Advancement of Computational Methods for Tunnelling and Underground Construction

Lead Guest Editor: Pengjiao Jia
Guest Editors: Jianyong Han, Yang Chen, and Yanqing Su

Advancement of Computational Methods for Tunnelling and Underground Construction

Advancement of Computational Methods for Tunnelling and Underground Construction

Lead Guest Editor: Pengjiao Jia
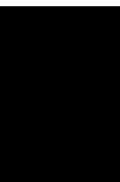Guest Editors: Jianyong Han, Yang Chen, and Yanqing Su

Zhaofei Chu, China
Wonseok Chung, Republic of Korea
Donato Ciampa, Italy
Gian Paolo Cimellaro, Italy
Francesco Colangelo, Italy
Romulus Costache, Romania
Liviu-Adrian Cotfas, Romania
Antonio Maria D'Altri, Italy
Bruno Dal Lago, Italy
Amos Darko, Hong Kong
Arka Jyoti Das, India
Dario De Domenico, Italy
Gianmarco De Felice, Italy
Stefano De Miranda, Italy
Maria T. De Risi, Italy
Tayfun Dede, Turkey
Sadik O. Degertekin, Turkey
Camelia Delcea, Romania
Cristoforo Demartino, China
Giuseppe Di Filippo, Italy
Luigi Di Sarno, Italy
Fabio Di Trapani, Italy
Aboelkasim Diab, Egypt
Thi My Dung Do, Vietnam
Giulio Dondi, Italy
Jiangfeng Dong, China
Chao Dou, China
Mario D'Aniello, Italy
Jingtao Du, China
Ahmed Elghazouli, United Kingdom
Francesco Fabbrocino, Italy
Flora Faleschini, Italy
Dingqiang Fan, Hong Kong
Xueping Fan, China
Qian Fang, China
Salar Farahmand-Tabar, Iran
Ilenia Farina, Italy
Roberto Fedele, Italy
Guang-Liang Feng, China
Luigi Fenu, Italy
Tiago Ferreira, Portugal
Marco Filippo Ferrotto, Italy
Antonio Formisano, Italy
Guoyang Fu, Australia
Stefano Galassi, Italy

Junfeng Gao, China
Meng Gao, China
Giovanni Garcea, Italy
Enrique García-Macías, Spain
Emilio García-Taengua, United Kingdom
DongDong Ge, USA
Khaled Ghaedi, Malaysia
Khaled Ghaedi, Malaysia
Gian Felice Giaccu, Italy
Agathoklis Giaralis, United Kingdom
Ravindran Gobinath, India
Rodrigo Gonçalves, Portugal
Peilin Gong, China
Belén González-Fonteboa, Spain
Salvatore Grasso, Italy
Fan Gu, USA
Erhan Güneyisi, Turkey
Esra Mete Güneyisi, Turkey
Pingye Guo, China
Ankit Gupta, India
Federico Gusella, Italy
Kemal Hacıefendioğlu, Turkey
Jianyong Han, China
Song Han, China
Asad Hanif, Macau
Hadi Hasanzadehshooiili, Canada
Mostafa Fahmi Hassanein, Egypt
Amir Ahmad Hedayat, Iran
Khandaker Hossain, Canada
Zahid Hossain, USA
Chao Hou, China
Biao Hu, China
Jiang Hu, China
Xiaodong Hu, China
Lei Huang, China
Cun Hui, China
Bon-Gang Hwang, Singapore
Jijo James, India
Abbas Fadhil Jasim, Iraq
Ahad Javanmardi, China
Krishnan Prabhakan Jaya, India
Dong-Sheng Jeng, Australia
Han-Yong Jeon, Republic of Korea
Pengjiao Jia, China
Shaohua Jiang, China

Chayut Ngamkhanong (iD), Thailand
Trung Ngo, Australia
Tengfei Nian, China
Mehdi Nikoo (iD), Canada
Youjun Ning (iD), China
Olugbenga Timo Oladinrin (iD), United
Kingdom
Oladimeji Benedict Olalusi, South Africa
Timothy O. Olawumi (iD), Hong Kong
Alejandro Orfila (iD), Spain
Maurizio Orlando (iD), Italy
Siti Aminah Osman, Malaysia
Walid Oueslati (iD), Tunisia
SUVASH PAUL (iD), Bangladesh
John-Paris Pantouvakis (iD), Greece
Fabrizio Paolacci (iD), Italy
Giuseppina Pappalardo (iD), Italy
Fulvio Parisi (iD), Italy
Dimitrios G. Pavlou (iD), Norway
Daniele Pellegrini (iD), Italy
Gatheeshgar Perampalam (iD), United
Kingdom
Daniele Perrone (iD), Italy
Giuseppe Piccardo (iD), Italy
Vagelis Plevris (iD), Qatar
Andrea Pranno (iD), Italy
Adolfo Preciado (iD), Mexico
Chongchong Qi (iD), China
Yu Qian, USA
Ying Qin (iD), China
Giuseppe Quaranta (iD), Italy
Krishanu ROY (iD), New Zealand
Vlastimir Radonjanin, Serbia
Carlo Rainieri (iD), Italy
Rahul V. Ralegaonkar, India
Raizal Saifulnaz Muhammad Rashid,
Malaysia
Alessandro Rasulo (iD), Italy
Chonghong Ren (iD), China
Qing-Xin Ren, China
Dimitris Rizos (iD), USA
Geoffrey W. Rodgers (iD), New Zealand
Pier Paolo Rossi, Italy
Nicola Ruggieri (iD), Italy
JUNLONG SHANG, Singapore

Nikhil Saboo, India
Anna Saetta, Italy
Juan Sagaseta (iD), United Kingdom
Timo Saksala, Finland
Mostafa Salari, Canada
Ginevra Salerno (iD), Italy
Evangelos J. Sapountzakis (iD), Greece
Vassilis Sarhosis (iD), United Kingdom
Navaratnarajah Sathiparan (iD), Sri Lanka
Fabrizio Scozzese (iD), Italy
Halil Sezen (iD), USA
Payam Shafigh (iD), Malaysia
M. Shahria Alam, Canada
Yi Shan, China
Hussein Sharaf, Iraq
Mostafa Sharifzadeh, Australia
Sanjay Kumar Shukla, Australia
Amir Si Larbi (iD), France
Okan Sirin (iD), Qatar
Piotr Smarzewski (iD), Poland
Francesca Sollecito (iD), Italy
Rui Song (iD), China
Tian-Yi Song, Australia
Flavio Stochino (iD), Italy
Mayank Sukhija (iD), USA
Piti Sukontasukkul (iD), Thailand
Jianping Sun, Singapore
Xiao Sun (iD), China
T. Tafsirojjaman (iD), Australia
Fujiao Tang (iD), China
Patrick W.C. Tang (iD), Australia
Zhi Cheng Tang (iD), China
Weerachart Tangchirapat (iD), Thailand
Xiaxin Tao, China
Piergiorgio Tataranni (iD), Italy
Elisabete Teixeira (iD), Portugal
Jorge Iván Tobón (iD), Colombia
Jing-Zhong Tong, China
Francesco Trentadue (iD), Italy
Antonello Troncone, Italy
Majbah Uddin (iD), USA
Tariq Umar (iD), United Kingdom
Muahmmad Usman, United Kingdom
Muhammad Usman (iD), Pakistan
Mucteba Uysal (iD), Turkey

Ilaria Venanzi ID, Italy
Castorina S. Vieira ID, Portugal
Valeria Vignali ID, Italy
Claudia Vitone ID, Italy
Liwei WEN ID, China
Chunfeng Wan ID, China
Hua-Ping Wan, China
Roman Wan-Wendner ID, Austria
Chaohui Wang ID, China
Hao Wang ID, USA
Shiming Wang ID, China
Wayne Yu Wang ID, United Kingdom
Wen-Da Wang, China
Xing Wang ID, China
Xiuling Wang ID, China
Zhenjun Wang ID, China
Xin-Jiang Wei ID, China
Tao Wen ID, China
Weiping Wen ID, China
Lei Weng ID, China
Chao Wu ID, United Kingdom
Jiangyu Wu, China
Wangjie Wu ID, China
Wenbing Wu ID, China
Zhixing Xiao, China
Gang Xu, China
Jian Xu ID, China
Panpan ID, China
Rongchao Xu ID, China
HE YONGLIANG, China
Michael Yam, Hong Kong
Hailu Yang ID, China
Xu-Xu Yang ID, China
Hui Yao ID, China
Xinyu Ye ID, China
Zhoujing Ye , China
Gürol Yildirim ID, Turkey
Dawei Yin ID, China
Doo-Yeol Yoo ID, Republic of Korea
Zhanping You ID, USA
Afshar A. Yousefi ID, Iran
Xinbao Yu ID, USA
Dongdong Yuan ID, China
Geun Y. Yun ID, Republic of Korea

Hyun-Do Yun ID, Republic of Korea
Cemal YİĞİT ID, Turkey
Paolo Zampieri, Italy
Giulio Zani ID, Italy
Mariano Angelo Zanini ID, Italy
Zhixiong Zeng ID, Hong Kong
Mustafa Zeybek, Turkey
Henglong Zhang ID, China
Jiupeng Zhang, China
Tingting Zhang ID, China
Zengping Zhang, China
Zetian Zhang ID, China
Zhigang Zhang ID, China
Zhipeng Zhao ID, Japan
Jun Zhao ID, China
Annan Zhou ID, Australia
Jia-wen Zhou ID, China
Hai-Tao Zhu ID, China
Peng Zhu ID, China
QuanJie Zhu ID, China
Wenjun Zhu ID, China
Marco Zucca, Italy
Haoran Zuo, Australia
Junqing Zuo ID, China
Robert Černý ID, Czech Republic
Süleyman İpek ID, Turkey

Contents

Contents

Research Article

Seismic Response Analysis of Secondary Lining Polymer Grouting Debonding Repair for Tunnel Construction Based on Parameter Inversion

Fengyang Miao [ID],[1] Chunyu Liang [ID],[2] Weiguo Li [ID],[3] Zhengxuan Huang [ID],[4] Jianguo Xu [ID],[1] Yingchun Cai [ID],[1] Xiaoyu Feng [ID],[3] and Yiming Xu [ID][5]

[1]*College of Water Conservancy Science and Engineering, Zhengzhou University, Zhengzhou 450000, China*
[2]*Yellow River Engineering Consulting Co Ltd, Zhengzhou 450003, China*
[3]*Henan Highway Engineering Bureau Group Co Ltd, Zhengzhou 450052, China*
[4]*Hefei Gotion High-Tech Power Energy Co Ltd, Hefei 230000, China*
[5]*Sippr Engineering Group Co Ltd, Zhengzhou 450003, China*

Correspondence should be addressed to Jianguo Xu; jianguoxu@zzu.edu.cn

The void phenomenon behind the tunnel lining has become the main cause of tunnel disease, easily triggering tunnel lining structure damage, shedding, water seepage, and other diseases that seriously threaten the normal operation of the tunnel. The void area behind the lining seriously reduces the seismic capacity of the tunnel. In this paper, the mechanical parameters of the surrounding rock are calculated by optimizing the inversion of the improved system identification sensitivity analysis method, and the numerical model of the tunnel's dynamic response is optimized using the improved inversion results to study the repair effect and seismic capacity of the Longmenshan tunnel using polymer grouting to repair the void area behind the lining under the action of a seismic load. The results show that the displacement and stress at the top of the tunnel secondary lining void area are significantly reduced and close to normal after the repair of polymer grouting; however, the stress and displacement at the top of the secondary lining are significantly different under the action of seismic waves at the same peak at different site conditions, which indicates that the dynamic response of this tunnel model has obvious sensitivity to the seismic wave spectrum.

1. Introduction

Over the past few decades, there have been many reports of varying degrees of tunnel damage caused by earthquakes, such as the Tokachi-Oki (Japan) earthquake in 1952, the Tonghai (China) earthquake in 1970, the Chi-Chi (Taiwan, China) earthquake in 1999, the Niigataken-Chetu (Japan) earthquake in 2004, the Wenchuan (China) earthquake in 2008, and the Kumamoto (Japan) earthquake in 2016 [1]. Scholars such as Ye et al. [2–5] found that voids behind the lining are common in tunnels and have become the main cause of tunnel disease. Xin et al. studied the seismic response and damage patterns of tunnels with/without voids behind the linings by shaking table tests [6]. Yasuda et al. studied the seismic response of cylindrical tunnels with void areas under 3D earthquakes, and the results showed that the large stress concentration on the lining caused by voids under the action of the earthquake resulted in the destruction of the tunnel [7]. Min et al. studied the effect of voids behind linings on the cracking performance of asymmetric double-arch tunnels, and the results show that due to the influence of the void area, the cracking of the tunnel area opposite the void area is more serious [8]. The research of the above scholars shows that the void area behind the tunnel lining seriously reduces the seismic performance of the tunnel, the lining in the void area

generates tensile stresses under seismic action, and the surrounding rock around the void area deforms severely in plasticity, leading to rockfall impacting the lining and serious lining damage.

The demolition and reconstruction method, backfill grouting method, and shotcrete concrete combined with the steel arch reinforcement method are often used to repair and fill void areas [9]. Jinlong et al. used secondary grouting to repair the void area of the tunnel. During the secondary grouting process, it was found that higher grouting pressure, a larger grout amount, and improper grouting position would lead to cracks in the tunnel [10]. In order to solve the problem of tunnel disease caused by cracks in the tunnel lining, Zhou et al. adopted the plate-short bolt assembly structure to reinforce the tunnel cracks [11]. Han et al. explored the reinforcement effect of the fiber-reinforced plastic (FRP)-polymer cement mortar (PCM) method on the void area of the tunnel [12]. Liu et al. used crack grouting, shotcrete support, and reconstruction of the secondary lining to repair the damaged lining [13]. However, due to the inherent defects of concrete, which limit the effect of tunnel disease management, many scholars have applied polymer grouting technology to tunneling projects in view of the advantages of early strength, lightweight, and good durability of polymer materials [14, 15]. At present, the research in this field mainly focuses on the rapid repair of buried pipeline leakage and settlement, railway track settlement, and pavement voids and collapse. Wang et al. repaired the void under the pipeline with polymer, and the results showed that polymer grouting can effectively restore the strength and resilience of the pipeline to its normal state [16, 17]. Li et al. developed an innovative trenchless concrete pipeline corrosion and void defect pretreatment technology called membrane bag pile polymer grouting pretreatment (MBP-PGP) technology, which can be used for pipeline corrosion and voiding repair [18]. Fang et al. showed through experiments that polymers can effectively repair the settlement of high-speed railways and provide sufficient long-term durability under dynamic train loads [19, 20]. The research of Li et al. shows that high polymer can effectively repair cracks and voids in pavement and effectively prevent pavement settlement [21, 22]. The polymer grouting material can sufficiently and densely fill the damaged area, thereby controlling the unfavorable deformation and better restoring the structural integrity. Therefore, the combination of polymer grouting repair technology and tunnel nondestructive testing can quickly find and repair tunnel disaster problems.

The abovementioned study did not investigate the effect of the seismic response of the tunnel after polymer grouting repair. This paper takes the Longmenshan tunnel project as an example. In order to simulate the Longmenshan tunnel more precisely, this paper deduces the inversion formula of the three-dimensional parameters of the physical mechanics of the surrounding rock of the tunnel based on the basic theory of system identification and improves the inversion method with the help of numerical simulation software. The improved inversion results are used to optimize the mechanical parameters of the surrounding rock of the tunnel and then study the repair effect and seismic capacity of the Longmenshan tunnel using polymer grouting to repair the void area behind the lining under the action of an earthquake load so as to provide the tunnel void space. Polymer grouting repair provides a theoretical basis.

2. Project Overview

Longmenshan Mountain tunnel is located at the junction of Tangchi town of Liuan city and Daguan town of Tongcheng city, Anhui province, China. It is a detached tunnel, buried at a depth of 50 m−300 m, with starting pile number K81 + 834 (ZK81 + 830) and ending pile number K84 + 47 (ZK84 + 450), a total length of 2644 (2620 m). The surrounding rock grade of the tunnel is mainly III, IV, and V grades surrounding rock, where III and IV grades surrounding rock is mainly medium weathered granite, and V grade surrounding rock is mainly full weathered granite.

2.1. Tunnel Construction Monitoring and Measurement. As is shown in Figure 1, the measurement items of the Longmenshan tunnel include surface subsidence observation, vault subsidence observation, and peripheral convergence measurement. As shown in the arch settlement diagram (Figure 2) of the K83 + 020 void section of the Longmenshan tunnel, the surrounding rock basically reached a stable state after 40 days, the accumulated settlement value was kept below 10 mm, and the development trend of the arch settlement curve was approximately a logarithmic function curve, which was finally kept at 9.4 mm. As is shown in Figure 3. The settlement rate of the vault also tended to decrease slowly on the whole, and after 40 days, the settlement rate remained relatively stable, between 0.1 mm/d and 0 mm/d. The maximum settlement rate was 0.6 mm/d on day 5, which occurred during the excavation of the lower step. Due to the relatively short duration of the maximum change in the settlement rate, it would not have much impact on the overall stability and safety of the tunnel excavation process. Overall, the vault deformation of this section is in a reasonable range at all stages; no abnormality is seen, the surrounding rock is basically stable, and the excavation method is reasonable.

As is shown in Figure 4, analysis of the convergence deformation data around the K83 + 020 void section of the Longmenshan tunnel right line shows that the accumulated peripheral convergence value of this section is smaller than the arch settlement value, and the regularity of its deformation process is more scattered than that of the arch deformation, and the result still tends to convergence. As is shown in Figure 5, analysis of the convergence deformation data around the K83 + 020 void section of the Longmenshan tunnel right line shows that during the whole process of convergence deformation, the convergence rate is higher in the first period, the peak reaches 0.4 mm/d, the duration is still short, and then drops sharply, the convergence rate is stabilized between 0.3 mm/d and 0.1 mm/d, the phenomenon of negative growth of convergence deformation appears in the 25th day, and there is no obvious sign of damage to the
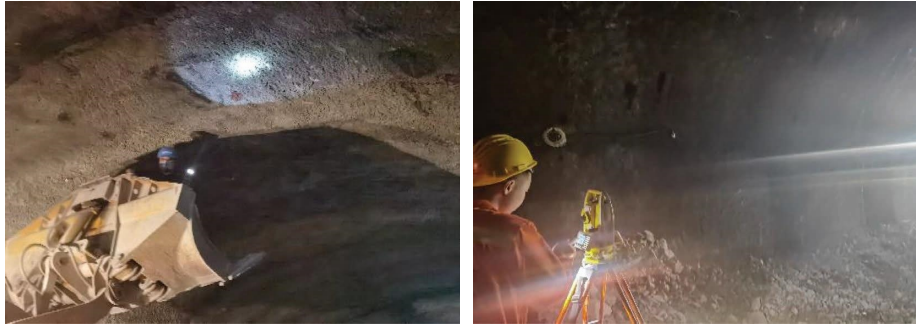
Figure 1: LongmenShan tunnel right line K83 + 020 void cross-section monitoring and measurement data.
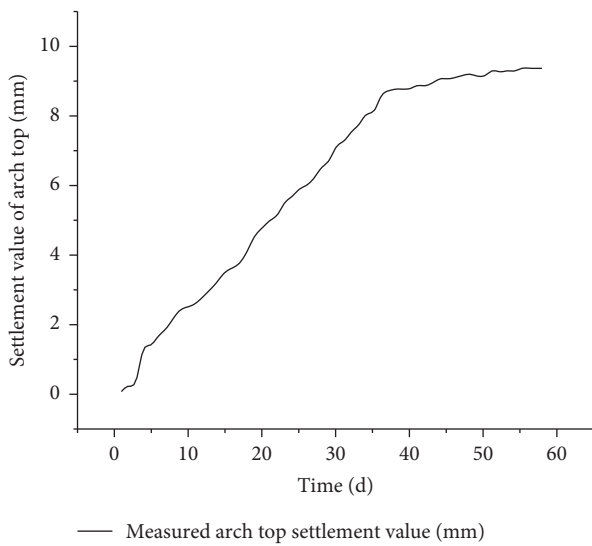
Figure 2: Settlement curve of K83 + 020 void section vault.
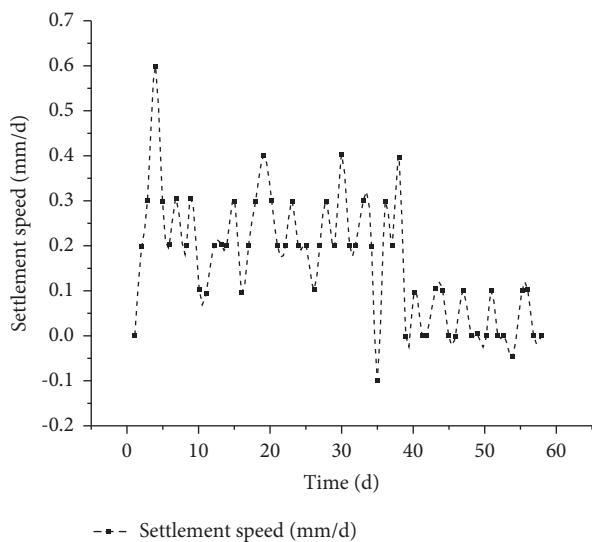
Figure 3: Settlement rate curve of K83 + 020 void section vault.

cave body in this process. After the 40th day, the convergence value of the cave body was kept at about 7 mm, and it could be affirmed as basic convergence when it reached

7.3 mm. The convergence rate was stabilized within 0.1 mm/d at the end, and the cave was basically stable without any abnormalities.

3. Numerical Simulation of Tunnel Excavation

3.1. Tunnel Excavation Process Simulation. Numerical simulation object for Longmenshan tunnel right line K83 + 010~K83 + 90 section, excavation length 80 m, tunnel burial depth of about 100~110 m, the terrain is relatively gentle, the section is IV grade surrounding rock, rock type for the medium weathering granite, the tunnel using the up-and-down step method of boring. The tunnel is excavated by the up-and-down step method. The inner contour of the main tunnel of the tunnel is a three-centered circle with diameters of 10.5 m, 12.8 m, and 10.5 m, respectively. The total height of the main tunnel is 7.45 m, and the total width is 11.93 m. For the creation of soil, according to Saint-Venant's principle, the stress redistribution caused by excavation is only within the range of 3–5 times the excavation width from the cavern, and will not cause too much impact on other areas. Therefore, the left and right boundaries of the model are three times the diameter of the tunnel, and the width is 100 m. The lower boundary is 3.5 times the diameter of the hole. According to the real terrain, the height is selected to be 150–160 m. The height of the tunnel from the bottom of the soil is 50 m, and the buried depth is 100–110 m. Combined with the tunnel ground investigation report, the soil model adopts the Mohr–Coulomb model in the elastoplastic principal model. The physical parameters of the soil are its density of 1.8 g/cm^3, modulus of elasticity of 2.6 GPa, Poisson's ratio of 0.32, friction angle of 34°, and cohesion of 0.5 MPa. The overrun support structure of the tunnel is a Φ25 mm overrun hollow grouting anchor with a density of 7.8 g/cm^3, a modulus of elasticity of 200 GPa, and Poisson's ratio of 0.2. The lining is made of C25 plain waterproof concrete; the density is 2.4 g/cm^3, the elastic modulus is 20 GPa, and Poisson's ratio is 0.2. The inverted arch and the secondary lining are made of C30 concrete with a density of 2.5 g/cm^3 and an elastic modulus of 25 GPa and Poisson's ratio of 0.2. The lining and the surrounding rock are bound together by tie constraints. Normal constraints were applied to the front, back, left, and right boundaries of the tunnel model, with the bottom boundary being fully constrained and the upper boundary being free. The vertical
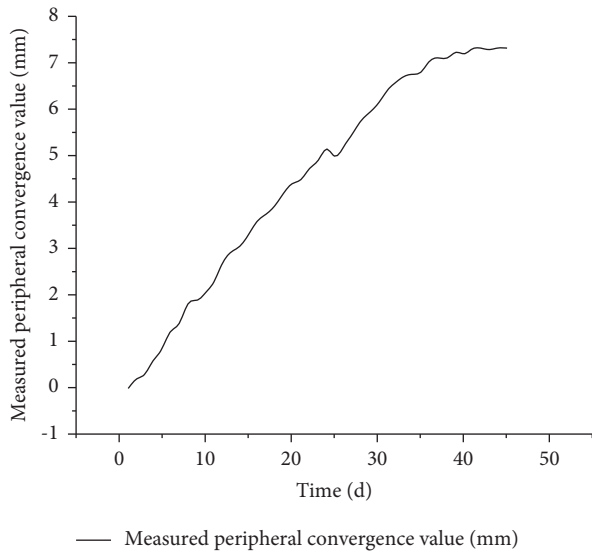
FIGURE 4: Peripheral convergence curve of K83 + 020 void section.
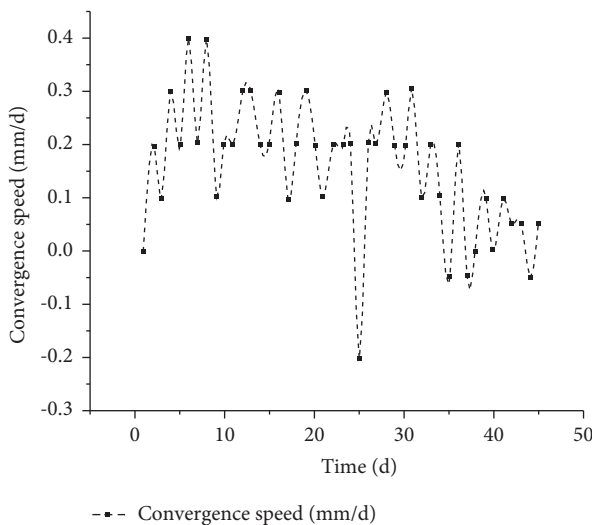
FIGURE 5: Peripheral convergence rate curve of K83 + 020 void section.

downward gravity load acts on the whole model. The overall meshing of the tunnel model is sparse in the overall soil and dense in the boundary of the tunnel. The neutral axis algorithm is used. The element type of the anchor is the truss and the total number of mesh elements is 126,600. The tunnel model of the lattice is shown in Figure 6.

3.2. Analysis of Results.
It can be seen from Figure 7 that the top of the arch is the maximum vertical displacement of the primary support structure, which reaches 6.267 mm. The maximum lateral displacement of 2.456 mm occurred in the arch waist area, while the measured settlement value of the arch top and the convergence value around the target section were 9.4 mm and 7.3 mm, respectively, with a large difference of 3.133 mm in the accumulated vault settlement value and 2.31 mm in the accumulated convergence value. To

better verify the accuracy of the numerical model, the vertical displacement at monitoring point 1 of the liner and the summation of the transverse displacement at monitoring points 2 and 3 were extracted (the locations of the points taken are shown in Figure 8), plotted as curves, and analyzed to compare the deformation trend of the measured vault subsidence value and the peripheral convergence value of the section where the liner is located.

As shown in Figure 9, a comparison of the analysis of the settlement values of the vault (the vertical displacement value at monitoring point 1) of void section K83 + 020, the peripheral convergence values (the sum of the lateral displacement values at monitoring points 2 and 3), and the calculated values of the model simulation reveals that the analysis results obtained also differ from the real situation due to the difference between the selected soil mechanical parameters and the real surrounding rock mechanical parameters. However, the theoretical analysis of the change in the initial lining displacement during the numerical simulation of tunnel excavation is consistent with the deformation law of the real tunnel excavation process, indicating that the numerical simulation of the Longmenshan Mountain tunnel excavation process is consistent with the real excavation process and the difference in stress and strain is caused by the unreasonable setting of the mechanical parameters of the tunnel surrounding rock during the simulation process, which can be analyzed by the inversion of the surrounding rock mechanical parameters to obtain The inversion analysis of the mechanical parameters of the surrounding rock can be used to obtain the mechanical parameters of the surrounding rock that are close to the real situation.

4. Inversion Analysis of Tunnel Envelope Mechanical Parameters

4.1. 3D Mechanical Parameter Inversion Analysis of Surrounding Rock. Some scholars [23–29] have already applied the system identification sensitivity analysis method in the inverse calculation of layered pavement structure, foundation excavation deformation analysis, and asphalt pavement aging inversion analysis, but at present, the system identification sensitivity analysis method is mainly applied to the inversion of two-dimensional parameters of tunnel envelope, and less tunnel monitoring data are used in the inversion analysis. In this paper, based on the forward model established for the Longmenshen Mountain tunnel as the Mohr–Coulomb 3D numerical model, a system identification method is introduced in the field of 3D parameter inversion analysis of the tunnel envelope. As shown in Figure 10, the three parameters of static elastic modulus, Poisson's ratio, and internal friction angle of the surrounding rock are calculated by inversion based on the measured peripheral convergence value S_1', vault settlement value S_2', and vault settlement value S_3' of the measured section of a tunnel, which can realize the high-precision and efficient automation of the model parameter adjustment process, and the basic process is as follows:
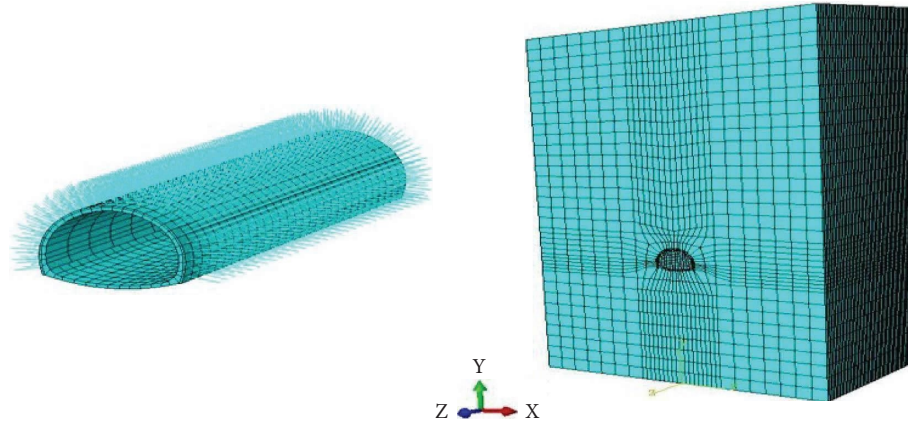
FIGURE 6: Tunnel model.
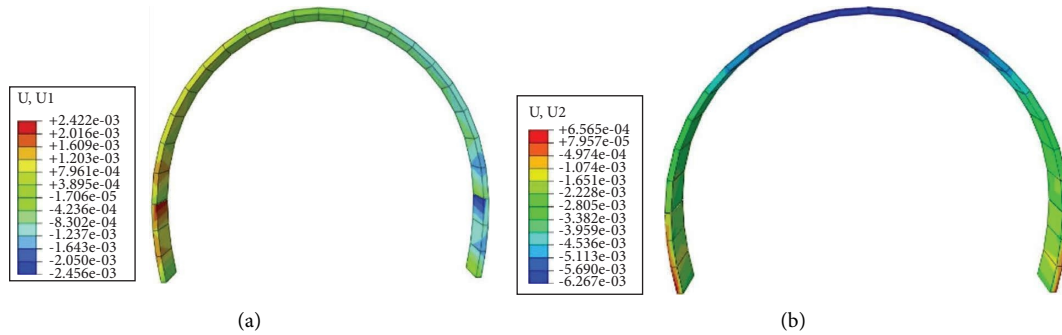
FIGURE 7: LongMianShan tunnel right line K83 + 020 section initial lining, transverse displacement cloud map, and vertical displacement cloud map: (a) a transverse displacement cloud map of the initial lining when the surrounding rock is stable; (b) a vertical displacement cloud map of the initial lining when the surrounding rock is stable.
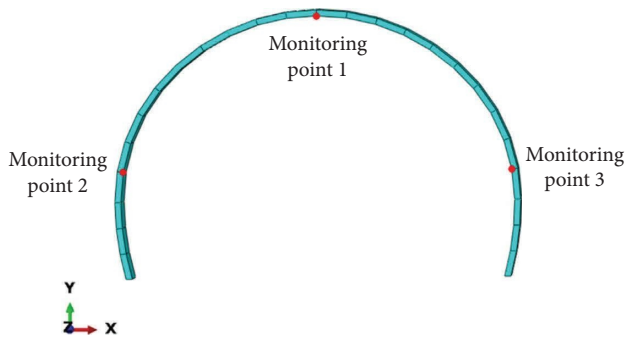
FIGURE 8: Location of the target section's primary lining monitoring points in the tunnel model.

(1) Setting the initial surrounding rock mechanical parameters

The initial internal friction angle φ_0, the modulus of elasticity E_0, and the initial Poisson's ratio μ_0 are assumed. φ_0, E_0, and μ_0 are input into the finite element forward model to calculate the displacement values of the section corresponding to the measured values

$$\{s\} = \begin{bmatrix} s_1 & s_2 & s_3 \end{bmatrix}^T. \qquad (1)$$

(2) Comparing the calculated value $\{s\}$ with the measured value $\{s'\}$

If the absolute value of the difference between the calculated value and the measured value is small, that is, the calculated result meets the requirements, take $\max\left\{\{\Delta s\}^T\{\Delta s\}\right\} \leq e$ (e is the calculation accuracy), immediately terminate the inverse analysis calculation, at this time the model elastic modulus E, Poisson's ratio μ and internal friction angle φ is the actual surrounding rock material static elastic modulus E_s, Poisson's ratio μ and internal friction angle φ.

(3) Establishing the sensitivity matrix

Using the forward difference method to build the sensitivity matrix, we find the calculated values $\{s(E_0, \mu_0, \varphi_0)\}$ for the initial elastic modulus E_0, initial Poisson's ratio μ_0, and initial internal friction angle φ_0; then we find $\{s(E_0 + \Delta E, \mu_0, \varphi_0)\}$ for the elastic modulus $E_0 + \Delta E$, Poisson's ratio μ_0, and internal friction angle φ_0; then we find $\{s(E_0, \mu_0 + \Delta \mu, \varphi_0)\}$; for the elastic modulus is E_0, the internal friction angle φ_0, and Poisson's ratio is $\mu_0 + \Delta \mu$; then find the $\{s(E_0, \mu_0, \varphi_0 + \Delta \varphi)\}$ when the modulus of elasticity E_0 Poisson's ratio μ_0 is constant, and the internal friction angle is $\varphi_0 + \Delta \varphi$ by taking $\Delta E = 1\%E$, $\Delta E = \Delta \mu = 1\%\mu$, and $\Delta \varphi = 1\%\varphi$ thus getting

(a)

(b)
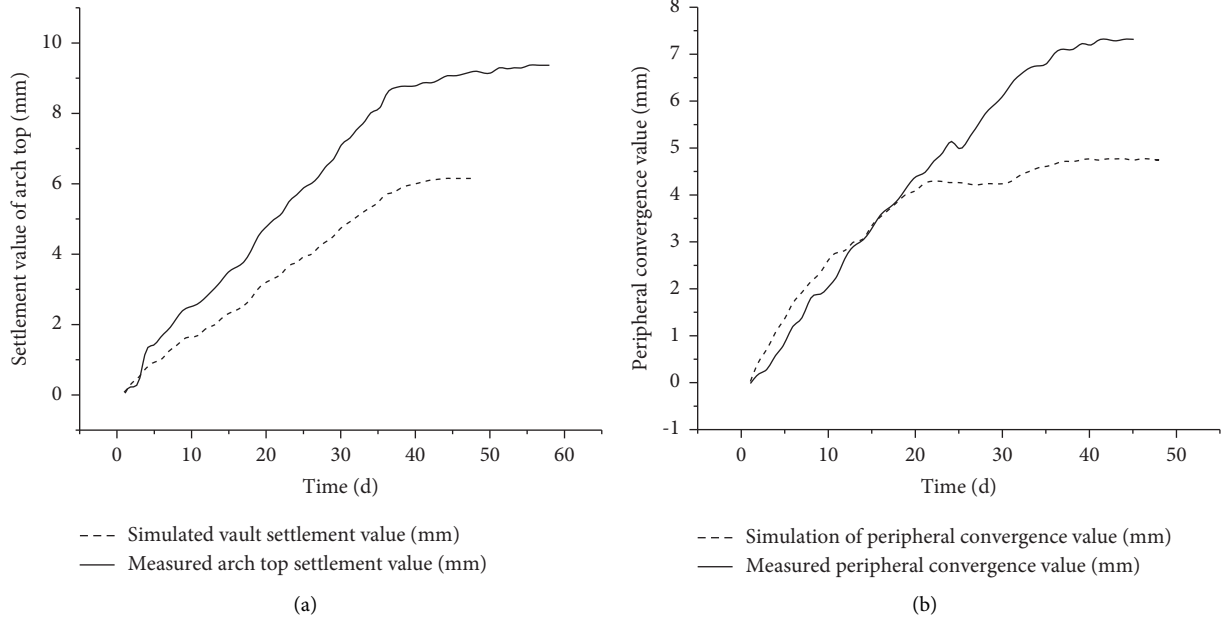
FIGURE 9: Comparison of measured and simulated values of vault settlement and peripheral convergence at void section K83 + 020: (a) comparison between measured and simulated values of vault settlement (monitoring point 1); (b) comparison between measured and simulated values of peripheral convergence (monitoring points 2 and 3).

$$
\begin{cases}
\dfrac{\partial s_1}{\partial E} = \dfrac{s_1\left(E_0 + \Delta E, \mu_0, \varphi_0\right) - s_1\left(E_0, \mu_0, \varphi_0\right)}{\Delta E}, \\[2mm]
\dfrac{\partial s_1}{\partial \mu} = \dfrac{s_1\left(E_0, \mu_0 + \Delta \mu, \varphi_0\right) - s_1\left(E_0, \mu_0, \varphi_0\right)}{\Delta \mu}, \\[2mm]
\dfrac{\partial s_1}{\partial \omega} = \dfrac{s_1\left(E_0, \mu_0, \varphi_0 + \Delta \varphi\right) - s_1\left(E_0, \mu_0, \varphi_0\right)}{\Delta \varphi}, \\[2mm]
\dfrac{\partial s_2}{\partial E} = \dfrac{s_2\left(E_0 + \Delta E, \mu_0, \varphi_0\right) - s_2\left(E_0, \mu_0, \varphi_0\right)}{\Delta E}, \\[2mm]
\dfrac{\partial s_2}{\partial \mu} = \dfrac{s_2\left(E_0, \mu_0 + \Delta \mu, \varphi_0\right) - s_2\left(E_0, \mu_0, \varphi_0\right)}{\Delta \mu}, \\[2mm]
\dfrac{\partial s_2}{\partial \omega} = \dfrac{s_2\left(E_0, \mu_0, \varphi_0 + \Delta \varphi\right) - s_2\left(E_0, \mu_0, \varphi_0\right)}{\Delta \varphi}, \\[2mm]
\dfrac{\partial s_3}{\partial E} = \dfrac{s_3\left(E_0 + \Delta E, \mu_0, \varphi_0\right) - s_3\left(E_0, \mu_0, \varphi_0\right)}{\Delta E}, \\[2mm]
\dfrac{\partial s_3}{\partial \mu} = \dfrac{s_3\left(E_0, \mu_0 + \Delta \mu, \varphi_0\right) - s_3\left(E_0, \mu_0, \varphi_0\right)}{\Delta \mu}, \\[2mm]
\dfrac{\partial s_3}{\partial \omega} = \dfrac{s_3\left(E_0, \mu_0, \varphi_0 + \Delta \varphi\right) - s_3\left(E_0, \mu_0, \varphi_0\right)}{\Delta \varphi}.
\end{cases}
\tag{2}
$$

(4) Calculating the parameter adjustment vector $\{\Delta x\}$

Calculating the difference $\{\Delta s\} = \{s\} - \left\{s'\right\}$ $= \begin{Bmatrix} s_1 - S_1' \\ s_2 - S_2' \\ s_3 - S_3' \end{Bmatrix}$ between the measured values and the calculated values under the initial modulus of elasticity E_0, the initial Poisson's ratio μ_0, and the initial angle of internal friction φ_0. Then, construct the sensitivity equation

$$
\{\Delta s\} = D\{\Delta x\},
\tag{3}
$$

where the sensitivity matrix $D = \begin{bmatrix} \partial s_1/\partial E & \partial s_1/\partial \mu & \partial s_1/\partial \varphi \\ \partial s_2/\partial E & \partial s_2/\partial \mu & \partial s_2/\partial \varphi \\ \partial s_3/\partial E & \partial s_3/\partial \mu & \partial s_3/\partial \varphi \end{bmatrix}$ and the parameter adjustment vector $\{\Delta x\} = \begin{bmatrix} \Delta E \\ \Delta \mu \\ \Delta \varphi \end{bmatrix}$.

The difference $\{\Delta s\}$ between the measured values and the calculated values under the initial elastic modulus E_0, the initial Poisson's ratio μ_0, the initial internal friction angle φ_0, and the sensitivity matrix D is input to the prepared numerical analysis program, which will calculate the parameter adjustment vector $\{\Delta x\}$.

(5) Performing the first iteration

Establishing the following equation:

$$
\begin{cases}
E_1 = E_0 + \Delta E, \\
\mu_1 = \mu_0 + \Delta \mu, \\
\varphi_1 = \varphi_0 + \Delta \varphi.
\end{cases}
\tag{4}
$$
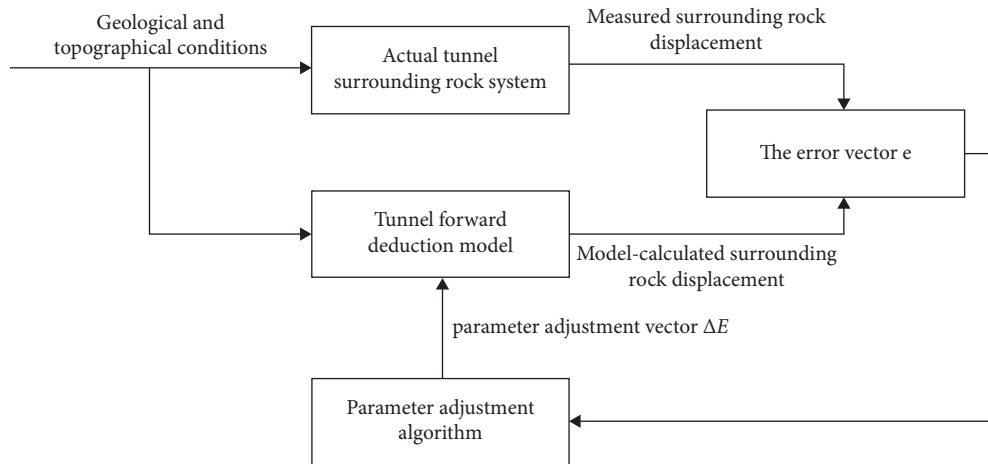
FIGURE 10: The basic process of identification of tunnel envelope parameter inverse calculation system.

Finding the calculated values ${s}^{(1)} = \left\{ s(E_1, \mu_1, \varphi_1) \right\}^{(1)}$ under the modulus of elasticity E_1, Poisson's ratio μ_1, and the angle of internal friction φ_1, with the upper mark "(1)" representing the first parameter adjustment, and then go back to step 2 until the requirements are met.

4.2. Inversion of Mechanical Parameters of Longmenshan Tunnel Enclosure. After several parameter adjustments, assuming that the initial mechanical properties of the surrounding rock parameters $E_0 = 2.0$ GPa, $\mu_0 = 0.32$, $\varphi_0 = 32°$, the inversion calculation is carried out according to the 3D mechanical parameters inversion method proposed in this paper, and four iterations are carried out to obtain $E = 1.82$ GPa, $\mu = 0.32$, $\varphi = 35°$, at which time the tunnel finite element model calculates the peripheral convergence value s_1 as 7.2554 mm, s_2 is 9.5317 mm, and s_3 is 8.8206 mm. According to the measured cumulative peripheral convergence value s_1' is 7.3224 mm, the measured cumulative vault settlement value s_2' is 9.4669 mm, and the measured cumulative vault settlement value s_3' is 8.7128 mm, it can be found that the simulated value is very close to the measured value as well. According to the model results, the measured results of the tunnel can be obtained, as shown in Table 1.

At this point $\{\Delta s^T\}\{\Delta s\} = 0.0466$ mm, satisfying the condition max $\max \left\{ \{\Delta s\}^T \{\Delta s\} \right\} \leq 1.0E - 5$m, the real surrounding rock mechanical parameters of the grade IV section of the Longmenshan tunnel numerically simulated are static elastic modulus $E_s = 1.82$ GPa, Poisson's ratio $\mu = 0.32$, and internal friction angle $\varphi = 35°$. Based on the system identification sensitivity analysis method for inversion to obtain the final surrounding rock parameters to establish the forward model, extract the simulated value of displacement change of its tunnel right line K83 + 020 section and the actual measurement to draw the fitting curve as shown in Figure 11.

Comparing the simulated and measured displacement variation curves of the target sections, it can be seen that the mechanical parameters obtained by applying the system identification sensitivity analysis method to the mechanical parameters of the tunnel envelope after displacement measurement inversion analysis and then substituting into the finite element model for the forward evolution have small error between the simulation results and the measured values. In each stage of tunnel construction, the error values of vault deformation and peripheral convergence of each target section in the numerical model and the actual monitoring and measurement results are small, within 0.3 mm. Through the inversion analysis of the Longmenshan tunnel, the actual surrounding rock parameters were reasonably determined for the section from K83 + 020 to K83 + 90, with a static elastic modulus $E_s = 1.82$ GPa, Poisson's ratio $\mu = 0.32$, and an internal friction angle $\varphi = 35°$. The results all meet the requirements of highway tunnel design specifications and prove the feasibility of the system identification sensitivity analysis method, which provides important application value for the real-time detection and evaluation of the tunnel under construction in Longmenshan Mountain and provides a basis for subsequent related scientific research.

5. Seismic Response Analysis of Tunnel Void Polymer Grouting Repair

5.1. Tunnel Void Inspection and Repair. In the right line of the Longmenshan tunnel section from K83 + 140 to K83 + 350, a geological radar method was used to inspect the quality of lining construction, and it was found that there was a void area with a maximum depth of 20 cm and a longitudinal length of about 2~3 m between the lining and the rock body at the top of the tunnel, as shown in Figures 12 and 13.

According to the data provided by radar, grouting repair of the void area, compared with concrete grouting material, has excellent antiseepage performance, compressive performance, tensile performance, and corrosion resistance. After the polymer repair material reaction, it can not only rapidly occur volume expansion (volume expansion 10~20 times), but also can automatically compact and reinforce the void area, and recompact and reinforce the structural disease area. More importantly, it is light in weight, high in construction efficiency, low in time cost, and high in economy, and the polymer material can reach 90% sufficient strength

TABLE 1: Tunnel section displacement change comparison table.

Construction stage	Lower step application initial lining		Palm surface advance 20 m		Palm surface advance 40 m		Pouring of second lining	
	Real measurement (mm)	Finite element model (mm)	Real measurement (mm)	Finite element model (mm)	Real measurement (mm)	Finite element model (mm)	Real measurement (mm)	Finite element model (mm)
Peripheral convergence (K83 + 020)	2.6	2.3	4.7	4.5	6.5	6.3	7.3	7.2
Vault settlement (K83 + 020)	2.8	2.5	5.2	5.5	7.5	7.6	9.4	9.5
Vault settlement (K83 + 040)	3.3	3	5.4	5.6	7.7	7.8	8.7	8.8

(a)

(b)

(c)
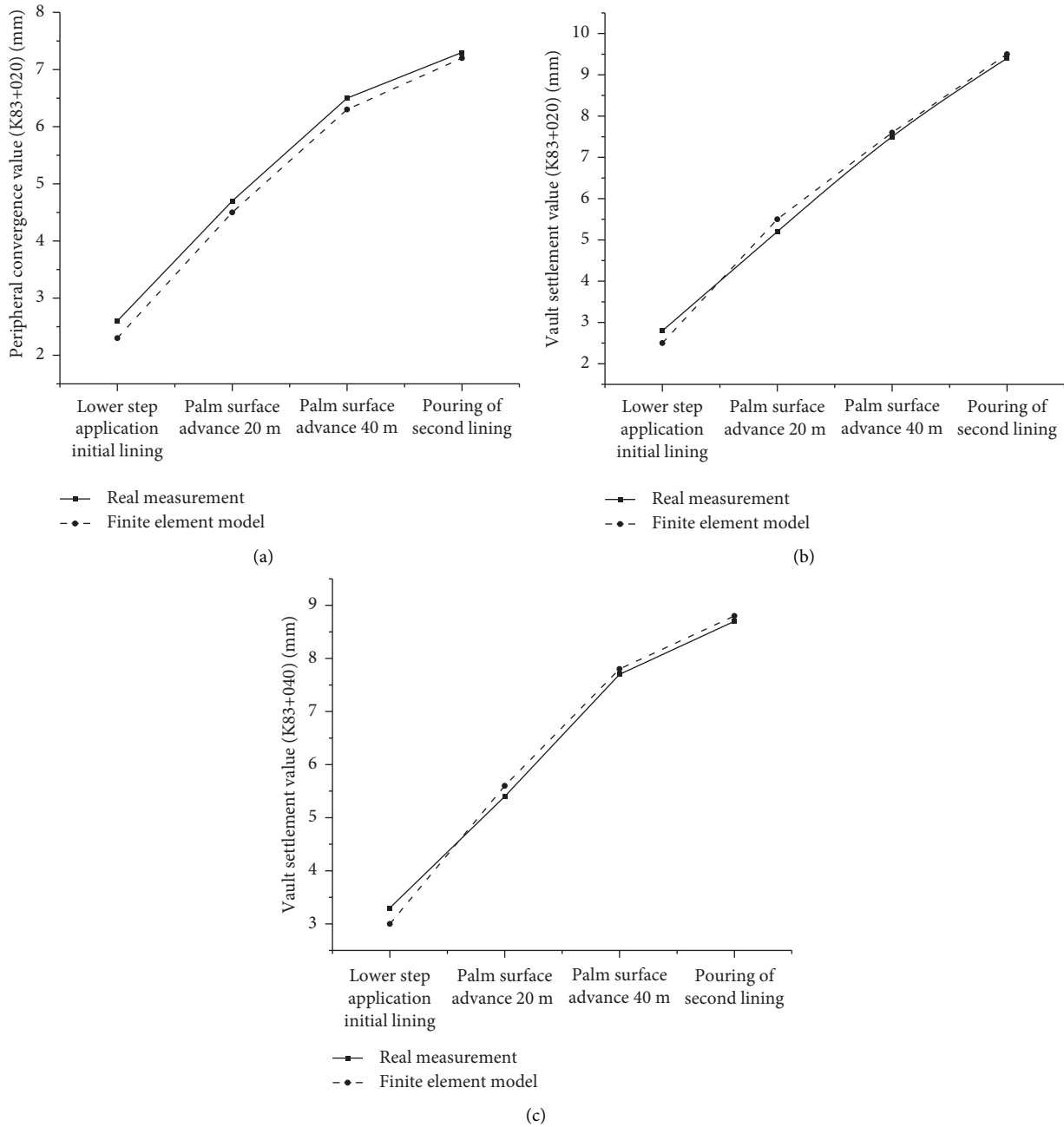
FIGURE 11: Comparison between simulated and measured values of arch top settlement in the target section of the tunnel: (a) K83 + 020 cross-sectional convergence around the simulated value and the measured value fitting curve; (b) K83 + 020 fitting curve between simulated and measured values of vault settlement; (c) K83 + 040 fitting curve between the simulated and measured values of vault settlement.

within 15 minutes after injection [16–20]. The grouting material used is a nonwater-reactive polymer. By comparing the radar detection spectra before and after the polymer grouting in Figure 14, it is found that the grouting effect in the void area behind the lining is good and that the integrity and compactness of the lining structure are significantly improved. To better verify the effect of polymer material for tunnel debonding repair, this paper carries out a comparative analysis of the seismic response before and after the tunnel polymer grouting repair under seismic action.

5.2. Numerical Model Creation. The numerical model was established based on the surrounding rock grade and tunnel burial depth of the Longmenshan tunnel section K83 + 140 to K83 + 350; the tunnel burial depth is 70 m the excavation depth is 160 m, and the tunnel debris area is located at the tunnel excavation depth of 80~83 m. The static modulus of elasticity $E_s = 1.82$ GPa, Poisson's ratio $\mu = 0.32$, internal friction angle $\varphi = 35°$, and the correlation between the static modulus of elasticity E_s and the dynamic modulus of elasticity E_d is considered according to the literature [30], which

Figure 12: Lining construction quality inspection site.

Figure 13: Void behind the lining.

results in the dynamic modulus of elasticity $E_d = 18.63$ GPa for the tunnel geotechnical body. The polymer material used for grouting is a nonwater-reactive polymer material with a density of 1.6 g/cm^3, an elastic modulus $E = 20.2$ MPa, and Poisson's ratio of $\mu = 0.3$. The model with a well-defined grid is shown in Figure 15. The seismic fortification standard of the Longmenshan tunnel is 0.1 g peak ground motion acceleration and 7-degree earthquake basic intensity. The three natural seismic waves selected for conducting seismic analysis are the Northridge wave (Class I site), the Taft wave (Class II site), and the EL-Centro wave (Class III site), which correspond to a peak acceleration of 0.1 g, a time interval of 0.02 s, and an effective duration of 19.2 s.

5.3. Analysis of the Seismic Mechanical Response of Tunnel and Grouting Repair

5.3.1. Displacement Analysis of Seismic Load Action. Since the debris area is located at the top of the tunnel, the vertical displacement and vertical acceleration at the top node of the secondary lining can visually reflect the improvement of the debris area by polymer grouting. It can be seen from Figures 16–19 that under the same earthquake, the displacement and acceleration time-history curves of the top of the secondary lining of the tunnel under normal, void, and polymer grouting repair conditions are basically the same. It can be seen that during the whole time course of vibration, the vertical displacement and vertical acceleration of the top of the secondary lining under normal conditions are the

smallest, and the vertical displacement and vertical acceleration are the largest when the top is void, which is significantly improved after grouting repair of the void area. Under each working condition of the Northridge wave action, the maximum vertical displacement at the top of the secondary lining under normal conditions, when the top is void, and after the void repair is 5.33 mm, 6.15 mm, and 5.68 mm, respectively, and the maximum vertical acceleration is 1.32 m/s^2, 1.56 m/s^2, and 1.43 m/s^2, respectively. Compared with the normal condition, the maximum vertical displacement at the top of the secondary lining when the top is void and after the void repair is 5.68 mm. Compared with the normal situation, the increase in maximum vertical displacement and maximum vertical acceleration at the top of the secondary lining was 15.4% and 18.5% when the top was void, and after the grouting repair, the increase of maximum vertical displacement and maximum vertical acceleration was 6.6% and 8.3%, which was 7.6% and 8.3% less than the increase when the top was void. Under the conditions of Taft wave action, the vertical displacements and vertical accelerations of the top of the secondary lining were 3.78 mm, 4.07 mm, and 3.95 mm under normal conditions, when the top was void and after the void repair, respectively, and the vertical accelerations were 1.08 m/s^2, 1.17 m/s^2, and 1.12 m/s^2, respectively. Compared with the normal conditions, the increase of the vertical displacement and vertical acceleration of the top of the secondary lining when the top was void was The increase of vertical displacement and vertical acceleration at the top of the secondary lining was 7.7% and 8.3% compared with the normal condition, and after the grouting repair, the increase of vertical displacement and vertical acceleration was 4.5% and 3.7%, which was 2.9% and 4.3% less than the increase at the time of top debonding. Under each working condition of the EL-Centro wave action, the vertical displacement at the top of the secondary lining under normal conditions, when the top is void and after the void repair is 2.97 mm, 3.85 mm, and 3.44 mm, respectively, and the maximum value of vertical acceleration is 0.91 m/s^2, 1.04 m/s^2, and 0.97 m/s^2, respectively, compared with the normal condition, the increase of vertical displacement and vertical acceleration at the top of the secondary lining when the top is void is 29.6% and 14.3%. Compared with the normal condition, the increase of vertical displacement and vertical acceleration at the top of the secondary lining was 29.6% and 14.3%, and after the grouting repair, the increase of vertical displacement and vertical acceleration was 15.8% and 6.6% compared with the normal condition, which was 10.6% and 6.7% less than the increase when the top was void. From the above analysis, it can be seen that the void has a greater impact on the tunnel, which will significantly increase the seismic response of the tunnel. After repairing the tunnel with polymer grouting, the maximum tunnel displacement will be significantly reduced, coming close to the displacement of the normal tunnel. It reflects the repair effect of polymer grouting on tunnel voids.

It can be seen from Figure 19 that, under the action of seismic waves with the same peak value in different site conditions, there are obvious differences in the vertical

(a)   (b)
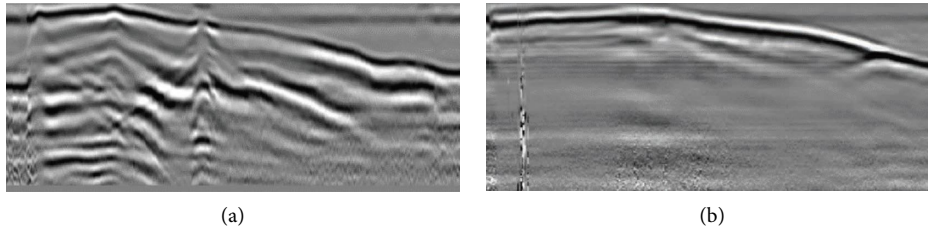
FIGURE 14: Geological radar detection spectra before and after grouting: (a) geological radar detection spectrum before polymer grouting; (b) geopolymer grouting after georadar detection spectrum.
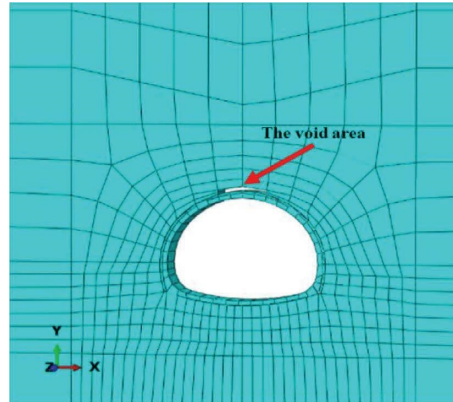
FIGURE 15: Schematic diagrams of the decommissioning area.

acceleration and vertical displacement of the top of the secondary lining. The vertical displacement and vertical acceleration of the top of the secondary lining of the tunnel under the excitation of the Northridge wave (type I site) are the largest, and the vertical displacement and vertical acceleration under the excitation of the EL-Centro wave (type III site) are the smallest. Hard, medium hard, or medium soft, the influence on the displacement and acceleration response of the top of the secondary lining gradually decreases, indicating that the dynamic response of the tunnel model has obvious seismic wave spectrum sensitivity.

5.3.2. Stress Analysis of Seismic Load Action. From Figures 20 to 23, it can be seen that under the three vertical seismic loads, the overall tunnel support structure in different working conditions behaves as a compressed state. Under the action of Northridge waves, the maximum absolute values of the maximum principal stresses at the top of the secondary lining in normal conditions, when the top is void, and after grouting repair are 0.211 MPa, 0.260 MPa, and 0.241 MPa, respectively, and the maximum values of the minimum absolute principal stresses are 7.49 MPa, 8.85 MPa, and 8.15 MPa. Compared with the normal condition, the increase in the maximum absolute values of the maximum principal stresses and the minimum absolute values of the principal stresses at the top of the secondary lining when the top is compared with the normal condition, the increase in the maximum absolute value of the maximum principal stress and the minimum absolute value of the principal stress at the top of the secondary lining was 23.2%

and 18.2%, and after the grouting repair, the increase in the maximum absolute value of the maximum principal stress and the minimum absolute value of the principal stress was 14.2% and 8.8% compared with the normal condition, and the increase was 7.3% and 7.9% less than the increase at the top of the lining when it was void. Under the action of Taft wave, the maximum absolute values of maximum principal stress at the top of secondary lining in normal condition, when the top is void and after grouting repair are 0.196 MPa, 0.241 MPa, and 0.218 MPa, respectively, and the maximum values of minimum absolute principal stress are 6.90 MPa, 7.95 MPa, and 7.21 MPa, compared with normal condition, the maximum values of maximum principal stress at the top when the top is void and the maximum values of minimum absolute principal stress at the top of secondary lining compared with the normal condition, the increase in the maximum value of absolute principal stress and the maximum value of absolute minimum principal stress at the top was 23.0% and 15.2%, and after the grouting repair, the increase in the maximum value of absolute principal stress and the maximum value of absolute minimum principal stress was 11.2% and 4.5% compared with the normal condition, and the increase was reduced by 8.3% and 9.5% compared with the increase when the top was void. The maximum values of absolute values of maximum principal stress under the EL-Centro wave are 0.187 MPa, 0.233 MPa, and 0.208 MPa, respectively. The maximum values of the absolute minimum principal stress at the top of the secondary lining in normal conditions, when the top is void, and after grouting repair are 6.57 MPa, 7.55 MPa, and 6.95 MPa, respectively, compared with the normal
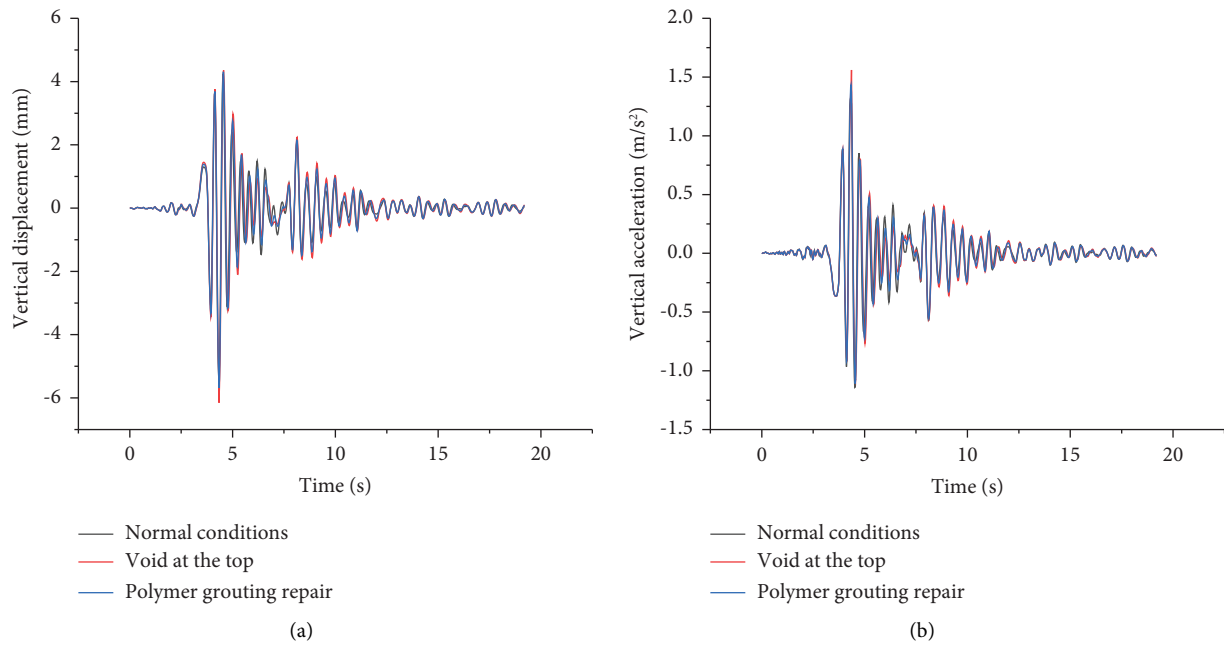
FIGURE 16: Vertical displacement and acceleration time curves of the top of the secondary lining under different working conditions of the tunnel under the action of the Northridge wave (Class I site): (a) the time course curve of vertical displacement at the top of the secondary lining; (b) the time course curve of vertical acceleration at the top of the secondary lining.
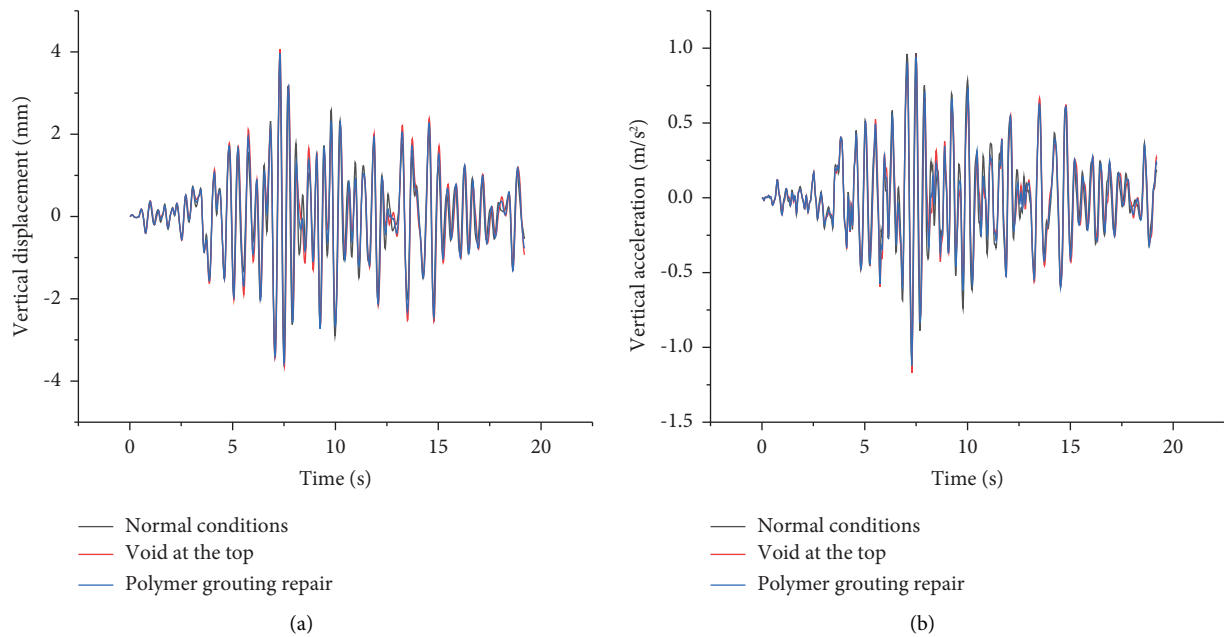
FIGURE 17: Vertical displacement and acceleration time curves of the top of the secondary lining under different working conditions of the tunnel under the action of Taft waves (Class II site): (a) the time course curve of vertical displacement at the top of the secondary lining; (b) the time course curve of vertical acceleration at the top of the secondary lining.

condition, when the top is void compared with the normal condition, the increase in the maximum absolute value of the maximum principal stress and the minimum absolute value of the principal stress at the top of the secondary lining was 24.6% and 14.9%, and after the grouting repair, the increase in the maximum absolute value of the maximum principal stress and the minimum absolute value of the principal stress was 11.2% and 5.8% compared with the normal condition, and the increase decreased by 10.7% and 7.9% compared with the top of the lining when the top was void. Compared with the top void condition, the compressive stress at the top of the secondary lining after grouting repair is obviously
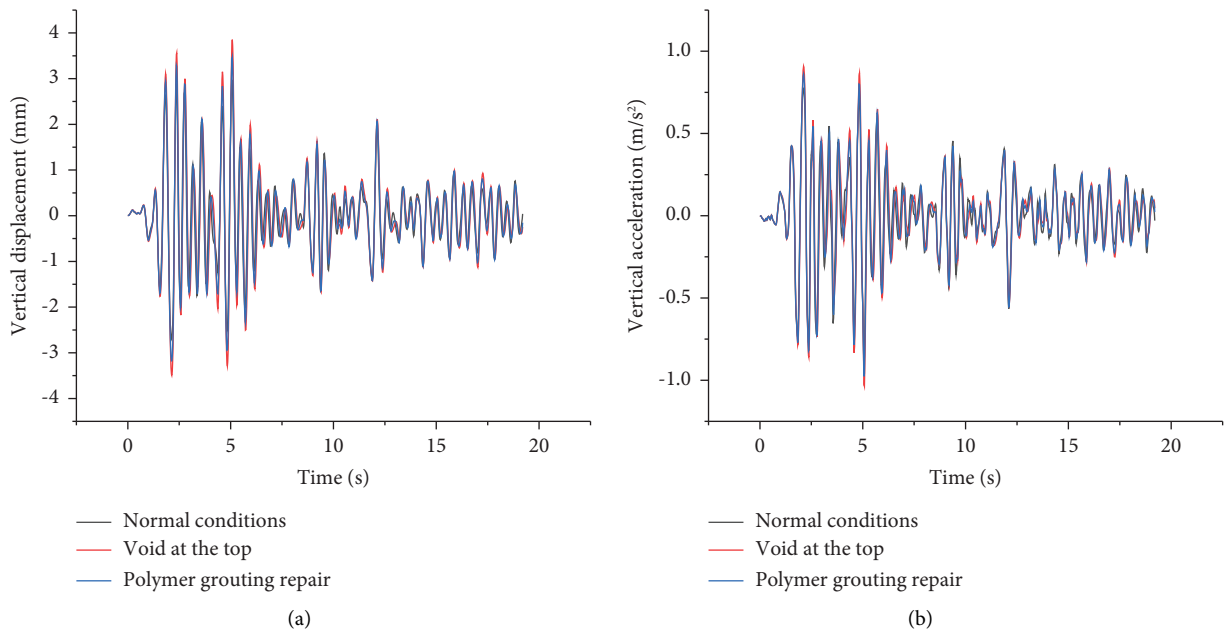
FIGURE 18: Vertical displacement and acceleration time curves of the top of the secondary lining under different working conditions of the tunnel under the action of the EL-Centro wave (Class III site): (a) the time course curve of vertical displacement at the top of the secondary lining; (b) the time course curve of vertical acceleration at the top of the secondary lining.
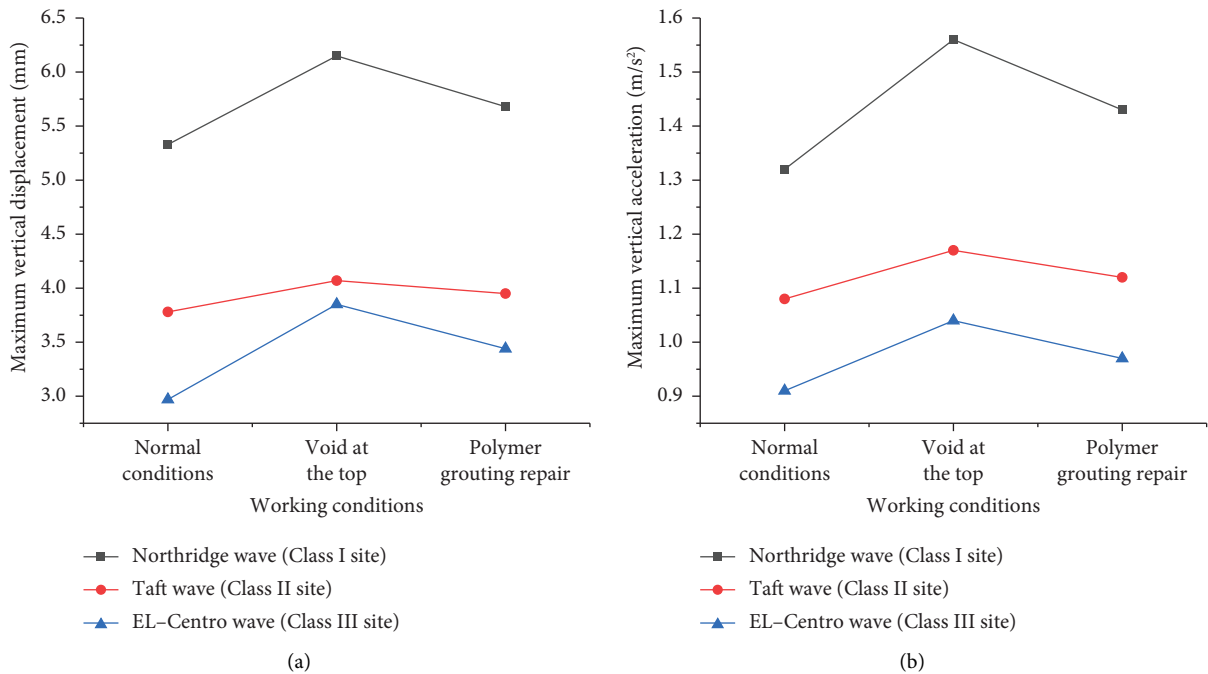
FIGURE 19: The maximum vertical displacement and maximum vertical acceleration of the top of the secondary lining of the tunnel under the action of seismic waves at different sites: (a) the maximum vertical displacement of the top of the secondary lining; (b) the maximum vertical acceleration at the top of the secondary lining.

small and close to the normal condition, which achieves the expected repair effect and makes the overall force deformation of the support structure safer and more stable.

It can be seen from Figure 23 that, under the action of seismic waves with the same peak value in different site conditions, there are obvious differences between the maximum absolute value of the maximum principal stress and the maximum absolute value of the minimum principal stress at the top of the secondary lining. The maximum absolute value of the maximum principal stress and the maximum absolute value of the minimum principal stress under Northridge wave (type I site) excitation are the largest,
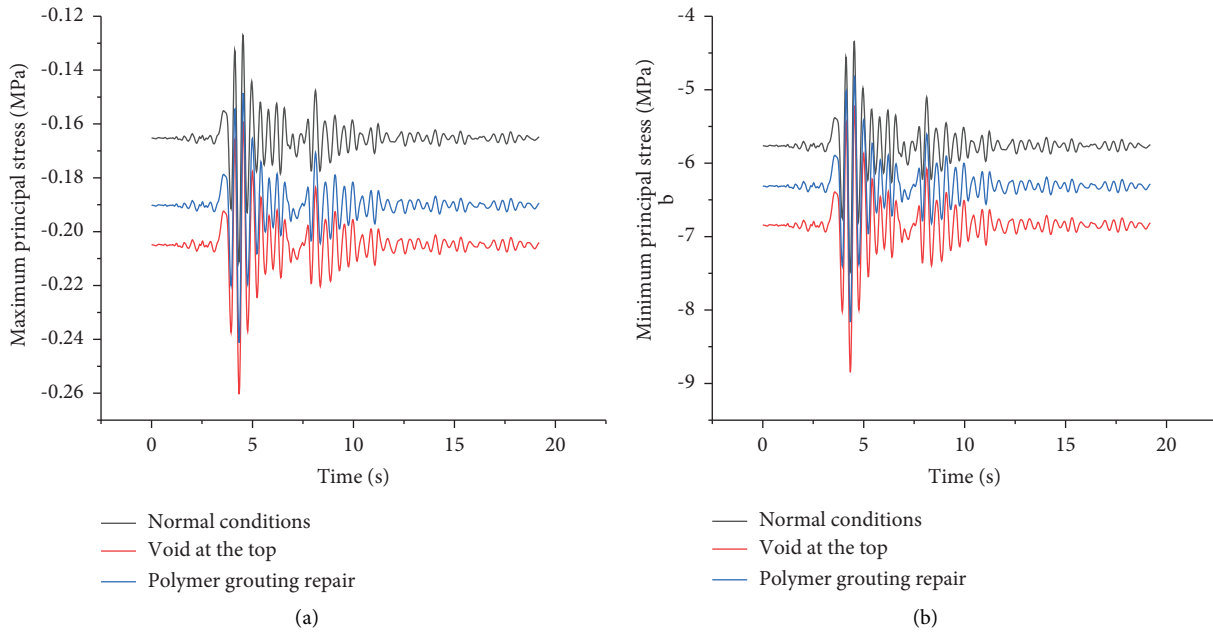
FIGURE 20: Stress variation curves at the top of the secondary lining for different working conditions of the tunnel under the action of the Northridge waves (Class I site): (a) the variation curve of the maximum principal stress at the top of the secondary lining; (b) A minimum principal stress variation curve at the top of the secondary lining.
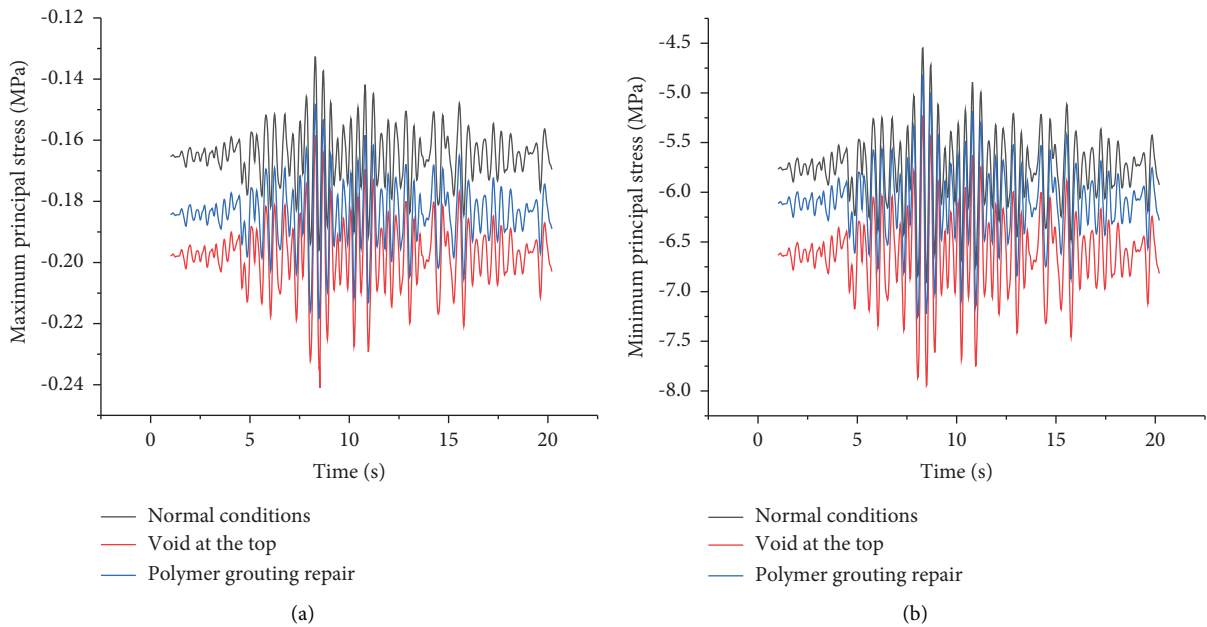
FIGURE 21: Stress variation curves of the top of the secondary lining under different working conditions of the tunnel under the action of the Taft waves (Class II site): (a) the variation curve of the maximum principal stress at the top of the secondary lining; (b) a minimum principal stress variation curve at the top of the secondary lining.

and the maximum absolute value of the vertical maximum principal stress under the excitation of EL-Centro wave (type III site), The maximum value of the absolute value of the minimum principal stress is the smallest; that is, as the site

type changes from hard, medium hard, to medium soft, the stress effect on the top of the secondary lining gradually weakens, indicating that the dynamic response of the tunnel model has obvious sensitivity to the seismic wave spectrum.
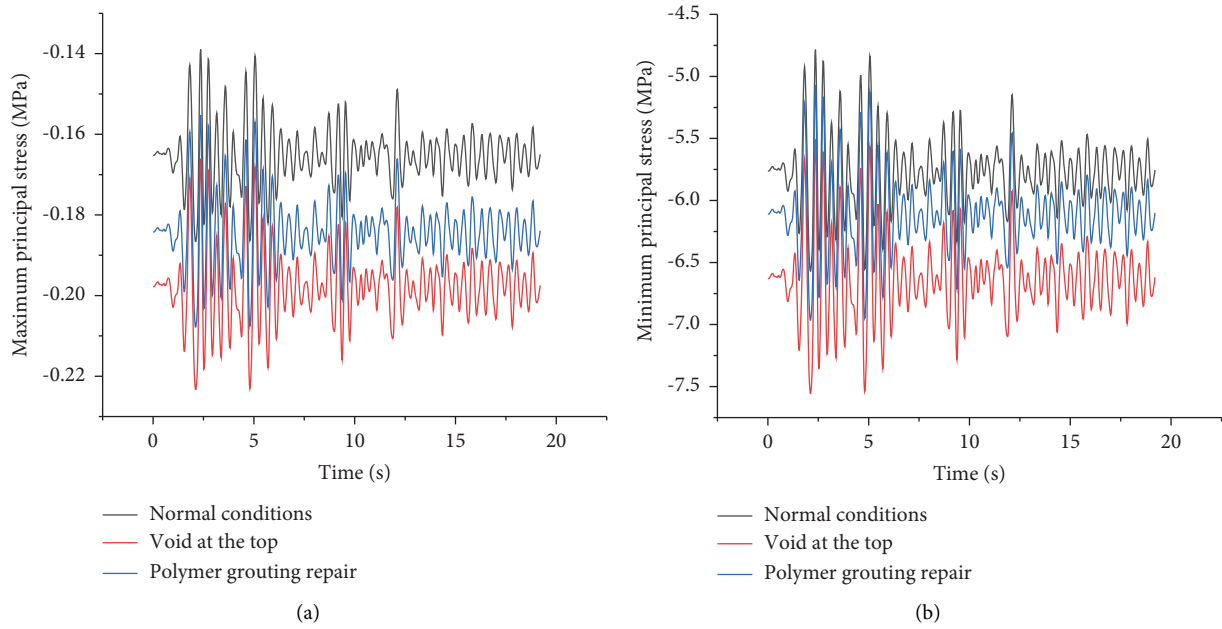
FIGURE 22: Stress variation curves at the top of the secondary lining for different working conditions of the tunnel under the action of the EL-Centro wave (Class III site): (a) the variation curve of the maximum principal stress at the top of the secondary lining; (b) a minimum principal stress variation curve at the top of the secondary lining.
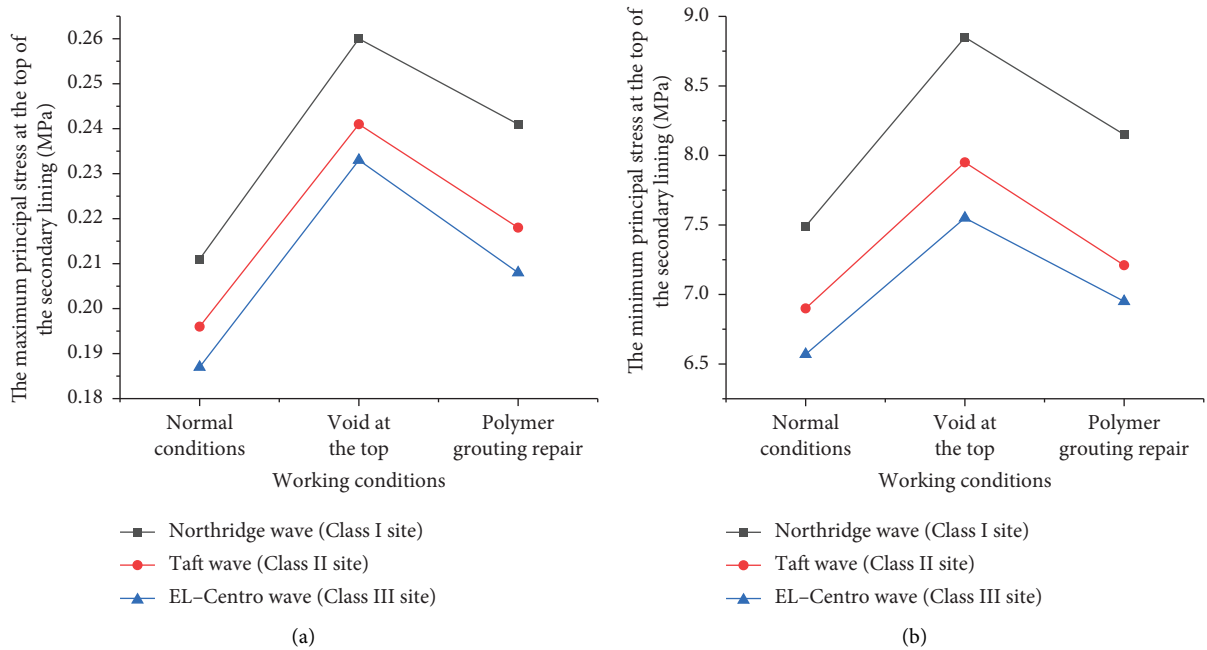
FIGURE 23: The maximum stress and minimum principal stress at the top of the secondary lining of the tunnel are determined by the action of seismic waves at different sites: (a) the maximum principal stress at the top of the secondary lining; (b) the minimum principal stress at the top of the secondary lining.

6. Conclusion

In this paper, the construction process of the Longmenshan Mountain tunnel under construction was numerically simulated using the Longmenshan Mountain tunnel as the engineering background, and the inversion of the physical parameters of tunnel envelope mechanics was carried out for the grade IV envelope section using the system identification sensitivity analysis method. Finally, the analysis of the effect of high polymer grouting to repair the tunnel debonding was carried out under the seismic mechanical response, and the following conclusions were obtained:

(1) Numerical simulation of the Longmenshan Mountain tunnel project using finite element software, found that the deformation law and stress distribution law of its tunnel envelope and support structure are in line with the site construction, but the amount of deformation such as vault settlement and peripheral convergence is different from the actual monitoring and measurement data, and this difference is caused by the discrepancy between the surrounding rock mechanical parameters selected by the numerical model and the actual difference is mainly caused by the discrepancy between the surrounding rock mechanical parameters selected by the numerical model and the actual ones.

(2) Based on the system identification sensitivity analysis method, the two-dimensional parameter inversion method is improved, the formula for three-dimensional physical and mechanical parameter inversion analysis of the surrounding rock is derived, and the three-dimensional mechanical parameter inversion analysis of the surrounding rock in the right line of the Longmenshan tunnel section from K83 + 010 to K83 + 90 is carried out. The final mechanical parameters of the surrounding rock, in line with reality, are the static elastic modulus $E_s = 1.82$ GPa, Poisson's ratio $\mu = 0.32$, and the internal friction angle $\varphi = 35°$, proving the feasibility of the system identification sensitivity analysis method. It has an important reference value for the real-time detection of the Longmenshan tunnel project under construction and provides a guarantee for accurately establishing the finite element model of the overall structure of the tunnel and surrounding rock and carrying out dynamic response analysis.

(3) The seismic mechanical response analysis verified the significant effect of polymer grouting to repair the tunnel debonding. The displacement and stress at the top of the tunnel's secondary liner debonding area were significantly reduced after the slurry repair, which was close to the normal condition. However, the stress and displacement of the top of the secondary lining under the action of seismic waves from the same peak at different site conditions are significantly different, and the effect on the displacement and stress response of the top of the secondary lining gradually decreases as the site type changes from hard, medium hard, to medium soft, indicating that the dynamic response of this tunnel model has obvious sensitivity to the seismic wave spectrum.

Data Availability

The data presented in this study are available in the main text of the article.

Conflicts of Interest

The authors declare that they have no conflicts of interest regarding the publication of this paper.

Acknowledgments

References

[1] X. Zhang, Y. Jiang, and K. Maegawa, "Mountain tunnel under earthquake force: a review of possible causes of damages and restoration methods," *Journal of Rock Mechanics and Geotechnical Engineering*, vol. 12, no. 2, pp. 414–426, 2020.

[2] F. Ye, N. Qin, X. Liang, A. Ouyang, Z. Qin, and E. Su, "Analyses of the defects in highway tunnels in China," *Tunnelling and Underground Space Technology*, vol. 107, Article ID 103658, 2021.

[3] P. Li, C. Feng, H. Liu, Y. Zhao, Z. Li, and H. Xiong, "Development and assessment of a water pressure reduction system for lining invert of underwater tunnels," *Marine Georesources and Geotechnology*, vol. 39, no. 3, pp. 365–371, 2021.

[4] Y. Luo and J. Chen, "Research status and progress of tunnel frost damage," *Journal of Traffic and Transportation Engineering*, vol. 6, no. 3, pp. 297–309, 2019.

[5] J. Fu, J. Xie, S. Wang, J. Yang, F. Yang, and H. Pu, "Cracking performance of an operational tunnel lining due to local construction defects," *International Journal of Geomechanics*, vol. 19, no. 4, Article ID 4019019, 2019.

[6] C. L. Xin, Z. Z. Wang, and B. Gao, "Shaking table tests on seismic response and damage mode of tunnel linings in diverse tunnel-void interaction states," *Tunnelling and Underground Space Technology*, vol. 77, pp. 295–304, 2018.

[7] N. Yasuda, K. Tsukada, and T. Asakura, "Three-dimensional seismic response of a cylindrical tunnel with voids behind the lining," *Tunnelling and Underground Space Technology*, vol. 84, pp. 399–412, 2019.

[8] B. Min, C. Zhang, X. Zhang, H. Wang, P. Li, and D. Zhang, "Cracking performance of asymmetric double-arch tunnels due to the voids behind linings," *Thin-Walled Structures*, vol. 154, Article ID 106856, 2020.

[9] J. X. Zhang, N. Zhang, A. Zhou, and S. L. Shen, "Numerical evaluation of segmental tunnel lining with voids in outside backfill," *Underground Space*, vol. 7, no. 5, pp. 786–797, 2022.

[10] L. Jin-long, O. Hamza, K. Sian Davies-Vollum, and L. Jie-qun, "Repairing a shield tunnel damaged by secondary grouting," *Tunnelling and Underground Space Technology*, vol. 80, pp. 313–321, 2018.

[11] P. Zhou, M. Lin, F. Zhou, L. Gong, and W. Ao, "Bearing characteristics and failure mechanism of a novel plate-short anchor structure for tunnel crack reinforcement," *Engineering Failure Analysis*, vol. 135, Article ID 106160, 2022.

[12] W. Han, Y. Jiang, N. Li, G. Wang, H. Luan, and C. Liu, "Failure behavior and reinforcing design of degraded tunnel linings based on the three-dimensional numerical evaluation," *Engineering Failure Analysis*, vol. 129, Article ID 105677, 2021.

[13] C. Liu, D. Zhang, and S. Zhang, "Characteristics and treatment measures of lining damage: a case study on a mountain tunnel," *Engineering Failure Analysis*, vol. 128, Article ID 105595, 2021.

[14] M. Shi, F. Wang, and J. Luo, "Compressive strength of polymer grouting material at different temperatures," *Journal of Wuhan University of Technology-Materials Science Edition*, vol. 25, no. 6, pp. 962–965, 2010.

[15] F. M. Wang, M. S. Shi, H. J. Li, and Y. H. Zhong, "Experimental study on the anti-permeability properties of polymer grouting materials," *Advanced Materials Research*, vol. 284-286, pp. 1952–1955, 2011.

[16] R. Wang, F. Wang, J. Xu, Y. Zhong, and S. Li, "Full-scale experimental study of the dynamic performance of buried drainage pipes under polymer grouting trenchless rehabilitation," *Ocean Engineering*, vol. 181, pp. 121–133, 2019.

[17] H. Fang, B. Li, F. Wang, Y. Wang, and C. Cui, "The mechanical behaviour of drainage pipeline under traffic load before and after polymer grouting trenchless repairing," *Tunnelling and Underground Space Technology*, vol. 74, pp. 185–194, 2018.

[18] B. Li, F. Wang, H. Fang, K. Yang, X. Zhang, and Y. Ji, "Experimental and numerical study on polymer grouting pretreatment technology in void and corroded concrete pipes," *Tunnelling and Underground Space Technology*, vol. 113, Article ID 103842, 2021.

[19] H. Fang, Y. Su, X. Du, F. Wang, and B. Li, "Experimental and numerical investigation on repairing effect of polymer grouting for settlement of high-speed railway unballasted track," *Applied Sciences*, vol. 9, no. 21, p. 4496, 2019.

[20] X. Bian, X. Duan, W. Li, and J. Jiang, "Track settlement restoration of ballastless high-speed railway using polyurethane grouting: full-scale model testing," *Transportation Geotechnics*, vol. 26, Article ID 100381, 2021.

[21] S. Li, Y. Niu, B. Wang, Y. Gao, and Y. Zhu, "Research on mechanical response of polymer grouting repair for longitudinal cracks in reconstructed and expanded expressway pavement," *Mathematical Problems in Engineering*, vol. 2022, Article ID 5760674, 8 pages, 2022.

[22] C. Cui, Q. Lu, C. Guo, and F. Wang, "Analysis of the coupling effect of thermal and traffic loads on cement concrete pavement with voids repaired with polymer grout," *Advances in Materials Science and Engineering*, vol. 2022, Article ID 2517250, 17 pages, 2022.

[23] V. Vemuri, J. A. Dracup, R. C. Erdmann, and N. Vemuri, "Sensitivity analysis method of system identification and its potential in hydrologic research," *Water Resources Research*, vol. 5, no. 2, pp. 341–349, 1969.

[24] A. A. Javadi, R. Farmani, V. V. Toropov, and C. Snee, "Identification of parameters for air permeability of shotcrete tunnel lining using a genetic algorithm," *Computers and Geotechnics*, vol. 25, no. 1, pp. 1–24, 1999.

[25] Y. M. A. Hashash, S. Levasseur, A. Osouli, R. Finno, and Y. Malecot, "Comparison of two inverse analysis techniques for learning deep excavation response," *Computers and Geotechnics*, vol. 37, no. 3, pp. 323–333, 2010.

[26] L. T. Nguyen and T. Nestorović, "Unscented hybrid simulated annealing for fast inversion of tunnel seismic waves," *Computer Methods in Applied Mechanics and Engineering*, vol. 301, pp. 281–299, 2016.

[27] X. Luo, H. Wang, Y. Deng, and H. Li, "Automatic inverse analysis of asphalt pavement field aging based on system identification," *IEEE Transactions on Intelligent Transportation Systems*, vol. 23, no. 11, Article ID 22106, 2022.

[28] H. B. Zhou and R. D. Li, "Back analysis of the elastic modulus and horizontal crustal stress of tunnel surrounding rock with system identification method," *Applied Mechanics and Materials*, vol. 127, pp. 412–414, 2011.

[29] F. Wang and R. L. Lytton, "System identification method for backcalculating pavement layer properties," 1993, http://onlinepubs.trb.org/Onlinepubs/trr/1993/1384/1384-001.pdf.

[30] M. Hu, Q. Zhou, Z. Ji, and L. Liang, "Study on dynamic and static modulus of rock mass in nuclear island area of some nuclear power plants in China," *Industrial Construction*, vol. 45, no. 9, pp. 37–39, 2015.

Research Article

Stability Analysis of the Lining Reinforcement Structure of a Double-Track Heavy-Haul Railway Tunnel

Weibin Ma [ID],[1,2] **Jinfei Chai** [ID],[1,2] **Xiaoyan Du** [ID],[1,2] **Yao Li,**[1,2] **Peng Zhao,**[1,2] **and Shanduo Li**[1,2]

[1]*Railway Engineering Research Institute, China Academy of Railway Sciences Corporation Limited, Beijing 100081, China*
[2]*State Key Laboratory for Track Technology of High-Speed Railway, Beijing 100081, China*

Correspondence should be addressed to Jinfei Chai; chaijinfei@rails.cn and Xiaoyan Du; 466074024@qq.com

An increasing number of railway tunnels are afflicted with railway tunnel lining diseases. Through on-site detection of lining diseases in double-track railway tunnels, this paper analyzed its causative factors and developed a section steel arch frame lining reinforcement. Through a simulation of its mechanical performance, both the steel plate and concrete met the tensile strength code requirements for railway tunnel design (TB 10003-2016). It effectively repaired the damage from lining diseases under narrow-site and short maintenance "window" time conditions without affecting the normal operation of catenary and power supply facilities. This reinforcement has great practical significance and broad application prospects.

1. Introduction

By the end of 2021, China's railway network reached 145,000 km, which includes 17,532 railway tunnels having a combined length of about 21,055 km [1]. As the train axle load and transportation density increase, so do the dynamic-load strength and fatigue effect of heavy-duty railway tunnels. In addition, seismic disturbances and corrosion from water and salt increase the probability of structure diseases; in fact, many tunnel linings have cracks, blocks, and voids. In addition, the dynamic stress and vibrations of the heavy-vehicle and light-vehicle lines unbalance the double-track heavy-haul railways, resulting in a deteriorating lining, which affects the train's long-term operational safety [2].

Ma et al. tested the in situ stress distribution of the railway tunnels in Southwest China based on the complete temperature compensation technology. Ma et al. [3] analyzed the vibration law of railway tunnel substructure under different axle loads and health conditions, and Ma et al. [4] researched the design parameters and fatigue life of tunnel bottom structure of single-track ballasted heavy-haul railway tunnel with 40-ton axle load [5]. Han et al. [6] developed a treatment technology for

optimizing the stress state of railway tunnel bottom structure. Chai [7, 8] analyzed the dynamic response characteristics for basement structure of heavy-haul railway tunnel with defects and researched the multijoint rock failure mechanism based on moment tensor theory.

Zhao [9] divided the crack reinforcement of a railway tunnel lining into crack treatment and structural reinforcement. Cracks with a small width and no penetration are generally filled with epoxy resin or mortar. Grout, shotcrete, or reinforced concrete behind the lining is used on wide, penetrating cracks. For a lining structure without a load-bearing capacity, it is removed and a new lining is reconstructed. Cheng et al. [10] divided tunnel cracks into four grades according to width and length: AA, A1, B, and C, from heavy to light. They proposed that grade AA be reinforced by W-shaped steel-belted mesh shotcrete; grade A1 by cross-seam anchor-bolt grouting; and the lighter-grade B and C cracks by appropriate shotcrete. Because the code has strict provisions regarding the effective clearance area of a high-speed railway tunnel, reinforcement measures should not be adopted when repairing cracks. Therefore, Cheng [11] put forward treatment measures for different levels of cracks.

In view of the deficiency in lining thickness and strength, Niu et al. [12] proposed structural reinforcement in the form of anchor spraying or sticking fiber cloth with a steel plate inside. In addition, Yu [13] summarized and pointed out that backfill grouting measures are generally adopted for small cavities behind the railway tunnel lining, while arch sleeve reinforcement is generally adopted for large cavities. Ma et al. [14] proposed that a corrugated steel plate has certain advantages, such as good ductility, for strengthening railway tunnels and can be applied to sections that have large deformations. In general, for some minor diseases such as cracks and cavities, grouting backfill reinforcement is generally carried out. For diseases of great structural impact, secondary reinforcement by means of an arch covering or pasted steel plates for backfilling is required. Wu et al. [15] and Cheng et al. [16] developed the hybrid complex variable element-free Galerkin method for 3D elasticity problems. Li and Wu [17] studied the basic formula of elastoplastic damage constitutive model of concrete.

Finding an effective means of repairing the lining of narrow, double-track heavy-haul railway tunnels that have limited maintenance "window" time, without affecting the normal operation of catenary and power supply facilities, is an urgent problem. Therefore, conducting research into current lining methods is of great practical significance and could have broad application.

To address these lining diseases, this paper is divided as follows. Section 1 introduces previous research results. Section 2 introduces the general situation of tunnel and lining diseases. Section 3 offers a preliminary analysis of the causes of tunnel lining diseases through data collection, field investigation, and detection. Section 4 introduces the design principles and maintenance methods of a reinforced steel arch frame lining. Section 5 analyzes the steel arch frame reinforcement using a numerical simulation. Section 6 draws conclusion and offers suggestions for further research.

2. Project Overview

Daheishan Tunnel, completed in 1984 under the management of the Chawu Railway Engineering Section of a heavy haul railway in northern China, is located between Yanqing North Station and Xiazhuang Station northeast of the Changping District of the Daqin Railway. It is a double-track tunnel.

The center mileage is K 299 + 700, with a total length of 2715 m. The lining of the tunnel is mainly a curved wall structure, and the line is downhill 10.1–10.8‰ in the direction of tunnel exit. The tunnel passes through the main peak of Daheishan mountain in the Yanshan Mountains, and all the tunnels pass through the Yanshanian granite layer. It is a gray-yellow, flesh-red medium grain structure on complex terrain and developed gullies. The maximum buried depth of the tunnel is 303 m. The lining was constructed according to the special tunnel 0025 drawing. It is a double-track electrified tunnel with curved wall concrete masonry.

The transportation load of this line is heavy, and the Daheishan Tunnel has been in operation for nearly 40 years. Over that time, its structural concrete has deteriorated

severely. In March 2021, according to data provided by the tunnel management and maintenance unit and through geological radar detection and three-dimensional laser scanning, it was found that the lining of the tunnel 1605–1625 m away from the tunnel entrance had cavities, falling blocks, wrong platforms, and other diseases seriously affecting driving safety, as shown in Figure 1. The size of the cavity opening is $0.1 \times 0.8 \times 0.3$ m; the thickness of lining concrete is about 30 cm; the deterioration is serious; and no reinforcement was found. The depth of the cavity was about 1 m and extended for 10 m in the direction of tunnel entrance. According to the *Evaluation Standard for Deterioration of Railway Bridge and Tunnel Buildings Part 2: Tunnel* (Q/CR 405.2-2019) of China, the disease grade was evaluated as AA, which meant treatment had to be taken immediately because of the risk to traffic safety (see Figures 2 and 3).

3. Cause Analysis of Lining Disease

By means of data collection, field investigation, and detection, the preliminary analysis showed that the causes of lining disease are as follows:

(1) *Design Factors*. Tunnel construction began in the 1980s, and there was a large gap between the design standard and the engineering technology of the time, which was generally low.

(2) *Construction Factors*. To reduce the amount of shotcrete after tunnel overbreak, during shotcrete construction, surrounding loose rock was not cleared in place, resulting in a cavity not being fully backfilled behind the initial support; as a result, the performance of the concrete lining was poor. The construction quality was also poor and insufficiently thick. With the progress of geological changes, the rock blocks above the cavity suddenly failed to support the concentrated load, causing the lining to break, resulting in falling blocks, a cavity, and other problems.

(3) *Deterioration Factors*. The tunnel is nearly 40 years old, and as its lining concrete continues to deteriorate, its bearing, bending, and shear capacity declines. Under continuous rock pressure, the deteriorating thin lining shell cracks, leading to falling blocks and cavities.

(4) *Fault Factor*. The diseased lining section crosses the reverse fault, and fault activity leads to stress changes around the tunnel.

(5) *Influencing Factors of Train Load*. The vibration of heavy-haul trains is considerable and causes the lining concrete to crack easily.

4. Design Principles and Maintenance Method

4.1. Design Principles. Due to limited operating space, poor working environment, and safety of the operating line tunnel, disease treatment is a very complex project.

FIGURE 1: Real map of lining diseases of Daheishan Tunnel on Datong to Qinhuangdao Railway.
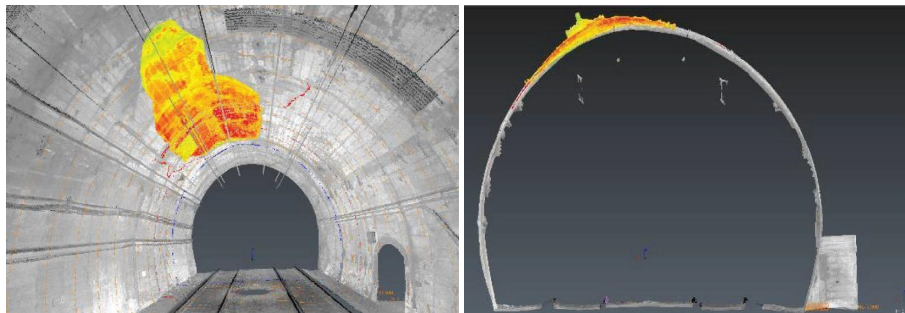
FIGURE 2: Three-dimensional laser scan of lining diseases in Daheishan Tunnel on Datong to Qinhuangdao Railway.
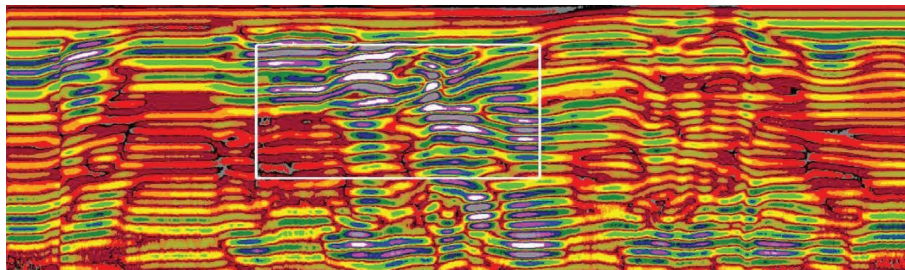
FIGURE 3: Geological radar detection of lining disease of Daheishan Tunnel on Datong to Qinhuangdao Railway.

Therefore, the following principles concerning tunnel reinforcement construction organization design had to be followed:

(1) Given the current state of tunnel diseases, the reinforcement design was carried out to ensure safe operation of the line.

(2) Factors such as the construction environment and amount of daylight were considered to minimize the influence on normal operation of the line as far as possible.

(3) The state of the surrounding rock and tunnel structure had to be under constant observation, and increased monitoring and measurement were done if necessary.

(4) Because of the complexity, particularity, and uncertainty of tunnel engineering construction, close communication and cooperation among the construction, design, equipment management, and other units were required, and construction was adjusted as necessary to match the actual conditions.

(5) The construction scheme was controlled according to the comprehensive minimum construction clearance size of Daheishan Tunnel.

(6) The insulation distance between temporary and permanent measures and the electrified body had to meet the requirements set out in the Code for Design of Railway Electric Traction Power Supply (TB10009-2016).

(7) During construction, the cables in the diseased section had to be effectively protected.

4.2. Remediation Plan

4.2.1. Technical Introduction. To prevent further cracking and deformation of the tunnel lining or serious water leakage, arch reinforcement was performed: an arch

structure was added along the surface of the original lining to form a common bearing body with the original lining. It is the most effective method for solving serious lining leakage because it gives good reinforcement, and construction quality is easy to control.

The main content of the treatment plan is to add circumferential H-shaped steel on the lining surface, weld steel plates between the H-shaped steel on the side away from the lining, and fill concrete between the steel plate and the lining.

The specific measures were as follows. An H175 steel arch frame was erected on the inner side of the lining according to the clearance requirements, and spacing of the steel arch frame was 1.0 m. The two steel arches were longitudinally connected with 20 mm in diameter deformed steel bars. The circumferential spacing was 1 m. Deformed steel bars were connected longitudinally with a circumferential spacing of 1 m; short anchor bolts were constructed between the steel arches; circumferential reinforcing mesh was erected; cavity grouting behind the lining was carried out; 6 mm thick steel plates were welded, and C35 concrete was poured inside, as shown in Figures 4 and 5.

4.2.2. Specific Steps

(1) During construction, the loose concrete lining was chiseled out; the concave groove was excavated at the erection position on the top surface of the tunnel trench; and the footing was used to support the grouting anchor pipe. The erection steel plate was welded at the end of the anchor pipe. After erecting the H175 steel arch, drill and install the anchor bolt and weld the end of the anchor bolt to the steel arch. Then, the micro-expansion concrete was filled manually behind the flange of the H-steel arch to ensure that the steel arch was close to the original lining.

(2) The H-shaped steel arch frame was processed outside the tunnel in five sections and assembled in the tunnel. The steel at both ends was connected with a 1 cm thick steel plate and high-strength bolts at the section connection and was firmly welded. The section length of the H-shaped steel arch frame was appropriately adjusted according to different mileage and sections.

(3) Before grade II welding, rust spots at the welding position had to be cleared, and there had to be no pores, undercuts, cracks, or other phenomena during welding. All welds were fully welded.

(4) In addition to chiseling the loose and cracked concrete in the reinforced section of the steel arch frame, it also had to be chiseled in combination with the tunnel clearance to embed the frame.

(5) Drill holes at the foot of the wall using a down-the-hole drill, lock the steel arch frame in the depth of the surrounding rock using anchor pipes and anchor rods, transfer as much load as possible to the deep part of the surrounding rock, and clean the connection between the steel arch frame, steel plate, and anchor pipe.

(6) After the steel arch frame was erected, M20 cement mortar was used to fill the chisel groove and the gap between the profile steel flange and the concrete lining surface to bring the frame close to the original concrete lining and give full play to its bearing capacity.

(7) Inspect the welds between the sections of the original steel arch and repair and strengthen those that failed to meet the requirements.

(8) Short anchor bolt with 20 mm in diameter threaded reinforcement with a circumferential spacing of 0.5 m was welded with steel plate and anchored in the lining using a coil anchoring agent.

(9) Erect three steel arches between two adjacent steel arches (20 mm in diameter) to form a circumferential reinforcement mesh.

(10) Grout the cavity behind the lining by a small conduit (42 mm in diameter) that injected micro-expansion material with a grouting pressure of 0.3 MPa.

(11) Remove the loose concrete between the arch frame and the lining, roughen and clean the tunnel lining surface, and then brush with a concrete interface agent.

(12) Erect the steel plate from bottom to top from the top surface of the tunnel trench. Weld the steel plat on the inner side of the outer edge of the section steel and at the end of the short anchor bolt. Weld the plate with a ring spacing of 0.5 m in diameter. Weld the steel plate with a flange of the steel arch frame with a length of 100 cm and a circumferential width of 500 cm. Bend the steel plate according to the radian of the steel arch frame on site. After each steel plate was installed, vibrate C35 concrete filled in the space between the steel plate and the original lining to ensure filling.

(13) Remove rust, polish, and spray red lead primer on exposed steel members and then brush dark gray antirust paint twice.

4.3. Mechanical Analysis Method of Steel Arch Structure.
Taking the stress condition of the circular arch as an example, the internal force was calculated and solved (see Figures 6 and 7). As shown in Figure 8, the arch as divided into n segments, where C_i represents the Ith segment from bottom to top; the stiffness is E_i; the node length is expressed as Li; and the arch crown had no nodes. The semistructural analysis is shown in Figure 9.
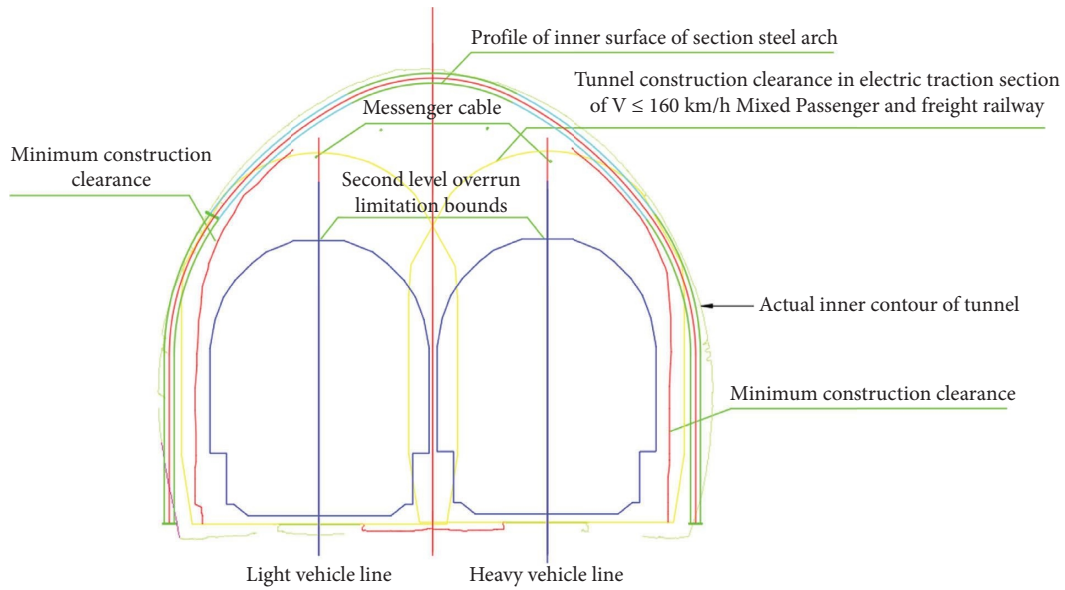
Figure 4: Gauge comparison.
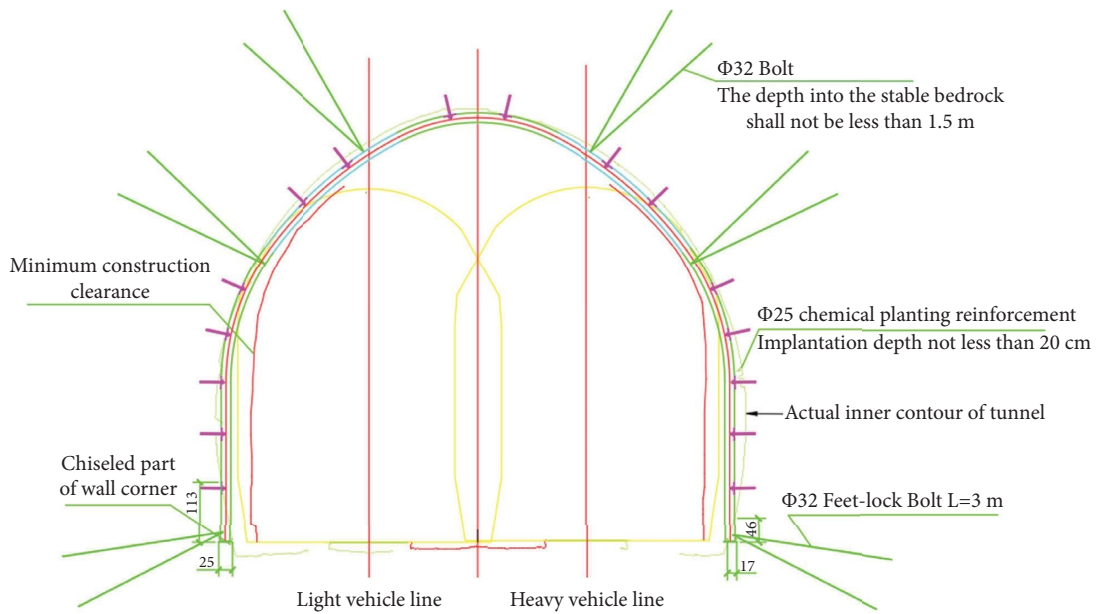
Figure 5: Overall cross section layout.

4.4. Establishing Equilibrium Equation.

The half structure of the steel arch structure is a statically indeterminate structure, and the internal force of the statically indeterminate structure was solved according to the force method. The equation established by the external force balance condition of the structure is as follows:

$$
\begin{cases}
F_{Ax} = F_{Cx} = q_2 R, \\
M_A = M_C.
\end{cases}
\tag{1}
$$

4.4.1. Establishing Force Method Equation.

Take M_c as the redundant unknown force and M_1 as the basic unknown force, and the force method equation is shown in the following formula:

$$
\delta_{11} M_1 + \Delta_{1P} = 0.
\tag{2}
$$

4.4.2. Solving Δ_{1P}.

According to the generalized diagram multiplication method, only internal forces caused by bending moments are considered, so the following is obtained:

$$
\nabla_{1P} = \int \frac{M \overline{M}}{EI} \, ds.
\tag{3}
$$

According to the calculus formula, the accumulated displacement of each segment is added to obtain
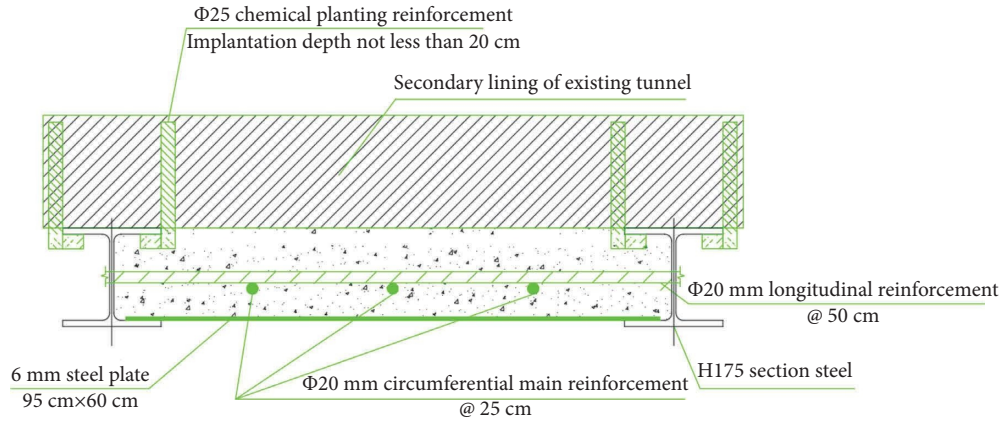
FIGURE 6: Structural cross section design drawing.
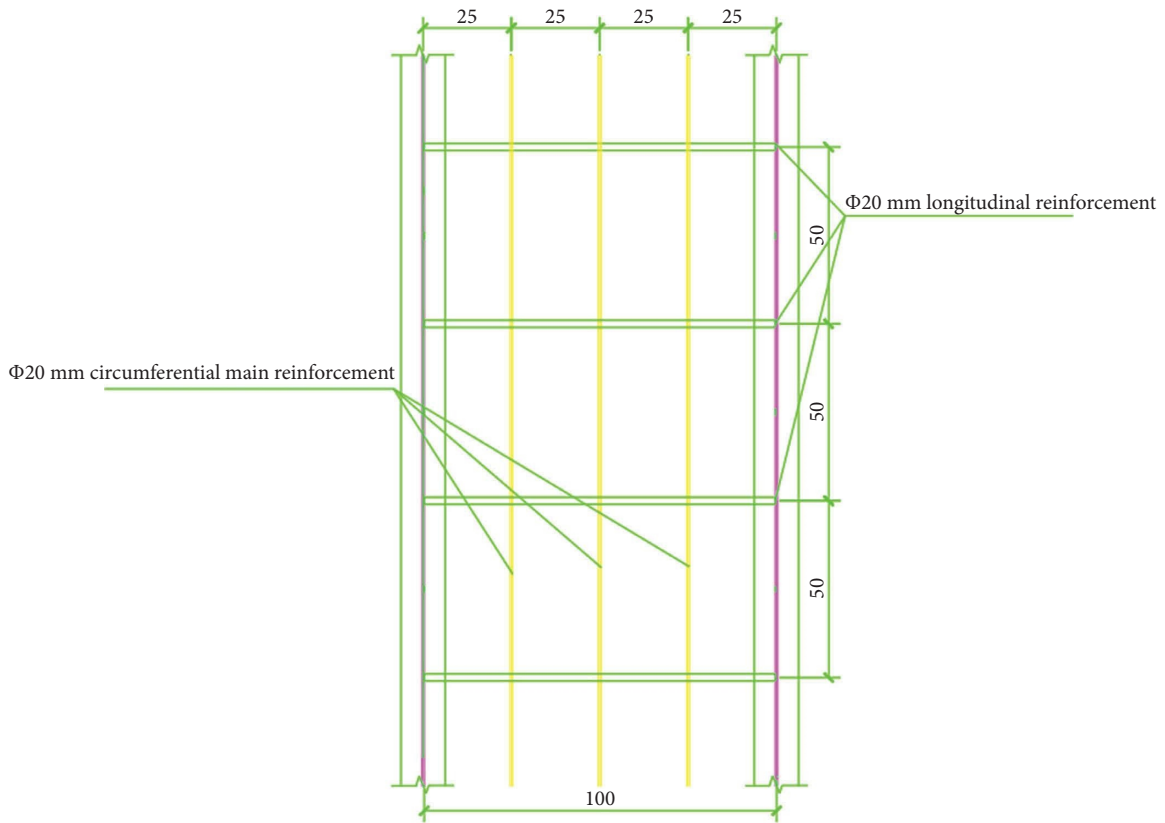
FIGURE 7: Reinforcement layout drawing.

$$\Delta_{1P} = \int \frac{M\overline{M}}{EI} ds = \int_0^{\theta_1/2} \frac{M\overline{M}}{EI_1'} Rd\varphi + \int_{\theta_1/2}^{\alpha_2-\theta_1/2} \frac{M\overline{M}}{EI} Rd\varphi + \cdots + \int_{\alpha_2-\theta_1/2}^{\alpha_2+\theta_1/2} \frac{M\overline{M}}{EI_1'} Rd\varphi$$

$$+ \int_{\alpha_i+\theta_i/2}^{\alpha_{i+1}-\theta_{i+1}/2} \frac{M\overline{M}}{EI} Rd\varphi + \cdots + \int_{\alpha_n+\theta/2}^{\pi} \frac{M\overline{M}}{EI} Rd\varphi,$$

(4)

of which the radian of steel arch section $L_i = R_i \bullet \theta_i$ is

$$\theta_1 = \theta_2 = \cdots = \theta_n = \theta. \quad (5)$$

The equivalent bending stiffness of the segment is

$$EI_1' = EI_2' = \cdots = EI_i' = \cdots = EI_n'. \quad (6)$$
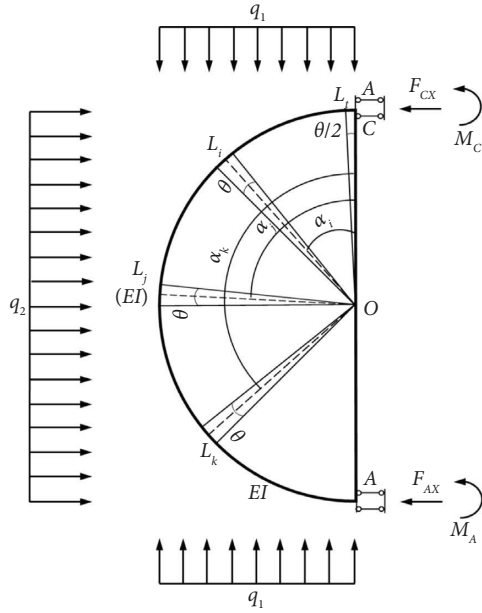
Figure 8: Stress analysis diagram.
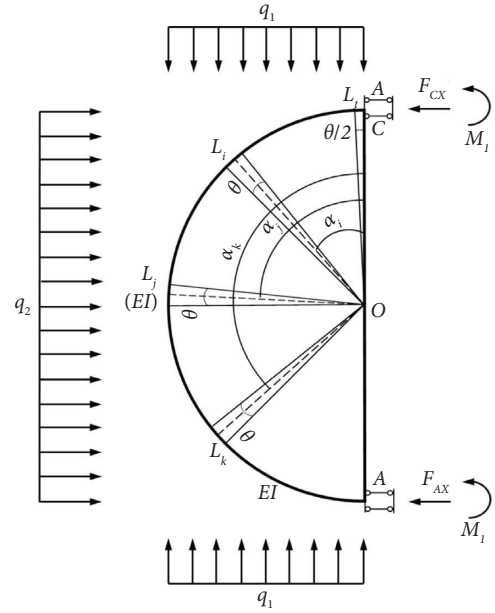
Figure 9: Basic system of force method.

So, equation (3) can be simplified as

$$\Delta_{1P} = \sum_{1}^{m} \int_{\alpha_i - \theta_i/2}^{\alpha_i + \theta_i/2} \frac{M\overline{M}}{EI_i'} R d\varphi + \int_{\alpha_i + \theta/2}^{\alpha_{i+1} - \theta/2} \frac{M\overline{M}}{EI} R d\varphi, \quad (7)$$

of which $\alpha_1 = \theta_1/2, \alpha_{n+1} - \theta_{n+1} = \pi/2$.

4.4.3. Solving δ_{11}

$$\delta_{11} = \int \frac{M\overline{M}}{EI} ds. \quad (8)$$

Accumulating the integral by segment number gives

$$\delta_{11} = \int \frac{M\overline{M}}{EI} ds = \sum_{1}^{m} \int_{\alpha_i - \theta_i/2}^{\alpha_i + \theta_i/2} \frac{M\overline{M}}{EI_i'} R d\varphi$$

$$+ \int_{\alpha_i + \theta_i/2}^{\alpha_{i+1} - \theta_{i-1}/2} \frac{M\overline{M}}{EI} R d\varphi, \quad (9)$$

in which $\alpha_1 = \theta_1/2, \alpha_{n+1} - \theta_{n+1} = \pi/2$.

In general, for the convenience of design and construction, a unified arc length segment was adopted so that $\theta_1 = \theta_2 = \cdots = \theta_n = \theta$.

The equivalent bending stiffness of the segment is $EI_1' = EI_2' = \cdots = EI_i' = \cdots = EI_n'$.

4.4.4. Solving Support Reaction.
Substitute equation (9) into equation (3) to obtain the unknown force M_C and bring it into the balance equation (10) to obtain the reaction force M_C of other supports.

$$[K]\{\delta\} = \{P\}, \quad (10)$$

where $[K]$ is the overall stiffness matrix of lining structure; $\{\delta\}$ is the node displacement matrix of lining structure, $\{\delta\} = [\delta_1 \, \delta_2 \delta_m]^T$; and $\{P\}$ is the lining node load matrix $\{P\} = [P_1 \, P_2 \, P_m]^T$. In the structural calculation, the structure was generally divided into many micro-elements, and the local element stiffness $[K]^e$, element displacement $\{\delta\}^e$, and element load matrixes $\{P\}^e$ were established. Finally, the element stiffness, displacement, and load matrixes were assembled into the overall stiffness, displacement, and overall load matrixes, respectively.

4.4.5. Internal Force Solution.
After the bearing reaction was obtained, the axial force and bending moment of the internal force of each element was solved as

$$F_{N\varphi} = F_{CX}\cos\varphi + q_1 R \sin^2\varphi - q_2 R \cos\varphi(1 - \cos\varphi),$$

$$M_\varphi = M_C + F_{CX}R(1 - \cos\varphi) - \frac{1}{2}q_1 R^2 \sin^2\varphi - \frac{1}{2}q_2 R^2(1 - \cos\varphi)^2. \quad (11)$$
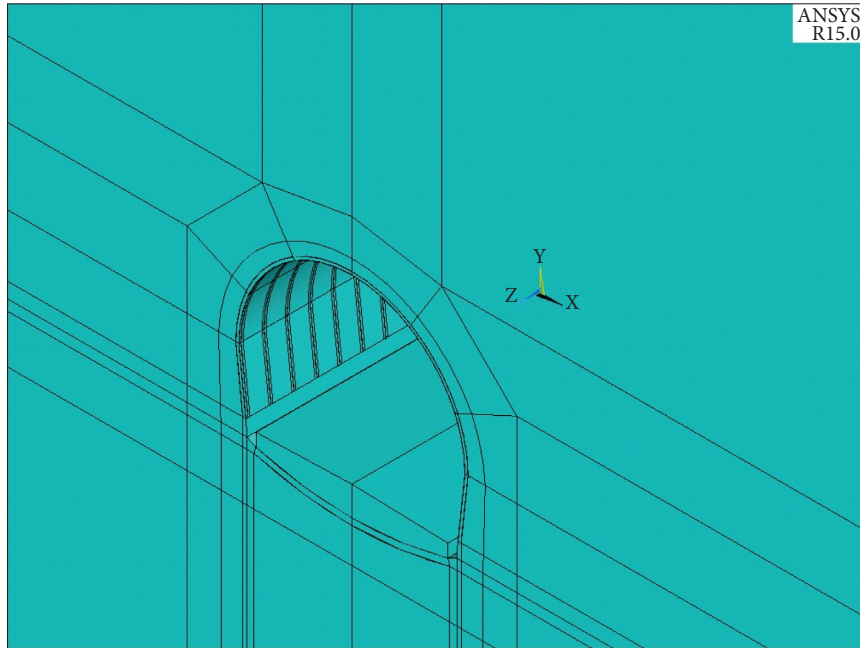
FIGURE 10: Numerical model.
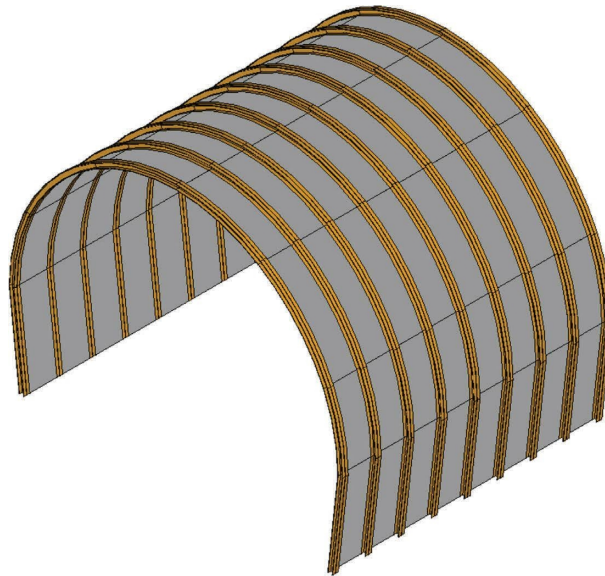
FIGURE 11: Steel frame and steel plate assembly.

4.5. Boundary Conditions. The left and right sides, bottom, front, and rear are fixed constraints.

4.6. Model Dimensions. The dimensions were 16 m along the longitudinal direction of the tunnel, 4 times the tunnel diameter on both sides, 2 times the tunnel diameter at the bottom, and the value at the top taken according to the actual buried depth. The model is shown in Figures 8–11.

4.6.1. Material Parameters. The surrounding rock parameters were selected according to the intermediate value of class IV in the *Code for Design of Railway Tunnel of China* (TB 10003-2016) (see Tables 1 and 2).

The existing structural C30 concrete was selected after being weakened by 50%. The parameters of a newly poured C30 concrete structure were selected according to the equivalent elastic modulus of internal reinforcement.
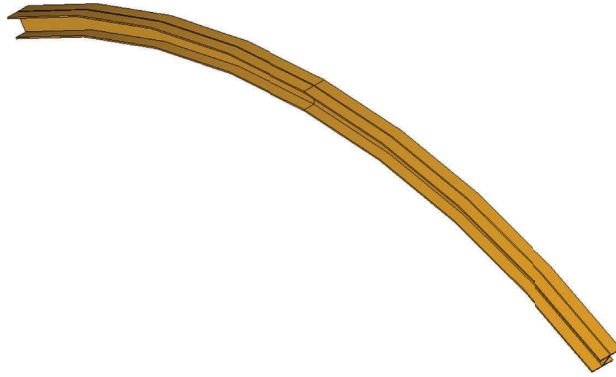
FIGURE 12: Steel frame model.
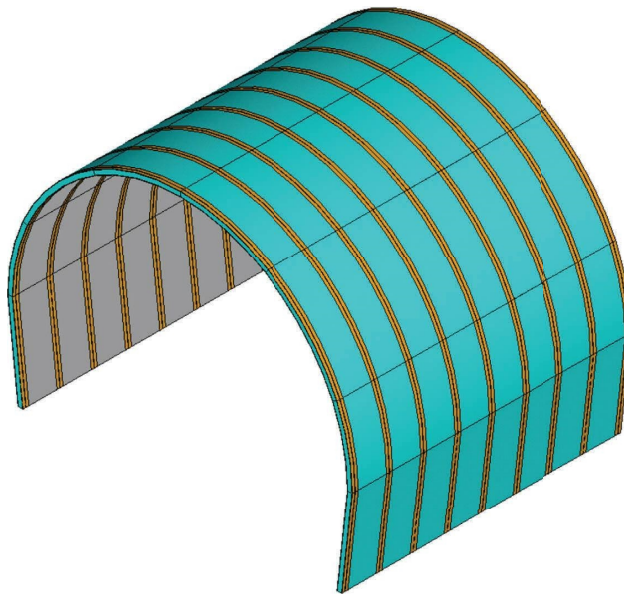
FIGURE 13: Steel frame steel plate concrete composite model.

The steel frame parameters were selected according to the code for railway tunnel design (TB 10003-2016).

4.6.2. Analysis Results

① *H175 Steel Frame (Spacing: 1.0 m)*

The maximum tensile stress of the steel frame was 28.9 MPa, which occurred at the top of the side wall, meeting the specification requirements (Figure 12).

The maximum tensile stress of the steel plate was 3.09 MPa, which occurred at the bottom of the side wall, meeting the specification requirements (Figure 13).

The maximum tensile stress of the newly poured concrete structure was 2.03 MPa, which occurred at the top of the side wall. It met specification requirements but was close to the tensile limit of the concrete.

② *H125 Steel Frame (Spacing: 1.0 m)*

The maximum tensile stress of the steel frame was 30.9 MPa, which occurred at the top of the side wall, meeting the specification requirements (Figure 14).

The maximum tensile stress of the steel plate was 3.42 MPa, which appeared at the bottom of the side wall, meeting the specification requirements (Figure 15).

4.7. Application Effect. In 2021, after the Daheishan Tunnel was reinforced with the lining steel arch frame structure (Figures 16 and 17), the crack and cavity of the tunnel lining were effectively repaired; the service capacity of the lining structure was effectively improved; the speed limit of the train in the diseased section was lifted; and the train returned to normal operation (see Figures 18 and 19).

TABLE 1: Parameters of surrounding rock.

Surrounding rock level	Bulk density γ (kN/m^3)	Elastic reaction coefficient K (MPa/m)	Deformation modulus E (GPa)	Poisson ratio ν	Internal friction angle φ (°)	Cohesion c (MPa)	Calculated friction angle φc (°)
IV	20–23	200–500	1.3–6	0.3–0.35	27–39	0.2–0.7	50–60

TABLE 2: Material parameters.

Project	Elastic modulus (GPa)	Poisson ratio	Ultimate tensile value (MPa)	Density (kg/m^3)
Existing concrete lining	15.75	0.2	1.1	2500
Fresh concrete	31.5	0.2	2.2	2500
Steel frame	210	0.3	420	7850

-.238E+07   .456E+07   .115E+08   .185E+08   .254E+08
        .109E+07   .804E+07   .150E+08   .219E+08   .289E+08
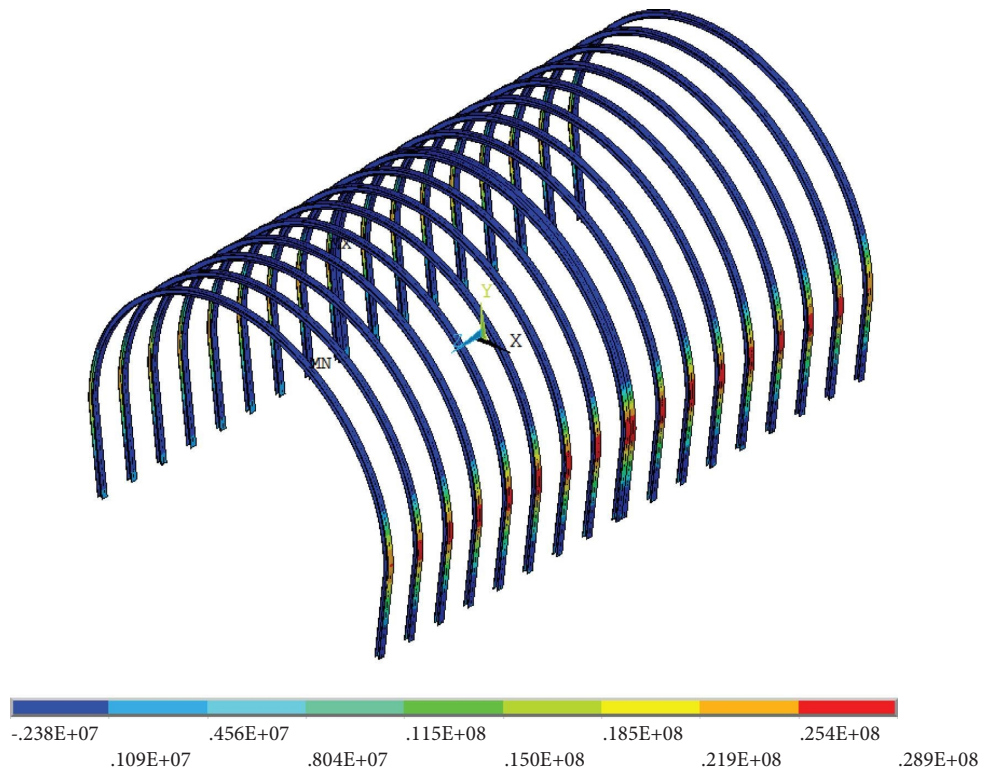
FIGURE 14: Stress diagram of steel frame with H175 steel.

−380587   390482   .116E+07   .193E+07   .270E+07
        4947.5   776016   .155E+07   .232E+07   .309E+07
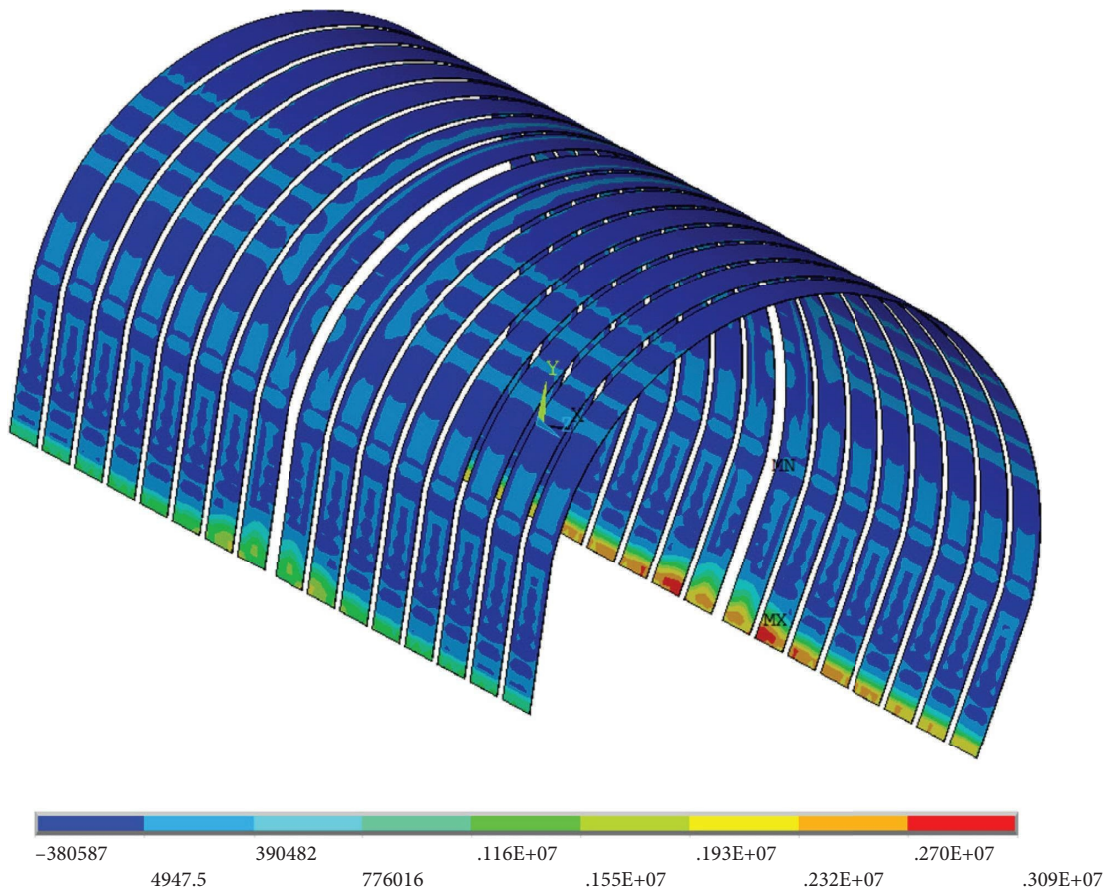
FIGURE 15: Stress diagram of steel plate with H175 steel frame.

.289E+07 .461E+07 .121E+08 .196E+08 .271E+08
861111 .836E+07 .159E+08 .234E+08 .309E+08
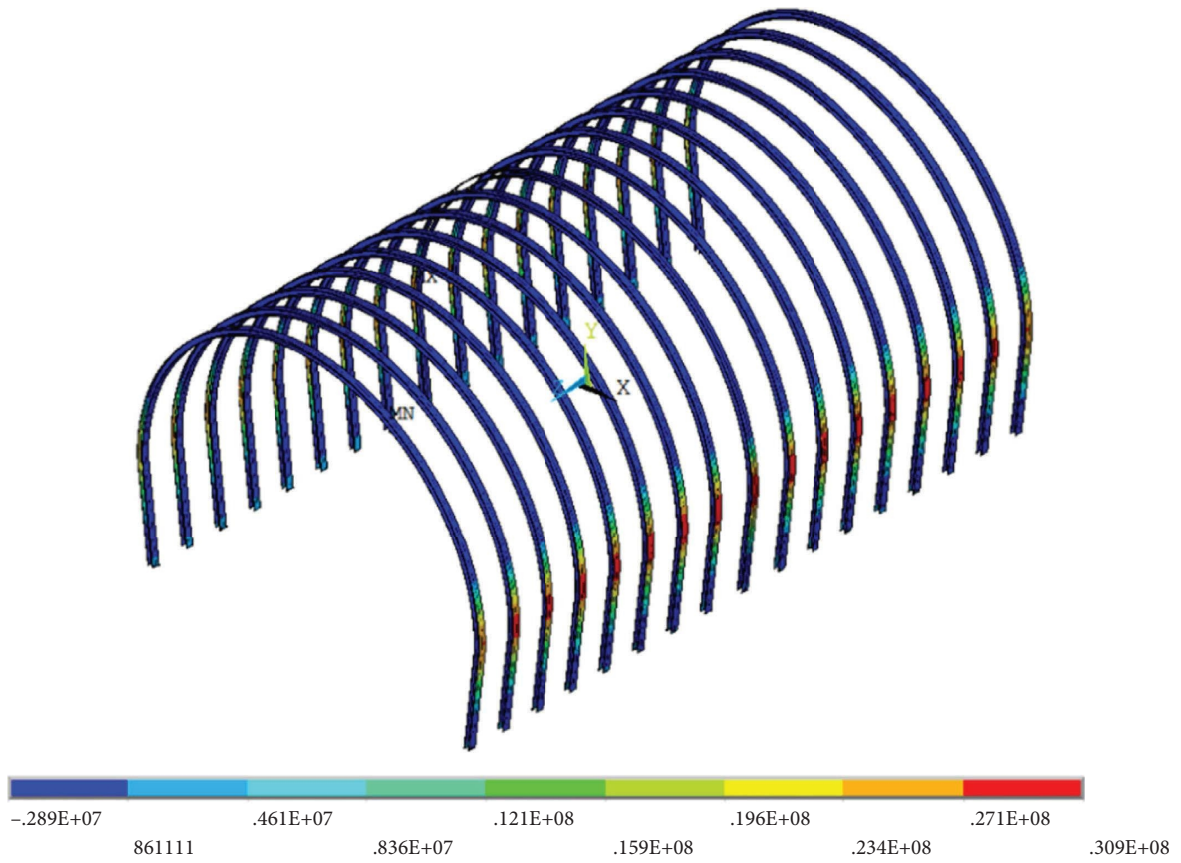
Figure 16: Stress diagram of steel frame with H125 steel frame.

−415643 436722 .129E+07 .214E+07 .299E+07
10539.6 862905 .172E+07 .257E+07 .342E+07
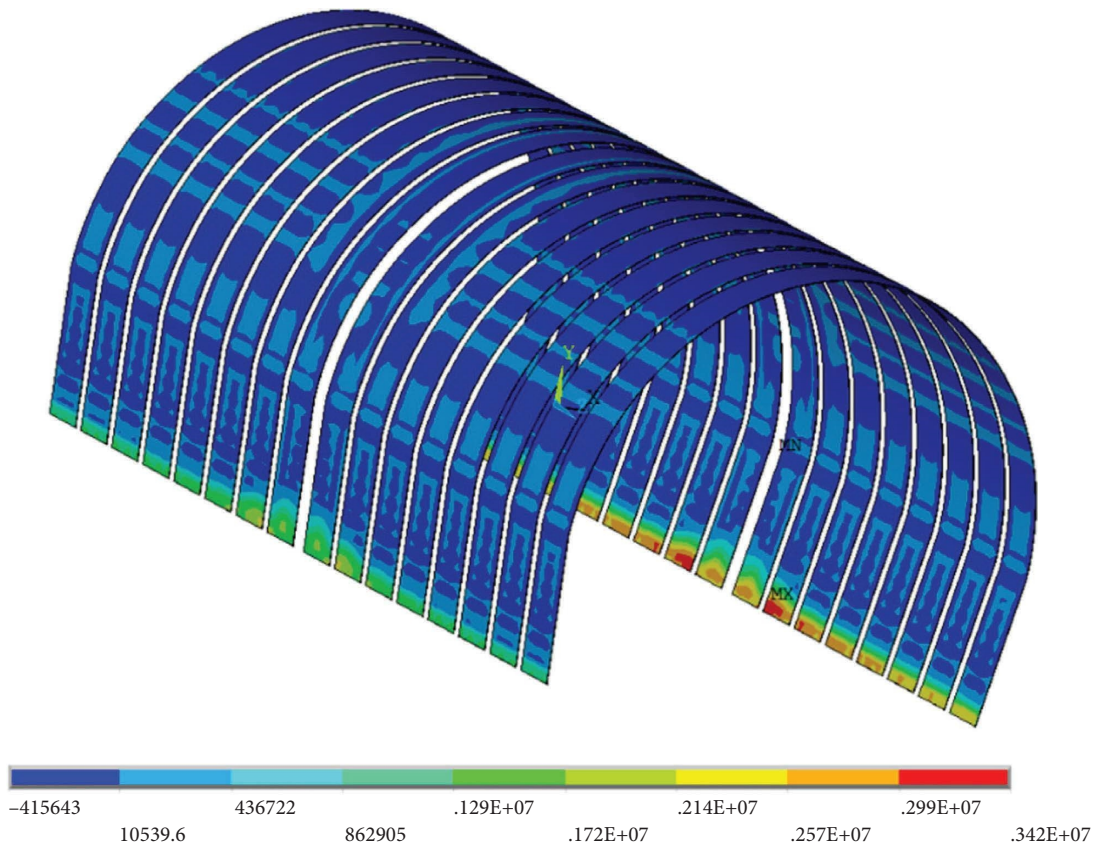
Figure 17: Stress diagram of steel plate with H125 steel frame.

FIGURE 18: Installation site of steel arch.

FIGURE 19: Installation site of connecting reinforcement and steel plate.

5. Conclusions and Further Observations

5.1. Conclusions

(1) The lining disease of narrow double-track heavy-haul railway tunnel can be repaired with limited maintenance "window" time without affecting the normal operation of the catenary and power supply facilities. This technology has great practical significance and broad application prospect.

(2) When H175 and H125 steel frames with an arrangement spacing of 1 m were used, the steel frame, steel plate, and concrete met the material tensile strength requirements set out in the *Code for Design of Railway Tunnel of China* (TB 10003-2016), indicating that the lining steel arch frame reinforcement structure of "circumferential H-section steel + welded steel plate between arches + filled concrete between slab walls" for a double-track railway tunnel is feasible as a whole.

5.2. Further Observations.
Through theoretical analysis and numerical simulation, the compressive strength of the reinforced structure of a lined steel arch frame in a double-track railway tunnel was analyzed, and the applicability and effectiveness of the reinforcement scheme were verified by field work. Although some conclusions were drawn, this paper had limitations due to time and conditions.

(1) This paper only analyzed the tensile capacity of each component of the reinforced structure and did not compare and analyze the stress state of the lining before and after reinforcement. In the next step, changes to the stress state of lining before and after reinforcement will be studied in depth.

(2) In the field verification, long-term health monitoring of the reinforced structure was not carried out. In subsequent research, sensors will be installed in the reinforced structure for real-time health monitoring.

6. Conclusion

(1) The technology is simple and can effectively repair the defects of railway tunnel bottom structure under the conditions of narrow site, short time of maintenance skylight, strict requirements of track size variation, and no interference with normal operation of train, which has great significance and broad application prospect.

(2) The drainage system of the existing railway tunnel bottom can be applied to the bottom structure renovation of railway tunnel. The high-strength transverse diversion structure at the bottom of the tunnel has the advantages of strong bearing capacity, high drainage capacity, and corrosion resistance, which can provide reference for the subsequent implementation of the reconstruction project of the bottom structure of railway tunnel.

Data Availability

The data used to support the findings of this study are included within the article.

Conflicts of Interest

The authors declare that there are no conflicts of interest regarding the publication of this paper.

Authors' Contributions

Weibin Ma and Jinfei Chai contributed to the central idea, analyzed most of the data, and wrote the initial draft of the paper. Xiaoyan Du interpreted the result. Yao Li contributed to the project overview and cause analysis. Peng Zhao contributed to the analyses. All authors discussed the results and revised the manuscript.

Acknowledgments

References

[1] J. F. Gong, G. R. Tang, and W. Wang, "Statistics of China's railway tunnels by the end of 2021 and design & construction overview of gaoligongshan tunnel," *Tunnel construction (Chinese and English)*, vol. 42, no. 3, pp. 508–517, 2022.

[2] C. F. Lu, "Maintenance mode and key technology of high speed railway bridge and tunnel engineering," *China Railway*, vol. 7, pp. 1–8, 2017.

[3] W. B. Ma, J. F. Chai, D. G. Cai et al., "Research on in situ stress distribution of the railway tunnels in southwest China based on the complete temperature compensation technology," *Shock and Vibration*, vol. 2021, Article ID 7170850, 14 pages, 2021.

[4] W. B. Ma, J. F. Chai, Z. F. Zhu et al., "Research on vibration Law of railway tunnel substructure under different axle loads and health conditions," *Shock and Vibration*, vol. 2021, Article ID 9954098, 14 pages, 2021.

[5] W. B. Ma, J. F. Chai, Z. L. Han et al., "Research on design parameters and fatigue life of tunnel bottom structure of single-track ballasted heavy-haul railway tunnel with 40-ton axle load," *Mathematical Problems in Engineering*, vol. 2020, Article ID 3181480, 9 pages, 2020.

[6] Z. L. Han, W. B. Ma, J. F. Chai et al., "A treatment technology for optimizing the stress state of railway tunnel bottom structure," *Shock and Vibration*, vol. 2021, Article ID 9191232, 13 pages, 2021.

[7] J. F. Chai, "Research on dynamic response characteristics for basement structure of heavy haul railway tunnel with defects," *Mathematics*, vol. 9, no. 22, p. 2893, 2021.

[8] J. F. Chai, "Research on multijoint rock failure mechanism based on moment tensor theory," *Mathematical Problems in Engineering*, vol. 2020, Article ID 6816934, 17 pages, 2020.

[9] G. Q. Zhao, "Treatment method of cracking in railway tunnel lining," *Chinese Journal of Rock Mechanics and Engineering*, vol. 15, no. 4, pp. 385–389, 1996.

[10] J. Cheng, J. S. Yang, and N. Cao, "Study on crack remediation and reinforcement to lining in railway tunnel," *Journal of Safety Science and Technology*, vol. 10, no. 9, pp. 134–139, 2014.

[11] D. Z. Cheng, *Study on the Lining Crack Disease of Tunnel and its Control Measures in High Speed Railway*, Ph.D. Thesis, Central South University, Changsha, China, 2012.

[12] Y. B. Niu, Q. L. Zhang, and W. B. Ma, "The Generating mechanism and control measures for disease of heavy-haul railway tunnel," *Railway Engineering*, vol. 56, no. 7, pp. 34–37, 2012.

[13] D. Y. Yu, *Study of Safety Evaluation and Treatment Measures of Cavity Defects behind Railway Tunnel Lining*, China Academy of railway sciences, Beijing, China, 2019.

[14] H. J. Ma, S. M. Tian, and B. X. Fu, "Application and development of corrugated pipe(plate) technology for railway engineering," *China Railway*, vol. 1, pp. 91–101, 2019.

[15] Q. Wu, P. P. Peng, and Y. M. Cheng, "The interpolating element-free Galerkin method for elastic large deformation problems," *Science China Technological Sciences*, vol. 64, no. 2, pp. 364–374, 2021.

[16] H. Cheng, M. J. Peng, Y. M. Cheng, and Z. Meng, "The hybrid complex variable element-free Galerkin method for 3D elasticity problems," *Engineering Structures*, vol. 219, Article ID 110835, 2020.

[17] J. Li and J. Wu, "Study on elastoplastic damage constitutive model of concrete I: basic formula," *Journal of Civil Engineering*, vol. 38, pp. 14–20, 2005.

Research Article

Numerical Investigation into the Effects of Controlled Tunnel Blast on Dynamic Responses of the Transmission Tower

Feng Wang,[1] Gaohai Zhang,[2] Wenwen Li [ID],[3] and Hongwei Nie[4]

[1]*China Railway 18th Bureau Group Co., Ltd., Tianjian, China*
[2]*China Railway Construction Investment Co., Ltd., Beijing, China*
[3]*Changshu Institute of Technology, Suzhou, China*
[4]*Soochow University, Suzhou, China*

Correspondence should be addressed to Wenwen Li; lwwgeo@hotmail.com

At present, the drill-and-blast method is still one of the main construction means in the road tunnel excavation process. When the tunnel penetrates underneath sensitive structures such as high-voltage transmission towers, the blasting and supporting parameters must be strictly controlled to ensure the stability and safety of the surface structures. In this paper, numerical simulations based on a large-section shallow buried tunnel project in Zhuhai are conducted to study the effect of controlled tunnel blast on the dynamic response of transmission towers. The numerical simulation results indicate that the blast vibration velocity of the rock generated by controlled blasting decreases rapidly along the tunnel excavation direction. The blast vibration velocity of the high-voltage transmission tower and its pile foundation gradually increases with the propagation of the blast waves, and the maximum vibration velocity is about 1.24 cm/s. The results indicate that the controlled blasting design of this project can effectively restrain the vibration velocity induced by the blasting load and could ensure the stability and safety of the transmission tower.

1. Introduction

With the rapid development of highways in China, large-section tunnels are widely used in highway construction because of their ability to significantly reduce road mileage and improve transport efficiency. The tunnels would sometimes inevitably penetrate beneath sensitive structures, such as transmission towers and other existing structures, which poses challenges for the design and construction of large-section tunnels.

At present, the drill-and-blast method is still one of the main construction methods in the road tunnel excavation process [1–3]. When the tunnel penetrates underneath sensitive structures such as high-voltage transmission towers, the blasting and support parameters need to be strictly controlled to ensure the stability and safety of the surface structures. To study the influence of vibration caused by controlled blasting on rock mass and sensitive structures, site test and numerical simulation methods are widely used

by researchers [4–7]. The site test can objectively reflect the influence of blasting vibration on the rock mass structure. However, due to the nonhomogeneity and the defects of the internal structure in the rock mass, the experimental conditions are difficult to control. Compared with the site tests, the numerical calculation can simulate the dynamic response problem in the complicated geological conditions, thus the numerical simulation method is widely used to analyze the blasting vibration response. Some studies [8–10] evaluated the vibration damage to transmission towers based on the finite element method. Luo et al. [11] analyzed the dynamic characteristic of the tunnel for surface explosion of 100 and 300 kg TNT charge, respectively. Duan et al. [12] investigated the vibration characteristic of high-voltage tower under the influence of adjacent tunnel blasting excavation. Beside the study on the influence of vibration induced by controlled blasting on transmission tower, more research focuses on the dynamic responses of adjacent structures. Zhao et al. [13] used field monitoring

experiments and numerical simulation to study the effect of blast-induced vibration from adjacent tunnel on existing tunnel. Jiang et al. [14] investigate the effect of excavation blasting vibration on adjacent buried gas pipeline in a metro tunnel. However, the dynamic responses of the transmission tower system remain one of the most challenging tasks in the civil engineering as a complex, continuous, and mechanical system.

Based on a large-section shallow buried tunnel project in Zhuhai, China, this paper studies the effects of controlled tunnel blasting on the dynamic responses of high-voltage transmission towers. Three-dimensional numerical analyses were conducted in the finite difference program FLAC3D, and the dynamic responses of the tunnel surrounding rock and high-voltage transmission towers under the blast loading were studied. The vibration velocity, deformation responses of surrounding rock and high-voltage transmission towers were predicted to provide scientific basis and reference for relevant construction optimization and decision-making.

2. Overview of the Project

The Black and White General Hill tunnel is a large-section shallow buried tunnel under construction in Zhuhai, China, which is built to enhance the transportation links between different districts in Zhuhai. The exit section of the tunnel penetrates directly underneath a high-voltage transmission tower. A schematic view of the locations of the tunnel and transmission tower is shown in Figure 1. The transmission tower is a 2F-SJ2 type tower with a total height of 41.5 m, supported by four piles with a diameter of 2.1 m and a length of 12 m. The vertical distance from the top of the tunnel to the pile toe is about 7.5 m, and the smallest horizontal distance from the tunnel to the transmission tower is about 1.9 m.

The surrounding rocks at the tunnel exit consisted of medium strongly weathered quartz amphibolite. The arches and sidewalls of the tunnel exit are of poor stability, which could lead to rock collapse and drops at drill-and-blast excavation. The uneven weathering of the surrounding rocks has an impact on the stability of the tunnel portal and the side slopes. These geological conditions would pose a threat to the stability of the transmission tower.

According to the geological survey, the soil stratum from top to bottom within the exploration depth is divided into clay, fully weathered, strongly weathered, medium weathered, and slightly weathered quartz amphibolite. Based on the results of the wave velocity test and other geotechnical tests, the physical properties of the soil and rock are shown in Table 1.

3. Numerical Investigation

3.1. Numerical Model. A 100 m range of tunnel exit (mileage YK4 + 820–YK4 + 920) is selected as the modelling area, with the tunnel and transmission tower included. The numerical model built in FLAC3D is shown in Figure 2. Considering the influence of tunnel depth and blasting, the total length
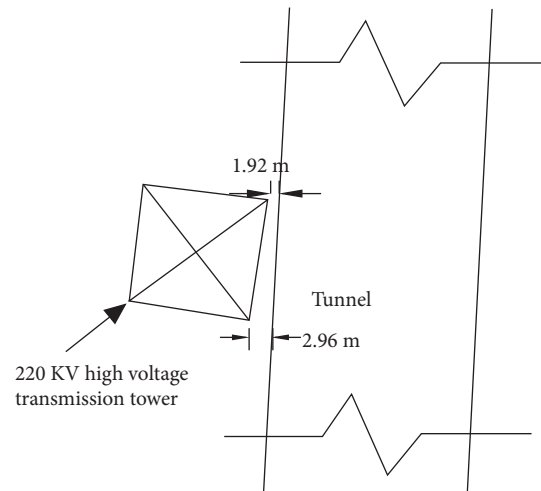
Figure 1: Schematic view of the locations of the tunnel and transmission tower.

and width of the model are selected as 100 m and 52 m, respectively, which could effectively reduce the boundary effect. The axis used in the numerical model is defined as follows: X axis is along the direction of tunnel excavation; Y axis is along the cross-section of the tunnel; and Z axis is along the gravity direction. The numerical model mainly consisted of the tunnel, surrounding rocks, transmission tower, and its file foundation. It is noted that the transmission tower and its pile foundation are modelled using the structure elements implanted in FLAC3D to reduce model complexity and increase calculation speed. The total number of zones in the 3D numerical model is 112,400, and the total number of nodes is 12033.

The high-voltage transmission tower is built upon a hill which the tunnel penetrates through. The curved surface of the hill needs to be considered in the numerical model to obtain a correct initial stress condition in the surrounding rocks. The curved surface is generated in SketchUp by importing the contour lines of the hill. Then, the 3D hill surface is exported to FLAC3D, and it connects with the tunnel model built in FLAC3D to form the 3D numerical model. The process of model generation is shown in Figure 3. The soil layer distribution is generated based on the geological data using the curved surface import method.

3.2. Constitutive Model and Material Parameters. The Mohr–Coulomb model is selected as the constitutive model for the soil and rock in this project. The parameters of density, cohesion, and friction angle are adopted directly from the geological survey data, which is shown in Table 1. The transmission tower is modelled with the beam element implemented in FLAC3D, which is a two-noded, straight, finite element with six degrees of freedom per node. The beam element has three material parameters, density, elastic modulus, and Poisson's ratio, which are set to be 7850 kg/m^3, 200 GPa, and 0.3, respectively. The pile foundation of the transmission tower is modelled using the pile element, which could effectively simulate the normal-directed

TABLE 1: Property parameters of the soil.

Soil layer	Name	Density (kN/m³)	Cohesion (kPa)	Friction angle (°)	Elastic modulus (MPa)	Poisson's ratio
1	Clay	19.8	25	20	20	0.38
2	Fully weathered quartz amphibolite	23.0	26	28	48	0.35
3	Strongly weathered quartz amphibolite	27.7	28	30	70	0.32
4	Medium weathered quartz amphibolite	28.9	5.5×10^3	41	4.0×10^4	0.30
5	Slightly weathered quartz amphibolite	30.0	7.0×10^3	42	6.5×10^4	0.23
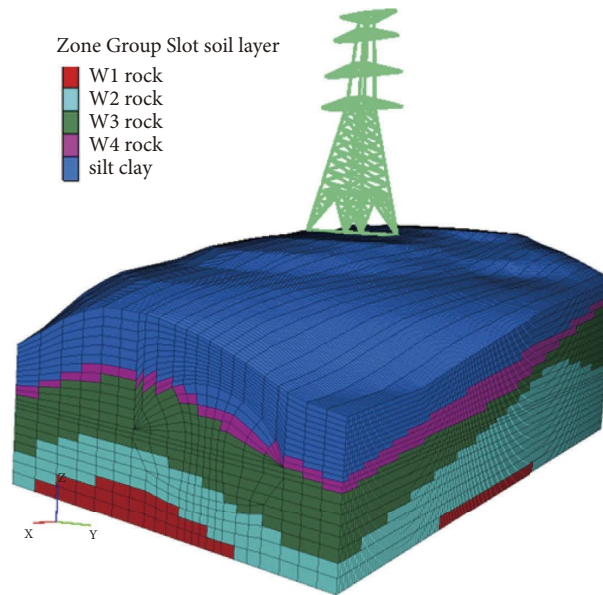
FIGURE 2: 3D numerical model.

(perpendicular to the pile axis) and shear-directed (parallel with the pile axis) frictional interaction between the pile and the soil. The soil-pile interaction is considered by the shear and normal coupling springs. The coupling springs are nonlinear, spring-slider connectors that transfer forces and motion between the pile and the grid at the pile nodes. The shear behavior of the pile-grid interface is cohesive and frictional in nature. The lining and anchors used as tunnel supporting are simulated with the liner element and cable element, respectively. The parameters of the structure element (pile, liner, and cable) adopted in this paper are shown in Tables 2–4.

3.3. Blasting Load. Due the short distance from the tunnel and the sensitivity of the transmission tower, the controlled blast and double-sided guide-pit method are adopted in the excavation and initial support of tunnel exit to ensure the stability of the transmission tower. The detailed blast-hole distribution and blasting sequences for the double-sided guide-pit method are shown in Figure 4. There are about 330 blast-holes in each blast section, distributed in a cross-sectional area of 305 m². The unit explosive consumption is about 0.9 kg/m³ for the controlled blast design. In order to study the effect of controlled blast on the dynamic responses of the transmission tower and surrounding rock, the blast load generated by millisecond delay blasting needs to be applied at the tunnel.

In the process of blasting, the interaction of stress waves generated by blasting will make cracks spread along the connecting line of adjacent blastholes. With the growth of the blast induced crack and interpenetration throughout the rock, a new free surface will be created along the blasthole line, which is the designed blasting excavation boundary. Therefore, the blasting excavation boundary is taken as the inner boundary of the numerical model. Thus, the full scale blastholes are not included in this model, and the blasting pressure is applied equivalently to the excavation boundary, which avoids tremendous model meshing and computational work due to detonations of too many tiny blastholes.

In this paper, an equivalent pulse load of the multihole blasts is applied at the blasting excavation boundary of the tunnel. This simplified equivalent load method certainly causes some deviation in the immediate vicinity of blastholes. However, this study is to investigate the dynamic responses of the transmission tower and surrounding rocks outside the blasting boundary rather than the explosion-induced rock fracture and fragmentation process around blastholes. Therefore, this equivalent pulse load simplification is acceptable to a certain degree. Following the procedure used by Yang et al. [15, 16], the equivalent pulse load applied in this paper is shown in Figure 5.
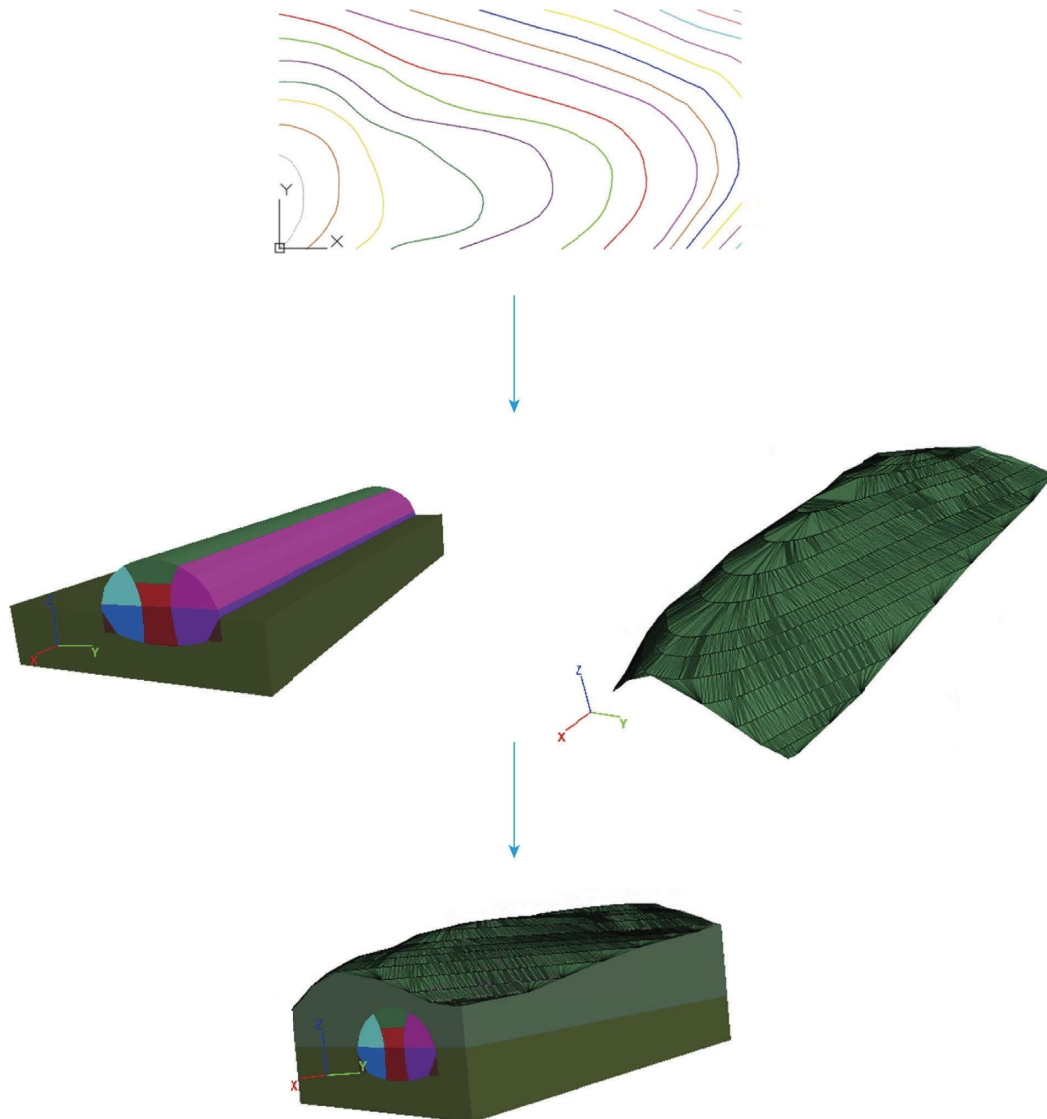
Figure 3: Process of 3D surface model generation.

3.4. Analysis Procedures and Boundary Condition. The focus of the research in this paper is to investigate the dynamic responses of the transmission tower under tunnel blasting to ensure the stability and functionality of the transmission tower. Therefore, the numerical study chooses the condition where the tunnel has been excavated directly underneath the transmission tower, and the initial support and cables have been installed in the excavated part of the tunnel, which is shown in Figure 6. The blast load generated by the first section of the tunnel (as shown in Figure 4) beneath the transmission tower is applied at the numerical model, when the influence of the blast on the transmission tower is the most obvious.

Before the blast loading is applied, the boundary of the numerical model is set to be fixed in their normal direction to calculate the initial stress condition. In static analysis, fixed boundaries applied here are realistic since the model size is large enough and the boundary is placed at some distance from the region of interest. However, such boundary conditions cause the reflection of outward

propagating waves back into the model and do not allow the necessary energy radiation. Therefore, the fixed boundary condition is converted into a viscous boundary by using independent dashpots in the normal and shear directions at the model boundaries in the dynamic loading stage.

4. Results and Discussions

4.1. Responses of the Surrounding Rock. To ensure the stability of the transmission tower, the dynamic responses of the surrounding rock are analyzed first. Figure 7 shows the time histories of blast velocities measured at different distances from the blast surface. The maximum blast velocities along X, Y, and Z axis caused by controlled blasting of section 1 are about 9 cm/s, 0.58 cm/s, and 3 cm/s, respectively. It can be concluded that the control blasting of section 1 of the tunnel generates main vibration of surrounding rock in the tunnel excavation direction, while the Y and Z axis component is relatively small.

TABLE 2: Parameters of pile elements.

Type	Density (kg/m³)	Elastic modulus (GPa)	Poisson's ratio	Cross-sectional area (m²)	Coupling stiffness (GPa)	Coupling friction angle	Coupling cohesion (kPa)
Pile	2400	80	0.3	3.464	13	25	25

TABLE 3: Parameters of liner elements.

Type	Density (kg/m³)	Thickness (m)	Elastic modulus (GPa)	Poisson's ratio	Normal coupling stiffness (GPa)	Shear coupling stiffness (GPa)
Liner	2000	1	30	0.25	9.77	9.77

TABLE 4: Parameters of cable elements.

Type	Density (kg/m³)	Cross-sectional area (cm²)	Elastic modulus (GPa)	Grout cohesion (kPa)	Grout friction angle
Cable	2000	5.9	100	50	35
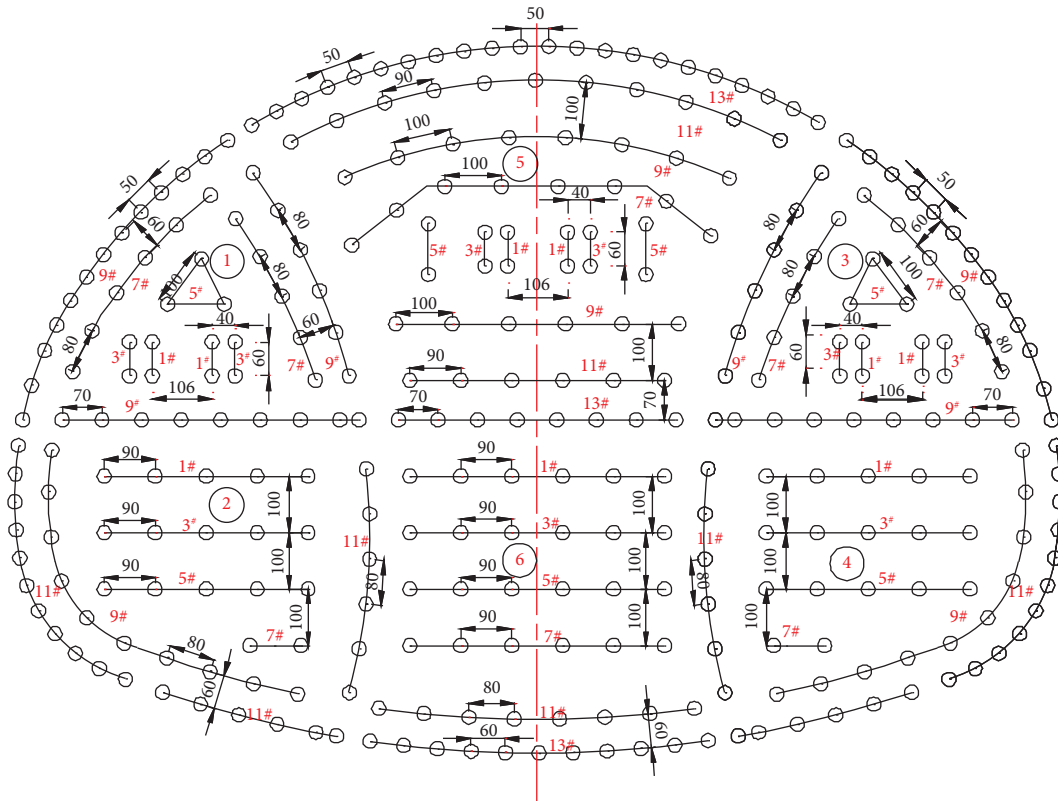
FIGURE 4: Blasting sequences of the double sidewall guide pit method.
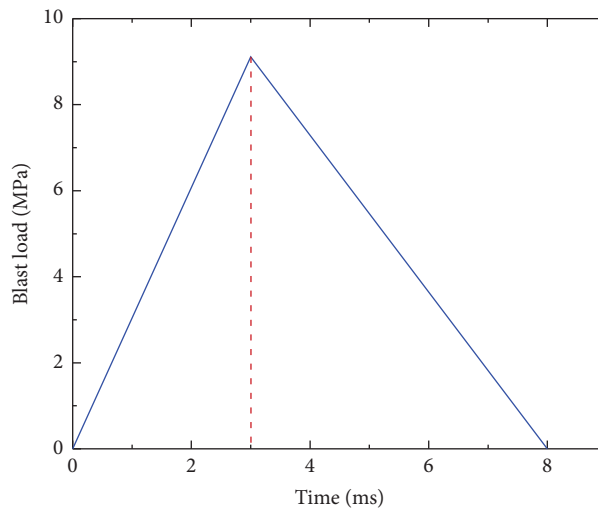
FIGURE 5: Time history of the equivalent pulse load.
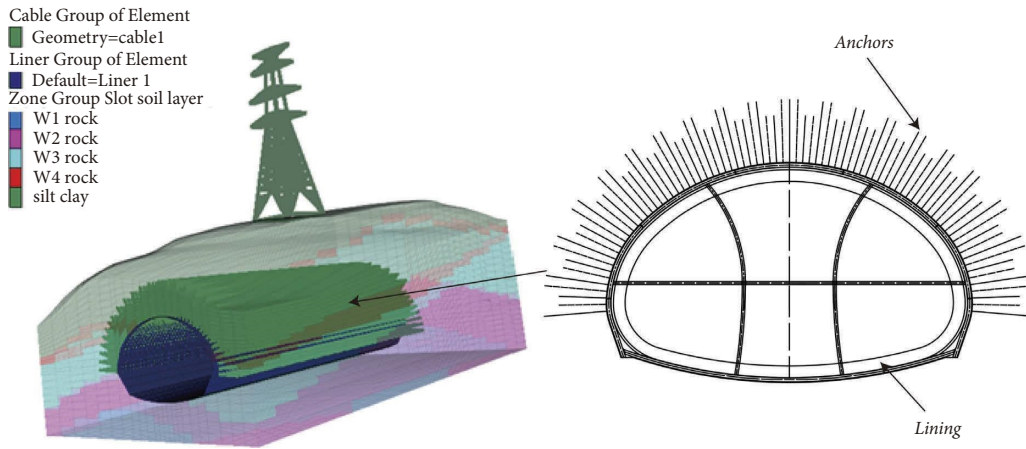
FIGURE 6: Initial support and cables of the tunnel.

(a)

(b)

(c)
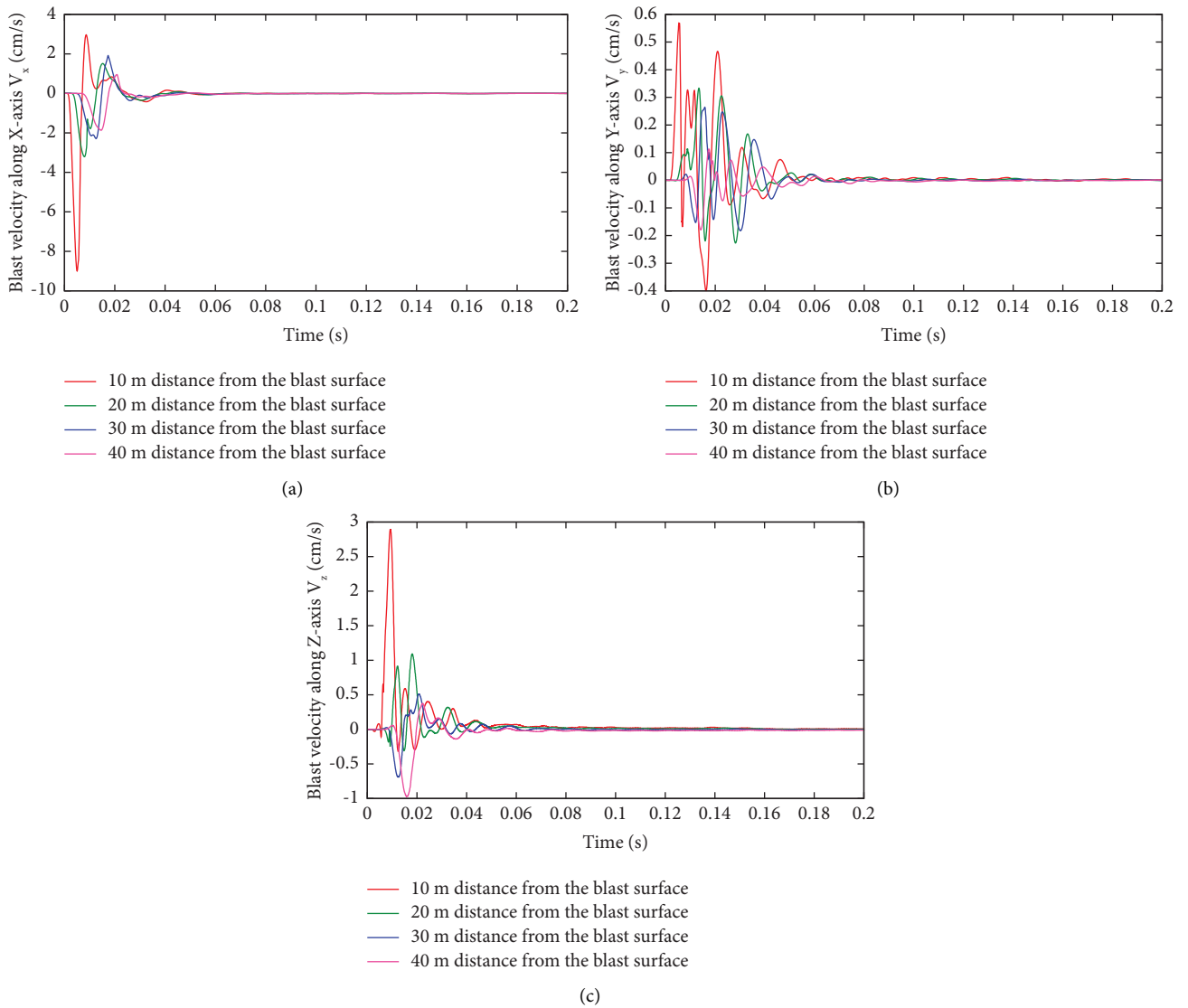
FIGURE 7: Time histories of blast velocities.
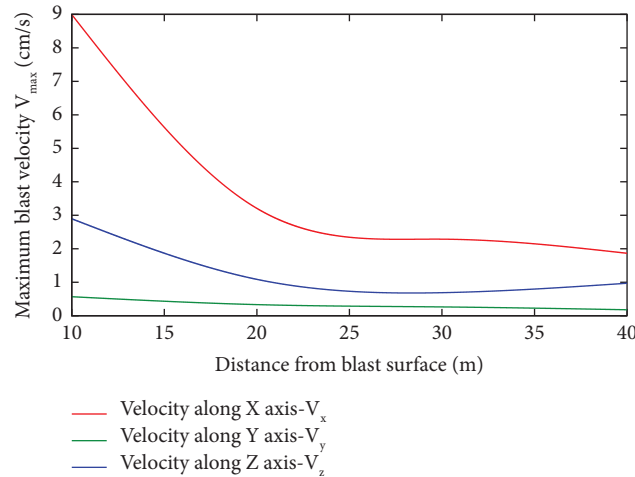
FIGURE 8: The maximum blast velocity distribution.
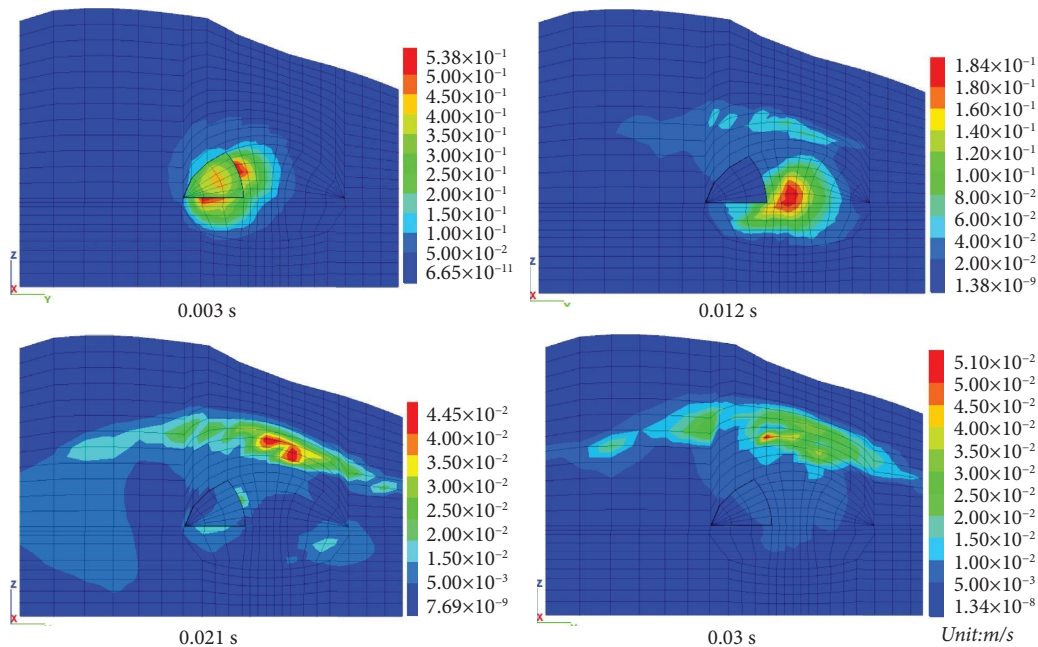
FIGURE 9: Blast velocity contour of the rock mass.

Figure 8 shows the decay curves of the maximum blast velocity along the tunnel excavation direction caused by controlled blasting in section 1, where the red, blue, and green curves are the velocity components in X, Y, and Z direction, respectively. As shown in the figure, the magnitude of blast velocity components in the three axes decreases rapidly in the range from 10 m to 20 m from the blast surface. Beyond that distance, the maximum blast velocity basically remains constant.

Figure 9 shows the blast velocity contour of the rock mass due to controlled blasting in section 1. The four contour graphs are captured at 0.003 s, 0.012 s, 0.021 s, and 0.03 s after blasting. It can be seen that at 0.003 s after blasting, the rock disturbance caused by controlled blasting of section 1 is basically concentrated within 4 m of the tunnel perimeter. With the increase of time, the range of rock

disturbance gradually expands, but its peak size decreases rapidly. After 0.02 s from the start of blasting, the blast velocity around the tunnel has basically decayed to zero, while the vibration velocity above the tunnel is the largest part of the rock mass at this time. Therefore, the controlled blasting design of this project can effectively control the blasting vibration velocity of the rock around the tunnel, which meets the safety requirements of the specification and can effectively ensure the safety and stability of tunnel blasting.

Figure 10 shows the maximum dynamic stress induced by the controlled blast, which is measured at 3 ms. As shown in the figure, the maximum dynamic stress occurred at the surrounding rock located near the blast section, with a value about 10 MPa. The dynamic stress decreases dramatically with the increase of distance from the blast section, with an
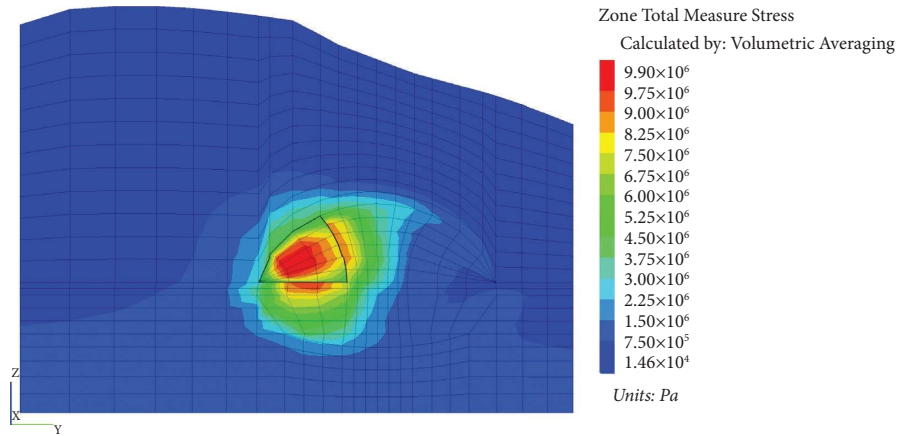
FIGURE 10: The maximum dynamic stress measured at the blasting surface.
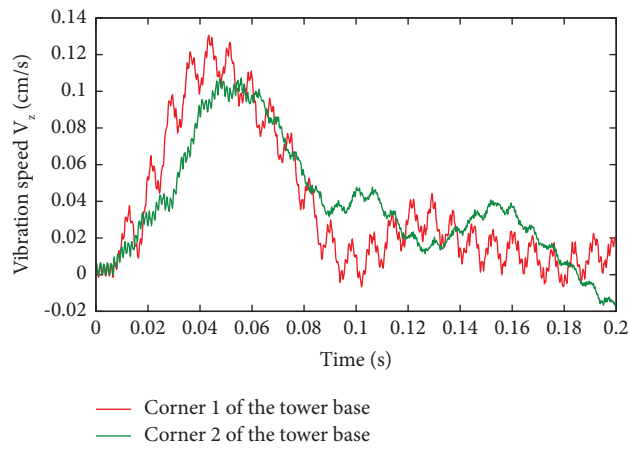
FIGURE 11: Vibration speed time histories at the tower base.
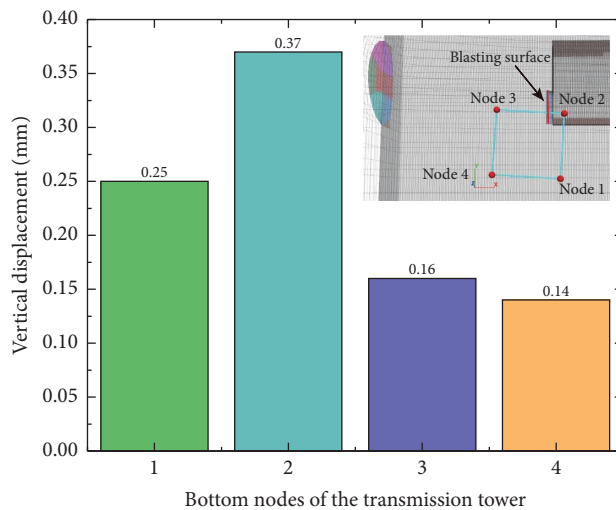
FIGURE 12: Vertical displacement measured at the tower base.

80% reduction in the peak value at the location with a distance of two times the largest dimension of the blast section from the blast center.

4.2. Responses of the Transmission Tower. Figure 11 shows the time histories of blasting velocity in Z direction at the corners of the base of the high-voltage tower. During the
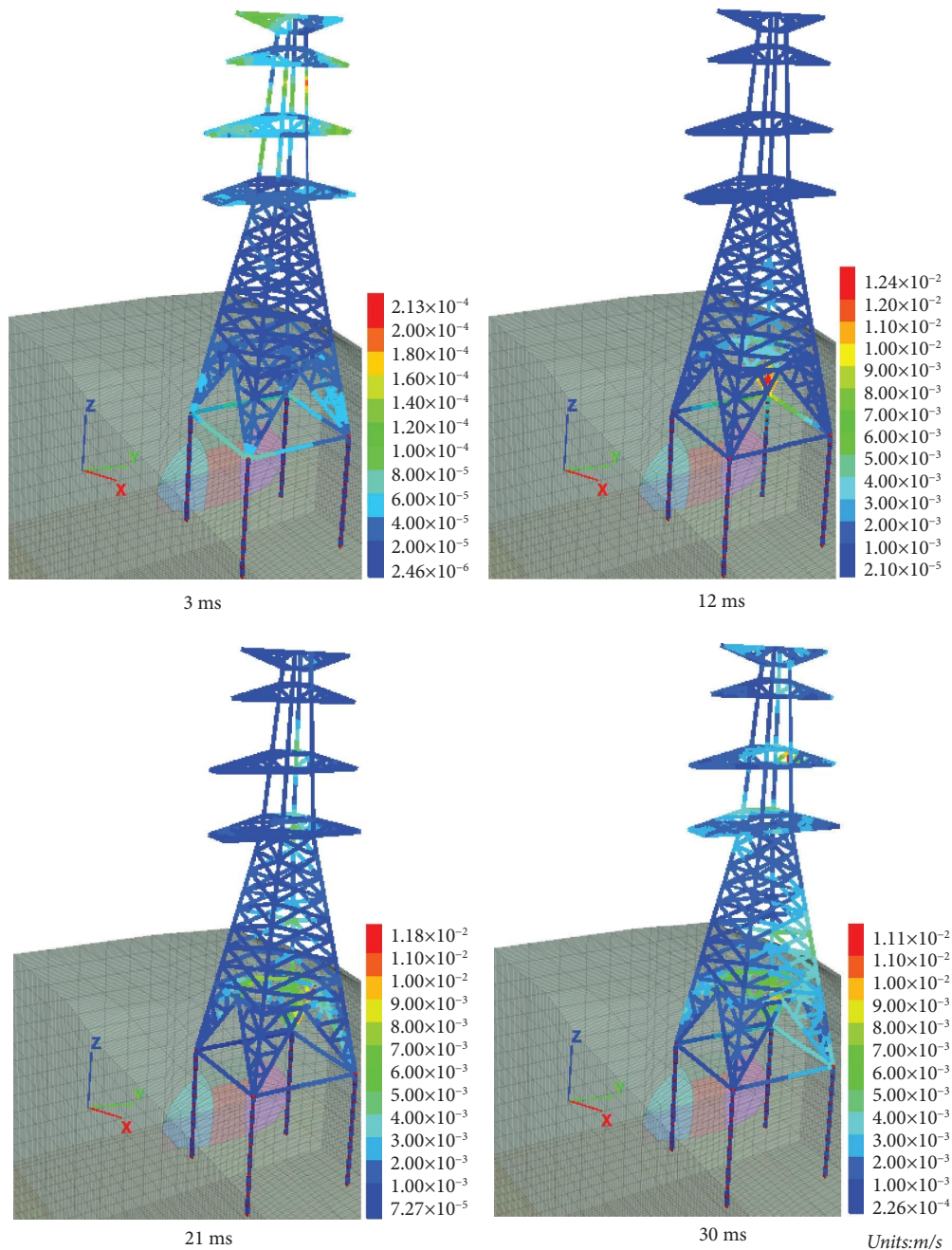
FIGURE 13: Vibration speed contour of the transmission tower.

controlled blasting of tunnel section 1, the blasting vibration in Z direction first increases and then decreases, with a peak value of about 0.12 cm/s. The blasting vibration velocity Vz in the Z-axis direction decreases to zero at about 0.2 s after the blasting. Therefore, the magnitude of velocity measured at the base of the transmission tower is relatively small and will not pose a threat to the stability of the transmission tower, which demonstrates the validity of the controlled blasting design.

The differential settlement of the transmission tower is a key factor to monitor in practice to ensure the stability of the transmission tower. Therefore, the vertical displacements

of the tower base are measured at the end of blast loading. Figure 12 presents the vertical displacement at the four corner nodes of the tower base and their relative position to the blasting surface. The maximum and minimum vertical displacements of the tower base are about 0.37 and 0.14 mm, respectively, which would result in a differential settlement of 0.23 mm. It can be concluded that the differential settlement would only cause a neglectable tilt angle and would not threaten the stability of the transmission tower.

Figure 13 shows contour of vibration speed of the transmission tower generated by controlled blasting. As can be seen, the maximum vibration speed of the transmission
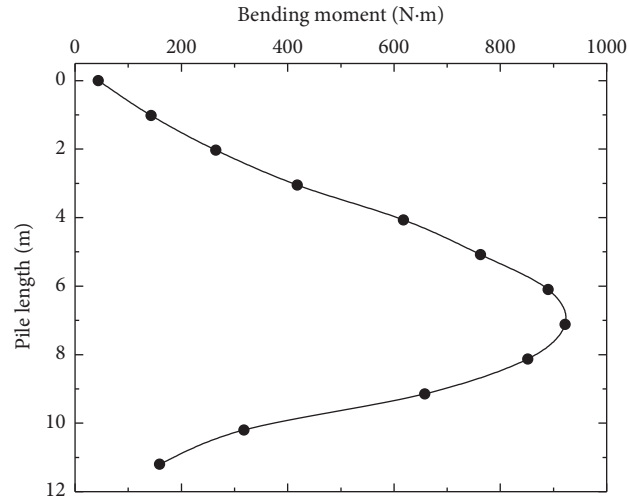
Figure 14: Maximum bending moment of the pile foundation.

tower and its pile foundation is about 0.02 cm/s at 0.003 s after the controlled blasting. As the blast wave in the rock propagates to the surface, the vibration speed of the transmission tower and its pile foundation gradually increases and its maximum vibration velocity is about 1.24 cm/s, which occurs at the location of the tower base 0.012 s after the blasting. Then, the vibration speed gradually decreases. It can be concluded that the design of controlled blasting of this project can ensure that the vibration speed of the transmission tower is below the safe vibration speed of 3.5 cm/s in the Chinese specification.

Due to the short distance between the pile foundation and the undercrossing tunnel, the dynamic responses of the pile foundation would also affect the stability of the transmission tower. Therefore, the maximum bending moment of the pile is measured during the controlled blasting, which is shown in Figure 14. The peak value of the bending moment developed in the pile is about 920 N·m, which is developed at 7 m below the pile top. Therefore, the blasting wave generated by controlled blast would not significantly affect the internal force in the pile. This result indicates that the pile foundation and the transmission tower remained stable during the blasting construction.

5. Conclusions

This paper investigates the dynamic effects of controlled tunnel blasting on surrounding rock and high transmission tower. A three-dimensional numerical analysis of a large section shallow buried tunnel under a transmission tower was conducted. The dynamic responses of the surrounding rock and the high transmission tower were analyzed in detail. The main conclusions can be drawn as follows:

(1) The vibration speed generated by controlled blasting decays rapidly along the tunnel excavation direction

(2) At 0.003 s after the start of blasting, the rock disturbance caused by controlled blasting of section 1 is basically concentrated within 4 m of the tunnel perimeter, and with the increase of time, the rock

disturbance range gradually expands, but its peak size decays rapidly

(3) As the blast wave in the rock mass propagates to the ground surface, the vibration speed of the transmission tower and its pile foundation gradually increases with a maximum vibration velocity of about 1.24 cm/s

(4) The controlled blasting design of this project can effectively restrain the vibration velocity of the surrounding rock and the transmission tower, which could ensure the stability and safety of the transmission tower.

Data Availability

The data come partly from the project site and engineering survey and partly from numerical simulations. All the data used to support the findings of this study are available from the corresponding author upon request.

Conflicts of Interest

The authors declare that they have no conflicts of interest.

Acknowledgments

References

[1] B. Duan, W. Gong, G. Ta, X. Yang, and X. Zhang, "Influence of small, clear distance cross-tunnel blasting excavation on existing tunnel below," *Advances in Civil Engineering*, vol. 2019, Article ID 4970269, 16 pages, 2019.

[2] X. Xia, H. B. Li, J. C. Li, B. Liu, and C. Yu, "A case study on rock damage prediction and control method for underground tunnels subjected to adjacent excavation blasting," *Tunnelling and Underground Space Technology*, vol. 35, pp. 1–7, 2013.

[3] Q. Liang, J. Li, D. Li, and E. Ou, "Effect of blast-induced vibration from new railway tunnel on existing adjacent railway tunnel in Xinjiang, China," *Rock Mechanics and Rock Engineering*, vol. 46, no. 1, pp. 19–39, 2013.

[4] N. Jiang and C. Zhou, "Blasting vibration safety criterion for a tunnel liner structure," *Tunnelling and Underground Space Technology*, vol. 32, pp. 52–57, 2012.

[5] M. Mohamadnejad, R. Gholami, and M. Ataei, "Comparison of intelligence science techniques and empirical methods for prediction of blasting vibrations," *Tunnelling and Underground Space Technology*, vol. 28, pp. 238–244, 2012.

[6] J.-H. Shin, H.-G. Moon, and S.-E. Chae, "Effect of blast-induced vibration on existing tunnels in soft rocks," *Tunnelling and Underground Space Technology*, vol. 26, no. 1, pp. 51–61, 2011.

[7] M. Monjezi, M. Ghafurikalajahi, and A. Bahrami, "Prediction of blast-induced ground vibration using artificial neural networks," *Tunnelling and Underground Space Technology*, vol. 26, no. 1, pp. 46–50, 2011.

[8] L. Tian, H. Li, and G. Liu, "Seismic response of power transmission tower-line system subjected to spatially varying ground motions," *Mathematical Problems in Engineering*, vol. 2010, Article ID 587317, 20 pages, 2010.

[9] F. Wang, Z. Su, Q. Li, and J. Yang, "Response analysis of cathead transmission tower seismic performance based on Open Sees," in *Proceedings of the 2014 Fifth International Conference on Intelligent Systems Design and Engineering Applications*, pp. 893–896, IEEE, Hunan, China, June 2014.

[10] H.-N. Li, W.-L. Shi, G.-X. Wang, and L.-G. Jia, "Simplified models and experimental verification for coupled transmission tower–line system to seismic excitations," *Journal of Sound and Vibration*, vol. 286, no. 3, pp. 569–585, 2005.

[11] K. Luo, Y. Wang, Y. Zhang, and L. Huang, "Numerical simulation of section subway tunnel under surface explosion," *Journal of PLA University of Science and Technology (Natural Science Edition)*, vol. 6, 2007.

[12] L. Duan, W. Lin, J. Lai, P. Zhang, and Y. Luo, "Vibration characteristic of high-voltage tower influenced by adjacent tunnel blasting construction," *Shock and Vibration*, vol. 2019, Article ID 8520564, 16 pages, 2019.

[13] H. Zhao, Y. Long, X. Li, and L. Lu, "Experimental and numerical investigation of the effect of blast-induced vibration from adjacent tunnel on existing tunnel," *KSCE Journal of Civil Engineering*, vol. 20, no. 1, pp. 431–439, 2016.

[14] N. Jiang, T. Gao, C. Zhou, and X. Luo, "Effect of excavation blasting vibration on adjacent buried gas pipeline in a metro tunnel," *Tunnelling and Underground Space Technology*, vol. 81, pp. 590–601, 2018.

[15] C. Z. Yang, Z. J. Yu, and S. F. Wang, "Analysis of the dynamic influence of the input blasting load on the tunnel surrounding rock," *Materials Research Innovations*, vol. 19, no. 8, pp. S8-S923–S8-930, 2015.

[16] J. H. Yang, C. Yao, Q. H. Jiang, W. B. Lu, and S. H. Jiang, "2D numerical analysis of rock damage induced by dynamic in-situ stress redistribution and blast loading in underground blasting excavation," *Tunnelling and Underground Space Technology*, vol. 70, pp. 221–232, 2017.

Hindawi

Research Article

Long-Term Effect Analysis of a High Slope with Tunnel Structure Based on Three-Dimensional Mesh Reconstruction

Youzhi Shi [ID],[1] Ganglie Yuan [ID],[2] Ailan Che [ID],[2] and Shixiong Qian [ID][3]

[1]School of Civil Engineering and Architecture, Xiamen University of Technology, Xiamen 361024, China
[2]Shanghai Key Laboratory for Digital Maintenance of Buildings and Infrastructure, School of Naval Architecture,
 Ocean and Civil Engineering, Shanghai Jiao Tong University, 800 Dongchuan-Road, Shanghai 200240, China
[3]Xiamen Road and Bridge Engineering Investment and Development Co., Ltd., Xiamen 361000, China

Correspondence should be addressed to Ganglie Yuan; yuanganglie@sjtu.edu.cn

The instability of high rock slopes with tunnel structures increases under the effects of earthquakes and rainfall. Limited studies have been conducted on the long-term effect analysis of high rock slopes with tunnels. Field electrical measurements on rock slopes have been conducted to study the response of high rock slopes with large cross-section tunnels during rainfall and seismic loading. The material threshold was determined using the resistivity probability density statistical method, and a three-dimensional geological visualization model was obtained. A three-dimensional mesh reconstruction method consisting of material segmentation, cluster filtering, mesh generation, and material attribute mapping modules was proposed. The three-dimensional model of high-cutting rock slope was reconstructed, and the three-dimensional finite element model of the rock slope with tunnel was obtained. The response analysis of the slope was performed during rainfall and seismic loading by employing the El-Centro wave. The results demonstrated that plastic strain was generated in the fracture zone of the upper part of the tunnel during rainfall, and the strain value was 8.135×10^{-4}. In the subsequent stages, it had a tendency to expand into the tunnel under continuous rainfall. The maximum principal strain was 3.324×10^{-2} under the effect of a strong earthquake. A large strain was generated in the fracture zone at the upper part of the tunnel. It had a tendency to expand under long-term load, which significantly affected the safety of the tunnel.

1. Introduction

The continuous increase in highway construction has led to the development of tunnels through high slopes with existing tunnel structures owing to the limitation of land use [1]. In a few cases, the tunnel is initially excavated, and the stress in the rock mass is allowed to gradually reach its equilibrium state untill the deformation of the rock mass becomes constant. The surface rock mass is excavated to form a slope. However, the slope stability and excavation response in such cases are different from those in cases without tunnel excavation in the rock mass because they affect the stress and deformation of the rock mass. The interaction between the slope and tunnel should be considered [2]. The presence of the tunnel might cause the

collapse or instability of the excavated slope. Additionally, the excavation and disturbance of the slope affect the stability of the tunnel [3]. Cracks develop on the slope due to the construction disturbance, particularly on high slopes. These cracks expand during rainfall and earthquakes, which damage the tunnel and slope. For example, extensive cracking occurred at the top of the slope, and landslides occurred in the Nanshan Tunnel of the Wankai Highway in Chongqing, China, due to disturbances caused during the excavation of the roadbed and frequent precipitation [4].

The stability of rock slopes and tunnels is mainly affected by factors such as rainfall [5], earthquakes [6, 7], geological structures (such as folds, discontinuities, and faults) [8, 9]. The unloading and blasting performed during the excavation process directly reduce the integrity of the rock mass, which

leads to fractures and cracks in the weak structural plane [10]. The weak structural surfaces significantly affect the stabilization of rock slopes [11]. Fractures and cracks expand during rainfall and earthquakes, and directly trigger the occurrence of landslides [12]. The tunnel structure and surrounding rock are vulnerable to damage in fracture zones under strong ground motion [13]. The tunnel-fault system can be divided into five main stages, strain localization, fracture initiation, crack acceleration, spontaneous crack growth and stabilization, which is a nonlinear failure process [14].

Several studies have been conducted on the stability of tunnels and slopes by various methods. Jiang et al. [15] proposed a modified BUS approach for the probabilistic back analysis of soil parameters and reliability updating of slopes in spatially variable soils, which facilitates the identification of the causes of slope failures and an understanding of the performance of in-service slopes. Shu et al. [16] analyzed the stability of 3D slopes characterized by spatially variable undrained shear strength based on the plastic limit analysis upper-bound theorem. Vo-Minh et al. [17] presented an isogeometric analysis (IGA) based on Bezier extraction to investigate the stability of a circular tunnel in cohesive-frictional soils subjected to uniform surcharge loading. Rasmussen et al. [18] developed the classic lattice spring model combined with the synthetic rock mass technique and Barton–Bandis joint constitutive model to analyze the probabilistic stability of rock tunnels in low in situ stress environments. Moreover, several studies have been conducted on the stability of high slopes with tunnel structure.

Numerical simulation, model testing, and field monitoring are mainly used to study the interaction between the tunnel and slope under excavation and earthquake [19]. He et al. [20] studied the effect of existing tunnels on the construction of intersecting tunnels in a shallow slope burial context through 3D numerical analysis and field monitoring. Causse et al. [21] focused on the mechanism of slope instability and damages that affect the structure of tunnels parallel to the slope. Kaya et al. [22] performed kinematic, limited equilibrium, and numerical stability analyses to investigate the mechanism of a failure of rock slope with a tunnel. Sun et al. [23] conducted a 1 : 25 large-scale shaking table model test on the bias loess tunnel, and the seismic responses and failure modes of the loess slope and bias tunnel were analyzed. The interaction between the tunnel structure and loess slope was studied. However, the previous studies conducted that the effect of weak structural surfaces on slopes with tunnels are inadequate, and deficiencies were observed in the analysis of the long-term effects of structures under the effects of rainfall and earthquakes.

Field drilling and geophysical exploration techniques are common methods that are used to determine the weak structural surfaces of rock slopes. Geological structures, including weak structural surfaces, can be identified through highly efficient geophysical exploration techniques [24]. In this study, field electrical measurements were conducted to determine the geological structures of the slope with tunnel structure and to study the response of a high-cutting slope with an existing large cross-section tunnel during rainfall and under seismic load. A three-dimensional mesh reconstruction method was proposed to develop a three-dimensional finite element model of the slope with tunnel structure. The long-term effect of the structure was analyzed by simulating rainfall and earthquakes.

2. Three-Dimensional Mesh Reconstruction

2.1. Material Segmentation. The three-dimensional mesh reconstruction method consisted of material segmentation, cluster filtering, mesh generation, and material attribute mapping. Material segmentation is a material processing method that is widely used in three-dimensional mesh model reconstruction. Material segmentation is used to classify the voxels in the three-dimensional visualization model, and each voxel corresponds to a material. Material segmentation can be divided into three types: threshold, edge, and region segmentation. Threshold segmentation is used to obtain the segmentation threshold through various algorithms, which can be considered the boundary of materials. Different material segmentation bases and segmentation methods result in different segmentation effects. The threshold (T) was determined using Otsu's method [25]. The discrete data points in the three-dimensional visualization model $F(i, j, k)$ were divided into different value range segments with different materials $G(i, j, k)$.

$$G(i, j, k) = \begin{cases} 0, F(i, j, k) \le T, \\ 1, T < F(i, j, k), \end{cases} \tag{1}$$

where i, j, k are the coordinate values in the three-dimensional visualization model, $F(i, j, k)$ is the discrete data points in the three-dimensional visualization model, and $G(i, j, k)$ is the value of data points after material segmentation.

2.2. Cluster Filtering. A cumulative marking method was proposed for a discrete data lattice to quickly and accurately determine the aggregation clusters in the three-dimensional data lattice. While accessing each data point, the marking of the current data point was determined, and the data points along the three axes, with the marking states of the previous adjacent points were combined. The data points were grouped according to the marking state to perform the identification of the scale of the data points in the aggregation cluster.

The position relationship of the data point (i, j, k) with six adjacent data points is shown in Figure 1. The six adjacent points were divided into three front and back points. The values $G(i, j, k)$, $G(i - 1, j, k)$, $G(i, j - 1, k)$, and $G(i, j, k - 1)$ of the current data point and the three front neighbors were recorded as G_S, G_1, G_2, and G_3, respectively.

The data lattice was sequentially marked by scanning along the positive directions of i, j, and k. If the data point of $G(i, j, k) = 1$ is the target to be marked first, the data point of $G(i, j, k) = 0$ was not marked temporarily. The cluster data points were combined, and eight previous states of the current element and the integration of the cluster are listed

FIGURE 1: Schematic diagram of adjacent points.

TABLE 1: Cluster integration.

Case	G_s	G_1	G_2	G_3	Aggregation cluster	m
1	1	0	0	0	New group	1
2	1	1	0	0	Group unchanged	$m_1 + 1$
3	1	0	1	0	Group unchanged	$m_2 + 1$
4	1	0	0	1	Group unchanged	$m_3 + 1$
5	1	1	1	0	Group merge	$m_1 + m_2 + 1$
6	1	1	0	1	Group merge	$m_1 + m_3 + 1$
7	1	0	1	1	Group merge	$m_2 + m_3 + 1$
8	1	1	1	1	Group merge	$m_1 + m_2 + m_3 + 1$
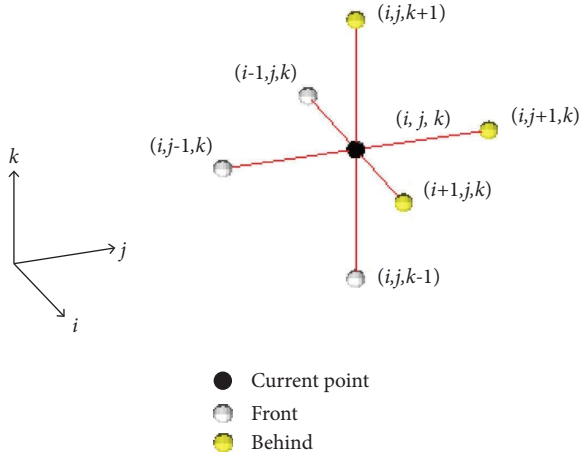
in Table 1, where m is the number of data points in the original cluster, and m_1, m_2, and m_3 are the number of data points in the original cluster where the three front adjacent points $(i-1, j, k)$, $(i, j-1, k)$, and $(i, j, k-1)$ are located, respectively.

The abovementioned cumulative mark scanning was performed, and the data point with $G(i, j, k) = 0$ was considered the target to be marked and was scanned again. The data points were assigned to different clusters according to their previous states. The cluster with data points m less than that of a certain value was defined as an outlier cluster, and the material attribute value $G(i, j, k)$ of the outlier cluster was converted, i.e., the cluster filtering was performed.

2.3. Mesh Generation. A three-dimensional mesh model was established that formed a mapping relationship with the data dot matrix. The three-dimensional mesh model consisted of eight node hexahedral elements, and each data point corresponded to a unit. The data point was located at the center of the unit, and the size of the unit along the three axes was similar to that of the three-axis spacing of the data point. The nodes of the grid model were numbered, as shown in Figure 2.

The coordinates of the Nth node of the model were

$$
\begin{cases}
x_N = \{(N-1)\% [(U+1)(V+1)]\}\% (W+1)\alpha - \dfrac{1}{2}\alpha, \\[2ex]
y_N = \left[\dfrac{(N-1)\% [(U+1)(V+1)]}{(W+1)}\right]\beta - \dfrac{1}{2}\beta, \\[2ex]
z_N = \left[\dfrac{N-1}{(U+1)(V+1)}\right]\lambda - \dfrac{1}{2}\lambda, \\[2ex]
N = 1, 2, \cdots, (U+1)(V+1)(W+1),
\end{cases}
\tag{2}
$$

where N is the number of node. x, y, and z are the co-ordinates of the Nth node in three directions. U, V, and W are

FIGURE 2: Schematic diagram of adjacent points.

the number of triaxial discrete data points. α, β, and λ are the values of the spacing of discrete data points along three axes. The 8 nodes in the cell were arranged counterclockwise and the number of the 8 nodes (N) in the nth element was determined using the following formula:

$$
\begin{cases}
N_n^1 = n + \left\lfloor \dfrac{n-1}{U} \right\rfloor + \left\lfloor \dfrac{n-1}{UV} \right\rfloor (U+1), \\[2ex]
N_n^2 = N_n^1 + 1, \\[2ex]
N_n^3 = N_n^1 + U + 2, \\[2ex]
N_n^4 = N_n^1 + U + 1, \\[2ex]
N_n^r = N_n^{r-4} + (U+1)(V+1), r = 5, 6, 7, 8,
\end{cases}
\tag{3}
$$

$$
n = 1, 2, \cdots UVW,
$$

where n is the number of element and r is the number of node.

2.4. Material Attribute Mapping. The material properties of the nth element in the model were determined using following formula:

$$\begin{cases} i = (n-1)\%U + 1, \\\\ j = \left\lfloor \dfrac{(n-1)\%(UV)}{U} \right\rfloor + 1 \\\\ k = \left\lfloor \dfrac{n-1}{UV} \right\rfloor. \end{cases} \tag{4}$$

The algorithms were developed according to the abovementioned steps to realize 3D mesh reconstruction. The 3D mesh reconstruction method can control the cell size of the 3D mesh model and improve the calculation efficiency to ensure the accuracy of the analysis.

3. Field Electrical Measurement and 3D Mesh Reconstruction of Slope with Tunnel

3.1. Project Overview. An interchange overpass was built on the Xiang'an Airport Highway, Xiamen, wherein a ramp crossed the existing Xiasha tunnel. The Xiasha tunnel was a separated shallow buried tunnel. The ramp was mainly excavated, and the maximum excavation depth was 19 m, as shown in Figure 3.

The results of geological drilling demonstrated the presence of gravelly and strongly weathered granite, fragmentary and strongly weathered granite, and moderately granite from top to bottom, as shown in Figure 4. The rock mass was disturbed, and the cracks expanded during the process of the rock slope excavation.

3.2. Field Test

3.2.1. Test Equipment. The electrical measurement system consisted of a dataset acquisition instrument, battery, booster, cable, and electrodes, as shown in Figure 5. The current and voltage were measured by the electrodes, and the signal was transmitted by the cable. The data acquisition instrument received signals and acquired data. The Wenner method was adopted for this high-density electrical exploration owing to the exploration depth and surface conditions. The electrode spacing was 2 m, and the power supply voltage was 480 V.

3.2.2. Survey Line Layout and Data Acquisition. Two survey lines were arranged to perform electrical measurements along the tunnel direction. Survey line 1 was arranged in tunnel 1, whereas survey line 2 was arranged in tunnel 2. Additionally, 120 electrodes were arranged on each survey line with a spacing of 2 m and a total length of 240 m. The maximum detection depth was 35 m. The layout of the survey line is shown in Figure 6.

3.2.3. Analysis of Test Results. The apparent resistivity profile obtained through field testing was inversely calculated in combination with the least square method, and the resistivity profiles of two survey lines were obtained, as shown in Figure 7. In the case of line 1, a low value of resistivity

(Resistivity = 0–100000 Ω·m) was measured on the surface of the slope area (Distance = 60–240 m), with a thickness of approximately 5–10 m. The results were compared with the drilling data, and it was preliminarily determined that strongly weathered granite was present on the surface of the slope. The resistivity gradually increased with an increase in depth, and the resistivity was greater than 100000 Ω·m. This was preliminarily determined to be moderately weathered granite. The slope was in a state of semiexcavation. Therefore, the area (Distance = 0–60 m) was a temporary construction road with large compactness and high resistance in survey line 2. A strongly weathered granite layer with a thickness of approximately 5–10 m was present on the surface, and the resistivity was in the range of 0–100000 Ω·m. Additionally, the deeper layer was a moderately weathered granite layer. The resistivity increased due to the effect of the buried tunnel.

The resistivity was logarithmically converted, and the Gaussian distribution model was introduced, as shown in Figure 8. The resistivity exhibited an approximate normal distribution, and the data were processed according to the law of Gaussian distribution. The distribution exhibited multipeak characteristics, and the thresholds were 10000 and 100000 Ω·m. Combined with the geological survey data, it was determined that the gravelly strongly weathered granite had a resistivity of less than 10000 Ω·m, the fragment strongly weathered granite had a resistivity in the range of 10000–100000 Ω·m, and the moderately weathered granite had a resistivity greater than 100000 Ω·m.

The slope materials were determined in combination with the mathematical statistics method and the material profile of each survey line was obtained, as shown in Figure 9. According to the frequency statistical results, the materials were divided into two categories: strongly and moderately weathered granite. Compared with that of the information from BLK2 drilling points passed by survey line 1, the thickness of strongly weathered granite was approximately 5-6 m. This was in good agreement with the value (5.8 m) obtained from the drilling point. The deeper part was moderately weathered granite, which was further divided based on different joints and fissure states.

4. Long-Term Effect Analysis of the High Slope with Tunnel Structure

4.1. Construction of a Finite Element Model. The inversion was performed using the least square method after format conversion, noise removal, smoothing, and interpolation. The three-dimensional spatial distribution of resistivity was obtained based on the two-dimensional electrical profiles spread in space through block Kriging interpolation. The resistivity of rock is dependent upon various factors such as rock properties, joints and fissures, and moisture content. Different types of rock have significant differences in electrical conductivity, while the resistivity of the same material is concentrated in a certain range. The three-dimensional resistivity model was combined with mathematical statistical
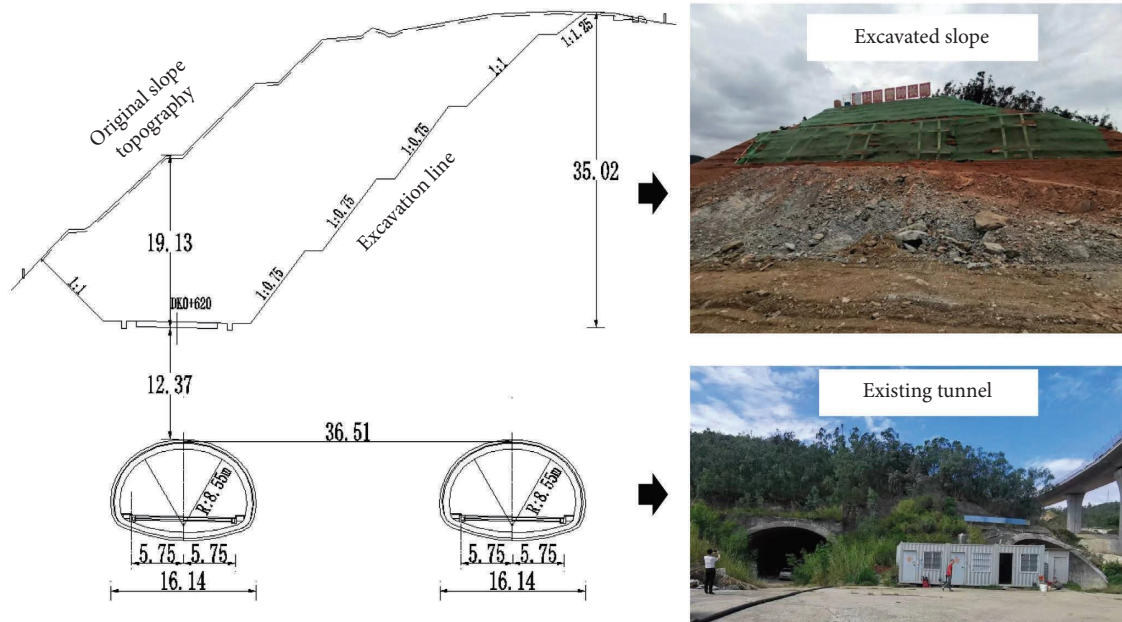
FIGURE 3: Relationship between the existing tunnel and slope (unit: m).
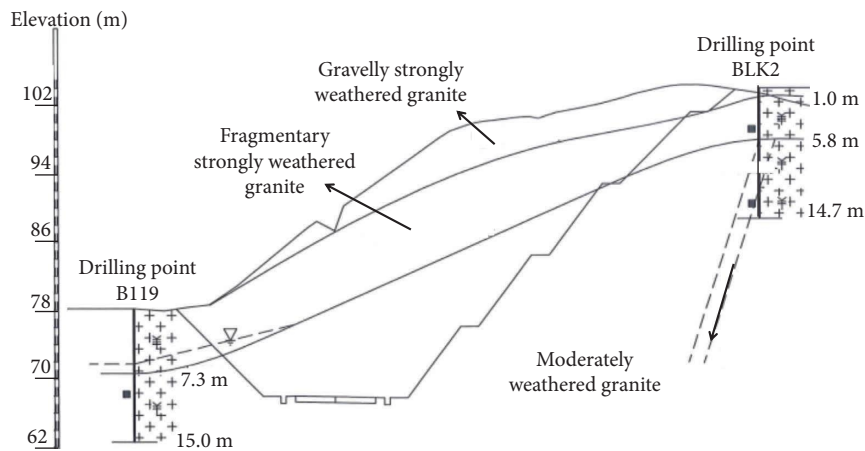
FIGURE 4: Engineering geological section (unit: m).

methods such as frequency analysis and cluster analysis and divided into several materials with different conductive properties to generate a three-dimensional geological model.

Combined with the 3D geological model, two 3D grid models were obtained through the three-dimensional mesh reconstruction method, which were affected by rainfall and earthquakes, respectively. The 3D grid model was composed of eight-node hexahedral units, and the size of the unit along the three axes was similar, which was $1 \, m \times 1 \, m \times 1 \, m$. The nodes of the mesh model were numbered, as shown in Figure 10. The length and width of the model were 130 and 45 m, respectively. The height above and below the surface was 31 and 46 m, respectively. The surface layer was strongly weathered granite, and the lower part was moderately weathered granite. The model affected by rainfall had 269,747 elements, while the model affected by the earthquake had 292,900 elements. For both models affected by

rainfall and earthquake, horizontal displacement was constrained on lateral surfaces, while horizontal and vertical displacement was constrained on the bottom surface. To reduce edge effects on the model affected by the earthquake, infinite elements were adopted on the boundary of the model. Combined with the geological exploration data, the mapping relationship between grid elements and material properties was established, and different material parameters such as elastic modulus and internal friction angle were assigned to the materials defined by the three-dimensional models.

4.2. Material Parameters.

Weathered granite is a rock material with weak nonlinear properties, and the Mohr–Coulomb criterion can fulfill the analysis accuracy, whose parameter is simple and has a physical meaning.
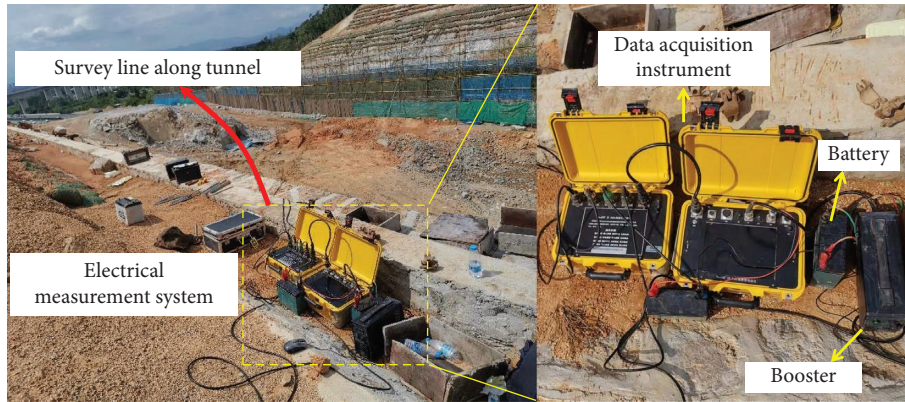
FIGURE 5: Electrical measurement system.
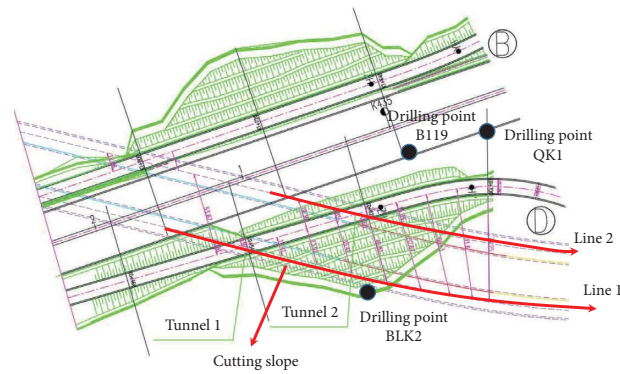
FIGURE 6: Survey line layout.

(a)

(b)
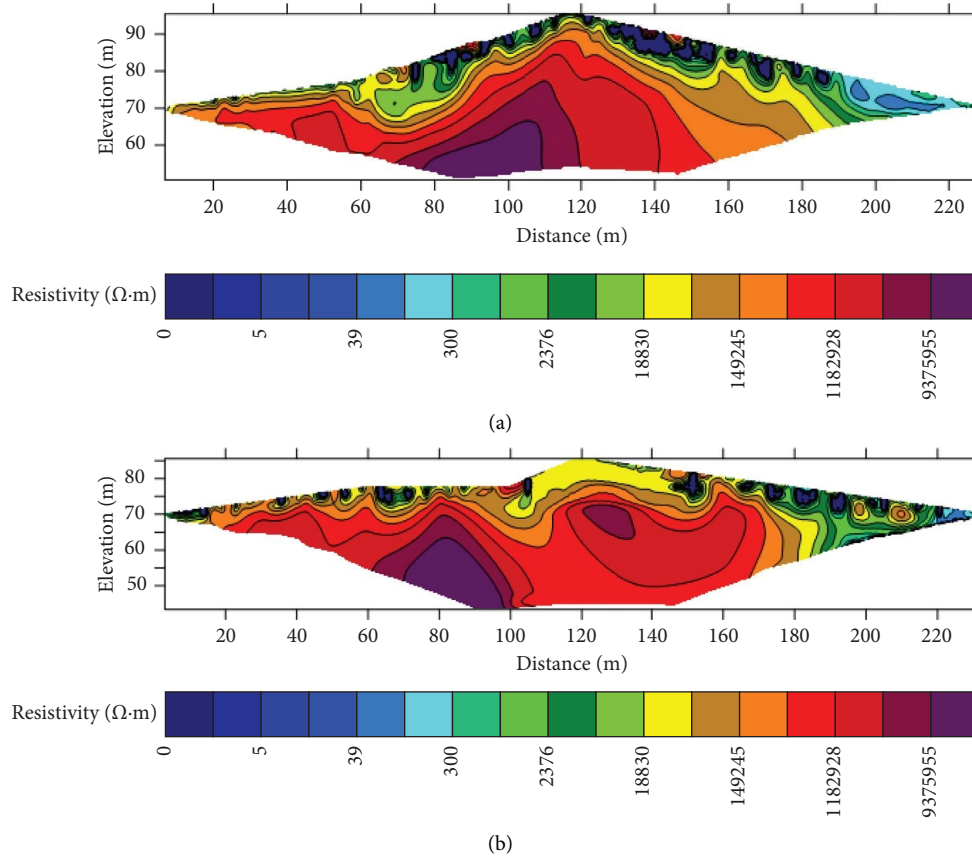
FIGURE 7: Resistivity profile. (a) Line 1. (b) Line 2.
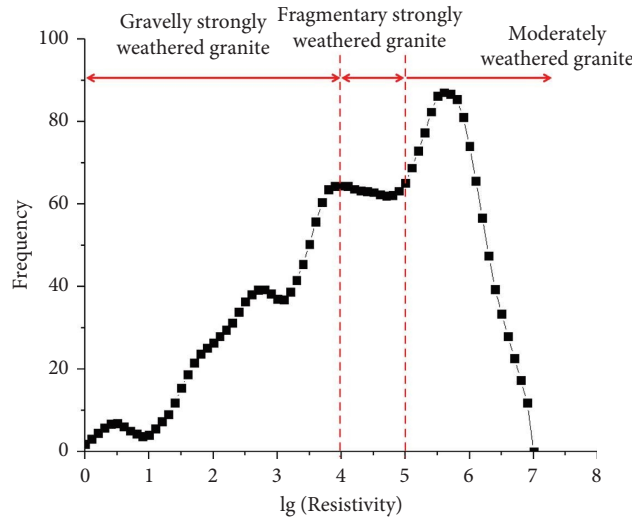
FIGURE 8: Resistivity frequency statistics.
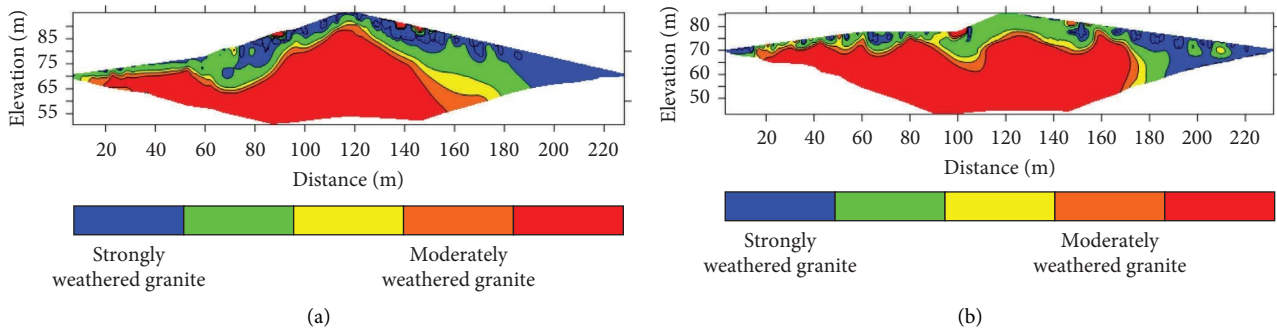
FIGURE 9: Material segmentation. (a) Line 1. (b) Line 2.

Weathered granite was sampled by drilling on-site. The unit weight (γ), cohesion (c'), internal friction angle (φ'), Young's modulus (E), and Poisson's ratio (v) were determined by mechanical experiments. The material parameters are shown in Table 2.

4.3. Load and Cases.

Rainfall and seismic force were selected as loads, and the cases are shown in Table 3. The change of strongly weathered rock water content was performed for case 1 under a gravity load to simulate rainfall. Based on the relationship between strongly weathered rock mechanical parameters and water content obtained by relevant literature and mechanical property tests [26], the reduction coefficient of 0.7 was determined when the soil reaches an approximately saturated state. And the stress-strain state of the slope and tunnel rock was observed. A dynamic calculation was performed for cases 2–6 to simulate an earthquake. A horizontal ground motion load was exerted at the bottom of the model, and the El-Centro wave was employed. The seismic time interval was 0.02 s and the duration was 30 s, as shown in Figure 11. The dynamic responses of the slope and tunnel, including acceleration, stress, strain, and earth pressure, were analyzed.

4.4. Responses of Slope and Tunnel under Rainfall.

The stress and strain distribution of the slope and tunnel, considering the reduction of soil parameters to simulate rainfall, is shown in Figures 12(a)–12(c). A stress concentration area was observed in the tunnel area, and the maximum Mises stress value was 3.576 MPa and the maximum principal strain was 3.268×10^{-5}. The plastic strain appeared in the fracture zone in the upper part of the tunnel, and the strain was 8.135×10^{-4}. A tendency to expand the tunnel was observed under continuous rainfall. The displacement of the slope and tunnel was small, and the maximum displacement was 9.579×10^{-6} m, as shown in Figure 12(d).

4.5. Responses of Slope and Tunnel under Earthquake.

The acceleration response of the slope and tunnel is shown in Figure 13. The maximum accelerations at VI and VIII degrees were 0.57 and 2.97 m/s², respectively, which had an amplification effect on the slope.

The infinite element boundary was adopted and the seismic load was continuously applied at the bottom of the model. The stress-strain state of the slope and tunnel is shown in Table 4. The maximum Mises stress value of the slope and tunnel under different seismic intensities at peak seismic wave acceleration ($t = 5$ s) is shown in Figure 14. The
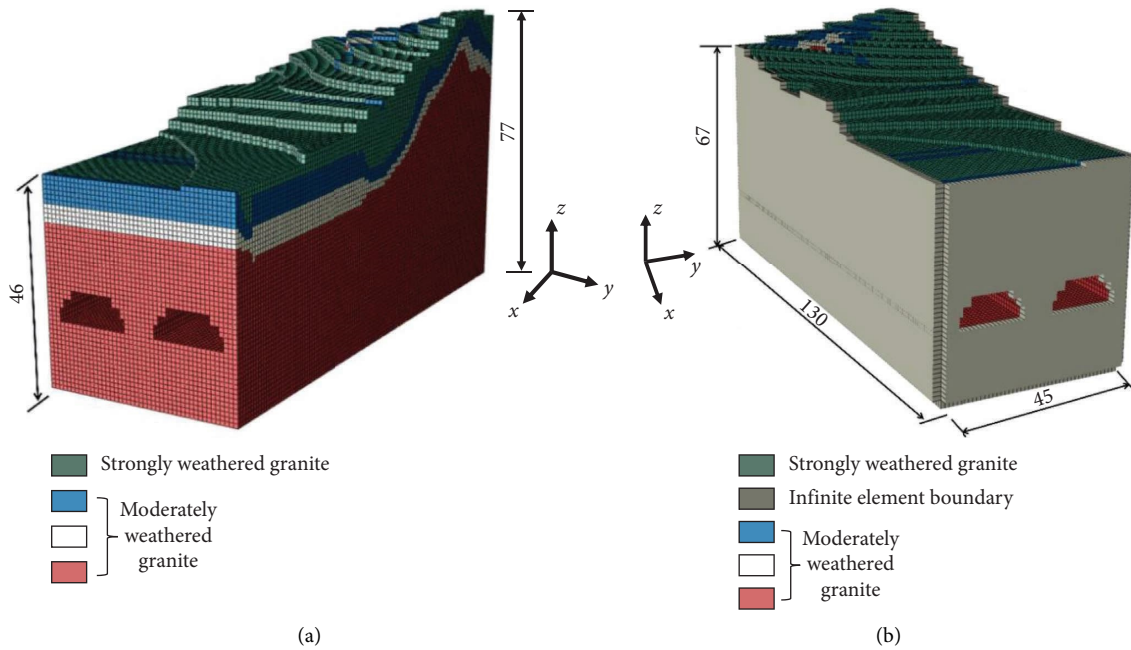
FIGURE 10: Finite element model: (a) The model affected by rainfall. (b) The model affected by earthquake.

TABLE 2: Material parameters for numerical analysis.

Material	Constitutive model	Unit weight (kN/m^3)	Young's modulus (kN/m^2)	Poisson's ratio	Cohesion (kN/m^2)	Internal friction angle (°)
Strongly weathered granite	Mohr–Colomb	21	70000	0.3	60	40
Moderately weathered granite	Mohr–Colomb	25	1500000	0.2	130	45

TABLE 3: Calculation cases.

Cases		Load intensity	Peak acceleration of seismic wave
Rainfall	1	Reduction of soil parameters	—
	2	Seismic intensity VI	70 gal
	3	Seismic intensity VII	140 gal
Seismic	4	Seismic intensity VIII	350 gal
	5	Seismic intensity IX	700 gal
	6	Seismic intensity > IX	1400 gal

maximum principal strain under different seismic intensities is shown in Figure 15. The maximum Mises stress initially increased under the same seismic intensity and then subsequently decreased. The stress rapidly increased with an increase in seismic intensity. Stress concentration areas were observed in the tunnel area. The maximum Mises stress values at $t = 0$, 5, and 10 s were 1.694, 11.640, and 4.367 MPa when the seismic intensity was IX. A large strain was observed in the upper fracture zone of the tunnel with a tendency to expand into the tunnel under the long-term load, which significantly affected the safety of the tunnel.

Compared with other monitoring points, the strain at D3 is higher due to the existence of a fracture zone, which is about 10.76×10^{-4}. Four settlement monitoring points were

arranged at the vault of the tunnel on-site to obtain the change in the tunnel settlement during excavation, as shown in Figure 16. The monitored settlement data along the tunnel is 0, −2.3 mm, −4.2 mm, and −3.5 mm. The trend is consistent with the strain calculation results, and the settlement at D3 is higher due to the existence of a fracture zone.

5. Discussion

5.1. Responses of the High Slope with Tunnel Structure under the Combination of Rainfall and Earthquake. It is inevitable that a tunnel will be close to a noncausative fracture zone during the line selection design of a tunnel. Several studies have been conducted on the seismic dynamic interaction
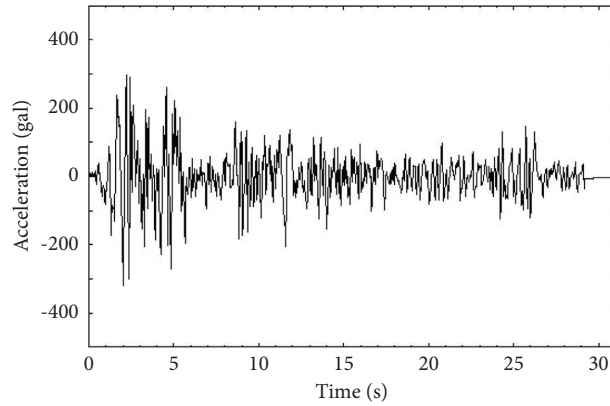
FIGURE 11: El-Centro wave.
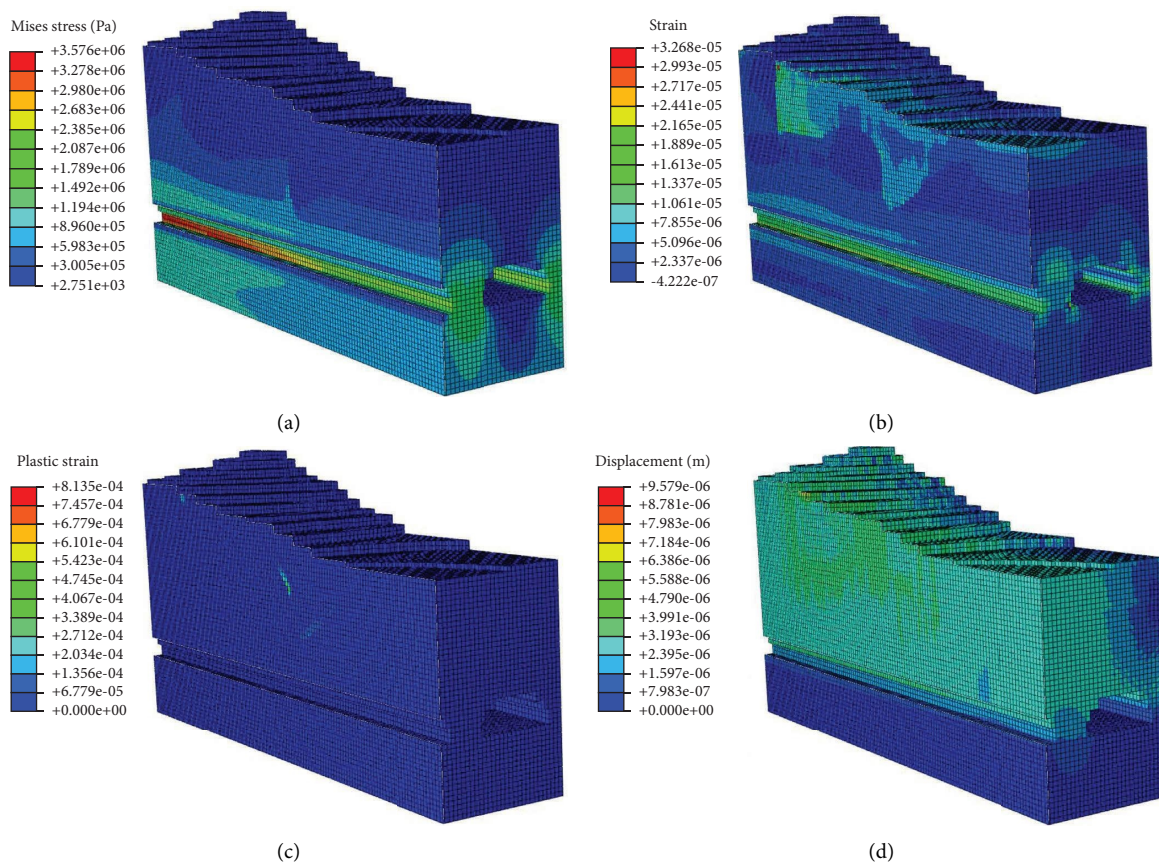
FIGURE 12: Stress, strain, and displacement of a slope and tunnel under rainfall: (a) Mises stress. (b) Strain. (c) Plastic strain. (d) Displacement.

between a noncausative fracture zone and lined tunnel. The stress amplification effect of the lined tunnel increased when the lined tunnel was in the foot wall of the fracture zone [27]. However, the disturbance on the fracture zone in the upper part of the tunnel was not considered, and the distribution of the fracture zone was mostly artificially assumed. The slope with tunnel model was developed using the three-dimensional mesh reconstruction method, and the distribution area of the fracture zone was accurately obtained.

Fracture growth was observed with a release of high geo-energies due to the excavation of the high slope [28]. Additionally, the thickness of the overlying soil layer of the tunnel decreased, and the rock in the fracture zone was further disturbed due to rainfall. The degradation of the mechanical parameters of the rock under the effect of rainfall was observed owing to the presence of the fracture zone. This severely affected the ground motion of earthquakes due to the multiple reflections of waves in the fault fracture zone

(a)

(b)

(c)

(d)
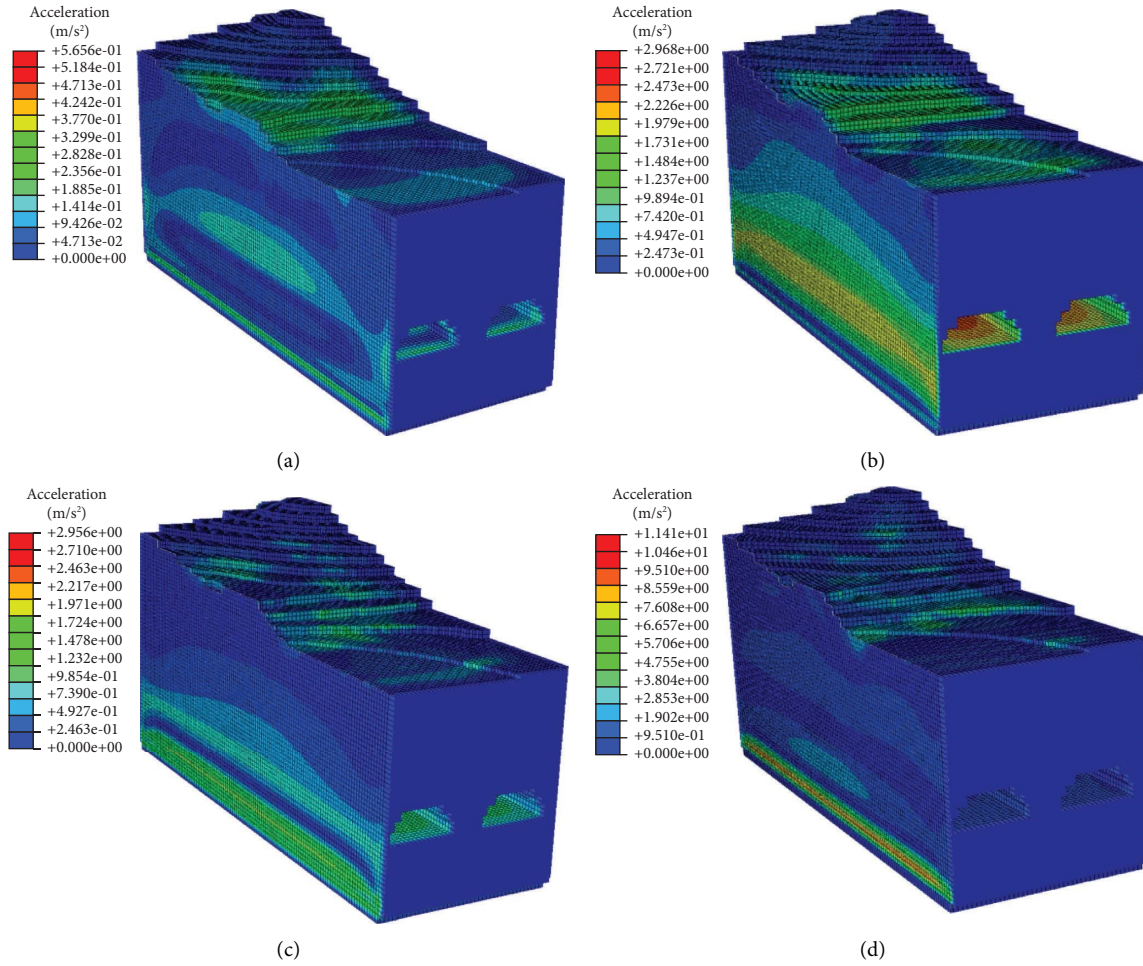
FIGURE 13: Acceleration responses under different seismic intensities: (a) VI. (b) VIII. (c) IX. (d) >IX.

TABLE 4: Maximum Mises stress and strain of tunnel under different seismic intensities.

Seismic intensity	Maximum Mises stress (MPa)			Maximum principal strain		
	$t = 0$ s	$t = 5$ s	$t = 10$ s	$t = 0$ s	$t = 5$ s	$t = 10$ s
VI	1.694	1.834	1.721	7.519×10^{-6}	8.979×10^{-4}	5.104×10^{-4}
VII	1.694	2.736	1.847	7.519×10^{-6}	3.311×10^{-3}	9.053×10^{-4}
VIII	1.694	5.960	2.690	7.519×10^{-6}	7.933×10^{-3}	1.847×10^{-3}
IX	1.694	11.640	4.367	7.519×10^{-6}	1.492×10^{-2}	4.308×10^{-3}
>IX	1.694	21.460	8.366	7.519×10^{-6}	3.324×10^{-2}	8.770×10^{-3}

[29, 30]. The concentration of stress and plastic strain appeared in the fracture zone. There was a tendency to expand to the tunnel under the long-term load. It is crucial to study the failure mechanism of a high slope with tunnel structure under rainfall and earthquake.

5.2. Failure Mechanism Analysis of the High Slope with Tunnel Structure. The combined finite-discrete element method (FDEM) can be employed to investigate the failure mechanism and failure process of rock masses and the effect of different factors on the failure mode [31]. The fracture zone and tunnel can be divided into discontinuous elements, and other areas can be set as continuous elements to obtain the three-dimensional numerical model [32]. Combined with the damage evolution of rock under rainfall and earthquake, the damage effects of rainfall and earthquake can be coupled into the constitutive model of rock based on continuous damage mechanics and statistical theory [33]. An elasto-plastic constitutive model considering damage deterioration can be established, and the mechanical parameters of continuous elements can be determined [34]. Combined with the quantitative correlation between the characteristic parameters of rock microstructure and macroparameters under rainfall and earthquake, the mechanical parameters of discontinuous elements can be defined. The interaction

(a)

(b)

(c)
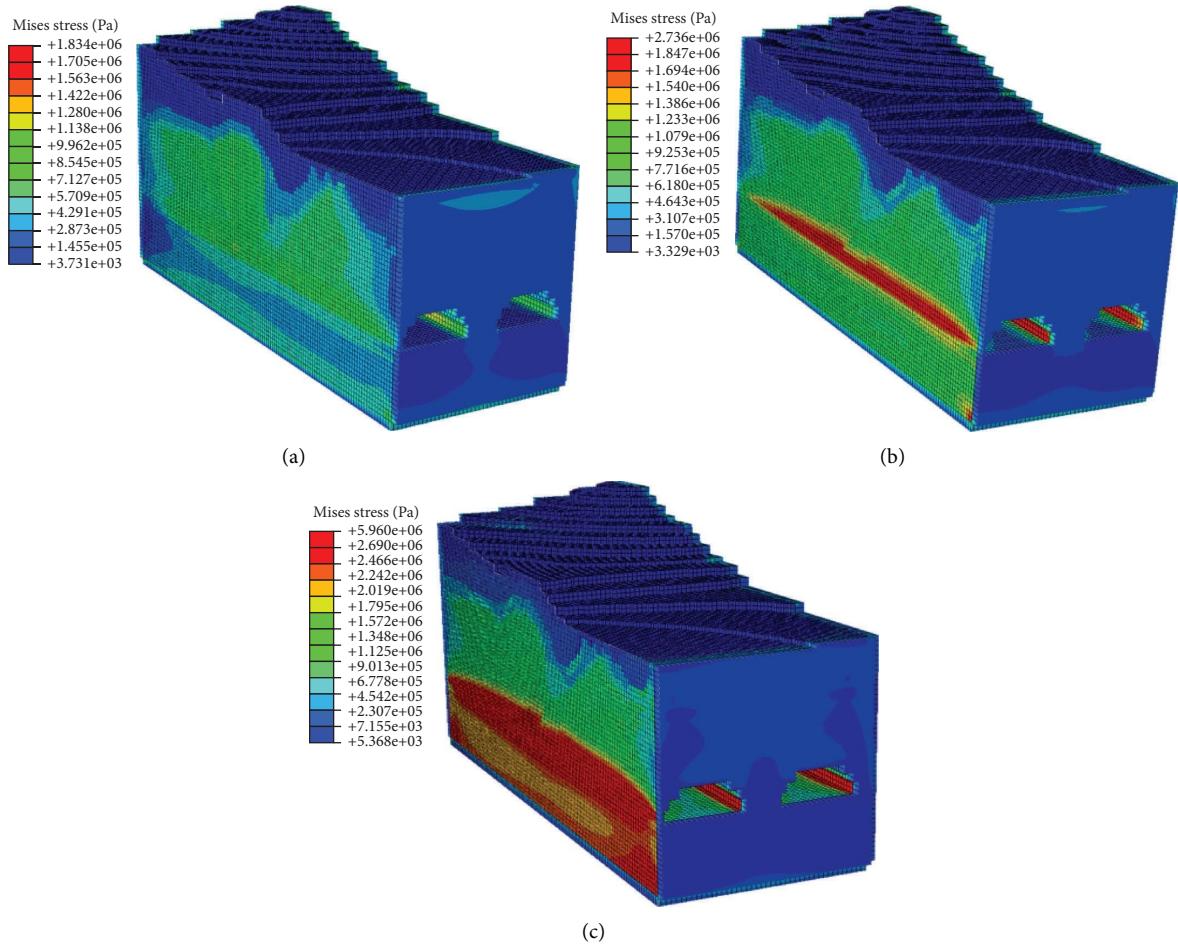
Figure 14: Mises stress under different seismic intensities ($t = 5$ s). (a) VI. (b) VII. (c) VIII.

(a)

(b)
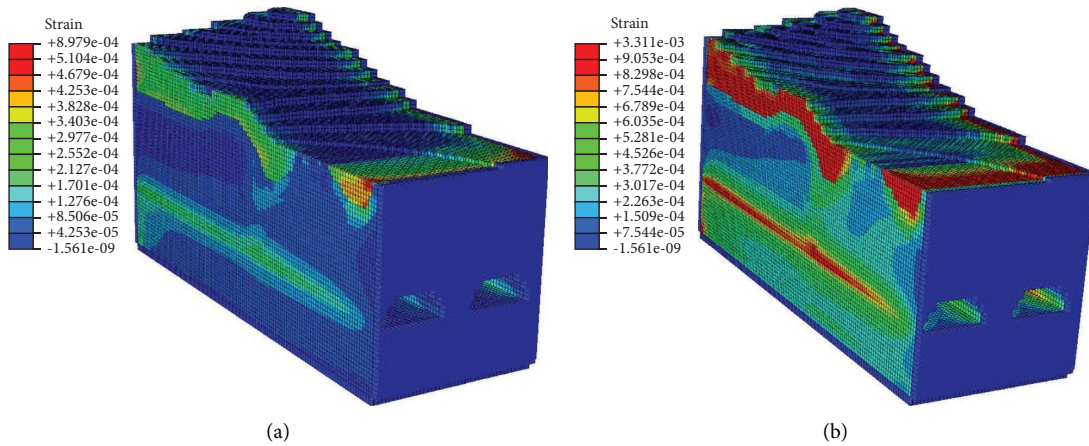
Figure 15: Continued.

(c)
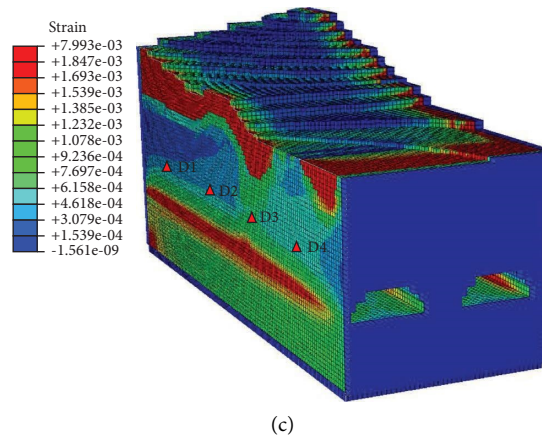
Figure 15: Maximum principal strain under different seismic intensities ($t = 5$ s). (a) VI. (b) VII. (c) VIII.
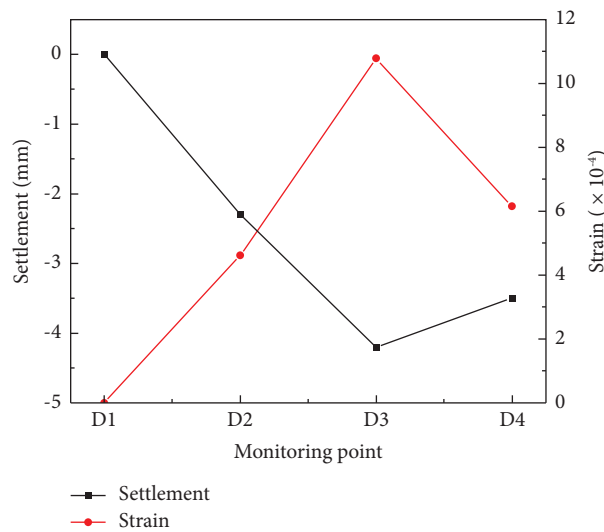
Figure 16: Comparison between calculation results and on-site displacement monitoring results.

relationship between discontinuous elements can be determined based on the contact constitutive law, and the boundary conditions of the coupling domain can be determined [35]. Research can be performed on the deformation and failure processes of a high slope with the tunnel structure considering the effects of rainfall and earthquake, and its failure patterns and mechanisms can be determined.

6. Conclusions

(1) A field test was performed on the cutting slope with an existing large cross-section tunnel through electrical measurement. To obtain the 3D geological visual model, a mathematical statistics method was used to determine the material thresholds of strongly weathered and moderately weathered granite, which were 10000 and 100000 Ω·m. The three-dimensional mesh reconstruction method was used to reconstruct the 3D mesh model of the slope with the tunnel for the long-term effect analysis.

(2) The rainfall and seismic cases were simulated based on the reconstructed finite element models. For the effect of the rainfall, plastic strain was observed in the fracture zone of the upper part of the tunnel. The strain value was 8.135×10^{-4} with a tendency to expand in the tunnel. For the effect of the earthquake, the maximum principal strain was 3.324×10^{-2}. A large strain was observed in the fracture zone at the upper part of the tunnel with a tendency to expand into the tunnel, which significantly affected the safety of the tunnel.

Data Availability

The data used to support the findings of this study are available from the corresponding author upon request.

Conflicts of Interest

The authors declare that they have no conflicts of interest.

Acknowledgments

References

[1] L. He, D. W. Zhong, Y. H. Liu, and K. Song, "Prediction of bench blasting vibration on slope and safety threshold of blasting vibration velocity to undercrossing tunnel," *Shock and Vibration*, vol. 2021, pp. 9939361–14, 2021.

[2] G. Y. Lu, Z. Q. Zhu, Q. Y. Liu, and J. B. Yang, "Three dimensional computer modeling for the stress and deformation interaction of rock slope and tunnel," in *Proceedings of the 2010 2nd IEEE International Conference on Information Management and Engineering*, pp. 169–172, Chengdu, China, April 2010.

[3] R. Vassallo, M. Mishra, G. Santarsiero, and A. Masi, "Modeling of landslide–tunnel interaction: the Varco d'izzo case study," *Geotechnical & Geological Engineering*, vol. 37, no. 6, pp. 5507–5531, 2019.

[4] Z. G. Zhang, Q. H. Zhao, C. Xu, and X. Y. Xu, "Interaction analyses between tunnel and landslide in mountain area," *Journal of Mountain Science*, vol. 14, no. 6, pp. 1124–1139, 2017.

[5] Q. Xu, X. Fan, and X. Dong, "Characteristics and formation mechanism of a catastrophic rainfall-induced rock avalanche–mud flow in Sichuan, China, 2010," *Landslides*, vol. 9, no. 1, pp. 143–154, 2012.

[6] G. Fan, J. Zhang, J. Wu, and K. Yan, "Dynamic response and dynamic failure mode of a weak intercalated rock slope using a shaking table," *Rock Mechanics and Rock Engineering*, vol. 49, no. 8, pp. 3243–3256, 2016.

[7] B. Tang and Y. Ren, "Study on seismic response and damping measures of surrounding rock and secondary lining of deep tunnel," *Shock and Vibration*, vol. 2021, pp. 1–9, 2021.

[8] D. H. Kim, I. Gratchev, and A. Balasubramaniam, "Determination of joint roughness coefficient (JRC) for slope stability analysis: a case study from the Gold Coast area, Australia," *Landslides*, vol. 10, no. 5, pp. 657–664, 2013.

[9] Y. S. Shen, Z. Z. Wang, J. Yu, X. Zhang, and B. Gao, "Shaking table test on flexible joints of mountain tunnels passing through normal fault," *Tunnelling and Underground Space Technology*, vol. 98, Article ID 103299, 2020.

[10] V. E. Mirenkov, "Zonal disintegration of rock mass around an underground excavation," *Journal of Mining Science*, vol. 50, no. 1, pp. 33–37, 2014.

[11] M. Jiang, T. Jiang, G. B. Crosta, Z. Shi, H. Chen, and N. Zhang, "Modeling failure of jointed rock slope with two main joint sets using a novel DEM bond contact model," *Engineering Geology*, vol. 193, pp. 79–96, 2015.

[12] C. Yang, L. Zhang, Y. Liu, D. Tian, X. Guo, and Y. Liu, "Shaking table test on dynamic response of bedding rock slopes with weak structural plane under earthquake," *Frontiers in Physics*, vol. 8, Article ID 556714, 2020.

[13] M. Kun and T. Onargan, "Influence of the fault zone in shallow tunneling: a case study of Izmir Metro Tunnel," *Tunnelling and Underground Space Technology*, vol. 33, pp. 34–45, 2013.

[14] Z. Yang, H. Lan, Y. Zhang, X. Gao, and L. Li, "Nonlinear dynamic failure process of tunnel-fault system in response to strong seismic event," *Journal of Asian Earth Sciences*, vol. 64, pp. 125–135, 2013.

[15] S. H. Jiang, J. S. Huang, X. H. Qi, and C. B. Zhou, "Efficient probabilistic back analysis of spatially varying soil parameters for slope reliability assessment," *Engineering Geology*, vol. 271, Article ID 105597, 2020.

[16] S. Shu, B. Ge, Y. Wu, and F. Zhang, "Probabilistic assessment on 3D stability and failure mechanism of undrained slopes based on the kinematic approach of limit analysis," *International Journal of Geomechanics*, vol. 23, no. 1, Article ID 06022037, 2023.

[17] T. Vo-Minh, L. Nguyen-Son, G. Nguyen-Van, and T. Thai-Phuong, "Upper bound limit analysis of circular tunnel in cohesive-frictional soils using isogeometric analysis based on Bezier extraction," *Tunnelling and Underground Space Technology*, vol. 114, Article ID 103995, 2021.

[18] L. L. Rasmussen, P. P. Cacciari, M. M. Futai, M. M. de Farias, and A. P. de Assis, "Efficient 3D probabilistic stability analysis of rock tunnels using a Lattice Model and cloud computing," *Tunnelling and Underground Space Technology*, vol. 85, pp. 282–293, 2019.

[19] Z. Liu, H. Zhang, A. Cheng, C. Wu, and G. Yang, "Seismic interaction between a lined tunnel and a hill under plane SV waves by IBEM," *International Journal of Structural Stability and Dynamics*, vol. 19, no. 02, p. 1950004, 2019.

[20] Z. He, C. Li, Q. He, Y. Liu, and J. Chen, "Numerical parametric study of countermeasures to alleviate the tunnel excavation effects on an existing tunnel in a shallow-buried environment near a slope," *Applied Sciences*, vol. 10, no. 2, p. 608, 2020.

[21] L. Causse, R. Cojean, and J. A. Fleurisson, "Interaction between tunnel and unstable slope - influence of time-dependent behavior of a tunnel excavation in a deep-seated gravitational slope deformation," *Tunnelling and Underground Space Technology*, vol. 50, pp. 270–281, 2015.

[22] A. Kaya, A. Akgün, K. Karaman, and F. Bulut, "Understanding the mechanism of slope failure on a nearby highway tunnel route by different slope stability analysis methods: a case from NE Turkey," *Bulletin of Engineering Geology and the Environment*, vol. 75, no. 3, pp. 945–958, 2016.

[23] W. Y. Sun, S. H. Yan, Q. Ma et al., "Dynamic response characteristics and failure mode of a bias loess tunnel using a shaking table model test," *Transportation Geotechnics*, vol. 31, Article ID 100659, 2021.

[24] R. M. Cosentini, G. Della Vecchia, S. Foti, and G. Musso, "Estimation of the hydraulic parameters of unsaturated samples by electrical resistivity tomography," *Géotechnique*, vol. 62, no. 7, pp. 583–594, 2012.

[25] N. Otsu, "A threshold selection method from gray level histograms," *IEEE Transactions on Systems, Man and Cybernetics*, vol. 9, no. 1, pp. 62–66, 1979.

[26] E. T. Mohamad, N. Latifi, A. Arefnia, and M. F. Isa, "Effects of moisture content on the strength of tropically weathered granite from Malaysia," *Bulletin of Engineering Geology and the Environment*, vol. 75, no. 1, pp. 369–390, 2016.

[27] Z. X. Liu, J. Q. Liu, Q. Pei, H. T. Yu, C. C. Li, and C. Q. Wu, "Seismic response of tunnel near fault fracture zone under incident SV waves," *Underground Space*, vol. 6, no. 6, pp. 695–708, 2021.

[28] G. Wang, A. Cao, Z. Dun, L. Ren, and X. Sun, "Numerical simulation of the dynamic responses and cumulative damage of underground caverns under multiple explosions," *Shock and Vibration*, vol. 2020, Article ID 8836375, 18 pages, 2020.

[29] H. Karabulut and M. Bouchon, "Spatial variability and nonlinearity of strong ground motion near a fault," *Geophysical Journal International*, vol. 170, no. 1, pp. 262–274, 2007.

[30] L. S. Wang, Z. H. Wang, and H. Kong, "Seismic response analysis of the fault fracture zones with saturated soil under incident SV waves," *Applied Mechanics and Materials*, vol. 638–640, pp. 1863–1868, 2014.

[31] P. H. Deng, Q. S. Liu, X. Huang, Y. C. Pan, and J. Wu, "FDEM numerical modeling of failure mechanisms of anisotropic rock masses around deep tunnels," *Computers and Geotechnics*, vol. 142, Article ID 104535, 2022.

[32] F. Zarate, J. M. Gonzalez, J. Miquel, R. Lohner, and E. Onate, "A coupled fluid fem-dem technique for predicting blasting operations in tunnels," *Underground Space*, vol. 3, no. 4, pp. 310–316, 2018.

[33] X. S. Liu, J. G. Ning, Y. L. Tan, and Q. H. Gu, "Damage constitutive model based on energy dissipation for intact rock subjected to cyclic loading," *International Journal of Rock Mechanics and Mining Sciences*, vol. 85, pp. 27–32, 2016.

[34] Y. W. Li, D. Jia, Z. H. Rui, J. Y. Peng, C. K. Fu, and J. Zhang, "Evaluation method of rock brittleness based on statistical constitutive relations for rock damage," *Journal of Petroleum Science and Engineering*, vol. 153, pp. 123–132, 2017.

[35] L. Chen, A. B. Jin, S. C. Wu, C. Q. Chu, and X. Li, "Numerical study on spalling failure of rock surrounding deep buried tunnel based on DEM," *Computers and Geotechnics*, vol. 145, Article ID 104653, 2022.

Hindawi

Research Article

Study of the Instantaneous Water Level Measurement Method on Unsteady Flow Based on Single Camera and Fixed Scale Compensation in the Tunnel Model

Weihua Ding [ID],[1,2,3] **Hu Li** [ID],[1,2,3] **Fan Yang,**[1,2,3] **Bin Hou,**[1,2,3] **Haibin Xue** [ID],[1,2,3] **Feihu Wang,**[2,3,4] **Zongxiao Zhang,**[2,3,4] **and Xinhong Wang**[2,3,4]

[1]*School of Civil Engineering and Architecture, Xi'an University of Technology, Xi'an 710048, China*
[2]*State Key Laboratory of Eco-Hydraulics in Northwest Arid Region, Xi'an University of Technology, Xi'an 710048, China*
[3]*Shaanxi Key Laboratory of Loess Mechanics and Engineering, Xi'an University of Technology, Xi'an 710048, China*
[4]*Institute of Water Resources and Hydro-Electric Engineering, Xi'an University of Technology, Xi'an 710048, China*

Correspondence should be addressed to Hu Li; 2200720068@stu.xaut.edu.cn

The shape of instantaneous water surface profiles for the unsteady flow in the tunnel model can be determined by measuring the instantaneous water levels at multiple points synchronously. However, the measurement accuracy of the ultrasonic method is affected greatly because of the complex state of the water surface when water level changes rapidly. Using an optical method, multicamera synchronous measurement is difficult to control, and the cost is high. For single camera measurement, the reading of the steel ruler in the image cannot be clearly seen when the distance between the measuring point and single camera is far. When the distance is short, all steel rulers cannot be captured at the same time. Hence, in this paper, a single camera and fixed scale compensation method for instantaneous water level observation in unsteady flow is proposed. A series of fixed scales is placed with the same height and width near the water surface to be measured. In order to capture dynamic images of all fixed scales with a clear water surface, a single camera is set at a far position to continuously record the water level change process within the model range. According to the height of the fixed scale, the image accuracy is compensated and the effect of the wide-angle image distortion is automatically avoided. The water level elevation is obtained according to the relationship between the fixed scale and the water surface. In this paper, the unsteady flow model measuring test is applied to the Southern Main Tunnel and the Water Distribution Pool of the Huangchigou Water Diversion Project. The accuracy of this method in measuring the dynamic water level is 1–2 mm, which meets the accuracy requirement and greatly reduces the observation cost of the model test. The proposed method may also be suitable for measuring the instantaneous water level of the unsteady flow in other similar hydraulic model tests.

1. Introduction

The instantaneous water surface profile of unsteady flow reflects the water flow state and the water-passing capacity of the hydraulic structure, and it is an important basis for determining the structure size and the operation mode of the control gate. In the tunnel model test, the instantaneous water surface profile needs to determine multipoint simultaneous water levels. At present, the main methods for measuring unsteady flow surface profiles include the

tracking water level meter method, ultrasonic method, and optical method.

Zhang and Cui [1] analyzed the structure and principle of the water level measuring instrument in the Yangtze River flood control model. In the water level instrument, resistance is used as an arm of the measuring bridge, but it could not get rid of the bridge output drift caused by the change in water temperature and water quality. Since the inertia in the rotating part of the instrument cannot be completely eliminated, it is still unable to track the situation where the

water level changes rapidly. When multiple water level meters are adopted to work at the same time, it becomes difficult to realize synchronization, and the cost is very high.

Qu et al. [2] verified the reliability of the instrument by installing an ultrasonic water level gauge at the Zhuangzi station. After 4 months of comparative observation, the instrument can meet the requirement of water level observation, but temperature has a great influence on the sensor.

Khuntia et al. [3] studied turbulence characteristics in a rough open channel under unsteady flow conditions, and three-point gauges with a Vernier scale were fixed to measure the flow depth from different positions along the centerline of the flume. Hu et al. [4], Liu et al. [5], and Song and Graf [6] have carried out indoor experiments on unsteady flow wave propagation characteristics, sediment transport capacity, flow velocity, and vortex in channel models. The authors have used the ultrasonic water level meter to measure the water level, and the corresponding cost is high. Jalili Ghazizadeh et al. [7] studied characteristics of water surface profiles over rectangular side weirs for supercritical flows. Water surface profiles were measured at different sections in the longitudinal and transverse direction of the main channel next to the side weir using piezometers and a movable point gauge with 0.1 mm accuracy.

Optical measurement is a method to measure water level using a camera to capture the water gauge reading image. This method has the advantages of noncontact measurement, no temperature drift, traceable results, and low system cost.

Zhong [8] proposed a method using a camera to capture a video containing a water gauge and intercepted the water level image from the video in real time. After grayscale conversion, median filtering, and edge detection, the image containing the scale calibration is obtained. According to the water gauge readings identified, the water level is calculated in the subsequent process. The method for calculating the water level results, compared with the manually direct reading of the water gauge, has an accuracy of 0.6 cm. This method is suitable for remote measurement of water level in lakes, reservoirs, and culverts. Ruan et al. [9] proposed an observation method for measuring the tidal water level by working together with an artificial noncalibration water gauge and a ruler with a standard scale, which can measure the dynamic water level at a fixed point. In this method, the pixel height in the image is determined by using the ruler. The water level is obtained proportionally according to the distance from the baseline of the noncalibration water gauge to the water surface, that is, the number of pixels. The idea of this method is novel.

Aiming at the water level operation control mode of large-scale water transmission open channels, Cui et al. [10] studied the constant water level operation control mode in front of the gates on a large-scale water transmission open channel in the Trunk Canal at the middle route of the South-to-North Water Diversion Project in China. Fang et al. [11] studied the water level variation lawcaused by the flow changes at the water outlet in the main canal in the middle water transfer channel of the South-to-North Water

Diversion Project. Li et al. [12] took a canal section in the middle water transfer channel of the South-to-North Water Diversion Project as a typical example and studied the hydraulic characteristics of the open channel water delivery system under the control of the gate. Litrico and Fromion [13], Bautista and Clemmens [14], and Clemmens et al. [15] used the method of feedforward control and storage compensation to simulate the operation scheduling of irrigation channels. In the above research studies, the numerical simulation method was adopted, and in contrast, the multipoint water level measurement for the unsteady flow in the open channel hydraulic model has an important reference value to test the rationality and objectivity of the unsteady flow water level simulation results.

Therefore, in this paper, considering the synchronous measurement and image resolution of multipoint water levels in unsteady flow instantaneous water levels, an observation method based on a single camera and fixed scale compensation is proposed. The method will be applied to the open channel water level measurement in the Southern Main Tunnel of the Hanjiang-to-Weihe Valley Water Diversion Project. The instantaneous water levels at multiple points of the Water Distribution Pool and the Southern Main Tunnel are measured when the inflow from the Qinling Tunnel is 0.0173 m^3/s, and the inlet gate of the Southern Main Tunnel is quickly opened or closed. Through the measurement and research, the instantaneous water surface profiles of unsteady flow are obtained in the Water Distribution Pool and the Southern Main Tunnel at any time. Moreover, the measurement accuracy and feasibility of the method are verified by comparing with the measurement results using a steel ruler with a single camera and close-up shot.

2. Engineering Background and Problems

2.1. Engineering Background. The Hanjiang-to-Weihe Valley Water Diversion Project is a water diversion project from the Yangtze River to the Yellow River drainage, which is a cross-basin water transfer project in Shaanxi province, China. It consists of two major parts: the water transfer project (the first stage) and the water transmission and distribution project (the second stage).

The Huangchigou Water Distribution Project, as the connection center of the water transfer project and the water transmission and distribution project, is a core water distribution structure. It plays a decisive role in the safe and rapid water distribution in the whole project.

According to the characteristics of linear distribution of water-receiving objects, two main water delivery routes are arranged. The Southern Main Route is an open channel flow tunnel. The section of the Southern Main Tunnel model has a horseshoe shape with a size 0.398 m × 0.239 m. How to measure the instantaneous water level in the model tunnel becomes a key issue.

Based on the hydraulic physical model of the Huangchigou Water Distribution Project, considering the sudden rise and fall of the inlet gate in the Southern Main Tunnel due to various operating conditions, it will cause a significant change in the water level at the Water Distribution Pool and

the Southern Main Tunnel model. Therefore, it is necessary to conduct a real-time observation on the water level in the Water Distribution Pool and the Southern Main Tunnel model.

2.2. Problem of Measuring the Instantaneous Water Level at Multiple Points with a Single Camera.

Figure 1 shows the original scheme for measuring the instantaneous water level of the Southern Main Tunnel model with a single camera.

In order to obtain the instantaneous water level of each measuring point at the Water Distribution Pool and the Southern Main Tunnel, a steel ruler was erected at the Water Distribution Pool, and several steel rulers were erected at multiple measurement points in the Southern Main Tunnel. Because the model of the Southern Main Tunnel is long (about 20 m), in order to display all measuring points in a single camera, it is necessary to ensure that the camera and the model have a sufficient distance. Under this condition, since the camera is too far from the water surface to be measured, the reading of each steel ruler in the image cannot be seen clearly, causing difficulty to implement this measurement scheme.

2.3. Principle of Measuring the Instantaneous Water Level Using the Single Camera and Fixed Scale Compensation Method.

In order to overcome the problem that the single camera is too far from the point to be measured and the reading of each steel ruler in the image cannot be seen clearly, naturally, the multicamera and multipoint measurement method can be considered. That is, a camera is set up in front of each steel ruler. All frames of images are extracted from the video collected by using the camera and saved, and the instantaneous water level of each measuring point at the same time is obtained according to the extracted images. However, this method requires multiple cameras, and its synchronization is difficult to control with high cost.

To solve the problem, considering that the water surface profiles in the polymethyl methacrylate model is clearly visible within a certain distance, an instantaneous water level observation method for unsteady flow based on the single camera and fixed scale compensation is proposed. First, we erect multiple noncalibration fixed scales with the same height at each point to be measured. Second, the water surface profile is photographed. Third, the instantaneous water level is calculated according to the relative position relationship between the water surface profile and the bottom edge of the fixed scale in the intercepted image. The fixed scale plays a vital role in compensating image accuracy and automatically avoiding the effect caused by wide-angle image distortion.

3. Test Procedure

3.1. Installation of Fixed Scales and Camera Equipment.

The specifications of the fixed scales are unified as a red polymethyl methacrylate plate with a height of 60.0 cm and a width of 5.0 cm. All scales are sequentially set at the measuring position with the numbers clearly visible in the image.

The distance between adjacent fixed scales in the model is about 0.80 m.

We used Canon 5DIII professional digital camera + Canon 16–35 mm, f/2.8 lens as a single camera to conduct panoramic photography in the test process. Figure 2 shows the relationship between the single camera and the position of the fixed scale. The wide-angle mode camera can capture 2–14 fixed scales in the photo at a close distance, and the telephoto mode camera can capture 1–24 fixed scales in the photo at a long distance. The wide-angle mode measurement scheme is adopted in this study.

In order to check the measurement accuracy of this method, a steel ruler is set beside the No. 12 fixed scale, as shown in Figure 3. Another Canon EOS70D + EFS18-200 mm camera was set up to take a close-up photo of the water surface profile near the steel ruler, and the instantaneous water level measurement results of the two methods were compared.

3.2. Calibration of Relative Elevation at the Bottom of the Fixed Scale.

When installing each fixed scale, we use the hanging hammer method to ensure the verticality of the fixed scale. Since relative elevation at the bottom of each scale is unknown, it needs to be calibrated. When the outlet gate of the Qinling Tunnel and the inlet gate of the Southern Main Tunnel of the model are fully opened, the water is in flow condition. Closed the outlet gates of the Qinling Tunnel andthe SouthernMain Tunnel of the model, the Water Distribution Pool and the Southern Main Tunnelmodel reaches static water condition. The needle is used to read the static water surface relative elevation in the Water Distribution Pool and the static water level is denoted as H0 . The single camera fixed scale measurement method was used to take photos of the fixed scales under the static water condition, as shown in Figure 4. The height $H_{\text{fixedscale}}$ of each fixed scale and the height $h_{\text{fixedscale}}$ between the water surface and the bottom of the fixed scale in the image were measured using CAD software. The actual distance H_{water} from the water surface to the bottom of the fixed scale can be calculated according to formula (1). The relative elevation of thebottom of each fixed scale can be obtained by H0-Hwater.

$$\frac{H_{fixed\,scale}}{H_{water}} = \frac{60}{h_{fixed\,scale}}. \tag{1}$$

The relative elevation of thesteel ruler bottom can be obtained by H0-Hruler.Hruler is the measuring depth fromwater surface to the steel ruler bottom, which can be obtained through reading the steel ruler scale. In this way, the instantaneous water level at the No. 12 fixed scale measuring point can be obtained by the single camera and fixed scale measurement method or can be read from the image captured using the camera at a close range with the steel ruler, so as to verify the accuracy of this method.

The calibration results of the bottom edge relative elevation of the fixed scale are shown in Table 1, in which the geometric scale of the model is 1 : 15. It should be noted that the relative elevation of the water level and the bottom edge
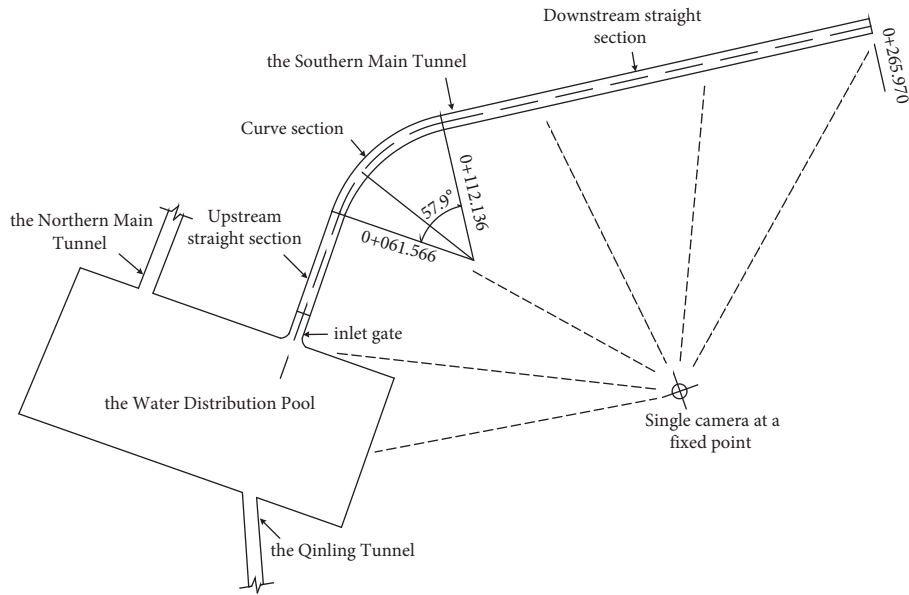
Figure 1: The original scheme for measuring the instantaneous water level by erecting steel rulers at multiple points using a single camera.
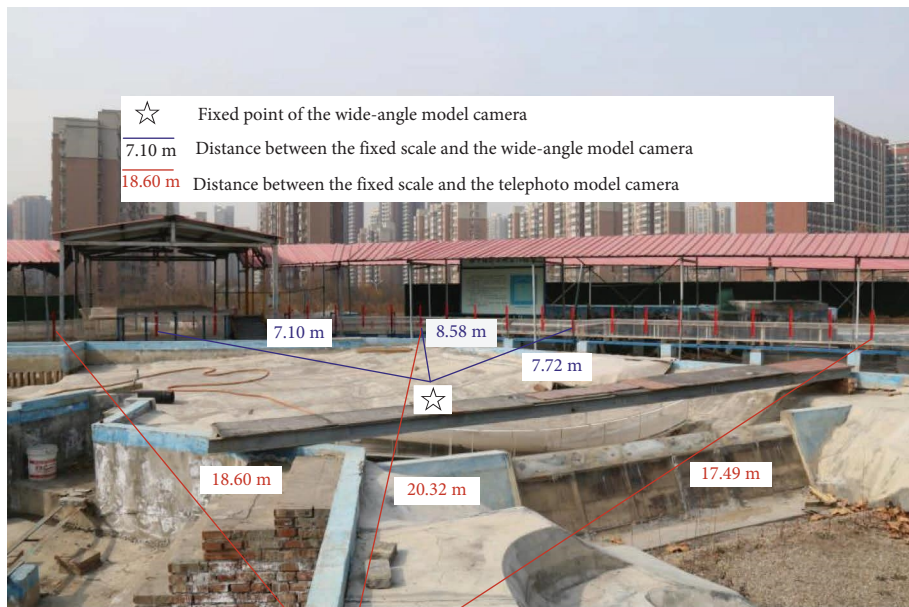
Figure 2: The position relationship between the single camera position and the fixed scale (two options).
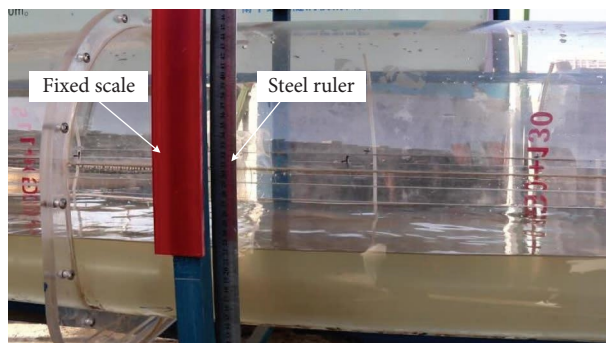
Figure 3: The position relationship between the No. 12 fixed scale and the steel ruler.
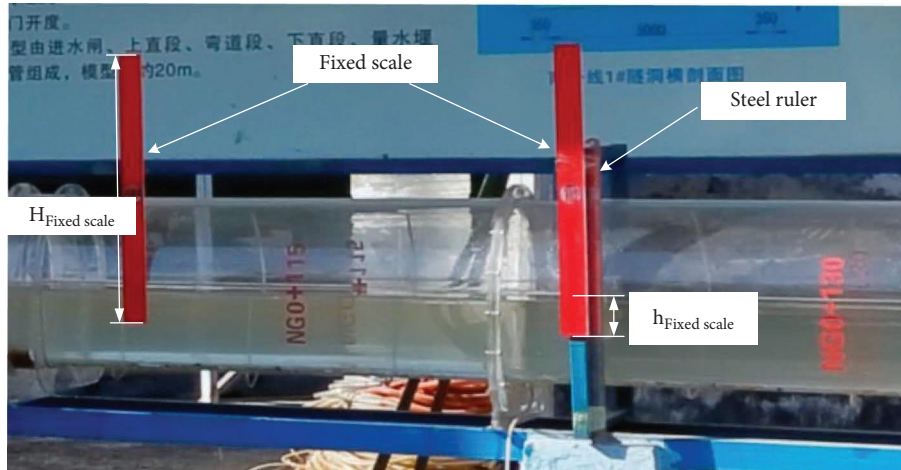
Figure 4: A schematic diagram of water level measurement.

Table 1: The position number of each fixed scale and the elevation of the bottom edge of the scale.

Fixed scale no.	Pile no.	Bottom edge elevation of the fixed scale (m)
3	NG0-012.300	661.266
4	NG0+027.175	661.228
5	NG0+035.275	661.235
6	NG0+046.459	661.180
7	NG0+059.101	661.339
8	NG0+071.519	661.391
9	NG0+084.461	661.333
10	NG0+098.038	661.259
11	NG0+109.948	661.283
12	NG0+123.718	661.318
13	NG0+137.743	661.451
14	NG0+149.623	661.383

of the fixed scale adopts the relative elevation of the prototype, and the other parameters adopt the model parameters in this paper. This makes it easy for the reader to understand design characteristic parameters of the prototype.

3.3. Measuring Process of the Instantaneous Water Level. When the inlet gate of the Southern Main Tunnel model is suddenly closed or opened, an unsteady flow process will occur in the Water Distribution Pool and the Southern Main Tunnel model. The instantaneous fluctuation of the water surface is large, and the influence range is wide. Therefore, the water surface change process can only be recorded by a video.

A series of pictures of the water level on fixed scales at multiple measuring points is intercepted from the video at an interval of 0.5 s. The height from the water surface of each measuring point to the bottom edge of the fixed scale at different times is read out in turn using CAD software, and the relative elevation of the water level at each measuring point is obtained by H0-Hwater. At the same time, the relative elevation points at the water level from the Water Distribution Pool to each measuring point in the Southern Main Tunnel model are connected in turn to form the instantaneous water surface profile at that time.

By repeating the above steps, the entire change process of the unsteady flow surface profiles can be obtained.

4. Application Research Measuring Instantaneous Water Levels of Unsteady Flow Using the Single Camera and Fixed Scale Compensation Method

4.1. Qualitative Analysis of the Instantaneous Water Level in the Water Distribution Pool and the Southern Main Tunnel Model. Considering Qinling Tunnel's model inflow of $0.0173 \, \text{m}^3/\text{s}$, the inlet gate of the Southern Main Tunnel model is initially closed. The gate is suddenly opened when the water level of the Water Distribution Pool rises to 664.88 m, and the change process at the instantaneous water level in the Water Distribution Pool and the Southern Main Tunnel model is analyzed. Typical instantaneous water surface photos taken from the video using a wide-angle camera are shown in Figure 5.

Figure 5(a) shows a picture of the water flow state of the Water Distribution Pool and the Southern Main Tunnel model at 2.0 s before opening the inlet gate. The water surface of the Water Distribution Pool is calm at a water level of 664.88 m. Figure 5(b) shows a panoramic view at 1.0 s after opening the inlet gate of the Southern Main Tunnel

(a)
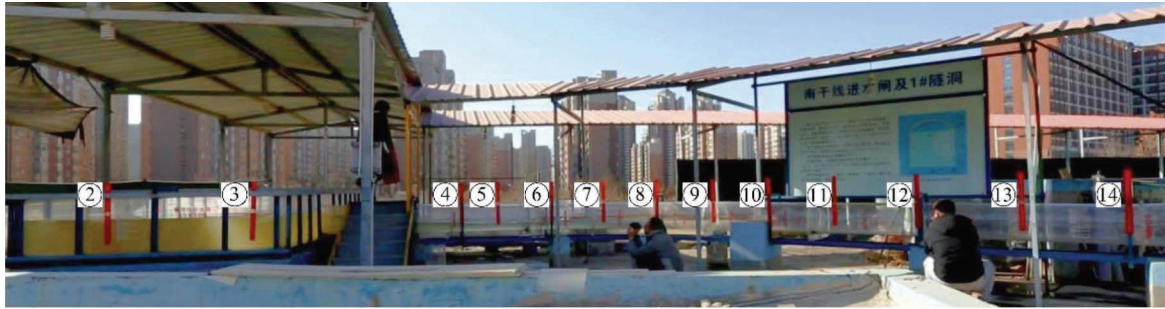
(b)

(c)

(d)

FIGURE 5: A panoramic view of the instantaneous water surface in the Water Distribution Pool and the Southern Main Tunnel model (a) A panoramic view at 2.0 s before opening the gate. (b) A panoramic view at 1.0 s after opening the gate. (c) A panoramic view at 3.0 s after opening the gate. (d) A panoramic view at 204.0 s after opening the gate.

model suddenly. The water surface of the Water Distribution Pool close to the inlet gate drops obviously, and the water surface fluctuates obviously. There is an open channel flow behind the gate of the Southern Main Tunnel model, which fluctuates greatly, and the front peak of the water wave reached the No. 8. fixed scale. Figure 5(c) shows a panorama view at 3.0 s after opening the inlet gate. The water level of

the Water Distribution Pool fluctuates obviously. The water level close to the inlet gate has a greater decrease and greater fluctuation. The water coming reaches the No. 11~12 fixed scale in the Southern Main Tunnel model. The water level close to the wave forehead gets lower and lower. Figure 5(d) shows a panoramic view at 204.0 s after opening the inlet gate. The water level of the distribution hub has a greater

decrease, and the Southern Main Tunnel model has the same level as the Water Distribution Pool, while water reaches a constant flow state.

4.2. Quantitative Analysis of the Instantaneous Water Level in the Water Distribution Pool and the Southern Main Tunnel Model. Using the single camera and fixed scale compensation method to measure the instantaneous water level at different positions in the model, the water levels in the Water Distribution Pool and the Southern Main Tunnel model were obtained. The instantaneous water levels are sorted out at No. 3, 7, 8, 10, and 14, respectively, as shown in Figure 6. It can be seen that the water level of the Water Distribution Pool continued to decrease, and the water level of each measuring point in the Southern Main Tunnel model increased sequentially from upstream to downstream and gradually stabilized after 9.5 s.

The instantaneous water surface profiles at different times are shown in Figure 7. It can be seen that the water level at the Water Distribution Pool is 664.88 m before opening the inlet gate and that there is no water in the Southern Main Tunnel model. At 0.5 s after opening the inlet gate, the front peak of the water wave in the Southern Main Tunnel model reaches the No. 6 scale, and the water level difference between upstream and downstream is very large. At 1.5 s after opening the inlet gate, the water front reaches the No. 11 scale, and the water level changes relatively little between the 4th and 8th scales, while the water level drops rapidly in downstream. At 3.5 s after opening the inlet gate, the water flow reaches the No. 14 scale. At 9.5 s after opening the inlet gate, the water level in the Southern Main Tunnel model is close to the highest.

4.3. Image Distortion Analysis. In the panoramic image obtained using the wide-angle camera, the measured height of each fixed scale is shown in Figure 8. It can be seen that the fixed scales with the same height obviously have different heights in the panoramic image due to the influence of the camera view field. The ratio of the maximum height to the minimum height is 1.599. The panoramic image distortion shows that the middle fixed scale is smaller and that at two sides is larger. Consequently, the height measured directly in the image needs to be corrected, and setting a fixed scale can avoid this distortion influence, which reflects the superiority of the method in this paper.

5. Accuracy Analysis of the Instantaneous Water Level by the Single Camera and Fixed Scale Compensation Method

The instantaneous water level at the No. 12 fixed scale measuring point can be obtained by the single camera and fixed scale measurement method, or it can be read from the image taken by using the camera at a close distance with a steel ruler. The specific results are shown in Figure 9. It can be seen that the instantaneous water levels obtained by the two
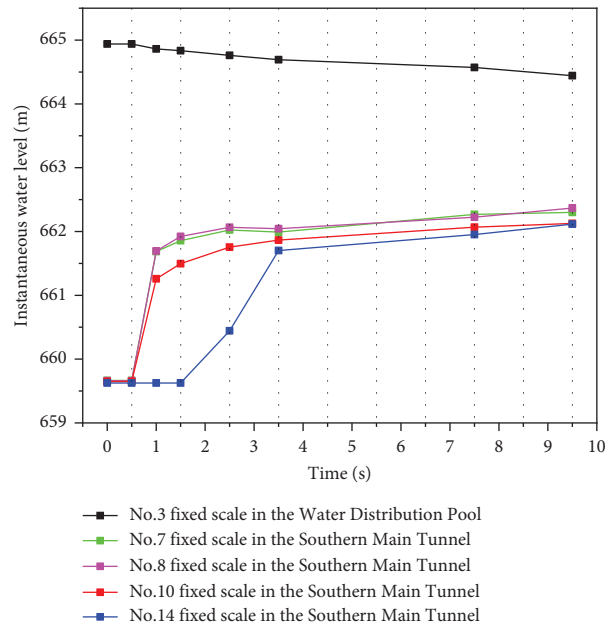
FIGURE 6: Instantaneous water level at each measuring point.
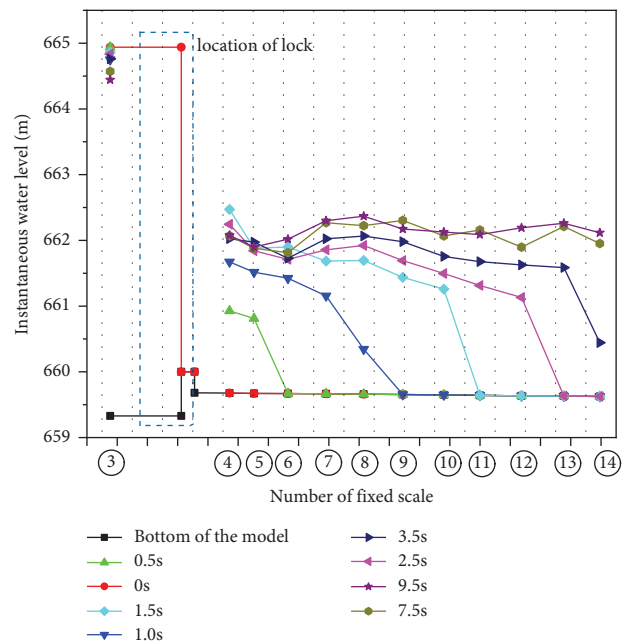
FIGURE 7: Instantaneous water surface profiles at different times.

measurement methods are in good agreement. At 8.0 s, 10.0 s, 16.0 s, 29.0 s, and 41.0 s, the water surface fluctuates obviously. The biggest difference between the results by the two methods is 0.7 cm in the model. The reason is that the position at the instantaneous water level read by using the steel ruler is slightly different from that at the No. 12 fixed scale. When water flow is unstable and the liquid level fluctuates greatly, the instantaneous water levels have a large difference. When water flow tends to be stable, that is, at 310.0 s, 320.0 s, and 328.0 s, it can be seen that the water level difference measured by the two methods is 1~2 mm in the model.
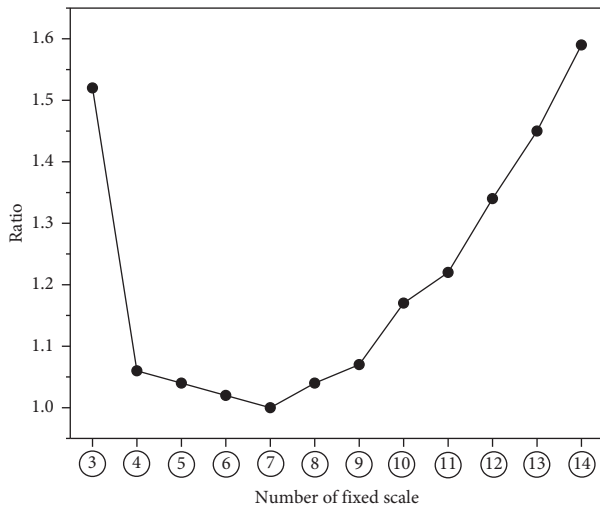
FIGURE 8: The ratio of each fixed scale height to the minimum height of the fixed scale in the image.

— ■ — Result with single camera and fixed scale compensation
— ● — Result with steel ruler
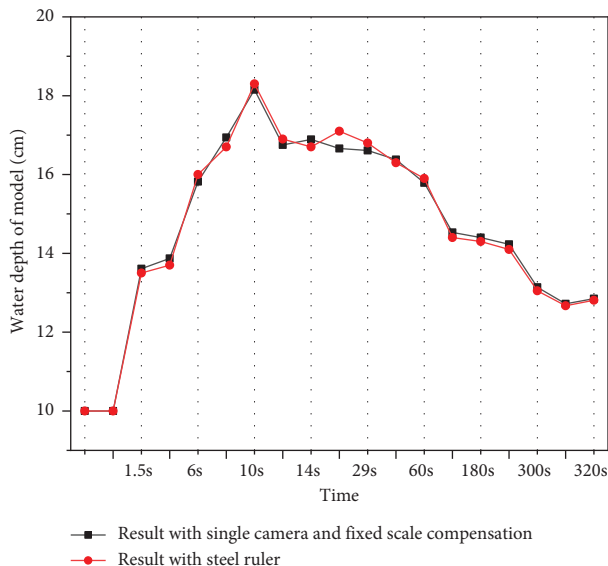
FIGURE 9: The instantaneous water depth at the unsteady water level at the same position by two measuring methods.

From the above analysis results, the single camera and fixed scale compensation method proposed in this paper can be implemented to measure the instantaneous water level accurately and meet measuring accuracy requirements of the hydraulic tunnel model.

6. Mechanism Analysis of Instantaneous Water Level Measurement by the Single Camera and Fixed Scale Compensation Method

Since a panoramic image needs to be obtained including all the fixed scales at the measuring points and the camera is far from the water surface to be measured, the readings of all fixed scales in the image cannot be seen clearly. Therefore, it

is not feasible to obtain the instantaneous water level by shooting all fixed scales using a camera.

The core of the proposed method in this paper is to make the fixed scale very high so that the image including all the fixed scales at the measuring points captured by using the wide-angle camera is clearly visible. The image height of the fixed scale can be accurately measured in the image, and the water surface level can be read and corrected. Image distortion effects can be avoided by erecting a huge fixed scale at each measuring point. The fixed scale can be subdivided in the image, and the precise water level can be read.

This method compensates the measurement resolution, and the idea of this paper is innovative. To the best of our knowledge, it has not been reported in all previous hydraulic model tests.

7. Conclusion

Aiming at the simultaneous water level measurement and image resolution at multipoint water levels in unsteady flow, a single camera and fixed scale compensation method is proposed. This method is applied to the open channel flow model test in the Water Distribution Pool and the Southern Main Tunnel of the Huangchigou Water Distribution Project, and the instantaneous water surface profile of unsteady flow at any time is obtained. The measurement accuracy of the method in this paper is verified. The specific conclusions are as follows:

(1) The principle and implementation process of the single camera and fixed scale compensation method to measure the instantaneous water level are proposed. This approach solves synchronization problems at multipoint measuring. The installation of a patternless fixed scale is equivalent to setting a magnification in the image. A clearly visible scale acts as a ruler, which objectively compensates or improves the image resolution. At the same time, it can avoid the geometric distortion influence caused by using the wide-angle camera in the captured image.

(2) When the results of measuringinstantaneous water level at the same point are compared with those of directreading steel ruler, the single camera and fixed scale compensation method has very high measurement accuracy. The 1~2 mm measuring accuracy meets the requirements of the instantaneous water level measurement in the unsteady flow model test.

(3) The method proposed in this paper was applied to the hydraulic model test in the Water Distribution Pool and the Southern Main Tunnel of the Huangchigou Water Distribution Project. The multipoint instantaneous water level research in the tunnel model was carried out, and the variation law of the instantaneous water level was analyzed. The quantitative water level measuring results are consistent with the macroscopic observation and water level analysis of unsteady flow, indicating that the method proposed in this paper is feasible for the unsteady flow tunnel model test.

Data Availability

The raw/processed data required to reproduce these findings cannot be shared at this time as the data also form part of an ongoing study.

Conflicts of Interest

The authors declare that they have no conflicts of interest.

Acknowledgments

References

[1] Y. J. Zhang and C. F. Cui, "Design and implementation of the high-precision tracking mode water level measuring instrument," *Computer Engineering and Applications*, vol. 41, no. 05, pp. 101–103, 2006.

[2] Z. Y. Qu, X. Qu, and Y. Wang, "Systematic error analysis of observation value with ultrasonic water level meter [J]," *Ground Water*, vol. 33, no. 04, pp. 44-45, 2011.

[3] J. R. Khuntia, K. Devi, and K. K. Khatua, "Turbulence characteristics in a rough open channel under unsteady flow conditions," *ISH Journal of Hydraulic Engineering*, vol. 27, no. 1, pp. 354–365, 2019.

[4] J. Hu, S. F. Yang, and X. H. Fu, "Experimental investigation on propagating characteristics of sinusoidal unsteady flow in open-channel with smooth bed," *Scientia Sinica*, vol. 42, no. 7, pp. 788–797, 2012.

[5] C. J. Liu, Z. S. Qu, D. X. Li, and X. Wang, "Experimental study on bed-load transport in unsteady open channel flows," *Journal of Hydroelectric Engineering*, vol. 25, no. 02, pp. 31–37, 2006.

[6] T. Song and W. H. Graf, "Velocity and turbulence distribution in unsteady open-channel flows," *Journal of Hydraulic Engineering*, vol. 122, no. 3, pp. 141–154, 1996.

[7] M. Jalili Ghazizadeh, H. Fallahi, and E. Jabbari, "Characteristics of water surface profile over rectangular side weir for supercritical flows," *Journal of Irrigation and Drainage Engineering*, vol. 147, no. 5, Article ID 04021011, 2021.

[8] Z. Y. Zhong, "Method of water level data capturing based on video image recognition," *Foreign Electronic Measurement Technology*, vol. 36, no. 06, pp. 96–99, 2017.

[9] R. Ruan, B. Zhang, and Y. F. Deng, "A new technology of water level measurement with photography," *Hydrographic Surveying and Charting*, vol. 30, no. 03, pp. 56–58, 2010.

[10] W. Cui, W. X. Chen, X. Yao, S. Wen, and J. Jiang, "Research on canal control of large scale water transfer project," *South-to-North Water Transfers and Water Science& Technology*, vol. 7, no. 5, pp. 6–10, 2009.

[11] S. G. Fang, B. S. Wu, X. D. Fu, J. H. Wei, Y. F. Huang, and G. Q. Wang, "Effect of diversions in the middle route of the South-to-North water transfer channel," *Journal of Tsinghua University*, vol. 47, no. 9, pp. 1452–1456, 2007.

[12] Y. J. Li, B. Ma, and F. Zhou, "Research on hydraulic characteristics of open channel water diversion system under the control of regulating gates," *China Rural Water and Hydropower*, vol. 5, pp. 46–50, 2017.

[13] X. Litrico and V. Fromion, "Simplified modeling of irrigation canals for controller design," *Journal of Irrigation and Drainage Engineering*, vol. 130, no. 5, pp. 373–383, 2004.

[14] E. Bautista and A. J. Clemmens, "Volume compensation method for routing irrigation canal demand changes," *Journal of Irrigation and Drainage Engineering*, vol. 131, no. 6, pp. 494–503, 2005.

[15] A. J. Clemmens, E. Bautista, B. T. Wahlin, and R. J Strand, "Simulation of automatic canal control systems," *Journal of Irrigation and Drainage Engineering*, vol. 131, no. 4, pp. 324–335, 2005.

Research Article

Numerical Studies of Floor Heave Control in Deep Mining Roadways with Soft Rocks by the Rock Bolts Reinforcement Technology

Ivan Sakhno [ID] **and Svitlana Sakhno** [ID]

Donetsk National Technical University, 29 Sofia Kovalevska Street, Lutsk, Volyn Region 43012, Ukraine

Correspondence should be addressed to Ivan Sakhno; ivan.sakhno@donntu.edu.ua

The floor heave is one of the key factors that can restrict high-efficiency and safety mining, especially in the deep roadways with soft rock. Considering the influences of rock fracturing over time on rock mass properties, a case study of the floor heave evolution and rock bolts reinforcement technology was performed in this paper. A numerical simulation was used to study the stress-strain state and displacement of surrounding rocks. It was found that significant floor heave caused by nonlinear deformation of laminated immediate floor under an increase in rock fracturing. The post-peak strain regions appear in the bottom corners of the roadway, after which strata in the immediate floor are destroyed one by one. The joint spacing of 0.45 m on the immediate floor is critical. At this step, post-peak strain regions merge in the central part of the roadway floor, which is the cause of uncontrolled floor heave. Rock bolts reinforcement was proposed to control the floor heave. Three floor support schemes with two types of support elements, different bolt orientations, and lengths of reinforcement were studied. The numerical simulation demonstrated that after reinforcement, post-peak plastic strain in the floor strata was reduced effectively. The optimal floor support scheme and depth of reinforcement were determined by the allowable floor heave. Ideally, the floor heaves could be reduced by rock bolts with a steel belt installed according to the support scheme III and reinforcement length of 2.0 m for outer bolts and 3.0 m for central bolts.

1. Introduction

With the increase in mining depth, the instability of roadways in soft rock has become a major challenge for deep coal mines [1, 2]. According to statistics, the actual repair rate of roadways in Ukraine is as high as 80%. A similar repairing rate is noted by researchers from other countries [3, 4]. The instability problems that are exacerbated due to deep mining are roadway surrounding rock large deformation, floor heave, support failure, and roof fall. In the case of the rock mass composed of soft fissured rock, the roadways stability issue is further relevant.

Current roadway support systems, including rock bolting, steel arch, hydraulic supports, and combined supports, are commonly successfully used to control the deformation of the roof and side walls of roadways. However, often a floor heave is still a serious failure phenomenon in mine roadways [5–7].

Many scholars have used theoretical analysis, physical experiments, and numerical simulations to study the floor heave in deep roadways with soft rock and have proposed various solutions. Existing technologies of floor heave controlling are quite advanced; these include the steel closed supports and concrete inverted arches, stress relief slots in the floor or wall of roadway, and reinforcement of surrounding rock.

Zhao et al. [8] researched and proposed a U-shaped steel closed support with an inverted steel arch in the floor as a method for improving the support effect of the surrounding rock during the process of floor heaving. Li et al. proposed the double-yield shell coupling support technology for high-stress soft rock roadways [9]. Wang et al. [10] managed to

control floor heave by using the high resistance yieldable multiple support for roadways excavated in extremely soft rocks.

Zheng et al. [11] designed a composite structure, including concrete antiarches and bolts, to control the floor heave. By means of field investigation, theoretical analysis, numerical calculation, and engineering practice. Wang et al. [12] established the instability reasons for the inverted arch structure and proposed a 36U-shaped steel round frame with bolt-mesh-shotcrete-combined support to control the floor heave.

Chen et al. [13] proposed an innovative "relief-retaining" control scheme of floor heave, which is the comprehensive measure of "cutting groove in floor + drilling for pressure relief at roadway side + setting retaining piles at the junction of roadway side and floor." Yang and Zhang [14] put forward the pressure-relief slot to prevent floor heave, established the mechanical model of the pressure-relief slot, and gave a method to determine the width of the pressure-relief slot.

The most worldwide floor heave control technology is reinforcement. Chang et al. [15] proposed hydraulic expansion bolts to prevent the development and flow of the plastic zone in the floor rock to control floor heave. He et al. [16] proposed a new method to control floor heave with bolt-net-anchor coupling support technology, with the anchor wire at a key location, with the rigid bolt, and corner grouting. Yang et al. [17] studied the floor heave control method of high-stress soft rock roadway and proposed new coupling support technology of a bolt-mesh-anchor-base angle bolt-flexible layer truss for controlling roadway floor heave. Wang et al. [18], using numerical simulations and theoretical analysis determined that an effective method for controlling floor heave is "self-drilling anchor bolt" + "high-strength reinforcement anchor bolt" + "W type steel belt" + "steel mesh" + anchor cable with birdcage.

Some scholars have focused on the bottom corners of the roadway where the critical stress concentration causes failure. Chen et al. [19] controlled the floor heave of gob-side entry retaining by reinforcing sides and corners of the solid coal body, and obtained an influence on the floor heave of gob-side entry retaining of sides supporting strength and the bottom bolt orientation in coal side. Cao et al. [20], based on the modelling by FLAC3D, proposed the floor support method, which includes optimal bolt parameters and arrangement, floor beam layout by grooving, and full-length grouting. Guo et al. [21] showed that intensive bolts with steel belt, wire mesh, and cable, can significantly reduce the floor heave in the roadway, the roof, and the side walls, compared with lower supporting intensity.

Zhang and Shimada [22] managed to control floor heave in retained goaf-side gate road by using grouting reinforcement. Shimada et al. [23] studied the reinforcement effect of cement grouting materials with different water-cement ratios on the floor. Sun et al. put forward the technology of reinforcing surrounding rocks to realize floor stability in inclined strata and soft rock [24].

To solve the problem of roadway floor heave, Zhou et al. [25] put forward three rock bolt support optimization schemes. The support effect of each scheme was simulated

and finally was determined that scheme 3 (the base plate anchor bolt adopts a pair of bottom angle anchor bolts in each row plus three vertical anchor bolts) is the best support optimization scheme.

Most studies are based on the results of numerical simulations because there are the best ways to model the magnitudes and spatial distribution of deformations [26]. Zhao et al. [8], Chen et al. [13], Guo et al. [21], Zhang and Shimada [22], and Zhou et al. [27] used a FLAC3D simulation. Kulatilake et al. used 3DEC software to simulate high-stress roadways and proposed the use of 3 m bolts and inverted arch roadways to control the surrounding rock [25]. Qi et al. [3], and Zhang et al. [28] simulated the failure mechanism of soft rock roadway by UDEC. Sakhno et al. [29] performed numerical modelling of controlling a floor heave of roadways in the soft rock by ANSYS. Małkowski et al. [26] used a phase 2 program.

In this paper, the mine roadway floor heave evolution during an increase in rock fracturing over time and rock bolts reinforcement technology were studied to effectively control the large nonlinear deformation of soft laminated floor rock. The mechanical properties of the surrounding rocks were studied using laboratory tests. The floor heave evolution and characteristics of the stress-strain state of surrounding rocks were analyzed by using the ANSYS. At the same time, physical and mechanical properties of the rocks were changed during the simulation. The degree of rock mass discontinuity was carried out by changing the Hoek–Brown parameters. This paper proposed coupling floor support technology of rock bolts with steel belt, which includes optimal bolt parameters and arrangement. The specific parameters suitable for controlling the floor heave of the roadway were determined using the numerical simulation method.

2. Engineering Background

2.1. Project Overview.
Surgaya coal mine is located in Vugledar city, Donbas region of Ukraine. At present, the main producing coal seam is the C11 coal seam. The average thickness of the C11 coal seam is 1.6 m, while the dip angle ranges from 7° to 10°. The studied roadway is presented in Figure 1(a). It was an air-return roadway of the 14th eastern panel of level 824 m. The dip angle of the roadway was 8°. The width and length of the 13th eastern panel were 182 m and 1600 m, respectively. This panel was extracted. At present, the 14th eastern transport roadway is being developed to create a new 14th eastern longwall panel. There are 45 m and 56 m coal pillars between the air-return roadway of the 14th eastern panel and the stop mining line. The surrounding rock of the roadway is mainly composed of mudstone and sandy mudstone. The detailed strata histogram and position of the roadway are illustrated in Figure 1(b).

2.2. Supporting System and Deformation Characteristics.
The section shape of the studied roadway was a semi-circular arch, 5.5 m in width and 4.2 m in height. The height of the straight wall was 1.8 m and the radius of the arch was 2.64 m.

Column	Lithology	Thickness (m)	Geologic description, uniaxial strength σ_c, (MPa)
	sandy mudstone	21.2	gray, horizontal bedding, σ_c=30-35 MPa
	sandy mudstone	8.6	dark gray, σ_c=22 MPa
	coal C11	1.4	semibright coal, fractured, σ_c=7-10 MPa
	mudstone	6.0	gray, laminated σ_c=18.5 MPa
	sandstone	22.5	gray, horizontal bedding, σ_c=32-37 MPa

(a)   (b)
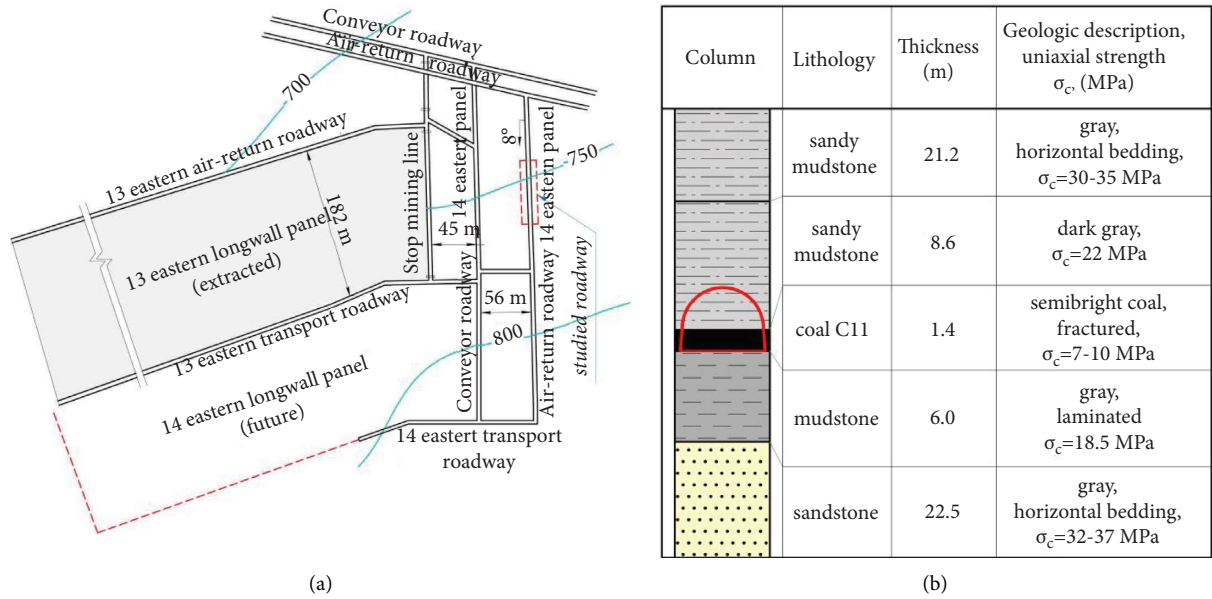
FIGURE 1: The studied area and geological conditions: (a) the locations of the studied roadway; (b) strata histogram.

The support used in the roadway was U-shape steel arches (U33) with wooden boards as filling material.

Field observations revealed a serious overall deformation of the roadway that has significantly reduced the roadway section. The characteristic points of failure of the roadway were the roof, floor, and roadway side walls.

The average roof subsidence and side walls convergences were 370 mm and 280 mm, respectively. In some sections of the roadway, the rate of deformation was as large as 1.5 times. This was the reason for the failure of the legs and the shed top of U-shaped steel arches (Figures 2(a) and 2(b)). As a rule, these locations were associated with different degrees of water inflow. Despite this, the deformations of the roof and side walls overall were not critical. The main problem was a floor heave up to 0.5-0.6 m (Figure 2(c)). The floor heave was aggravated in zones of the increased water content of the rocks. The deformation and failure of the roadways and supports are shown in Figure 2(d). The track laid in the roadway was seriously deformed. The roadway had to be repaired to ensure transport and supply the necessary amount of air to ventilate the 13 longwall panels. This process wasted a lot of manpower and material resources. So, it is necessary to optimize the support scheme to control the floor heave of the roadway and ensure the normal production of the 14th longwall panel and the next ones after it.

The results of observation are in good agreement with measurements in situ. The floor heave on stations, which were built in roadways D-2 and F-33b, was monitored over two years [30]. In roadway D-2, the maximum value of upheaval after almost 800 days of monitoring was 0.54 m, and in roadway F-33b 0.6 m. The average value of floor heave on monitoring stations in the conveyor roadway of 5 longwalls of 3 m seam was 0.7 m [31]. The zone of rock cracking in the floor of the roadway was more than 7 m. The floor heave of the roadway of the Qitaihe Longhu coal mine [27] was very serious; the maximum floor heave was 0.9 m,

which seriously restricted the efficient production of the coal mine.

2.3. Laboratory Tests. The specimens of intact rocks were selected during excavated of the floor and reconstruction of the roadway for the uniaxial compressive strength tests. Rectangular prism-shaped specimens with a rib size of about 55 mm were made. The tests were completed using a universal testing machine (Figure 3(a)). Test results for a specimen of mudstone and coal are shown in (Figure 3(b)) as an example.

Then, the average deformation modulus (E_{def}) was calculated in the pre-peak region of the stress-strain curve. The deformation modulus fluctuations for the last stage of loading of specimens are shown in Figure 3(b). The average value of E_{def} of mudstone was 1955 MPa, and E_{def} of coal was 1145 MPa. The uniaxial compressive strength (σ_c) of mudstone was 19.3 MPa, and (σ_c) of coal was 9.1 MPa.

Due to the previous long exploitation time of the roadway (more than 4 years), and water inflow the surrounding soft rocks were fractured. Therefore, to model rock masses, it is necessary to correct the parameters of intact rock.

The Hoek–Brown Failure Criterion [32] was used, which is widely accepted and applied in many projects and applications around the world. Based on the physical and mechanical measurements and analysis of the joint, the surrounding rocks were determined Hoek–Brown Parameters: the Geological Strength Index (GSI), values of the constant m_i and the disturbance factor (D). For example, the Hoek–Brown parameters used the modelling for the floor rocks not exposed to the water and for the waterlogged floor rocks in the project [26].

Since the main problem with the stability of the roadway was floor heaving, floor rocks were studied more carefully.

(a)

(b)

(c)

(d)
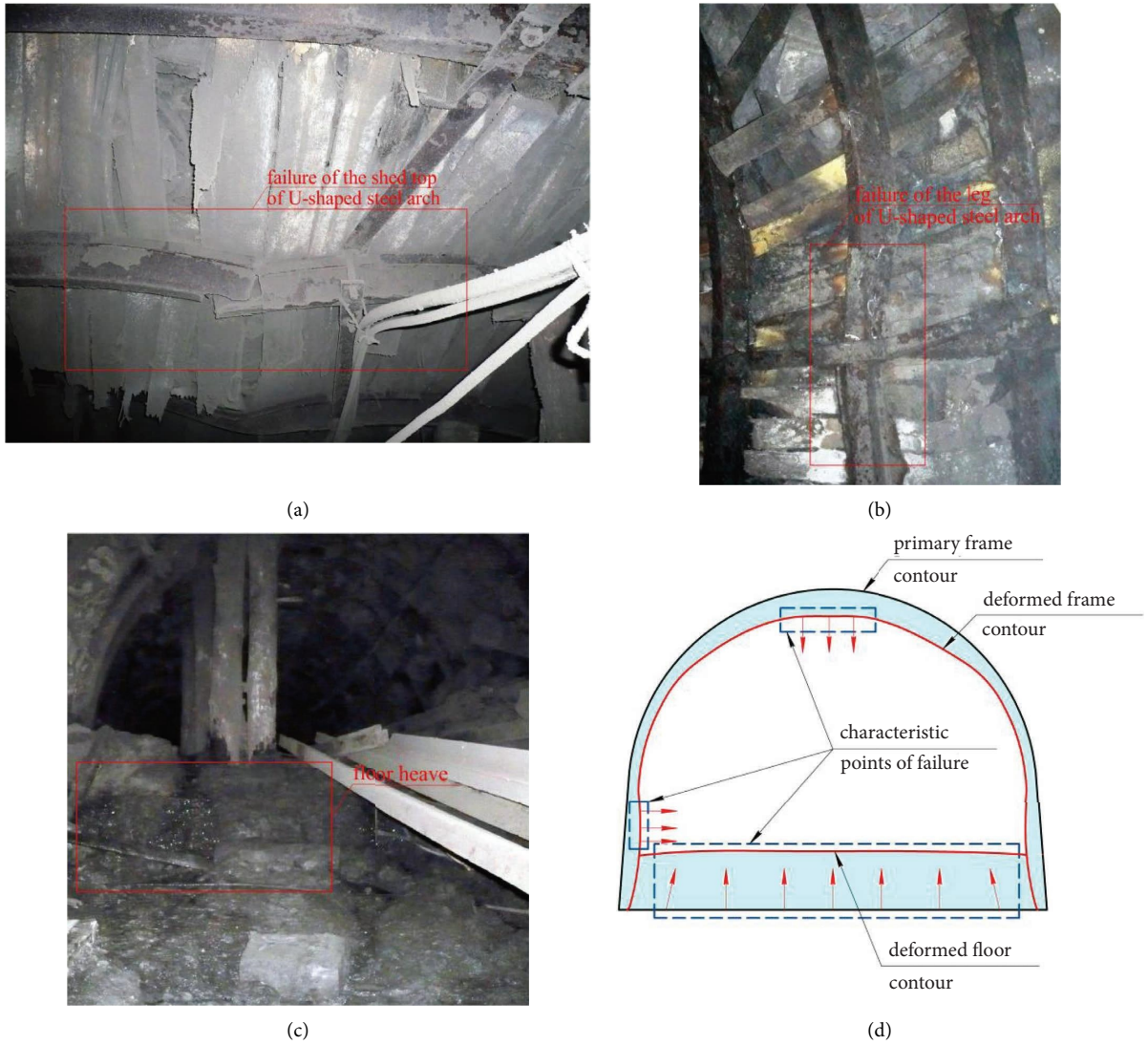
FIGURE 2: The characteristics of rupture of the roadway: (a) the failure of the shed top of the U-shaped steel arch; (b) the failure of the leg of the U-shaped steel arch; (c) the floor heave; (d) the characteristic failures of the studied roadway.

(a)

(b)
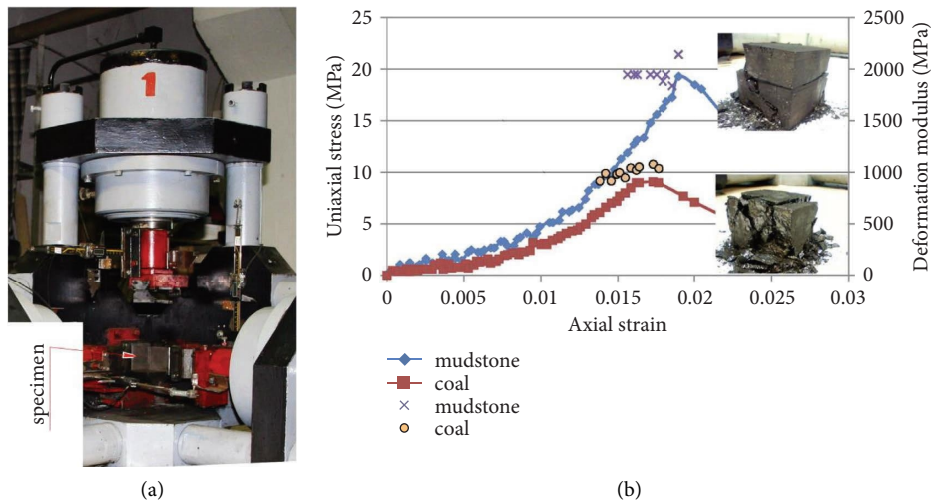
FIGURE 3: Laboratory equipment and test results: (a) the universal testing machine; (b) stress-strain curve and deformation modulus fluctuations for coal and mudstone specimens.

The study of the degree of disturbance of floor rock mass showed that the average joint spacing was about 30 cm, so the minimum GSI value was taken to be 63 (Figure 4) [33]. The disturbance factor for the floor was $D = 0.7$.

The Geological Strength Index for surrounding rocks was calculated as GSI = RMR$_{89}$−5 [26, 32], and it has been in the range of 74–63 since mining, as shown in Figure 4.

For estimating rock mass, deformation modulus used the empirical method [34]. The following equation was used:

$$E_{rm} = E_i \left(0.02 + \frac{1 - D/2}{1 + e^{(60+15D-GSI/11)}} \right), \tag{1}$$

where E_{rm} and E_i represent the deformation modulus of the rock mass and the intact rock, respectively.

The following equations were used for the angle of friction (φ) and the cohesive strength (c):

$$\varphi = \sin^{-1} \left[\frac{6am_b \left(s + m_b \sigma_{3n}^1 \right)^{a-1}}{2(1+a)(2+a) + 6am_b \left(s + m_b \sigma_{3n}^1 \right)^{a-1}} \right],$$

$$c = \frac{\sigma_{ci} \left[(1+a)s + (1-a)m_b \sigma_{3n}^1 \right] \left(s + m_b \sigma_{3n}^1 \right)^{a-1}}{(1+a)(2+a)\sqrt{1 + 6am_b \left(s + m_b \sigma_{3n}^1 \right)^{a-1} / ((1+a)(2+a))}}, \tag{2}$$

where m_b, s, and a represent peak strength parameters of Hoek–Brown [32]; σ_{ci}-uniaxial compressive strength of the intact rock; $\sigma_{3n}^1 = \sigma_{3\max}^1 / \sigma_{ci}$-the upper limit of confining stress over which the relationship between the Hoek–Brown and the Mohr–Coulomb criteria is considered [32].

The uniaxial compressive strength of the rock mass was calculated as follows:

$$\sigma_{crm} = \sigma_{ci} s^a. \tag{3}$$

The tensile strength of the rock mass was calculated as follows:

$$\sigma_{trm} = -\frac{\sigma_{ci} s}{m_b}. \tag{4}$$

The properties of the rock mass were calculated for the studied strata. They are listed in Table 1.

According to the classification of the International Society for Rock Mechanics (ISRM), the surrounding rocks were "weak" because their average uniaxial compressive strength (UCS) was in the range of 5–25 MPa [35]. In addition, the surrounding rocks were fissured and wet, and the immediate floor of the roadway was laminated. This explains the large deformations in the roadway. The reliability of ventilation of the 14th eastern panel depends on the deformations degree of the air-return roadway, especially on the rate of floor heave. Therefore, it is imminent to research the control technology of the floor heave.

3. Study of the Floor Heave in Soft Rock

3.1. Numerical Model. The numerical simulation by means of ANSYS was performed to analyze the characteristics of the stress and strain distributions of surrounding rock before and after reinforcing of floor. To simulate the behavior of rock mass, the Drucker–Prager model was used. The model enables simulating plastic deformation of rock and its other pressure-dependent material, which corresponds to the properties of rocks in a fracture zone.

The model simulates a cross-section of roadway with the unit thickness (1 m). The distance between the rows of bolts is 1.0 m. Thus, the support is set in the middle along the thickness of the model (with the coordinate $z = 0.5$). Thus, the condition of symmetry and uniformity is satisfied. When the distance between the rows of anchors is less or more than 1.0 m, then the result obtained should be multiplied by the support density factor $F_d = 1/a$, where a is the actual distance between the rows of anchors.

The numerical model was established according to the actual geological engineering conditions. The model was 1 m long, 60 m wide, and 60 m high. Horizontal displacements were fixed at the lateral boundaries. Vertical displacements were fixed at the bottom boundary. The top boundary was set free. A vertical pressure of 20 MPa, that equivalent to the weight of rocks at a depth of development (800 m), was applied on the top of the model. A 5.5×4.2 m arch shape roadway was adopted, and the beam unit was used to simulate the U-shaped steel support. The filling material (wooden boards) was modeled between rock mass and frames (Figure 5).

For investigation of the evolution on the floor heave of soft rock mass in the deep roadway, the physical and mechanical properties of the rocks were changed during the simulation. This simulated an increase in rock fracturing over time. Numerical accounting of the degree of rock mass discontinuity was carried out by changing the Hoek–Brown parameters: GSI (from 74 to 63) and D (from 0 to 0.7). The initial value of the Hoek–Brown parameters corresponded to the stage of development, and the final state of the parameters corresponded to the roadway reconstruction stage (critical floor heave). The numerical modelling process had 9 steps: 1 step for intact rock and 8 steps for the rock mass. The most detailed was the simulation of the immediate floor, the joint spacing of which was 1.8–0.25 m for steps 2–9, respectively. Properties of the main roof and main floor did not change because these strata were out of the influence of the roadway. Table 2 presents the mechanical parameters of rock mass for each step. The dilatancy angle was taken equal
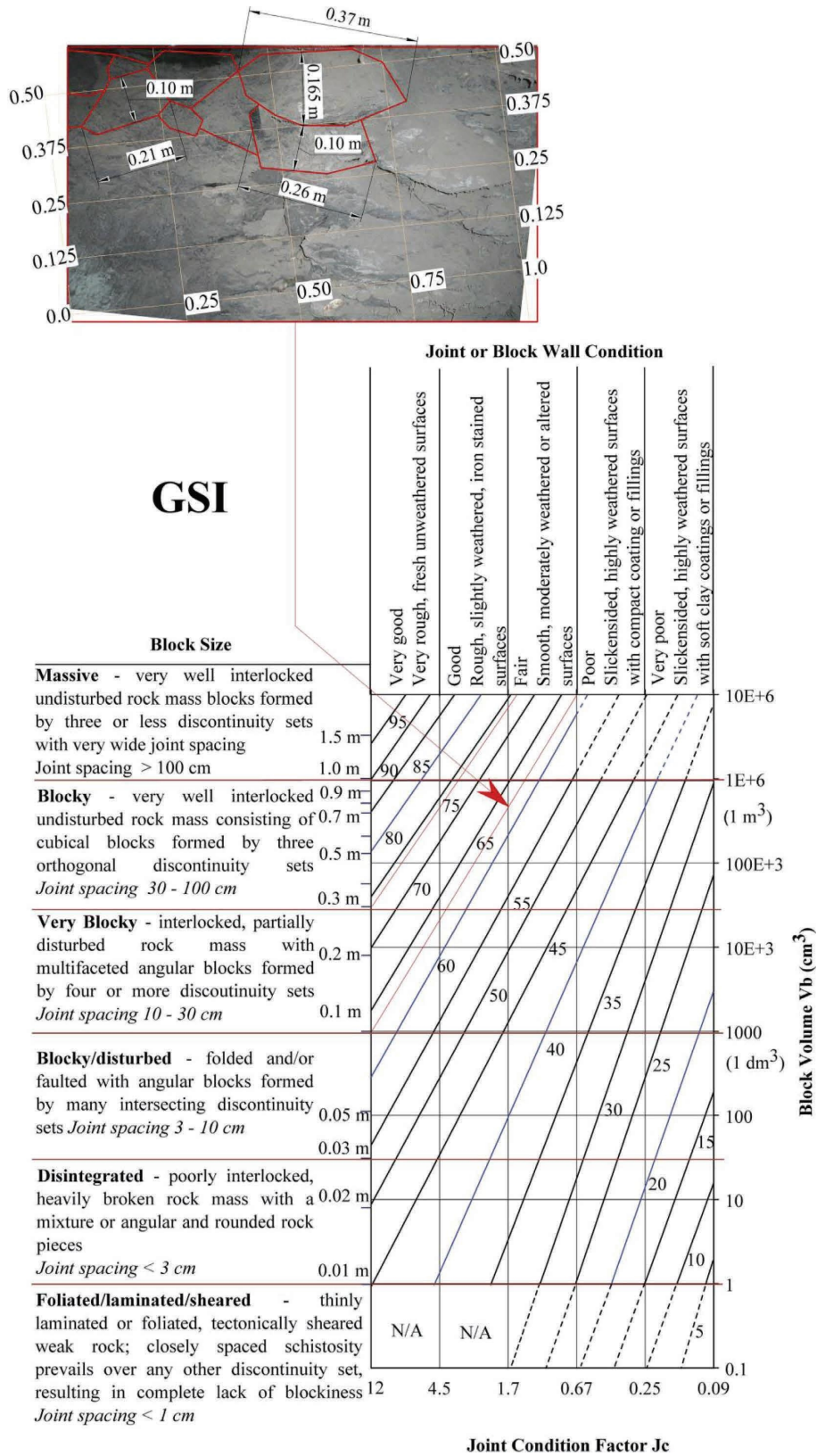
FIGURE 4: Quantification of GSI chart [33] with indicating region for the studied roadway.

TABLE 1: Intact rock properties and calculated rock mass properties.

| Rock strata | Density (kg/m³) | Intact rock | | GSI/D/m_i | Rock mass | | |
		Young's modulus (MPa)	Compressive strength (MPa)		Young's modulus (MPa)	Compressive strength (MPa)	Tensile strength (MPa)
During reconstruction of roadway							
Sandy mudstone	2400	3600	40.0	71/0.3/7	2040	6.7	0.55
Sandy mudstone	2400	2245	35.0	67/0.6/7	760	3.5	0.28
Coal C11	1300	1145	9.1	66/0.5/15	420	1.9	0.07
Mudstone	2300	1955	19.3	63/0.7/7	460	1.3	0.10
Sandstone	2400	6120	55.0	72/0.3/7	3573	9.7	0.80
During development of roadway							
Sandy mudstone	2400	3600	40.0	74/0/7	2881	9.4	0.80
Sandy mudstone	2400	2245	35.0	74/0/7	1797	8.3	0.70
Coal C11	1300	1145	9.1	70/0/15	838	3.4	0.12
Mudstone	2300	1955	19.3	73/0/7	1536	4.3	0.36
Sandstone	2400	6120	55.0	74/0/7	4889	13.0	1.20
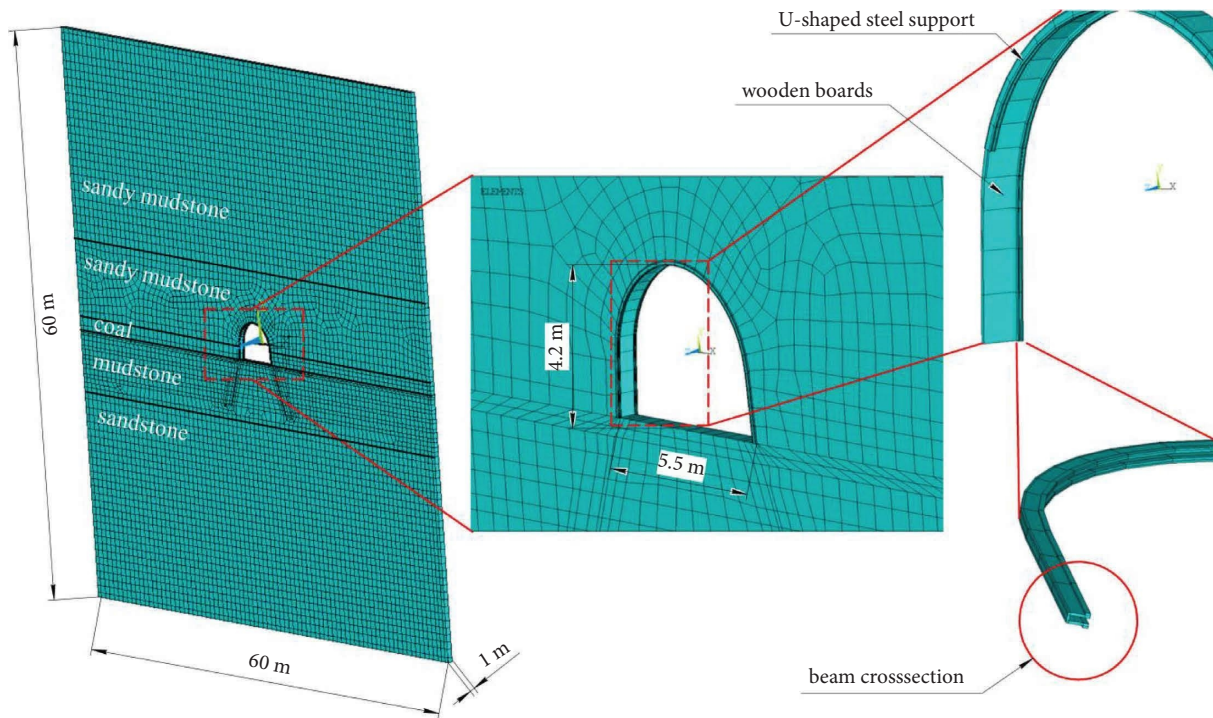
FIGURE 5: Numerical simulation model and supporting units.

to the angle of internal friction, which corresponded to the unfavorable option. Mechanical parameters of U-shaped steel support are shown in Table 3.

3.2. Simulation Results.

The stress distributions of the surrounding rocks are shown in Figure 6. It is seen that the zone of reduced maximum principal stresses σ_1 is formed on the floor of the roadway (Figure 6(a)). In the distance from the floor surface to deep equal to the roadway width, the stress σ_1 is 2-3 times less than out of the roadway influence. The level of tensile stresses near the contour of the floor in the central part of a cross-section of the roadway is greater than the tensile strength of mudstone.

It is the potential zone of rock fracture. This region is highlighted in gray color. On the side of the roadway, the size

TABLE 2: Rock mass parameters for numerical simulation.

Steps	GSI/ D	Compressive strength (MPa)	Tensile strength (MPa)	Deformation modulus (GPa)	Poisson's ratio	Cohesion value (MPa)	Angle of internal friction (deg)	Dilatancy angle (deg)
				Main roof (sandy mudstone)				
1	—	40.0	3.50	3.60	0.3	5.35	30	30
2–9	71/ 0.3	6.7	0.55	2.04	0.3	4.20	28	28
				Immediate roof (sandy mudstone)				
1	—	35.0	3.05	2.24	0.3	6.40	32	32
2	74/0	8.2	0.7	1.79	0.3	5.20	30	30
3	72/ 0.2	6.6	0.54	1.40	0.3	3.30	27	27
4	71/ 0.3	5.8	0.47	1.29	0.3	2.95	26	26
5	70/ 0.4	5.1	0.41	1.09	0.3	2.63	25	25
6	68/ 0.5	4.1	0.35	0.93	0.3	2.37	24	24
7	67/ 0.7	3.5	0.27	0.76	0.3	2.11	23	23
8	67/ 0.7	3.5	0.27	0.76	0.3	2.11	23	23
9	67/ 0.7	3.5	0.27	0.76	0.3	2.11	23	23
				Coal C11				
1	—	9.1	0.10	1.14	0.3	2.60	26	26
2	70/0	3.4	0.12	0.84	0.3	2.30	24	24
3	70/ 0.2	3.0	0.11	0.68	0.3	2.11	23	23
4	69/ 0.3	2.7	0.09	0.60	0.3	1.82	23	23
5	68/ 0.4	2.3	0.08	0.51	0.3	1.64	22	22
6	67/ 0.5	2.0	0.07	0.44	0.3	1.47	21	21
7	66/ 0.5	1.9	0.08	0.42	0.3	1.43	21	21
8	66/ 0.5	1.9	0.08	0.42	0.3	1.43	21	21
9	66/ 0.5	1.9	0.08	0.42	0.3	1.43	21	21
				Immediate floor (mudstone)				
1	—	19.3	1.60	1.80	0.3	4.30	28	28
2	73/0	4.3	0.36	1.53	0.3	3.42	27	27
3	72/ 0.2	3.6	0.30	1.25	0.3	2.89	26	26
4	71/ 0.3	3.2	0.26	1.10	0.3	2.63	25	25
5	70/ 0.4	2.8	0.23	0.96	0.3	2.37	24	24
6	68/ 0.5	2.3	0.18	0.79	0.3	2.11	23	23
7	65/ 0.6	1.7	0.13	0.59	0.3	1.82	23	23
8	64/ 0.7	1.4	0.11	0.50	0.3	1.64	22	22
9	63/ 0.7	1.3	0.10	0.46	0.3	1.47	21	21
				Main floor (sandstone)				
1	—	55.0	3.50	6.12	0.3	19.10	35	35
2–9	72/ 0.3	9.7	0.80	3.50	0.3	5.00	32	32

TABLE 3: Properties of support elements used in the model.

Primary support	Type of elements	Material behaviour option	Elastic modulus (GPa)	Poisson's ratio	Yield strength (MPa)	Tangent modulus (GPa)
U-shaped steel support	Beam	Bilinear isotropic hardening	200	0.3	342	52.2
Filling material (wooden boards)	Solid	Isotropic	750	0.3	—	—

of the zone of reduced σ_1 reaches half the roadway width. An insignificant decrease in stresses also occurs in the roof of the roadway.

The analysis of the distribution patterns of the minimum principal stresses σ_3 (Figure 6(b)) shows that an area of increased σ_3 is formed on the sides of the roadway in the distance from the side wall surface to the deep equal to the roadway width. The largest σ_3 are formed at the bottom corners of the roadway.

After the development of the roadway, deformations of the roof, side wall, and floor are not large. The distribution of vertical displacement of the roof and floor after development is shown in Figure 6(c). The floor heave of the roadway is 0.072 m. The roof subsidence is 0.03 m. Maximum principal strains of surrounding rocks are within the limits of elasticity, except for the bottom corners of the roadway (Figure 6(d)).

The results of laboratory tests show that the failure strain of mudstone is 0.018–0.02, and of the coal is 0.012–0.016 (Figure 3). This corresponds with the results of testing soft rock specimens in a volumetric field [36–38] and under uniaxial compression [39, 40]. According to the results of tests, it was found that for mudstone, siltstone, argillite, and sandstone with uniaxial strength of 25–40 MPa, the failure criteria for strain is about 0.02-0.03. Thus, for this study, the failure limit is in the range of "−0.02"–"+0.02".

Figure 7 shows the distributions of minimum principle stress (σ_3) around the roadway in the simulation increasing in rock fracturing. The evolution of σ_3 shows that on the roof and on the floor of the roadway the reduced stress areas increase step by step. At the same time, roof subsidence occurs, and floor heave grows. The σ_3 in the bottom corners of the roadway significantly exceed the compressive strength of the mudstone. Under the foot of the arch support, there is a high probability of rock destruction.

The size of the increased σ_3 zone on the side wall increases. So the width of the increased stress zone, in which σ_3 is 5–30% greater than σ_3 before excavation, exceeded the width of the roadway (W) at the last step of the simulation by 1.5 times. Near the contour of the roadway, the nature of the stress changes significantly. The monitoring line A-A[1] was arranged along the horizontal axis, and the stress on this line changed with the number of calculation steps (Figure 8(a)). Figure 8(a) shows that at 2, 3, and 4 steps in the near-contour area with a depth of 0.7 m, a decrease in stresses is observed; however, at subsequent steps, stresses increase in this area. This can be explained by the compression of rocks near the contour of the roadway, caused by the resistance of the frame support, which increases with the increasing displacement of rocks.

The stress concentration factor is defined as the stress value at that point divided by the stress before excavation. For simulation steps, 2 and 9 the stress concentration factor on the right side of the roadway is presented in (Figure 8(b)). It is observed that σ_3 concentrates on the roadway sides at a depth of 1.2 m, with a stress concentration factor of 1.16. With an increase in the number of calculation steps, the σ_3 concentration factor continuously increases, and the concentration of stress shifts to the deep part. At the last simulation step, σ_3 concentrates at the depth of 1.8 m, with a stress concentration factor of 1.19.

Figures 9 and 10 show the distributions of maximum principle stress and maximum principle strain, respectively, for the surrounding rocks with calculation steps. Figure 9 shows that the size of the reduced stress zone in the floor and the roof of the roadway with an increase in the number of calculation steps increases gradually. Thus, the size of the reduced stress zone, in which σ_1 is 2.8 times less than before excavation, increases from 0.68 W to 1.0 W. At the same time, as the reduced stress zone in the floor increases, on the wall sides of the roadway, the stresses become less intense. The size of the reduced stress zone with an increase in the number of calculation steps increases.

The σ_1 in the central part of the roadway floor significantly exceed the mudstone tensile strength, which indicates a high probability of rock failure. Obviously, the evolution of σ_1 correlates with the growth of the floor heave.

The maximum principle strain of surrounding rocks of the roadway is increased nonlinearly with an increase in the number of calculation steps, as shown in Figure 10.

The maximum principle strains in the immediate floor exceed the failure limit (+0.02). This indicates the formation of cracks in the floor. Initially, post-peak strain regions appear in the bottom corners of the roadway, after which they develop into the depths. In this way, strata on the immediate floor are destroyed one by one, starting from the corners of the roadway. At the 6th simulation step, these regions merge in the roadway floor at a depth of about 2.0 m, forming a closed contour. The gray color in Figure 10 highlights the regions of rocks in which the maximum principle strain is 2.5 times greater than the post-peak ones. It can be seen that at the 9th step, the strata on the immediate floor to a depth of more than 2.0 m are included in this region. Thus, a high degree of floor destruction is evident there. Dilatancy and plastic flow of rocks are observed in this region, which causes significant floor heave.

Figure 11 shows the floor heave on monitoring line B-B[1] and vertical plastic strain distribution at 1, 6, 8, and 9 steps. Post-peak plastic strains appear at the 6th simulation step. The nonlinear nature of floor heave is clearly seen in the

(a)

(b)

(c)

(d)
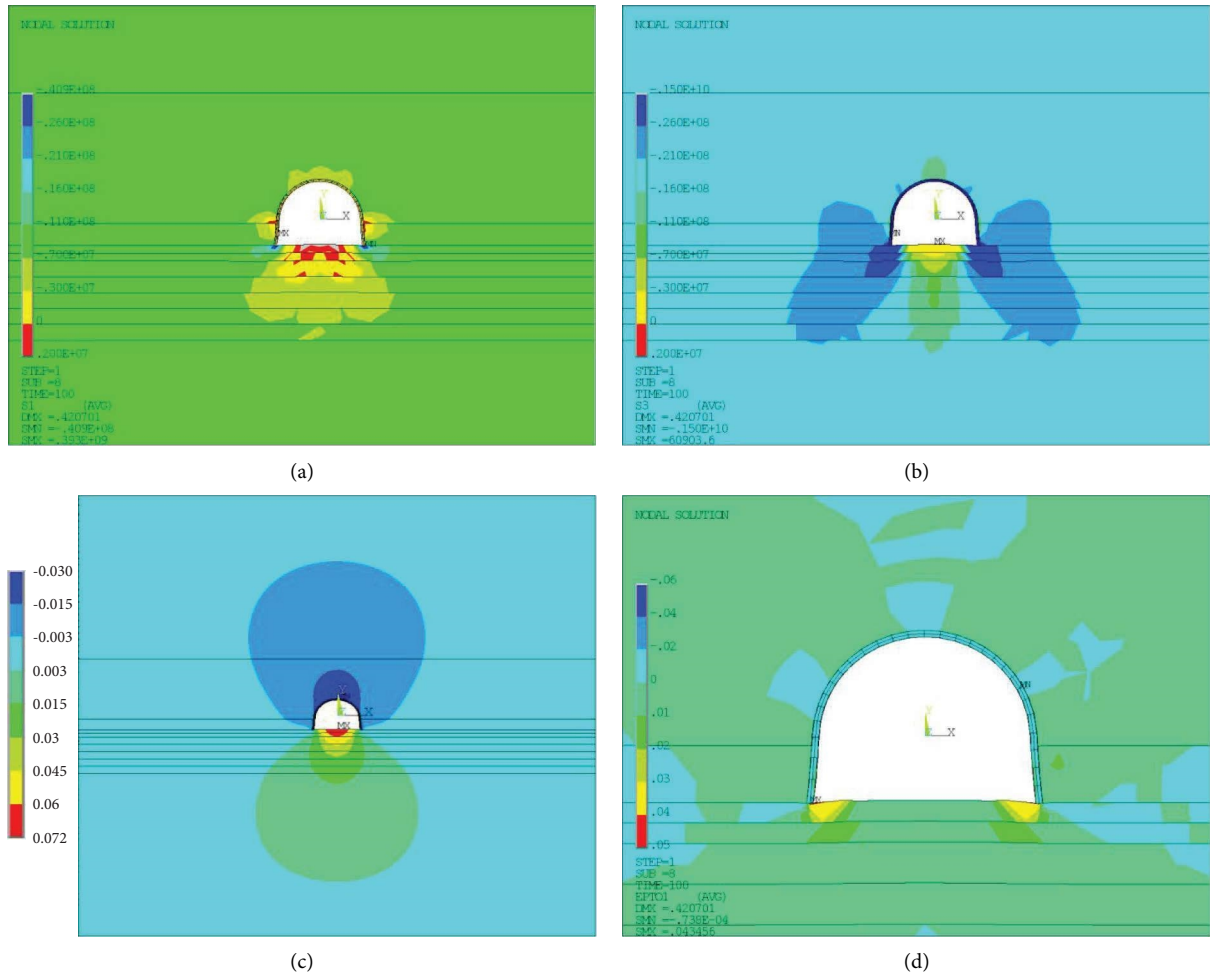
FIGURE 6: The results of numerical calculation in the case of roadway development: (a) distribution of maximum (σ_1) principal stresses; (b) distribution of minimum (σ_3) principal stresses; (c) distribution of vertical displacement; (d) distribution of maximum principal strains.

graphs in Figure 11. Thus, the nonlinear increase in heaving is a consequence of the transition of rocks to the stage of plastic deformation.

3.3. Simulation Discussions. Several conclusions can be drawn according to the above analyses:

(1) The roof and side walls were controlled adequately by the original steel arch support. In this, the simulation results correspond with observations of the roadway in situ.

(2) The stress analysis shows that with an increase in rock mass fracturing (number of calculation steps), the σ_3 concentration factor on the side wall of the roadway continuously increases, and the concentration of stress shifts to the deep rock mass part. The σ_3 in the bottom corners of the roadway significantly exceed the compressive strength of the immediate floor, which indicates a high probability of rock cracking under the foot of the arch support. At the same time, the size of the reduced σ_1 stress zone in the floor and the roof of the roadway increases

gradually. The σ_1 in the central part of the roadway floor significantly exceed the tensile strength of the immediate floor, which indicates a high probability of rock crushing.

(3) The strain analysis shows that the size of the post-peak maximum principle strain zone in the floor and side wall of the roadway increases nonlinearly with an increase in rock mass fracturing (number of calculation steps). The analysis shows that a significant proportion of maximum principle strains are plastic strains. They exceed the failure limit more than 2.5 times and cause the floor heave. Initially, post-peak strain regions appear in the bottom corners of the roadway, after which strata in the immediate floor are destroyed one by one, into the depth. After that post-peak strain regions merge in the central part of the roadway floor at a depth of about 2.0 m. Finally, the strata in the immediate floor to a depth near 2.0 m are included in the post-peak strain region, which indicates a high probability of rock crushing. This region of the surrounding rocks is mainly involved in the development of floor heave.
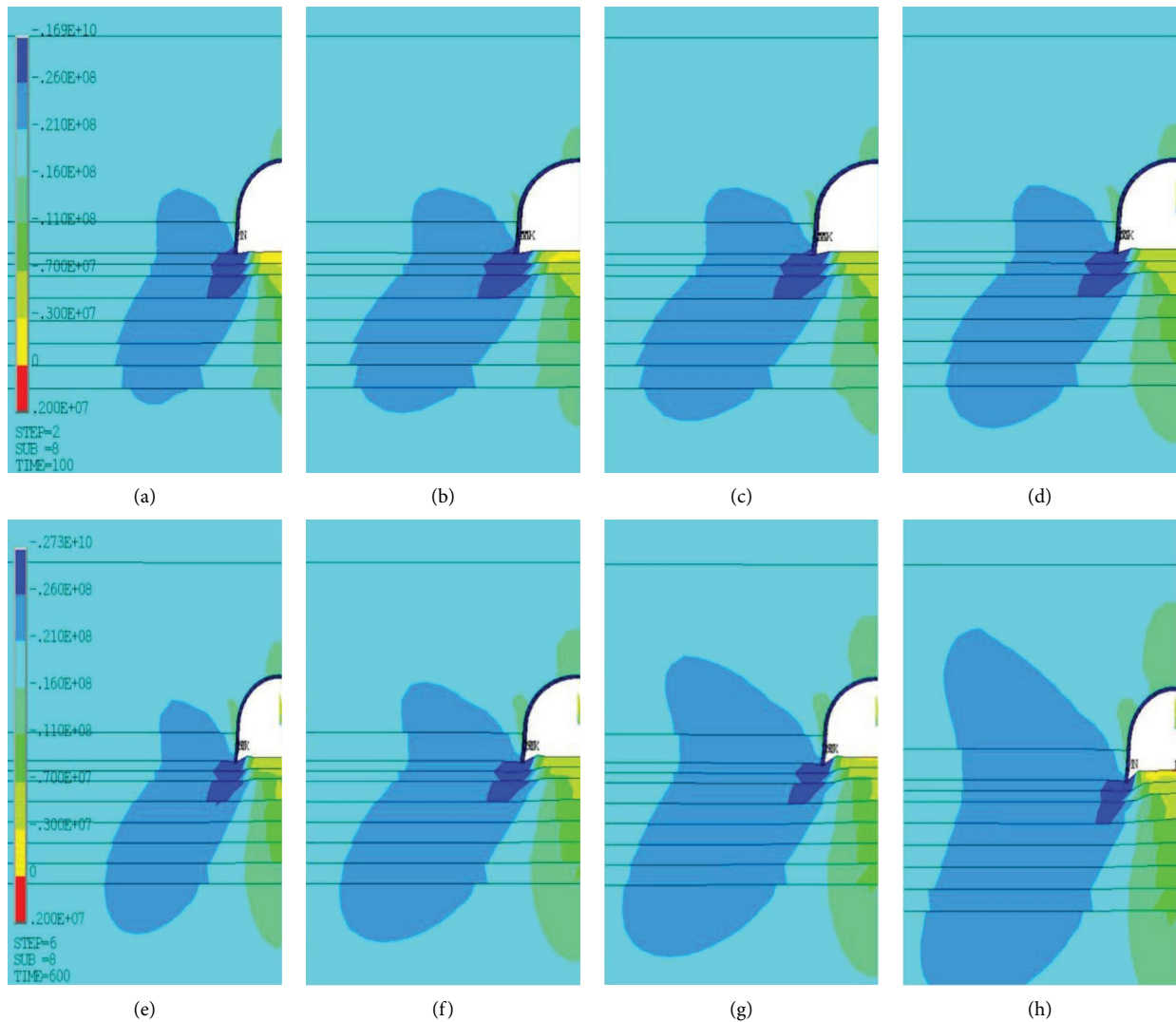
FIGURE 7: Minimum principle stress (σ_3) distribution around the roadway with a step-by-step increase in rock fracturing: (a) step 2; (b) step 3; (c) step 4; (d) step 5; (e) step 6; (f) step 7; (g) step 8; (h) step 9.

Dilatancy and plastic flow of rocks are observed in this region, which causes significant floor heave.

(4) The key to floor heaving control is to control the development of the crushing zone on the immediate floor. It is necessary to limit the development of post-peak strains from the bottom corners of the roadway deep into the massif and prevent their merging on the immediate floor. This will limit plastic deformations and dilatancy in the immediate floor, which will have a positive effect on the floor heave intensity. The critical is the 6th simulation step, which corresponds to an average joint spacing of 0.45 m in the immediate floor, as shown in Figure 12. After the merging of the post-peak strain regions and the formation of a closed contour in the immediate floor by them (simulation step 7), the heaving growth acquires an obvious nonlinear character. At this step, significant plastic deformation begins, which is the cause of uncontrolled floor heave.

4. Floor Heave Control Technology

Based on the above analysis results, the rock bolts reinforcement was proposed for the floor heave control. This technology has been widely applied in mining. Taking into account the evolution of stresses and strain in the floor of the roadway, the proposed support method should include optimal bolt parameters and arrangement.

4.1. Design of Floor Heave Control Scheme.
The region of critical stress and post-peak strain in the immediate floor is limited to a depth of 2.25 m. Three rock bolt arrangements were proposed in which the orientation of the bolts was varied. Fully grouted resin bolts were used. In modelling, the length of the bolts was different for different schemes. At the same time, the bolts lengths were assumed to multiple ones to the length of the reinforcement zone: 5 m; 4 m; 3 m; 2 m; and 1 m. When the anchoring depth was significant, the bolts consisted of sections.

(a)

(b)
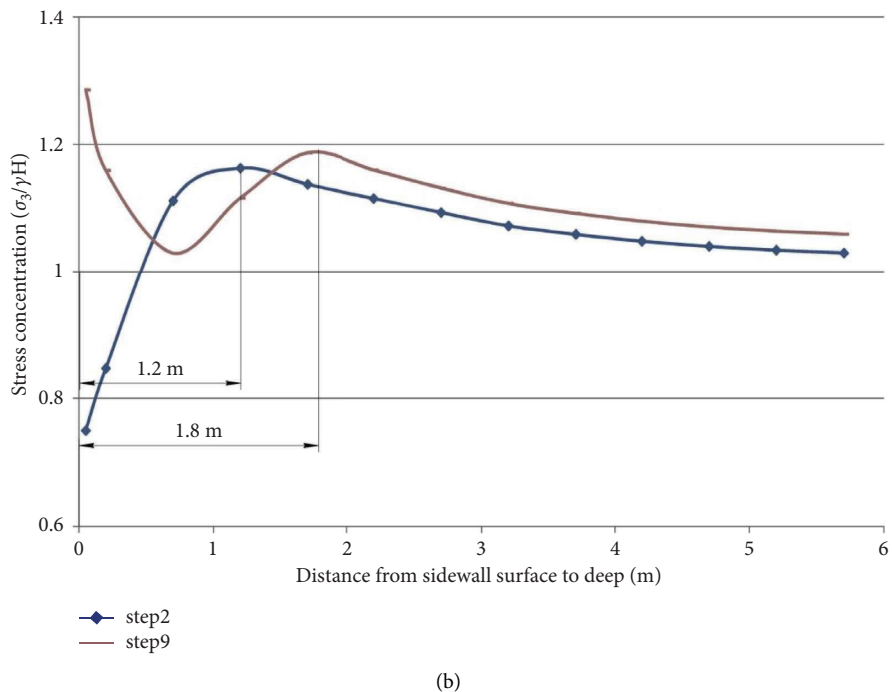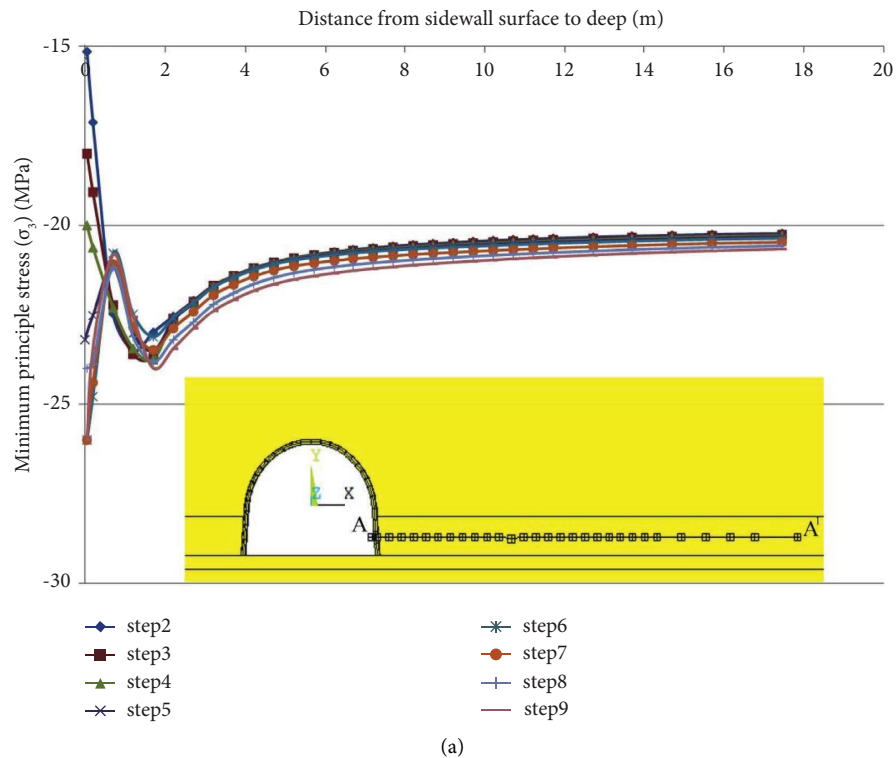
Figure 8: (a) Characteristics of minimum principle stress (σ_3) on monitoring line A-A^1 with calculation steps; (b) characteristics of stress concentration factor ($\sigma_3/\gamma H$) on monitoring line A-A^1 for steps 2 and 9.

The maximum length of the bolts was limited by the strata level $L_{max} = 5.0$ m. The bolts with traditional bearing plates were used firstl, and then bolts with steel belts were used. The original U-shaped steel support was still unchanged. Table 4 shows the setting of mechanical parameters of the rock bolts and other supporting components in the numerical model.

Figure 13 shows the support schemes of the roadway with the rock bolts reinforcement. The optimal floor heave control scheme provides an acceptable floor heave with a minimum rock bolt length. The floor support elements that were used in the model are shown in Figure 14.
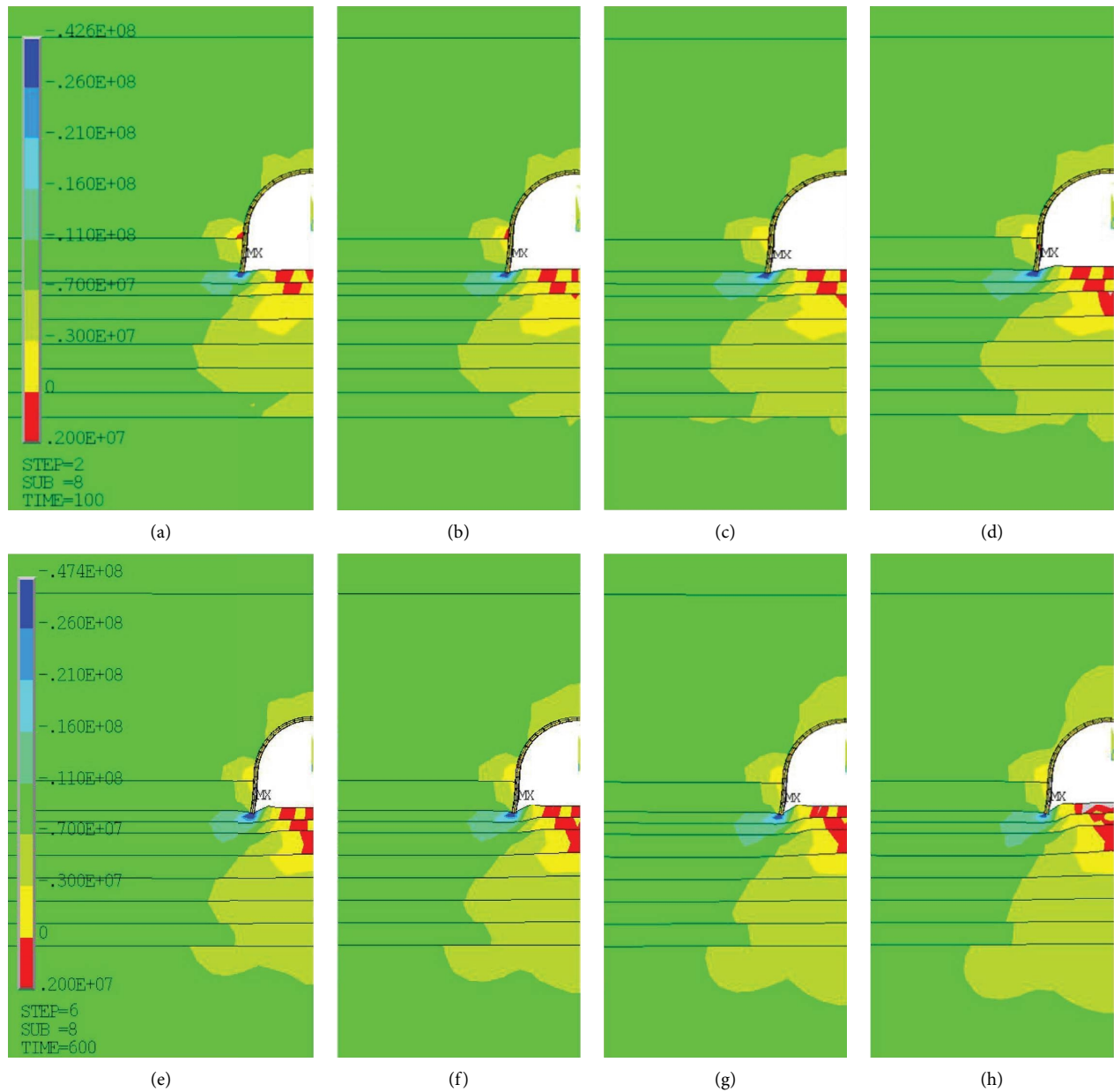
FIGURE 9: Maximum principle stress (σ_1) distribution around the roadway with a step-by-step increase in rock fracturing: (a) step 2; (b) step 3; (c) step 4; (d) step 5; (e) step 6; (f) step 7; (g) step 8; (h) step 9.

4.2. Effectiveness of Rock Bolts Reinforcement. Firstly rock bolts with bearing plates were modeled. Although the minimum principal stress in rock bolts and in the frame is less than the tensile strength of steel, the loading results in significant deformation of the frame and bolts, as shown in Figure 15(a). Most of all, the rock bolts located at the edges are bent. The analysis of vertical strains shows that the installation of bolts without additional elements generally has a positive effect on the heaving intensity. However, with this variant of floor support, post-peak strains are observed near the corners of the roadway in the near-contour of the immediate floor, as shown in Figure 15(b). This reduces the effectiveness of the reinforcement and can lead to further development of rock crushing on the immediate floor. As an

element of coupling steel belt was proposed across the entire width of the roadway's floor. A comparison of the effectiveness of floor support by bolts with steel belts and without it was made for the last simulation step, which corresponds to an average joint spacing of 0.10 m in the immediate floor.

Figure 16 shows the distributions of maximum principle stress for the surrounding rocks at the last simulation step after reinforcement for different floor support schemes. The zone of reduced stress σ_1 in the roadway floor as a result of rock bolts reinforcement is reduced in size compared to the case without reinforcement (Figure 9(h)). However, near the contour of the roadway in the immediate floor, σ_1 are formed that exceed the tensile strength of rock. The regions of critical σ_1 are located between the rock bolts. In the case of
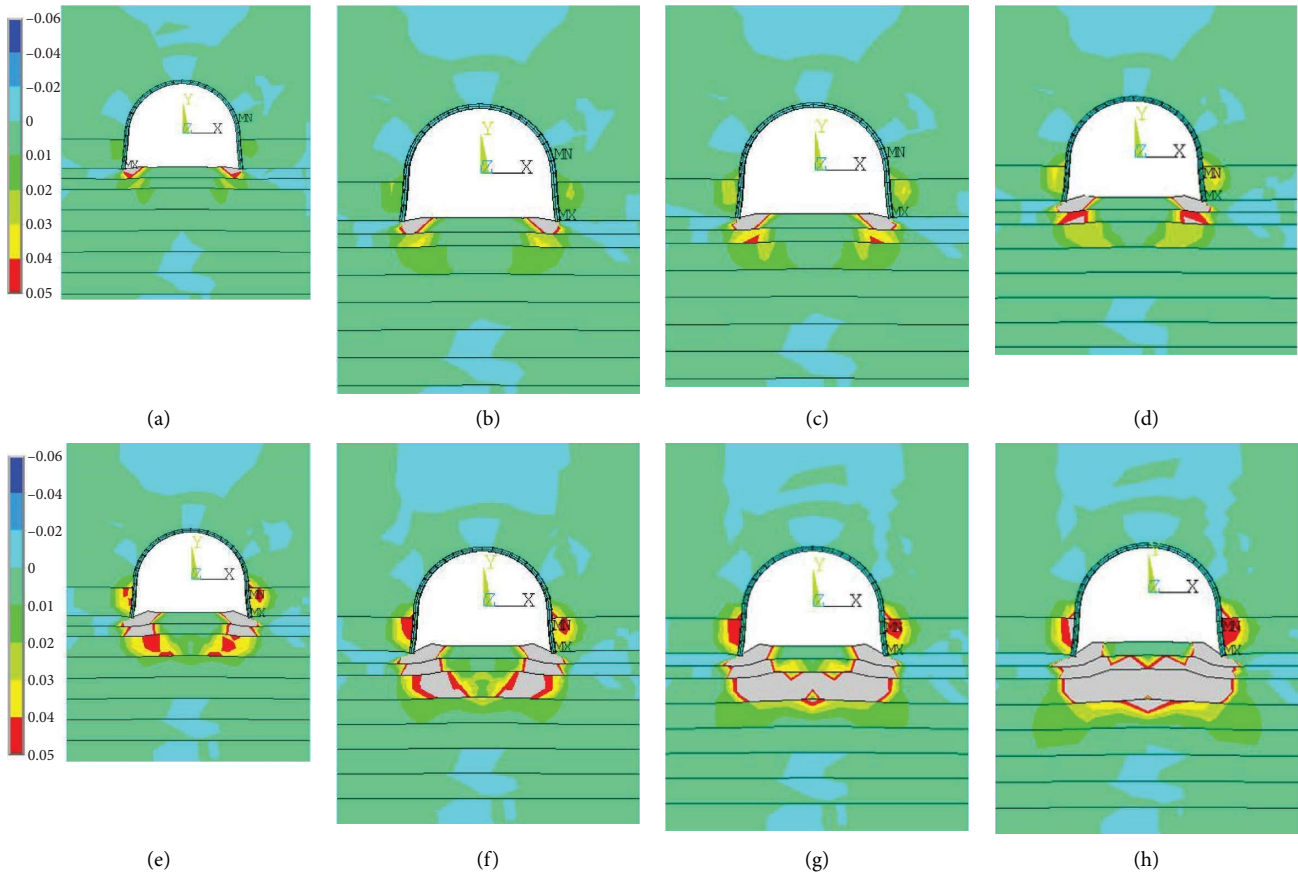
Figure 10: Total maximum principle strain distribution around the roadway with a step-by-step increase in rock fracturing: (a) step 2; (b) step 3; (c) step 4; (d) step 5; (e) step 6; (f) step 7; (g) step 8; (h) step 9.
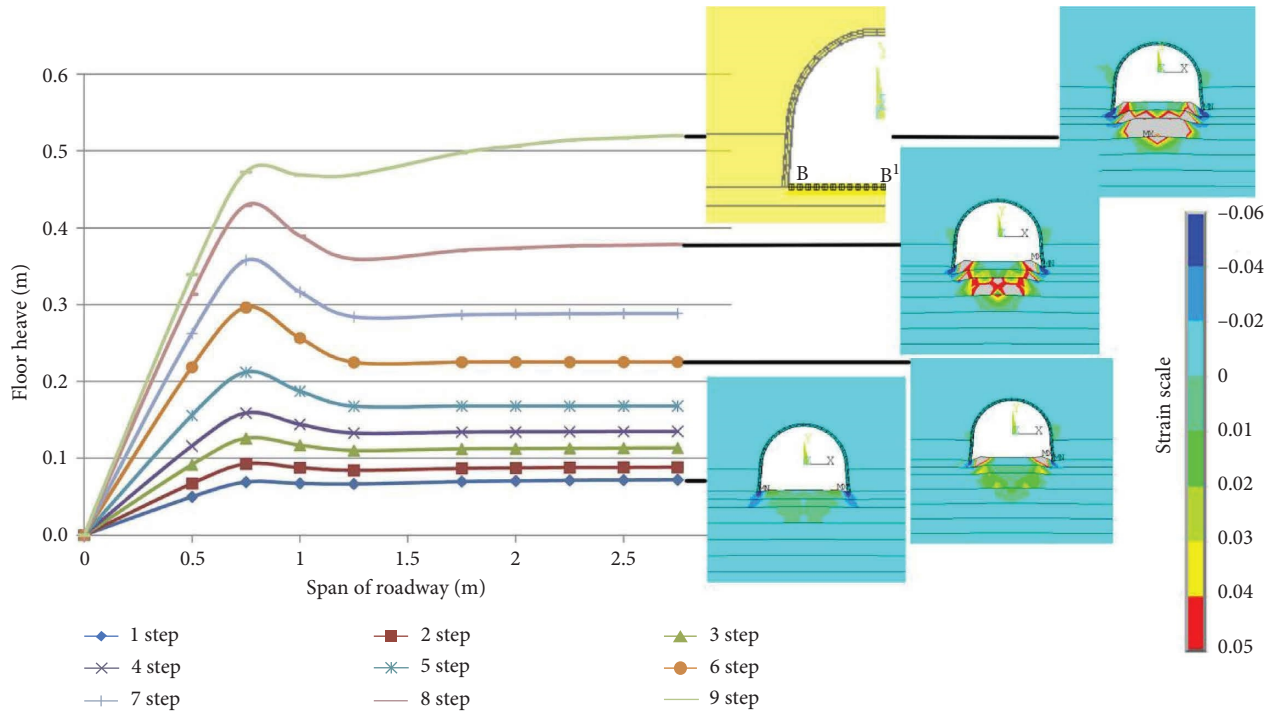
Figure 11: Floor heave on monitoring line B-B^1 and vertical plastic strain distribution around the roadway.
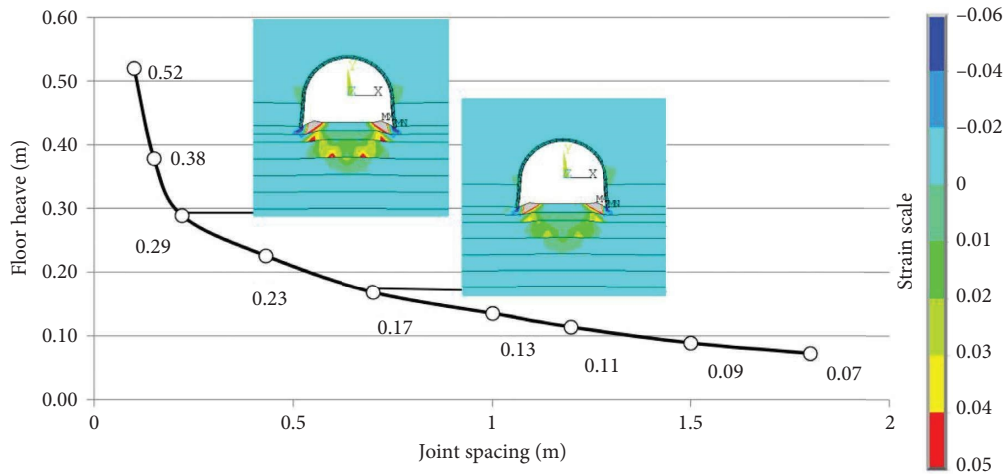
FIGURE 12: The relationship between joint spacing in the immediate floor and floor heave and vertical plastic strain distribution around the roadway for steps 5 and 7.

TABLE 4: Properties of floor support elements used in the model.

Floor support element	Cross-sectional area (m²)	Material behaviour option	Elastic modulus (GPa)	Poisson's ratio	Yield s/trength (MPa)	Tangent modulus (GPa)
Bolt	8.04×10^{-4}	Bilinear isotropic hardening	200	0.3	342	52.2
Steel belt	7.5×10^{-4}	Isotropic	200	0.3	—	—

using rock bolts with steel belts, such regions do not occur, the zone of reduced stress is smaller, and the contour of the roadway floor is smoother. There is also a tendency to change the size of the zone of reduced stress σ_1 with a change in the installation angle of rock bolts. The maximum vertical sizes of this zone are formed at support scheme I and the minimum ones are formed at support scheme III. This is true both for the case of bolts without steel belts and for the case with steel belt. The analysis of Figure 16 gives grounds to believe that the presence of a steel belt in the floor support system leads to a change in the distribution of stress on the immediate floor.

Figure 17 shows the distribution of maximum principle strain for the surrounding rocks before and after reinforcement with different support elements for support scheme II. The analysis of the figure helps to trace the influence of each floor support element on the distribution of strain on the immediate floor. The installation of a steel belt without rock bolts makes it possible to reduce the size of the post-peak strain region in the roadway floor, as shown in Figure 17(b). At the same time, the contour of the floor in the bottom corners of the roadway is smoothed out. However, a zone of immediate floor to a depth of about 2.0 m is still in the region where the strains exceed the post-peak ones by more than 2.5 times. Thus, the destruction of the immediate floor is very probable, and the effectiveness of such reinforcement is low.

The installation of rock bolts without a steel belt significantly changes the size and shape of the post-peak strain regions, as shown in Figure 17(c). These regions are located under the bottom corners of the roadway along the rock

bolts and no longer form a closed contour. The total value of floor heave is reduced. The coupled use of rock bolts with a steel belt reduces the size of the region with a post-peak strain by 1.5 times compared to the case without the steel belt. The optimal effect of such reinforcement is obvious, as shown in Figure 17(d).

Figure 18 shows the floor heave on monitoring line B-B[1] and vertical plastic strain distribution around the roadway before and after reinforcement with different supporting elements for floor support scheme III. The roadway support is symmetrical about the axis of its cross-section, so the graphs in Figure 18 are shown only half of the roadway span. Analysis of the figure makes it possible to track the proportion of the contribution of each supporting element to the decrease of floor heave. The installation of a steel belt without rock bolts reduces floor heave by 17% while smoothing it out in the bottom corners of the roadway. At the same time, the region of post-peak vertical plastic strain is formed on the immediate floor. Reinforcement by rock bolts without a steel belt reduces floor heave by 44%. However, in the bottom corners of the roadway, vertical plastic strain forms regions with a depth of 0.5 m in which the strain is more than 2.5 times than the post-peak one. The destruction of rocks in these regions is highly probable, which reduces the effectiveness of reinforcement in the future. In the case of coupled use of rock bolts with steel belt, the total value of floor heave is reduced by 48%, and post-peak vertical strain is not formed in the near-contour area. Still, there are insignificant regions of post-peak vertical strains under the legs of the frame. However, the sizes of these
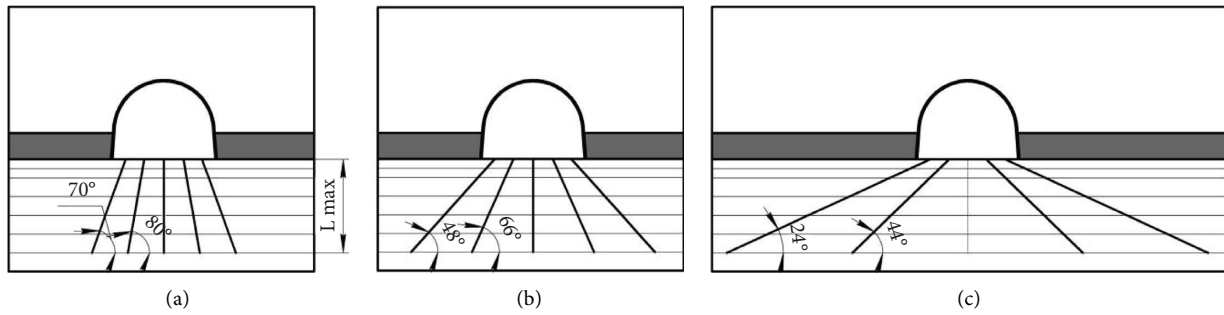
FIGURE 13: The floor support schemes with different bolt orientations: (a) scheme I; (b) scheme II; (c) scheme III.
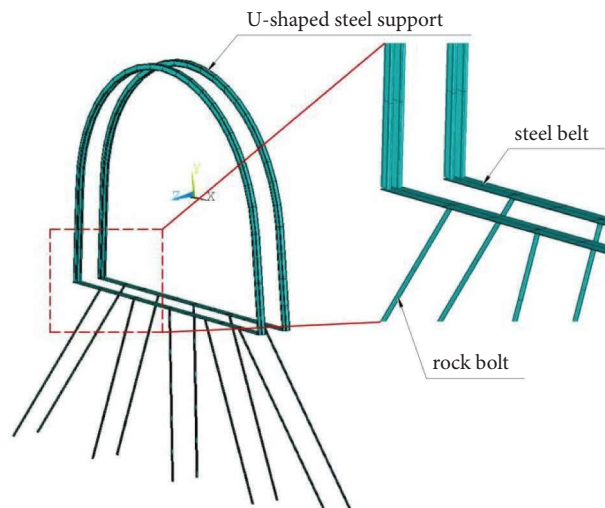
FIGURE 14: Support elements in the numerical model.
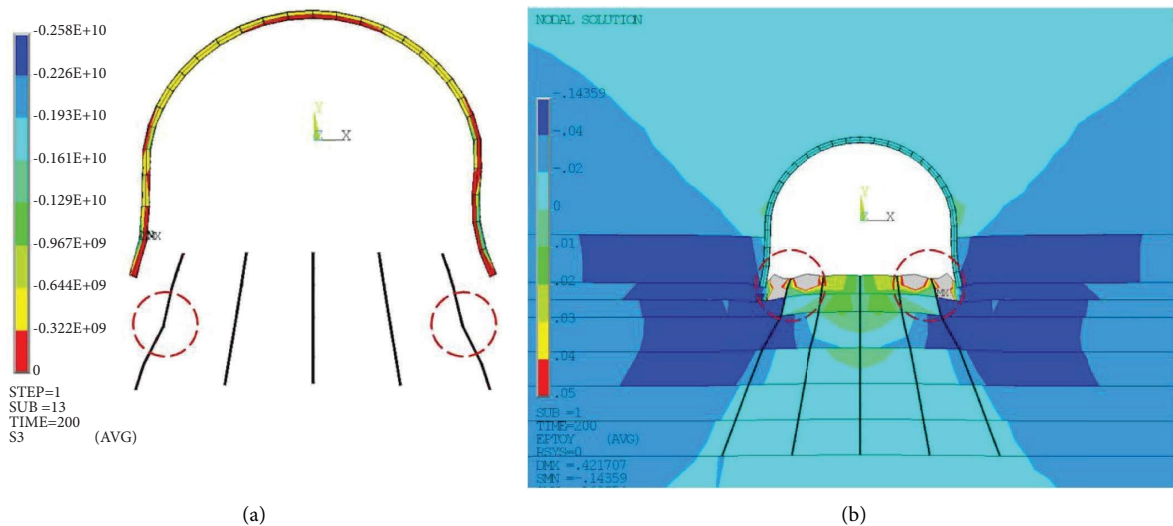
FIGURE 15: (a) Minimum principle stress (σ_3) distribution in support elements; (b) vertical total strain distribution around the roadway.

regions and, accordingly, the cracking floor rocks are noticeably lower than in other cases. Thus, it is obvious that the best floor supporting effect is in the case of coupled installation of rock bolts with a steel belt. The absence of a steel belt reduces the effectiveness of floor stabilization.

The most effective floor heave support scheme should provide the maximum bearing capacity of the rocks. Rock bolt arrangement highly influences the maximum principle strain distribution around the roadway, as shown in Figure 19. Reducing the angles of the bolts leads to a decrease in the size of the post-peak strain region in the roadway floor.

(a)

(b)
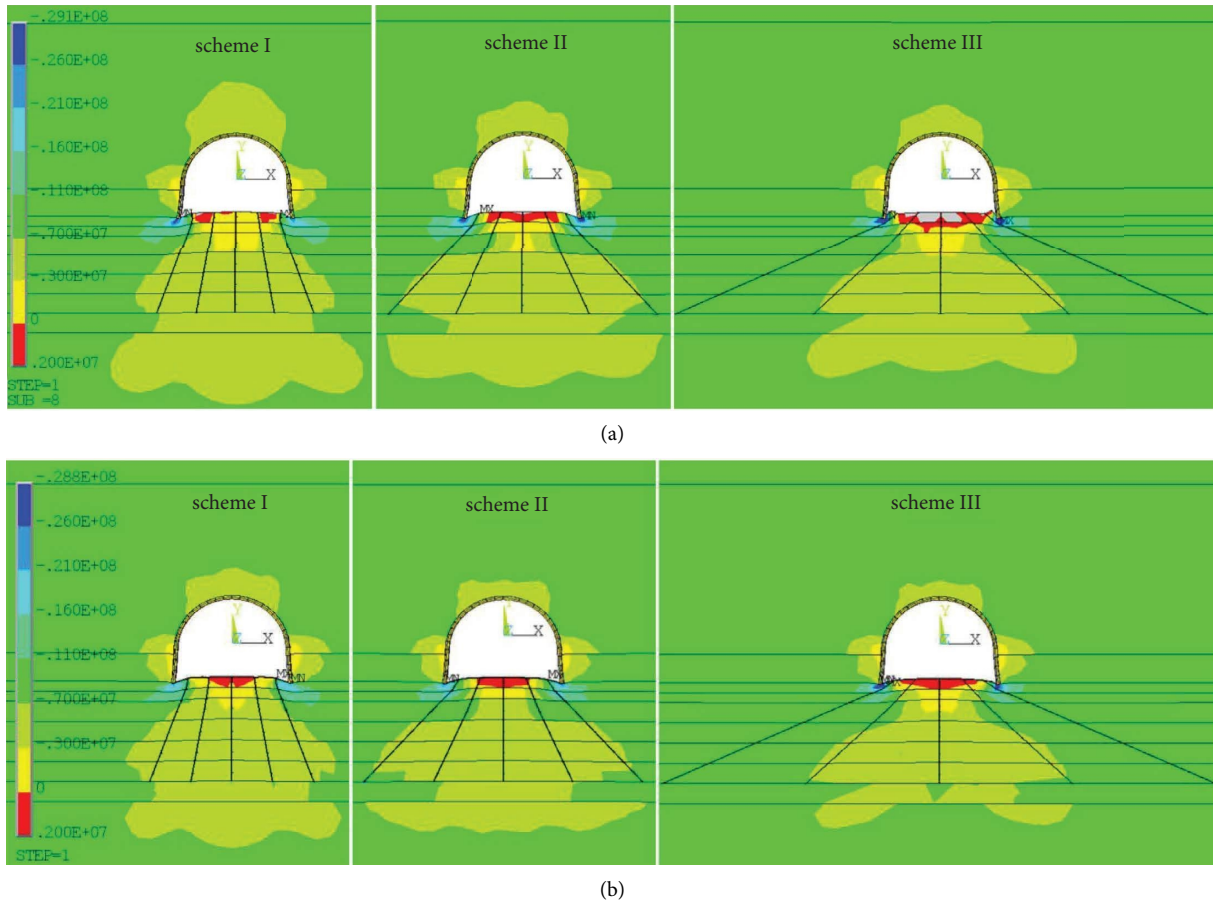
FIGURE 16: Maximum principle stress distribution around the roadway after floor bolting: (a) rock bolts without additional supporting elements; (b) rock bolts with steel belt.

(a)   (b)   (c)   (d)
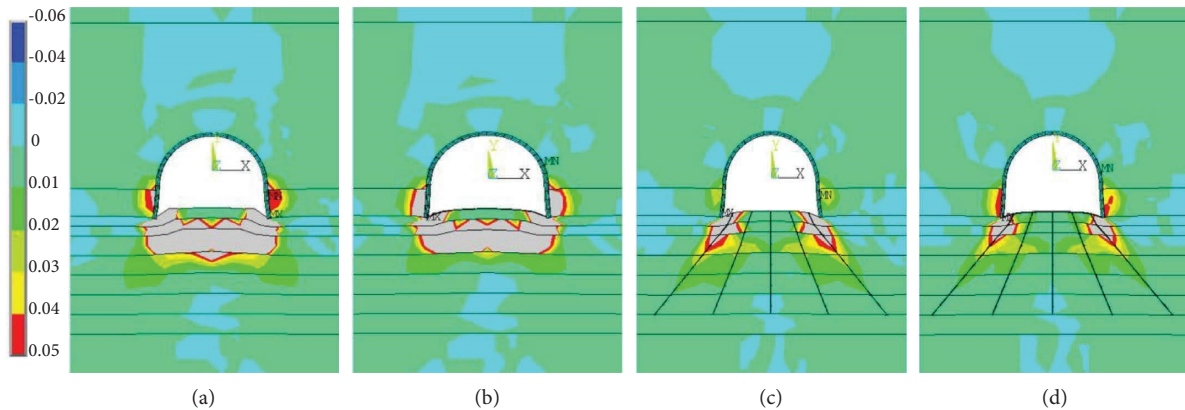
FIGURE 17: Total maximum principle strain distribution around the roadway: (a) without floor support; (b) with steel belt; (c) with rock bolts; (d) with rock bolts and steel belt.

The best floor support scheme is scheme III, in which the region of post-peak maximum principle strain, which is highlighted in Figure 19 with gray color, is much smaller than in other cases.

This conclusion is also confirmed by the maximum decrease of floor heave in scheme III, as shown in Figure 20. Although the difference in the value of floor heave between different schemes is insignificant, the distribution of vertical plastic deformation confirms that scheme III is more efficient. Thus, in the case of using scheme I in the near-contour area in the corners of the roadway, both post-peak plastic strains of compression and tension appear, which can serve as an indicator of crack and crash rocks. With scheme II, post-peak plastic compressive strains are formed under the legs of the frame. In the case of using scheme III, only very small regions of post-peak
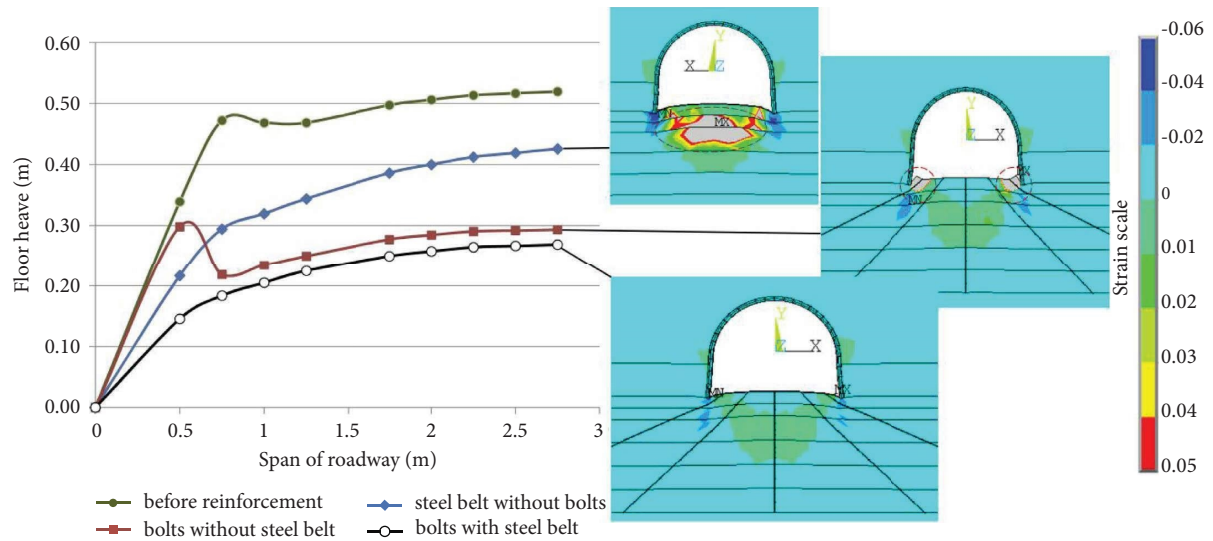
FIGURE 18: Floor heave on monitoring line B-B[1] and vertical plastic strain distribution around the roadway before and after reinforcement with different support elements (floor support scheme III).

(a)   (b)   (c)
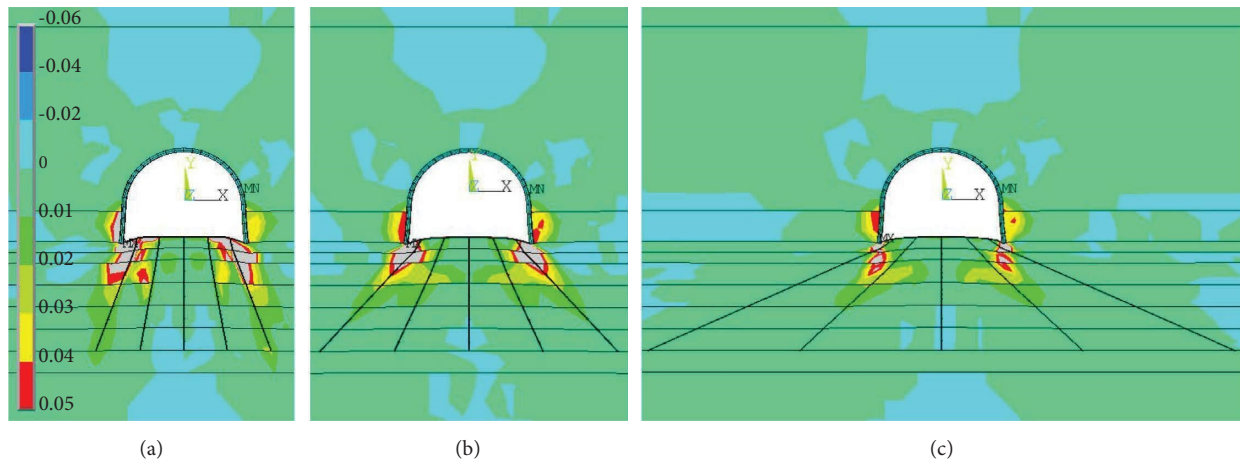
FIGURE 19: Total maximum principle strain distribution around the roadway after reinforcement: (a) floor support scheme I; (b) floor support scheme II; (c) floor support scheme III.

compressive strains are formed. Obviously, scheme III is the most effective for floor support.

During the simulation, the immediate floor was reinforced to a depth of 1.0 to 5.0 m. This made it possible to determine the optimal length of the rock bolts. The corresponding simulation results for floor support scheme III are shown in Figures 21 and 22.

As shown in Figure 21, the reduction of the reinforced zone size (L_r) from 5.0 to 2.0 m does not significantly affect the distribution of the total maximum principle strain. The sizes and configuration of the regions of post-peak strain in the roadway floor are almost unchanged. When L_r is reduced to 1.0 m, the pattern of strain distribution noticeably changes. The regions of post-peak strain increase significantly in size. At the same time, post-peak strains exceed the limits by more than 2.5 times. These regions merge in the central part of the roadway floor. Thus, the zone of the probable crash of rocks has a closed contour. Dilatancy and plastic flow of rocks are observed below the reinforcement

length. These processes lead to intense floor heave. Their development will reduce the effectiveness of reinforcement in the future. A significant increase in floor heave with a decrease in L_r from 2.0 to 1.0 m is also noted on the floor heave curve, as shown in Figure 22. In the case when L_r has a size from 5.0 to 2.0 m the floor heave does not change significantly, the results are within the accuracy of the calculations. Taking into account the margin of safety, it was proposed to limit the length of the outer bolts with a reinforcing depth of 2.0 m and the length of the central bolts with a depth of 3.0 m. The total maximum principle strain distribution around the roadway is shown in Figure 22.

4.3. Support Scheme of the Surrounding Rock. Through field observations and numerical calculations, it became clear that the current support system cannot maintain the stability of the surrounding rocks, especially of the immediate floor. The original support method must be improved and optimized. Based on the analysis of the literature review and results of
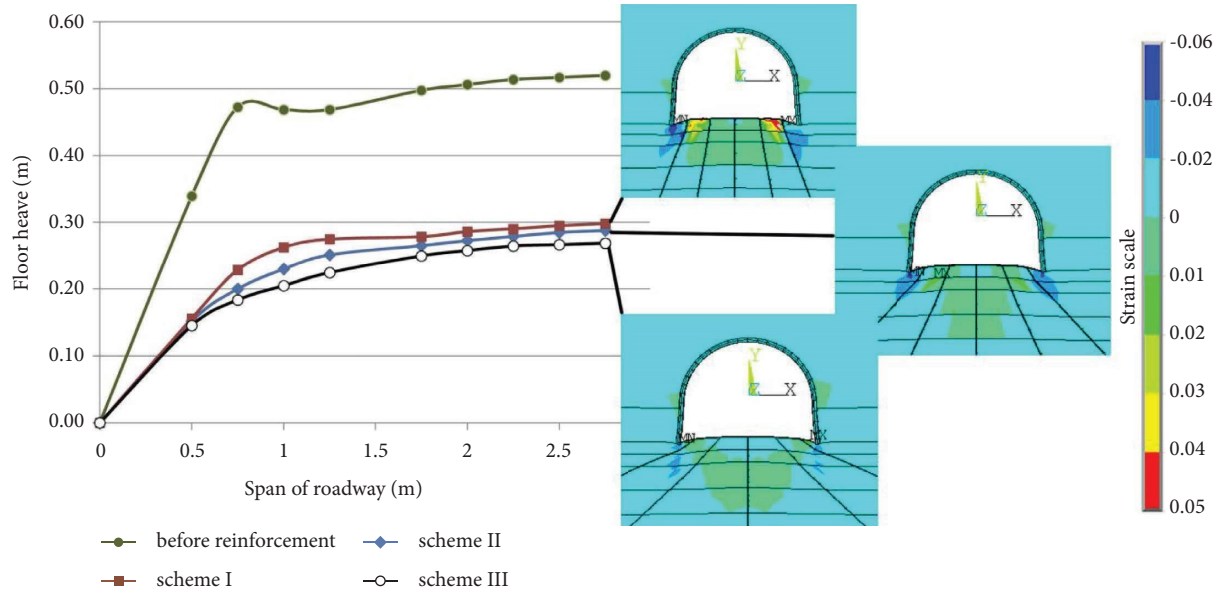
FIGURE 20: Floor heave on monitoring line B-B[1] and vertical plastic strain distribution around the roadway before and after reinforcement with different floor support schemes.

(a)

(b)

(c)

(d)
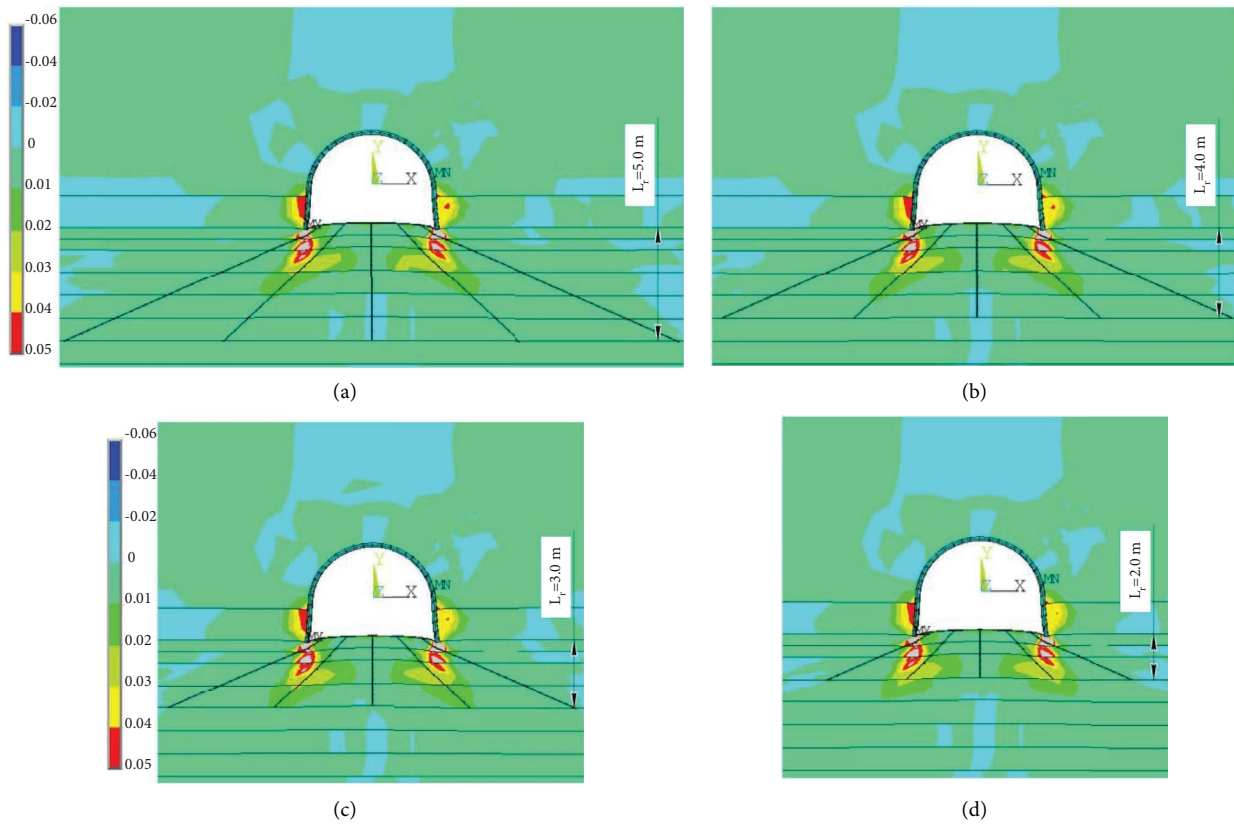
FIGURE 21: Continued.

(e)
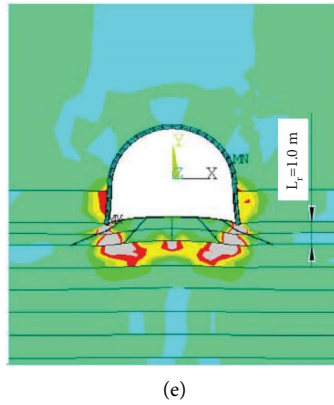
Figure 21: Total maximum principle strain distribution around the roadway after floor supporting with different lengths of reinforcement (L_r): (a) 5 m; (b) 4 m; (c) 3 m; (d) 2 m; (e) 1 m.
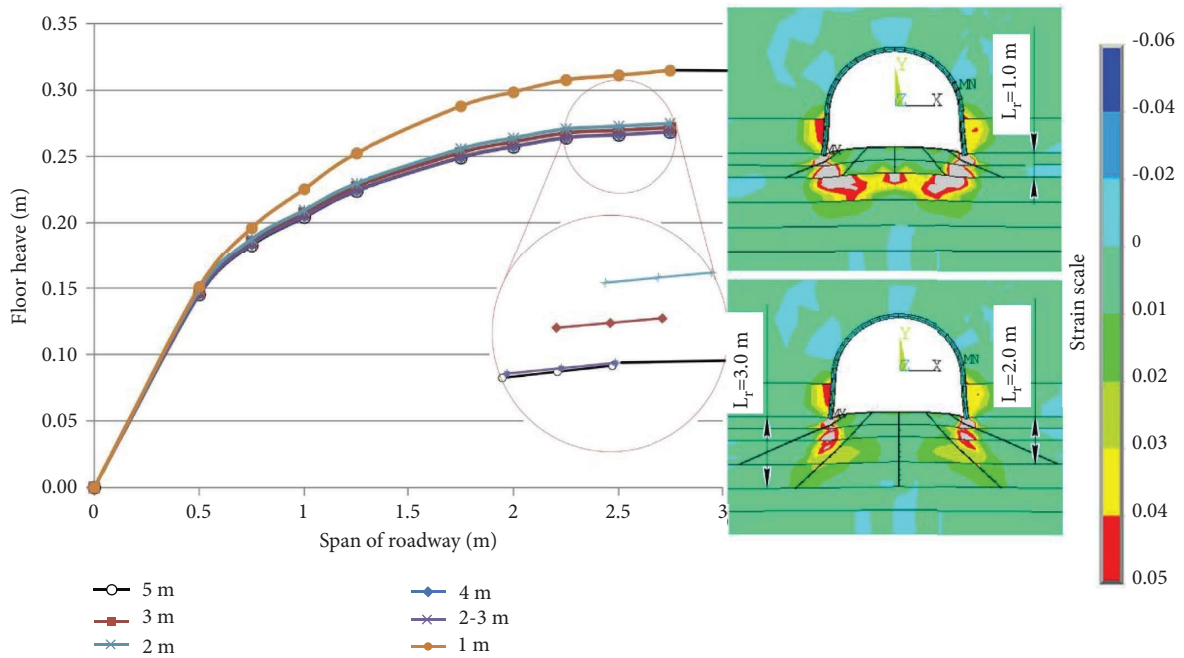
Figure 22: Floor heave on monitoring line B-B^1 (Figure 11) and total maximum principle strain distribution around the roadway after floor supporting with different lengths of reinforcement.
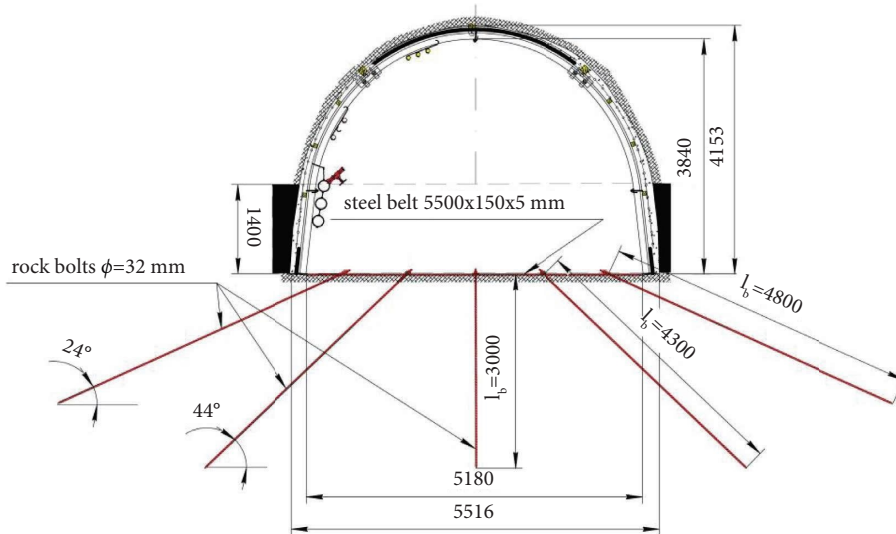
Figure 23: Design of support scheme.

numerical simulation, the rock bolts reinforcement was proposed for the floor heave control. Based on the results of the numerical simulation, the most effective floor support scheme was proposed, and the optimal bolt length is justified. Figure 23 shows the proposed design of the support scheme.

5. Conclusions

In this study, deep mining roadway in soft rock was considered as the research subject. We focused on the floor heave evolution and the effectiveness of rock bolts reinforcement of the roadway. A numerical simulation was used to study the stress-strain state and displacement of surrounding rocks in the underground coal mine 800 m in the depth of Ukraine. The results demonstrated that significant floor heavecaused nonlinear deformation of the laminated immediate floor under an increase in rock fracturing. This was followed by investigating the effectiveness of rock bolts reinforcement. Based on the results of this investigation, the following conclusions can be drawn:

(1) The numerical analysis shows that with an increase in rock mass fracturing, the σ_3 in the bottom corners of the roadway significantly exceed the compressive strength of the immediate floor, which indicates a high probability of rock cracking under the foot of the arch support. The σ_1 in the central part of the roadway floor significantly exceed the tensile strength of the immediate floor, which indicates a high probability of rock crushing. At the same time, the size of the reduced σ_1 stress zone in the floor of the roadway increases gradually. The size of post-peak maximum principle strain regions in the floor of the roadway is increased nonlinearly with an increase in rock mass fracturing. The analysis shows that a significant proportion of maximum principle strains are plastic ones. They exceed the failure limit more than 2.5 times and cause the floor heave.

(2) Initially, post-peak strain regions appear in the bottom corners of the roadway, after which strata in the immediate floor are destroyed one by one into the depth. After that, post-peak strain regions merge in the central part of the roadway floor at a depth of about 2.0 m. Finally, the strata in the immediate floor to a depth near 2.0 m are included in the post-peak strain region, which indicates a high probability of rock crushing. This region of the surrounding rocks is mainly involved in the development of floor heave. The joint spacing of 0.45 m on the immediate floor is critical. At this step, significant plastic deformation begins, which is the cause of uncontrolled floor heave.

(3) Considering the floor heave mechanism of the soft rock, rock bolts reinforcement was proposed to control the floor heave. Three floor support schemes with two types of support elements, different bolt orientations, and lengths of reinforcement were studied during many numerical simulations. After reinforcement, post-peak plastic strain in the floor strata was reduced effectively. The optimal floor support scheme and depth of reinforcement were determined by the allowable floor heave. Ideally, the floor heaves could be reduced by rock bolts with steel belts installed according to the support scheme III and reinforcement length of 2.0 m for outer bolts and 3.0 m for central bolts. This can provide suggestions for the specific parameters suitable for controlling the floor heave of the roadway through rock bolts reinforcement technology.

Data Availability

The data of numerical simulation in ANSYS that were used to support the findings of this study are available from the corresponding author upon request.

Conflicts of Interest

The authors declare that they have no conflicts of interest.

References

[1] F. Zhang, J. Liu, X. Zhang, H. Ni, and Y. Liu, "Research on excavation and stability of deep high stress chamber group: a case study of Anju Coal Mine," *Geotechnical & Geological Engineering*, vol. 39, no. 5, pp. 3611–3626, 2021.

[2] J. C. Chang, D. Li, T. F. Xie, W. B. Shi, and K. He, "Deformation and failure characteristics and control technology of roadway surrounding rock in deep coal mines," *Geofluids*, vol. 2020, pp. 1–15, Article ID 8834347, 2020.

[3] F. Qi, Z. Ma, D. Yang et al., "Stability control mechanism of high-stress roadway surrounding rock by roof fracturing and rock mass filling," *Advances in Civil Engineering*, vol. 2021, Article ID 6658317, pp. 2021–17, 2021.

[4] Q. Wang, B. Jiang, R. Pan et al., "Failure mechanism of surrounding rock with high stress and confined concretesupport system," *International Journal of Rock Mechanics and Mining Sciences*, vol. 102, pp. 89–100, 2018.

[5] S. Mo, K. Tutuk, and S. Saydam, "Management of floor heave at Bulga Underground Operations—a case study," *International Journal of Mining Science and Technology*, vol. 29, no. 1, pp. 73–78, 2019.

[6] H. P. Kang, J. Lin, and M. J. Fan, "Investigation on support pattern of acoal mine roadway within soft rocks—a case study," *International Journal of Coal Geology*, vol. 140, pp. 31–40, 2015.

[7] X. P. Lai, H. C. Xu, P. F. Shan, Y. L. Kang, Z. Y. Wang, and X. Wu, "Research on mechanism and control of floor heave of mining influenced roadway in top coal caving working face," *Energies*, vol. 13, no. 2, p. 381, 2020.

[8] Y. M. Zhao, N. Liu, X. Zheng, and N. Zhang, "Mechanical model for controlling floor heave in deep roadways with U-shaped steel closed support," *International Journal of*

Mining Science and Technology, vol. 25, no. 5, pp. 713–720, 2015.

[9] C. Li, Z. Wang, and T. Liu, "Principle and practice of coupling support of double yielding shell of soft rock roadway under high stress," *International Journal of Mining Science and Technology*, vol. 24, no. 4, pp. 513–518, 2014.

[10] C. Wang, Y. Wang, and S. Lu, "Deformational behaviour of roadways in soft rocks in underground coal mines and principles for stability control," *International Journal of Rock Mechanics and Mining Sciences*, vol. 37, no. 6, pp. 937–946, 2000.

[11] W. Zheng, Y. Zhao, and Q. Bu, "The coupled control of floor heave based on a composite structure consisting of bolts and concrete antiarches," *Mathematical Problems in Engineering*, vol. 2018, Article ID 3545423, pp. 1–14, 2018.

[12] C. Wang, X. Y. Chen, J. D. Zhang, and Y. P. Wu, "Stability mechanism and repair method of U-shaped steel reverse arch support in soft floor roadway," *Advances in Civil Engineering*, vol. 2020, Article ID, 8814365, pp. 1–12, 2020.

[13] A. Chen, X. B. Li, X. S. Liu, Y. L. Tan, K. Xu, and H. L. Wang, ""Relief-Retaining" control technology of floor heave in mining roadway with soft rock: a case study," *Advances in Civil Engineering*, vol. 2021, Article ID 1455052, pp. 1–13, 2021.

[14] T. Yang and J. Zhang, "Research on the treatment technology of soft rock floor heave based on a model of pressure-relief slots," *Arabian Journal of Geosciences*, vol. 14, no. 13, p. 1278, 2021.

[15] Q. Chang, H. Zhou, Z. Xie, and S. Shen, "Anchoring mechanism and application of hydraulic expansion bolts used in soft rock roadway floor heave control," *International Journal of Mining Science and Technology*, vol. 23, no. 3, pp. 323–328, 2013.

[16] M. C. He, G. F. Zhang, G. L. Wang, Y. L. Xu, C. Z. Wu, and Q. D. Tang, "Research on mechanism and application to floor heave control of deep gateway," *Chinese Journal of Mechanical Engineering*, vol. 28, pp. 2593–2598, 2009.

[17] J. Yang, K. Zhou, Y. Cheng, Y. Gao, Q. Wei, and Y. Hu, "Mechanism and control of roadway floor heave in the paleogene soft rock surroundings," *Geotechnical & Geological Engineering*, vol. 37, no. 6, pp. 5167–5185, 2019.

[18] Y. Wang, P. Wang, W. Li, and J. Bai, "Floor heave control technology in deep and soft rock mining roadway: a case study," *Arabian Journal of Geosciences*, vol. 15, no. 6, p. 500, 2022.

[19] Y. Chen, J. Bai, S. Yan, Y. Xu, X. Wang, and S. Ma, "Control mechanism and technique of floor heave with reinforcing solid coal side and floor corner in gob-side coal entry retaining," *International Journal of Mining Science and Technology*, vol. 22, no. 6, pp. 841–845, 2012.

[20] R. Cao, P. Cao, and H. Lin, "Support technology of deep roadway under high stress and its application," *International Journal of Mining Science and Technology*, vol. 26, no. 5, pp. 787–793, 2016.

[21] G. Guo, H. Kang, D. Qian, F. Gao, and Y. Wang, "Mechanism for controlling floor heave of mining roadways using reinforcing roof and sidewalls in underground coal mine," *Sustainability*, vol. 10, no. 5, p. 1413, 2018.

[22] Z. Y. Zhang and H. Shimada, "Numerical study on the effectiveness of grouting reinforcement on the large heaving floor of the deep retained goaf-side gateroad: a case study in China," *Energies*, vol. 11, no. 4, p. 1001, 2018.

[23] H. Shimada, A. Hamanaka, T. Sasaoka, and K. Matsui, "Behaviour of grouting material used for floor reinforcement in underground mines," *International Journal of Mining, Reclamation and Environment*, vol. 28, no. 2, pp. 133–148, 2014.

[24] X. m. Sun, F. Chen, M. c. He, Wl. Gong, Hc. Xu, and H. Lu, "Physical modeling of floor heave for the deep-buried roadway excavated in ten degree inclined strata using infrared thermal imaging technology," *Tunnelling and Underground Space Technology*, vol. 63, pp. 228–243, 2017.

[25] X. M. Zhou, S. Wang, X. L. Li et al., "Research on theory and technology of floor heave control in semicoal rock roadway: taking longhu coal mine in Qitaihe mining area as an Example," *Lithosphere*, vol. 2022, no. 11, Article ID 3810988, 2022.

[26] P. Małkowski, Ł. Ostrowski, and J. Stasica, "Modeling of floor heave in underground roadways in dry and waterlogged conditions," *Energies*, vol. 15, no. 12, p. 4340, 2022.

[27] H. Y. Liu, B. Y. Zhang, X. L. Li et al., "Research on roof damage mechanism and control technology of gob-side entry retaining under close distance gob," *Engineering Failure Analysis*, vol. 138, no. 5, Article ID 106331, 2022.

[28] D. Zhang, J. Bai, Sh. Yan, R. Wang, N. Meng, and G. Wang, "Investigation on the failure mechanism of weak floors in deep and high-stress roadway and the corresponding control technology," *Minerals*, vol. 11, no. 12, p. 1408, 2021.

[29] I. Sakhno, S. Sakhno, and V. Kamenets, "Mechanical model and numerical analysis of a method for local rock reinforcing to control the floor heave of mining-affected roadway in a coal mine," *IOP Conference Series: Earth and Environmental Science*, vol. 970, no. 1, Article ID 012035, 2022.

[30] P. Małkowski, Ł. Ostrowski, and Ł. Bednarek, "The effect of selected factors on floor upheaval in roadways-in situ testing," *Energies*, vol. 13, no. 21, p. 5686, 2020.

[31] I. Sakhno, O. Isayenkov, and S. Rodzin, "Local reinforcing of footing supported in the destroyed rock massif," *Mining of Mineral Deposits*, vol. 11, no. 1, pp. 9–16, 2017.

[32] E. Hoek, C. Carranza-Torres, and B. Corkum, "Hoek-Brown failure criterion – 2002 edition," in *Proceedings of the 5th North American Rock Mechanics Symposium and the 17th Tunnelling Association of Canada Conference, NARMS-TAC, Toronto, Canada,* et al. pp. 267–271, Rocscience Inc, Toronto, Canada, 2002.

[33] M. Cai, P. K. Kaiser, H. Uno, Y. Tasaka, and M. Minami, "Estimation of rock mass deformation modulus and strength of jointed hard rock masses using the GSI system," *International Journal of Rock Mechanics and Mining Sciences*, vol. 41, no. 1, pp. 3–19, 2004.

[34] E. Hoek and M. Diederichs, "Empirical estimation of rock mass modulus," *International Journal of Rock Mechanics and Mining Sciences*, vol. 43, no. 2, pp. 203–215, 2006.

[35] E. T. Brown, *Suggested Methods for Rock Characterization Testing and Monitoring*p. 211, Oxford Pergamon Press, Oxford, UK, 1981.

[36] H. Zhou, C. Zhang, Z. Li, D. Hu, and J. Hou, "Analysis of mechanical behavior of soft rocks and stability control in deep tunnels," *Journal of Rock Mechanics and Geotechnical Engineering*, vol. 6, no. 3, pp. 219–226, 2014.

[37] M. Josh, L. Esteban, C. Delle Piane, J. Sarout, D. N. Dewhurst, and M. B. Clennell, "Laboratory characterisation of shale properties," *Journal of Petroleum Science and Engineering*, vol. 88-89, pp. 107–124, 2012.

[38] I. G. Sakhno, A. V. Molodetskyi, and S. V. Sakhno, "Identification of material parameters for numerical simulation of the behavior of rocks under true triaxial conditions,"

Naukovyi Visnyk Natsionalnoho Hirnychoho Universytetu, vol. 5, pp. 48–53, 2018.

[39] O. A. Almisned and N. B. Alqahtani, "Rock analysis to characterize Saudi soft sandstone rock," *Journal of Petroleum Exploration and Production Technology,* vol. 11, no. 6, pp. 2381–2387, 2021.

[40] Q. Liu, B. Liang, W. Sun, and H. Zhao, "Experimental study on the difference of shale mechanical properties," *Advances in Civil Engineering,* vol. 2021, Article ID 6677992, 14 pages, 2021.

Research Article

Progressive Failure Analysis of Soil Slope with Strain Softening Behavior Based on Peridynamics

Chen Wang [ID],[1] **Jianhui Zhao** [ID],[1] **and Weifeng Zheng** [ID][2]

[1]*College of Energy Engineering, Xi'an University of Science and Technology, Xi'an 710054, China*
[2]*Institute of Foundation Engineering, China Academy of Building Research, Beijing 100013, China*

Correspondence should be addressed to Chen Wang; baggio40@tom.com

In this study, the nonlocal, nonordinary state-based peridynamics (NOSBPD) is introduced as a novel regularization technique to study the strain localization and progressive failure of soil slopes due to strain softening behavior. The NOSBPD formulations are introduced first, and then the strain-softening Mohr–Coulomb model is incorporated into the nonlocal framework. The implicit formulations of the nonlinear NOSBPD model under the plane strain condition combined with the energy dissipation-based arc-length method to avoid the limitations of the force and displacement control in the nonlinear analysis are given. Numerical examples, including the plane strain biaxial experiments and slope models, validate the effectiveness of the proposed method in terms of alleviating mesh sensitivity. The results show that this nonlocal method can remove the mesh dependence, and the localized shear band is related to the nonlocal parameter δ. The proposed method involves being able to capture strength mobilization in different parts of the sliding surface during the progressive failure process of the soil slope. It can avoid the dilemma that the peak strength is too dangerous and the residual strength is too conservative due to the rigid body assumption in the limit equilibrium method.

1. Introduction

Strain localization is a common phenomenon in geotechnical engineering, and its occurrence is often accompanied by strain softening and progressive failure of structures. Regarding the study of strain localization in geomaterials, many attempts have been made in experimental, theoretical, and numerical aspects. In terms of experiments [1–3], there are many studies on soil samples with significant strain-softening behavior, such as dense sand and hard clay, including the plane strain test and the centrifugal model test. From the theoretical point of view [4, 5], the occurrence of shear bands is commonly predicted by the bifurcation theory. In recent years, the introduction of noncoaxial theory [6] has made the prediction more effective, but bifurcation theory cannot simulate the behavior of materials after bifurcation. For the numerical simulation methods for crack initiation and propagation in brittle or quasi-brittle material, there are two types of methods, namely separation

and smearing methods. The numerical method for the strain localization analysis can also be roughly divided into separated and continuous models according to the relationship between shear band width (h) and element size (d). Separation models can be further divided into weak discontinuities [7], strong discontinuities [8], shear elements [9, 10], etc. In this method, the relationship between the element size and the width of the shear band is generally expressed as $d \geq h$ (in the strong discontinuities method, $h = 0$). However, the continuous model is generally required $d < h$. The current study focuses on continuous methods.

For the conventional finite element method without internal length scale, when it deals with strain localization problems, the static control equations are transformed from elliptical to hyperbolic, and the dynamic control equations are changed from hyperbolic to elliptical, due to the strain softening or asymmetric stiffness matrix obtained by the nonassociative flow rule. Thus, the solution to the boundary value problem depends heavily on the size of the finite

element. In particular, as the size of the finite element decreases, the width of the shear band decreases, which means that with the mesh refinement, the energy consumption would approach zero. It obviously violates the laws of physics. Therefore, considerable regularization mechanisms have been introduced to overcome the mesh sensitivity, such as viscous models [11], the Cosserat continuum model [12], the gradient plasticity model [13], and the nonlocal model [14, 15], among others.

The peridynamic (PD) theory originally proposed by Silling [16] uses the form of differential-integral to describe the equation of motion of the continuum medium, avoiding the displacement derivative term, so it can obtain a continuous-discontinuous unified expression. The PD theory, including PD-FEM coupled models, has great advantages in dealing with discontinuity failure problems, as illustrated in previous studies [17–19]. At the same time, PD naturally has the nonlocal parameter, i.e., neighborhood radius (or called the horizon, δ). Thus, it can seem like a consistent nonlocal model in the sense that in some existing nonlocal models, only nonlocal averaging of stress-strain is performed in the postprocessing stage, while constitutive models are still local models. The peridynamic theory is widely used in composite materials [20], concrete [21], and other fields [22], but it is rarely seen in the field of predicting the progressive failure process of soil slopes. Song et al. [23, 24] initially applied peridynamics for the analysis of chemical plastic strain localization in unsaturated soils, but the strain softening properties, one of the main factors causing strain localization [25–27], have not yet been discussed thoroughly.

The main objective of the current study is to use the PD theory as a regularization technique for the strain localization analysis in soil induced by strain-softening behavior. The effectiveness of this method for relieving the mesh dependency is emphatically analyzed by a plane strain element test and a slope model, and the influence of a neighborhood radius of δ is discussed. The analysis in this paper is based on a small deformation assumption and does not consider soil-water interactions. The rest of the manuscript is organized as follows: In Section 2, the governing equations of the numerical model and the constitutive model are introduced. The plane strain test is simulated by the proposed method in Section 3. Numerical studies for the progressive failure of soil slopes are conducted in Section 4. A summary and conclusions are drawn in Section 5.

2. Numerical Method and Constitutive Model

2.1. Nonordinary State-Based Peridynamics Theory.
The state-based peridynamics theory was proposed by Silling to overcome the limitations of the fixed Poisson's ratio of the bond-based peridynamic theory [27]. By introducing the *state* concept, the existing constitutive models expressed in terms of stress and strain quantities in classical continuum mechanics can be easily incorporated into the nonordinary state-based peridynamics (NOSBPD) framework. For self-completeness, the basic formulations of NOSBPD are briefly outlined in this subsection. More details about this theory can be found in [28].

The notations and kinematics of NOSBPD are illustrated in Figure 1. The reference position vector state is defined as

$$\mathbf{X}\langle\boldsymbol{\xi}\rangle = \boldsymbol{\xi} = \mathbf{x}' - \mathbf{x}. \tag{1}$$

As deformation proceeds, the deformed position vector state is given by

$$\mathbf{Y}\langle\mathbf{x}' - \mathbf{x}\rangle = \boldsymbol{\eta} + \boldsymbol{\xi} = (\mathbf{u}' + \mathbf{x}') - (\mathbf{u} + \mathbf{x}). \tag{2}$$

The nonlocal deformation gradient is approximated as

$$\mathbf{F}(\mathbf{x}) = \left[\int_{H_x} \omega(|\boldsymbol{\xi}|)\Big(\mathbf{Y}(\boldsymbol{\xi}) \otimes \boldsymbol{\xi}\Big)dV_{\boldsymbol{\xi}}\right] \cdot \mathbf{K}(\mathbf{x}), \tag{3}$$

where the shape tensor $\mathbf{K}(\mathbf{x})$ is defined as

$$\mathbf{K}(\mathbf{x}) = \left[\int_{H_x} \omega(|\boldsymbol{\xi}|)(\boldsymbol{\xi} \otimes \boldsymbol{\xi})dV_{\boldsymbol{\xi}}\right]^{-1}, \tag{4}$$

where H_x denotes the horizon of a material point $\boldsymbol{x}$. It is a circle in two dimensions with a cut-off radius of δ.

Based on the principle of virtual work, the force state can be derived as follows in terms of the stress tensor as an intermediate step:

$$\mathbf{T}[\mathbf{x}]\langle\mathbf{x}' - \mathbf{x}\rangle = \omega\Big(|\mathbf{x}' - \mathbf{x}|\Big)[\boldsymbol{\sigma}(\mathbf{F})]^T \cdot \mathbf{K}(\mathbf{x}) \cdot \boldsymbol{\xi}. \tag{5}$$

Subsequently, the governing equation of the NOSBPD in the static or quasi-static conditions ignoring the inertial effects reads

$$\int_{H_x} \left\{\mathbf{T}[\mathbf{x}]\langle\mathbf{x}\prime - \mathbf{x}\rangle - \mathbf{T}[\mathbf{x}]\langle\mathbf{x}\prime - \mathbf{x}\rangle\right\}dV_{\mathbf{x}'} + \mathbf{b}(\mathbf{x}) = \mathbf{0}. \tag{6}$$

2.2. Strain-Softening Constitutive Model for Soil.
In the current study, to describe the strain-softening behavior of the soil, the modified Mohr–Coulomb model, considering a variation in the cohesion strength c with the accumulated plastic strain is employed. The celebrated Mohr–Coulomb constitutive model has been widely used for describing the shear failure of soils, and it can reflect the soil failure dependence on the hydrostatic pressure. The dilatancy can be reflected by the nonassociative flow law. It is noted that the model in this paper does not consider hat-shaped yielding under isotropic compression.

The yield criterion of this model (see Figure 2(a)) is given by

$$\Phi(\boldsymbol{\sigma}, c) = (\sigma_{\max} - \sigma_{\min}) + (\sigma_{\max} + \sigma_{\min})\sin\varphi - 2c\cos\varphi, \tag{7}$$

where $\sigma_{\max}$ and $\sigma_{\min}$ are the major and minor principle of effective stress (the compression components of the stress are positive), respectively. c is the cohesion intercept, and φ is the friction angle. The flow rule is a nonassociated type with a dilatancy angle ψ, which satisfies $\psi < \varphi$.

Following the previous studies [14], the strain-softening behavior of soil can be described by decreasing the strength parameters (c and/or φ). In this study, the attenuation of the friction angle is not considered during softening (see
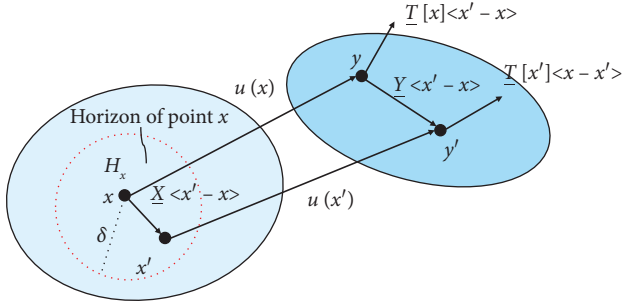
FIGURE 1: NOSB PD notations and kinematics.

Figure 2(b)), and the strain softening characteristics are solely reflected by the attenuation of the cohesion force with the development of the accumulated plastic strain. In specific, the cohesion intercept is linearly reduced with the accumulated plastic strain after the occurrence of the initial yield, as shown in Figure 2(c).

2.3. Numerical Implementation. The meshless method proposed by Silling is employed herein for spatial discretization [29]. That is, a particle with a certain volume at the center of the grid is used to represent the movement of the entire cell. The explicit solution algorithm is often used for peridynamics, while the time step of the explicit

algorithm is commonly very short and it takes a long time for the structure to reach a stable state. In this study, a nonlinear implicit solution algorithm is used. It differs from the previous study [30] in that it is expressed in a nonlinear framework.

The shape tensor in a discretized form is given by

$$\mathbf{K}(\mathbf{x}_j) = \left[\sum_{n=1}^{m} \omega\left(\left|\mathbf{x}_n - \mathbf{x}_j\right|\right) \left[(\mathbf{x}_n - \mathbf{x}_j) \otimes (\mathbf{x}_n - \mathbf{x}_j)\right] V_n \right]^{-1}, \tag{8}$$

where $\mathbf{x}_j$ is the source point; $\mathbf{x}_n$ is the field point; V_n is the volume of the particle $\mathbf{x}_n$.

Correspondingly, the discretized deformation gradient tensor reads

$$\mathbf{F}(\mathbf{x}_j) = \left[\sum_{n=1}^{m} \omega\left(\left|\mathbf{x}_n - \mathbf{x}_j\right|\right) \left[(\mathbf{u}_n - \mathbf{u}_j) \otimes (\mathbf{x}_n - \mathbf{x}_j)\right] V_n \right] \mathbf{K}(\mathbf{x}_j) + \mathbf{I}. \tag{9}$$

With the infinitesimal deformation assumption, the strain tensor can be calculated as

$$\boldsymbol{\varepsilon} = \frac{1}{2}\left(\mathbf{F} + \mathbf{F}^T\right) - \mathbf{I}. \tag{10}$$

Thus, the strain tensor can be approximated as

$$\boldsymbol{\varepsilon}(\mathbf{x}_j) = \frac{1}{2} \sum_{n=1}^{m} \omega\left(\left|\mathbf{x}_n - \mathbf{x}_j\right|\right) \left[(\mathbf{u}_n - \mathbf{u}_j) \otimes (\mathbf{x}_n - \mathbf{x}_j) + (\mathbf{x}_n - \mathbf{x}_j) \otimes (\mathbf{u}_n - \mathbf{u}_j)\right] V_n \cdot \mathbf{K}(\mathbf{x}_j). \tag{11}$$

For the plane strain problem considered herein, the strain is expressed in a matrix form as

$$\boldsymbol{\varepsilon} = \left[\varepsilon_{11} \ \varepsilon_{22} \ 2\varepsilon_{12} \right]^T = \mathbf{BNU}, \tag{12}$$

where the matrix $\mathbf{B}$, $\mathbf{N}$, and $\mathbf{U}$ are

$$\mathbf{B} = \begin{bmatrix} k_{11} & 0 & k_{12} & 0 \\ 0 & k_{12} & 0 & k_{22} \\ k_{12} & k_{11} & k_{22} & k_{12} \end{bmatrix},$$

$$\mathbf{N} = \begin{bmatrix} \cdots & \omega\xi_{xn}V_n & 0 & \cdots & N^{(1)} & 0 \\ \cdots & 0 & \omega\xi_{xn}V_n & \cdots & 0 & N^{(1)} \\ \cdots & \omega\xi_{yn}V_n & 0 & \cdots & N^{(2)} & 0 \\ \cdots & 0 & \omega\xi_{yn}V_n & \cdots & 0 & N^{(2)} \end{bmatrix}, \tag{13}$$

$$N^{(1)} = -\sum_{n=1}^{m} \omega(|\xi|)\xi_{xn}V_n,$$

$$N^{(2)} = -\sum_{n=1}^{m} \omega(|\xi|)\xi_{yn}V_n,$$

$$\mathbf{U} = \left[\cdots \ u_n \ v_n \ \cdots \ u_j \ v_j \right]^T.$$

The stress tensor can be expressed as

$$\boldsymbol{\sigma} = \left[\sigma_{11} \ \sigma_{22} \ \tau_{12} \right]^T = \boldsymbol{\sigma}(\boldsymbol{\varepsilon}, \boldsymbol{\zeta}), \tag{14}$$

where $\boldsymbol{\zeta}$ denotes the state variables, herein it is the accumulated plastic strain.

Consequently, the force state can be rewritten as

$$\mathbf{T}\left[\mathbf{x}\right]\langle\mathbf{x}' - \mathbf{x}\rangle = \omega\left(\left|\mathbf{x}' - \mathbf{x}\right|\right)\mathbf{Q} \cdot \boldsymbol{\sigma}(\boldsymbol{\varepsilon}, \boldsymbol{\zeta}), \tag{15}$$

where the matrix $\mathbf{Q}$ is

$$\mathbf{Q} = \begin{bmatrix} Q_1 & 0 & Q_2 \\ 0 & Q_2 & Q_1 \end{bmatrix},$$

$$Q_1 = \sum_{i=1}^{2} K_{1i}\xi_i, \tag{16}$$

$$Q_2 = \sum_{i=1}^{2} K_{2i}\xi_i.$$

It is noted that the imposition of boundary conditions for the nonlocal PD model is more complicated than the local models. In this paper, both the boundary displacement constraints and the external force are applied through a particle layer with a thickness of δ (δ is the neighborhood radius). The traction force is applied as a body force as
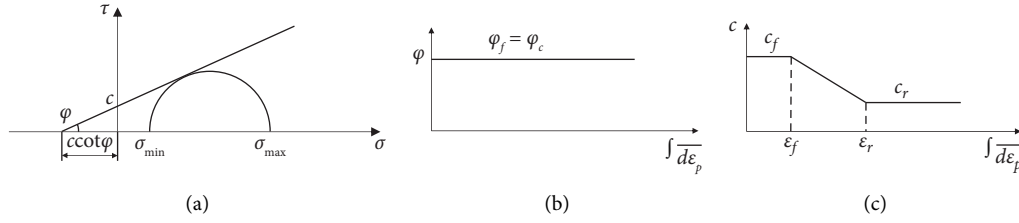
FIGURE 2: The strain-softening Mohr–Coulomb model: (a) yield criterion; (b) variation of φ with the accumulated plastic strain; and (c) variation of c with the accumulated plastic strain.

$$\mathbf{b}(\mathbf{x}) = -\frac{1}{\Delta}\mathbf{p}(\mathbf{x})\mathbf{n}, \qquad (17)$$

where Δ is the thickness of the boundary layer, and $\mathbf{p}(\mathbf{x})$ is the pressure.

The implementation method of the elastic-plastic model in the NOSBPD framework is almost identical to the local one [20]. The fully implicit backward Euler stress integration algorithm is employed for the strain-softening Mohr–Coulomb constitutive model [31]. It should be noted that in the Mohr–Coulomb model, the flow directions of the plastic potential at the corners of the plane are a combination of multiple yield surface normal vectors [31].

In the nonlinear analysis of strain softening materials, the force control loading method cannot simulate the descending section, and the displacement control cannot deal with the problem of snap-back, so the arc-length method needs to be used for control. Although the conventional arc-length method is effective for geometric nonlinear control, the arc-length governing equations for material nonlinear problems often have complex roots. Thus, it is difficult to identify the occurrence of local damage and failure. Therefore, the force control and the energy dissipation-based arc-length method are used jointly to control the nonlinear iteration process. That is, a force control constraint is used at first before switching to the energy dissipation-based arc-length method once the plastic energy dissipates. The details of this solution algorithm can be found in [32].

The aforementioned solution scheme has been incorporated into a C++ in-house platform. The flowchart of the computational program is outlined in Figure 3.

3. Evaluation of the Proposed Method

In this section, a plane strain biaxial test is presented to show the capability of the proposed method overcoming the mesh sensitivity. The classical finite element method is also employed for comparison. All simulations are conducted with the plain strain assumption.

The geometric dimensions and boundary conditions of the plane strain specimen are shown in Figure 4. The soil specimen has a width of 40 mm and a height of 80 mm. Herein, the edge friction constraint is applied to the model for stimulating the generation of shear bands; that is, the upper end is a constraint in the x-direction. The calculation parameters are listed in Table 1 by referring to []. The

calculation is divided into two steps: the first step is to apply isotropic consolidation pressure σ_3, and the second step is to apply deviatoric stress $\sigma_1 - \sigma_3$.

Two discretization schemes for FEM are employed for the purpose of comparison, where the fine mesh is composed of 3200 elements with an element size of 1 mm, whereas the element size of the coarse model becomes 2 mm. Figure 5 plots the shear band predicted by FEM with different mesh densities. The stress-strain curves of the point located in the shear band under the two cases are shown in Figure 6. It is readily apparent that the local FEM model yields nonobjective results. Upon mesh refinement, a thinner shear band and a more brittle response at the postpeak stage could be obtained. If the mesh is too fine, then the thickness of the shear band becomes zero, and energy dissipation would also tend to be zero. This nonphysical energy dissipation phenomenon is unacceptable.

With regard to the PD model, comparisons of the simulations with different cases are studied to address the following two questions: (1) can the simulation yield objective results in terms of thickness of the shear band and stress-strain relations? (2) What is the factor to determine the simulation results?

For the first question, we use the PD models, which have different grid densities but the same horizon. That is, the coarse grid model is set $\Delta x = 2$ mm and $\delta = 2\Delta x = 4$ mm, while the fine grid model is set as $\Delta x = 1.333$ mm and $\delta = 3\Delta x = 4$ mm. The shear band width and the stress-strain relation curve under different grid densities were compared in Figures 7 and 8(a), respectively. It can be seen from the two figures that, under the same internal scale parameter (δ), the nonlocal model can obtain a stable shear band width and stress-strain curve independent of mesh density.

For the second question, the PD models have different horizon sizes, but the grid spacing is kept fixed. That is, the small horizon model is set $\Delta x = 2$ mm and $\delta = 2\Delta x = 4$ mm, while the fine grid model $\Delta x = 2$ mm and $\delta = 4\Delta x = 8$ mm. It is employed to investigate the influence of the internal scale parameters (δ) on the simulation results. The width of the shear band and the stress-strain curves obtained from different models are shown in Figures 7(a), 7(c), and 8. It can be seen from that the width of the shear band is basically proportional to the nonlocal parameter δ, and the width of the shear band is roughly equal to δ. In addition, the stress-strain curves also vary at the postpeak stage with different nonlocal parameters. Therefore, in practices, the
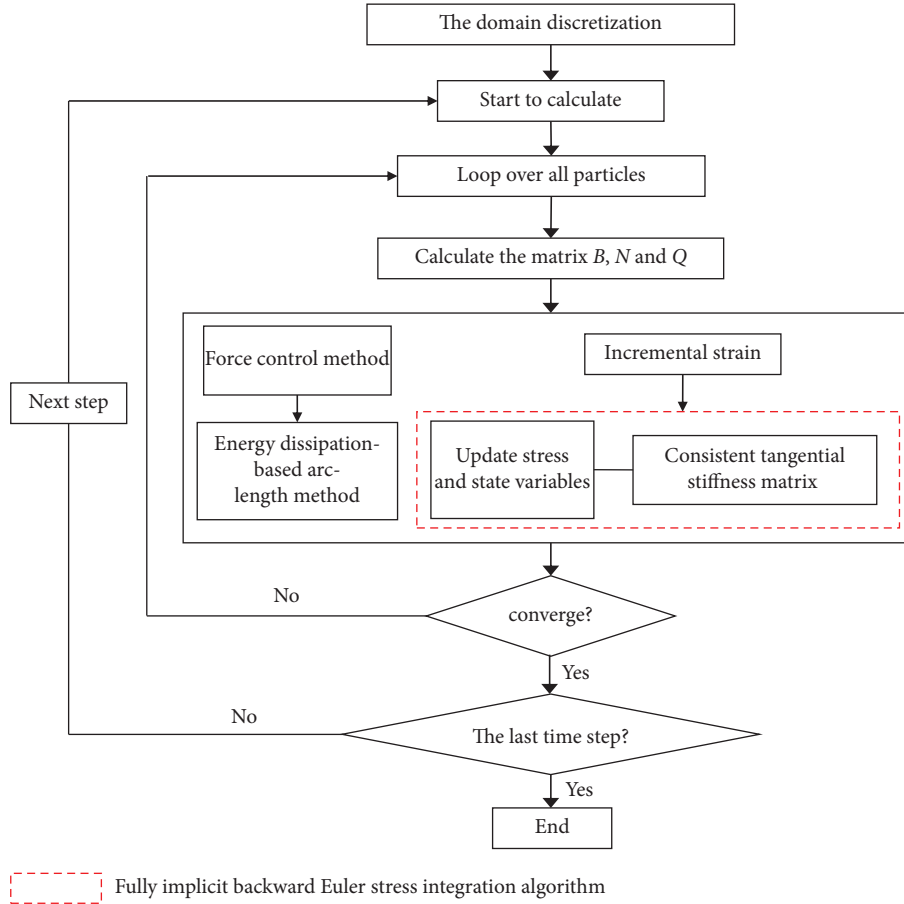
FIGURE 3: Flow chart of the computational program.

TABLE 1: Material parameters for the strain-softening Mohr–Coulomb constitutive model.

Parameters	Biaxial models	Slope models	Units
Young's modulus E	10.0	10.0	MPa
Poisson's ratio v	0.40	0.40	—
Unit of weight r	2.0	2.0	kN/m^3
Friction angle $\varphi_f = \varphi_c$	20°	30°	°
Dilatancy angle ψ	10°	10°	kPa
Peak strength of cohesion intercept c_f	30	60	kPa
Residual strength of cohesion intercept c_r	5	5	kPa
Hardening modulus	−500	−550	kPa
Threshold of strain ε_r	0.05	0.1	—

experimentally measured stress-strain curves can be used to determine the nonlocal parameters, and then one can use the calibrated parameters to investigate the strain localization failure in an objective manner.

From the above analysis, the correctness of the proposed method incorporating the strain-softening Mohr–Coulomb constitutive model is ensured, and it is confirmed that the NOSBPD model can be used as an effective regularization technique for strain localization analysis and that the localized shear band is related to the nonlocal parameter δ.

In addition, the nonlocal PD model is indeed more computationally intensive than the local FEM model under the same condition. For instance, for the FEM model with

40×80 elements, the computational time is 18 min, while for the PD model with 40×80 particles, the corresponding time is 335 min. Thus, the PD-FEM model [32] with the advantage of enhancing computational efficiency, merits consideration.

4. Progressive Failure Analysis of Soil Slope

In this section, the proposed NOSBPD method is used to analyze the progressive failure process of the soil slope with strain-softening behavior. The main departure is to illustrate the postfailure behavior of the soil slope in a progressive manner that can be effectively captured by the proposed method.
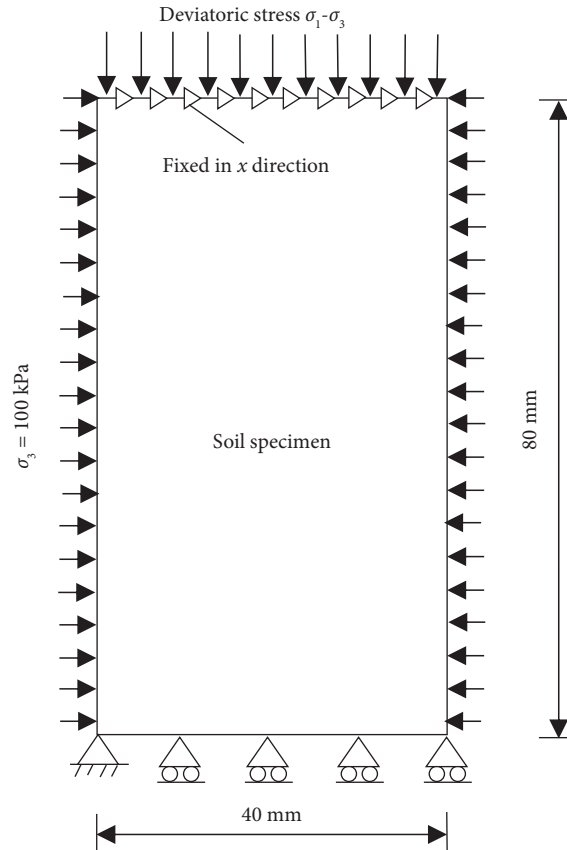
FIGURE 4: Geometry and boundary conditions for the biaxial test.

The geometry and boundary conditions of the slope model are shown in Figure 9. The slope with a height of 10.0 m is subjected to a gradually increasing surcharge load P. The calculation is also divided into two steps. First, the initial stress field is constructed by applying the gravity force, and then a uniform load is applied at the top surface of the slope, covering a length of 3 m. The arc-length method controls the gradual, increasing loading process until the slope fully fails. Material parameters are listed in Table 1. The slope is discretized into uniformly spaced particles with a grid spacing of $\Delta x = 0.3$ m. The horizon is set to $\delta = 2\Delta x$.

Figure 10 shows the displacement contours and typical point (located in the shear band) stress-strain curves. It is observed that the slope with strain-softening behavior under the surcharge load has a tendency to slide outward and downward. Comparisons of the slip surface obtained by the limit equilibrium method (LEM; herein, we use the Morgenstern-Price method) using the peak and residual strengths, respectively, and the NOSBPD model are illustrated in Figure 11. It can be seen from the figure that the position of the slip surface obtained by the NOSBPD model is located between those obtained by the LEM with peak and residual strength. In Figure 11(c), interestingly, different portions of the slip surface exhibit different cohesion

strengths. That is, the peak and residual strength are mobilized at the toe and top of the slope, respectively. The middle position of the slip surface near the toe is basically at the residual strength, while the strength parameters of the middle part near the top are intermediate between the peak and residual strength. It means that the slope starts to slide from the top of the slope and gradually expands downward. This nonuniform mobilization of the strength parameter indicates the occurrence of progressive failure of the soil slope.

As carried out in [14], an index referred to as the residual cohesion coefficient is defined to investigate the progressive failure process further:

$$I_c = \frac{c_f - c}{c_f - c_r}, 0 \le I_c \le 1, \tag{18}$$

where c_f and c_r are the peak and residual cohesion strength, respectively. It characterizes the reduction of the material strength parameters of the slope with respect to the peak strength. Figure 12 shows the variation of the residual cohesion coefficient with the progressive failure process of the slope. With the occurrence and development of the plastic zone on the sliding surface of the slope, the material strength parameters gradually weaken to the residual strength.

(a)   (b)
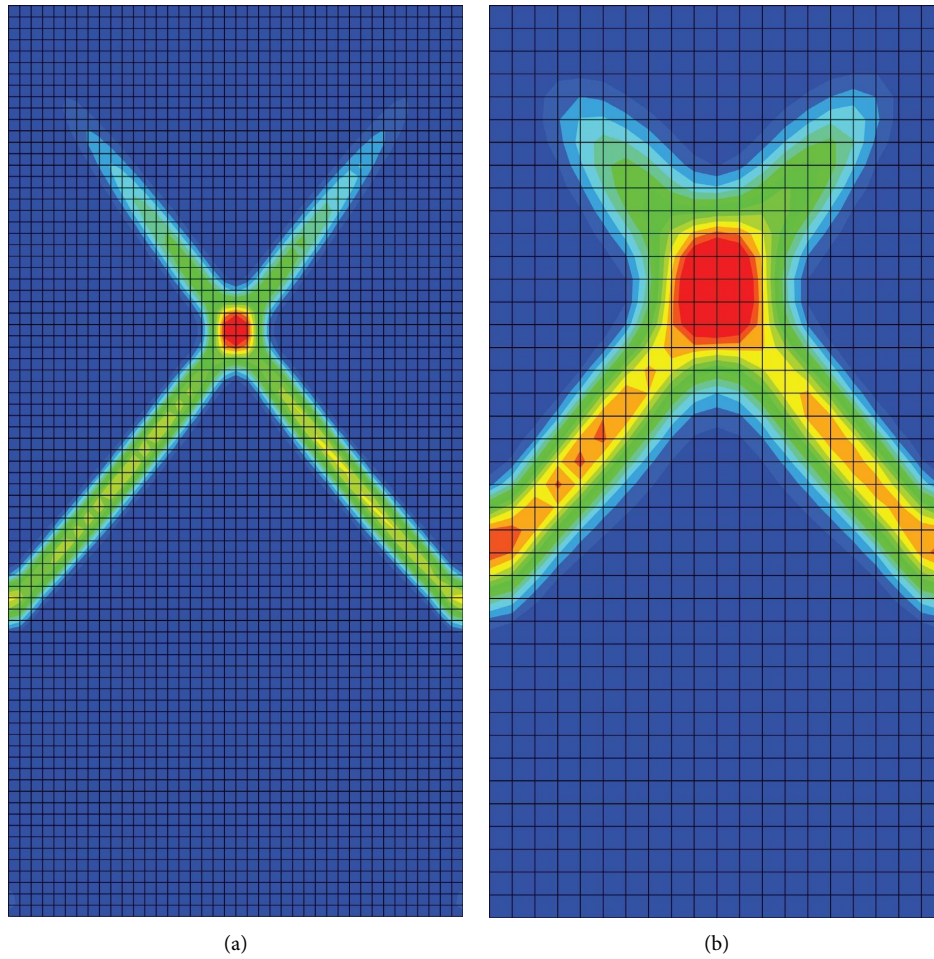
FIGURE 5: Distributions of the shear band under different mesh densities using FEM: (a) fine mesh (the element size is 1 mm); (b) coarse mesh (the element size is 2 mm).

—— fine mesh: the element size is 1 mm
- - - coarse mesh: the element size is 2 mm
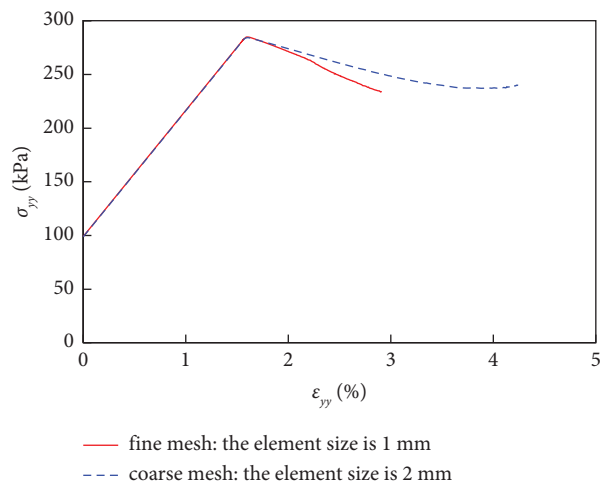
FIGURE 6: Stress-strain curves (σ_{yy}–ε_{yy}) of the point located in the shear band under different mesh densities using FEM.

(a)   (b)
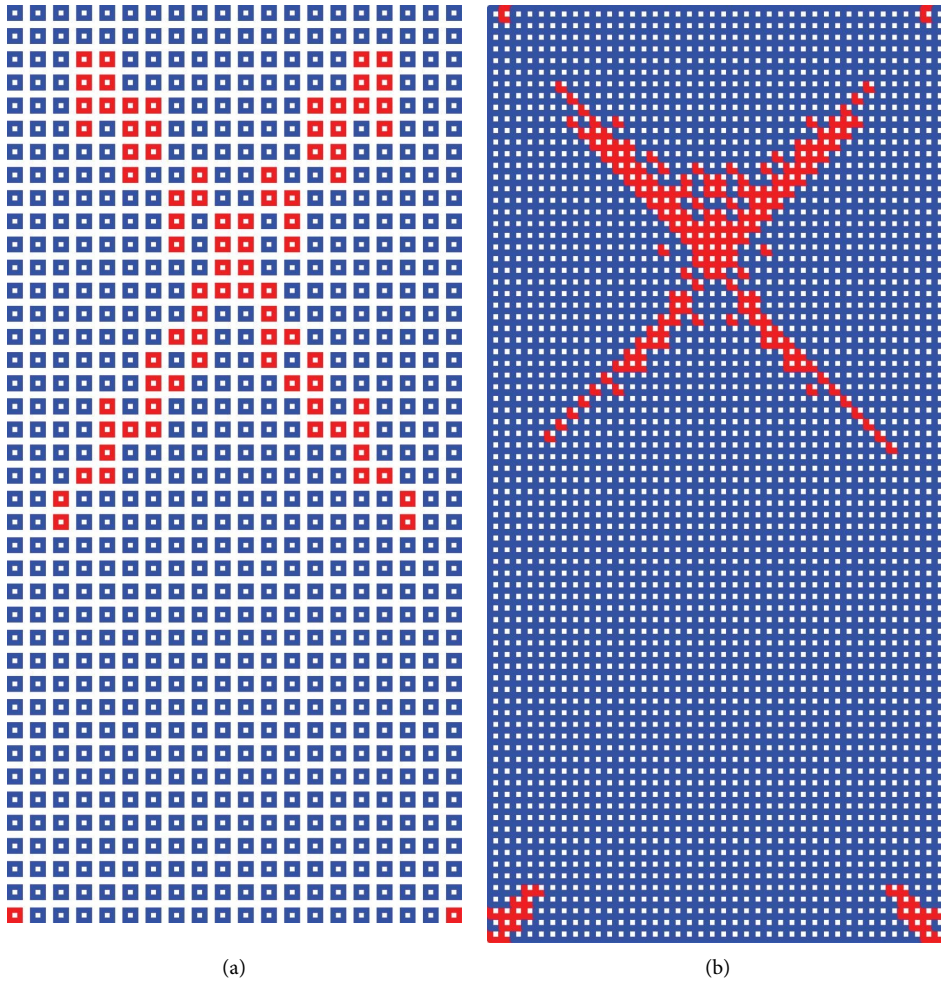
Figure 7: Continued.

(c)
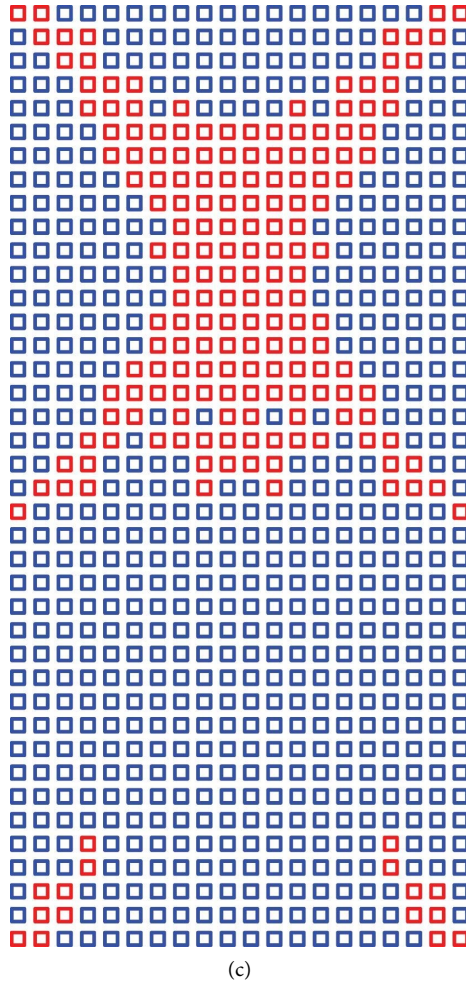
FIGURE 7: Distributions of the shear band under different particle densities: (a) coarse grid model ($\Delta x = 2$ mm, $\delta = 2\Delta x = 4$ mm); (b) fine grid model ($\Delta x = 1.333$ mm, $\delta = 3\Delta x = 4$ mm); (c) large horizon model ($\Delta x = 2$ mm, $\delta = 4\Delta x = 8$ mm).

fine grid; $\Delta x = 1.333$ mm, $\delta = 3\Delta x = 4$ mm

coarse grid; $\Delta x = 2$ mm, $\delta = 2\Delta x = 4$ mm

(a)

large horizon: $\Delta x = 2$ mm, $\delta = 4\Delta x = 8$ mm

small horizon: $\Delta x = 2$ mm, $\delta = 2\Delta x = 4$ mm

(b)
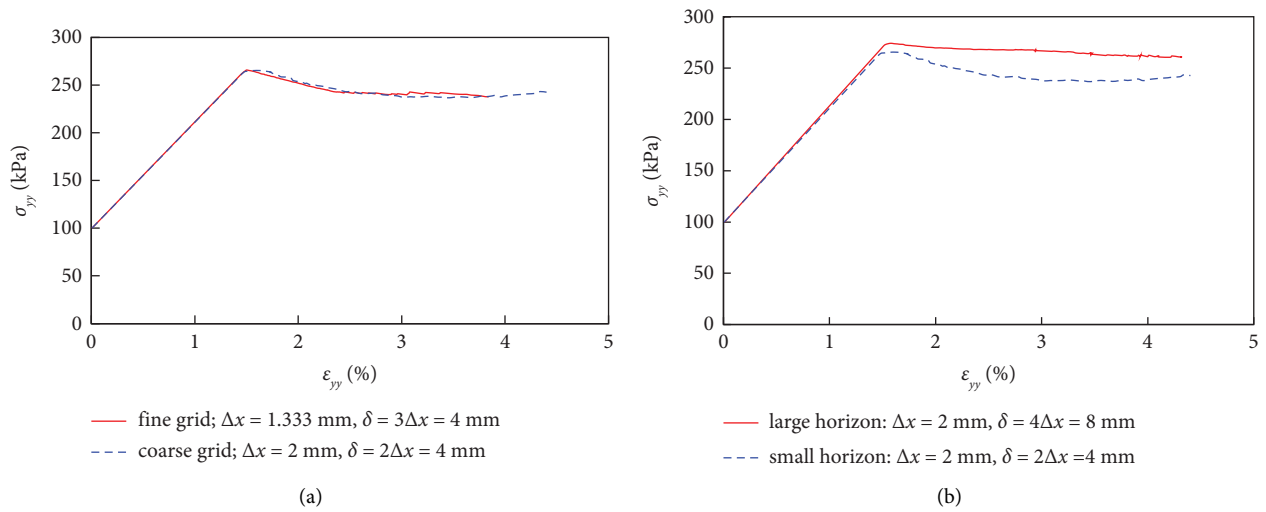
FIGURE 8: Stress-strain curves (σ_{yy}–ε_{yy}) of the point located in the shear band under different PD models: (a) different grid densities, but the horizon is kept fixed; (b) different horizons, but the grid spacing is kept fixed.
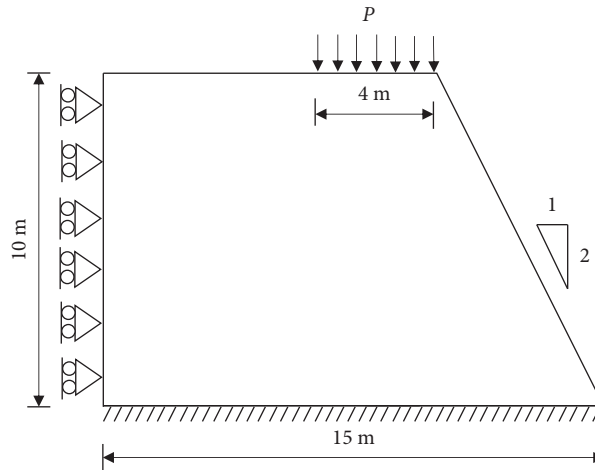
FIGURE 9: Geometry and boundary conditions for the slope model.

(a)

(b)

(c)
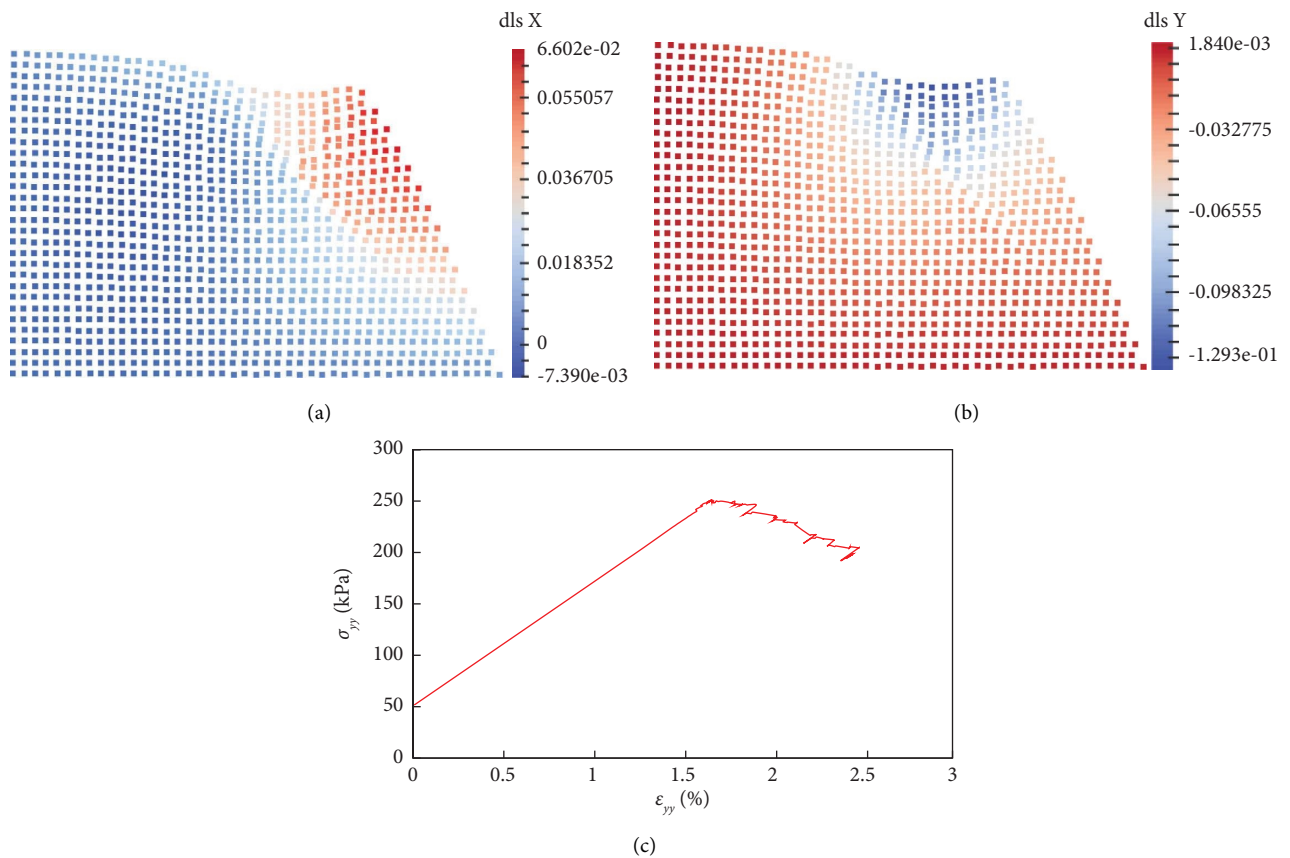
FIGURE 10: Displacement contours and stress-strain curves of the point located in the shear band under the surcharge load at the upper surface of the slope: (a) horizontal displacement; (b) vertical displacement; (c) stress-strain curve in the shear band (units of displacement: m).

It can be seen from the abovementioned analysis that there is stress redistribution and strength mobilization near the slip surface during the progressive failure of the slope, which cannot be assumed as a rigid body as made by the limit equilibrium method. Using the proposed method, it can avoid the dilemma that the peak strength is too dangerous and the residual strength is too conservative in the limit equilibrium method.

(a)

(b)

—— residual strength intermediate

—— strength (between peak and residual)

—— peak strength

(c)
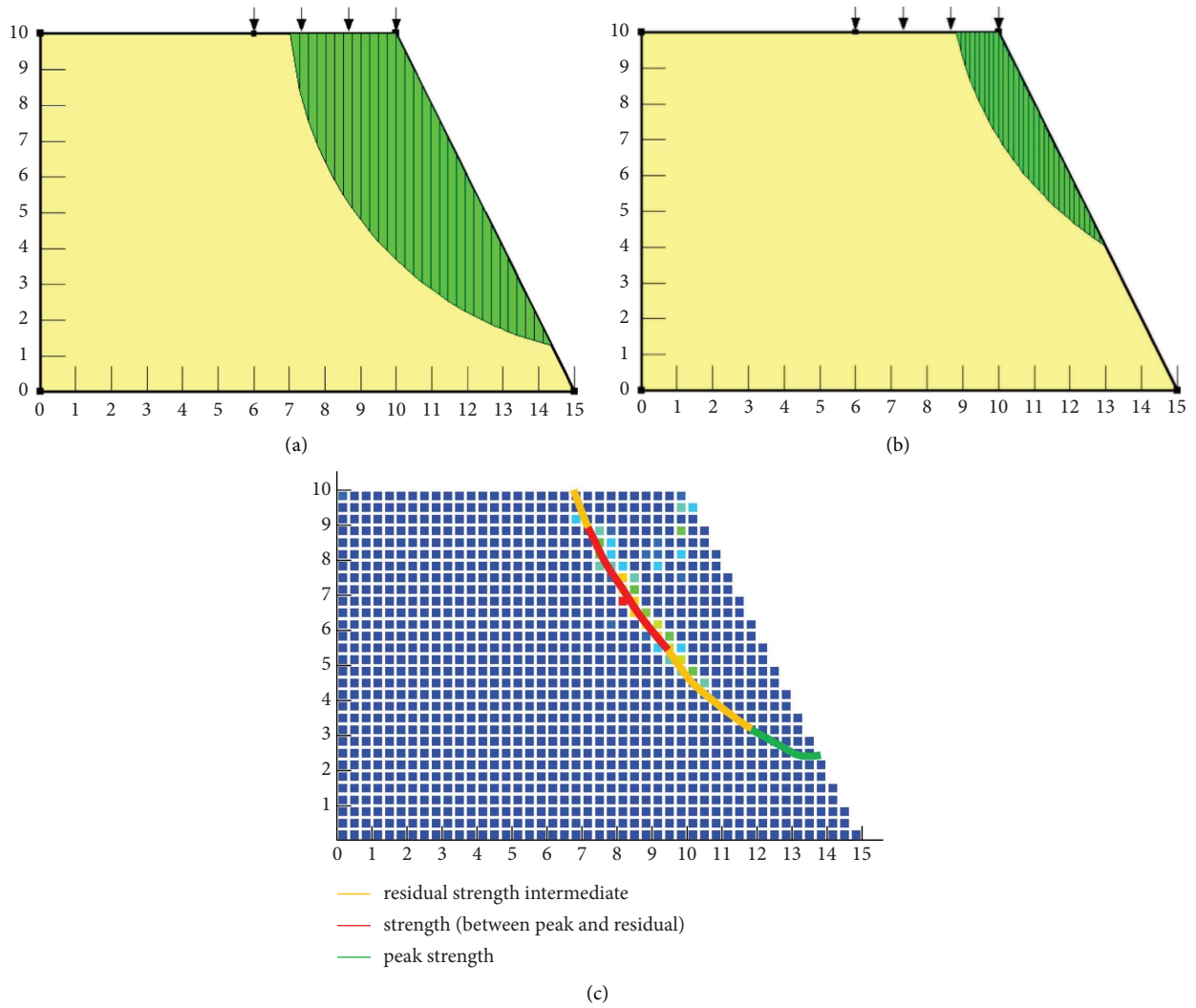
FIGURE 11: Slip surfaces obtained from the limit equilibrium method (LEM) and NOSBPD: (a) slip surface obtained by LEM using the peak strength parameters; (b) slip surface obtained by LEM using the residual strength parameters; (c) slip surface obtained by NOSBPD with a nonuniform mobilization of soil strength.

(a)

(b)
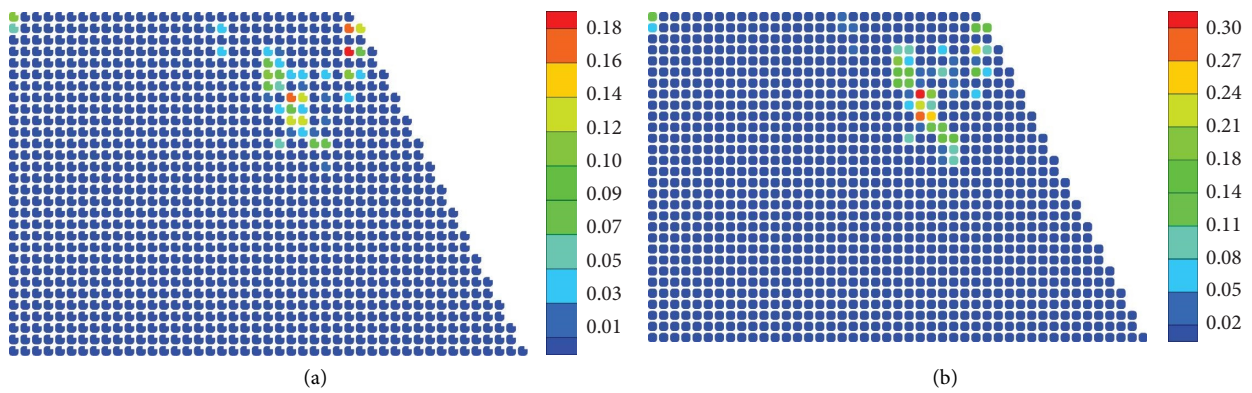
FIGURE 12: Continued.

(c)
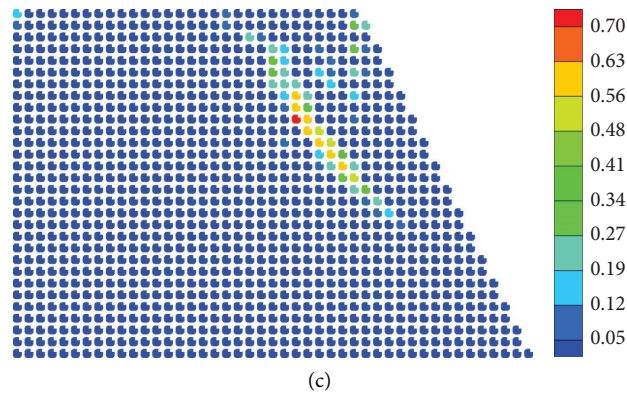
FIGURE 12: Variations of the residual cohesion parameter with the progressive failure process of the slope: (a) step = 200; (b) step = 250; (c) step = 300.

5. Conclusion

In this paper, the NOSBPD model is used as a regularization technique for the strain localization analysis of soil with strain-softening behavior. The Mohr–Coulomb constitutive model, by reducing the strength parameters linearly with the increase of the accumulative plastic strain, is incorporated into the NOSBPD framework to describe the strain-softening behavior of the soil. The plane strain test and the progressive failure of the soil slope are analyzed. The main conclusions obtained from the analyses are as follows:

(1) The nonlocal method can remove the mesh dependence, and the NOSBPD model can be used as an effective regularization technique for strain localization analysis.

(2) The localized shear band is related to the nonlocal parameter δ, which can be calibrated by the experimentally measured stress-strain curves.

(3) With the occurrence and development of the plastic zone on the sliding surface of the slope, the material strength parameters gradually weaken to the residual strength. Different portions of the slope are mobilized with different strength parameters. The stress redistribution and strength mobilization along the slip surface render the assumption made by the limit equilibrium method incorrect. That is, it is not a rigid body.

(4) The proposed method involves being able to capture strength mobilization in different parts of the sliding surface during the progressive failure process of the soil slope. It can avoid the dilemma that the peak strength is too dangerous and the residual strength is too conservative due to the rigid body assumption in the limit equilibrium method.

As a nonlocal theory, NOSBPD is much more computationally intensive than conventional FEM. There is a necessity to apply the FEM-NOSBPD coupled method [32] for soil strain localization analysis. In addition, there is a need to remove the constraint of the small deformation assumption for simulating the progressive failure of slope in the large deformation regime. Also, considering the interaction of soil and water, incorporating a more advanced constitutive model of soil will also require further research.

Data Availability

The datasets generated and analyzed during the current study are available from the corresponding author upon reasonable request.

Conflicts of Interest

The authors declare that they have no conflicts of interest.

References

[1] K. A. Alshibli and S. Sture, "Shear band formation in plane strain experiments of sand," *Journal of Geotechnical and Geoenvironmental Engineering*, vol. 126, no. 6, pp. 495–503, 2000.

[2] X. Cheng, "Localization in Dutch Dune Sand and Organic clay: New Insight into Localization Mechanisms," doctoral thesis, Delft University Press, Delft Netherlands, 2004.

[3] L. P. Wang and G. Zhang, "Progressive failure behavior of pilereinforced clay slopes under surface load conditions," *Environmental Earth Sciences*, vol. 71, no. 12, pp. 5007–5016, 2014.

[4] R. Borst, "Numerical methods for bifurcation analysis in geomechanics," *Ingenieur-Archiv*, vol. 59, no. 2, pp. 160–174, 1989.

[5] M. Huang, "Analysis methods for stability and bearing capacity of soils," *Chinese Journal of Geotechnical Engineering*, vol. 38, no. 1, pp. 1–34, 2016.

[6] M. Huang, Z. Chen, and X. Lu, "Bifurcation prediction of shear banding in sand with non-coaxial critical state model considering inherent anisotropy," *Soils and Foundations*, vol. 58, no. 3, pp. 641–653, 2018.

[7] T. Belytschko, J. Fish, and B. E. Engelmann, "A finite element with embedded localization zones," *Computer Methods in Applied Mechanics and Engineering*, vol. 70, no. 1, pp. 59–89, 1988.

[8] R. I. Borja, "A finite element model for strain localization analysis of strongly discontinuous fields based on standard Galerkin approximation," *Computer Methods in Applied Mechanics and Engineering*, vol. 190, no. 11-12, p. 21, 2000.

[9] G. S. Wang, L. W. Kong, A. G. Guo, and Z. W. Wang, "Element model with shear band and its application to progressive failure analysis of slopes," *Chinese Journal of Rock Mechanics and Engineering*, vol. 24, no. 21, pp. 3852–3857, 2005.

[10] G. Zhang and Y. Hu, "Numerical modeling of failure process of soil slopes," *International Journal of Geomechanics*, vol. 17, no. 4, Article ID 06016031, 2017.

[11] M. Lazari, L. Sanavia, and B. A. Schrefler, "Local and non-local elasto-viscoplasticity in strain localization analysis of multiphase geomaterials: local/non-local Elasto-viscoplastic Modeling of Multiphase Materials," *International Journal for Numerical and Analytical Methods in Geomechanics*, vol. 39, no. 14, pp. 1570–1592, 2015.

[12] R. De Borst, "Simulation of strain localization: a reappraisal of the cosserat continuum," *Engineering Computations*, vol. 8, no. 4, pp. 317–332, 1991.

[13] R. De Borst and H.-B. Mühlhaus, "Gradient-dependent plasticity: formulation and algorithmic aspects," *International Journal for Numerical Methods in Engineering*, vol. 35, no. 3, pp. 521–539, 1992.

[14] E. Conte, F. Silvestri, and A. Troncone, "Stability analysis of slopes in soils with strain-softening behaviour," *Computers and Geotechnics*, vol. 37, no. 5, pp. 710–722, 2010.

[15] M. Huang, X. Qu, and X. Lü, "Regularized finite element modeling of progressive failure in soils within nonlocal softening plasticity," *Computational Mechanics*, vol. 62, no. 3, pp. 347–358, 2018.

[16] S. A. Silling, "Reformulation of elasticity theory for discontinuities and long-range forces," *Journal of the Mechanics and Physics of Solids*, vol. 48, no. 1, 2000.

[17] W. Sun, J. Fish, and P. Lin, "Numerical simulation of fluid-driven fracturing in orthotropic poroelastic media based on a peridynamics-finite element coupling approach," *International Journal of Rock Mechanics and Mining Sciences*, vol. 158, Article ID 105199, 2022.

[18] F. Liu and J. Fish, "Modeling cohesive fracture propagation in partially saturated porous media with the assumed enhanced strain method," *Acta Geotechnica*, vol. 17, no. 5, pp. 1605–1626, 2022.

[19] W. Sun, J. Fish, and P. Ni, "Superposition based concurrent multiscale approaches for poromechanics," *International Journal for Numerical Methods in Engineering*, vol. 122, no. 24, pp. 7328–7353, 2021.

[20] E. Madenci and E. Oterkus, *Peridynamic Theory and its Applications*, Springer, New York, NY, USA, 2014.

[21] W. Sun, G. Zhang, and Z. Zhang, "Damage analysis of the cut-off wall in a landslide dam based on centrifuge and numerical modeling," *Computers and Geotechnics*, vol. 130, Article ID 103936, 2021.

[22] W. Sun and J. Fish, "Coupling of non-ordinary state-based peridynamics and finite element method for fracture propagation in saturated porous media," *International Journal for Numerical and Analytical Methods in Geomechanics*, vol. 45, no. 9, pp. 1260–1281, 2021.

[23] X. Song and S. Menon, "Modeling of chemo-hydromechanical behavior of unsaturated porous media: a nonlocal approach based on integral equations," *Acta Geotechnica*, vol. 14, no. 3, pp. 727–747, 2019.

[24] X. Song and N. Khalili, "A peridynamics model for strain localization analysis of geomaterials," *International Journal for Numerical and Analytical Methods in Geomechanics*, vol. 43, no. 1, pp. 77–96, 2019.

[25] G. Zhang and J. M. Zhang, "Stability evaluation of strain-softening slope based on Swedish slice method," *Rock and Soil Mechanics*, vol. 28, no. 1, pp. 12–16, 2007.

[26] G. Zhang and J.-M. Zhang, "Simplified method of stability evaluation for strain-softening slopes," *Mechanics Research Communications*, vol. 34, no. 5-6, pp. 444–450, 2007.

[27] G. Zhang, Y. Hu, and L. P. Wang, "Behaviour and mechanism of failure process of soil slopes," *Environmental Earth Sciences*, vol. 73, no. 4, pp. 1701–1713, 2015.

[28] S. A. Silling, M. Epton, O. Weckner, J. Xu, and E. Askari, "Peridynamic states and constitutive modeling," *Journal of Elasticity*, vol. 88, no. 2, pp. 151–184, 2007.

[29] S. A. Silling and E. Askari, "A meshfree method based on the peridynamic model of solid mechanics," *Computers & Structures*, vol. 83, no. 17–18, pp. 1526–1535, 2005.

[30] M. S. Breitenfeld, P. H. Geubelle, O. Weckner, and S. A. Silling, "Non-ordinary state-based peridynamic analysis of stationary crack problems," *Computer Methods in Applied Mechanics and Engineering*, vol. 272, pp. 233–250, 2014.

[31] E. A. de Souza Neto, D. Peric, and D. R. Owen, *Computational Methods for Plasticity: Theory and Applications*, John Wiley & Sons, New York, NY, USA, 2011.

[32] W. Sun, J. Fish, and G. Zhang, "Superposition of non-ordinary state-based peridynamics and finite element method for material failure simulations," *Meccanica*, vol. 55, no. 4, pp. 681–699, 2020.

Research Article

Based on the CT Image Rebuilding the Micromechanics Hierarchical Model of Concrete

Lei Guangyu [ID] [1,2,3] **and Han Jichang**[1,2,3]

[1]*Shaanxi Land Engineering Construction Group, Xi'an 710048, China*
[2]*Institute of Land Engineering and Technology, Shaanxi Provincial Land Engineering Construction Group Co Ltd, Xi'an 710048, China*
[3]*Key Laboratory of Degraded and Unused Land Consolidation Engineering, The Ministry of Natural Resources, Xi'an 710048, China*

Correspondence should be addressed to Lei Guangyu; leiyugogo@163.com

Establishing a mesoscopic numerical model to investigate the mechanical properties of concrete has very important significance. This paper considers the random distribution of aggregate in concrete. The aggregate is assumed to be spherical, respectively, to simulate the interface layer as the entity unit or the contact elements. The random aggregate model and the interface model of random aggregate were established. Based on the CT image and the application of MATLAB and MIMICS software, the different characteristics of the concrete model for 3D reconstruction were set up. Through comparative analysis of the advantages and disadvantages of different models, considering the CT number included in the CT images, this paper establishes the reconstruction model, which includes the shape of concrete aggregates, gradation, holes, etc. The analysis results have shown that the model can infer realistic concrete behavior, providing a new approach for studying concrete properties at the mesoscale.

1. Introduction

Concrete is a composite material consisting of water, cement, and coarse aggregates. The special properties of the composite material determine its macroscopic mechanical properties [1]. The destruction process involves the interaction of various scales, from the microscopic to the macroscopic [2, 3] . Currently, the mesoscale is considered the linking bridge between the microscopic and macroscopic scales. The micromechanical numerical method, based on the finite element method, uses the concrete micromechanical model to study its failure process and obtain the intrinsic relationship between mesoscopic failure and macrodestruction, thus investigating the failure mechanism of concrete materials [4–9].

With the improvement of theoretical methods and computer hardware components, graphics processing software and meshing tools have been continuously upgraded, resulting in easier simulation of concrete mesostructures. Nowadays, using numerical methods to investigate the mechanical properties of concrete has received extensive attention from researchers. Indeed, the development of numerical models has an important influence on the simulation results. Among the most representative models in the literature are the random particle model [10], lattice model [11, 12], stochastic mechanical property model [13], and statistical damage constitutive model [14–16].

The micromechanical method is typically utilized to analyze the concrete characteristics using numerical experiments. Under the condition that the calculation model is reasonable and the material parameters of each concrete phase are sufficiently accurate, some tests can be realistically replicated to overcome the objective limitations of the test conditions and human factors [29]. This has greatly promoted the study of the mechanical properties of concrete [17]. Nevertheless, previous research has outlined some

limitations and drawbacks in the above models. At present, digital image processing technology is becoming significantly important for developing numerical models. Recently, concrete computed tomography (CT) scan image reconstruction models have become a hotspot and frontier of research on the numerical simulation of construction materials [18–21].

The real shape and location of aggregate particles in concrete were assumed in numerical analyses based on X-ray CT scans. Reference [22] found that satisfactory agreement regarding the vertical force versus crack mouth opening displacement evolution and crack geometry was achieved between analyses and laboratory tests. Two-dimensional mesoscale finite element models with realistic aggregates, cement paste, and concrete voids are developed using microscale X-ray CT images. Cohesive elements with traction-separation laws are pre-embedded within cement paste and aggregate-cement interfaces. Reference [23] simulated complex nonlinear fracture and tension tests using a large number of images. Reference [24] proposed an objective judgment criterion of unit attribute recognition based on the method of mesh mapping and established the 3D finite element model with the same aggregate proportion as the specimen in the experiment.

This study combines the literature sources' achievements over the years to develop different microscopic concrete numerical models and analyze their respective deficiencies. After that, it establishes a concrete reconstruction model based on CT images. The model considers the concrete mesostructure to simulate its behavior realistically. This study is expected to provide a reference for future investigations of the mesoconcrete's mechanical properties.

2. Mesoscopic Concrete Stochastic Model

Generally, the concrete random model is used to replicate testing samples numerically using the knowledge of the random sampling method and statistics along with the actual mixture proportions. The advantage of this approach is the ability to simulate the influence of different factors on concrete behavior. At present, the method is considered mature and independent of the data size, and its development is relatively perfect. Perform calculations on different types of specimens.

2.1. Random Aggregate Model. The random aggregate model is a three-phase heterogeneous composite consisting of aggregates, mortar, and a bond zone between the two. Previously, the Monte Carlo method was used to generate random numbers [25]. Based on the self-programmed model generation procedure, the projected grid method is used to assign the corresponding material properties according to the unit type. Due to the involvement of different material parameters in each phase, the load-deformation relationship of the concrete specimen is nonlinear. It can be used to simulate the specimen's crack propagation process and damage patterns [26].

This approach to determining the position of aggregates with different particle sizes in the sample involves calculating the number of aggregates using the actual mix ratio of concrete and assuming spherical-shaped aggregates with four variables each. The diameter of the sphere is used to distinguish the size of the aggregate, and the position of the sphere center (XYZ) is used to determine the location of the aggregate. According to the self-programming procedure, the spherical center coordinates are generated randomly using the Monte Carlo method. Generally, different spheres meet objective conditions by setting constraints and adopting a cyclical comparison method. A 3D random distribution geometric model of concrete aggregates can be obtained by compiling the generated random variables into corresponding FORTRAN programs and reading them into ANSYS in the command flow mode.

Once the concrete geometric model is generated, the aggregate, mortar, and interface are given corresponding parameters. Moreover, the material is meshed using the finite element method to obtain a 3D random distribution model of concrete aggregates. The overall model diagram is shown in Figure 1, and the section diagram is shown in Figure 2.

2.2. Random Aggregate Contact Surface Model. The concrete's random aggregate contact surface model is a two-phase material that consists of mortar and aggregate and uses an ANSYS contact surface unit to simulate their interface joint. This method starts by establishing a concrete cylinder body in ANSYS, then randomly generating aggregate spheres in the entity using the self-programming procedure to separate the cylinder and aggregate spheres for the BOOLEANS calculations. The position of the aggregate formed at this time is a hollow concrete specimen. Use the program again to read the position coordinates of the aggregate and generate its entity. The overall mesh is typically selected using the SOLID45 element. Besides, the aggregate projection grid method is used to distinguish the fundamental material properties. Moreover, the contact elements between the aggregate and the mortar are defined using the TARGE170 and CONTA174 unit types [27]. The model contact element is shown in Figure 3, and the cross-section of the random aggregate contact surface model is shown in Figure 4.

Compared with the random aggregate model, this technique uses a contact element instead of an interface element, resulting in considerably lower computational time and cost. The results of the two calculations are shown in Figure 5. It can be seen that their destruction rules are the same, indicating that the random aggregate contact surface model can be a good substitute for the random aggregate model.

3. Mechanical Model Based on Three-Dimensional Reconstruction of Concrete Images

Due to the difference between the random model and the actual concrete internal structure, the research and analysis cannot lead to a complete correspondence with the test. Therefore, studying the mechanical model based on concrete
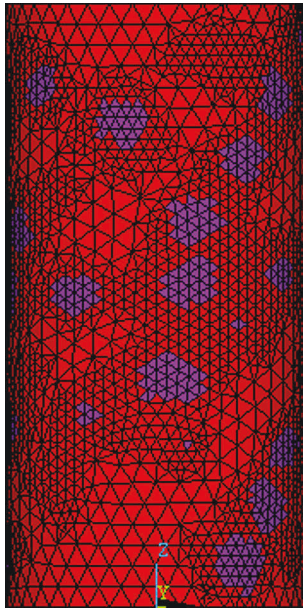
FIGURE 1: Model of random aggregate.

FIGURE 2: Section of random aggregate.

FIGURE 3: Contact element of model.
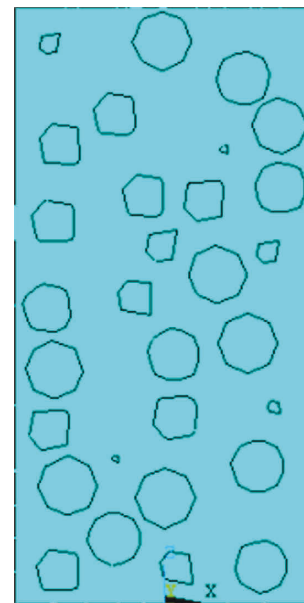
FIGURE 4: Section of the contact element.

images for 3D reconstruction has gradually gained attention and progress. The 3D reconstruction model is a model that is closer to the mesostructure of the actual concrete and is an important foundation for future research on the mechanical properties of mesoconcrete.

3.1. Three-Dimensional Reconstruction Model of Concrete Based on the Joint Unit Method.

Unlike previously explained techniques, the three-dimensional reconstruction model is closer to the real mesostructure of concrete and can be compared with the physical experiment. The 3D finite element model of concrete based on the joint-element method

abandons the modeling order of points, lines, surfaces, and bodies by discretely separating the concrete into many nodes in the space, which are then connected to generate the unit. Then the material properties of the specimen are determined from the elements containing the node attributes, thereby establishing a 3D finite element model of the concrete mesostructure. The modeling procedure in this method is described as follows:

(1) Each CT image is processed to save its CT number and spatial position as a cross-section file.

(a)   (b)
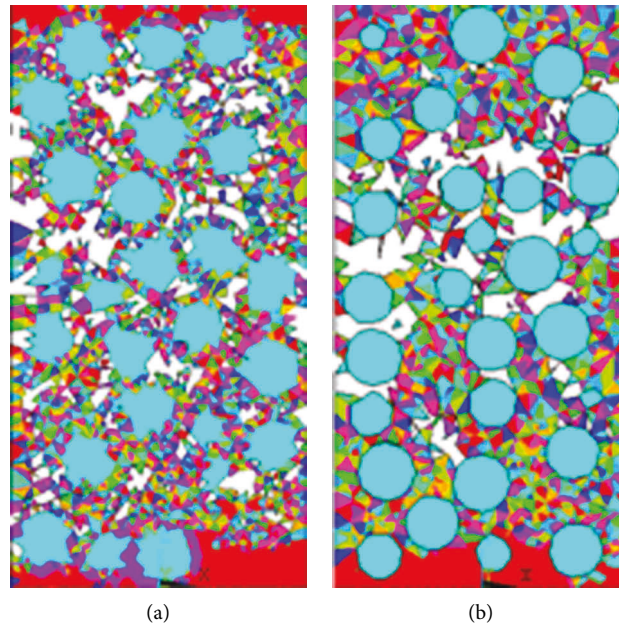
FIGURE 5: Different damaged sections of the model. (a) Model of random aggregate. (b) Interface model of random aggregate.

(2) The image quality is enhanced using the threshold segmentation method to distinguish the aggregate from the mortar.

(3) The image information is saved as a two-dimensional matrix using MATLAB.

(4) The pixel attribute value matrix in MATLAB is read into the ANSYS array using a self-programming code to generate a model.

The model is shown in Figure 6.

On the other hand, this method cannot yet rebuild a complete concrete test piece due to using many elements. In order to reduce the amount of data, the influence of holes, small aggregate particles, etc., is not taken into account in the reconstruction process, resulting in relatively low simulation accuracy.

3.2. Three-Dimensional Reconstruction Model of CT Images Based on MIMICS Software. Some large-scale image creation and editing software, such as MIMICS, has a 3D entity reconstruction function. MIMICS software can directly read Dicom format CT scan images through the following procedure:

(1) Interpolate the picture using image positioning.

(2) set different thresholds for different materials.

(3) modify the pixels of the image by different pixel modification methods.

(4) once each layer of the image is processed to remove redundant data, a 3D geometric concrete model can be established based on the calculation.

(5) use ANSYS software to read the list file of the 3D concrete built in the MIMICS software and generate the finite element model directly.

The overall model is shown in Figure 7,

Based on the concrete reconstruction model obtained from the above CT images, a complete calculation cannot be performed at present due to the model's large number of elements and relatively low accuracy.

4. Key Issues and Technical Approaches to Concrete Micromechanical Models

The numerical model of mesoconcrete is the basis for studying the material's mechanical properties. The diversity in the concrete's constituent materials and the randomness in the preparation process increase the complexity and nonuniformity of the model compared to other materials. Therefore, there are many key problems in the numerical model of the mesoconcrete. At present, this method cannot perform one-to-one comparative analysis with physical tests because the simulated aggregate shape and position are different from those of real concrete specimens, and the model rarely considers the influence of holes in the specimen. The 3D reconstruction model of concrete relies on CT images. Based on the digital image processing method and large-scale image processing software for finite element modeling, the mesostructure of the real specimen is well simulated. The advantage of this method is that, according to the actual concrete shape, a consistent finite element model can be generated to perform concrete mechanical tests better. Accordingly, the development of concrete reconstruction models is the direction of future concrete property investigations. This research topic is still facing some deficiencies. For instance, image information data compression results in large amounts of data that cause the completeness of a full model computation to be prevented. Moreover, the model's accuracy is low due to the unit selection of feature points. Besides, the model cannot
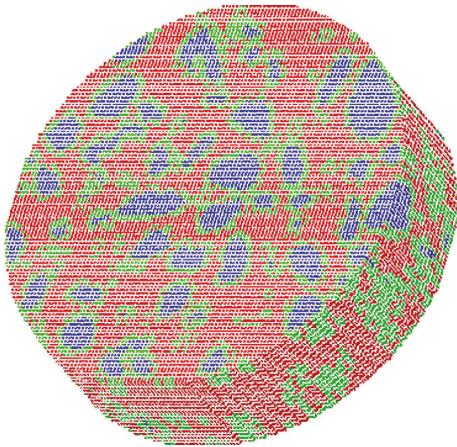
FIGURE 6: The specimen FEM elements.
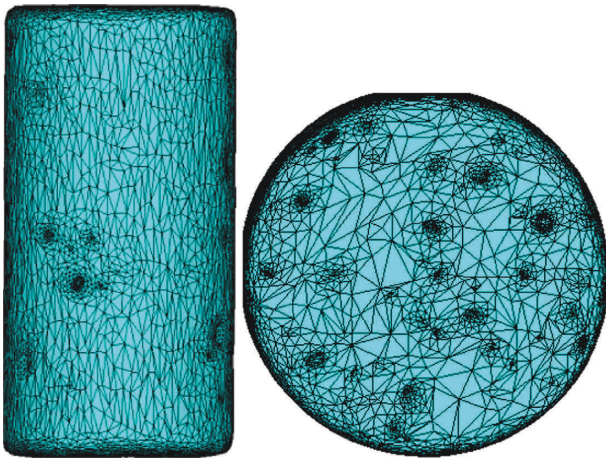
FIGURE 7: 3D FEM elements of concrete.
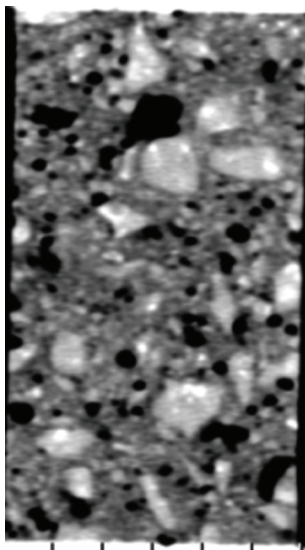
FIGURE 8: Initial graph of the CT section.
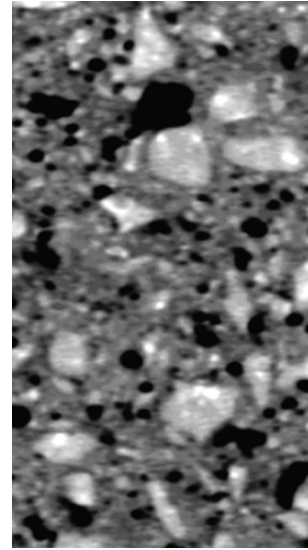
FIGURE 9: After extraction of the CT section.

consider the impact of small aggregates, holes, and other factors during the reconstruction process. These factors have an important influence on the mechanical properties of concrete. Combining the above problems with the concrete random model and the concrete reconstruction model, the common limitation of the two is that the influence of small volume components such as holes and fine aggregates has not been taken into account, along with the influence of different aggregate parameters. These are problems that cannot be ignored in the study of concrete mechanics. Accordingly, a concrete mesoscopic model that reflects actual conditions is the basis for investigating concrete mechanical properties and obtaining reasonable and correct results. Therefore, based on the problems existing in the above models, starting from concrete CT images, reconstructing the concrete mechanical model, taking into account the influence of different aggregate parameters and concrete holes, reflecting these characteristics in the reconstruction model is the trend to study the numerical calculation model of the microscopic concrete.

5. Microscopic Concrete Reconstruction Model Based on CT Number

The CT machine scans the concrete sample layer by layer to obtain CT slices of any scanned surface inside the concrete. Each slice contains the material information and density of the layer. Finally, the material properties can be represented by the CT values of each pixel [28].

5.1. Image Processing. In a single test specimen, the number of CT digital regions and the number of scanned CT slices vary due to the difference in the resolution of the CT machine and the scanning thickness. Before processing an image, it is first necessary to determine the resolution of the image and the geometric location of the CT slice in the
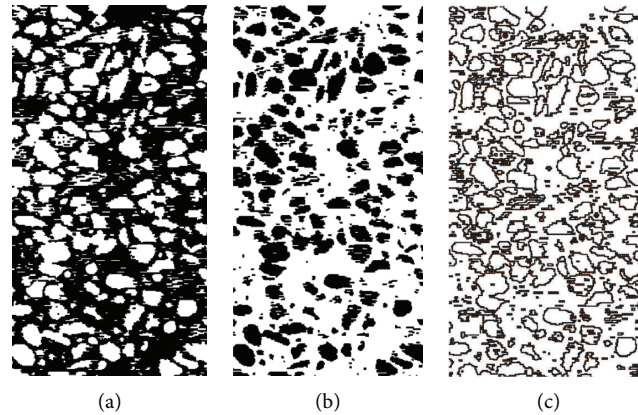
FIGURE 10: Profile of every material in the CT section after reconstruction. (a) Mortar. (b) Aggregate. (c) Interface.

concrete specimen, and then select the CT slice that needs to be reconstructed. At the same time, since the CT machine scans the concrete specimens and the parts around the specimens, CT slice images also contain this information. The image is first divided into study areas, and the areas that need to be investigated for reconstruction are selected. A raw CT slice map is shown in Figure 8. The figure contains the scanned parts of the test specimen and the information on the surrounding blank parts. In the analysis, if the CT image is not processed, it will cause errors when analyzing the image data. Therefore, the image study area is extracted, as shown in Figure 9.

Once the extraction of the CT slice image is completed, the size of the image should be determined to obtain the pixel matrix of the image. Then use the ENVI software to extract the CT value at each pixel. At this point, the coordinate value at the pixel point and the CT value are in a one-to-one correspondence and represent the material information at this position. For the convenience of calculation and statistics, CT values are normalized. Thereafter, the position information and material quantity are determined. Finally, the data, including the position coordinates of the aggregate, mortar, and holes and the size of the CT value, is saved.

5.2. Model Reconstruction. The ABAQUS software generated a two-dimensional geometric model with the same dimensions as the CT slices. The two-dimensional plane geometry model was meshed. Each unit represented a pixel, and the ".inp" file was proposed once the partition was completed. According to the Fortran language, the corresponding program is compiled, and the node information in the ".inp" file is replaced with the information of the node coordinates of the aggregate, mortar, and hole in the CT slice, and the file is saved and read again. At this point, the information contained in the model's elements and nodes are the aggregates, mortar, and hole information. In this study, a new unit was added between the aggregate and the mortar, considered a transitional layer, giving it corresponding material properties. The reconstruction of the
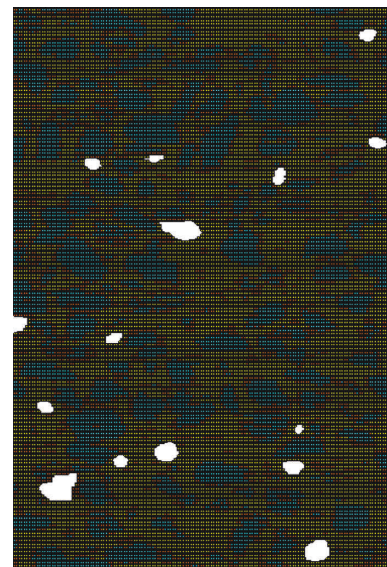
FIGURE 11: Whole reconstruction model.
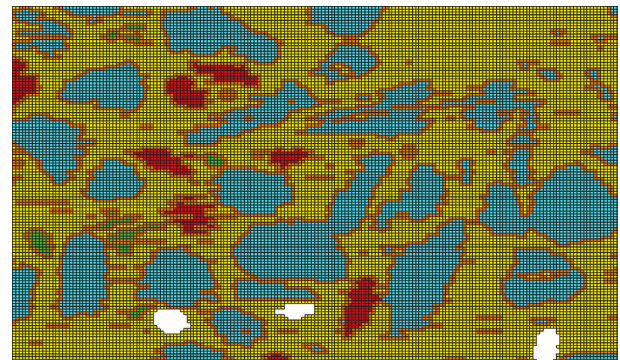
FIGURE 12: Reconstruction partial enlarged.

model is complete. Each material section is shown in Figure 10, and the whole is shown in Figure 11.

After selecting the image and processing the data, the CT image is finally converted into a numerical model. It can be seen from the partial enlargement of Figure 12 that the

reconstructed model contains aggregates, interfaces, mortar, and holes at all levels.

This model integrates the characteristics of the random models and CT reconstruction techniques. The interface influence in the random model and the aggregate shape and gradation effects in the CT reconstruction model were taken into account, and the influence of holes that both models did not consider was increased.

In order to verify the rationality of the model, a mechanical analysis was performed under pressure and tensile loads. This paper used the plastic damage model of concrete. The damage factor D is calculated separately according to the compression and tension conditions. The mechanical parameters of each material are shown in Table 1. This paper applied dynamic compression and tension forces using a displacement-controlled protocol. The loading curve is shown in Figures 13 and 14. The dynamic compression loading time was 0.1 s, and the loading displacement was 1 mm. Besides, the loading time for the dynamic tensile case was 0.05 s, and the loading displacement was 0.12 mm.

5.3. Pressure Load. The dynamic pressure load is applied to the model top, and the bottom surface of the model is restrained. The computation results are shown in Figures 15 and 16. In the initial loading stage, when the specimen is not damaged, the displacement of the material changes regularly, where the top displacement is the largest, the bottom is the smallest, and the layering changes sequentially. When the specimen is destroyed, the displacement varies locally. Under the dynamic pressure load, the damage starts at the top ends of the specimen. As the load increases, the damage range gradually expands over the whole section. When the stress reaches a certain value, damage in some areas begins to increase and gradually penetrate, and finally, several macroscopic cracks penetrating the entire specimen are formed. It can be seen from the figure that the hole has a certain impact on the concrete damage where the stress concentration is easy to occur first around the hole, causing the damage to initiate. Moreover, the hole influences the development of the damage path and affects the final failure surface.

Figure 17 shows the analysis of different materials' damage. It can be seen that the crack is mainly developed along the intersection of the mortar and the aggregate. Two major failure cracks can be observed in the mortar, indicating that the crack mainly occurs. The damage diagram of the interface is slightly amplified in Figure 18, where it suffered damage, and some interfaces collapsed. However, because the interface is relatively small, thin, and isolated, it cannot form a unified damage surface. Therefore, from an overall point of view, the damage mainly occurs in the mortar. However, in the initial damage stage, crack initiation starts at the interface, and when the damage accumulates to a certain extent, due to the interaction of stress between the interface, aggregate, mortar, and holes, the cracks begin to develop and penetrate. In addition to the mortar, some aggregates have experienced damage. The partial damage enlargement shows that most cracks propagate around the

TABLE 1: Material parameters.

Material	Elastic modulus/ Pa	Poisson's ratio	Tensile strength/ Pa
Aggregate	5.8731×10^{10}	0.2407	$9.25e6$
Mortar	1.7458×10^{10}	0.1960	$2.78e6$
Interface	1.3967×10^{10}	0.2000	$1.56e6$
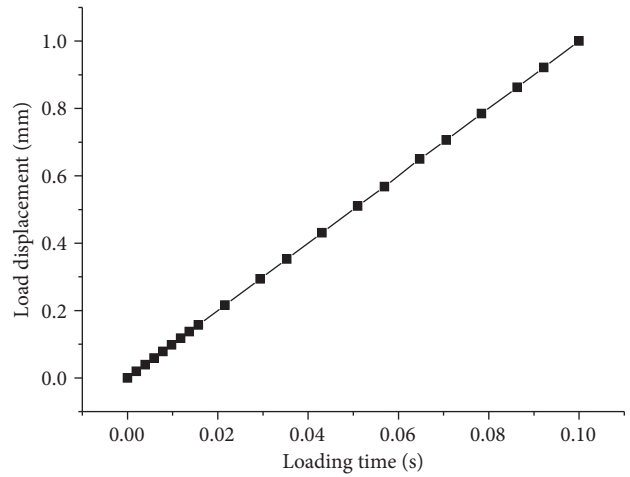
FIGURE 13: The load curve of dynamic pressure load.
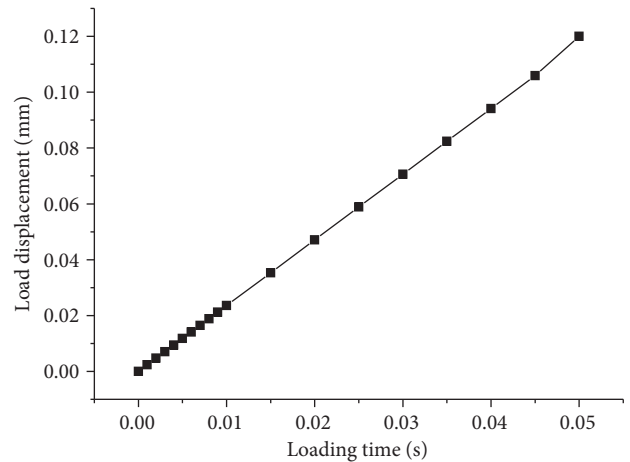
FIGURE 14: The load curve of dynamic tensile load.

aggregate, but some of them pass through the aggregate particles. Therefore, under the dynamic pressure load, the concrete as a composite material has a complicated failure process, and each material's stress interaction determines the cracks' development.

5.4. Tensile Load. This study applies the dynamic tensile load to the model top while its bottom surface is restrained. The analysis results are shown in Figures 19 and 20. It can be seen that when a concrete specimen is subjected to a dynamic tensile load, its failure mode is completely different from that of a dynamic compression load. For instance, it can be observed that at the beginning of the loading, the specimen's
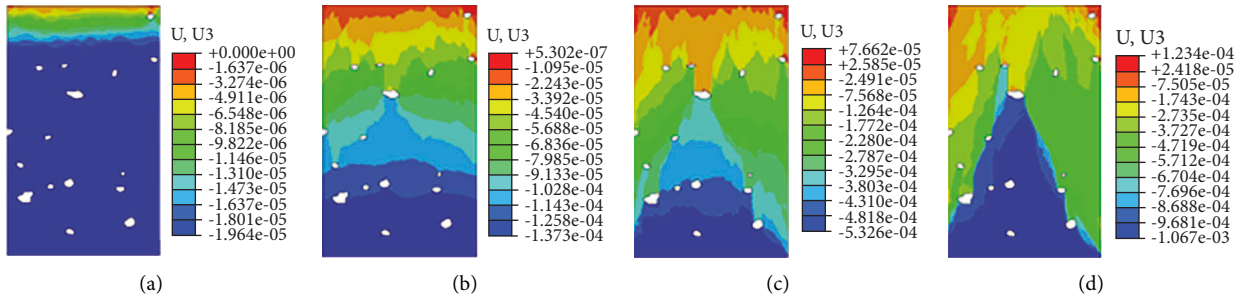
Figure 15: Vertical displacement graphs under different loading displacement. (a) $s = 0.02$ mm. (b) $s = 0.137$ mm. (c) $s = 0.533$ mm. (d) $s = 1$ mm.
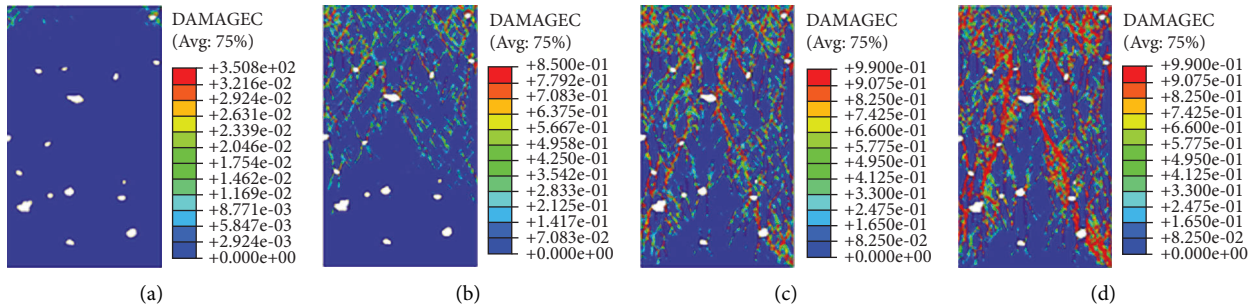
Figure 16: Damage failure graphs under different loading displacement. (a) $s = 0.02$ mm. (b) $s = 0.137$ mm. (c) $s = 0.533$ mm. (d) $s = 1$ mm.
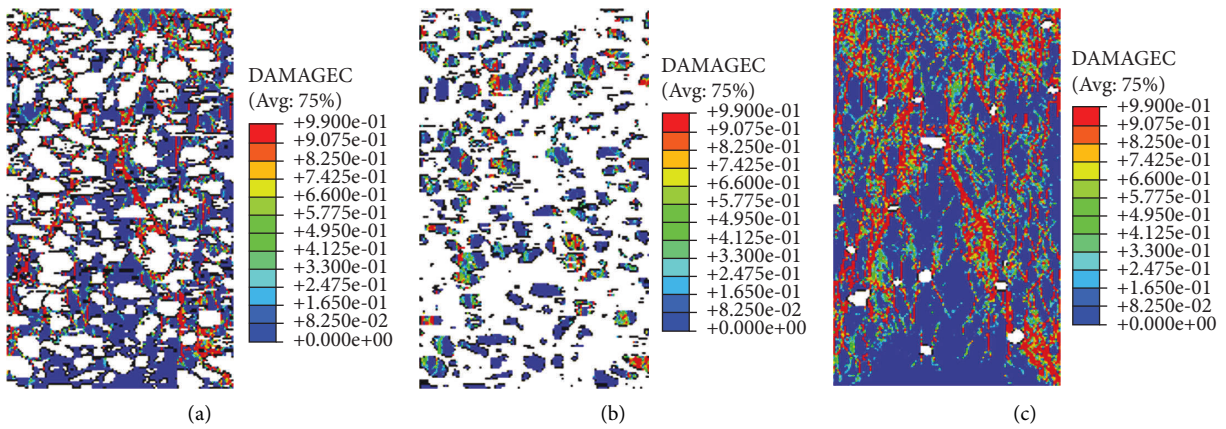
Figure 17: Damage graphs of different materials when the loading displacement is 1 mm. (a) Mortar. (b) Aggregate. (c) Concrete.
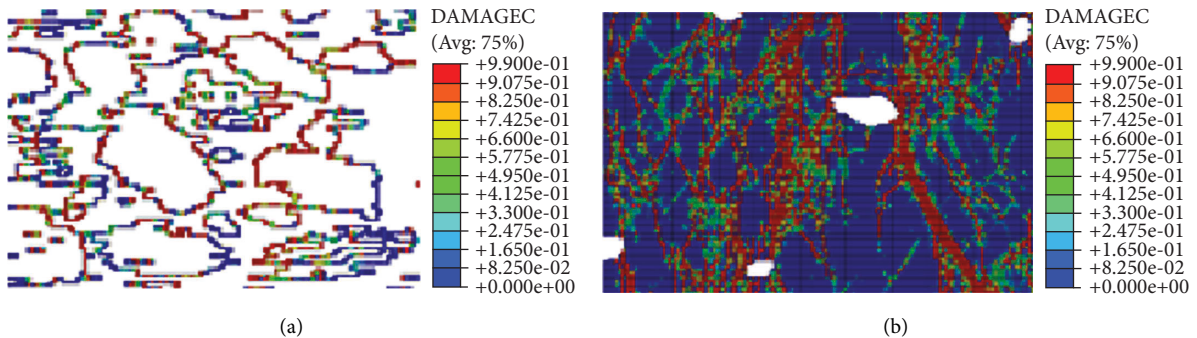
Figure 18: Local failure graph of material. (a) Interface. (b) Concrete.
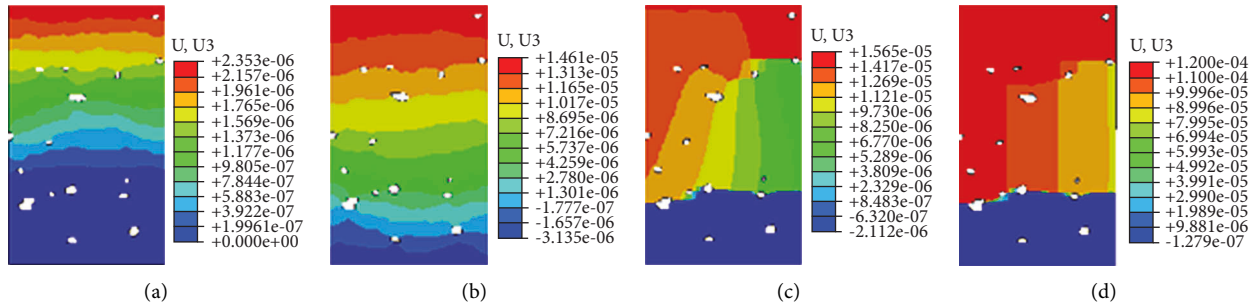
FIGURE 19: Vertical displacement graphs under different loading displacement. (a) $s = 0.002$ mm. (b) $s = 0.015$ mm. (c) $s = 0.016$ mm. (d) $s = 0.12$ mm.
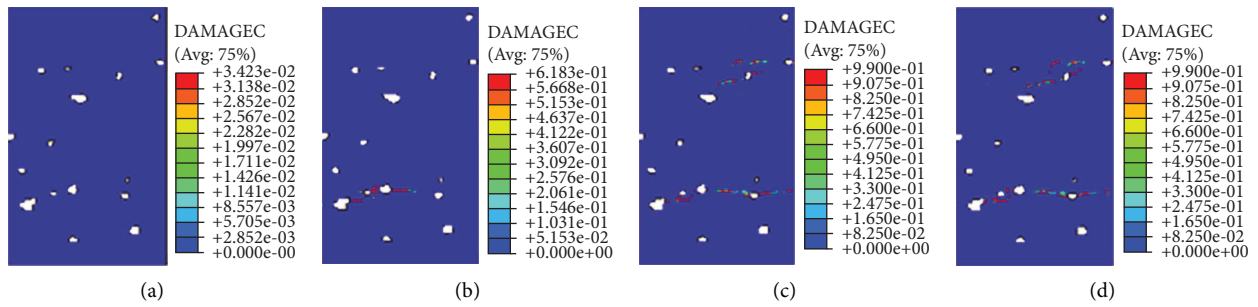
FIGURE 20: Damage failure graphs under different loading displacement. (a) $s = 0.002$ mm. (b) $s = 0.015$ mm. (c) $s = 0.016$ mm. (d) $s = 0.12$ mm.
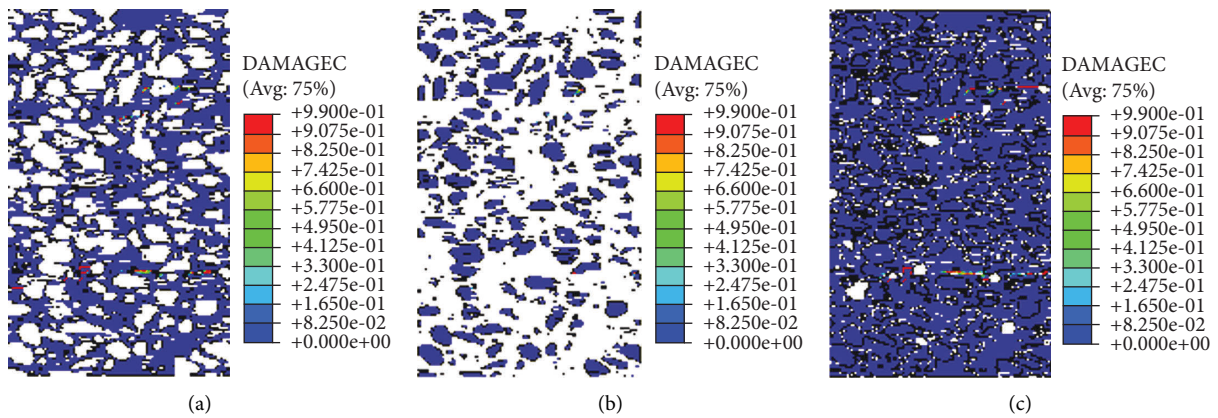
FIGURE 21: Damage graphs of different materials when the loading displacement is 0.12 mm. (a) Mortar. (b) Aggregate. (c) Concrete.

top displacement changed the most, and the damage did not occur. As the load increases, the change in displacement fluctuates, and the damage slowly develops. The vertical displacement begins to change unevenly, and the damage begins to occur slowly. Initially appearing around the hole, continuing to load, the damage begins to develop and gradually forms a damaged area throughout the specimen and perpendicular to the direction of loading. At the same time, there is intermittent damage in other parts of the test piece. When the loading reaches a certain value, the displacement has a significant mutation, indicating the occurrence of a complete collapse. From Figure 20, the degree of the damaged area throughout the specimen is more serious, and the damage accumulation eventually leads to the

destruction of the specimen, while one fracture surface runs through the specimen.

Further analysis of the mechanical changes of various materials during the stress process. As shown in Figure 21, the damage mainly occurs in the mortar, and there are many cracks under the dynamic pressure load, but there is only one main crack under the dynamic tensile load where the aggregate has slight damage. The failure surface from the overall damage figure is relatively straight and passes through part of the aggregate and most of the mortar. The interface has also suffered damage, mainly concentrated at the location of the failure surface, as shown in Figure 22. In the partially enlarged view of the overall damage, it can be clearly seen that the crack passes through small aggregate,

(a)   (b)
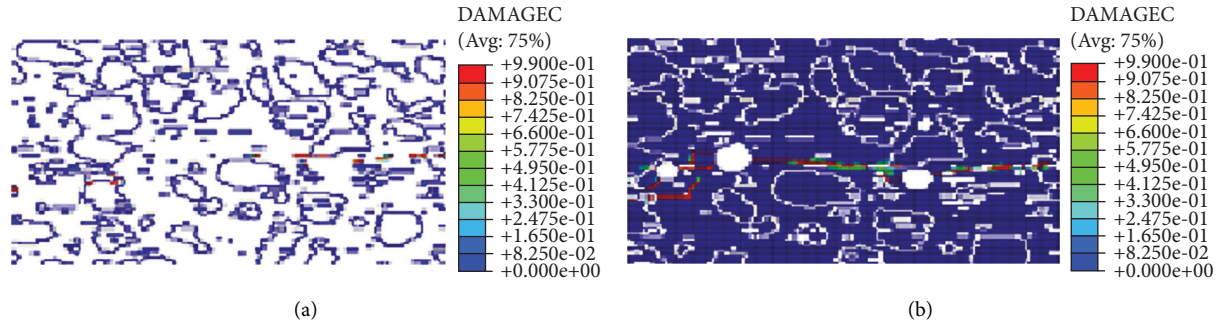
FIGURE 22: Local failure enlarged graph of material. (a) Interface. (b) Concrete.

mortar, and their interface, stops at the hole, and forms on its other side.

6. Model Verification

6.1. Dynamic Pressure Test Results. The CT scanned sections under dynamic compressive load show that the concrete specimens' damage occurs abruptly. As a result, unlike damage characteristics under static pressure, it is difficult to capture the microcrack initiation process, propagation, and final development using CT. Figure 23 and 24 show the final failure modes. It can be seen that under dynamic pressure, the damaged area is large, the damage is relatively complete, the aggregate is destroyed, and the damage is "double cone" extrusion damage.

6.2. Dynamic Tensile Test Results. The CT scanning section of the concrete specimen (Figure 25) shows that the concrete specimen's damage specimen occurs suddenly under dynamic tensile load. Before the damage, each loading stage's CT image remained unchanged. After the damage, a horizontal main crack was formed in the weakest section of the whole specimen, and the crack passed through part of the aggregate. As shown in Figure 26, the fracture surface is relatively flat, the aggregate is divided into two parts, the two specimens after the failure are completed, and the concrete surface is intact.

The numerical calculation of the CT reconstruction model shows that under the dynamic load, the model's simulation results and the experimental ones from the CT test have a high similarity. The crack is mainly developed along the intersection of the mortar with the aggregate. Additionally, some aggregates are damaged, and the hole has a certain influence on the development path of the crack. There are many cracks under dynamic pressure load with a high failure degree, a large failure area, and a double cone failure. On the other hand, there is one crack only under the dynamic tensile load, the fracture surface is relatively flat, and the failure mode is the fracture surface perpendicular to the loading direction. Compared with the CT test, in which the development of cracks before failure cannot be observed due to the limitations of test conditions, the numerical tests can solve this problem by their calculation characteristics. It can be observed that the initiation and development path of

FIGURE 23: CT scan sectional drawings.

FIGURE 24: The failure of specimens under dynamic pressure.
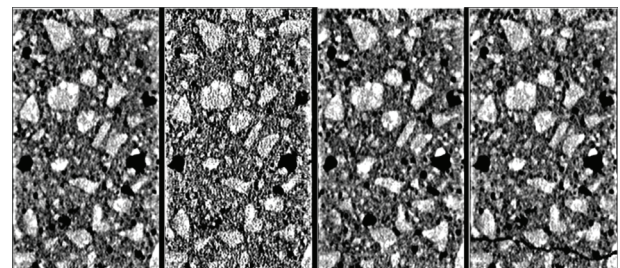
FIGURE 25: CT scan sectional drawings.

internal cracks in the concrete specimens occurs under the action of force in real-time.

Numerical experiments and CT physics tests are complementary. By establishing a numerical reconstruction model of mesoconcrete based on CT images, the two are well combined to provide effective help for further study of the mesomechanical mechanism of concrete.

FIGURE 26: The failure of specimens under dynamic tensile.

7. Conclusion

As the basis of numerical experiments, numerical models have a crucial influence on the simulation test results. Therefore, choosing a suitable numerical model is critical for obtaining accurate results.

This paper develops a reconstruction model based on CT images to perform the mechanical analysis. The results of CT experiments are compared and verified, and the main conclusions are as follows:

(1) Both the random aggregate model and the random aggregate interface model can simulate the force characteristics of the mesoconcrete. When simulating the bond between the aggregate and the mortar in the concrete, the interface elements in the random aggregate model are relatively thick, and the contact parameters in the random aggregate contact surface model are not easily determined. Besides, both models do not consider aggregate shape and hole influence.

(2) The 3D reconstruction models based on the joint-element method and the MIMICS CT image are closer to the actual concrete behavior than the random aggregate model. This observation is mainly attributed to the low precision and the lack of consideration of the unit compression. As a result, a complete primary mechanical analysis cannot be performed at present.

(3) The CT image reconstruction model based on CT number considers the aggregate gradation influence, including the shape and hole, to provide the advantages of the random aggregate model, thus achieving realistic concrete behavior compared to other models.

(4) The damage to concrete is affected by the hole, and the location of the hole is prone to cracking. Moreover, the initiation of cracks often occurs at the interface and eventually extends through the mortar. The strength of its weak specimen parts mainly determines the strength of concrete [29].

Data Availability

All data, models, and code generated or used during the study are included in the article.

Conflicts of Interest

The authors declare that they have no conflicts of interest.

Acknowledgments

References

[1] Z. W. Qu, Z. H. Liu, R. Z. Si, and Y. Zhang, "Effect of various fly ash and ground granulated blast furnace slag content on concrete properties: experiments and modelling," *Materials*, vol. 15, no. 9, p. 3016, 2022.

[2] S. Afroz, Y. D. Zhang, Q. D. Nguyen, T. Kim, and A. Castel, "Effect of limestone in General Purpose cement on autogenous shrinkage of high strength GGBFS concrete and pastes," *Construction and Building Materials*, vol. 327, Article ID 126949, 2022.

[3] Q. D. Nguyen, S. Afroz, Y. D. Zhang, T. Kim, W. Li, and A Castel, "Autogenous and total shrinkage of limestone calcined clay cement (LC3) concretes," *Construction and Building Materials*, vol. 314, no. 12, Article ID 125720, 2022.

[4] I. Carol, C. M. López, and O. Roa, "Micromechanical analysis of quasi-brittle materials using fracture-based interface elements," *International Journal for Numerical Methods in Engineering*, vol. 52, no. 12, pp. 193–215, 2001.

[5] F. Dupray, Y. Malecot, L. Daudeville, and E. Buzaud, "A mesoscopic model for the behaviour of concrete under high confinement," *International Journal for Numerical and Analytical Methods in Geomechanics*, vol. 33, no. 11, pp. 1407–1423, 2009.

[6] S. M. Kim and R. K. A. Alrub, "Meso-scale computational modeling of the plastic-damage response of cementitious composites," *Cement and Concrete Research*, vol. 41, no. 3, pp. 339–358, 2011.

[7] S. Shahbeyk, M. Hosseini, and M. Yaghoobi, "Mesoscale finite element prediction of concrete failure," *Computational Materials Science*, vol. 50, no. 7, pp. 1973–1990, 2011.

[8] M. Du, L. Jin, and D. Li, "Mesoscopic simulation study of the influence of aggregate size on mechanical properties and specimen size effect of concrete subjected to splitting tensile loading," *Engineering Mechanics*, vol. 34, no. 9, pp. 54–62, 2017.

[9] W. Wang, Z. Yi, B. Tian, Y. Zhang, and S. Lu, "Nonlinear finite element analysis of PBL shear connectors in hybrid structures," *Structures*, vol. 33, no. 10, pp. 4642–4654, 2021.

[10] G. D. Schutter and L. Taerwe, "Random particle model for concrete based on delaunay triangulation," *Materials and Structures*, vol. 26, no. 2, pp. 67–73, 1993.

[11] E. Schlangen and E. J. Garboczi, "Fracture simulations of concrete using lattice models: computational aspects," *Engineering Fracture Mechanics*, vol. 57, no. 2–3, pp. 319–332, 1997.

[12] J. P. B. Leite, V. Slowik, and H. Mihashi, "Computer simulation of fracture processes of concrete using mesolevel models of lattice structures," *Cement and Concrete Research*, vol. 34, no. 6, pp. 1025–1033, 2004.

[13] C. A. Tang and W. C. Zhu, *Numerical Simulation Tests of Concrete Damnification and Fracture*, Science Press, Beijing, China, 2003.

[14] A. R. Mohamed and W. Hansen, "Micormechanical modeling of crack-aggregate interaction in concrete materials," *Cement and Concrete Composites*, vol. 21, no. 5/6, pp. 349–359, 1999.

[15] W. F. Bai, J. Y. Chen, and S. L. Fan, "Statistical damage constitutive model for concrete material under uniaxial compression," *Journal of Harbin Institute of Technology*, vol. 17, no. 3, pp. 338–344, 2010.

[16] H. F. Ma, H. Q. Chen, and C. L Yang, "Numerical tests of meso-scale damage mechanism for full graded concrete under complicated dynamic loads," *China Civil Engineering Journal*, vol. 45, no. 7, pp. 175–182, 2012.

[17] X. L. Du and L. Jin, "Meso-element equivalent model for macro-scopic mechanical properties analysis of concrete materials," *Chinese Journal of Computational Mechanics*, vol. 29, no. 5, pp. 654–661, 2012.

[18] K. Gopalakrishnan, H. Ceylan, F. Inanc, and M. Heitzman, "Characterization of asphalt materials using X-ray high-resolution computed tomography imaging techniques," in *Proceedings of the 2006 T&DI Airfield and Highway Pavement Specialty Conference*, pp. 437–454, Atlanta, Georgia, May 2006.

[19] Q. Dai, "Two- and three-dimensional micromechanical viscoelastic finite element modeling of stone-based materials with X-ray computed tomography images," *Construction and Building Materials*, vol. 25, no. 2, pp. 1102–1114, 2011.

[20] I. Onifade, D. Jelagin, A. Guarin, B. Birgisson, and N. Kringos, *Asphalt Internal Structure Characterization with X-Ray Computed Tomography and Digital Image Processing*, pp. 139–158, Springer, Netherlands, 2013.

[21] Ł. Skarżyński, M. Nitka, and J. Tejchman, "Modelling of concrete fracture at aggregate level using FEM and DEM based on X-ray μCT images of internal structure," *Engineering Fracture Mechanics*, vol. 147, pp. 13–35, 2015.

[22] W. Trawiński, J. Tejchman, and J. Bobiński, "A three-dimensional meso-scale modelling of concrete fracture, based on cohesive elements and X-ray μCT images," *Engineering Fracture Mechanics*, vol. 189, 2018.

[23] W. Y. Ren, Z. Yang, R. Sharma, C. Zhang, and P. J. Withers, "Two-dimensional X-ray CT image based meso-scale fracture modelling of concrete," *Engineering Fracture Mechanics*, vol. 133, pp. 24–39, 2015.

[24] W. Qin and C. B. Du, "Meso-level model of three-dimensional concrete based on the CT slices," *Engineering Mechanics*, vol. 29, no. 7, pp. 186–193, 2012.

[25] N. Metroplis and S. U. Lam, "Monte Carlo method," *Amerrican: J. Amer.states*, vol. 44, no. 247, pp. 335–341, 1949.

[26] Y. N. Zheng, *Three-Dimensional Numerical Simulation on Mesolevel and CT Experiment Verification of Failure Process in Concrete*, Xi'an University of Technology, Xi'an, China, 2005.

[27] X. Y. Liang, F. N. Dang, and W. Tian, "Study on numerical model of concrete based on 3D meso-mechanics," *Chinese Journal of Applied Mechanics*, vol. 28, no. 2, pp. 129–134, 2011.

[28] G. Y. Lei, J. C. Han, and Y. Zhang, "Based on the CT image rebuilding the micromechanics hierarchical model of concrete," *Journal of Hydroelectric Engineering*, vol. 35, no. 3, pp. 105–112, 2016.

[29] Y. D. Zhang, S. Afroz, Q. D. Nguyen et al., "Analytical model predicting the concrete tensile stress development in the restrained shrinkage ring test," *Construction and Building Materials*, vol. 307, Article ID 124930, 2021.

Research Article

Mechanical and Thermal Properties of Shale Ceramsite Concrete: Experimental Study on the Influence Law due to Microencapsulated Phase-Change Material Content and Phase-Change Cycle Numbers

Weihua Ding [ID],[1,2,3] **Lin Zhu** [ID],[1,2,3] **Hu Li,**[1,2,3] **Bin Hou,**[1,2,3] **and Fan Yang**[1,2,3]

[1]*School of Civil Engineering and Architecture, Xi'an University of Technology, Xi'an 710048, China*
[2]*State Key Laboratory of Eco-hydraulics, Northwest Arid Region, Xi'an University of Technology, Xi'an 710048, China*
[3]*Shaanxi Key Laboratory of Loess Mechanics and Engineering, Xi'an University of Technology, Xi'an 710048, China*

Correspondence should be addressed to Lin Zhu; zhulin_xaut@163.com

The addition of microencapsulated phase-change materials (MPCM) to concrete will inevitably cause changes in the mechanical and thermal properties of concrete, and this is vitally important for the safety and energy saving of concrete building components. In this research, shale ceramsite and shale ceramics sand were used as the main raw materials to produce lightweight aggregate concrete (LWAC) mixed with MPCM. In order to investigate the effect of MPCM content and phase-change cycle numbers on the mechanical and thermal properties of MPCM-LWAC, two groups of MPCM-LWAC specimens were prepared. One group consists of specimens containing 2.5%, 5.0%, 7.5%, and 10% MPCM, respectively, and they are used to reveal the change law of tensile strength, compressive strength, enthalpy, and specific heat capacity of LWAC integrated into MPCM. The other group includes specimens with the same MPCM content, but the specimens are subjected to different phase-change cycle numbers of 50, 100, 150, and 200 at the environment temperature of −10–60°C to study the thermal properties of MPCM-LWAC. Findings from the experimental results include the following: (1) The tensile and compressive strengths of MPCM-LWAC concrete are negatively correlated with the MPCM content, while the enthalpy and specific heat capacity are positively correlated with the MPCM content. When the MPCM content reaches 10%, the compressive and tensile strengths of MPCM-LWAC decreased, respectively, by 45.49% and 52.63% than the LWAC without MPCM. (2) Under heating and curing condition, the corresponding maximum specific heat capacity of LWAC with 10% MPCM is 328.35% and 249.50% higher than the LWAC without MPCM, respectively, and the average specific heat capacities increase 71.21% and 44.94%, respectively. (3) The melting enthalpy of MPCM-LWAC is slightly larger than the curing enthalpy, and the difference is more noticeable with the increase of MPCM content. In addition, when the number of phase-change cycle is below 200, the compressive strength and splitting tensile strength of MPCM-LWAC decrease by less than 5%, and the specific heat capacity decreases by less than 1.33%. Hence, it concludes that shale ceramsite concrete with MPCM has promising application prospects.

1. Introduction

Reduction in energy consumption has major significance for the mitigation of global warming. Three sectors of transportation, industry, and construction together account for 97.88% of the global energy consumption. Particularly, the construction sector alone accounts for approximately 30% of the total energy consumption. Energy used for refrigeration and heating to maintain indoor comfort temperature is one of the major parts of building energy consumption [1, 2].

The use of fossil fuels to maintain indoor comfort temperature increases the emission of harmful gases. Hence, renewable energy is a prime option to boost the energy efficiency of buildings, such as solar energy, wind energy,

and geothermal energy. However, the intermittent characteristics of these renewable energies limit their applications, except for phase-change materials (PCM). PCM has been the present hotspot in the field of building energy saving materials due to its unique advantages, especially large heat storage per unit volume, absorbing and releasing heat under constant temperature [3–5]. More importantly, PCM maintains good thermal stability when they are added to building materials.

PCM undergo phase changes according to the change of ambient temperature, which is accompanied by the absorption and release of heat. When the ambient temperature is greater than the minimum phase-change temperature of PCM, it transforms from solid to liquid and absorbs heat from the environment, causing the ambient temperature to decrease. When the ambient temperature is less than the maximum phase-change temperature, it transforms from liquid to solid and releases heat into environment, raising an increase of the ambient temperature. This endothermic and exothermic process under different ambient temperatures helps adjust the amplitude of the ambient temperature fluctuation. Therefore, embedding PCM into building materials can significantly increase the thermal inertia of building materials and prevent excessive abrupt changes in indoor temperature.

Scholars around the world have carried out extensive research on the application of PCM in the field of building materials, such as adding PCM into concrete, mortar, gypsum, and wood. [6–9]. Among them, PCM concrete can not only be used as a structural material in different building structures but also be utilized as a functional material to maintain indoor comfort temperature, which shows a good application prospect in the field of building energy conservation [10, 11].

At present, scholars have carried out substantive researches in many aspects, such as the development of PCM, addition methods of PCM, and mechanical and thermal properties of energy storage concrete [12–14]. According to these research findings, PCM commonly used in construction field are organic and inorganic solid-liquid PCM with phase transition temperature between 10 and 30°C, such as paraffin wax and hydrated salt. However, for inorganic PCM, its application is limited in the construction field due to the two serious shortcomings of undercooling and phase separation.

For solid-liquid PCM, some serious problems were encountered in the process of repeated solid-liquid conversion, such as leakage, interaction between PCM and concrete matrix, and reduced heat transfer efficiency. In order to solve these problems, shaped phase-change aggregate [15], macro-PCM [7], and micro-PCM [13] came into being. MPCM is a new type of composite materials, composed of solid-liquid PCM particles wrapped by stable polymer film. MPCM not only provides a very high heat transfer area but also avoids leakage of PCM [16, 17]. Moreover, adding MPCM to concrete can improve the energy storage capacity of concrete material, but exists a negative effect on the mechanical properties. Pilehvar et al.

[18] investigated the effects of curing time, phase state, and PCM content on the compressive strength of silicate concrete and geopolymer concrete through experiments. They found that the compressive strength of PCM geopolymer concrete was larger than that of PCM silicate concrete under the same conditions. Hunger et al. [19] measured the thermal conductivity and specific heat capacity of PCMconcrete by using the method of transient hot wire and homemade improvised device for studying the effect of MPCM content on the thermal properties. Their finding is that the increase of MPCM content will decrease the thermal conductivity and increase the specific heat capacity of concrete, thus beneficial to improve the thermal performance of concrete. However, scanning electron microscope (SEM) images exposes the problem that MPCM may be destroyed in the mixing process, which will cause the paraffin to penetrate into the concrete matrix. Ouni et al. [20] added different amounts of MPCM to Portland cement concrete and found that the addition of MPCM to concrete improved the heat storage capacity of concrete.

Good mechanical and thermal stability are the most fundamental premise for the development and utilization of PCM-concrete. The above literatures indicates that the energy storage concrete in raw material selection and production technology is different. The energy storage capacity of present concrete containing PCM lacks reasonable comparisons. However, the mechanical and thermal properties of different types of PCM-concrete are quite different. Therefore, it is necessary to further study the mechanical and thermal properties of energy storage concrete with application prospect.

In this research, MPCM-LWAC partition wall is regarded as the research background. Shale ceramsite, shale ceramics sand, MPCM, and Portland cement as the main raw materials are used to prepare MPCM-LWAC specimens. A series of experiments on mechanical and thermal properties of MPCM-LWAC were carried out to study the effects of MPCM content and phase-change cycle numbers on the tensile strength, compressive strength, enthalpy, and specific heat capacity of MPCM-LWAC. Under the heating and curing condition, a comparative study was conducted to reveal the change law of mechanical and thermal properties of MPCM-LWAC with MPCM content and phase-change cycle numbers. The above research lays a foundation for the development and application of MPCM-LWAC partition wall.

2. Materials and Methods

2.1. Basic Properties of Raw Materials

2.1.1. Lightweight Aggregate. In this research, shale ceramsite with diameters of 8–20 mm and 5–8 mm was selected to be mixed as lightweight coarse aggregate (LWCA) by a mass ratio of 4 : 6, and shale ceramic sand with diameters of 3–5 mm and 1–3 mm was chosen to be mixed with a mass ratio of 4 : 6 as lightweight fine aggregate (LWFA). Basic properties of lightweight aggregate are shown in Table 1.

TABLE 1: The properties of lightweight aggregate.

Shale ceramsite	Size (mm)	Packing density (kg/m3)	Water absorption of 1 h (%)	Cylinder pressure strength (MPa)
LWCA	8~20	641	4.50	4.37
	5~8	795	3.63	6.43
LWFA	3~5	857	3.27	7.37
	1~3	930	—	—

2.1.2. Microencapsulated Phase-Change Materials (MPCM). MPCM with polymethyl methacrylate as the shell material and n-octadecane as the core material is produced by Hebei Ruo-sen Technology Co., Ltd. Experiment was carried out to investigate the micromorphology of MPCM by using scanning electron microscopy (SEM). From the SEM image of MPCM (Figure 1), it can be found that MPCM with a diameter of 1–3 um is spherical. In addition, the thermal properties of MPCM were investigated by conducting differential scanning calorimeter (DSC) test. The DSC curve of MPCM is shown in Figure 2, which presents clearly the change curve of heat flux with temperature during the melting and curing process. The phase transition temperature range of MPCM is from 24.9°C to 28.9°C in the melting process. On the contrary, its phase transition temperature range is from 20°C to 25.1°C during the curing process.

2.1.3. Cement. Cement with the grade of P.O 42.5 is a commercial ordinary Portland cement. According to General Portland Cement (GB175-2007), the physical properties and quality of cement were detected, as shown in Tables 2 and 3. The compressive strength of the cement for 3 d and 28 d is 27.2 MPa and 54.9 MPa, and its flexural strength is 5.7 MPa and 8.8 MPa, respectively.

2.1.4. Water. Tap water was used as the test water. It needs to emphasize that chemical admixtures such as fly ash, air entraining agent, and water reducing agent were not used in the preparation of MPCM-LWAC to avoid chemical reaction between such admixtures and MPCM.

2.2. Mix Proportion Design. The strength of MPCM-LWAC specimens prepared in this study is less than 10 MPa due to lightweight partition wall as the research background. According to the Technical Specification for Lightweight Aggregate Concrete (JGJ51-2002), the sand ratio and water-cement ratio are determined to be 0.65 and 0.6, respectively. Meanwhile, the MPCM content meeting the strength requirements should not be more than 10% [21]. The mixture ratio of MPCM-LWAC is selected as given in Table 4 to satisfy these conditions. MPCM-LWAC-0.0% was designed as a control experiment. MPCM-LWAC specimens were prepared by replacing the LWFA with the same amount of MPCM. The cubic concrete specimen has the size of $100 \times 100 \times 100$ mm^3.

3. Experimental Procedures

3.1. Mechanical Test. In order to ensure that MPCM-LWAC can meet the strength requirements of lightweight partition wall, it is necessary to determine the tensile and compressive strengths of MPCM-LWAC and study its influencing factors. The tensile and compressive strengths of MPCM-LWAC with MPCM content of 0%, 2.5%, 5.0%, 7.5%, and 10.0% and phase-change cycle numbers of 0, 50, 100, 150, and 200 were determined by using a microcomputer-controlled electro-hydraulic servo pressure testing machine.

3.2. Thermal Tests

3.2.1. Testing Program. Differential scanning calorimeter (DSC) based on power compensation was used to test enthalpy and specific heat capacity of MPCM-LWAC with MPCM content of 0%, 2.5%, 5.0%, 7.5%, and 10.0% and the same items of MPCM-LWAC with phase-change cycle numbers of 0, 50, 100, 150, and 200, respectively. Figure 3 gives the process of making specimen and test instruments.

3.2.2. Calculation Principle of Enthalpy. DSC test is based on power compensation, and it can reflect the change of enthalpy of the sample by monitoring the power difference between the sample and the reference (sapphire) [22]. DSC curve with the abscissa of time or temperature and the ordinate of heat flow can be obtained by DSC test. The main feature of power compensation DSC test is that the sample and reference have independent heaters and heat sensors. The temperature difference between the sample and the reference is equal to 0°C by adjusting the heating power of the sample, so that the heat flow rate can be directly calculated from the compensated power using

$$\Delta W = \frac{dQ_s}{dt} - \frac{dQ_r}{dt}$$
$$= \frac{dH}{dt},$$

(1)

where ΔW is the compensated power; dQ_s/dt is the heat supplied to the sample per unit time; dQ_r/dt is the heat supply per unit time of the reference object, and dH/dt is the rate of change in enthalpy.

The heat absorbed or released per unit mass of PCM in the process of phase transformation is known as the phase-change enthalpy, which is equal to the change in enthalpy of
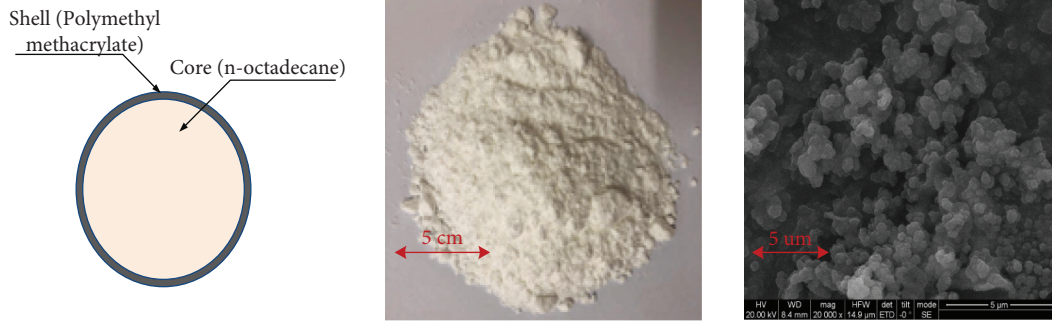
FIGURE 1: Morphology picture of MPCM.
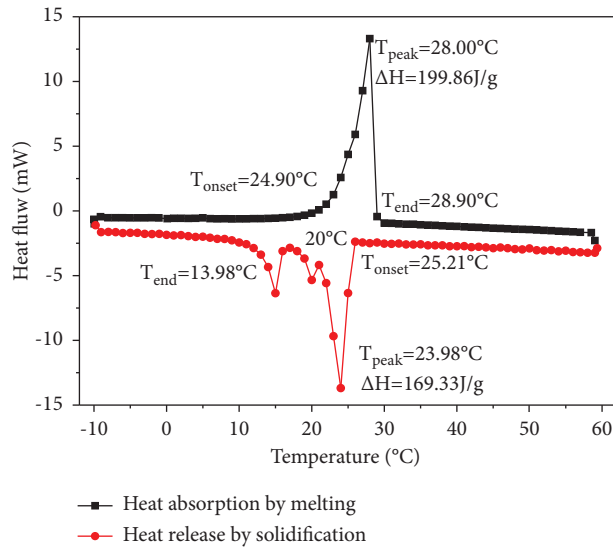
FIGURE 2: Heat flux curve with temperature during its melting and curing process.

TABLE 2: Physical properties of cement.

Testing items	Specific area (m^2/kg)	Standard consistency	Setting time (min)		Soundness	Compressive strength (MPa)		Flexural strength (MPa)	
			Initial set	Final set		3 d	28 d	3 d	28 d
P·O42.5	327	27.2	162	213	Qualified	27.2	54.9	5.7	8.8

TABLE 3: Quality testing of P·O42.5 cement.

Testing item	Loss on ignition (%)	SO_3 (%)	MgO (%)	Chlorine ion content (%)	Alkali content (%)
P·O42.5	0.34	2.81	2.30	0.023	0.52

TABLE 4: Mix proportion of MPCM-LWAC specimens by using the method of equal mass substitution.

Specimens	Water (kg/m^3)	Cement (kg/m^3)	LWAC (kg/m^3)	LWFA (kg/m^3)	MPCM (kg/m^3)	Water-cement ratio	Sand ratio
MPCM-LWAC-0.0%	187.0	311.7	455.5	845.800	0.000		
MPCM-LWAC-2.5%	187.0	311.7	455.5	824.655	21.145		
MPCM-LWAC-5.0%	187.0	311.7	455.5	803.510	42.290	0.60	0.65
MPCM-LWAC-7.5%	187.0	311.7	455.5	782.370	63.435		
MPCM-LWAC-10%	187.0	311.7	455.5	761.220	84.580		
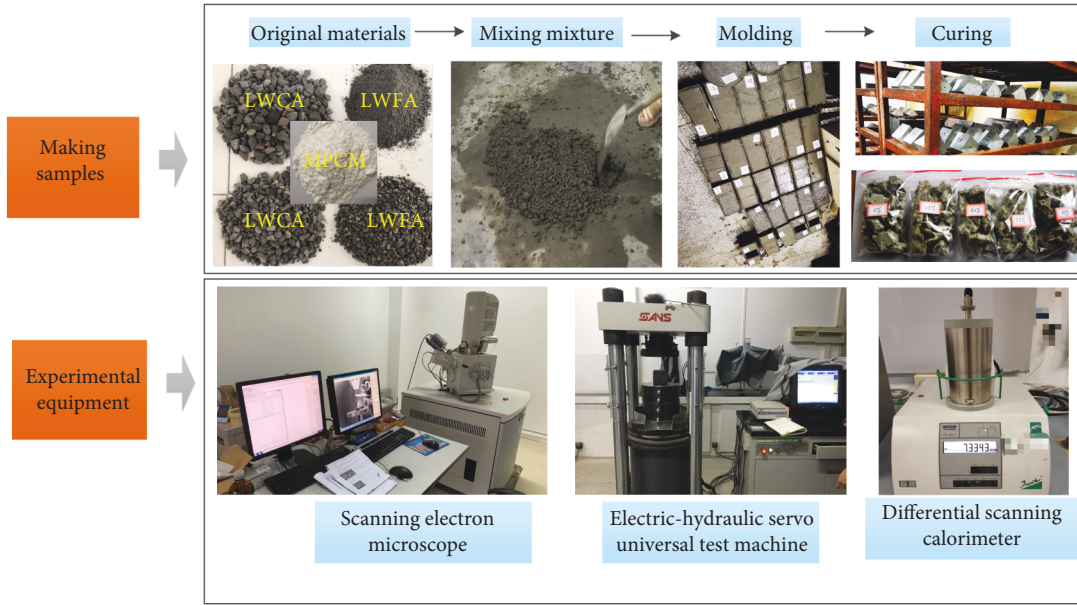
FIGURE 3: Specimen making and experimental equipment.

the system in the process of phase transformation in quantity. Therefore, the enthalpy of tested sample can be calculated according to equation (2).

$$\Delta H = \int_{t_1}^{t_2} \frac{dH}{dt} \, dt, \qquad (2)$$

where ΔH is the enthalpy of PCM, t_1 and t_2 are the start time and end time of DSC peak respectively, and dH/dt is the rate of change in enthalpy.

3.2.3. Calculation Principle of Specific Heat Capacity.

Specific heat capacity of tested sample was determined by using the comparative method (Figure 4). The DSC curves of empty crucible, sapphire, and the sample were tested from T1 to T2 under the same experimental conditions. The DSC curve of the empty crucible was taken as the baseline. According to the DSC curve position of sample and sapphire, the calculation formula of specific heat capacity of sample was deduced:

$$C_p = \overline{C}_p \cdot \frac{\overline{m}}{m} \cdot \frac{y}{\overline{y}}, \qquad (3)$$

where C_p and $\overline{C}_p$ are the specific heat capacity of sapphire and the sample to be determined, respectively, J/g•°C. m and $\overline{m}$ are the mass of sapphire and sample to be determined, respectively, g. y and $\overline{y}$ are the range differences between the sample to be determined and sapphire on the ordinate.

4. Analysis of Experimental Result

4.1. Mechanical Properties Analysis of MPCM-LWAC

4.1.1. Effect of MPCM Content on Tensile and Compressive Strengths of MPCM-LWAC. The tensile and compressive strengths of MPCM-LWAC with different MPCM content are shown in Figures 5 and 6. From Figures 5 and 6, it can be found that the tensile and compressive strengths of MPCM-
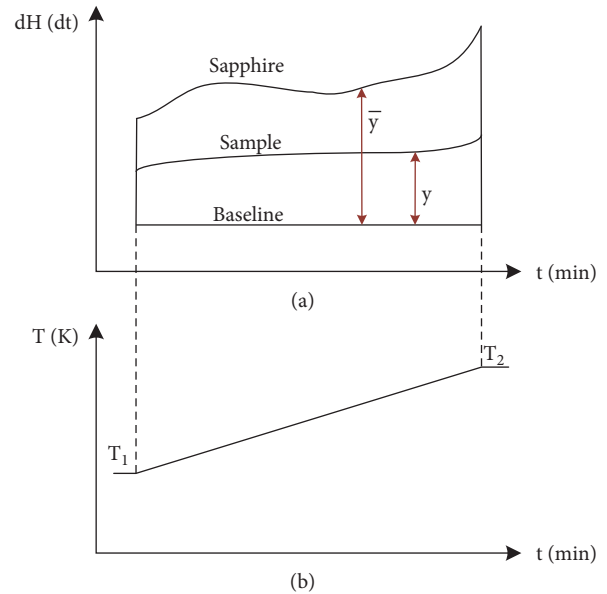
FIGURE 4: Calculation principle diagram of specific heat capacity based on the DSC curve.

LWAC decreased with the increase of MPCM content. Compared with MPCM-LWAC-0.0% specimen, the tensile strength of MPCM-LWAC-2.5%, MPCM-LWAC-5.0%, MPCM-LWAC-7.5%, and MPCM-LWAC-10.0% specimen decreased by 10.66%, 21.31%, 34.84%, and 45.49%, and their compressive strength decreased by 8.27%, 22.3%, 49.62%, and 52.63%, respectively. The functional relationship showing the influence of MPCM content on the tensile and compressive strengths conforms with

$$\sigma_c = -1.46\varepsilon_{MPCM} + 26.85, \qquad (4)$$

$$\sigma_t = -0.11\varepsilon_{MPCM} + 2.45, \qquad (5)$$
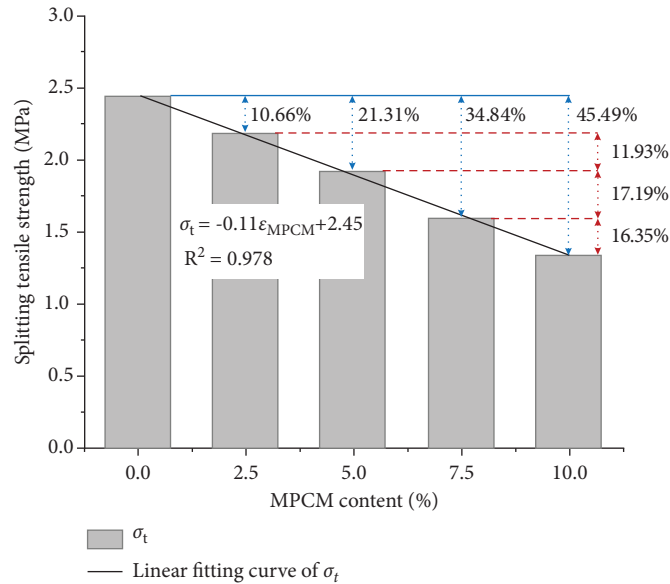
FIGURE 5: The relation curve between splitting tensile strength and MPCM content.
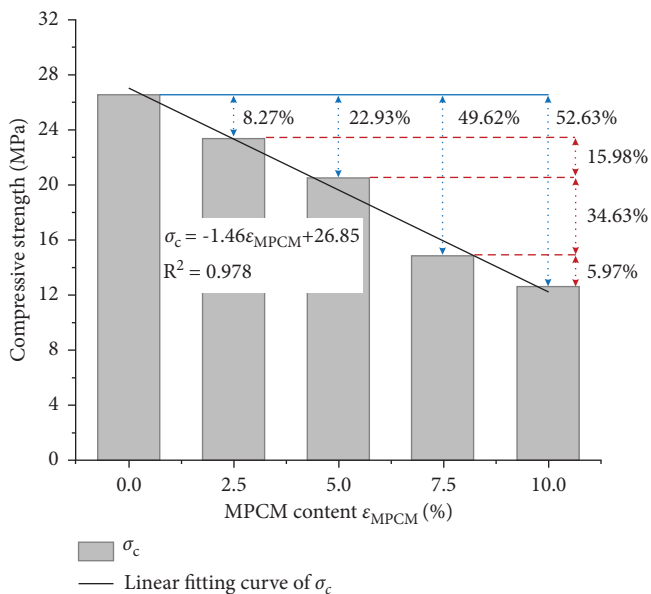
FIGURE 6: The relation curve between compressive strength and MPCM content.

where σ_c and σ_t are the compressive strength and tensile strength of MPCM-LWAC, respectively, MPa; ε_{MPCM} is mass fraction of MPCM content, %.

4.1.2. Effect of Phase-Change Cycle Numbers on Tensile and Compressive Strengths of MPCM-LWAC.
Figures 7(a) and 8(a) show the change law of compressive and tensile strength of MPCM-LWAC with the number of phase-change cycle. Figures 7(b) and 8(b) show the change amount of compressive and tensile strength of MPCM-LWAC specimen subjected to different phase-change cycle numbers.

According to Figures 7(a) and 7(b), the compressive strength of MPCM-LWAC-0.0% specimen undergoing phase-change cycle numbers of 50, 100, 150, and 200 varied by decreasing −0.38%, 0.77%, 0.38%, and 1.14%, respectively. The compressive strength of MPCM-LWAC-5.0% specimens decreased by −0.47%, −0.09%, 0.46%, and 1.93%, respectively. The compressive strength of MPCM-LWAC-10.0% specimens decreased by 0.58%, 1.75%, 2.92%, and 3.51%, respectively. When the MPCM content was 2.5% and the phase-change cycle numbers was 200, the compressive strength variation decreased the maximum value of 3.72%.

From Figures 8(a) and 8(b), after the specimen subjected to phase-change cycle numbers of 0, 50, 100, 150, and 200, the splitting tensile strength variation of MPCM-LWAC-0.0% specimen decreased by 0.81%, 0.41%, 0.81%, and 1.22%, respectively. The variations of the tensile strength of MPCM-LWAC-5.0% specimens decreased by 0.51%, 1.02%, 2.03%, and 3.04%, respectively. The compressive strength variations of the MPCM-LWAC-10.0% specimens decreased by 1.44%, 2.16%, 2.88%, and 4.32%, respectively. When the MPCM content was 7.5% and the phase-change cycle numbers were 200, the splitting tensile strength variation decreased the maximum value of 4.90%.

According to the above results, it can be concluded that the compressive strength and splitting tensile strength of MPCM-LWAC exhibit decreasing trend with the increase of phase-change cycle numbers. However, the decreasing amount for both strengths are not more than 5%, which is not enough to affect the normal use of the material.

4.2. Analysis of Thermal Properties of MPCM-LWAC

4.2.1. Effect of MPCM Content on Enthalpy of MPCM-LWAC.
Figures 9(a) and 9(b) are the DSC curves of MPCM-LWAC specimens with different MPCM contents.

(a)

(b)
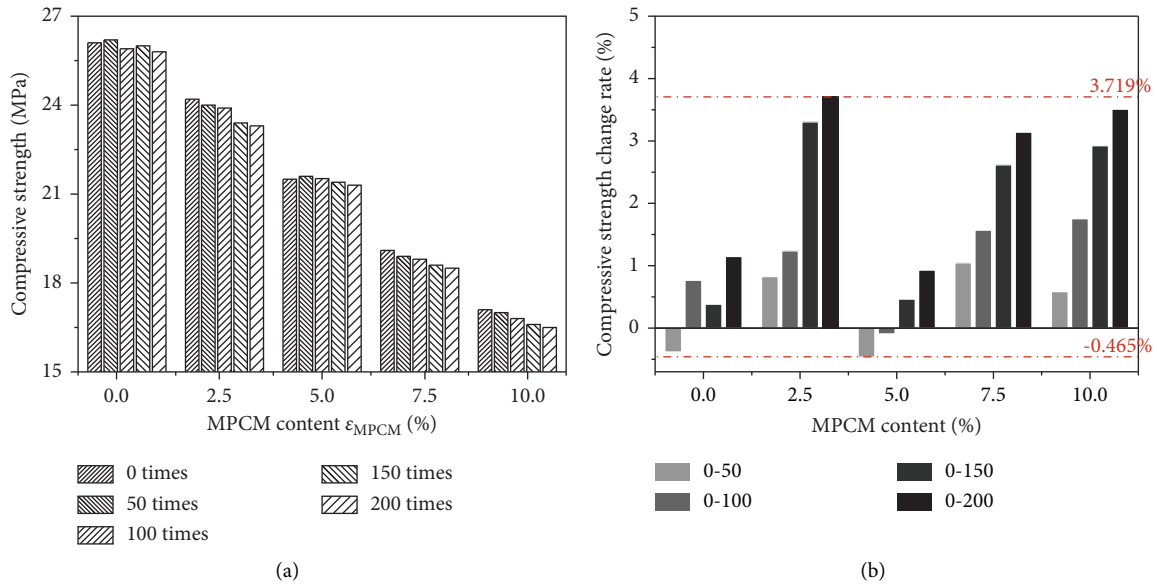
FIGURE 7: The relation curve between the numbers of phase-change cycle and compressive strength with the numbers of phase-change cycle. (a) The change law of compressive strength. (b) The change law of compressive strength variation.

(a)

(b)
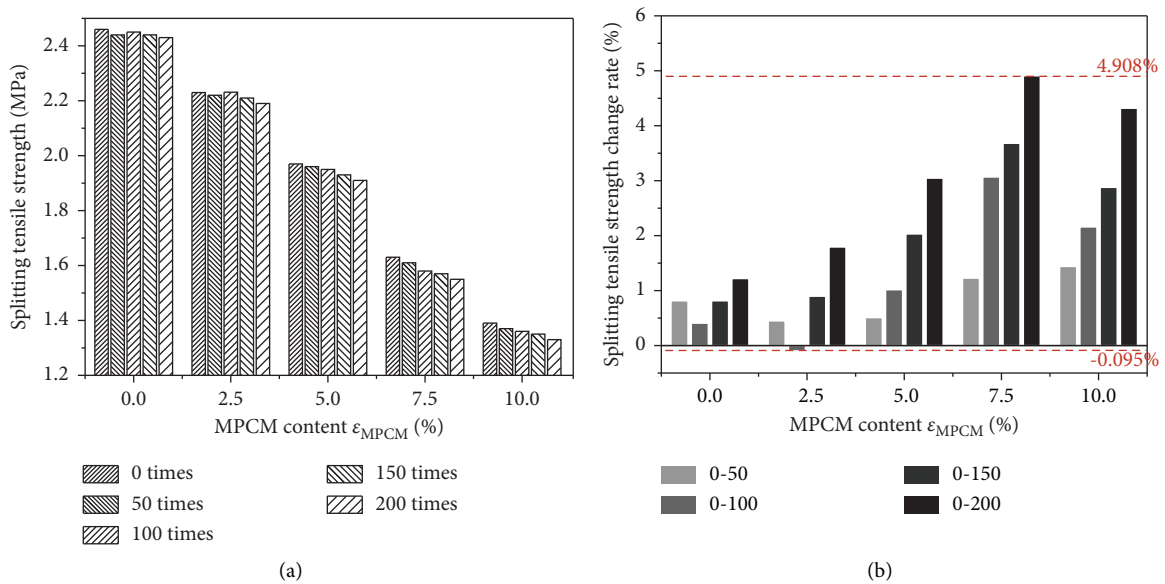
FIGURE 8: The relation curve between the numbers of phase-change cycle and splitting tensile strength with the numbers of phase-change cycle. (a) The change law of splitting tensile strength. (b) The change law of splitting tensile strength variation with the numbers of the phase-change cycle.

It can be seen from Figures 9(a) and 9(b) that the phase-change temperature range and calorimetric signal shape displayed on the DSC curve of MPCM-LWAC depend on the DSC curve of MPCM (Figure 2). In addition, there are two obvious differences between DSC curves in the melting and curing process. One is that there are two peaks in DSC curves during the curing process, which are caused by the solid-liquid phase transformation of MPCM. Other is that the peak temperature of MPCM-LWAC in the curing process lags behind its peak temperature in the melting process.

The melting enthalpy and curing enthalpy of MPCM-LWAC with different MPCM contents were calculated according to (2). As can be seen from Figure 10, the melting enthalpy and curing enthalpy of MPCM-LWAC are positively correlated with the MPCM content. The mixture of LWAC with MPCM does not affect the enthalpy of MPCM.

(a)

(b)
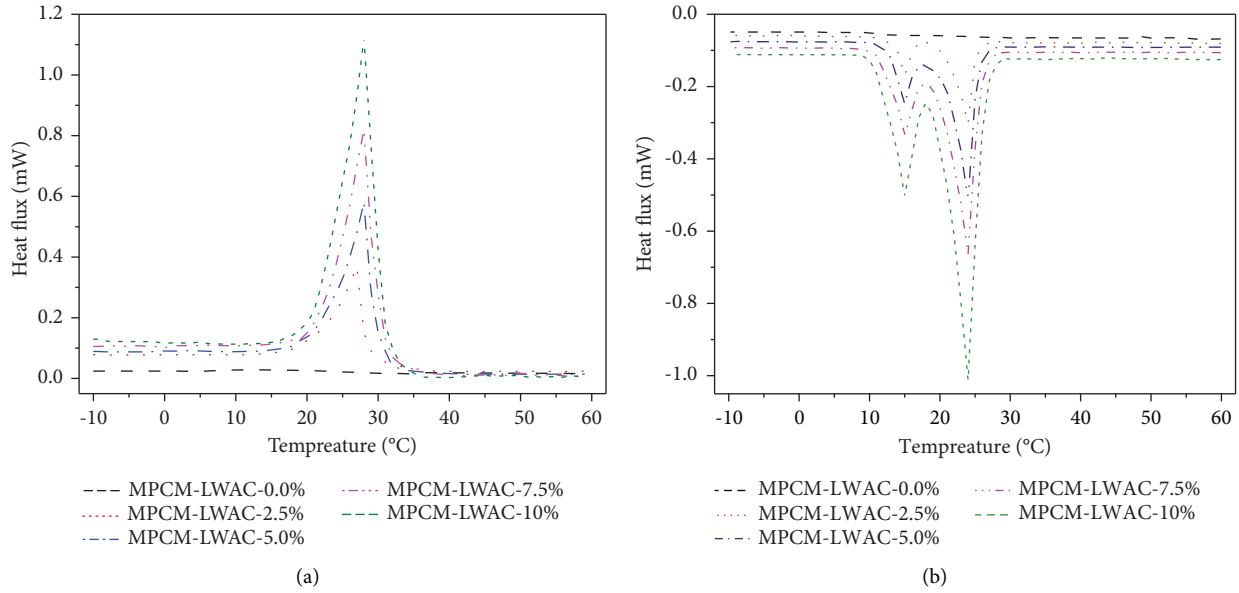
FIGURE 9: DSC curves of MPCM-LWAC with different MPCM contents. (a) Heat absorption by melting. (b) Heat release by solidification.
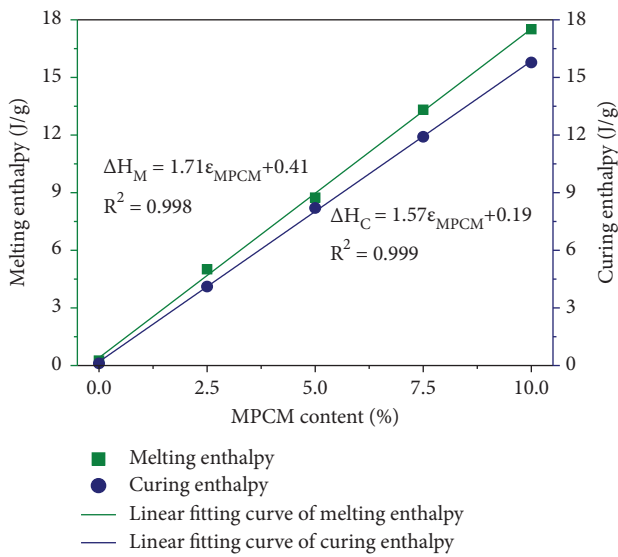
FIGURE 10: Effect of the MPCM content on melting and curing enthalpy.

Melting enthalpy of MPCM-LWAC is slightly larger than its curing enthalpy, and the difference is more obvious with the increasing amount of MPCM.

4.2.2. Effect of Phase-Change Cycle Numbers on the Enthalpy of MPCM-LWAC. DSC test was carried out to measure specific heat capacity of MPCM-LWAC with the different phase-change cycle numbers of 0, 50, 100, 150, and 200. The specific heat capacity of MPCM-LWAC was calculated according to (3) (here, specific heat capacity refers to the average of the specific heat capacity at each temperature point). The calculation results are shown in Figure 11. From Figure 11, the maximum and minimum enthalpy of MPCM-LWAC with different MPCM contents were obtained.

Undergoing 0, 50, 100, 150, and 200 phase-change cycle numbers, the variation in enthalpy of MPCM-LWAC with different MPCM contents of 2.5%, 5.0%, 7.5%, and 10% during the melting process are 7.16%, 9.49%, 6.57%, and 3.94%, respectively. The variation in enthalpy during the curing process are 6.22%, 3.11%, 5.30%, and 1.16%, respectively. This suggests that when the phase-change cycle numbers are less than 200, the phase-change cycle has little influence on the latent heat.

Under different phase-change cycle numbers, the enthalpy obtained by DSC test has no obvious and regular trend. That is, the enthalpy of MPCM-LWAC may increase or decrease with the increase of phase-change cycle numbers. The reason for this phenomenon is that DSC test requires the sample to be uniform. However, it cannot be guaranteed that the MPCM content contained in each group of samples is fixed, nor that the content of other components is consistent.

4.2.3. Effect of MPCM Content on Specific Heat Capacity of MPCM-LWAC. The specific heat capacity of MPCM-LWAC is calculated according to (3), and the results are shown in 12.

Comparing Figures 12(a) and 12(b), the specific heat capacity of MPCM-LWAC-0.0% always stays within the range of 1.210 ± 0.05 J/g°C during the whole process of heating and curing, which suggests that temperature has little effect on the specific heat capacity of MPCM-LWAC-0.0%.

Within the phase transition temperature range (20–30°C), the specific heat capacities of MPCM-LWAC-2.5%, 5.0%, 7.5%, and 10% increase rapidly, and the increase of specific heat capacity is proportional to the MPCM content, which is determined by the phase-change characteristics of MPCM. The specific heat capacity of MPCM-

(a)

(b)
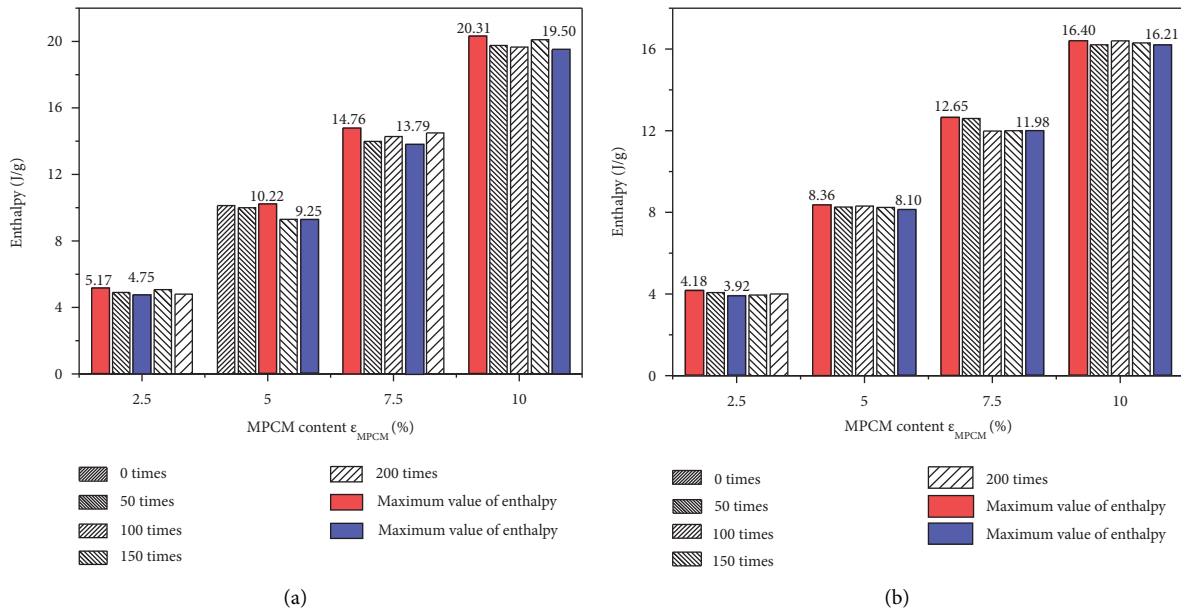
FIGURE 11: Effect of the phase-change cycle numbers on the enthalpy of MPCM-LWAC. (a) Heat absorption by melting. (b) Heat release by curing.

(a)

(b)
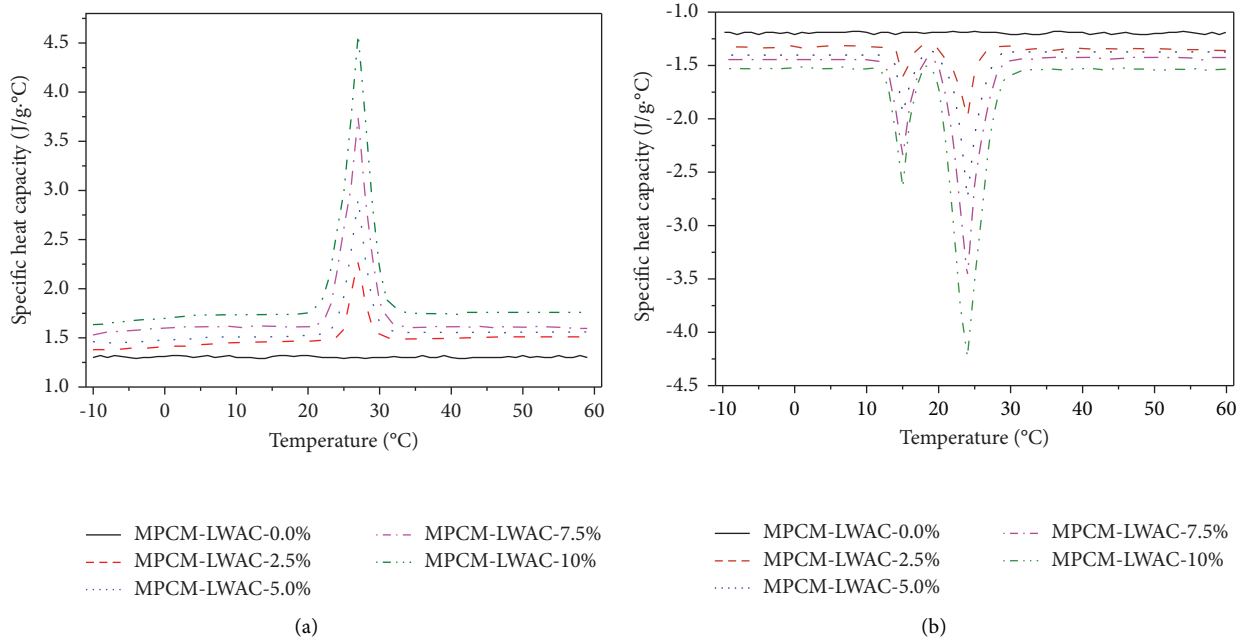
FIGURE 12: Curve of specific heat capacity of MPCM-LWAC with temperature. (a) Heat absorption by melting. (b) Heat release by solidification.

LWAC remains unchanged outside the phase transition temperature range.

The change trend of specific heat capacity of MPCM-LWAC with temperature is consistent with that of MPCM, and the horizontal coordinate of peak point is also the same as that of MPCM, which indicates that the phase-change characteristics of MPCM determine that of MPCM-LWAC.

4.2.4. Effect of Phase-Change Cycle Numbers on Specific Heat Capacity of MPCM-LWAC. Figures 13(a) and 13(b) are the effect of the phase-change cycle numbers on the specific heat capacity of MPCM-LWAC.

From Figures 13(a) and 13(b), it can be found that when the phase-change cycle numbers are less than 200, the phase-change cycle has little influence on the specific heat capacity.
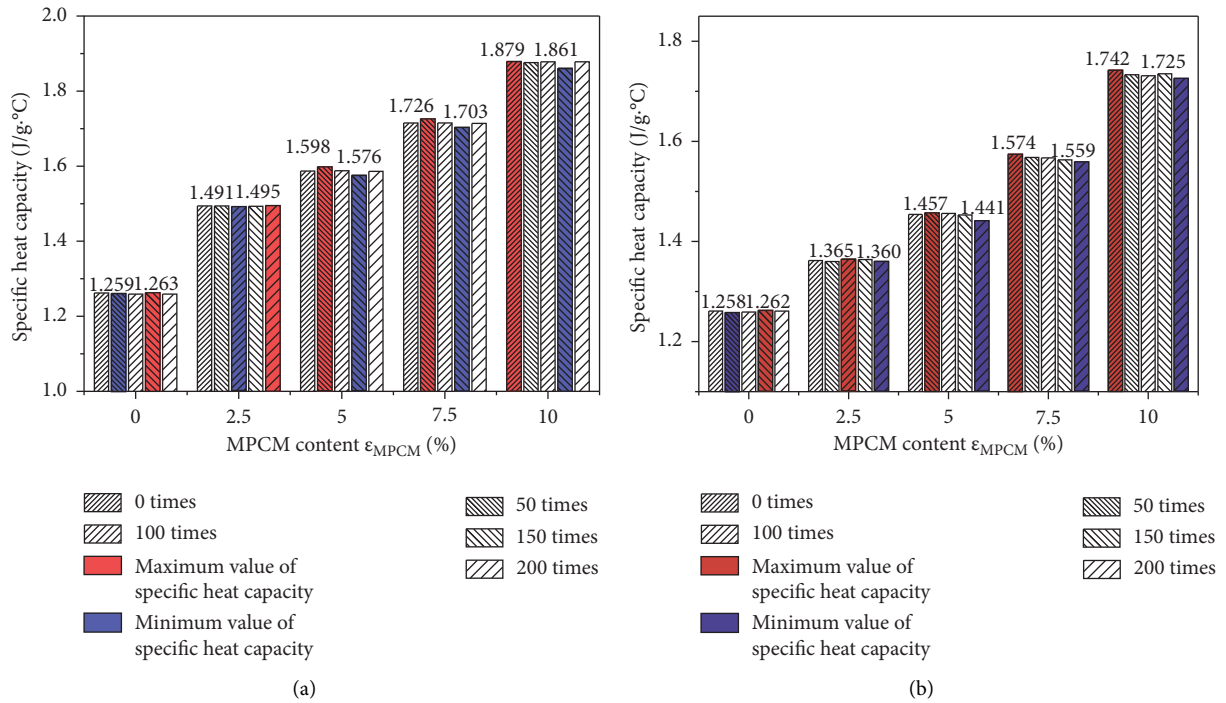
FIGURE 13: Effect of the phase-change cycle numbers on the specific heat capacity of MPCM-LWAC. (a) Heat absorption by melting. (b) Heat release by curing.
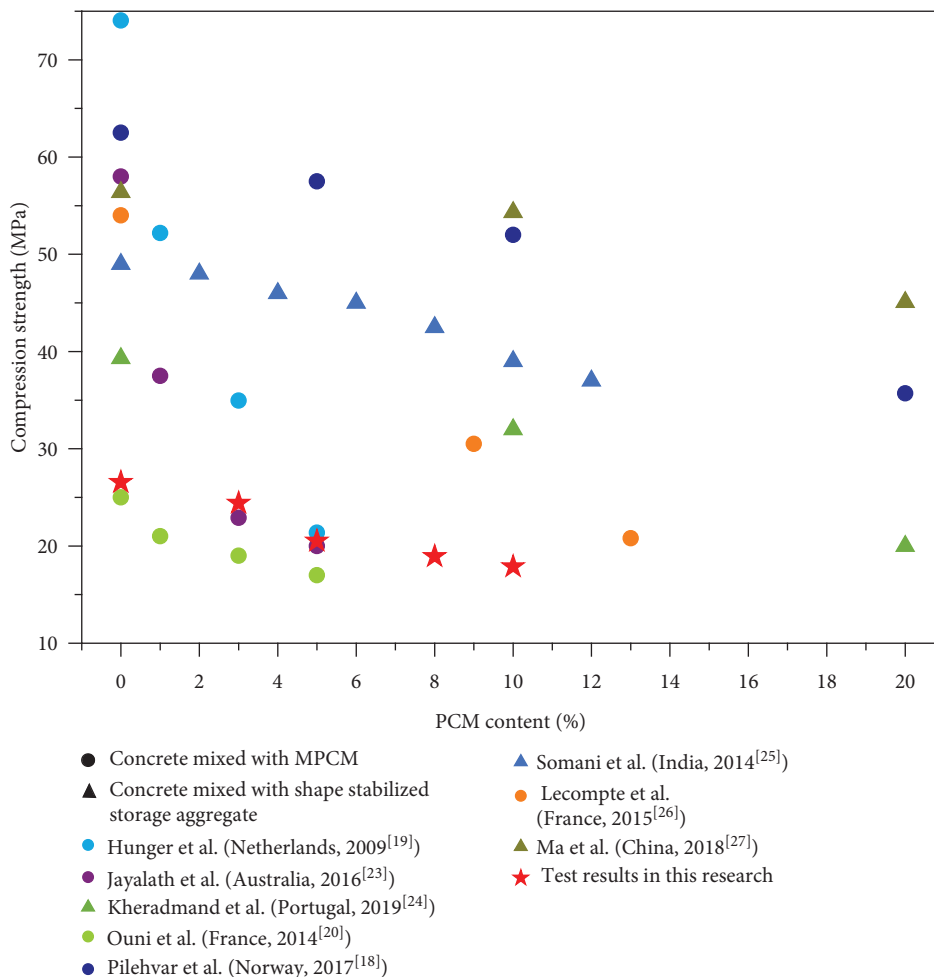
FIGURE 14: The relation curve between compressive strength and PCM content by different researchers.
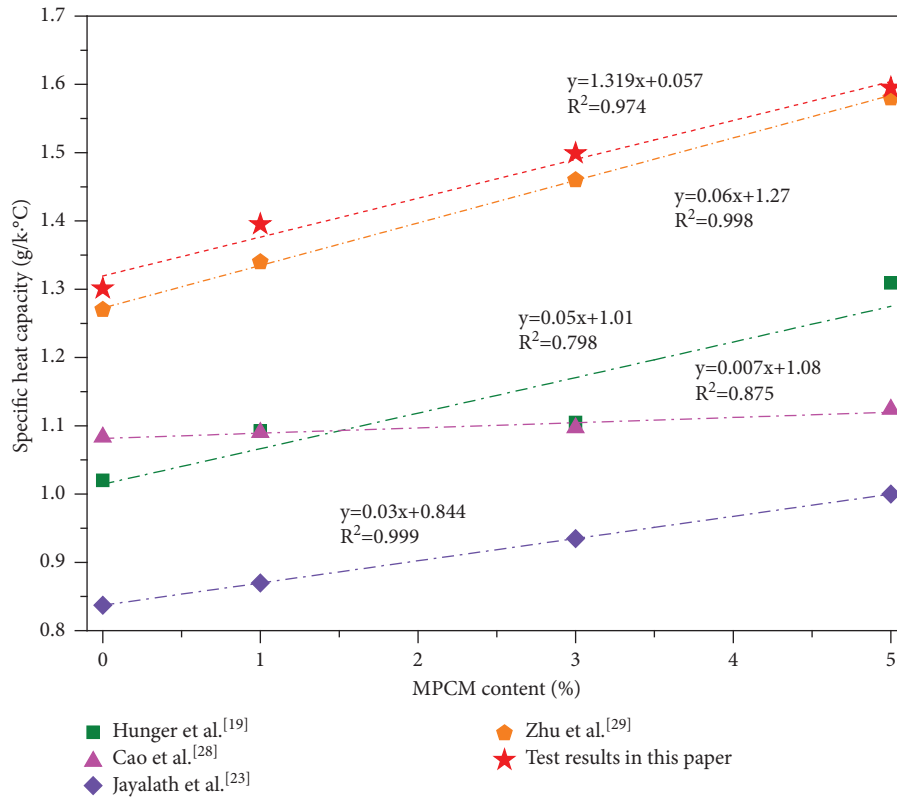
FIGURE 15: The relation curve between specific heat capacity and MPCM content by different researchers.

The maximum variation of the specific heat capacity is 1.33% (the specific heat capacity refers to the average of the specific heat capacity in the range of $-10\sim60°C$).

Based on the influence of the phase-change cycle numbers on the specific heat capacity of MPCM-LWAC, it is concluded that the MPCM-LWAC exhibits a good thermal stability, which is of great significance to the application of energy storage lightweight aggregate concrete.

5. Discussion

In order to reveal the influence of PCM content, preparation method and testing method on mechanical and thermal properties of PCM-concrete, experimental results from different scholars are summarized and presented in Figures 14 and 15, respectively, and they are compared with the results of this study.

From Figure 14, the compressive strength of PCM-concrete tested by different scholars has a wide range (varying from 17 to 75 MPa), which is mainly caused by the differences in raw material selection, mix ratio determination, and preparation process. The trend of experimental results in this study is similar with that of other researchers in Figure 14, namely, the addition of PCM will inevitably lead to the reduction of concrete compressive strength. Notably, the main difference between the research results of various scholars in Figure 14 is that the compressive strength of different PCM-concrete varies greatly. The MPCM-LWAC selected in this paper has lower strength, which

mainly depends on the properties and content of raw materials.

There are three main reasons for the reduction of concrete strength caused by the addition of MPCM. The first reason is that the mechanical properties of MPCM are weaker than that of the replaced sand, the second reason is that the porosity of the MPCM-LWAC increases with the increase of MPCM content, and the third reason is that the larger the MPCM content, the stronger the aggregation effect of MPCM, causing uneven distribution of concrete compositions.

From Figure 15, the addition of PCM will inevitably lead to an increase in the specific heat capacity of concrete, and the increase is positively correlated with the amount of PCM. This phenomenon indicated that the PCM content greatly affects the specific heat capacity of PCM concrete. In addition, PCM shows good chemical stability in the hydration reaction of concrete mix. In terms of function, the larger the specific heat capacity of PCM concrete, the more beneficial it is to adjust the indoor temperature. Compared with the experimental results from other scholars in Figure 15, the MPCM-LWAC selected in this research has larger specific heat capacity.

According to literature [30], the strength of MPCM-LWAC in this research can be further improved by adjusting the cement grade, increasing the content of cement and sand rate, while keeping the specific heat capacity unchanged, which helps to expand the scope of application of this material.

6. Conclusion

Mechanical and thermal properties of shale ceramsite concrete with different MPCM contents and different phase-change cycle numbers have been investigated. The optimal mixture ratio is determined, and the MPCM-LWAC specimens with different MPCM content were prepared. Subsequently, the mechanical and thermal properties of MPCM-LWAC specimens were studied. The experimental results are as follows:

(1) The mechanical properties of MPCM-LWAC are negatively correlated with the MPCM content. The tensile and compressive strengths of MPCM-LWAC decrease linearly with the increase of the MPCM content. Compared with MPCM-LWAC-0.0% specimens, the tensile strengths of MPCM-LWAC-2.5%, MPCM-LWAC-5.0%, MPCM-LWAC-7.5%, and MPCM-LWAC-10.0% specimens decreased by 10.66%, 21.31%, 34.84%, and 45.49%, respectively. The compressive strengths decreased by 8.27%, 22.93%, 49.62%, and 52.63%, respectively.

(2) The enthalpy of MPCM-LWAC is positively correlated with the MPCM content. Outside the phase-change temperature range, the specific heat capacity of MPCM-LWAC does not change with the change of temperature, but inside the phase-change temperature range, the specific heat capacity of MPCM-LWAC changes greatly with the change of temperature.

(3) With the increase of phase-change cycle numbers, the compressive strength, tensile strength, and specific heat capacity of MPCM-LWAC gradually decrease, but the strength decrease percentage is less than 5%, and the maximum specific heat capacity decrease percentage is 1.33%, which is not enough to affect the normal use of the MPCM-LWAC.

(4) The mechanical and thermal properties of MPCM-LWAC are comprehensively revealed in this paper, which provides a basis for the use of this material as partition wall.

In further research, the mechanical and thermal properties of MPCM-LWAC are expected to improve by adjusting cement grade, cement and MPCM content, sand rate, etc. Such research studies help to optimize the mechanical and thermal properties and then to expand the application range of MPCM-LWAC materials.

Data Availability

The raw/processed data required to reproduce these findings cannot be shared at this time as the data also form part of an ongoing study.

Conflicts of Interest

The authors declare that they have no conflicts of interest.

References

[1] S. Xian, A. M. Shazim, and C. Wai, "Experimental assessment of position of macro encapsulated phase change material in concrete walls on indoor temperatures and humidity levels [J]," *Energy and Buildings*, vol. 71, pp. 80–87, 2014.

[2] J. Wang, J. Han, and J. Chen, "Experimental and numerical study on the dynamic response of a superthick backfill subgrade under high-speed railway loading: a case study of Qianjiang-Zhangjiajie-Changde Railway [J]," *Journal of Construction Engineering and Management*, vol. 14, no. 15, p. 3215, 2022.

[3] S. Drissi, T. C. Ling, K. H. Mo, and A. Eddhahak, "A review of microencapsulated and composite phase change materials: a," *Renewable and Sustainable Energy Reviews*, vol. 110, pp. 467–484, 2019.

[4] A. Alessandro, A. L. Pisello, and C. F. Fabiani, "Multifunctional smart concretes with novel phase change materials: mechanical and thermo-energy investigation [J]," *Applied Energy*, vol. 212, pp. 1448–1461, 2018.

[5] Y. Xue, J. Liu, P. G. Ranjith, Z. Gao, and S. Wang, "Experimental investigation of mechanical properties, impact tendency, and brittleness characteristics of coal mass under different gas adsorption pressures," *Geomechanics and Geophysics for Geo-Energy and Geo-Resources*, vol. 8, no. 5, p. 131, 2022.

[6] T. C. Ling and C. S. Poon, "Use of phase change materials for thermal energy storage in concrete: an overview," *Construction and Building Materials*, vol. 46, no. 8, pp. 55–62, 2013.

[7] M. Z. Haider, X. H. Jin, R. Sharma, and J. W. Pei Hu, "Enhancing the compressive strength of thermal energy storage concrete containing a low-temperature phase change material using silica fume and multiwalled carbon nanotubes," *Construction and Building Materials*, vol. 314, Article ID 125659, 2022.

[8] Y. Xue, P. G. Ranjith, Y. Chen, G. Cai, and X. Liu, "Nonlinear mechanical characteristics and damage constitutive model of coal under CO2 adsorption during geological sequestration," *Fuel*, vol. 331, Article ID 125690, 2023.

[9] J. Y. Liu, S. F. Jia, X. X. Lin, W. Cao, and W Guo Sun, "Fabrication of thermal energy storage wood composite based on shape-stable phase change material," *Materials Research Express*, vol. 8, no. 5, Article ID 055304, 2021.

[10] J. Han, D. Liu, Y. Guan, L. Chen, J. Yan, and Y. Zhao, "Study on shear behavior and damage constitutive model of tendon-grout interface," *Construction and Building Materials*, vol. 320, Article ID 126223, 2022.

[11] U. Berardi and A. A. Gallardo, "Properties of concretes enhanced with phase change materials for building applications," *Energy and Buildings*, vol. 199, pp. 402–414, 2019.

[12] Z. Na, S. Li, and P. Hu, "A review on applications of shape-stabilized phase change materials embedded in building enclosure in recent ten years [J]," *Sustainable Cities and Society*, vol. 43, pp. 251–264, 2018.

[13] Y. Xue, J. Liu, and P. G. Ranjith, "Changes in Microstructure and Mechanical Properties of Low-Permeability Coal Induced by Pulsating Nitrogen Fatigue Fracturing Tests [J]," *Rock Mechanics and Rock Engineering*, 2022.

[14] Y. P. Cui, J. C. Xie, J. P. Liu, and S. WangChen, "A review on phase change material application in building," *Advances in Mechanical Engineering*, vol. 9, no. 6, pp. 168781401770082–15, 2017.

[15] M. Li and J. Shi, "Review on micropore grade inorganic porous medium based form stable composite phase change materials: preparation, performance improvement and effects on the properties of cement mortar," *Construction and Building Materials*, vol. 194, pp. 287–310, 2019.

[16] P. K. S. Rathore, N. K. Gupta, D. Yadav, k. Shu, and S. Kaul, "Thermal performance of the building envelope integrated with phase change material for thermal energy storage: an updated review," *Sustainable Cities and Society*, vol. 79, Article ID 103690, 2022.

[17] O. Pons, A. Aguado, A. I. Fernández, and J. M. Cabeza Chimenos, "Review of the use of phase change materials (PCMs) in buildings with reinforced concrete structures," *Materiales de Construcción*, vol. 64, no. 315, pp. e031–11, 2014.

[18] S. Pilehvar, V. D. Cao, A. M. Szczotok, S. Valentini, P. Magistri, and A. L. Kjøniksen, "Mechanical properties and microscale changes of geopolymer concrete and Portland cement concrete containing micro-encapsulated phase change materials," *Cement and Concrete Research*, vol. 100, pp. 341–349, 2017.

[19] M. Hunger, A. G. Entrop, I. Mandilaras, and M. Brouwers Founti, "The behavior of self-compacting concrete containing micro-encapsulated Phase Change Materials," *Cement and Concrete Composites*, vol. 31, no. 10, pp. 731–743, 2009.

[20] A. E. Ouni, S. Drissi, and J. Colin, "Experimental and multi-scale analysis of the thermal properties of Portland cement concretes embedded with microencapsulated Phase Change Materials (PCMs) [J]," *Applied Thermal Engineering*, vol. 64, pp. 32–39, 2014.

[21] L. Zhu, F. N. Dang, Y. Xue, and W. Jiao Ding, "Multivariate analysis of effects of microencapsulated phase change materials on mechanical behaviors in light-weight aggregate concrete," *Journal of Building Engineering*, vol. 42, Article ID 102783, 2021.

[22] Z. S. Chen and X. S. Ge, *Calorimetry and Determination of thermal Properties [M]*, University of Science and Technology of China Press, Hefei, Anhui, China, 1990.

[23] A. Jayalath, R. San Nicolas, M. Sofi, N. A. Shanks, and P. Mendis, "Properties of cementitious mortar and concrete containing micro-encapsulated phase change materials," *Construction and Building Materials*, vol. 120, pp. 408–417, 2016.

[24] M. Kheradmand, R. Vicente, M. Azenha, and J. L. de Aguiar, "Influence of the incorporation of phase change materials on temperature development in mortar at early ages: experiments and numerical simulation," *Construction and Building Materials*, vol. 225, pp. 1036–1051, 2019.

[25] P. Somani and A. Gaur, "Evaluation and reduction of temperature stresses in concrete pavement by using phase changing material," *Materials Today Proceedings*, vol. 32, pp. 856–864, 2020.

[26] T. Lecompte, P. Le Bideau, P. Glouannec, L. Nortershauser, and S Masson, "Mechanical and thermo-physical behaviour of concretes and mortars containing phase change material," *Energy and Buildings*, vol. 94, pp. 52–60, 2015.

[27] Q. Y. Ma and M. Bai, "Mechanical behavior, energy-storing properties and thermal reliability of phase-changing energy-storing concrete," *Construction and Building Materials*, vol. 176, no. 10, pp. 43–49, 2018.

[28] V. D. Cao, S. Pilehvar, C. Salas-Bringas, R. Szczotok, A. M. Carmona, and A. L. Kjøniksen, "Microencapsulated phase change materials for enhancing the thermal performance of Portland cement concrete and geopolymer concrete for passive building applications," *Energy Conversion and Management*, vol. 133, pp. 56–66, 2017.

[29] L. Zhu, F. N. Dang, Y. Xue, and K. Ding Jiao, "Experimental investigation of the thermal and mechanical properties of lightweight aggregate concrete mixed with microencapsulated phase change materials," *International Journal of Energy Research*, vol. 45, no. 9, pp. 12864–12878, 2021.

[30] P. J. Li and X. b. Liu, "Fundamental mechanical properties of concrete with high strength expanded shale [J]," *Journal of Building Materials*, vol. 7, no. 1, pp. 113–116, 2004.

Research Article

Simplified Calculation Method for Overlying Pipeline Deformation Induced by Tunnel Construction in Soil Based on the Energy Principle

Minghui Yang [iD],[1,2] **Tao Yang,**[1] **and Bo Deng** [iD][3]

[1]*College of Civil Engineering, Hunan University, Changsha 410082, Hunan, China*
[2]*Department of Civil Engineering, Xiamen University, Xiamen 361005, Fujian, China*
[3]*College of Civil Engineering, University of South China, Hengyang 421001, Hunan, China*

Correspondence should be addressed to Bo Deng; parl_d@126.com

The deformation of the overlay pipeline caused by the excavation of the soil tunnel in the case of small spacing cannot be ignored. Based on the experience of previous engineering, this paper assumes that the settlement of the overlying pipeline caused by tunnel excavation satisfies the basic morphology of Gaussian distribution. On this basis, the soil displacement is converted into load acting on the pipeline, and the energy variation principle is introduced, and the energy variation equation of the pipe-soil system is established, which is iteratively solved based on the principle of minimum potential energy, so as to obtain the calculation method of overlay pipeline vertical deformation caused by soil tunnel excavation, which is more simple and practical than the previous method. The calculation results were compared with the existing tests and engineering examples to verify the correctness of the proposed formula. Finally, the influence of pipeline material, formation loss rate, and intersection angle between the tunnel and pipeline on pipeline vertical deformation was analyzed. The comparative analysis shows that the pipeline deformation decreases with the increase of tunnel angle and pipeline elastic modulus, but increases with the increase of formation loss rate.

1. Introduction

There are a large number of deep loess in Northwest and North China, with a maximum thickness of more than 400 meters [1], so most tunnel projects in this area do not enter the rock stratum, but cross the soil layer to form soil tunnels. In addition, due to the large number of pipeline projects such as west to east gas transmission pipeline and municipal pipeline in this region, there are many soil tunnels under the existing pipeline projects [2–4]. Compared with the rock tunnel, the excavation stability of soil tunnel is relatively poor, which may cause large deformation of the overlying soil, and then cause the disturbance of the pipeline, and even affect the normal use of the overlying pipeline in serious cases. Therefore, the reasonable calculation of the deformation value of the overlying pipeline during the excavation of the soil tunnel has become one of the most concerned issues in this type of engineering [5, 6].

For the calculation of the deformation of the overlying pipeline caused by the tunnel excavation, the commonly used methods for predicting the deflection of the pipeline mainly include theoretical calculation [7–10], numerical simulation [11–13], and model test [14–16]. Among them, the accuracy of numerical simulation depends to a large extent on the selection of soil constitutive model and parameters, and the complexity of modeling is not convenient for engineering popularization and application; however, the input of the model test is large, time-consuming, and often different from the engineering practice, which affects the prediction results. Therefore, under the

premise of the allowable accuracy of the design, according to the pipe-soil interaction model caused by tunnel excavation, the analytical approximate solution which is convenient for engineering practice is still the first choice to solve this problem.

The elastic foundation beam method and the energy variational method are common methods for analyzing the deformation of pipelines, both of which assume that the pipeline is an elastic foundation beam and its bending deformation occurs along the longitudinal direction. Among them, the former generally uses the difference method to solve the fourth-order deflection differential control equation, and the calculation process is complicated and requires more segments to achieve better calculation accuracy, which is not suitable for engineering applications. Compared with the former, the latter has the advantages of simple integral solution, no need to discretize the pipeline, and easy to achieve ideal calculation accuracy, which is convenient for popularization and application in practical engineering [17–19]. For example, Zhou et al. [20] solved the deformation of shield tunnel caused by foundation pit excavation under the effect of the faulting of lining rings based on the energy method; Zhu et al. [21] proposed a dynamic analytical model for the vibration reduction system of a floating foundation supported by elastic components based on the energy method and the Lagrange equation of motion. In terms of pipeline deformation caused by tunnel excavation, Liu et al. [22] calculated the vertical displacement of single- and double-track tunnels passing through underground pipelines based on the energy method. On this basis, Wei et al. [23] further considered the characteristics of different soils and proposed the calculation method of pipeline deformation caused by the construction of quasirectangular shield or double-circle shield. It is still slightly complicated, which limits its engineering promotion and application.

In view of this, based on the previous research results, this paper further simplifies the calculation on the basis of clarifying the basic form of soil and overlying pipeline deformation caused by tunnel excavation and puts forward a concise calculation method of pipeline deformation caused by soil tunnel excavation based on energy method and compared with the results of centrifuge test, engineering example, and existing literature. It has certain guiding significance for practical engineering.

2. Computational Models and Assumptions

Due to the complexity of the tunnel-pipe-soil interaction in the process of tunnel excavation, it is difficult to use direct modeling for analysis, and most of them use the two-stage method for approximate theoretical analysis [24, 25]. First, calculate the vertical displacement of soil caused by tunnel excavation at the pipeline axis (ignoring the influence of pipeline). On this basis, a pipe-soil interaction model is established, the soil deformation result is regarded as an external load, the obtained soil-free displacement is applied to the pipeline, the vertical load deformation balance differential equation of the pipeline is established and solved, and then an energy equation to solve for pipe deformation

was constructed. For the convenience of calculation, the basic assumptions used in this paper are as follows:

(1) Both the pipeline and the soil are continuous homogeneous bodies, and the sectional dimension change caused by the pipeline deformation is ignored.

(2) The foundation under the pipeline is regarded as the Pasternak foundation, and the pipeline is regarded as a homogeneous, continuous Euler beam.

(3) The pipe and soil are always in contact, and the stratum loss remains unchanged.

2.1. Tunnel Excavation-Induced Formation Deformation Mode.
According to the above ideas, the deformation of soil layer during tunnel excavation can be calculated first. From Reference [26], according to a large number of engineering examples, it is found that the stratum settlement curve perpendicular to the tunnel axis caused by ground loss during tunnel excavation roughly conforms to the following function (see in Figure 1):

$$S(x') = S_{\max} \exp\left[-\frac{(x')^2}{2i_s^2}\right],$$

$$S_{\max} = \frac{\pi R^2 \eta}{i_s \sqrt{2\pi}},$$

(1)

where x' is the distance from the tunnel axis; $S(x')$ is the ground surface settlement at x' and $S_{\max}$ is the maximum value of ground surface settlement; η is the formation loss rate; R is the tunnel radius; and i_s is the distance from the center of symmetry of the soil settlement curve to the inflection point of the curve, which is generally called "settlement trough width." According to Jiang et al. [27], the inflection point of soil settlement curve is as follows:

$$i_s = 1.15R\left(\frac{H}{2R}\right)^{0.9}\left(1 - \frac{z_s}{H}\right)^{0.3},$$

(2)

where z_s is the depth from the surface. If it is assumed that there is an angle θ between the soil profile and the tunnel axis, the Peck formula can be modified as follows:

$$S(x) = S_{\max} \exp\left[-\frac{(x\sin\theta)^2}{2i_s^2}\right].$$

(3)

2.2. Pipeline Deformation Induced by Tunnel Excavation.
Tunnel excavation will inevitably cause deformation of the overlying pipeline. For flexible pipelines, Zhu et al. [14] and Wang et al. [15] showed through similar indoor model test results that the deformation of the overlying pipeline is in a good agreement with the distribution of Gaussian curve during tunnel excavation. While Han et al. [7], Gu et al. [8], and Klar et al. [9] proved that the pipeline deformation mode using Gaussian distribution is more reasonable from the point of view of theoretical analysis. For this reason, the
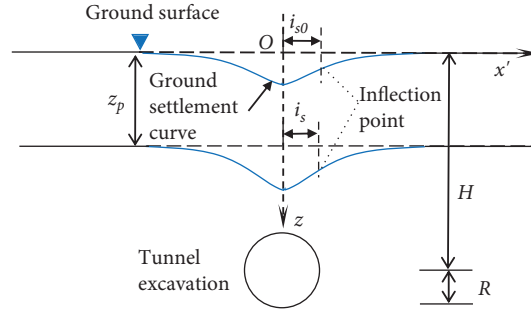
FIGURE 1: Soil settlement caused by tunnel excavation.

pipeline deformation model is still used in this paper, and the calculation model is shown in Figure 2, and the pipeline deformation function is as follows:

$$w(x) = A \exp\left[-\frac{x^2}{2i_p^2}\right], \qquad (4)$$

where x is the distance from a point on the pipeline to the center of symmetry of the settlement curve; $w(x)$ is the vertical deformation at coordinate x on the pipeline; A is the maximum vertical deformation of the pipeline; and i_p is the distance from the center of symmetry of the pipeline settlement curve to the inflection point of the curve, which is called "pipeline settlement tank width." According to equation (4), the vertical deformation of the pipeline can be solved only if the values of A and i_p are required.

3. Solution of Pipeline Deformation by Energy Method

3.1. Construction of Energy Equation of Pipe-Soil System. Figure 3 shows the interaction between the existing pipeline and the newly excavated tunnel. The excavation of the tunnel below will inevitably lead to the release of surface stress, resulting in soil movement, and ultimately leading to the longitudinal displacement difference of the overlying pipeline. If the overlying pipeline and the soil between the tunnel and the tunnel are taken as the research system, the deformation effect of the soil above the pipeline is transformed into load acting on the pipeline, while the soil below the pipeline provides support for the pipeline, and the pipeline is placed on an elastic foundation.

Among the common foundation models, the Winkler foundation model and the Pasternak foundation model are widely used, as shown in Figure 4. The Winkler foundation is assumed to be composed of a series of continuously distributed, nonconnected discrete springs, which can give satisfactory results to many practical problems. However, the Winkler foundation cannot account for shearing between adjacent springs. Adopting the Winkler foundation will overestimate the bending moment of the elastic beam due to the discontinuity of adjacent springs [28].

If the Pasternak foundation model is used to simulate the foundation soil beneath the pipeline, according to the assumption (3) that tunnel excavation does not change the formation loss rate, then the soil settlement function and

pipeline deformation function should meet the following requirements:

$$\frac{\sqrt{2\pi}i_s S_{\max}}{\sin\theta} = \sqrt{2\pi}i_p A, \qquad (5)$$

$$i_{s\theta} = \frac{i_s}{\sin\theta}. \qquad (6)$$

Due to the existence of pipeline, there is a difference between the vertical displacement of soil and the pipeline deformation at the axis of the pipeline, that is, the relative displacement of soil and pipe is $S_{rel} = S(x) - w(x)$, then the external force acted by soil displacement on the pipeline is as follows:

$$F = K \cdot S_{rel} - G\frac{d^2 S_{rel}}{dx^2}, \qquad (7)$$

where K is the modified elastic modulus of soil, which can be calculated by the method proposed by Vesic [29] and modified by Attewell et al. [30] as follows:

$$K = \frac{1.30E}{1 - v^2} \cdot \sqrt[12]{\frac{Ed^4}{E_p I_p}}, \qquad (8)$$

where $E_p I_p$ is the bending stiffness of pipeline, d is the pipeline diameter, v is the soil Poisson's ratio, and E is the soil elastic modulus.

The work by the soil displacement on the pipeline can be expressed as follows:

$$\Pi_s = \frac{1}{2}\int_{-\infty}^{+\infty}(S(x) - w(x))$$

$$\cdot\left[K(S(x) - w(x)) - G\left(\frac{d^2 S(x)}{dx^2} - \frac{d^2 w(x)}{dx^2}\right)\right]dx, \qquad (9)$$

where G is the foundation shear stiffness, which can be calculated by the value suggested by Tanahashi [28]:

$$G = \frac{Eh}{6(1 + v)}d, \qquad (10)$$

where h is the depth affected by the tunnel deformation in the Pasternak foundation model. Xu [31] suggested that h should be 2.5 times the diameter of the pipeline, that is, $h = 2.5\,d$.
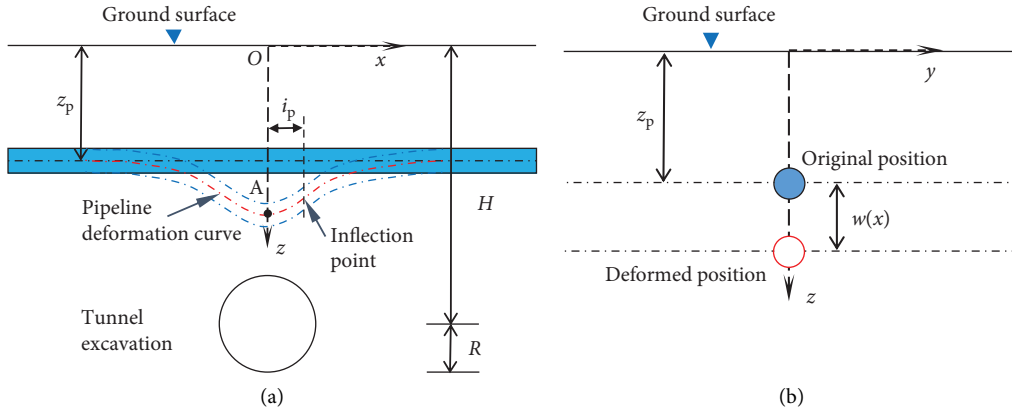
FIGURE 2: Deformation calculation diagram of pipeline during tunnel excavation. (a) In the x-z plan and (b) in the y-z plan.
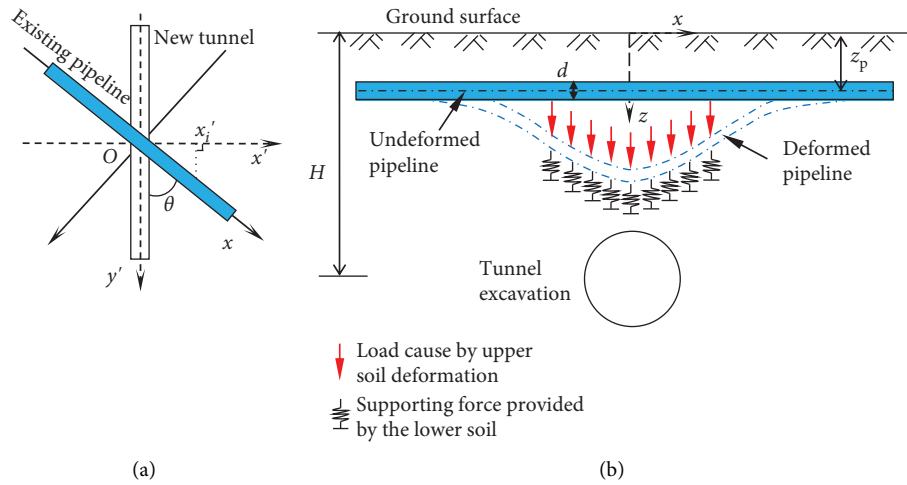
FIGURE 3: Deformation calculation diagram of pipeline during tunnel excavation. (a) Plan view. (b) Cross section view.
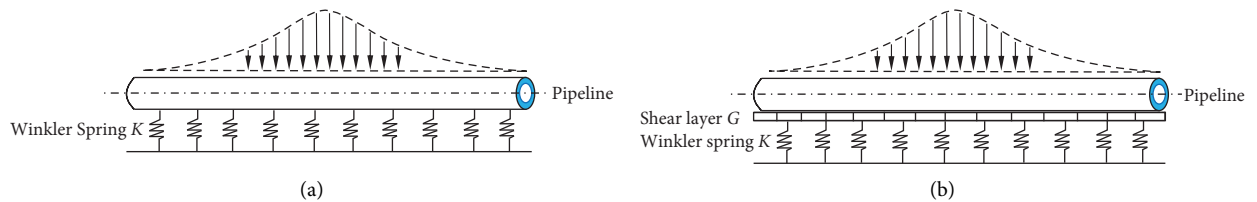
FIGURE 4: Two different foundation models. (a) Winkler foundation model. (b) Pasternak foundation model.

The bending strain energy of the pipeline is as follows:

$$\Pi_p = \frac{E_p I_p}{2} \int_{-\infty}^{+\infty} \left(\frac{d^2 w(x)}{dx^2} \right)^2 dx. \tag{11}$$

Then, the total potential energy of the system is $\prod = \prod_P + \prod S$.

3.2. Pipeline Deformation Solution. According to the principle of minimum potential energy, the real displacement field of the pipe-soil system makes the total potential energy functional take the minimum value, then:

$$\frac{\delta \Pi}{\delta A} = \frac{\delta \Pi_p}{\delta A} + \frac{\delta \Pi_S}{\delta A} = 0. \tag{12}$$

Substituting equations (9) and (11) into equation (12) yields the following:

$$E_p I_p \int_{-\infty}^{+\infty} \frac{\partial^2 w(x)/\partial x^2}{\partial A} \cdot \frac{\partial^2 w(x)}{\partial x^2} dx - K \int_{-\infty}^{+\infty} \frac{\partial w(x)}{\partial A} (S(x) - w(x)) dx$$

$$+ \frac{G}{2} \int_{-\infty}^{+\infty} \frac{\partial w(x)}{\partial A} \left(\frac{d^2 S(x)}{dx^2} - \frac{\partial^2 w(x)}{\partial x^2} \right) + (S(x) - w(x)) \frac{\partial^2 w(x)/\partial x^2}{\partial A} dx = 0, \tag{13}$$

$$\int_{-\infty}^{+\infty} \left[\frac{\partial^2 w(x)/\partial x^2}{\partial A} \cdot \frac{\partial^2 w(x)}{\partial x^2} + \lambda \frac{\partial w(x)}{\partial A} w(x) \right] dx - \frac{\varepsilon}{2} \int_{-\infty}^{+\infty} \frac{\partial w(x)}{\partial A} \cdot \frac{\partial^2 w(x)}{\partial x^2} dx + \frac{\partial^2 w(x)/\partial x^2}{\partial A} w(x) dx$$

$$= \lambda \int_{-\infty}^{+\infty} \frac{\partial w(x)}{\partial A} S(x) dx - \frac{\varepsilon}{2} \int_{-\infty}^{+\infty} \frac{\partial w(x)}{\partial A} \cdot \frac{d^2 S(x)}{dx^2} dx + \frac{\partial^2 w(x)/\partial x^2}{\partial A} S(x) dx, \tag{14}$$

where $\lambda = K/E_p I_p$ and $\varepsilon = G/E_p I_p$.

Substituting equations (2) and (4) and (5) and (6) into equation (14) yields the following:

$$\int_{-\infty}^{+\infty} A \left(\frac{x^2}{i_p^4} - \frac{1}{i_p^2} \right)^2 \exp\left[-\frac{x^2}{i_p^2} \right] dx + \lambda \int_{-\infty}^{+\infty} A \exp\left[-\frac{x^2}{i_p^2} \right] dx - \varepsilon \int_{-\infty}^{+\infty} A \left(\frac{x^2}{i_p^4} - \frac{1}{i_p^2} \right) \exp\left[-\frac{x^2}{i_p^2} \right] dx$$

$$= \lambda \int_{-\infty}^{+\infty} S_{max} \exp\left[-\left(\frac{1}{2i_p^2} + \frac{1}{2i_{s\theta}^2} \right) x^2 \right] dx - \frac{\varepsilon}{2} \int_{-\infty}^{+\infty} S_{max} \left[\left(\frac{1}{i_{s\theta}^4} + \frac{1}{i_p^4} \right) x^2 - \left(\frac{1}{i_{s\theta}^2} + \frac{1}{i_p^2} \right) \right] \exp\left[-\left(\frac{1}{2i_p^2} + \frac{1}{2i_{s\theta}^2} \right) x^2 \right] dx. \tag{15}$$

Since equation (15) is difficult to calculate directly, it is first expressed separately as follows, and then integrated and simplified, respectively:

$$\int_{-\infty}^{+\infty} A \left(\frac{x^2}{i_p^4} - \frac{1}{i_p^2} \right)^2 \exp\left[-\frac{x^2}{i_p^2} \right] dx = \frac{3\sqrt{\pi} A}{4 i_p^3}, \tag{16}$$

$$\lambda \int_{-\infty}^{+\infty} A \exp\left[-\frac{x^2}{i_p^2} \right] dx = \lambda A \sqrt{\pi} i_p, \tag{17}$$

$$-\varepsilon \int_{-\infty}^{+\infty} A \left(\frac{x^2}{i_p^4} - \frac{1}{i_p^2} \right) \exp\left[-\frac{x^2}{i_p^2} \right] dx = \frac{\sqrt{\pi} \varepsilon A}{2 i_p}, \tag{18}$$

$$\lambda \int_{-\infty}^{+\infty} S_{max} \exp\left[-\left(\frac{1}{2i_p^2} + \frac{1}{2i_{s\theta}^2} \right) x^2 \right] dx = \frac{\sqrt{2\pi} \lambda S_{max} i_p i_{s\theta}}{\sqrt{i_p^2 + i_{s\theta}^2}}, \tag{19}$$

$$-\frac{\varepsilon}{2}\int_{-\infty}^{+\infty} S_{\max}\left[\left(\frac{1}{i_{s\theta}^4}+\frac{1}{i_p^4}\right)x^2-\left(\frac{1}{i_{s\theta}^2}+\frac{1}{i_p^2}\right)\right]\exp\left[-\left(\frac{1}{2_{ip}^2}+\frac{1}{2i_{s\theta}^2}\right)x^2\right]dx = \frac{\sqrt{2\pi}\varepsilon S_{\max}i_p i_{s\theta}}{\left(i_{s\theta}^2+i_p^2\right)^{1.5}}. \tag{20}$$

Substituting equations (5) and (16)-(20) into equation (15) yields the following:

$$\frac{3}{4}\frac{1}{i_p^4}+\lambda+\frac{\varepsilon}{2i_p^2}=\frac{\sqrt{2}\left(\lambda i_{s\theta}^2+\varepsilon\right)}{\left(i_p^2+i_{s\theta}^2\right)^{1.5}}i_p+\frac{\sqrt{2}\lambda}{\left(i_p^2+i_{s\theta}^2\right)^{1.5}}i_p^3. \tag{21}$$

Equation (21) is relatively complex and difficult to solve directly. Therefore, this paper establishes the following iterative formula to solve i_p:

$$i_p=\left[\frac{\left(i_p^2+i_s^2/sin^2\theta\right)^{1.5}}{4\sqrt{2}\lambda}\left(3+4\lambda i_p^4+2\varepsilon i_p^2\right)-\left(\frac{i_s^2}{sin^2\theta}+\frac{\varepsilon}{\lambda}\right)i_p^5\right]^{1/7}. \tag{22}$$

If the Winkler foundation model is used to simulate the foundation soil beneath the pipeline, it is only necessary to substitute $\varepsilon=0$ into equation (21), then equation (22) degenerates into:

$$i_p=\frac{1}{\sqrt{2}}\left[\frac{3+4\lambda i_p^4}{\lambda\sin\theta}\sqrt{i_s^2+\left(i_p\sin\theta\right)^2}\right]^{1/5}, \tag{23}$$

where θ is the angle between pipeline and tunnel. The author suggests that the initial iteration value should be $i_{p0}=(2\sim3)R$, so as to quickly obtain the final iteration value.

The parameters i_p and A are obtained by solving simultaneous equations (5) and (16) to complete the calculation of pipeline deformation.

4. Example Verification

4.1. Comparison with Field Measured Data. Ma [32] provided the measured data of shield tunnel excavation in a certain section of the Shenzhen metro project (the Phase 1). This section of the tunnel is located in gravelly clay and sandy clay, which is a typical soil tunnel. The comparison calculation parameters are as follows: the tunnel depth $H=14.4$ m, the tunnel diameter $D=6$ m, the pipeline diameter $d=3$ m, the pipeline wall thickness $t=0.12$ mm, the pipeline elastic modulus $E_p=25$ GPa, the pipeline depth $z_p=8.7$ m, the formation loss rate $\eta=0.77\%$, the soil elastic modulus $E=8.2$ MPa, the soil Poisson's ratio $v=0.3$, the bending stiffness of pipeline $E_pI_p=2.819\times10^{10}$ N m^2, and the tunnel is orthogonal to the pipeline, that is, $\theta=90$ degree.

The comparison between the calculated results and the measured values using equations (22) and (23) is shown in Figure 5. The measured average maximum settlement value of the pipeline is 8.30 mm, and the maximum settlement values calculated based on the Pasternak foundation and Winkler foundation are 8.63 mm and 8.55 mm, respectively. The deviations between the two foundation models and the measured values are 3.98% and 3.01%, respectively. It can be seen that the calculation method in this paper is basically consistent with the measured results, while the Pasternak

foundation is slightly larger than the Winkler foundation, but the difference is small.

4.2. Comparison with the Centrifuge Test. Marshall et al. [5] measured the vertical deformation of the pipeline caused by tunnel excavation under the condition of centrifugal acceleration of 75 g. Select $\eta=0.5\%$, 1% for analysis, the main calculation parameters are as follows: the tunnel depth $H=13.65$ m, the tunnel diameter $D=4.65$ m, the diameters of the two pipelines $d=2.6$ m and 0.66 m, the bending stiffness of pipeline $E_pI_p=2.56\times1010$ N m2, 2.04×108N·m2, and the pipeline depth $z_p=5.6$ m. The soil elastic modulus $E=19.52$ MPa, the soil Poisson's ratio $v=0.4$, the test soil sample is dry sand, and the tunnel is orthogonal to the pipeline, that is, $\theta=90$ degree

For pipelines with small stiffness, the comparison between calculation results and test values by using the formula in this paper is shown in Figure 6(a), Case 1: the formation loss rate $\eta=0.5\%$, the maximum deformation measured in the test is 5.25 mm, the maximum deformation calculated based on Pasternak foundation is 5.574 mm, while the maximum deformation calculated based on Winkler foundation is 5.573 mm, and the deviations between the calculated results and the measured values of the two foundation models are 6.17% and 5.80%, respectively; Case 2: the formation loss rate $\eta=1\%$, the maximum deformation measured in the test is 11.25 mm, the maximum deformation calculated based on Pasternak foundation is 11.148 mm, while the maximum deformation calculated based on Winkler foundation is 11.147 mm, and the deviations between the calculated results and the measured values of the two foundation models are -0.907% and -0.915%, respectively.

For pipelines with large stiffness, the comparison between calculation results and test values by using the formula in this paper is shown in Figure 6(b), Case 3: the formation loss rate $\eta=0.5\%$, the maximum settlement measured in the test is 4.5 mm, the maximum deformation calculated based on Pasternak foundation is 3.984 mm, while the maximum settlement calculated based on Winkler foundation is 3.959 mm, and the deviations between the calculated results and the measured values of the two foundation models are -11.47% and -12.02%, respectively; Case 4: the formation loss rate $\eta=1\%$, the maximum deformation measured in the test is 7.5 mm, the maximum deformation calculated based on Pasternak foundation is 7.97 mm, while the maximum deformation calculated based on Winkler foundation is 7.92 mm, and the deviations between the calculated results and the measured values of the two foundation models are 6.27% and 5.60%, respectively. In conclusion, the pipeline settlement calculated by the method in this paper is in a good agreement with the experimental values, and there is little
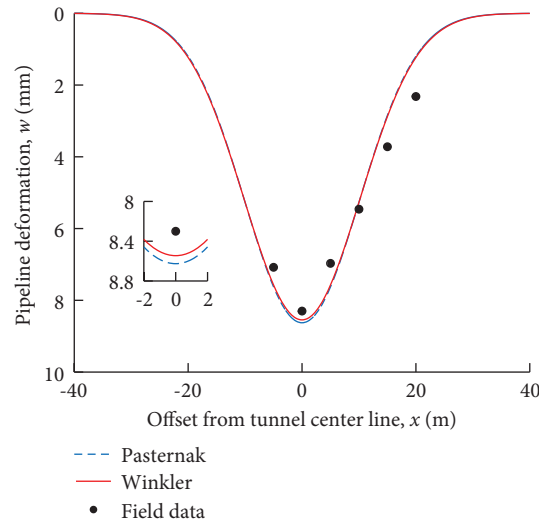
FIGURE 5: Comparison of analytical solution against field data.

(a)

(b)
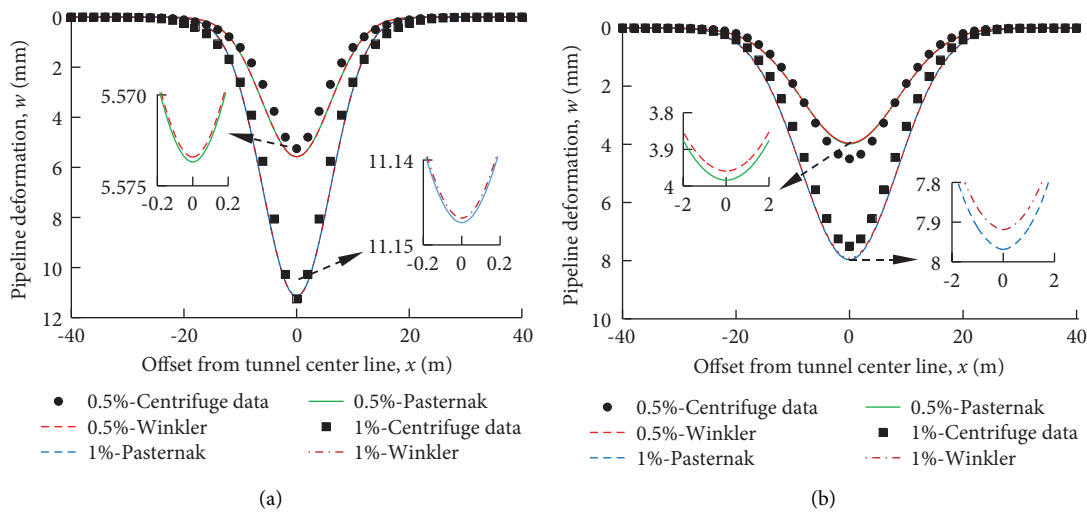
FIGURE 6: Comparison of analytical solution against centrifuge test data. (a) Small stiffness pipeline and (b) large stiffness pipeline.

difference in the pipeline deformation calculated by the two foundation modes for large and small stiffness pipelines.

4.3. Compared with the Existing Literature.

Compared with the calculation method of Vorster et al. [33], the calculation parameters are as follows: the tunnel depth $H = 5$ m, the excavation diameter $D = 1.5$ m, the pipeline diameter $d = 0.8$ m, the bending stiffness of pipeline $E_p I_p = 1.05 \times 10^8$ N m2, the pipeline depth $z_p = 1.5$ m, the soil elastic modulus $E = 14.32$ MPa, the soil Poisson's ratio $\nu = 0.25$, and the tunnel is orthogonal to the pipeline, that is, $\theta = 90°$. Vorster et al. [33] gave the maximum settlement value of free soil displacement Smax = 13.6 mm, and the inflection point of settlement trough is = 2.6 m in the buried depth of the pipeline.

The calculated results are shown in Figure 7. In this paper, the maximum settlement of pipeline is calculated by using Pasternak foundation and Winkler foundation as 11.93 mm and 11.89 mm, respectively. The maximum value of pipeline settlement calculated by Vorster et al. is 12 mm, and the difference between the results calculated by Pasternak foundation and Vorster et al. is −0.583%, and the difference between the results calculated by Winkler foundation and Vorster et al. is −0.917%.

5. Parametric Studies

According to the influencing factors of pipeline deformation, the factors such as pipeline material, formation loss rate, and pipe-tunnel intersection angle are analyzed. The selected calculation parameters are as follows: buried depth of tunnel axis $H = 15$ m, the tunnel diameter $D = 6$ m, the
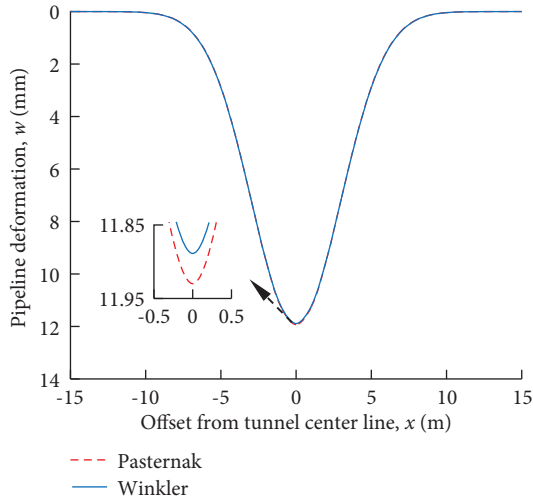
FIGURE 7: Comparison of analytical solution and other method.

pipeline diameter $d = 2$ m, and the pipeline wall thickness $t = 0.12$ mm. The soil elastic modulus $E = 15$ MPa and the soil Poisson's ratio $v = 0.3$. To simplify the calculation, only Pasternak foundation model calculation is used as an example in the parameter analysis.

5.1. Pipeline Material.
When the buried depth of the pipeline axis is selected to be 3 m, which corresponds to the distance between the axis of the pipe and the tunnel is 12 mm, the angle between the tunnel and the pipeline θ = 90 degree, and the formation loss rate $\eta = 2\%$, the commonly used pipeline material parameters are shown in Table 1.

The calculation results of pipeline deformation for different pipeline materials are shown in Figure 8. It can be seen from the figure that as the stiffness of the pipeline increases, the maximum deformation value of the pipeline decreases gradually, while the width of the pipeline settlement tank increases gradually.

5.2. Formation Loss Rate.
The cast iron material in Table 1 is selected to analyze the influence of formation loss rate on pipeline deformation, and the intersection angle between the tunnel and the pipeline θ = 90 degree, and the formation loss rate $\eta = 1\%$, 2%, and 3%. The calculation results are shown in Figure 9. It can be found from the figure that the maximum settlement value of the pipeline gradually increases with the increase of the formation loss rate, but the width of the pipeline settlement tank remains unchanged, indicating that the formation loss rate has a significant impact on the pipeline deformation.

5.3. Intersection Angle.
Selecting the formation loss rate $\eta = 2\%$ and the cast iron pipe in Table 1, the calculation results of pipeline deformation under different tunnel intersection angles between the tunnel and the pipeline (e.g., 90 degree, 60 degree, and 30 degree) are shown in Figure 10. It can be seen from the figure that as the angle between the tunnel and the pipeline decreases, the maximum

TABLE 1: Material parameters of different pipelines.

Material name	Elastic modulus (GPa)	Bending stiffness
PVC pipe	3	9.432×10^8 N·m²
Concrete pipe	25	7.860×10^9 N·m²
Cast iron pipe	150	4.716×10^{10} N·m²
Steel pipe	210	6.602×10^{10} N·m²
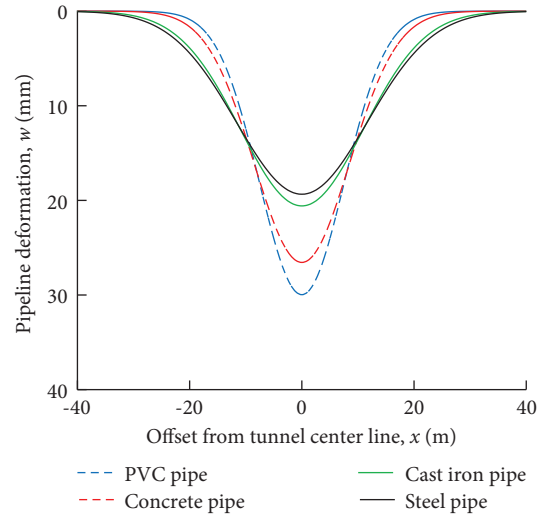
FIGURE 8: Pipeline deformation under different pipeline materials.
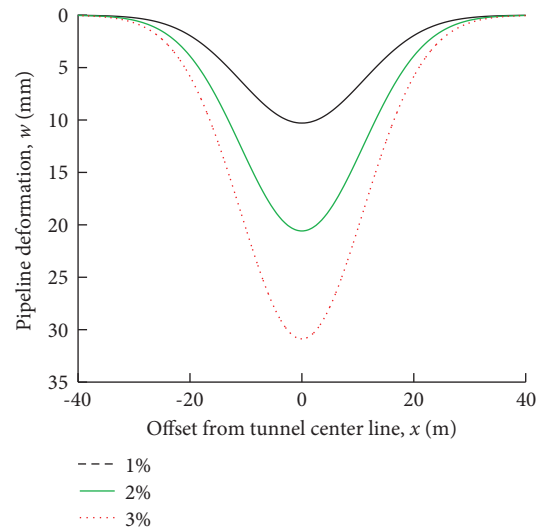
FIGURE 9: Pipeline deformation under different formation loss rates.

deformation value of the pipeline gradually increases, and as the angle between the tunnel and the pipeline decreases, the problem is gradually transformed into a plane problem and the corresponding maximum value of pipeline deformation gradually approached the maximum value of soil settlement. In addition, when the intersection angle between the tunnel and the pipeline changes from 90 degree to 60 degree, the increase in the maximum settlement of the soil is less than that when the angle changes from 60 degree to 30 degree. To
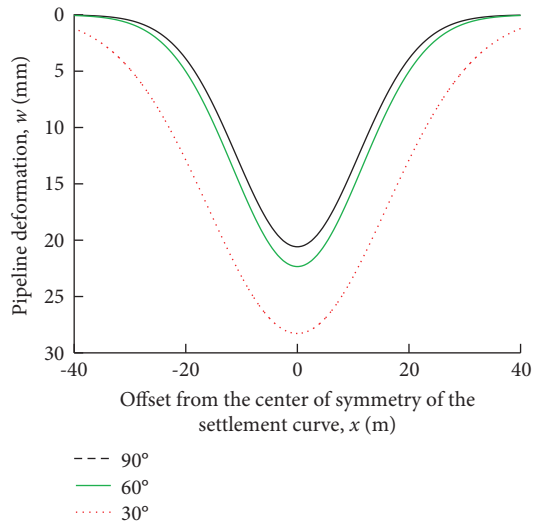
Figure 10: Pipeline deformation under different intersection angles.

speak it simply, the width of the pipe settlement tank gradually increases with the decrease of the intersection angle between the pipe and tunnel. When the intersection angle between the pipe and tunnel is close to 90 degree, the calculation as 90 degree can meet the accuracy requirements, but when the intersection angle between the pipe and tunnel is far away from 90 degree, the intersection angle between the pipe and tunnel cannot be ignored.

6. Conclusion

For the special condition of soil tunnel under the existing pipeline, this paper proposes a calculation method of pipeline deformation based on the principle of minimum potential energy based on the previous test experience. The effectiveness of the method in this paper is verified by comparison with engineering examples and centrifuge test results, and the influencing factors of pipeline deformation are analyzed. The main conclusions are as follows:

(1) As the stiffness of the pipeline increases, the maximum settlement value of the pipeline gradually decreases, while the width of the deformation trough gradually increases.

(2) With the increase of formation loss rate, the maximum deformation value of pipeline increases gradually, but the width of the pipeline settlement tank remains unchanged.

(3) With the decrease of the angle between the tunnel and the pipeline, the maximum deformation of the pipeline increases gradually, and the width of the pipeline settlement tank increases gradually.

Data Availability

The data used to support the findings of this study are included within the article.

Conflicts of Interest

The authors declare that they have no conflicts of interest.

Acknowledgments

References

[1] Z. J. Xue, Z. G. Lin, and M. S. Zhang, "Loess in China and loess landslides," *Chinese Journal of Rock Mechanics and Engineering*, vol. 26, no. 7, pp. 1297–1312, 2007, in Chinese.

[2] L. Zhang, X. Wu, Y. Qin, M. J. Skibniewski, and W. Liu, "Towards a fuzzy Bayesian network based approach for safety risk analysis of tunnel-induced pipeline damage," *Risk Analysis*, vol. 36, no. 2, pp. 278–301, 2016.

[3] Y. K. Sun, W. Y. Wu, and T. Q. Zhang, "Analysis on the pipeline settlement in soft ground induced by shield tunneling across buried pipeline," *China Railway Science*, vol. 30, no. 1, pp. 80–85, 2009, in Chinese.

[4] N. Jiang, T. Gao, C. Zhou, and X. Luo, "Effect of excavation blasting vibration on adjacent buried gas pipeline in a metro tunnel," *Tunnelling and Underground Space Technology*, vol. 81, pp. 590–601, 2018.

[5] A. M. Marshall, A. Klar, and R. J. Mair, "Tunneling beneath buried pipes: view of soil strain and its effect on pipeline behavior," *Journal of Geotechnical and Geoenvironmental Engineering*, vol. 136, no. 12, pp. 1664–1672, 2010.

[6] A. Klar, "Elastic continuum solution for tunneling effects on buried pipelines using fourier expansion," *Journal of Geotechnical and Geoenvironmental Engineering*, vol. 144, no. 9, Article ID 4018062, 2018.

[7] X. Han, C. H. Lei, and P. Zhang, "A modified stiffness approach to predict tunnelling induced deformation and force of pipelines," *Journal of Civil & Environmental Engineering*, vol. 34, no. 3, pp. 21–27, 2012, in Chinese.

[8] S. C. Gu, H. W. He, and G. F. Ru, "Analysis of underground pipeline stress caused by metro tunneling," *Urban Mass Transit*, vol. 5, pp. 14–18, 2015, in Chinese.

[9] A. Klar and A. M. Marshall, "Linear elastic tunnel pipeline interaction: the existence and consequence of volume loss equality," *Géotechnique*, vol. 65, no. 9, pp. 788–792, 2015.

[10] C. Lin, M. Huang, F. Nadim, and Z. Liu, "Tunnelling-induced response of buried pipelines and their effects on ground settlements," *Tunnelling and Underground Space Technology*, vol. 96, Article ID 103193, 2020.

[11] Y. Wang, J. Shi, and C. W. W. Ng, "Numerical modeling of tunneling effect on buried pipelines," *Canadian Geotechnical Journal*, vol. 48, no. 7, pp. 1125–1137, 2011.

[12] M. Xu and L. Shi, "A Numerical study on the effect of tunneling on adjacent buried pipelines," in *Proceedings of the International Conference on Pipelines and Trenchless Technology*, pp. 1376–1387, Beijing, China, October 2011.

[13] J. Shi, Y. Wang, and C. W. W. Ng, "Numerical parametric study of tunneling-induced joint rotation angle in jointed pipelines," *Canadian Geotechnical Journal*, vol. 53, no. 12, pp. 2058–2071, 2016.

[14] Y. T. Zhu, H. Zhang, Z. X. Zhang, X. Huang, and K. Liu, "Physical model test study of influence of advance of shield

tunnel on adjacent underground pipelines," *Rock and Soil Mechanics*, vol. 37, no. 2, pp. 151–160, 2016, in Chinese.

[15] H. T. Wang, H. Jin, and D. J. Yuan, "Model test study on influence of pipeline caused by tunnel construction in sand," *China Civil Engineering Journal*, vol. 50, no. 2, pp. 118–126, 2017, in Chinese.

[16] S. Ma, Y. Shao, Y. Liu, J. Jiang, and X. Fan, "Responses of pipeline to side-by-side twin tunnelling at different depths: 3D centrifuge tests and numerical modelling," *Tunnelling and Underground Space Technology*, vol. 66, pp. 157–173, 2017.

[17] J. L. Figueroa, A. S. Saada, L. Liang, and N. M. Dahisaria, "Evaluation of soil liquefaction by energy principles," *Journal of Geotechnical Engineering*, vol. 120, no. 9, pp. 1554–1569, 1994.

[18] M. Z. Chen, X. N. Gong, and J. X. Ying, "Variational solution for pile group–pile cap (raft)," *China Civil Engineering Journal*, vol. 34, no. 6, pp. 67–73, 2001, in Chinese.

[19] H. S. Shang, H. Zhang, and F. Y. Liang, "Lateral bearing capacity of pile foundation due to shallow tunneling," *Chinese Journal of Geotechnical Engineering*, vol. 35, no. z2, pp. 740–743, 2013, in Chinese.

[20] S. H. Zhou, J. H. Xiao, and C. He, "Energy method for calculating deformation of adjacent shield tunnels due to foundation pit excavation considering step between rings," *China Railway Science*, vol. 37, no. 3, pp. 53–60, 2016, in Chinese.

[21] L. J. Zhu, L. H. Wen, and S. Hei, "Analytical model of floating foundation vibration reduction system based on energy method," *Earthquake Engineering and Engineering Dynamics*, vol. 42, no. 2, pp. 104–112, 2022, in Chinese.

[22] X. Q. Liu, F. Y. Liang, H. Zhang, and F. Chu, "Energy variational solution for settlement of buried pipeline induced by tunneling," *Rock and Soil Mechanics*, vol. 35, no. 2, pp. 217–222, 2014, in Chinese.

[23] G. Wei, C. H. Cui, and X. Xu, "Calculation of pipeline settlement induced by double-o-tube shield tunneling based on energy method," *Chinese Journal of Underground Space and Engineering*, vol. 15, no. 4, pp. 1106–1111, 2019, in Chinese.

[24] A. Klar, T. E. B. Vorster, K. Soga, and R. J. Mair, "Soil—pipe interaction due to tunnelling: comparison between Winkler and elastic continuum solutions," *Géotechnique*, vol. 55, no. 6, pp. 461–466, 2005.

[25] H. Zhang and Z. X. Zhang, "Vertical deflection of existing pipeline due to shield tunnelling," *Journal of Tongji University*, vol. 41, no. 8, pp. 1172–1178, 2013, in Chinese.

[26] R. B. Peck, "Deep excavations and tunnelling in soft ground," in *Proceedings of the 7th International Conference on soil Mechanics and Foundation Engineering*, pp. 225–290, Mexico, 1969.

[27] X. L. Jiang, Z. M. Zhao, and Y. Li, "Analysis and calculation of surface and subsurface settlement trough profiles due to tunneling," *Rock and Soil Mechanics*, vol. 25, no. 10, pp. 1542–1544, 2004, in Chinese.

[28] H. Tanahashi, "Formulas for an infinitely long Bernoulli-Euler beam on the Pasternak model," *Soils and Foundations*, vol. 44, no. 5, pp. 109–118, 2004.

[29] A. B. Vesic, "Bending of beams Resting on Isotropic elastic Solid," *Journal of the Engineering Mechanics Division*, vol. 87, no. 2, pp. 35–53, 1961.

[30] P. B. Attewell, J. Yeates, and A. R. Selby, *Soil Movements Induced by Tunnelling and Their Effects on Pipelines and Structures*, Blackie & Son, London, UK, 1986.

[31] L. Xu, *Study on Longitudinal Settlement of Soft Soil Shield Tunnel*, Tongji University, Shanghai, China, 2005, in Chinese.

[32] T. Ma, *The Research of Tunneling- Induced Ground Surface Movements and Their Influence to Adjacent Utilities*, Changsha University of Science & Technology, Changsha, China, 2005, in Chinese.

[33] T. E. Vorster, A. Klar, K. Soga, and R. J. Mair, "Estimating the effects of tunneling on existing pipelines," *Journal of Geotechnical and Geoenvironmental Engineering*, vol. 131, no. 11, pp. 1399–1410, 2005.

Research Article

Dynamic Response Analysis of Buried Drainage Pipes for Polymer Grouting Trenchless Rehabilitation under the Traveling Wave Effect

Fengyang Miao ![ORCID],[1] **Weiguo Li** ![ORCID],[2] **Jianguo Xu** ![ORCID],[1] **Zhihao Chen** ![ORCID],[3] **and Xiaoyu Feng** ![ORCID][2]

[1]*School of Water Conservancy Engineering, Zhengzhou University, Zhengzhou 450001, Henan, China*
[2]*Henan Highway Engineering Bureau Group Co. LTD, Zhengzhou 450052, Henan, China*
[3]*Zhongshui Northeast Survey Design and Research Co. LTD, Changchun 130021, Jilin, China*

Correspondence should be addressed to Jianguo Xu; jianguoxu@zzu.edu.cn

The polymer grouting nonexcavation repair technology has been widely used in the repair of underground pipeline leaks, but the seismic response to the polymer repair pipeline is currently using a consistent excitation of seismic input without considering the influence of the traveling wave effect. This paper establishes the longitudinal and transverse vibration models of the polymer grout repair pipeline considering the traveling wave effect based on the elastic foundation beam theory. The seismic input uses artificially generated random seismic waves and solves the differential equations for pipeline vibration to carry out seismic response analysis of long-buried pipelines under three conditions: normal, vacant, and polymer grouting repair. The results show that after considering the traveling wave effect, the reaction of each measuring point on the pipeline has obvious phase characteristics, and the waveform of the distant measuring point has an obvious hysteresis phenomenon; the seismic wave velocity has a great influence on the deformation of the pipeline, and the displacement amplitude of the pipeline increases with the increase of the seismic wave velocity. The peak of pipeline displacement after vacancy will increase by 100%~300% more than normal, while the difference in pipeline deformation after high polymer grouting is about 25% compared with normal, which means that the bottom vacant will have a great influence on pipeline deformation, and high polymer repair can restore the pipeline mechanical properties to normal levels.

1. Introduction

The polymer grouting repair technology is used to fill the void, seal the leakage, and lift and settle the pipeline by injecting polymer grouting material into the leaky part of the pipeline structure, and as a minimally invasive and efficient underground pipeline trenchless repair technology, this technology has been successfully applied in many underground pipeline repair projects [1–3]. Studies have also been conducted on the seismic response of polymer-repaired pipes [4–7], but the seismic inputs used in all of these studies were consistent excitation. For small-span structures, it is reasonable not to consider the spatial variation of ground shaking. However, studies have shown that the use of seismic input with consistent excitation for large-span structures such as pipelines is not practical and may lead to unreasonable seismic design [8–11]. Therefore, it is necessary to perform a nonuniform excitation seismic response analysis for polymer grouting to repair underground drainage pipes.

The variability of ground shaking includes temporal and spatial differences, mainly traveling wave effects, local site effects, and partial coherence effects with traveling-wave effects dominating [12, 13]. Therefore, this paper will consider the dynamic response of the high polymer repair pipe under the traveling wave effect and establish the vibration equation of the high polymer repair pipe considering the traveling wave effect based on the elastic foundation beam theory. The seismic input uses artificially generated random

seismic waves and then analyzes the effect of different apparent wave speeds on the traveling wave effect.

2. Solving Vibration Equations for Polymer Repaired Pipes under the Traveling Wave Effect

As shown in Figure 1, for the dynamic response of the polymer repair pipeline under the traveling wave effect, this paper assumes the underground pipeline as an infinitely long homogeneous long beam on an elastic foundation and combines the analytical model of pipe-soil-polymer interaction previously proposed by the authors [7], neglecting the internal damping of the pipeline, to obtain a computational model of the seismic response of the polymer repair pipeline.

$$m\frac{\partial^2 u(x,t)}{\partial t^2} + c\frac{\partial u(x,t)}{\partial t} + ku(x,t) - \mathrm{EA}\frac{\partial^2 u(x,t)}{\partial x^2} = ku_g(x,t) + c\frac{\partial u_g(x,t)}{\partial t}, \tag{1}$$

where m is the mass of the pipe, c is the damping factor of the surrounding medium, k is the longitudinal stiffness of the surrounding medium, EA is the axial stiffness of the pipe, $u(x,t)$ is the longitudinal displacement of the pipe, and $u_g(x,t)$ is the longitudinal ground displacement.

To solve the above-given vibration equation, the proposed static displacement method [14] is used to consider the effect of the traveling wave effect, and the longitudinal displacement of the pipe in equation (1) is decomposed as shown in equation (2), which is the proposed static displacement $u^s(x,t)$ caused by the ground motion and the dynamic displacement $u^d(x,t)$ caused by the inertia and damping of the structure, respectively.

$$u(x,t) = u^s(x,t) + u^d(x,t). \tag{2}$$

The dynamic term in equation (1) is removed to obtain the proposed static displacement ordinary differential equation.

$$ku^s(x,t) - \mathrm{EA}\frac{d^2 u^s(x,t)}{dx^2} = ku_g(x,t). \tag{3}$$

The general solution of the chi-square equation corresponding to equation (3) is

$$u^s(x,t) = Ae^{-\sqrt{k/\mathrm{EA}}x} + Be^{\sqrt{k/\mathrm{EA}}x}. \tag{4}$$

Expanding the site displacement and pipe displacement on the interval A as a cosine series leads to the special solution of equation (3) as

$$u^s(x,t) = \frac{1}{2}a_0(t) + \sum_{n=1}^{\infty} \frac{ka_n(t)}{k - \mathrm{EA}(n\pi)^2/l^2} \cos\frac{n\pi}{l}x. \tag{5}$$

2.1. Solving the Longitudinal Vibration Response Equation for Pipelines.
The underground continuous pipeline is usually very long, and when doing the actual calculation, you can take one of the pipe sections to calculate. When the length of the calculated pipe section is large enough, the influence of the boundary conditions on the middle part of the calculated pipe section is small, so the calculated pipe section can be regarded as a free boundary, and when the pipe generates longitudinal vibration, its calculation model and boundary conditions are shown in Figure 2.

Assuming that the medium around the underground pipe is uniformly distributed along the direction of the pipe axis, the longitudinal vibration equation of the pipe is shown as follows:

Adding equations (4) and (5) and substituting the boundary conditions yields the solution of the differential equation as

$$u^s(x,t) = \frac{1}{2}a_0(t) + \sum_{n=1}^{\infty} \frac{ka_n(t)}{k - \mathrm{EA}(n\pi)^2/l^2} \cos\frac{n\pi}{l}x. \tag{6}$$

Then, the dynamic term in formula (1) is proposed, and the following equation can be obtained:

$$m\frac{\partial^2 u^d(x,t)}{\partial t^2} + c\frac{\partial u^d(x,t)}{\partial t} + ku^d(x,t) - \mathrm{EA}\frac{\partial^2 u^d(x,t)}{\partial x^2} = -m\frac{\partial u_g(x,t)}{\partial t^2}. \tag{7}$$

The dynamics of displacement can be solved by the vibration superposition method [15]. Firstly, the damping term and nonflush term in equation (7) are removed, and the self-oscillation frequency and vibration shape are obtained by substituting the boundary conditions using the separation of variables method as follows:

$$\omega_n = \sqrt{\frac{n^2\pi^2 EA}{l^2 m} + \frac{k}{m}}, \tag{8}$$

$$\phi_n(x) = \cos\frac{n\pi}{l}x.$$

Then,

$$u^d(x,t) = \sum_{n=0}^{\infty} q_n(t)\phi_n(x). \tag{9}$$

Substituting the above equation into equation (7), we get

$$m \sum_{n=1}^{\infty} \frac{d^2 q_n(t)}{dt^2} \cos \frac{n\pi}{l} x + c \sum_{n=1}^{\infty} \frac{dq_n(t)}{dt} \cos \frac{n\pi}{l} x + k \sum_{n=1}^{\infty} q_n(t) \cos \frac{n\pi}{l} x$$

$$-\text{EA} \sum_{n=1}^{\infty} q_n(t) \left(\frac{n\pi}{l} \right)^2 \cos \frac{n\pi}{l} x = -mf(t) \sum_{k=0}^{N} C_k \cos(\omega_k t + \phi_k). \tag{10}$$

Decoupling equation (10) using the vibration superposition method, we obtain

$$m \sum_{n=1}^{\infty} \frac{d^2 q_n(t)}{dt^2} \cos \frac{n\pi}{l} x \cdot \cos \frac{m\pi}{l} x + c \sum_{n=1}^{\infty} \frac{dq_n(t)}{dt} \cos \frac{n\pi}{l} x \cdot \cos \frac{m\pi}{l} x + k \sum_{n=1}^{\infty} q_n(t) \cos \frac{n\pi}{l} x \cdot \cos \frac{m\pi}{l} x$$

$$- \text{EA} \sum_{n=1}^{\infty} q_n(t) \left(\frac{n\pi}{l} \right)^2 \cos \frac{n\pi}{l} x \cdot \cos \frac{m\pi}{l} x$$

$$= -mf(t) \sum_{k=0}^{N} C_k \cos(\omega_k t + \phi_k) \cdot \cos \frac{m\pi}{l} x. \tag{11}$$

Equation (11) is integrated over the interval $(0, l)$, and according to the orthogonality of the vibration pattern, we get

$$m \frac{d^2 q_n(t)}{dt^2} + c \frac{q_n(t)}{dt} + k q_n(t) - \text{EA} q_n \left(\frac{n\pi}{l} \right)^2 = -m \sum_{k=1}^{N} A \sin\left(\omega_k - \frac{\omega_k l}{c} + \phi_k + n\pi\right) - A \sin(\omega_k t + \phi_k)$$

$$+ B \sin\left(\omega_k - \frac{\omega_k l}{c} + \phi_k - n\pi\right) - B \sin(\omega_k t + \phi_k), \tag{12}$$

where $A = 1/ - \omega_k/c + n\pi/l \cdot C_k/2\omega_k^2$, $B = 1/ - \omega_k/c - n\pi/l \cdot C_k/2\omega_k^2$.

Take the first N vibration types for calculation, and after finding the corresponding a, the dynamic displacement can be approximated according to equation (9).

$$u^d(x,t) \approx \sum_{n=0}^{N} q_n(t) \phi_n(x). \tag{13}$$

Finally, the proposed static displacement and dynamic displacement are summed to obtain the displacement solution of the longitudinal vibration equation of the pipe under the traveling wave effect, and the strain and internal force of the pipe can be further obtained from the displacement.

2.2. Pipeline Transverse Vibration Response Equation Solving. The pipeline transverse vibration calculation model and boundary conditions are shown in Figure 3, and the transverse vibration equation is

Although the equations of motion and boundary conditions for longitudinal and transverse vibrations are different, the solution ideas are the same, so we will not repeat them here. By replacing a with b in the above longitudinal vibration, the proposed static displacement of the transverse vibration can be obtained as

$$m \frac{\partial^2 u(x,t)}{\partial t^2} + c \frac{\partial u(x,t)}{\partial t} + k u(x,t) + \text{EI} \frac{\partial^4 u(x,t)}{\partial x^4} = k u_g(x,t) + c \frac{\partial u_g(x,t)}{\partial t}. \tag{14}$$

$$u^s(x,t) = \frac{1}{2} a_0(t) + \sum_{n=1}^{\infty} \frac{k a_n(t)}{k + \text{EI}(n\pi)^4/l^4} \cos \frac{n\pi}{l} x. \tag{15}$$

Correspondingly, its differential equation for solving a is

$$m\frac{d^2 q_n(t)}{dt^2} + c\frac{q_n(t)}{dt} + kq_n(t) + EIq_n\left(\frac{n\pi}{l}\right)^4 = -m\sum_{k=1}^{N} A\sin\left(\omega_k - \frac{\omega_k l}{c} + \phi_k + n\pi\right) - A\sin(\omega_k t + \phi_k)$$

$$+ B\sin\left(\omega_k - \frac{\omega_k l}{c} + \phi_k - n\pi\right) - B\sin(\omega_k t + \phi_k). \tag{16}$$

3. Artificial Random Seismic Wave Generation

Since the actual seismic waves cannot match the corresponding seismic environment and site conditions, the actual seismic records are discrete and cannot be used for subsequent calculations. Therefore, the seismic wave input in this paper adopts artificially generated random seismic waves. The seismic input uses artificially generated random seismic waves, whose generation method is based on the Clough–Penzien power spectrum of a smooth ground shaking process [16], and introduces a generalized evolutionary power spectrum model of a nonsmooth ground shaking acceleration process and associated parameters. The generalized evolutionary power spectrum model fully takes into account the time-varying characteristics of the ground shaking duration, peak ground shaking acceleration, site soil circular frequency, and damping ratio, and the expression of this power spectrum density function is

$$S_a(\omega, t) = A^2(t)\frac{\omega_g^2(t) + 4\xi_g^2(t)\omega_g^2(t)\omega^2}{\left(\omega^2 - \omega_g^2(t)\right)^2 + 4\xi_g^2(t)\omega_g^2(t)\omega^2} \times \frac{\omega^4 S_0(t)}{\left(\omega^2 - \omega_j^2(t)^2 + +4\xi_j^2(t)\omega_j^2(t)\omega^2\right)},$$

$$A(t) = \left[\frac{t}{t_{\max}}\exp\left(1 - \frac{t}{t_{\max}}\right)\right]^d, \tag{17}$$

$$S_0(t) = \frac{\overline{a}_{\max}^2}{\gamma^2 \pi \omega_g(t)\left[2\xi_g(t) + 1/2\xi_g(t)\right]},$$

where $A(t)$ is called the forced modulation coefficient, $t_{\max}$ is the moment corresponding to the peak acceleration, d is the modulation coefficient shape control index, $S_0(t)$ is the spectral parameter indicating the ground vibration intensity, $\overline{a}_{\max}$ is the average peak acceleration, and γ is the equivalent peak factor. $\omega_g(t), \xi_g(t)$ are the site soil self-oscillation circle frequency and damping ratio, respectively; $\omega_j(t), \xi_j(t)$ are the filtering parameters. Site parameters and filtering parameters are linear functions of time, respectively.

For a zero-mean nonsmooth ground shaking acceleration time series $a(t)$, if its evolutionary power spectral density function is $S_a(\omega_i, t)$, the nonsmooth earthquake acceleration time series can be modeled as

$$a(t) = \sum_{i=1}^{N}\sqrt{S_a(\omega_i, t)\Delta\omega}\left[\cos(\omega_i t)X_i + \sin(\omega_i t)Y_i\right]. \tag{18}$$

The calculated response spectrum $S_a(\omega, \zeta)$ can be approximated to the design response spectrum $S_a^T(\omega, \zeta)$ by iterative correction of the amplitude spectrum according to equation (19) using the numerical analysis software calculation program.

$$S_a^{i+1}(\omega_k, t) = S_a^i(\omega_k, t) \cdot \left[\frac{S_a^T(\omega_k, \zeta)}{S_a(\omega_k, \zeta)}\right]^2. \tag{19}$$

The evolving power spectrum density function $S_a(\omega, t)$ used in this paper can be determined from the standard response spectrum of hydraulic design, and the relevant parameters can be determined according to SL203-97 "Code for Seismic Design of Hydraulic Buildings" [14]. Then, the artificial seismic waves generated based on the above process are shown in Figure 4.

4. Analysis of Calculation Results

Based on the above solution process, a calculation program was prepared using numerical analysis software, and the calculation and analysis of the example were carried out. For the calculation, the length of the pipe is 1000 m, and three measurement points are selected at 200 m, 500 m, and 800 m along the pipe axis to analyze the deformation of the pipe under normal, vacant, and repair conditions [17, 18]. A vacant is assumed to occur at the bottom of the entire pipe (approximately 1/8 of the circular area of the entire pipe), along the direction of the pipe axis, through the entire bottom of the pipe [3].

The standard spectrum of artificial random seismic wave design is determined according to SL203-97 "Seismic Design Code for Hydraulic Buildings," and the loading direction is divided into two directions: longitudinal and transverse [14]. Although the propagation velocity of seismic waves in soft soil is generally 50 m/s~250 m/s, the propagation velocity of
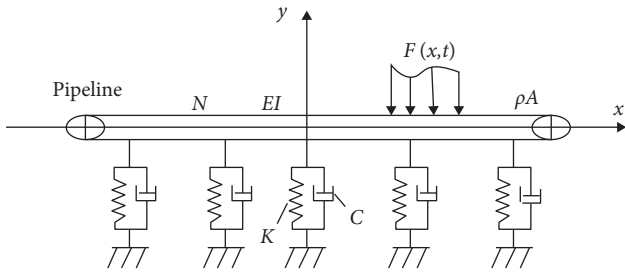
FIGURE 1: Seismic response calculation model for polymer rehabilitation pipeline.

FIGURE 2: Pipeline longitudinal vibration calculation model and boundary conditions.

FIGURE 3: Pipeline transverse vibration calculation model and boundary conditions.

FIGURE 4: Artificial seismic waves generated using numerical analysis software.

TABLE 1: The basal apparent wave velocity of the EI-Centro station.

Depth/ m	Thickness (m)	Soil	Apparent wave velocity (m/s)
4.2	4.2	Clay	122
5.6	1.2	Sand clay	122
15.7	10.1	Sandy clay-silting clay	175
21.8	6.1	Sand silt clay	213
34.8	13.0	Fine sand soil	251
42.3	7.5	Silted clay	251
45.9	3.6	Silt fine sand	251
65.5	19.6	Silted clay	305
68.5	13.0	Silt fine sand	—

TABLE 2: Calculated stiffness values for normal, vacant, and repair conditions.

Work conditions	Calculated stiffness (10^7 N/m^2)	
	Longitudinal vibration	Transverse vibration
Normal	7.13	6.33
Vacant	8.94	8.01
Polymer grouting repair	6.04	5.97

apparent wave velocity of the EI-Centro wave station is shown in Table 1 in the manuscript. Therefore, three-wave velocities of 100 m/s, 200 m/s, and 500 m/s are used to analyze the seismic waves in this paper.

The values of the medium stiffness around the pipe in the vibration equation under normal, vacant, and repair conditions can be calculated according to the equations in the previous research results [7], and the specific data can be found in Table 2, and for space reasons, the detailed solution process will not be repeated. The damping is viscous damping, and the damping ratio taken in this paper is 0.05.

4.1. Analysis of Calculation Results of Longitudinal Vibration of Pipes. Figure 5 shows the comparison of the maximum values of the longitudinal vibration displacement at the three corresponding observation points for different seismic wave velocities under three working conditions, namely, normal, decoupled, and repaired. From Figure 5(b), it can be seen that the maximum values of pipe displacements at different locations do not differ much under the action of the same seismic wave. The maximum value of displacement at the 500 m measurement point is 21.012 mm when the wave speed is 500 m/s under the vacant condition, compared with 14.461 mm at the 200 m measurement point and 15.338 mm at the 800 m measurement point. The difference is 6.551 mm and 5.674 mm, respectively, and the difference is the largest at this time, and the difference is between 1 and 4 mm for the rest of the working conditions.

For the same measurement point, when the seismic wave velocity is different, the maximum value of its longitudinal vibration displacement increases with the increase of wave

seismic waves increases with the increase of soil depth [19, 20], and the propagation velocity in bedrock increases significantly, reaching 2000 m/s~2500 m/s [21, 22]. The basic

(a)

(b)

(c)
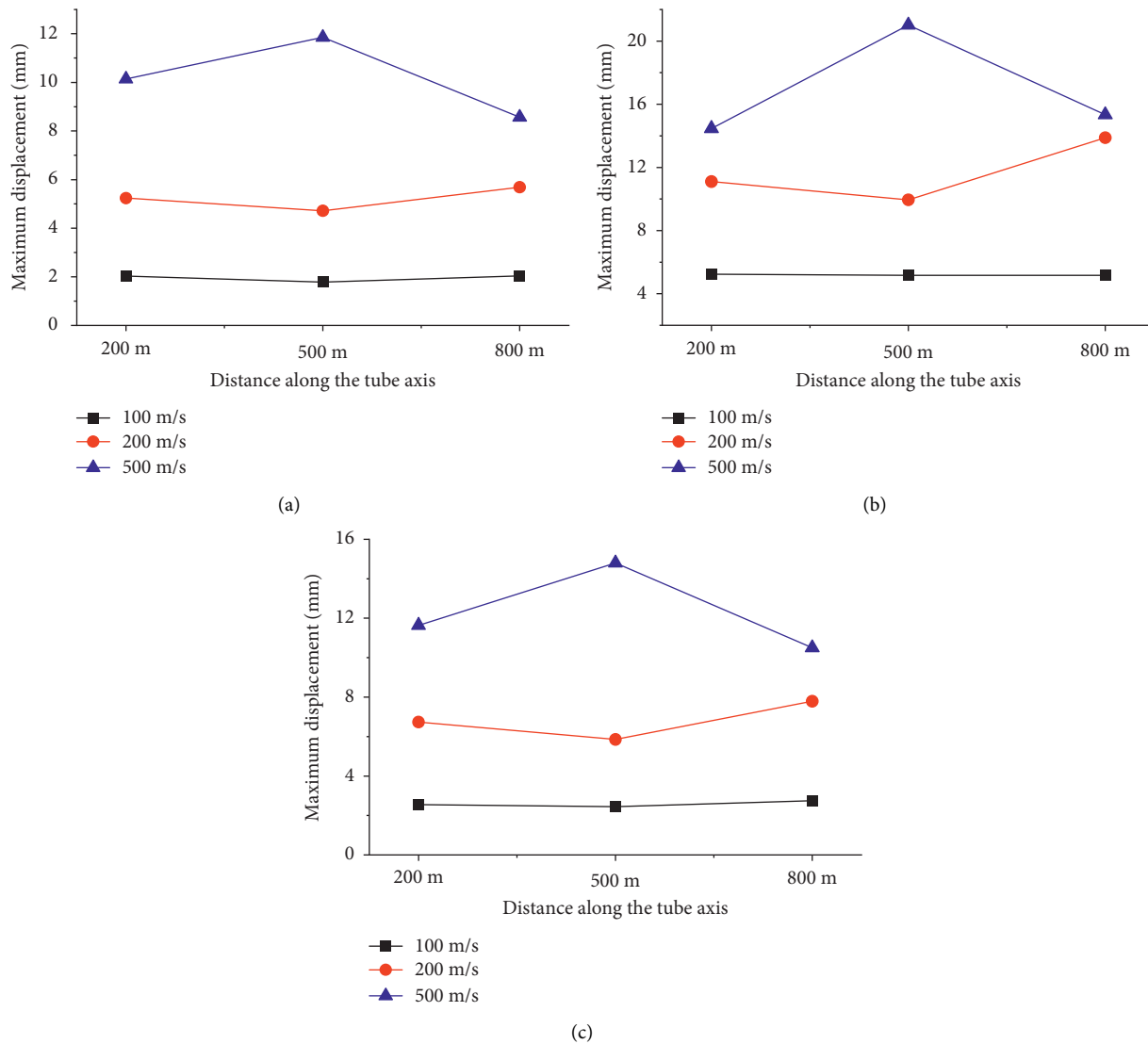
FIGURE 5: Maximum value of longitudinal vibration displacement of the pipeline under different wave velocities. (a) Normal, (b) vacant, and (c) polymer grouting repair.

velocity. From Figure 5(a), it can be seen that the maximum values of pipe displacement at 200 m of the measurement point under normal conditions are 2.030 mm, 5.240 mm, and 10.139 mm with the increase of seismic wave velocity, and the maximum values of displacement at wave velocity 200 m/s and wave velocity 500 m/s are increased by 2.58 times and 4.99 times, respectively, compared with that at wave velocity 100 m/s. Similarly, from Figure 5(c), it can be seen that the maximum values of displacement at 200 m after repair are 2.548 mm, 6.733 mm, and 11.634 mm, respectively, which are 2.64 times and 4.56 times higher compared to the wave speed of 100 m/s.

As can be seen from Figure 5, the displacement maximum value of the pipeline increases significantly for the pipeline vacant case relative to the normal burial condition of the pipeline. For example, at the 500 m measurement point, the displacement maxima of the decoupled pipe at wave velocities of 100 m/s, 200 m/s, and 500 m/s increased by 3.374 mm, 5.226 mm, and 9.156 mm, respectively, compared with normal conditions. The displacement maxima of the repaired pipeline are small compared with the normal condition. At the 500 m measurement point, the displacement maxima of the repaired pipeline with polymer are 2.442 mm, 5.856 mm, and 14.793 mm, respectively, and the errors are 20%, 21%, and 13%, respectively, compared with the displacement maxima under normal conditions at the same wave speed, which are small. From the above analysis, it can also be seen that the vacant has a greater impact on the pipeline, which will make the seismic response of the pipeline increase significantly, and the maximum value of the pipeline displacement will be significantly reduced after the repair by polymer deformation close to the longitudinal displacement deformation of the normally buried pipeline, reflecting the repair effect of polymer grouting on the pipeline vacant.

Figure 6 shows the comparison of the longitudinal vibration displacement time curves of the pipe at different positions. As can be seen from Figure 6, the trend of the

(a)

(b)

(c)
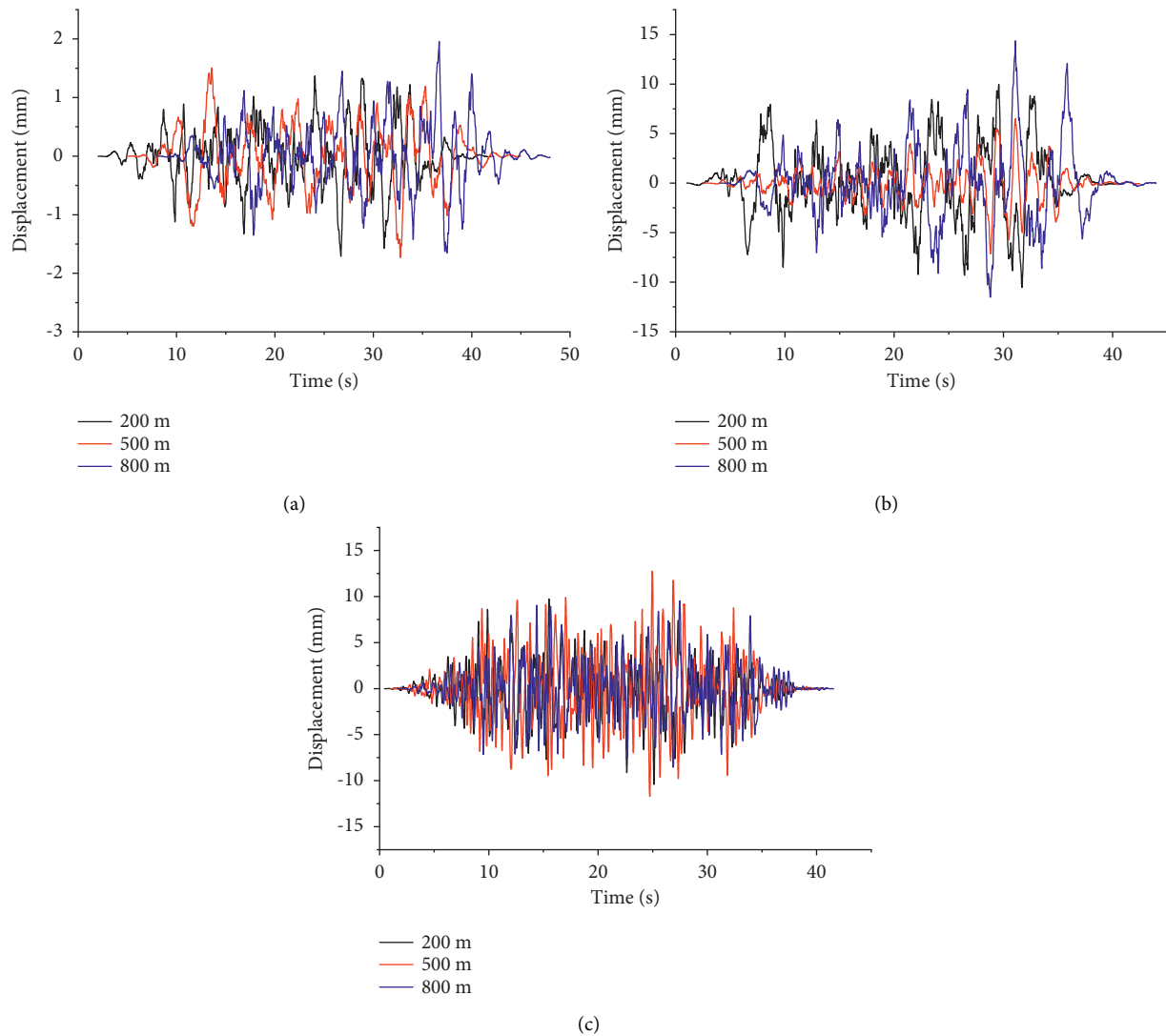
FIGURE 6: Longitudinal vibration displacement time course curves of pipes at different positions. (a) Wave speed $v = 100 \, \text{m/s}$ (normal). (b) Wave speed $v = 200 \, \text{m/s}$ (vacant). (c) Wave speed $v = 500 \, \text{m/s}$ (polymer grouting repair).

displacement time curve at different locations of the pipeline under normal, vacant, and repair conditions under the same seismic action is basically the same, while the response of each measurement point of the pipeline has obvious phase characteristics. From Figure 6(a), it can be seen that when the wave speed is 100 m/s, the displacement time curve at the measurement point 800 m has a significant lag relative to that at 200 m, and the lag time is approximately equal to the propagation time of the seismic wave between the two. This hysteresis can also be seen in Figure 6(b) for a wave speed of 200 m/s. This hysteresis is not obvious in Figure 6(c) due to the faster wave speed, which is in general agreement with the results obtained in the literature [23]. From Figure 6, it can be seen that the peak values of pipes at different locations are slightly different for the same seismic wave velocity. This is because the length of pipes used in the actual calculation is

taken as a constant value compared to the theoretical assumption of infinite length pipes, which cannot eliminate the effect of boundary effects.

Figure 7 shows the comparison of the longitudinal vibration displacement time curves of the pipe at the same position under different wave velocity conditions. From Figure 7, it can be obtained that the displacement time curves at the same location of the pipeline under normal, vacant, and repair conditions are basically of the same waveform under different wave velocity conditions, and the displacement amplitude increases with the increase of seismic wave velocity. Figure 7(a) shows the displacement time curve at 200 m under the normal condition, and the displacement maximum increases by 392% and 56% with increasing wave speed, and the displacement maximum increases by 307% and 111% at 500 m in Figure 7(b) under
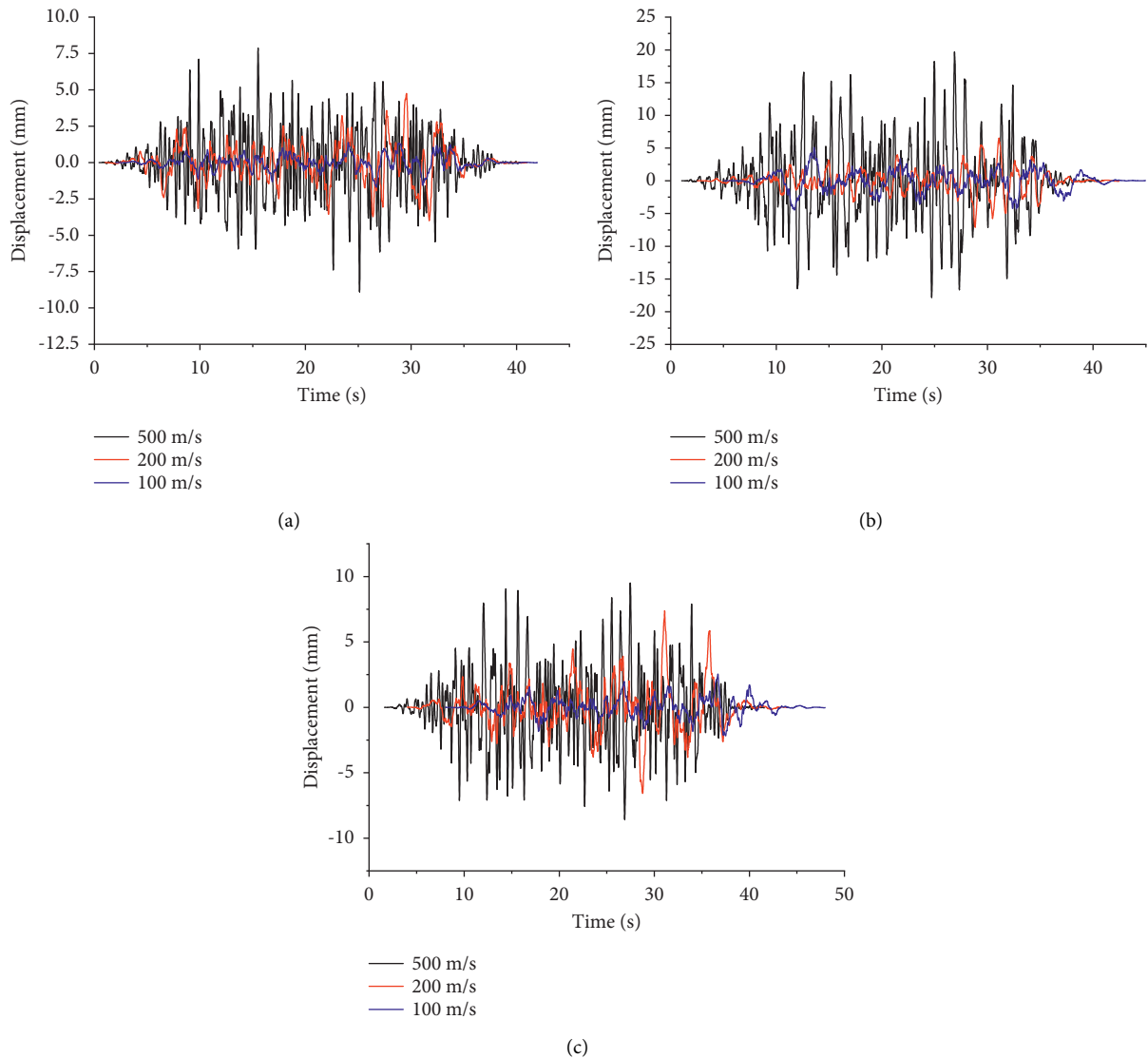
FIGURE 7: Longitudinal vibration displacement time curve of the pipeline under different wave velocity conditions. (a) Displacement time course curve at 200 m (normal). (b) Displacement time course curve at 500 m (vacant). (c) Displacement time course curve at 800 m (polymer grouting repair).

the vacant condition, and Figure 7(c) shows the displacement time curve at 800 m after restoration, which increases by 281% and 34% relative to 2.752 mm at 100 m/s and 200 m/s at 7.789 mm, an increase of 281% and 34%. It can be seen that after considering the traveling wave effect, the seismic wave velocity has a greater influence on the deformation of the pipeline.

Figure 8 shows the comparison of the longitudinal vibration displacement time curves of the pipe at the same position under three conditions: normal, vacant, and repaired. As can be seen from 8, the displacement amplitude of the dehollowed pipe will increase significantly compared to the normal condition at different locations and under different wave speed conditions, while the displacement value of the pipe will return to the normal level after repair. Figure 8(a) shows the comparison of

normal, vacant, and repaired displacement time curves at 800 m measurement point at wave speed 100 m/s. It can be seen that the displacement value of the pipe will increase overall after being vacant, and its maximum value appears at 36.7 s as 5.164 mm, at which time the displacement is 1.993 mm under the normal condition and 2.494 mm after being repaired. Compared with the normal condition, the displacement of the dehollowed pipe increases compared with the normal situation, the displacement of the decoupled pipe increases by 159%, and the displacement of the repaired pipe only increases by 25%. As shown in Figure 8(b), when the wave speed is 200 m/s, the maximum value of the displacement of the decoupled pipe at the 500 m measurement point occurs at 31.1 s as 6.975 mm, compared with the normal situation (displacement maximum value of 3.133 mm), the

(a)

(b)

(c)
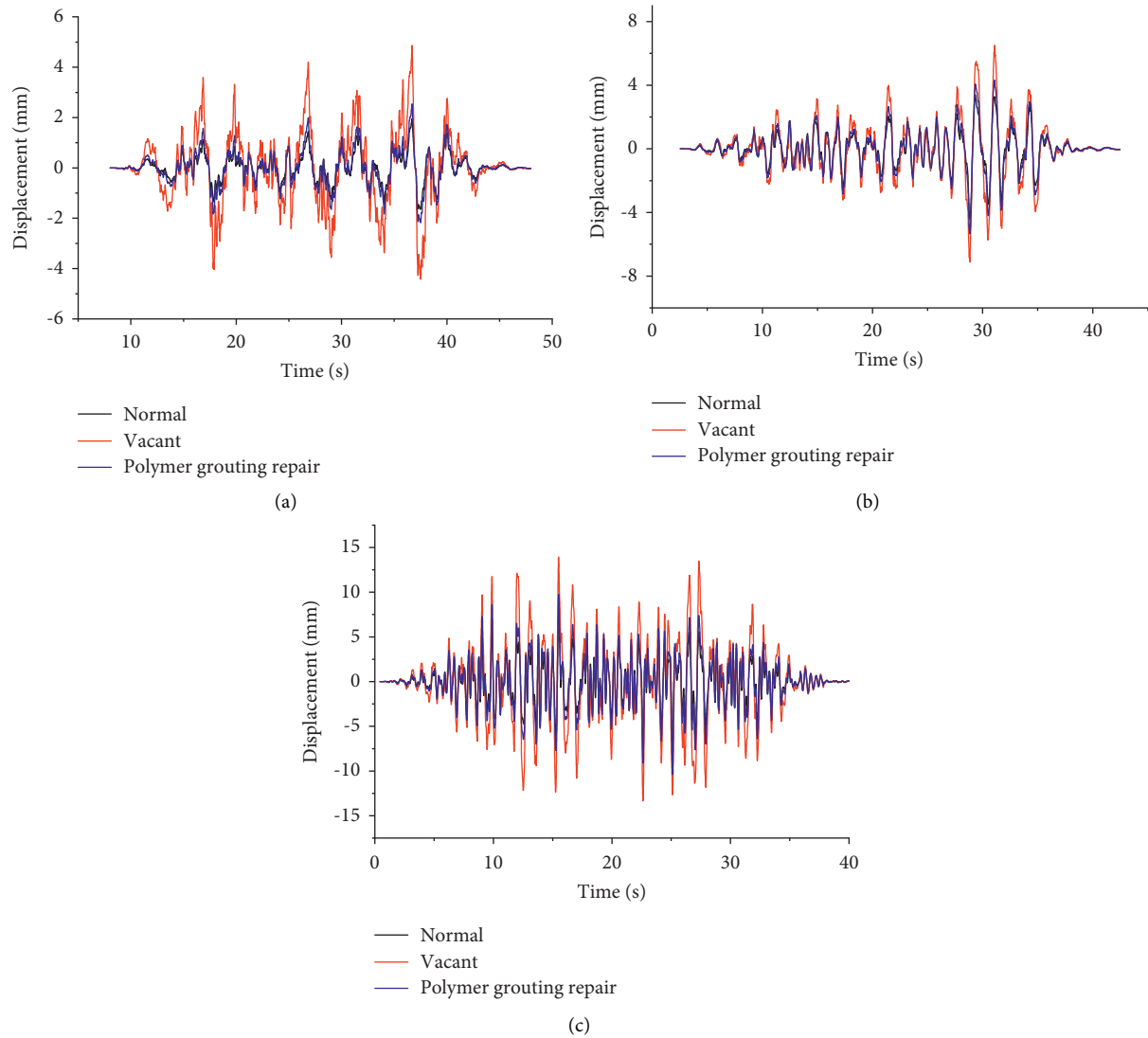
FIGURE 8: Longitudinal vibration displacement time curve of the pipe under normal, vacant, and polymer grouting repair. (a) At 800 m, wave speed $v = 100$ m/s. (b) At 500 m, wave speed $v = 200$ m/s. (c) At 200 m, wave speed $v = 500$ m/s.

displacement of the decoupled pipe increases by 123%, and the displacement of the repaired pipe (displacement maximum value of 4.352 mm) increases by 38%. Also, in Figure 8(c), the displacement of the dehollowed pipe is maximum at 15.6 s, 7.432 mm, at which time the displacement of the dehollowed pipe increases by 83% compared to the normal condition (displacement maximum of 4.045 mm), and the displacement of the repaired pipe (displacement maximum of 4.352 mm) increases by 7%. This shows that the bottom vacant will have a great influence on the deformation of the pipeline, and the deformation of the pipeline as a whole will increase under the vacant condition, while the deformation of the pipeline after polymer grouting will only increase by about 20% compared with the normal burial condition, bringing the deformation of the pipeline close to returning to the normal level.

4.2. Analysis of Pipeline Transverse Vibration Calculation Results.

Figure 9 shows the comparison of the maximum values of transverse vibration displacement at the three measurement points for different seismic wave velocities under three working conditions, namely, normal, decoupled, and repaired. As in Figure 5, it can be seen that under the transverse vibration conditions, the displacement maximum value at the three measurement points changes basically the same law as the longitudinal vibration. Under the same seismic wave action, as shown in Figure 9(b), the maximum value of displacement at the 500 m measurement point is 37.462 mm when the wave speed is 500 m/s under repair conditions, compared with 27.618 mm at the 200 m measurement point and 26.423 mm at the 800 m measurement point; the difference is 9.834 mm and 11.039 mm, respectively, at which time the difference is the maximum. The rest of the

(a)

(b)

(c)
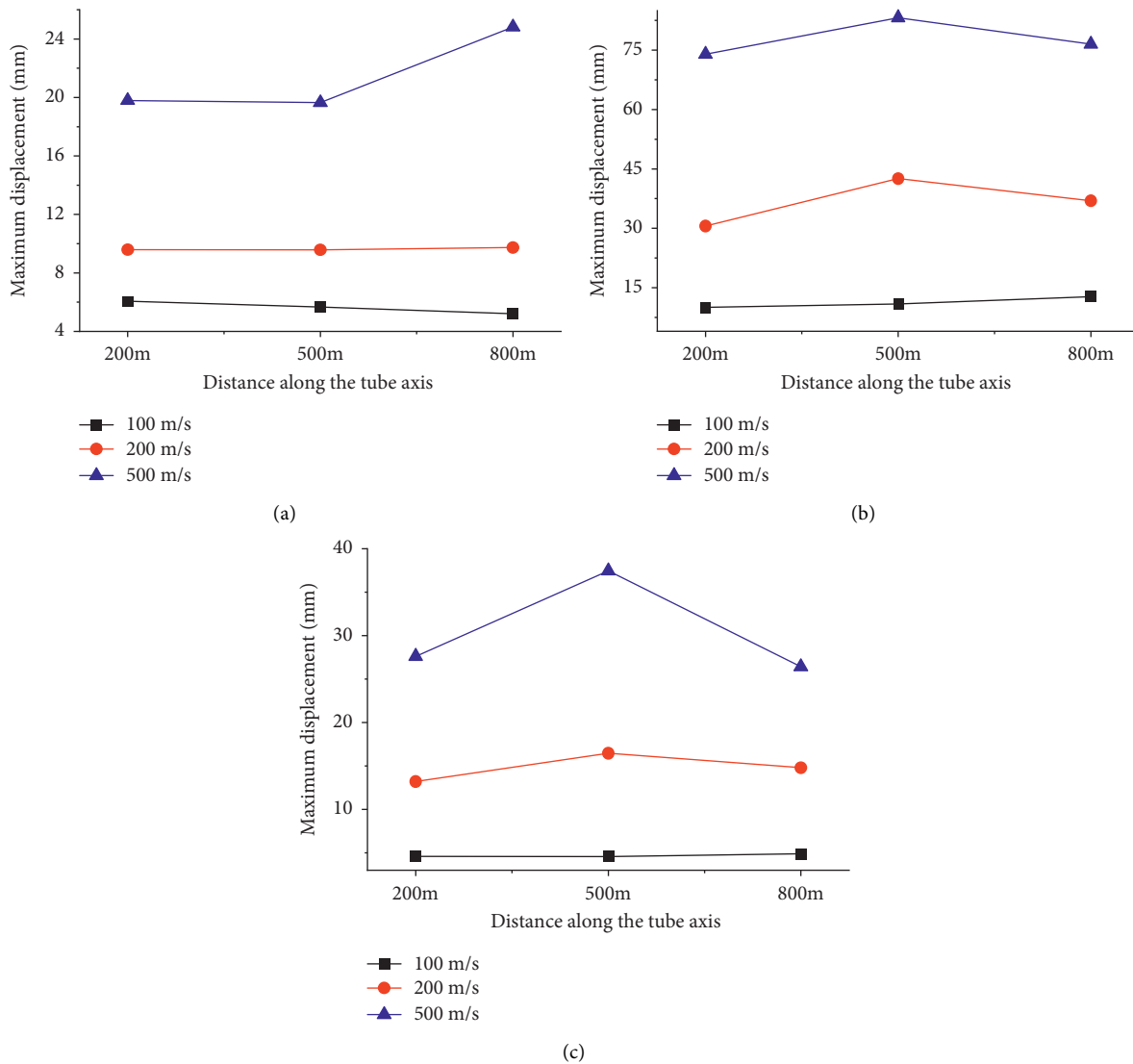
FIGURE 9: Maximum value of transverse vibration displacement of the pipeline under different wave velocities. (a) Normal, (b) vacant, and (c) polymer grouting repair.

working condition difference values are between 1 and 7 mm, and the maximum value of pipe displacement at different positions is not much different. For the same measurement point, when the seismic wave velocity is different, the maximum value of its longitudinal vibration displacement increases with the increase of wave velocity. The vacant has a greater impact on the pipeline, which will cause a significant increase in the maximum value of the pipeline displacement. After repair by polymer, the maximum value of the pipeline displacement will be significantly reduced, the error will be smaller compared with the normal condition, and the deformation will be close to the deformation in normal use.

Figure 10 shows the comparison of the time course curves of transverse vibration displacement of the pipeline at different locations. From Figure 10, it can be seen that the time course curves of transverse vibration displacement at

different locations of the pipeline under normal, vacant, and repair conditions under the action of the same earthquake also have basically the same trend, while the response of each measurement point of the pipeline has the same phase characteristics as the longitudinal vibration. From Figure 10(a), it can be seen that this hysteresis phenomenon is most obvious when the wave speed is 100 m/s. In Figure 10(c), the waveforms at different locations roughly overlap when the wave speed is 500 m/s, which shows that the hysteresis phenomenon becomes less and less obvious as the wave speed increases.

Figure 11 shows the comparison of the time course curves of transverse vibration displacement of the pipeline under different wave velocity conditions at the same location. It can be seen from the figure that the transverse vibration displacement amplitude of the pipe increases with the increase of seismic wave speed. Figure 11(c)

(a)

(b)

(c)
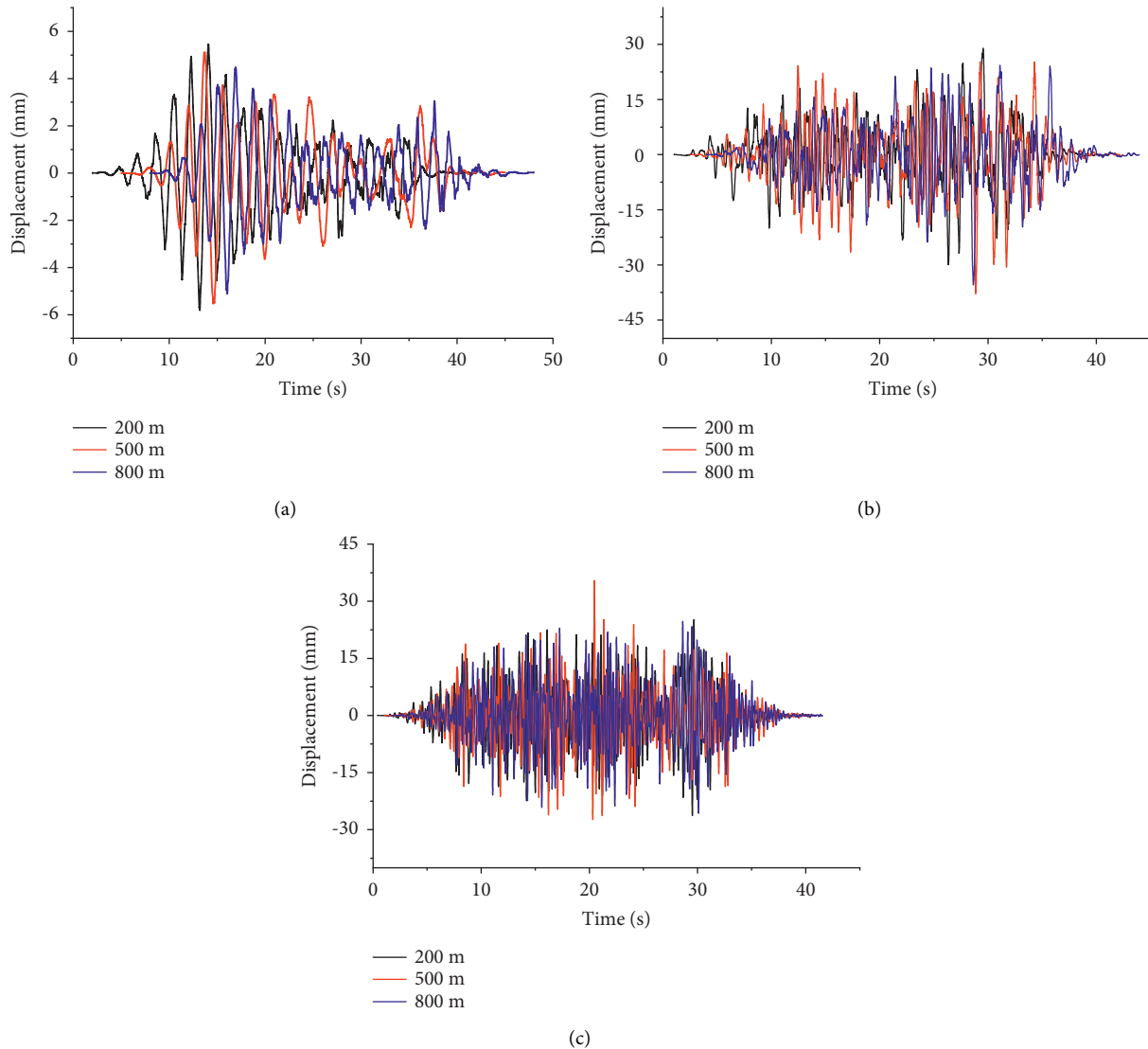
FIGURE 10: Time course curve of transverse vibration displacement of pipes at different positions. (a) Wave speed $v = 100$ m/s (normal). (b) Wave speed $v = 200$ m/s (vacant). (c) Wave speed $v = 500$ m/s (polymer grouting repair).

shows the displacement time course curve at 800 m after repair. The peak seismic displacement is the largest when the wave speed is 500 m/s, and the maximum displacement value is 26.423 mm at this time, which increases by 438% and 131% compared to 4.907 mm at 100 m/s and 11.403 mm at 200 m/s, respectively. Similarly, Figure 11(a) shows the displacement time curve at 200 m in the normal case with 257% and 166% increase in the displacement maximum and 717% and 166% increase in the displacement maximum at 500 m in Figure 11(b) in the off-air case. It can be seen that the seismic wave velocity has a large effect on the lateral deformation of the pipeline after considering the traveling wave effect.

Figure 12 shows the comparison of the lateral vibration displacement time curves of the pipe at the same position under normal, dehollowed, and repaired conditions. From Figure 12, it can be seen that the displacement amplitude of

the dehollowed pipe increases significantly compared with the normal condition at different positions and different wave velocities, while the displacement value of the rehabilitated pipe returns to the normal level. Figure 12(a) shows the comparison of normal, vacant, and repaired displacement time curves at 800 m measurement point at wave speed 100 m/s. It can be seen that the displacement value of the pipe will increase overall after being vacant, and its maximum value appears at 12.541 mm at 36.7 s, at which time the displacement is 3.993 mm under the normal condition and 4.913 mm after being repaired. Compared with the normal condition, the displacement of the dehollowed pipe increases compared with the normal situation, the displacement of the decoupled pipe increased by 214%, and the displacement of the repaired pipe increased by 23%. As shown in Figure 12(b), when the wave speed is 200 m/s, the maximum value of the displacement

(a)

(b)

(c)
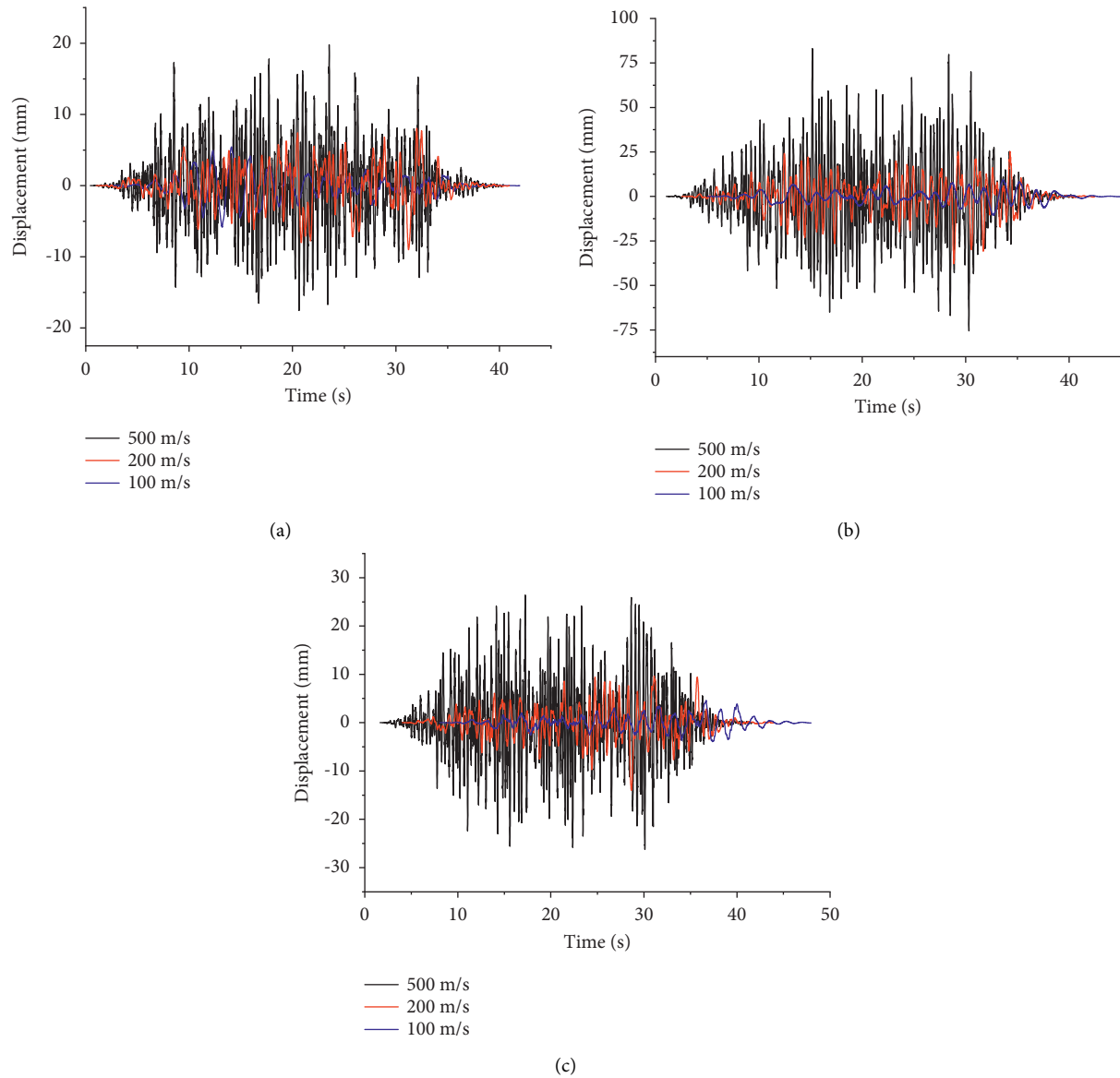
FIGURE 11: Time course curve of transverse vibration displacement of the pipeline under different wave velocity conditions. (a) At 200 m (normal). (b) At 500 m (vacant). (c) At 800 m (polymer grouting repair).

of the decoupled pipe at the 500 m measurement point appears at 28.8 s as 42.557 mm, at which time the displacement of the decoupled pipe increases by 193% compared with the normal situation (displacement maximum value of 14.506 mm), and the displacement of the repaired pipe (displacement maximum value of 11.805 mm) increases by 18%. Similarly, in Figure 12(c), the displacement of the dehollowed pipe is maximum at 24.8 s, which is 72.459 mm, at which time the displacement of the

dehollowed pipe increases by 302% compared with the normal condition (displacement maximum is 18.013 mm), and the displacement of the repaired pipe (displacement maximum is 24.352 mm) increases by 35%. It shows that the bottom of the vacant will have a great influence on the deformation of the pipe, and the overall deformation of the pipe will increase under the vacant condition, while polymer grouting can make the deformation of the pipe basically return to the normal level.

(a)

(b)

(c)
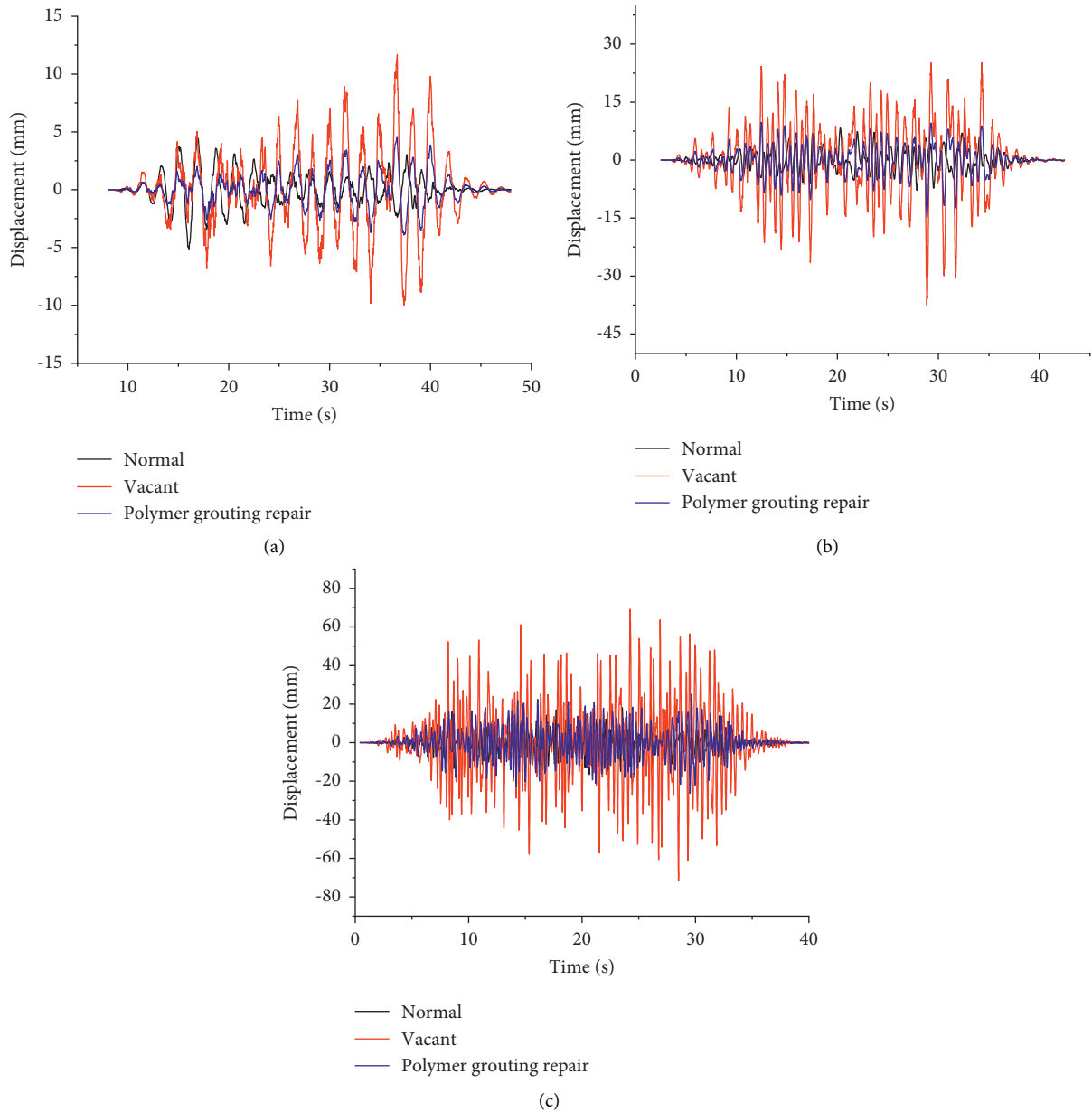
FIGURE 12: Time course curves of transverse vibration displacement of pipes under normal, vacant, and polymer grouting repair. (a) At 800 m, wave speed $v = 100$ m/s. (b) At 500 m, wave speed $v = 200$ m/s. (c) At 200 m, wave speed $v = 500$ m/s.

5. Conclusion

In this paper, the underground pipeline is assumed to be an infinitely long homogeneous long beam on an elastic foundation, and the seismic response calculation model of the polymer repair pipeline is established by combining the proposed analytical model of pipe-soil-polymer interaction and neglecting the internal damping of the pipeline, while the longitudinal and transverse vibration equations of the pipeline are solved by using the vibration superposition method, and finally, based on the above solution process, artificial random seismic waves are input to carry out the analysis of the seismic response of the pipeline under the traveling wave effect. The seismic response analysis of

pipeline polymer repair under the effect of traveling waves was carried out based on the above solution process and inputting artificial random seismic waves. The following conclusions were obtained.

(1) Under the action of the same seismic wave, the trend of the displacement time curve at different locations of the pipeline under normal, vacant, and repair conditions is basically the same, and the difference between the maximum value of positive displacement and the maximum value of negative displacement of the pipeline at different locations is not large. At the same time, the response of each measurement point of the pipeline has obvious phase

characteristics, and the waveform of the measurement point at a farther distance has an obvious hysteresis phenomenon, but with the increase of wave speed, the hysteresis phenomenon becomes less and less obvious.

(2) The displacement time curves at the same location of the pipeline under normal, decoupled, and repaired conditions are basically the same under different wave velocities, and the displacement amplitude increases with the increase of seismic wave velocity. After considering the traveling wave effect, the seismic wave speed has a greater influence on the deformation of the pipeline.

(3) The displacement amplitude of the dehollowed pipe will increase significantly compared with the normal condition under different positions and different wave speed conditions, while the maximum displacement value of the repaired pipe basically returns to the normal level. The peak displacement of the pipe after being vacant will increase by 100%~300% compared with the normal condition, while the deformation of the pipe after polymer grouting will only increase by about 20% compared with the normal condition. It can be concluded that the bottom vacant will have a great influence on the deformation of the pipe, and the pipe deformation can be nearly restored to the normal level after the repair of polymer grouting.

Data Availability

The data presented in this study are available within the main text of the article.

Conflicts of Interest

The authors declare that they have no conflicts of interest regarding the publication of this paper.

Acknowledgments

References

[1] M. S. Shi, F. M. Wang, and J. Luo, "Compressive strength of polymer grouting material at different temperatures," *Journal of Wuhan University of Technology*, vol. 25, no. 6, pp. 962–965, 2010.

[2] S. Mohammadi Esfarjani and M. Salehi, "Inspection of aboveground pipeline using vibration responses," *Journal of Pipeline Systems Engineering and Practice*, vol. 11, Article ID 04020021, 3 pages, 2020.

[3] R. Wang, F. Wang, J. Xu, Y. Zhong, and S. Li, "Full-scale experimental study of the dynamic performance of buried drainage pipes under polymer grouting trenchless rehabilitation," *Ocean Engineering*, vol. 181, pp. 121–133, 2019.

[4] M. H. Hajmohammad, M. Maleki, and R. Kolahchi, "Seismic response of underwater concrete pipes conveying fluid covered with nano-fiber reinforced polymer layer," *Soil Dynamics and Earthquake Engineering*, vol. 110, pp. 18–27, 2018.

[5] S. Alzabeebee, "Seismic response and design of buried concrete pipes subjected to soil loads," *Tunnelling and Underground Space Technology*, vol. 93, Article ID 103084, 2019.

[6] M. S. Zarei, R. Kolahchi, M. H. Hajmohammad, and M. Maleki, "Seismic response of underwater fluid-conveying concrete pipes reinforced with SiO2 nanoparticles and fiber reinforced polymer (FRP) layer," *Soil Dynamics and Earthquake Engineering*, vol. 103, pp. 76–85, 2017.

[7] J. g. Xu, Z. h. Chen, and R. Wang, "Mechanical characteristic analysis of buried drainage pipes after polymer grouting trenchless rehabilitation," *Advances in Civil Engineering*, vol. 2021, Article ID 6679412, 14 pages, 2021.

[8] L. I. Zhengying, M. U. Dejian, and D. Pengpeng, "Influence of traveling wave effect on passive seismic control of long-span bridge," *Procedia Engineering*, vol. 14, pp. 2307–2314, 2011.

[9] P. Zhang, Y. Wang, and G. Qin, "Fuzzy damage analysis of the seismic response of a long-distance pipeline under a coupling multi-influence domain," *Energies*, vol. 12, no. 1, p. 62, 2018.

[10] Z. h. Zong, R. Zhou, X. y. Huang, and Z. h. Xia, "Seismic response study on a multi-span cable-stayed bridge scale model under multi-support excitations. Part I: shaking table tests," *Journal of Zhejiang University - Science*, vol. 15, no. 5, pp. 351–363, 2014.

[11] B. Yan and G. Dai, "Seismic pounding and protection measures of simply-supported beams considering interaction between continuously welded rail and bridge," *Structural Engineering International*, vol. 23, no. 1, pp. 61–67, 2013.

[12] W. Xie, L. Sun, and M. Lou, "Shaking table test verification of traveling wave resonance in seismic response of pile-soil-cable-stayed bridge under non-uniform sine wave excitation," *Soil Dynamics and Earthquake Engineering*, vol. 134, Article ID 106151, 2020.

[13] J. B. Dai, G. D. Zhang, C. T. Hu, and K. K. Cheng, "Study on synthesis method of multipoint seismic waves for buried oil and gas pipeline in shaking table tests," *Shock and Vibration*, vol. 2021, Article ID 4624871, 8 pages, 2021.

[14] E. L. Wilson, *Three Dimensional Static and Dynamic Analysis of Structures: A Physical Approach with Emphasis on Earthquake Engineering*, Computers and Structures Incorporated, Walnut Creek, CA, USA, 1998.

[15] T. Itoh, "Damped vibration mode superposition method for dynamic response analysis," *Earthquake Engineering & Structural Dynamics*, vol. 2, no. 1, pp. 47–57, 1973.

[16] R. W. Clough and J. Penzien, *Dynamics of Structures*, pp. 121–133, McGraw-Hill, New York, 1975.

[17] D. Covas, H. Ramos, and A. B. De Almeida, "Standing wave difference method for leak detection in pipeline systems," *Journal of Hydraulic Engineering*, vol. 131, no. 12, pp. 1106–1116, 2005.

[18] H. Shamloo and A. Haghighi, "Leak detection in pipelines by inverse backward transient analysis," *Journal of Hydraulic Research*, vol. 47, no. 3, pp. 311–318, 2009.

[19] K. L. Wen, "Non-linear soil response in ground motions," *Earthquake Engineering & Structural Dynamics*, vol. 23, no. 6, pp. 599–608, 1994.

[20] E. Şafak, "Local site effects and dynamic soil behavior," *Soil Dynamics and Earthquake Engineering*, vol. 21, no. 5, pp. 453–458, 2001.

[21] A. M. Chandler, N. T. K. Lam, H. H. Tsang, and M. N. Sheikh, "Estimation of near-surface attenuation in bedrock for

analysis of intraplate seismic hazard," *Journal of Seismology and Earthquake Engineering*, vol. 7, 2005.

[22] S. Dardaei, H. Shakib, M. Khalaf Rezaei, and M. Mousavi, "Analytical and experimental seismic evaluation of confined masonry walls retrofitted by steel-fiber and polypropylene shotcrete," *Journal of Seismology and Earthquake Engineering*, vol. 16, no. 4, pp. 271–280, 2015.

[23] T. Qu and Q. Wang, "Method for solving bending vibration of underground pipeline under spatially varying seism," *Engineering Mechanics*, vol. 14, no. 03, pp. 88–96, 1997.

Research Article

Potential Roof Collapse Analysis of Tunnel Considering the Orthotropic Weak Interlayer on the Detaching Surface

Tong Xu [ID],[1] **Dingli Zhang,**[1] **Zhenyu Sun,**[1] **Lin Yu,**[1] **Ran Li,**[2] **and Jiwei Luo**[3]

[1]*Key Laboratory of Urban Underground Engineering of Ministry of Education, Beijing Jiaotong University, Beijing 100044, China*
[2]*China Tiesiju Civil Engineering Group Co., Ltd., Hefei 230023, China*
[3]*Tianjin Research Institute for Water Transport Engineering, M.O.T, Tianjin 300456, China*

Correspondence should be addressed to Tong Xu; 16115280@bjtu.edu.cn

The evaluation of the roof collapse in tunnels or cavities remains one of the most complex issues in geotechnical engineering. Taking the detaching surface of the tunnel roof collapse as an orthotropic weak interlayer, an analytical approach for determining the limit collapse range considering the arch effect of the tunnel is presented in this paper by the variation calculus. A discontinuity criterion moving from the anisotropic criterion proposed by the present authors is applied to the orthotropic interlayer. The phenomenon of sharp points in collapse blocks is further analyzed. Based on the proposed approach, illustrated examples are analyzed to investigate the effect of the strength parameters and the consideration of the collapse cusp, which show different influence laws on the range of collapse blocks. Those interesting conclusions can provide guidance for the prediction of the collapse mechanism of the tunnel.

1. Introduction

The stability problems of tunnels have always been of overriding significance in geotechnical engineering. The possible collapse of the tunnel remains one of the most challenging problems. Due to the natural uncertainties of the properties of the rock mass in situ, such as mechanical parameters and the random variability of cracks or fractures [1–8], the collapse mechanism of a cavity roof has yet to be thoroughly grasped [9]. Because the limit analysis method requires no elastic characterization and only refers to the limit behavior, this approach can obtain more rigorous results with fewer assumptions [10]. As a result, the limit analysis method is very suitable for analyzing the collapse mechanism of tunnel roofs and has been rapidly developed in recent years.

Lippmann [11] firstly applied the limit analysis method to the roof stability problems of tunnels considering the Mohr–Coulomb (M-C) criterion. For many years, the roof stability of tunnels is analyzed in this framework [10]. Guarracino and Guarracino [12] made encouraging progress with the help of plasticity theory and calculus of variations, and a closed-form solution of the collapsed outline was obtained with the Hoek–Brown (H-B) criterion considered instead of the M-C rule. Since then, many researchers furthered their work by considering various cases of cavities such as different excavation profiles [13], layered rock masses or soils [9, 14–17], the presence of the karst cave [18], the solutions for shallow tunnels [19–22] or progressive collapse [23–26], consideration of the supporting pressure [27–29], and the case considering the groundwater [30–33].

These extending works moving from the approaches of Guarracino and Guarracino [12] only focused on the H-B rule expressed in the M-C form (nonlinear). In fact, a weak interlayer may appear between the detaching surface when roof collapse occurs [34]. The rock mass at the detaching surface of the collapse zone can be taken as a weak interlayer with thin thickness, which is related to the failure mechanism of the surrounding rock [35, 36]. Under the influence of the dislocation of the rock masses, the weak interlayer exhibits different strength characteristics in the orthogonal direction. For this reason, analysis considering the

orthotropic characteristics of the weak interlayer between the detaching surface can better describe the roof collapse problems of tunnels or cavities. This consideration requires a special criterion that can describe the failure behavior of the orthotropic weak interlayer on the detaching surface.

In addition, we notice that most researchers obtained a smooth collapse curve, which can be derivable at the axis of symmetry [24]. In fact, a collapse cusp (not derivable at the axis of symmetry) is usually observed in model tests or numerical analysis [34, 37, 38], which means that the condition at the axis of symmetry should be treated with caution (Figure 1). To further explain this phenomenon, the sharp point of the collapse curve is discussed in our study. Once the assumption of a smooth curve (at the axis of symmetry) is not applied to the analysis, it becomes more difficult to get the collapse curve. As a result, we need to find a reasonable restriction as an alternative to the smooth assumption when considering the collapse cusp.

Based on the above considerations, a discontinuity yield criterion for an orthotropic interlayer that moves from a pressure-dependent, anisotropic criterion is applied in this research. Then, the theoretical formulas for the cases with and without considering the collapse cusp are deduced to figure up the collapse block. Finally, some examples are analyzed, and the discrepancy between different cases is further discussed in this paper. The results can help constitute guidance for the prediction of the collapse range of tunnels or cavities.

2. Problem Description

2.1. Orthotropic Criterion at the Velocity Discontinuity.
The orthotropic yield criterion can move from the anisotropic criterion. Given the pressure-dependent of the rock material, Caddell et al. [39] proposed an anisotropic yield criterion in the following form:

$$
\% \quad
\begin{aligned}
A_{yz}\left(\sigma_y - \sigma_z\right)^2 + A_{zx}\left(\sigma_z - \sigma_x\right)^2 + A_{xy}\left(\sigma_x - \sigma_y\right)^2 \\
+ B_{yz}\tau_{yz}^2 + B_{zx}\tau_{zx}^2 + B_{xy}\tau_{xy}^2 + K_1\sigma_x + K_2\sigma_y + K_3\sigma_z = 1,
\end{aligned}
\tag{1}
$$

where the parameters A_{yz}, A_{zx}, A_{xy}, B_{yz}, B_{zx}, B_{xy}, K_1, K_2, and K_3 characterize the properties of anisotropy. The subscript x, y, and z denote the reference axes of anisotropy. In consideration of the orthotropic materials, these parameters satisfy the following relations:

$$
A_{yz} = A_{zx}, B_{yz} = B_{zx}, B_{xy} = 2\left(A_{yz} + 2A_{xy}\right), K_1 = K_2. \tag{2}
$$

Because the detaching surface is consistent with the weak layer, we take the normal direction of the detaching surface as the z axis (Figure 2). As a result, the failure on the detaching surface only depends on σ_z, τ_{zy}, and τ_{zx}, which leads to an orthotropic yield criterion in the degenerative form:

$$
B_{zx}\left(\tau_{zx}^2 + \tau_{zy}^2\right) + K_3\sigma_z = 1. \tag{3}
$$

For the plane strain problems, the equation (3) can be further simplified as

$$
B\tau^2 + K\sigma_n = 1, \tag{4}
$$

where σ_n denotes the stress of normal direction (the compressive stress is taken as positive in this paper), and the parameters B and K can be determined according to the shear (τ_0) and tensile (σ_T) strengths of the weak interlayer on the detaching surface.

$$
B = \frac{1}{\tau_0^2}, K = -\frac{1}{\sigma_T}. \tag{5}
$$

On the basis of the above consideration, the discontinuity yield criterion at the detaching surface of velocity can be obtained as

$$
f = \tau^2 - \tau_0^2\sigma_T^{-1}\sigma_n - \tau_0^2 = 0. \tag{6}
$$

2.2. Collapse Mechanism of the Tunnel Roof.
The key point about the roof stability of tunnels or cavities is to determine the shape and range of the potential collapsing blocks (Figure 3). As it is usual, this paper considers the problem in a plane and only makes reference to the cross section of a long tunnel or cavity. The rock material is assumed to be ideally plastic, and the plastic strain rate follows the associated flow rule. Besides, strain within the collapsing body is regarded as insignificant when the roof collapse occurs (rigid-plastic behavior). Based on the above conditions, the shape of the potential collapsing region can be given by using the calculus of variations [12, 40].

In order to investigate the roof collapse on account of the gravity field and refer to the upper bound principle [41], a kinematically admissible field of vertical velocity, which fulfills the compatibility with the strain rates, must be assumed at first [42]. As shown in Figure 3, the collapse velocity $\dot{u}_v$ is in the negative direction of the y-axis, and the symmetrical collapse curve is expressed as $f(x)$. Moreover, as shown in Figure 4, the value of the vertical velocity is considered a variable that decreases from $\dot{u}$ ($x = 0$) to zero ($x = R$) linearly. As a result, the field of the variable vertical velocity can be expressed as

$$
\dot{u}_v = \dot{u}\left(1 - \frac{x}{R}\right). \tag{7}
$$

According to the geometric conditions, the plastic strain rate (the tensile strain rate is taken as negative) components in the tangential ($\dot{\gamma}$) and normal ($\dot{\varepsilon}_n$) directions can be obtained as

$$
\dot{\gamma} = -\left(1 - \frac{x}{R}\right)\left(\frac{\dot{u}}{w}\right)f'(x)\left[1 + f'(x)^2\right]^{-\frac{1}{2}},
\tag{8}
$$

$$
\dot{\varepsilon}_n = -\left(1 - \frac{x}{R}\right)(\dot{u}/w)\left[1 + f'(x)^2\right]^{-\frac{1}{2}}.
$$

(a)   (b)
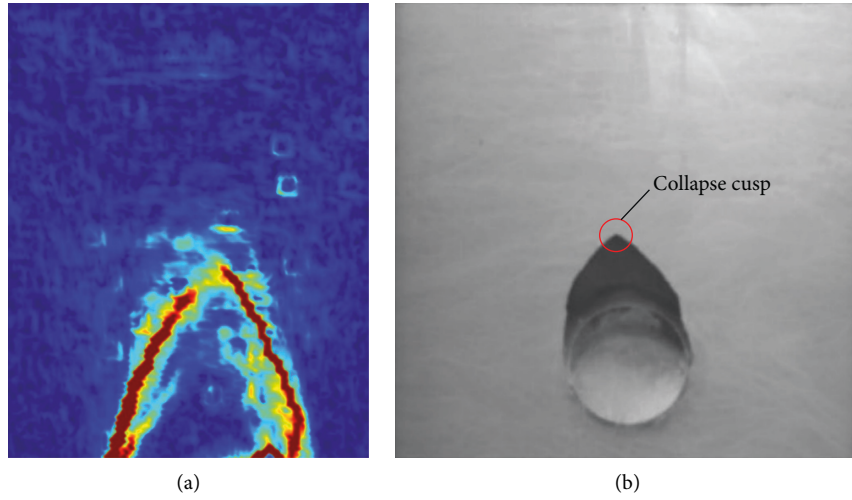
FIGURE 1: Roof collapse in (a) an active trapdoor numerical test [34]; (b) a model test [38].
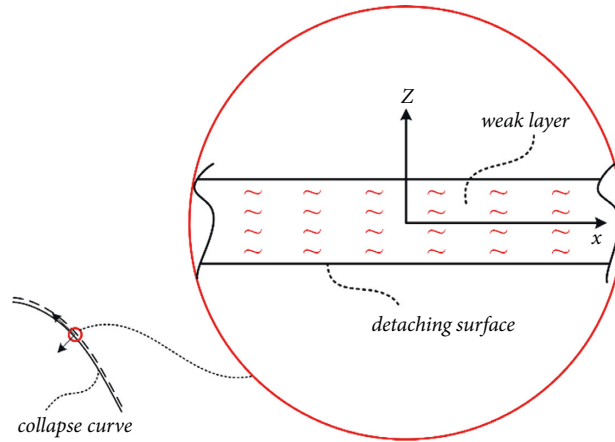
FIGURE 2: Orthotropic interlayer on the detaching surface.
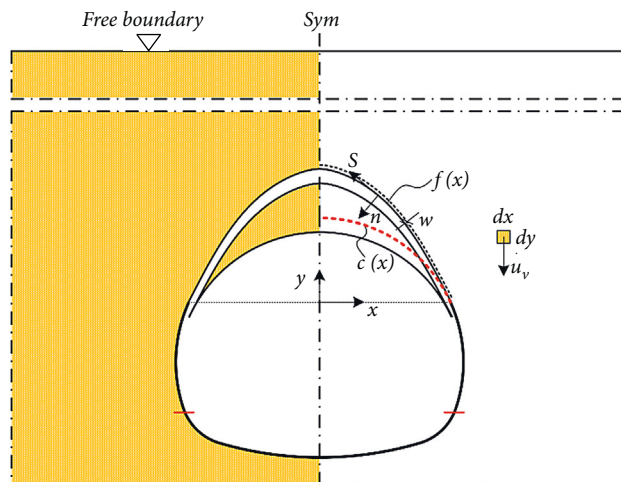
FIGURE 3: Possible collapsing area of the tunnel roof.
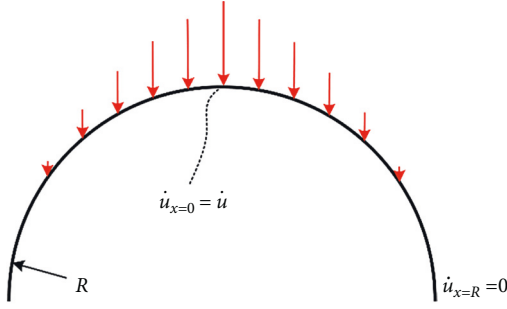
FIGURE 4: The field of the variable vertical velocity.

Coincident with the failure criterion mentioned in Section 2.1 (obeying to the associated flow rule), the plastic potential function ξ can be expressed as

$$\xi = \tau^2 - \tau_0^2 \sigma_T^{-1} \sigma_n - \tau_0^2. \tag{9}$$

Further, the plastic strain rate can also be written in the form:

$$\dot{\gamma} = \lambda \frac{\partial \xi}{\partial \tau} = 2\lambda \tau,$$

$$\dot{\varepsilon}_n = \lambda \frac{\partial \xi}{\partial \sigma_n} = -\lambda \tau_0^2 \sigma_T^{-1}. \tag{10}$$

The association of equations (7) and (9) leads to the following results:

$$\lambda = \tau_0^{-2} \sigma_T \left(1 - \frac{x}{R}\right)\left(\frac{\dot{u}}{w}\right)\left[1 + f'(x)^2\right]^{-\frac{1}{2}} \tag{11}$$

$$\tau = -\frac{\tau_0^2 \sigma_T^{-1}}{2} f'(x). \tag{12}$$

Finally, by substituting equations (10) into (6), we can obtain

$$\sigma_n = \frac{\tau_0^2 \sigma_T^{-1}}{4} f'(x)^2 - \sigma_T. \tag{13}$$

According to the equations (11) and (12), the tangential and normal stress components are expressed by using the derivative of the collapse function. Because a cusp (Figure 1) can occur in roof collapse [34, 37, 38], the stress at the axis of symmetry should be treated with caution (no derivative). In particular, the shear stresses around the collapse cusp can be described in Figure 5. Based on symmetry, the magnitude of the shear stresses in the symmetrical tilt directions at the cusp point must be equal. As a result, the inner horizontal shear stress at the axis of symmetry naturally satisfies the condition of being equal to zero, so long as the collapse curves on both sides are symmetrical to each other.

3. Analysis without Considering Collapse Cusp

Because most researchers assumed a smooth collapse curve in their studies [23, 24], the collapse curve is derivable at the axis of symmetry, which must lead to zero of derivative
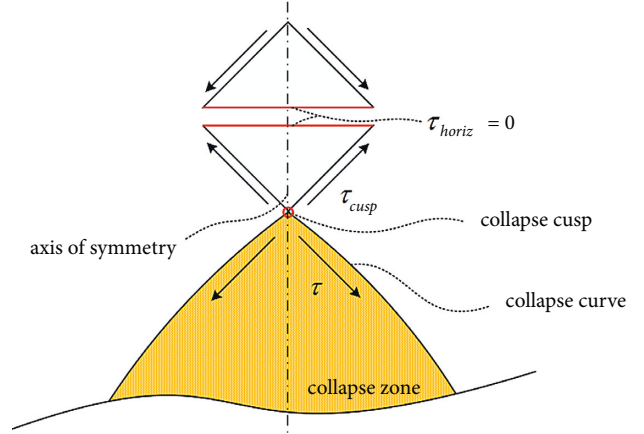
FIGURE 5: The shear stresses around the collapse cusp.

function $f'(x)$. For comparison, we analyze the collapse curve without considering collapse cusp in this section. Meanwhile, a different criterion (i.e., the orthotropic yield criterion proposed in section 2.1) is applied at the velocity discontinuity.

Associating the equations (7), (11), and (12), the dissipated power density of the internal stresses at the discontinuity ($\dot{D}$) is expressed as

$$\dot{D} = \sigma_n \dot{\varepsilon}_n + \tau \dot{\gamma}$$

$$= \left\{ \left(\frac{\tau_0^2 \sigma_T^{-1}}{4} f'(x)^2 + k\sigma_T \right) \Big/ \left(w\sqrt{1 + [f'(x)]^2} \right) \right\} \left(1 - \frac{x}{R}\right)\dot{u}. \tag{14}$$

Besides, the power density of the applied loads is

$$\dot{W}_e = \gamma[f(x) - c(x)]\left(1 - \frac{x}{R}\right)\dot{u}, \tag{15}$$

where γ denotes the gravity per unit volume of the rock mass.

Here, we consider the right half of the symmetrical block (with respect to the y-axis). The total dissipated power of the collapse system is further deduced as

$$\dot{U} = \int_0^L \dot{D}w\sqrt{1 + [f'(x)]^2}dx - \int_0^L \dot{W}_e dx$$

$$= \int_0^L F[f(x), f'(x), x]\dot{u}dx, \tag{16}$$

where the $F[f(x), f'(x), x]$ can be expressed as

$$F[f(x), f'(x), x] =$$

$$\left\{ \frac{\tau_0^2 \sigma_T^{-1}}{4} f'(x)^2 + \sigma_T - \gamma[f(x) - c(x)] \right\} \left(1 - \frac{x}{R}\right)\dot{u}. \tag{17}$$

Because the effective collapse curve can be obtained when the total dissipation power makes a minimum [13], the problem can be solved by using the calculus of variations. In order to obtain an extremum of the total dissipated power $\dot{U}$ over the interval of 0-L, the functional F must satisfy Euler's equation:

$$\delta \dot{U} = 0 \Rightarrow \frac{\partial F}{\partial f(x)} - \frac{d}{dx}\left(\frac{\partial F}{\partial f'(x)}\right) = 0. \tag{18}$$

From equation (14), we can deduce that

$$\frac{\partial F}{\partial f(x)} = -\gamma\left(1 - \frac{x}{R}\right)\dot{u}, \frac{\partial F}{\partial f'(x)}$$

$$= \frac{1}{2}\tau_0^2 \sigma_T^{-1} f'(x)\left(1 - \frac{x}{R}\right)\dot{u}, \tag{19}$$

$$\frac{d}{dx}\left(\frac{\partial F}{\partial f'(x)}\right) = \frac{1}{2}\tau_0^2 \sigma_T^{-1}\left[f''(x)\left(1 - \frac{x}{R}\right) - \frac{1}{R}f'(x)\right]\dot{u}.$$

By substituting equations (16) into (15), it is

$$\left\{-\gamma\left(1 - \frac{x}{R}\right) - \frac{1}{2}\tau_0^2 \sigma_T^{-1}\left[f''(x)\left(1 - \frac{x}{R}\right) - \frac{1}{R}f'(x)\right]\right\}\dot{u} = 0. \tag{20}$$

Integrating the equation (17), we can obtain the first derivative of $f(x)$ as follows:

$$f'(x) = \gamma\tau_0^{-2}\sigma_T\left(R - x - \frac{R^2}{R - x}\right) + \frac{C_1 R}{R - x}. \tag{21}$$

Here, C_1 is an unknown parameter which needs to be further determined. Similar to existing studies, $f'(x = 0)$ should be equal to zero because a smooth symmetrical collapse curve is assumed in this section, which results in $C_1 = 0$. Then, the collapse curve $f(x)$ can be deduced by integrating the equation (18):

$$f(x) = \gamma\tau_0^{-2}\sigma_T\left(Rx - \frac{1}{2}x^2 + R^2 \ln (R - x)\right) + C_2, \tag{22}$$

where C_2 is a pending parameter. Considering an implicit constraint $f(x = L) = 0$, we can obtain that

$$C_2 = -\gamma\tau_0^{-2}\sigma_T\left(RL - \frac{1}{2}L^2 + R^2 \ln (R - L)\right), \tag{23}$$

$$c(x) = \sqrt{R^2 - x^2} - \sqrt{R^2 - L^2}. \tag{24}$$

Then, L can be further determined by equating the total dissipated power to zero. Substituting equations (15) and (20)–(23) into (14), we can obtain the equation which L yields. It is

$$\frac{\gamma^2 \sigma_T R^3}{4\tau_0^2}\left\{\frac{L}{R} + \frac{1}{2}\left(\frac{L}{R}\right)^2 - \left(\frac{L}{R}\right)^3 + \frac{1}{4}\left(\frac{L}{R}\right)^4 - \ln\left(\frac{R}{R - L}\right)\right\}$$

$$- \gamma\left\{\frac{R^2}{3} - \frac{R^2}{2}\arcsin\left(\frac{L}{R}\right) + \frac{R}{6}\left[\frac{3L}{R} - \left(\frac{L}{R}\right)^2 - 2\right](R^2 - L^2)^{\frac{1}{2}}\right\}$$

$$+ \frac{\sigma_T L}{2}\left(2 - \frac{L}{R}\right) = 0 \tag{25}$$

Note that equation (23) can be easily solved by using the numerical method. After L is obtained, the collapse curve is finally written as

$$f(x) = \begin{cases} \gamma\tau_0^{-2}\sigma_T\left(R(x - L) + \frac{1}{2}(L^2 - x^2) + R^2 \ln\left(\frac{R - x}{R - L}\right)\right), & (x \geq 0) \\ \\ \gamma\tau_0^{-2}\sigma_T\left(R(-x - L) + \frac{1}{2}(L^2 - x^2) + R^2 \ln\left(\frac{R + x}{R - L}\right)\right), & (x < 0) \end{cases}. \tag{26}$$

4. Analysis Considering Collapse Cusp

When a possible collapse cusp (Figure 5) is considered in the collapse analysis, the condition at the axis of symmetry should be handled with care due to no derivative. As a result, C_1 in equation (19) cannot be simply determined by equating $f'(x = 0)$ with zero. So, $f(x)$ coming from equation (18) should be written as

$$f(x) = \gamma\tau_0^{-2}\sigma_T\left(Rx - \frac{1}{2}x^2 + R^2 \ln (R - x)\right)$$
$$- C_1 R \ln (R - x) + C_2. \tag{27}$$

Then, the pending parameter C_2 can be deduced by considering $f(x = L) = 0$. It results

$$C_2 = -\gamma\tau_0^{-2}\sigma_T\left(RL - \frac{1}{2}L^2 + R^2 \ln (R - L)\right) + C_1 R \ln (R - L). \tag{28}$$

Substituting equations (17), (24), (27), and (28) into (14) and equating the total dissipated power to zero, C_1 and L yield

$$\frac{\gamma^2 \sigma_T R^3}{4\tau_0^2}\left\{\frac{L}{R} + \frac{1}{2}\left(\frac{L}{R}\right)^2 - \left(\frac{L}{R}\right)^3 + \frac{1}{4}\left(\frac{L}{R}\right)^4 - \ln\left(\frac{R}{R - L}\right)\right\}$$

$$- \frac{\gamma R^2}{6}\left\{\begin{array}{c} 2 - 3\arcsin\left(\dfrac{L}{R}\right) \\ \\ + \left[\dfrac{3L}{R} - \left(\dfrac{L}{R}\right)^2 - 2\right]\left(1 - \left(\dfrac{L}{R}\right)^2\right)^{\frac{1}{2}} \end{array}\right\} \tag{29}$$

$$+ \frac{\sigma_T L}{2}\left(2 - \frac{L}{R}\right) + \frac{C_1^2 \tau_0^2 R}{4\sigma_T}\ln\left(\frac{R}{R - L}\right) = 0.$$

In addition, the fracturing azimuth is related to the friction angle (φ) of the surrounding rock. Taking a stress element at the collapse cusp of the tunnel and considering the friction angle (Figure 6), we can get the angle between directions of the fracture and maximum principal stress (the horizontal and vertical shear stresses, i.e., τ_{horiz} and τ_{verti}, are zero at the axis of symmetry) as ($\pi/4 - \varphi/2$). Then, the one-sided derivative $f'_+(x)$ can be expressed as
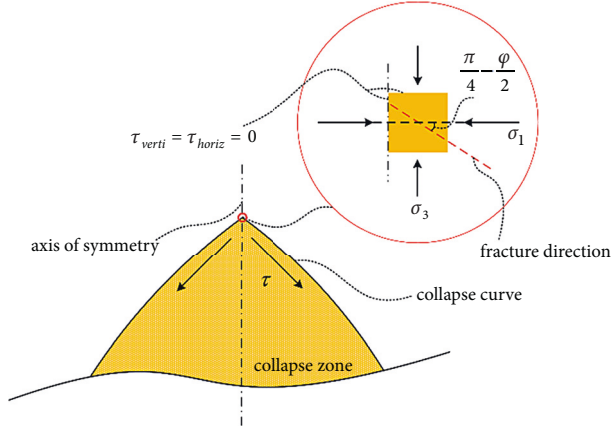
FIGURE 6: Microdescription of the fracture direction at the collapse cusp.
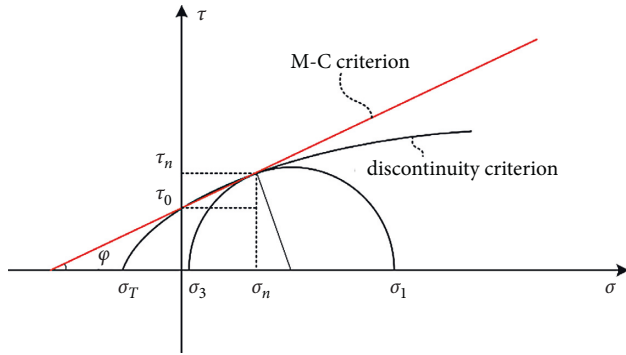
FIGURE 7: Acquisition of the friction angle by applying the M-C criterion.

$$f'_+ (x = 0) = C_1 = -\tan\left(\frac{\pi}{4} - \frac{\varphi}{2}\right). \tag{30}$$

The friction angle corresponding to the M-C criterion at the collapse cusp can be described in Figure 7. Considering

* variation of method by Fraldi and Guarracino
— no collapse cusp
— with collapse cusp

FIGURE 8: Comparison between cases considering and not considering the collapse cusp.

equation (30) and the approximate geometric conditions of σ_n and τ, the friction angle φ yields

$$\tan\varphi \tan^2\left(\frac{\pi}{4} - \frac{\varphi}{2}\right) - 2\tan\left(\frac{\pi}{4} - \frac{\varphi}{2}\right) \\ + 4\tau_0^2 \sigma_T \left(\tau_0 - \sigma_T \tan\varphi\right) = 0. \tag{31}$$

Finally, by considering equations (29), (30), and (31) together, we can get C_1 and L numerically. Then, the collapse curve considering a collapse cusp at the axis of symmetry ($x = 0$) can be written as

$$f(x) = \begin{cases} \gamma\tau_0^{-2}\sigma_T\left(R(x-L) + \frac{1}{2}\left(L^2 - x^2\right) + R^2\ln\left(\frac{R-x}{R-L}\right)\right) - C_1 R\ln\left(\frac{R-x}{R-L}\right), & (x \geq 0) \\ \\ \gamma\tau_0^{-2}\sigma_T\left(R(-x-L) + \frac{1}{2}\left(L^2 - x^2\right) + R^2\ln\left(\frac{R+x}{R-L}\right)\right) - C_1 R\ln\left(\frac{R+x}{R-L}\right), & (x < 0) \end{cases} \tag{32}$$

5. Examples and Discussion

5.1. The Discrepancy between Different Cases. In the preceding sections, two different analytical results are obtained by considering and not considering the collapse cusp, respectively. The two results obtained under different conditions are compared through an example. The parameters involved in the example are $\tau_0 = 20$ kPa, $\sigma_T = 22$ kPa, $\gamma = 25$ kN/m³, and $R = 3$ m. As a result, the comparison between these two analytical results of the collapse curve is shown in Figure 8.

The results indicate that the collapse curve obtained by considering the collapse cusp is higher than that obtained without considering the collapse cusp. According to the analytical results obtained in this paper, the height of the collapse block can increase by 0.78 m when considering the collapse cusp in the analysis. The span of the collapse curve does not change whether the cusp is considered or not. Due to the increase in the collapse height, the weight of the collapse block will also increase. The gravity of the collapse block can be calculated by using the following equation:
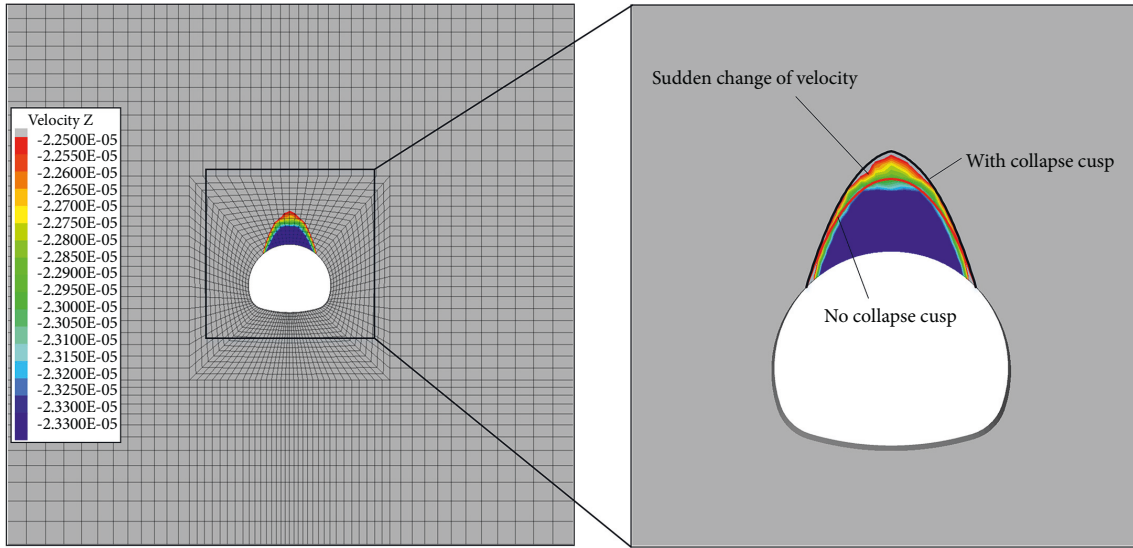
FIGURE 9: Comparison of collapse block shapes in terms of vertical velocities.

(a)

(b)
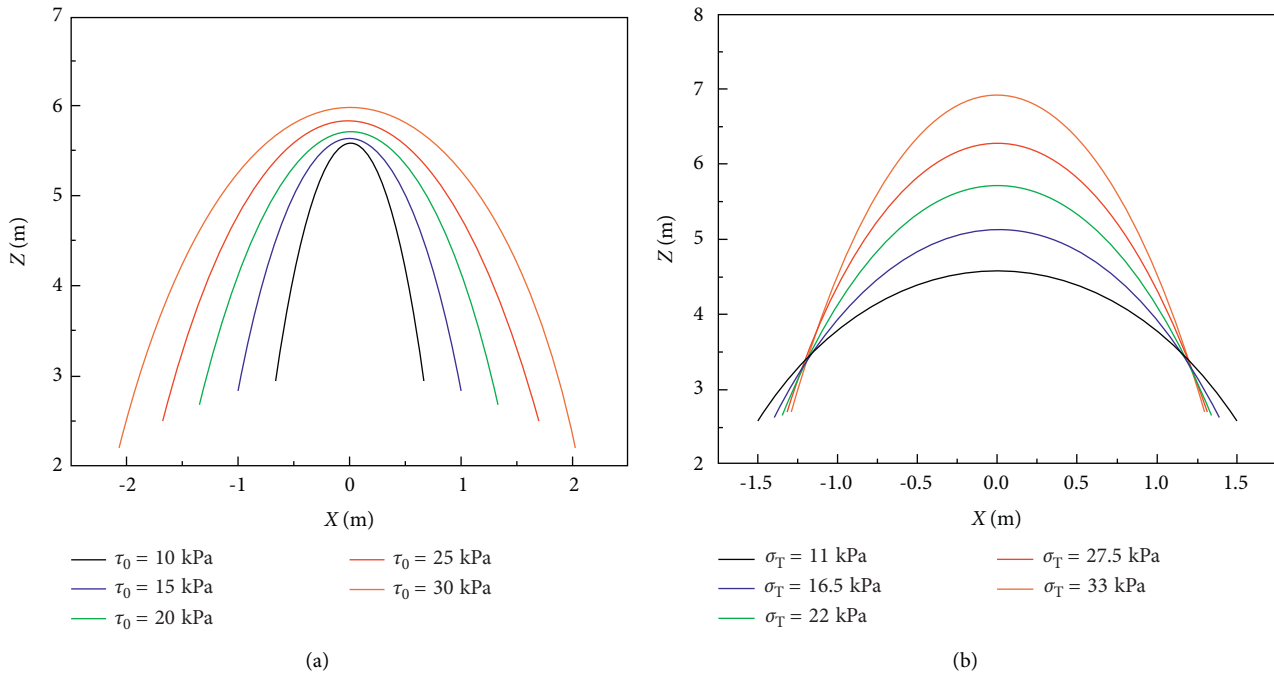
FIGURE 10: Effects of strength parameters involved in our analysis on the potential collapse of the tunnel roof without considering the collapse cusp: (a) shear strength; (b) tensile strength.

$$P = 2 \int_0^L \gamma [f(x) - c(x)] dx. \tag{33}$$

Substituting equations (24) and (30) into (31), respectively, we can easily calculate the gravity corresponding to the collapse block for both cases. The results show that the gravity obtained by considering the collapse cusp is increased by 23% compared to the gravity obtained without considering the collapse cusp. Therefore, taking the collapse cusp at the axis of symmetry into account when predicting the collapse block can help ensure the safety of the tunnel roof.

5.2. Comparison with Numerical Analysis. A numerical analysis has been performed to further verify the above analyses. The numerical parameters are consistent with those mentioned in Section 5.1. The M-C friction angle can be calculated from equation (29). The results for the example in terms of vertical velocities have been obtained by FLAC3D. The collapse block described the sudden change of vertical velocities as shown in Figure 9.

By comparing the collapse block shapes as shown in Figure 9, it is worth highlighting the similarity of the collapse block shape from numerical analysis to that obtained by the proposed analytical method. Both analytical results can

(a)

(b)

(c)
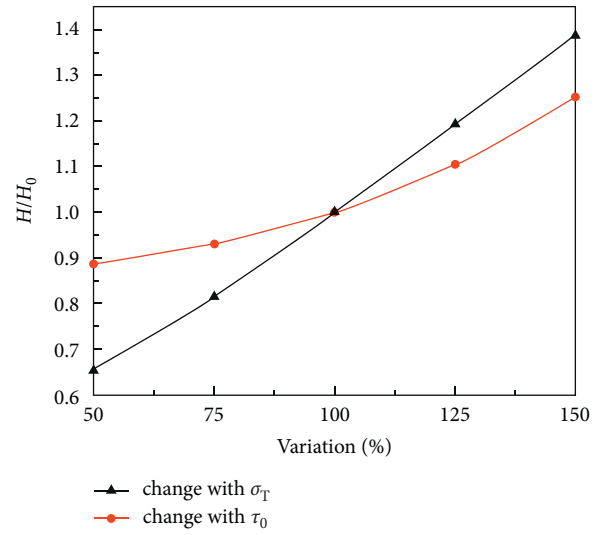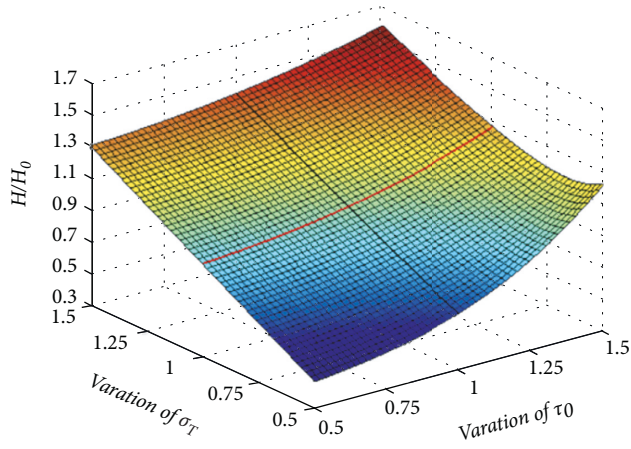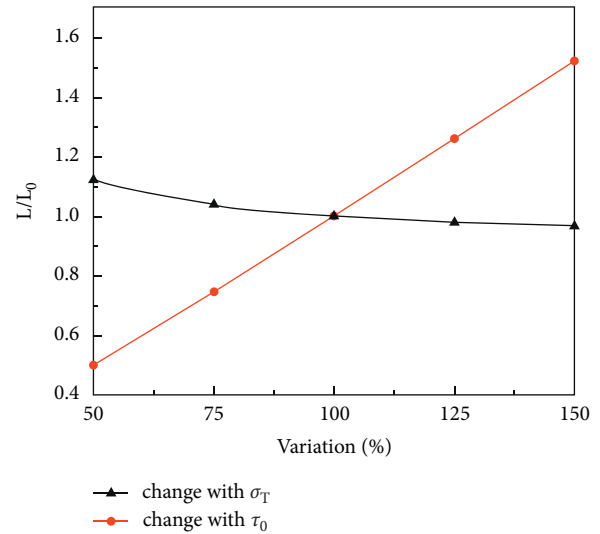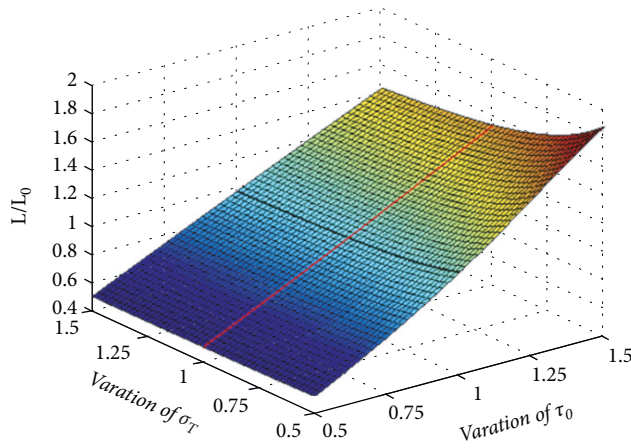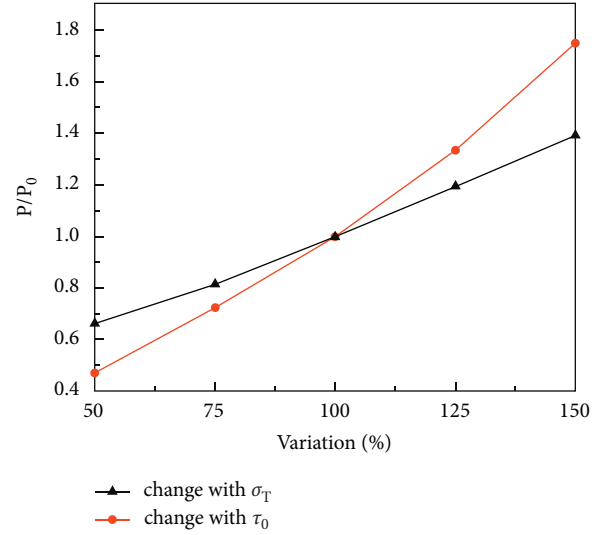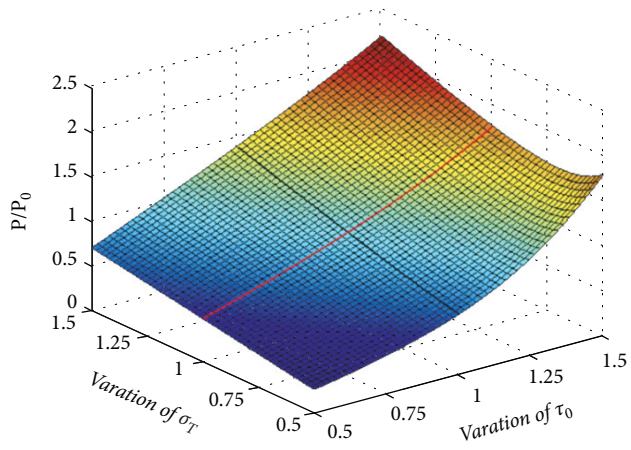
FIGURE 11: Comparison of the influences of shear and tensile strengths on (a) H/H_0; (b) L/L_0; (c) P/P.

(a)

(b)
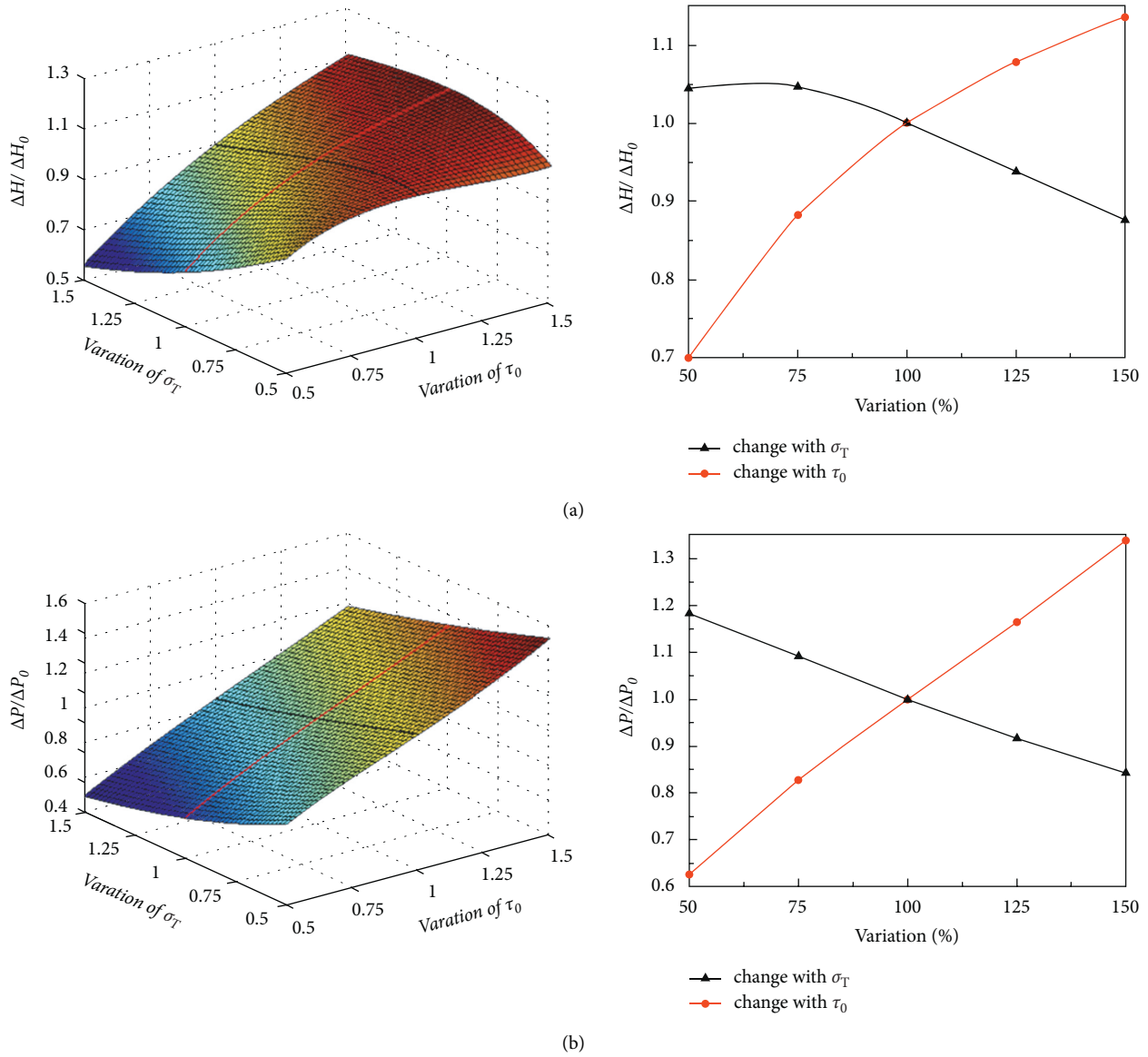
Figure 12: Comparison of the influences of shear and tensile strengths on the discrepancy between considering and not considering collapse cusp: (a) $\Delta H/\Delta H_0$; (b) $\Delta P/\Delta P_0$.

describe the collapse block shape well. As described in Section 5.1, the analytical result will lead to a wider range of collapse blocks when considering the phenomenon of sharp points in roof collapse behavior.

5.3. Influence of Strength Parameters of the Weak Interlayer. In the process of predicting the potential collapse of the tunnel roof, the shear and tensile strengths of the weak interlayer on the detaching surface are involved in our analysis. In order to investigate the influence of these two important parameters, we first discuss the different cases without considering the collapse cusp. Figures 10(a) and 10(b) show the different results considering different values of the shear and tensile strengths, respectively.

Figure 10(a) shows that the collapse curves obtained from our proposed analytical result are significantly affected by the shear strength of the weak interlayer on the detaching surface. The width and the height of the collapse block increase as the shear strength increases. Obviously, with the increase in shear strength, a greater gravity of surrounding rock can be maintained in the short term, but it also means that once the collapse occurs, there will be a wider range of primary failures.

Figure 10(b) shows that the collapse curves obtained from our proposed analytical result are also significantly affected by the tensile strength of the weak interlayer on the detaching surface. The height of the collapse block increases as the tensile strength increases. However, the width of the collapse block decreases as the tensile strength increases, which is different from the effect of the shear strength. Similar to the influence of shear strength, although the increase in tensile strength may maintain a greater gravity of surrounding rocks, there will be a wider range of primary failure once the collapse occurs.

Furthermore, in order to compare the different effects of shear and tensile strengths on the collapse block, the changes in height, width, and gravity of the collapse block are shown in Figures 11(a), 11(b), and 11(c), respectively. The example described in Section 5.1 is taken as the original case. By comparing the change rates of each index with different strength parameters, we can find that the height of the collapse block is more sensitive to the change in tensile strength. However, the width and the gravity of the collapse block are more sensitive to the change in shear strength.

As described in Section 5.1, the height and weight of the collapse block increase when considering the collapse cusp compared to those without considering the collapse cusp, while the span of the collapse curve does not change whether the cusp is considered or not. As a result, when considering the collapse cusp, only the changes in the collapse block height (ΔH) and gravity (ΔP) relative to the results without considering the collapse cusp are discussed. Figure 12 shows the comparison of the influences of shear and tensile strengths on the discrepancies of the collapse block height and gravity.

According to Figure 12, the discrepancies in the collapse block height and gravity between the two cases generally decrease with the increase in the tensile strength. On the contrary, the discrepancies in the collapse block height and gravity between the two cases increase with the increase in the shear strength. It is worth noting that these changes are more sensitive to the change of shear strength than the change of tensile strength, which is of directive functions when considering the effect of the consideration of the collapse cusp.

6. Conclusions

By using the orthotropic yield criterion which moves from the anisotropic criterion proposed by Caddell et al. [39] for the rock material, an exact solution to tunnel roof collapse has been obtained with the help of the traditional plasticity theory and the calculus of variations. In order to further illustrate the impact of collapse cusps which have been observed in previous studies [34, 37, 38], two different cases according to whether the collapse cusp is considered are analyzed in this paper. Our new theoretical results lead to the following conclusions:

(1) Taking the detaching surface of the tunnel roof collapse as an orthotropic weak interlayer, the theoretical formulas figuring up the collapse block are obtained with and without considering the collapse cusp, respectively. A case analysis shows that considering the collapse cusp can lead to a higher range of collapse blocks.

(2) The strength parameters of the weak interlayer have a significant impact on the range of collapse blocks. The shear and tensile strength have similar effects on the height of the collapse block, but their effects on the width have the opposite trend. Moreover, because the increase in shear and tensile strengths may maintain a greater gravity of surrounding rocks,

there will be a wider range of primary failures once the collapse occurs. By sensitivity analysis, we can find that the height of the collapse block is more sensitive to the change in tensile strength, but the width and the gravity of the collapse block are more sensitive to the change of shear strength.

(3) The discrepancies between the two cases according to whether the collapse cusp considered are related to the strength parameters. The discrepancies between the two cases generally decrease with the increase in the tensile strength but increase with the increase in the shear strength. These changes are more sensitive to the change of shear strength than the change of tensile strength, which is of directive functions when considering the effect of the consideration of the collapse cusp.

Our theoretical results can provide guidance on the collapse mechanism in tunnels or natural cavities, especially they can explain the phenomenon of sharp points in collapse blocks. Moreover, based on our proposed approach, many extensions including various cases such as layered rock masses and the presence of the karst cave can be further studied in future research.

Data Availability

All data used to support the findings of this study are included within the article.

Conflicts of Interest

The authors declare that there are no conflicts of interest regarding the publication of this paper.

Acknowledgments

References

[1] Z. Chu, Z. Wu, Q. Liu, B. Liu, and J. Sun, "Analytical solution for lined circular tunnels in deep viscoelastic burgers rock considering the longitudinal discontinuous excavation and sequential installation of liners," *Journal of Engineering Mechanics*, vol. 147, no. 4, 2021.

[2] Z. Chu, Z. Wu, Q. Liu, L. Weng, Z. Wang, and Y. Zhou, "Evaluating the microstructure evolution behaviors of saturated sandstone using NMR testing under uniaxial short-term and creep compression," *Rock Mechanics and Rock Engineering*, vol. 54, no. 9, pp. 4905–4927, 2021.

[3] Z. Chu, Z. Wu, Z. Wang, L. Weng, Q. Liu, and L. Fan, "Micromechanism of brittle creep in saturated sandstone and its mechanical behavior after creep damage," *International Journal of Rock Mechanics and Mining Sciences*, vol. 149, no. 3–4, p. 104994, 2022.

[4] Z. Sun, D. Zhang, Q. Fang, G. Dui, and Z. Chu, "Analytical solutions for deep tunnels in strain-softening rocks modeled by different elastic strain definitions with the unified strength theory," *Science China Technological Sciences*, vol. 65, 2022.

 [5] Z. Sun, D. Zhang, Q. Fang, G. Dui, Q. Tai, and F. Sun, "Analysis of the interaction between tunnel support and surrounding rock considering pre-reinforcement," *Tunnelling and Underground Space Technology*, vol. 115, Article ID 104074, 2021.

 [6] Z. Sun, D. Zhang, Q. Fang, D. Liu, and G. Dui, "Displacement process analysis of deep tunnels with grouted rockbolts considering bolt installation time and bolt length," *Computers and Geotechnics*, vol. 140, p. 104437, 2021.

 [7] K. Wu, Z. Shao, M. Sharifzadeh, S. Hong, and S. Qin, "Analytical computation of support characteristic curve for circumferential yielding lining in tunnel design," *Journal of Rock Mechanics and Geotechnical Engineering*, vol. 14, no. 1, pp. 144–152, 2022.

 [8] D. Zhang, Z. Sun, and Q. Fang, "Scientific problems and research proposals for Sichuan-Tibet railway tunnel construction," *Underground Space*, vol. 7, no. 3, pp. 419–439, 2022.

 [9] C. Chian and S. C. Chian, "Revisiting crown stability of tunnels deeply buried in non-uniform rock surrounds," *Tunnelling and Underground Space Technology*, vol. 73, no. December, pp. 154–161, 2018.

 [10] M. Fraldi, R. Cavuoto, A. Cutolo, and F. Guarracino, "Stability of tunnels according to depth and variability of rock mass parameters," *International Journal of Rock Mechanics and Mining Sciences*, vol. 119, no. May, pp. 222–229, 2019.

 [11] H. Lippmann, "Plasticity in rock mechanics," *International Journal of Mechanical Sciences*, vol. 13, no. 4, pp. 291–297, July 1970.

 [12] M. Guarracino and F. Guarracino, "Limit analysis of collapse mechanisms in cavities and tunnels according to the Hoek-Brown failure criterion," *International Journal of Rock Mechanics and Mining Sciences*, vol. 46, no. 4, pp. 665–673, 2009.

 [13] M. Guarracino and F. Guarracino, "Analytical solutions for collapse mechanisms in tunnels with arbitrary cross sections," *International Journal of Solids and Structures*, vol. 47, no. 2, pp. 216–223, 2010.

 [14] C. Chian and S. C. Chian, "2D and 3D stability analysis of tunnel roof collapse in stratified rock: a kinematic approach," *International Journal of Rock Mechanics and Mining Sciences*, vol. 100, no. October, pp. 269–277, 2017.

 [15] X. L. Yang, T. Zhou, and W. T. Li, "Reliability analysis of tunnel roof in layered Hoek-Brown rock masses," *Computers and Geotechnics*, vol. 104, no. June, pp. 302–309, 2018.

 [16] X. L. Yang and C. Yao, "Axisymmetric failure mechanism of a deep cavity in layered soils subjected to pore pressure," *International Journal of Geomechanics*, vol. 17, no. 8, Article ID 04017031, 2017.

 [17] X. L. Yang and C. Yao, "Stability of tunnel roof in nonhomogeneous soils," *International Journal of Geomechanics*, vol. 18, no. 3, Article ID 06018002, 2018.

 [18] C. Lyu, L. Yu, M. Wang, P. Xia, and Y. Sun, "Upper bound analysis of collapse failure of deep tunnel under karst cave considering seismic force," *Soil Dynamics and Earthquake Engineering*, vol. 132, p. 106003, 2020.

 [19] C. Zeng and Z. Zeng, "Upper bound limit analysis of unsymmetrical progressive collapse of shallow tunnels in inclined rock stratum," *Computers and Geotechnics*, vol. 116, no. May, Article ID 103199, 2019.

 [20] H. T. Wang, P. Liu, C. Liu, X. Zhang, Y. Yang, and L. Y. Liu, "Three-Dimensional upper bound limit analysis on the collapse of shallow soil tunnels considering roof stratification and pore water pressure," *Mathematical Problems in Engineering*, vol. 2019, pp. 1–15, 2019.

 [21] X. L. Huang and F. Huang, "Collapse mechanism of shallow tunnel based on nonlinear Hoek-Brown failure criterion," *Tunnelling and Underground Space Technology*, vol. 26, no. 6, pp. 686–691, 2011.

 [22] L. h. Zhao, S. h. Hu, X. P. Yang, F. Huang, and S. Zuo, "Limit variation analysis of shallow rectangular tunnels collapsing with double-layer rock mass based on a three-dimensional failure mechanism," *Journal of Central South University*, vol. 26, no. 7, pp. 1794–1806, 2019.

 [23] M. Guarracino and F. Guarracino, "Limit analysis of progressive tunnel failure of tunnels in Hoek-Brown rock masses," *International Journal of Rock Mechanics and Mining Sciences*, vol. 50, pp. 170–173, 2012.

 [24] K. Han, J. W. W. Ju, H. Kong, and M. Wang, "Functional catastrophe analysis of progressive failures for deep tunnel roof considering variable dilatancy angle and detaching velocity," *Rock Mechanics and Rock Engineering*, vol. 52, no. 10, pp. 3987–3997, 2019.

 [25] C. B. Qin, S. C. Chian, and X. L. Yang, "3D limit analysis of progressive collapse in partly weathered Hoek–Brown rock banks," *International Journal of Geomechanics*, vol. 17, no. 7, Article ID 04017011, 2017.

 [26] C. B. Qin, X. L. Yang, Q. J. Pan, Z. B. Sun, L. L. Wang, and T. Miao, "Upper bound analysis of progressive failure mechanism of tunnel roofs in partly weathered stratified Hoek-Brown rock masses," *International Journal of Rock Mechanics and Mining Sciences*, vol. 74, pp. 157–162, 2015.

 [27] Y. Gao, Z. Yang, Z. Cheng, Y. Jiang, and Y. Ren, "Limit analysis of tunnel collapse according to the Hoek-Brown criterion and bolt parameter research," *Arabian Journal for Science and Engineering*, vol. 44, no. 10, pp. 8171–8180, 2019.

 [28] K. Guan, W. C. Zhu, L. L. Niu, and Q. Y. Wang, "Three-dimensional upper bound limit analysis of supported cavity roof with arbitrary profile in Hoek-Brown rock mass," *Tunnelling and Underground Space Technology*, vol. 69, no. June, pp. 147–154, 2017.

 [29] B. Jiang, Q. Wang, S. C. Li et al., "The research of design method for anchor cables applied to cavern roof in water-rich strata based on upper-bound theory," *Tunnelling and Underground Space Technology*, vol. 53, pp. 120–127, 2016.

 [30] F. Yang and X. L. Yang, "Upper bound limit analysis of collapse shape for circular tunnel subjected to pore pressure based on the Hoek-Brown failure criterion," *Tunnelling and Underground Space Technology*, vol. 26, no. 5, pp. 614–618, 2011.

 [31] C. Qin, S. C. Chian, X. Yang, and D. Du, "2D and 3D limit analysis of progressive collapse mechanism for deep-buried tunnels under the condition of varying water table," *International Journal of Rock Mechanics and Mining Sciences*, vol. 80, pp. 255–264, 2015.

 [32] L. Yu, C. Lyu, M. Wang, and T. Xu, "Three-dimensional upper bound limit analysis of a deep soil-tunnel subjected to pore pressure based on the nonlinear Mohr-Coulomb criterion," *Computers and Geotechnics*, vol. 112, no. April, pp. 293–301, 2019.

 [33] R. Zhang and X. Yang, "Limit analysis of active and passive mechanisms of shallow tunnels in nonassociative soil with changing water table," *International Journal of Geomechanics*, vol. 18, no. 7, Article ID 04018063, 2018.

 [34] S. W. Jacobsz, "Trapdoor experiments studying cavity propagation," *Proceedings of the First Southern African Geotechnical Conference*, in *Proceedings of the 1st Southern African Geotechnical Conference*, pp. 159–165, 2016. November.

[35] F. Huang, H. Zhu, Q. Xu, Y. Cai, and X. Zhuang, "The effect of weak interlayer on the failure pattern of rock mass around tunnel - scaled model tests and numerical analysis," *Tunnelling and Underground Space Technology*, vol. 35, pp. 207–218, 2013.

[36] D. P. Xu, X. T. Feng, Y. J. Cui, and Q. Jiang, "Use of the equivalent continuum approach to model the behavior of a rock mass containing an interlayer shear weakness zone in an underground cavern excavation," *Tunnelling and Underground Space Technology*, vol. 47, pp. 35–51, 2015.

[37] Y. Zhao, Q. Gong, Y. Wu, Z. Tian, S. Zhou, and L. Fu, "Progressive failure mechanism in granular materials subjected to an alternant active and passive trapdoor," *Transportation Geotechnics*, vol. 28, Article ID 100529, 2021.

[38] C. p. Zhang, K. h. Han, Q. Fang, and D. l. Zhang, "Functional catastrophe analysis of collapse mechanisms for deep tunnels based on the Hoek-Brown failure criterion," *Journal of Zhejiang University - Science*, vol. 15, no. 9, pp. 723–731, 2014.

[39] R. M. Caddell, R. S. Raghava, and A. G. Atkins, "A yield criterion for anisotropic and pressure dependent solids such as oriented polymers," *Journal of Materials Science*, vol. 8, no. 11, pp. 1641–1646, 1973.

[40] H. J. Greenberg, *On the Variational Principles of Mechanics*, 1949.

[41] W.-F. Chen, *Limit Analysis and Soil Plasticity*, 1975.

[42] T. Yang and X. Yang, "Limit analysis of failure mechanism of tunnel roof collapse considering variable detaching velocity along yield surface," *International Journal of Rock Mechanics and Mining Sciences*, vol. 100, no. October, pp. 229–237, 2017.

Research Article

Numerical Analysis on Seismic Responses of a Large Metro Station in Sandy Area

Yu Liu [1,2] **and Xiao Liu** [1,2]

[1]*School of Architectural and Civil Engineering, Shenyang University, Shenyang 110044, China*
[2]*Key Lab of Environmental Geotechnical Engineering, Shenyang University, Shenyang 110044, China*

Correspondence should be addressed to Xiao Liu; liuxiao@syu.edu.cn

A new assessment method is proposed considering shortcomings of the current investigations for the assessment of underground structures considering seismic load. First, the dynamic elastic modulus and damping ratio of sand are studied based on the dynamic characteristic experiment of the soil. Subsequently, a series of design acceleration time history curves are obtained using the proposed methods. Finally, the seismic response of underground structures is evaluated by a three-dimensional numerical simulation. The results indicate that the dynamic elastic modulus of sand decreases with the increase of dynamic elastic strain and increases with the increase of confining pressure. The influence of confining pressure on the damping ratio of sand is slight, but it can still be seen that the damping ratio decreases with the increase of confining pressure, especially when the dynamic elastic strain is relatively low. The interlayer displacement between the top and middle plate is 2.1 mm and the interlayer displacement angle is 1/2650. The interlayer displacement between the middle and bottom plate is 1.7 mm and the interlayer displacement angle is 1/4117. Under the action of fortification earthquake, the interlayer displacement angles of Taiyuan Street station are less than 1/550, indicating that the structure meets the seismic requirements.

1. Introduction

With the strategy of a country with a strong transportation network, the construction of an urban subway has entered a stage of rapid development in China. Although the complex structure of the subway station has rich functions and can promote regional development, its seismic response is also difficult to obtain accurately because of its complex structure under earthquakes [1, 2]. With the emergence of cases of serious damage to underground structures caused by earthquakes, more and more scholars began to do a lot of research work in this field [3, 4].

In the theoretical analysis, Newmark [5] and Kuesel [6] proposed a simplified algorithm for free field strain under the condition of the simple harmonic incident at any angle in isotropic elastic homogenization. Luco and Barros [7] studied the seismic response of circular underground structures in semi-infinite elastic space under SH wave by using the method of combining finite elements with a wave function and the indirect boundary integral method based on two-dimensional Green's function. Davis et al. [8] derived the analytical solution of P-wave and SV-wave scattering by underground structures in semi-infinite space through the large arc assumption method. Pang et al. [9] proposed a novel model to analyze the seismic response and reliability level of a subway station, and the presented model can generate completely nonstationary ground motions. The characteristics of earthquakes have notable influences on the dynamic structural behavior of underground structures. Qiu et al. [10] proposed a modified simplified analysis method to evaluate seismic responses of a large subway station in a complex area. Based on the presented model, the seismic response of the support structure was

divided into two categories such as the kinematic interaction effect and the inertial interaction effect.

In the physical model experiments, Tomari and Towhata [11] used a shaking table test to explore the seismic response of flexible section structure under the condition of a liquefiable site and discussed the influence of natural vibration frequency and backfill dilatancy on structural characteristics. The shaking tests on the seismic response characteristics of the underground structure in the liquefiable site are investigated by An et al. [12]. Wu et al. [13] studied the dynamic response and spectrum characteristics of a tunnel using shaking table tests. A centrifuge shaker model test of a subway station on a liquefiable foundation was carried out, which studied the process in which damage occurs during an earthquake. Several dynamic centrifuge tests were conducted to investigate the seismic structural response and failure model of the underground structure system. The vertical load notably increases the axial forces on the frame columns to reduce the horizontal deformation capacity [14]. Miao et al. [15] investigated soil-structure interactions on the seismic response of metro stations using a series of experiments.

In the aspect of numerical simulation, Chen [16] et al. conducted numerical research on the dynamic response of subway stations under seismic load in shallow soft soil sites. Taking the interval tunnel of Beijing Metro Line 7 as an example, Li et al. [17] established the numerical model of the cross tunnel by using FLAC3D software and studied the seismic response characteristics of a closed pasted cross tunnel under strong earthquakes. Lu and Huang [18] established the three-dimensional refined model of the upper and lower intersecting metro tunnel using MIDAS software, and the dynamic response law of the subway cross tunnel is analyzed. Ma et al. [19] established the finite element model of tunnel soil and the dynamic response of the silty sand layer is analyzed. Liu et al. [20] proposed a seismic control technology for shallow buried underground structures. The finite element models are established and evaluated for the support system. The results indicate that the technology can effectively reduce the horizontal displacement of the central support system and provide a reference for the ability of earthquake prevention. Du et al. [21, 22] proved that the axial compression ratio of the central column increased notably under the combined action of horizontal-vertical loads, which reduced deformation capacity in the horizontal direction.

In summary, the dynamic response of a large metro station has been investigated using theoretical analyses, physical experiments, and numerical simulations. Due to the rapid development of computer technology, numerical software is widely used in geotechnical engineering. However, it is little for investigation of the seismic responses using numerical software considering the local seismic load. Thereby, considering shortcomings of the aforementioned investigations, the structural deformation of subway station under seismic load is further evaluated and several key contents are as follows: (1) The dynamic elastic modulus and damping ratio of sand are studied based on the dynamic characteristic experiment of soil. (2) A series of design acceleration time history curves are obtained using the proposed methods. (3) The seismic response of underground structures is evaluated by a three-dimensional numerical simulation.

2. Engineering Survey

Taiyuan Street Station of line 4 is located in a prosperous commercial area, mainly surrounded by shopping malls and business buildings. The passenger flow is relatively concentrated and the risk source is large, as shown in Figure 1. The auxiliary structure of Taiyuan Street station includes 3 entrances and exits, 2 air ducts, 1 transfer channel, and 2 emergency exits. The station is a three-span island platform station on the second floor underground, with a length of 231.7 m, a standard section width of 25.3 m, and a platform width of 14 m. The buried depth of the bottom plate of the station is approximately 27 m and the covering soil of the top plate is 10.57 m. The main structure of the station is constructed by the PBA method of concealed excavation, as shown in Figure 2. The main measures of the PBA method are as follows: bored cast-in-place piles(φ1000@1200) are mainly used for side piles, a steel support is set, and the dewatering scheme outside the pit is adopted. The proposed site is mainly composed of miscellaneous fill, a cohesive soil layer, a silty soil layer, and a sandy soil layer (Table 1).

3. Experimental Study on Dynamic Characteristics of the Soil

Considering that the dynamic shear modulus and damping ratio of soil are important parameters of soil dynamic characteristics, they are indispensable in the seismic safety evaluation of the engineering site and the seismic response analysis of the soil layer. The rationality of parameter selection will directly affect the safety and economy of the engineering building structure. The variation law of dynamic elastic modulus and damping ratio of sand is studied in this section..

3.1. Experiment Preparation. The dynamic characteristic test of soil was completed with the assistance of the laboratory of Northeast University. The indoor test was carried out according to the typical sandy soil in Shenyang. Silt is the soil sample of the bidirectional dynamic triaxial test system produced by GDS company, as shown in Figure 3. Remolded soil samples with a diameter of 39.1 mm and a height of 80 mm were used in the test. The remolded sample is prepared by the multilayer wet tamping method, which is carried out in five layers. The dry density of the silty sand sample is 1.55 g/cm^3. The consolidation stress of the silt sample is 50 kPa, 100 kPa, and 150 kPa respectively. The weight of each layer of the soil sample is determined according to the dry density and predesigned water content of the soil sample and compacted to the corresponding height. The contact surface of each layer is scratched to ensure a good upper and lower contact.
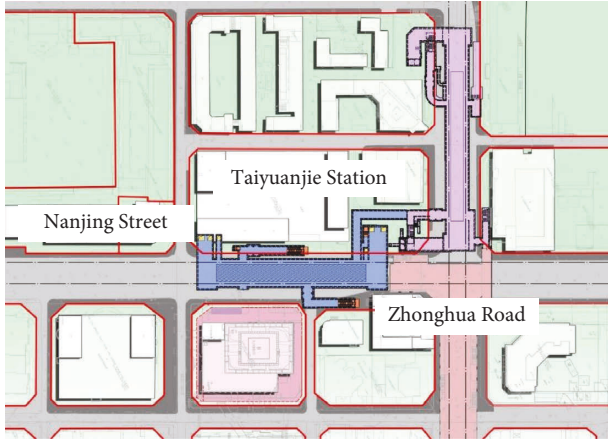
FIGURE 1: General plan.
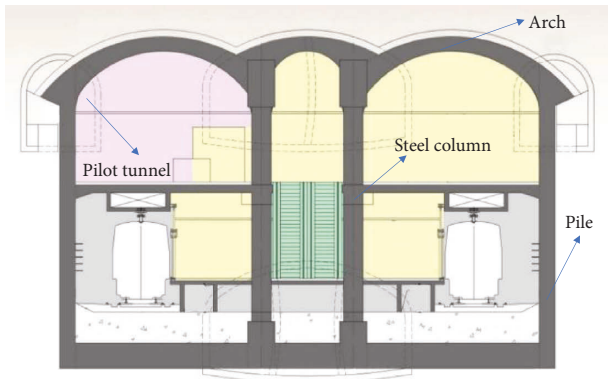
FIGURE 2: Cross section.

3.2. Result Analysis

3.2.1. Dynamic Elastic Modulus.
The relationship curve between dynamic elastic modulus and dynamic elastic strain of the sample under different confining pressures is shown in Figure 4. It can be seen from the figure that with the gradual increase of dynamic elastic strain, the dynamic elastic modulus decreases and the stiffness softening phenomenon occurs. At the beginning of the cycle, the curve is steep and the stiffness softening rate is fast. Then, with the increase of dynamic elastic strain, the curve tends to be flat and the stiffness softening rate decreases. For the same strain level, when the confining pressure increases, the dynamic elastic modulus increases. The dynamic elastic modulus tends to increase with the increase of confining pressure because the void ratio of the sample decreases with the increase of confining pressure, the relative density increases, and the contact point of soil particles increases, which makes the stress wave propagate faster in the soil, thus increasing the dynamic elastic modulus. The dynamic elastic modulus of sand decreases with the increase of dynamic elastic strain and increases with the increase of confining pressure.

3.2.2. Damping Ratio.
The relationship curve between the damping ratio and dynamic elastic strain under different confining pressures is shown in Figure 5. It can be seen from

the figure that the damping ratio of sand increases with the increase of dynamic elastic strain. In a small strain, the damping ratio increases rapidly with the increase of dynamic elastic strain; then, the curve tends to be flat. It shows that the change of strain lags behind the change of stress in the process of vibration is limited. At the same time, the influence of confining pressure on the damping ratio of sand is not significant, but it can still be seen that the damping ratio decreases with the increase of confining pressure, especially when the dynamic elastic strain is relatively low.

4. Site Design Ground Motion Parameters

4.1. Synthetic Ground Motion Time History of Bedrock. In the seismic response time history analysis, the selection of an appropriate ground motion acceleration time process is very important. Although the number of actual seismic records has greatly increased in the past few decades, the site conditions of the recording sites may be very different from the construction site conditions we are concerned about. We need a set of ground motion samples that meet the same statistical characteristics as the seismic response input. In this section, based on the above-ground motion characteristic parameters of the project site, the triangular series superposition simulation method is used to synthesize the bedrock ground motion time history. The calculation model is as follows:

$$x''(t) = f(t) \sum_{k=0}^{n} C_k \cos(\omega_k t + \varphi_k) = f(t)a(t), \quad (1)$$

$$a(t) = \sum_{k=0}^{n} C_k \cos(\omega_k t + \varphi_k). \quad (2)$$

In the formula, φ_k is the random phase angle uniformly distributed in the $(0, 2\pi)$ interval; C_k and ω_k is the amplitude and frequency of the k-th frequency component, respectively; $f(t)$ is the strength envelope function, which is a definite function of time; and $a(t)$ is a stationary Gaussian process.

It can be seen from equation (1) that the synthetic acceleration time history $x''(t)$ with the characteristics of a nonstationary random process is the product of a Gaussian process $a(t)$ with the characteristics of a stationary random process and an intensity envelope function $f(t)$.

The coefficient C_k in equation (2) can be determined by a given power spectral density function $S(\omega_k)$, where we obtain as follows:

$$\begin{cases} C_k = \sqrt{4S(\omega_k)\Delta\omega}, \\ \\ \omega_k = \dfrac{2\pi k}{T}, \\ \\ \Delta\omega = \dfrac{2\pi}{T}, \end{cases} \quad (3)$$

where t is the total holding time of the stationary random process. In order to use the acceleration response spectrum

TABLE 1: Soil parameters.

Soil	Depth (m)	Weight (kN/m³)	Dynamic elastic modulus (MPa)	Dynamic Poisson ratio	Cohesion (kPa)	Internal friction angle (°)
Backfill soil	2.0	17	93.7	0.41	0	6
Fine sand	2.7	19.5	279.6	22	3	26
Medium coarse sand	2.2	19.8	611.5	30	0	32
Gravel sand	8.7	20	660.9	32	0	34
Silty clay	2.1	19	283.3	20	18	14
Boulder clay	7	20.0	1036.8	—	—	

FIGURE 3: Dynamic triaxial test of sandy soil.
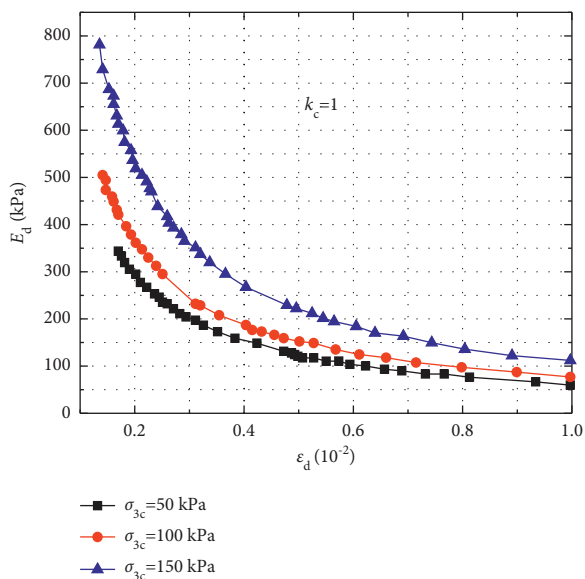
FIGURE 4: E_d-ε_d relation curve of silt under different confining pressures.
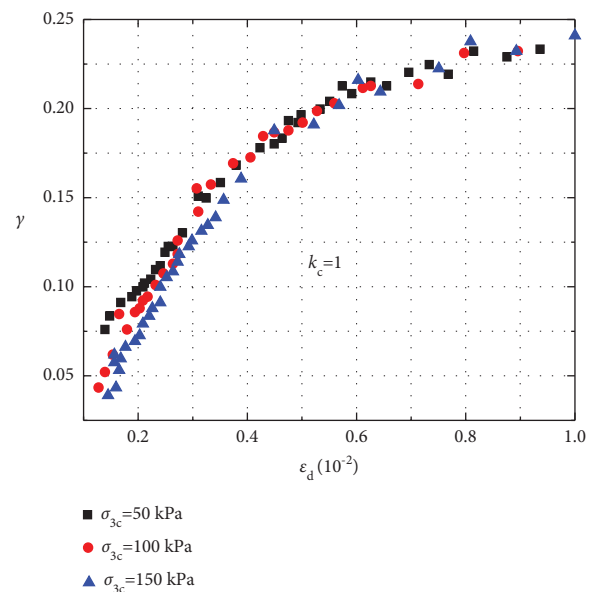
FIGURE 5: λ-ε_d relation curve of silt under different confining pressures.

as the target spectrum of artificial acceleration time history, the following approximate relationship between the response spectrum and power spectrum can be used to replace $S(\omega_k)$ in equation (3);

$$S(\omega_k) = -\frac{\zeta}{\pi\omega}\left[S_a^T(\omega)\right]^2\frac{1}{\ln\left[-\pi/\omega T\ln(1-P)\right]}. \qquad (4)$$

In the formula, $S_a^T(\omega)$ is the given target acceleration response spectrum, ζ is the damping ratio, t is the duration, and P is the exceedance probability of the response.

The intensity envelope function $f(t)$ is related to the magnitude, epicenter distance, geological structure background, site soil conditions, and other factors and reflects the unstable characteristics of ground motion with time. Generally, the strength envelope function $f(t)$ is expressed by the following piecewise function:

$$f(t) = \begin{cases} (t/t_1)^2, & 0 \le t \le t_1, \\ 1, & t_1 < t \le t_2, \\ e^{-c(t-t_2)}, & t_2 < t \le t_d, \end{cases} \qquad (5)$$

where $(0, t1)$ is the rising section, (t_1, t_2) is the stationary section, (t_2, t_d) is the attenuation section, and C is the attenuation coefficient. Since the relationship between the response spectrum and the power spectrum represented by equation (4) is approximate, the response spectrum calculated according to the initial time history is generally only approximate to the target response spectrum. In order to improve the fitting accuracy, iterative adjustment is required. When the difference between the calculated response spectrum and the target response spectrum is less than the control accuracy (take 5%), the iteration is stopped.

4.2. Dynamic Response Analysis of Site Soil

4.2.1. Calculation Model of Dynamic Response of the Site Soil Layer.
The results of site engineering seismic conditions show that within the scope of the project site, the changes in medium characteristics and terrain are not very significant along the horizontal direction. Therefore, the influence of site conditions on seismic ground motion is considered based on a one-dimensional site model. The equivalent linearization method of one-dimensional soil shear dynamic response analysis is used in the study of the influence of the one-dimensional site model on earthquake ground motion. Its basic principle is as follows:

It is assumed that the shear wave is incident vertically from the viscoelastic semi-infinite bedrock space into the horizontal layered (N-layer) nonlinear soil and propagates upward. For this calculation model, according to the wave propagation theory, the dynamic response value of the field ground medium can be calculated by using the time-frequency transformation technology, combined with the complex damping simulation of the nonlinear characteristics of soil and the equivalent linearization method.

A shear harmonic is set to incident vertically upward from the calculated base and propagate in the soil layer.

According to the wave theory and complex damping theory, the medium motion in each soil layer must meet the wave equation:

$$\rho_j\frac{\partial^2 U_j(x.t)}{\partial t^2} = G_j^c\frac{\partial^2 U_j(x,t)}{\partial x^2}, \qquad (6)$$

where $U_j(x,t)$ is the displacement value of medium reaction in the soil layer j, ρ_j is the density of the medium in the soil layer j, G_j^c is the dynamic complex shear modulus of the medium in the soil layer j, G_j^c is given by the following equation:

$$G_j^c = \left[1 + 2\lambda_j(\gamma_{je})i\right]G_{jd}(\gamma_{je})G_{jo}, \qquad (7)$$

where G_{jo} is the maximum dynamic shear modulus of medium in soil layer, $jG_{jd}(\gamma_{je}), \lambda_j(\gamma_{je})$ is the dimensionless coefficient of equivalent dynamic shear modulus and hysteretic damping ratio of the medium in soil layer, and $j\gamma_{je}$ is the maximum dynamic shear modulus of the medium in soil layer j

The medium motion between soil layers meets the conditions of displacement continuity and stress continuity.

$$\begin{aligned} U_j(x,t)\big|_{x=H_j} &= U_{j+1}(x,t)\big|_{x=0}, \\ \tau_j(x,t)\big|_{x=H_j} &= \tau_{j+1}(x,t)\big|_{x=0}, \\ \tau_1(x,t)_{x=0} &= 0. \end{aligned} \qquad (8)$$

In the formula, H_j is the layer thickness of the j-th soil layer, and it is specified that the vertically downward direction is the positive direction of the X coordinate and the coordinate origin is placed at the top of each soil layer. Through formula (6), the frequency domain value of the medium reaction quantity in the soil layer can be obtained by using the known calculated base incident wave value, and then, the time domain value of the medium reaction quantity in the soil layer can be obtained by using the Fourier transform method.

Considering the nonlinear characteristics of soil, the dimensionless coefficient of equivalent dynamic shear modulus and hysteretic damping ratio of each soil layer are functions of equivalent shear strain. Therefore, in the actual calculation, the initial equivalent dynamic shear strain of the medium reaction in each soil layer is assumed and the response calculation is carried out by using the abovementioned method. Then, the maximum shear strain response of the medium at the midpoint of each soil layer is calculated. Finally, the maximum shear strain of the medium reaction at the midpoint of each soil layer multiplied by the reduction coefficient (0.65) is taken as the calculated value of the equivalent shear strain of the medium in the soil layer. We compare the equivalent shear strain used in the calculation with the equivalent dynamic shear modulus and hysteretic damping ratio corresponding to the calculated equivalent shear strain. If the relative error is less than the given allowable error (0.05), it is considered that the consideration of the nonlinear characteristics of soil meets the requirements. Otherwise, we replace the initial equivalent shear strain value with the latest calculated equivalent shear strain value and repeat the

abovementioned calculation process until the relative error is less than the allowable error.

4.2.2. Determination of Dynamic Parameters of the Site Soil Layer. Focal characteristics, propagation path, and local site conditions are the main factors affecting the ground motion of the site, and the influence of local site conditions is particularly prominent in a small area. Therefore, the engineering geological exploration in the proposed site and the determination of the type, stratification, and thickness of the site soil are essential work in the seismic response calculation. The analysis and determination of dynamic mechanical indexes of site soil (such as bulk density, shear wave velocity, shear modulus ratio curve, and damping ratio curve) are very important for site dynamic response analysis.

In this work, the existing data are sorted out according to the requirements of soil seismic response analysis and calculation. According to the borehole data of the site, a borehole with shear wave velocity data is taken as the calculation control point for each station site and station-to-station interval. In the seismic response calculation, the medium with a shear wave velocity greater than 500 m/s is determined as the seismic input interface and the shear wave velocity of the soil below this layer is greater than 500 m/s.

4.3. Site Design Ground Motion Parameters. On the basis of the seismic response calculation results of the site soil layer obtained in the previous section, the design ground motion parameters of the project site in this section will be given, including the design peak ground motion acceleration and acceleration response spectrum. The design peak ground acceleration is determined by comprehensively considering the peak value of the sample and the short-period acceleration response spectrum. The design acceleration response spectrum is determined by using the average fitting method for the calculated acceleration response spectrum.

The design ground motion acceleration response spectrum of the project site is taken as follows:

$$S_a(T) = A_{max}\beta(T),$$

$$\alpha_{max} = \frac{A_{max}\beta_{max}}{g}, \tag{9}$$

where A_{max} is the design peak ground acceleration, α_{max} the maximum value of seismic influence coefficient, g is the gravitational acceleration, and $\beta(T)$ is given in the form of 《Code for seismic design of Highway Engineering》(JTG B02-2013):

$$\beta(T) = \begin{cases} 1 + \dfrac{(\beta_{max} - 1)T}{T_1}, & 0 \le T < T_1\,(s), \\[2ex] \beta_{max}, & T_1 \le T \le T_g\,(s), \\[2ex] \beta_{max}\left(T_g/T\right)^{\gamma}, & T > T_g\,(s), \end{cases} \tag{10}$$

where T is the natural vibration period of the structure, β_{max} is the maximum value of the response spectrum, T_1 is the initial period of the platform section with the maximum response spectrum, T_g is the characteristic period, and γ is the attenuation index of the falling section of the response spectrum.

4.4. Design Acceleration Time History. In this work, the artificial ground motion is synthesized according to the calculated peak value and response spectrum results. Formula (10) is used to calculate the horizontal ground motion acceleration response spectrum results combined with the 50-year exceedance probability of the project site of 10%. The relative error between the time history response spectrum and the target spectrum is less than 5%. The synthesis takes 0.02 seconds as the step length, and the envelope function mainly considers the influence of long-period ground motion. By calculating the equivalent magnitude and equivalent distance of ground motion corresponding to the natural vibration period of the structure, the envelope parameters used are determined. The horizontal acceleration time history curve of each exceedance probability and its fitting with the target spectrum are shown in Figures 6 and 7.

5. Response Analysis of the Structure

5.1. Finite Element Model. The finite element model of the subway station is established by Midas-GTS software, and the response analysis of the subway station under seismic load is carried out using the time history method. The dimension of the numerical model is selected as $100\,\text{m} \times 40\,\text{m} \times 47\,\text{m}$ to include most of the soil affected by the excavation. That is, the side artificial boundary of the calculation model is 3 times the horizontal effective width of the subway station. The lower boundary is to the equivalent bedrock surface, and the upper surface is taken to the actual surface. Horizontal and vertical seismic acceleration loads are applied at the bottom of the model, and the peak value of vertical acceleration is 65% of the horizontal acceleration. Free field boundary conditions are set around the calculation model. To prevent seismic wave reflection, the unit width of the free boundary is set to 1000 km and the bottom of the model is a fixed constraint. To ensure calculation accuracy and reduce the calculation time as much as possible, the grid near the main structure of the station is densified. The stratum is simulated by a three-dimensional solid element, the station secondary lining is simulated by a plate element, and the middle column and longitudinal beam are simulated by a beam element. The Mohr–Coulomb model is adopted for the soil constitutive relationship and the elastic-plastic model is adopted for station lining. The calculation model is shown in Figure 8.

5.2. Result Analysis. The safety of the station under earthquake is directly affected by the relative displacement of the top and bottom plates of the subway station. It can be seen from Figure 9 that under the seismic conditions of
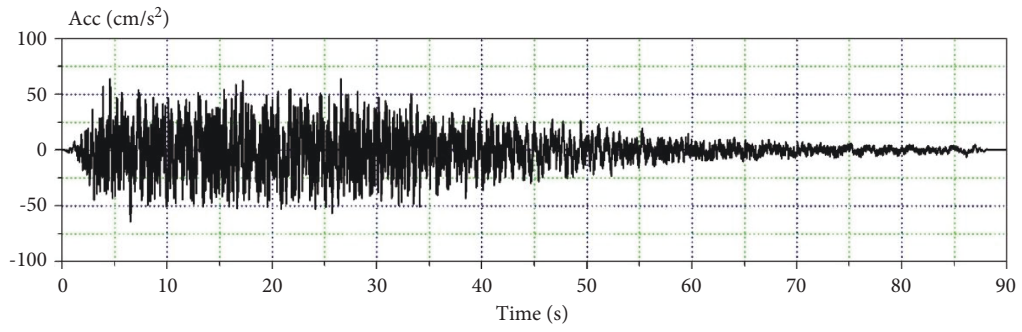
FIGURE 6: Time history of horizontal design ground motion acceleration of 10% section II foundation surface.
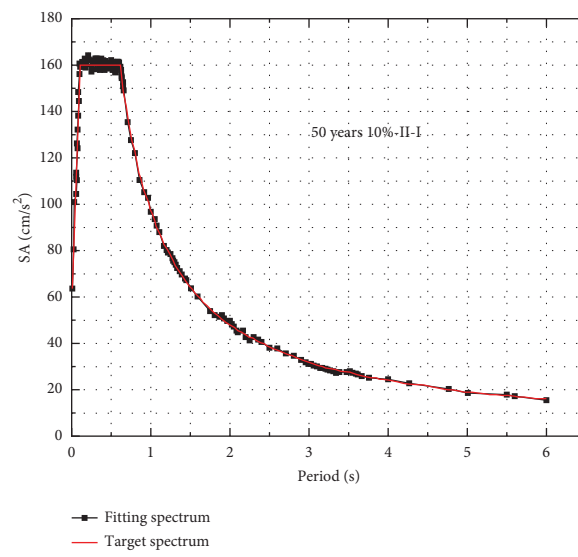
FIGURE 7: Fitting of the response spectrum.
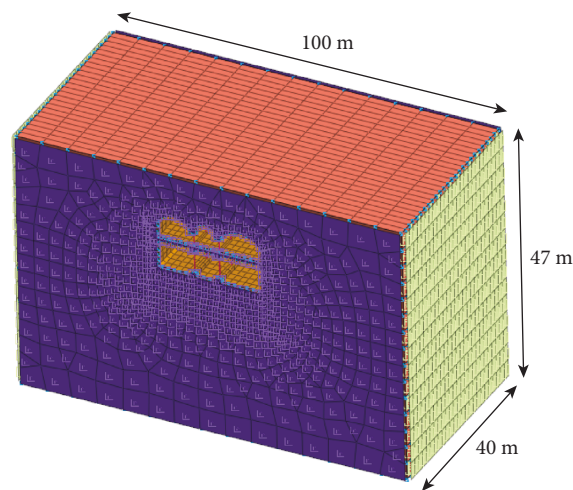
FIGURE 8: Calculation model.
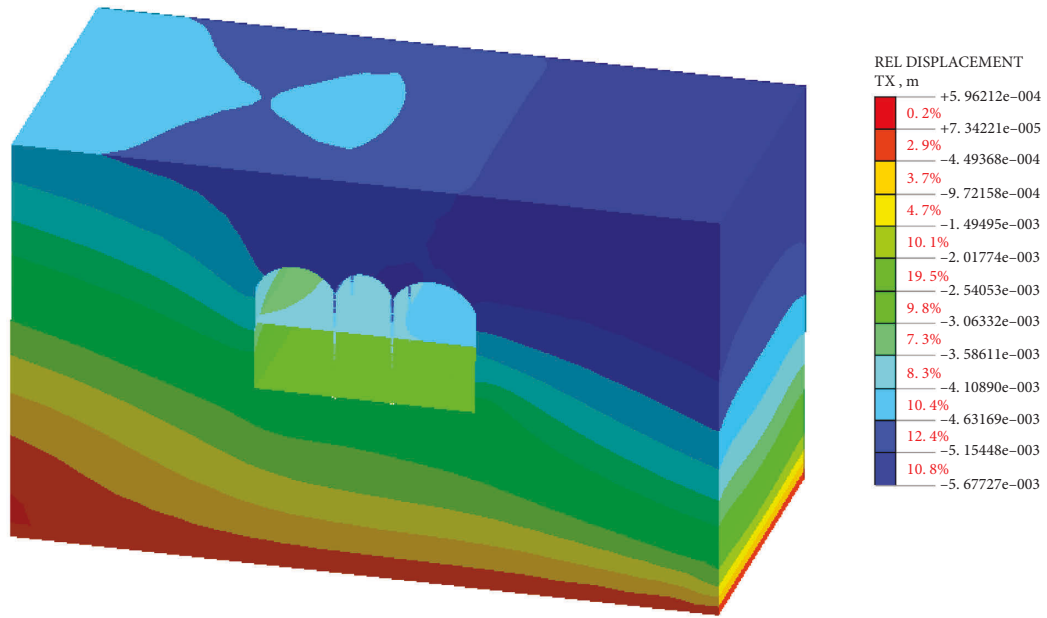
(a)
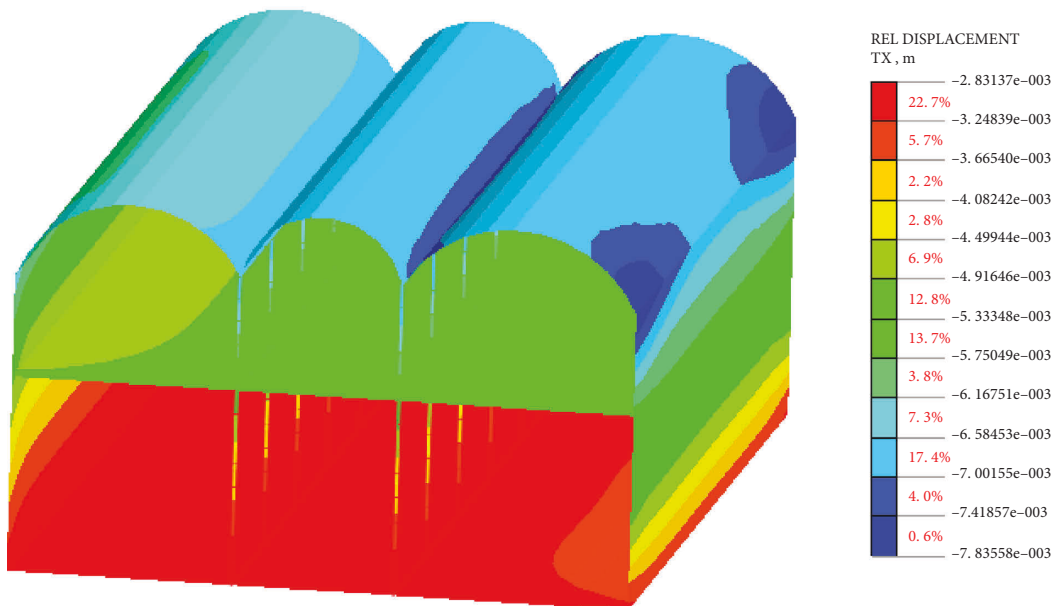
(b)

FIGURE 9: Horizontal displacement at the moment of maximum relative deformation of the top and bottom plates. (a) Overall horizontal displacement. (b) Horizontal displacement of the structure.

fortification intensity, the maximum horizontal displacement of the bottom plate is 18.8 mm. The horizontal displacement of the middle plate and the bottom plate are 16.7 and 15.0 mm, respectively. Therefore, the interlayer displacement between the top plate and the middle plate is 2.1 mm and the interlayer displacement angle is 1/2650. The interlayer displacement between the middle baseplates is 1.7 mm and the interlayer displacement angle is 1/4117, see Figure 10. Under the action of a fortification earthquake, the inter story displacement angle of Taiyuan Street station is less than 1/550, indicating that the structure meets the seismic requirements.
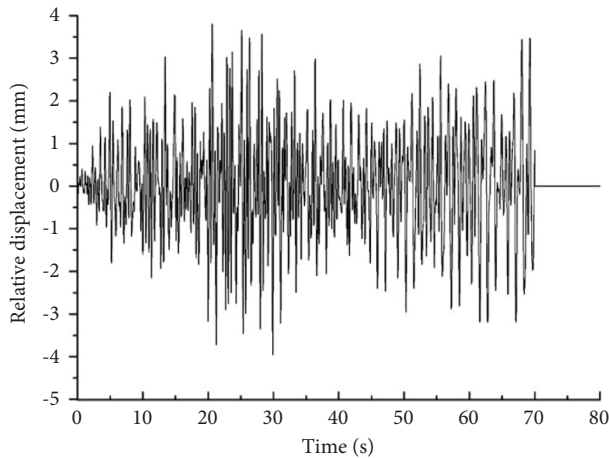
Figure 10: Relative displacement history curve of the top and bottom plates.

6. Conclusions

(1) The dynamic elastic modulus of sand decreases with the increase of dynamic elastic strain and increases with the increase of confining pressure. The influence of confining pressure on the damping ratio of sand is slight, but it can still be seen that the damping ratio decreases with the increase of confining pressure, especially when the dynamic elastic strain is relatively low.

(2) The interlayer displacement between the top and middle plate is 2.1 mm and the interlayer displacement angle is 1/2650. The interlayer displacement between the middle and bottom plate is 1.7 mm and the interlayer displacement angle is 1/4117. Under the action of a fortification earthquake, the interlayer displacement angles of Taiyuan Street station are less than 1/550, indicating that the structure meets the seismic requirements.

Data Availability

The data used to support the findings of this study are included in the article.

Conflicts of Interest

The authors declare that they have no conflicts of interest.

Acknowledgments

References

[1] S. Chen, B. Lang, H. Liu, D. Li, and C. Gao, "DNS covert channel detection method using the LSTM model," *Computers & Structures*, vol. 104, Article ID 102095, 2021.

[2] H. Zhu, X. Wang, X. Chen, and L. Zhang, "Similarity search and performance prediction of shield tunnels in operation through time series data mining," *Automation in Construction*, vol. 114, Article ID 103178, 2020.

[3] Z. Z. Wang and Z. Zhang, "Seismic damage classification and risk assessment of mountain tunnels with a validation for the 2008 Wenchuan earthquake," *Soil Dynamics and Earthquake Engineering*, vol. 45, no. 1, pp. 45–55, 2013.

[4] M. C. Pakbaz, A. Yareevand, and A. Yareevand, "2-D analysis of circular tunnel against earthquake loading," *Tunnelling and Underground Space Technology*, vol. 20, no. 5, pp. 411–417, 2005.

[5] N. M. Newmark, "Problems in wave propagation in soil and rock," in *Proceedings of the International Symposium on Wave Propagation and Dynamic Properties of Earth Materials*, pp. 7–26, New Mexico, August 1967.

[6] T. R. Kuesel, "Earthquake design criteria for subways," *Journal of the Structural Division*, vol. 95, no. 6, pp. 1213–1231, 1969.

[7] J. E. Luco and F. C. P. D. Barros, "Dynamic displacements and stresses in the vicinity of a cylindrical cavity embedded in a half-space," *Earthquake Engineering & Structural Dynamics*, vol. 23, no. 3, pp. 321–340, 2010.

[8] C. A. Davis, V. W. Lee, and J. P. Bardet, "Transverse response of underground cavities and pipes to incident SV waves," *Earthquake Engineering & Structural Dynamics*, vol. 30, no. 3, pp. 383–410, 2010.

[9] R. Pang, K. Chen, Q. Fan, and B. Xu, "Stochastic ground motion simulation and seismic damage performance assessment of a 3-D subway station structure based on stochastic dynamic and probabilistic analysis," *Tunnelling and Underground Space Technology*, vol. 126, Article ID 104568, 2022.

[10] Y. J. Qiu, H. R. Zhang, Z. Y. Yu, and J. K. Zhang, "A modified simplified analysis method to evaluate seismic responses of subway stations considering the inertial interaction effect of adjacent buildings," *Soil Dynamics and Earthquake Engineering*, vol. 150, Article ID 106896, 2021.

[11] Y. Tamari and I. Towhata, "Seismic soil-structure interaction of cross sections of flexible underground structures subjected to soil liquefaction," *Soils and Foundations*, vol. 43, no. 2, pp. 69–87, 2003.

[12] J. An, L. Tao, L. Jiang, and H. Yan, "A shaking table-based experimental study of seismic response of shield-enlarge-dig type's underground subway station in liquefiable ground," *Soil Dynamics and Earthquake Engineering*, vol. 147, no. 3, Article ID 106621, 2021.

[13] H. Wu, H. Lei, and T. Lai, "Shaking table tests for seismic response of orthogonal overlapped tunnel under horizontal seismic loading," *Advances in Civil Engineering*, vol. 2021, no. 2, pp. 1–19, 2021.

[14] C. Xu, Z. Zhang, Y. Li, and X. Du, "Validation of a numerical model based on dynamic centrifuge tests and studies on the earthquake damage mechanism of underground frame structures," *Tunnelling and Underground Space Technology*, vol. 104, Article ID 103538, 2020.

[15] Y. U. Miao, Y. I. Zhong, B. Ruan, K. E. Cheng, and G. Wang, "Seismic response of a subway station in soft soil considering the structure-soil-structure interaction," *Tunnelling and Underground Space Technology*, vol. 106, Article ID 103629, 2020.

[16] J. X. Chen, R. Z. Wen, and P. Q. Yu, "Numerical analysis of seismic response of a shallow-buried subway station structure in soft soil," *World Earthquake Engineering*, vol. 25, no. 02, pp. 46–53, 2009.

[17] X. L. Du, H. T. Liu, and C. S. Xu, "Experimental study on seismic performance of precast column in assembled monolithic subway station under different axial compression ratio," *Journal of Building Structures*, vol. 39, no. 11, pp. 11–19, 2018.

[18] Y. Lu and W. Huang, "Numerical simulation of dynamic response law of intersecting metro tunnels in upper and lower strata," *Geotechnical & Geological Engineering*, vol. 38, no. 4, pp. 3773–3785, 2020.

[19] X. Ma, W. Zhang, and J. Ren, "Dynamic response of silty fine sand layer beneath single-hole double-track subway tunnel," *J Disaster Prev Mitig Eng*, vol. 39, no. 01, pp. 106–116, 2019.

[20] D. Liu, X. Du, H. M. El Naggar, C. Xu, and Q. Chen, "Seismic mitigation performance analysis of underground subway station with arc grooved roller bearings," *Soil Dynamics and Earthquake Engineering*, vol. 153, Article ID 107082, 2022.

[21] X. L. Du, C. Ma, D. C. Lu, C. S. Xu, and Z. G. Xu, "Collapse simulation and failure mechanism analysis of the Daikai station under seismic loads," *China Civil Engineering Journal*, vol. 50, no. 1, pp. 53–62, 2017.

[22] X. L. Du, Y. Li, C. S. Xu, D. C. Lu, Z. G. Xu, and L. Jin, "Review on damage causes and disaster mechanism of Daikai subway station during 1995 Osaka-Kobe earthquake," *Chinese Journal of Geotechnical Engineering*, vol. 40, no. 2, pp. 223–236, 2018.

Research Article

Estimation of Critical Safety Thickness of the Base against Confined Water Inrush for a Rectangular Foundation Pit

Qin-xing Li,[1] **Hong-tao Wang** ⓘ **,**[1,2] **Yan-qing Men** ⓘ **,**[1] **Xiao Yu,**[1] **Chi Liu,**[1] **and Hua-jun Zhang**[1]

[1]*Jinan Rail Transit Group Co., Ltd., Jinan, Shandong, China*
[2]*School of Civil Engineering, Shandong Jianzhu University, Jinan, Shandong, China*

Correspondence should be addressed to Hong-tao Wang; wanghongtao918@163.com and Yan-qing Men; ky_jnyt@163.com

Received 15 June 2022; Accepted 26 July 2022; Published 12 September 2022

Academic Editor: Pengjiao Jia

Affected by confined aquifer, basal inrush accidents caused by excavation are common in foundation pits, and accurate estimation of the safety thickness of the base is a big concern of engineers. In this paper, a three-dimensional failure mechanism of base inrush was constructed for a rectangular foundation pit. In this mechanism, the strength of the soil mass was assumed to be nonhomogeneous along the depth, and the soil-mass failure satisfied the linear and nonlinear Mohr–Coulomb strength criteria. Then, based on the limit equilibrium theory, the prediction method for the safety thickness of the base against confined water inrush was deduced, and a comparison with existing research works was conducted. Furthermore, the influence laws of soil strength parameters, pit design parameters, and confined water pressure on the critical safety thickness were analyzed. The results show that the critical safety thickness of the base is positively correlated with nonlinear coefficient and confined water pressure but negatively correlated with cohesion, internal friction angle, nonhomogeneity coefficient, and unit weight. The soil strength is a key factor affecting the base safety thickness, which should be paid enough attention to in engineering design and construction. The research findings in this paper can provide a theoretical reference for the prevention and control of basal inrush accidents in confined water strata.

1. Introduction

In recent years, with the continuous advancement of urbanization in the world, the scale of all kinds of infrastructure construction is increasing, and the surface space is gradually becoming crowded. A series of problems such as population surge, traffic congestion, and environmental pollution have also become increasingly prominent. Rational development and utilization of underground space can effectively alleviate the above problems; it is one of the important ways to achieve sustainable and healthy urban development in the future. In the development process of urban underground space, the open-cut method is one of the most commonly used construction methods. In this method, accompanied by a series of complex projects such as urban subways, utility tunnels, and high-rise buildings, a large number of deep foundation pits with complex geological conditions have emerged in recent years, bringing great challenges to project safety construction. According to the existing data, the foundation pit accidents caused by groundwater account for about 45%–70% of all kinds of accidents. Especially in the confined water area, the inrush disaster caused by the action of the bottom confined water is more common, and it is easy to induce the collapse of foundation pits and destruction of supporting structures, which are big concerns of engineering design and construction personnel.

At present, the basal inrush failure mechanism of the foundation pit subjected to confined water has always been the concern of many scholars. The commonly used research methods include theoretical analysis, numerical simulation, and laboratory tests. For instance, Terzaghi [1] concluded that the seepage failure zone of the foundation pit base is mainly near the enclosure structure according to the model

test and established the foundation pit inrush discriminant based on the test results. Marsland [2] conducted model tests at a building research station to determine the types of failures that occur due to water seepage in strutted sheeted excavations in noncohesive soils and investigated the influences of the cofferdam width, the penetration depth of the sheeting, and the soil conditions. Liu and Wang [3] analyzed the influence of the pressure water in shallow silty on excavation and proposed a series of measures to ensure safety during the pit excavation. Fontana [4] assessed the safety coefficient by comparing the exit gradient with the critical gradient and concluded that the experimental data and theoretical values were close if the thickness of the sheet pile and the ground surface deformation were properly taken into account. Wudtke [5] investigated the kind and the mechanism of hydraulic heave at excavations in cohesive soils and carried out a series of tests to visualize the failure mechanism in cohesive soil; finally, he proposed a series of factors that the failure type basically depends on. Do et al. [6] investigated basal heave stability of deep excavations in soft clay and employed three methods to estimate factors of safety against basal heave. Do et al. [7] investigated four failure mechanisms of excavations and proposed that reasonable stability of excavations was estimated by the FEM in the case of elastoplastic support system. Ding et al. [8] analyzed the influence laws of induced factors (confined water head, length, and width of the foundation pit) on the plastic deformation failure of foundation pit inrush based on the three-dimensional finite element calculation model. The results show that the uplift deformation and inrush plastic deformation failure of the soil under the foundation pit have a nonlinear relationship with the confined water head and the width of the foundation pit. Goh [9] assessed the basal heave stability of diaphragm wall supported circular excavations in clays using the finite element method and proposed a simplified method for assessing the basal heave factor of safety for axisymmetric supported excavations. Huang et al. [10] proposed a new failure mechanism to evaluate the basal stability of excavations with embedded walls in undrained clay and analyzed two failure field cases in anisotropic clay using this mechanism.

In strata containing confined water, sufficient base safety thickness of the foundation pit is very necessary to prevent inrush disaster. For example, in the current foundation pit codes of China and Japan, the theoretical prediction formula of basal inrush disaster is given on the basis of the pressure balance method. In this method, it is considered that inrush failure occurs if the dead weight of the bottom soil mass is smaller than the confined water pressure; the influence of soil strength is ignored. Specific to this problem, Ma et al. [11] proposed a calculation method for the critical thickness of the foundation pit base based on the relevant theories of structural mechanics. Yang and Zheng [12] took the excavation of a subway station as an example and put forward the calculation formula of base inrush to correct the code method by considering the shearing strength of soil mass. Wang et al. [13] obtained the method for determining the critical thickness of the base plate of the foundation pit based

on elastic theory. Liu et al. [14] derived a new checking formula for anti-inrush of the foundation pit by considering shear strength and the dead weight of the foundation pit base and considering seepage factors of the foundation pit base. Sun [15] conducted a series of centrifugal model tests to investigate the failure mechanism of the foundation pit and proposed a theoretical approach to the basal stability analysis of deep excavation against a confined aquifer. Chen et al. [16] established the numerical model of PIP braced excavation in Shanghai soft clay overlying a confined aquifer and investigated the coupling effects of re-excavation and hydraulic uplift on base instability. Hu et al. [17] proposed the basic equation of unsteady seepage and stress coupling and investigated the stability of a deep foundation pit adjacent to water.

It should be noted that the above research works are all conducted on the basis of the linear Mohr–Coulomb failure criterion. A large number of laboratory tests [18–21] have shown that the strength envelope of soil mass is closer to an outer convex curve rather than the traditional linear relationship. Therefore, a nonlinear criterion is more accurate to describe the failure of soil masses. Meanwhile, under the action of long-term overloading within the strata, the soil mass may present obvious nonhomogeneity. By considering these factors and based on the existing research work, the nonlinear failure characteristics and the nonhomogeneity of soil masses are further incorporated in this paper, and a three-dimensional basal inrush failure mechanism for a rectangular foundation pit is constructed. Then the formula for predicting the critical safety thickness of the base is derived on the basis of the limit equilibrium method. The influence laws of different soil parameters, foundation pit design parameters, and confined water pressure on the critical thickness are obtained. The research findings in this paper can provide a theoretical reference for the basal inrush failure of foundation pits in confined water strata.

2. Inrush Failure Mechanism for a Rectangular Foundation Pit

2.1. Calculation Model in Current Technical Codes. At present, in the technical codes of foundation pits in China and Japan, the calculation model of base inrush is established on the basis of the pressure balance method, as shown in Figure 1. In this model, it is assumed that there is a confined aquifer below the pit bottom and that the water head of the confined aquifer is higher than that of the pit bottom. The formula for calculating the inrush stability subjected to the confined water can be expressed as follows:

$$\frac{D_s \gamma}{H_w \gamma_w} \geq K_{ty}, \tag{1}$$

where K_{ty} is a safety factor that is greater than or equal to 1.1, γ is the unit weight of the soil mass, γ_w is the unit weight of the water, D_s is the critical safety thickness of the base against confined water inrush, and H_w is the height of the confined water head.
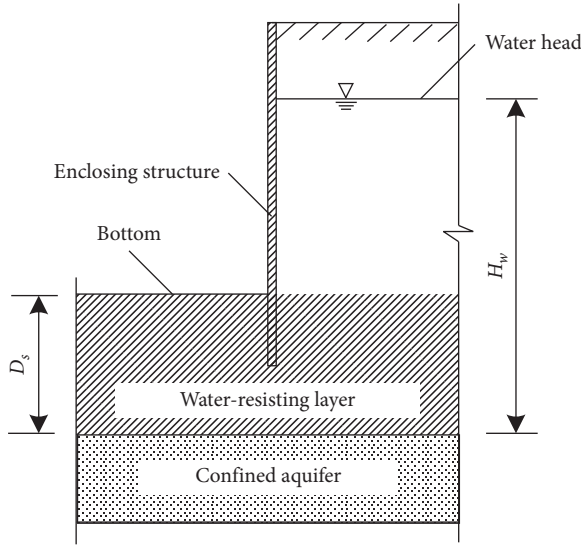
FIGURE 1: The calculation model of base inrush stability in current codes.

2.2. The Inrush Failure Mechanism Proposed in This Paper. In this paper, a rectangular foundation pit with depth H, width B, and length L is selected for analysis. According to the current codes and the research works by Yang and Zheng [12], Liu et al. [14], and Sun [15], a three-dimensional failure mechanism of base inrush is constructed, as shown in Figure 2. The inrush failure range is considered to be a red cube in Figure 2. Specifically, it is assumed that when the confined water pressure at the bottom exceeds the strength and dead weight of the upper soil mass, the inrush failure will occur. The bottom soil mass will slide upward along the vertical failure surface. The corresponding critical safety thickness is D_s. Meanwhile, the influence of supporting structure is neglected in the proposed mechanism, which can be regarded as the most unfavorable failure case and can ensure the safety of engineering design. Compared with the calculation model in current codes, the presented failure mechanism in Figure 2 considers the influence of soil shear strength, which may be closer to reality. Accordingly, the normal stress at the corresponding soil failure surface is σ_n, and the shear stress is τ_n.

In the mechanism shown in Figure 2, we assume that the failure of the basal soil mass meets the following two criteria.

2.2.1. Mohr–Coulomb Failure Criterion. Mohr–Coulomb failure criterion is one of the most widely used strength criteria in geotechnical engineering. And its form is simple and can effectively describe the shear failure characteristics of soil masses. Accordingly, the normal stress σ_n and shear stress τ_n at any point on the soil failure surface should meet the following expression:

$$\tau_n = \sigma_n \tan \varphi + c, \tag{2}$$

where c and φ are the cohesion and internal friction angle, respectively.

2.2.2. Nonlinear Mohr–Coulomb Failure Criterion. A large number of laboratory tests [18–21] have shown that the relationship between the normal stress and shear stress corresponding to soil failure is not strictly linear. Especially in the low-stress region, the strength envelope of soil masses is closer to an outer convex curve. Thus, a nonlinear Mohr–Coulomb failure criterion is also used to describe the nonlinear characteristics of soil masses, as shown in Figure 3. The corresponding expression is

$$\tau_n = c_0 \left(1 + \sigma_n / \sigma_t\right)^{1/m}, \tag{3}$$

where c_0 is the cohesion of soil mass, σ_t is the tensile strength, and m is a nonlinear coefficient. When $m = 1.0$, the nonlinear Mohr–Coulomb failure criterion in equation (3) can be converted to the linear Mohr–Coulomb failure criterion.

In addition, due to long-term overburden and sedimentation, the soil mass may present a property of non-homogeneity, which will have a significant impact on its shear strength of itself. According to the research works by Huang et al. [22], Wang et al. [23], and Liu et al. [24], it is assumed that the cohesion of the soil mass increases linearly with depth in Figure 2, as shown in Figure 4.

Based on the nonhomogeneity model in Figure 4, the soil cohesion at the ground surface is assumed to be c_{01}. Then, in the linear and nonlinear Mohr–Coulomb expressions in equations (2) and (3), the cohesion at any depth inside the basal soil mass can be expressed as follows:

$$c(z) = c_{01} \left[1 + \frac{\lambda (H + z)}{H + D_s} \right], \tag{4}$$

where λ is a coefficient reflecting the nonhomogeneity of soil mass.

3. Determination of Critical Safety Thickness of the Base

3.1. Critical Safety Thickness Based on Mohr–Coulomb Failure Criterion. According to the inrush failure mechanism of the base in the rectangular foundation pit in Figure 2, the vertical dead weight stress at any position of the soil failure surface is

$$\sigma_v = \gamma (H + z). \tag{5}$$

Correspondingly, the normal stress at the soil failure surface is

$$\sigma_n = \gamma K_0 (H + z), \tag{6}$$

where K_0 is the lateral pressure coefficient. According to the linear Mohr–Coulomb failure criterion and soil non-homogeneity and by using equations (2), (4), and (6), the shear stress at any point of the soil failure surface can be expressed as follows:

$$\tau_n = \sigma_n \tan \varphi + c = \gamma K_0 (H + z)\tan \varphi + c_{01} \left[1 + \frac{\lambda (H + z)}{H + D_s} \right]. \tag{7}$$
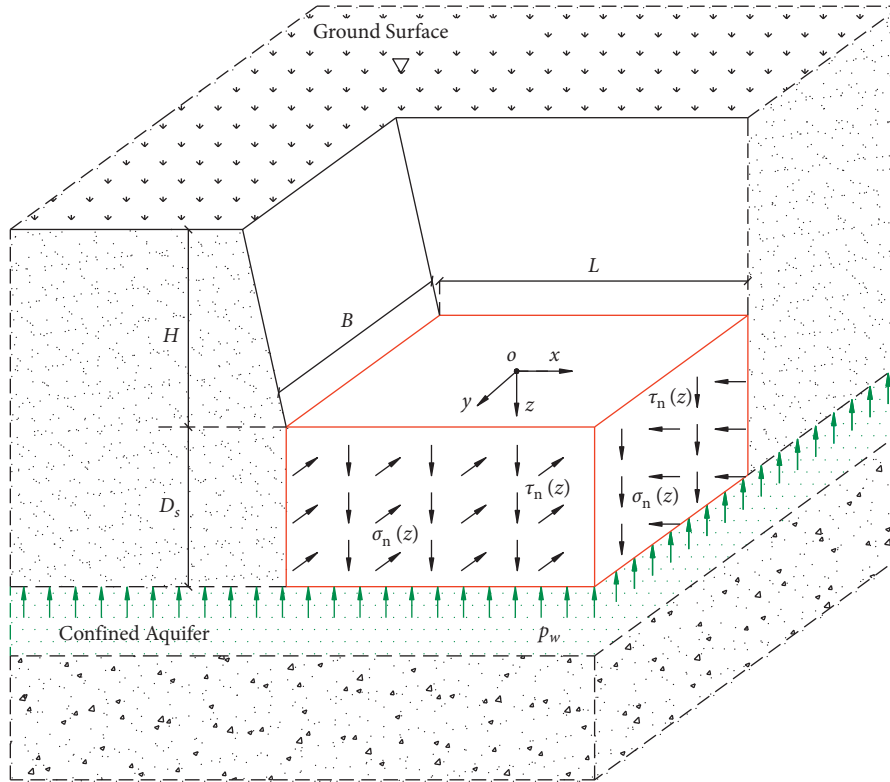
FIGURE 2: Inrush failure mechanism for a rectangular foundation pit.
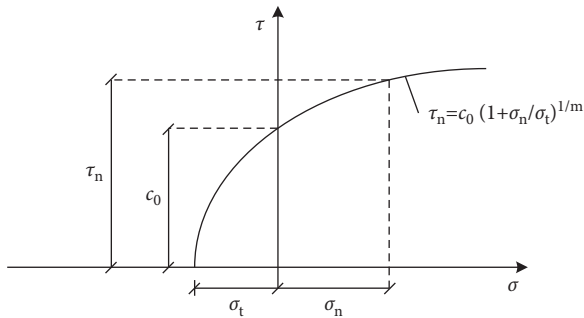
FIGURE 3: Nonlinear Mohr–Coulomb failure criterion.
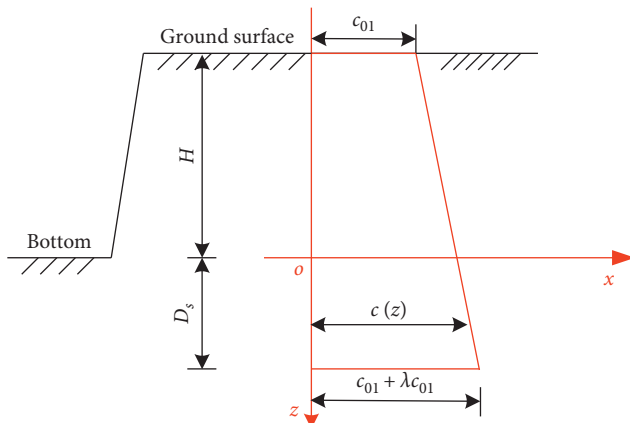
FIGURE 4: Nonhomogeneity of soil mass.

The total shear force at the failure surface of the soil mass can be obtained by integrating equation (7) and can be expressed as follows:

$$
\begin{aligned}
F &= 2(B+L)\int_0^{D_s} \tau_n dz \\
&= 2(B+L)D_s \\
&\cdot \left\{ \gamma K_0 \left(H + \frac{D_s}{2}\right)\tan\varphi + c_{01}\left[1 + \frac{\lambda(H+D_s/2)}{H+D_s}\right]\right\}.
\end{aligned}
\tag{8}
$$

The total weight of the soil mass within the inrush failure area of the foundation pit base is

$$
G = BLD_s\gamma. \tag{9}
$$

The total inrush destructive force generated by confined water under the foundation pit base is:

$$
F_{pw} = BLp_w. \tag{10}
$$

The inrush failure of the foundation pit base is jointly borne by the dead weight of the upper soil mass and the shear force at the failure surfaces. In order to ensure the safety of the foundation pit base, by referring to the calculation formula in equation (1) given in the current code, the following calculation formula can be constructed:

$$
\frac{G+F}{F_{pw}} \geq K_{ty}, \tag{11}
$$

where K_{ty} is a safety factor for characterizing the inrush stability of the foundation pit base.

By substituting equations (8)–(10) into equation (11), the following calculation formula of the critical safety thickness D_s against basal inrush in rectangular foundation pits can be obtained:

$$\gamma K_0 (B+L)\tan\varphi \cdot D_s^3$$
$$+\left\{\gamma BL + (B+L)\cdot\left[3\gamma HK_0\tan\varphi + c_{01}(2+\lambda)\right]\right\}$$
$$\cdot D_s^2 + H\left\{\gamma BL + (B+L)\left[2\gamma HK_0\tan\varphi + 2c_{01}(1+\lambda)\right]\right.$$
$$\left.-K_{ty}BLp_w\right\}\cdot D_s - BLHK_{ty}p_w \geq 0. \tag{12}$$

When the soil strength parameters and design parameters of the foundation pit are known, the theoretical calculation value of critical safety thickness D_s can be obtained by using equation (12) according to the inrush safety factor.

3.2. Critical Safety Thickness Based on Nonlinear Mohr–Coulomb Failure Criterion.

According to the nonlinear Mohr–Coulomb failure criterion, by substituting equations (4) and (6) into equation (3), the shear stress at any height of the failure surface of the foundation pit base can be expressed as follows:

$$\tau_n = c_0\left(1+\frac{\sigma_n}{\sigma_t}\right)^{1/m}$$
$$= c_{01}\left[1+\frac{\lambda(H+z)}{H+D_s}\right]\cdot\left[1+\frac{\gamma K_0(H+z)}{\sigma_t}\right]^{1/m}. \tag{13}$$

By integrating equation (13) along the inrush failure surfaces of the foundation pit base, the total shear force generated at the failure surfaces can be obtained as follows:

$$F = 2(B+L)\int_0^{D_s}\tau_n dz$$
$$=\frac{2c_{01}(B+L)m\sigma_t}{(1+m)\gamma K_0}\left\langle(1+\lambda)\left[\frac{\sigma_t+\gamma K_0(H+D_s)}{\sigma_t}\right]^{(1+m)/m}\right.$$
$$-\left(1+\frac{\lambda H}{H+D_s}\right)\left(\frac{\sigma_t+\gamma K_0 H}{\sigma_t}\right)^{(1+m)/m}-\frac{\lambda m\sigma_t}{(H+D_s)(1+2m)\gamma K_0}$$
$$\left.\cdot\left\{\left[\frac{\sigma_t+\gamma K_0(H+D_s)}{\sigma_t}\right]^{(1+2m)/m}-\left(\frac{\sigma_t+\gamma K_0 H}{\sigma_t}\right)^{(1+2m)/m}\right\}\right\rangle. \tag{14}$$

According to equation (9) and (10), equation (14) is substituted into equation (11), and the calculation formula of critical safety thickness D_s can also be obtained as follows:

$$\frac{2c_{01}(B+L)m\sigma_t}{(1+m)\gamma K_0}\left\langle(1+\lambda)\left[\frac{\sigma_t+\gamma K_0(H+D_s)}{\sigma_t}\right]^{(1+m)/m}\right.$$
$$-\left(1+\frac{\lambda H}{H+D_s}\right)\left(\frac{\sigma_t+\gamma K_0 H}{\sigma_t}\right)^{(1+m)/m}$$
$$-\frac{\lambda m\sigma_t}{(H+D_s)(1+2m)\gamma K_0}$$
$$\cdot\left\{\left[\frac{\sigma_t+\gamma K_0(H+D_s)}{\sigma_t}\right]^{(1+2m)/m}-\left(\frac{\sigma_t+\gamma K_0 H}{\sigma_t}\right)^{(1+2m)/m}\right\}\right\rangle$$
$$+BLD_s\gamma - K_{ty}BLp_w \geq 0. \tag{15}$$

At this time, when the nonlinear strength parameters and the design parameters of the foundation pit are known, the critical safety thickness D_s of the rectangular foundation pit base under the nonlinear Mohr–Coulomb failure criterion can be obtained by using equation (15).

4. Discussion and Analysis

4.1. Comparison with Existing Research Works.

In the current codes, the inrush calculation model of the foundation pit base is established on the basis of the pressure balance method without considering the influence of soil strength. To solve this problem, Sun [15] carried out the centrifugal model test of foundation pit inrush and proposed a theoretical prediction method of critical base thickness based on the Mohr–Coulomb criterion. In order to further verify the effectiveness of the calculation method in this paper, when the size B(width) $\times L$(length) of the foundation pit is $8\,m \times 16\,m$, $10\,m \times 20\,m$, and $12\,m \times 24\,m$, respectively, the method proposed in this paper, the current code method, and the method proposed by Sun [15] are used for a comparative analysis in this section. The specific calculation parameters are as follows: excavation depth $H = 3\,m$, soil cohesion $c_{01} = 30\,kPa$, internal friction angle $\varphi = 30°$, unit weight $\gamma = 18\,kN/m^3$, and lateral pressure coefficient $K_0 = 0.8$. Meanwhile, this section considers two nonhomogeneity coefficients of $\lambda = 0$ and $\lambda = 0.5$, respectively, for comparative analysis. Figures 5–7 show the variation curves of the critical safety thickness of the foundation pit base inrush with confined water pressure P_w. It can be seen from Figures 5–7 that the critical safety thickness of the foundation pit base under the three calculation methods increases with the increase of confined water pressure. Meanwhile, the calculation results of this method are slightly smaller than those of the method proposed by Sun [15], but the results of these two methods are close to each other, and both are smaller than the code calculation results. This shows that the code method is relatively conservative under the premise of ensuring the safety of the foundation pit base, while the proposed method in this paper is relatively economical. In addition, by comparing the calculation results in Figures 5–7, it can also be seen that the excavation size of the foundation pit also has a certain influence on base stability.
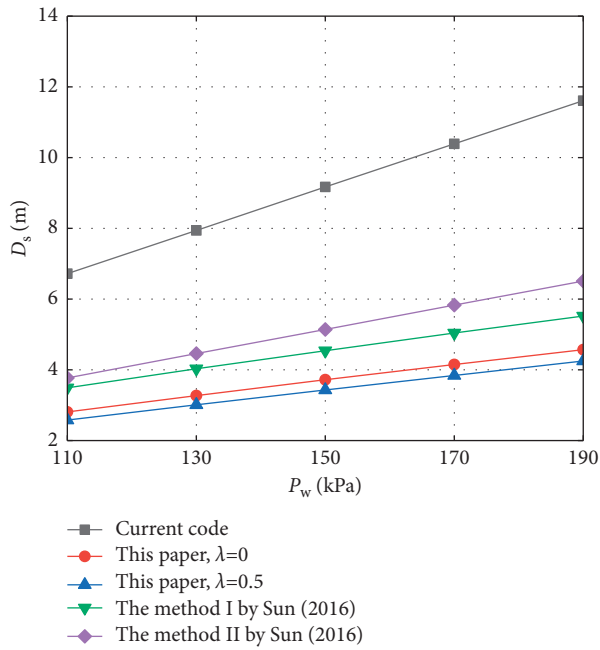
FIGURE 5: Critical safety thickness of the base corresponding to $B \times L = 8\,\text{m} \times 16\,\text{m}$.
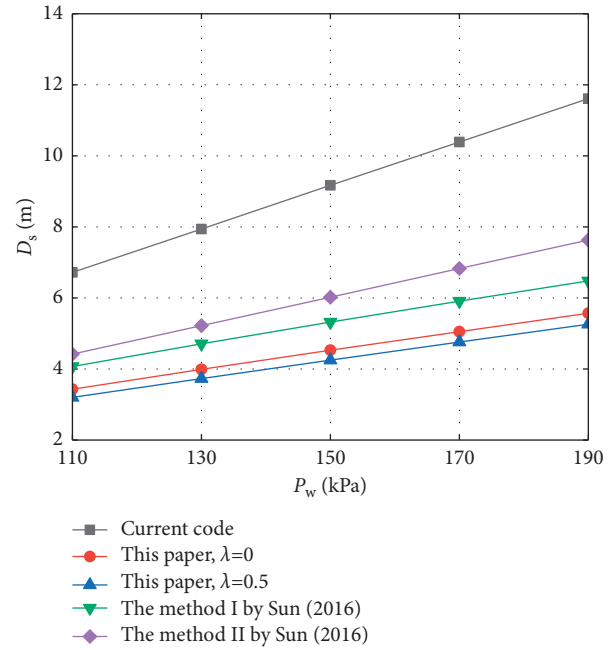
FIGURE 7: Critical safety thickness of the base corresponding to $B \times L = 12\,\text{m} \times 24\,\text{m}$.
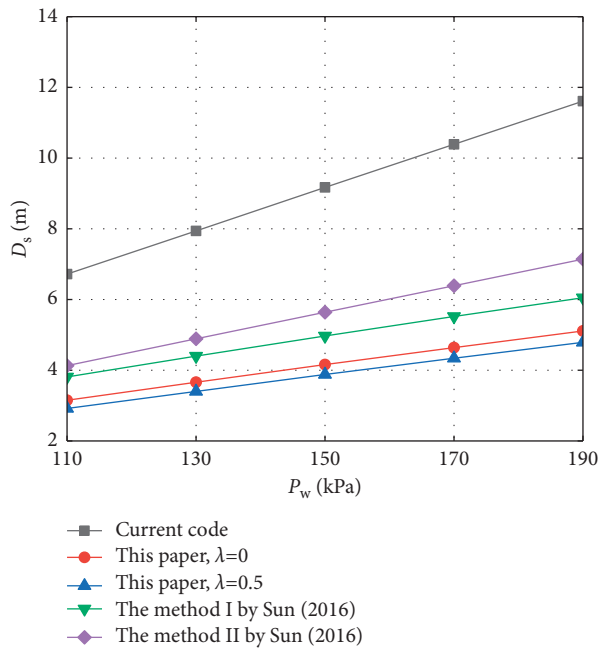
FIGURE 6: Critical safety thickness of the base corresponding to $B \times L = 10\,\text{m} \times 20\,\text{m}$.

As the excavation size increases, the critical safety thickness of the base also increases accordingly.

4.2. Effects of Different Linear Mohr–Coulomb Parameters. Based on the traditional linear Mohr–Coulomb failure criterion, this section analyzes the influence laws of non-homogeneity coefficient, cohesion, internal friction angle,

and unit weight on the critical safety thickness of the foundation pit base under different excavation sizes. The following parameters are selected as a standard group for calculation: foundation pit size $B \times L = 10\,\text{m} \times 20\,\text{m}$, excavation depth $H = 6\,\text{m}$, cohesion $c_{01} = 30\,\text{kPa}$, internal friction angle $\varphi = 30°$, unit weight $\gamma = 18\,\text{kN/m}^3$, lateral pressure coefficient $K_0 = 0.8$, confined water pressure $P_w = 150\,\text{kPa}$, and safety factor $K_{ty} = 1.1$. When analyzing the change of one soil parameter, the other parameters remain unchanged. When cohesion c_{01} is $10 \sim 50\,\text{kPa}$, internal friction angle φ is $22° \sim 38°$, unit weight γ is $14 \sim 22\,\text{kN/m}^3$, and nonhomogeneity coefficient λ is $0 \sim 1.0$, the corresponding variation curves of the basal critical safety thickness are shown in Figure 8. It can be seen from Figure 8 that under the traditional linear Mohr–Coulomb strength criterion, with the increase of cohesion, internal friction angle, unit weight, and nonhomogeneity coefficient, the whole strength of the soil mass and the capacity of the base against inrush increase accordingly, and the corresponding critical safety thickness of the foundation pit base decreases.

4.3. Effects of Different Nonlinear Mohr–Coulomb Parameters. Similarly, based on the nonlinear Mohr–Coulomb strength criterion, this section analyzes the influence laws of initial cohesion at the ground surface, nonhomogeneity coefficient, nonlinear coefficient, and unit weight on the critical safety thickness of the base under different excavation sizes. In the calculation process, the foundation pit size, excavation depth, initial cohesion at the ground surface, lateral pressure coefficient, unit weight, confined water pressure, and safety factor are the same as those of the standard group in Section 4.2. When the initial cohesion at the ground surface c_{01} is $10 \sim 50\,\text{kPa}$, the unit weight γ is $14 \sim 22\,\text{kN/m}^3$, the
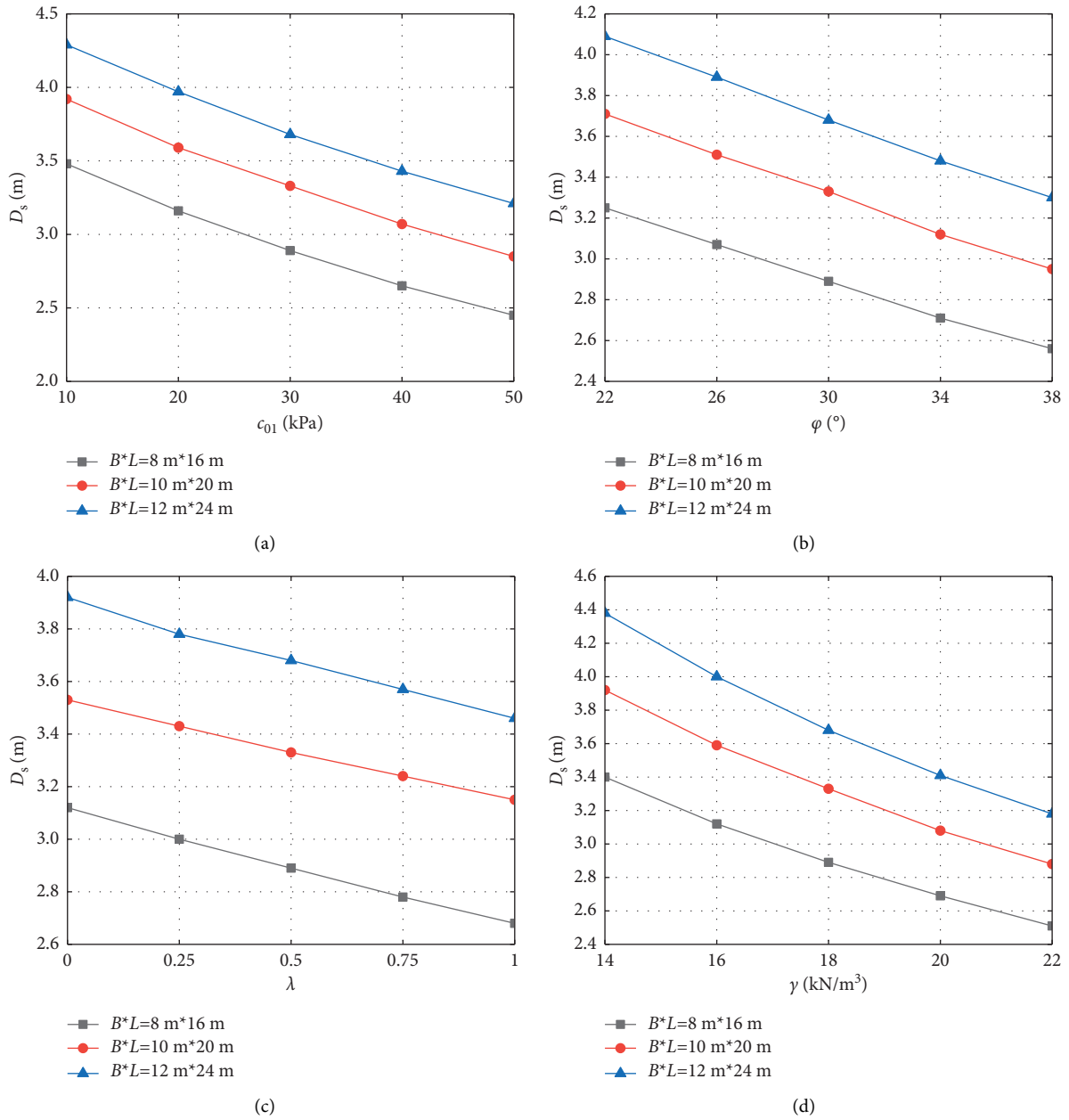
Figure 8: Effects of different linear Mohr–Coulomb parameters on critical safety thickness: (a) cohesion, (b) internal friction angle, (c) nonhomogeneity coefficient, and (d) unit weight.

nonhomogeneity coefficient λ is $0 \sim 1.0$, and the nonlinear coefficient m is $1 \sim 3$, the variation curves of the basal's critical safety thickness under different nonlinear strength parameters are shown in Figure 9. It can be seen from Figure 9 that under the nonlinear Mohr–Coulomb strength criterion, the critical safety thickness of the base is negatively correlated with the initial cohesion at the ground surface, nonhomogeneity coefficient, and unit weight, which is consistent with the conclusion in Section 4.2. However, the critical safety thickness is positively correlated with the nonlinear coefficient m. That is, as the nonlinear coefficient of the soil mass increases, the overall

strength of the soil mass decreases, and the corresponding critical safety thickness of the base increases.

4.4. Recommendations for Engineering Projects.
According to the influence laws of different parameters on the critical safety thickness of the base, in order to further guide the design of the foundation pit support and inrush disaster prevention in confined water strata, this paper provides the following recommendations for engineering projects:
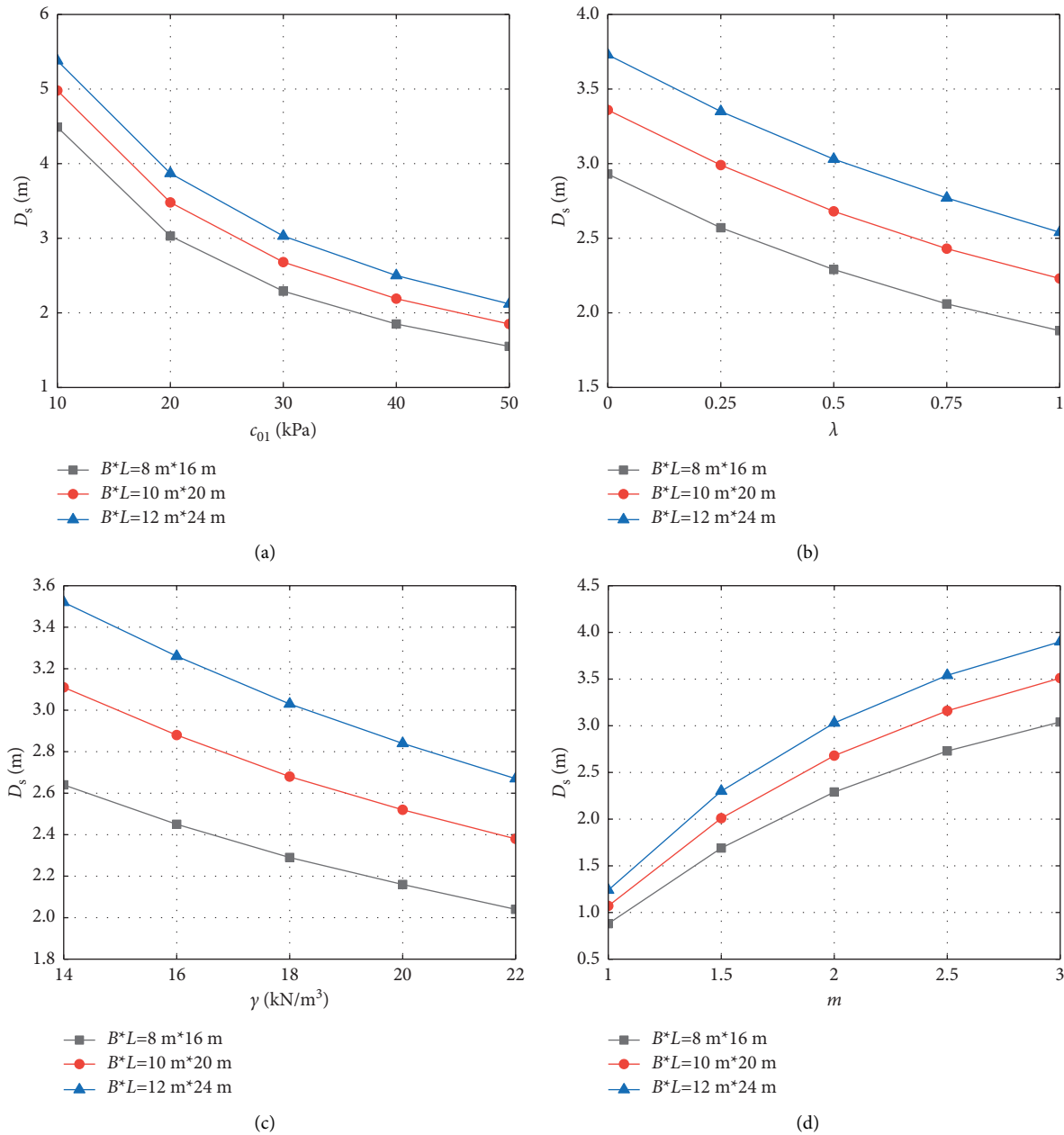
FIGURE 9: Effects of different nonlinear Mohr–Coulomb parameters on critical safety thickness: (a) initial cohesion at the ground surface, (b) nonhomogeneity coefficient, (c) unit weight, and (d) nonlinear coefficient.

(1) Due to the consideration of soil strength parameters in the method proposed in this paper, the corresponding calculation results are smaller than those in the current codes. This shows that the current code method is relatively conservative. Especially in practical engineering, if the soil strength of the foundation pit base is high, it is more economical to adopt the method in this paper; it can reduce the cost of prevention and control of inrush disasters to a certain extent.

(2) The influence of soil strength parameters on the inrush failure of the foundation pit base is significant.

If the strength of the bottom soil mass is low, the reinforcement of the bottom soil mass can be carried out in advance by a cement-soil mixing pile, high-pressure jet grouting pile, or grouting reinforcement measures, so as to improve the strength parameters of the soil mass and the safety of the base.

(3) Increasing the unit weight of basal soil mass is also one of the effective measures to prevent the inrush of the foundation pit. In engineering practice, the basal safety can be improved by means of surcharging load or replacing soil layer with stone to prevent inrush disaster.

5. Conclusions

(1) In this paper, focusing on a rectangular foundation pit, a three-dimensional failure mechanism of basal inrush is proposed. By using this mechanism, the theoretical formula for calculating the critical safety thickness against basal inrush is derived on the basis of the limit equilibrium method, and the linear and nonlinear Mohr–Coulomb strength criterion. In addition, the corresponding engineering suggestions are given, which can provide some theoretical reference for the prevention and control of basal inrush disasters of foundation pits in confined water strata.

(2) The proposed method is validated by comparing with the current code and the existing research works. The calculation results in this paper are close to those in the existing literature and are smaller than those in the current code. This shows that the results obtained by the current code are conservative, while the method presented in this paper is relatively economical.

(3) The influence laws of different excavation sizes, soil strength parameters, and confined water pressure on the basal critical safety thickness are analyzed. The results show that the critical safety thickness decreases with the increase of cohesion, internal friction angle, nonhomogeneity coefficient, and unit weight but increases with the increase of nonlinear coefficient and confined water pressure. The influence of soil strength parameters on the basal inrush failure is significant, and enough attention should be paid to it in engineering design and construction.

Abbreviations

D_s: The critical safety thickness of the base against confined water inrush
γ: The unit weight of the soil mass
H_w: The height of the confined water head
P_w: Confined water pressure
K_{ty}: A safety factor to characterizing the inrush stability of the foundation pit base
σ_n: The normal stress at the soil failure surface
τ_n: The shear stress at the soil failure surface
c: Cohesion
φ: Internal friction angle
c_0: Initial cohesion
σ_t: Tensile strength
m: A nonlinear coefficient
λ: A coefficient reflecting the nonhomogeneity of soil mass
H: The depth of the rectangular foundation pit
B: The width of the rectangular foundation pit
σ_v: The vertical stress at any position of the soil failure surface
K_0: Lateral pressure coefficient
L: The length of the rectangular foundation pit
G: The total weight of the soil mass within the inrush failure area
F_{pw}: The total inrush destructive force generated by confined water
F: The total shear force at the failure surface of soil mass.

Data Availability

The data used to support the findings of this study are included within the article.

Conflicts of Interest

The authors declare that there are no conflicts of interest regarding the publication of this paper.

Acknowledgments

References

[1] K. Terzaghi, "Simple tests determine hydrostatic uplift," *Engineering News-Record*, vol. 116, no. 6, pp. 872–875, 1936.

[2] A. Marsland, "Model experiments to study the influence of seepage on the stability of a sheeted excavation in sand," *Géotechnique*, vol. 3, no. 6, pp. 223–241, 1953.

[3] G. B. Liu and H. X. Wang, "Influence of the pressure water in shallow silty sand in Shanghai on excavation," *Chinese Journal of Geotechnical Engineering*, vol. 24, no. 6, pp. 790–792, 2002, in Chinese.

[4] N. Fontana, "Experimental analysis of heaving phenomena in sandy soils," *Journal of Hydraulic Engineering*, vol. 134, no. 6, pp. 794–799, 2008.

[5] R. B. Wudtke, "Failure mechanisms of hydraulic heave at excavations," in *Proceedings of the Young Geotechnical Engineers' Conference (EYGEC)*, Győr, Hungary, September 2008.

[6] T.-N. Do, C.-Y. Ou, and A. Lim, "Evaluation of factors of safety against basal heave for deep excavations in soft clay using the finite-element method," *Journal of Geotechnical and Geoenvironmental Engineering*, vol. 139, no. 12, pp. 2125–2135, 2013.

[7] T.-N. Do, C.-Y. Ou, and R.-P. Chen, "A study of failure mechanisms of deep excavations in soft clay using the finite element method," *Computers and Geotechnics*, vol. 73, pp. 153–163, 2016.

[8] C. Ding, Z. Li, X. Wu, and K. Wu, "Analysis on inducing factors to inrushing plastic deformation failure of foundation pit with confined water," *Tunneling And Underground Construction*, pp. 491–501, 2014.

[9] A. T. Goh, "Basal heave stability of supported circular excavations in clay," *Tunnelling and Underground Space Technology*, vol. 61, pp. 145–149, 2017.

[10] M. S. Huang, H. Y. Wang, Z. Tang, and J. Yu, "Basal stability analysis of braced excavations in anisotropic and non-homogeneous undrained clay using streamline velocity fields," *Acta Geotechnica*, vol. 16, no. 4, pp. 1175–1186, 2020.

[11] S. C. Ma, C. J. Yin, and Y. S. Zou, "Analysis and calculation of the pit base plate thickness of bearing resistance water foundation," *Engineering Mechanics*, vol. 2, pp. 204–208, 2004.

[12] J. M. Yang and G. Zheng, "Classification of seepage failures and opinion to formula for check bursting instability in dewatering," *Rock and Soil Mechanics*, vol. 30, no. 1, pp. 261–264, 2009.

[13] Y. L. Wang, K. H. Xie, M. M. Lu, and K. Wang, "A method for determining critical thickness of base soil of foundation pit subjected to confined water," *Rock and Soil Mechanics*, vol. 31, no. 5, pp. 1539–1544, 2010.

[14] Z. R. Liu, S. Z. Ma, Y. Yang, and J. P. Wang, "Consider soil shear strength, seepage pit formulas check bursting analysis," *Science Technology and Engineering*, vol. 13, no. 35, pp. 10727–10730, 2013.

[15] Y. Y. Sun, "Experimental and theoretical investigation on the stability of deep excavations against confined aquifers in Shanghai, China," *KSCE Journal of Civil Engineering*, vol. 20, no. 7, pp. 2746–2754, 2016.

[16] F. Q. Chen, G. J. Miao, and F. W. Lai, "Base instability triggered by hydraulic uplift of pit-in-pit braced excavations in soft clay overlying a confined aquifer," *KSCE Journal of Civil Engineering*, vol. 24, no. 6, pp. 1717–1730, 2020.

[17] Z. Hu, Q. Wang, S. Yang et al., "Numerical simulation of soil displacement and settlement in deep foundation pit excavations near water," *Geofluids*, vol. 2021, Article ID 5559009, 14 pages, 2021.

[18] P. V. Lade, "Elastoplastic stress-strain theory for cohesionless soil with curved yield surfaces," *International Journal of Solids and Structures*, vol. 13, no. 11, pp. 1019–1035, 1977.

[19] J. G. Agar, N. R. Morgenstern, and J. D. Scott, "Shear strength and stress—strain behaviour of Athabasca oil sand at elevated temperatures and pressures," *Canadian Geotechnical Journal*, vol. 24, no. 1, pp. 1–10, 1987.

[20] F. J. Santarelli, *Theoretical and Experimental Investigation of the Stability of the Axisymmetric Borehole*, University of London, London, UK, 1987.

[21] X. L. Yang, *Limit Analysis Method and its Application to Geotechnical Engineering with Linear and Nonlinear Failure Criterias*, Zhongnan Univ, Changsha, China, 2002.

[22] M. S. Huang, K. L. Qin, and Y. C. Guo, "Upper bound solution for bearing capacity of nonhomogeneous and anisotropic clay foundation," *Chinese Journal of Rock Mechanics and Engineering*, vol. 3, pp. 511–518, 2008.

[23] H. T. Wang, Q. Wang, C. A. You, S. C. Li, D. C. Wang, and X. Wang, "Study of ultimate pullout force of anchor cable considering non-homogeneity and anisotropy of soil mass," *Rock and Soil Mechanics*, vol. 34, no. 8, pp. 2204–2210, 2013.

[24] Z. D. Liu, J. W. Zhang, W. P. Chen, D. Wu, and A. Szekrenyes, "Influence of anisotropy and nonhomogeneity on stability analysis of fissured slopes subjected to seismic action," *Mathematical Problems in Engineering*, Article ID 6582787, 13 pages, 2020.

Research Article

Influence of Parallel Joint Spacing and Rock Size on Rock Bulk Modulus

Tao Zhao,[1,2,3] Gaojian Hu [ID],[4,5] Tao Wang,[2] and Huan Zhang[2]

[1]*College of Safety Science and Engineering, Liaoning Technical University, Huludao, Liaoning 125105, China*
[2]*School of Safety and Emergency Management Engineering, Taiyuan University of Technology, Taiyuan, Shanxi 030024, China*
[3]*Key Laboratory of Mine Thermodynamic Disasters and Control, Ministry of Education, Liaoning Technical University, Huludao, Liaoning 125105, China*
[4]*School of Civil Engineering, Shaoxing University, Shaoxing, Zhejiang 312000, China*
[5]*Key Laboratory of Rock Mechanics and Geohazards of Zhejiang Province, Shaoxing, Zhejiang 312000, China*

Correspondence should be addressed to Gaojian Hu; hugaojian8@163.com

The size effect on the bulk modulus of rocks has been reported by previous studies. The accuracy in selecting the parameter for the rock mechanics analysis determines further accuracy of the calculation results. Moreover, given the influence of the size effect and joint spacing, the rock bulk modulus often changes. Thus, it is essential to examine the size effect on the bulk modulus. This study elucidated the influence of rock size and parallel joint spacing on the bulk modulus using the regression analysis and 12 sets of numerical plans. The results demonstrated that the bulk modulus decreased with an increase in rock size, and the curve represents an exponential function. The bulk modulus linearly increased as the parallel joint spacing increased. Furthermore, the characteristic size of the bulk modulus linearly decreased as the parallel joint spacing increased. In contrast, the characteristic bulk modulus linearly increased as the parallel joint spacing increased. The specific forms of these relationships were also elucidated in this study.

1. Introduction

The rock bulk modulus reflects the ability of a rock to resist deformation under external loads, using which one can characterize the mechanical characteristics of rocks. The bulk modulus is a comprehensive response of the rock mineral composition, fluid, pore, and structure under the action of the original internal environment, such as the formation pressure and temperature [1]. These unique characteristics make the bulk modulus an important parameter to study.

The joints in a rock fundamentally affect its bulk modulus. For instance, parallel joints can exist in sedimentary rocks, thereby significantly affecting the bulk modulus [2]. At the same time, the number of parallel joint spacings (PJS) in the rock causes a difference in the bulk modulus. For instance, Zhao et al. [3] have used the finite element method to study the bulk modulus of rock.

Moreover, some scholars have studied the effects of different factors on bulk modulus. For instance, Blake and Faulkner [4] have conducted seepage tests on granite to examine the effect of bulk modulus on fracturing permeability. Furthermore, Davarpanah et al. [5] studied the relationship between the modulus ratio and bulk modulus. Liu and Zhang [6] conducted an indoor triaxial creep test and found that the absolute value of the bulk modulus decreases with an increase in creep stress. Scholars have also addressed the calculation methods for bulk modulus. For instance, Shen et al. [7] studied the relationship between the tensile failure strain of rock and the initial fracture density spacing. They ultimately established a calculation method for the rock bulk modulus under tensile conditions. Zhao et al. [8] studied the failure and cracking characteristics of a broken rock mass cut using joints. Li et al. [9] obtained the volumetric fracture and crack propagation law of rocks through a dynamic load test.

Overall, research literature extensively examined bulk modulus, but only a few studies have considered the size and PJS, while the relationship between bulk modulus and PJS is poorly understood.

The rock has a side effect, and the change in rock size also affects the rock bulk modulus. For instance, the change in the size of some sedimentary rocks rich in joints fundamentally affects the change in the rock bulk modulus [10]. In this regard, Pang et al. [11] demonstrated that the bulk modulus of coal increases with a decrease in particle size. Jiang [12] reported that the size of the rock particles affects the rock pore structure, thereby triggering changes in the rock bulk modulus. Zhang and Yang [13] quantified the bulk modulus of montmorillonite by measuring changes in the length and density of the sample. Some other scholars have studied the effect of irregular particles on the bulk modulus. For instance, Kerimov et al. [14] have elucidated the effects of irregularly shaped particles and particle size on the porosity, permeability, and bulk modulus of granular porous media. Researchers also examined the effect of size on bulk modulus, but the elements of PJS, as well as the relationship between bulk modulus and size, are both poorly understood.

The mechanical parameters of rocks fundamentally vary with the size of the jointed rock and eventually tend toward a stable value, which is defined as the representative essential volume (REV). Some researchers have previously proposed various methods to evaluate the REV, whereas Hu and Ma [15] used a realistic failure process analysis (RFPA) to study the characteristic size. Ying et al. [16] established a method based on volume rupture strength (P32) and a statistical test method to estimate rock mass REV. Wu et al. [17] studied the effect of size on bulk modulus, while taking into account the effect of the model location, and reported that the REV size was 18 m. Liu et al. [18] elucidated the size effect of the defective rock mass strength through uniaxial and confining pressure tests and obtained a REV size of $5\,m \times 10\,m$. Hu et al. [19] obtained the relationship between the characteristic size of the rock elastic modulus and the PJS. Overall, although the bulk modulus has been extensively studied, only a few researchers investigated the relationship between the characteristic size of the bulk modulus (CSBM) and PJS and established a model of the CSBM and PJS.

This study established 12 numerical models to investigate the influence of the PJS and rock size on rock K. Within this research aim, (1) the corresponding stress-strain curves were analyzed, (2) the relationship between K and PJS, as well as the relationship between K and size were both established. Finally, (3) a model of the CSBM and PJS and a model of the rock characteristic bulk modulus (CBM) and PJS were established.

2. Numerical Simulation Plans

This study primarily focuses on two aspects: (1) elucidating the influence of PJS on rock K, with PJS of 10, 20, 30, 40, and 50 mm and (2) elucidating the effect of rock size with PJS on rock K, with the rock sizes of 100, 200, 400, 600, 800, 1,000, and 1,200 mm. Table 1 summarizes the research plans of this study based on [15].

This study uses RFPA as the simulation software. The boundary conditions and rock mechanical parameters used in the numerical simulation are summarized in referred to [15].

The roughness coefficient of the joint applied for the numerical simulations was 3, its elastic modulus was 1.5 MPa, its compressive strength was 2 MPa, its Poisson's ratio was 0.3, and its internal friction angle was 30°.

3. Numerical Results and Analysis

3.1. Stress-Strain Curve Analysis. The research analysis included plotting of the stress-strain curves in the plans 1 to 7 (Figure 1). Furthermore, the stress-strain curves in plans 8 to 12 were plotted as well (Figure 2).

Figure 1 illustrates the effect of the PJS on the compressive strength of rocks with different rock sizes. As seen in Figures 1(a)–1(g), the laws of the stress-strain curves were similar as the rock size increased from 100 to 1,200 mm. The strain of the rock gradually increased with the increase of the stress under the pressure effect. Moreover, it exhibited a linear elastic failure, which was further exacerbated by a plastic failure. Figure 1(a) is shown as an example, where the rock size is 100 mm. As seen, the compressive strength of the rock gradually increased, as the PJS increased from 10 to 50 mm.

Figure 2 displays the effect of the rock size on the compressive strength of the rock at different PJS. As seen from Figures 2(a)–2(e), when the PJS increased from 10 to 50 mm, the laws of rock stress-strain curves were also similar. Like in Figure 2, the rock was also destroyed by the elastic deformation first, which was further exacerbated by plastic deformation. Figure 2(e) is shown as an example with a PJS of 50 mm. As seen, the compressive strength of the rock gradually decreased with the increase of the rock size from 100 mm to 1,200 mm, thereby somewhat manifesting the size effect. Notably, the law of the curve is consistent with the law from [15], thereby indicating that the size effect of the rock was the same when the parameters of the joints changed.

The elastic modulus fundamentally reflects the proportional relationship between the stress and strain of a material during the elastic deformation stage. Figures 1 and 2 shows the obtained values of the elastic modulus and Poisson's ratio for each working condition, as summarized in Tables 2 and 3.

Bulk modulus is a relatively stable material constant. Fundamentally, there is a relationship between bulk modulus K, elastic modulus E, and Poisson's ratio v: $K = (E/3) \times (1 - 2v)$. Furthermore, the bulk modulus K of each working condition was solved according to this equation and the values from Tables 2 and 3, as shown in Table 4.

3.2. Influence of PJS on K. Table 3 summarizes the statistical data, which revealed no clear relationship between Poisson's ratio, rock size, and PJS, and the data obtained are relatively discrete.

TABLE 1: Research plans [15].

| Numerical simulation | PJS (mm) | Research plans | | | | | | |
		Plan 1 $l = 100$ mm	Plan 2 $l = 200$ mm	Plan 3 $l = 400$ mm	Plan 4 $l = 600$ mm	Plan 5 $l = 800$ mm	Plan 6 $l = 1000$ mm	Plan 7 $l = 1200$ mm
Plan 8	$s = 10$	10×100	10×200	10×400	10×600	10×800	10×1000	10×1200
Plan 9	$s = 20$	20×100	20×200	20×400	20×600	20×800	20×1000	20×1200
Plan 10	$s = 30$	30×100	30×200	30×400	30×600	30×800	30×1000	30×1200
Plan 11	$s = 40$	40×100	40×200	40×400	40×600	40×800	40×1000	40×1200
Plan 12	$s = 50$	50×100	50×200	50×400	50×600	50×800	50×1000	50×1200

s is the parallel joint spacing, and l is the rock size.

(a)

(b)

(c)

(d)

(e)

(f)
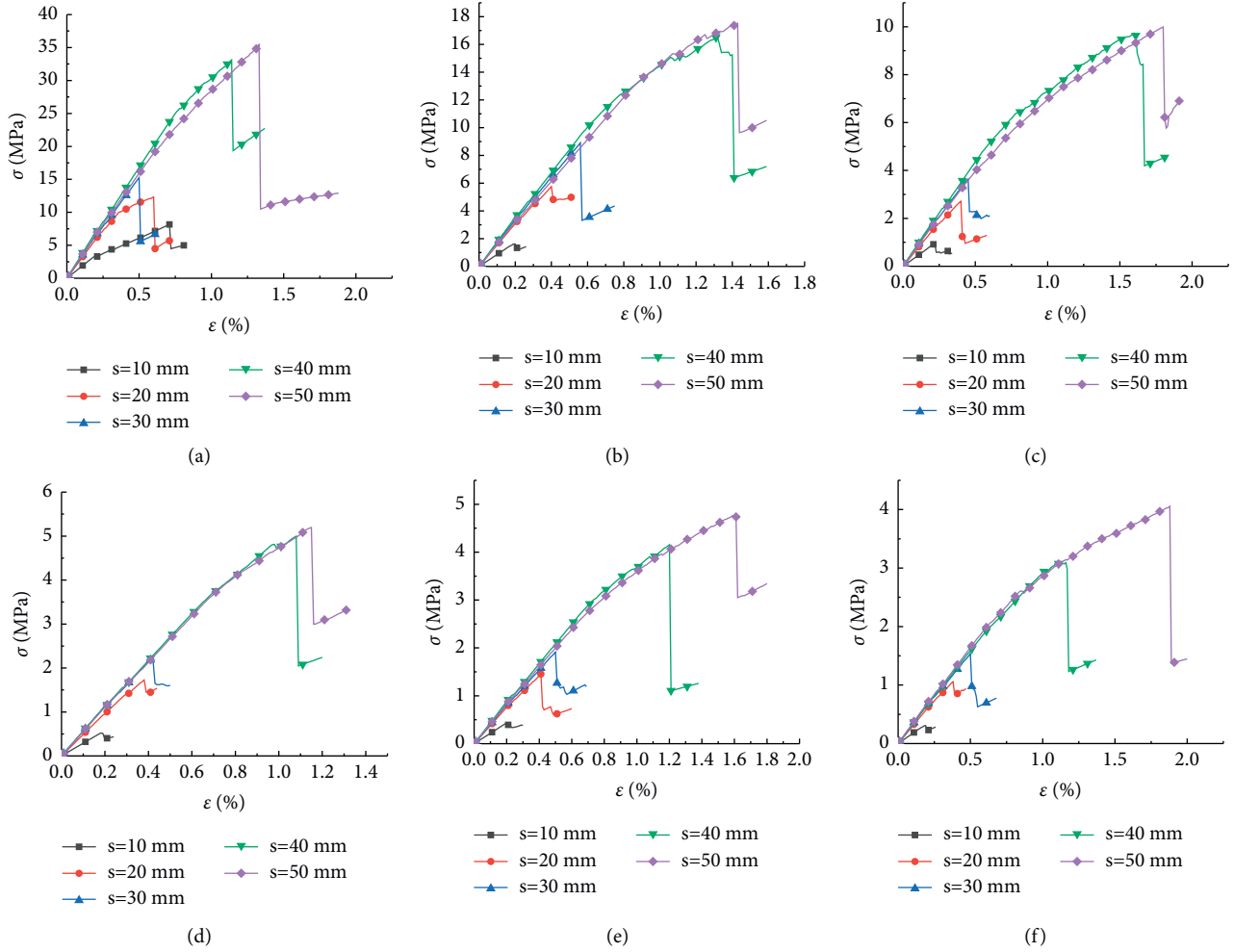
FIGURE 1: Continued.

(g)
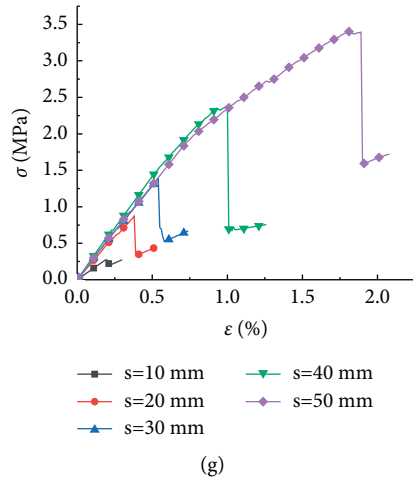
Figure 1: Stress-strain curves of rocks of different sizes. (a) $l = 100$ mm, (b) $l = 200$ mm, (c) $l = 400$ mm, (d) $l = 600$ mm, (e) $l = 800$ mm, (f) $l = 1000$ mm, and (g) $l = 1200$ mm.

(a)

(b)

(c)
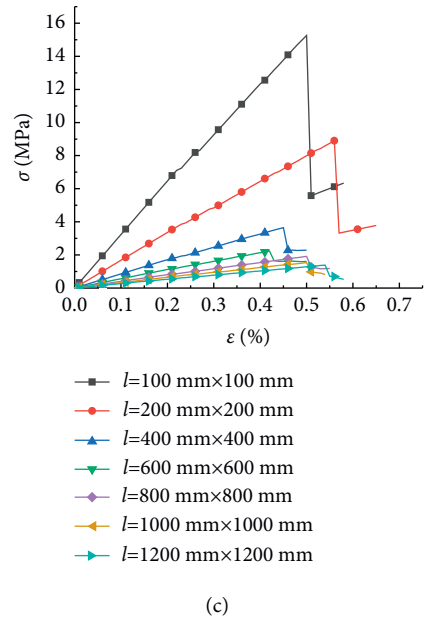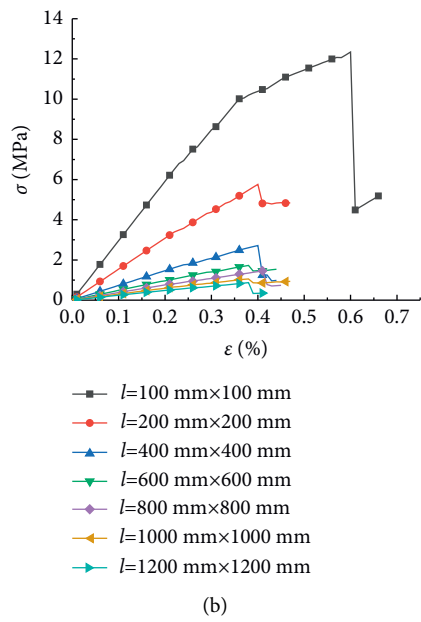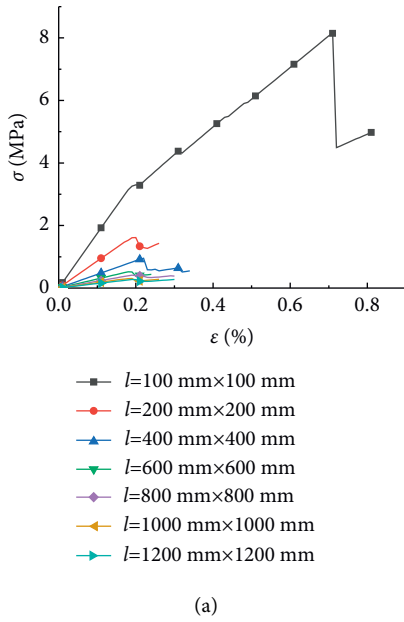
Figure 2: Continued.

(d)

(e)
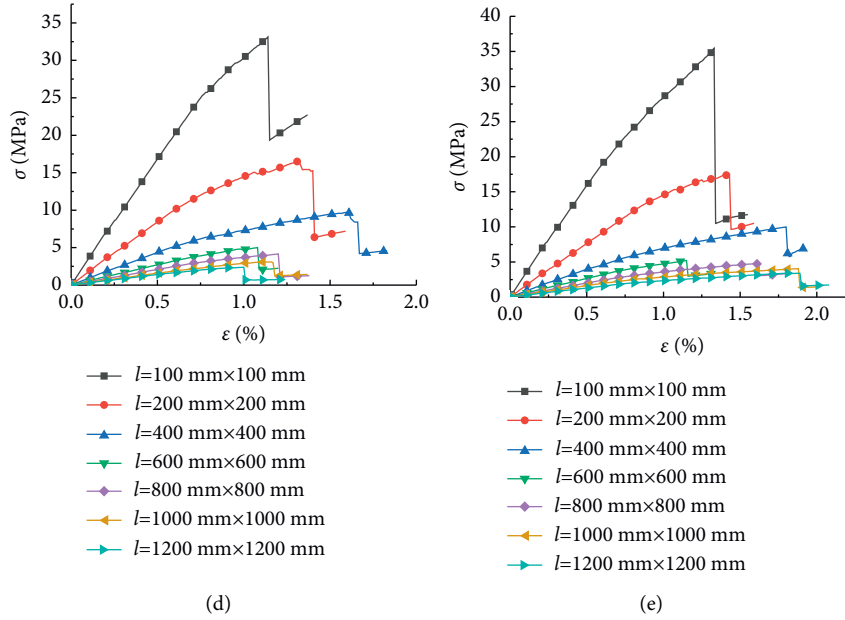
Figure 2: Stress-strain curves of rocks with different PJS. (a) $s = 10$ mm, (b) $s = 20$ mm, (c) $s = 30$ mm, (d) $s = 40$ mm, and (e) $s = 50$ mm.

Table 2: Values of elastic modulus.

| Numerical plans | Rock size (mm) | Elastic modulus (GPa) | | | | |
		Plan 8 $s = 10$ mm	Plan 9 $s = 20$ mm	Plan 10 $s = 30$ mm	Plan 11 $s = 40$ mm	Plan 12 $s = 50$ mm
Plan 1	$l = 100$	1.750	2.957	3.236	3.519	3.338
Plan 2	$l = 200$	0.864	1.542	1.681	1.769	1.607
Plan 3	$l = 400$	0.438	0.734	0.859	0.911	0.834
Plan 4	$l = 600$	0.290	0.488	0.563	0.570	0.557
Plan 5	$l = 800$	0.218	0.380	0.406	0.439	0.418
Plan 6	$l = 1000$	0.172	0.298	0.327	0.333	0.344
Plan 7	$l = 1200$	0.145	0.243	0.272	0.297	0.273

Table 3: Values of Poisson's ratio.

| Numerical plans | Rock size (mm) | Poisson's ratio | | | | |
		Plan 8 $s = 10$	Plan 9 $s = 20$	Plan 10 $s = 30$	Plan 11 $s = 40$	Plan 12 $s = 50$
Plan 1	100	0.3000	0.2049	0.2200	0.2369	0.2930
Plan 2	200	0.2326	0.1667	0.1429	0.1654	0.2396
Plan 3	400	0.1523	0.2000	0.2111	0.2754	0.2861
Plan 4	600	0.1754	0.1875	0.1867	0.2118	0.2486
Plan 5	800	0.1875	0.1964	0.2097	0.2177	0.2638
Plan 6	1000	0.1053	0.1750	0.2340	0.2689	0.2673
Plan 7	1200	0.1586	0.1667	0.1607	0.1944	0.3013

Table 4: Values of bulk modulus.

| Numerical plans | Rock size (mm) | Bulk modulus (GPa) | | | | |
		Plan 8 $s = 10$	Plan 9 $s = 20$	Plan 10 $s = 30$	Plan 11 $s = 40$	Plan 12 $s = 50$
Plan 1	100	1.458	1.670	1.926	2.229	2.687
Plan 2	200	0.538	0.771	0.784	0.881	1.028
Plan 3	400	0.210	0.408	0.495	0.676	0.650
Plan 4	600	0.149	0.260	0.299	0.330	0.369
Plan 5	800	0.117	0.209	0.233	0.259	0.295
Plan 6	1000	0.073	0.153	0.205	0.240	0.246
Plan 7	1200	0.071	0.122	0.134	0.162	0.229

The statistical data, shown in Table 4, demonstrate that K gradually increased as the PJS increased. A data point plot of K and PJS for each size was drawn, and the corresponding curve was fitted, as shown in Figure 3.

As seen in Figure 3, when the rock size was fixed and unchanged, K was affected by the PJS and increased with the increasing PJS. This pattern of variation remained the same even when the rock size varied. When the PJS was fixed and unchanged, K was affected by the rock size and decreased with an increase in the rock size. This finding indicates that K of the rock with parallel joints exhibited a positive correlation with the PJS and a negative correlation with the rock size. To illustrate this relationship in detail, see the formulae for the regression curves in Table 5.

The fitting formula from Table 5 was further used. The relationship indicated that K and PJS exhibited a linear relationship, and the mathematical model for K and PJS was formalized as

$$K(s) = as + b, \quad (1)$$

where $K(s)$ is K when PJS is s (GPa) and s is PJS (mm); a and b are the parameters.

The values of the parameters a and b from Table 5 are listed in Table 6 according to (1). The values from Table 6 were used to draw the fitting curves of the rock size and the parameters a and b (see Figure 4).

Figure 4 shows that the parameters a and b exhibited a power function relationship to s. Thus, we established the following formulae:

$$a = 1.241 l^{-0.833}, \quad (2)$$

$$b = 381.501 l^{-1.272}. \quad (3)$$

From equations (1)–(3), we obtained a special relational formula for K and PJS:

$$K(s) = 1.241 s l^{-0.833} + 381.501 l^{-1.272}. \quad (4)$$

(3) was used to quantify K, thereby providing a special relationship between K and PJS. Overall, it is applicable for solving K on a two-dimensional plane. In particular, for a known rock size, K can be obtained when the PJS was determined.

3.3. Influence of the Size Effect of K.

A data point plot of K and the rock size under each PJS was drawn according to the values from Table 4. The corresponding curve was fitted, as shown in Figure 5.

Figure 5 shows that when the PJS was fixed and unchanged, K was affected by the rock size and decreased with the increase in size. This pattern of variation remained the same even if PJS differed. Furthermore, when the rock size was fixed and unchanged, K was affected by rock size and increased accordingly. This phenomenon suggests that, for a rock with parallel joints, its K would have a positive correlation with the PJS, but a negative correlation with the rock size. For details of this relationship, see the formula of the regression curves summarized in Table 7.

The fitting formula in Table 7 was used to infer an exponential relationship between K and the rock size. The mathematical model for K and rock size was proposed:

$$K(l) = d + f e^{-gl}, \quad (5)$$

where $K(l)$ is K at the size l and the unit is GPa; $d, f,$ and g are parameters.

The values of the parameters $d, f,$ and g in Table 7 are listed in Table 8 according to (5). Furthermore, the values from Table 8 were used to draw the fitting curves of the rock size ($d, f,$ and g are drawn), as shown in Figure 6.

Figure 6 shows that the parameters $d, f,$ and g all were linearly associated to s, thereby laying the foundation for the following formulae:

$$d = 0.005s + 0.072, \quad (6)$$

$$f = 0.083s + 2.051, \quad (7)$$

$$g = 1.048 \times 10^{-4} s + 0.008. \quad (8)$$

Furthermore, equations (5)–(8) were used to obtain a special relational formula for K and the rock size:

$$K(l) = (0.0083s + 2.051) e^{-\left(1.048 \times 10^{-4} s + 0.008\right)l}$$
$$+ 0.005s + 0.072. \quad (9)$$

(9) quantifies K, while also providing a special relationship between K and the rock size. Moreover, it can be used for solving K on a two-dimensional plane. Thus, K can be obtained when PJS is known and when the rock size is determined.

3.4. Relationships of CSBM, CBM, and PJS

3.4.1. Derived Formula of CSBM.

The size effect of K can be characterized by the characteristic size of the bulk modulus (CSBM). In particular, Liang et al. [20] previously provided the method for quantifying the characteristic size; one can solve the CSBM by

$$|k| = \left| f g e^{(-gl)} \right|,$$
$$|k| \le \gamma, \quad (10)$$
$$l \ge \frac{\ln(gf) - \ln \gamma}{g},$$

where γ is the acceptable absolute value of the inclination.

3.4.2. Relationship of CSBM and PJS.

The CSBM was solved, as summarized in Table 9, when the PJS was 10, 20, 30, 40, and 50 mm. The regression curves for the CSBM and PJS are shown in Figure 7.

Figure 7 shows that, as the PJS increased from 10 to 50 mm, the CSBM decreased from 690.66 mm to 574.1 mm. Moreover, a linear relationship between CSBM and PJS was discerned, where the slope of the curve was found to be
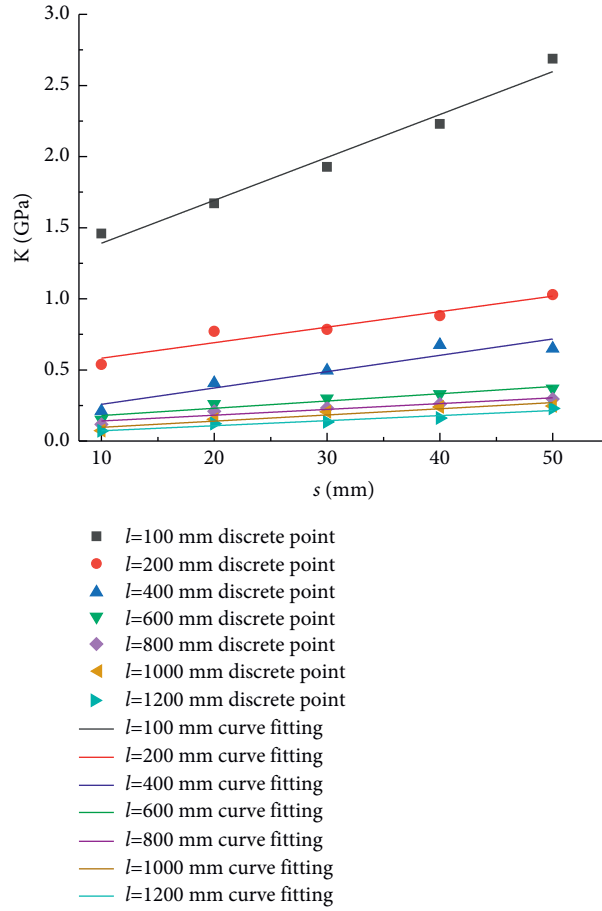
FIGURE 3: Fitting curves of bulk modulus and PJS.

TABLE 5: Fitting relationships between K and PJS.

Rock size (mm)	Fitting formula	Fitting coefficient (R^2)
100	$K(s) = 0.027s + 1.089$	0.976
200	$K(s) = 0.013s + 0.473$	0.927
400	$K(s) = 0.012s + 0.143$	0.907
600	$K(s) = 0.005s + 0.128$	0.917
800	$K(s) = 0.004s + 0.100$	0.916
1000	$K(s) = 0.004s + 0.053$	0.907
1200	$K(s) = 0.004s + 0.036$	0.942

TABLE 6: Values of a and b under different rock sizes.

Parameter	Values						
	$l = 100$ mm	$l = 200$ mm	$l = 400$ mm	$l = 600$ mm	$l = 800$ mm	$l = 1000$ mm	$l = 1200$ mm
A	0.027	0.013	0.012	0.005	0.004	0.004	0.004
B	1.089	0.473	0.143	0.128	0.100	0.053	0.036

negative. Thus, according to the fitting curve, the following specific relationship was formalized:

$$B(s) = -3.464s + 732.144, \qquad (11)$$

where $B(s)$ is the characteristic size of bulk modulus (unit: mm).

(11) quantifies the CSBM, thereby providing a special relationship between the CSBM and PJS, which can be used for solving the CSBM in a two-dimensional plane. Note that, in field applications, the CSBM can be generally obtained when the PJS is measured.

3.4.3. Relationship of CBM and PJS. The value of CSBM was substituted into (5), and the characteristic bulk modulus (CBM) of rocks with different PJS values is described in Table 10.

(a)

(b)
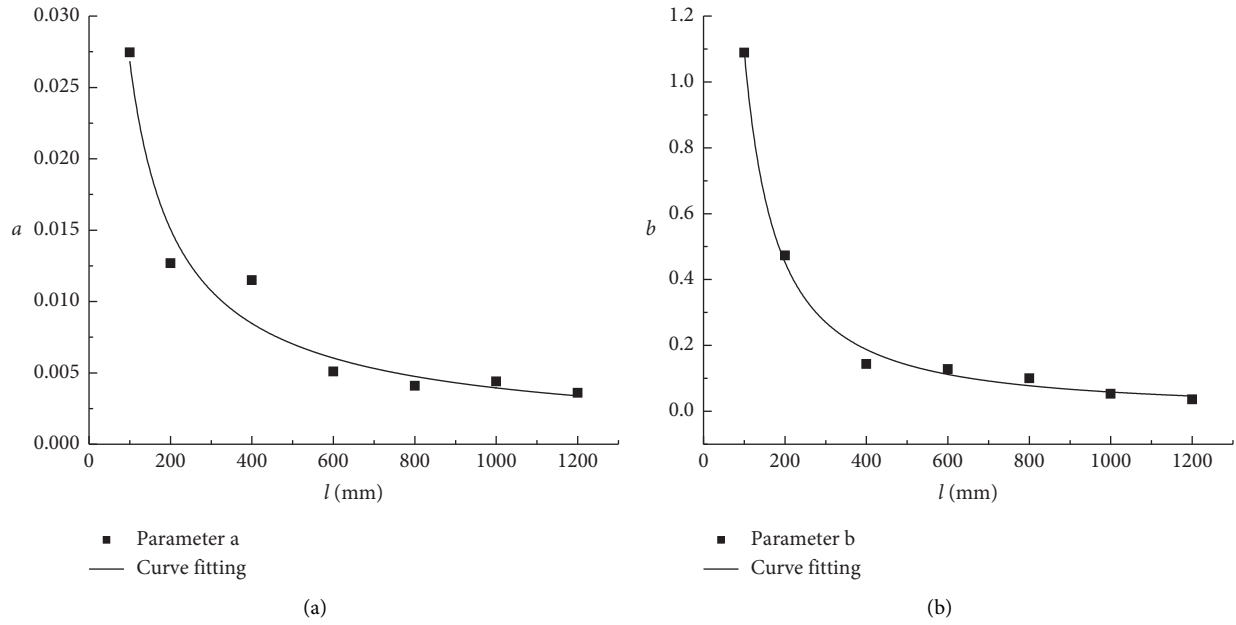
FIGURE 4: Fitting curve diagrams. (a) Parameter a; (b) parameter b.
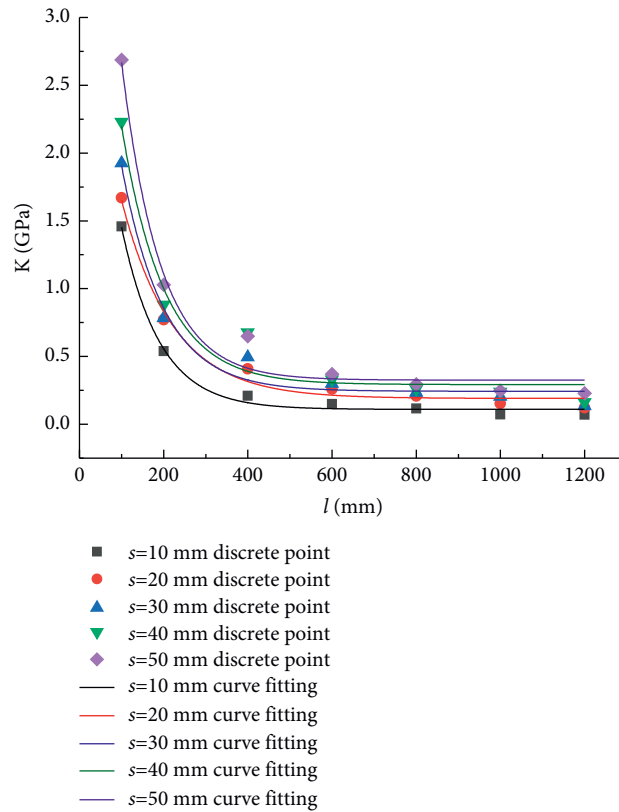
FIGURE 5: Fitting curves of bulk modulus and rock size.

Figure 8 shows that the CBM increases gradually with the increase of the PJS, thereby exhibiting a linear relationship. On this basis, the special relation was obtained:

$$K_w(s) = 0.005s + 0.078, \qquad (12)$$

where $K_w(s)$ is the CBM (unit: GPa).

(12) quantifies the CBM and provides a special relationship between the CBM and PJS. It can be used for solving the CBM on a two-dimensional plane. In field applications, the CBM can be obtained when the PJS is measured.

TABLE 7: Fitting relationships between K and rock size.

PJS (mm)	Fitting formula	Fitting coefficient (R^2)
10	$K(l) = 0.110 + 3.254e^{-0.0093l}$	0.995
20	$K(l) = 0.191 + 3.321e^{-0.0094l}$	0.988
30	$K(l) = 0.243 + 4.517e^{-0.0111l}$	0.979
40	$K(l) = 0.293 + 5.132e^{-0.0126l}$	0.963
50	$K(l) = 0.326 + 6.507e^{-0.0129l}$	0.983

TABLE 8: Values of d, f, and g.

Parameters	Values				
	$s = 10$ mm	$s = 20$ mm	$s = 30$ mm	$s = 40$ mm	$s = 50$ mm
d	0.1096	0.1905	0.2431	0.2927	0.3255
f	3.2541	3.3206	4.5174	5.1317	6.5067
g	0.0093	0.0094	0.0111	0.0126	0.0129
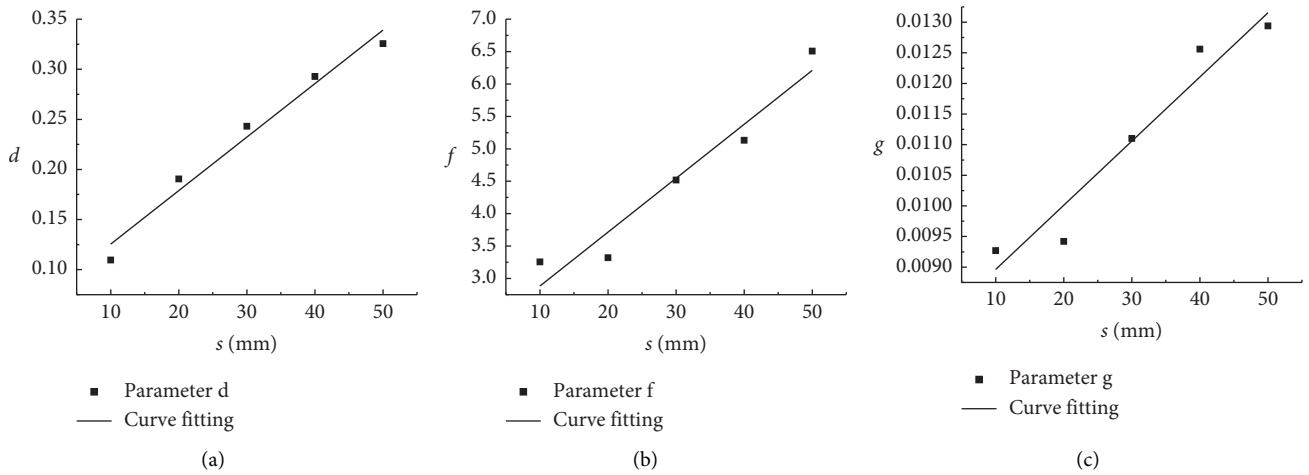
FIGURE 6: Fitting curves of parameters and PJS. (a) Parameter d; (b) parameter f; (c) parameter g.

TABLE 9: Relationship between CSBM and PJS.

PJS (mm)	10	20	30	40	50
Characteristic size of bulk modulus (mm)	690.66	683.52	622.58	570.2	574.1
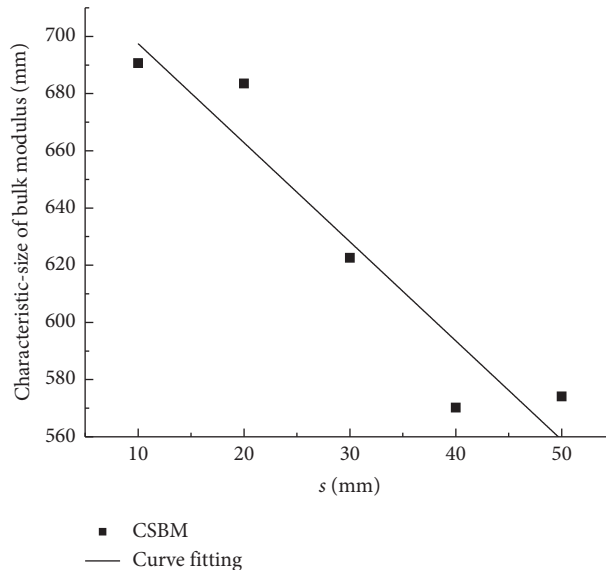
FIGURE 7: Fitting curve of CSBM and PJS.

Table 10: Relationship between CBM and PJS.

PJS (mm)	10	20	30	40	50
Characteristic bulk modulus (GPa)	0.115	0.196	0.248	0.297	0.329

Table 11: Elastic modulus and bulk modulus with different rock sizes.

Rock size	2 m	4 m	8 m	12 m	16 m
Elastic modulus (GPa)	11.38	8.06	7.66	7.39	7.29
Bulk modulus (GPa)	2.0484	1.4508	1.3788	1.3302	1.3122
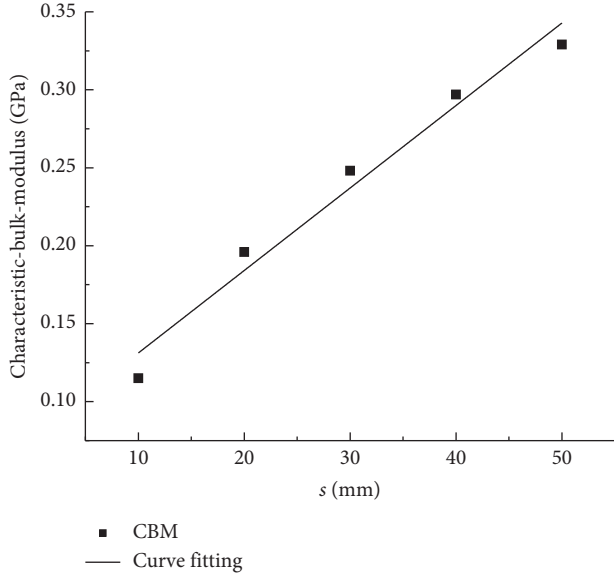
Figure 8: Fitting curve of CBM and PJS.
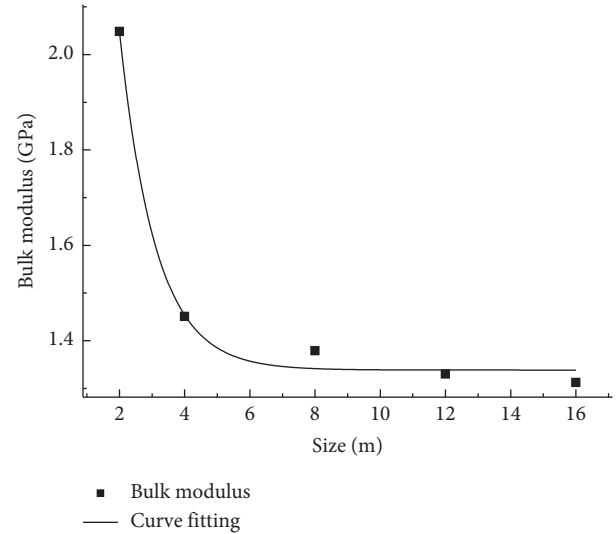
Figure 9: Fitting curves of bulk modulus with different sizes.

3.5. Verification Analysis. To evaluate the accuracy of our results, we analyzed the applicability of (5). The verification was conducted using the data of elastic moduli for different rock sizes from Figure 3.11 (page 44) in reference [21], as shown in Table 11. From these elastic modulus, the corresponding bulk modulus were calculated and summarized in Table 11. According to Table 11, we obtained a scatter plot and relationship curve of the bulk modulus and rock size (see Figure 9).

The relationship between the bulk modulus and different sizes is shown in Figure 9 and was formalized as follows:

$$K(l) = 1.34 + 4.37e^{-0.91l}, \qquad (13)$$

where $K(l)$ (GPa) is K of the rock when the rock size is l and l (m) is the rock size.

The function type of (13) generally conformed to the mathematical model, introduced in (5). It can be therefore concluded that the numerical simulation and experimental conclusions were consistent. Moreover, the evaluation analysis indicates that the mathematical model, proposed in (5), is applicable for the solution of the bulk modulus with respect to the size.

4. Discussion

The K values of rocks of different sizes varied with the PJS. Importantly, this study established the following four relationships: (1) K and PJS; (2) K and rock size; (3) CSBM and PJS; as well as (4) CBM and PJS. Only a few previous studies considered the size effect of rocks with PJS on K. Moreover, the effect of rock size changes on the K of rocks with PJS, and

the effect of the changes in PJS on the size effect of K; both remained understudied.

In this study, the K values of rocks with different sizes were obtained using the data from [21], and (15) was obtained, which confirmed the accuracy of (5). Moreover, it proved that the formula, proposed in the study, stands out with certain universality, thereby also confirming the high accuracy of the research results. However, some differences between the numerical and experimental results were discerned. In addition, the two-dimensional model is limited in simulating three-dimensional samples. Both these challenges can be alleviated in future studies.

Overall, the specific relationships of rock K were obtained in this study. The information about the rock size effect and the PJS is essential as input for the setting of mechanical parameters such as K in rock engineering, which can prevent rock engineering disasters. When the PJS and rock size are available, rock K, CSBM, and CBM can be quickly obtained for a selected engineering site, thereby providing valuable data-driven guidelines for engineering purposes.

5. Conclusions

This study elucidated the size effect of rocks with a PJS on K using numerical simulations. The following conclusions can be drawn:

(1) The relationship between K and PJS is linear.

$$K(s) = as + b. \qquad (14)$$

We also obtained the special relationship.

$$K(s) = 1.241sl^{-0.833} + 381.501l^{-1.272}. \quad (15)$$

Moreover, the relationship between K and rock size is exponential:

$$K(l) = d + fe^{-gl}. \quad (16)$$

And we obtained the special relationship.

$$K(l) = (0.0083s + 2.051)e^{-\left(1.048\times10^{-4}s+0.008\right)l} \\ + 0.005s + 0.072. \quad (17)$$

(2) CSBM is fundamentally associated with PJS. This study obtained the following relationship:

$$B(s) = -3.464s + 732.144. \quad (18)$$

(3) The CBM was found to be related to PJS. This study provided the following relationship:

$$K_w(s) = 0.005s + 0.078. \quad (19)$$

Data Availability

The data supporting the findings of this study are available from the corresponding author upon reasonable request.

Conflicts of Interest

The authors declare no conflicts of interest regarding the publication of this paper.

Authors' Contributions

G Hu contributed to conceptualization, software, and funding acquisition. T Zhao contributed to methodology, data curation, investigation, writing, and original draft preparation. T Wang contributed to data curation and formal analysis. H Zhang was responsible for funding acquisition and formal analysis.

Acknowledgments

References

[1] X. Wang, H. Kang, and F. Gao, "Numerical study on the formation of pressure arch in bolted gravel plate," *Computers and Geotechnics*, vol. 130, Article ID 103933, 2021.

[2] B. Li, J. Lan, G. Si, G. Lin, and L. Hu, "NMR-based damage characterisation of backfill material in host rock under dynamic loading," *International Journal of Mining Science and Technology*, vol. 30, no. 3, pp. 329–335, 2020.

[3] J. Zhao, H. Chen, and N. Li, "The study of elastic properties of fractured porous rock based on digital rock," *IOP Conference Series: Earth and Environmental Science*, vol. 514, no. 2, Article ID 022022, 2020.

[4] O. O. Blake and D. R. Faulkner, "Using velocities, density, and bulk modulus to predict the permeability evolution of microfractured rocks," *Rock Mechanics and Rock Engineering*, vol. 53, no. 9, pp. 4001–4013, 2020.

[5] M. Davarpanah, G. Somodi, L. Kovács, and B Vasarhelyi, "Experimental determination of the mechanical properties and deformation constants of mórágy granitic rock formation (Hungary)," *Geotechnical & Geological Engineering*, vol. 38, no. 3, pp. 3215–3229, 2020.

[6] W. Liu and S. Zhang, "Research on rock creep model based on the dual influence of stress and time," *Journal of Central South University*, vol. 51, no. 8, pp. 2256–2265, 2020.

[7] C. Shen, H. Wang, X. Li, and Y. Wang, "Theoretical calculation method of tensile deformation modulus of damaged rock," *Chinese Journal of Underground Space and Engineering*, vol. 14, no. 06, pp. 1466–1475, 2018.

[8] Y. Zhao, X. Feng, Q. Jiang et al., "Large deformation Control of deep roadways in fractured hard rock based on cracking-restraint method," *Rock Mechanics and Rock Engineering*, vol. 54, no. 5, pp. 2559–2580, 2021.

[9] B. Li, J. Lan, G. Si, G. Lin, and L. Hu, "NMR-based damage characterisation of backfill material in host rock under dynamic loading," *International Journal of Mining Science and Technology*, vol. 30, no. 3, pp. 329–335, 2020.

[10] P. Wang, Y. Liu, L. Zhang, Z. Huang, and M. Cai, "A preliminary study on the uniaxial compression characteristics of fractured rock mass based on 3D printing technology," *Chinese Journal of Rock Mechanics and Engineering*, vol. 37, no. 2, pp. 364–373, 2018.

[11] L. Pang, Y. Yang, L. Wu, F. Wang, and H. Meng, "Effect of particle sizes on the physical and mechanical properties of briquettes," *Energies*, vol. 12, no. 19, p. 3618, 2019.

[12] L. Jiang, *Numerical Simulation of Acoustic and Electrical Properties of Natural Gas Reservoir Rock Based on Digital core*, China University of Petroleum, Beijing China.

[13] M. Zhang and X. Yang, "Experiment on elastic properties of montmorillonite," *Earthquake Geology*, vol. 42, no. 05, pp. 1229–1239, 2020.

[14] A. Kerimov, G. Mavko, T. Mukerji, J. Dvorkin, and M. A. Al Ibrahim, "The influence of convex particles' irregular shape and varying size on porosity, permeability, and elastic bulk modulus of granular porous media: insights from numerical simulations," *Journal of Geophysical Research: Solid Earth*, vol. 123, no. 12, pp. 10, 563–10, 582, 2018.

[15] G. Hu and G. Ma, "Size effect of parallel-joint spacing on uniaxial compressive strength of rock," *PLoS One*, vol. 16, no. 9, pp. 1–16, 2021.

[16] L. Ying, Q. Wang, J. Chen, S. Song, J. Zhan, and X. Han, "Determination of geometrical REVs based on volumetric fracture intensity and statistical tests," *Applied Sciences*, vol. 8, no. 5, p. 800, 2018.

[17] Q. Wu, H. Tang, L. Wang, G. Lei, and K. Fang, "Three-dimensional distinct element simulation of size effect and spatial anisotropy of mechanical parameters of jointed rock mass," *Chinese Journal of Rock Mechanics and Engineering*, vol. 33, no. 12, pp. 2419–2432, 2014.

[18] X. Liu, S. He, and D. Wang, "Numerical analysis of the anisotropy and scale effects on the strength characteristics of

defected rockmass," *Advances in Civil Engineering*, vol. 2020, no. 5, pp. 1–21, 2020.

[19] G. Hu, G. Ma, W. Liang, L. Song, and W. Fu, "Influence of the number of parallel-joints on size effect of elastic modulus and characteristic elastic modulus," *Frontiers of Earth Science*, vol. 10, pp. 1–11, 2022.

[20] Z. Liang, Y. Zhang, S. Tang, L. Li, and C. Tang, "Size effect of rock masses and associated representative element properties," *Chinese Journal of Rock Mechanics and Engineering*, vol. 32, no. 6, pp. 1157–1166, 2013.

[21] W. Cheche, *DEM Simulation Analysis of Size Effect of Jointed Rock Mass and its Multi-Scale Calculation Method*, Shandong University, China, 2021.

Research Article

Transient Electromagnetic 1-Dimensional Inversion Based on the Quantum Particle Swarms Optimization-Smooth Constrained Least Squares Joint Algorithm and Its Application in Karst Exploration

Xue Liu [iD],[1,2] **Chunwei Pan,**[3] **Fangkun Zheng** [iD],[1,2] **Ying Sun,**[1,2] **and Qingsong Gou**[4]

[1]*CCCC Fourth Harbor Engineering Institute Co., Ltd., Guangzhou 510230, China*
[2]*CCCC Key Laboratory of Environment Protection and Safety in Foundation Engineering of Transportation, Guangzhou 510230, Guangdong, China*
[3]*Guangdong Transportation Industrial Investment Co., Ltd., Guangdong, Guangzhou 510000, China*
[4]*Chongqing Institute of Geology and Mineral Resources, Chongqing 401120, China*

Correspondence should be addressed to Xue Liu; lxue1@cccc4.com

Before the construction of the bridge bored pile in the karst area, geological conditions of the excavation area should be investigated. In order to avoid the karst caves in underground space making adverse impacts on the construction, bearing capacity, and stability of pile foundation, in this paper, we use the transient electromagnetic method to detect the karst development in the bearing layer of the pile foundation, which is different from the traditional karst survey method. To improve the interpretation accuracy of transient electromagnetic detection for karst caves, the quantum particle swarm optimization (QPSO) algorithm was combined with the smooth constrained least squares (CLS) algorithm, and the transient electromagnetic inversion based on the QPSO-CLS joint algorithm was generated. Better inversion results were achieved by the proposed method in this study. Based on the inversion calculation results of simulation data and field test data, it is further demonstrated that the QPSO-CLS joint algorithm has high optimization efficiency without manually setting the initial model. The interpretation results are consistent with the theoretical model and drilling logging results, which proves the adaptability of the proposed algorithm.

1. Introduction

Karst has been widely developed in Yunnan and Guizhou areas in China and also has been frequently distributed in northern Guangdong, western Hunan, western Hubei, and eastern Sichuan of China [1]. If the development of the underground unfavorable geological body is not found out when drilling cast-in-place pile in karst area, then safety accidents such as hole collapse, ground subsidence, buried drill, and cracking of surrounding building structure can be caused [2]. The transient electromagnetic method has the advantages of low cost, simple operation, large detection depth, strong sensitivity to water, and mud bearing karst cave and is less susceptible to external interference.

Therefore, a transient electromagnetic method for karst cave detection has become an efficient method [3–6]. However, the apparent resistivity profile of transient electromagnetic is a comprehensive response of underground medium, and its interpretation has low accuracy. To obtain more accurate results, the geophysical inversion method is often used to process transient electromagnetic detection data.

In fact, geophysical inversion is a highly nonlinear problem, and a reliable initial model is difficult to be defined for geophysical inversion. To this end, researchers introduced a fully nonlinear algorithm into geophysical inversion. Somanash has made some research achievements on a simulated annealing method, a genetic algorithm, and an artificial neural network algorithm [7]. Li et al. proposed a

nonlinear programming genetic algorithm and applied it to 1D inversion of ground transient electromagnetic and achieved good results [8]. Through the integral equation numerical simulation, Chen studied the transient electromagnetic response characteristics in the full space of a mine and obtained the best response component [9]. Sun et al. introduced the simulated annealing nonlinear global optimization algorithm into transient electromagnetic inversion calculation, took L1 norm as the objective function, and achieved good inversion results [10]. However, the above algorithm has the disadvantages of slow convergence speed and low accuracy.

Particle swarm optimization (PSO) is a crowd-based algorithm [11]. Compared with the algorithms mentioned above, PSO has strong adaptability and can be based on the global optimization algorithm. Many scholars have studied the application of the PSO algorithm in the field of geophysics. Shaw and Srivastava evaluated the adaptability of the PSO algorithm in geophysical data inversion by inverting synthetic data with noise interference retrieved on a multilayer one-dimensional model [12]. Monteiro Santos used the PSO algorithm to retrieve spontaneous potential data to detect shallow anomalies [13]. Cheng et al. proposed the PSO algorithm based on the transient electromagnetic method and the direct current method. The research shows that the proposed algorithm can obtain better results and has been successfully applied in the advanced exploration of coal mine roadways [14]. Li et al. combined the particle swarm optimization algorithm with a damped least square method and realized the inversion calculation of full space transient electromagnetic data. The results show that the combined algorithm can invert the transient electromagnetic detection data of roadways with high accuracy [15]. Similar to other global optimization algorithms, the PSO algorithm is also prone to fall into local extremum and premature convergence. To solve this problem, Li and Li fused the improved QEA (quantum-inspired evolutionary algorithm) with the PSO algorithm and proposed a fast convergence and abundant algorithm of quantum particle swarm optimization (QPSO) [16]. However, in recent years, scholars have found through research that the QPSO algorithm also has the disadvantages of premature convergence and is easy to fall into the local minimum [17]. Moreover, the QPSO algorithm is rarely applied in the field of geophysics.

The smooth constrained least square method (CLS) is commonly used to solve nonlinearity fittings. Based on the Newton optimized nonlinearity least square method, it can adjust the damping coefficient and the smoothing filter to keep its forward value close to the true value and measure the gap between them by the mean square deviation RMS. When the RMS tends to be stable, the result is the final inversion result [18, 19]. This algorithm is faster than the conventional least square method and takes up less memory [20].

Based on the above, in this manuscript, the quantum particle swarm optimization (QPSO) algorithm was combined with the smooth constrained least squares algorithm. The QPSO algorithm was used to carry out the preliminary iterative search, and the preliminary inversion results were taken as the initial model for the following inversion

calculation in the smooth constrained least squares (CLS) algorithm. Subsequently, the reliability and accuracy of the proposed inversion algorithm were further verified by a series of numerical experiments of test functions, simulation synthesis, and field measured data.

2. The Inversion of the QPSO-CLS Joint Algorithm

Based on the strong global search ability of the QPSO algorithm, the application of the QPSO algorithm to loop source transient electromagnetic nonlinear inversion can help the algorithm deviate from the local optimal value and provide a more reliable initial value for the next CLS algorithm.

2.1. Basic Principle. In this study, the quantum particle swarm optimization (QPSO) algorithm is applied to the inversion of layer resistivity and layer thickness simultaneously. Assuming that the initial inversion layer number is N, the resistivity value $\rho_1, \rho_2, \rho_3, ..., \rho_N$ and the thickness of each layer $h_1, h_2, h_3, ..., h_{N-1}$ need to be reversely calculated. The total number of variables to be solved is $2N - 1$. Then, this problem can be transformed into a $2N - 1$ dimensional optimization problem. The basic calculation principle is as follows:

(1) Initialization and transformation. It is different from the ordinary PSO algorithm; the qubit phase plays the role of random initial population, which is in the range of $[0, 2\pi]$. Then, the qubit can be calculated by probability amplitude. After then, by solving the solution space transformation formula, the qubit can be transformed into the corresponding value in the domain of the independent variable so that the corresponding appropriate value can be calculated.

(2) Update. The updated rules of particle state are as follows, including the update of the qubit angle and the probability amplitude of qubit:

(a) The incremental update of the qubit angle on particles is as follows:

$$\Delta\theta_{ij}(t+1) = \omega\Delta\theta_{ij}(t) + c_1 r_1 (\Delta\theta_l) + c_2 r_2 (\Delta\theta_g), \tag{1}$$

where

$$\Delta\theta_l = \begin{cases} 2\pi + \theta_{ilj} - \theta_{ij} (\theta_{ilj} - \theta_{ij} < -\pi) \\ \theta_{ilj} - \theta_{ij} (\pi \leq \theta_{ilj} - \theta_{ij} \leq \pi) \\ \theta_{ilj} - \theta_{ij} - 2\pi (\theta_{ilj} - \theta_{ij} > \pi) \end{cases},$$
$$\Delta\theta_g = \begin{cases} 2\pi + \theta_{gj} - \theta_{ij} (\theta_{gj} - \theta_{ij} < -\pi) \\ \theta_{gj} - \theta_{ij} (\pi \leq \theta_{gj} - \theta_{ij} \leq \pi) \\ \theta_{gj} - \theta_{ij} - 2\pi (\theta_{gj} - \theta_{ij} > \pi) \end{cases} \tag{2}$$

ω is a random number with inertia weight; c_1, c_2 is a self-factor and a global factor, respectively; r_1, r_2 is a random number of (0,1).
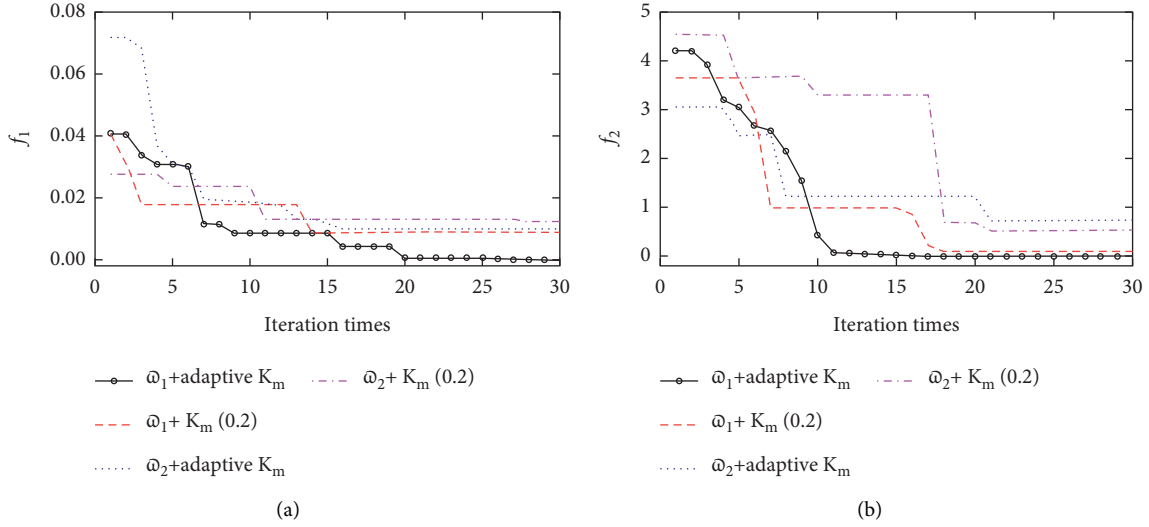
FIGURE 1: The decline curve of the moderate value of an objective function of the QPSO algorithm. (a) Griewank function (b) Ackley function.

(b) The probability amplitude of qubit on particles is updated as follows:

$$
\begin{bmatrix} \cos\left(\theta_{ij}(t+1)\right) \\ \sin\left(\theta_{ij}(t+1)\right) \end{bmatrix}
$$

$$
= \begin{bmatrix} \cos\left(\Delta\theta_{ij}(t+1)\right) - \sin\left(\Delta\theta_{ij}(t+1)\right) \\ \sin\left(\Delta\theta_{ij}(t+1)\right)\cos\left(\Delta\theta_{ij}(t+1)\right) \end{bmatrix}
$$

$$
\begin{bmatrix} \cos\left(\theta_{ij}(t)\right) \\ \sin\left(\theta_{ij}(t)\right) \end{bmatrix} \tag{3}
$$

$$
= \begin{bmatrix} \cos\left(\theta_{ij}(t) + \Delta\theta_{ij}(t+1)\right) \\ \sin\left(\theta_{ij}(t) + \Delta\theta_{ij}(t+1)\right) \end{bmatrix}.
$$

Among them, $i = 1, 2, ..., n$; $j = 1, 2, ..., d$; n and d are the number of population and the dimension of unknown variables, respectively.

(3) Mutation treatment. The quantum nongate is used to mutate particles. It gives each particle a random number $[rand]i$ between $(0,1)$. When the random number $[rand]i$ is lower than the set value K_m, the $[n/2]$ qubits are randomly selected, for the mutation operation using equations (2) and (3).

$$
\begin{bmatrix} 01 \\ 10 \end{bmatrix} \begin{bmatrix} \cos(\theta_{ij}) \\ \sin(\theta_{ij}) \end{bmatrix} = \begin{bmatrix} \sin(\theta_{ij}) \\ \cos(\theta_{ij}) \end{bmatrix}
$$

$$
= \begin{bmatrix} \cos\left(\theta_{ij} + \dfrac{\pi}{2}\right) \\ \sin\left(\theta_{ij} + \dfrac{\pi}{2}\right) \end{bmatrix}, \tag{4}
$$

where $i = 1, 2, ..., n$; $j = 1, 2, ..., d$ [21].

2.2. Regulation Mechanism of Inertia Weight and Mutation Operator.
In particle swarm optimization, inertia weight ω is an important parameter. If the value of ω is increased, the global search ability will be enhanced. If the value of ω is decreased, the local search ability will be enhanced. In this study, the commonly used nonlinear method is employed to adjust the inertia weight. Besides, two methods of adjusting inertia weight are comprehensively compared, as shown in Figures 1(a) and 1(b). It is found that better results can be obtained by equations (2)–(4) rather than equations (2)–(5). Therefore, equations (2)–(4) are used as the inertia weight adjustment strategy of the QPSO algorithm.

Adjustment strategy 1: equations (2)–(4) are used to realize the nonlinear dynamic adjustment of inertia weight as follows:

$$
\omega_1 = \begin{cases} \omega_{\min} - \dfrac{(\omega_{\max} - \omega_{\min}) * (f - f_{\min})}{f_{\text{avg}} - f_{\min}}, & f \le f_{\text{avg}}, \\[3mm] \omega_{\max}, & f > f_{\text{avg}}, \end{cases} \tag{5}
$$

where f represents the real-time objective function value of particles; $f_{\min}$ and f_{avg} are the minimum and average moderate values of all particles [21].

Adjustment strategy 2: equations (2)–(5) are used to realize the nonlinear dynamic adjustment of inertia weight as follows:

$$
\omega_2 = 0.99^k * \frac{r}{2} + a, \tag{6}
$$

where k is the current evolution algebra, r is a random number of $(0, 1)$, and a is a decimal greater than zero, ranging from $[0, 0.5]$.

To increase the diversity of the population, equations (2)–(6) are used to adaptively adjust the mutation operator as follows:
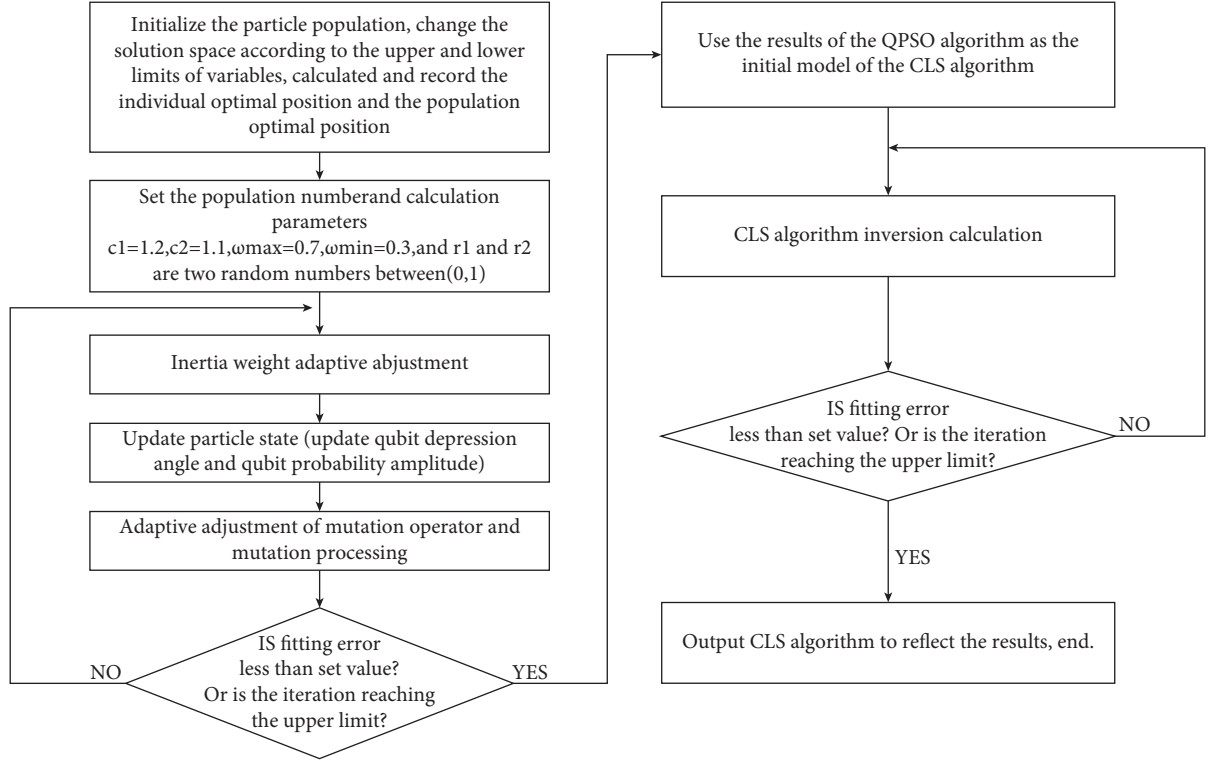
FIGURE 2: Flow chart of the QPSO-CLS joint algorithm.

$$K_m(t) = K_m * 2^{e^{(1-G_m/G_m+1-t)}}, \tag{7}$$

where K_m is the maximum mutation probability, G_m is the maximum number of iterations, and t is the current number of iterations.

As shown in Figures 1 and 2 (a) and (b), better performance can be obtained by using an adaptive mutation operator.

To verify the ability of the adjusted QPSO algorithm, two functions are set for the optimization test as follows:

① Griewank function

$$f_1 = \frac{1}{4000} \sum_{i=1}^{n} x_i^2 - \prod_{i=1}^{n} \cos\left(\frac{x_i}{\sqrt{i}}\right) + 1. \tag{8}$$

② Ackley function

$$f_2 = 20 + e - 20 \exp\left(-0.2\sqrt{\frac{1}{n}\sum_{i=1}^{n} x_i^2}\right)$$
$$\tag{9}$$
$$- \exp\left(\frac{1}{n}\sum_{i=1}^{n} \cos\left(2\pi x_i\right)\right).$$

As shown in Figures 1(a) and 1(b), the performance of the QPSO algorithm under the ϖ_1 adaptive strategy of K_m is better. Therefore, this strategy is used in this study.

2.3. The QPSO-CLS Joint Algorithm. The QPSO algorithm is improved by equations (2)–(4) and equations (2)–(6) and then combined with smooth constrained least squares (CLS). Finally, a QPSO-CLS joint transient electromagnetic 1D inversion method is formed. In the initial stage of inversion,

the improved QPSO algorithm is used to invert the layer resistivity and thickness of the model, and reasonable parameters such as the number of particles and the number of iterations are set according to the actual needs. After the algorithm iterates to a certain extent, the QPSO algorithm is terminated. The inversion results of the QPSO algorithm are taken as the initial model of the CLS algorithm, and the CLS algorithm is started for iterative inversion until the inversion results meet the requirements. The flow chart of the QPSO-CLS algorithm is shown in Figure 2.

Since the one-dimensional layered Earth model belongs to the mutation model, the resistivity and thickness of each layer are not continuous. Considering the calculation time and accuracy, the L1 norm of observation data and model data is selected as the objective function. The objective function is as follows:

$$F\left[\rho_1, \rho_2, \rho_3, ..., \rho_N\right] = \frac{1}{n}\sum_{i=1}^{n}\left|\widehat{\rho}_t^{(i)} - \rho^{(i)}\right|, \tag{10}$$

where ρ_N is the apparent resistivity value of the n-th recording time trace, $\widehat{\rho}_t^{(i)}$ is the apparent resistivity value of t iterations of the i-th recording time trace, and $\rho^{(i)}$ is the actual resistivity value of the i-th recording time trace.

3. Numerical Simulation

The data collected by the transient electromagnetic sounding instrument used in this paper are the induced EMF (electromotive force), which can be normalised to give a late apparent resistivity by the late apparent resistivity formula. However, late apparent resistivity is assumed to be derived approximately as time tends to infinity, so in the early stages,
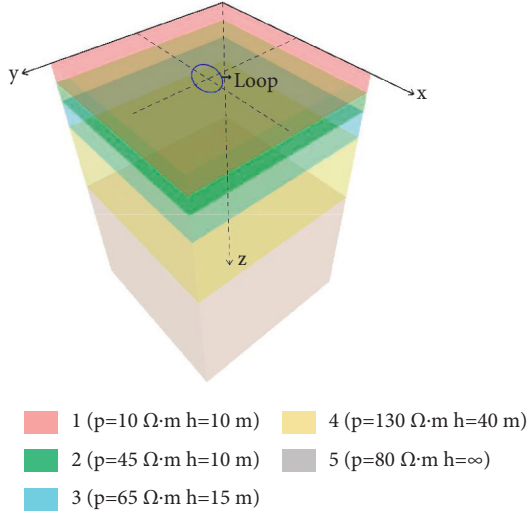
Figure 3: Forward modeling of TEM.

1 (p=10 Ω·m h=10 m)
2 (p=45 Ω·m h=10 m)
3 (p=65 Ω·m h=15 m)
4 (p=130 Ω·m h=40 m)
5 (p=80 Ω·m h=∞)

Table 1: Test model parameters.

Layer number	1	2	3	4	5
Resistivity ρ (Ω·m)	10	45	65	130	80
Thickness h (m)	10	10	15	40	∞

the apparent resistivity curve is severely distorted and cannot be imaged well for shallow areas, becoming one of the distractions of shallow geological interpretation, so many scholars have proposed the concept of area-time apparent resistivity. The all-time apparent resistivity calculated directly from the magnetic field strength is a more realistic reflection of the shallow geological conditions and is closer to the true apparent resistivity definition. In this paper, the area-wide apparent resistivity is adopted as the fitting parameter for the QPSO-CLS inversion algorithm.

For 1D forward of the central loop TEM, the strength of the magnetic field perpendicular to the central loop can be solved directly. Suppose a geoelectric model with N layers, the resistivity of layer j as ρ_j, and the thickness as h_j, so the magnetic field intensity response in frequency domain is

$$H_z = aI(\omega) \int_0^\infty \frac{\lambda^2}{\lambda + u^{(1)}} J_1(\lambda a) d\lambda, \tag{11}$$

where a represents the equivalent radius of the transmitting wireframe. The recurrence formula of u is as follows:

$$\begin{cases} u_j = \sqrt{\lambda^2 - k_j^2}, k_j^2 = -\frac{i\omega\mu_0}{\rho_j}, j = 1, 2, 3, \cdots, n, \\ \\ u^{(j)} = u_j \frac{u^{(j+1)} + u_j \tan h(u_j h_j)}{u_j + u^{(j+1)} \tan h(u_j h_j)}, \\ \\ u^{(n)} = u_n. \end{cases} \tag{12}$$
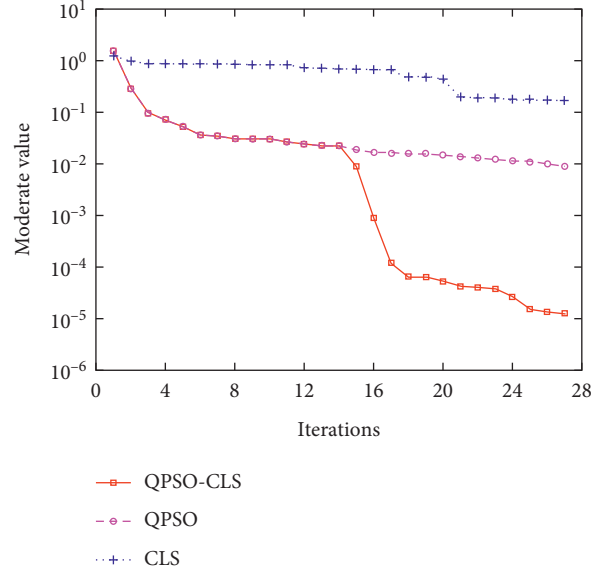
Figure 4: Descent curves of iterative computation obtained by different inversion algorithms.

— QPSO-CLS
– ○ – QPSO
···+··· CLS
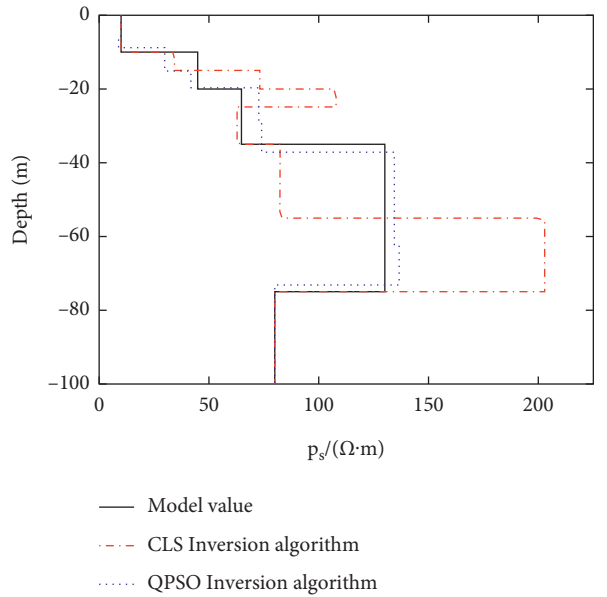
Figure 5: Inversion results of the QPSO algorithm and the CLS algorithm.

— Model value
–·– CLS Inversion algorithm
······ QPSO Inversion algorithm

The transient detection instrument used in this paper adopts a square wave with a duty cycle of 1 : 1, so only half a period of the waveform needs to be considered in the forward simulation, which can be regarded as a step-by-step wave as follows:

$$I(t) = \begin{cases} I_0, t < 0, \\ 0, t > 0, \end{cases} \tag{13}$$

where I_0 is the emission current. Fourier transforms the above formula to obtain the expression of emission current in frequency domain as follows:

(a)

(b)
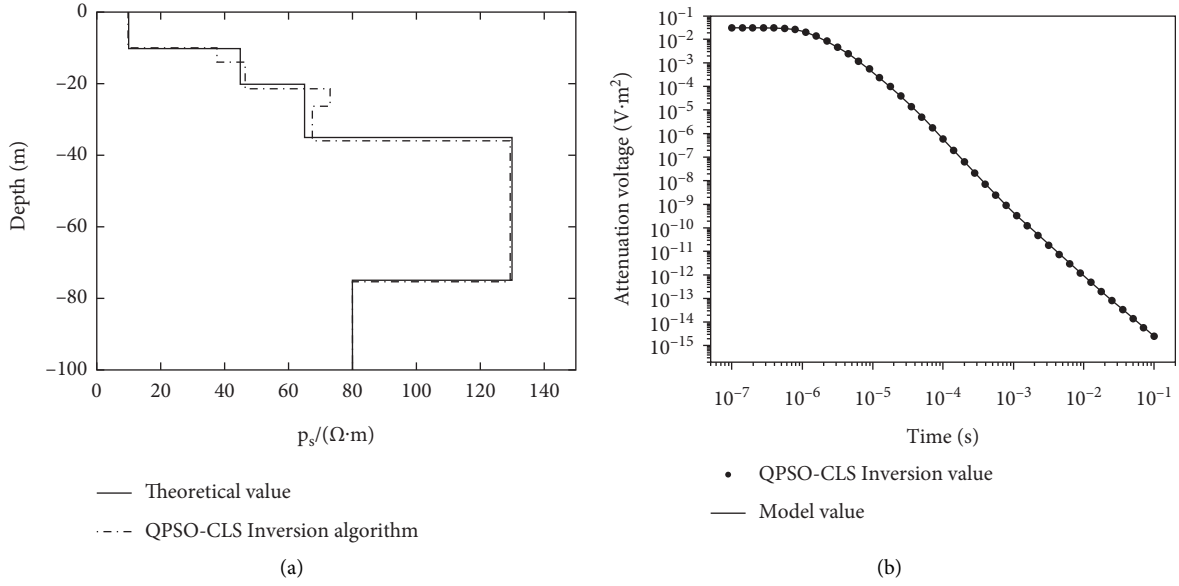
FIGURE 6: Inversion results of the QPSO-CLS joint algorithm, (a) model fitting curve, and (b) fitting curve of attenuation voltage.
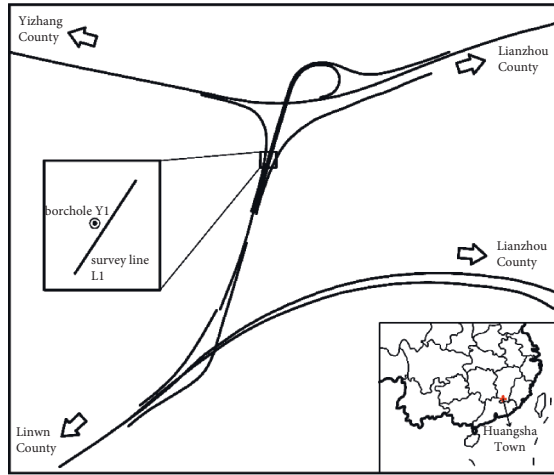
FIGURE 7: Schematic diagram of work area location.

$$I(\varpi) = \int_{-\infty}^{\infty} I(t)e^{i\varpi t}dt = -\frac{1}{\varpi}I_0. \tag{14}$$

Therefore, the magnetic field strength can be simplified as follows:

$$H_z = \frac{2}{\pi}\int_0^{\infty} Im\left[\frac{H_z(\varpi)}{\varpi}\right]\cos(\varpi t)d\varpi,$$

$$= \frac{2I_0}{\pi}\int_0^{\infty} Im\left[\frac{1}{\varpi}\int_0^{\infty}\frac{\lambda^2}{\lambda+u^{(1)}}J_1(\lambda a)d\lambda\right]\cos(\varpi t)d\varpi. \tag{15}$$

Let the inner integral kernel function be $func = \lambda^2/\lambda + u^{(1)}$. Hankel transform is represented by

$HT\{*\}$, and the cosine transform is represented by $CT\{*\}$. So, formulas (3)–(5) can be abbreviated as follows:

$$H_z = \frac{2I_0}{\pi} \cdot CT\left\{\frac{HT\{Im(func)\}}{\varpi}\right\}. \tag{16}$$

For the uniform half space geoelectric model, the analytical expression of H_z can be derived as follows:

$$H_z(t,x) = \frac{I_0}{2a}\left[\frac{3}{\sqrt{\pi}}\frac{1}{x}e^{-x^2} + \left(1 - \frac{3}{2x^2}\right)\text{erf}(x)\right], \tag{17}$$

where $\text{erf}(x)$ is the error function. Normalize H_z to obtain the following function:

$$Z(x) = \frac{3}{\sqrt{\pi}}\frac{1}{x}e^{-x^2} + \left(1 - \frac{3}{2x^2}\right)\text{erf}(x)$$

$$= \frac{4a}{\pi}CT\left\{\frac{HT\{Im(func)\}}{\varpi}\right\}. \tag{18}$$

Calculate the inverse function x of $Z(x)$ and derive the region-wide apparent resistivity based on magnetic field strength as follows:

$$\rho_a = \frac{\mu_0 a^2}{4x^2 t}. \tag{19}$$

Since the function $Z(x)$ is an implicit function, its inverse function cannot be obtained; therefore, it cannot be solved analytically. However, the numerical solution can be obtained by using the dichotomous finding method or the golden section method due to $Z(x)$ being monotonically increasing between 0 and 1.

To verify the effectiveness of the inversion algorithm, five-layer model forward data are established in this study, and the model is shown in Figure 3. Table 1 shows the layer thickness and resistivity of the model. The square loop of
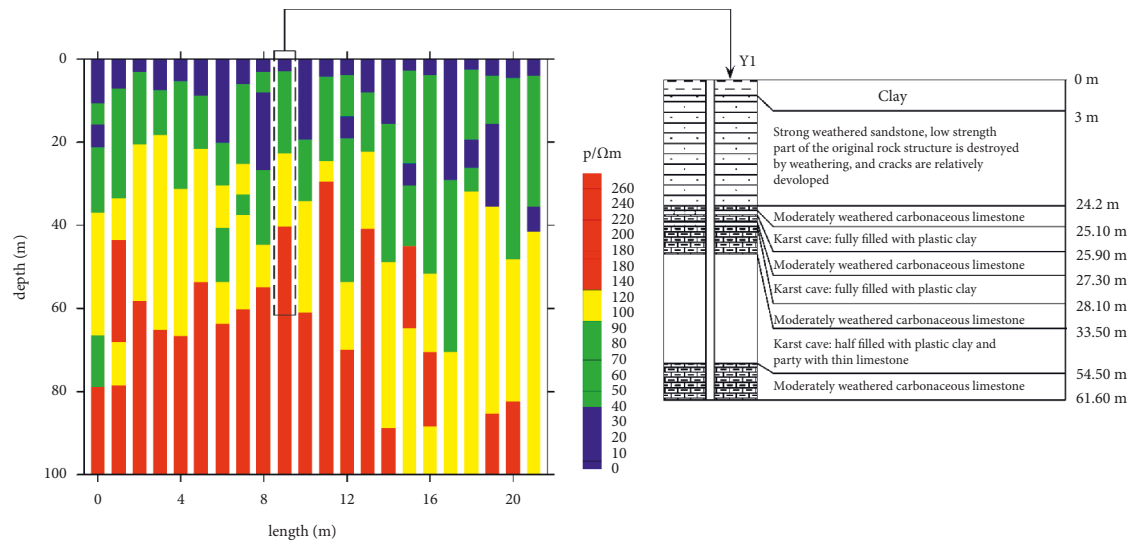
F<small>IGURE</small> 8: Comparison of inversion results (left) and borehole logging results (right).

10 m × 10 m is used as transmitting coil, the emission current is 1A, and the receiving mode of common center point receiving is adopted. In the inversion algorithm, 10 layers of the initial model are set for calculation.

The descent curves of iterative computation obtained by different inversion algorithms are shown in Figures 4 and 5.

Figure 6 shows the results of the QPSO-CLS joint algorithm.

The results of different inversion algorithms are compared. It is found that the QPSO-CLS joint algorithm can effectively break through the local optimal extremum and presents better inversion results. By comparing Figures 4 and 5, the inversion results of the QPSO-CLS joint algorithm are more consistent with the theoretical model, and the results have a higher reduction degree and higher fitting degree for the layer thickness and resistivity of the model.

4. Field Test

4.1. Location Overview and Data Acquisition. The field data were collected at pile Y1 (112.70 E, 25.14 N) of the Caojiaben interchange main line bridge of Linwu-Lianzhou (Hunan-Guangdong Boundary) expressway project in Yizhang County, Hunan Province. The specific location is shown in Figure 7 as follows. The terrain conditions of the Caojiaben junction interchange are relatively simple, with relatively gentle terrain and local steep area, and the natural slope is 20°–40°. According to the boring results illustrated in Figure 8, the strata revealed in site include Holocene deluvial and eluvial clay and the underlaying bedrock: Devonian carbonaceous limestone and sandstone. The grimy highly weathered carbonaceous limestone with texture and structure partially destroyed is closely sectioned by joints and fractures and drilling core recovered as detritus and gravel. The moderately weathered carbonaceous limestone with cryptocrystalline texture and layered structure is broken by joints and fractures with calcite veins filled in the fissures. The moderately weathered rock that is widely distributed

within the site and karst is discovered locally by borings. According to the data of borehole Y1, within 24.2–33.5 m in the underground, the surrounding rock is mainly moderately weathered carbonaceous limestone with broken joints and developed karst caves. The geological conditions are complex.

The transient electromagnetic survey line in Figure 7 is named L1, with a length of 20 m and a fundamental frequency of 25 Hz. A total of 21 measuring points were set up, with an interval of 1 m. Then, 25 channels of data were collected at each point, and the emission line of 1.9 m × 1.9 m and the receiving coil of 110.16 m^2 were used, as well as the common central point detection method was adopted. The circle in Figure 7 is located in borehole Y1, and the logging information can be compared with the inversion results.

4.2. Inversion Analysis of Field Data. Figure 8 shows the comparison of inversion results and borehole logging results. The comparative analysis shows that the uppermost layer is the clay layer, which is humid and has high water content. Thus, the formation resistivity of about 0 m–5 m is low. Due to the existence of strongly weathered sandstone with low strength, developed fractures, and poor integrity within 5 m–25 m, the resistivity value of this layer is higher than that of the overlying clay layer, and the local low resistivity area is probably caused by the development of fracture water. The borehole revealed that there are karst caves and moderately weathered carbonaceous limestone intercalations within 25 m–54.5 m. There are both fully filled and semifilled karst caves (the filling material is plastic clay). Thus, this section presents the characteristics of high resistivity value. The local high resistivity anomaly area is probably caused by the karst cavity, and the local low resistivity anomaly area is probably caused by the high-water content plastic clay-filled area in the karst cave. The strata below 54.5 m show the characteristics of medium and high resistance values. It is inferred that the rock structure in this

area is complete and dense. As the known borehole depth is 61.60 m, only the borehole logging information is compared within this range. When the detection distance is greater than 61.60 m, the transient electromagnetic detection results are obtained. It can be seen that the inversion results are generally consistent with all kinds of strata exposed by drilling, indicating that the inversion results are accurate in the strata division. Thus, the effectiveness of the QPSO-CLS joint algorithm and its application value in engineering are verified.

5. Conclusion

(1) The proposed transient electromagnetic 1D inversion algorithm based on the QPSO-CLS joint algorithm can be used to effectively depict the formation boundary of the model and efficiently inverse the information of formation thickness and formation resistivity.

(2) The inversion calculation of simulated data shows that the QPSO-CLS joint algorithm has better inversion results and has a higher reduction degree for the inversion of layer thickness and resistivity value of the model, which is superior to a single algorithm. The inversion results of field test data show that the inversion results of the QPSO-CLS joint algorithm are consistent with the results of borehole logging, and the proposed QPSO-CLS joint algorithm can accurately reveal the formation information.

(3) The QPSO-CLS joint algorithm improves the interpretation accuracy of transient electromagnetic. It provides a new inversion interpretation idea for the transient electromagnetic detection of the bored pile, reduces the engineering cost, and enriches the detection means of karst geological conditions.

The QPSO-CLS joint inversion algorithm proposed in this manuscript is only aimed at the 1-dimensional model which assumes that the strata under the exploration area are evenly distributed in layers. However, it has certain limitations in the 2-dimensional section imaging. In the future, relevant research and testing can be carried out so that the joint algorithm can be applied to the two-dimensional inversion to increase the accuracy of the exploration of the spatial position and shape of the cave.

Data Availability

The [TEM data.DTE] data used to support the findings of this study are available from the corresponding author upon request.

Conflicts of Interest

The authors declare no conflicts of interest.

Authors' Contributions

Xue Liu conducted conceptualization, methodology, validation, writing, review, and editing, as well as supervision. Chunwei Pan conducted methodology, model analysis, validation, and data curation. Fangkun Zheng conducted methodology, formal analysis, investigation, and data curation. Ying Sun conducted data curation, writing, review, and editing. Qingsong Gou conducted writing, review, and editing.

Acknowledgments

References

[1] X. F. Shi, *Study on the Roof Stability of Concealed Karst Cave under Pile Foundation*, The Chinese Academy of Sciences, Wuhan, China, 2005.

[2] H. B. Zhou, "Built-in-rock bored pile construction technology of pre-treatment to cover layer and karst cave in karst geology," *Construction Technology*, vol. 40, pp. 198–202, 2011.

[3] X. Li, J. J. Wu, and D. M. Cao, "Advanced geologic forecasting for unfavorable geological body with water-transient electromagnetic method," *Geotechnical Investigation and Surveying*, vol. 34, no. 3, pp. 70–75, 2006.

[4] D. M. Tan, T. Y. Qi, and C. L. Liu, "Research on the transient electromagnetic response in tunnel whole space and its application," *Hydrogeology & Engineering Geology*, vol. 36, no. 3, pp. 111–116, 2009.

[5] D. J. Yu, L. Huang, and W. Zhang, "Application of transient electromagnetic method in advance geologic prediction technique of Mingyuexia tunnel," *Site Investigation Science and Technology*, vol. 2, pp. 48–50, 2010.

[6] S. C. Li, S. Li, Q. Zhang et al., "Predicting geological hazards during tunnel construction," *Journal of Rock Mechanics and Geotechnical Engineering*, vol. 2, no. 3, pp. 232–242, 2010.

[7] M. Somanath, *Global optimization with application to geophysics*, vol. 73, pp. R71–R82, University of Alberta, Edmonton, Canada, 2008.

[8] F. P. Li, H. Y. Yang, and X. H. Liu, "Nonlineat programming geneic algorithm in transient electromagnetic invesion," *Geophysical and Gewchemical Exploration*, vol. 41, no. 2, pp. 347–353, 2017.

[9] D. Cheng, J. L. Cheng, and A. M. Wang, "Numerical simulation of drillhole transient electromagnetic response in mine roadway whole space using integral equation method," *Chinese Journal of Geophysics*, vol. 61, pp. 4182–4193, 2018.

[10] H. F. Sun, N. Y. Zhang, and S. B. Liu, "Ll-norm based nonlinear inversion of transient electromagnetic data," *Chinese Journal of Geophysics*, vol. 62, no. 12, pp. 4860–4873, 2019.

[11] J. Kennedy and R. C. Eberhart, "Particle swarm optimization [R]," in *Proceedings of the IEEE International Conference on Neural Networks*, WA, Australia, December 1995.

[12] R. Shaw and S. Srivastava, "Particle swarm optimization: a new tool to invert geophysical data," *Geophysics*, vol. 72, no. 2, pp. F75–F83, 2007.

[13] F. A. Monteiro Santos, "Inversion of self-potential of idealized bodies' anomalies using particle swarm optimization," *Computers & Geosciences*, vol. 36, no. 9, pp. 1185–1190, 2010.

[14] J. L. Cheng, F. Li, S. P. Peng, X. Sun, J. Zheng, and J Jia, "Joint inversion of TEM and DC in roadway advanced detection based on particle swarm optimization," *Journal of Applied Geophysics*, vol. 123, pp. 30–35, 2015.

[15] M. X. Li, J. Y. Cheng, and P. Wang, "Transient electromagnetic 1D inversion based on the PSO–DLS combination algorithm," *Exploration Geophysics*, vol. 5, pp. 1–9, 2019.

[16] S. Y. Li and P. C. Li, "Quantum particle swarms algorithm for continuous space optimization," *Chinese Journal of Quantum Electronics*, vol. 24, no. 5, pp. 569–574, 2007.

[17] X. S. Zhao, S. W. Wang, and X. Shao, "Cooperative task allocation for multiple UCAV based on improved quantum-behaved particle swarm optimization algorithm," *Journal of Sichuan Ordnance*, vol. 10, pp. 120–124, 2015.

[18] B. X. Su, P. H. Zhai, and Z. Zhang, "Application of three-dimensional high-density electrical method in detection of sandstone water on coal," *Roof Coal Technology*, vol. 40, no. 3, pp. 43–45, 2021.

[19] Z. ., Y. Zhang, "Application of 3 D high-density electrical method in detection of water-accumulated gob," *Mining Safety & Environmental Protection*, vol. 1, pp. 76–79, 2015.

[20] M. H. Loke and R. Barker, "Rapid least-squares inversion of apparent resistivity pseudosections by a quasi-Newton method1," *Geophysical Prospecting*, vol. 44, no. 1, pp. 131–152, 1996.

[21] W. X. Zhang, J. S. Liu, L. Yu, and B Jin, "Nonlinear inversion for complex resistivity method based on QPSO-BP algorithm," *Open Journal of Geology*, vol. 11, no. 10, pp. 494–508, 2021.

Research Article

Study on Seismic Response Characteristics of Shield Tunnel in Soil-Rock Combination Stratum

Guang-Biao Shao [ID],[1,2] **Xi-Sen Fan** [ID],[1] **Jin-Hua Shang** [ID],[3] **and Li-Xin Lu** [ID][1]

[1]*School of Civil Engineering, Shandong Jianzhu University, Jinan 250101, China*
[2]*Key Laboratory of Building Structural Retrofitting and Underground Space Engineering,*
 Ministry of Education, Jinan 250101, China
[3]*Jinan Rail Transit Group Co, Ltd, Jinan 250200, China*

Correspondence should be addressed to Li-Xin Lu; 595812889@qq.com

The sharp change of stiffness in the soil-rock combination stratum is the weak point in the seismic design of the tunnel structure. To explore the influence of soil-rock combination stratum vibration on the shield tunnel, the section of Jinan rail transit line 4 at the Olympic Sports Center is used as the research background. Firstly, the two-dimensional numerical model is established, and the internal force calculation and distribution law of the structure are studied. Then, based on the third similarity theory, the model similarity physical relationship is derived. The shaking-table model test of the soil-rock-structure system is carried out. The seismic response law of tunnel cross-section is studied by the model test and numerical analysis. The results revealed the following: (1) the peak bending moment distribution diagram derived from numerical calculation is consistent with that obtained from the shaking-table model test, which has shown that the numerical and experimental methods are correct, and the research results are available for the seismic resistance of shield tunnels. (2) The deformation, axial force, shear force, and bending moment of the tunnel structure in the soil-rock combination stratum under the action of S-wave change abruptly and significantly at the soil-rock interface section, and the difference in structural stress between the upper and lower sides of the soil-rock interface increased by 65.5%. The excessive stress difference changes the damage mode of the tunnel. (3) The relative difference and abrupt change of bending moment and shear force at the interface is more significant than the axial force, so that the tunnel structure at the soil-rock interface is most prone to bending-shear damage.

1. Introduction

The shield method [1, 2], as one of the main methods of tunnel construction, has been widely used in the field of urban underground rail transit engineering construction. Many underground structures were severely damaged by the Kobe earthquake, and the structures were either completely collapsed or could not be used as they became irreparable. It fully exposed the problem of underground structures resisting earthquakes [3, 4]. With the development of urban subway tunnels, there are more records of earthquake damage to underground structures [5, 6]. For tunnel structures in complex geological conditions, the strength of the restraint effect of the surrounding strata on the tunnel

results in different damage states, where the lateral force characteristic of the tunnel sheet is the key point for seismic performance control, especially when the tunnel structure crosses the stratigraphic interface, where the soil stiffness and shear properties change sharply.

The existing analysis methods are divided into the pseudostatic method [7] and the dynamic analysis method [8] in terms of mechanical characteristics, and the dynamic analysis method is one of the most effective analytical methods to study the interaction between the structure and the soil medium under seismic excitation in complex geological conditions. Liu et al. [9] established a three-dimensional finite element model to analyze the seismic response of immersed tube tunnels in different sites. Huang

et al. [10] carried out shaking-table model tests for longitudinal soil-rock abrupt change strata and studied the effect of the input angle of seismic waves on the longitudinal dynamic response of the tunnel structure. Shen [11] designed a shaking-table test based on the longitudinal equivalent stiffness of shield tunnel to study its dynamic response characteristics for the shield tunnel, crossing soft and hard strata. Cheng [12] used the ABAQUS software to establish a refined numerical model of three-dimensional soil-concrete pipe sheet structure and bolts between pipe rings to obtain the structural response law of a large-diameter shield tunnel through soft and hard abruptly changing strata under longitudinal seismic effects. Wang et al. [13] carried out the shaking-table tests of shield tunnels under cracks in the strata and conducted the shaking-table tests of loess-free field as well as horseshoe-shaped tunnel structure foundation interactions.

The above studies mainly focus on the effect of sharp changes in tunnel longitudinal stratigraphy on the seismic response of the structure, however, most of these studies only use a single research method. Usually, it is difficult to verify the validity of the results obtained by a single research method. Using a variety of mutually verifiable research methods may effectively improve the reliability of the results. Therefore, in this study, establish a two-dimensional dynamic analysis model, study the interaction response law of the soil-rock stratum tunnel system through numerical analysis, and obtain the response values of soil-rock geological structure changes to the internal force and acceleration of shield tunnel. Then, shaking-table tests are conducted for shield tunnels under soil-rock combination fields to visualize the seismic response mechanism of the structure; meanwhile, the shaking table test reveals the dynamic response of the geological changes to the cross-section of the shield tunnel structure.

2. Engineering Research Background

Rail transit line 4 is the main rail transportation line linking the west and east city regions, and the area where the traffic line project is located belongs to the North China Seismic Zone. In this paper, the crossing node of the selected tunnel is located in the section of the Olympic Sports Center Station of Rail Transit Line 4, with a minimum embedded depth of about 10.3 m and a maximum depth of about 12.2 m, as shown in Figure 1. The tunnel passes through a complex stratigraphic environment with mixed fill, loess-like silty clay, silty clay, limestone, etc. The state of the upper silty clay layer is mainly plastic to hard plastic, while the lower layers of rock are mainly Paleozoic Ordovician limestone with rock quality class III and RQD = 20~80. The upper soft and lower hard strata are in close contact, so that the cross-section of the shield tunnel is in the upper soil and lower rock strata at the same time, and the soil and rock stiffness changes along the depth direction because of the abrupt material change in the soil-rock stratum and the difference in the embedment restraint mechanism of soil and rock. These unfavorable factors bring more uncertainty and challenge to the seismic design of shield tunnels and other underground structures in this stratum distribution form. Therefore, it is important to
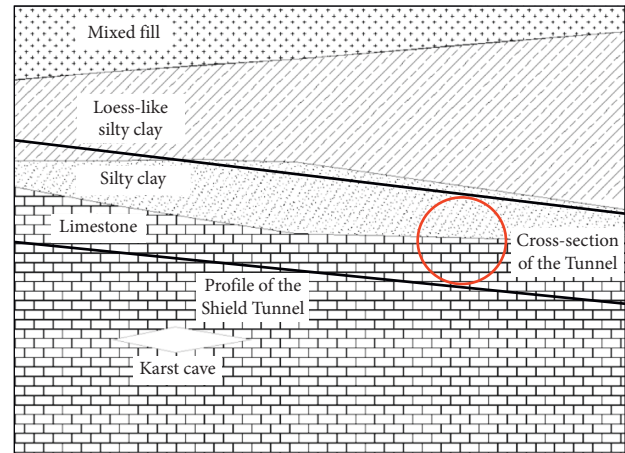
Figure 1: Schematic diagram of rail transit no. 4 line.

carry out the lateral seismic study of the tunnel under relevant geological conditions. The typical soil and rock combination stratum was selected for this study. The stratum was simplified into two types of hard and soft strata, and the direction of the interface was parallel to the longitudinal axis of the tunnel.

3. Numerical Simulation of Shield Tunnel in Soil and Rock Combination Stratum

3.1. Soil-Rock Combination Stratum Model. Based on MIDAS/GTS finite element software, an equivalent linear model is used for the soil and rock, an elastic model is used for the pipe sheet material, a fixed boundary condition is used at the bottom, an interface element layer is set between the soil and the structure, and a dynamic finite element model is established, as shown in Figure 2. The numerical analysis model is easier to solve and obtain the detailed distribution of the internal force of the shield tunnel structure and provide suggestions on model making, sensors arrangement, and ground motion input for the subsequent shaking-table test. The element type of stratum is two-dimensional planar element. Mixed fill, silty clay, and limestone are used in the Mohr-Coulomb elastoplastic principal model, considering the reduction of segment stiffness caused by segment joint and the influence of segment joint assembly. The segment ring has ηEI ($\eta \leq 1$, EI is the bending stiffness of the cross-section of the homogeneous tunnel), and the transverse stiffness of the tunnel is reduced by a coefficient of 0.6~0.8 [14], which is taken as $\eta = 0.8$. The material parameters of the structure and stratum are taken, as shown in Table 1. The relative sliding or detachment of the tunnel structure and the soil body occurs, resulting in the inability to transfer the forces exerted by the forced displacement of the soil body, and to simulate the actual contact condition, considering the frictional shear effect at the contact surface because of the change in stiffness between different materials, an interface elements layer is set up between the stratum and the tunnel [15]. The interface element defines the contact behavior automatically by MIDAS according to the stiffness value between two materials. The
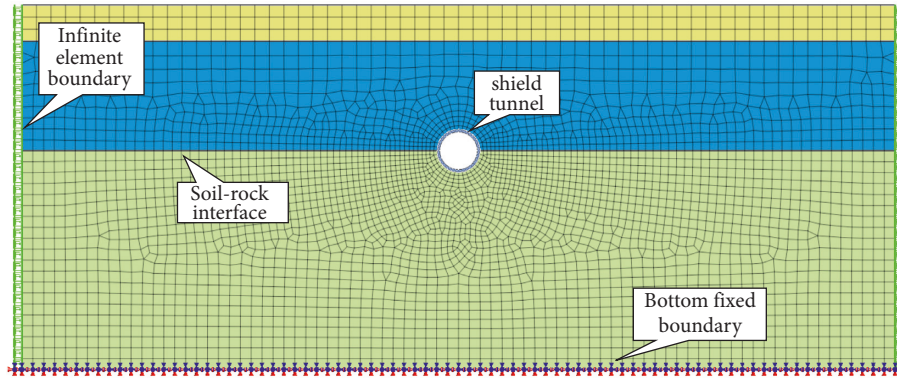
FIGURE 2: Finite element model of soil-rock combination field.

TABLE 1: Structure and stratigraphic physical parameters.

Material	Severe γ (kN·m^{-3})	Modulus of elasticity E (MPa)	Cohesion c (kPa)	Internal friction angle φ (°)	Poisson's ratio μ
Mixed fill	19.2	12	18.0	12.0	0.37
Silty clay	17.9	25	30.2	17.8	0.32
Limestone	21.2	6000	217.0	35.0	0.39
Bedrock	25.6	17200	—	—	0.20
C50 concrete	25.0	34500	—	—	0.20

bedrock is used at a depth of 5 times the diameter of the tunnel below to ensure good convergence and stability of the numerical calculation.

3.2. Seismic Wave Selection and Loading Conditions.
El-Centro wave is selected for numerical simulation in this study. El-Centro wave is a typical near-field strong earthquake wave, which is suitable for cohesive soil sites. The input bedrock seismic waves are E1 frequent earthquakes with a peak acceleration of 0.05 g, E2 fortification earthquakes with a peak acceleration of 0.10 g, and unidirectional x seismic waves are input from the bottom of the model.

The free-field eigenvalue analysis was performed on the soil-rock site to obtain the first two orders of self-oscillation periods, where the sum of the maximum mass participation coefficients of the model exceeded 80% for calculation. In the soil-rock tunnel model, the cross-section of the structure is in the dual media of powder clay and rock, and the stratigraphic partition interface is at 1/2 cross-section.

3.3. Structural Internal Force Analysis.
The internal force values of the tunnel structure in the soil-rock combination stratum are shown in Table 2. The values of the internal force of the tunnel structure on the upper and lower sides of the stratigraphic interface are extracted for two different sets of seismic loading conditions. The shear force relative differences were 31.2% and 50.0%. The relative value difference percentage of the bending moment was 41.6% and 50.2%. The relative value differences percentage of the structural internal force values increased gradually with the increase of seismic load level, in which the difference of shear force and bending moment at the soil-rock partition interface was significantly larger than the abrupt changes of axial force.

Even if the abrupt change of the axial force at the partition interface is an unfavorable section, the axial force is not the dominant factor in the seismic design at the soil-rock partition interface because of the large compressive bearing capacity of concrete. Since the shear and flexural bearing capacity of concrete structures is mainly provided by internal reinforcement, the tunnel structure at the soil-rock interface is most prone to bending and shear damage, and the tunnel structure bending-shear structural measures should be strengthened during the seismic design.

The time history curves of maximum Mises stress at rock side (lower interface) and soil side (upper interface) are shown in Figure 3. The stress value of the tunnel structure at the soil-rock transition section increases from 7286 kN·m^{-2} to 21,144 kN·m^{-2}, and the structural stress increased by 65.5%. The excessive stress difference causes secondary stresses inside the structure to change the damage pattern of the structure, resulting in the tunnel structure at the soil-rock transition interface damage pattern changing from compression-bending damage state to bending-shear damage state.

3.4. Distribution Law of Structural Internal Force.
According to existing studies, the tunnel is mainly controlled by the static load under the action of medium and small earthquakes in the soil field, and the structural bending moment gradually changes to the antisymmetric form as the seismic load level increases. The axial force distribution is compressed in the full section, and the shear force is distributed in 45° antisymmetric form along the counterclockwise direction [16].

In the soil-rock combination field, the soil properties change sharply along with the soil depth, and the stiffness and shear properties of the surrounding rock are significantly different from those of the clay. Figure 4 presents the structural

TABLE 2: Internal forces of the tunnel structure.

Seismic waves (g)	Location	The right side of structure			The left side of structure		
		Axial force N (kN)	Bending moment M (kN·m)	Shear force V (kN)	Axial force N (kN)	Bending moment M (kN·m)	Shear force V (kN)
0.05	Upper interface	−860.7	−168.8	167.2	−891.1	−175.3	158.6
	Lower interface	−755.2	−116.2	97.6	−795.2	−120.4	93.7
0.10	Upper interface	−1 065.6	−273.2	352.1	−1 125.6	−293.6	264.2
	Lower interface	−892.1	−155.2	241.3	−867.2	−146.9	131.5
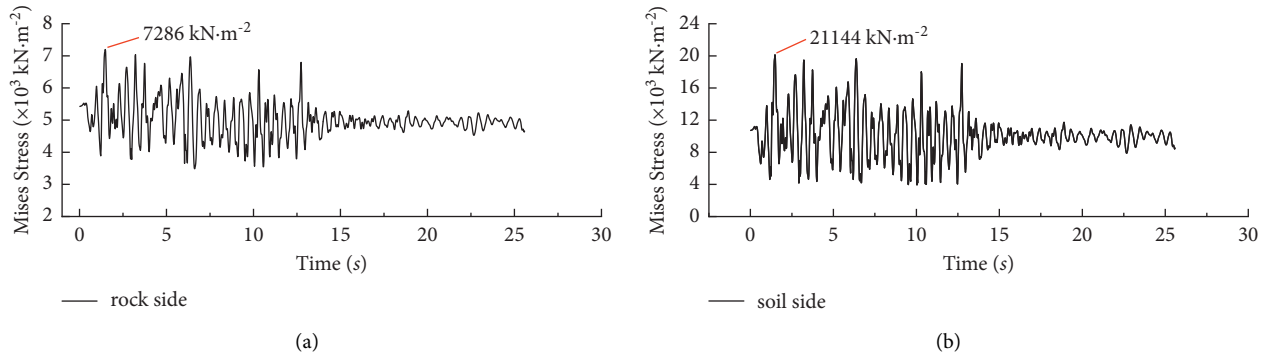
FIGURE 3: Time history curves of Mises stress at the soil-rock partition interface of the tunnel structure, (a) rock side of soil-rock partition interface of tunnel, and (b) soil side of the soil-rock partition interface of tunnel.
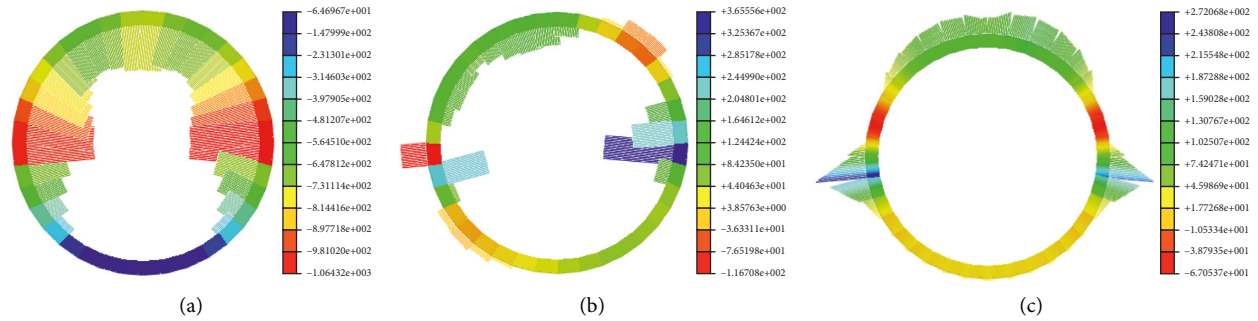
FIGURE 4: Internal force distribution of tunnel structure, (a) structural axial force cloud diagram, (b) structural shear force cloud diagram, and (c) structural bending moment cloud diagram.

cloud diagram of the tunnel structure in the soil-rock combination field under the action of 0.10 g seismic wave for the axial force, shear force, and bending moment of the tube piece. The analysis results show that the axial force of the tunnel structure in the soil-rock stratum under the action of seismic waves is still symmetrically distributed in the full-section compressed state. The bending moment shows a four-peak phenomenon, with the maximum value occurring at the soil-rock interface in an axisymmetric distribution. The shear force distribution of the structure in the interface region undergoes a significant abrupt change. On both sides of the soil-rock partition interface, the internal force response of the structure on the soil side is larger. This phenomenon may be because the main deformation of the tunnel tube is the forced displacement caused by the deformation of the surrounding soil layer during the seismic action, especially in the section of abrupt changes in the ground stiffness, shear parameters, etc., which

will cause unfavorable situation areas of stress. Therefore, the lateral seismic design of the tunnel structure should focus on the case of abrupt changes in geological conditions.

4. Shaking-Table Model Test

The shaking-table test is mainly to further study the dynamic response law of the tunnel structure cross-section under the earthquake action. The numerical analysis and the response law of the structure obtained from the shaking-table test are used to verify the accuracy of the study.

4.1. Shaking-Table Testing System. The test was conducted on a three-way hydraulic servo-driven seismic simulation test bench of Shandong Jianzhu University, with a table size of 3 m × 3 m, the system frequency range of 0–100 Hz, the

maximum load of 10 t, the maximum acceleration of 1.5 g in *X, Y,* and *Z* directions, and the maximum amplitude of ±125 mm, with a laminated shear model box of 2.0 m × 1.5 m × 1.5 m assembled on the shaking-table. The excitation direction is along the long side of the model box horizontal excitation, and the model box is as shown in Figure 5.

4.2. Similarity Ratio Design.

The model did not reach the damage stage in the test. Hence, the ultimate strength similarity of the material is not all required. The geometric similarity ratio of the tunnel model is selected as 1/25, the similarity ratio of the unit weight is 1/1, and the similarity ratio of the elastic modulus is 1/125, with the length *l*, density *ρ*, and elastic modulus *E* as the basic physical quantities. In the dynamic test of the underground structure, the similarity ratio of the soil is very important to the influence of the shaking-table test, which is mainly based on the shear wave velocity and density as the basic physical quantities, assuming that the model soil density similarity ratio is 1. According to the similarity principle [17–20], a volume analysis can be performed to derive other relevant parameter ratios, as shown in Table 3.

4.3. Similar Materials for Tunnels and Rock

4.3.1. Tunnel Structure Similar Materials.

A similar model of the tunnel structure is made using gypsum, which is made of water and gypsum according to a certain mass ratio. The cross-sectional deformation of the shield tunnel consists of two parts: the bending deformation of the tube piece and the rotational deformation of the longitudinal joint [18]. Considering the discounting of the structural stiffness by the circumferential tube piece splicing, the rotational stiffness *Kθ* of the tunnel model splice joint and the prototype splice joint should be kept in a similar relationship. In this test, a single-sided model slotting is used to simulate the effect of splice joint stiffness weakening, and its slotting parameters are calculated according to the subsequently given formula [21, 22]. The slotted thickness *h'* of the model is as follows:

$$h' = \sqrt[3]{\frac{12L_2kI}{b(EI + kL)}}$$
$$= \sqrt[3]{\frac{12Ika(D_1 + D_2)}{2bEI + bka(D_1 + D_2)}}.$$

(1)

The external slotted curved beam thickness cubic equation is as follows:

$$(EI + kL_2)bh'^3 - 6kIah' - 6D_2kIa = 0,$$

(2)

where *a* is the rounding angle corresponding to the slotted section of the model, *b* is the ring width of the prototype tube sheet ring, *D*1 is the outer diameter of the prototype tube ring, *D*2 is the inner diameter of the prototype tube sheet ring, *E* is the modulus of elasticity of the prototype tube material, *I* is the cross-sectional moment of inertia of the

FIGURE 5: Shaking-table testing system.

TABLE 3: Similarity relationship and similarity ratio of each physical quantity of the model.

Physical quantity	Similar relationship	Similarity ratio
Length/*l*	C_l	1/25
Modulus of elasticity/*E*	C_E	1/125
Unit weight/*γ*	1	1
Strain/*ε*	1	1/
Stress/*σ*	$C_E C_\sigma$	1/125
Effective overpressure/*F*	C_l	1/25
Time/*t*	$C_l\sqrt{C_P/C_G}$	1/12.5
Frequency/*w*	$1/C_t$	12.5
Acceleration/*a*	C_l/C_t^2	2.3

prototype tube ring in the transverse direction, *L*2 is the prototype slotted width, and *k* is the stiffness of the prototype tube sheet joint. The center angle of the tube sheet ring corresponding to the single-sided slotted model joint is taken as 3°. Table 4 shows the gypsum tube sheet slotting parameters. The pipe model with slotted section is shown in Figure 6.

4.3.2. Similar Materials for Soil-Rock Combination Stratigraphy.

According to the geotechnical investigation report and the similar ratio relationship, the prototype site soil is selected for the silty clay stratum, controlling the same water content and weight. The surrounding rock is with quartz sand and gravel as aggregate, along with silicate cement and gypsum as the binder material. Density, cohesion, internal friction angle, and other physical and mechanical parameters have a large impact on the structural response. The mixed materials are subjected to the direct shear test and laboratory geotechnical test to determine the above parameters. The mass ratio of the surrounding rock in this model is shown in Table 5, and the physical parameters of the prototype foundation and the model are shown in Table 6.

4.4. Experimental Design and Seismic Wave Loading

4.4.1. Test Sensor Arrangements.

The test requires the acquisition of structural acceleration, strain, and other data. The principle of sensor arrangement is based on the research content. One observation surface A–A was set up in the model. To reduce the unfavorable influence of the boundary effect on the test, strain sensors S1~S14 are arranged on the A–A observation surface in the circular direction along the

TABLE 4: Slotting parameters for model splice joints at a 3° rounding angle.

Name	Flexural stiffness	Slotting depth (mm)	Slotting width (mm)
Arch top/arch bottom	50	3.5	7.6
Arched waist	35	2.2	7.6

(a)   (b)

FIGURE 6: The slotted model of shield tunnel, (a) model pipe casting and forming, and (b) model pipe piece slotting.

TABLE 5: Mass ratio of each constituent of the surrounding rock material.

Molding materials	Quartz sand	Stone	Gypsum powder	Silicate cement
Mass ratio	10	0.2	4	1

TABLE 6: Similar physical parameters of the foundation material model.

Material	Unit weight γ (kN·m^{-3})	Modulus of elasticity E/(MPa)	Cohesion c/(kPa)	Internal friction angle φ (°)
Silty clay	17.9	0.6	30.2	17.8
Surrounding rocks	21.2	200	217	35

inside and outside of the tunnel to obtain the bending moment of the cross-section of the structure, as shown in Figure 7. Accelerometers A1–A2 were arranged on the surface of the soil, A3–A7 were arranged in the surrounding soil and rock, and A8 was located on the table of the shaking-table as the reference acceleration input monitoring point, as shown in Figure 8.

4.4.2. Test Loading Scheme. The test is proposed using the El-Centro wave as input ground motion. The bedrock seismic waves are referred to the seismic waves provided by the Earthquake Engineering Research Institute of Shandong Province with a 50-year probability of exceedance of 10% (multiple encounter earthquake, peak acceleration 0.05 g), and a 50-year probability of exceedance of 5% (fortified earthquake, peak acceleration 0.10 g), and the corresponding acceleration peaks are 0.115 g and 0.230 g after baseline adjustment and similar relationship conversion, with a seismic wave duration of 26.324 s and a time step of 0.00616 s. The frequency scanning with the white noise of the amplitude of 0.05 g is performed before and after each level of loading to observe the changes in self-oscillation frequency and damping of the soil-model structure interaction system. The specific test conditions are shown in Table 7, and the seismic wave time history curves are shown in Figure 9.
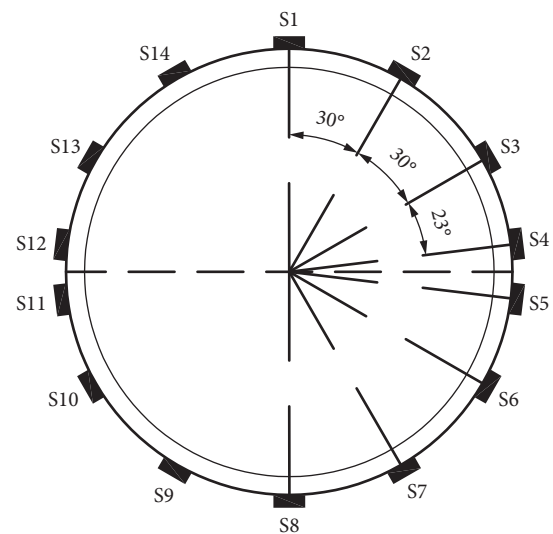
FIGURE 7: Strain sensors arrangement.

5. Result Analysis of Shaking-Table Model Testing

5.1. Shear Box Boundary Effect Verification. Since the soil range in the laminar shear box is finite and cannot truly simulate the infinite domain state, its boundary effect is
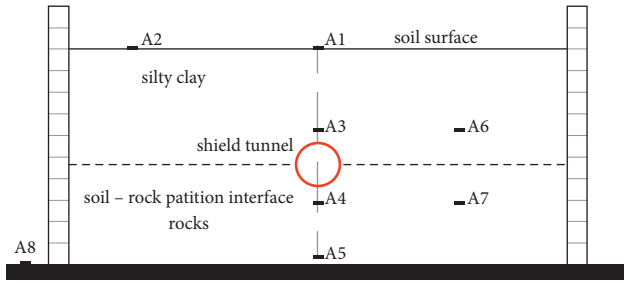
Figure 8: Stratum accelerometers arrangement.

Table 7: Shaking-table test loading scheme.

Name	Waveform	Acceleration	Duration (s)	Direction
1	White noise	0.05 g	30	
2	El-Centro	0.115 g	30	
3	White noise	0.05 g	30	One-way x
4	El-Centro	0.230 g	30	
5	White noise	0.05 g	30	
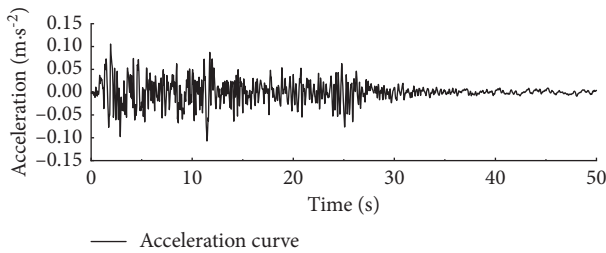
Figure 9: Acceleration time history of El-Centro wave.

inevitable. The acceleration response peaks of different measurement points at the same elevation are extracted in the test, and the boundary effect of the test shear box is verified by the calculation of the acceleration difference ratio between measurement points A1 and A6 near the boundary of the model box and measurement points A2 and A3 at the center of the site, citing the two-van deviation index [23]. The two-parameter deviation index μ was calculated using the following equation:

$$\mu = \frac{\left\| X_i - X_o \right\|}{\left\| X_O \right\|}, \tag{3}$$

where X_O, X_i-refers to the values of the reference sensor and the target sensor, respectively, μ, which is the reasonable range of index, is 0.01~0.25.

The acceleration curves of the two measurement points A1 and A2 have the same trend of change and show the same acceleration dynamic response change law. Figure 10 shows the diophantine coefficient curve, with the increase of the ground vibration input peak index μ increasing roughly linearly, indicating that the boundary effect is gradually enhanced with the increase of earthquake intensity, and the maximum of the collecting data results is 0.16, which meets the test error requirements.
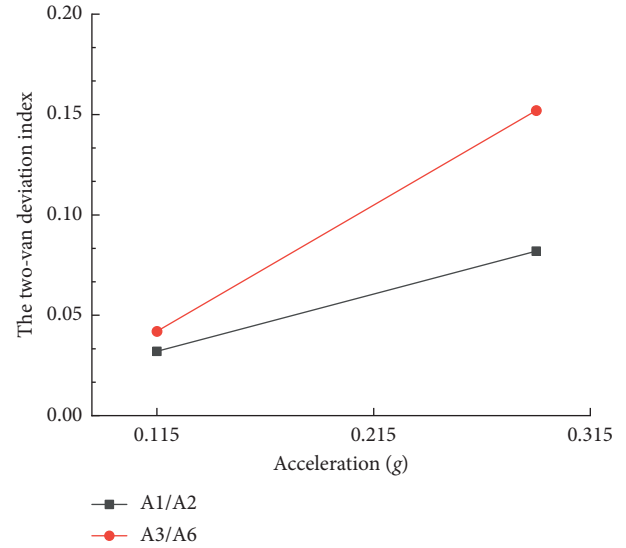
Figure 10: Soil-rock combination stratum two-van deviation curve.

5.2. Predominant Period in Soil-Rock Combination Stratum.
Site natural vibration period is an important index parameter for the seismic design of underground structures and the vibration characteristics inherent to the underground structure and soil system. In this study, the self-vibration characteristics of free sites are usually determined by the white noise signal scanning method. The A1 acceleration sensor on the surface of the foundation is the white noise transfer curve measurement point, and the scanned frequency data is filtered and processed with Fourier transform using MATLAB to obtain the predominant period variation trend of the test model, as shown in Figure 11. In the soil-rock combination field, the predominant period of the site is more inclined to the first modal frequency of 13.68 Hz, and with the increase of the peak loading load, the soil-rock field is enhanced by the second-order modal influence. The first-order modal frequency is reduced to 12.05 Hz, and the change of modal distribution tends to the characteristics of the silty clay, which is because the damage characteristics of the limestone are more easily broken under the action of external forces, and the lower surrounding rock enters the damage state to decrease the transmission efficiency of seismic waves.

5.3. Structural Dynamic Response Analysis

5.3.1. Model Structural Strain.
In the shaking-table test, the time history curves of dynamic strains under 0.115 g peak acceleration were extracted from the measurement points on the soil side and the surrounding rock side at the soil-rock interface, as shown in Figure 12. The strains at the lower and upper parts of the interface are 127.8 $\mu\varepsilon$ and 218.6 $\mu\varepsilon$. The stress time history curves on the upper and lower sides of the soil-rock interface of the tunnel structure in the numerical analysis, as shown in Figure 3, are the same as the test strain curves roughly, which intuitively reflect the influence of soil-

(a)

(b)
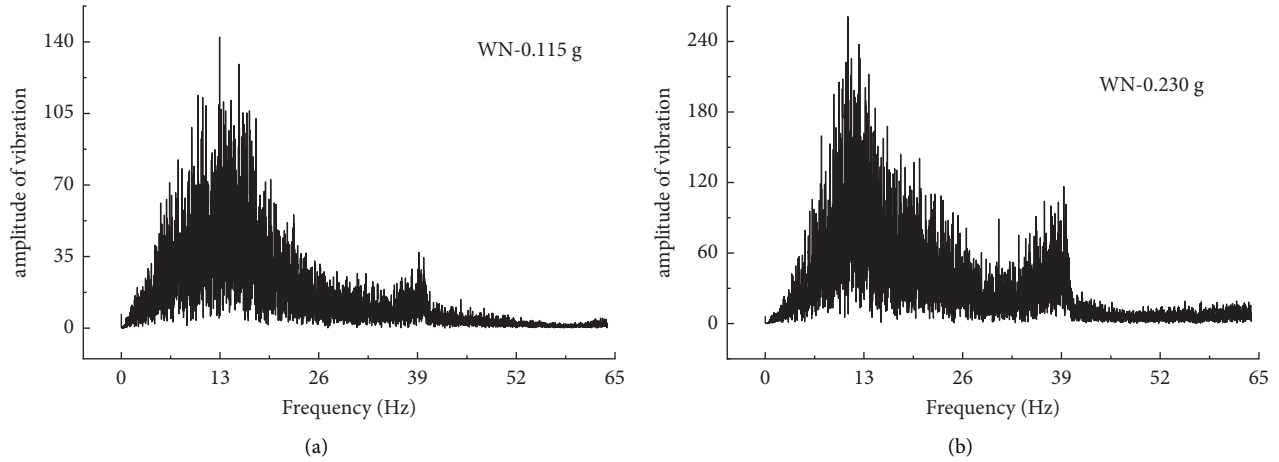
FIGURE 11: White noise spectrum curve of soil-rock combination field. (a) White noise −0.115 g. (b) White noise −0.230 g.
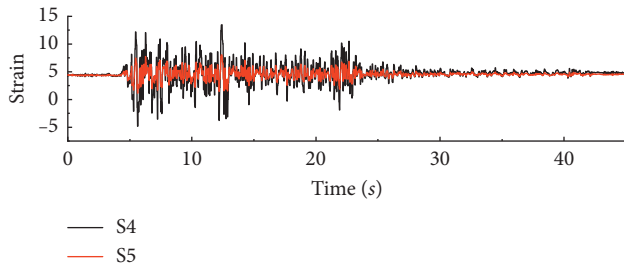
FIGURE 12: Time history of dynamic strain at S4 and S5 measurement points at the soil-rock partition interface.

rock abrupt changes on the internal force of the structure and indicate that the abrupt change in the interface area of the strata is an unfavorable factor for the seismic design of the structure.

5.3.2. Distribution Law of Peak Bending Moment of the Tunnel Structure.

As the tunnel model structure is dominated by bending deformation, structure bending resistance is the dominant factor in the design phase. In this model test, the structure is in an elastic state. The internal force of the structure mainly considers the bending moment of the model section. The internal force is calculated based on tension on the outer surface of the tunnel model structure. The strain value of the structure is obtained through the strain gauges pasted on the inner and outer sides of the same measuring point of the tunnel, and the structural bending moment is calculated through formula (4).

$$
\begin{aligned}
M &= \frac{(\varepsilon_1 - \varepsilon_2)E_c W}{2} \\
&= \frac{(\varepsilon_1 - \varepsilon_2)E_c bh^2}{12},
\end{aligned}
\tag{4}
$$

where ε_1 is the inner edge strain value, ε_2 is the outer edge strain value, EC is the model elastic modulus, W is the model section resistance moment, b is the model width, and h is the model thickness.

The peak bending moment distribution of the structure is calculated from the peak strain at each measurement point of the tunnel structure, as shown in Figure 13. The distribution of peak bending moment under 0.115 g acceleration from the shaking-table test in figure 13(a) is consistent with the distribution of bending moment in figure 4(c), obtained from a numerical analysis under 0.05 g peak acceleration to verify the reliability of the analysis.

The comparison of the bending moment distribution of the model test with the numerical analysis of the structural bending moment distribution (i.e., Figures 13 and 4(c)) shows that the bending moments at the soil-rock partition interface change abruptly, and the second peak phenomenon appears at 45° counterclockwise of the structure, which is symmetrically distributed. As the seismic load level increases, the second peak gradually transitions to the vault. The second peak bending moment occurs between ±45° and 60° of the structure, which is because of the vertical overlying soil self-weight on the tunnel structure and the embedded constraint of the lower surrounding rock on the structure, and the forced displacement imposed by the soil body on the structure under the action of the seismic load is mainly borne by the tunnel structure on the soil side, and the direction of the synthetic force by the action is mainly in ±45° to ±60°, so that the second peak of the strain is generated. Therefore, the overall strength of the shield tunnel on one side of the soil should be strengthened in the seismic design.

5.3.3. Tunnel Structure Acceleration Analysis.

The acceleration time curves of the vault and arch of the tunnel structure are derived and Fourier transformed. The response law of different frequency bands of the tunnel structure under the action of seismic waves are obtained, as shown in Figure 14. The tunnel structure in the rock has an amplification effect on the high-frequency 6–8 Hz band of seismic waves and a low frequency 1.5–2.5 Hz band in the soil layer. At the same time, compared with the amplification effect of the high-frequency band of the tunnel structure in the rock, the percentage of the high-frequency band of seismic waves at the location of the tunnel vault shows a significant

bending moment M, unit (10^{-4} kN · m)
- ■ Tunnel prototype
- ● Structural peak bending moment

(a)

bending moment M, unit (10^{-4} kN · m)
- ■ Tunnel prototype
- ● Structural peak bending moment

(b)
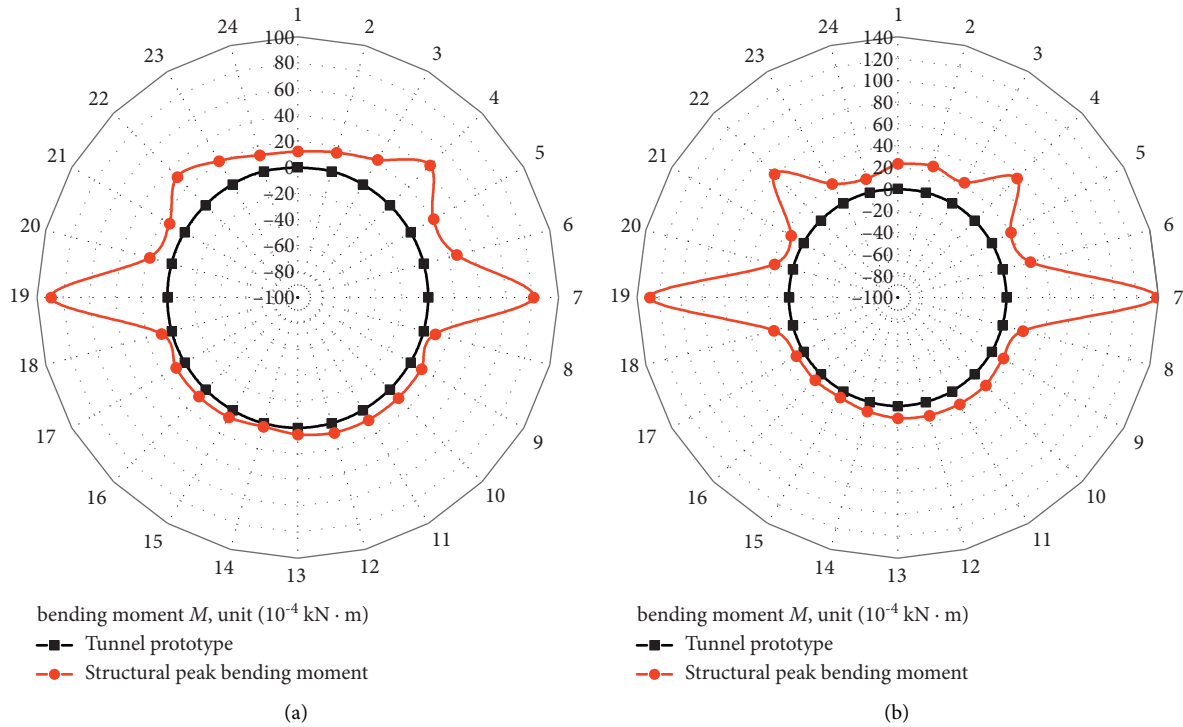
FIGURE 13: Peak bending moment diagram of the model tunnel structure. (a) 0.115 g. (b) 0.230 g.

— Tunnel arch bottom

(a)

— Tunnel arch top

(b)
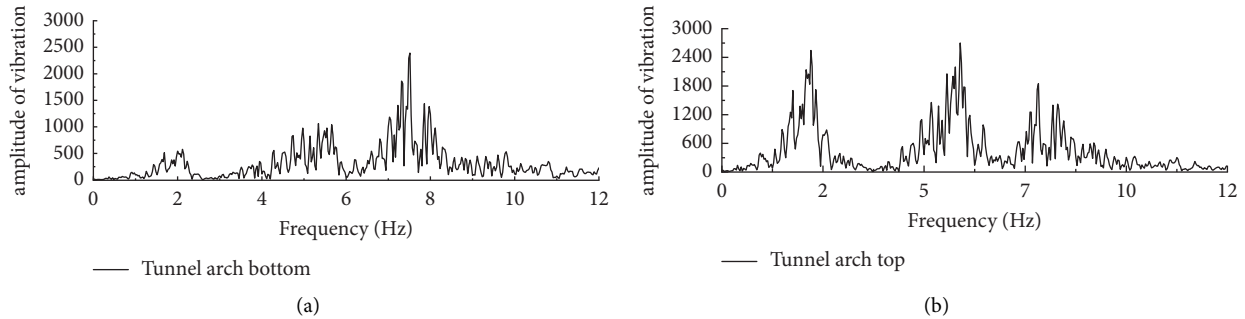
FIGURE 14: Fourier transform curves of the acceleration of the tunnel structure. (a) Bottom of tunnel structure. (b) Top of tunnel structure.

decrease, and the seismic waves in a certain high-frequency band will be filtered by the soil layer during the propagation of seismic waves in the soil layer.

6. Conclusion

The focus was on the Jinan shield tunnel through the soil-rock binary combination stratum. The analysis conditions were designed according to the typical soil-rock combination stratum geological conditions. The seismic response characteristics of the shield tunnel were studied by the finite element simulation and shaking-table test. The conclusions drawn were mainly as follows:

(1) Under the earthquake loading, the internal force values of the shield tunnel structure in the soil-rock combination stratum increased significantly from the lower side rock to the upper side soil, and the tunnel structural stress increased by 65.5%. The excessive stress difference causes secondary stresses inside the structure and changes the damage pattern of the tunnel.

(2) The abrupt increase of the shear force at the soil-rock interface is significantly higher than the increase of axial force. Meanwhile, the shear bearing capacity of the concrete structure is mainly provided by the internal reinforcement. Hence, the tunnel structure at the soil-rock interface is most susceptible to bending-shear damage.

(3) Compared with the amplification effect of the high-frequency band of the tunnel structure in the rock, the percentage of the high-frequency band of seismic waves at the tunnel vault shows a significant decrease, i.e., the high-frequency band of seismic waves will be filtered by the soil layer during earthquake waves propagated from the lower rock to the upper soil layer.

(4) Since the tunnel tube pieces are prefabricated structures, in the process of seismic design of the structure, the local stiffness of the structure should be enhanced in the soil-rock combination stratum, and the bending-shear structural measures of the shield tunnel should be strengthened to improve the seismic performance.

Data Availability

Some or all data, models, or codes that support the findings of this study are available from the corresponding author upon reasonable request.

Conflicts of Interest

The authors declare that there are no conflicts of interest regarding the publication of this paper.

Acknowledgments

References

[1] D.-Y. Wang, "Seismic damage mechanism and treatment technologies of construction landslide section of highway tunnels in highly seismic region," *Chinese Journal of Geotechnical Engineering*, vol. 40, no. 2, pp. 353–359, 2018.

[2] T. An, "Review of seismic damage and anti-seismic analysis method of underground structures," *Value Engineering*, vol. 37, no. 11, pp. 244-245, 2018.

[3] X.-L. Du, G. Wang, and D. C. Lu, "Earthquake damage mechanism analysis of dakai metro station by Kobe earthquake," *Journal of Disaster Prevention and Mitigation Engineering*, vol. 36, no. 2, pp. 165–171, 2016.

[4] B.-C. Zhang, "Key construction techniques for metro lines with shield tunneling method under-crossing existing lines in upper-soft lower-hard stratum," *Urban Mass Transit*, vol. 24, no. 9, pp. 132–136, 2021.

[5] Y. Su and B. M. Zhao, "Analysis of longitudinal seismic of shield tunnelwith longitudinal equivalent continuous model," *Communications Science and Technology Heilongjiang*, vol. 32, no. 4, pp. 80–82, 2009.

[6] B.-H. Wu, *Research on Seismic Safety Evaluation of Subway Shield Tunnel under Construction*, Xi'an Technological University, Xi'an, China, 2020.

[7] Y. S. Yu, *Analysis of Dynamic Response of Shield Tunnel under Strongearthquake*, Dalian University of Technology, Dalian, China, 2020.

[8] X. Cai, J.-W. Liang, and An Xu, *Longitudinal seismic analysis of Mawan sea-crossing large diameter shield tunnels.Journal of Natural Disaeters*, vol. 29, no. 6, pp. 13–20, 2020.

[9] Q. Liu, Y. Liu, and J.-W. Liang, "Seismic transverse analysis of shield tunnels in complex soft soil through response deformation method," *China Earthquake Engineering Journal*, vol. 42, no. 5, pp. 1217–1224, 2020.

[10] L.-Y. Huang, C. H. Wang, and Y. Shuxin, "Seismic design and engineering application of tunnels based on coseismic displacement," *China Earthquake Engineering Journal*, vol. 41, no. 01, pp. 29–35, 2019.

[11] H. Shen, *Seismic Response Analysis of Shield Tunnel*, Dalian University of Technology, Dalian, China, 2006.

[12] J. X. Cheng, "Experimental study and numerical analysis on seismic responses of immersed tunnel," *Recent Developments in World Seismology*, vol. 10, pp. 65-66, 2019.

[13] W. Wang, "The study of seismic response of shield tunnel crossing interface of soft and hard strata," Southwest Jiaotong University, Sichuan, China, 2015.

[14] J. Han, D. Liu, Y. Guan et al., "Study on shear behavior and damage constitutive model of tendon-grout interface," *Construction and Building Materials*, vol. 320, Article ID 126223, 2022.

[15] W. Zhao, P.-J. Jia, L. Zhu et al., "Analysis of the additional stress and ground settlement induced by the construction of double-O-tube shield tunnels in sandy soils," *Applied Sciences*, vol. 9, no. 7, Article ID 1399, 2019.

[16] Y.-L. Jiao, *Study on Longitudinal Seismic Response of Large Diameter Shield Tunnel with Hardand Soft Abrupt Formation*, Tianjin University, Tianjin, China, 2018.

[17] J. Y. Han, W. Zhao, P. J. Jia, Y. P. Guan, Y. Chen, and B. F. Jiang, "Risk analysis of the opening of shield-tunnel circumferential joints induced by adjacent deep excavation," *Journal of Performance of Constructed Facilities*, vol. 32, no. 1, 2018.

[18] C. He and P. Geng, "Research on practical seismic analysis methods of shield tunnel," *China Journal of Highway and Transport*, vol. 33, no. 12, pp. 15–25, 2020.

[19] G.-X. Chen, X. Zuo, and H.-Y. Zhuang, "A comparison between large-size shaking-table test results and numerical simulation of a subway station structure," *Journal of Earthquake Engineering and Engineering Vibration*, vol. 28, no. 1, pp. 157–164, 2008.

[20] F. Gao, "Experimental study of seismic response shaking-table for tunnels with different burial depths," *Rock and Soil Mechanics*, vol. 36, no. 9, pp. 2617–2522, 2015.

[21] D.-W. Huang, "Design method for longitudinal segment joints of shield tunnel model," *Chinese Journal of Geotechnical Engineering*, vol. 37, no. 6, pp. 1068–1076, 2015.

[22] Q.-R. Chen, "Research of shaking-table test for large-scale shield tunnel under non-uniform ground motion excitation," Guangzhou University, Guangzhou, China, 2020.

[23] G.-D. Gong, "Seismic transverse time-history analysis of shield tunneling complex soft soil," *Journal of Tianjin University*, vol. 52, no. S1, pp. 106–111, 2019.

Research Article

Optimal Selection of Earthquake Resisting Schemes for Jakarta-Bandung High-Speed Railway

Wei Quan [ID],[1,2] **Lin Deng** [ID],[1,2] **Xuzheng Liu** [ID],[3] and **Bibo Gao** [ID][4]

[1]*School of Civil Engineering and Architecture, Huangshan University, Huangshan 245041, China*
[2]*Prefabricated Building Technology Innovation Center of Huangshan City, Huangshan 245041, China*
[3]*School of Civil Engineering and Architecture, East China Jiaotong University, Nanchang 330013, China*
[4]*China Railway Design Corporation, Tianjin 300308, China*

Correspondence should be addressed to Lin Deng; 95635486@qq.com

The Jakarta-Bandung high-speed railway is the first overseas project involving China's high-speed railway. Owing to the high seismic intensity in this area, the optimal selection of earthquake resisting schemes is critical for short-span bridges, and such schemes are related to the safety and cost-effectiveness of the entire line. This study compares the safety and cost-effectiveness of four earthquake resisting schemes: (i) prestressed concrete (PC) simply-supported box beams using common spherical steel bearings; (ii) PC simply-supported box beams using seismic isolation bearings; (iii) steel-concrete (SC) composite simply-supported beams using seismic isolation bearings; (iv) reinforced concrete (RC) rigid frames. The results indicate that PC beams using more expensive seismic isolation bearings reduce the cost of the substructure, making it more cost-effective. In contrast, the scheme of SC composite beams is the most expensive one, and the associated maintenance costs are also the highest. Although the scheme of RC rigid frames is the cheapest among the evaluated schemes, it is only suitable for relatively stiff sites with low pier heights. Overall, PC beams with isolation bearings exhibit good seismic performance and are suitable for prefabricated construction; therefore, this scheme can be applied in various soil conditions with relatively low costs, and it is recommended for use throughout the entire Jakarta-Bandung high-speed railway.

1. Introduction

High-speed railway construction has entered a rapid development period all over the world. To reduce land coverage, the rule of "substituting a bridge for subgrade" is often adopted in the design and construction of high-speed railways. Bridges account for up to 70%–80% of the entire rail line in terms of length, and most are short-span bridges [1–6]. Therefore, selecting the optimal earthquake resisting scheme for short-span bridges is crucial to maximizing the safety, serviceability, and economy of high-speed railways in high seismic intensity regions. Such schemes are influenced by various factors, including the natural climatic conditions, the traffic requirements, and the local site-specific conditions. The beam must be sufficiently stiff to allow the trains to run smoothly enough to meet the high standards required

for a high-speed railway. Meanwhile, the weight of the superstructure should be reduced to minimize the seismic response. Prestressed concrete (PC) simply-supported box beams are generally implemented for short-span bridges in China's high-speed railways [1–6], whereas reinforced concrete (RC) rigid frame bridges are adopted for Japanese Shinkansen railways on a large scale [7, 8], and steel-concrete composite (SC) beams are often used in France [1].

For high-speed railway bridges in strong earthquake conditions, both ductility seismic and isolation seismic systems have been introduced by designers [9–25]. Kang et al.[9] evaluated the seismic damage to high-speed railway bridge components under various earthquake excitation intensities. Chen et al. [10] studied the seismic response of a high-speed railway simply-supported girder bridge. Wei et al. [11] investigated the seismic vulnerabilities of a high-

speed railway bridge by considering track-bridge interactions. Li et al. [12, 13] studied the effects of seismic isolation on the seismic response of a high-speed rail prototype bridge in California. Xia et al. [14] investigated the seismic damage and seismic performance of various bridge types. Bai [15] compared structural form selections for small and medium-sized bridges along the Beijing-Shanghai high-speed railway in China. Xie et al. [16] systematically identify and quantify the damage states, repair actions, repair costs, and travel delay losses for China's high-speed railway multi-span simply-supported bridge system. Cui et al. [17] conducted the seismic fragility and risk assessment of a typical high-speed continuous girder bridge. Guo et al. [18] investigated the seismic damage features of high-speed railway simply-supported bridges under near-fault earthquakes. Shan et al. [19] proposed a novel fragility analysis method for irregular bridges in high-speed railways. Meng et al. [20] assessed the design and seismic mitigation performance of shock absorbers for a railway bridge with a simply-supported beam. Zheng et al. [21, 22] studied the application of seismic devices, including friction pendulum bearings and E-shaped metallic dampers. Xia et al. [23] evaluated the seismic performance of friction pendulum bearings. Jiang et al.[24] studied the effects of friction-based fixed bearings on seismic performance of high-speed railway simply-supported bridge. Guo et al. [25] proposed an improved equivalent energy-based design procedure for seismic isolation system of simply-supported bridges in China's high-speed railways. Other related research works include train-track-bridge interaction of high-speed railway bridges, seismic design method research of bridge bents, and so on. Guo et al. [26] studied the train-track-bridge interaction in high-speed railways and proposed a real-time hybrid simulation method using the moving load convolution integral method. Shi et al. [27] proposed a toggle BRB system for the seismic retrofit of bridge bents and the corresponding design method. Mitoulis et al. [28] conducted a cost-effective analysis related to the earthquake-resisting system of multispan motorway bridges. However, limited studies are comparing the economy and safety of common earthquake resisting schemes applied to bridges on high-speed railways.

Indonesia's Jakarta-Bandung high-speed railway represents a successful application and major breakthrough concerning the "going out" policy of China's high-speed railway. It provides an important demonstration that supports the brand of "China's high-speed railway" throughout the world. This study takes the short-span bridge of the Jakarta-Bandung high-speed railway as an example and compares the following bridge earthquake resisting schemes: (i) PC simply-supported box beams using common spherical steel bearings, (ii) PC simply-supported box beams using seismic isolation bearings, (iii) SC composite simply-supported beams using seismic isolation bearings, and (iv) RC rigid frames. The safety and cost-effectiveness of these four schemes are evaluated and compared in detail. The results provide a useful basis for the selection of the earthquake resisting systems throughout the entire line and offer a reference for similar high-speed railway projects in high seismic intensity regions.

2. Description of the Project and Earthquake Input

The total length of Indonesia's Jakarta-Bandung high-speed railway is 142.3 km. The project is part of the high-speed railway line that connects Jakarta to Surabaya, which has a total length of approximately 800 km. The designed running speed is 350 km/h. After completing the railway, the traveling time from Jakarta to Bandung will be reduced from the current 3 hours to only 40 minutes. The high-speed railway will adopt a cooperation mode involving joint venture construction and management by China and Indonesia enterprises.

As the first "going out" project of China's high-speed railway, the Jakarta-Bandung high-speed railway will apply the technical standards, surveys, designs, facilities, engineering construction, management, and operation of China's high-speed railways, and it will promote China's "one belt and one road" policy.

According to the seismic ground motion parameters zoning map developed based on the Indonesian code for seismic design of bridges [29], the peak acceleration along the Jakarta-Bandung high-speed railway line is equal to that of a site with a seismic intensity of 8 or 9 in China [30]. Therefore, the seismic response of bridges is a decisive parameter for selecting the resisting scheme. Moreover, comparative results depend on the geological conditions and seismic parameters of the site. The standard technical parameters are as follows: design speed = 350 km/h; track type = ballastless track; mainline design = double track; design load = Chinese ZK live load. The design parameters influencing the ground motion are as follows: site soil type = Type II (moderately firm soil where the interval range of the shear wave velocity is between 250 and 500 m/s). The peak acceleration and characteristic period are 0.14 g and 0.5 s, respectively, for low-level earthquakes (i.e., earthquake recurrence interval ≈50 years); the peak acceleration and characteristic period are 0.34 g and 0.74 s, respectively, for design earthquakes (i.e., earthquake recurrence interval ≈ 475 years); peak acceleration and characteristic period are 0.57 g and 0.89 s for high-level earthquakes (i.e., earthquake recurrence interval ≈ 2475 years). Figure 1 presents the design response spectra for these three earthquake levels. Time history analyses have been conducted by matching the seismic time curves against the spectra given in the code governing the seismic design of railway engineering in China (China Railway Code, an abbreviation for the code) [30].

3. Seismic Calculation Principles

The Eurocode for the earthquake resistance of bridge structures [31] dictates that in regions of moderate to high seismicity, it is generally preferable (for economic and safety reasons) to design a bridge with ductile behavior, i.e., to provide reliable means to dissipate a significant amount of the input energy under severe earthquake conditions. This is accomplished via an intended configuration of flexural plastic hinges or by using isolating devices.
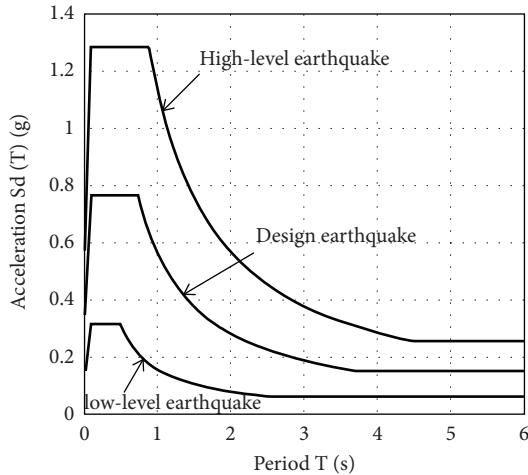
Figure 1: Design response spectra.

induce significant damage to the bridges, but they would not collapse.

For the seismic design of the ductility system, pier reinforcement should be monitored under low-level earthquake conditions. The strength of the connection between the superstructure and substructure should be checked under design earthquake conditions, and the ductility calculation should be conducted to prevent collapse following high-level earthquakes. Nonlinear time historical analysis should be implemented to assess the elastic-plastic deformation under rare earthquake conditions according to equation (1) [30]:

$$\mu_u = \frac{\Delta_{\max}}{\Delta_y} < [\mu_u], \tag{1}$$

where μ_u is the nonlinear displacement ductility ratio; $[\mu_u]$ is the allowable displacement ductility ratio (herein defined as 4.8 in provision 7.3.3 of China Railway Code [30]. The value has considered safety assurances rate, thus can guarantee the safety of bridges.);$\Delta_{\max}$ is the largest nonlinear displacement of piers;Δ_y is the yielding displacement of piers.

For the seismic design of the isolation system, pier reinforcement should be monitored under low-level earthquake conditions in the same way. In a rare earthquake scenario, piers should remain elastic and may sustain slight damage owing to the protection of isolation devices. Moreover, the working conditions of the isolation devices should be checked regularly to ensure proper functioning under rare earthquake conditions.

In seismic bridge design specifications for the United States [32], for Seismic Design Category (SDC) C or D, all bridges and their foundations must have a clearly identifiable earthquake resisting system that satisfies the life safety criteria. Moreover, the design should be based on one of three earthquake resisting systems: (1) a ductile substructure with an essentially elastic superstructure (e.g., for conventional concrete bridges), where seismic energy can be dissipated through the plastic hinges in piers and bents; (2) an essentially elastic substructure with a ductile superstructure (e.g., only for steel superstructures), where ductility is derived from ductile elements in the pier cross-frames; (3) an elastic superstructure and a substructure with a fusion mechanism between the two (e.g., for seismically isolated structures and structures with supplemental energy dissipation devices, such as dampers, to control inertial forces transferred between the superstructure and substructure).

In China Railway Code [30], bridges in regions with seismic intensities >7 should undergo ductile checks of the RC piers under rare earthquake conditions. Additional mitigation and isolation design strategies can be applied for bridges in areas with higher seismic intensities.

Considering the codes or specifications of various countries, the two most applicable earthquake resisting systems are ductility seismic and isolation seismic systems. In this study, the first and fourth schemes involve ductility seismic systems, whereas the second and third schemes use isolation seismic systems.

The Jakarta-Bandung high-speed railway is the first overseas project of China's high-speed railway, and therefore, the seismic design of bridges should be completed according to China Railway Code [30]. The three levels of seismic fortification goals are as follows: (1) low-level earthquakes (63% probability exceedance in 50 years) cause the bridges to sustain negligible or slight damage, and they can still work elastically; (2) design earthquakes (10% probability exceedance in 50 years) cause damage, but bridges can be readily inspected and repaired; (3) high-level earthquakes (2% probability exceedance in 50 years) may

4. Prestressed Concrete Simply-Supported Box Beams with Common Bearings

PC simply-supported box beams are generally implemented for short-span bridges along China's high-speed railway. This structure has various advantages, including high stiffness, simple working mechanism, and beautiful appearance. Moreover, PC beams can be constructed quickly using a prefabricated construction method. The most extensively used beams have a span of 32 m. The calculated length of the beam is 31.5 m, and the total length is 32.6 m. Since the gap between the adjacent beams is 0.1 m, the standard span of the beam is 32.7 m as shown in Figure 2.

Therefore, PC simply-supported box beams with a span of 32 m were used in this study. According to the Jakarta-Bandung high-speed railway statistics, the average height of the piers is approximately 15 m. A multi-span simply-supported beam with a height of 15 m is depicted in Figure 2.

In order to eliminate the boundary effect, the four-span 32-m beam was taken as an example. Common spherical steel bearings were used on the pier top. There were two fixed bearings and two longitudinal sliding bearings. Soil springs under the bottom of the piers were modeled to simulate the interactions between the foundation and the structures. The overall computed seismic beam model is shown in Figure 3x, y and z axes represent the longitudinal, transverse, and vertical axis of the bridge, respectively.
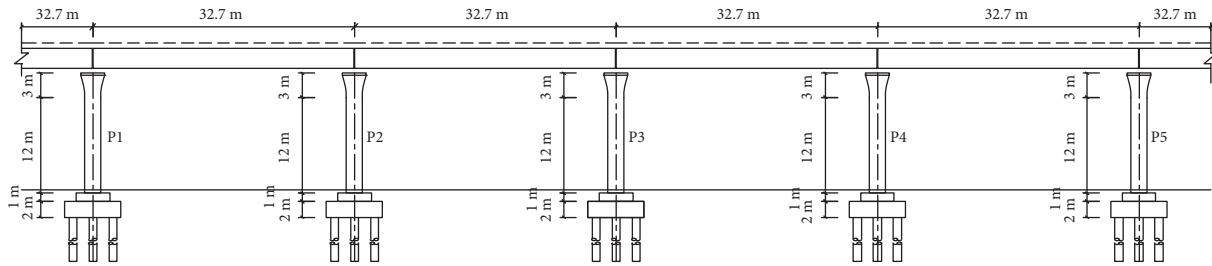
FIGURE 2: Longitudinal section of a multi-span simply-supported beam.
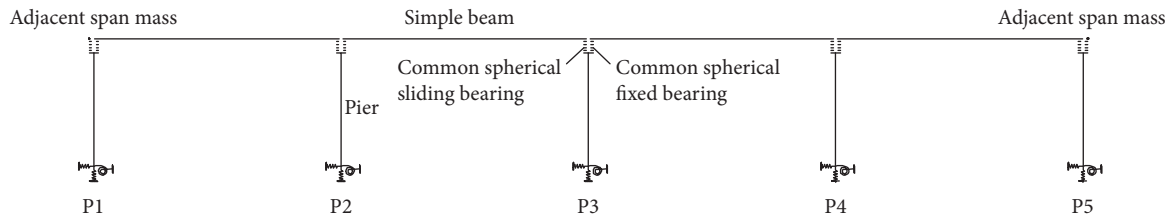
FIGURE 3: Stick model of the multi-span simply-supported beam.

The cross-section of the deck is a box-girder with a total width of 12.4 m (Figure 4). The bridge deck arrangement for a double ballastless track is also shown in Figure 4. The piers are wall-like columns (Figure 5), and their cross-sections are rounded. The bridge piers are founded on Type II ground, as defined by China Railway Code [30], via 11 pile groups, each with a diameter of 1.0 m. Concrete C50 and C40 and steel rebar HRB400 (Hot-rolled Ribbed Bar) as defined in Chinese code for the design of concrete structures of the railway bridge and culvert [33] were used in the scheme. The mechanical properties of concrete and steel rebar are shown in Tables 1 and 2, respectively. The concrete of the beam is C50, and the concrete of the piers, pile caps and piles is all C40. The primary load-bearing steel rebar used in the piers is HRB400. The longitudinal cross-section of the common steel fixed bearings is shown in Figure 6.

The total flexibility of the foundations was taken into account by implementing linear soil spring elements. The translational and rotational stiffness values of the springs are given in Table 3. These values adopted were determined by the geotechnical in situ tests conducted for the bridge.

The seismic design was prepared in accordance with China Railway Code [30]. Pier reinforcement should be checked under low-level earthquake conditions. The strength of the connection between the superstructure and substructure should be monitored under the design earthquake scenario, and ductility calculations should be performed to prevent collapse under high-level earthquake conditions.

4.1. Low-Level Earthquake. A low-level earthquake controls the reinforcement ratio of the piers. The peak ground acceleration of the low-level earthquake is 0.14 g, which is equal to a seismic intensity of 9 in the China Railway Code [30]. Table 4 gives the pier bottom internal forces of the P3 pier following longitudinal and transverse earthquakes. The

HRB400 reinforcement bar with a diameter of 32 m was used, and the reinforcement ratio was 1.63%, as shown in Figure 7. For the longitudinal earthquake, the largest stress of the concrete and steel rebar is 13.5 MPa and 300.0 MPa, respectively. For the transverse earthquake, the largest stress of the concrete and steel rebar is 15.9 MPa and 308.9 MPa, respectively.

4.2. Design Earthquake. The longitudinal force of the bearing should be checked under the design earthquake scenario. The ratio between the longitudinal force and the vertical capacity can then be calculated. The longitudinal force of the bearing is approximately 5605 kN, which is 1.25 times the vertical bearing capacity of 4500 kN. Generally, along with the increasing of the horizontal force of the bearing, the difficulty of manufacturing is also increasing. Thus, the cost of the bearing would increase significantly.

4.3. High-Level Earthquake. Under high-level earthquake conditions, ductility analysis of the pier bottom must be conducted to determine whether the bridge pier is damaged. If ductile damage has occurred, the nonlinear displacement ductility ratio is calculated. According to provision 7.3.3 of the China Railway Code [30], the allowable displacement ratio is 4.8. For the studied bridge, the displacement at the yielding moment is 9.5 cm, and the ultimate displacement is 22.59 cm. Thus, the calculated ductility ratio is 2.38, which is smaller than the allowable ratio of 4.8, and the performance level required for "no-collapse" under rare earthquake conditions is satisfied.

According to capacity protection theory, the piles should work elastically before the piers suffer from plastic damage. Therefore, the pile length and reinforcement area should be increased. Table 5 presents the corresponding pile length and reinforcement area under low-level and high-level earthquake conditions.

WITH ELECTRIFICATION SYSTEM

WITHOUT ELECTRIFICATION SYSTEM
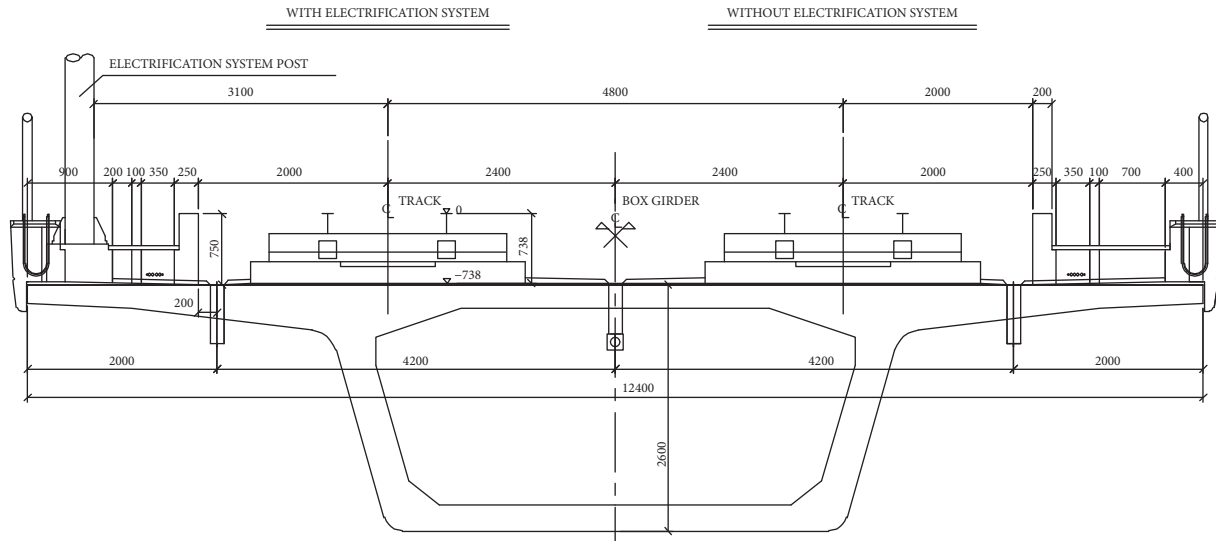
Figure 4: Cross-section of the box beam at the middle span (unit: mm).

Figure 5: Pier and foundation: (a) cross-section of a pier; (b) longitudinal section; (c) overall plan.

Table 1: Mechanical properties of concrete.

Concrete grade	C50	C40
Elastic modulus E(MPa)	35500	34000
Shear modulus G(MPa)	15265	14620
Poisson's ratio μ	0.2	0.2
Axial compression strength of concrete f_c(MPa)	33.5	27
Axial tensile strength of concrete f_{ct}(MPa)	3.1	2.7
Coefficient of linear expansion	0.00001	0.00001

Table 2: Mechanical properties of steel rebar.

Steel rebar Grade	HRB400
Standard tensile strength f_{sk}(MPa)	400
Elastic modulus E_s(MPa)	2.0×10^5

According to Table 5, following a low-level earthquake, the calculated pile length is 48 m, and the reinforcement area is 102.1 cm². Following a high-level earthquake, capacity protection theory indicates that the pile length should increase to 56 m, while the reinforcement area should increase

to 204.0 cm². The concrete volume increases to 483.8 m³, and the rebar weight increases to 98.7 t. The integrated unit price of rebar is RMB 4342.9, and the integrated unit price of concrete is RMB 1368.7. Thus, the total cost increases by approximately 339k RMB.

5. Prestressed Concrete Simply-Supported Box Beams with Isolation Bearings

The piers of bridges with common spherical steel bearings in high-intensity seismic regions may suffer significant damage, which is difficult and costly to repair. Moreover, the bearings themselves may also be damaged, and the longitudinal and transverse restrainers would likely be broken. The fixed bearings would become movable bearings and, in consequence, the entire structural system would be a pure sliding friction system. Although such a system (with no restoring ability) is beneficial for the substructures, the superstructures cannot be restored to their original state.

Bridges with isolation bearings exhibit better seismic performance. Under rare earthquake conditions, the shear
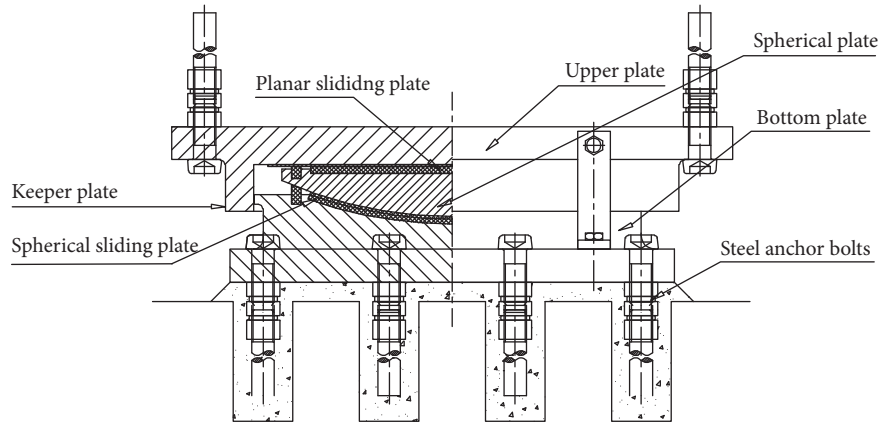
FIGURE 6: Longitudinal cross-section of the common steel bearings.

TABLE 3: Stiffness values of the soil springs.

K_x	(kN/m)	$5.53 \cdot 10^6$
K_y	(kN/m)	$6.09 \cdot 10^6$
K_z	(kN/m)	$6.07 \cdot 10^7$
K_{rx}	(kN m/rad)	$7.84 \cdot 10^8$
K_{ry}	(kN m/rad)	$5.29 \cdot 10^8$
K_{rz}	(kN m/rad)	$1.00 \cdot 10^{12}$

TABLE 4: Pier bottom internal forces under low-level earthquake.

Pier bottom internal force	Longitudinal earthquake	Transverse earthquake
Axial force, F_x(kN)	16270	16270
Longitudinal shear force, F_y(kN)	4476	0
Transverse shear force, F_z(kN)	0	5551
Longitudinal moment, M_y(kN·m)	64709	0
Transverse moment, M_z(kN·m)	0	94126

key of the bearings would be broken (as designed), and the upper and bottom bearing plates would slide. This mitigation effect sufficiently protects the substructure, including the piers and piles. Moreover, this structural system has self-restoring abilities. After a rare earthquake, the bearings can readily be repaired. Therefore, a PC simple beam with isolation devices is included in the comparison.

The most common isolation devices include lead rubber bearings, high damping laminated rubber bearings, elastoplastic steel damping bearings, and double-curved spherical seismic isolation bearings, among others. The vertical loading capacity and durability are limited for the lead rubber bearings and high damping laminated rubber bearings. The design life of a rubber bearing is approximately 30 years. Therefore, during the 100-year design life of the bridge, several bearing replacements are required. It is very costly and difficult to replace the numerous bridge bearings along the entire high-speed railway line, which is fully closed. However, the design life of a steel bearing can reach 100 years with normal maintenance and rehabilitation procedures. In the case of elastoplastic steel damping bearings, the affordable bending times of the damping components are limited, and permanent yielding

deformation would occur after a rare earthquake. It is costly to replace the elastoplastic components, and therefore, they are not recommended. Double-curved spherical isolation bearings, which have a large loading capacity, good durability, and self-restoring capacity, are suitable for the seismic design of high-speed and general-speed railway bridges.

When using common double-curved spherical isolation bearings, the beam will rise slightly when moving because of the influence of the double sphere. This slight rise is tolerable for common highway bridges, while it is intolerable for high-speed railway bridges. Therefore, specific double-curved spherical seismic isolation bearings were designed and developed for railway bridges. Considering the features of common double-curved spherical isolation bearings, a planar sliding plate was added to the bearings to prevent the rise during operation. The railway double-curved spherical seismic isolation bearings have been applied in several national projects in China, including the Sutong Yangtze River Bridge, Hongkong-Zhuhai-Macao Major Bridge, and bridges along the Fuzhou-Xiamen Railway.

Thus, the railway double-curved spherical seismic isolation bearings were adopted in this study, and the corresponding overall seismic computational model is shown in

TABLE 5: Parameters for low-level and high-level earthquakes.

Item	Low-level earthquake	High-level earthquake	Difference
Reinforcement area(cm^2)	102.1	204.0	101.9
Pile length(m)	48	56	8
Number of piles	11	11	0
Rebar(t)	42.3	98.7	56.4
Concrete(m^3)	414.7	483.8	69.1
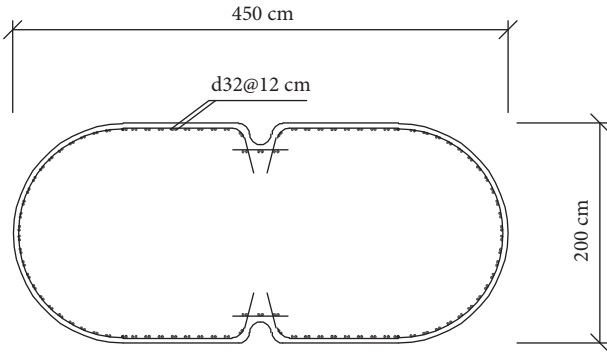
FIGURE 7: Pier reinforcement detail (cross-section).

Figure 8. The beam and pier sizes and the materials adopted are as same as the scheme (i).

The curved surface radius of the double-curved spherical seismic bearings is 2.3 m, and the friction coefficient under earthquake is 0.06. The vertical loading capacity of the bearings is 4500 kN. The longitudinal cross-section of railway double-curved spherical seismic isolation bearings is shown in Figure 9. The hysteresis curve of bearings is given in Figure 10:

The post-yielding stiffness of the bearing can be obtained:

$$K_d = \frac{W}{R}. \tag{2}$$

The equivalent stiffness can be expressed as follows:

$$K_{eff} = \frac{W}{R} + \mu_d \frac{W}{D_d}. \tag{3}$$

The equivalent damping can be expressed as follows:

$$\xi_{eff} = \frac{2\mu_d}{\pi(D_d/R + \mu_d)}. \tag{4}$$

Where W is the vertical force of the bearings under dead load; R is the curved surface radius of the bearing; D_d is the design horizontal displacement of the bearings; μ_d is the sliding frictional coefficient of the bearings.

The two-stage seismic design was carried out using the railway's double-curved spherical seismic bearings according to China Railway Code [30].

5.1. Low-Level Earthquake. Under low-level earthquake conditions, the isolation devices of the simple beam would not function. Therefore, the mechanical performance of the bridges is the same with the simple beam as it was with

common spherical bearings. The reinforcement ratio is also the same. The HRB400 reinforcement bar with a diameter of 32 m was used, and the reinforcement ratio was 1.63%.

5.2. High-Level Earthquake. With the isolation devices, the performance level of the bridges can be enhanced. In general, after a rare earthquake, the bridges work elastically or sustain little damage. Table 6 presents the pier bottom internal forces of the middle pier (P3) after a rare earthquake.

According to Table 6, the mitigation rates for longitudinal and transverse earthquakes reach 78.9% and 83.8%, respectively. The pier bottom internal forces following the high-level earthquake are lower than the corresponding forces of the low-level earthquake when the isolation devices are operating. The reinforcement can be calculated based on the internal forces of the low-level earthquake, and therefore, the piers remain elastic after a rare earthquake.

Owing to the favorable seismic effect, the seismic response to the rare earthquake does not dictate the design, and capacity protection design is not needed. With the isolation devices, the pile length and reinforcement under low-level earthquake conditions are adopted directly. Table 7 provides the mechanical status of various components under different loading cases.

It is clear that the piers and piles of the bridges with the isolation bearings all remain elastic. Only the shear keys of the bearings are broken, and these are easily repaired. Thus, the bridges have a higher seismic performance.

6. Steel-Concrete Composite Beams with Isolation Bearings

The SC composite beams are lighter than concrete beams, and therefore, they exhibit smaller seismic responses. Compared with pure steel beams, SC beams save steel materials, emit less noise, and exhibit better fatigue performance. SC beams are effective for the construction of high-speed railway bridges, especially in conditions involving limited clearance or where they are used as adjustable span beams.

The potential applicability of this type of beam in the high-intensity seismic region of the Jakarta-Bandung high-speed railway was studied. The weight of the superstructures can be reduced to a certain degree, and therefore, the seismic forces of the substructures can also be decreased.

The calculated span of the SC composite bridge is 31.5 m, and the total length of the beam is 32.6 m. According to the train-bridge coupling vibration results, the height of the steel beam is 2.7 m, and the steel parts adopt a double-I-shaped
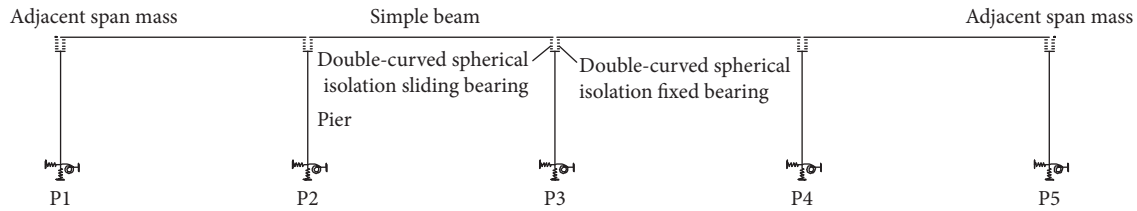
FIGURE 8: Stick model of the multi-span simply-supported beam.
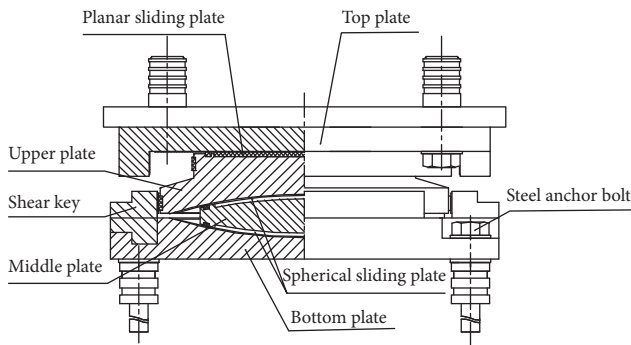
FIGURE 9: Longitudinal cross-section of railway double-curved spherical seismic isolation bearings.
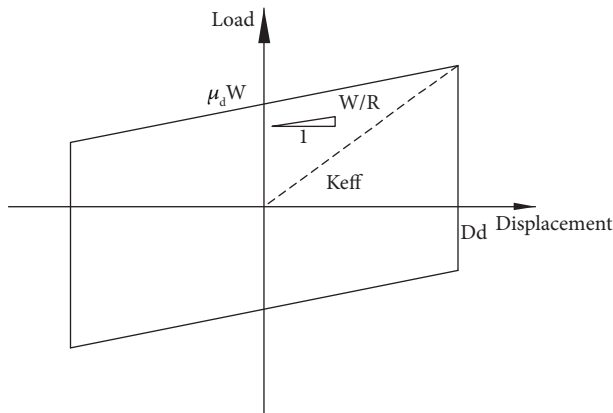
FIGURE 10: Hysteresis curve of bearings.

section. The thicknesses of the top and bottom steel plates are each 50 mm, and the thickness of the web plate is 24 mm, with a stiffening rib thickness of 20 mm. The concrete bridge deck is cast-in-situ. The overall seismic computational model is the same as scheme (ii) (PC simply-supported box beams using seismic isolation bearings), as shown in Figure 8.

Q370qE steel as defined in Chinese code for the design on steel structure of railway bridge [34] was used in the scheme. The mechanical properties of steel plates are shown in Table 8. The SC beam comprises a Q370qE steel beam and C50 concrete deck. The concrete of the piers, pile caps, and piles is all C40. The primary load-bearing steel rebar used in the piers is also HRB400.

The cross-section of the SC composite beam is shown in Figure 11.

The piers are double-column piers (height = 15 m), and the cross-section of the piers and foundation pile plan are shown in Figure 12.

Considering the inherent defects of common spherical steel bearings, the double curved spherical seismic isolation bearings were used in this scheme. Although the no-collapse performance after a rare earthquake can be reached through rational reinforcement, significant damage cannot be avoided for SC composite beams with common spherical steel bearings. According to the calculated results of scheme (ii) (P.C. simply-supported box beams using seismic isolation bearings), although the isolation devices are more expensive than common bearings, the total cost is lower because of the action of isolation devices. Two-stage seismic design can therefore be conducted according to China Railway Code [30].

6.1. Low-Level Earthquake. Low-level earthquakes control the reinforcement ratio of the piers. The peak ground acceleration of a low-level earthquake is 0.14 g. Table 9 shows the pier bottom internal forces of the P3 pier under longitudinal and transverse earthquake conditions. The HRB 400 reinforcement bar with a diameter of 28 mm was used, and the reinforcement ratio was 0.98%, as shown in Figure 13. For the longitudinal earthquake, the largest stress of the concrete and steel rebar is 13.3 MPa and 297.8 MPa, respectively. For the transverse earthquake, the largest stress of the concrete and steel rebar is 9.0 MPa and 163.4 MPa, respectively.

6.2. High-Level Earthquake. With the isolation devices, the seismic performance of the bridges increases. In general, after a rare earthquake, the bridges work elastically or sustain little damage. Table 10 presents the pier bottom internal forces of the middle pier (P3) after a rare earthquake. The mitigation rates for longitudinal and transverse earthquakes reach 88% and 87%, respectively. The pier bottom internal forces of the high-level earthquake are less than those of low-level earthquakes when the isolation devices are operating. The reinforcements are monitored according to the internal forces of a low-level earthquake, and therefore, the piers remain elastic after a rare earthquake.

7. Reinforced Concrete Rigid Frames

The RC rigid frame scheme is economical and has a simple structure, good mechanical performance, good integrity, and facile construction. As a result, this structural system is

TABLE 6: Pier bottom internal forces with isolation devices under high-level earthquake.

Pier bottom internal force	Longitudinal earthquake	Transverse earthquake
Axial force, F_x(kN)	16002	16002
Longitudinal shear force, F_y(kN)	4012	0
Transverse shear force, F_z(kN)	0	3970
Longitudinal moment, M_y(kN·m)	55921	0
Transverse moment, M_z(kN·m)	0	62175
Mitigation rates	78.9%	83.8%

TABLE 7: Mechanical status of different components with isolation devices.

Load case	Piers	Piles	Bearings
Normal operating condition	Elastic	Elastic	Normal
Low-level earthquake	Elastic	Elastic	Normal
1.1 times low-level earthquake	Elastic	Elastic	Broken
Design earthquake	Elastic	Elastic	Broken
High-level earthquake	Elastic	Elastic	Broken

TABLE 8: Mechanical properties of steel plate.

Steel plate grade	Q370qE
Elastic modulus Es(MPa)	2.1×10^5
Shear modulus G(MPa)	8.1×10^4
Poisson's ratio μ	0.3
Coefficient of linear expansion	0.000012
Axial allowable strength $[\sigma]$(MPa)	210
Bending allowable strength$[\sigma]$(MPa)	220
Allowable shear strength $[\tau]$(MPa)	120
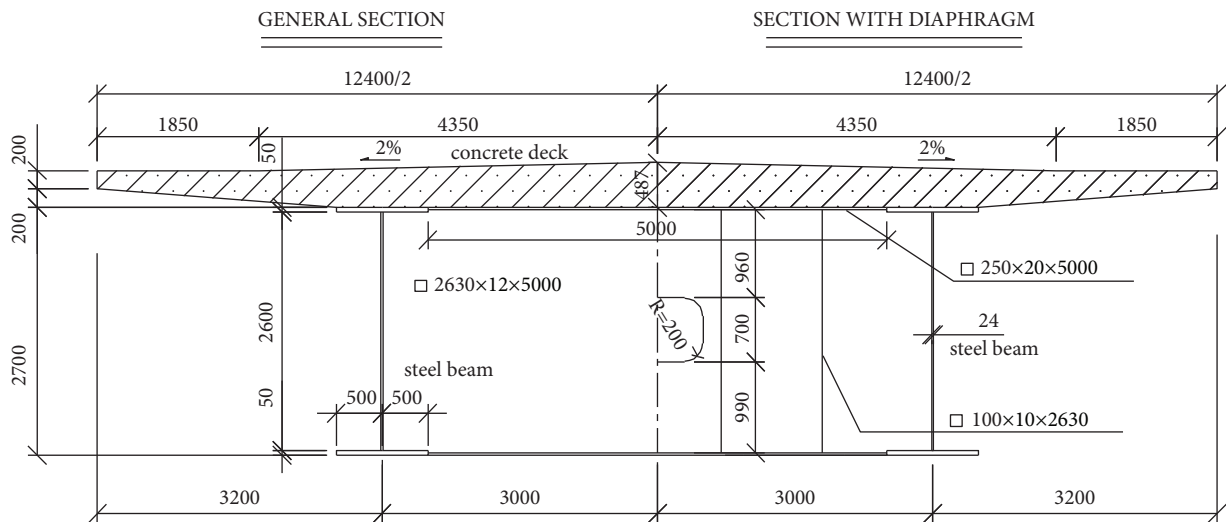
FIGURE 11: Cross-section of the SC composite beam (unit: mm).

widely used in various countries, especially in Japan's Shinkansen. In China, many RC rigid frame bridges have been used, e.g., in the Beijing-Shanghai high-speed railway and Datong-Xi'an passenger dedicated line.

The RC rigid frame scheme was evaluated in the context of the Jakarta-Bandung high-speed railway. One unit of RC rigid frame bridge comprises a 3 × 12 m rigid frame and an 8-m simple plate. The total length of the structure is 46.4 m, and the double-column piers have a transverse distance of 6 m between columns. The width of the deck is 12.4 m, and the height of the rigid frame is 15 m. The heights of the cross beams at the two ends and in the middle are 1.48 m and 1.1 m, respectively. The elevation and cross-section of the RC rigid frame are depicted in Figure 14.
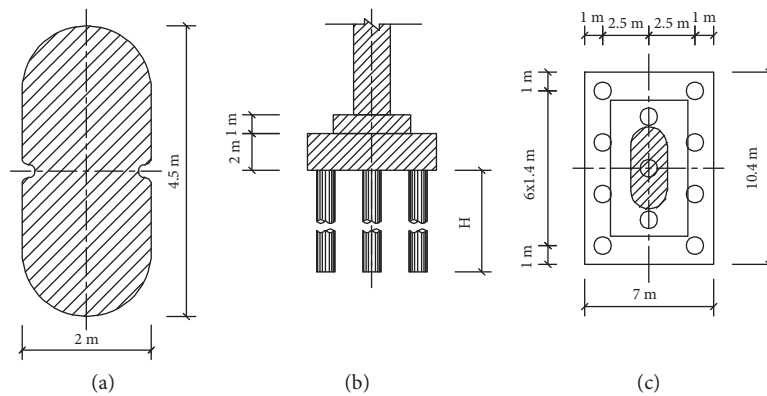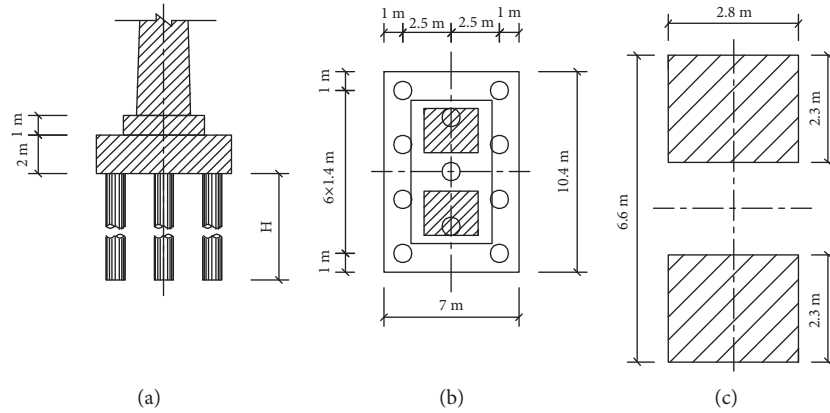
FIGURE 12: Pier and foundation: (a) cross-section of piers; (b) longitudinal section; (c) overall plan.

TABLE 9: Pier bottom internal forces under low-level earthquake.

Pier bottom internal force	Longitudinal earthquake	Transverse earthquake
Axial force, F_x(kN)	7393	7393
Longitudinal shear force, F_y(kN)	2302	0
Transverse shear force, F_z(kN)	0	2673
Longitudinal moment, M_y(kN·m)	27260	0
Transverse moment, M_z(kN·m)	0	13918

A finite element analysis model was built using the Midas Civil software program as shown in Figure 15. Space beam elements were used to model the piers and beams. The secondary dead loads were transferred to mass. Soil springs were modeled under the bottom of the piers to simulate the interactions between the foundation and the structures. The RC rigid frame comprises C40 concrete and an HRB400 steel rebar.

7.1. Low-Level Earthquake. Low-level earthquakes control the reinforcement ratio of the piers. Taking P2 piers (see Figure 15) as an example, Table 11 presents the pier bottom internal forces under longitudinal and transverse low-level earthquakes. The HRB 400 rebar with a diameter of 28 mm was used, and the reinforcement ratio was 3.06%, as shown in Figure 16. For the longitudinal earthquake, the largest stress of the concrete and steel rebar are 11.8 MPa and 206.0 MPa, respectively. For the transverse earthquake, the largest stress of the concrete and steel rebar are 8.7 MPa and 166.1 MPa, respectively.

7.2. High-Level Earthquake. The no-collapse performance under rare earthquake conditions should be satisfied. According to China Railway Code [30], when the outermost steel rebar begins to yield, the displacement at this moment is defined as the yielding displacement of the piers. Taking the P2 piers as an example, under a longitudinal earthquake, the displacement at the yielding moment is 8.56 cm, while the ultimate displacement is 12.42 cm. Thus, the calculated ductility ratio is 1.45, which is smaller than the allowable ratio of 4.8. Under a transverse earthquake, the displacement at the yielding moment is 7.42 cm, and the ultimate
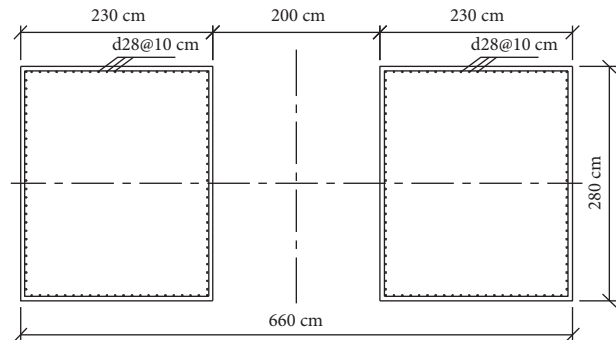
FIGURE 13: Pier reinforcement detail (cross section).

displacement is 11.68 cm. Thus, the calculated ductility ratio is 1.57, which is also smaller than the allowable ratio of 4.8. The no-collapse performance under rare earthquake conditions is therefore satisfied. For an RC rigid frame bridge under a high-intensity earthquake, the piers will yield at the pier bottom, and ductility hinges are formed to dissipate the seismic energy.

8. Technical and Economic Comparison

For the 32-m simply-supported box beam, a prefabricated erection method was adopted. The overall cost of the bridges considers the cost of the prefabricated yards and the temporary roads. For a simply-supported bridge, the erection cost of a simple beam is approximately 220k RMB. For the RC rigid frame bridge, full framing is used for the construction, and the cost for one unit of the frame is approximately 593k RMB.

TABLE 10: Pier bottom internal forces with isolation devices under high-level earthquake.

Pier bottom internal force	Longitudinal earthquake	Transverse earthquake
Axial force, F_x(kN)	7270	7270
Longitudinal shear force, F_y(kN)	2125	0
Transverse shear force, F_z(kN)	0	1877
Longitudinal moment, M_y(kN·m)	21349	0
Transverse moment, M_z(kN·m)	0	8796
Mitigation rates	88.0%	87.0%
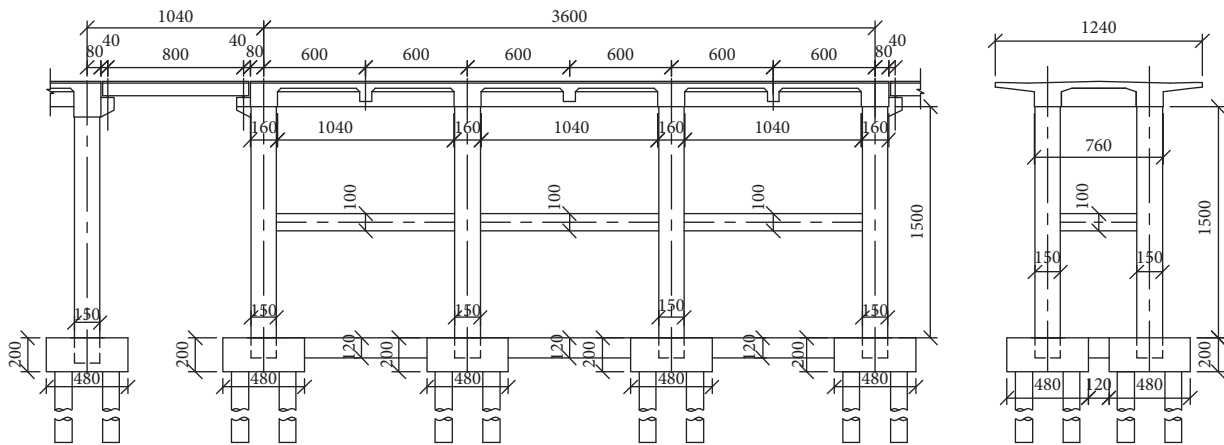
FIGURE 14: Elevation and cross-section of a RC rigid frame (unit: cm).
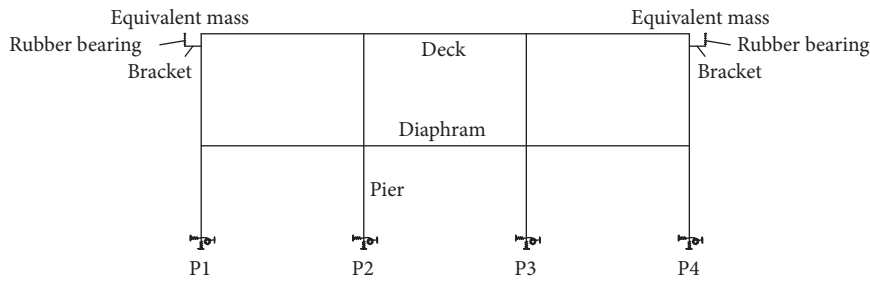
FIGURE 15: Seismic computational model of an RC rigid frame.

TABLE 11: Pier bottom internal forces under low-level earthquakes.

Pier bottom internal force	Longitudinal earthquake	Transverse earthquake
Axial force, F_x(kN)	1179	210
Longitudinal shear force, F_y(kN)	1100	0
Transverse shear force, F_z(kN)	0	1300
Longitudinal moment, M_y(kN·m)	7653	0
Transverse moment, M_z(kN·m)	0	5804

FIGURE 16: Pier reinforcement detail (cross section).

Economic analysis was conducted for the four evaluated schemes, and the costs of the substructures and super-structures are shown in Table 12.

Overall, the cost of RC rigid frames is the lowest among the four evaluated schemes, whereas the cost of SC composite beams is the highest. The cost of PC simply-supported box beams with isolation bearings is 7.4% cheaper than scheme (i) (PC simple beams with common bearings), whereas the cost of SC composite beams is 3.3% more expensive than scheme (i) and the cost of RC rigid frames is 11.0% cheaper than scheme (i). In conclusion, RC rigid frames are advantageous in terms of costs. Table 13 presents a technical comparison of the four schemes considering parameters besides costs.

TABLE 12: Economic comparison of the four earthquake resisting schemes.

Item	PC simple beam (common bearing)	PC simple beam (isolation bearing)	SC composite beam (isolation bearing)	RC rigid frame
Piles(k RMB)	1516.7	1177.7	905	1851.3
Piers(k RMB)	412.3	412.3	285	785.6
Pile caps(k RMB)	201.4	201.4	205	392.1
Foundation + Piers(k RMB)	2130.4	1791.4	1495	3029.0
Beams + Bearings (k RMB)	1789.9	1839.9	2230	1950.3
Total costs(k RMB)	3920.3	3631.3	4062	4979.2
Cost indicator per meter (k RMB/per meter)	120.255	111.390	124.220	107.311

TABLE 13: Technical comparison of the four earthquake resisting schemes.

Items	PC simple beam (common bearing)	PC simple beam (isolation bearing)	SC composite beam (isolation bearing)	RC rigid frame
Structural system	Static determinate	Static determinate	Static determinate	Static indeterminate
Construction method	Precast; fast	Precast; fast	Factory manufacture for steel beams, cast-in-situ for concrete deck; medium	Cast-in-situ; slow
Seismic system	Ductility system	Isolation system	Isolation system	Ductility system
Low-level earthquake	Elastic	Elastic	Elastic	Elastic
High-level earthquake	Piers damaged; difficult to repair	Piers elastic, shear key broken; easy to replace	Piers elastic, shear key broken; easy to replace	Piers damaged; difficult to repair

According to investigations in Indonesia, SC composite beams are rarely used, and the corresponding design, construction, and maintenance experiences are lacking. Since Indonesia is located in a tropical rainforest zone, there is abundant rain throughout the year, and the air humidity is ~80%. The railway line traverses a sea climate, which makes maintenance and rehabilitation difficult and costly. Thus, considering the lifetime costs, it is even more expensive. Moreover, the noise of SC composite beams is higher than that of concrete beams, which can increase the damping of the structure, thereby reducing the vibration and noise of the bridge. In contrast, concrete beams have advantages in terms of maintenance and rehabilitation, and have less noise pollution and better durability. Therefore, concrete beams are generally preferred.

Considering the overall structural systems, for a simple beam, advanced isolation devices can be implemented in the seismic design because of the favorable separation between piers and beams, leading to a better seismic performance. The integrity of the RC rigid frame is better because of the rigid pier-beam connection. Therefore, only a ductile design method can be applied (at the price of pier damage). From the perspective of the project timeline, PC beams are faster to build because of their construction method (i.e., prefabricated erection). In contrast, the RC rigid frames are constructed using a full framing method, and the construction period is the longest. The construction period for SC composite beams is between that of PC beams and RC rigid frames. Although the scheme of RC rigid frames has economic advantages, its overall applicability is relatively low. Under high-level earthquake conditions, piers would undergo significant damage, which would be difficult to repair. Earthquakes in Japan have caused massive disruption of RC rigid frame bridges, leading to significant economic losses for the north-eastern Shinkansen [8]. The present study indicates that PC simply-supported beams with double-curved spherical seismic isolation bearings are optimal for the entire railway line. The other schemes can also be applied to some specific bridges.

9. Conclusions

The optimum selection of a rational earthquake resisting scheme is crucial for high-speed railway lines. Based on the comparison of four bridge earthquake resisting schemes relevant for the Jakarta-Bandung high-speed railway considering technical and economic aspects, the following conclusions can be drawn.

(1) PC simply-supported beams are generally constructed using a prefabricated method, and the construction quality can be guaranteed. The construction form and devices can be used repeatedly, and the beams are suitable for large-scale manufacturing. These simple beams have static determinate structures and are suitable for various types of soils.

(2) PC simply-supported beams are connected to the piers through bearings, and therefore, advanced isolation bearings or other energy dissipation devices can be applied. The seismic performance of the bridge is thus improved, and the total cost of the project can be minimized. Under high-level earthquake conditions, the shear key can easily be replaced after broken. Although the isolation bearings are more expensive than common spherical steel bearings, the cost of the substructure can be reduced to a larger extent. The total cost is, therefore, smaller for beams with isolation bearings.

(3) The SC composite beam is the most expensive, especially when considering the subsequent costs associated with maintenance and rehabilitation. Moreover, SC composite beams exhibit less rigidity and require longer construction processes than concrete beams. The noise from SC composite beams is also relatively larger than from concrete beams.

(4) In RC rigid frame bridges, the piers and beams are rigidly connected, and the advanced isolation devices cannot be integrated into this system. Therefore, only a ductile design method can be used (at the price of bridge pier damage). Moreover, RC rigid frame bridges, which are indeterminate structures, are not applied to soft site regions. The cast-in-situ construction method requires a longer period of time and more manpower, and the RC rigid frame bridges show only limited economic advantages.

In conclusion, considering their high seismic performance, convenient construction, and beam type integrity, the PC simply-supported beams with isolation bearings are recommended for use throughout the entire railway line of the Jakarta-Bandung high-speed railway. Considering the

economic advantages of RC rigid frame bridges, this bridge type can be employed for certain locations with relatively low pier heights when the bridge girder erection machine and transporting girder vehicle are difficult to run, but the soil conditions are suitable and the site allows for full framing construction.

Data Availability

Conflicts of Interest

The authors declare no conflicts of interest.

Acknowledgments

References

[1] J. Zheng, *High-speed Railway Bridge of China*, People's Railway Press, Beijing, China, 2012.

[2] B. Yan, G. L. Dai, and N. Hu, "Recent development of design and construction of short span high-speed railway bridges in China," *Engineering Structures*, vol. 100, pp. 707–717, 2015.

[3] W. Guo, Y. Hu, H. Y. Gou et al., "Simplified seismic model of CRTSII ballastless track structure on high-speed railway bridges in China," *Engineering Structures*, vol. 211, Article ID 110453, 2020.

[4] L. Z. Jiang, Y. T. Zhang, Y. L. Feng, W. Zhou, and Z. Tan, "Simplified calculation modeling method of multi-span bridges on high-speed rail ways under earthquake condition," *Bulletin of Earthquake Engineering*, vol. 18, no. 5, pp. 2303–2328, 2020.

[5] J. Yu, L. Z. Jiang, W. B. Zhou, J. Lu, T. Zhong, and K. Peng, "Study on the influence of trains on the seismic response of high-speed railway structure under lateral uncertain earthquakes," *Bulletin of Earthquake Engineering*, vol. 19, no. 7, pp. 2971–2992, 2021.

[6] Z. H. Zhu, Y. J. Tang, Z. N. Ba, K. Wang, and W. Gong, "Seismic analysis of high-speed railway irregular bridge–track system considering V-shaped canyon effect," *Rail. Eng. Science*, vol. 30, no. 1, pp. 57–70, 2022.

[7] W. L. Xie, "Overview of Japan shinkansen bridge," *Railway Investigation and Surveying*, vol. 4, pp. 10–17, 2000.

[8] M. Akiyama, D. M. Frangopol, and K. Mizuno, "Performance analysis of Tohoku-Shinkansen viaducts affected by the 2011 Great East Japan earthquake," *Structure and Infrastructure Engineering*, vol. 10, no. 9, pp. 1228–1247, 2014.

[9] X. Kang, L. Z. Jiang, Y. Bai, and C. C. Caprani, "Seismic damage evaluation of high-speed railway bridge components under different intensities of earthquake excitations," *Engineering Structures*, vol. 152, pp. 116–128, 2017.

[10] L. K. Chen, L. Z. Jiang, Z. W. Yu, and Y. Li, "Seismic response characteristics of a high-speed railway simply-supported girder bridge," *Journal of Vibration and Shock*, vol. 12, pp. 216–222, 2011.

[11] B. Wei, T. H. Yang, L. Z. Jiang, and X. He, "Effects of uncertain characteristic periods of ground motions on seismic vulnerabilities of a continuous track–bridge system of high-speed railway," *Bulletin of Earthquake Engineering*, vol. 16, no. 9, pp. 3739–3769, 2018.

[12] Y. Li and J. P. Conte, "Probabilistic performance-based optimum design of seismic isolation for a California high-speed rail prototype bridge," *Earthquake Engineering & Structural Dynamics*, vol. 47, no. 2, pp. 497–514, 2018.

[13] Y. Li and J. P. Conte, "Effects of seismic isolation on the seismic response of a California high-speed rail prototype bridge with soil-structure and track-structure interactions," *Earthquake Engineering & Structural Dynamics*, vol. 45, no. 15, pp. 2415–2434, 2016.

[14] X. S. Xia, X. C. Chen, and C. F. Wang, "Bridge damage analysis and reasonable seismic systems," *Earthquake resistant engineering and Retrofitting*, vol. 6, pp. 132–136, 2011.

[15] X. K. Bai, "Structural form analysis of small and medium bridge of Beijing-Shanghai high-speed railway," *Railway Standard Design*, vol. 6, pp. 35–39, 2002.

[16] X. Xie and T. Y. Yang, "Performance evaluation of Chinese high-speed railway bridges under seismic loads," *International Journal of Structural Stability and Dynamics*, vol. 20, no. 05, Article ID 2050066, 2020.

[17] S. G. Cui, C. Guo, J. Su, E. Cui, and P. Liu, "Seismic fragility and risk assessment of high-speed railway continuous girder bridge under track constraint effect," *Bulletin of Earthquake Engineering*, vol. 17, no. 3, pp. 1639–1665, 2019.

[18] W. Guo, X. Gao, P. Hu et al., "Seismic damage features of high-speed railway simply supported bridge–track system under near-fault earthquake," *Advances in Structural Engineering*, vol. 23, no. 8, pp. 1573–1586, 2020.

[19] D. S. Shan, F. X. Qu, and X. D. Deng, "Seismic fragility analysis of irregular bridges with non-circular tall piers considering ground motion directionality," *Bulletin of Earthquake Engineering*, vol. 18, no. 4, pp. 1723–1753, 2020.

[20] X. Meng, R. Gao, and C. G. Li, "Design and seismic mitigation performance study of shock absorber for railway simply-supported beam bridge," *Bridge Construction*, pp. 81–86, Article ID 3, 2014.

[21] X. L. Zheng and Y. X. Jin, "Design and seismic isolation performance analysis of friction pendulum bearings," *Journal of Railway Engineering Society*, vol. 10, pp. 81–87, 2014.

[22] X. L. Zheng, Y. X. Jin, and N. Lv, "The design and seismic isolation performance analysis of bearings with E-shape metallic dampers," *Journal of Railway Engineering Society*, vol. 2, pp. 70–75, 2015.

[23] X. S. Xia, H. D. Zhao, and H. L. Ouyang, "Study on seismic isolation of high speed railway bridge with friction pendulum bearings," *Earthquake Resistant Engineeringand Retrofitting*, vol. 3, pp. 21–26, 2014.

[24] L. Z. Jiang, S. S. Cao, and B. Wei, "Effects of friction-based fixed bearings on seismic performance of high-speed railway simply supported girder bridges and experimental validation," *Advances in Structural Engineering*, vol. 22, no. 3, pp. 687–701, 2019.

[25] W. Guo, Q. D. Du, Z. Huang, H. Gou, X. Xie, and Y. Li, "An improved equivalent energy-based design procedure for seismic isolation system of simply supported bridge in China's high-speed railway," *Soil Dynamics and Earthquake Engineering*, vol. 134, Article ID 106161, 2020.

[26] W. Guo, C. Zeng, H. Y. Gou et al., "Real-time hybrid simulation of high-speed train-track-bridge interactions using the moving load convolution integral method," *Engineering Structures*, vol. 228, Article ID 111537, 2021.

[27] Y. Shi, Z. W. Zhong, H. G. Qin, J. Han, and Z. Sun, "Toggle buckling-restrained brace systems and a corresponding designmethodfor the seismic retrofit of bridge bents," *Engineering Structures*, vol. 221, Article ID 110996, 2020.

[28] S. A. Mitoulis, I. A. Tegos, and K. C. Stylianidis, "Cost-effectiveness related to the earthquake resisting system of multispan bridges," *Engineering Structures*, vol. 32, no. 9, pp. 2658–2671, 2010.

[29] Rsni3 2833, *201X, Seismic Design of Bridges*, National Standard of Indonesia, China, 2013.

[30] Gb 50111-2006, *Code of Seismic Design of Railway Engineering*, National Standard of People's Republic of China, China, 2009.

[31] B. S. En1998-2, *Eurocode 8-Design of Structures for Earthquake Resistance-Part 2: Bridges*, European Committee for standardization, China, 2018.

[32] Aashtolfrdseis-1, *AASHTO Guide Specifications for LRFD Seismic Bridge Design*, American Association of State Highway and Transportation Officials, China, 2011.

[33] Tb 10091-2017, *Code for Design of Concrete Structuresof Railway Bridge and Culvert*, National Standard of People's Republic of China, China, 2017.

[34] Tb 10091-2017, *Code for Design on Steel Structure of Railway Bridge*, National Standard of People's Republic of China, China, 2017.

Research Article

Analysis of Bridge Health Detection Based on Data Fusion

Ying Chen,[1] Jiuhong Zhang,[1] Yanfeng Li ⑩,[2] and Jialong Li ⑩[2]

[1]*JangHo Architecture, Northeastern University, Shenyang 110169, China*
[2]*School of Transportation and Geomatics Engineering, Shenyang Jianzhu University, Shenyang 110168, China*

Correspondence should be addressed to Yanfeng Li; lyfneu@126.com

By integrating rough set theory and neural network theory, this study combined their advantages. Drawing on the existing theoretical results for bridge influencing factors, a method for numerical simulation and data fusion was used in the application of multifactor data fusion for cable-stayed bridge safety evaluation. Based on studying existing bridge safety evaluation methods, a neural network and rough set theory were combined to perform a safety evaluation of PC cable-stayed bridge cables, which provided a new means for bridge safety evaluation. First, a cable-stayed bridge in Shenyang was used as the engineering background, the safety level of its cables was divided into five levels, and a safety evaluation database was established, clustered by a Kohonen neural network. This provided specific evaluation indicators corresponding to the five safety levels. A rough neural network algorithm integrating the rough set and neural network was applied to data fusion of the database, with the attribute-reduction function of the rough set used to reduce the input dimension of the neural network. *Conclusions*. The neural network was then trained and the resulting trained network was applied to the safety evaluation of the cables of the cable-stayed bridge. Four specific attribute index values, corresponding to the bridge cables, were directly input to obtain the safety status of the bridge and provide corresponding management suggestions.

1. Introduction

Artificial intelligence (AI) is a branch of computer science and a new research direction that has emerged in recent years. AI can solve many complex problems with strong nonlinearity and large uncertainty, which are difficult to solve by traditional methods, through simulation of the decision-making process of human thinking. Recently, AI tools represented by neural networks have been successfully applied to bridge evaluation [1, 2].

Scholars have also optimized the evaluation method, index system, evaluation standard, and other factors based on manual detection. Sun et al. [3] have provided the weights of each bridge component and realized the performance evaluation layer by layer according to fuzzy weighting and the weak segmentation method and have formulated different maintenance plans for structures with different ratings. Based on the Dempster-Shafer evidence theory and Yager combination rule, Bolar et al. [4] have proposed a hierarchical assessment method for bridge status, which

reduces the uncertainty of multisource index information. Based on field test data, Caglayan et al. [5] have carried out dynamic corrections to the model of a railway bridge, simulated testing of most of the dynamic indices of the whole bridge, and completed the safety assessment of damaged bridge components. Kim [6] has calculated 36 load combinations on steel box girder bridge models with different spans and predicted the load response distribution of the actual structure. Wang [7] has established a time-varying probability model of resistance as well as a probability model of vehicle loading based on the probability model of resistance parameters. The main failure modes and correlation coefficients of bridge structures were also derived through the principle of minimum load increment and a failure tree model. Wang [8] has defined the concept of "generalized post progress," weighted the main load-bearing members of a steel truss-tied arch bridge, and completed a comprehensive evaluation of the safety of the whole bridge through the fuzzy comprehensive evaluation method. Yan et al. [9] have identified and extracted the structural response signals

under car load and crowd load and established a mathematical model for bridge safety monitoring and evaluation based on hesitant fuzzy set. Wang et al. [10] have proposed an influence line-based moving load test method for a rapid bridge capacity evaluation. Mohammad et al. [11] have used a comprehensive and coherent reliability approach to assess the safety of TSBG bridges after the complete fracture of one steel girder.

In recent years, security issues of bridges have received widespread attention from governments and communities around the world. Security research on the later stage of bridge operation has also become a hot research topic. Carrying out safety assessment of bridges can quickly and accurately obtain the current safety status of bridges. The actual bearing capacity of bridges is obtained, such that the actual working state of the bridge in service can be understood. Based on assessment conclusions, the corresponding measures are then taken in time to ensure that bridges remain in safe operational state.

Although the current bridge-evaluation field has been developing rapidly, there are still some problems to be solved in terms of data sources, indicator empowerment, and evaluation methods. Division of the scoring interval cannot be completely accurate and reasonable and the weights of indicators have a great influence on evaluation results. However, the current subjective weighting method is too arbitrary and the objective weighting results are easily inconsistent with human cognition.

This study was based on a current situation, in which a cable-stayed bridge is vulnerable and difficult to repair during its operation and takes detection, monitoring, and finite elements as the source of index data. Then, research on the comprehensive evaluation method for the reliability of the cable-stayed bridge box girder was performed and the applicability and effectiveness of the method were verified by taking the background engineering as an example. The main contributions were as follows:

(1) Many relevant publications were consulted and the relevant overviews, necessity, and research status of bridge safety evaluation were summarized. The commonly used bridge structure safety-evaluation methods were proposed and the basic concept of multisource data fusion and the feasibility of its application in bridge evaluation were expounded.

(2) Various existing data fusion algorithms and their practicality were comprehensively considered. A rough set and neural network were integrated to complement each other in constructing a rough neural algorithm. The accuracy of data fusion was further improved, reducing the time required for fusion.

(3) On the basis of relevant literature, the existing study addressed and integrated stress amplitude, corrosion degree, sheath damage, and damping system influencing factors. A safety evaluation database of stay cables was established and specific grading standards for safety evaluation grades were obtained by cluster analysis. A rough set was used to reduce the attribute index of the database. After simplification, a database is obtained and the designed neural network trained using this data.

(4) The trained neural network was then applied to the evaluation of the selected Fumin Bridge. The safety level corresponding to the bridge was provided based on the prediction result produced by the neural network.

The research background of this study was the situation of the Fumin Bridge in Shenyang, described as follows.

The main bridge of Shenyang, Fumin Bridge, is a single-plane PC cable-stayed bridge with a length of 420 m and span arrangement of $89 + 242 + 89$ m (see Figure 1). The material of the main girder is C50 concrete, with a nearly triangular section formed with good wind resistance, a single box with three rooms, and girder height of 3.414 m. The dimensions of each part of the midspan were the upper edge thickness of the two chambers at 25 cm, upper edge thickness of the middle chamber at 40 cm, lower edge thickness at 30 cm, side web thickness at 25 cm, and middle web thickness at 40 cm (see Figure 2). The thickness of each part of the side-span included the upper edge of both chambers at 40 cm, upper edge of the middle chamber at 50 cm, lower edge at 40 cm, middle web at 50 cm, and side web at 30 cm (see Figure 3). The main tower is cast with C50 concrete, with a box-shaped section, tower height above the bridge deck at 67.5 m, and folded angle of the main tower located 33.9 m above the bridge deck. The angle between the lower tower body and horizontal plane is 75° and the angle between the upper and lower tower bodies is 7.5°. The stay cables are made of galvanized high-strength steel wires, with four specifications of 301-Φ7, 241-Φ7, 211-Φ7, and 151-Φ7. They are arranged in a fan shape, with 15 pairs arranged on each main tower and a total of 120 cables in the whole bridge. The cable force of the bridge is 5500–9500 kN. The 4# pier is a fixed connection system of towers, girders, and piers and 5# pier is a tower-girder fixed connection and girder-pier separation system.

2. Safety Assessment Level

Cable-stayed cables are vulnerable force-transmitting components in cable-stayed bridges which also determine the performance of the entire bridge. It is necessary to evaluate the durability of cable-stayed cables to provide guidance for management and maintenance and to reduce life cycle costs.

2.1. Stay Cables Reliability Risk Recognition. Different risk types determine different risk factors. For example, the risk factors of bridge earthquakes and fires are totally different. It is necessary to recognize and confirm risk types before risk
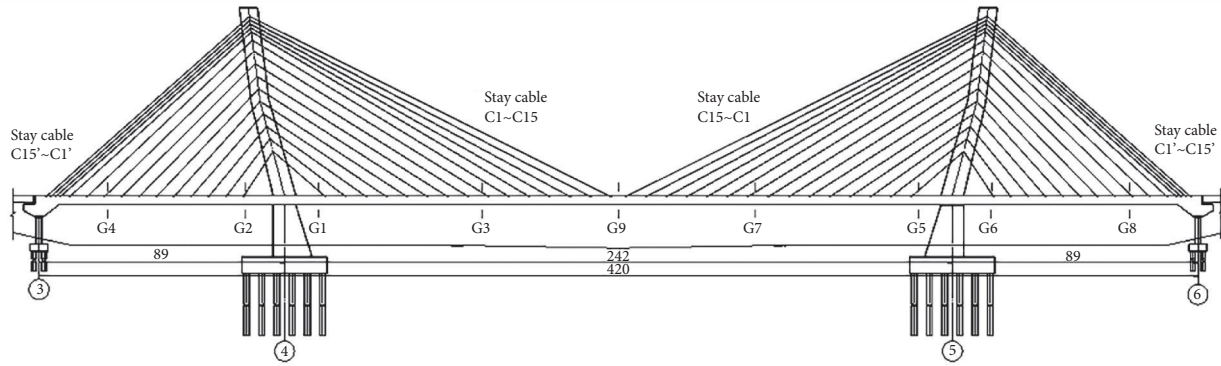
FIGURE 1: Arrangement of the main bridge (m).
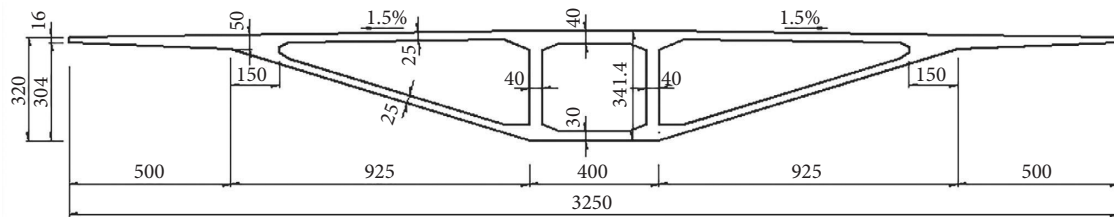
FIGURE 2: Cross section of midspan girder (cm).
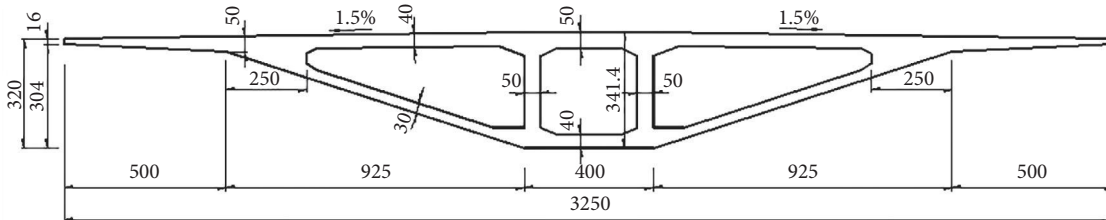
FIGURE 3: Cross section of side-span girder (cm).

assessment. The reliability of the project refers to the ability to complete the intended functionality within the intended environment and intended time, which mainly includes safety, applicability, and durability. Therefore, the reliability risk recognition of the cable must be carried out separately from these three aspects.

2.1.1. Safety Risk. The safety of structural components is closely related to the bearing capacity, which is controlled by strength, stiffness, or stability. For typical tensile members, such as stay cables, the problem of stability is generally not considered. High-strength steel wire materials have a high stiffness and low elongation rate, with deformation not controlling its failure. In fact, the safety risk of stay cables is the strength failure risk. Without considering the impact of durability degradation on the risk of cable breaking, the safety risks can be attributed to excessive tensile stress in stay cables.

2.1.2. Adaptability Risk. Applicability refers to the ability to maintain good functions in the normal use process, such as not producing excessive deformation which affects the normal use of components. As the regulating unit of the whole bridge mechanical state, good performance of stay cables is mainly reflected in ensuring the uniform and reasonable force of the beam and tower members. Therefore, the applicability risk can be attributed to increase and decrease of the cable force value under constant loading.

2.1.3. Durability Risk. Different scholars have different understandings of durability. The definitions of durability have been summarized in some references (see Table 1). Through comparison, the durability of existing structures is defined here as follows: the ability of the structure to maintain a minimum predetermined function under the conventional level of maintenance due to deterioration of the design, construction defects, use environment, material

TABLE 1: Definition of durability.

	Reference [12]	Reference [13]	Reference [14]	Reference [15]	Reference [16]
Duration	Design duration	Design duration	Intended duration	Design duration	Specified duration
Effect	Intended effect	Design environment effect	Deterioration effect	Use environment, material deterioration	Various adverse factors
Condition	Intended use maintenance	Design use maintenance	Intended use maintenance	Optimization funds	Normal use maintenance
Performance	Safety, applicability	Safety, applicability	Necessity	Safety, applicability	Intended function

TABLE 2: Durability risk factors of stay cables.

Environment	Material	Stress	Human Factor
Corrosion	Aging	Fatigue	Low construction quality
Vibration	Prestress relaxation	Sheath cracking	Not timely inspection
	Material defects		

Note. Aging is the degradation of materials due to the decrease in molecular coalescence. Sheath cracking is the cracking caused by repeated cooperative deformation of sheath and steel wire under high stress state.

TABLE 3: Grading standard of risk indexes.

	Probability		Harmfulness		Premonitory	
	Quality	Quantity	Quality	Quantity	Quality	Quantity
1	Rare	$P \leq 0.003$	Insignificant	$Q \leq 0.125\%$	Common sense judgment	$t > 12$ h
2	Occasional	$0.003 < P \leq 0.03$	Sight	$0.125\% < Q \leq 1.25\%$	Infer with professional knowledge	3 h $< t \leq 12$ h
3	Possible	$0.03 < P \leq 0.3$	Serious	$1.25\% < Q \leq 12.5\%$	Professional tool calculation	0.5 h $< t \leq 3$ h
4	More possible	$P > 0.3$	Extremely serious	$Q > 12.5\%$	Unpredictable	$t \leq 0.5$ h

properties, and other factors during the remaining service life of the structure. The main intended function of the stay-cable system is to deliver the bridge surface load. The risk of existing durability can be expressed as follows: During the remaining use phase, durability risk is a factor that has adverse effects on the performance of the cable force-transmission system (high-strength steel wire and anchorage system) at the level of normal pipe curing.

The harmfulness of the durability risk is reflected in the form of disease. Existing references list the main diseases of the cable system [17], and, on this basis, the durability risk identification of the cable is realized by combining retrieval experience and expert interviews. The durability risks of common stay cables were sorted out according to the environment, material, force, and human factors, and evaluations were made for these nine risks (see Table 2).

2.2. Risk Matrix Expansion.
In [18], the indicators and standards suitable for engineering risk assessment have been proposed. The absolute value of direct economic losses is used as an assessment standard for harmfulness, which is not applicable to the risk assessment of small and medium structures with low cost. This study used relative economic losses as a harmfulness evaluation standard. The internal rate of return of engineering projects is generally 12%, with this standard conforming to national conditions.

Premonitory sign is a sign that occurs before an incident. The important manifestation of premonitory risk is the advancement value of forecast time, which is of great significance to reduce risk losses, as discussed in [19]. The safe evacuation time for the risk population in a fire is stipulated in [20]. Different grades of premonitory indices have been roughly described, which yields it difficult to form normative standards, as discussed in [21]. At present, there are few studies of premonitory risk and few references have incorporated it into risk assessment.

The advancement value of forecast time "t" is introduced as a quantitative standard for "premonitory." Combined with the corresponding qualitative description, the risk matrix was extended to a three-dimensional (3D) risk space. The risk indices and grading standards are shown in Table 3 and 3D risk space is shown in Figure 4. Note. Risk sample corresponding to different risk areas (see Table 4).

2.3. Evaluation Index System.
The durability of stay cables is mainly affected by fatigue and corrosion. Following the principles of effectiveness [22–26], measurability, comprehensiveness, and independence, a durability evaluation index system for stay cables was established (see Table 5).

2.4. Durability Qualitative Description.
As the reduction of the performance of structural components must be manifested in the form of external diseases, the formulation of durability standards can be considered from the perspective of disease conditions and service performance [27, 28]. The qualitative criteria of evaluation indicators and evaluation
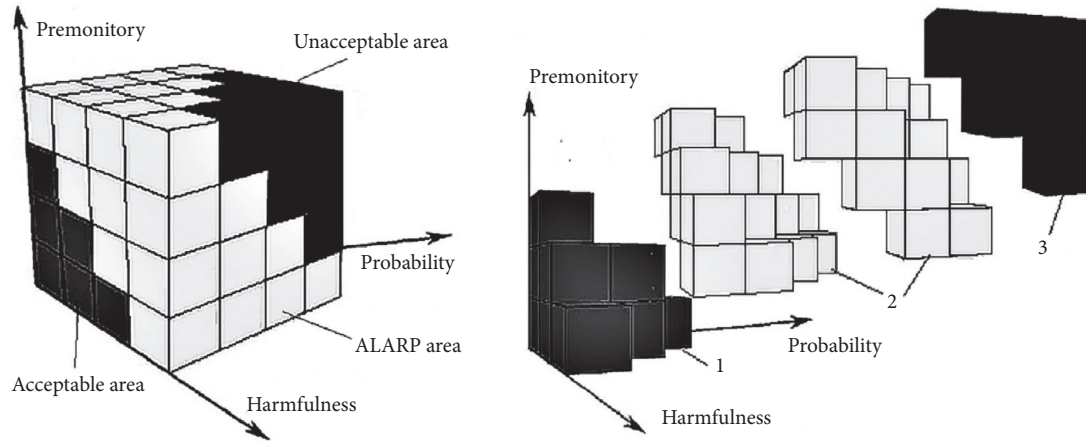
Figure 4: Three-dimensional risk space.

Table 4: Combination of risk factors.

Risk grade	Risk sample
Acceptable	Aa1, Aa2, Aa3, Ab1, Bb1, Ab2, Ac1, Ba1, Ba2, Ca1, Bb2
ALARP	Aa4, Ba4, Ba3, Ca3, Ca2, Da2, Da1, Db1, Ab4, Ab3, Ac3, Ac2, Ad2, Ad1, Bd1, Bb3, Cb2, Bc2, Cb1, Bc1, Cc1, Dd1, Dc1, Dc2, Db2, Db3, Da3, Da4, Ca4, Cb4, Bb4, Bc4, Ac4, Ad4, Cd1, Cd2, Bd2, Bd3, Ad3, Cc2, Cb3, Bc3
Unacceptable	Dd4, Dd3, Dd2, Dc3, Cd3, Dc4, Cd4, Db4, Bd4, Cc4, Cc3

Note. A-D, a-d, and 1–4 represent probability, harmfulness, and premonitory indicators 1–4.

Table 5: Durability index system of stay cables.

Index	Upper limit	Lower limit	Weights
Stress amplitude	250 MPa	110 MPa	0.3
Corrosion degree	Quantitative	Quantitative	0.3
Sheath damage	Qualitative	Qualitative	0.2
Damping system	Quantitative	Quantitative	0.2

Note. Weights are not the focus of this study. Stress amplitude is the difference between maximum tensile stress and minimum tensile stress in each stress cycle. Corrosion degree is divided into four grades: serious corrosion, medium corrosion, weak corrosion, and no corrosion. Sheath damage is mainly affected by aging and fatigue.

results might be inconsistent, but the focus here was on verification of method applicability. The qualitative scale of indicators and evaluation results are shown in Table 6.

2.5. Safety Assessment Level.
According to the approximate derivation results of the bridge structure evaluation grade, the evaluation grade standard of a stay cable is shown in Table 7.

For the evaluation standard of safety level, 20 experts and scholars were determined by asking for advice using distributed questionnaires. Statistical results of the questionnaires are shown in Table 8.

This study used Clementine 12.0 [7] as a data mining tool to establish a Kohonen neural network for clustering and analyzing the database data flow. Training of the Kohonen neural network entailed the expert mode, with the width at 5, length 1, and number of neurons in the output layer 5, and the network clustered the samples into 5 classes. After cluster

Table 6: Qualitative description of durability rating.

Level	Qualitative description
1	Excellent performance, no disease, completely normal use
2	General performance, weak disease, partially affecting use
3	Performance degradation, moderate disease, affecting normal use
4	Performance deviation, serious disease, difficult to use normally
5	Poor performance, badly ill, barely useable

analysis, the entire evaluation database was clustered into five categories, with the specific evaluation standards shown in Table 9.

The evaluation standard obtained by the Kohonen neural network was seen to be very close to the recommended evaluation standard given by most experts, indicating that it possessed high reliability. It was thus determined as the safety level evaluation standard for the main girder of the bridge.

3. Processing of Evaluation Data

3.1. Calculation of Sample Data.
Taking the case of bridge operation as an example, the calculation process of one sample of data was considered and the method for obtaining other sample data was the same as this example. When the bridge was built and operated for the 5th year, the corrosion degree did not reach the critical maximum corrosion degree. Therefore, it was considered that the prestressed steel bars in the bridge stay cables were not corroded and the prestress condition was not lost, such that the prestress was taken as

TABLE 7: Rating standards for stay cables.

Type of structure or member	a	b	c	d
Safety identification factor K	$K \geq 1.0$	$0.95 \leq K < 1.0$	$0.86 \leq K < 0.95$	$K < 0.86$

TABLE 8: Statistical table of questionnaire survey results.

Supporters (%)	Plan	Evaluation standards				
		Level 1	Level 2	Level 3	Level 4	Level 5
35	Plan 1	$K \geq 1.30$	$1.20 \leq K < 1.30$	$1.10 \leq K < 1.20$	$1.00 \leq K < 1.10$	$K \leq 1.00$
40	Plan 2	$K \geq 1.20$	$1.10 \leq K < 1.20$	$1.00 \leq K < 1.10$	$0.90 \leq K < 1.10$	$K \leq 0.90$
25	Plan 3	$K \geq 1.25$	$1.15 \leq K < 1.25$	$1.00 \leq K < 1.15$	$0.95 \leq K < 1.00$	$K \leq 0.95$

TABLE 9: Safety rating standard table.

Evaluation standards				
Level 1	Level 2	Level 3	Level 4	Level 5
$K \geq 1.20$	$1.00 \leq K < 1.20$	$0.95 \leq K < 1.00$	$0.90 \leq K < 0.95$	$K \leq 0.90$

FIGURE 5: Data flow diagram for data discretization.

FIGURE 6: Data flow diagram for training a neural network.

1.00. The bridge had endured a 5-year operation period, which meant that the elastic modulus should have been reduced to a certain extent. According to the time-varying formula of steel strength, the reduction coefficient was 0.832. After 5 years of operation, the bridge should appear to be damaged and the apparent score thus decreased with operation time, such that there was great uncertainty. Therefore, by randomly generating a set of values between 0 and 1 to simulate the visual inspection (sheath damage) score, the resulting score was 0.9437. At this point, the sample data corresponding to the 5th year of bridge operation had been obtained.

3.2. Rough Set Attribute Reduction. Before performing rough set attribute reduction on the data, the data needed to be processed. Because the data in the information table was complete and some value ranges of the condition and decision attributes were continuous, it was not necessary to complete them and only the information table needed to be discretized. With Clementine 12.0 as a data mining tool, the data flow for the sample data was discretized using mean-standard deviation grouping (see Figure 5).

Using the sufficiency theory of rough set knowledge to simplify the sample data, processing was divided into two steps, one to simplify summation of the conditional attribute set of the decision table and the other to simplify the conditional attribute value. Using rough set theory for data preprocessing, no additional information needed to be known in advance and the reduction algorithm simple was beneficial for realizing automatic operation with the help of a computer or software [29–31].

4. Neural Network Training and Prediction

The performance and correctness of the training model based on the rough neural network were tested by extracting 545 sets of data samples from the reduced database as the training set, with inputting to the neural network for training the neural network. The remaining 120 sets of data samples were used as verification data to test the prediction accuracy of the network [32, 33]. The neural network was created and trained through the neural network node. The data flow diagram is shown in Figure 6.
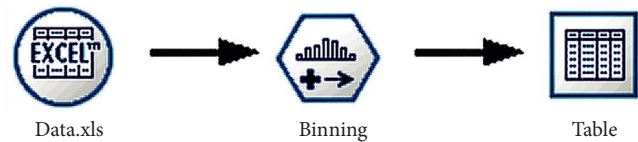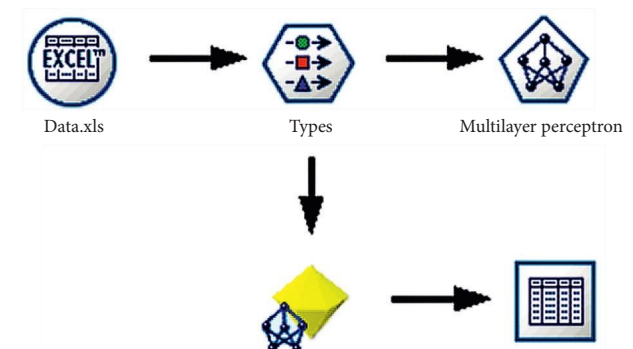
Neural networks were created and trained through neural network nodes and used to simulate the work of a large number of interconnected processing units arranged in layers. Neural networks often consist of 3 parts: First is the input layer, whose units represent the input fields. Second, one or more layers are hidden layers. Third, one is the output layer, whose units represent output fields. Units are connected by changing connection strengths or weights. Clementine provides 6 training modes to train neural network models: fast, dynamic, multiple, pruned, radial basis function network (RBFN), and thorough pruning.

The training method selected in this study was the fast method, with the number of neurons in the input layer being $n = 7$ and the number of neurons in the output layer being $m = 1$. The neural network had 3 hidden layers, with the

FIGURE 7: The parameter settings of neural network.

number of neurons in the first, second, and third layers being $l = 20$, 15, and 10, respectively, and the number of continuations was set to 200 times. The accuracy of the neural network training error was set to $k = 0.0001$ and the correct rate of the neural network was >95%. The learning efficiency of the neural network was set as follows: Alpha = 0.3, initial Eta = 0.3, Eta decay = 30, high Eta = 0.1, and low Eta = 0.01. The parameter settings are shown in Figure 7.

The prediction accuracy of the categorical output variable is the proportion of the model's correctly predicted samples to the total samples. For a numeric output variable, the prediction accuracy was calculated as follows:

$$\frac{1 - |Y_i - Y'_i|}{Y_{max} - Y_{min}} \times 100\%, \tag{1}$$

where $|Y_i - Y'_i|$ is the absolute error between the ith actual observed and model predicted values and Y_{max} and Y_{min} are the actual maximum and minimum values of the output variable, respectively. Note that the values refer to values after normalization. The prediction accuracy needed to be calculated for each observation and the average value was the total prediction accuracy of the model.

After the neural network training was completed [34, 35], 120 sets of verification data were input into the neural network to obtain a predicted value based on the coarse neural network algorithm. The data flow diagram predicted by the neural network is shown in Figure 8.

The K value of the 120 groups of data in the original safety assessment database was taken as the theoretical value and the value output by the neural network was taken as the predicted value. The relative sizes of the two data groups were compared and used as the basis for evaluating the prediction accuracy of the neural network model. The network prediction error curve is shown in Figure 9.

The neural network was seen to have high accuracy, with the relative error not exceeding 3%. This completely met the needs of the actual situation and thus could be applied to practical projects.

5. Example Verification

5.1. Testing Results of Single-Plane Cable-Stayed Bridges. A cable-stayed bridge in Shenyang is located 2 km downstream of the Changqing Bridge on the Hunhe River in the south of Shenyang City. The bridge was built in 2003 and belongs to urban class I bridges. The bridge is China's first double-tower single-plane prestressed-concrete cable-stayed bridge in the shape of a broken line. The bridge shape is partially unbalanced to form an overall balance, which is in line with traditional Chinese architectural aesthetics. The overall combination of bridges has a sense of rhythm, reflecting the perfect combination of strength and beauty. Its unique polyline-shaped tower shape and its special location in Hunhe Park make it a landmark building in Shenyang City and Hunnan New District. In April 2011, the Transportation Experiment Center of Harbin Institute of Technology carried out dynamic and static load testing as well as appearance inspections of the bridge. The test (Figure 10) results were as follows:

(1) During inspection of the appearance, it was found that the PE sheath of the stay cable in the midspan part of the main span was broken. There were cracks in the main and diaphragm girders, most of the crack widths were stable, and individual crack widths tended to increase. Although these cracks were not enough to cause cable damage, this affected the aesthetic of this bridge. The aesthetic characteristics of the bridge building determined that, with its entire exposed structure and clear image of each component's function, a harmonious landscape aesthetic effect had been formed in synergy. The cracks of the cable-stayed sheath and main girder of the bridge first had an intuitive deterioration effect on the aesthetic expression of the bridge building itself and the quality of the environmental landscape. Appearances observations are shown in Figure 10.

(2) When the bridge was completed in November 2003; the actual measured bridge deck elevation in the middle of the main span was 18 mm lower than the design elevation. After seven years of operation, the theoretically calculated value of the lower deflection in the middle of the main span was 59 mm, but the measured value of the lower deflection in the middle of the main span was 87 mm, which was an actual 28 mm lower deflection than the theoretical lower deflection. When the bridge was completed in 2003, the measured elevation of the main span should have been higher than the design value. The higher part should have been equal to the 10-year shrinkage creep value plus 0.5 times the deflection value generated by the live-car load. In fact, the measured elevation of the main span was 56.743 m, which was 18 mm lower than the designed elevation of
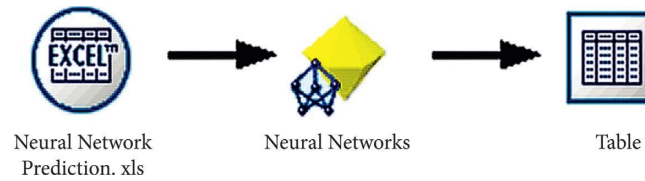
FIGURE 8: Data flow diagram of neural network prediction.
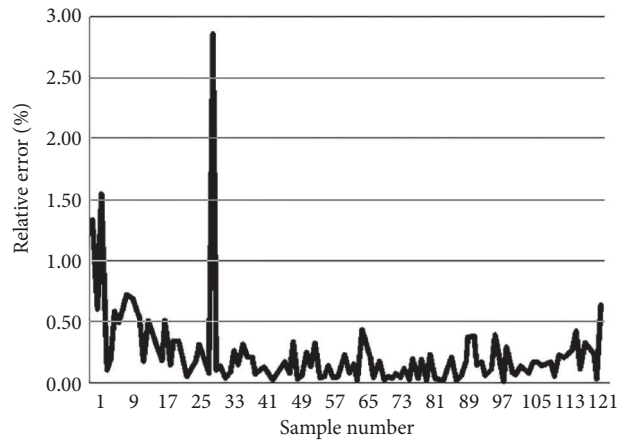
FIGURE 9: Network prediction error curve.

FIGURE 10: Appearance images.

56.761 m. Clearly, the bridge deck alignment of the main span was significantly lower than the design value. This was known from comprehensive test results and theoretical results of the whole bridge cable force and linear shape. Seven years after the bridge was opened to traffic, the change range of the cable force-line shape was within a small range and the line-shape change value was basically consistent with the theoretical value. Change in the cable force was not large, but there was a slight difference from the theoretical value in the specific change trend. At the same time, there was a large deviation between the current actual and designed alignments. The actual measurements of the bridge deck alignment are shown in Figure 11.

Based on the above two inspection contents, according to the ratio of bridge deflection change

and the influence of sheath rupture on the galvanized high-strength (Figure 11) steel wire of the inner stay cable, the safety evaluation index from the appearance inspection was given as $P1 = 0.8764$.

(3) In the state of no vehicle load on the bridge deck, data collection was performed on the permanent strain detection points embedded in the stay cables. Comparison results showed that there was no clear tensile strain at each measuring point during monitoring. Therefore, it was considered that there has been no prestress loss in the stay cable and the stress state of the stay cable had not changed significantly. The bridge safety assessment index for the stay cable was given as $P3 = 0.9544$.

(4) During monitoring, the natural frequency of the bridge was observed and the data analyzed in the frequency domain of a sports car, thus establishing a
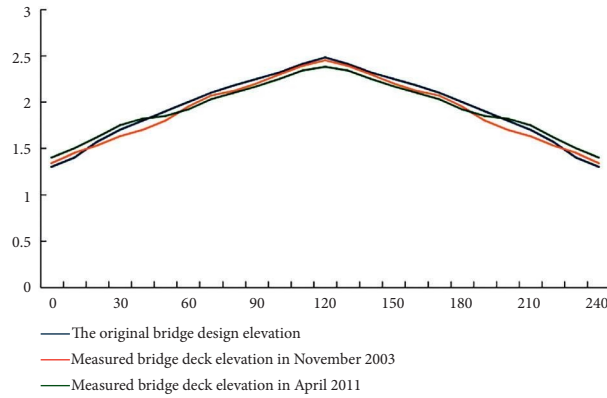
FIGURE 11: Alignment of main girder monitoring summary.
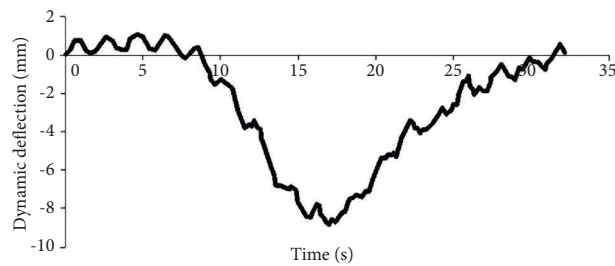
FIGURE 12: Time-history of the midspan dynamic deflection of the main span.

TABLE 10: Summary of security assessment indicators.

Indicator name	Stress amplitude	Corrosion degree	Sheath damage	Damping system
Value	0.9544	0.9821	1.10	1.20

dynamic model of the bridge. At measuring points in the middle of the main span, the frequencies of grades 1–8 were 0.51, 1.37, 2.85, 2.95, 3.09, 3.24, 3.38, and 5 Hz, respectively. The time-history of the midspan dynamic deflection of the main span was then plotted (see Figure 12).

Through the above dynamic testing and theoretical calculations, the first-order symmetrical vertical bending of the midspan was found to be 0.490106 Hz with the test value being 0.51 Hz. The first-order antisymmetric vertical bending of (Figure 12) the midspan was 0.759268 Hz and the test value was 0.86 Hz. The measured value of the bridge frequency was seen to be greater than the theoretical value (but the difference was small), which indicated that the bridge's dynamic stiffness met the design requirements. At the same time, it should be noted that the two most important frequencies were basically the same as the test values of the completion test in November 2003, with the difference also being very small. This showed that the dynamic characteristics of the bridge's structure corresponding to the second-order frequency did not change and the stay-cable damping system was intact.

5.2. Safety Evaluation Index of Single-Plane Cable-Stayed Bridge. Combined with previous theoretical research, the bridge safety assessment indicators were determined (see Table 10).

6. Conclusions

By considering various existing data fusion algorithms and their practicality, this study integrated rough sets and neural networks, which learned from each other's strengths and complemented each other. From this, a rough neural algorithm was constructed, which was then applied to bridge safety evaluation. Four indicators were input into the trained neural network model, yielding a predicted value of 1.041 (see Table 10). According to the safety level evaluation standard, the safety level of the bridge was seen to be Class II (see Table 9). The safety reserve of the bridge met the current use requirements, which was consistent with the direct detection conclusion. The validity and accuracy of the evaluation model were demonstrated and the specific conclusions are as follows:

(1) The Kohonen neural network was applied to the safety evaluation of a cable-stayed bridge with reference to the building structure appraisal and rating method. The evaluation database was clustered and the evaluation labels corresponding to the five types of safety levels were obtained, which provided a corresponding reference for the safety evaluation of similar bridge types.

(2) Combined with bridge safety evaluation data, four indices of stress amplitude, corrosion degree, sheath damage, and damping system were selected as attribute indices. Taking the bridge structure safety appraisal coefficient K as the decision-making index, the safety evaluation database of Fumin Bridge was established.

(3) The training time of the simplified neural network was shortened and the training speed improved. Also, the neural network model possessed high simulation accuracy and the absolute error value between the predicted and theoretical values did not exceed 3%. This showed that the coarse neural network data fusion method could be used for bridge safety evaluation.

(4) During the safety evaluation of a cable-stayed bridge, entering the four specific attribute indices of the bridge directly, the current safety status of the bridge was quickly determined to be Class II. That is to say, the safety reserve of the bridge met the current use requirements and was consistent with the results of the testing unit. This showed that these evaluation results of this method were objective and could thus improve bridge evaluation work efficiency.

Data Availability

The data used to support the findings of this study are available from the corresponding author upon request.

Conflicts of Interest

The authors declare that there are no conflicts of interest regarding the publication of this paper.

Acknowledgments

References

[1] R. W. Soares, L. R. Barroso, and O. A. S. Al-Fahdawi, "Response attenuation of cable-stayed bridge subjected to central US earthquakes using neuro-fuzzy and simple adaptive control," *Engineering Structures*, vol. 203, Article ID 109874, 2020.

[2] H. Bonakdari, I. Ebtehaj, A. H. Azimi et al., "Pareto design of multiobjective evolutionary neuro-fuzzy system for predicting scour depth around bridge piers," *Water Engineering Modeling and Mathematic Tools*, vol. 2021, pp. 491–517, 2021.

[3] P. Sun, X. M. Hou, W. Z. Zheng, H. Qin, and G. Shao, "Risk assessment for bridge structures against blast hazard via a fuzzy-based framework," *Engineering Structures*, vol. 232, Article ID 111874, 2021.

[4] A. Bolar, S. Tesfamariam, and R. Sadiq, "Condition assessment for bridges: a hierarchical evidential reasoning (HER) framework," *Structure and Infrastructure Engineering*, vol. 9, no. 7, pp. 648–666, 2013.

[5] O. Caglayan, K. Ozakgul, O. Tezer, and E. Uzgider, "Evaluation of a steel railway bridge for dynamic and seismic loads," *Journal of Constructional Steel Research*, vol. 67, no. 8, pp. 1198–1211, 2011.

[6] Y. J. Kim, "Safety assessment of steel-plate girder bridges subjected to military load classification," *Engineering Structures*, vol. 38, pp. 21–31, 2012.

[7] Q. Wang, *Security Assessment Based on Time-dependent Reliability for Bridges*, Chongqing University, Chongqing, China, 2016.

[8] Q. Wang, *Safety Evaluation for Large-Span Steel Truss Tied Arch Bridges Based on Fuzzy Analytic Hierarchy Process*, Harbin Institute of Technology, China, 2016.

[9] Y. Yan, X. T. Wu, and Z. Y. Wu, "Bridge safety monitoring and evaluation based on hesitant fuzzy set," *Alexandria Engineering Journal*, vol. 61, no. 2, pp. 1183–1200, 2022.

[10] N. B. Wang, W. Shen, C. Guo, and H. P. Wan, "Moving load test-based rapid bridge capacity evaluation through actual influence line," *Engineering Structures*, vol. 252, Article ID 113630, 2022.

[11] M. Abedin, A. B. Mehrabi, M. Ghosn, A. Azizinamini, A. S. Nowak, and A. R. Babu, "Reliability evaluation of twin steel box girder bridges using a simplified metho," *Engineering Structures*, vol. 259, Article ID 114122, 2022.

[12] S. Dai, *Durability Evaluation of Concrete Structure*, Construction and Design for Project, 2013.

[13] R. Douglas Hooton, "Future directions for design, specification, testing, and construction of durable concrete structures," *Cement and Concrete Research*, vol. 124, Article ID 105827, 2019.

[14] S. Demis and V. G. Papadakis, "Durability design process of reinforced concrete structures Service life estimation, problems and perspectives," *Journal of Building Engineering*, vol. 26, Article ID 100876, 2019.

[15] H. K. Sugandhini, N. Sivadas, N. Sivadas, G. Nayak, and K. K. Shetty, "A review on concrete's durability in India Framework for performance-based approach," *Materials Today Proceedings*, vol. 60, no. 1, pp. 545–551, 2022.

[16] K. F. Zhang, "Research on durability design of concrete structure under chloride environment," *Advanced Materials Research*, vol. 926-930, pp. 623–626, 2014.

[17] H. H. Sun, J. Xu, W. Z. Chen, and J. X. Yang, "Time-dependent effect of corrosion on the mechanical characteristics of stay cable," *Journal of Bridge Engineering*, vol. 23, no. 5, 2018.

[18] B. Y. Zhao, X. P. Wang, C. Zhang, W. Li, R. Abbassi, and K. Chen, "Structural integrity assessment of shield tunnel crossing of a Railway Bridge using orthogonal experimental

design," *Engineering Failure Analysis*, vol. 114, Article ID 104594, 2020.

[19] X. K. Yan, "Analysis on safety management and risk early warning application of railway tunnel construction," *Value Engineering*, vol. 38, no. 30, 2019.

[20] *Ministry of Housing and Urban-Rural Development of the People's Republic of China," Code for Fire Protection Design of Building*, China Planning Press, China, 2014.

[21] H. Deng, C. Wen, and X. Wang, *Research on Structural Robustness for Cable-stayed Bridge without Back-Stays*, Journal of Shijiazhuang Tiedao University, China, 2016.

[22] X. Wu, J. Yuan, and A. Ben, "A novel magnetic testing method for the loss of metalliccross-sectional area of bridge cables," *International Journal of Applied Electromagnetics and Mechanics*, vol. 39, no. 1-4, pp. 195–201, 2012.

[23] D. H. Dan, Y. M. Zhao, T. Yang, and X. F. Yan, "Health condition evaluation of cable-stayed bridge driven by dissimilarity measures of grouped cable forces," *International Journal of Distributed Sensor Networks*, vol. 9, no. 10, Article ID 818967, 2013.

[24] D. Zonta, F. Bruschetta, and R. Zandonini, "Analysis of monitoring data from cable-stayed bridge using sensor fusion techniques," *Sensors and Smart Structures Technologies for Civil, Mechanical and Aerospace Systems*, vol. 8692, pp. 643–650, 2013.

[25] W. Zhang, S. Liu, B. Sun, Y. Liu, and M. Pecht, "A cloud model-based method for the analysis of accelerated life test data," *Microelectronics Reliability*, vol. 55, no. 1, pp. 123–128, 2015.

[26] S. Q. Qin, J. B. Zhang, C. L. Huang, L. Gao, and Y. Bao, "Fatigue performance evaluation of steel-UHPC composite orthotropic deck in a long-span cable-stayed bridge under in-service traffic," *Engineering Structures*, vol. 254, Article ID 113875, 2022.

[27] Y. F. Li, X. L. Sun, and L. S. Bao, "PC cable-stayed bridge main girder shear lag effects: assessment of single cable plane in construction stage," *Advances in Materials Science and Engineering*, vol. 2020, pp. 1–16, Article ID 2646513, 2020.

[28] B. Chen, X. Wang, D. Z. Sun, and X. Xie, "Integrated system of structural health monitoring and intelligent management for a cable-stayed bridge," *The Scientific World Journal*, vol. 2014, Article ID 689471, 12 pages, 2014.

[29] H. D. Peng, D. W. Liu, J. Ma, and G. Yang, "Quality degrading evaluation for the lining structure of longtime shutdown tunnels based on cloud model," *Journal of Safety and Environment*, vol. 17, no. 04, pp. 1232–1236, 2017.

[30] B. W. Wei, H. P. Huang, and K. W. Xu, "Two-dimensional evaluation model of rock mass based on combination weighting and cloud model," *Chinese Journal of Rock Mechanics and Engineering*, vol. 35, no. I, pp. 3092–3099, 2016.

[31] Y. Ren, Z. Y. Zhu, Z. Y. Fan, Q. Huang, and T. T. Zhang, "Estimation of extreme cable forces of cable-stayed bridges based on monitoring data and random vehicle models," *Advances in Civil Engineering*, vol. 2021, pp. 1–15, Article ID 8897427, 2021.

[32] M. R. Kaloop, J. W. Hu, and J. W. Xiang, "Stayed-cable bridge damage detection and localization based on accelerometer health monitoring measurements," *Shock and Vibration*, vol. 2015, pp. 1–11, Article ID 102680, 2015.

[33] H. L. Fu, Z. Huang, H. W. Huang, and J. B. Zhang, "Health diagnosis method of shield tunnel structure based on cloud theory," *Journal of Engineering Science*, vol. 39, no. 05, pp. 794–801, 2017.

[34] P. Wen, I. Khan, H. Jie, C. Qiaofeng, and Y. Shiyu, "Online intelligent identification of modal parameters for large cable-stayed bridges," *Shock and Vibration*, vol. 2020, pp. 1–17, Article ID 2040216, 2020.

[35] J. Wang, J. Han, J. Chen et al., "Experimental and numerical study on the dynamic response of a superthick backfill subgrade under high-speed railway loading: a case study of Qianjiang-Zhangjiajie-Changde Railway," *Journal of Construction Engineering and Management*, 2022.

Research Article

Analysis of Extent of Deformation Range and Failure Characteristics of Rocks Surrounding a Tunnel Crossing Fault Zone Based on FDEM

Guo Xiaoxiong,[1,2] Wang Ning [iD],[3] Xu Xueliang,[1,2] and Ye Zihui[3]

[1]*Railway Engineering Research Institute, China Academy of Railway Sciences Corporation Limited, Beijing 100081, China*
[2]*State Key Laboratory for Track Technology of High-Speed Railway, Beijing 100081, China*
[3]*Jiangxi Key Laboratory of Infrastructure Safety Control in Geotechnical Engineering, East China Jiaotong University, Nanchang 330013, China*

Correspondence should be addressed to Wang Ning; wn1290@163.com

The combined finite-discrete element method (FDEM) and laboratory test were selected to study the extent of deformation range and time-dependent deformation of surrounding rock during tunnel excavation without support in a fault-crossing tunnel project. FDEM was found to accurately reflect the deformation and failure characteristics of different surrounding rocks during stress release, including conjugate shear and extrusion. Analysis of the results showed that the disturbance range of surrounding rocks could reach 1.5 to 2.5 times the tunnel diameter when crossing the fault zone. The rock surrounding the tunnel was found to incur significant conjugate shear deformation and extrusion deformation: conjugate shear deformation was identified as dominant in the deep rock mass, whereas extrusion deformation prevailed in the rock mass near the cave wall. The conjugate shear distribution was represented as a spiral line of deformation circling around the tunnel section, with an elliptical main deformation zone with its long axis parallel to the fault plane. Compared with the findings when crossing the intact rock mass, the deformation of the surrounding rocks when crossing the fault zone was characterized by rapid development, deep expansion area, and large deformation. The study conclusions were that supporting bolts and steel arches should be implemented timely when excavating fault zones and that both lithology and optimal construction timing were essential considerations in determining the length of the supporting bolts.

1. Introduction

Due to the diversity of stratigraphic conditions, it may be necessary for many mountain tunnels to cross fault zones, some of which may be active. Active fault zones are often accompanied by varying degrees of unfavorable geological conditions. For example, rock mass characteristics within fault zones usually include high susceptibility to fracturing and weathering, poor strength, and significant differences from the surrounding rock. When a tunnel passes through a fault zone, considerable deformation occurs, potentially alongside serious problems such as tunnel face instability, collapsing of the tunnel wall, and supporting structural failure [1–5]. In his study, Terzaghi [6] ascribed the large extrusion deformation in the tunnel to the considerable amount of clay minerals present in the rock, suggesting that the volume of this rock mass slowly increased and then intruded into the tunnel clearance. The actual sampling at the engineering site showed that the rock mass within a certain range of the fault zone and its surrounding area contained very high clay minerals. Terzaghi [6] therefore concluded that the deformation in the vicinity of the tunnel crossing fault zone could be attributed to the significant deformation of local soft rocks.

Extensive research has been carried out on fault-crossing tunnels, including analysis models, experiments, and numerical

simulation. Key influencing factors of fault zones studied have included the fault zone width, soil properties, and the intersection angle between tunnel axis and fault zone [7, 8]. Tunnelling research subjects have encompassed surrounding rock deformation, internal forces, tunnel lining deformation, and the advantages and drawbacks of a range of construction measures [9–13]. In many research hotspots, the deformation of surrounding rocks during excavation has been ignored, that is, the development of crack or deformation of rock mass around the tunnel in the vertical direction, especially in the engineering project crossing the active fault zone. Since active fault zones are usually accompanied by high tectonic stresses, tunnel excavations produce a release of initial stress in the rock mass. This stress release leads to a deep deformation of surrounding rocks, the most significant instance being the rock burst phenomenon of hard rock with high ground stress. A stress release gradient change occurs from the inner wall of the tunnel to the rock mass, causing problematic issues such as the area of influence of rock mass deformation, and the potential presence of cracks in the rock mass. Fractures within the rock mass have important repercussions on the waterproofing and drainage maintenance systems throughout the tunnel operation period. Rigorous research is therefore urgently required on this subject.

To date, numerical simulation has been the most favored method for tunnel analysis, commonly using numerical software such as FLAC3D, Plaxis, and ABAQUS [14–17]. The finite-discrete element method is a common numerical tool to analyze fracture development, in particular the typical one is the combined finite-discrete element method (FDEM) [18–23]. It can simulate the behavioral process of materials from continuous deformation to discontinuous deformation. In the field of civil engineering, this method has been applied to analyze the deformation of rocks surrounding highway construction and the development of cracks in concrete structures and to perform simulation tests of the mass strength of various rock and soil types [24–27], all of which demonstrated good computational and simulation performances.

In the present study, set in an engineering context of a tunnel crossing a fault zone, laboratory testing and the FDEM were implemented to establish the law determining the area affected by rock mass deformation caused by tunnel excavation around the site where the tunnel crossed the fault zone. The failure mechanism of rock mass within the fault zone was revealed, which in the authors' view provided valuable references for preventive measures against rock deformation in future projects involving tunnel excavations.

2. Basic Principles of FDEM Numerical Simulation

FDEM was first proposed by Munjiza et al. [28–30] in 1995. In 2004, they proposed a complete set of theories and developed the corresponding calculation program Y-Code. However, as the initial version of the computation program, the Y-Code still presents numerous problems to this day. For example, quasistatic friction is not achieved, contact energy

dissipation is not considered, and the Mohr–Coulomb shear strength criterion is not realized. Therefore, Mahabadi et al. proposed an improved version of Y-Geo in 2012 based on the Y-Code [31], which made the FDEM constitutive model and strength criterion more consistent with the mechanical properties of rock materials. Moreover, a corresponding preprocessor Y-GUI [32] was developed to quickly assign corresponding attributes to model elements and nodes.

The basic principle of FDEM can be summarized as follows: the intact material was divided into triangular elements, and quadrilateral joint elements with initial zero thickness were inserted at the boundary of the triangular elements. The longest side of the quadrilateral elements was shared with a triangular element, and the shortest side of the quadrilateral elements coincided with the line of adjacent nodes, as shown in Figure 1(a) (the initial thickness exists). The triangular elements represented the constant strain elements, and their Cauchy deformation stress was solved by the generalized application of Hooke's law. Moreover, the triangular elements only sustained elastic deformation, as opposed to plastic deformation or fracture failures. The plastic yield and fracture failure of rock materials were represented by the quadrilateral joint elements. The state of the quadrilateral joint elements was determined according to the relative tensile or shear displacement between nodes, as shown in Figure 1(b). When two of the three nodes in the quadrilateral elements (points A, B, and C in Figure 1(a)) reached either the ultimate tensile displacement or the shear displacement sr, the fracture failure occurred in the joint elements. The triangular elements were transformed on both sides from a bonding relationship to a contact relationship. The bond stress calculation program for the joint elements was no longer implemented and the contact stress was solved by potential functions. The advantage of potential functions was that the contact stress consisted of distributed stress rather than concentrated stress, which was more consistent with the real contact relationship of the block, thus avoiding the need to conduct fillet processing.

The constitutive equations of the quadrilateral joint element were

$$\sigma_n = \begin{cases} \dfrac{o}{o_p} \cdot f_t, o < o_p, \\ \\ z \cdot f_t, o_p < o < o_t, \end{cases}$$

$$\tau = \begin{cases} \dfrac{s}{s_p} \cdot c, s < s_p \text{ and } \sigma_n > 0, \\ \\ \dfrac{s}{s_p} \cdot (c - \sigma_n \tan \varphi_i), s < s_p \text{ and } \sigma_n < 0, \\ \\ z \cdot c, s_p < s < s_t \text{ and } \sigma_n > 0, \\ \\ z \cdot c - \sigma_n \tan \varphi_i, s_p < s < s_t \text{ and } \sigma_n < 0, \end{cases} \tag{1}$$

where σ_n and τ are normal and tangential stresses ($\sigma_n > 0$ represents tensile stress, and $\sigma_n < 0$ represents compressive stress); o and s are normal and tangential displacements; o_p
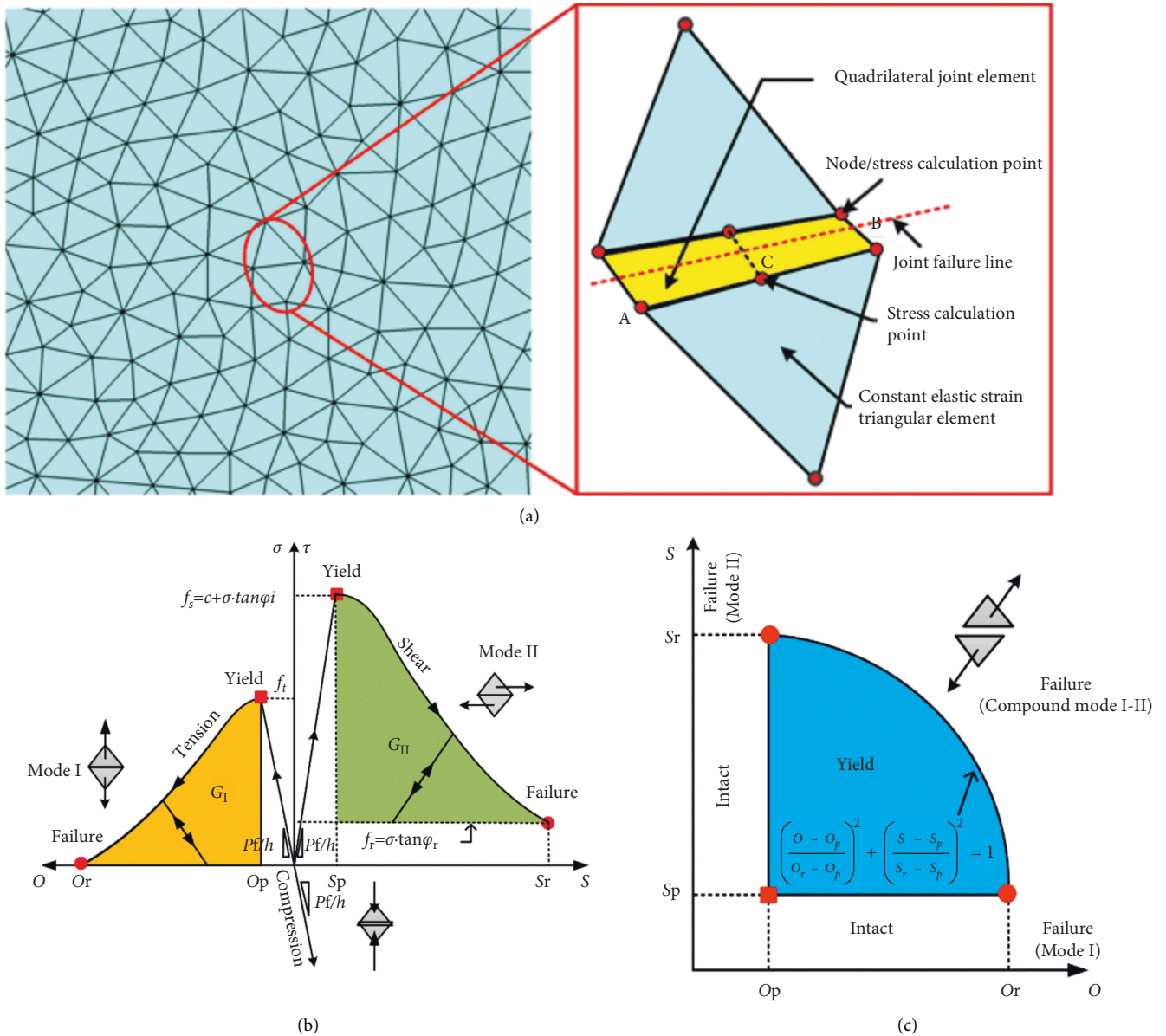
FIGURE 1: Triangular meshing and failure modes of joint elements. (a) Triangular and quadrilateral grids. (b) Failure modes I and II. (c) Compound failure modes I and II.

and s_p are normal and tangential peak displacements; and o_t and s_t are normal and tangential ultimate displacements. It can be observed that when the tensile or shear displacement of the joint element reached its corresponding limit value, the joint element fractured and failed; c is the cohesion; φ_i is the internal friction angle; f_t is the tensile strength; and z is the post-peak softening function [33].

3. Project Overview

The rock strata around the tunnel line mainly consisted of quartz sandstone, slate, and quartz diorite. The tunnel crossed an active fault zone with a small angle. The fault zone was a normal fault with a dip angle of 64~80°. The width of the core fault zone was about 7 m, and the width of the fault

zone was about 60 m. The tunnel was about 235 m deep, while the depth of groundwater was about 5 m. The results of the ground stress tests showed that the horizontal ground stress of surrounding rocks was dominant, which was measured at about 17.5 MPa. At the same time, the rock mass near the fault zone was fractured and formed part of an area of significant, widespread deformation, which was prone to major tunnel deformation. The tunnel was a double-line tunnel with a diameter (d) of about 13.5 m and an included angle between the tunnel axis and fault strike of about 14°. The plane relationship between tunnel and fault is shown in Figure 2. According to the tunnel crossing the strata, three working cases were selected: (I) the tunnel crossed the intact rock mass; (II) the tunnel crossed the fault fracture zone; and (III) the tunnel crossed the fault core

(a)

(b)

(c)

(d)
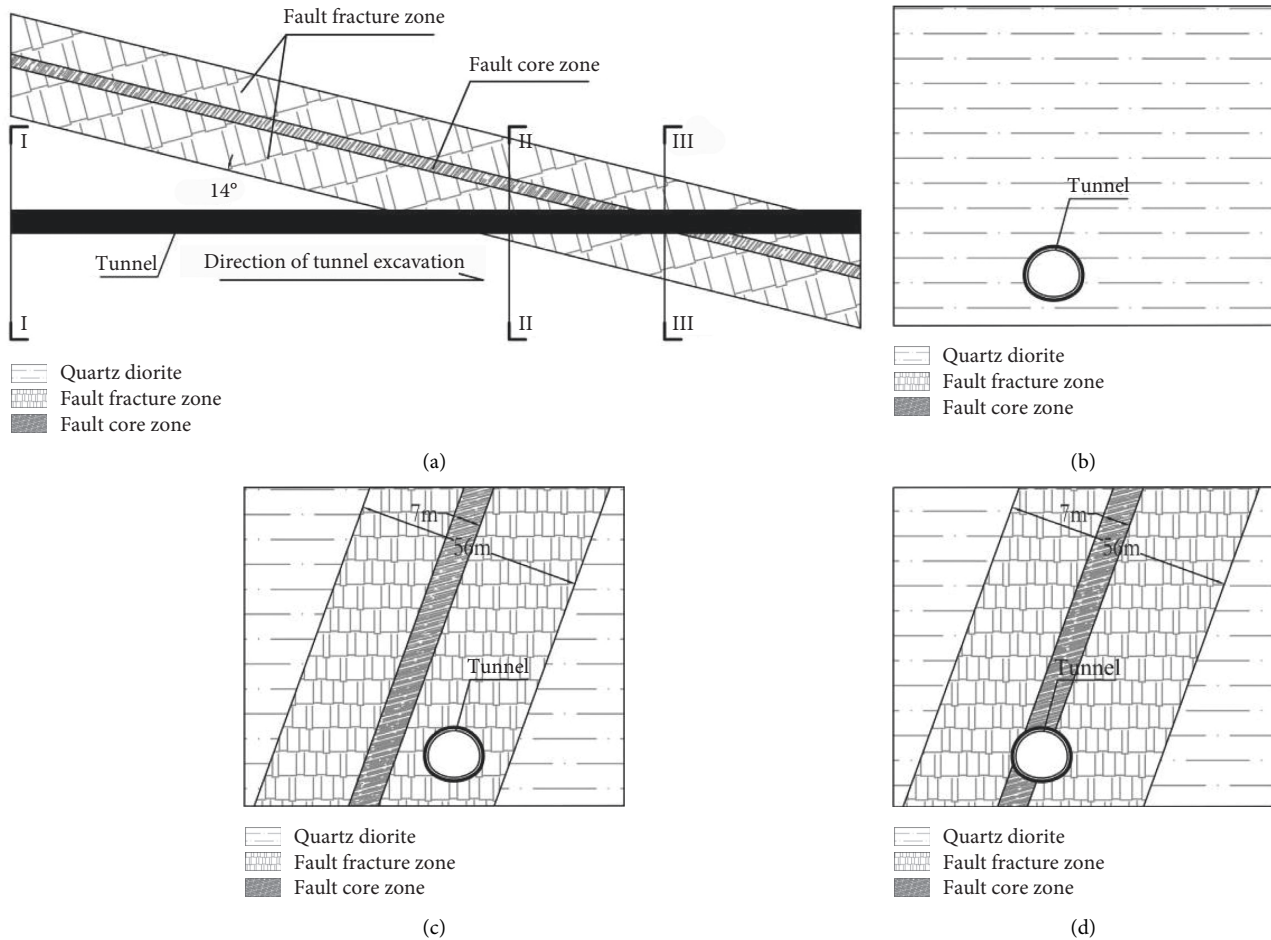
FIGURE 2: Plane schematic diagram of tunnel crossing fault zone. (a) Cross-section. (b) I-I profile section. (c) II-II profile section. (d) III-III profile section.

zone. Then, the difference in deformation of the surrounding rocks was compared and analyzed at the point where the tunnel effectively crossed the fault zone.

4. Soil Parameter Test

Rock samples representing different rock masses in three typical sections were obtained from different excavation locations along the tunnel. The three types of rock samples were as follows: (a) weakly weathered quartz diorite representing the original rock; (b) highly weathered quartz sandstone representing the fault zone; and (c) fully weathered soil representing the fault core zone.

The production process and core samples of quartz diorite are shown in Figure 3. The core size was 50 mm in diameter and 100 mm in height. The mineral composition and mechanical properties of the rock samples were tested. The main minerals in the rock samples were potassium feldspar, albite, and quartz. Saturated uniaxial compressive strength tests and Brazilian splitting tests were conducted on the samples, and the test results are shown in Table 1.

The rock samples of strongly weathered quartz sandstone are shown in Figure 4. In their natural state, the rock samples were massive and without any obvious structural cleavage. It thus proved challenging to obtain regular cores

using the sampler, and the rock samples could be crushed by hand. The saturated uniaxial compressive strength of the rock samples was less than 1 MPa. The initial average water content and initial density of the rock samples were 1.8% and 2.49 g/cm^3, respectively. The rock samples were mainly composed of albite and quartz with poor resistance to disintegration. Due to the weakness of the rock samples, they were destroyed and remodeled; the triaxial consolidated drained tests were carried out. The soil parameters obtained in the test are shown in Table 2.

The rock mass in the fault core zone had essentially been fully weathered into the soil, as shown in Figure 5. The soil samples were found to belong to gravel soil, and the grains mainly consisted of sand while also containing some clay and block stones. The block stone size distribution was mainly between 20 and 150 mm. A triaxial consolidated drained test was performed on the undisturbed soil samples containing block stones. The soil parameters obtained in the test are shown in Table 2.

5. Numerical Model

The FDEM numerical simulation model was established on the basis of three different profiles, as shown in Figure 6. The model size was 140 m × 140 m and was divided into three

(a)   (b)   (c)

FIGURE 3: Production process and core samples of quartz diorite. (a) Core processing. (b) Rock samples. (c) Rock triaxial loading device.

TABLE 1: Strength parameters of rock samples.

Experiment content	Test strength (MPa)	Mean value (MPa)
Saturated uniaxial compressive strength	93.00	102.44
	97.86	
	116.45	
Saturated Brazilian splitting test	2.55	2.18
	2.26	
	1.73	

(a)   (b)

FIGURE 4: Strongly weathered quartz sandstone and test instruments. (a) Strongly weathered quartz sandstone. (b) GDS hollow cylinder torsional shear instrument.

TABLE 2: Test soil parameters.

Soil name	Density (g/cm^3)	Cohesion (kPa)	Internal friction angle (°)
Strongly weathered quartz sandstone	2.49	14.5	35.4
Fully weathered soil in the fault core zone	2.26	3.7	35.8

sectors: a tunnel sector, a mesh refinement sector, and a far-field sector. The diameters of the tunnel and the mesh refinement areas were 13.5 m and 60 m, respectively. The mesh sizes of the tunnel boundary and the model boundary were 0.15 m and 10 m, respectively. Under two-dimensional plane strain conditions, the tunnel excavation process could be divided into two stages: a ground stress loading stage and a tunnel excavation stage. The model boundary was free at the ground stress stage and fixed at the tunnel excavation stage. After the ground stress had been applied and the model reached equilibrium, a core material softening method was adopted to reflect the gradual weakening process of the radial support effect on the tunnel face. In other words, the elastic modulus and viscous damping of the material in the tunnel region were gradually weakened, and the softening of each step had to ensure that the response of surrounding rocks caused by the softening of the previous step reached equilibrium before it could be performed. The input parameters are the ones listed in Table 3.

(a)   (b)   (c)
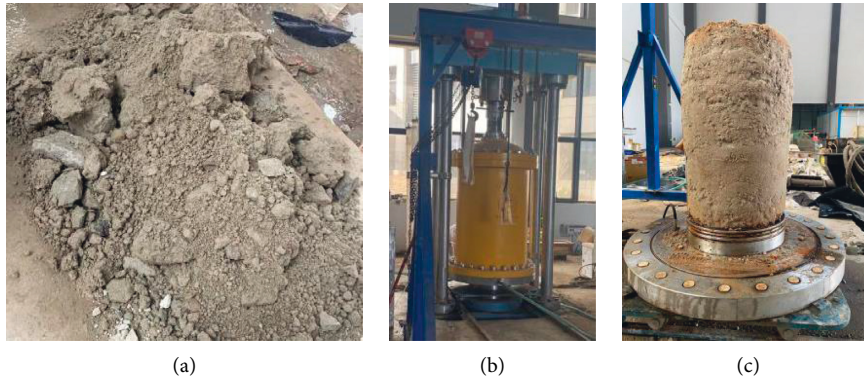
FIGURE 5: Soil samples in the fault core zone and testing instruments. (a) Soil sample in the fault core zone. (b) Triaxial tester. (c) Soil sample after the test.

(a)   (b)   (c)
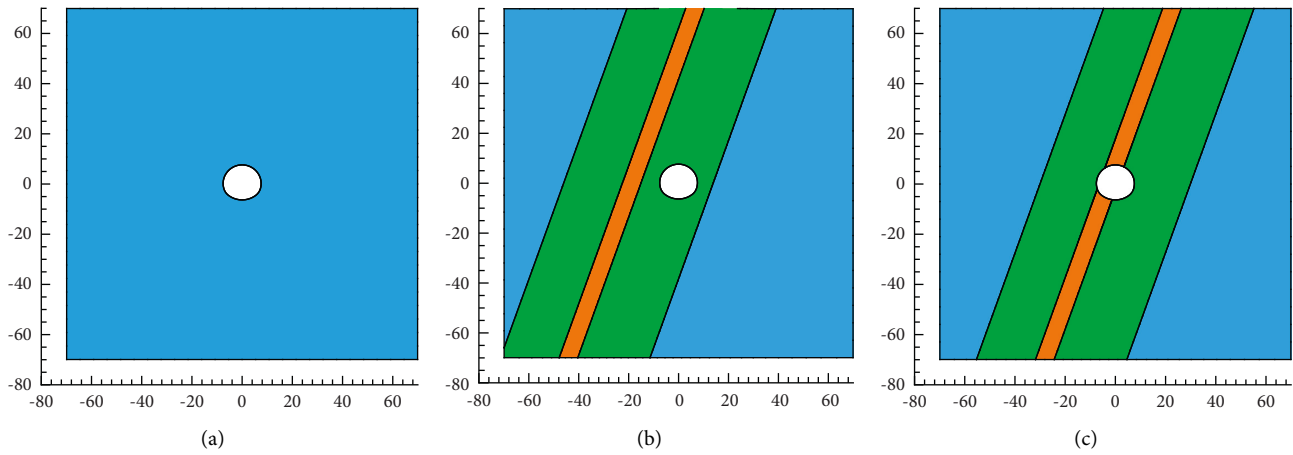
FIGURE 6: The FDEM numerical model. (a) Crossing the intact rock (case 1). (b) Crossing the fault fracture zone (case 2). (c) Crossing the fault core zone (case 3).

TABLE 3: Input parameters of tunnel excavation introduced in the FDEM numerical model.

Parameter	Mildly weathered quartz diorite	Strongly weathered quartz sandstone	Fully weathered soil
Triangular element parameter			
Density, ρ (kg/m^3)	2490	2490	2260
Elastic modulus, E (GPa)	50	25	20
Poisson's ratio, v	0.25	0.25	0.25
Mesh size around the tunnel, h(m)	0.15	0.15	0.15
Viscous damping, μ (kg/m·s)	$2h\sqrt{E\rho}$		
Calculation step, Δt (s)	1e-7		
Quadrilateral joint element parameter			
Tensile strength, f_t (kPa)	2180	4.2	1.3
Cohesion, c (kPa)	7000	14.5	3.7
Type I fracture energy, G_I (J/m^2)	10,000	1,000	400
Type II fracture energy, G_{II} (J/m^2)	20,000	4,000	1,000
Internal friction angle, φ_i (°)	28	35.4	35.8
Sliding friction angle, φ_r (°)	28	35.4	35.8
Normal contact stiffness, P_n (GPa)	100	50	40
Tangential contact stiffness, P_t (GPa)	100	50	40
Joint penalty, P_f (GPa)	100	50	40
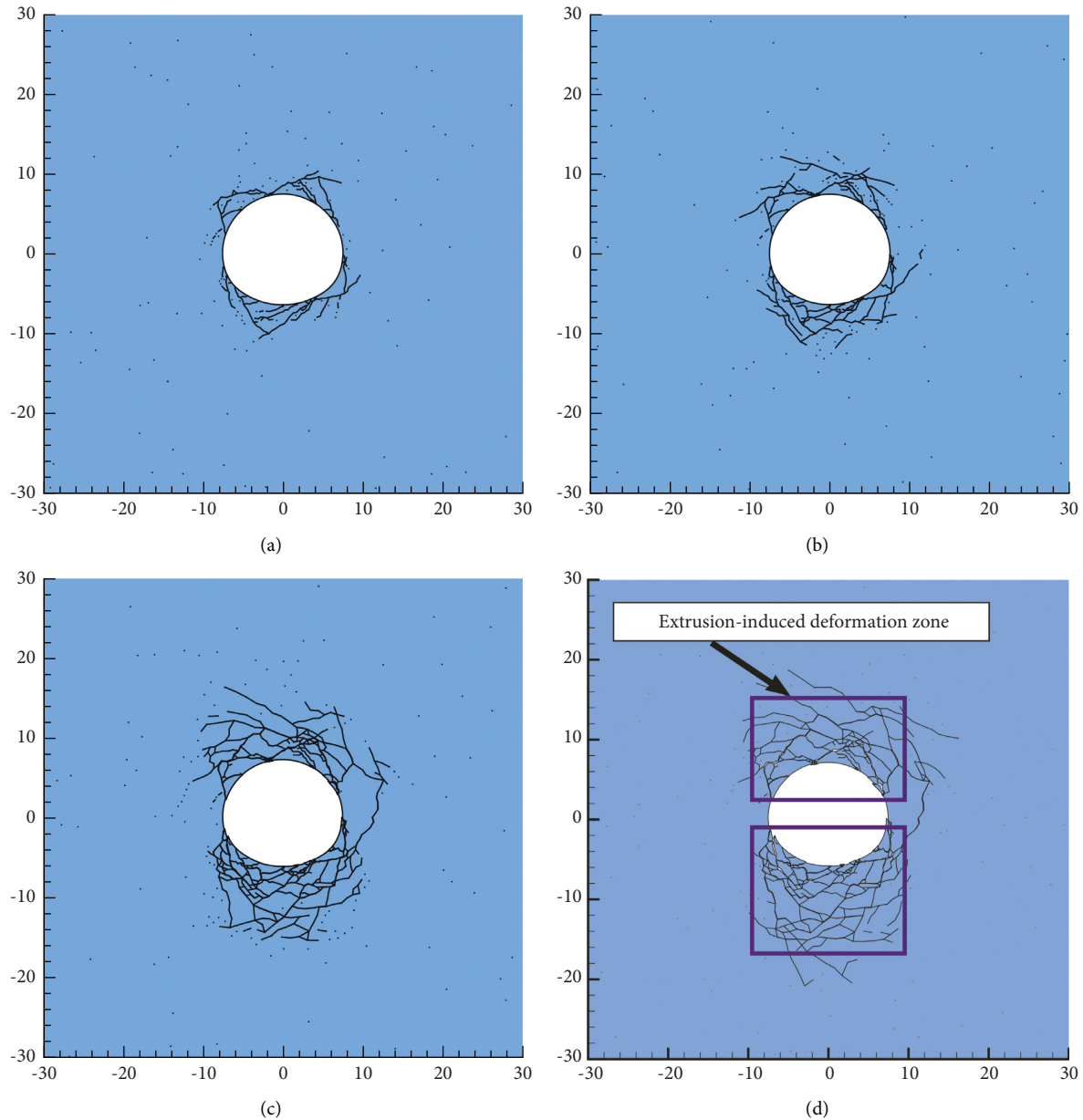
FIGURE 7: Development of the law determining the area of surrounding rock deformation (case 1). (a) 2.1 million step. (b) 2.4 million step. (c) 3.0 million step. (d) 4.2 million step.

6. Data Calculation and Analysis

6.1. Development of an Analysis Method of the Area of Surrounding Rock Deformation during Excavation of the Intact Rock Mass. Figure 7 shows the regional development of deep deformation of surrounding rocks caused by stress release during tunnel excavation of the intact rock mass without support. At the initial stage of excavation, the deformation development area was found to be shallow, mainly occurring at the top and bottom of the tunnel. With the further distribution of stress release of the surrounding rock to the deep area, the deformation zone expanded further and eventually reached an area equal to one time the hole diameter. Within 0.1 d of the vault, the obvious surrounding rock fracture occurs.

6.2. Analysis Development of the Area of Surrounding Rock Deformation during Excavation of the Fault Fracture Zone. Figure 8 shows the regional development of deep deformation of surrounding rocks caused by stress release during tunnel excavation of the fault fracture zone without support. At the initial stage of excavation, the deformation only occurred within the crushing zone and mainly at the top and bottom of the tunnel, showing distinct conjugate shear deformation characteristics. With the wider distribution of stress release to the deep area of the surrounding rock, the deformation zone expanded further. The side close to the fault core zone was found to have a deeper development area which could exceed 1.5 times the cavity diameter. The conjugate shear line density was significantly
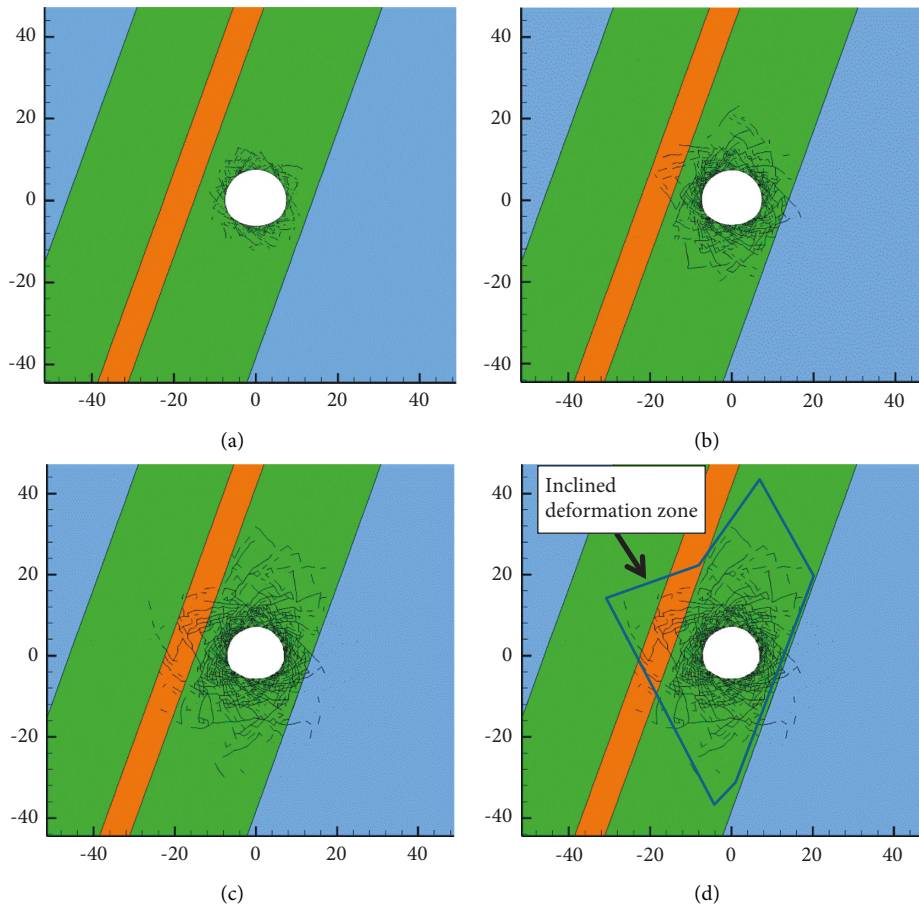
FIGURE 8: Development of the law determining the area of surrounding rock deformation (case 2). (a) 2.1 million step. (b) 2.4 million step. (c) 3.0 million step. (d) 4.2 million step.

higher than that of the intact rock mass excavated. The surrounding rock near the tunnel wall shifted from incurring shear failure to extrusion failure.

6.3. Analysis Development of the Area of Surrounding Rock Deformation during Excavation of the Fault Core Zone. Figure 9 shows the regional development of deep deformation of the surrounding rocks caused by stress release during tunnel excavation of the fault core zone without support. It can be observed that when the fault core zone was being crossed, the surrounding rock deformation zone quickly expanded and that shear deformation and extrusion deformation coexisted at the initial stage of excavation. With the continuous release of stress into the surrounding rock, the deformation zone increased rapidly, whereas the rock mass near the tunnel was mainly characterized by extrusion deformation, the deep rock mass predominantly incurred conjugate shear deformation. The approximate elliptic deformation range was established by taking the axis close to the fault core zone as the long axis, while the main deformation zone could approximately exceed twice the cavity diameter. The conjugate shear line could bypass the tunnel to form a long spiral that snaked its way through up and down, while the main deformation zone formed an ellipse with the long axis parallel to the fault plane.

6.4. Comparative Analysis of Surrounding Rock Deformation Development in Different Excavation Areas. Figure 10(a) shows the final development trend of the surrounding rock deformation zone when crossing the intact rock mass or the fault zone, and the range varied by 2.5 times. Compared with Figures 10(b) and 10(c), the final development depth of the surrounding rock deformation zone was close when crossing the fault fracture zone or the fault core zone, and the deformation was relatively intense. When crossing the fault fracture zone, the dense area of deformation fissures was within the range of 1.0 d. When crossing the fault core zone, the dense area of deformation fissures was within the range of 1.5 d.

The development of the deformation zone can be better observed from the displacement field nephogram of surrounding rocks illustrated in Figure 11. When crossing the intact monolayer rock mass, the main deformation of surrounding rocks was in the range of 7 m (about 0.5 d). The maximum deformation had occurred in the upper and lower sectors adjacent to the tunnel, with a value of about 0.5 m. When crossing the fault fracture zone, the deformation zone of surrounding rocks was within 15 m of the tunnel wall (about 1.0 d). The deformation at the top and bottom of the tunnel was significant, with a maximum of about 0.8 m. When crossing the fault core zone, the deformation area of
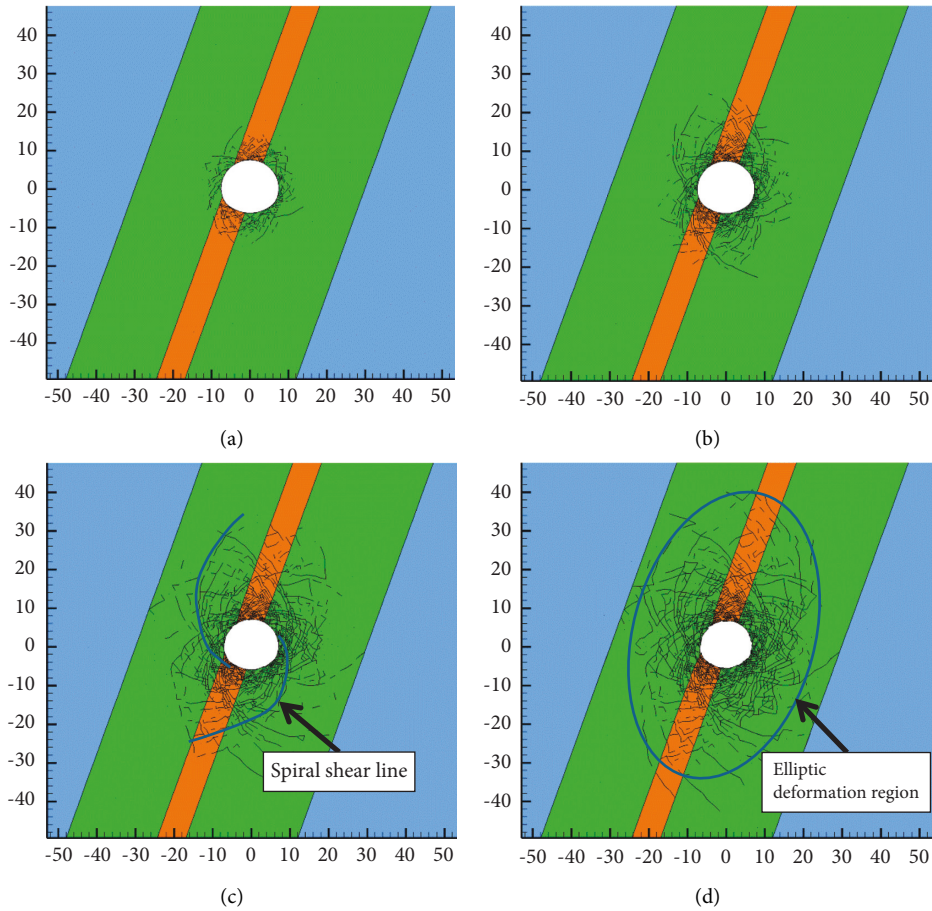
FIGURE 9: Development of the law determining the surrounding rock deformation zone (case 3). (a) 2.1 million step. (b) 2.4 million step. (c) 3.0 million step. (d) 4.2 million step.
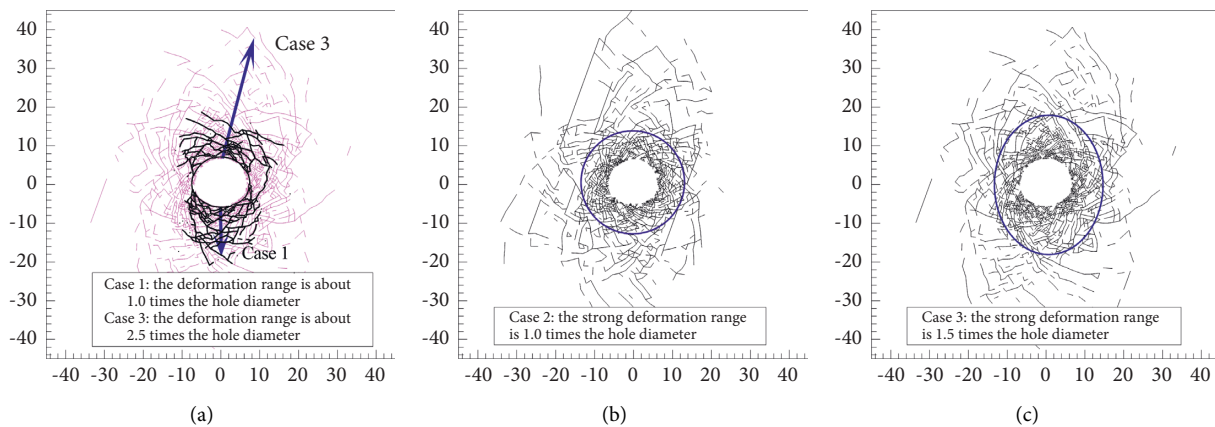
FIGURE 10: Schematic diagram of the development of surrounding rock deformation. (a) Comparison of the deformation range between working cases 1 and 3. (b) Schematic diagram of the strong deformation range in working case 2. (c) Schematic diagram of the strong deformation range in working case 3.

surrounding rocks was within 20 m of the tunnel wall (about 1.5 d). The deformation at the top of the tunnel was significant, with a maximum of about 1.2 m.

Figure 12 shows the maximum development range of surrounding rock deformation zones under different analysis steps (time) after excavation of different rock masses. The slope of the two curves during the excavation of the fault

zone can obviously be observed to be steeper than that during the excavation of the intact rock mass, indicating that the initial deformation developed faster in the fault zone due to the poor properties of the surrounding rocks.

The above analysis is based on unsupported excavation, which is corresponding to the situation in the time interval between the completion of tunnel excavation and the
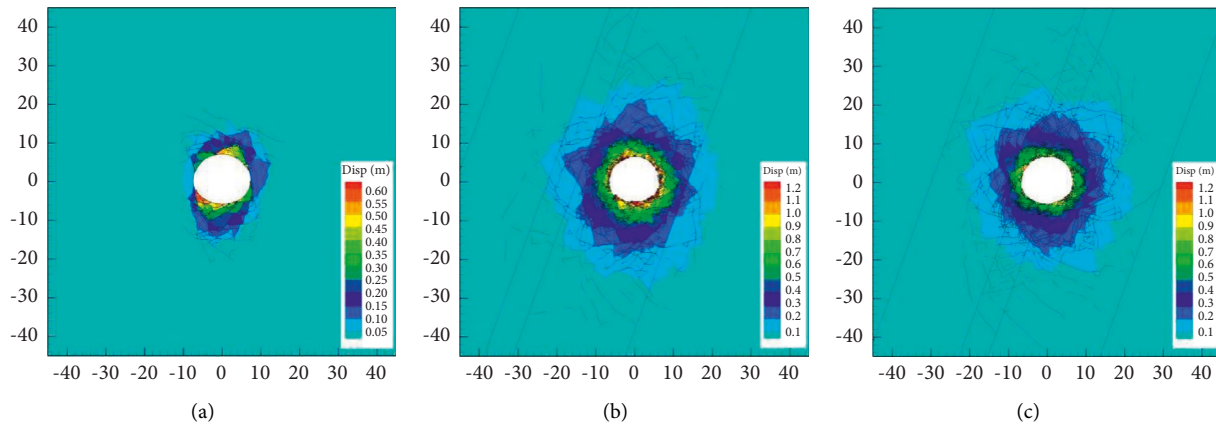
FIGURE 11: Nephogram of surrounding rock deformation and displacement. (a) Crossing the intact rock (case 1). (b) Crossing the fault fracture zone (case 2). (c) Crossing the fault core zone (case 3).
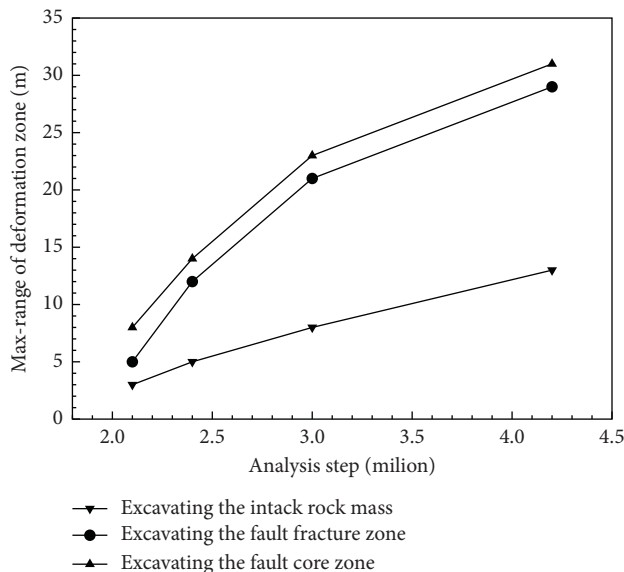
FIGURE 12: Maximum range of the surrounding rock deformation zone at different steps.

implementation of the support system. The increase in the analysis step represents the increase in the time. It can be seen that the deformation range of the surrounding rock is smaller if the supporting system (supporting bolts) is timelier completed. The development rule of the deformation range of the surrounding rock further indicates that the supporting bolt length is correlated with the construction promptness of the support system and the property of the rock mass.

7. Conclusions

In this study based on an actual project, the real rock mass parameters were obtained by analyzing the test results of different surrounding rock samples obtained from the project site. On this basis, the deformation development characteristics of surrounding rocks without support following tunnel excavation were analyzed by using the FDEM. The analysis results showed that

(1) The rock mass is more disturbed by the stress release from tunnel excavations when these cross a fault zone than under the conditions where tunnel excavations cross an intact rock mass. The range of disturbance can reach 1.5 to 2.5 times the tunnel diameter, and the strong disturbance area (where the displacement exceeds 0.2 m) can reach 1.0 to 1.5 times the tunnel diameter. This will provide guidance for determining the length of the supporting bolts.

(2) Compared with the extrusion deformation that occurs when a tunnel crosses an intact rock mass, conjugate shear deformation and extrusion deformation coexist when a tunnel crosses a fault zone. Conjugate shear deformation is dominant in the deep rock mass, and extrusion deformation is dominant in the rock mass near the cave wall. Therefore, appropriate supporting measures should be adopted in different zones with different deformation mechanisms.

(3) When crossing an intact rock mass, the surrounding rock deformations mainly occur in an approximately rectangular range that includes the top and bottom of the cave. No penetrating deformation line bypassed the tunnel section. When a tunnel crosses a fault zone, a spiral deformation line is formed around the tunnel section, and the main deformation zone takes an elliptical shape, the long axis of which lies parallel to the fault plane. This conclusion can provide a reference for the selection of the length of supporting bolts in different directions on the tunnel cross-section.

(4) Compared with the condition of a tunnel crossing an intact rock mass, the surrounding rock deformation develops more rapidly when a tunnel crosses a fault zone. Depending on the speed and range of development of deformation zones, the difference in length of any supporting bolts affixed to different surrounding rocks is significant. The length of applied bolts is determined both by the properties of

the surrounding rock and the timing of application. In addition, when being implemented in a fault zone, the construction and fitting of supporting bolts and steel arches must be completed timely, thus the fracture deformation of deep surrounding rock can be more efficiently controlled.

Data Availability

Some or all data, models, or code that support the findings of this study are available from the corresponding author upon reasonable request.

Conflicts of Interest

The authors declare that they have no conflicts of interest.

Acknowledgments

References

[1] J. G. Liu, X. J. Zhou, Q. H. Xiao, and W. Zhao, "Fault-related instability problems of tunnels - the host rock slip criterion and characteristics of the tunneling-induced shear displacements," *Stavebni Obzor Civil Engineering Journal*, vol. 26, no. 4, pp. 441–458, 2017.

[2] G. Bruneau, D. Tyler, J. Hadjigeorgiou, and Y. Potvin, "Influence of faulting on a mine shaft a case study: part I Background and instrumentation," *International Journal of Rock Mechanics and Mining Sciences*, vol. 40, pp. 95–111, 2003.

[3] L. Meng, T. Li, Y. Jiang, R. Wang, and Y. Li, "Characteristics and mechanisms of large deformation in the Zhegu mountain tunnel on the Sichuan–Tibet highway," *Tunnelling and Underground Space Technology*, vol. 37, pp. 157–164, 2013.

[4] M. Kun and T. Onargan, "Influence of the fault zone in shallow tunneling: a case study of Izmir Metro Tunnel," *Tunnelling and Underground Space Technology*, vol. 33, pp. 34–45, 2013.

[5] F. Suorineni, D. Tannant, and P. Kaiser, "Determination of fault-related sloughage in open stopes," *International Journal of Rock Mechanics and Mining Sciences*, vol. 36, no. 7, pp. 891–906, 1999.

[6] K. Terzaghi, "Rock defects and loads on tunnel supports," in *Rock Tunneling with Steel Supports*, R. V. Proctor and T. L. White, Eds., Commercial Shearing and Stamping Company, Ohio, OH, USA, 1946.

[7] S. Ma, L. Zhang, D. Wang, X. R. Tan, S. Li, and Y. Liu, "Analysis of tunnel lining failure mechanism under the action of active fault," *Shock and Vibration*, vol. 2021, Article ID 9918021, 11 pages, 2021.

[8] M. Ghafari, H. Nahazanan, Z. Md Yusoff, and N. N. Nik Daud, "A novel experimental study on the effects of soil and faults' properties on tunnels induced by normal and reverse faults," *Applied Sciences*, vol. 10, no. 11, p. 3969, 2020.

[9] P. Oreste and D. Pella, "Modelling progressive hardening of shotcrete in convergence-confinement approach to tunnel design," *Tunnelling and Underground Space Technology*, vol. 12, no. 3, pp. 425–431, 1997.

[10] F. Kimura, N. Okabayashi, and T. Kawamoto, "Tunnelling through squeezing rock in two large fault zones of the Enasan Tunnel II," *Rock Mechanics and Rock Engineering*, vol. 20, no. 3, pp. 151–166, 1987.

[11] T. Kondo, "The management problem of measurement and control in tunnel construction with the NATM," *Construction Technology*, vol. 11, pp. 76–80, 1977.

[12] D. Zhang, S. Liu, and S. Reng, "Research on selection of steel and steel grid for tunnel support in soft rock with high geostress," *Chinese Journal of Rock Mechanics and Engineering*, vol. 33, no. 11, pp. 2258–2266, 2014.

[13] G. Li and Y. Zhu, "Control technology for large deformation of high land stressed weak rock in wushaoling tunnel," *Journal of Railway Engineering Society*, vol. 3, pp. 54–59, 2008.

[14] Y. Ma, Q. Sheng, G. Zhang, and Z. Cui, "A 3D discrete-continuum coupling approach for investigating the deformation and failure mechanism of tunnels across an active fault: a case study of xianglushan tunnel," *Applied Sciences*, vol. 9, no. 11, p. 2318, 2019.

[15] H. Lan, C. D. Martin, and B. Hu, "Effect of heterogeneity of brittle rock on micromechanical extensile behavior during compression loading," *Journal of Geophysical Research*, vol. 115, no. B1, 2010.

[16] W. C. Zhu and C. A. Tang, "Micromechanical model for simulating the fracture process of rock," *Rock Mechanics and Rock Engineering*, vol. 37, no. 1, pp. 25–56, 2004.

[17] J. F. Hazzard, R. P. Young, and S. C. Maxwell, "Micromechanical modeling of cracking and failure in brittle rocks," *Journal of Geophysical Research: Solid Earth*, vol. 105, no. B7, Article ID 16683, 2000.

[18] T. M. He, Q. Zhao, J. Ha, K. Xia, and G. Grasselli, "Understanding progressive rock failure and associated seismicity using ultrasonic tomography and numerical simulation," *Tunnelling and Underground Space Technology*, vol. 81, pp. 26–34, 2018.

[19] H. Han, D. Fukuda, H. Liu et al., "Combined finite-discrete element modellings of rockbursts in tunnelling under high in-situ stresses," *Computers and Geotechnics*, vol. 137, Article ID 104261, 2021.

[20] A. Lisjak, Q. Liu, Q. Zhao, O. K. Mahabadi, and G. Grasselli, "Numerical simulation of acoustic emission in brittle rocks by two-dimensional finite-discrete element analysis," *Geophysical Journal International*, vol. 195, no. 1, pp. 423–443, 2013.

[21] A. Lisjak, B. S. A. Tatone, O. K. Mahabadi et al., "Hybrid finite-discrete element simulation of the EDZ formation and mechanical sealing process around a microtunnel in opalinus clay," *Rock Mechanics and Rock Engineering*, vol. 49, no. 5, pp. 1849–1873, 2016.

[22] P. Deng, Q. Liu, X. Huang, Q. Liu, H. Ma, and W. Li, "Acquisition of normal contact stiffness and its influence on rock crack propagation for the combined finite-discrete element method (FDEM)," *Engineering Fracture Mechanics*, vol. 242, no. 6, Article ID 107459, 2021.

[23] P. Deng and Q. Liu, "Influence of the softening stress path on crack development around underground excavations: insights from 2d-fdem modelling," *Computers and Geotechnics*, vol. 117, Article ID 103239, 2020.

[24] I. Vazaios, M. S. diederichs, and N. Vlachopoulos, "Assessment of strain bursting in deep tunnelling by using the finite-

discrete element method," *Journal of Rock Mechanics and Geotechnical Engineering*, vol. 11, no. 1, pp. 12–37, 2019.

[25] W. Wang, Q. Liu, H. Ma, H. Lu, and Z. Wang, "Numerical analysis of material modeling rock reinforcement in 2d fdem and parameter study," *Computers and Geotechnics*, vol. 126, Article ID 103767, 2020.

[26] Z. Wu, X. Ji, Q. Liu, and L. Fan, "Study of microstructure effect on the nonlinear mechanical behavior and failure process of rock using an image-based-fdem model," *Computers and Geotechnics*, vol. 121, Article ID 103480, 2020.

[27] A. Farsi, A. Bedi, J. P. Latham, and K. Bowers, "Simulation of fracture propagation in fibre-reinforced concrete using fdem: an application to tunnel linings," *Computational Particle Mechanics*, vol. 7, no. 5, pp. 961–974, 2020.

[28] A. Munjiza, D. R. J. Owen, and N. Bicanic, "A combined finite-discrete element method in transient dynamics of fracturing solids," *Engineering Computations*, vol. 12, no. 2, pp. 145–174, 1995.

[29] A. Munjiza, *The Combined Finite-Discrete Element Method*, John Wiley & Sons, London, UK, 2004.

[30] A. Munjiza, T. Bangash, and N. W. M. John, "The combined finite-discrete element method for structural failure and collapse," *Engineering Fracture Mechanics*, vol. 71, no. 4-6, pp. 469–483, 2004.

[31] O. K. Mahabadi, A. Lisjak, A. Munjiza, G. Grasselli, and Y. Geo, "Y-geo: new combined finite-discrete element numerical code for g applications," *International Journal of Geomechanics*, vol. 12, no. 6, pp. 676–688, 2012.

[32] O. K. Mahabadi, G. Grasselli, A. Munjiza, and Y. Gui, "Y-GUI: a graphical user interface and pre-processor for the combined finite-discrete element code, Y2D, incorporating material heterogeneity," *Computers & Geosciences*, vol. 36, no. 2, pp. 241–252, 2010.

[33] B. S. A. Tatone and G. Grasselli, "A calibration procedure for two-dimensional laboratory-scale hybrid finite–discrete element simulations," *International Journal of Rock Mechanics and Mining Sciences*, vol. 75, pp. 56–72, 2015.

Research Article

Experimental Study on Bearing Capacity of Normal- and High-Strength Steel Screw Anchors

Guodong Shao,[1] Xiao Lyu [ID],[2] Wenming Wang,[2] Shijun Ding [ID],[3] Jing Li,[1] Mintao Ding,[3] and Hanke Sheng[2]

[1]*PowerChina SEPCO1 Electric Power Construction Co., Ltd., Jinan 250102, China*
[2]*School of Civil Engineering, Shandong Jianzhu University, Jinan 250101, China*
[3]*China Electric Power Research Institute, Beijing 102401, China*

Correspondence should be addressed to Xiao Lyu; xiaolv_seu@126.com

In order to study the bearing capacity of high-strength steel screw anchors, six groups of screw anchors with different parameters are carried out in in situ construction and tensile capacity test, and the load-displacement curves of screw anchors with different parameters are obtained. The bearing mechanism, design method, and key design parameters of screw anchors are analyzed. Meanwhile, the test results are compared with theoretical calculation and numerical simulation, respectively. The results show that the drawing capacity of high-strength screw anchor calculated by the existing standard theoretical calculation formula is conservative. The load capacity of high-strength steel screw anchor is significantly higher than that of ordinary strength steel screw anchor. Taking steel strength, buried depth, quantity, distance, and diameter as the influencing factors, parametric analysis is conducted on the uplift capacity of high-strength steel screw anchor in this paper. The embedding depth of screw anchor, the number, spacing, and diameter of anchor plates have significant influence on the drawing capacity of screw anchor. The construction technology of high-strength steel screw anchor is reliable, and the bearing capacity is good, which can be applied in the soft-soil power transmission line projects, such as bog and coastal beach. Meanwhile, the research results can provide reference for the design and construction of screw anchor foundation.

1. Introduction

Foundation design must adhere to the principle of protecting environment and saving resources, according to the line topography, construction conditions, geotechnical engineering investigation data, and comprehensive consideration of foundation type and design scheme so as to achieve the purpose of safety and economic and reasonable foundation design [1]. Screw anchor foundation is mainly suitable for general soil, river, such as mud, coastal tidal flats soft-soil conditions, is a use of deep-soil anchor structure of the role of resistance to the upper structure, composed of a single weak screw anchor plate or one or more pieces of spacing and nonuniform welding in the round or square steel rod or long screw, when using installation of machinery in the top up a torque and spinning it straight into the ground. Manual drilling, mechanical drilling, and other construction methods can be adopted [2–5]. This type of foundation has the advantages of simple manufacturing, convenient installation and construction, fast drilling speed, and fast bearing capacity, can shorten the construction period, reduce the cost of the project, has small damage to the environment, high bearing capacity, and small deformation; screw anchor foundation has unique advantages in these aspects. The earliest use of screw anchors is dated back to Alexander Mitchell in the year 1833 [6]. Around the inner Tidal Bays of England, lighthouses were supported by screw anchors. The highest voltage grade of China's national high-voltage dc project has reached ±1100 kV [7]. With the development of extra-high-voltage direct current transmission projects towards higher voltage levels and larger transmission capacity, higher requirements will be put forward for

TABLE 1: Specimen profile.

| Type | Number | Anchor plate | | | | | Anchor arm | | Depth L (mm) |
		Diameter D_1 (mm)	Space h_1 (mm)	Thickness t_1 (mm)	Strength (MPa)	Strength (MPa)	Diameter D_2 (mm)	Thickness t_2 (mm)	
SY-1	1	$\varphi400$	—	10	355	355	$\varphi133$	8	4500
SY-2	2	$\varphi400$	1200	10	355	355	$\varphi133$	8	4500
SY-3	3	$\varphi400$	1200	10	355	355	$\varphi133$	8	5700
SY-4	2	$\varphi400$	1200	10	355	355	$\varphi133$	8	5700
SY-5	1	$\varphi600$	—	10	420	690	$\varphi127$	6	4500
SY-6	2	$\varphi600$	1200	10	420	690	$\varphi127$	8	4500

the bearing capacity of spiral anchor single pile. In order to study the applicability of screw anchor foundation and promote its application in gravel soil foundation, the axial uplift static load tests of screw anchor full die and half die were carried out in laboratory. The test results show that the overall shear failure and the bearing capacity of the anchor plate in shallow gravel soil tend to be weakened, while the local shear failure of the upper soil and the deformation of the deeply buried anchor plate increase gradually [8–10]. In view of the engineering geological conditions of transmission lines in the hills and mountains of southern Anhui province, which are covered with sandy clay and weathered rock below the soil layer, the environment-friendly straight pillar anchor composite foundation is put forward [11–13]. Screw anchor tilt when drawing strong coupling effect between the horizontal and vertical; the flat circular anchor simulation for this single blade screw anchor in Micronesia sand drawing model experiment by a homemade transparent chamber combined with digital photography measurement technology further reveals flat circular anchor oblique drawing bearing mechanism and effects of various factors [14, 15]. In order to master the nonlinear characteristics of dynamic interaction between steel pipe screw anchor foundation and soil under horizontal excitation, Zhang et al. [16] studied the horizontal vibration response characteristics of steel pipe screw anchor with different anchor geometry in sand based on the self-made model test system of dynamic interaction between anchor and soil. Qian et al. [17], based on the model test in the laboratory, designed and selected two kinds of screw bolt foundation and proposed a method to calculate the ultimate bearing capacity of uplift, which was verified in the field test and proved to be a practical and feasible basic form. Dong et al. [18] studied the failure mode of spiral pile foundation, pile type design, calculation of ultimate bearing capacity of single pile and pile group under ultimate load condition, established the failure mode of its foundation, and deduced the proportional relationship between pitch (blade spacing) and blade diameter, namely, minimum pitch and control pitch. The calculation methods of ultimate bearing capacity of single pile and group pile under different pitch are obtained. The pull-out performance of screw anchor is studied in clay by numerical calculation and clarified the main factors affecting the bearing capacity of the foundation [19–21]. By comparing the results of numerical simulation with those of existing formulas, a method to correct the calculation of pulling capacity on screw anchor foundation

is proposed. Zorany et al. [22] adopted the method of experiment and numerical calculation to reveal the influence mechanism of uplift bearing capacity of screw anchor in dense sand by installation disturbance and put forward the calculation method of bearing capacity considering the influence of disturbance. Kwon et al. [23] carried out pull-out test on a single anchor under the action of inclined updraft load. By changing the included Angle between the updraft load and the horizontal direction, the influence law of the inclination of updraft load on the updraft capacity of a single anchor was explained. Due to its unique variable cross section design, the work and load-bearing mechanism of screw piles are more complex than those of common smooth-rod piles.

To sum up, there are many researches on the bearing capacity of ordinary steel screw anchors by scholars at home and abroad, but few literature focus on the bearing capacity of high-strength steel screw anchors. Therefore, it is necessary to carry out researches on the bearing capacity and force mechanism of high-strength steel screw anchors.

2. Screw Anchor Pull-Out Test

2.1. Specimens Design. In this paper, the control variable method is used to analyze the influencing factors of the bearing capacity of high-strength screw anchor. The effects of different burial depths, number of anchor plates, distance between anchor plates, and diameter of anchor plates on the bearing capacity of high-strength screw anchor are compared based on parametric analysis.

Six kinds of specimens with different specifications were designed to study the influence of different variables on the bearing capacity of single anchor. As we know, steel has excellent mechanical properties at ambient temperature. The normally used mild steel in the paper is Q355. The high-strength steel with a nominal yield strength equal to 420 MPa and 690 MPa is adopted too. High-strength steel offers higher performance in tensile stress, yield stress, bending, weld ability, and corrosion resistance compared to mild steel. Specific parameters are shown in Table 1. The design of specimens is shown in Figure 1.

2.2. Engineering Geological Conditions. The soil layer of the site is characterized by silty clay and yellowish brown, wet, plastic soft, no shaking reaction, moderate dry strength and toughness, slightly shiny, and 8.8∼8.9 m thickness.

(a)

(b)

(c)

(d)
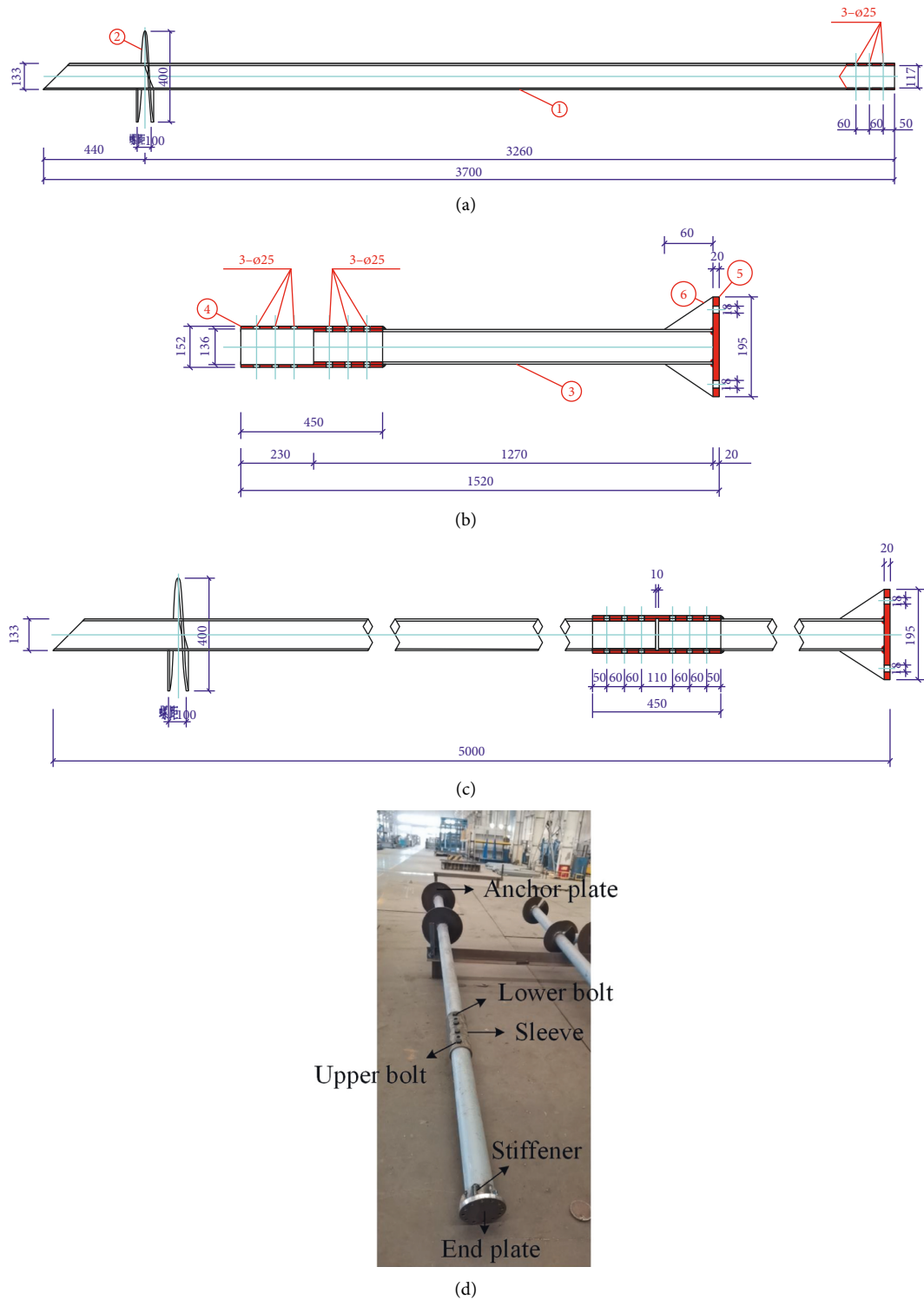
FIGURE 1: Spiral anchor specimen design. (a) Guide section: (1) lower bolt and (2) anchor plate. (b) Rod cap segment: (3) upper bolts, (4) sleeves, (5) end plates, and (6) stiffeners. (c) Integral assembly. (d) Specimens.

2.3. Full-Scale Test.

In order to determine the allowable tensile capacity of high-strength steel screw anchors and verify the formulas of tensile capacity, the researchers carried out drawing tests on high-strength steel screw anchors and ordinary strength steel screw anchors in an open field. During the test, a box steel beam was added at the end of the rod head as a reaction beam, and both ends of the reaction beam were supported on the steel pier column. In the middle of the reaction beam, a 50-ton oil pressure jack was placed. The oil pressure jack was firmly connected with the screw bolt head and the load was applied to the screw anchor, as shown in Figure 2.
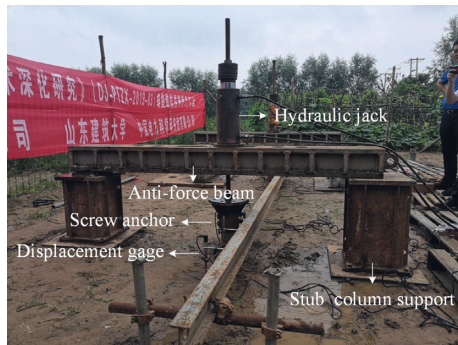
FIGURE 2: Test of screw anchor.

FIGURE 3: Load-displacement curve of screw anchor.

Each level of load is kept for 60 min. After the load is applied, the vertex displacement of pile is measured at 5 min, 15 min, 30 min, 45 min, and 60 min, respectively. When the pile top displacement rate reaches relatively stable (i.e., the pile top displacement does not exceed 0.5 m within an hour), the next load can be applied. Loading can be terminated when one of the following conditions occurs:

(1) Under a certain level of load, the vertex displacement of pile is 5 times greater than that under the previous level of load, and the total vertex displacement of pile exceeds the predetermined limit displacement.

(2) The maximum load has reached the requirement and the settlement of the vertex of pile has reached the relatively stable standard.

(3) The pulling amount on the base or anchor pile has reached the allowable value.

(4) When the load-displacement curve is slowly deformed, the total displacement of the pile top under vertical load is 60 mm~80 mm, and that of the pile top under horizontal load is no less than 40 mm. When the pile tip resistance is not fully exploited, the cumulative vertical settlement of pile top can be more than 80 mm, and the cumulative horizontal displacement can be more than 60 mm.

2.4. Test Results and Analysis

2.4.1. Load versus Displacement of Specimens. The load-displacement curve of the tensile capacity test of screw anchor is shown in Figure 3. According to the bearing characteristics, it shows that the stress process of screw anchor can be divided into elastic stage and elastic-plastic stage. With the increase of drawing load, the screw anchor position shift gradually increases, and the load and displacement are linearly proportional. This stage is the elastic stage. When the drawing load increases to a certain extent, the screw anchor force enters the elastic-plastic stage, and when the load increases to a small value, the displacement increases obviously, the slope decreases, and the elastic-plastic characteristics are significant. When the number of anchor plates increases, the pulling capacity of screw anchor increases. Compared with SY-1 and SY-2, when the spacing of anchor plates is 1.2 m, the number of anchor plates
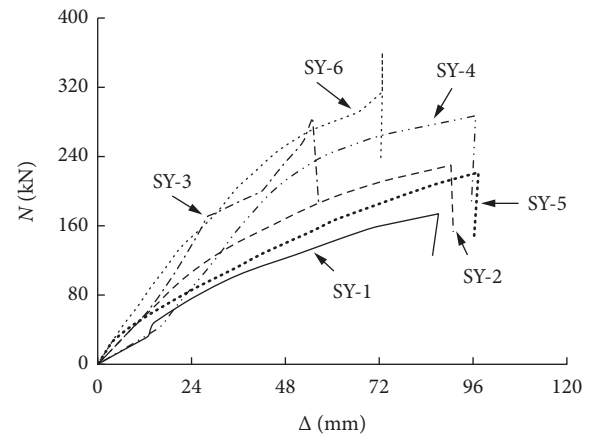
increases from 1 to 2, and the bearing capacity of screw anchor increases by about 32%. As can be seen from specimens SY-4 and SY-2, when the number of anchor plates remains unchanged, the buried depth increases from 4.5 m to 5.7 m, and the screw anchor bearing capacity increases by about 25%. By comparing SY-6 and SY-2 specimens, it is seen that under the condition that the number of anchor plates and burial depth remain unchanged, increasing the diameter of anchor plates and increasing the strength of steel can significantly increase the bearing capacity of screw anchors. The diameter of anchor plates increases from 0.4 m to 0.6 m, the strength of steel increases from 355 MPa to 420 MPa, and the bearing capacity of screw anchors increases by about 57%.

2.4.2. Torque versus Depth of Specimens. The torque motors that could be used to drive the helical piles into the ground will be relatively quiet, at least when compared with conventional piling, and they could be sited over water or under water. Importantly, the measurement of the torque during installation will provide a quality assurance on the pile capacity, as good evidence exists (from current field measurements and theory) that relates torque resistance to vertical capacity. The design can be further refined from torque data gathered during pile installation, and this might lead to cost savings.

The torque-depth curve of the screw anchor is shown in Figure 4. Seen from Figure 4, the construction torque of screw anchor is related to the buried depth, and the construction torque increases with the increase of the buried depth. By comparing the test results of two specimens, SY-2 and SY-4, both of which are provided with two anchor plates, when the buried depth of screw anchor increases from 4.5 m to 5.7 m, the construction torque increases from 20.4 kNm to 34.5 kNm; in other words, the buried depth increased by 27% and the construction torque increased by 69%. In addition, the number of anchor discs also has an impact on the construction torque value. By comparing SY-1 with SY-2, the construction torque value increases by about 13% when the number of anchor discs is doubled. Similarly, by comparing SY-5 with SY-6, the construction torque value
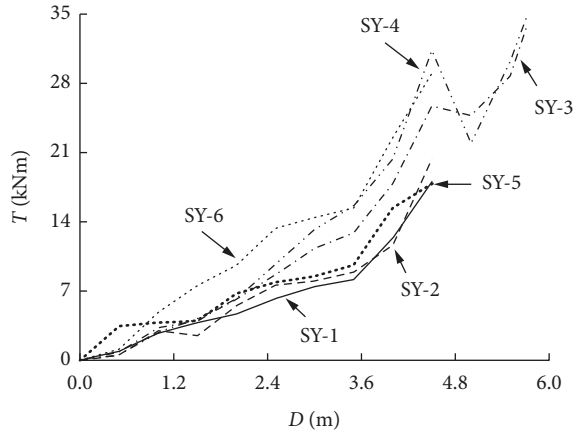
FIGURE 4: Torque-depth curve of screw anchor.

increases by about 63% when the number of anchor discs is doubled. This is because of the high-strength steel used in SY-5 and SY-6. Therefore, comparing SY-2 with SY-6, they both have double anchor plates and the buried depth is 4.5 m. Due to the use of high-strength steel Q420 and Q690 in specimen SY-6, the value of construction torque increases by 43%. It shows that material strength and buried depth have a significant impact on screw anchor construction torque.

3. Theoretical Analysis and Numerical Simulation

3.1. Theoretical Analysis. The tensile bearing capacity of screw anchor foundation can be calculated based on the combination of cap, anchor plate, and anchor bolt. Here, only the tensile bearing capacity of screw anchor is studied. Therefore, the bearing capacity of screw anchor consists of anchor plate and anchor bolt. The formula of the bearing capacity of screw anchor is as follows:

$$T_m = T_{pi} + T_g, \tag{1}$$

where T_m is the standard value of hoisting capacity of screw anchor, kN; T_{pi} is the standard value of hoisting capacity of anchor plate, kN; and T_g is the standard value of hoisting capacity of single bolt, kN.

The formula for calculating the uplift capacity of spiral anchor plate by cylindrical shear method is as follows:

$$T_{pi}\left(0.65 D_p C_w h_l + 0.4 \frac{\pi}{4} D_p \gamma_s h_l^2\right) + Q_p$$

$$C_w \begin{cases} C + 2\dfrac{90\% - S_r}{10\%}, & S_r < 90\%, \\[2mm] C - 2\dfrac{90\% - S_r}{10\%}, & S_r > 90\%, \end{cases} \tag{2}$$

where C_w is the calculation of cohesion of soil, kPa; C is cohesion determined by saturated undrained shear or equivalent method, kPa; D_p is the diameter of anchor plate, m; h_l is the effective buried depth of spiral anchor plate, the

effective depth of the first piece of anchor plate above is the vertical distance from the ground to the anchor plate, the effective buried depth of the second piece of anchor plate is the distance from the first piece to the second piece of anchor plate, and the same for other anchor plates, m; γ_S is the weighted average weight of soil above screw anchor plate, kN/m^3; Q_p is self-gravity of screw anchor plate, kN; and S_r is actual saturation of foundation soil, %.

3.2. Numerical Simulation. In order to verify the superiority of high-strength screw anchor over ordinary screw anchor, the finite software ABAQUS is adopted to establish the overall fine numerical model of screw anchor and surrounding soil. According to the test results of soil samples, the soil model is set as silty clay, and the Moore–Coulomb plastic constitutive model is selected. The specific material parameters are shown in Table 2.

Considering the interaction between soil and screw anchor, the cylinder soil model is adopted in this paper. The height of the cylinder soil model is greater than two times the embedding depth of the bolt, and the diameter is 6 m. For the interaction between screw anchor foundation and soil, the constitutive relationship is a mechanical model with mutual friction. The friction is divided into normal and tangential directions. The normal direction is set as hard contact, the tangential direction is set as penalty contact, and the friction coefficient is 0.3. In the process of setting boundary conditions, two horizontal constraints were set around the soil model and vertical constraints were set at the bottom. Tarawneh et al. [9] conducted field test and numerical simulation of bearing capacity of flat plate screw anchor and spiral plate screw anchor; the calculation results of the two are consistent, and the maximum error of stress value between flat plate anchor model and spiral anchor model is only 5%. Therefore, flat plate screw anchor model is used for analysis in this paper. At the same time, each component of the whole model was assigned element types, and linear geometric order and hourglass control were used to enhance the model convergence.

In this paper, Q355 steel is used for ordinary screw anchor, and two kinds of high-strength steel are used for high-strength screw anchor, namely, Q420 steel for anchor plate and Q690 steel for anchor rod. Ideal elastic-plastic constitutive model is used for all steels. Specific material parameters of each steel model are shown in Table 3.

Figures 5–7, respectively, show the screw anchor soil model, screw anchor model, and screw anchor stress distribution. As can be seen from the screw anchor stress distribution cloud diagram in Figure 6, the stress at the connection between screw anchor plate and bolt is large, while the stress at the overhanging part of anchor plate is small. The stress gradually decreases from the connection point to the overhanging edge of anchor plate. The stress value of anchor plate closer to the ground is generally larger than that of the lower anchor plate.

Comparison of load-displacement curves between test and numerical simulation is shown in Figures 8(a)–8(f). It can be seen from Figures 8(a)–8(f) that the numerical

TABLE 2: Material properties of the soil.

Soil density (kg/m^3)	Modulus (MPa)	Poisson's ratio	Cohesion (kPa)	Internal friction angle (°)	Expansion angle (°)	Tensile strength (kPa)
1900	2.4	0.35	35	26	13	40

TABLE 3: Steel material parameters.

Type	Steel density (kg/m^3)	Modulus (MPa)	Poisson's ratio	Yield strength (MPa)
Q355	7850	2.06×10^5	0.3	355
Q420	7850	2.06×10^5	0.3	420
Q690	7850	2.06×10^5	0.3	690
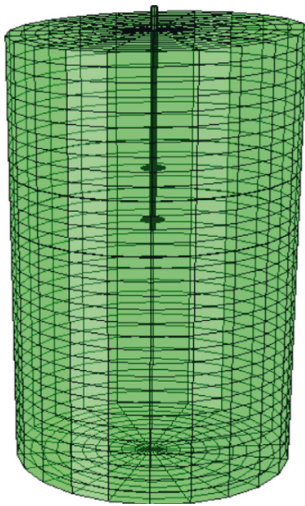
FIGURE 5: Screw anchor—soil integral model.

simulation is in good agreement with the test load-displacement curve. At the beginning, the vertex displacement of the screw anchor increases with the increase of the drawing load and presents a linear ratio relationship. When the load increases to a certain value, the load value increases slightly but the displacement increases rapidly, as shown in Figures 8(a), 8(b), and 8(f). Therefore, soil model, screw anchor model, and unit division are reasonable in numerical simulation, which can provide reference for parametric analysis of uplift capacity of high-strength steel screw anchor.

The comparison of theoretical calculation, numerical calculation, and experimental results is shown in Table 4. As seen from Table 4, for mild steel screw anchor specimens, the bearing capacity results of theory are similar to the numerical and experimental results. But for the high-strength steel screw anchor specimens, the theoretical results are different from the numerical and experimental results. It is shown that the bearing capacity of steel screw anchor calculating by theory formula is not suitable for high-strength materials. Besides, with the capacity of specimen rising, the resilience rate is higher too.

3.3. Parametric Analysis. Considering the material parameters used in the test and according to the relevant

FIGURE 6: Screw anchor model.

specifications and the parameter variation range commonly used in engineering practice, the influence of parameter variation on the bearing capacity of high-strength steel screw anchor is studied. The range of each parameter in the paper is determined as follows:

Steel strength (f_y): 355 MPa, 390 MPa, 420 MPa, 460 MPa, 550 MPa, and 690 MPa

Anchor plate buried depth (h): 4.5 m, 5.5 m, 6.5 m, 7.5 m, 8.5 m, 9.5 m, and 10.5 m

Anchor plate number (n): 1, 2, 3, 4, and 5

S, Mises

(平均 : 75%)

+3.154e+08
+2.894e+08
+2.634e+08
+2.373e+08
+2.113e+08
+1.853e+08
+1.593e+08
+1.333e+08
+1.073e+08
+8.124e+07
+5.523e+07
+2.921e+07
+3.193e+06
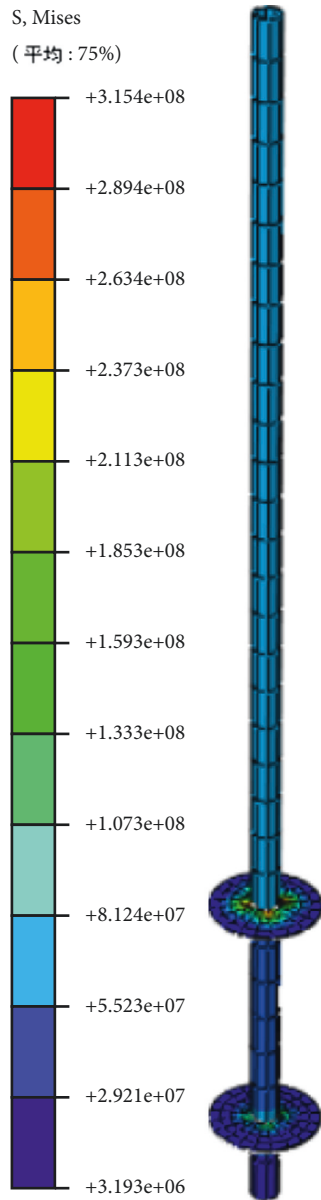
Figure 7: Stress distribution of screw anchor.

Anchor plate spacing (l): 0.6 m, 1.2 m, 1.8 m, 2.4 m, and 3 m

Anchor plate diameter (D_p): 0.3 m, 0.4 m, 0.5 m, 0.6 m, and 0.7 m

3.3.1. Steel Strength. The basic situation of the calculation example is as follows: the buried depth of anchor plate is 4.5 m, the number of anchor plate is 1, the diameter of anchor plate is 0.4 m, the thickness of anchor plate is 10 mm, the diameter of anchor bolt is 133 mm, and the wall thickness of anchor bolt is 8 mm. The influence of steel strength on the bearing capacity of screw anchor is shown in Figure 9. The drawing capacity of screw anchor increases with the increase of steel strength, the steel strength increases from 355 MPa to 390 MPa, the strength increases by 10%, the

bearing capacity of screw anchor increases by 6%, the steel strength increases from 550 MPa to 690 MPa, the strength increases by 25%, and the bearing capacity increases by 9%. It is seen that when the steel strength increases to a certain extent, the contribution of the steel strength to the uplift capacity of the screw anchor decreases, because when the steel strength increases to a certain value, soil conditions become the main factors affecting the bearing capacity of the screw anchor.

3.3.2. Buried Depth of Anchor Plate. The basic situation of the calculation example is as follows: steel strength 690 MPa, anchor plate number 1, anchor plate diameter 0.4 m, anchor plate thickness 10 mm, anchor bolt diameter 133 mm, and anchor bolt wall thickness 8 mm. Figure 10 shows the influence of anchor plate burial depth on the bearing capacity of screw anchor. When the buried depth of screw anchor plate increases from 4.5 m to 5.5 m, the buried depth increases about 22% and the uplift capacity of screw anchor increases about 27%. When the buried depth of screw anchor plate increases from 9.5 m to 10.5 m, the buried depth increases about 11% and the uplift capacity of screw anchor increases about 17%. It is seen that the pull-out bearing capacity of screw anchor increases with the increase of the buried depth of screw anchor plate, which has a significant influence on the pull-out bearing capacity of screw anchor.

3.3.3. Number of Anchor Plates. The basic information of the calculation example is as follows: steel strength 690 MPa, anchor plate buried depth 4.5 m, anchor plate diameter 0.4 m, anchor plate spacing 0.5 m, anchor plate thickness 10 mm, anchor bolt diameter 133 mm, and anchor bolt wall thickness 8 mm. The influence of the number of anchor plates on the bearing capacity of screw anchors is shown in Figure 11. When the number of screw anchors increases from 1 to 2, the bearing capacity of screw anchors increases about 15%. When the number of screw anchors increases from 4 to 5, the bearing capacity of screw anchors increases about 7%. It is seen that the pull-out bearing capacity of screw anchor increases with the increase of the number of anchor plates, but not the better, and the increase rate of bearing capacity decreases with the increase of the number of anchor plate.

3.3.4. Anchor Plate Spacing. The basic situation of the calculation example is as follows: steel strength 690 MPa, anchor plate buried depth 4.5 m, anchor plate number 2, anchor plate diameter 0.4 m, anchor plate thickness 10 mm, anchor bolt diameter 133 mm, and anchor bolt wall thickness 8 mm. The influence of anchor plate spacing on the bearing capacity of screw anchor is shown in Figure 12. When the spacing of anchor plates increases from 0.6 m to 1.2 m, the uplift capacity of screw anchors increases by about 9%; when the spacing of anchor plates increases from 2.4 m to 3.0 m, the uplift capacity of screw anchors increases by about 3.5%. It shows that when the distance between anchor plates increases appropriately, the pulling capacity of screw
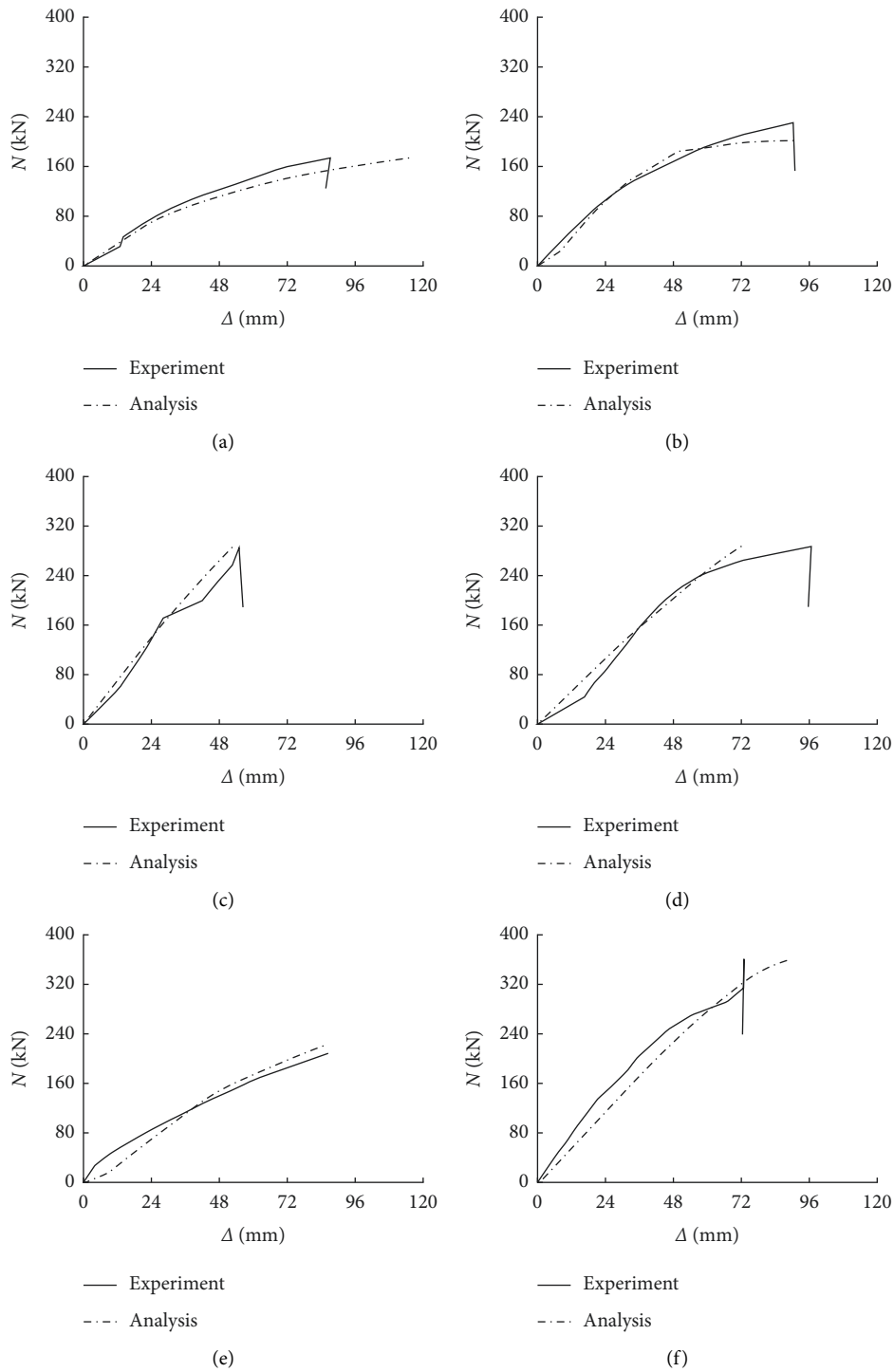
Figure 8: Comparison of load-displacement curves between test and numerical analysis: (a) SY-1; (b) SY-2; (c) SY-3; (d) SY-4; (e) SY-5; (f) SY-6.

Table 4: Comparison of bearing capacity of screw anchor.

Type	Theoretical results (kN)	Numerical results (kN)	Experimental results (kN)	T/E	N/E	Resilience rate (%)
SY-1	160	170	174	0.94	0.98	10
SY-2	221	223	230	0.96	0.97	13
SY-3	310	315	285	1.09	1.11	19
SY-4	265	281	287	0.92	0.98	14
SY-5	170	218	222	0.77	0.98	20
SY-6	285	355	360	0.79	0.99	17
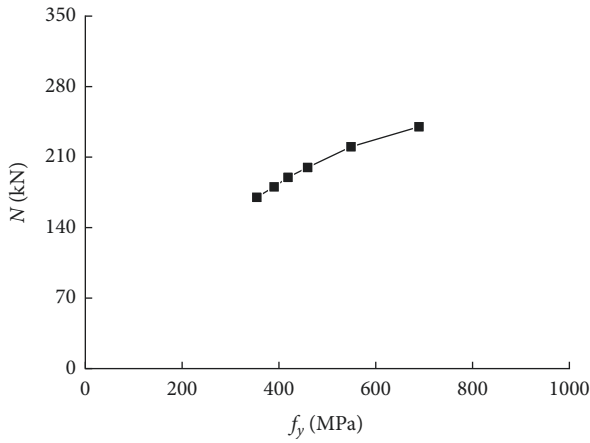
FIGURE 9: Influence of steel strength.
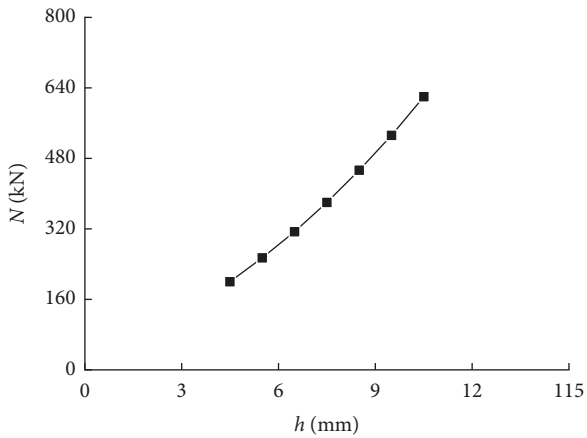
FIGURE 10: Influence of anchor plate burial depth.

FIGURE 11: Influence of anchor plate number.

FIGURE 12: Influence of anchor plate spacing.

FIGURE 13: Influence of anchor plate diameter.

3.3.5. Diameter of Anchor Plate. The basic situation of the calculation example is as follows: steel strength 690 MPa, anchor plate buried depth 4.5 m, anchor plate number 1, anchor plate thickness 10 mm, anchor bolt diameter 133 mm, and anchor bolt wall thickness 8 mm. Figure 13 shows the influence of anchor disc diameter on the bearing capacity of screw anchor. When the diameter of anchor plate increases from 0.3 m to 0.4 m, the pull-out bearing capacity of screw anchor increases by about 19%, and when the diameter of anchor plate increases from 0.6 m to 0.7 m, the pull-out bearing capacity of screw anchor increases by about 8.3%. It is seen that the pull-out bearing capacity of the screw anchor increases with the increase of the diameter of the anchor plate. Too large diameter of anchor plate will cause local stability problem of anchor plate itself, and too large diameter to thickness ratio will reduce the pulling capacity of spiral anchor.

4. Conclusions

Based on theoretical calculation, numerical analysis, and experimental study of the tensile capacity of high-strength steel screw anchor, the following conclusions are obtained:

anchor increases with the increase of the distance between anchor plates. If the distance between anchor plates is too large, the cooperative working capacity between anchor plates deteriorates. Therefore, the pulling capacity of screw anchor decreases.

(1) The bearing capacity of high-strength steel screw anchor increases significantly compared with that of normal-strength steel screw anchor, and the rebound rate is larger after unloading.

(2) Parametric analysis of the uplift capacity of spiral anchors shows that steel strength, buried depth, and number of anchor plates, distance between anchor plates and diameter of anchor plates are the main influencing factors of bearing capacity of spiral anchors, among which the buried depth of anchor plates has the most significant influence on tensile bearing capacity of spiral anchors.

(3) The tensile bearing capacity of high-strength screw anchor calculated by the theoretical formula in the existing code is small, which needs to be modified by the calculation formula of uplift bearing capacity.

Data Availability

The data used to support the findings of this study are currently under embargo while the research findings are commercialized. Requests for data, 6/12 months after publication of this article, will be considered by the corresponding author.

Conflicts of Interest

The authors declare that there are no conflicts of interest regarding the publication of this article.

Acknowledgments

References

[1] M. N. Isa, P. Kypros, and G. Maurizio, "Shear behaviour of E-UHPC containing recycled steel fibres and design of E-UHPC screw piles[J]," *Construction and Building Materials*, p. 304, 2021.

[2] A. N. Tarawneh, E. F. Saleh, and S. A. Majdalaweyh, "Reliability assessment and strength reduction factor calibration for screw anchors concrete breakout," *ACI Structural Journal*, vol. 119, no. 2, pp. 113–122, 2022.

[3] S Sakr, "Performance of laterally loaded helical piles in clayey soils established from field experience," *DFI Journal - The Journal of the Deep Foundations Institute*, vol. 12, no. 1, pp. 28–41, 2018.

[4] C. Cerfontaine, K. Knappett, M. J Brown, C Davidson, and Y Sharif, "Optimised design of screw anchors in tension in sand for renewable energy applications," *Ocean Engineering*, vol. 217, Article ID 108010, 2020.

[5] S. Nassiri, Z. Chen, A. Lamanna, and W Cofer, "Numerical simulation of failure mechanism in screw anchors under static tension," *Advances in Structural Engineering*, vol. 23, no. 16, pp. 3385–3400, 2020.

[6] F. Fang, H.-Xi Gao, and W.-W. Duan, "Theoretical analysis and experimental research on upward capacity of screw anchor," *Advanced Materials Research*, pp. 3029–3035, 2011.

[7] L. Yan-Qiao, Q.-H. Wu, and S. Jing-Jing, "Uhv transmission technology in China has achieved a leap from "following" to "leading"," *China Survey and Design*, no. S1, pp. 19–21, 2021, (In Chinese).

[8] F. Xue, S.-J. Ding, Li Hai-Mei et al., "Model tests of pull-out resistance for helical anchors and bearing characteristic analysis in remolded gravel foundation," *Industrial Construction*, vol. 51, no. 6, pp. 150–155, 2021, (In Chinese).

[9] A. Tarawneh, Y. Momani, and R. Alawadi, "Leveraging artificial intelligence for more accurate and reliable predictions of anchors shear breakout capacity in thin concrete members," *Structures*, vol. 32, pp. 1005–1014, 2021.

[10] C. Chen, N. Nassiri, and L. Lamanna, "Investigation of a combined failure mode for screw anchors under tension," *Advances in Structural Engineering*, vol. 23, no. 13, pp. 2803–2812, 2020.

[11] W. Feng-Xian and W.-F. Zheng, "Experimental study on newly column anchor composited foundation in transmission line engineering," *Geotechnical Investigation & Surveying*, vol. 46, no. 10, pp. 20–24, 2018, (In Chinese).

[12] H. M. Ho, A. A. Malik, J. Kuwano, and H M A Rashid, "Influence of helix bending deflection on the load transfer mechanism of screw piles in sand: experimental and numerical investigations," *Soils and Foundations*, vol. 61, no. 3, pp. 874–885, 2021.

[13] F. Feng, W-D. Fu, and C. Chen, H X Li, Y L Xie, and J Li, "Field tests of micro screw anchor piles under different loading conditions at three soil sites," *Bulletin of Engineering Geology and the Environment*, vol. 80, no. 1, pp. 127–144, 2021.

[14] M. Mohyeddin, F Gad, and J Lee, "Failure modes and tensile strength of screw anchors in non-cracked concrete," *Construction and Building Materials*, vol. 221, pp. 501–513, 2019.

[15] Z. Lin, W. Hu, Pu Zhao et al., "Experimental study on the uplift behavior of circular anchor plate inclined drawing in sand," *Rock and Soil Mechanics*, vol. 42, no. 11, pp. 3059–3068+3168, 2021, (In Chinese).

[16] X.-C. Zhang, B. Yun-Can, Ze-Q. He, and A. Zhu, "Experimental study on vibration response characteristics of screw pile foundation in sand under lateral dynamic loading," *Chinese Journal of Applied Mechanics*, vol. 37, no. 2, pp. 601–930, 2020, (In Chinese).

[17] S. Qian, L. Yi-Liang, Li Cui-Hua, and J. Luo, "Experimental research on application of screw anchored foundation to transmission route," *J.Wuhan Univ. of Hydr. & Elec. Eng.*vol. 31, no. 4, pp. 30–33, 1998, (In Chinese).

[18] T.-W. Dong, Li Liang, M.-S. Wang, and C.-J. Zhang, "Pitch of screws and bearing capacity of screw piles under ultimate load," *Chinese Journal of Geotechnical Engineering*, vol. 28, no. 11, pp. 2031–2034, 2006, (In Chinese).

[19] R. S. Merifield, "Ultimate uplift capacity of multiplate helical type Anchors in clay," *Journal of Geotechnical and Geoenvironmental Engineering*, vol. 137, no. 7, pp. 704–716, 2011.

[20] C. Tang and K. K. Phoon, "Model uncertainty of cylindrical shear method for calculating the uplift capacity of helical anchors in clay," *Engineering Geology*, vol. 207, pp. 14–23, 2016.

[21] C. Tang and K. K. Phoon, "Statistics of model factors and consideration in reliability-based design of axially loaded helical piles," *Journal of Geotechnical and Geoenvironmental Engineering*, vol. 144, no. 8, Article ID 04018050, 2018.

[22] A. P. Zorany, A. S. José, C. D. H. C. Tsuha, and D Dias, "Numerical and experimental study on influence of installation effects on behaviour of helical anchors in very dense sand," *Canadian Geotechnical Journal*, vol. 55, no. 1, pp. 1067–1080, 2018.

[23] O. Kwon, J. Lee, G. Kim, I. Kim, and J Lee, "Investigation of pullout load capacity for helical anchors subjected to inclined loading conditions using coupled Eulerian-Lagrangian analyses," *Computers and Geotechnics*, vol. 111, pp. 66–75, 2019.

Research Article

Study on the Bearing Capacity of High-Cap Inclined Pile Foundations

Guodong Shao,[1] Juan Liu,[2] Tonglei Wang,[1] and Yuping Liu [3]

[1]*Powerchina Sepco1 Electric Power Construction Co. Ltd., Jinan 250102, China*
[2]*China Power Construction Corporation Ltd., Beijing 100044, China*
[3]*School of Civil Engineering, Shandong University, Jinan 250061, China*

Correspondence should be addressed to Yuping Liu; civil_sdu@163.com

To analyze the bearing capacity of high-cap inclined pile foundations based on foundation design in practical engineering, finite element models of single cap foundations and multi-cap foundations are established. The influence of the inclination direction and angle of the inclined pile on the lateral displacement of the foundation and internal force of the pile body is investigated. The influence of uneven settlement on inclined pile foundations is examined by weakening the soil strength. This paper suggests that the lateral bearing capacity of a negatively inclined pile is better than that of a positively inclined pile. When the inclination angle of a negatively inclined pile changes within a certain range, it can significantly affect the lateral displacement of the pile body. Under uneven settlement, the change in the internal force of the inclined pile is larger than that of the vertical pile, the horizontal displacement difference of each bearing platform is small, and the vertical displacement is quite different.

1. Introduction

A pile foundation is suitable for building structures with an insufficient bearing capacity of shallow soil and high requirements for foundation displacement and bearing capacity. A high-pile cap foundation is a special pile foundation. The cap is located above the Earth's surface. When the cap is subjected to horizontal load, it will produce a large lateral displacement [1]. For structures controlled by horizontal loads, the horizontal bearing capacity of pile foundations should be considered. A large-span transmission tower is a typical high-rise structure and wind-sensitive system. Horizontal load is an important factor in the design of pile group foundations of transmission towers and often has a controlling role. The horizontal bearing capacity of the foundation should be considered.

The vertical bearing capacity of a pile foundation can be easily adjusted by changing the pile diameter, pile length, and pile number [2]. Usually, the horizontal bearing capacity of a foundation is improved by increasing the pile diameter and pile spacing [3, 4]. Increasing the pile spacing and pile

diameter will increase the construction cost of the cap, and improvement of the horizontal bearing capacity of the foundation is limited by the pile diameter and pile spacing. To explore a more economical and effective method for improving the horizontal bearing capacity of pile foundations, scholars worldwide have proposed setting inclined piles in pile group foundations to improve their horizontal bearing capacity [5, 6].

Dezi et al. [7] proposed a simplified numerical model for the dynamic analysis of inclined pile foundations. Compared with the stricter calculation method and fine finite element model, the calculation difficulty is reduced, and the loss of accuracy is not obvious. The calculation method proposed by Dezi et al. [7] simplifies the pile to an Euler–Bernoulli beam element, and the soil is composed of an infinite viscoelastic horizontal layer. The pile–soil interaction is considered by Green's elastic mechanics function. The pile–soil interaction of a 2×2 inclined group pile foundation under lateral load based on a scale test was explored by Goit et al. [8]. A semiempirical formula for predicting the soil reaction is proposed by analyzing the variation in the soil reaction along

the pile depth. Carbonari et al. [9] selected the bridge foundation as the object and examined the influence mechanism of pile–soil-structure interactions with different inclined pile shapes and pile inclination angles. By considering the pile–soil interaction by the Green function, the stress distribution law and foundation filtering effect of inclined pile group foundations under earthquakes were analyzed. Álamo et al. [10] established the foundation of an inclined pile group to investigate its dynamic response law in heterogeneous foundations. By setting different soil profiles and soil parameters, the influence of different geological conditions on the impedance function of inclined piles and pile groups was investigated, and it was considered necessary to analyze inclined pile groups by selecting the soil layer that was consistent with the actual engineering situation.

Presently, scholars worldwide have focused on the bearing performance, dynamic response, and simplified calculation method of inclined pile group foundations under loads. There is a lack of research on the bearing performance of inclined piles, especially research on the bearing performance of inclined pile foundations under uneven settlement.

2. Model Establishment

Based on a practical project in Brazil, this paper establishes a refined finite element model of high-pile cap-pile–soil. This project involves a river-crossing engineering section of an ultrahigh voltage transmission tower. The foundation is set at the river bank, and the shallow soil has insufficient bearing capacity and is easily scoured by water flow. The selected foundation type is a high pedestal, concrete-filled, steel tube pile foundation. The pile body is a concrete-filled, steel tube pile, and the pile length and steel pipe length are 10.3 m. Concrete is filled within 5.0 m above the steel tube, and the strength of concrete is equivalent to that of cap concrete. The lower part of the pile foundation is a hollow steel tube with a wall thickness of 12.7 mm. To resist the large horizontal force of the transmission tower, inclined piles are set in the pile group foundation to improve the lateral bearing capacity of the foundation. There are 22 concrete-filled, steel tubular piles under the cap, 5 of which are inclined piles. Figure 1 shows the left and front elevations of the single cap foundation. Geological survey reports provide standard penetration hammer counts for soils. In this paper, the elastic modulus of the soil is estimated by a standard penetration test (SPT). Sand can be estimated by the following formula: $E\,0.5\,(N+15)$; clay can be estimated by the following formula: $E\,0.6\,(N+5)$.

2.1. Element Type and Constitutive Model.
The selection rationality of element and material constitutive determines the accuracy of numerical model calculation [11]. When the size of a component in one direction is much smaller than that in the other direction, the beam element, shell element, and other simplified elements can be utilized according to the characteristics of the structure. For components with the same dimension size, a solid element with high calculation
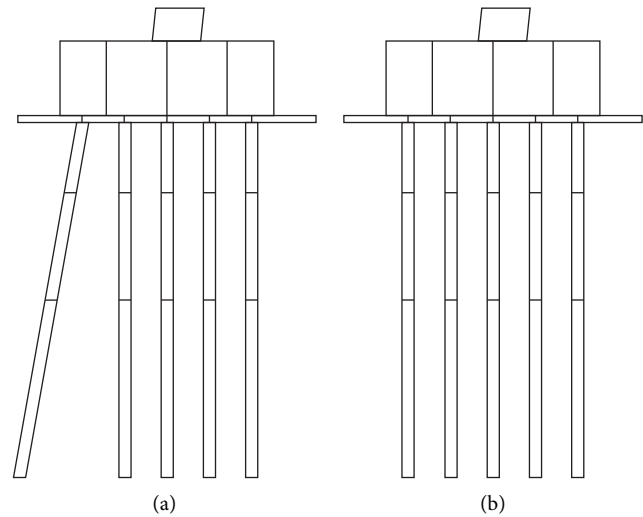
Figure 1: Facade plan of single cap: (a) left elevation; (b) front elevation.
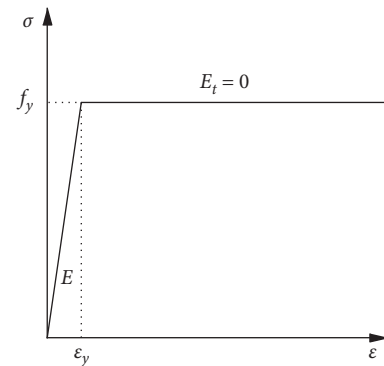
Figure 2: Ideal elastoplastic constitutive model.

accuracy can be applied. Solid elements are employed in the pile cap, pile body, coupling beam, and soil when establishing the pile group foundation model.

The appropriate constitutive model is selected according to the characteristics of different materials, and the ideal elastoplastic model is selected for plastic materials such as steel. The stress–strain curve of the model is shown in Figure 2. The ideal elastic–plastic constitutive model assumes that the material is completely elastic before the yield limit and completely plastic after the yield limit. A complete elastic model is adopted to simplify brittle materials such as concrete, and the plasticity and damage conditions of materials are not defined. Setting the soil constitutive model is the key to guaranteeing the accuracy of the calculation [12–14]. The Mohr–Coulomb model is a material constitutive model based on the shear strength theory of soil, which requires five parameters: elastic modulus, dilatancy angle, Poisson's ratio, internal friction angle, and cohesion. The latter two parameters are selected to define the yield conditions, and the model can better simulate the shear failure behavior of the excavated body.

(a)   (b)
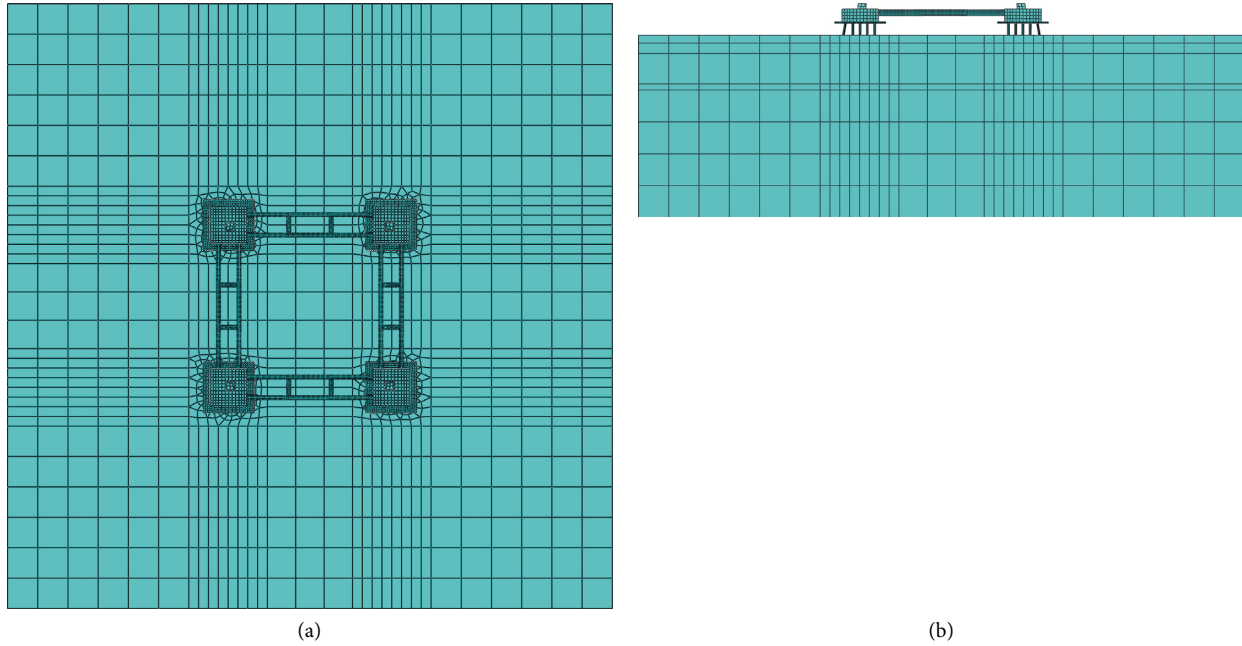
FIGURE 3: Diagram of grid division: (a) vertical view; (b) lateral view.

The interaction between the pile and the soil is transmitted through contact, and the correct definition of the pile–soil interface is the key to ensuring the accuracy and reliability of the simulation results [15, 16]. General contact is set between the pile and the soil; tangential behavior of the contact surface is hard contact; and normal behavior is defined as penalty contact. The friction coefficient, which is determined according to the internal friction angle of the soil, is set to normal. The pile cap and pile body interact through a tie command.

The calculation units of different sizes are divided according to the size and force complexity of different parts. Considering the calculation speed and calculation cost, the large components are divided into medium-sized grids, the grids are encrypted in the complex local stress region, and the small components are divided into small grids. A schematic of the grid division is shown in Figure 3.

2.2. Model Calibration. The correctness of the numerical model needs to be tested based on the existing calculation formula or related test results. Presently, there are no full-scale test data of large high-cap inclined pile group foundations, and it is difficult to verify the correctness of the model by test data [17]. In this paper, the single pile model, which adopts the same element type, constitutive relation, and contact condition as the pile group foundation model, is established. The vertical bearing capacity of a single pile is calculated by the formula, and the correctness of the model is verified by comparing the numerical calculation results with the formula calculation results [18].

The single pile model is shown in Figure 4, and the model setting is equivalent to that of the pile group foundation model. Figures 4(b)–4(d) show the overall stress cloud

diagram of the model and the stress cloud diagram of each component. The stress of the pile is obviously greater than that of the soil, and the stress of the soil gradually increases from top to bottom. The soil around the pile is affected by extrusion and friction, and the stress of the soil layer around the pile is obviously greater than that of the other soil layers in the same plane. The stress distribution of the soil layer is consistent with the actual situation. When the vertical load is transferred downward along the pile, the vertical friction force provided by the pile wall increases with increasing pile depth, and the load transferred to the lower pile decreases. The pile stress gradually decreases from top to bottom, which is consistent with the simulation results.

The mechanical calculation method can be used to calculate the bearing capacity of a pile. The bearing capacity of the pile is derived from the pile side friction and pile bottom bearing capacity. The soil is stratified according to the properties of the soil, and the lateral friction resistance of the pile is calculated and summed according to the standard value of the lateral resistance of different soil layers multiplied by the corresponding friction area. The bottom bearing force of the pile is the area of the pile bottom multiplied by the standard value of the end resistance and the corresponding reduction coefficient.

$$Q_{uk} = Q_{sk} + Q_{pk} = u\Sigma q_{sik}l_i + \lambda_p q_{pk} A_p,$$

$$\frac{h_d}{d} < 5, \lambda_p = \frac{0.16 h_b}{d},$$

$$\frac{h_d}{d} \geq 5, \lambda_p = 0.8,$$

(1)

where Q_{sk} and Q_{pk} are the standard value of the total ultimate lateral resistance and the standard value of the total
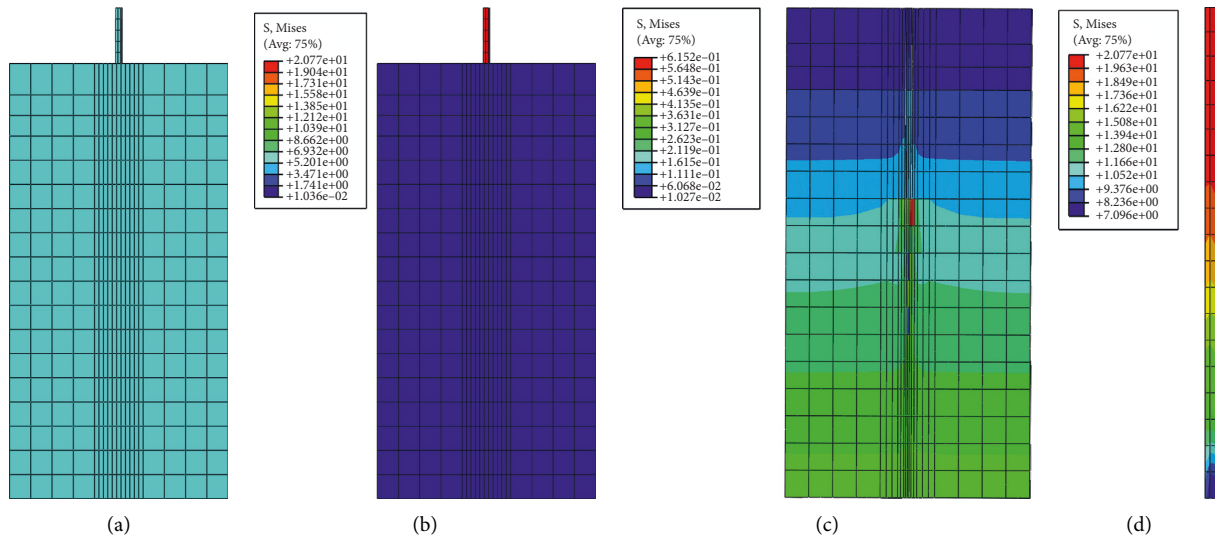
FIGURE 4: Single pile model: (a) mesh subdivision; (b) overall stress nephogram; (c) soil stress nephogram; (d) pile stress nephogram.
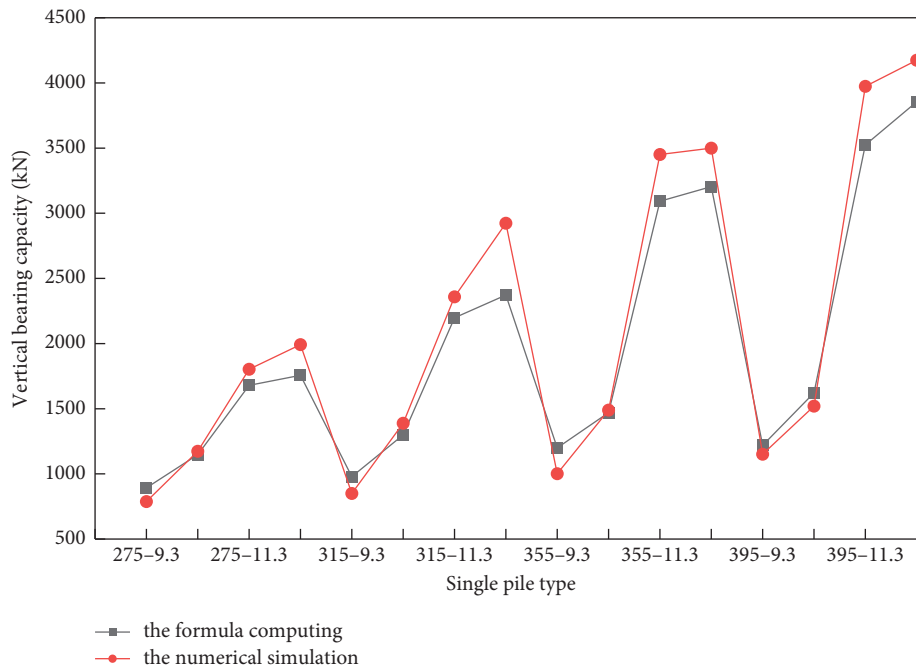
FIGURE 5: Comparison diagram of vertical bearing capacity of single pile.

ultimate end resistance, respectively, of the steel pipe pile; u is the circumference of the pile; l_i is the thickness of layer i soil; and q_{sik} and q_{pk} are the standard value of the initial limit lateral resistance and the standard value of the initial limit end resistance, respectively, of the i soil layer of the steel pipe pile.

Figure 5 shows the comparison between the vertical bearing capacity of a single pile calculated by the formula and that of the numerical simulation. The single pile model 275–9.3 represents pile diameter of 275 mm and pile length of 9.3 m. The finite element calculation results of the vertical bearing capacity of single piles with different pile lengths and diameters are similar to those of formula mechanics; the

bearing capacity of different single piles has the same variation trend; and the bearing capacity curves basically coincide. Therefore, the constitutive model, constraint conditions, boundary conditions, and interaction of soil selected for establishing the finite element model show agreement with the actual project, and the correctness and rationality of the model are verified.

3. Parametric Study of Inclined Pile Foundations

The large-span pile group foundation of the transmission tower investigated in this paper is composed of four caps,
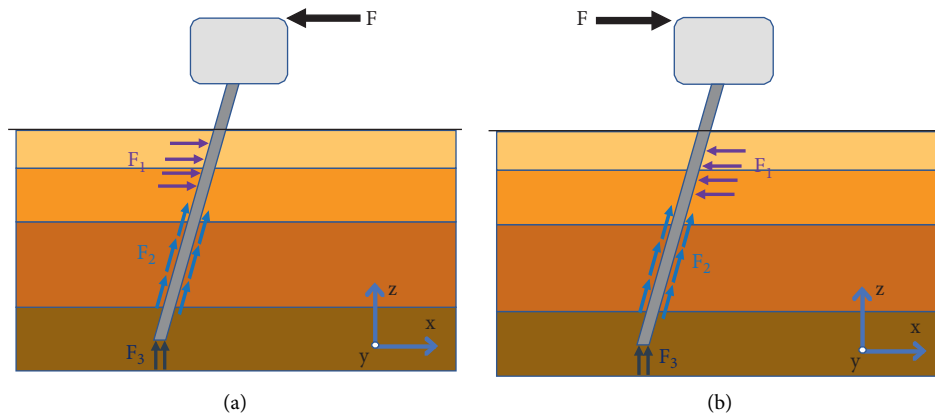
FIGURE 6: Schematic of inclined pile: (a) schematic of negative inclined pile; (b) schematic of positive inclined pile.

under which 18 vertical piles and 5 inclined piles are set. To control a single variable, a single cap model was established to study the influence of the inclined angle and direction of the pile on the bearing performance of the cap.

3.1. Vergence Direction. When the vertical pile is subjected to downward pressure, the lateral friction resistance and the bearing force at the bottom of the pile jointly resist vertical load. When the horizontal force is applied to the vertical pile, the pile wall compresses the surrounding soil to resist horizontal load. When the strength of the soil around the pile is insufficient or the horizontal force is large, the soil cannot provide enough horizontal resistance to the pile so that the horizontal displacement of the foundation exceeds the limit [19, 20].

As shown in Figure 6(a), when the horizontal force direction is opposite to the inclined direction of the pile, it is referred to as a negative inclined pile. As shown in Figure 6(b), when the horizontal force direction is equivalent to the inclined direction of the pile, it is referred to as a positive inclined pile. Generally, the horizontal load and vertical load simultaneously act on the pile top, and the negatively inclined pile produces a horizontal component along the positive x direction under the action of the downward pressure load, which is opposite to the direction of horizontal load F, thereby reducing the horizontal load F acting on the pile body. After the downward load is applied to the positive inclined pile, the load component of the pile is consistent with the direction of the horizontal load, which increases the horizontal force acting on the pile.

Since the vertical loads on the four caps of the pile group foundation are different, the requirement of a single variable cannot be met, and the influence rule of the pile inclination direction on the horizontal bearing capacity of the foundation cannot be determined. Therefore, a single cap foundation was established, and both vertical and horizontal loads were applied to the cap to investigate the influence rule of the pile tilt direction on the horizontal bearing capacity of the foundation. The single cap model and grid division are shown in Figure 7.

Figure 8 shows the displacements of the positive inclined pile, negative inclined pile, and vertical pile under load. The horizontal coordinate represents the amplitude of the downward pressure load. The red broken line, blue broken line, and black broken line represent the horizontal displacement of the positive inclined pile, negative inclined pile, and vertical pile, respectively. The horizontal displacement of the negative inclined pile is obviously smaller than that of the positive inclined pile and vertical pile, and the lateral bearing capacity of the negative inclined pile is better than that of the vertical pile and positive inclined pile. The vertical load can affect the lateral bearing capacity of the pile foundation. With an increase in vertical load, the lateral displacement of the vertical pile and negative inclined pile decreases, while that of the positive inclined pile increases. The top of the pile is 2.0 m above the ground; the displacement of the top of the negative inclined pile is slightly larger than that of the ground; and the displacement of the top of the positive inclined pile is obviously larger than that of the ground. The displacement difference between the pile top and the ground depends on the horizontal force acting on the pile top. With an increase in the horizontal load, the bending degree of the pile increases, and the displacement difference between the pile top and the ground increases.

When the downward load and horizontal load simultaneously act, the negatively inclined pile generates a horizontal component along the inclined direction of the pile under the vertical load, which can offset part of the horizontal force. When the vertical displacement of the negative inclined pile is limited by the cap, the axial force along the inclined pile will be generated when the horizontal force acts on the pile top. The axial force can be decomposed into a vertical force and horizontal force. The horizontal component is opposite to the horizontal load, which further reduces the horizontal resultant force acting on the inclined pile. Under the action of vertical force, the horizontal component of the positive inclined pile is produced in the same direction as the horizontal force, which increases the horizontal force acting on the pile top. There is no horizontal component of the vertical pile under vertical force. Therefore, under the combined action of vertical and horizontal forces, the lateral bearing capacity of the negative inclined pile is the maximum, while that of the positive inclined pile is the minimum.

(a)   (b)
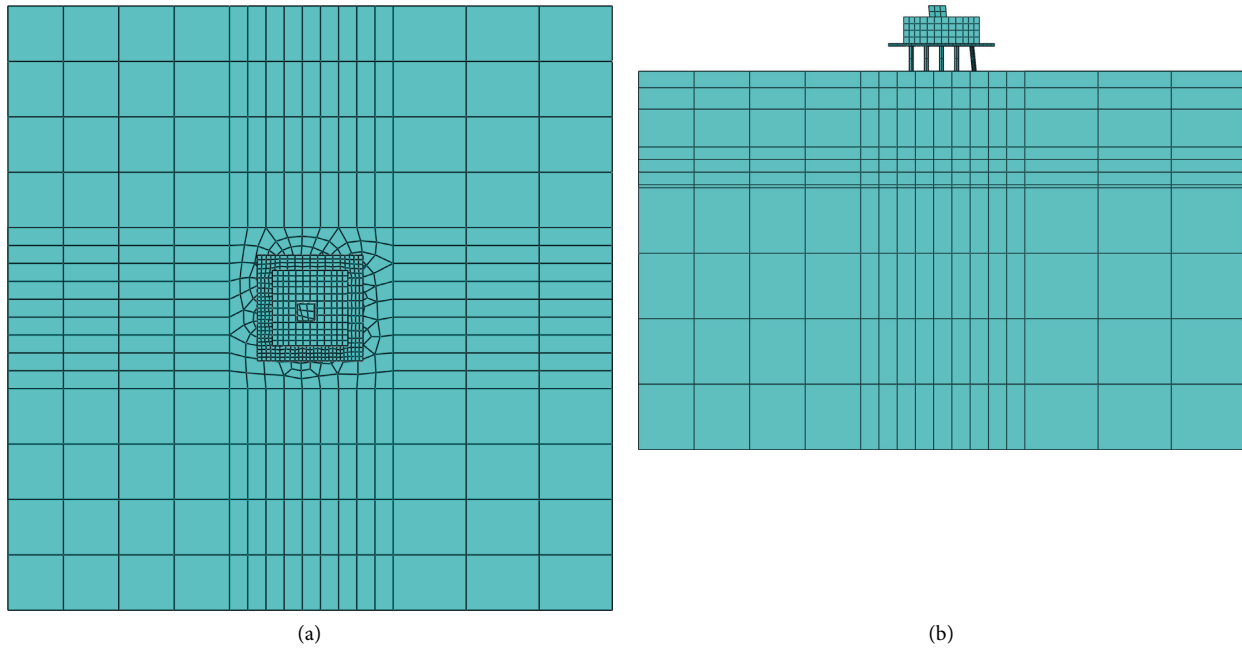
Figure 7: Single cap model: (a) vertical view of single cap model; (b) lateral view of single cap model.
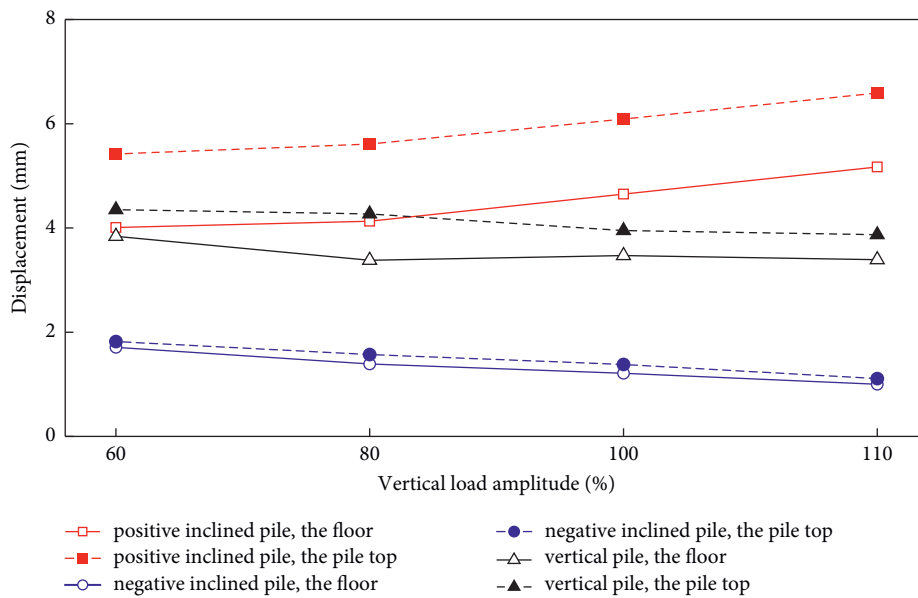
Figure 8: Pile displacement line chart.

Figure 9 shows a comparison of the bending moments of piles in different inclined directions. The bending moment diagrams of the positive inclined pile, vertical pile, and negative inclined pile have the same shape, a circular arc; the maximum bending moment is located in different parts. The shape of the bending moment diagram is the same, which indicates that the soil has the same constraint behavior on the pile side, and the change in the inclined direction of the pile does not affect the interaction between the pile side and the soil. The bending moment values of different piles vary. The positive inclined pile has the largest bending moment value, and the negative inclined pile has the smallest bending

moment value. The bending moment of the pile depends on the horizontal force acting on the pile top. The horizontal force of the positive inclined pile is the largest, so the bending moment is the largest. The positions of the maximum bending moments of the positive inclined pile, vertical pile, and negative inclined pile are −1.6 m, −1.1 m, and −0.9 m, respectively. With a decrease in the pile bending moment, the position of the maximum bending moment increases.

The inclined direction of the pile has a great influence on its lateral bearing capacity. The inclined pile indirectly changes the horizontal bearing capacity of the foundation by
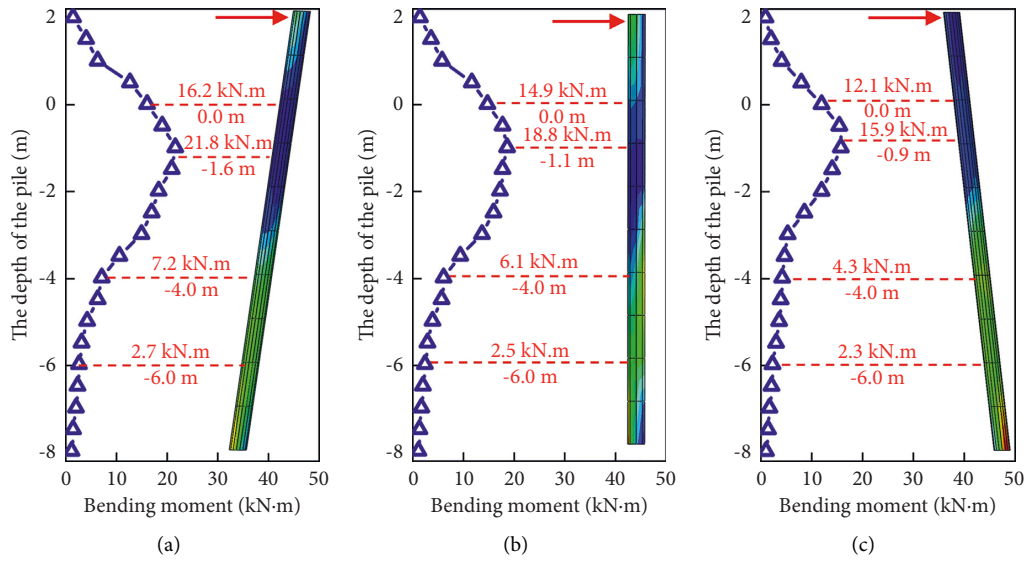
FIGURE 9: Pile bending moment comparison diagram: (a) bending moment of positive inclined pile; (b) bending moment of vertical pile; (c) bending moment of negative inclined pile.

affecting the horizontal resultant force, which can be divided in two ways. For the first method, when the vertical force acts on the inclined pile, the pile interacts with the soil to produce the horizontal component. When the direction of the horizontal component is opposite to the direction of the horizontal force, the lateral bearing capacity of the foundation can be improved; when the direction is the same, the horizontal bearing capacity of the foundation will be reduced. For the second method, the pile top limits the vertical displacement. When the horizontal load acts on the pile top or cap, the inclined pile will produce the horizontal component, which increases or decreases the horizontal force acting on the pile.

As shown in Figure 9, the stress of the lower part of the pile is significantly greater than that of the upper part of the pile, which is caused by the pile structure. The upper part of the pile is filled with concrete, and the stiffness is large. The lower part of the pile is a hollow steel tube, and the stiffness is small. The stress in the lower part of the pile is greater than that in the upper part of the pile under the bending moment.

3.2. Pile Inclination Angle. Setting a negative inclined pile in a pile group foundation can reduce the lateral displacement, and the inclination of the pile will not only affect its vertical bearing capacity but also cause some difficulties in construction. Therefore, piles with inclination angles of 0°, 5°, and 10° are selected as the research objects, and the influence of the inclination of the pile body on the horizontal bearing capacity of the pile group foundation is analyzed through numerical simulation. In this study, the same depth of the pile is maintained. When the inclination angle of the pile is changed, the length of the pile is appropriately changed to ensure that the depth of the pile into the soil remains unchanged.

The inclined angle of the pile influences the horizontal bearing capacity of the foundation. Figure 10 shows a
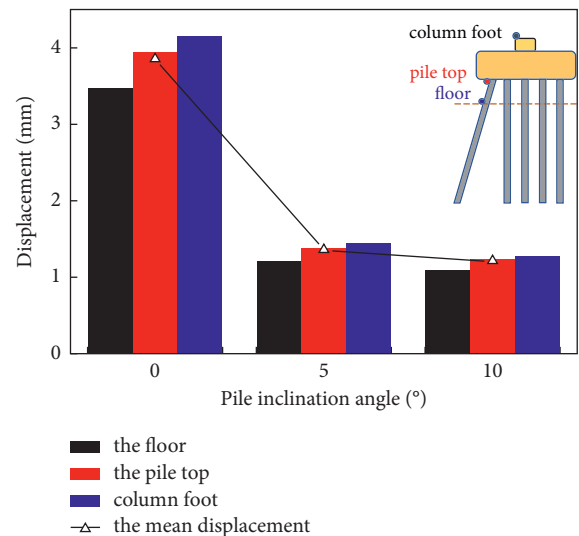
FIGURE 10: Contrast diagram of foundation displacement.

comparison of the foundation lateral displacement at different inclined angles of the pile body. The inclined angle 0° represents the vertical pile, and 5° and 10° are the negative inclined pile angles. The lateral displacement of vertical piles is obviously larger than that of negative piles with inclined angles of 5° and 10°. Setting negative piles can effectively reduce the lateral displacement of the foundation. The displacement of the 5° negatively inclined pile is smaller than that of the vertical pile, decreasing by 60.5%. The displacement of the 10° negatively inclined pile is smaller than that of the 5° negatively inclined pile, decreasing by 13.3%. The larger the inclination angle of the negative inclined pile, the smaller the horizontal displacement of the foundation. When the inclination angle is greater than 5°, a further increase in the inclination angle cannot effectively reduce the lateral displacement of the foundation. An excessively large

(a)

(b)
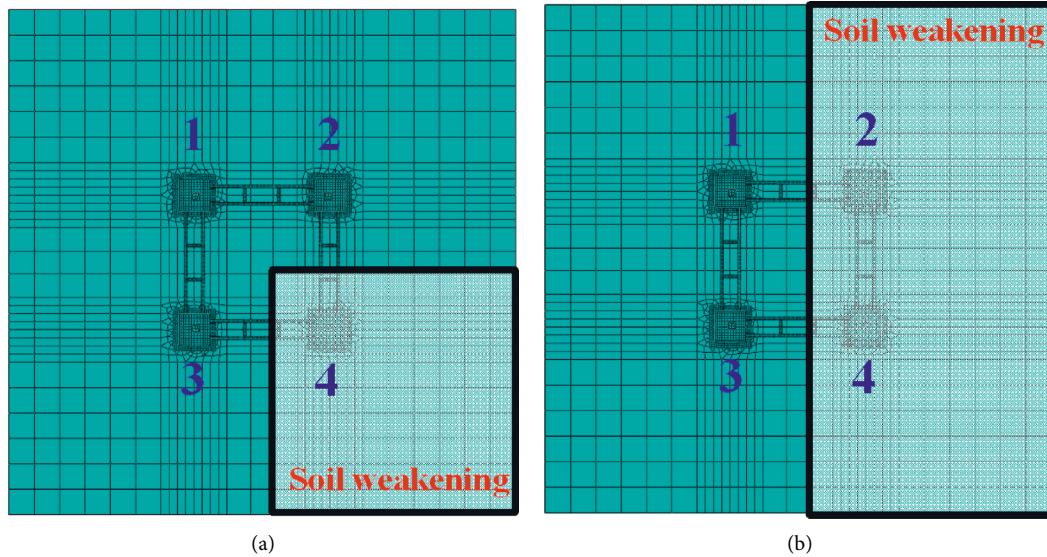
FIGURE 11: Uneven settlement condition of foundation: (a) single foundation settlement; (b) double foundation settlement.

inclined angle will weaken the vertical bearing capacity of the pile. To improve the lateral bearing capacity without reducing the vertical bearing capacity of the inclined pile, an inclined pile with an inclination greater than 10° should not be set.

4. Influence of Uneven Settlement on the Bearing Capacity of Inclined Pile Foundations

A full-scale numerical model of a transmission tower foundation was established to analyze the distribution of the internal force and displacement of an inclined pile foundation under the action of uneven settlement. The most unfavorable load is applied to the foundation, and the settlement of the foundation is caused by weakening the soil in different parts. To simulate the settlement condition of a single foundation, the strength of the soil under a single foundation is weakened, and the strength of the other soils is kept constant. To simulate the settlement condition of the double foundation, the strength of the soil under the double foundation is weakened, and the strength of the other soil remains constant. Different foundation settlement conditions are shown in Figure 11. In this study, the same depth of the pile is maintained. When the inclination angle of the pile is changed, the length of the pile is appropriately changed to ensure that the depth of the pile into the soil remains unchanged.

4.1. Analysis of Foundation Displacement. Figure 12 shows a comparison of the basic vertical displacement. The upward movement of the vertical displacement is positive, and the downward movement is negative. When the soil is uniform, the displacement of each cap is small. The maximum upward displacement is 1.7 mm, and the maximum downward displacement is 4.7 mm. When the soil under foundation
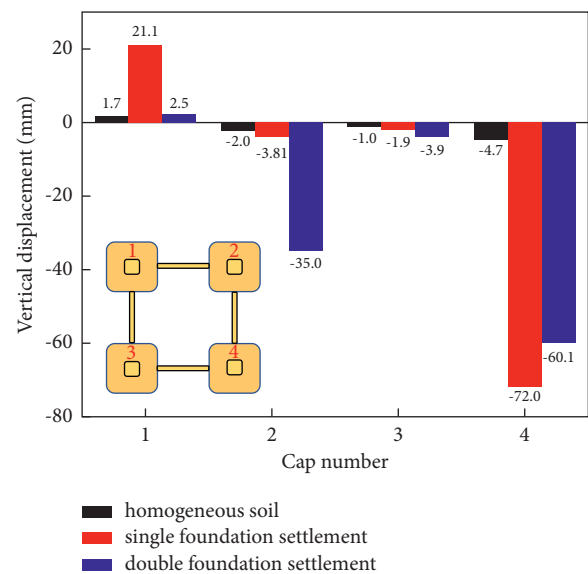
FIGURE 12: Vertical displacement contrast diagram of cap.

No. 4 weakens, the maximum upward displacement is 21.1 mm, and the maximum downward displacement is 72.0 mm. The settlement of a single foundation significantly affects the vertical displacement of the whole foundation and changes the stress states of different caps, and the four caps interact through connecting beams. The soil under foundation No. 4 weakens; the cap is unloaded; and part of the load is transferred to other caps through connecting beams. The vertical displacement of cap No. 4 increases to 72.0 mm, and the vertical displacement of cap Nos. 1, 2, and 3 increases due to the increase in load transmitted from cap No. 4. In the case of double foundation settlement, the vertical displacement of foundations No. 2 and No. 4 obviously increases, while the vertical displacement of foundations No. 1
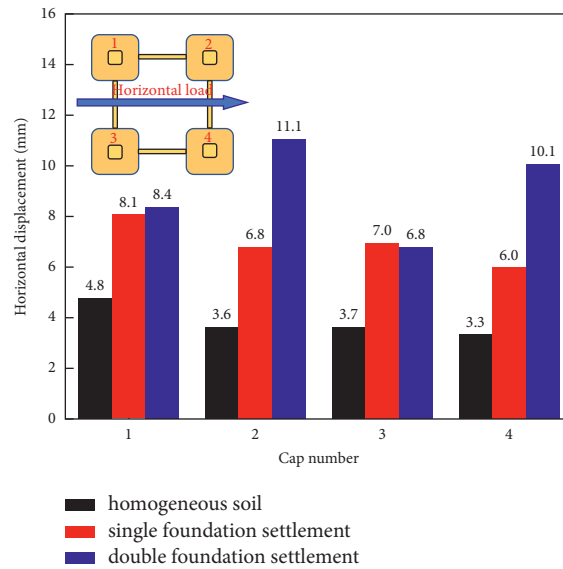
FIGURE 13: Horizontal displacement contrast diagram of cap.

and No. 3 slightly increases. Part of the load of foundations No. 2 and No. 4 is transferred to foundations No. 1 and No. 3 through connecting beams, and the displacement of foundations No. 1 and No. 3 is slightly increased.

Figure 13 shows a comparison of the horizontal displacement of the cap; the direction of the horizontal force is also shown. When the soil is uniform, the minimum displacement of the cap is 3.3 mm and the maximum displacement is 4.8 mm. Due to the constraint of the beam, the horizontal displacement of the four caps is evenly distributed. When the single foundation is settled, the horizontal displacements of the four caps are larger than those of the uniform foundation. The distribution law of the horizontal displacements is equivalent to that of the uniform foundation. The maximum displacements appear in cap No. 1, and the minimum displacements appear in cap No. 4. In the case of double foundation settlement, the increase in the displacements of the four caps is obvious, and the distribution law of horizontal displacements is quite different from that in the case of uniform soil. The horizontal displacements of caps No. 2 and No. 4 are obviously larger than those of caps No. 1 and No. 3. When the double foundation is settled, half of the soil is weakened, and the ability of the foundation to bear the horizontal load is obviously weakened. As a result, the horizontal displacement of the whole foundation is obviously larger than the horizontal displacement of the foundation when the soil is uniform, and the constraint effect of the beam on the horizontal displacement of the foundation is weakened.

Figure 14 shows the displacement cloud diagram of the caps. The vertical displacements of the four caps are obviously different. The vertical integrity of the foundation is poor, and the ability of connecting beams to adjust the vertical displacements of the caps is limited. The lateral displacement of the whole foundation is uniform, the displacement difference between different caps is small, and the foundation beam has a strong ability to adjust the horizontal displacement.

The displacement variation of inclined pile foundations under uneven settlement is analyzed by weakening the strength of the corresponding soil. The horizontal displacement of the pile group foundation increases with uneven settlement, but the difference in horizontal displacement between the four caps is small. The vertical displacement of the foundation with uneven settlement obviously increases, while the vertical displacement of the other three caps exhibits no obvious change.

4.2. Analysis of Foundation Internal Force. The uneven settlement of the foundation affects the displacement of the cap and the internal force of the pile foundation. To study the influence of uneven foundation settlement on the internal force of inclined piles, the maximum stress of piles under uniform soil, single foundation settlement, and double foundation settlement was compared. Figure 15 shows the maximum stress of different pile bodies under different caps.

As shown in the figure, the stress of the inclined pile is greater than that of the vertical pile. The stress of the pile under cap No. 1 is the minimum; that of the pile under cap No. 4 is the maximum; and that of the pile under caps No. 2 and No. 3 is at the same level. When the soil is uniform, the difference in the maximum stress of the pile under different caps is caused by different loads acting on the caps. When the single foundation is settled, the stress of the inclined pile and vertical pile under cap No. 4 decreases, while the stress of the inclined pile under cap No. 2 and cap No. 3 obviously increases. The increase in the vertical pile stress is smaller than that of the inclined pile, and the pile stress under cap No. 1 exhibits no obvious change. When the double foundation is settled, the maximum stress of caps No. 2 and No. 4 slightly decreases, while the maximum stress of caps No. 1 and No. 3 increases. In conclusion, the stress variation of the inclined pile is obviously greater than that of the vertical pile when the foundation undergoes uneven settlement.

(a)   (b)   (c)

(d)   (e)   (f)
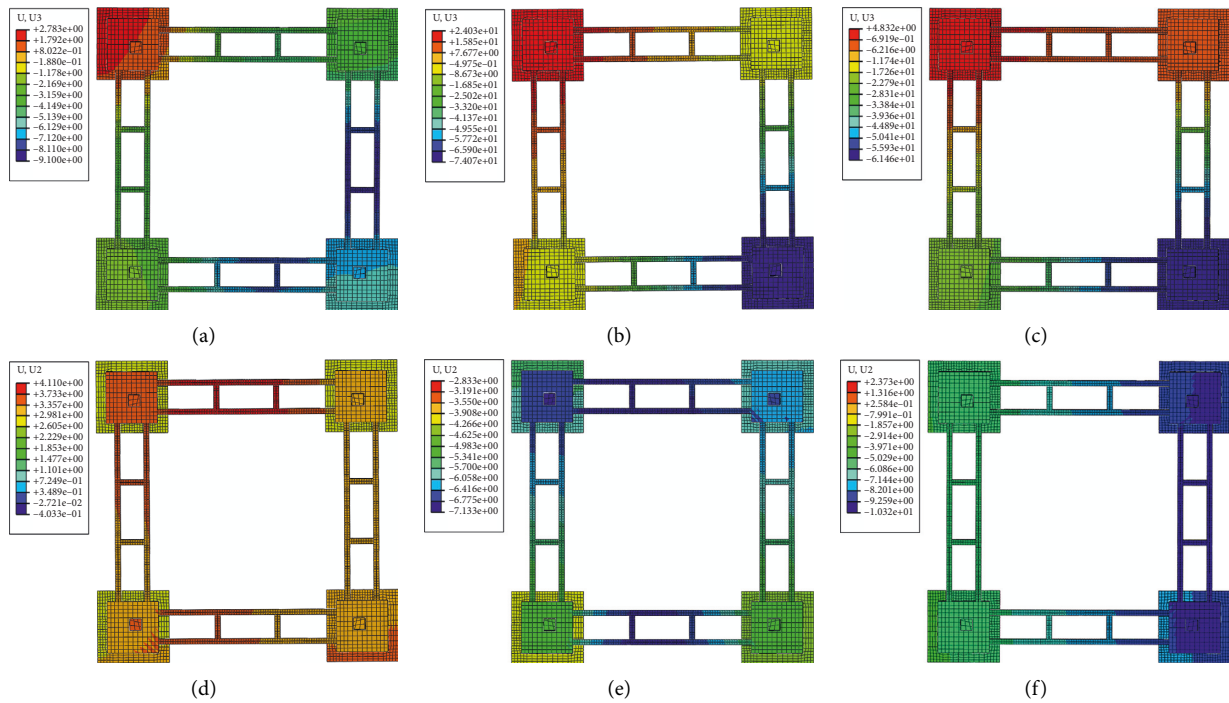
FIGURE 14: Displacement contrast diagram of cap: (a) homogeneous soil vertical displacement; (b) single foundation settlement vertical displacement; (c) double foundation settlement vertical displacement; (d) homogeneous soil horizontal displacement; (e) single foundation settlement horizontal displacement; (f) double foundation settlement horizontal displacement.
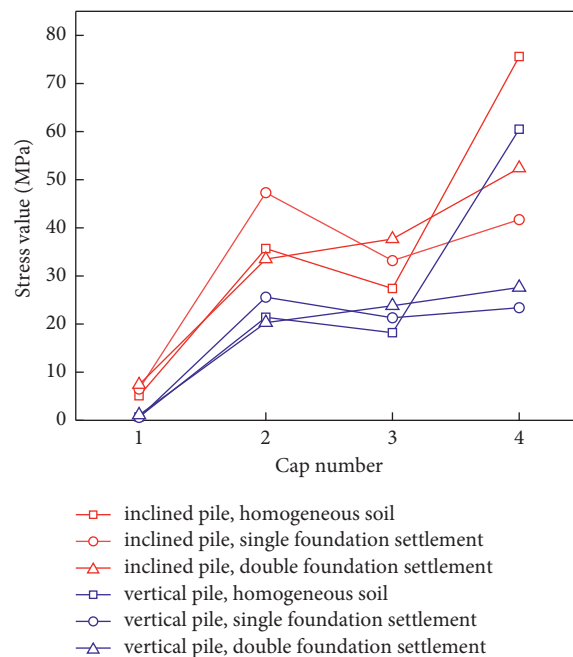
FIGURE 15: Maximum stress contrast diagram of pile.

The bending moment diagram of the inclined pile under uneven settlement is shown in Figure 16. The bending moment of cap pile No. 1 is the smallest, while the bending moments of cap pile Nos. 2, 3, and 4 obviously change under different settlement conditions. Under the action of uneven settlement, the bending moment of cap pile No. 1 increases, but the variation is small. The bending moment of the inclined pile under cap No. 2 is the smallest when the soil is uniform; the foundation settlement increases the bending moment; and the influence of the double foundation settlement is greater than that of the single foundation settlement. The bending moment of the inclined pile under cap
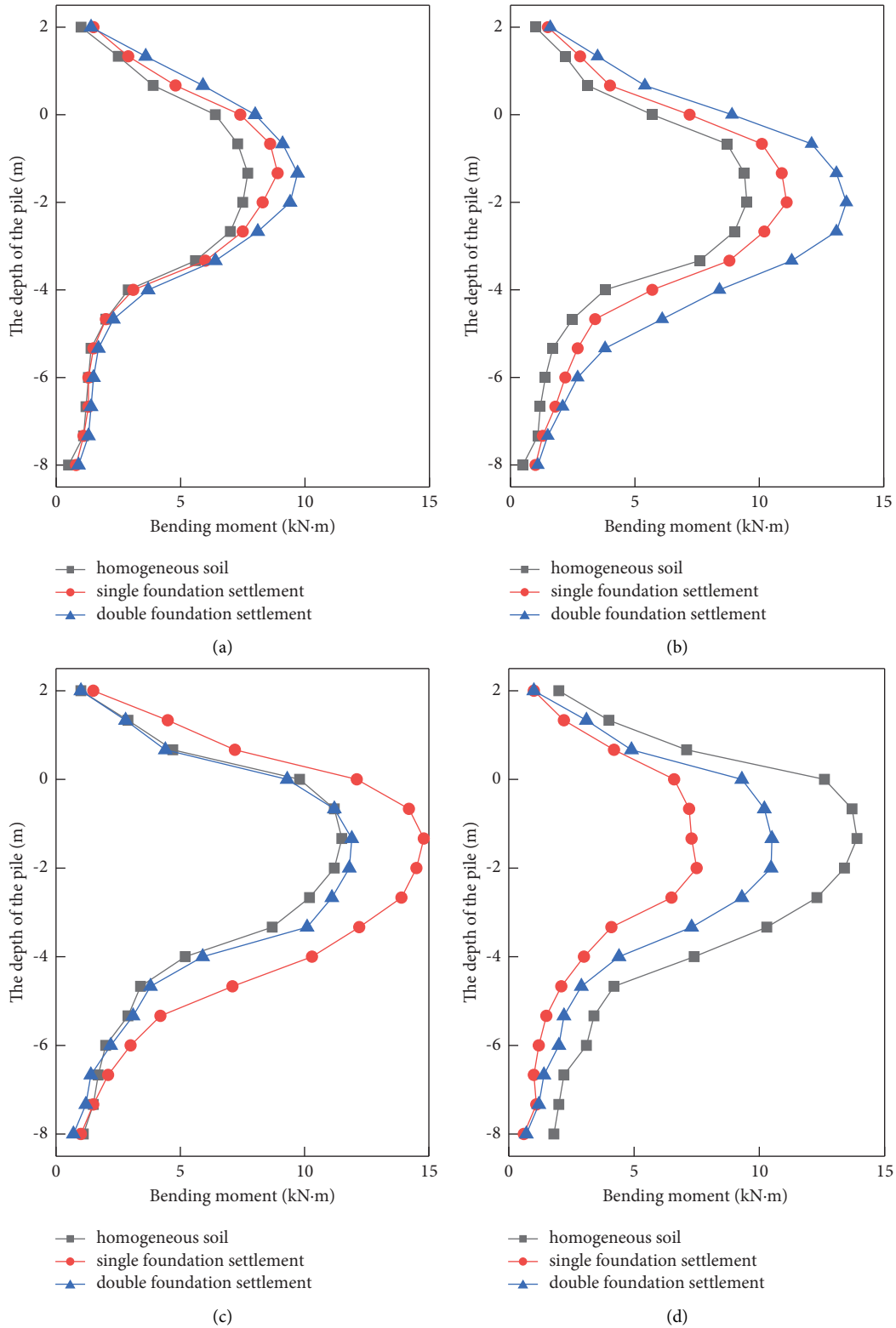
Figure 16: Bending moment diagram of inclined pile: (a) No. 1 pile cap, (b) No. 2 pile cap; (c) No. 3 pile cap; (d) No. 4 pile cap.

No. 3 is the largest when the single foundation is settled. The bending moment of pile No. 4 under the cap is the maximum when the soil is uniform, and when the soil layer is weakened, the bending moment of pile No. 4 decreases.

5. Conclusions

In this paper, a single cap finite element model is established to study the influence of pile tilt direction and angle on the lateral bearing capacity of foundations. A multi-cap finite element model is established to analyze the influence of uneven settlement on the displacement and internal force of inclined pile foundations. The following conclusions can be drawn:

(1) The lateral displacement of the negatively inclined pile is the smallest, while that of the positively inclined pile is the largest under the combined action of horizontal load and downward load. Setting a negative inclined pile can improve the lateral bearing capacity of the foundation.

(2) The inclination angle of a negatively inclined pile has a significant influence on its lateral bearing capacity. When the inclination angle is less than 5°, the lateral bearing capacity obviously increases with increasing angle. When the inclination angle exceeds 5°, the lateral bearing capacity does not significantly increase with increasing angle.

(3) Under the action of uneven settlement, the difference in vertical displacement between each cap is obvious, but the difference in horizontal displacement is small. The basic type has good horizontal integrity but insufficient vertical integrity.

(4) The stress variation of the inclined pile is obviously greater than that of the vertical pile when the foundation settlement is uneven. The bending moment of the inclined pile decreases in weakened soil but increases in unweakened soil.

Data Availability

The data used to support the findings of this study are available from the corresponding author upon request.

Conflicts of Interest

The authors declare that they have no conflicts of interest.

Acknowledgments

References

[1] D. Kong, M. Deng, and Y. Li, "Numerical simulation of seismic soil-pile interaction in liquefying ground," *IEEE Access*, vol. 8, pp. 195–204, 2020.

[2] J. Li, X. Wang, Y. Guo, and X. B Yu, "Vertical bearing capacity of the pile foundation with restriction plate via centrifuge modelling," *Ocean Engineering*, vol. 181, pp. 109–120, 2019.

[3] M. Iovino, R. M. S. Maiorano, L. de Sanctis, and S. Aversa, "Failure envelopes of pile groups under inclined and eccentric load," *Géotechnique Letters*, vol. 11, no. 4, pp. 247–253, 2021.

[4] A. Franza, M. J. DeJong, M. Morici, and C. F. Dezi, *Artificial neural networks for the evaluation of impedance functions of inclined pile groups [M] Numerical Methods in Geotechnical Engineering IX*, CRC Press, Boca Raton, Florida, United States, pp. 823–828, 2018.

[5] M. Bharathi, R. N. Dubey, and S. K. Shukla, "Experimental investigation of vertical and batter pile groups subjected to dynamic loads," *Soil Dynamics and Earthquake Engineering*, vol. 116, pp. 107–119, 2019.

[6] R. Daher and J. M Abbas, "The behavior of pile group under inclined static load with different angle of inclination in sandy soil," *Diyala Journal of Engineering Sciences*, vol. 14, no. 2, pp. 52–61, 2021.

[7] F. Dezi, S. Carbonari, and M. Morici, "A numerical model for the dynamic analysis of inclined pile groups," *Earthquake Engineering & Structural Dynamics*, vol. 45, no. 1, pp. 45–68, 2016.

[8] C. S. Goit and M. Saitoh, "Model tests on horizontal impedance functions of fixed-head inclined pile groups under soil nonlinearity," *Journal of Geotechnical and Geoenvironmental Engineering*, vol. 140, no. 6, 2014.

[9] S. Carbonari, M. Morici, F. Dezi, F. Gara, and G Leoni, "Soil-structure interaction effects in single bridge piers founded on inclined pile groups," *Soil Dynamics and Earthquake Engineering*, vol. 92, pp. 52–67, 2017.

[10] G. M. Álamo, A. E. Martínez-Castro, L. A. Padrón, J. J. Aznarez, R. Gallego, and O Maeso, "Efficient numerical model for the computation of impedance functions of inclined pile groups in layered soils," *Engineering Structures*, vol. 126, pp. 379–390, 2016.

[11] H. Kheradi, Y. Morikawa, G. Ye, and F Zhang, "Liquefaction-Induced buckling failure of group-pile foundation and countermeasure by partial ground improvement," *International Journal of Geomechanics*, vol. 19, no. 5, 2019.

[12] S. Ye, Z. Zhao, and Y. Zhu, "Study on negative friction of pile foundation in single homogeneous soil layer in collapsible loess area of Northwest China," *Arabian Journal of Geosciences*, vol. 14, no. 12, p. 1137, 2021.

[13] H. Ghasemzadeh, M. Tarzaban, and M. M. Hajitaheriha, "Numerical analysis of pile–soil–pile interaction in pile groups with batter piles," *Geotechnical & Geological Engineering*, vol. 36, no. 4, pp. 2189–2215, 2018.

[14] P. J. Imrich, C. Kirchlechner, and G. Dehm, "Influence of inclined twin boundaries on the deformation behavior of Cu micropillars," *Materials Science and Engineering A*, vol. 642, pp. 65–70, 2015.

[15] X. Zhang, X. Chen, Y. Wang, M. Ding, J. Lu, and H. Ma, "Quasi-static test of the precast-concrete pile foundation for railway bridge construction," *Adv. Concrete Construct*, vol. 10, no. 1, pp. 49–59, 2020.

[16] E. Conte, L. Pugliese, A. Troncone, and M Vena, "A simple approach for evaluating the bearing capacity of piles subjected to inclined loads," *International Journal of Geomechanics*, vol. 21, no. 11, 2021.

[17] T. Sui, C. Zhang, D. s Jeng et al., "Wave-induced seabed residual response and liquefaction around a mono-pile foundation with various embedded depth," *Ocean Engineering*, vol. 173, pp. 157–173, 2019.

[18] R. P. Chen, W. H. Zhou, and Y. M. Chen, "Influences of soil consolidation and pile load on the development of negative skin friction of a pile," *Computers and Geotechnics*, vol. 36, no. 8, pp. 1265–1271, 2009.

[19] J. Wang, D. Zhou, T. Ji, and S. Wang, "Horizontal dynamic stiffness and interaction factors of inclined piles," *International Journal of Geomechanics*, vol. 17, no. 9, 2017.

[20] C. Y. Chen and H. Q. Hsu, "Modeling of batter pile behavior under lateral soil movement [C] //IOP Conference Series: materials Science and Engineering," *IOP Conference Series: Materials Science and Engineering*, vol. 216, no. 1, 2017.

Research Article

Observation System Optimization of Offshore Acoustic Exploration for Estimating Submarine Geological Structures via Directivity Analysis

Chao Fu [ID],[1] **Lei Hao,**[1] **Pengfei Zhou,**[2] **Lei Chen** [ID],[1] **Xiaobin Xu,**[2] **Kai Wang,**[2] **and Miaojun Sun**[3]

[1]*Geotechnical and Structural Engineering Research Center, Shandong University, Jinan 250061, China*
[2]*Shandong Hi-speed Group Co., Ltd., Jinan 250101, China*
[3]*Huadong Engineering Co., Ltd., Zhejiang 311122, China*

Correspondence should be addressed to Lei Chen; clei667@163.com

To better understand the shallow sea geological information and avoid the risk caused by potential geo-disasters, the efficient offshore geological exploration methods are required. Better detection resolution can be obtained by using a spark source. As the foundation, the observation system plays an important role for geological detection. The influence of the variation of the parameters of the observation system on the detection accuracy is analysed theoretically. Then, the numerical simulations based on the finite difference method was applied, and imaging characteristics of observation system with different parameter were studied. For submarine acoustic exploration, the spark source with frequency over 200 Hz can obtain the clear reflections for geological interpretation; besides, the receiver array with the interval of 5 m–10 m helps to obtain better wave signals when the buried depth of a geological body is less than 300 m, and the width is more than 10 m. Based on numerical simulations, the observation system was optimized and designed. The results of numerical examples show that the accurate position information of the structure can be obtained by using the observation system proposed in this paper. Different imaging performances are obtained by adjusting the parameters of the observation system. On this basis, combined with directivity analysis, the optimal observation system parameters are proposed. Finally, the proposed observation system is used to image the fault model. The research results of this paper can provide reference for the observation system design in similar projects.

1. Introduction

With the rapid development of social economy, the resources and living space are required urgently [1]. Rational utilization of offshore resources and protection of the marine environment are important strategies [2]. In recent years, the rapid development of marine resources (such as oil and gas) and offshore engineering (such as cross-sea bridges and subsea tunnels) has led to a growing concern on the marine geological environment [3]. Marine geo-disasters (such as submarine landslides and submarine faults) enormously threaten and often destroy the offshore engineering [4]. For example, in 1969, Hurricane Camille induced a submarine landslide, and the fast-moving landslide body destroyed three offshore platforms (loss over one million dollars) [5].

Therefore, accurate geological detection and warning on geo-hazards risk in time are critical to the safety of offshore engineering [6].

At present, the traditional methods [7] mainly include echo sounding systems [8, 9], side sonar systems [10–13], shallow profile systems, and high-resolution seismic detection systems [14]. In practice, the detection of marine geo-disasters is often based on the combination of seabed topography and various means of detection [15, 16]. Among them, acoustic exploration has been widely used [17]. Research on the detection of marine geo-disasters has been the core of marine geologists [18]. Many researchers have done a lot of work for them, such as OOI (the Ocean Observatories Initiative) program and the DONET (Development of Dense Ocean-floor Network System for Earthquake and Tsunami)

systems in Japan, as well as the ESONET (the European Sea Observatory Network) system and the COSTA (Continental Slope Stability) program [19–21]. These research works promoted the progress in the formation mechanism of marine geo-disasters and detection techniques [22]. However, for the specific environment and requirement, the observation system and processing approach should be optimized for the best result, improving the accuracy of geological interpretation (depth less than 300 m, width greater than 10 m).

This method is suitable for the detection in the offshore and seabed engineering survey period. The observation system can be adaptively adjusted according to the difference of underground geological disaster, and the fault can be imaged with higher resolution. The remainder of the paper was organized as follows. First, combined with engineering requirements, we propose an optimization method for the observation system under the condition of array reception. Then, based on the imaging results, different parameters are evaluated by the observation system evaluation method, and the optimal observation parameters are obtained. Finally, the optimized observation system parameters are used for data processing and imaging. Numerical model examples show that the directivity parameter is a valid method for evaluating the observation system and can obtain the exact position of the interface.

2. Observation System and Methodology

The observation system is the key foundation for exploration. A better observation system can effectively improve the exploration result. For acoustic exploration, the key factors are the source and receiver array. We used the acoustic directivity parameter to initially evaluate the observation system. The directivity parameter can be expressed as follows:

$$F_\theta(\alpha) = \left| \frac{\sin[N\pi f d/v(\sin\alpha - \sin\theta)]}{N\sin[\pi f d/v(\sin\alpha - \sin\theta)]} \right|, \tag{1}$$

where N represents the number of sources, f represents the dominant frequency of source, d represents the source spacing, v represents the medium velocity, and α represents the scanning angle, $\alpha \in [-\pi/2, \pi/2]$. θ is the special angle. In this manuscript, it is equal to 90. With the increase of the number of sources or geophones, the detection effect will be improved. However, it will reduce the detection efficiency and improve the cost. Therefore, we use the ratio of the side lobe to main lobe of the directivity parameter as the criterion. When the side lobe ratio is higher than 0.6, we think the detection effect is higher.

2.1. Main Parameters of the Observation System.

The typical sources for acoustic exploration are the air gun and spark. The main parameter is frequency. Frequency determines the depth and the resolution of the migration result. In general, the high frequency wavelet has a better resolution. However, the attenuation of the high frequency is larger than that of the lower frequency signal, resulting in a shallower detection

depth [23]. The detection demand of landslides along the offshore is no more than 200 m, and the detection target scale is about 10 m. Therefore, we choose the high frequency spark source as the excitation signal.

The geophone interval of the receiver array. The geophone interval of the receiver array is the basic parameter of the observation system, relating to the resolution and the coverage of acoustic exploration. In general, the observation system (including the source and receivers) is placed under the sea surface. The following principles should be met [24]: firstly, the track pitch should be smaller than the first Fresnel zone; secondly, the track pitch should satisfy the sampling theorem to avoid spatial aliasing; thirdly, the application cost should be minimum.

To reveal the imaging characteristics of the receiver array with different intervals, the numerical simulations and directivity analysis are introduced to evaluate the observation system. In simulation, the total number of sources is 20. Four geophone intervals are adopted by 2 m, 5 m, 10 m, and 20 m, and the total number of corresponding geophones are 251, 101, 51, and 26. The sampling rate is 0.5 ms, and the Ricker wavelet of 200 Hz is adopted.

2.2. Numerical Simulation Method.

The typical acoustic numerical modelling method includes a geometric ray and wave equation. The wave equation method is better at simulating the seismic propagation in complex geological models. In this study, the finite difference method based on the two-dimensional wave equation is adopted. For two-dimensional models, the wave equation is as follows:

$$\frac{\partial^2 U(x,z)}{\partial x^2} + \frac{\partial^2 U(x,z)}{\partial z^2} = \frac{1}{V(x,z)^2} \frac{\partial^2 U(x,z)}{\partial t^2} + s(x,z,t), \tag{2}$$

where $V(x,z)$ represents the velocity in the vertical direction of the particle at (x,z); U represents pressure field; and s(x, z, t) represents the source function. In the acoustic wave equation, the properties of the medium are usually designed by wave velocity $V(x,z)$. Then, the equation can be transferred based on the Taylor formula, and the equation of high-order finite difference is as follows [25]:

$$U_{i,j}^{n+1} - 2U_{i,j}^n + U_{i,j}^{n-1}$$

$$= V_{i,j}^2 \cdot \Delta t^2$$

$$\cdot \left(\frac{U_{i+m,j}^n - 2U_{i,j}^n + U_{i-m,j}^n}{\Delta x^2} + \frac{U_{i,j+m}^n - 2U_{i,j}^n + U_{i,j-m}^n}{\Delta z^2} \right). \tag{3}$$

2.3. Data Processing Method.

To compare observation systems with different parameters, the seismic data are processed for imaging the geological condition. The processing scheme mainly consists of three parts: preprocessing, waveform processing, and imaging. To obtain more accurate imaging, we use Gaussian smoothing (window size equal to
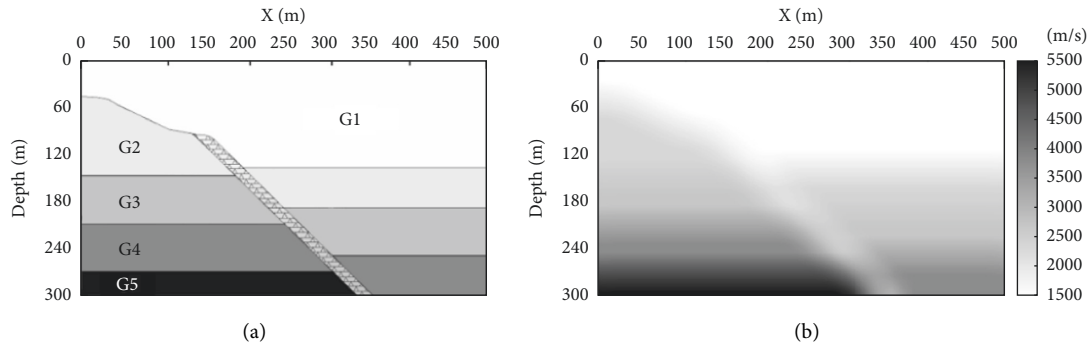
FIGURE 1: The submarine geological model with layered media and an inclined fault. (a) True velocity model. (b) Initial velocity model for imaging.

10) for the initial model to obtain the model after imaging. The preprocessing includes data conversion. The waveform processing mainly includes direct wave removing, attenuation compensation, spectrum analysis, amplitude balance, generate common middle point (CMP) gather, velocity analysis, and normal moveout (NMO) correction. Meanwhile, the filtering method is used to extract effective signals and remove noise in reflected waves [26–28]. In addition, the imaging method includes stack, Kirchhoff poststack migration [29], and time-depth conversion.

3. Numerical Examples

To design and optimize the parameters of the observation system, a submarine geological model with a fault was built and studied as an example. As is shown in Figure 1(a), the model has the length of 500 m with the depth of 300 m. The first layer which marked G1 represents the seawater. The inclined fault is located at the middle of the geological model. The bedrock is composed by 3 or 4 layers. The geological parameters of G1 are Vp= 1500 m/s. The geological parameters of G2 are Vp= 2200 m/s. The geological parameters of G3 are Vp= 2500 m/s. The geological parameters of G4 are Vp= 3500 m/s. The geological parameters of G5 are Vp= 5500 m/s. The fault is filled by broken rocks and water. Therefore, the wave speed of Vp is 1700 m/s. To obtain more accurate imaging, we use Gaussian smoothing for the initial model (Figure 1(a)) to obtain the model after imaging Figure 1(b). In practice, the velocity can be obtained by velocity scanning or tomography imaging method calculations.

3.1. Imaging Difference of the Observation System Using the Wavelet with Different Frequencies.

At first, the influence of wavelet frequency on the imaging result was studied. To study the difference, the same receiver array with the geophone interval of 5 m and the source with the wave spreading around were adopted. Meanwhile, the common source gather (CSG) mode with one source was adopted in data acquisition. Figure 2 shows the imaging results in time domain using the wavelet with the frequency of 50 Hz, 100 Hz, 200 Hz, and 400 Hz.

According to the imaging results, it is easy to find that the wavelength of these four results are different. Figure 2(a) is the imaging result using the wavelet with the frequency of 50 Hz, which shows the reflected waves have the length of about 40 m. In that case, the boundary between the seabed and the stratum of the large scale (A1) can be basically displayed, but the fractured zone in the middle is blurred (A2). Although the existence of interfaces (A1) can be judged, it is hard to accurately locate the interfaces. Figure 2(b) is the imaging result using the wavelet with the frequency of 100 Hz, which shows the clearer reflected waves with the increasing frequency. In that case, the wavelength is about 20 m, and the existence of the fracture zone (B1) can be judged. Figure 2(c) is the result using the wavelet with the frequency of 200 Hz, the image is the clearest, and the boundary and the thickness (C1) are easily estimated. Figure 2(d) is the result using the wavelet with the frequency of 400 Hz, and the wavelet length is the smallest of all. However, when the high-frequency wave propagates in the stratum, the energy of the reflected signal is weaker (D2). The interface position is obtained for both 200 Hz and 400 Hz frequency wavelets. However, when the frequency is 400 Hz, the energy of the event is obviously weakened, and the imaging sharpness is decreased. As the frequency increases, the artifacts in the imaging results become more and more significant. Moreover, the acoustic waves are attenuated, and the low frequencies excited by the spark source are more stable. Combining the above information, we finally chose the 200 Hz frequency as the excitation frequency.

3.2. Imaging Difference of the Observation System with Different Geophone Intervals.

It is necessary to set the geophone interval reasonably for imaging resolution. According to the theoretical analysis, the geophone interval has influence on the coverage time and imaging result, as well as the detection cost. In that case, finding the maximum geophone interval (meeting the resolution requirement) is important to field exploration. In this part, the receiver arrays with different geophone intervals were studied, respectively.

Figure 3 shows the imaging results using the observation system with different intervals (2 m, 5 m, 10 m, and 20 m, respectively) as well as direction analysis (the greater the energy in a certain direction, the stronger the directivity. When the pointing distribution is uniform, it indicates that the acoustic wave beam has more balanced illumination in

(a)

(b)

(c)

(d)
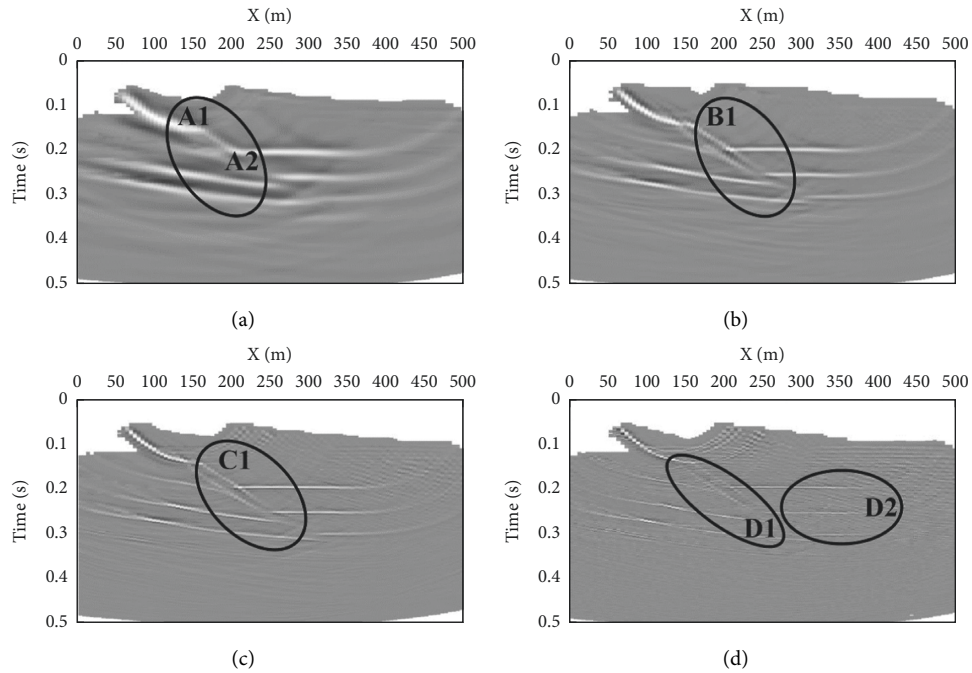
FIGURE 2: The imaging results in time domain using the wavelet with different frequencies: (a) imaging result of 50 Hz, (b) imaging result of 100 Hz, (c) imaging result of 200 Hz, and (d) imaging result of 400 Hz.

(a)

(b)

(c)

(d)
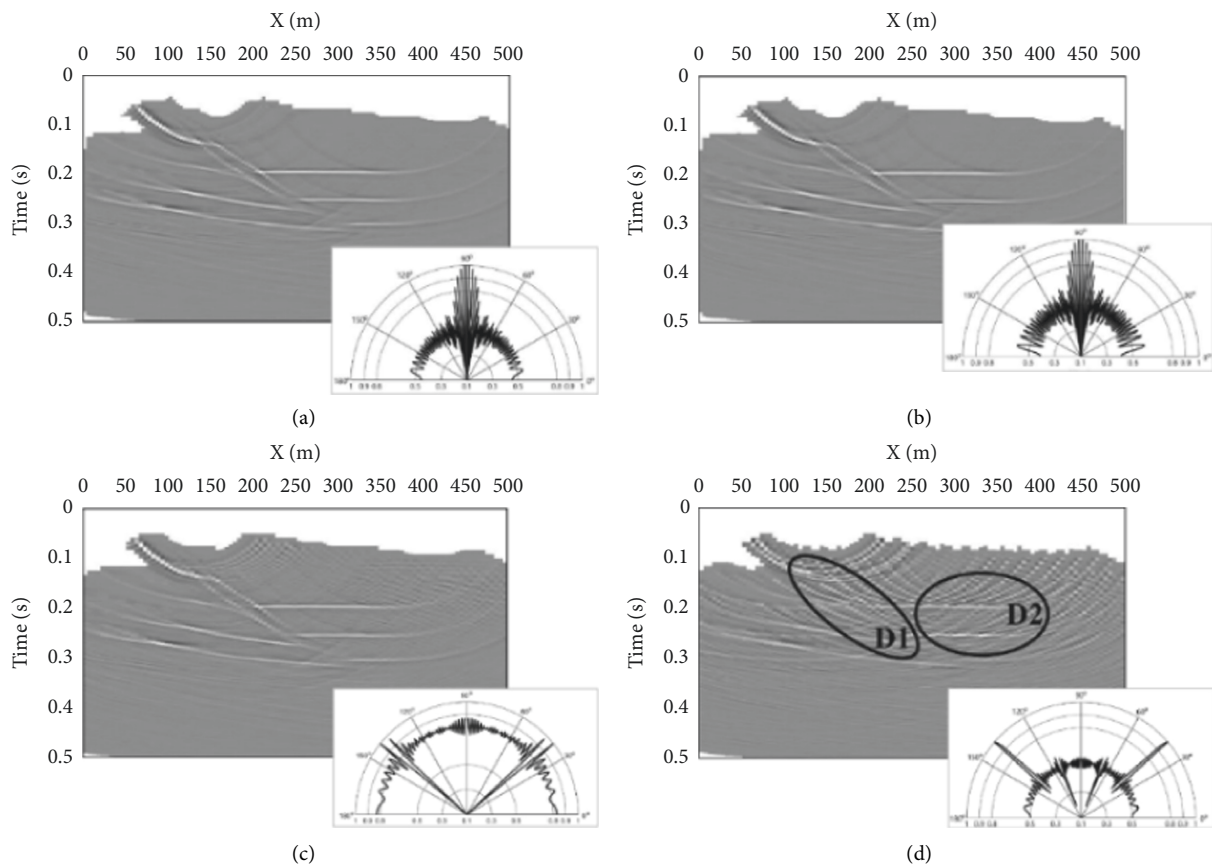
FIGURE 3: The imaging results in time domain using the receiver array with different geophone intervals: (a) the receiver array with the geophone interval of 2 m. (b) The receiver array with the geophone interval of 5 m. (c) The receiver array with the geophone interval of 10 m and (d) the receiver array with the geophone interval of 20 m.

all directions). Figure 3(a) is the imaging result using the observation array with the geophone interval of 2 m, in which the reflected waves of interfaces are clearly imaged. Figure 3(b) is the imaging result with the geophone interval of 5 m, and the position of interface can also be recognized. However, the resolution reduces when the geophone interval increases. Figure 3(c) is the imaging result with the geophone interval of 10 m, and the resolution of the stratum is further decreased. Meanwhile, the resolution is improved with the increasing depth. Figure 3(d) is the imaging result with the geophone interval of 20 m, and it is hard to recognize the reflected waves by interfaces (especially for the reflected waves of faults). In total, in the depth of 300 m range, 200 Hz acoustic wave can achieve better imaging results. The smaller the geophone interval, the greater the total number of geophones. Therefore, there are fewer artifacts. In the premise of ensuring the quality of imaging, we want to have less number of geophones, geophone interval of 2 m, 5 m is less imaging artifacts, but the number of geophones is too much (250, 100, respectively). With an interval of 20, although the number of geophones is less (25), it produces many artifacts that interfere with the identification of anomalies. In contrast, when the geophone interval is 10 m, the artifacts have a little effect on the anomaly identification. And the geophone data are relatively small (50), so the geophone interval range is from 5 m to 10 m.

The directivity of the wave field obtained by Figures 3(a) and 3(b) is clearer, and the direction of 90 degrees is stronger, indicating that most of the energy is incident into the medium perpendicular to the sea level. This is beneficial to receive more reflected artifact information. In addition, the channel with the spacing of 5 m (Figure 3(b)) requires fewer geophones to achieve the similar result, which is better to the massive data acquisition. Figure 3(c) shows two sharp peaks at 45 degrees and 135 degrees, which means that the sound waves are pointing and diverging. It can be clearly seen from the imaging results that many artifacts are produced. It is inconvenient for the identification of faults. Therefore, the source with the dominate frequency of 200 Hz and the geophone with the interval of 5 m to 10 m are chosen for this study.

3.3. Observation System for Submarine Acoustic Exploration.
According to the requirements of offshore geological exploration (the general depth of detection is 300 m) and the theoretical analysis above, an observation system suitable for offshore geological acoustic exploration is designed: (1) the propagation of the source should be mainly in the vertical direction to obtain clearer events. Meanwhile, the source should be placed under the depth of 5 m or more of sea level to couple the medium; (2) the frequency of the source could be 200 Hz to obtain high-resolution imaging of submarine structures; (3) the geophone interval of the receiver array should be 5–10 m to obtain continuous reflections of submarine structures.

Based on the parameters above, the imaging result in depth domain was carried out (Figure 4). The result shows that the estimated reflected waves of interfaces agree with the
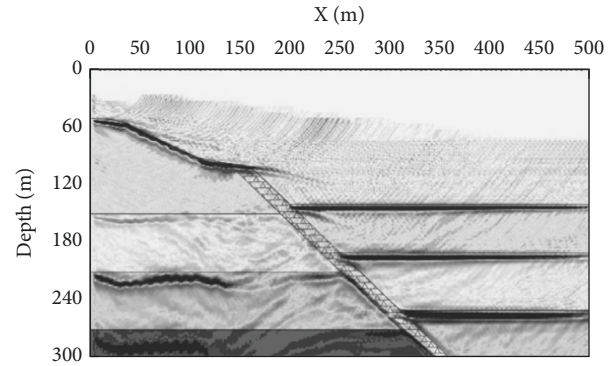
FIGURE 4: The imaging result in depth domain using the designed observation system.

interfaces in the geological model. Meanwhile, the thickness of the fault could be estimated according to the break point of reflected waves.

4. Verification and Discussion

4.1. Numerical Verification.
For submarine geological condition, there are more than 20 kinds of geo-disasters that can cause damage and threaten engineering safety [30]. In general, the most dangerous geo-disasters are submarine faults and landslides. To further examine the feasibility of the designed observation system, three geological models with typical adverse geologies (submarine landslides and submarine faults) were built, and the numerical simulations were conducted. Figure 5 shows the numerical simulation of submarine landslides and submarine faults. The optimized observation system was adopted to obtain seismic signals.

Figure 5(a) shows the numerical simulation of submarine landslides. Figure 5(b) shows the migration result in time domain, which indicates three interfaces under the seawater. To better realize the location, the time-depth conversion was adopted (Figure 5(c)). The submarine bedrock interface and the submarine landslide surfaces could be estimated, and the locations are consistent with the actual model.

To further verify the designed observation system, a geological model with multilayers was built (consists of six layers and an inclined fault). As Figure 5(d) shows, six layers are placed horizontally with an inclined fault. The fault has the thickness of 20 m. Figure 5(e) shows the migration result in time domain, which shows six interfaces under the sea level. However, the reflected waves of second horizontal interfaces are blurry due to the low difference of wave impedance on the two sides of this interface. Meanwhile, two reflected waves by the fault can be recognized obviously. Then, the time-depth conversion was adopted to get the location of geological interfaces (Figure 5(f)). In depth domain, the estimated layers interfaces and fault boundaries are consistent with the actual model. Meanwhile, with the number of layers increasing, the reflected waves of deep interfaces become blurry due to the multiples.

Figure 5(g) is the numerical simulation by using the geological model with six layers and two inclined faults. The
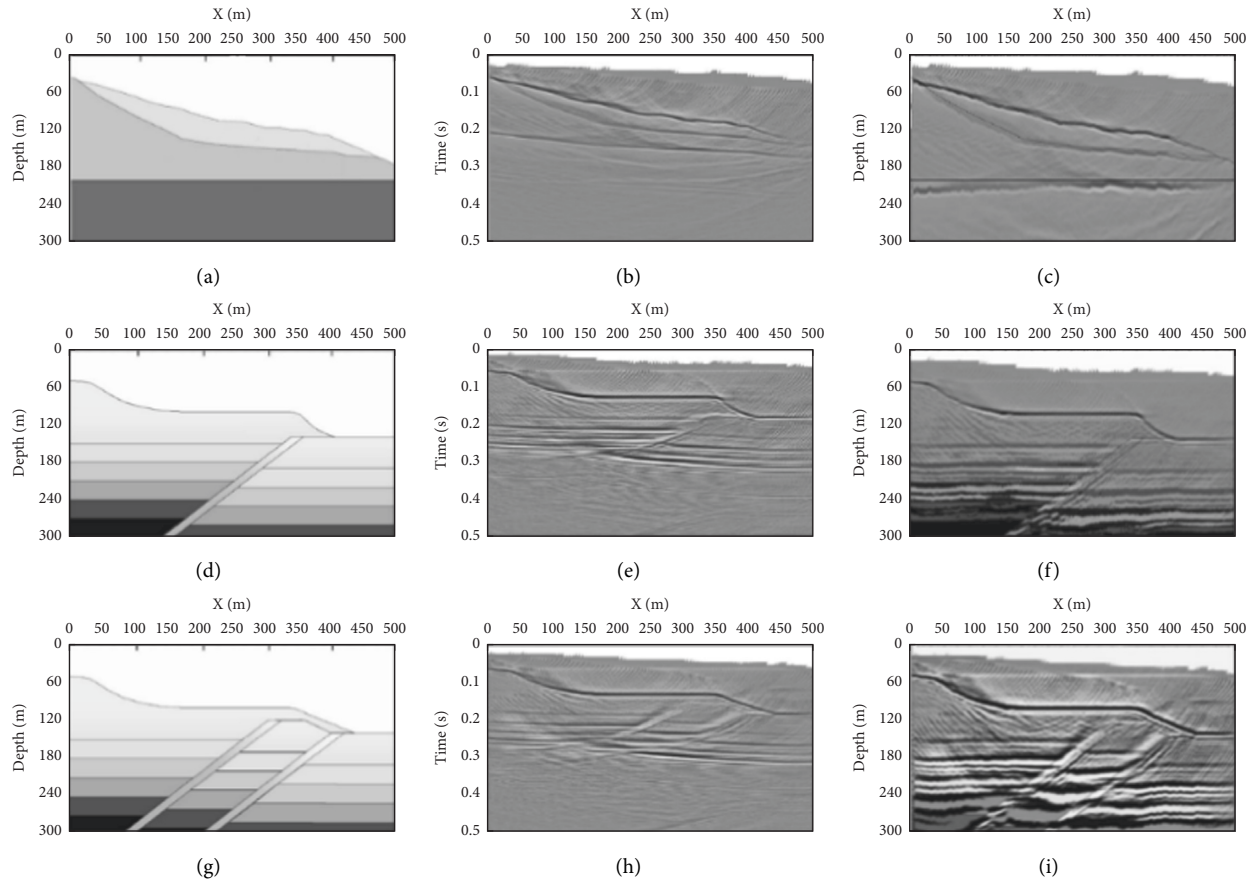
FIGURE 5: The numerical experiments: (a), (b), and (c) are the geological model, imaging in time domain, and imaging in depth domain of the submarine landslide, respectively; (d), (e), and (f) are the geological model, imaging in time domain, and imaging in depth domain of the submarine fault (single), respectively; (g), (h), and (i) are the geological model, imaging in time domain, and imaging in depth domain of the submarine fault (double), respectively.

two faults are parallel to each other and have the distance of 100 m in the horizontal direction. Figure 5(h) is the migration result in time domain, which shows the six interfaces under the seawater and two inclined interfaces. Due to the reason that velocity of layer increases with the increasing depth and the fault has lower velocity, the reflected wave by the interface under the fault are bent in time domain. Meanwhile, the thickness of faults could be recognized roughly. Then, the time-depth conversion was adopted to get the migration result in depth domain (Figure 5(i)). The result shows that the estimated layers interfaces and fault boundaries are consistent with the actual model.

5. Discussion

To optimize the observation system and support the imaging result of submarine geological structures, the main parameters of the observation system (the source frequency and geophone interval of the receiver array) were studied. The influence characteristics of the main parameters are as follows:

(1) The dominate frequency of the source has a great influence on the detection accuracy and imaging. Compared to the source with the dominate

frequency of 30 Hz (explosion source), the frequency of the air gun or spark source in the ocean is higher and helps to improve the resolution of geological conditions (especially for offshore landslides or faults). To balance the detection depth and resolution, the frequency of the source should be 200 Hz for offshore acoustic exploration. In order to improve the performance of imaging, data processing and imaging also need to be implemented. For example, random noise or regular noise attenuation and least-squares reverse time migration (RTM).

(2) In this manuscript, we assume that the medium is relatively intact; however, there is an attenuation of acoustic waves in the broken medium which is not negligible. Due to the attenuation of acoustic waves, the detection depth and imaging accuracy are reduced. For this problem, the Q-RTM can be introduced to solve it, and this will be our next step to study.

(3) The directivity parameter of phased array ultrasound is introduced to evaluate the performance of the observation system. For the geophone interval of the receiver array, the imaging test results show that the imaging result improves with the decreasing

geophone interval. Considering the detection cost, the geophone interval should be in the range from 5 m to 10 m. It should be noted that this observation system evaluation method can be used in other fields, such as ultrasonic structural health detection (SHD), array sonic ahead prediction (ASAP), and physical model on the digital ultrasonic system (PMDUS).

6. Conclusion

The observation system is the important foundation for acoustic detection. In this paper, we designed an observation system and analysed the imaging characteristics by this system.

(1) The main parameters of offshore acoustic detection are analysed. Based on the numerical simulation, the influence characteristics of different observation parameters are studied systematically. The theoretical analysis indicates a suitable frequency (200 Hz) and receiver interval (5 m–10 m) for offshore acoustic exploration when the geo-disasters are 300 m below the water surface. Then, an observation system for offshore acoustic exploration has been designed.

(2) Based on numerical simulation, the feasibility of the designed observation system was fully verified based on the geological model with typical adverse geologies (submarine landslides and submarine faults). When determining the parameters of the observation system using a numerical model, the imaging quality of the target depth can be used to determine. The migration result shows that the designed observation system helps to recognize the multi-interfaces and locate the position.

In the next research, the applicability of the designed observation system for submarine exploration using a passive source should be further studied. Meanwhile, the full waveform inversion is another research key point for accurately examining the velocity for imaging the geological conditions under the seabed.

Data Availability

The original data used to support the findings of this study may be released upon application to the corresponding author who can be contacted at clei667@163.com.

Conflicts of Interest

The authors declare that they have no conflicts of interest.

Acknowledgments

References

[1] J. Zhang and M. Zhao, "Monitoring system for circular deformation in metro shield tunnels in soft soils," *Advances in Civil Engineering*, vol. 2020, pp. 1–12, 2020.

[2] Z. Zhu and C. Yan, "Detection of offshore submarine faults based on shallow seismic exploration technology," *The Journal of Geology*, vol. 39, no. 2, pp. 258–262, 2015.

[3] X. Cheng, G. Li, J. Chen, K. Zhang, and X. Du, "Seismic response of a submarine tunnel under the action of a sea wave," *Marine Structures*, vol. 60, pp. 122–135, 2018.

[4] J. Frey-Martínez, J. Cartwright, and D. James, "Frontally confined versus frontally emergent submarine landslides: a 3D seismic characterisation," *Marine and Petroleum Geology*, vol. 23, no. 5, pp. 585–604, 2006.

[5] G. P. Williams and H. P. Guy, *Erosional and Depositional Aspects of Hurricane Camille in Virginia*, US Government Printing Office, 1973.

[6] K. A. Weitemeyer, A. M. Tréhu, and A. M. Tréhu, "A marine electromagnetic survey to detect gas hydrate at Hydrate Ridge, Oregon," *Geophysical Journal International*, vol. 187, no. 1, pp. 45–62, 2011.

[7] E. Sounding, "High-resolution sub-bottom profiling using parametric acoustics," *International Ocean Systems*, vol. 7, no. 4, pp. 6–11, 2003.

[8] D. W. Beran, W. H. Hooke, and S. F. Clifford, "Acoustic echo-sounding techniques and their application to gravity-wave, turbulence, and stability studies," *Boundary-Layer Meteorology*, vol. 4, no. 1, pp. 133–153, 1973.

[9] U. Nixdorf, D. Steinhage, U. Meyer et al., "The newly developed airborne radio-echo sounding system of the AWI as a glaciological tool," *Annals of Glaciology*, vol. 29, pp. 231–238, 1999.

[10] H. P. Johnson and M. Helferty, "The geological interpretation of side-scan sonar," *Reviews of Geophysics*, vol. 28, no. 4, pp. 357–380, 1990.

[11] C. De Moustier and H. Matsumoto, "Seafloor acoustic remote sensing with multibeam echo-sounders and bathymetric sidescan sonar systems," *Marine Geophysical Researches*, vol. 15, no. 1, pp. 27–42, 1993.

[12] W. H. Key, "Side scan sonar technology[C]//OCEANS 2000 MTS/IEEE Conference and Exhibition," *Conference proceedings*, IEEE, vol. 2, , pp. 1029–1033, 2000.

[13] F. Yu, B. He, and K. Li, "Side-scan sonar images segmentation for AUV with recurrent residual convolutional neural network module and self-guidance module," *Applied Ocean Research*, vol. 113, 2021.

[14] M. Greco and S. Watts, "Modeling and processing of radar signals for earth observation," *International Journal of Navigation and Observation*, vol. 2008, pp. 1-2, 2008.

[15] B. G. McAdoo, L. F. Pratson, and D. L. Orange, "Submarine landslide geomorphology, US continental slope," *Marine Geology*, vol. 169, no. 1-2, pp. 103–136, 2000.

[16] M. Canals, G. Lastras, R. Urgeles et al., "Slope failure dynamics and impacts from seafloor and shallow sub-seafloor geophysical data: case studies from the COSTA project," *Marine Geology*, vol. 213, no. 1-4, pp. 9–72, 2004.

[17] J. L. Deichmann, A. Hernández-Serna, C. M. Delgado, M. Campos-Cerqueira, and T. M. Aide, "Soundscape analysis and acoustic monitoring document impacts of natural gas

exploration on biodiversity in a tropical forest," *Ecological Indicators*, vol. 74, pp. 39–48, 2017.

[18] T. Y. Zhou and B. W. Lian, "A multipath processing technology based on multiparameter-combined observation in GNSS," *Mobile Information Systems*, vol. 2021, no. 2021, pp. 1–11, 2021.

[19] J. Mienert, "COSTA—continental slope stability: major aims and topics," *Marine Geology*, vol. 1, no. 213, pp. 1–7, 2004.

[20] Y. Osada, M. Kido, H. Fujimoto, and Y. Kaneda, "Development of a seafloor acoustic ranging system toward the seafloor cable network system," *Ocean Engineering*, vol. 35, no. 14-15, pp. 1401–1405, 2008.

[21] I. Puillat, R. Person, C. Leveque et al., "Standardization prospective in esonet noe and a possible implementation on the antares site," *Nuclear Instruments and Methods in Physics Research Section A: Accelerators, Spectrometers, Detectors and Associated Equipment*, vol. 602, no. 1, pp. 240–245, 2009.

[22] Xi Wang, T. Chen, D. Li, and S. Yu, "Processing methods for digital image data based on the geographic information system," *Complexity*, vol. 22, 2021.

[23] Y. Chen, S. Fomel, and J. Hu, "Iterative deblending of simultaneous-source seismic data using seislet-domain shaping regularization," *Geophysics*, vol. 79, no. 5, pp. 179–189, 2013.

[24] V. Cerveny, *Seismic ray Theory*, Cambridge University Press, 2005.

[25] H. Liu, N. Dai, F. Niu, and W. Wu, "An explicit time evolution method for acoustic wave propagation," *Geophysics*, vol. 79, no. 3, pp. T117–T124, 2014.

[26] Y. Chen, "Deblending using a space-varying median filter," *Exploration Geophysics*, vol. 46, no. 4, p. 5183, 2014.

[27] B. Liu, C. Fu, Y. Ren, Q. Zhang, X. Xu, and Y. Chen, "Structural complexity-guided predictive filtering," *Geophysical Prospecting*, vol. 68, no. 5, pp. 1509–1522, 2020.

[28] S. Yang, Z. Wang, J. Wang et al., "Defect segmentation: mapping tunnel lining internal defects with ground penetrating radar data using a convolutional neural network," *Construction and Building Materials*, vol. 319, 2022.

[29] C. Oren and R. L. Nowack, "An overview of reproducible 3D seismic data processing and imaging using Madagascar," *Geophysics*, vol. 83, no. 2, pp. F9–F20, 2018.

[30] Y. Xue, F. Kong, S. Li et al., "Water and mud inrush hazard in underground engineering: genesis, evolution and prevention," *Tunnelling and Underground Space Technology*, vol. 114, 2021.

Research Article

Mechanical Properties of Fast-Growing Poplar Reinforced with Carbon Fiber

Ying Gao,[1] Liwei Guo,[2] Xiao Zhang,[1] Yuzhuo Wang [iD],[2,3] Xiuying Yang,[4] ChuanGuo Fu,[2] and Ziqing Liu[5]

[1]*College of Engineering, Shandong Xiehe University, Jinan, Shandong Province 250109, China*
[2]*School of Civil Engineering, Shandong Jianzhu University, Jinan, Shandong Province 250101, China*
[3]*Key Laboratory of Building Structural Retrofitting and Underground Space Engineering (Shandong Jianzhu University), Ministry of Education, Jinan, Shandong Province, 250101, China*
[4]*School of Architecture and Civil Engineering, Liaocheng University, Liaocheng 252000, China*
[5]*School of Civil Engineering, Southeast University, Nanjing, Jiangsu Province 211189, China*

Correspondence should be addressed to Yuzhuo Wang; yuzhuowang@163.com

This paper presents mechanical properties of fast-growing poplar specimens reinforced with carbon fibers. A total of 90 specimens including 10 contrast specimens were tested to investigate the influence from the following parameters: (a) different carbon fiber ratios (0.167%, 0.251%, 0.334%, 0.401%, and 0.501%) and (b) different fiber locations. The failure mode, compressive strength, elastic modulus, and axial deformation of specimens were analyzed. The test results indicate the following: (1) The compressive strength, elastic modulus, and axial deformation of specimens reinforced with carbon fiber were significantly improved compared with that of fast-growing poplar specimens. The compressive strength, elastic modulus, and axial deformation increased by 54.1–76.03%, 11.58–22.89%, and 24.86–60.06%, respectively. (2) There was little effect on the compressive strength of the specimen with the increase of carbon fiber ratio. With the increase of carbon fiber ratio, the elastic modulus of specimens slightly decreased and the axial deformation increased. The elastic modulus decreased by 1.39–18.69%, and the axial deformation increased by 10%–48%. (3) The different locations of the carbon fiber distribution resulted in a large difference in the compressive strength of the specimens, while the effects on the modulus of elasticity and axial deformation were not significant. Finally, the compressive strength calculation formula was proposed.

1. Introduction

Timber structure is a popular structural form in various regions of the world for its seismic resistance and heat preservation [1]. The wood materials are in short supply because of policies of closing mountains for afforestation and no cutting. Fast-growing poplar is widely planted for its high survival rate and short growth period [2–4]. However, the application of fast-growing poplar is limited in the field of building for the loose texture and low strength. Improving the mechanical properties of rapid growth materials has become the focus of attention. The method of gluing fast-growing poplar reinforced with carbon fiber was used in this paper.

In recent years, the scholars have done a lot of work on the mechanical properties of fast-growing poplar, it is mainly focusing on chemical modification, glued wood, and glued fast-growing poplar reinforced with carbon fiber [5–24]. The main research results in chemical modification are as follows: Yue et al. [5, 6] studied the influence of boric acid phenolic formaldehyde resin (BPF) impregnation on the mechanical and combustion properties of fast-growing poplar timber specimens. The results showed that the strength of modified poplar timber specimens increased by 11.2–45.8% with the increase of BPF impregnation concentration. Pure lactic acid oligomers (OLA) and phenolic methylol urea were also commonly used in chemical

impregnation [7–9]. The internal reactive deposition of CaCl$_2$ and NaCO$_3$ was used in modification studies [10], and some studies even combined heat treatment, chemical impregnation, and other methods to improve the performance of poplar [11, 12]. Liu et al. [13] conducted bending tests on 31 laminated timber beam specimens, and the test results showed that the combination mode and size of laminates have significant influence on the mechanical properties of specimens.

With the deepening of the research on the modification of fast-growing poplar, it has been widely used that pasting or winding carbon fiber to improve mechanical properties [14–23]. Zuo et al. [14] studied the flexural performance of modified flax fiber reinforced glued laminated timber beams. The results showed that the flexural load capacity and flexural stiffness of glued laminated timber beam increased with the number of FFRP layers applied at the bottom. He et al. [15, 16] studied the mechanical properties of modified reconstituted wood structures and revealed that the improvement of the strength, modulus of elasticity, and strength-to-weight ratio of the reconstituted wood material, which effectively strengthened the interaction between the reconstituted wood beam, the reconstituted wood column, the bolts, and the steel infill plate, and the nodal force performance was significantly improved. Juliano Fiorelli et al. [17] studied the method used to produce glulam beams led to a higher efficiency of the structural elements. Zheng [18] used carbon fiber to wind the whole specimens, in order to improve its compressive bearing capacity. The compressive bearing capacity increased by 21.4% after first layer had been wound, and 83.1% after third layer had been wound. José Sena-Cruz [24] studied the bonding behavior between integrated material and GFRP by pull-out test. The stress-slip relationship for the local bonding was obtained by test data. A significant increase in flexural load capacity was found for reinforced, prestressed, and prestressed reinforced beams [25]. In addition, Wei et al. [26–29] conducted experimental research and simulation analysis on the mechanical properties of bamboo. It was found that the residual plastic strain ratio of bamboo scrimber was far lower than that of concrete, and new composite materials such as recombinant bamboo and steel-reinforced bamboo scrimber were proposed. This literature provides important insights into the study of mechanical properties of fast-growing poplar reinforced with carbon fiber.

The previous research on improvement methods of fast-growing poplar mainly focuses on chemical impregnation, physical compaction, or carbon fiber reinforcement. The chemical impregnation and physical compaction methods can improve the mechanical properties of fast-growing poplar; however, this method has little improvement. The carbon fiber was added between timber boards in this paper to form a new composite material, which can be better applied in the building field. Considering the influence of different carbon fiber ratio and different fiber location, the fast-growing poplar reinforced with carbon fiber was tested and the influence rule of mechanical properties of fast-growing poplar reinforced with carbon fiber was obtained.

2. Experimental Program

2.1. Design of Specimens. A total of 90 fast-growing poplar specimens were designed and tested, as shown in Table 1 and Figures 1–3. These included 10 comparison specimens and 80 specimens reinforced with carbon fiber, which are 100 mm × 100 mm × 100 mm cubes. Ten pieces of 10 mm × 100 mm × 100 mm timber boards were spliced together to form one specimen using structural adhesive. All the specimens were made in accordance with the code for design of timber structure [30].

In the production process, the fast-growing poplar lumber was cut, dried, cleaned, polished, and flattened to form the fast-growing poplar laminate. Carbon fiber cloth was cut into 100 mm × 100 mm size. All materials were bonded together by evenly brushing structural adhesive, as shown in Figure 1. The structural adhesive was made by mixing epoxy resin and curing agent in the ratio of 2:1. The finished specimens were cured and maintained under 0.4 MPa pressure for 48 hours.

2.2. Materials. The specimens were made of No. 108 artificially cultivated fast-growing poplar (diameter at a breast height of about 20 cm, tree height of about 9 m, no insect pests and other tree quality defects, and straight trunk), which is mainly produced in Jinan city, Shandong Province, China. The 0.167 mm thick (300 g) carbon fiber was used in the test. The main components of the structural adhesive were epoxy resin and curing agent (mainly phenol-4-sulfonic acid) at the ratio of 2:1, the density of structural adhesive is 2000 kg/m^3, and the structural adhesive between layers is 2000 g/m^2.

2.3. Moisture Content. The moisture content has a significant impact on the compression strength of the composite material. Ten cubic test blocks of 20 mm × 20 mm × 20 mm were made and measured according to Method for Determination of the Moisture Content of Timber GB/T 1931–2009 [31]. The average moisture content of the fast-growing poplar was 12.39%, which met the requirements of code GB/T 50708–2012 [32], as can be seen in Table 2.

3. Experimental Process

The test was carried out using a WAW-1000C universal testing machine (maximum test force 1000 KN) for loading in the vertical axis. The specimens reinforced with carbon fiber were placed in the testing machine, and geometric axis alignment was performed according to the standard for test method of timber structures. The test was loaded at a rate of 2 mm/min until the specimen cannot withstand the load and the test was terminated [33].

4. Experimental Results and Discussion

4.1. Failure Mode. The failure mode of Y1 was that all specimens had horizontal cracks, and some specimens had vertical cracks. From the observation of the failure

Table 1: Design parameters of the specimens.

Specimen		Carbon fiber position	Carbon fiber ratio R (%)
Comparison	Y1	--	--
	X1	--	--
Carbon fiber ratio	A1	2-3, 5-6, 8-9	0.167
	A2	2-3, 5-6, 8-9	0.251
	A3	2-3, 5-6, 8-9	0.334
	A4	2-3, 5-6, 8-9	0.401
	A5	2-3, 5-6, 8-9	0.501
Carbon fiber position	B1	1-2, 5-6, 9-10	0.501
	B2	1-2, 2-3, 5-6, 8-9, 9-10	0.501

Note. $R = \frac{V_{carbon\,fibre}}{V_{specimen}} \times 100\%$, R is the carbon fiber ratio, which is the ratio of the volume of the carbon fiber to the volume of the reinforced specimen; V_c is the volume of the carbon fiber; V_s is the volume of the specimen.
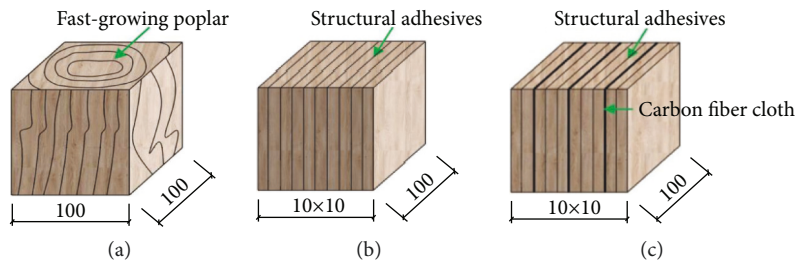
Figure 1: Layout of the specimens: (a) Y1, (b) X1, and (c) A1-5 and B1-2.
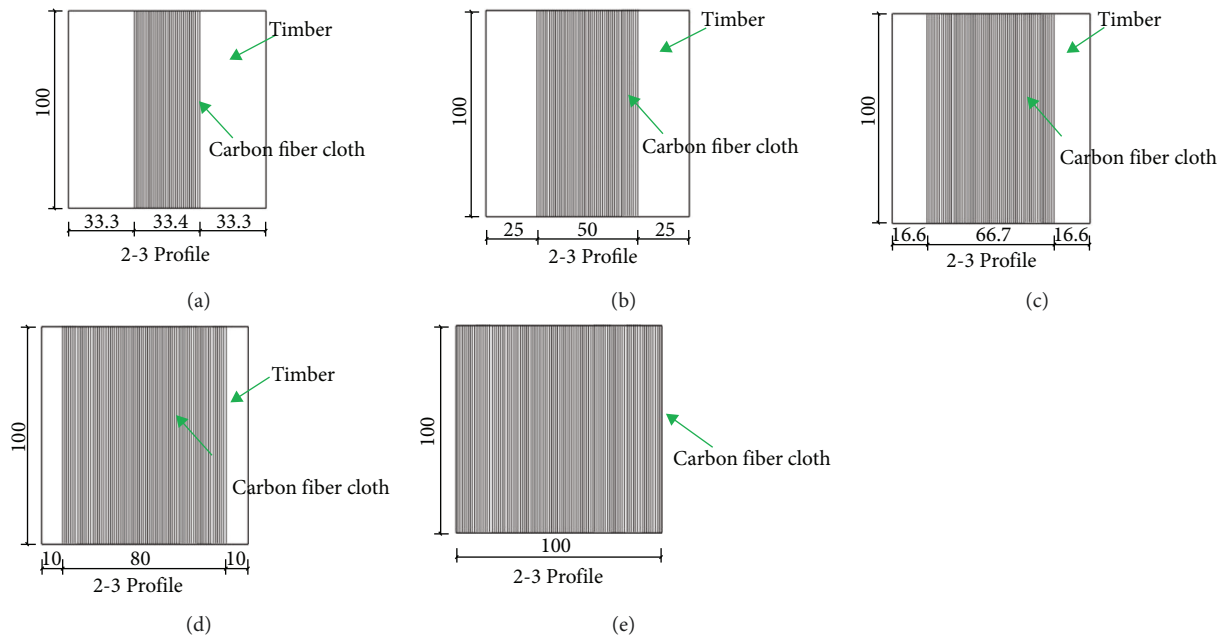
Figure 2: Different carbon fiber ratios: (a) A1, (b) A2, (c) A3, (d) A4, and (e) A5.

specimens, it can be seen that the wood fiber was severely squeezed, and the specimen showed obvious compression deformation. The specific phenomenon is shown in Figure 4.

The failure modes of specimens reinforced with carbon fiber are similar to that of fast-growing poplar specimens, as shown in Figure 5. Most specimens only appeared horizontal cracks, and some specimens simultaneously appeared horizontal cracks and a few vertical cracks. Compared with specimen Y1, horizontal cracks of specimens A1 to A5 were randomly distributed and had no continuity. The vertical cracks were mostly distributed in the adhesive location. With the carbon fiber ratio increases, the deformation of the specimen becomes greater and its damage reaches earlier. The outermost laminates of specimens A4 and A5 separated from the specimens, forming isolated laminates, and the continued loading of the test caused the outer laminates to buckle, and the test was ended.
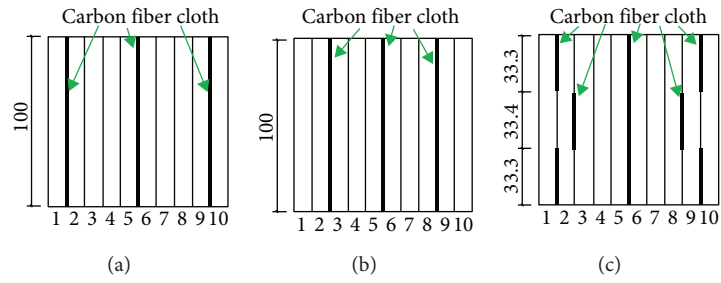
FIGURE 3: Different carbon fiber positions: (a) A5, (b) B1, and (c) B2.

TABLE 2: Moisture content test data.

Number	1	2	3	4	5	Average %
Moisture content %	11.56	11.96	12.27	12.53	13.14	
Number	6	7	8	9	10	12.39
Moisture content %	12.73	12.13	12.40	12.72	12.43	

FIGURE 4: Failure mode of the specimen Y1.
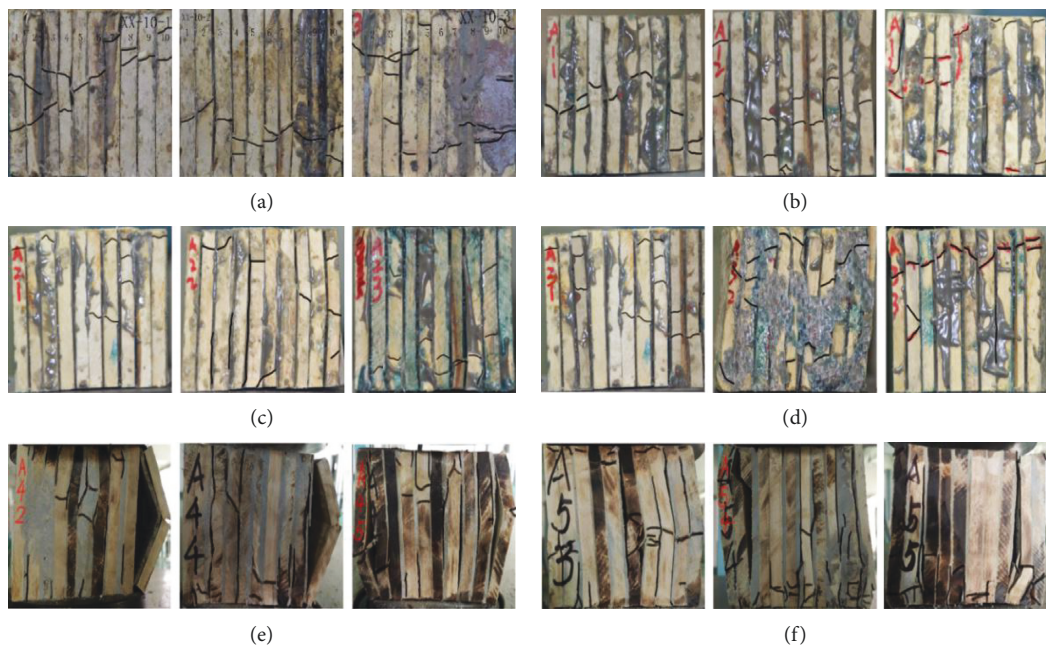
FIGURE 5: Failure mode of the specimens X1 and A1-5: (a) X1, (b) A1, (c) A2, (d) A3, (e) A4, and (f) A5.
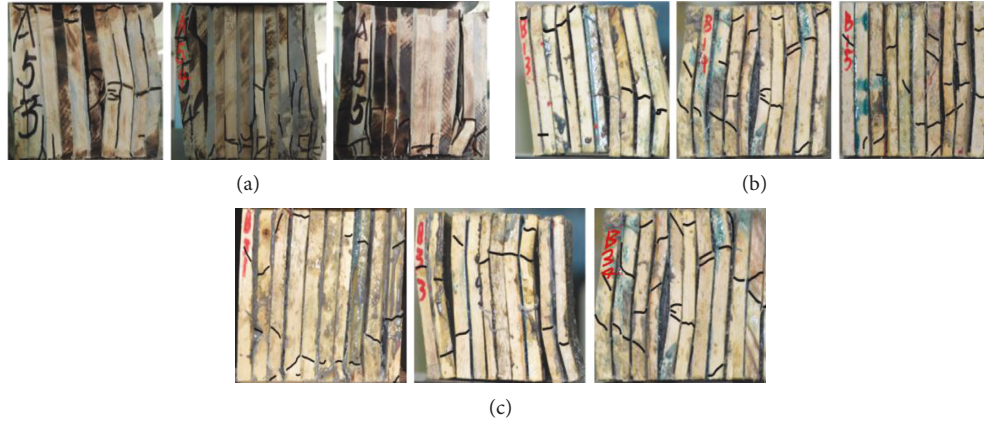
FIGURE 6: Failure mode of the specimens (a) *A*5, (b) *B*1, and (c) *B*2.

TABLE 3: Mechanical parameters of specimens with different carbon fiber ratios.

Specimen	f_a (MPa)	S (standard deviation)	f_k (MPa)	α_3	E_a (MPa)	Δ_a (mm)
*Y*1	22.84	2.593	17.38	—	1320	3.58
*X*1	27.74	1.509	24.56	1	1586	4.24
*A*1	35.69	3.27	28.81	1.1730	1564	4.47
*A*2	35.31	2.239	30.60	1.2459	1622	4.61
*A*3	34.42	2.767	28.60	1.1645	1508	4.80
*A*4	33.24	3.068	26.78	1.0904	1473	5.05
*A*5	31.59	2.15	27.07	1.1022	1291	5.73
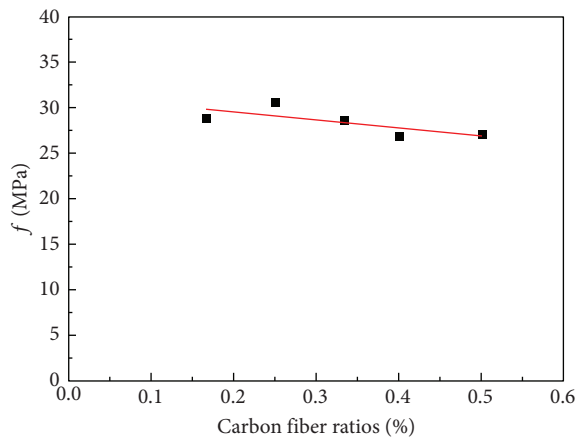
FIGURE 7: Compressive strength of specimens with different carbon fiber ratios.

According to the experimental phenomena, the carbon fiber positions of specimens *A*5, *B*1, and *B*2 were different, but their failure modes were similar, as shown in Figure 6. At the early stage of loading, specimens *A*5, *B*1, and *B*2 produced a slight wood extrusion sound. With the increase of load, the specimens showed obvious bending deformation and cracked seriously between some boards. The bond force was lost, some boards were separated from each other, and the outer boards of some specimens were even broken, and the test was ended.

4.2. Compressive Strength. The following data are taken from the data collection of the test machine, and the average of the 10 specimens is taken as the selected value, where f_a is average compressive strength of 10 specimens, S is standard deviation, f_k is standard value of compressive strength, and α_3 is the improvement coefficient. E_a is the average of elastic modulus of 10 specimens, and Δ_a is the average axial deformation of 10 specimens. Where f_k was collated according to GB 50005–2017 [30] and E_a and Δ_a were collated according to GB/T 50329–2012 [33], we have the results in Table 3 and Figures 7, 8, and 9.

Table 3 and Figure 7 show that the compressive strength of specimens *A*1 to *A*5 is significantly improved in comparison with that of specimens *Y*1 and *X*1. Compared with that of specimen *Y*1, the compressive strength of the specimens increased by 54.1–76.03%. Compared with that of specimen *X*1, the compressive strength of the specimens increased by 9.04–24.56%. The reason is that carbon fiber is a high strength and high modulus fiber, which increases the resistance of the specimen to bending deformation and therefore increases the compressive strength of the specimen. In addition, with the carbon fiber ratio increases, the effect on the compressive strength of the specimens is not significant. According to the above test data, the compressive strength formula of specimens with different carbon fiber ratio was obtained by fitting, as shown in the following equation:

$$y = (-0.4992x + 1.798)f_0, \tag{1}$$

where y is the measured compressive strength of carbon fiber specimen, x is the carbon fiber ratio, and f_0 is the compressive strength of fast-growing poplar specimen.

As shown in Table 3, the compressive strength of specimens *A*1 to *A*5 with different fiber proportion increased
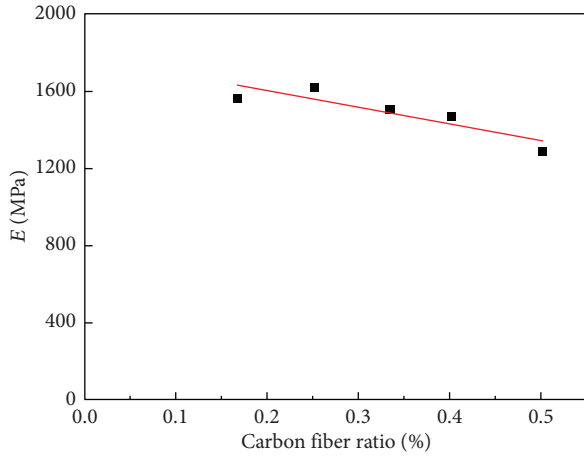
FIGURE 8: Elastic modulus of specimens with different carbon fiber ratios.
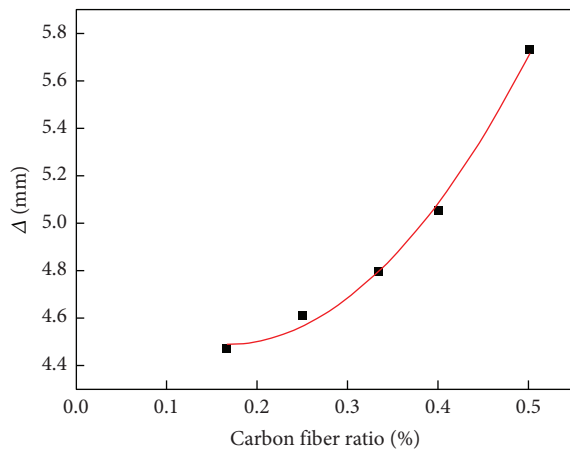
FIGURE 9: Axial deformation of specimens with different carbon fiber ratios.

by 17.3%, 24.6%, 16.4%, 9.0%, and 10.2%, respectively, compared with that of $X1$. Through data fitting, the calculation formula of α_3 was obtained, as shown in the following equation:

$$\alpha_3 = -0.3532\rho_c + 1.2721. \tag{2}$$

4.3. Elastic Modulus. It can be seen from Table 3 and Figure 8 that the elastic modulus of specimens $A1$ to $A5$ is improved in comparison with that of specimens $Y1$. Compared with that of specimen $Y1$, the elastic modulus of the specimens increased by 11.58–22.89%. Compared with that of specimen $X1$, the elastic modulus of the specimens decreased by 1.39–18.57%. The elastic modulus of specimens decreased in the range of 3.56–21.11% with the increase of carbon fiber ratio. As can be seen from the above research, when the ratio of carbon fibers increases, the area of the carbon fibers increases. The bond between the carbon fibers and the structural adhesive is less than the bond between the wood and the structural adhesive. The load-bearing capacity of the specimen depends on the adhesion between carbon

TABLE 4: Mechanical parameters of specimens with different fiber position.

Specimen	f_a (MPa)	S (standard deviation)	f_k (MPa)	E_a (MPa)	Δ_a (mm)
A5	31.59	2.15	27.07	1291	5.73
B1	30.46	4.79	20.38	1351	5.58
B2	31.62	1.62	28.21	1428	6.25

fiber and structural adhesive. It leads to a reduction in the modulus of elasticity of the specimen. According to the above test data, the elastic modulus formula of specimens with different carbon fiber ratio was obtained by fitting, as shown in the following equation:

$$y = (-0.673x + 1.413)E_0, \tag{3}$$

where y is the measured elastic modulus of carbon fiber specimen, x is the carbon fiber ratio, and E_0 is the elastic modulus of fast-growing poplar specimen.

4.4. Axial Deformation. Table 3 and Figure 9 show that the axial deformation of specimens A1 to A5 is significantly improved in comparison with that of specimens Y1 and X1. Compared with that of specimen Y1, the axial deformation of the specimens increased by 24.86–60.06%. Compared with that of specimen X1, the axial deformation of the specimens increased by 5.42–35.14%. When the carbon fiber ratio increased, the axial deformation increased, with a maximum increase of 48%. According to the above test data, the axial deformation formula of specimens with different carbon fiber ratio was obtained by fitting, as shown in

$$y = \left(3.05x^2 - 1.02x + 1.34\right)\Delta_0, \tag{4}$$

where y is the axial deformation of carbon fiber specimen, x is the carbon fiber ratio, and Δ_0 is the axial deformation of fast-growing poplar specimen.

4.5. Compressive Strength, Elastic Modulus, and Axial Deformation of Carbon Fiber Position. It can be seen from Table 4 and Figure 10 that the changing position of the carbon fibers has an effect on the compressive strength, but it has little effect on the modulus of elasticity and axial deformation. The maximum difference of compressive strength, elastic modulus, and axial deformation between specimens B1 and B2 and the comparison specimen A5 was 24.7%, 10.60%, and 9.1%, respectively.

5. Calculation of Compressive Strength

Although the specimens reinforced with carbon fiber were made of poplar timber, structural adhesive, and carbon fiber, the compressive strength was mainly provided by adhesive and timber. Carbon fiber itself has not compressive strength, but it can improve the ability of specimen to resist bending deformation, thus affecting the compressive strength of specimen. Therefore, the influence of carbon fiber on the
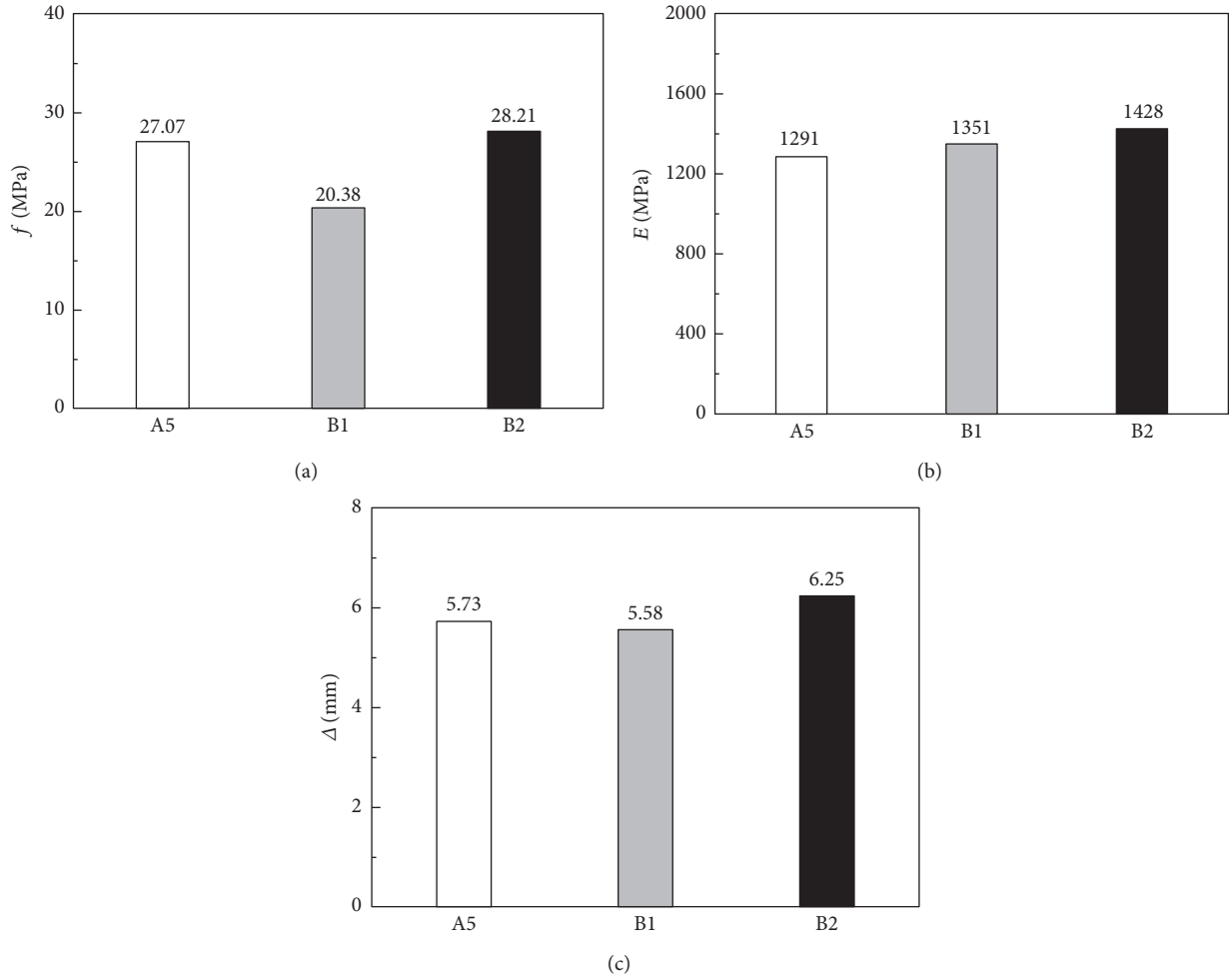
FIGURE 10: (a) Compressive strength, (b) elastic modulus, and (c) axial deformation of specimens with different carbon fiber positions.

TABLE 5: Value of α_1 and α_2.

	(5) + (6)	(5) + (7)	(5) + (8)	(6) + (7)	(6) + (8)	(7) + (8)	Average
α_1	0.742	0.583	0.714	0.416	0.702	0.894	0.675
α_2	1.245	1.463	1.283	2.190	1.361	0.113	1.276

strength of reinforced specimens was expressed by the improvement coefficient; that is, the compressive strength formula of fast-growing poplar specimens reinforced with carbon fiber could be expressed by the following equation:

$$f_c = \alpha_3 \left(\alpha_1 \rho_w f_w + \alpha_2 \rho_a f_a \right), \tag{5}$$

where f_c is the compressive strength of carbon fiber reinforced fast-growing poplar, f_w is the compressive strength of timber, f_a is the compressive strength of adhesive, ρ_w is the timber content $\rho_w = 100 \times t_w/99 \times t_w + 100$, ρ_a is the adhesive content $\rho_a = 100 - t_w/99 \times t_w + 100$, t_w is the thickness of the timber, α_1 is the combination coefficient of timber compressive strength, and α_2 is the combination coefficient of structural adhesive strength.

In Eq (5), specimen X1 did not consider the effect of carbon fibers on the compressive strength, so the coefficient α_3 is taken as 1 ($\alpha_3 = 1$). The compressive strength of the reinforced fast-growing poplar with the thickness of 5 mm, 10 mm (X1), 15 mm, and 20 mm were obtained from [34]. The test result of compressive strength was substituted into equation (5) to give equation (6). The values of α_1 and α_2 could be obtained by solving any pair of equations selected from equation (6). The average values of α_1 and α_2 were 0.675 and 1.276, respectively, as shown in Table 5.

$$\begin{cases} \alpha_1 \times 0.8403 \times 22.84 + \alpha_2 \times 0.1597 \times 87.6 = 31.66, \\ \alpha_1 \times 0.9174 \times 22.84 + \alpha_2 \times 0.0826 \times 87.6 = 24.56, \\ \alpha_1 \times 0.9434 \times 22.84 + \alpha_2 \times 0.0566 \times 87.6 = 19.82, \\ \alpha_1 \times 0.9615 \times 22.84 + \alpha_2 \times 0.0385 \times 87.6 = 20.01. \end{cases} \tag{6}$$

Equation (2) was substituted into equation (5) to give equation (7) for calculating the compressive strength of specimens reinforced with carbon fiber.

Here, ρ_c is the carbon fiber ratio.

$$f_c = \alpha_3\left(\alpha_1\rho_0 f_0 + \alpha_2\rho_a f_a\right) = \left(-0.3532\rho_c + 1.2721\right) \\ \left(0.675\rho_w f_w + 1.276\rho_a f_a\right). \tag{7}$$

6. Conclusion

This paper experimentally and analytically investigated mechanical properties of fast-growing poplar reinforced with carbon fiber. The following conclusions can be drawn:

(1) The compressive strength, elastic modulus, and axial deformation of specimens reinforced with carbon fiber are significantly improved compared with those of fast-growing poplar specimens. The compressive strength, elastic modulus, and axial deformation increase by 54.1–76.03%, 11.58–22.89%, and 24.86–60.06%, respectively.

(2) With the increase of carbon fiber ratio, the range of variation in compressive strength is insignificant, the elastic modulus of specimens slightly decreases, and the axial deformation increases. The elastic modulus decreases by 1.39–18.69%, and the axial deformation increases by 10%–48%.

(3) The different locations of the carbon fiber distribution resulted in a large difference in the compressive strength of the specimens, and the maximum difference of compressive strength is 8 MPa, while the effects on the modulus of elasticity and axial deformation are not significant.

(4) The compressive strength calculation formula of specimens reinforced with carbon fiber is established.

Data Availability

The numerical and measurement data used to support the findings of this study are included within the article.

Conflicts of Interest

The authors declare that they have no conflicts of interest.

Acknowledgments

References

[1] I. Smith and M. A. Snow, "Timber: an ancient construction material with a bright future," *The Forestry Chronicle*, vol. 84, no. 4, pp. 504–510, 2008.

[2] T. Johansson and A. Karačić, "Increment and biomass in hybrid poplar and some practical implications," *Biomass and Bioenergy*, vol. 35, no. 5, pp. 1925–1934, 2011.

[3] W.-j. Liang, H.-q. Hu, F.-j. Liu, and D.-m. Zhang, "Research advance of biomass and carbon storage of poplar in China," *Journal of Forestry Research*, vol. 17, no. 1, pp. 75–79, 2006.

[4] Z. Sun, Y. Zhang, and e tal, "Research status and prospect of organic-inorganic compound modified fast-growing wood," *Materials Reports*, vol. 35, no. 05, pp. 5181–5187, 2021.

[5] K. Yue, X. C. Cheng, and L. L. Wan, "Effect of modification on mechanical property and fire-retardant behavior of fast-growing poplar timber," *Journal of Combustion Science and Technology*, vol. 22, no. 5, pp. 426–432, 2016.

[6] K. Yue, Z. Chen, W. Lu et al., "Evaluating the mechanical and fire-resistance properties of modified fast-growing Chinese fir timber with boric-phenol-formaldehyde resin," *Construction and Building Materials*, vol. 154, pp. 956–962, 2017.

[7] G. Charlotte, N. Marion, F. T. Marie, R. Lauri, and G. Philippe, "Influence of water and humidity on wood modification with lactic acid," *Journal of Renewable Materials*, vol. 6, no. 3, pp. 259–269, 2018.

[8] H. Chen, X. Miao, Z. Feng, and J. Pu, "In situ polymerization of phenolic Methylolurea in cell wall and induction of pulse-pressure impregnation on green wood," *Industrial & Engineering Chemistry Research*, vol. 53, no. 23, pp. 9721–9727, 2014.

[9] F. Cheng, Y. Hu, and L. Li, "Interfacial properties of glass fiber/unsaturated polyester resin/poplar wood composites prepared with the prepreg/press process," *Fibers and Polymers*, vol. 16, no. 4, pp. 911–917, 2015.

[10] C. Qian, *Study on the Preparation and Properties of poplar Modified by Internal Reaction Deposition*, Nanjing Forestry University, China, 2020.

[11] Y. Dong, Y. Yan, Y. Zhang, S. Zhang, and J. Li, "Combined treatment for conversion of fast-growing poplar wood to magnetic wood with high dimensional stability," *Wood Science and Technology*, vol. 50, no. 3, pp. 503–517, 2016.

[12] W. D. Li, C. Wang, Y. Zhang, C. Jia, C. C. Gao, and J. W. Jin, "The influence of hot compression on the surface characteristics of poplar veneer," *Bioresources*, vol. 9, no. 2, pp. 2808–2823, 2014.

[13] W. Q. Liu and H. F. Yang, "Experimental study on flexural behavior of engineered timber beams," *Journal of Building Structures*, vol. 29, no. 1, pp. 90–95https, 2008.

[14] H. Zuo, Z. Wang, and Y. Li, "Flexural behavior of modified flax fiber reinforced polymer reinforced glulam beams," *Journal of Northeast Forestry University*, vol. 49, no. 4, pp. 76–80, 2021.

[15] M. He, Li Zheng, and L. Wu, "Study on mechanical properties and strength design index of modified reconstituted wood," *Journal of Building Structures*, vol. 41, no. S1, pp. 364–372, 2020.

[16] M. He, duo Tao, Li Zheng, and J. Zhang, "Experimental investigation of mechanical property of dowel-type post-and-beam connections made of wood scrimber composite," *Journal of Southeast University (Natural Science Edition)*, vol. 48, no. 06, pp. 1013–1020https, 2018.

[17] J. Fiorelli and A. A. Dias, "Glulam beams reinforced with FRP externally-bonded: theoretical and experimental evaluation," *Materials and Structures*, vol. 44, no. 8, pp. 1431–1440, 2011.

[18] Y. L. Zheng, Q. F. Wang, and Y. H. Huang, "Experimental study on axial compressive behaviors of timber column strengthened with GFRP," *Journal of Huaqiao University*, vol. 33, no. 3, pp. 321–324, 2012.

[19] Y. H. Guo, Y. B. Lin, and B. Na, "Evaluation of physical and mechanical properties of fiber-reinforced poplar scrimber," *Bioresources*, vol. 12, no. 1, pp. 43–55, 2017.

[20] P. X. Wei, J. H. Brad, and D. G. Wang, "Mechanical properties of poplar laminated veneer lumber modified by carbon fiber reinforced polymer," *Bioresources*, vol. 8, no. 4, pp. 4883–4898, 2013.

[21] S. Ahmad, J. Mohammad, T. H. S. Mohamed, and H. Azman, "Preliminary study on tensile and impact properties of kenaf/bamboo fiber reinforced epoxy composites," *Journal of Renewable Materials*, vol. 6, no. 5, pp. 529–535, 2018.

[22] S. H. Li, B. L. Gao, and G. Q. Li, "Experimental study on poplar LVL beams reinforced with CFRP sheets," *Journal of Building Structures*, vol. 39, no. 2, pp. 109–112, 2009.

[23] G. M. Raftery and A. M. Harte, "Low-grade glued laminated timber reinforced with FRP plate," *Composites Part B: Engineering*, vol. 42, no. 4, pp. 724–735, 2011.

[24] J. Sena-Cruz, J. Branco, M. Jorge, J. A. O. Barros, C. Silva, and V. M. C. F. Cunha, "Bond behavior between glulam and GFRP's by pullout tests," *Composites Part B: Engineering*, vol. 43, no. 3, pp. 1045–1055, 2012.

[25] H. Yang, D. Ju, W. Liu, and W. Lu, "Prestressed glulam beams reinforced with CFRP bars," *Construction and Building Materials*, vol. 109, no. 15, pp. 73–83, 2016.

[26] W. Yang, Si Chen, S. Tang, K. Zheng, and J. Wang, "Mechanical behavior of bamboo composite tubes under axial compression," *Construction and Building Materials*, vol. 245127681 pages, 2022.

[27] W. Yang, S. Tang, Ji Xuewei, K. Zhao, and G. Li, "Stress-strain behavior and model of bamboo scrimber under cyclic axial compression," *Engineering Structures*, vol. 209, no. 4, 110279 pages, 2020.

[28] Y. Wei, K. Zhao, C. Hang, S. Chen, and M. Ding, "Experimental study on the creep behavior of recombinant bamboo," *Journal of Renewable Materials*, vol. 8, no. 3, pp. 251–273, 2020.

[29] W. Yang, S. Yan, K. Zhao, F. Dong, and G. Li, "Experimental and theoretical investigation of steel-reinforced bamboo scrimber beams," *Engineering Structures*, vol. 223, no. 12, 111179 pages, 2020.

[30] "Ministry of housing and urban rural development of the people's Republic of China," in *GB50005-2017, Code for Design of Timber Structures*China Architecture & Building Press, Beijing , China, 2017.

[31] "Ministry of housing and urban rural development of the people's Republic of China," in *GB/T1931-2009, Method for Determination of the Moisture Content of Timber*China Architecture & Building Press, Beijing , China, 2009.

[32] "Ministry of housing and urban rural development of the people's Republic of China," in *GB/T50708- 2012, Technical Code of Glued Laminated Timber Structures*China Architecture & Building Press, Beijing , China, 2012.

[33] "Ministry of housing and urban rural development of the people's Republic of China," in *GB/T50329- 2012, Standard for Test Method of Timber Structures*China Architecture & Building Press, Beijing , China, 2012.

[34] Q. J. Liu, Y. Z. Wang, Y. Gao, B. J. Zhang, and B. Li, "The experimental study on mechanical behavior of modified fast-growing poplar," *Journal of Civil & Environmental Engineering*, vol. 41, no. 5, pp. 99–108, 2019.

Research Article

Semianalytical Solution for Thermal Consolidation of Viscoelastic Marine Clay with the Fractional Order Derivative

Minjie Wen,[1,2] Lichen Li,[3] Xinchen Qiu,[2] Yi Tian,[3] Kuihua Wang,[2] Kaifu Liu [ID],[1] and Wenbing Wu [ID][2,3]

[1]*School of Civil Engineering and Architecture, Zhejiang Sci-Tech University, Hangzhou, Zhejiang 310018, China*
[2]*Research Center of Coastal Urban Geotechnical Engineering, Zhejiang University, Hangzhou, Zhejiang 310058, China*
[3]*Faculty of Engineering, Zhejiang Institute, China University of Geosciences, Wuhan, Hubei 430074, China*

Correspondence should be addressed to Wenbing Wu; zjuwwb1126@163.com

The deformation property of marine clay under a heat source has received considerable attention in the geotechnical literature. In this paper, a three-parameter fractional order derivative model is introduced into the thermo-hydro-mechanical coupling governing equations with thermal filtration and thermo-osmosis to simulate viscoelastic characteristics of marine clay. The excess pore pressure, temperature increment, and displacement of marine clay are derived by using the Laplace transform method, and the semianalytical solution for the one-dimensional thermal consolidation in the time domain is derived by using a numerical inversion of the inverse Laplace transform. The influence of the order of the fractional derivative, material parameters, and phenomenological coefficient on thermal consolidation is investigated based on the present solutions. It is shown that the influence of the fractional derivative parameter on the excess pore pressure and displacement of marine clay depends on the properties of soil mass, and the temperature increment has an obvious effect on the thermal filtration and thermo-osmosis process.

1. Introduction

Over the past decades, more and more engineering activities have caused the change in the temperature field of the surrounding soil layers, which inevitably affects the physical and mechanical properties of the strata. These engineering activities involve a broad range of civil engineering topics such as deep geological disposal of radioactive waste [1], deep drilling and excavation [2, 3], extraction of geothermal energy [4–6], energy piles [7, 8], ground improvement using prefabricated vertical thermal drain [9–11], oil and gas pipelines [12], and frictional heating-induced large-scale landslides [13]. This huge engineering demand has stimulated scholars to pay their attention on the thermo-hydro-mechanical coupling theory of porous media, especially the deformation properties of marine clay under a heat source [14].

Biot originally proposed the constitutive equations considering the thermal effect and established the theoretical

framework for the thermodynamics of saturated porous media [15]. Following Biot's research, a number of scholars have investigated the thermal consolidation of elastic saturated porous media by considering the influence of the thermal effect. Booker and Savvidou studied the thermal consolidation of saturated soil under the action of the deep buried spherical and point heat source [16, 17]. Bai [18] derived an analytical solution for the wave response of porous materials under cyclic thermal load [18]. Smith and Booker [19] established the linear thermoelastic theory of homogeneous isotropic materials by using the Green function method [19]. Lu et al. [20] investigated the thermal-mechanical coupling response of saturated porous media under simple harmonic heat and load based on the generalized thermoelastic theory [20]. Ai and Wang [21] studied the axisymmetric thermal consolidation of layered elastic saturated porous media under the action of the heat source [21]. Furthermore, Ai et al. [22] studied the axisymmetric thermal consolidation of layered transversely isotropic

porous media [22]. Wen et al. [23] studied the thermal dynamic response of a lined circular tunnel in saturated elastic porous media with the help of a fractional order derivative [23].

Although the above-mentioned scholars have greatly promoted the development of the thermo-hydro-mechanical coupling theory of porous media, they neglect thermal filtration (the influence of the excess pore pressure gradient on heat flux) and thermo-osmosis (the influence of the temperature gradient on water flux). In reality, by conducting an experiment on thermo-osmosis of water through kaolinite, Srivastava and Avasthi [24] found that the water flux associated with thermo-osmosis in compacted kaolinite can reach 10^{-8} m/s under a temperature gradient of 20°C/m [24]. Considering the influence of thermal filtration and thermo-osmosis, Zhou et al. [25] presented a fully coupled thermo-hydro-mechanical model [25]. Considering the influence of seepage velocity on thermal diffusion and the temperature gradient on seepage velocity, Liu et al. [26] established a fully dynamic coupled thermo-hydro-mechanical model and investigated the influence of the thermal and water permeability coefficient of saturated porous media around cylindrical holes and spherical cavities on their thermodynamic response, respectively [26, 27]. Yang et al. [25] proposed a refined mathematical model to study the coupled effect of thermo-osmosis in saturated porous media [28]. All these references utilized the elastic theory to simulate stress-strain relationships in saturated porous media, which may not be applicable to the marine clay covering two-thirds of the Earth.

With the continuous development of marine development all over the world, more and more attention has been paid to the deformation characteristics of marine clay. Liu et al. [29] studied the one-dimensional consolidation of viscoelastic marine soft soil under load varying with depth and time [29]. Liu et al. [14] investigated the effect of viscosity on the one-dimensional thermal consolidation of marine soft soil [14]. Wang and Wang [30] studied the rheology and thermal consolidation of layered saturated soft soil under force and thermal load [30]. Although these works have promoted the understanding of the deformation characteristics of marine clay, the existing research is still far from being applied to the engineering applications in marine clay due to its complex rheological properties. In order to reasonably consider the rheological characteristics of soil, many scholars introduced the fractional constitutive model to study the consolidation characteristics of soil [31–35]. However, to the authors' knowledge, there is no report on the thermal consolidation of viscoelastic marine soil with a fractional order derivative.

In light of the above, the objective of this paper is to investigate the one-dimensional thermal consolidation of viscoelastic marine clay with the fractional order derivative. By introducing a three-parameter fractional order derivative model to consider thermal filtration and thermo-osmosis, the solutions of excess pore pressure, temperature increment, and displacement of viscoelastic marine clay are obtained by using the Laplace transform method and its numerical inverse transform. Based on the present solutions, the influence of the order of the fractional derivative, material parameters, and phenomenological coefficient on the thermal consolidation of viscoelastic marine clay is investigated.

2. Mathematical Modeling

Considering the effects of thermal filtration and thermo-osmosis, a fully coupled thermo-hydro-mechanical model was proposed by Zhou et al. [25]. On this basis, a three-parameter fractional order derivative model, consisting of two springs and one dashpot in parallel, is introduced into the thermo-hydro-mechanical coupling governing equations. The constitutive relationship of the fractional order derivative model is expressed as [36]

$$(1 + \tau_\varepsilon^\alpha D^\alpha)\sigma'(z,t) = (1 + \tau_\sigma^\alpha D^\alpha)(\lambda + 2G)\frac{\partial u(z,t)}{\partial z}. \quad (1)$$

Here, $\sigma'(z,t)$ denotes the vertical effective stress; λ and G are Lame constants; z represents the depth below the ground surface; t is time; τ_ε, and τ_σ are material parameters; and α is the fractional order parameter which can be obtained by the triaxial test and parameter inversion method, and $0 < \alpha < 1$; $u(z,t)$ is the displacement in the z direction. $D^\alpha = d^\alpha/dt^\alpha$ denotes α order Riemann–Liouville fractional derivative, and it is defined as [36]

$$D^\alpha[x(t)] = \frac{1}{\Gamma(1-\alpha)}\frac{d}{dt}\int_0^t \frac{x(\tau)}{(t-\tau)^\alpha}d\tau. \quad (2)$$

Here, $\Gamma(\varphi) = \int_0^\infty t^{\varphi-1}e^{-\varphi}dt$ is the Gamma function.

As shown in Figure 1, both the top and bottom surfaces are set as permeable. Instantaneous compressive stress q_0 and temperature T_1 are applied at the top surface, and a constant temperature T_0 is maintained at the bottom surface.

The viscoelastic characteristics of marine clay are simulated by the three-parameter fractional order derivative model, the equilibrium equation is given by [25]

$$\xi p + K'\beta T - \sigma' = q_0. \quad (3)$$

Here, $\xi = 1 - K'/K_s$ depends on the compressibility of the soil grains; K' represents the drained bulk modulus of the soil medium; K_s denotes the bulk modulus of the soil grains; β is the coefficient of volumetric expansion of the soil medium and T is the temperature increment; and p is excess pore pressure.

Substituting equation (1) into equation (3) yields

$$\xi p + K'\beta T - \frac{1 + \tau_\sigma^\alpha D^\alpha}{1 + \tau_\varepsilon^\alpha D^\alpha}(\lambda + 2G)\frac{\partial u}{\partial z} = q_0. \quad (4)$$

The fluid mass balance is governed by

$$k\frac{\partial^2 p}{\partial z^2} + S_w\frac{\partial^2 T}{\partial z^2} = c_1\frac{\partial^2 u}{\partial z \partial t} - c_2\frac{\partial T}{\partial t} + c_3\frac{\partial p}{\partial t}. \quad (5)$$

Here, k denotes the coefficient of permeability; S_w is a phenomenological coefficient associated with the influence of the thermal gradient on the water flux (thermo-osmosis); the parameters c_1, c_2, and c_3 are expressed as $c_1 = 1 - K'/K_s$,
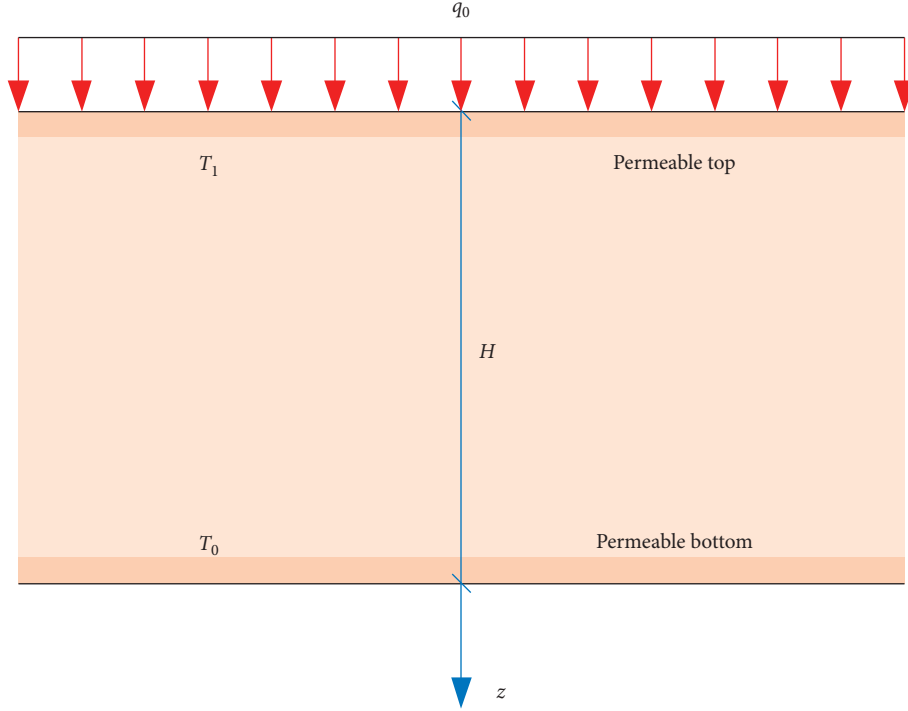
FIGURE 1: Mathematical model.

$c_2 = na_w + (1-n)a_s - \beta K'/K_s$, and $c_3 = n/\beta_w - (1-n)/K_s$, respectively; n is the porosity; a_w and a_s are volumetric thermal expansion coefficients of the pore water and soil grains, respectively; and β_w is the bulk modulus of pore water.

The thermal energy balance equation is given as

$$C_v \frac{\partial T}{\partial t} - T_0 K' \beta \frac{\partial^2 u}{\partial z \partial t} = (K - T_0 a_w \beta_w S_w) \frac{\partial^2 T}{\partial z^2} \tag{6}$$
$$+ T_0 (S_w - a_w \beta_w k) \frac{\partial^2 p}{\partial z^2},$$

where C_v is the volumetric specific heat of the soil medium; $C_v = (1-n)\rho_s C_s + n\rho_w C_w$; ρ_s is the density of soil grains; ρ_w is the density of water; C_s and C_w denote the gravimetric specific heats of soil grains and the pore water, respectively; and $K = (1-n)\lambda_s + n\lambda_w$ is the thermal conductivity of the soil medium, in which λ_s and λ_w are the thermal conductivities of the soil grain and the pore water.

The initial conditions of the problem are as follows:

$$p(z,0) = q_0,$$
$$u(z,0) = 0, \tag{7}$$
$$T(z,0) = 0.$$

The boundary conditions of the problem are as follows:

$$p(0,t) = 0. \tag{8}$$

$$p(H,t) = 0. \tag{9}$$

$$u(H,t) = 0. \tag{10}$$

$$T(0,t) = T_1. \tag{11}$$

$$T(H,t) = 0. \tag{12}$$

3. Solutions to Governing Equations

Laplace transform is introduced to solve governing equations (4)–(6), and the following Laplace transform equation is defined:

$$s^\gamma \overline{f}(s) = \int_0^\infty \frac{\partial^\gamma f(t)}{\partial t^\gamma} e^{-st} dt. \tag{13}$$

Applying Laplace transforms to equations (4)–(6), one can obtain transformed governing equations as

$$\xi \overline{p} + K' \beta \overline{T} - \frac{1 + \tau_\sigma^\alpha s^\alpha}{1 + \tau_\varepsilon^\alpha s^\alpha} (\lambda + 2G) \frac{\partial \overline{u}}{\partial z} = \frac{q_0}{s}. \tag{14}$$

$$k \frac{\partial^2 \overline{p}}{\partial z^2} + S_w \frac{\partial^2 \overline{T}}{\partial z^2} = sc_1 \frac{\partial \overline{u}}{\partial z} - sc_2 \overline{T} + c_3 (s\overline{p} - q_0). \tag{15}$$

$$C_v s \overline{T} - T_0 K' \beta s \frac{\partial \overline{u}}{\partial z} = (K - T_0 a_w \beta_w S_w) \frac{\partial^2 \overline{T}}{\partial z^2} \tag{16}$$
$$+ T_0 (S_w - a_w \beta_w k) \frac{\partial^2 \overline{p}}{\partial z^2}.$$

Here, s is the Laplace transform parameter; $\overline{p} = \int_0^\infty e^{-st} p\, dt$, $\overline{T} = \int_0^\infty e^{-st} T\, dt$, and $\overline{u} = \int_0^\infty e^{-st} u\, dt$.

The Laplace transform of equations (8)–(12) with respect to the time variable t is derived as

$$\bar{p}|_{z=0} = 0. \tag{17}$$

$$\bar{p}|_{z=H} = 0. \tag{18}$$

$$\bar{u}|_{z=H} = 0. \tag{19}$$

$$\bar{T}|_{z=0} = \frac{T_1}{s}. \tag{20}$$

$$\bar{T}|_{z=H} = 0. \tag{21}$$

Substituting equation (15) into equation (16) yields

$$a_1 \frac{\partial^2 \bar{T}}{\partial z^2} + a_2 \frac{\partial^2 \bar{p}}{\partial z^2} + a_3 s\bar{T} + a_4 s\bar{p} - a_4 q_0 = 0. \tag{22}$$

Here, $a_1 = -T_0 K'\beta S_w/c_1 - K + T_0 a_w \beta_w S_w$; $a_2 = -T_0 K' \beta k/c_1 - T_0(S_w - a_w \beta_w k)$; $a_3 = C_v - T_0 K'\beta c_2/c_1$; and $a_4 = T_0 K'\beta c_3/c_1$.

Substituting equation (15) into equation (14) gives

$$b_1 \frac{\partial^2 \bar{T}}{\partial z^2} + b_2 \frac{\partial^2 \bar{p}}{\partial z^2} + b_3 s\bar{T} + b_4 s\bar{p} + b_5 q_0 = 0, \tag{23}$$

where $b_1 = 1 + \tau_\sigma^\alpha s^\alpha/1 + \tau_\varepsilon^\alpha s^\alpha (\lambda + 2G)S_w/c_1$; $b_2 = 1 + \tau_\sigma^\alpha s^\alpha/1 + \tau_\varepsilon^\alpha s^\alpha (\lambda + 2G)k/c_1$; $b_3 = 1 + \tau_\sigma^\alpha s^\alpha/1 + \tau_\varepsilon^\alpha s^\alpha (\lambda + 2\;G)c_2/c_1 - K'\beta$; $b_4 = -\xi - 1 + \tau_\sigma^\alpha s^\alpha/1 + \tau_\varepsilon^\alpha s^\alpha (\lambda + 2G)c_3/c_1$; and $b_5 = 1 + \tau_\sigma^\alpha s^\alpha/1 + \tau_\varepsilon^\alpha s^\alpha (\lambda + 2G)c_3/c_1 + 1$.

Further transformation of equations (22) and (23) leads to

$$\bar{T} = \frac{h_1}{s} \frac{\partial^2 \bar{p}}{\partial z^2} + h_2 \bar{p} + h_3 \frac{q_0}{s}, \tag{24}$$

where $h_1 = a_2 b_1 - a_1 b_2/a_1 b_3 - a_3 b_1$; $h_2 = a_4 b_1 - a_1 b_4/a_1 b_3 - a_3 b_1$; and $h_3 = -a_4 b_1 + a_1 b_5/a_1 b_3 - a_3 b_1$.

Substituting equation (24) into equation (22) yields

$$g_1 \frac{\partial^4 \bar{p}}{\partial z^4} + g_2 s \frac{\partial^2 \bar{p}}{\partial z^2} + g_3 s^2 \bar{p} + \frac{s}{a_1}(a_3 h_3 - a_4)q_0 = 0, \tag{25}$$

where $g_1 = h_1$; $g_2 = h_2 + a_2/a_1 + a_3 h_1/a_1$; and $g_3 = a_3 h_2 + a_4/a_1$.

The general solution of equation (25) is derived as

$$\bar{p} = A_1 e^{\gamma_1 z} + A_2 e^{-\gamma_1 z} + B_1 e^{\gamma_2 z} + B_2 e^{-\gamma_2 z} - \frac{a_3 h_3 - a_4}{a_1 g_3 s} q_0, \tag{26}$$

where A_1, A_2, B_1, B_2 are undetermined coefficients. $\gamma_1^2 = -g_2 - \sqrt{g_2^2 - 4g_1 g_3}/2g_1 s$; $\gamma_2^2 = -g_2 + \sqrt{g_2^2 - 4g_1 g_3}/2g_1 s$

Substituting equation (26) into equation (24) gives

$$\bar{T} = \left(\frac{h_1 \gamma_1^2}{s} + h_2\right)\left(A_1 e^{\gamma_1 z} + A_2 e^{-\gamma_1 z}\right) + \left(\frac{h_1 \gamma_2^2}{s} + h_2\right)\left(B_1 e^{\gamma_2 z} + B_2 e^{-\gamma_2 z}\right)$$
$$-\frac{h_2(a_3 h_3 - a_4)}{a_1 g_3 s} q_0 + \frac{h_3 q_0}{s} \tag{27}$$

Substituting equation (26) into equations (17), (18), (20), and (21), the undermined coefficients can be obtained as

$$A_1 = -\frac{s(\phi_1 - c_{22}\phi_0)\left(1 - e^{-\gamma_1 H}\right) + T_1 e^{-\gamma_1 H}}{s(c_{11} - c_{22})\left(e^{\gamma_1 H} - e^{-\gamma_1 H}\right)},$$

$$A_2 = \frac{s(\phi_1 - c_{22}\phi_0)\left(1 - e^{\gamma_1 H}\right) + T_1 e^{\gamma_1 H}}{s(c_{11} - c_{22})\left(e^{\gamma_1 H} - e^{-\gamma_1 H}\right)},$$

$$B_1 = \frac{s(\phi_1 - c_{11}\phi_0)\left(1 - e^{-\gamma_2 H}\right) + T_1 e^{-\gamma_2 H}}{s(c_{11} - c_{22})\left(e^{\gamma_2 H} - e^{-\gamma_2 H}\right)},$$

$$B_2 = -\frac{s(\phi_1 - c_{11}\phi_0)\left(1 - e^{\gamma_2 H}\right) + T_1 e^{\gamma_2 H}}{s(c_{11} - c_{22})\left(e^{-\gamma_2 H} - e^{-\gamma_2 H}\right)}, \tag{28}$$

where $c_{11} = h_1\gamma_1^2/s + h_2$, $c_{22} = h_1\gamma_2^2/s + h_2$, $\varphi_0 = -a_3$ $h_3 - a_4/a_1g_3sq_0$, and $\varphi_1 = -(h_2(a_3h_3 - a_4)/a_1g_3s - h_3/s)q_0$.

Then, equation (26) can be rewritten as

$$
\begin{aligned}
\overline{p} &= -\frac{\theta_1\sinh[\gamma_1 z] - [T_1 - \theta_1]\sinh[\gamma_1(H - z)] - T_0\sinh[\gamma_1 z]}{h_1(\gamma_1^2 - \gamma_2^2)\sinh[\gamma_1 H]} \\
&\quad + \frac{\theta_2\sinh[\gamma_2 z] + [\theta_2 - T_1]\sinh[\gamma_2(H - z)] - T_0\sinh[\gamma_2 z]}{h_1(\gamma_1^2 - \gamma_2^2)\sinh[\gamma_2 H]} + \phi_0
\end{aligned}
\tag{29}
$$

where, $\theta_1 = s(\varphi_1 - \varphi_0 c_{22})$ and $\theta_2 = s(\varphi_1 - \varphi_0 c_{11})$.

Substituting equations (26) and (27) into equation (14) yields

$$
\begin{aligned}
\frac{\partial\overline{u}}{\partial z} &= \chi\left[K'\beta\left(\frac{h_1\gamma_1^2}{s} + h_2\right) + \xi\right](A_1 e^{\gamma_1 z} + A_2 e^{-\gamma_1 z}) + \chi\left[K'\beta\left(\frac{h_1\gamma_2^2}{s} + h_2\right) + \xi\right](B_1 e^{\gamma_2 z} + B_2 e^{-\gamma_2 z}) \\
&\quad + \chi q_0\left[-\frac{\xi(a_3h_3 - a_4)}{a_1g_3 s} - \frac{K'\beta h_2(a_3h_3 - a_4)}{a_1g_3 s} + \frac{K'\beta h_3 - 1}{s}\right]
\end{aligned}
\tag{30}
$$

where $\chi = 1/\lambda + 2G1 + \tau_\epsilon^\alpha s^\alpha/1 + \tau_\sigma^\alpha s^\alpha$.

Integrating both sides of equation (30) from zero to infinity gives

$$
\begin{aligned}
\overline{u} &= \frac{\chi}{\gamma_1}\left[K'\beta\left(\frac{h_1\gamma_1^2}{s} + h_2\right) + \xi\right](A_1 e^{\gamma_1 z} - A_2 e^{-\gamma_1 z}) + \frac{\chi}{\gamma_2}\left[K'\beta\left(\frac{h_1\gamma_2^2}{s} + h_2\right) + \xi\right](B_1 e^{\gamma_2 z} - B_2 e^{-\gamma_2 z}) \\
&\quad + \chi q_0\left[-\frac{\xi(a_3h_3 - a_4)}{a_1g_3 s} - \frac{K'\beta h_2(a_3h_3 - a_4)}{a_1g_3 s} + \frac{K'\beta h_3 - 1}{s}\right]z + D_1
\end{aligned}
\tag{31}
$$

Substituting equation (31) into equation (19), the coefficient D_1 can be obtained as

$$
\begin{aligned}
D_1 &= \frac{-\chi}{\gamma_1}\left[K'\beta\left(\frac{h_1\gamma_1^2}{s} + h_2\right) + \xi\right](A_1 e^{\gamma_1 H} - A_2 e^{-\gamma_1 H}) - \frac{\chi}{\gamma_2}\left[K'\beta\left(\frac{h_1\gamma_2^2}{s} + h_2\right) + \xi\right](B_1 e^{\gamma_2 H} - B_2 e^{-\gamma_2 H}) \\
&\quad - \chi q_0\left[-\frac{\xi(a_3h_3 - a_4)}{a_1g_3 s} - \frac{K'\beta h_2(a_3h_3 - a_4)}{a_1g_3 s} + \frac{K'\beta h_3 - 1}{s}\right]H
\end{aligned}
\tag{32}
$$

Through the above derivation, the analytical expressions of excess pore pressure, temperature increment, and displacement can be obtained accordingly. However, it is difficult to directly obtain the analytical solutions in the transformed space for some formulas are difficult to integrate. Therefore, it is necessary to utilize the numerical method to program and analyze the solution process in this paper. Currently, there exist many Laplace inverse transform methods, among which the Crump's numerical inversion results of Laplace transform is the most accurate [10].
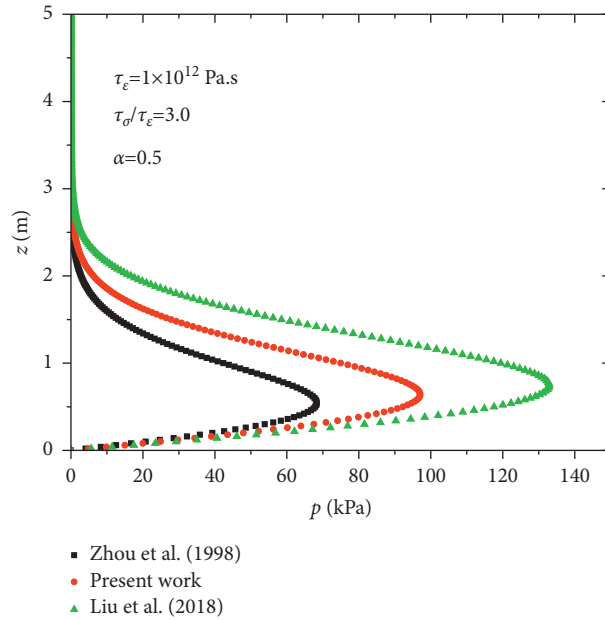
FIGURE 2: Comparison of excess pore pressure among solutions of Zhou et al. [25], Liu et al. [14], and present work.
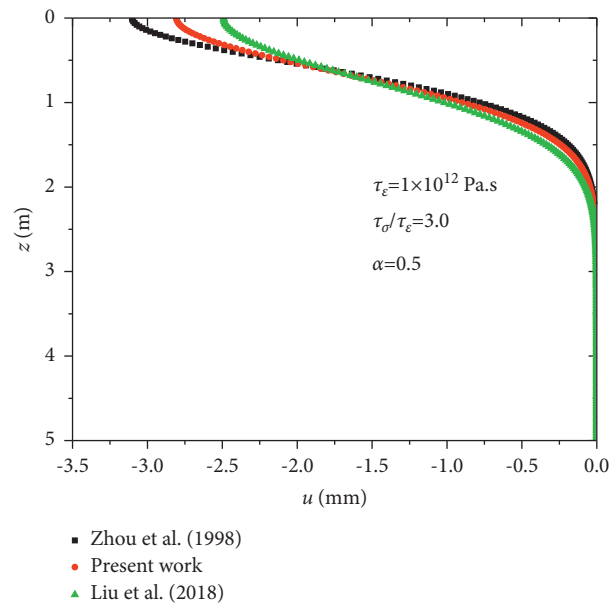
FIGURE 3: Comparison of displacement among solutions of Zhou et al. [25], Liu et al. [14], and present work.

Assuming that $F(s)$ is the Laplace transform of function $F(t)$, Crump's inversion algorithm of the Laplace inverse transform can be written as

$$F(t) \approx \frac{e^{at}}{T^*}\left\{\frac{1}{2}F(a) + \sum_{m=1}^{500}\left[\text{Re}\left[F\left(a + \frac{m\pi i}{T^*}\right)\right]\cos\frac{m\pi t}{T^*} - \text{Im}\left[F\left(a + \frac{m\pi i}{T^*}\right)\right]\sin\frac{m\pi t}{T^*}\right]\right\}, \tag{33}$$
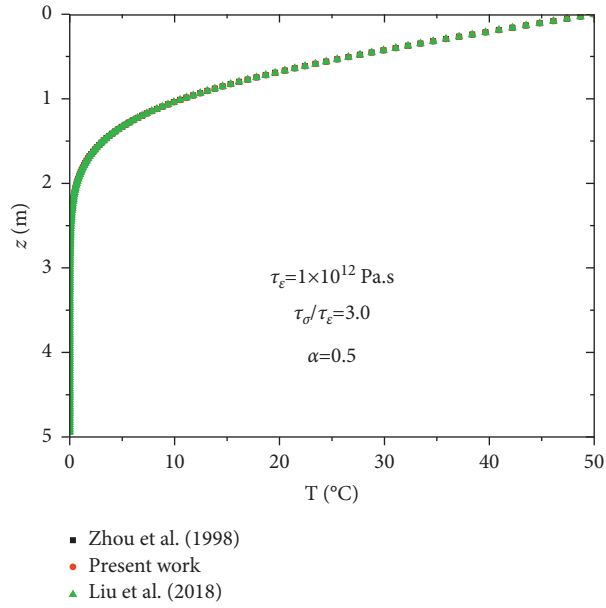
FIGURE 4: Comparison of temperature increment among solutions of Zhou et al. [25], Liu et al. [14], and present work.
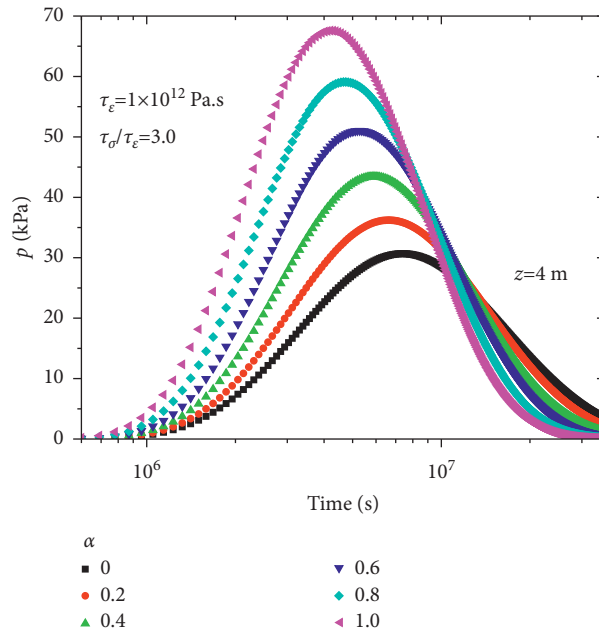
FIGURE 5: Influence of the order of the fractional derivative on excess pore pressure when $\tau_\sigma / \tau_\varepsilon = 3$.

where $T^* > t/2$. If $|F(t)| < Me^{\alpha t}$, the error $|\varsigma| \leq Me^v e^{-2T^*(a-v)}$.

4. Numerical Results and Discussion

Having illustrated and reviewed the obtained theoretical results in the preceding section, we now present some numerical results. Following the works of Liu et al. [14] and Zhou et al. [25], the parameters of marine clay in the calculation can be set as $\lambda = 6 \times 10^6$ Pa, $G = 8 \times 10^6$, $n = 0.25$, $S_w = 6.0 \times 10^{-11}$ m²/s/°C, $K' = 2.78 \times 10^6$ Pa, $k = 1.0 \times$ 10^{-14} m⁵/J/s, $\lambda_w = 0.582$ J/m/s/°C, $\lambda_s = 3.29$ J/m/s/°C, $K_s = 59 \times 10^9$ Pa, $\beta_w = 3.3 \times 10^9$ Pa, $\rho_w = 1000$ kg/m³, $\rho_s = 2610$ kg/m³, $C_w = 4186$ J/kg/°C, $C_s = 937$ J/kg/°C, $a_s = 3.0 \times 10^{-6}$°C⁻¹, $a_w = 3.0 \times 10^{-4}$°C⁻¹, $\tau_\varepsilon = 1 \times 10^{12}$Pa·s, $q_0 = 0$ Pa, $T_1 = 50$°C, and $T_0 = 23$°C.

4.1. Comparative Analysis. The Kelvin viscoelastic model is combined with the thermo-hydro-mechanical coupling governing equations for marine clay, and the influence of viscosity on one-dimensional thermal consolidation was
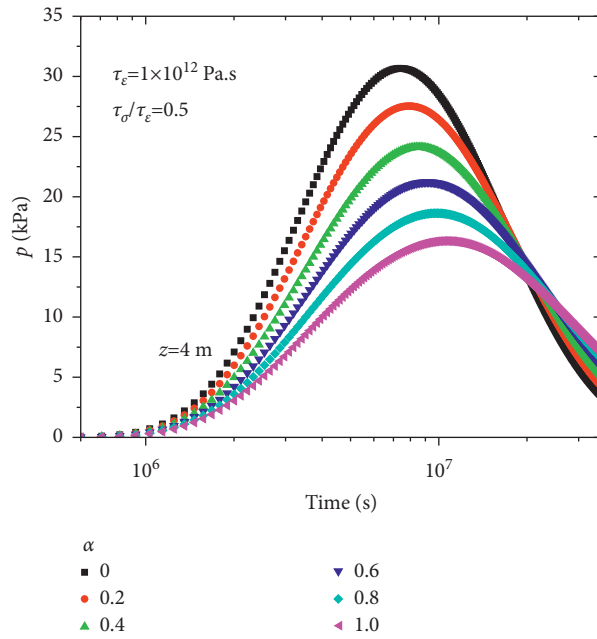
FIGURE 6: Influence of the order of the fractional derivative on excess pore pressure when $\tau_\sigma / \tau_\varepsilon = 0.5$.
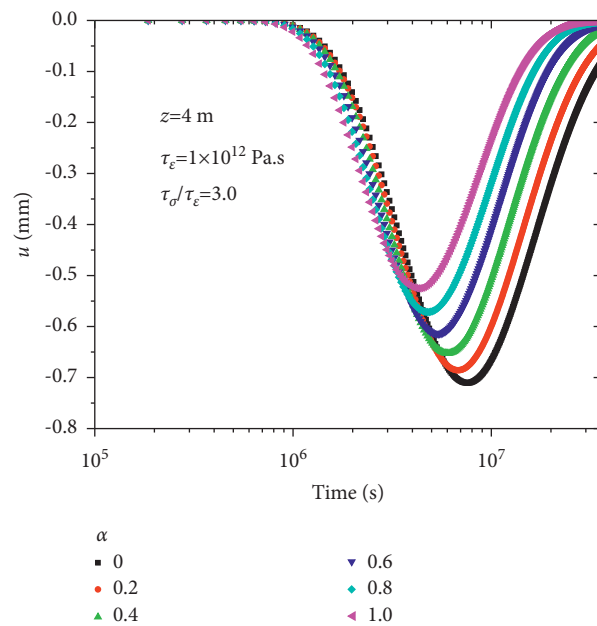
FIGURE 7: Influence of the order of the fractional derivative on displacement when $\tau_\sigma / \tau_\varepsilon = 3$.

investigated by Liu et al. [14]. In addition, Zhou et al. [25] proposed a fully coupled thermo-hydro-mechanical model with thermal filtration and thermo-osmosis. In this paper, for the purpose of verifying and presenting the differences of the three cases of the fractional derivative viscoelastic model (FDVM), Kelvin viscoelastic model (KVM), and elastic model (EM), the order of the fractional derivative α is assumed to be zero for the comparison of the FDVM with the EM, and the material parameter τ_ε^α is assumed to be zero,

and α is equal to 1 for the comparison of the FDVM with the KVM. Figures 2–4 illustrate the distribution of excess pore pressure, displacement, and temperature increment against depth among solutions of Zhou et al. [25], Liu et al. [14], and present work. It can be found that the KVM produces the largest excess pore pressure, followed by the results of the FDVM and EM. At depth above 0.6 m, the displacement value produced by the EM is the largest, followed by those of the FDVM and KVM. At larger depth, remarkable increase
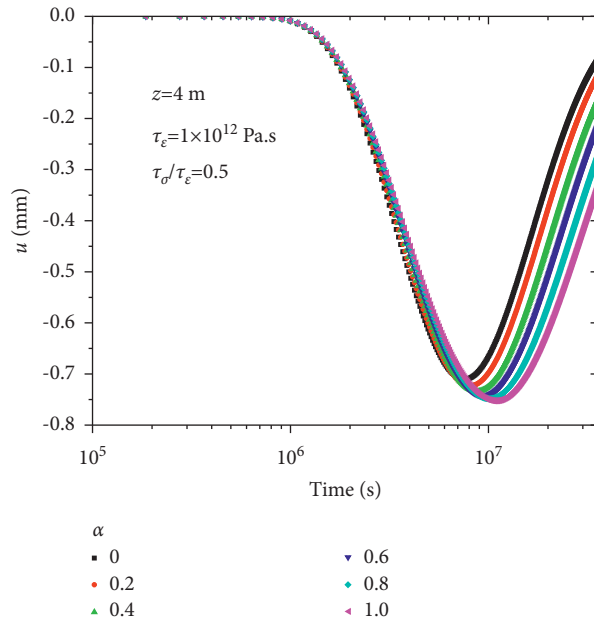
FIGURE 8: Influence of the order of the fractional derivative on displacement when $\tau_\sigma/\tau_\varepsilon = 0.5$.
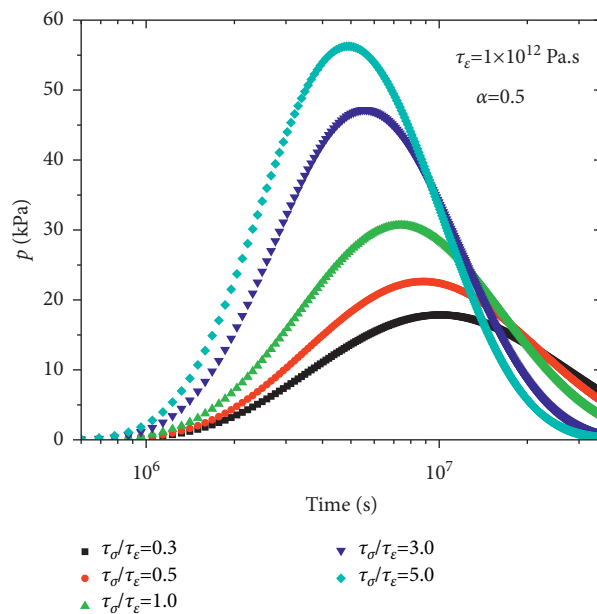
FIGURE 9: Influence of the material parameter $\tau_\sigma/\tau_\varepsilon$ on excess pore water pressure when $\alpha = 0.5$.

of the displacement value could be observed for all the three models. For the distribution of temperature, the three models produce similar results.

4.2. Influence of the Order of the Fractional Derivative α. Figures 5 and 6 show the influence of the parameter α on the development of excess pore pressure when the values of $\tau_\sigma/\tau_\varepsilon$ are 3.0 and 0.5, respectively. When $\tau_\sigma/\tau_\varepsilon = 3.0$, the excess pore pressure increases with the increase of α before the peak value. After the peak, the increase of α seems to

accelerate the dissipation of the excess pore pressure. When $\tau_\sigma/\tau_\varepsilon = 0.5$, an opposite trend could be observed. With increasing α, the peak value of excess pore pressure shows a decreasing trend, and the after-peak dissipation rate is smaller. It can be seen that the influence of the fractional derivative parameter α on the development of excess pore pressure depends on the characteristics of the soil mass.

Figures 7 and 8 show the influence of the parameter α on the displacement development under the same conditions. Similar trends to that of the excess pore pressure can be observed. Another finding is that the influence of α is more
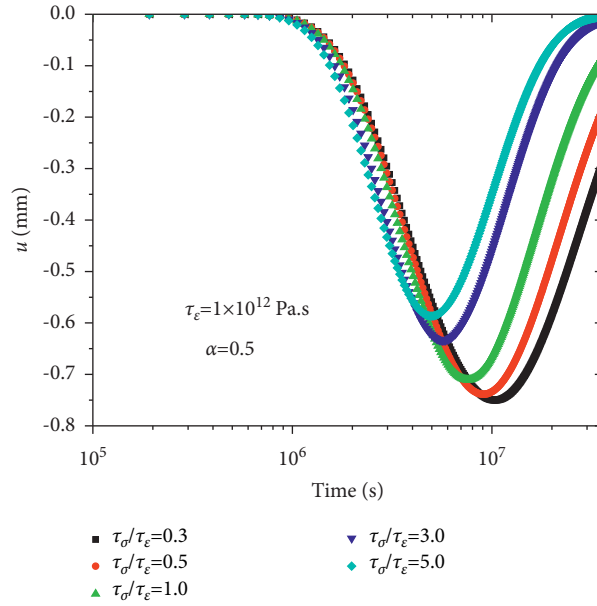
FIGURE 10: Influence of the material parameter $\tau_\sigma/\tau_\varepsilon$ on displacement when $\alpha = 0.5$.
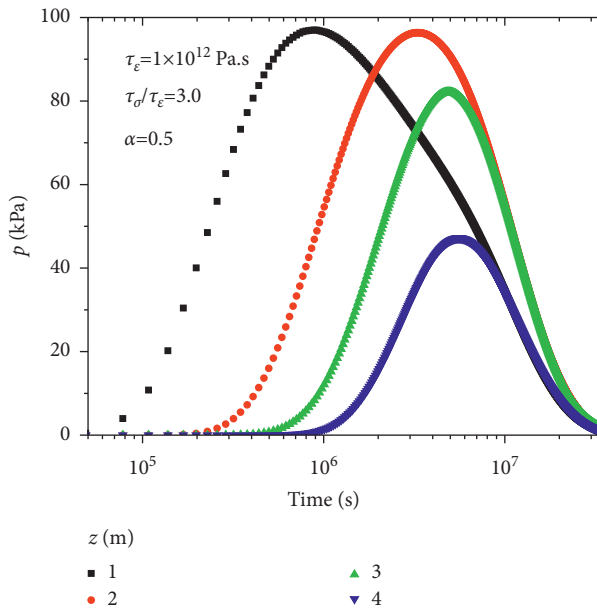
FIGURE 11: Influence of embedment depth on pore water pressure when $\tau_\sigma/\tau_\varepsilon = 3$.

obvious at $\tau_\sigma/\tau_\varepsilon = 3.0$. It can be seen that the soil property would influence the impact of the fractional derivative parameter on the development of displacement.

4.3. Influence of Material Parameters $\tau_\sigma/\tau_\varepsilon$. Figures 9 and 10 depict the influence of $\tau_\sigma/\tau_\varepsilon$ variance on the development of excess pore pressure and displacement with $\alpha = 0.5$. With increasing $\tau_\sigma/\tau_\varepsilon$, both the peak value of the excess pore value and the after-peak dissipation rate are much larger, while the net maximum displacement value decreases. The influence of $\tau_\sigma/\tau_\varepsilon$ on the trend of displacement development is less obvious.

The influence of embedment depth on the development of excess pore pressure and displacement is presented in Figures 11–14. As shown in Figures 11 and 12, the magnitude of excess pore pressure at $\tau_\sigma/\tau_\varepsilon = 3$ is much larger than that at $\tau_\sigma/\tau_\varepsilon = 0.5$. On the other hand, the development trend of excess pore pressure at different depths seems to be uninfluenced with the variance of $\tau_\sigma/\tau_\varepsilon$, but the peak excess pore pressure decreases with depth. As depicted in Figures 13 and 14, similar trends could be observed for the development of the displacement value. With increasing depth, the displacement value is much smaller.

$\tau_\varepsilon = 1 \times 10^{12}$ Pa.s
$\tau_\sigma / \tau_\varepsilon = 0.5$
$\alpha = 0.5$

z (m)
■ 1   ▲ 3
● 2   ▼ 4
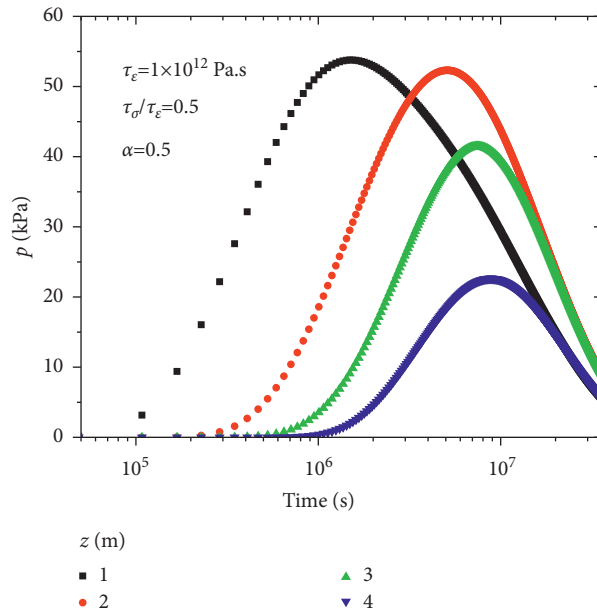
FIGURE 12: Influence of embedment depth on pore water pressure when $\tau_\sigma / \tau_\varepsilon = 0.5$.

$\tau_\varepsilon = 1 \times 10^{12}$ Pa.s
$\tau_\sigma / \tau_\varepsilon = 3.0$
$\alpha = 0.5$

z (m)
■ 1   ▲ 3
● 2   ▼ 4
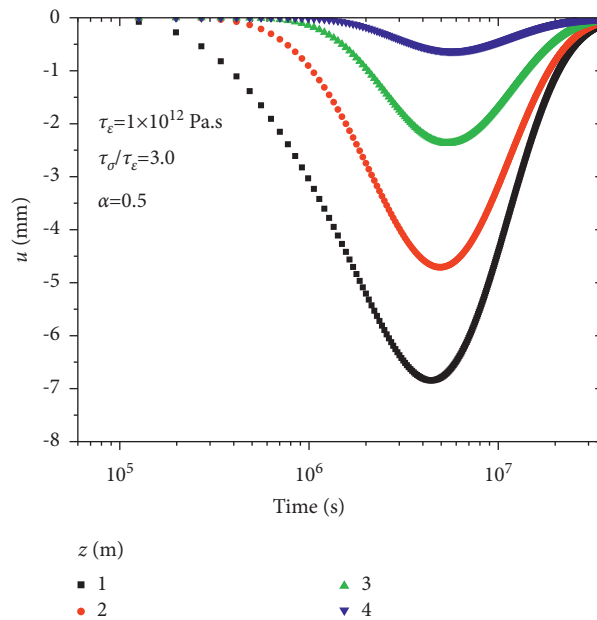
FIGURE 13: Influence of embedment depth on displacement when $\tau_\sigma / \tau_\varepsilon = 3$.

4.4. Influence of the Phenomenological Coefficient S_w. The influence of the phenomenological coefficient S_w on the development of excess pore pressure, displacement, and temperature increment is presented in Figures 15–17. It is clear that both the excess pore pressure and displacement increase with increasing S_w. On the other hand, the variance of S_w seems to have no impact on the development of temperature increment. This parametric analysis indicates
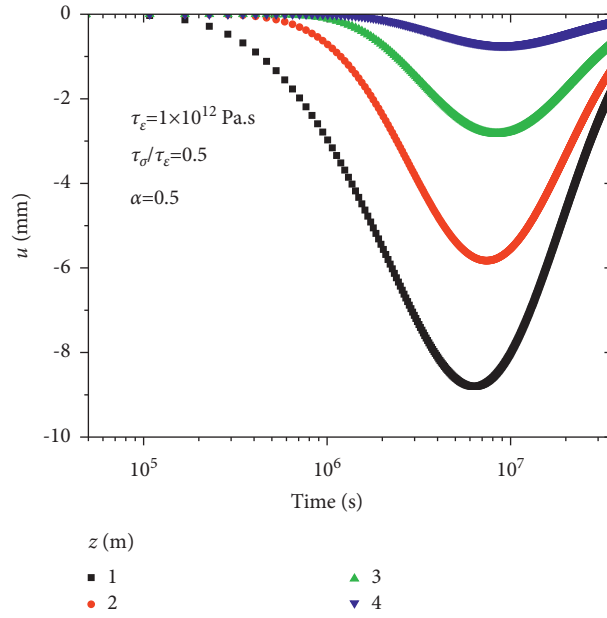
FIGURE 14: Influence of embedment depth on displacement when $\tau_\sigma/\tau_\varepsilon = 0.5$.
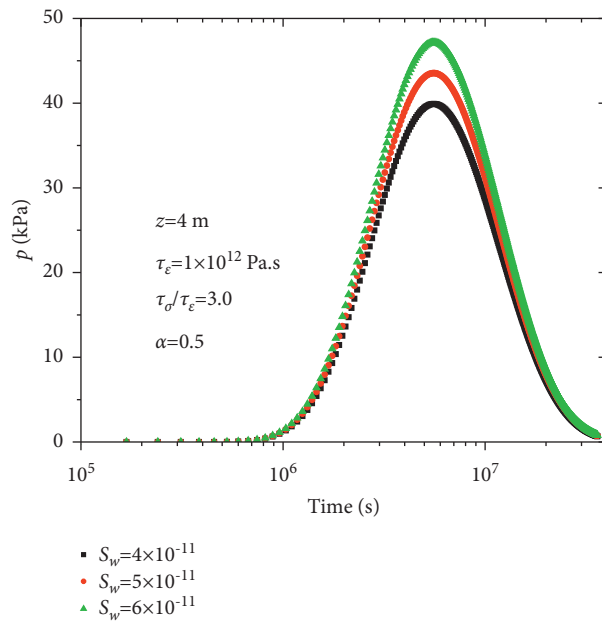
FIGURE 15: Influence of the phenomenological coefficient S_w on excess pore pressure.
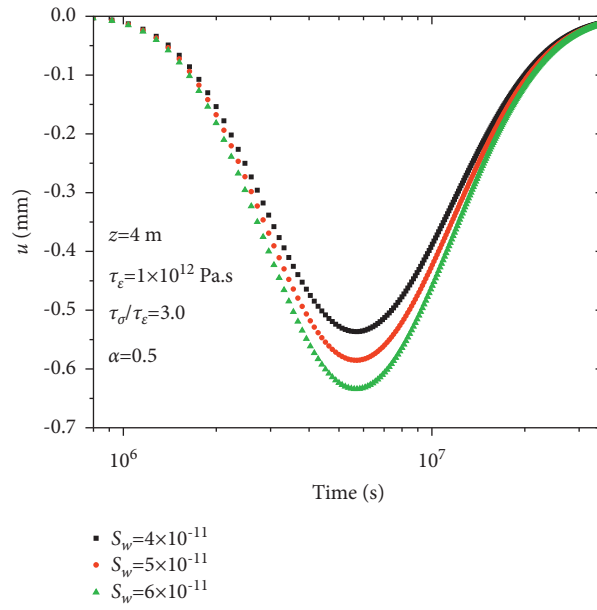
FIGURE 16: Influence of the phenomenological coefficient S_w on displacement.
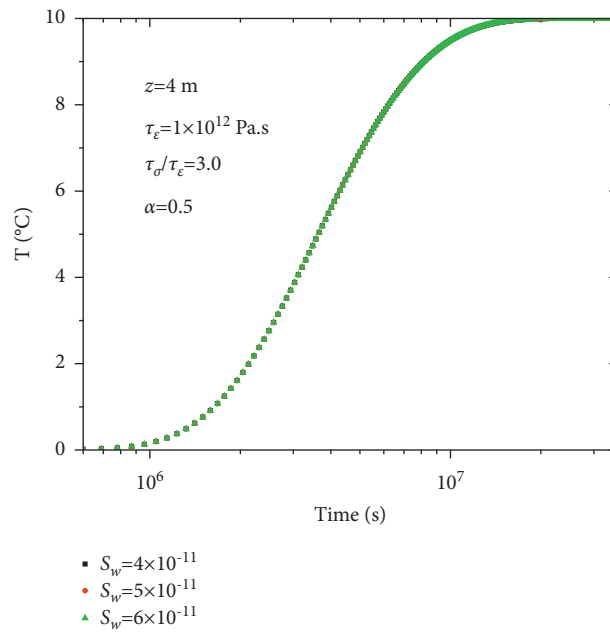
FIGURE 17: Influence of the phenomenological coefficient S_w on temperature increment.

that the thermal gradient has an obvious effect on the thermal filtration and thermo-osmosis process.

5. Conclusion

In this paper, a three-parameter fractional order derivative model is proposed based on the improved thermo-hydro-mechanical coupling theory by accounting for the viscoelastic behavior of marine clay. One-dimensional thermal consolidation of viscoelastic marine clay is analyzed, considering the thermal filtration and thermo-osmosis process. Solutions of excess pore pressure, temperature increment, and displacement are obtained by using the Laplace transform method and its numerical inverse transform. The influence of the order of the fractional derivative, material parameters, and phenomenological coefficient on the characteristics of thermal consolidation of marine clay is investigated. The performance of the proposed fractional derivative viscoelastic model (FDVM), Kelvin viscoelastic model (KVM), and elastic model (EM) is compared. The calculated excess pore pressure values from the three models are quite different, while the development of temperature increment seems to be uninfluenced by the selected model. For the development of the displacement value, there is an obvious turn of the displacement value for different models at the depth of 0.6 m. Further parametric analysis indicates that the influence of the fractional derivative parameter on the development of excess pore pressure and displacement depends on the properties of the soil mass, and the temperature increment has an obvious effect on the thermal filtration and thermo-osmosis process.

Data Availability

Data are available on request from the authors.

Conflicts of Interest

The authors declare that they have no conflicts of interest.

Acknowledgments

References

[1] F. G. F. Gibb, "A new scheme for the very deep geological disposal of high-level radioactive waste," *Journal of the Geological Society*, vol. 157, no. 1, pp. 27–36, 2000.

[2] Y. N. Abousleiman and S. Ekbote, "Solutions for the inclined borehole in a porothermoelastic transversely isotropic medium," *Journal of Applied Mechanics*, vol. 72, no. 1, pp. 102–114, 2005.

[3] Y. P. Zhang, G. S. Jiang, W. B. Wu et al., "Analytical solution for distributed torsional low strain integrity test for pipe pile," *International Journal for Numerical and Analytical Methods in Geomechanics*, vol. 46, no. 1, pp. 47–67, 2022.

[4] Y. Man, H. X. Yang, N. R. Diao, J. H. Liu, and Z. H. Fang, "A new model and analytical solutions for borehole and pile ground heat exchangers," *International Journal of Heat and Mass Transfer*, vol. 53, no. 13-14, pp. 2593–2601, 2010.

[5] M. J. Wen, H. R. Xiong, and J. M. Xu, "Thermo-hydro-mechanical response of a partially sealed circular tunnel in saturated rock under inner water pressure," *Tunnelling and Underground Space Technology*, vol. 126, Article ID 104552, 2022.

[6] W. B. Wu, Z. J. Yang, X. Liu et al., "Horizontal dynamic response of pile in unsaturated soil considering its construction disturbance effect," *Ocean Engineering*, vol. 245, Article ID 110483, 2022.

[7] A. F. Rotta Loria and L. Laloui, "Thermally induced group effects among energy piles," *Géotechnique*, vol. 67, pp. 374–393, 2017.

[8] Y. P. Zhang, Z. Q. Wang, M. H. El Naggar, W. B. Wu, L. X. Wang, and G. S. Jiang, "Three-dimensional wave propagation in a solid pile during torsional low strain integrity test," *International Journal for Numerical and Analytical Methods in Geomechanics*, vol. 2022, 2022.

[9] Y. Tian, W. B. Wu, M. J. Wen, G. S. Jiang, M. H. El Naggar, and G. X. Mei, "Nonlinear consolidation of soft foundation improved by prefabricated vertical drains based on elliptical cylindrical equivalent model," *International Journal for Numerical and Analytical Methods in Geomechanics*, vol. 45, no. 13, pp. 1949–1971, 2021.

[10] Y. Tian, G. S. Jiang, W. B. Wu et al., "Elliptical cylindrical equivalent model of PVD-assisted consolidation under surcharge combined with vacuum preloading and its application," *Computers and Geotechnics*, vol. 139, Article ID 104389, 2021.

[11] M. F. Zong, Y. Tian, R. Z. Liang, W. B. Wu, M. J. Xu, and G. X. Mei, "One-dimensional nonlinear consolidation analysis of soil with continuous drainage boundary," *Journal of Central South University*, vol. 29, no. 1, pp. 270–281, 2022.

[12] D. L. Slegel and L. R. Davis, "Transient heat and mass transfer in soils in the vicinity of heated porous pipes," *Journal of Heat Transfer*, vol. 99, no. 4, pp. 541–546, 1977.

[13] M. J. Wen, Y. Tian, L. C. Li, K. H. Wang, and W. B. Wu, "An imperfect thermal contact problem for consolidation of bilayered saturated soil subjected to ramp-type heating," *International Journal of Heat and Mass Transfer*, vol. 190, Article ID 122755, 2022.

[14] J. C. Liu, W. T. Shi, and G. H. Lei, "Influence of viscosity on one-dimensional thermal consolidation of marine clay," *Marine Georesources & Geotechnology*, vol. 37, no. 3, pp. 331–338, 2019.

[15] M. A. Biot, "Thermoelasticity and irreversible thermo-dynamics," *Journal of Applied Physics*, vol. 27, no. 3, pp. 240–253, 1956.

[16] J. R. Booker and C. Savvidou, "Consolidation around a spherical heat source," *International Journal of Solids and Structures*, vol. 20, no. 11-12, pp. 1079–1090, 1984.

[17] J. R. Booker and C. Savvidou, "Consolidation around a point heat source," *International Journal for Numerical and*

Analytical Methods in Geomechanics, vol. 9, no. 2, pp. 173–184, 1985.

[18] B. Bai, "Fluctuation responses of saturated porous media subjected to cyclic thermal loading," *Computers and Geotechnics*, vol. 33, no. 8, pp. 396–403, 2006.

[19] D. W. Smith and J. R. Booker, "Green's functions for a fully coupled thermoporoelastic material," *International Journal for Numerical and Analytical Methods in Geomechanics*, vol. 17, no. 3, pp. 139–163, 1993.

[20] Z. Lu, H. L. Yao, and G. B. Liu, "Thermomechanical response of a poroelastic half-space soil medium subjected to time harmonic loads," *Computers and Geotechnics*, vol. 37, no. 3, pp. 343–350, 2010.

[21] Z. Y. Ai and L. J. Wang, "Axisymmetric thermal consolidation of multilayered porous thermoelastic media due to a heat source," *International Journal for Numerical and Analytical Methods in Geomechanics*, vol. 39, no. 17, pp. 1912–1931, 2015.

[22] Z. Y. Ai, Z. Ye, Z. Zhao, Q. L. Wu, and L. J. Wang, "Time-dependent behavior of axisymmetric thermal consolidation for multilayered transversely isotropic poroelastic material," *Applied Mathematical Modelling*, vol. 61, pp. 216–236, 2018.

[23] M. J. Wen, J. M. Xu, and H. R. Xiong, "Thermo-hydro-mechanical dynamic response of a cylindrical lined tunnel in a poroelastic medium with fractional thermoelastic theory," *Soil Dynamics and Earthquake Engineering*, vol. 130, Article ID 105960, 2020.

[24] R. C. Srivastava and P. K. Avasthi, "Non-equilibrium thermodynamics of thermo-osmosis of water through kaolinite," *Journal of Hydrology*, vol. 24, no. 1-2, pp. 111–120, 1975.

[25] Y. Zhou, R. K. N. D. Rajapakse, and J. Graham, "A coupled thermoporoelastic model with thermo-osmosis and thermal-filtration," *International Journal of Solids and Structures*, vol. 35, no. 34–35, pp. 4659–4683, 1998.

[26] G. B. Liu, K. H. Xie, and R. Y. Zheng, "Model of nonlinear coupled thermo-hydro-elastodynamics response for a saturated porous medium," *Science in China, Series A: Technological Sciences)*, vol. 52, pp. 2373–2383, 2009.

[27] G. B. Liu, K. H. Xie, and R. Y. Zheng, "Thermo-elastodynamic response of a spherical cavity in saturated poroelastic medium," *Applied Mathematical Modelling*, vol. 34, no. 8, pp. 2203–2222, 2010.

[28] Y. Yang, K. Guerlebeck, and T. Schanz, "Thermo-osmosis effect in saturated porous medium," *Transport in Porous Media*, vol. 104, no. 2, pp. 253–271, 2014.

[29] J. C. Liu, G. H. Lei, and X. D. Wang, "One-dimensional consolidation of visco-elastic marine clay under depth-varying and time-dependent load," *Marine Georesources & Geotechnology*, vol. 33, no. 4, pp. 337–347, 2015.

[30] L. J. Wang and L. H. Wang, "Semianalytical analysis of creep and thermal consolidation behaviors in layered saturated clays," *International Journal of Geomechanics*, vol. 20, no. 4, Article ID 06020001, 2020.

[31] H. H. Zhu, C. C. Zhang, G. X. Mei, B. Shi, and L. Gao, "Prediction of one-dimensional compression behavior of Nansha clay using fractional derivatives," *Marine Georesources & Geotechnology*, vol. 35, no. 5, pp. 688–697, 2017.

[32] L. C. Li, X. Liu, H. Liu et al., "Experimental and numerical study on the static lateral performance of monopile and hybrid pile foundation," *Ocean Engineering*, vol. 255, Article ID 111461, 2022.

[33] L. C. Li, M. Y. Zheng, X. Liu et al., "Numerical analysis of the cyclic loading behavior of monopile and hybrid pile foundation," *Computers and Geotechnics*, vol. 144, Article ID 104635, 2022.

[34] M. H. Huang and J. C. Li, "Consolidation of viscoelastic soil by vertical drains incorporating fractional-derivative model and time-dependent loading," *International Journal for Numerical and Analytical Methods in Geomechanics*, vol. 43, no. 1, pp. 239–256, 2018.

[35] L. Wang, D. A. Sun, P. C. Li, and Y. Xie, "Semi-analytical solution for one-dimensional consolidation of fractional derivative viscoelastic saturated soils," *Computers and Geotechnics*, vol. 83, pp. 30–39, 2017.

[36] Y. A. Rossikhin and M. V. Shitikova, "Applications of fractional calculus to dynamic problems of linear and nonlinear hereditary mechanics of solids," *Applied Mechanics Reviews*, vol. 50, no. 1, pp. 15–67, 1997.

Research Article

Microscopic Bearing Behavior of Horizontally Loaded Vertical Plate Anchors in Sandy Soil

Sifeng Zhang [1,2] **Yushuai Wang,** [1] **Chao Li,** [1] **Qing Li,**[3] **and Dong Yang**[4]

[1]*School of Transportation Engineering, Shandong Jianzhu University, Jinan 250101, Shandong, China*
[2]*Shandong Provincial Key Laboratory of Road and Traffic Engineering in Colleges and Universities, Jinan 250101, Shandong, China*
[3]*Shandong Hi-Speed Maintenance Group Co., LTD., Ji'nan, Shandong 250032, China*
[4]*Tai'an Transportation Bureau, Tai'an, Shandong 271000, China*

Correspondence should be addressed to Chao Li; lichao21@sdjzu.edu.cn

Vertical plate anchors are an effective technique to enhance the stability of various structures, such as retaining walls and sheet piles. More research has been devoted to their bearing capacity and macroscopically affecting parameters, while less research can be found on their microscopic bearing behavior. In this paper, the microscopic bearing behavior of vertical plate anchors subjected to a horizontal pullout load in sandy soil was investigated with the particle flow code (PFC) based on the model test results. Results show that the larger-sized anchor plates withstand greater soil pressure and affect a broader range of soil during the pullout process. The soil not behind the anchor plate is pressed, and the pressure in front of the anchor plate increases with increasing size. The soil close to the plate anchor suffers larger pressure while the soil far away from the plate anchor is less affected, and the soil is redistributed to a more stable state during the pullout process of the plate anchor. The particles with a long axis distributed in the horizontal direction are the most stable, while those with a long axis distributed in the vertical direction are the most unstable.

1. Introduction

Plate anchors are widely used in rock and soil anchoring engineering because of their simple installation and low cost. The vertically installed plate anchor, by which the drawing force of the rod or cable is converted into the compressive stress on the surrounding but not behind rock or soil, provides an effective technique to enhance the stability of different structures. Because of its excellent bearing capacity and deformation resistance, the vertical plate anchor is often used in permanent anchoring engineering, such as retaining walls, sheet piles, etc. [1, 2]. Because the bearing capacity design has been a focus [3], the bearing behavior of vertical plate anchors becomes critical for its theoretical basis significance.

At present, many hypotheses and theoretical methods have been used to analyze and study the working mechanism of plate anchors. Cheng et al. [4] established a finite element model to calculate anchor resistance, and determined the method of the overall cyclic loading coefficient U_{cy}^* to determine the cyclic anchor resistance. Ali and Aziz [5] studied the uplift ability of horizontal anchor plates in non-cohesive soil and concluded that the ultimate uplift capacity of anchor plate increases with an increase in the burial depth of the anchor plate. Cheng et al. [6] used the three-dimensional finite element method to simulate the cyclic deformation process of vertically loaded anchors (VLAs) in soft soil, determined the failure displacement of VLAs under shallow and deep-embedded conditions, and revealed the variation rule of cyclic displacement, average displacement, and the cyclic bearing capacity of anchor bolts with the number of cycles. Al Hakeem and Aubeny [7] adopted the large deformation finite element (LDFE) analysis method to determine the bearing capacity and motion characteristics of vertical strip plate anchor in uniform non-cohesive soil. Jesmani et al. [8] used the finite element method to

determine the pulling-out resistance of anchor plates at different positions in different soils and concluded that the pulling-out resistance of plates with deeper burial depths increases with size. Based on discrete element method (DEM), Evans and Zhang [9] concluded that when the burial depth is shallow, no matter if the particle combination is dense or loose, the rupture coefficient linearly increases with an increase in burial depth ratio. In addition, the roughness of the bolt has little influence on the resistance of the plate anchor. El Sawwaf and Nazir [10] concluded that adding row piles in front of a bolt can improve the ultimate bearing capacity of the bolt plate. Pile row, pile length, pile spacing, pile diameter relative to anchorage plate position, and pile inclination affect the anchorage ability. Based on the finite element method, Chen et al. [11] studied the soil failure mechanism of a square plate in the drawing process of non-heavy earth and self-weight earth. They observed three different types of pulling-out failure. Bhattacharya [12] used the 3D finite element method (3D-FEM) to establish a reference solution of the ultimate translational resistance through plastic limit analysis and found that shear resistance decreases with increased plate length and is less affected by plate thickness. Niroumand et al. [13] conducted a parameterization study on symmetric anchor plates. They concluded that, compared with square and circular anchor plates, rectangular anchor plates have a higher pulled-out response, and symmetric rectangular anchor plates have greater lifting resistance in deeper burial depths. Tho et al. [14] used the finite element method to conduct simulation tests and concluded that the pullout force of a plate anchor in soil with a linear increase in strength was lower than that in uniform soil. Tilak and Samadhiya [15], through the ultimate pullout ability test of a multi-plate horizontal bolt, determined that, compared with a single-plate bolt, the pullout ability of a multi-plate bolt in shallow layers decreased and that of a multi-plate bolt in deep layers increased. Choudhary and Dash [16] showed that plate anchor failure displacement and bearing capacity are closely related to soil density and burial depth. Srinivasan et al. [17] studied the interaction of anchor groups and concluded that when the anchor spacing is smaller, the displacement is larger, and the pulling force is smaller. Zhang et al. [18] studied the pullout characteristics of plate anchor in structural soft clay in combination with laboratory tests and finite element analysis. Han et al. [19] used centrifugal tests and LDFE analysis to determine the performance of a plate anchor under continuous loading in normally consolidated clay. They established the continuous uplift deformation mechanism of soil around the anchor under different mono-bearing capacity ratios. Sabermahani and Nasirabadi [20] used particle image velocimetry (PIV) technology to found that the pullout ability and sand deformation of a bolt are greatly affected by the burial depth. Kumar and Rahaman [21] concluded that the vertical pullout resistance of water plate anchors in sand decreased with an increase in the eccentricity and vertical incline angle. Athani et al. [22] adopted the discrete element method to found that both the ratio of a bolt to grain size and the angle of internal friction in sandy soil affect the pull ability. Through model experiments, Yang

et al. [23] concluded that the pullout resistance of a bolt with a plate is affected by the slope foot and margin ratio, and the peak resistance of a bolt decreases with an increase in the slope foot and increases with an increase in the margin ratio. Liu et al. [24] used digital image cross-correlation (DIC) technology to determine that the unearthed density and the embedded depth of anchor significantly impact the pullout performance of a plate anchor and soil deformation. Liu et al. [25] obtained the prediction method of the pullout capacity coefficient of a rectangular bolt with a wide range of parameters by using the finite element method. Yang et al. [26] proposed an analysis method for a plate anchor to evaluate the ultimate embedding depth and bearing capacity.

Although numerous studies have been devoted to the bearing behavior of vertical plate anchors, the present body of work is concentrated on the macroscopic bearing capacity. For the microscopic bearing behavior of vertical plate anchors, such as the state variation of the soil particles, less work can be found. Therefore, it is necessary to conduct further studies on vertical plate anchor's microscopic bearing mechanical evolution. In this paper, by employing particle flow code (PFC), the microscopic bearing behavior of the vertical plate anchor was investigated based on the model test results. The results provide a theoretical basis for plate anchor design and guidance for engineering practice.

2. Model Test of Plate Anchor

2.1. Test Scheme and Design. When plate anchor anchors soil, the surrounding soil's displacement is difficult to observe. There are few studies on microscopic deformation of the surrounding soil. Moreover, monitoring the stress variation of an anchor plate in practical engineering requires an extended period, and the test results are difficult to obtain in real-time. In this paper, digital photographic deformation measurement technology (DPDM) and laboratory visual model tests were used to analyze the soil displacement and deformation around an anchor plate. Microscopic changes in displacement were obtained, and the stress of the anchor plate was experimentally studied. In the laboratory model tests, measurement analysis was carried out by the non-punctuation method.

The test model device is shown in Figure 1. The glass case's length, width, and height were 650 mm × 300 mm × 500 mm. A row of square holes with a spacing of one centimeter was drilled left at the edge of one side of the baffle, the diameter of which was slightly more than one centimeter, allowing a bolt to pass through, as shown in Figure 2.

The rod body of the plate anchor used in the test was square in section, with a side length of 10 mm. The shape of the anchor plate was semicircular. The diameter D of the anchor plate was $D = 3$ cm and $D = 5$ cm. After smooth treatment of the surface of the plate anchor, its friction with sand was able to be ignored. The style of the plate anchor is shown in Figures 3 and 4 show the assembled overall model diagram. In this section, three earth pressure gages were mounted on the anchor plate with thickness of 7 mm, surface diameter of 25 mm and maximum range of 40 kPa).

FIGURE 1: Test model equipment.

FIGURE 2: Detailed test model equipment.

FIGURE 3: Plate anchor style.

FIGURE 4: Assembled model.

FIGURE 5: Soil pressure gauge.
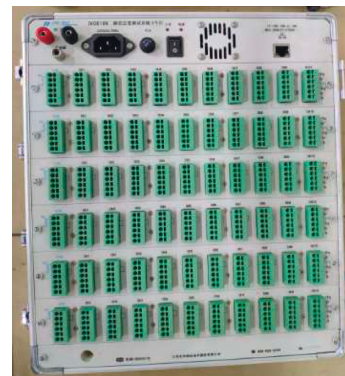
FIGURE 6: Static strain gauge.

And Donghua DH-3816 static strain gauge was used together with earth pressure gauge, which can timely monitor the stress of the soil in front of the anchor plate, as shown in Figures 5 and 6.

The soil samples were mixed with Fujian Pingtan standard sand and Yellow River soil in Shandong Province. The particles with a diameter greater than 0.65 mm accounted for 3%, 0.45–0.65 mm accounted for 40.5%, 0.25–0.45 mm accounted for 51.5%, and the particles with a diameter less than 0.25 mm accounted for 6%. The physical properties of the sand are shown in Table 1.

2.2. Bearing Behavior of Plate Anchor

2.2.1. Load-Displacement Behavior. The displacement variation of a plate anchor can directly reflect the influence of the

TABLE 1: Physical properties of sand.

Particle specific gravity G_s	Maximum dry density $\rho_{d\max}$ (g/cm^3)	Minimum dry density $\rho_{d\min}$ (g/cm^3)	Maximum porosity $e_{\max}$	Minimum porosity $e_{\min}$	The average particle size d_{50} (mm)
2.643	1.74	1.43	0.848	0.519	0.34
Coefficient of nonuniformity C_u	The curvature coefficient C_c	Relative density D_r (%)	Angle of internal friction φ (°)	Void ratio e	Density ρ (kg/m3)
1.542	1.104	23~32	30.2	0.823	1450

anchor plate on the surrounding soil. Therefore, the displacement analysis of a plate anchor under pulling action was carried out to explore the change in the surrounding soil during the pullout process. Figure 7 shows the load-displacement results of the anchor plate with $D = 5$ cm.

The load-displacement curve of the plate anchor loading process can be divided into three stages. When a pulling drawing force is applied to the anchor, the displacement linearly increases in the initial stage. The displacement gradually decreases with pulling tension, from a straight line to a curve, and the curve slope gradually becomes smaller. When the displacement curve is close to the horizontal direction, the displacement suddenly increases. In this stage, the soil suffers shear failure, and the plate anchor is pulled out.

The analysis of the curve variation trend shows that in the initial loading stage, the interaction between soil and the anchor plate is low. The anchor plate easily compresses the soil, and the displacement increases linearly. As the soil is gradually compressed, the effect of embedment and compression between the soil particles are enhanced. The soil can resist a larger force from the anchor plate and limit the anchor plate's displacement. With the continuous increase in tension, the soil has a limited bearing effect, and finally, failure occurs.

To study the influence of anchor plate size on the surrounding soil, two anchor plates ($D = 3$ cm and $D = 5$ cm) with the same rod length were selected for the model test. The obtained soil displacement variation is shown in Figure 8. As can be seen from the figure, an approximately circular area appears near the anchor plate. This area is caused by the compression of the soil by the anchor plate in front. The range of influence of anchoring plate when $D = 5$ cm is more extensive than that of anchor plate when $D = 3$ cm, indicating that the influence of an anchor plate with a larger area is more significant. There is a prominent small circular area along the rod body at the left end. This is because the bearing capacity of the small-diameter anchor plate is poor, leading to a slight swing up and down of the soil.

2.2.2. Stress of the Anchor Plate. The pressure of the anchor plate was tested during the pullout process. A continuous load was applied to ensure a uniform increase in external load as far as possible until the tensile failure of the anchor plate. The stress of the two anchor plates with different diameters of 3 cm and 5 cm are shown in Figure 9.

Because of the stress of the anchor plate, the anchoring plate with a diameter of 5 cm is subjected to a pressure value greater than that of 3 cm. It shows that the anchor plate with
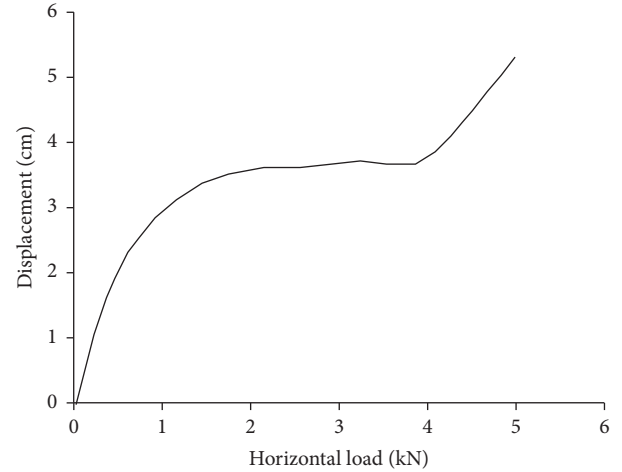
FIGURE 7: Load-displacement curve of a vertical plate anchor.

a larger diameter has a more substantial bearing capacity. Because of the stress variation, the stress reaches a peak value as the loading process continues. The stress variation shows that the surrounding soils have a limited bearing capacity, exceeding the relative motion, and redistribution of the soils occurs. When the loading process continues, the soil is destroyed, and the stress of the anchor plate rapidly decreases.

3. Numerical Simulation of Plate Anchor

3.1. Establishment of Numerical Model. Based on the particle flow theory and the PFC2D program, the physical and mechanical properties of plate anchors subjected to horizontal pullout load were studied using numerical simulations. PFC can simulate the mechanical properties and behaviors of the object from the microscopic perspective. It represents the macroscopic mechanical properties of the object by setting the mechanical and geometric properties of particles and bonds. The basic numerical simulation model boundary was composed of four walls, with a horizontal width of 6 m and a vertical height of 5 m. The soil had an initial porosity of 30% and was simulated using circular particles with a radius ranging from 10 mm to 12 mm that were generated according to gaussian normal distribution within the closed rectangular range walls. Gravity was applied to the generated particles to simulate soil particles. Under the action of gravity, the particles began to cycle down and compress each other, forming the initial stress field. When the particles were in an equilibrium state under circulation, the circulation ended, simulating the original

(a)

(b)
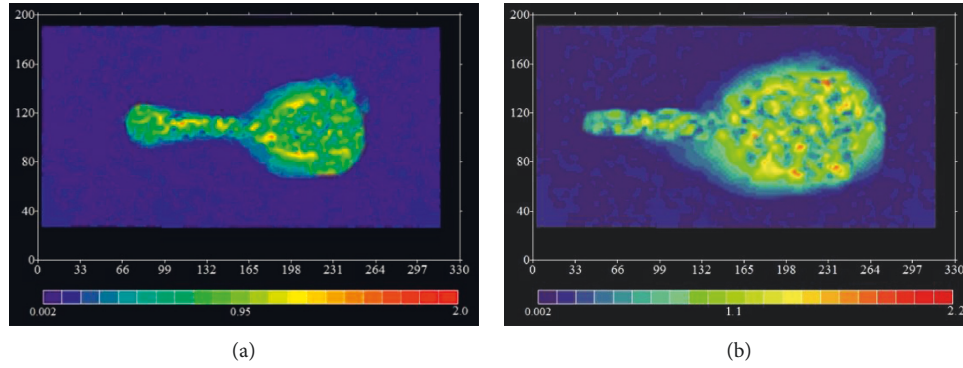
FIGURE 8: Soil displacement of with different anchor plate diameters. (a) $D = 3$ cm. (b) $D = 5$ cm.

FIGURE 9: The stress of the anchor plates with different diameters.

FIGURE 10: Simulation model of plate anchor.

state of the soil. The particles in the height range of 2.16–2.24 m in the y-direction and a width range of 3.96–4.04 m in the x-direction were deleted to form reserved holes for bolts and anchor plates. The anchor plates were set at the reserved holes with bolts with a diameter of 8 cm. The plates had a height of 1 m. Simulation model of plate anchor is shown in Figure 10. Mechanical parameters of the simulation model are shown in Table 2. The number and position of the measuring circles are shown in Figure 11.

3.2. Verification of Numerical Model. In this paper, the maximum horizontal pulling force of the anchor was applied step by step, and the appropriate horizontal load was 160 kN. Similarly, the displacement variation of the plate anchor was observed. The normalized values of the simulation results were compared with the test results, as shown in Figure 12. The figure shows the consistency of the two results. The displacement increases rapidly when the anchor plate is initially subjected to the drawing force. With an increase in the running time step, the displacement stabilizes and does not increase. This is because when the soil is initially loaded, the anchor compresses the soil and reduces the porosity. The

reverse force of the anchorage system caused by the soil particles is small, leading to the apparent displacement of the anchor. With the continuous compaction of the soil particles by the anchor plate, the internal stress of the soil is redistributed, and the resistance of the soil particles to the anchorage system increases. At this time, the resistance is equal to the applied load on the plate anchor, and the soil particles and the anchorage system reach a new equilibrium state.

Figure 13 is the displacement vector diagram of the soil particle under the action of the anchor plate. The anchor plate compresses the soil and "pushes" the soil forward. This part of soil moves along the plate anchor position and away from the plate anchor in the vertical direction perpendicular to the plate anchor. The soil particles above the rear side of the anchor plate have evident falling displacement, pointing to the position of the anchor plate. The anchor plate pushes the soil mass in front and forms a pullout area. The upper soil particles fall to fill the pullout area due to gravity, forming a prominent falling zone. In addition, the displacement of soil particles near the rod body also became apparent, which is due to the contact friction between the soil particles and the plate anchor. The friction force drives the nearby particles to move.

4. Microscopic Bearing Behaviour of Soil Particles

4.1. Stress of Soil Particles. When the vertical plate anchor is subjected to a horizontal load, it dramatically influences the

TABLE 2: Mechanical parameters of the soil particles.

Name	Friction coefficient μ	The normal stiffness K_n (N/m)	Shear stiffness K_s (N/m)	Particle radius (mm)	Normal bond strength (N)	Tangential bond strength (N)
The wall	1	$1e^8$	$1e^8$	—	—	—
Anchor particles	2.0	$1e^{10}$	$1e^{10}$	40	$1e^{30}$	$1e^{30}$
Anchor plate particles	10.0	$1e^{10}$	$1e^{10}$	40	$1e^{30}$	$1e^{30}$
Sand particles	6	$1e^7$	$1e^7$	10–12	$1e^7$	$1e^7$
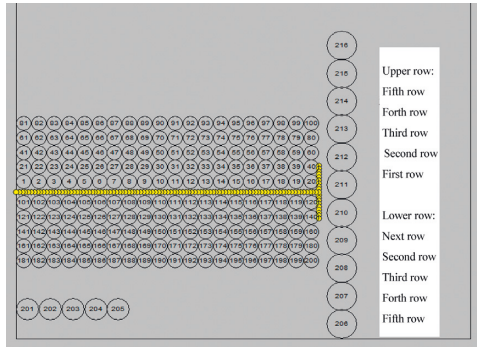
FIGURE 11: Measuring circle arrangement diagram.

FIGURE 12: Displacement-time step curve of the plate anchor.

FIGURE 13: Displacement vector diagram of the soil particles.

FIGURE 14: Contact stress before loading.

FIGURE 15: Contact stress after loading.

surrounding soil. In this paper, the axial stress and shear stress were analyzed, and the research scope was within the range of the four rows of measuring circles above and below the plate anchor (as shown in Figure 11). The average stress values obtained from each row of measuring circles were monitored and extracted for comparative analysis.

Figures 14 and 15 show the change of contact stress between soil particles before and after loading, respectively. Thicker the black lines in the figure indicate more significant contact stress between the particles.

Before loading, the contact stress between particles is mainly distributed under the plate anchor. After loading, the contact stress between soil particles under the anchor plate increases, and significant contact stress also appears above the plate anchor caused by the friction between the plate anchor and soil particles and compaction of the nearby soil. However, the contact stress between soil particles behind the anchor plate decreases significantly, indicating that with the movement of the anchor plate, the front soil is gradually
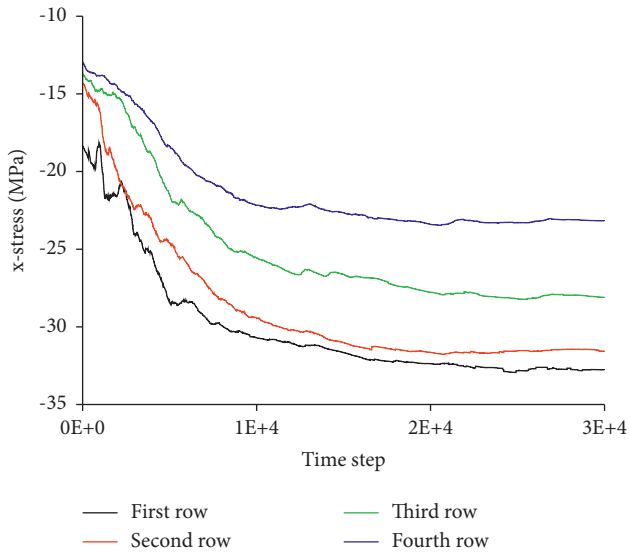
FIGURE 16: Upper average soil stress in the x-direction.
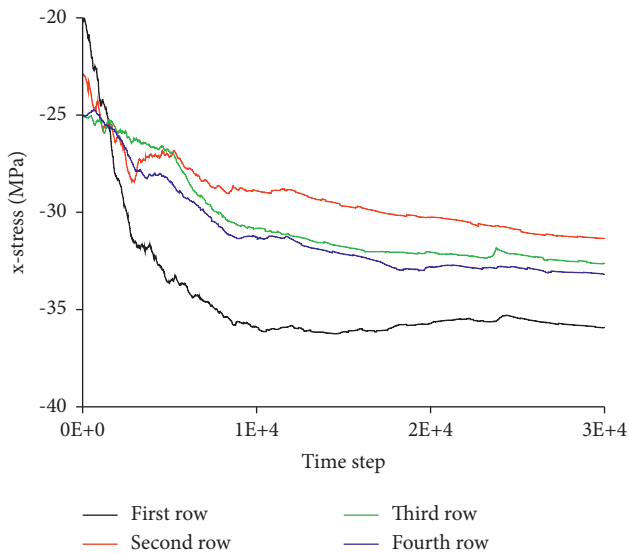
FIGURE 17: Lower average soil stress in the x-direction.

FIGURE 18: Average shear stress of upper soil.
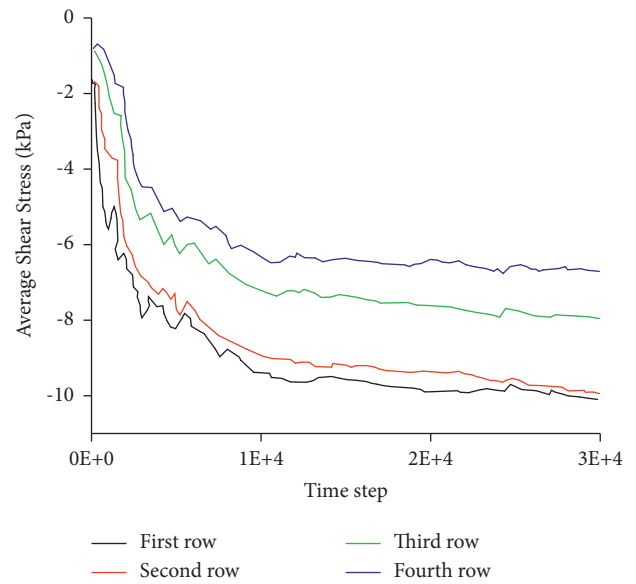
FIGURE 19: Average shear stress of lower soil.

compacted, while a certain gap forms in the rear. The nearby soil particles fill in the gap, and the compactness decreases. The contact between the soil decreases. Overall, in such projects, sufficient compaction should be ensured before prestressing the anchor plate to reduce the displacement caused by the anchor plate, reduce the disturbance to the soil behind the anchor plate, and improve the overall stability.

Figures 16 and 17 show the mean soil stress in the x-direction monitored by the four rows of measuring circles above and below the plate anchor. During the whole loading process, the average x-direction soil stress above and below the anchor is negative, indicating that the soil within this range is under pressure from the anchor. The average absolute value of the stress in the x-direction obtained by the following four rows of measuring circles is generally more significant than that obtained by the above four rows of

measuring circles. Among the above measuring circles, the closer the distance to the plate anchor, the greater the value, indicating that the external load spreads outward along the radial direction of the plate anchor body. Among the average stress obtained by the following four rows of measuring circles, the value measured by the next row of measuring circles near the plate anchor is the largest, indicating that the plate anchor greatly influences this area.

Figures 18 and 19 show the average shear stress of the soil obtained from the four rows of measuring circles above and below the plate anchor, respectively. Overall, the average shear stress is greater near the plate and decreases with distance. With an increase in the time step, the average shear stress increases rapidly, then decreases slightly, and finally
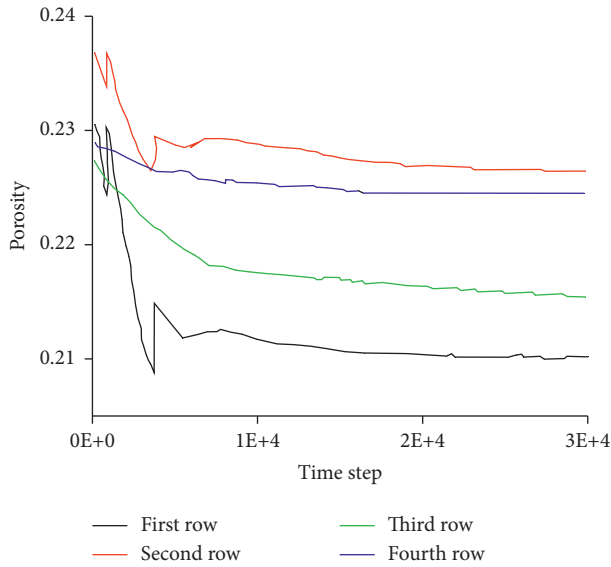
FIGURE 20: The porosity of upper soil particles change with increased load.
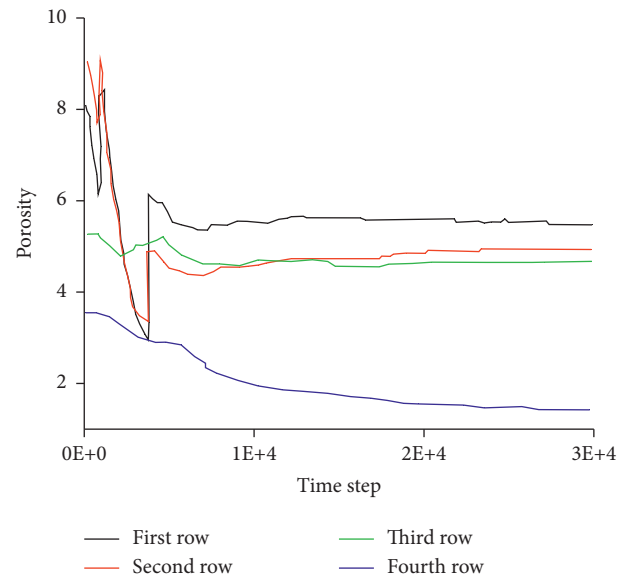
FIGURE 21: The porosity of the lower soil particles change with increased load.

gradually stabilizes. The stress of the upper soil decreases after reaching its maximum value, and the value stabilizes after falling to a certain extent. However, the lower soil stress continuously increases, and the reduction is no longer evident after reaching its maximum value. The results show that the soil particles move and change the internal stress due to the plate anchor's influence when compressed by the plate anchor load. The particles resist the shear force from the plate anchor. Due to the limited space, the shear resistance of the soil under the anchor continues to increase until it reaches equilibrium with the anchor. However, the soil particles above the anchor continue to move after the shear stress reaches its maximum value, decreasing the average shear stress and the phenomenon of decline.

4.2. Microscopic Parameters of Soil Particles.

Soil is a granular material, and the variation of its microscopic parameters affects the properties of the soil. In this section, the bearing characteristics of the plate anchor and the evolution law of the soil particles are studied by analyzing the porosity, coordination number, and rotation of the soil particles.

Figures 20 and 21 show the soil porosity variation obtained from the four rows of measuring circles above and below the plate anchor. When a horizontal load is applied to the plate anchor, the average porosity of the measured circles decreases both above and below the anchor. The law of the four rows of measuring circles above the plate anchor is the same as that in the x-direction stress of the soil above the plate anchor. The variation rule of the average porosity obtained from each row of measured circles below the anchor is from the upper soil section. Furthermore, porosity was the least at the deepest values (fourth row), similar to the x-direction stress at the same position. The above trends show that the porosity variation between soil particles is closely related to the x-direction stress variation, which is

affected by the plate anchor and the depth of the position; the influence of the dead weight stress is indispensable.

The particle coordination number is the degree of contact between soil particles and is a way to reflect the variation of force transmission between particles. It also represents the variation process of particles subjected to a horizontal load. A coordination value of 3 is the minimum index to maintain a stable state between two-dimensional circular particles.

Figures 22 and 23 show the soil particle coordination number variations obtained from the four rows of measuring circles above and below the plate anchor, respectively. The average coordination values obtained from the fourth row vary little, indicating that the force exerted by the horizontal load on the plate anchor is dispersed in the transmission process by the depth of the fourth row. The overall direct influence range is within three rows, here about 1.2 m.

Also, the mean coordination number variation is closely related to the time step. The measured average coordination number curve fluctuated in the first 10,000 steps, decreasing first and then increasing. However, after the 10,000th time step, the variation of the average coordination number decreased, and the degree of fluctuation of the curve decreased and stabilized. The average coordination number in the four rows of the lower part of the anchor was greater than that in the upper part of the anchor. This is because the particles below the anchor are in closer contact due to gravity acting on the particles.

When the plate anchor is loaded, the average coordination number of the first row of measured circles above the plate anchor varied greatly, decreasing rapidly from 3.17 to below 3, indicating that the particles are in a chaotic and unstable state and could no longer resist the external tension load. With an increase in time, the average coordination number gradually increased and finally stabilized, indicating
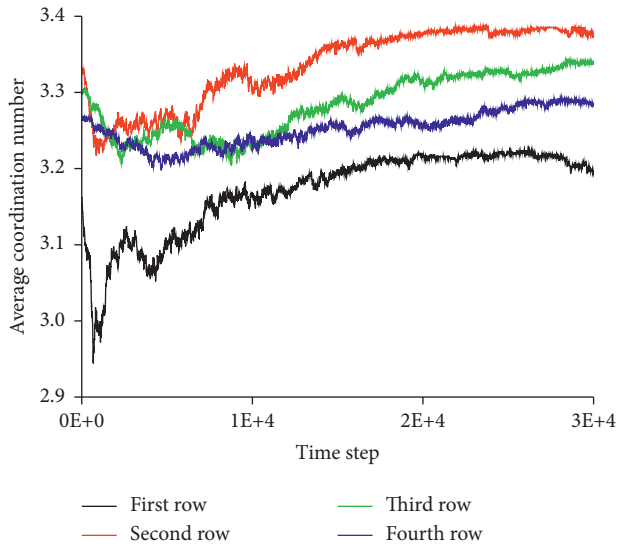
FIGURE 22: Coordination number above the plate.
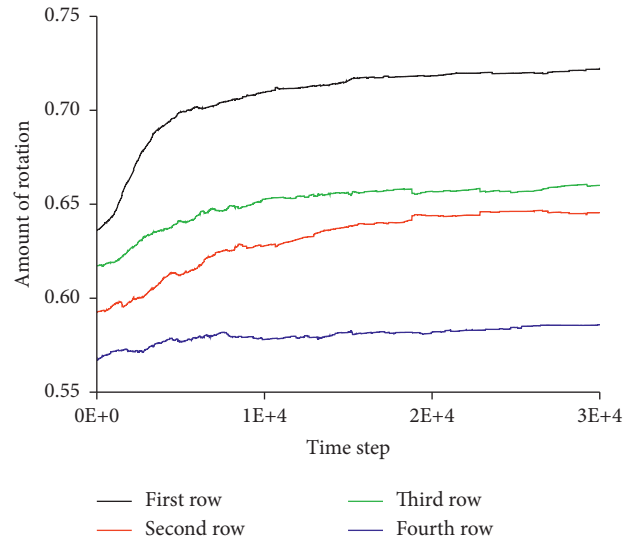
FIGURE 24: Rotation variation of particle above the plate.
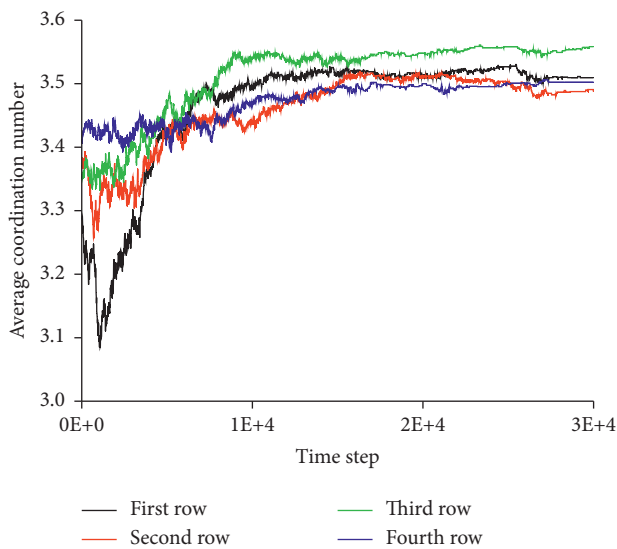
FIGURE 23: Coordination number below the plate.
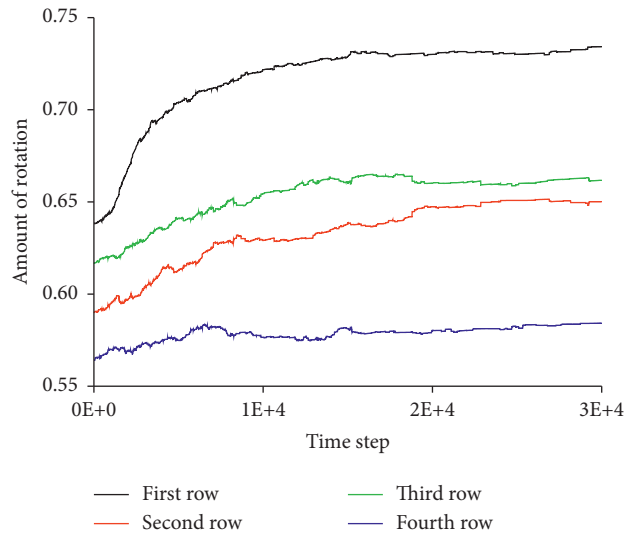
FIGURE 25: Rotation variation of particle below the plate.

that the load on the soil near the plate anchor is redistributed and stabilized once again. The first row below the anchor has the same variation trend as the previous row, but it is overall more stable. The minimum value of the coordination number in the next row is greater than 3, indicating no severe instability among particles within this range. The overall variation value ranges between 3.0 and 3.6, which also verifies the influence of the dead particle weight.

Particle rotation is the particle rotation value over time under an external load. In this model, the change of rotation quantity reflects the shear change between soil particles and the anchor plate. A larger particle rotation indicates a more substantial shear effect of the anchor plate.

Figures 24 and 25 show the rotation variation of the soil particles obtained from the four rows of measuring circles above and below the plate anchor, respectively. With the

increase in the time step, the rotation obtained by each row of measured circles first increases and then stabilizes, indicating that the external load's influence gradually decreases. With a continued external load, particle rotation mainly occurs within the range of the first and second rows of measuring circles, and the rotation angle has a nonlinear relationship with the running time step. In the radial direction along the bolt body, the rotation variation gradually decreases, and the values measured in the first, second, and fourth rows were greater than those in the third and fourth rows, indicating that with an increase in radial distance from the plate body, the influence of the external load gradually decreases. The values measured in the third row of the upper and lower measuring circles are larger than those in the second row, indicating that the soil further from the plate anchor is initially less affected when a load is applied. With the redistribution of the overall force on the model, the force on the soil near the plate anchor gradually transfers
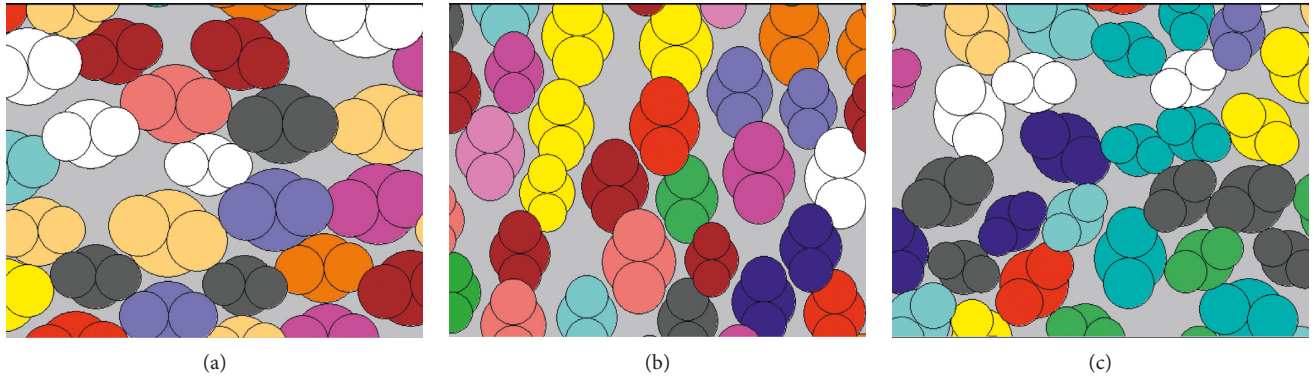
FIGURE 26: Three types of particles with different shapes. (a) H-type particles. (b) V-type particles. (c) R-type particles.

outwards. This results in the variation of the soil force with distance. The variation range of the values in the upper and lower fourth rows of measuring circles is minimal, indicating that the plate anchor load is not transmitted to this depth and is beyond the function range of the plate anchor.

4.3. Orientation Variation of Soil Particles in Different Surface Shapes. Soil particles are not perfectly round but complex non-round clusters. To study the orientation variation of soil particles in different surface shapes, three different combinations of elliptical particles, H-type (particles mainly distributed in the horizontal direction), V-type (particles mainly distributed in the vertical axis direction), and R-type (particles distributed within the range of 0°~360°), were chosen in this paper, as shown in Figure 26. The three types of particles can exhibit distinctive directional characteristics and represent common Earth materials.

Through the numerical simulation of the elliptic particles, the evolution of the orientation of the particles under the influence of horizontal loads was analyzed, including the variation of long-axis orientation and contact normal direction orientation. The development and change in the long-axis orientation of the particles reflect the rearrangement of particles and the evolution of structural anisotropy after loading. These are essential fabric parameters to describe the microstructural changes of the soil during loading. Contact normal direction orientation is the distribution and quantity of particle contact, which directly affects the transmission of the contact force and stability of the structure. The evolution law of meso-fabric anisotropy during soil changes is expressed quantitatively.

The mathematical expression for the long axis orientation is:

$$O(\theta) = \frac{[1 + \alpha_P COS2(\theta - \theta)]}{2\pi}. \tag{1}$$

Type: $O(\theta)$ is the percentage of particles falling in the long axis of the total number of particles. α_P is the directional anisotropy coefficient of the grain along the long axis, and its value mainly reflects the degree of anisotropy. θ_P is the main direction of particle orientation along the long axis.

The mathematical expression of contact normal is:

$$E(\theta) = \frac{[1 + \alpha COS2(\theta - \theta)]}{2\pi}. \tag{2}$$

Type: $E(\theta)$ is the percentage of the number of contact points falling in the contact normal direction of the total number of contact points. α is the contact normal anisotropy coefficient, and its value mainly reflects the strength of the anisotropy degree. θ_α is the main direction of contact normal. The long-axis orientation and contact normal direction orientation between the elliptic particles were obtained through the simulation, and the wind rose diagram was fitted.

Figure 27 shows the directional evolution law of the long axis orientation of the three types of particles before and after loading. Before loading, the H-and V-type particles have obvious initial orientation. The H-type particles of the long axis direction are mainly oriented 0° and 180° (horizontal direction). The V-type particles of the long axis direction are mainly concentrated in the approximate 90° direction (vertical direction), while the R-type particles did not have an obvious orientation compared to the other two particles. The long axis of the V-type particles are mostly horizontal before loading and changed slightly after loading, deflecting and evolving along the direction of 150° clockwise. The proportion of the long-axis falling in the direction of 150° increased, and the rose pattern changed from the original thin shape to a slight bulge in the middle quarter. The H-type particles also exhibit a similar situation, changing from vertical to 60°. R-type particles also rotated but in the opposite direction, moving counterclockwise.

It can be concluded that the plate anchor is displaced under a horizontal load, and the elliptic soil particles also rotate under the influence of the displacement of the anchor plate. The long axis direction of the particles also changed. The changing angle of the long axis is consistent with the axial displacement direction of the plate anchor. The random orientation of the long axis determines if the particle itself stabilizes under the action of gravity. The plate anchor played a minor role, and gravity became the main factor causing the change of its long axis direction.

Contact normal orientation analysis is an extension of the coordination number. The coordination number represents the change in contact number, and contact normal orientation represents the variation of the contact direction.
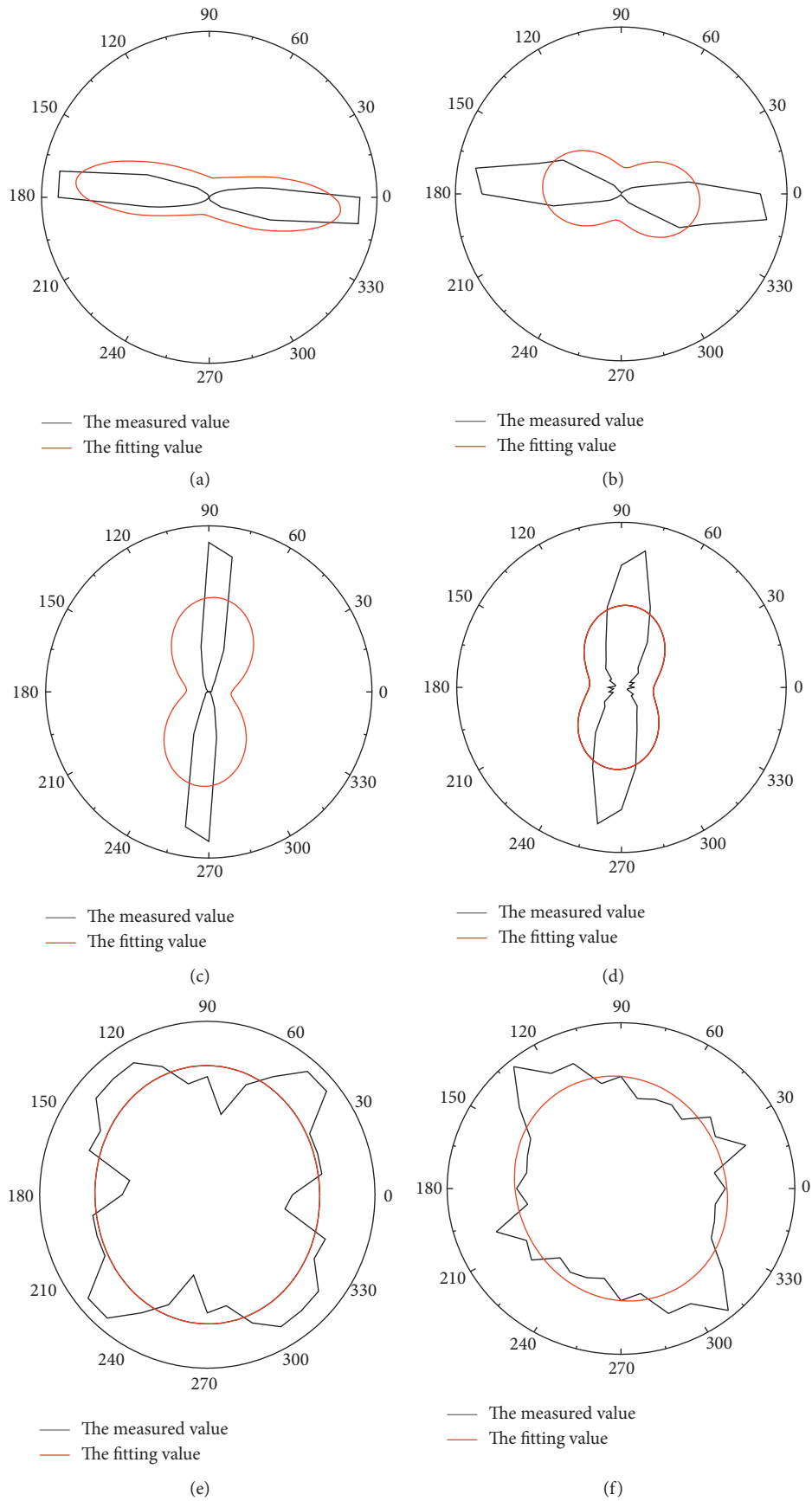
FIGURE 27: Long axis orientation evolution before and after loading. (a) H-type particles before loading. (b) H-type particles after loading. (c) V-type particles before loading. (d) V-type particles after loading. (e) R-type particles before loading. (f) R-type particles after loading.
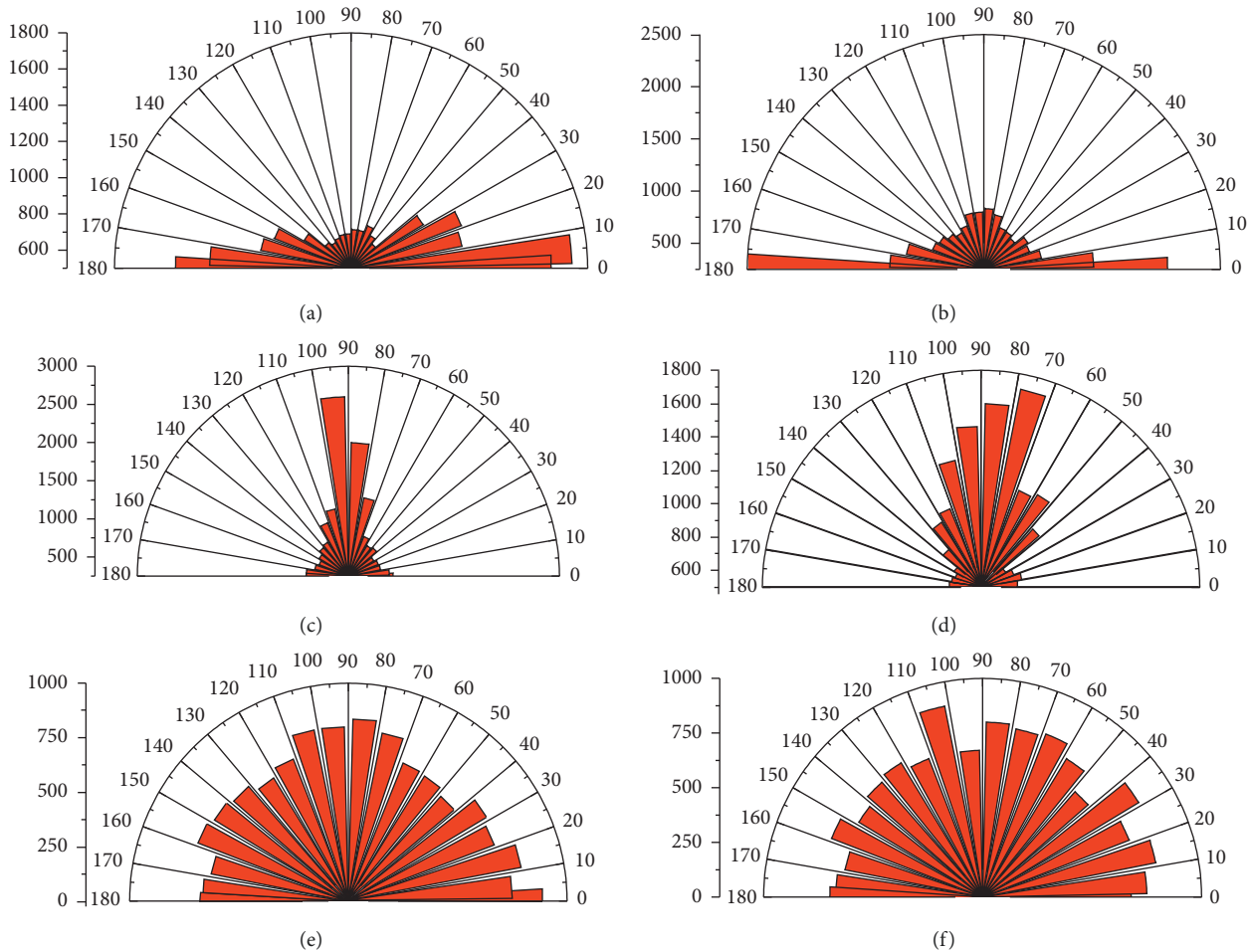
Figure 28: Contact normal orientation evolution before and after loading. (a) H-type particles before loading. (b) H-type particles after loading. (c) V-type particles before loading. (d) V-type particles after loading. (e) R-type particles before loading. (f) R-type particles after loading.

Figure 28 shows the directional evolution of the contact directions of the three types of particles before and after loading. Before loading, H-type particles and V-type particles have an apparent initial orientation in the contact direction, while R-type particles do not. After loading, the number of contacts between H-type particles in the normal direction of the main direction decreases significantly. The original contact direction mainly ranges from 0° to 30°, and after loading, the particle orientation ranges from 80° to 100°. H-type particles gradually shifted from transverse to vertical. The V-type particles deflected from the range of 80° to 100° to 70° to 110° and gradually became inclined. There is no noticeable change in the R-type particles with loading and no optimal direction. It can be concluded that, under the action of a horizontal load, the displacement movement of the plate anchor affects the elliptic particles and causes them to rotate, and decreases the contact normal angle.

5. Conclusions

This paper investigated the bearing behavior of horizontally loaded vertical plate anchors from a macroscope and microscope perspective. The results are as follows:

(1) When the anchor is subjected to a horizontal load, the anchor plate compresses the soil in front of it, moving the soil vertically away from the anchor. The soil behind the anchor plate also is displaced and moves towards the anchor plate.

(2) The soil near the anchor plate is mainly under pressure from the anchor plate. The pressure in front of the anchor plate is significant, regardless of the axial or shear stresses. The plate anchor affects the soil stress state and is related to the dead weight stress caused by the burial depth.

(3) The change trend of porosity reflects the change of axial stress. The soil near the anchor has a greater stress effect, while the soil far away from the anchor has a smaller impact. Particle coordination number reflects the change of contact number between particles. After the bolt is loaded, the soil particles close to the bolt are highly active and in a chaotic and unstable state, unable to resist the external tension load. Particle rotation is an important meso-physical quantity reflecting the shear evolution process of the interface between soil and anchor body. Under external load, particle rotation mainly occurs in the

range of the first and second row of measuring circles, and the rotation Angle has a nonlinear relationship with the running time step under load.

(4) Under the influence of the displacement of the anchor bolt, the elliptic particles move and rotate, and the long axis orientation of the particles also changes, and the angle of change is consistent with the axial displacement direction of the anchor bolt. The displacement motion of bolt affects the contact normal direction of elliptic particles, which makes them rotate. However, not only the deflection angle is changed, but the contact normal angle also decreases. The long axis orientation and contact normal of the three elliptic particle types vary. The particles with a long axis distributed in the horizontal direction are the most stable, while those with a long axis distributed in the vertical direction are the most unstable.

(5) The anchor plate with large size is subjected to larger pressure and has obvious influence on soil displacement. The force of anchor plate increases first and then decreases, and the soil force is redistributed.

Data Availability

The data used to support the findings of this study are included within the article.

Conflicts of Interest

The authors declare that they have no conflicts of interest.

References

[1] R. Ganesh and S. Khuntia, "Estimation of pullout capacity of vertical plate Anchors in cohesionless soil using MARS," *Geotechnical & Geological Engineering*, vol. 36, no. 1, pp. 223–233, 2018.

[2] H. Yue, P. Zhuang, H. Zhang, and X. Song, "Failure and deformation mechanisms of vertical plate Anchors subjected to lateral loading in sand," *International Journal of Geomechanics*, vol. 20, no. 11, Article ID 04020210, 2020.

[3] R. Jadid, A. R. Shahriar, M. R. Rahman, and T. Imtiaz, "Evaluation of theoretical models to predict the pullout capacity of a vertical anchor embedded in cohesionless soil," *Geotechnical & Geological Engineering*, vol. 37, no. 5, pp. 3567–3586, 2019.

[4] X. Cheng, Z. Jiang, P. Wang, Y. Zhao, and Z. Liu, "Bearing capacity of plate anchors subjected to average and cyclic loads in clays," *Ocean Engineering*, vol. 235, Article ID 109343, 2021.

[5] Z. S. Ali and L. J. Aziz, "Investigating the pull-out capacity of a horizontal plate Anchor embedded in sandy soil," *IOP Conference Series: Materials Science and Engineering*, vol. 1094, no. 1, Article ID 012048, 2021.

[6] X. Cheng, Y. Li, P. Wang, Z. Liu, and Y. Zhou, "Model tests and finite element analysis for vertically loaded anchors subjected to cyclic loads in soft clays," *Computers and Geotechnics*, vol. 119, Article ID 103317, 2020.

[7] N. Al Hakeem and C. Aubeny, "Numerical modeling of keying of vertically installed plate anchor in sand," *Ocean Engineering*, vol. 223, Article ID 108674, 2021.

[8] M. Jesmani, M. Kamalzare, and M. Nazari, "Numerical study of behavior of anchor plates in clayey soils," *International Journal of Geomechanics*, vol. 13, no. 5, pp. 502–513, 2013.

[9] T. M. E. N. Zhang and N. Zhang, "Three dimensional simulations of plate Anchor pullout in granular materials," *International Journal of Geomechanics*, vol. 19, no. 4, 10.1061/(asce)gm.1943-5622.0001367, 2019.

[10] M. El Sawwaf and A. Nazir, "The effect of soil reinforcement on pullout resistance of an existing vertical anchor plate in sand," *Computers and Geotechnics*, vol. 33, no. 3, pp. 167–176, 2006.

[11] Z. Chen, K. K. Tho, C. F. Leung, and Y. K. Chow, "Influence of overburden pressure and soil rigidity on uplift behavior of square plate anchor in uniform clay," *Computers and Geotechnics*, vol. 52, pp. 71–81, 2013.

[12] P. Bhattacharya, "Pullout capacity of strip plate anchor in cohesive sloping ground under undrained condition," *Computers and Geotechnics*, vol. 78, pp. 134–143, 2016.

[13] H. Niroumand, K. A. Kassim, and R. Nazir, "The influence of soil reinforcement on the uplift response of symmetrical anchor plate embedded in sand," *Measurement*, vol. 46, no. 8, pp. 2608–2629, 2013.

[14] K. K. Tho, Z. Chen, C. F. Leung, and Y. K. Chow, "Pullout behaviour of plate anchor in clay with linearly increasing strength," *Canadian Geotechnical Journal*, vol. 51, no. 1, pp. 92–102, 2014.

[15] B. V. Tilak and N. K. Samadhiya, "Pullout capacity of multiplate horizontal anchors in sand: an experimental study," *Acta Geotechnica*, vol. 16, no. 9, pp. 2851–2875, 2021.

[16] A. K. Choudhary and S. K. Dash, "Pull-out behaviour of vertical plate anchor in granular soil," *Proceedings of the Institution of Civil Engineers - Geotechnical Engineering*, vol. 171, no. 5, pp. 379–390, 2018.

[17] V. Srinivasan, P. Ghosh, and G. Santhoshkumar, "Experimental and numerical analysis of interacting circular plate Anchors embedded in homogeneous and layered cohesionless soil," *International Journal of Civil Engineering*, vol. 18, no. 2, pp. 231–244, 2020.

[18] N. Zhang, H. N. Wu, J. S. L. Shen, T. Hino, and Z.-Y. Yin, "Evaluation of the uplift behavior of plate anchor in structured marine clay," *Marine Georesources & Geotechnology*, vol. 35, no. 6, pp. 758–768, 2017.

[19] C. Han, D. Wang, C. Gaudin, C. D. O'Loughlin, and M. J. Cassidy, "Behaviour of vertically loaded plate anchors under sustained uplift," *Géotechnique*, vol. 66, no. 8, pp. 681–693, 2016.

[20] M. Sabermahani, "Displacement field around an uplifting innovated plate Anchor," *Acta Geodynamica et Geomaterialia*, vol. 17, no. 1, pp. 119–132, 2020.

[21] J. Kumar and O. Rahaman, "Vertical uplift resistance of horizontal plate anchors for eccentric and inclined loads," *Canadian Geotechnical Journal*, vol. 56, no. 2, pp. 290–299, 2019.

[22] S. Athani, P. Kharel, D. Airey, and P. Rognon, "Grain-size effect on uplift capacity of plate anchors in coarse granular soils," *Géotechnique Letters*, vol. 7, no. 2, pp. 167–173, 2017.

[23] M. Yang, Z. Ai, and B. Deng, "Experimental and analytical study on uplift loading capacity of strip plate Anchors near sand slope," *International Journal of Geomechanics*, vol. 20, no. 1, Article ID 04019136, 2020.

[24] J. Liu, M. Liu, and Z. Zhu, "Sand deformation around an uplift plate Anchor," *Journal of Geotechnical and Geoenvironmental Engineering*, vol. 138, no. 6, pp. 728–737, 2012.

[25] J. Liu, M. Tan, and Y. Hu, "New analytical formulas to estimate the pullout capacity factor for rectangular plate anchors in NC clay," *Applied Ocean Research*, vol. 75, pp. 234–247, 2018.

[26] Q. Yang, B. Cong, Z. Wang, and L. Yu, "An analytical solution for the ultimate embedment depth and potential capacity of vertically loaded anchors with a bridle shank," *Ocean Engineering*, vol. 187, Article ID 106216, 2019.

Research Article

Stability Analysis of Downstream Dam Expansion Tailings Pond

Jiaxu Jin,[1] **Hongyue Zhang** ⬤**,**[1] **Liang Xu,**[2] **Kelin Zhou,**[1] **and Xiangfeng Lv**[3]

[1]*Liaoning Technology University, Fuxin 123000, China*
[2]*Qingdao University of Technology, Qingdao 266000, China*
[3]*School of Civil and Resource Engineering, University of Science and Technology Beijing, Beijing 100083, China*

Correspondence should be addressed to Hongyue Zhang; lgd1232020@163.com

The buildup of tailings in China has expanded dramatically with economic development and industrial demand, and the safety of tailings reservoirs has become increasingly serious. Due to the difficulty in finding a new reservoir site, the expansion approach of building a new tailings dam downstream of the original reservoir area was investigated. The stability of the tailings reservoir after expansion was calculated using the traditional dynamic and static stability solution method and taking into account the unpredictability of dam construction materials and tailings material parameters in the reservoir area. The results reveal that throughout the tailings accumulation process in the new reservoir, the tailings will build a back pressure slope at the original reservoir's initial dam, which can considerably improve the original reservoir's dynamic and static stability. The Monte Carlo method clearly outperforms older methods for tailing pond stability analysis. The results of this paper's calculations will give a theoretical foundation and practical reference for the later management and maintenance of such tailings reservoirs, as well as fresh ideas and insights for comparable projects due to limited site selection.

1. Introduction

A tailings reservoir is a massive geotechnical structure that mining companies use to store tailings throughout the ore extraction and separation process. As the greatest geotechnical structure, the primary function of the tailings dam is to block tailings. There are approximately 24,605 tailings ponds in the world [1], and tailings dam breakdown events may create irrevocable catastrophic consequences [2–8] and long-term environmental pollution [9–12].

The stability of the tailings pond is crucial for preventing accidents. Numerous scientists have researched the seismic stability of tailings ponds [13–16]. Fu-Sheng L I et al. [15] estimated the infiltration line of a tailings dam slope, examined the dam body condition and stability safety factor after heightening and expansion, and demonstrated that the elevation and expansion scheme of a tailings rockfill dam is safe and dependable. Wei et al. [17] analyzed the successful cases of increasing and extending the service life of an existing tailings pond using the upper bend drainage system. Ozcan et al. [18] analyzed a copper-zinc tailings dam

elevated by 7 m in the Black Sea region of Turkey using static and pseudostatic analysis methods. The results indicate that the tailings dam has maintained its static and dynamic stability after being raised by 7 meters. Many scholars have used the Monte Carlo approach to calculate the stability of tailings ponds due to its less problem-limiting nature, high calculation accuracy, simple operation, and high adaptability [19–21]. Li et al. [22] examined the probability and sensitivity of spatial fluctuation of sand layer using the Monte Carlo test principle. It was believed that different sampling procedures created huge fluctuations in the chance of instability and the dependability index but did not appreciably alter the safety factor.

To sum up, there is no relevant literature utilizing the Monte Carlo approach to analyze the stability of the expansion mode of the new tailings dam downstream of the original reservoir area that forms twin reservoirs. This study employs the Monte Carlo approach to solve the dynamic and static stability of the tailings reservoir in the double reservoir area and compares it with the standard stability solution method to determine the "good formula" for the stability

solution of the double reservoir area project. The research results give recommendations for the project's future operation, maintenance, and safety warnings, as well as a theoretical foundation and numerical reference for similar initiatives in the future.

This paper's outline is as follows: in the second section, the engineering situation of the tailings pond, the distribution characteristics of the tailings, the physical parameters of the tailings material, and the calculation model are described. The third section elaborates on the static and dynamic analysis theory and Monte Carlo theory utilized in this study. The fourth section presents the static and dynamic stability calculation findings of tailings based on the traditional approach and Monte Carlo theory. The fifth section of this paper describes the research findings. The sixth section is the conclusion.

2. Enlargement Scheme of Tailings Pond

2.1. Engineering Overview. The working area is located in the western slope of Ailao Mountains in Yuxi City, Yunnan Province, China. The geographical location is shown in Figure 1 [23]. The initial dam of the expanded tailings pond is located at about 640.0 m downstream of the original tailings dam site in Banmao ravine, which is the same as the final accumulation elevation of the built tailings pond design, and finally forms the whole. The proposed initial dam height is 64.0 m, the dam crest width is 5.0 m, the dam bottom width is 255.0 m, the dam crest length is 180.0 m, and the dam type is rockfill dam; the total storage capacity is 1757.3 million m^3, and the effective storage capacity is 1521.9 million m^3, which belongs to the second-class storage. The final accumulation elevation is 1260.0 m, the accumulation slope is 1 : 4.5, and the projected service life is 19.4 years.

2.2. Physical and Mechanical Properties of Each Component Material in Tailings Pond. In this paper, field density measurement, consolidation test, undrained static triaxial shear test, and dynamic triaxial test are carried out. The test materials are mainly composed of tailings dam accumulation material, subdam, tailings silt, and tailings silty clay. The dam is built from the local soil in Yunnan. Tailings silt and silty clay are taken from the tailings site. Tailings dam accumulation material is a kind of mixed material. According to the results of field compaction test at dam site, the rockfill material is tested indoor, and the average value of field dam slope material is graded.

Tailings dam body and dam material have nonlinear characteristics. Its deformation not only changes with the load size, but also is related to the stress path of loading. The stress-strain relationship is obviously nonlinear. In order to better describe the nonlinear characteristics of tailings dam and dam material, the nonlinear model is used to calculate the material characteristics. In nonlinear models, the Duncan-Chang Hyperbolic model is commonly utilized because of its clear concept [24], extensive expertise in parameter determination, and greater consistency with engineering practice. Therefore, in this paper, the Duncan–Chang model is used to calculate the nonlinear stress-strain relationship of dam materials. The parameters of Duncan–Chang model determined by three-axis experiments are arranged as shown in Table 1.

The maximum dynamic shear modulus G_{max} is the main indicator of material dynamic parameters. At present, there are primarily three techniques for computing the dynamic shear modulus: field shear wave test calculation [25], calculation according to the undrained strength value [26], and empirical calculation considering physical properties [27]. In this paper, the empirical method is used to calculate the dynamic shear modulus of tailings dam materials. In the calculation process, the dynamic shear strain is 10^{-6}, and the relationship between the maximum dynamic shear modulus and confining pressure of silty tail soil and silty tail clay is shown in Figure 2.

The dynamic shear modulus ratio and damping ratio are crucial factors for evaluating the seismic safety of an engineering site and analyzing the seismic response of a soil layer. In this paper, the dynamic shear modulus ratio G/G_{max} and damping ratio are used as two indices to measure the dynamic parameters of tailings dam materials. The dynamic shear modulus ratio and damping ratio of initial dam, subdam, tailings silt, and tailings silt clay are calculated. Through the calculation and analysis of the accumulation height of each component in the tailings pond, the confining pressure of the initial dam rockfill is set to 200 kPa and 800 kPa, and the consolidation ratio Kc is 2; the confining pressures of subdam, tailing silt, and silty clay are set to 100 kPa, 150 kPa, and 200 kPa, respectively, and the consolidation ratio Kc is 1. The calculation results are shown in Figure 3.

2.3. Calculation Model of Tailings Pond Expansion. For the first case in China, a new tailings dam is constructed downstream of the old reservoir area, thereby upgrading the existing tailings reservoir from a third-level reservoir to a second-level reservoir. First, this extension is controlled by the local topography and geomorphology; second, the site selection in the area downstream of the original reservoir can focus on mitigating the reservoir's environmental impact. Simultaneously, the development of additional tailings in the area downstream of the original reservoir can utilize the same infrastructure and significantly reduce economic expenses.

Figure 4 is the calculation model of three working conditions; that is, the tailings beach in the new reservoir area accumulates to the initial dam top of the original reservoir area (condition 1), the tailings beach in the new reservoir area accumulates to the central point of the atomic dam in the original reservoir area (condition 2), and the beach in the new reservoir area accumulates to the top of the atomic dam in the original reservoir area (condition 3). Under the three working conditions, the infiltration line height is inferred by field hole measurement.

3. Stability Analysis Theory and Material Parameters of Tailings Pond

3.1. Static Stability Analysis. Finite element and limit equilibrium methods are the most commonly employed for

FIGURE 1: Geographical location and the actual prospect of a tailing pond in Yunnan.

TABLE 1: Duncan–Chang model parameters of each component in tailing pond area.

Name	c (kPa)	φ (°)	K	n	R_f	K_b	m
Initial dam	0.0	28.0	800	0.36	0.72	320	0.25
Subdam	12.1	29.0	150	0.51	0.8	65	0.21
Tailing silt	21.4	24.6	180	0.5	0.81	80	0.21
Tail silt clay	33.6	21.6	160	0.5	0.81	70	0.21

calculating the static stability of tailings ponds [28, 29]. The most extensively utilized technique among these approaches is the Swedish arc technique. Here, the static stability of the tailings pond is studied using the Swedish arc method and the finite element strength reduction method, and the following equation is established:

Swedish arc method is as follows:

$$F = \frac{\sum_{i=1}^{n}\left[c_i b_i \sec\theta_i + (\gamma h_i - \gamma_w h_{iw}) b_i \cos\theta_i \tan\phi_i\right]}{\sum_{i=1}^{n} W_i \sin\theta_i}. \quad (1)$$

Finite element strength reduction method is as follows:

$$\left.\begin{array}{c} \tau_r = \dfrac{\tau_f}{F_s} = \dfrac{\sigma \tan \phi}{F_s} = \sigma \sin \phi_r + c_r \\[2ex] \phi_r = \arctan \dfrac{\tan \phi}{F_s}, c_r = \dfrac{c}{F_s} \end{array}\right\}. \quad (2)$$

In the formula,

W_i is strip gravity, kN; c_i is cohesion, kPa; Φ_i is internal friction angle, °; b_i is the width of soil strip, m; n is the number of blocks; θ_i is the bottom slope angle, °; γ is the weight of soil, kN/m³; h_i is the average height of soil strip, m; γw is the weight of water, kN/m³; h_{iw} is the average height below the soil infiltration line, m; τ_r is the reduced shear strength, kPa; τ_f is shear strength before reduction, kPa; σ is the total stress, kPa; and F_s is the reduction coefficient.

3.2. Dynamic Stability Analysis

3.2.1. Establishment of a Dynamic Model considering Confining Pressure.
In dynamic calculations and analyses, dam body and foundation materials are typically considered viscoelastic. The dynamic shear modulus G and damping ratio D are used to reflect the nonlinearity and hysteresis of the dynamic stress-strain relationship and are expressed as the relationship between dynamic shear modulus, damping ratio, and dynamic shear strain. In this paper, the Hardin–Drnevich model [30] is used to calculate the dynamic shear modulus and damping ratio, as follows:

Dynamic shear modulus is as follows:

$$G = \frac{G_{\max}}{1 + \gamma/\gamma_r}. \quad (3)$$

Damping ratio is as follows:

$$D = D_{\max}\frac{D/D_r}{1 + D/D_r}. \quad (4)$$

Maximum shear modulus is as follows:

$$G_{\max} = K_2 Pa \left(\frac{\sigma'_m}{Pa}\right)^n. \quad (5)$$

In the formula, γ_r is the parameter shear strain, $\gamma_r = \tau_{\max}/G_{\max}$; γ is the total shear strain; K_2, n are test parameters; Pa is atmospheric pressure, MPa; and σ'_m is the average effective stress, kPa.

3.2.2. Dynamic Control Equation and Solution.
Wilson method is used to solve the dynamic control equation [31]. In the calculation process, it is assumed that the dynamic shear modulus G and damping ratio D of each unit in each period remain unchanged, and the time step is set as
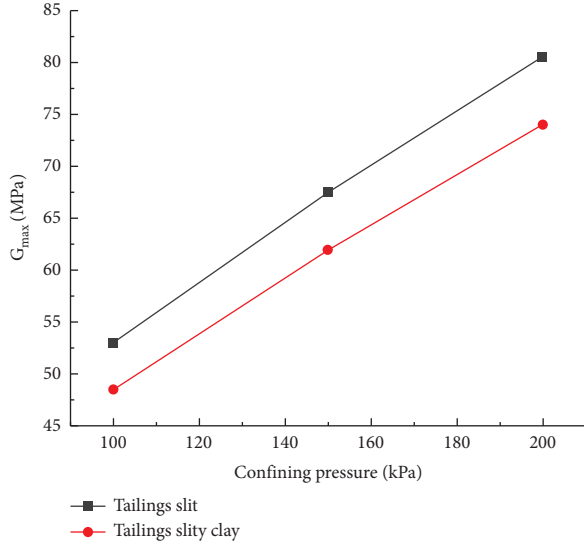
FIGURE 2: Relationship between maximum dynamic shear modulus and confining pressure.

$\Delta t = 0.01 \sim 0.02$ s. The 0.65 times of the maximum shear strain $\gamma_{\max}$ in this period is taken as the average shear strain $\overline{\gamma}$ of the unit in this period.

The dynamic control equation is

$$[M]\{\ddot{\delta}(t)\} + [C]\{\dot{\delta}(t)\} + [K]\{\delta(t)\} = \{F(t)\}. \qquad (6)$$

In the formula, $\delta(t)$, $\dot{\delta}(t)$, and $\ddot{\delta}(t)$ are node displacement, velocity, and acceleration; $F(t)$ is the dynamic load of the node, determined by the seismic acceleration; $[M]$ is the unit mass matrix; $[K]$ is the element stiffness matrix; and $[C]$ is the element damping matrix.

3.2.3. Earthquake Permanent Deformation.

The Newmark approach [32, 33], simplified analysis method [34], equivalent inertia force method [35], and probability analysis method [36, 37] are the most common seismic permanent deformation calculation methods. When Newmark method is used to calculate the permanent deformation of soil, the following fundamental assumptions are made: (1) the effect of earthquake on dam body can be equivalent to a quasistatic inertia force with a defined magnitude and direction; obvious potential sliding surface will be formed when dams are damaged in earthquakes. (2) When the seismic action exceeds its ultimate seismic capacity, rigid-plastic sliding occurs along the potential sliding surface; the strength of the sliding surface will not degrade significantly during the earthquake. (3) The quasistatic horizontal seismic acceleration applied when the potential landslide is in the critical limit equilibrium state or the antisliding safety factor is 1 is called the yield seismic acceleration $a_y = k_y g$ of the dam body, where the ratio of the yield seismic acceleration to the gravity acceleration is called the yield acceleration coefficient k_y. (4) When the total sliding force generated by the potential landslide under the action of seismic inertia force exceeds the total antisliding force on the sliding body, the potential landslide

will slide instantaneously along the potential sliding surface. The sliding deformation generated by this instantaneous overload will stop when the acceleration is reversed, and the velocity of the landslide reduces to zero. The seismic slip is the accumulation of the sliding displacement caused by all instantaneous overload pulses during the earthquake duration.

3.3. Monte Carlo Method.

The Monte Carlo approach is fundamentally a probability analysis technique. In the Monte Carlo sampling experiment, the material parameters are taken from the interval based on the assumption that the physical parameters of the material follow a particular probability distribution. The precision of the Monte Carlo sampling experiment is dependent on the sample size of the material characteristics and the number of extractions. When all requirements are qualified, the precision of the Monte Carlo sampling experiment can be ensured. In this article, 10,000 extractions are performed in order to calculate the stability of the new and original tailings using the Monte Carlo approach.

When the Monte Carlo method is used to analyze the stability of the tailings pond, the mean and standard deviation of the physical properties and mechanical parameters of the tailings material in Table 2 are input into the GeoStudio software. According to the normal distribution of the output parameters, the random values are substituted for n times in the solution equation of the dynamic and static stability. The n safety factors are Z_1, Z_2, Z_3, ..., Z_n; if there are m safety factors greater than 1, the probability of dam failure can be expressed as follows:

$$p_f = \frac{m}{n}. \qquad (7)$$

At this time, the mean μ_z and standard deviation σ_z of the safety factor of the tailings dam are

$$\begin{cases} \mu_z = \dfrac{1}{n} \sum_{i=1}^{n} Z_i, \\[4mm] \sigma_z = \sqrt{\dfrac{1}{n-1} \sum_{i=1}^{n} \left(Z_i - \mu_z \right)^2}. \end{cases} \qquad (8)$$

3.4. Seismic Acceleration Time-History Curve.

According to the engineering geological survey study, the Simao area has experienced tectonic earthquakes in the past. According to records, Honghe, Ailaoshan, Jiujia-Anding, three NW-trending faults, have rarely seen earthquakes, which were mainly concentrated in the NW-trending secondary fault zone on the west side of the Amojiang fault zone, constituting Pu'er-Simao seismic tectonic belt. The earthquakes mainly occurred in the south of latitude 23°40′. The seismic activities that occurred from 1983 to 1984 also concentrated in the area from Pu'er to Simao. The epicenter extended northward to the vicinity of Mohei. There were 9 strong earthquakes with magnitude $M \geq 6$, 4 moderate

(a)

(b)

(c)

(d)
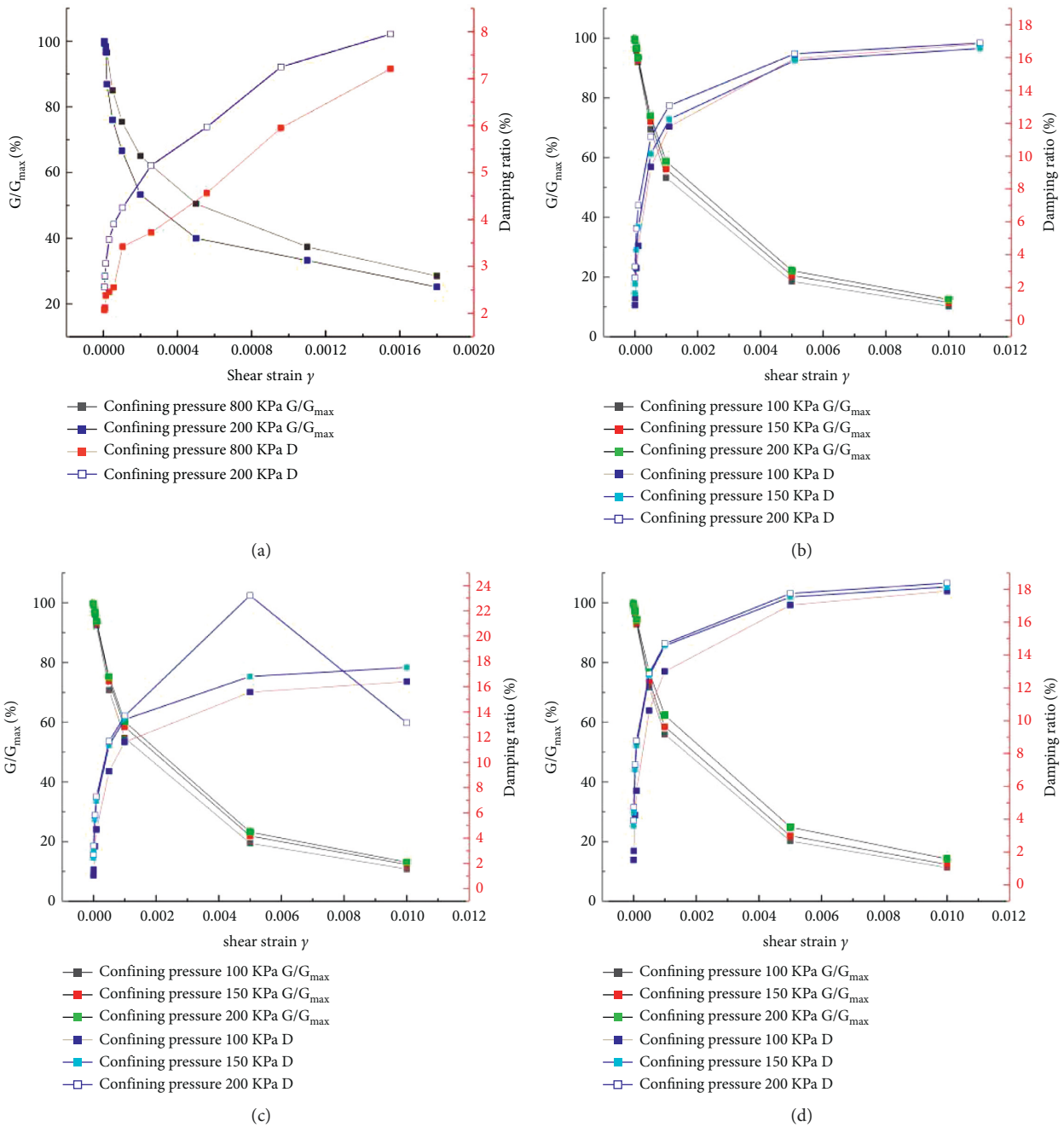
Figure 3: Dynamic parameters of each component in the tailing pond. (a) Dynamic parameters of initial dam. (b) Dynamic parameters of subdam. (c) Dynamic parameters of tailing silt. (d) Dynamic parameters of tailing silt clay.
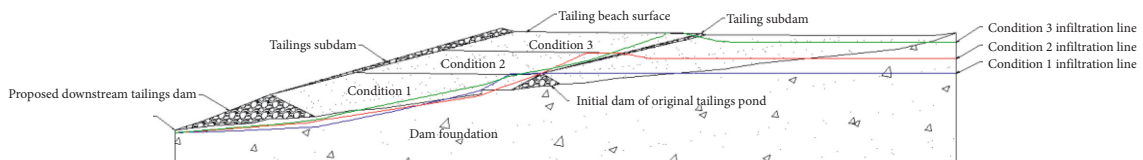
Figure 4: Calculation models of three working conditions.

earthquakes with magnitude $6 > M \geq 5$, and 12 earthquakes with magnitude $5 > M \geq 4$. All of them were weak earthquakes with magnitude below 4. The epicenters of the above strong and weak earthquakes are distant from the

engineering region and have minimal impact on its construction.

According to the feasibility study report of tailings pond expansion, the peak ground motion acceleration of the site is

TABLE 2: Physical property and force index table of tailing pond.

Material name	Volumetric weight				Effective stress shear index							
	Natural unit weight γ (kN/m^3)		Floating bulk density γ' (kN/m^3)		C (kPa)				φ (°)			
					Mean value		Standard deviation		Mean value		Standard deviation	
	Mean value	Standard deviation	Mean value	Standard deviation	Water	Underwater	Water	Under water	Water	Under water	Water	Under water
Starter dam	18.0	0.2	10.0	0.2	0.0	0.0	—	—	28.0	27.0	3.4	3.4
Tailings silt	16.9	0.5	9.2	0.6	21.4	15.7	4.4	4.5	24.6	22.1	3.4	3.7
Tailings silty clay	14.6	0.2	7.9	0.2	33.6	25.3	3.6	3.8	21.6	17.6	2.6	3.1
Tailings subdam	20.5	0.2	12.3	0.2	12.1	5.6	1.8	1.9	29.0	26.0	2.0	2.2
Dam foundation	24.0	—	24.0	—	30.0	30.0	—	—	38.0	38.0	—	—

0.10 g, the seismic fortification intensity is VII, and the characteristic period of the ground motion response spectrum is 0.45 s. In this calculation, two seismic waves are used, the time-history curves of El Centro waveform and Taft waveform are taken, and the maximum amplitude is reduced to 0.1 g and 0.15 g, as shown in Figure 5. In the dynamic calculation of tailings pond, the horizontal acceleration time history curve is input.

4. Calculation Results and Analysis

4.1. Static Stability. In order to analyze the stability of the tailings pond after adopting the new expansion method, three working conditions models of the tailings reservoir that the beach surface of the new reservoir area accumulates to different positions of the original reservoir area are designed. Since the new and the original two reservoir areas merge under #3 working condition, there is no stability calculation result of the original reservoir area under #3. Critical sliding surface for slope stability calculation by limit equilibrium method is selected based on experience; that is, failure surface is generated from the outer slope angle or outer slope surface of the initial dam and is penetrated at the top of the subdam.

Figure 6 is the calculation results of the new and original reservoir areas based on the traditional method (the left is the Swedish arc method, and the right is the finite element strength reduction method) under three working conditions. The figure demonstrates that the safety factors of the new and original reservoir areas solved by the new tailings reservoir expansion method of double reservoir areas are far more than the standard design value, and the minimum value is the result of the original reservoir area under the Swedish arc method #1 condition. According to the calculation results of the finite element strength reduction method, it can be seen that there are two shear stress concentration areas in the original reservoir area under #1 working condition, and the infiltration line can be obtained by comprehensive engineering speculation. The stress concentration area is near the intersection point of the infiltration line and the tail silt clay area of the original reservoir area. This is due to the saturation state of the tailings below the infiltration line, which leads to

the decrease of the effective stress and then affects the stress distribution in the nearby area. Therefore, the static stability of the original reservoir area should be paid attention to in the construction project of the new reservoir area of the tailings reservoir in the double reservoir area. With the gradual increase of the beach surface in the new reservoir area, the stress concentration point in the original reservoir area disappears. This is because the gradual increase of the beach surface in the new reservoir area causes the back pressure slope protection at the initial dam and the subdam of the original reservoir area, thereby improving the stability of the original reservoir area. The two traditional methods calculate that the safety factor of the original reservoir area increases with the increase of the beach surface in the new reservoir area, which also proves this point. Consequently, compared to the way of extending the expansion at the original dam, the novel expansion method of the double reservoir area significantly enhances the storage capacity and is beneficial to enhancing the stability of the tailings reservoir. In the process of the gradual rise of the beach surface in the new reservoir area and the formation of the whole reservoir area, the intensive shear stress gradient of the reservoir area is gradually transferred from the original reservoir area to the new reservoir area and finally uniformly distributed at the dam foundation of the new reservoir area. Therefore, in the practical engineering of the double reservoir area, when the reservoir area meets operational condition #2, the monitoring center of the stability of the reservoir area should be transferred from the original reservoir area to the new reservoir area.

Figure 7 is the Monte Carlo calculation results of the new reservoir area under #1 condition (MC-Swedish arc method on the left side and MC-strength reduction method on the right side). The calculation results of the new and original reservoir areas under other conditions are similar to those in Figure 7, so they are not listed. The findings of the MC-Swedish arc method and the MC-strength reduction approach are comparable to the normal distribution, whereas the standard calculation method yields a fixed value. This is because the traditional calculation method is to find the critical sliding surface in the calculation area and solve the stability, ignoring the discreteness and randomness of the soil, while the Monte Carlo method is to solve all the sliding
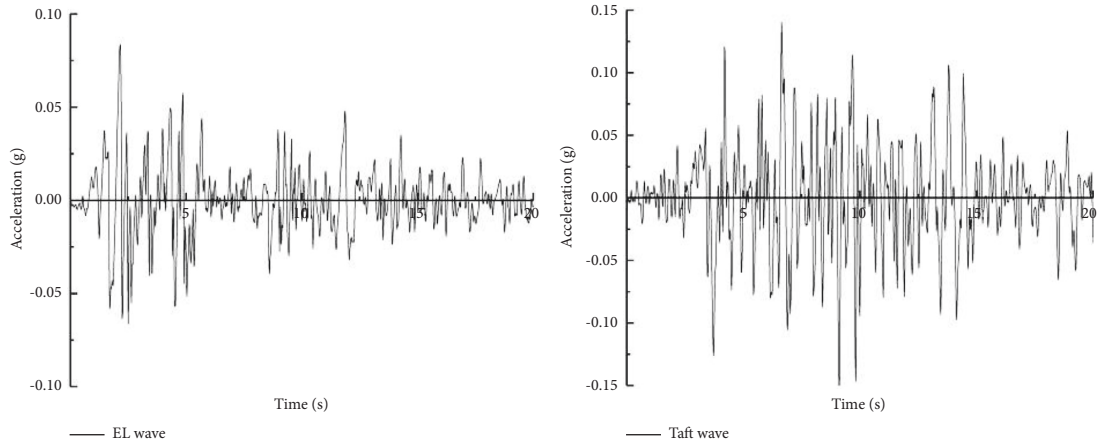
FIGURE 5: El Centro and Taft seismic acceleration time-history curves.
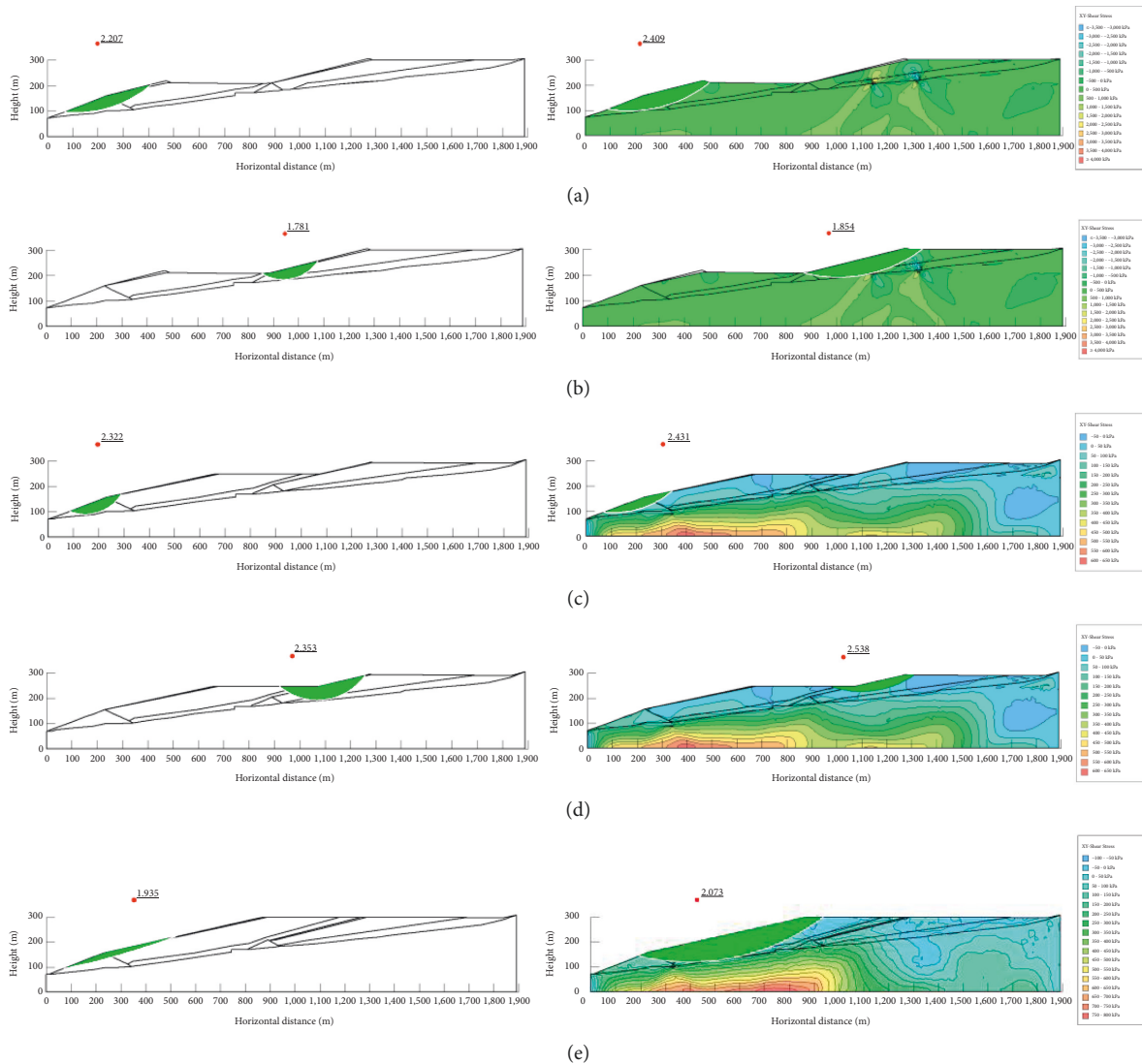
FIGURE 6: Calculation results of traditional methods under three working conditions. (a) Condition 1: new reservoir area. (b) Condition 1: original reservoir area. (c) Condition 2: new reservoir area. (d) Condition 2: original reservoir area. (e) Condition 3: new reservoir area.
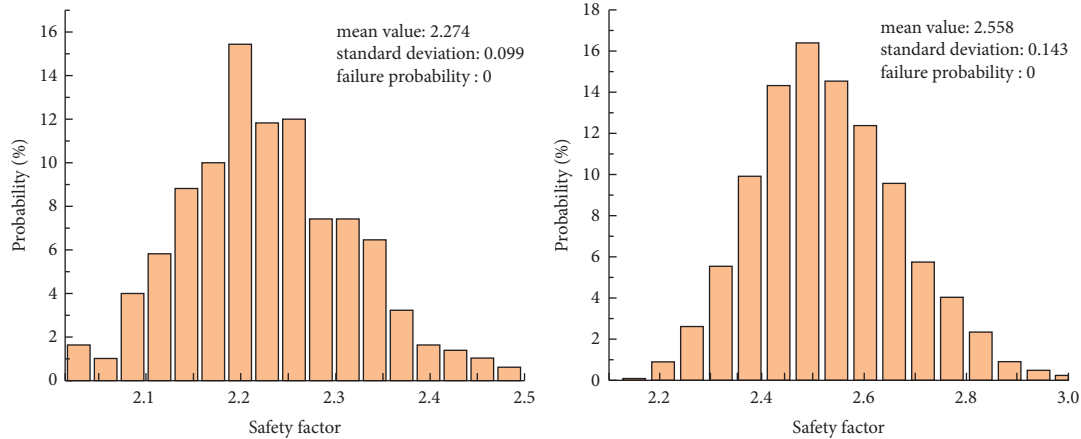
FIGURE 7: #1 condition calculation figure of Monte Carlo method for new reservoir area.

surfaces in the calculation area. Therefore, the Monte Carlo method's computation findings have greater practical relevance. When the minimum safety factor in the calculation area is obtained, the composition and distribution of the safety factor in the area can be mastered. Under three working conditions, Monte Carlo method provides comparable average value and safety factor as traditional calculation methods. However, in the original reservoir area, the safety factor calculated by Monte Carlo method increases abruptly, which is much larger than that of the traditional calculation method. This paper analyses that the safety factor calculated by Monte Carlo method is a closed interval, and the average value is calculated. The safety factor calculated by the Sweden arc method and finite element method is the minimum value of the critical sliding surface. With the progressive increase of the tailings beach in the new reservoir area, the back pressure slope is formed on the outer slope of the dam at the initial stage of the original reservoir area. Therefore, the safety factor of the other three conditions suddenly increases; MC-Swedish arc method and MC-strength reduction method calculate that the failure probabilities of the new and original reservoir areas under three working conditions are 0, which shows that the new and original reservoir areas under this condition have good static stability.

Table 3 shows the calculation results of the traditional method, MC-Swedish arc method, and MC-strength reduction method in the new and original reservoir areas under three working conditions. It can be seen from the table that several methods in the new reservoir area under three working conditions have good consistency, and the calculation error is minor. However, in the original reservoir area, the calculation results of Monte Carlo method are sharply increased and should be compared with other methods in practical engineering. The Monte Carlo method is combined with the Swedish arc method and the finite element strength reduction method to solve the static stability of the new original tailings pond after expansion. This calculation method compensates for the randomness and spatial variability of the tailings and dam material parameters that are overlooked in the traditional calculation method to solve the static stability of the tailings pond and replaces the fixed value

with the normal distribution of the calculated material parameters to analyze and evaluate the slope stability. Therefore, under the same design calculation model, the calculation results of this method are obviously more realistic.

4.2. Dynamic Stability. In order to systematically study the dynamic characteristics of a tailings reservoir in Yunnan, El Centro wave and Taft wave are selected to carry out the dynamic calculation of the height of the accumulation dam in three new reservoirs under six calculation conditions (confining pressure 800 kPa). Table 4 outlines the precise computation conditions.

4.2.1. Dynamic Displacement Response. The extreme value of dynamic displacement (i.e., the maximum absolute value of dynamic displacement in the whole earthquake duration) is a decisive index for evaluating the dynamic stability of tailings pond. The horizontal displacement, vertical displacement, and total displacement of condition A are introduced as examples, as shown in Figure 8.

The same method is used to simulate other working conditions, and the horizontal displacement, vertical displacement, and total displacement of the six working conditions are counted in Table 5.

From the dynamic displacement nephogram, it can be seen that under the action of seismic waves, the horizontal displacement to the contact between tailings beach and subdam is larger, especially in the original reservoir area; the vertical displacement of the reservoir area is small, and the total displacement is highly consistent with the horizontal displacement. This is because the input acceleration time history curve is horizontal in the dynamic calculation of the tailings pond.

Table 5 demonstrates that the new and old tailings reservoirs have distinct degrees of displacement when subjected to the action of two types of seismic waves. The minimum value of total displacement under the action of El Centro wave is 2.40 cm when the beach surface of the new reservoir area accumulates to the top of the initial dam in the original reservoir area, and the maximum value is 4.87 cm

TABLE 3: Safety factor values of different solving methods under three working conditions.

Condition	New/original reservoir area	Factor of safety				Failure probability (%)
		Limit equilibrium method	Finite element method	Combination of Monte Carlo method		
		Swedish circle method	SRM	Swedish circle method	SRM	
#1	New	2.207	2.409	2.274	2.558	0
	Original	1.781	1.864	4.597	4.743	0
#2	New	2.322	2.431	2.354	2.500	0
	Original	2.353	2.538	5.220	6.067	0
#3	New	1.936	2.073	2.074	2.147	0

TABLE 4: Six working conditions and corresponding waveforms.

Condition	Waveform	Cross-sectional view
A		Figure 4 condition 1
B	El Centro	Figure 4 condition 2
C		Figure 4 condition 3
a		Figure 4 condition 1
b	Taft	Figure 4 condition 2
c		Figure 4 condition 3

(a)

(b)

(c)
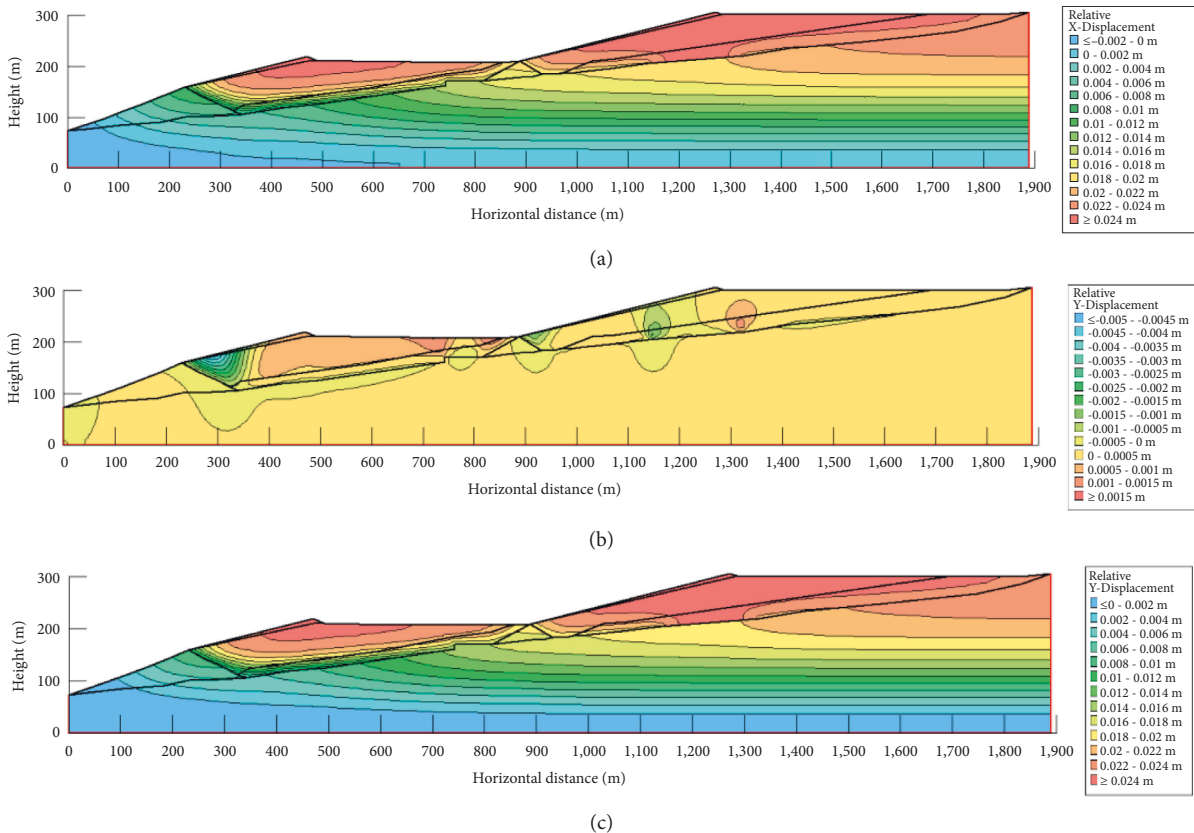
FIGURE 8: Dynamic displacement cloud of working condition A. (a) Horizontal dynamic displacement cloud of working condition A. (b) Vertical dynamic displacement cloud of working condition A. (c) Total dynamic displacement cloud of working condition A.

when the beach surface of the new reservoir area accumulates to the top of the subdam. When the total displacement of the reservoir is compared at different points of the tailings pond, it is discovered that the total displacement

of the reservoir gradually increases with the increase of the tailings beach under the action of the El Centro wave. The minimum value of total displacement under Taft wave action is 2.02 cm when the new reservoir beach accumulates to the

TABLE 5: Extreme values of dynamic displacement of tailing pond under various working conditions.

Condition	Horizontal displacement (cm)	Vertical displacement (cm)	Total displacement (cm)	Waveform
A	2.40	0.15	2.40	El Centro
B	3.78	0.12	3.78	El Centro
C	4.87	0.12	4.87	El Centro
a	2.17	0.14	2.17	Taft
b	2.02	0.09	2.02	Taft
c	2.09	0.09	2.09	Taft

(a)

(b)
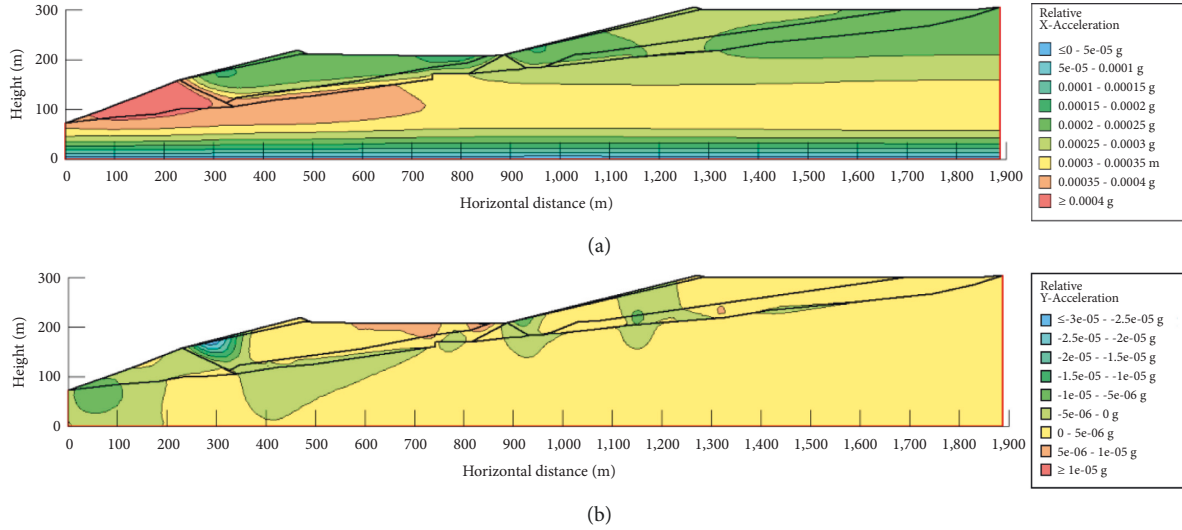
FIGURE 9: Acceleration cloud for working condition A. (a) Horizontal acceleration cloud of working condition A. (b) Vertical acceleration cloud of working condition A.

midpoint of the original reservoir dam height, and the maximum value is 2.17 cm when the new reservoir beach accumulates to the original reservoir's initial dam crest. When the variation law of the total displacement of the reservoir under the action of the two waveforms is compared, it is clear that the reservoir changes under the action of the El Centro wave. The El Centro waveform is closer to the eigenvalue period of the expansion tailings reservoir, yet its safety performance remains within the controllable range.

4.2.2. Acceleration Response. The acceleration extremum and amplification factor of the dam under six working conditions are calculated. The acceleration extremum and amplification factor of condition A are introduced as examples, as shown in Figure 9.

The same method is used to simulate other working conditions. The horizontal acceleration and vertical acceleration under six working conditions are counted, and the corresponding magnification is calculated in Table 6.

The comprehensive analysis of horizontal acceleration and vertical acceleration extremum nephogram and magnification summary table shows that different waveforms have different effects on new and original tailings reservoirs, especially to prevent seismic waves similar to El Centro waveform, which has a greater impact; under the action of earthquake, the overall distribution of acceleration nephogram of tailings reservoir under different working

conditions is reasonable, and the extreme value is mainly located at the initial dam of the new reservoir area, but due to the small value, its influence can be ignored; with the increase of the stacking height of the tailings beach in the new reservoir area, the seismic characteristic values of the new and original tailings reservoirs also change, resulting in different effects of the same waveform on different heights. Therefore, it is recommended that in the construction process of the new and original tailings, special attention should be paid to the seismic detection and early warning. With the increase of tailings beach in the new reservoir area, the extreme value of horizontal acceleration gradually increases, which is consistent with the conclusion in [38].

4.2.3. Seismic Stability. The Newmark method introduced above is used to calculate the seismic stability under three working conditions, and the variation law of the minimum safety factor and the sliding surface where the minimum safety factor is located in the seismic process of the reservoir area is obtained so as to comprehensively understand the seismic stability of the double reservoir area in the construction process.

Figure 10 shows the minimum safety factor and critical slip surface ((a), (c), (e), (g), and (i) show El Centro wave in the earthquake of the new and original tailings pond under six working conditions; (b), (d), (f), (h), and (j) show Taft wave). It can be seen from the figure that the safety factors

TABLE 6: Extreme values and amplification factors of acceleration under six working conditions (unit: m/s^2).

Condition	Horizontal direction		Vertical direction		Waveform
	Acceleration	Magnification	Acceleration	Magnification	
A	0.00673	0.00673	0.00025	0.00025	El Centro
B	0.00689	0.00689	0.00025	0.00025	El Centro
C	0.00706	0.00706	0.00015	0.00015	El Centro
a	0.00322	0.00322	0.00046	0.00046	Taft
b	0.00373	0.00373	0.00035	0.00035	Taft
c	0.00376	0.00376	0.00047	0.00047	Taft
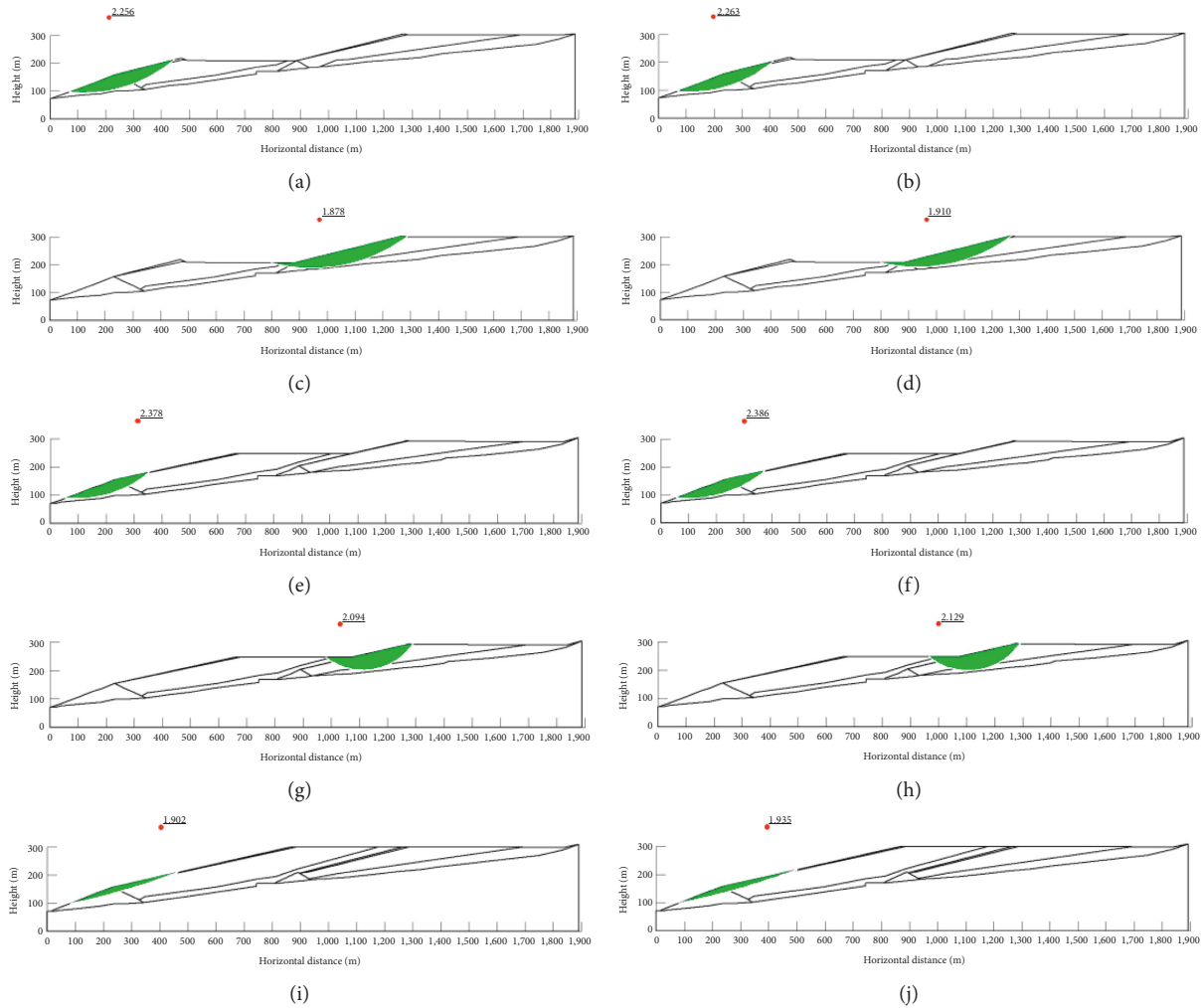
FIGURE 10: Minimum epicentral stability coefficient and the critical sliding surface of new and original tailings reservoirs under three working conditions. (a) A: new reservoir area, (b) a: new reservoir area, (c) A: original reservoir area, (d) a: original reservoir area, (e) B: new reservoir area, (f) b: new reservoir area, (g) B: original reservoir area, (h) b: original reservoir area, (i) C: new reservoir area, and (j) c: new reservoir area.

calculated by El Centro and Taft waves are similar; under the action of seismic waves, the safety factor of the original reservoir area of working conditions A and a will drop sharply, so the stability of the original reservoir area of working condition should be paid more attention in practical engineering. With the increase of the new reservoir beach, the back pressure slope will be formed in the original reservoir area, so the stability of the whole tailings reservoir can be restored to a higher level. Under the action of El Centro wave and Taft wave, the critical sliding surfaces under six working conditions have good consistency; the safety factor of El Centro wave is less than that of Taft wave, which further shows that the El Centro waveform is closer to the eigenvalue period of the expanded tailings pond.

Table 7 lists the calculation results of dynamic stability of new and original tailings reservoirs under different working

TABLE 7: Calculation results and failure probability of Monte Carlo method and Newmark method.

	Condition	Newmark	Monte Carlo method	Failure probability
A	New	2.256	2.3746	0
	Original	1.878	4.5515	0
B	New	2.378	2.5135	0
	Original	2.094	5.1876	0
C	New	1.902	2.078	0
a	New	2.263	2.3746	0
	Original	1.910	3.8172	0
b	New	2.386	2.5135	0
	Original	2.129	5.0243	0
c	New	1.935	2.0853	0

conditions by the Monte Carlo method. Based on Newmark method, the randomness of tailings and dam construction material parameters is considered. The simulation results are as follows.

It can be seen from Table 7 that when the Monte Carlo method is used to solve the dynamic stability of the new and original tailings reservoirs under different working conditions, the same situation appears as that when the static stability is solved, and there is a sudden increase in the calculated value of the safety factor at the original reservoir area of working conditions A, B, a, and b. The reasons for the above analysis have been explained in this paper, which is not repeated here. The calculation results of Monte Carlo method and Newmark method show that the new and original tailings reservoirs have high stability under El Centro wave and Taft wave under different working conditions. When the Monte Carlo method is used to calculate the dynamic and static stability of the double reservoir area, the calculation results of the new reservoir area are in good agreement with those of other methods, whereas the calculation value of the original reservoir area is higher. Attention should be paid to the comprehensive comparison with other methods in practical engineering application.

5. Discussion

The limitation of this study is that the linkage effect of tailings and dam material parameters with dam instability damage is not considered. It has been shown that when a slope has a tendency to destabilize, parameters such as soil pore space and permeability coefficient will increase with time, and then the values of parameters such as soil cohesion and internal friction angle and elastic modulus will decrease, and eventually the soil will be destabilized due to a vicious cycle. Therefore, the subsequent study can solve the stability of tailing ponds from the perspective of destabilization damage and material parameter degradation linkage, which will be more in line with the engineering reality.

6. Conclusions

In this study, we used the traditional dynamic and static stability solution method and Monte Carlo method to carry out the stability numerical calculation of the double reservoir area (three static conditions and six dynamic conditions) generated by the new expansion method. The results of the calculations indicate that the new expansion method is highly feasible and stable, and it will form a reverse pressure slope at the initial dam of the original reservoir area while significantly increasing the capacity of the tailings reservoir, which is more conducive to the stability of the tailings reservoir.

The traditional dynamic and static stability methods (Newmark method and Swedish arc method) disregard the randomness and spatial variability of tailings material when calculating the stability of a tailings pond and use the critical sliding surface in the calculation area as an index to evaluate the stability of the region, which makes it difficult to meet the engineering needs at this stage. The Monte Carlo method replaces the fixed value with the tailings material parameters obeying a specific distribution in the calculation process and takes into account the randomness of the calculation material parameters, and therefore it can exclude other influencing factors when calculating the failure probability of the tailings pond under different working conditions by sampling. Under the condition that the required number of samples and extraction times are met, Monte Carlo technique accuracy can also be guaranteed. Therefore, the Monte Carlo approach has greater reference importance and practical significance than traditional methods.

Monte Carlo approach predicts similar stability of the new reservoir area as other traditional methods, indicating its feasibility in solving the stability of the new reservoir area under the condition of double reservoir areas. However, this method may overestimate the stability of the original reservoir area, and therefore comparisons with other calculation methods are required.

Data Availability

All data supporting the findings in this study are available from the corresponding author upon reasonable request.

Conflicts of Interest

The authors declare that they have no conflicts of interest regarding the publication of this paper.

References

[1] T. Liang, T. T. Werner, X. Heping, Y. Jingsong, and S. Zeming, "A global-scale spatial assessment and geodatabase of mine areas," *Global and Planetary Change*, vol. 204, Article ID 103578, 2021.

[2] M. Rico, G. Benito, and A. Diez-Herrero, "Floods from tailings dam failures," *Journal of Hazardous Materials*, vol. 154, no. 1–3, pp. 79–87, 2008.

[3] S. Tian, X. Dai, G. Wang, Y. Lu, and J. Chen, "Formation and evolution characteristics of dam breach and tailings flow from dam failure: an experimental study," *Natural Hazards*, vol. 107, no. 2, pp. 1621–1638, 2021.

[4] G. Z. Yin, X. F. Jing, Z. A. Wei, and X. Li, "Experimental study of similar simulation of tailings dam-break[J]," *Chinese Journal*

of Rock Mechanics and Engineering, vol. 29, no. 2, pp. 3830–3838, 2010.

[5] F. Thompson, B. C. de Oliveira, M. C. Cordeiro et al., "Severe impacts of the brumadinho dam failure (minas gerais, Brazil) on the water quality of the paraopeba river," *The Science of the Total Environment*, vol. 705, Article ID 135914, 2020.

[6] C. A. de Paiva, A. da Fonseca Santiago, and J. F. do Prado Filho, "Content analysis of dam break studies for tailings dams with high damage potential in the Quadrilátero Ferrífero, Minas Gerais: technical weaknesses and proposals for improvements," *Natural Hazards*, vol. 104, no. 2, 2020.

[7] J. C. Santamarina, L. A. Torres-Cruz, and R. C. Bachus, "Why coal ash and tailings dam disasters occur," *Science*, vol. 364, no. 6440, pp. 526–528, 2019.

[8] J. Jin, Z. Qin, X. Lü et al., "Rheology control of self-consolidating cement-tailings grout for the feasible use in coal gangue-filled backfill," *Construction and Building Materials*, vol. 316, Article ID 125836, 2022.

[9] J. M. Mayoral and M. P. Romo, "Geo-seismic environmental aspects affecting tailings dams failures," *American Journal of Environmental Sciences*, vol. 4, no. 3, p. 212, 2008.

[10] N. M. Halden and L. A. Friedrich, "Trace-element distributions in fish otoliths: natural markers of life histories, environmental conditions and exposure to tailings effluence," *Mineralogical Magazine*, vol. 72, no. 2, pp. 593–605, 2008.

[11] F. M. Romero, M. A. Armienta, M. E. Gutiérrez, and G. Villasenor, "Eological and climatic factors determining hazard and environmental impact of mine tailings," *Revista Internacional de Contaminación Ambiental*, vol. 24, no. 2, pp. 43–54, 2008.

[12] C. M. K. Neuman, J. W. Boulton, and S. Sanderson, "Wind tunnel simulation of environmental controls on fugitive dust emissions from mine tailings," *Atmospheric Environment*, vol. 43, no. 3, pp. 520–529, 2009.

[13] G. Yin, W. Wang, W. Zuoan, G. Cao, and X. Jin, "Analysis of dynamic response and seismic performance of tailings pond raising and expansion dams," *Journal of Rock Mechanics and Engineering*, vol. 37, no. S1, pp. 3132–3142, 2018.

[14] J. Jin, C. Song, B. Liang, Y. Chen, and M. Su, "Dynamic characteristics of tailings reservoir under seismic load," *Environmental Earth Sciences*, vol. 77, no. 18, pp. 1–11, 2018.

[15] K. F. Morrison, J. M. Johnson, A. J. Augello, and B. Doughty, "Innovative expansion of a large centreline constructed tailings storage facility in a seismically-active area," in *Proceedings of the First International Seminar on the Reduction of Risk in the Management of Tailings and Mine Waste*, pp. 205–215, Australian Centre for Geomechanics, Perth, Australia, January 2010.

[16] L. Fusheng, H. Hongbin, Q. Hong, and L. Zhili, "Seepage stability analysis of elevation and expansion of manshanhong tailings dam," *Modern Mining*, vol. 28, no. 05, p. 25, 2012.

[17] Z. Wei, G. Yin, L. Wan, and G. Li, "A case study on a geotechnical investigation of drainage methods for heightening a tailings dam," *Environmental Earth Sciences*, vol. 75, no. 2, p. 106, 2016.

[18] N. T. Ozcan, R. Ulusay, and N. S. Isik, "A study on geotechnical characterization and stability of downstream slope of a tailings dam to improve its storage capacity (Turkey)," *Environmental Earth Sciences*, vol. 69, no. 6, pp. 1871–1890, 2013.

[19] G. S. Thallak and A. M. Hegde, "A case study of probabilistic seismic slope stability analysis of RockFill tailing dam," *International Journal of Geotechnical Earthquake Engineering*, vol. 10, no. 1, pp. 43–60, 2019.

[20] L. Zhang, Y. Huang, X. Wu, and M. J. Skibniewski, "Risk-based estimate for operational safety in complex projects under uncertainty," *Applied Soft Computing*, vol. 54, pp. 108–120, 2017.

[21] G. Bhattacharya, R. Chowdhury, and S. Metya, "Residual factor as a variable in slope reliability analysis," *Bulletin of Engineering Geology and the Environment*, vol. 78, no. 1, pp. 147–166, 2019.

[22] T. Li, G. Liu, C. Wang, X. Wang, and Y. Li, "The probability and sensitivity analysis of slope stability under seepage based on reliability theory," *Geotechnical & Geological Engineering*, vol. 38, no. 1, pp. 1–11, 2020.

[23] Google Maps, *Satellite Image of a Tailings Pond in Yunnan*, https://www.gugeditu.net, 2021.

[24] W. H. Gu, N. R. Morgenstern, and P. K. Robertson, "Progressive failure of lower San Fernando dam," *Journal of geotechnical engineering*, vol. 119, no. 2, pp. 333–349, 1993.

[25] M. Cha and G. C. Cho, "Shear strength estimation of sandy soils using shear wave velocity," *Geotechnical Testing Journal*, vol. 30, no. 6, pp. 484–495, 2007.

[26] Y. T. Huang, A. B. Huang, Y. C. Kuo, and M. D. Tsai, "A laboratory study on the undrained strength of a silty sand from Central Western Taiwan," *Soil Dynamics and Earthquake Engineering*, vol. 24, no. 9-10, pp. 733–743, 2004.

[27] J. Leng, G. Ye, B. Ye, and D. S. Jeng, "Laboratory test and empirical model for shear modulus degradation of soft marine clays," *Ocean Engineering*, vol. 146, pp. 101–114, 2017.

[28] S. Y. Liu, L. T. Shao, and H. J. Li, "Slope stability analysis using the limit equilibrium method and two finite element methods," *Computers and Geotechnics*, vol. 63, pp. 291–298, 2015.

[29] R. Kalatehjari and N. Ali, "A review of three-dimensional slope stability analyses based on limit equilibrium method," *Electronic Journal of Geotechnical Engineering*, vol. 18, pp. 119–134, 2013.

[30] X. Huang, X. Cai, J. Bo, S. Li, and W. Qi, "Experimental study of the influence of gradation on the dynamic properties of centerline tailings sand[J]," *Soil Dynamics and Earthquake Engineering*, vol. 151, Article ID 106993, 2021.

[31] I. Gladwell and R. Thomas, "Stability properties of the Newmark, houbolt and wilson θ methods," *International Journal for Numerical and Analytical Methods in Geomechanics*, vol. 4, no. 2, pp. 143–158, 1980.

[32] N. M. Newmark, "Effects of earthquakes on dams and embankments," *Géotechnique*, vol. 15, no. 2, pp. 139–160, 1965.

[33] S. L. Kramer and M. W. Smith, "Modified Newmark model for seismic displacements of compliant slopes," *Journal of Geotechnical and Geoenvironmental Engineering*, vol. 123, no. 7, pp. 635–644, 1997.

[34] N. Serff, H. B. Seed, and F. I. Makdisi, *Earthquake-induced Deformations of Earth Dams*, Univ of California, Los Aneles, CA, USA, 1976.

[35] E. Taniguchi, R. V. Whitman, and W. A. Marr, "Prediction of earthquake-induced deformation of earth dams," *Soils and Foundations*, vol. 23, no. 4, pp. 126–132, 1983.

[36] S. K. Pal, M. S. Rahman, and C. C. Tung, "A probabilistic analysis of seismically induced permanent movements in earth dams," *Soils and Foundations*, vol. 31, no. 1, pp. 47–59, 1991.

[37] J. M. Kim and N. Sitar, "Probabilistic evaluation of seismically induced permanent deformation of slopes," *Soil Dynamics and Earthquake Engineering*, vol. 44, pp. 67–77, 2013.

[38] J. Jin, Q. Ding, H. Cui, P. Zhang, X. Xiao, and X. Lv, "Dynamic response characteristics of a tailing dam determined by shaking-table tests," *Arabian Journal of Geosciences*, vol. 13, no. 18, pp. 1–12, 2020.

Research Article

Mechanical Analysis of Preventing Reflection Cracks Based on Stress Absorbing Layer

Lingjie Han,[1] **Shihao Zhang** (iD)**,**[2] **Zhengqi Zhang,**[3] **and Taotao Gao**[3]

[1]*Zhengzhou University of Science and Technology, Zhengzhou, Henan 450064, China*
[2]*Zhengzhou Railway Vocational and Technical College, Zhengzhou, Henan 451460, China*
[3]*Chang'an University, Xi'an, Shaanxi 710064, China*

Correspondence should be addressed to Shihao Zhang; 1187785731@qq.com

After asphalt concrete overlay, the reflection crack in the old pavement remains a great challenge. In order to overcome this problem, here, we report the effect of stress absorbing layer on the reflection crack. First, the concrete measures to prevent and reduce reflection cracks at home and abroad are analyzed. Then, the mechanism of the generation and development of reflection cracks is studied, the functional characteristics of stress absorbing layer are analyzed, and the principle of antireflection crack is clarified. Further, the effects of modulus thickness and porosity of stress absorbing layer on the stress of pavement structure layer are discussed. Finally, the effect of the stress absorbing layer on preventing reflective cracks is analyzed by numerical simulation. The analyses show that the stress absorbing layer is a thin asphalt concrete layer with good fatigue resistance and low modulus between the old pavement and asphalt pavement, which delays the expansion of pavement reflection cracks. The stress absorbing layer should have high elasticity and low temperature flexibility, water damage resistance, and interlayer bonding. The simulation results suggest that the modulus of the stress absorbing layer should be 400 MPa~600 MPa, and the thickness should be 1 cm~2.5 cm. When the thickness of the stress absorption layer is 2.5 cm, the values of tensile stress σ_X, equivalent stress σ_{Mises} and maximum shear stress τ_{Max} are 31.7%, 29.2%, and 25.7% lower than those of the layer without addition, respectively. The results demonstrate that the effect of stress reduction is obvious, which plays an important role in preventing or reducing the occurrence of reflective cracks. The designed void ratio of the mixture is between 1% and 2.5% for the indoor permeability resistance test. We believe that these findings have certain guiding significance for theoretical analysis and engineering application of stress absorbing layer.

1. Introduction

The asphalt concrete overlay on the old pavement not only improves the performance of the old cement concrete pavement, but also improves the driving comfort. At the same time, it makes full use of the residual strength of the old pavement and has little impact on traffic and environment [1, 2]. However, after adding the new asphalt surface, due to the crack defects of the old pavement in the structure, the new pavement is prone to produce reflection cracks under the combined action of external load and environment [3, 4]. Reflection cracks will not only lead to the deterioration of pavement performance, but also affect the beauty of pavement. Once the surface water infiltrates, the strength and stability of subgrade and pavement will be seriously reduced,

and the surrounding cracks will expand rapidly, greatly shortening the service life of asphalt overlay [5–8].

To reduce or prevent the occurrence of reflective cracks, many experts and scholars at home and abroad have done a lot of relevant research. Gu [9] and others conducted fatigue tests on cement concrete pavement with asphalt overlay, analyzed the influence of asphalt overlay thickness on the crack resistance of pavement structure, and concluded that when the asphalt overlay thickness is less than 10 cm, the fatigue life increases significantly with the increase of thickness, and there is an approximate linear relationship between them. However, when the thickness exceeds 10 cm, the growth rate of the antifatigue load slows down, and when the thickness exceeds 15 cm, the thickness resistance performance is unaffected. Zhang and others [10–12] carried

out crack prevention tests using glass fiber grille, geotextile, and geogrid. The research shows that this material can better prevent the occurrence of reflection cracks, and the crack prevention effect of glass fiber grille is better than that of geotextile and geogrid. If the old cement concrete slab has high damage rate, large damage area, and uneconomical replacement or grouting repair, the old cement concrete slab can be cracked and stabilized, and then the asphalt surface layer can be added to reconstruct the old road [13–18].

Compared with the method of thickening asphalt overlay, the stress absorbing layer can achieve the same antireflection crack effect, and the economic benefits of the stress absorbing layer are higher. Compared with geotextile method, the geotextile mainly plays the role of stirrup at the bottom of the asphalt layer, and the stress absorbing layer plays the role of "absorbing" the stress of base cracking through its own flexibility. Compared with the isolation layer method, the asphalt macadam or graded gravel uses its larger void ratio to make the reflection not reflect upward. The stress absorption layer can achieve the same effect, but it will also cause waterproof damage. Compared with the crushing method, the construction of the crushing method is difficult, the crushing particle size is uneven, resulting in environmental pollution, the remaining life of the old plate is not fully utilized, and the construction of the stress absorption layer is as simple as that of the ordinary asphalt surface layer.

How to effectively prevent the occurrence of reflection cracks and make the pavement continue to bear the repeated action of traffic load after the overlay is a prominent problem to be solved urgently in the asphalt overlay of old pavement. Therefore, this paper summarizes and analyzes the research on preventing reflection cracks at home and abroad and then explores the characteristics of the stress absorbing layer and the principle of reflection crack prevention according to analyzing the mechanism of reflection cracks. It secondly discusses the influence of finite element stress absorbing layer modulus, thickness, and void ratio on the stress of pavement structure layer. Finally, the effect of stress absorbing layer on preventing reflection crack is analyzed through numerical simulation. In this paper, the effect of the stress absorbing layer on the old pavement is systematically studied, which has important practical value for theoretical research and engineering application in the future.

2. Mechanism of Reflection Crack Generation and Development

According to the existing research basis, in the professional field, the formation of reflection cracks is usually divided into two stages: the first stage is the generation stage of reflection cracks; the second stage is the expansion stage of reflection cracks [19].

2.1. Mechanism of Reflection Crack Formation. The sudden change of temperature will cause two kinds of deformation of the pavement structure: one is the cracking of the cement concrete pavement in the asphalt surface: when the temperature rises, the cracks in the old pavement will increase

the opening deformation due to temperature shrinkage, resulting in additional stress on the asphalt surface and cracks on new asphalt surface; second, the temperature distribution of each structural layer of the pavement is uneven, resulting in different shrinkage and warping deformation of different materials. Under the cyclic action of temperature difference, the cracks produce large stress, resulting in further cracking.

When the driving load repeatedly acts on the pavement cracks, its impact on the surface layer can be divided into three stages, as shown in Table 1.

When the driving load approaches and leaves, the surface will produce shear stress in the opposite direction. When the driving load acts on the upper surface of the original crack, the surface will be subjected to bending tensile stress. The above two forces increase the cracking of the crack.

2.2. Reflection Crack Propagation. From its generation to expansion, the reflection crack will undergo a crack propagation stage, that is, the reflection crack along the asphalt overlay in the direction of longitudinal extension and transverse extension of the surface.

2.2.1. Longitudinal Propagation of Reflection Cracks. Temperature stress leads to cracking; driving load mainly leads to open type and shear-type cracks. When the wheel is driven directly above the cracks, it is easy to produce open cracks. The driving passing through the crack side is shear-type. For the gap-type reflection cracks generated under the positive load of the vehicle, they usually appear at the bottom of the cover layer and expand vertically upward through the repeated action of the load. Shear reflection cracks appear in the asphalt overlay, extending from the bottom of the overlay to the top at an angle of about 45°.

2.2.2. Transverse Propagation of Reflection Cracks. Once cracks appear, they will inevitably expand to both sides. Usually, reflection cracks often appear on one side of the road surface. The comprehensive action of environment and load will accelerate the crack propagation. The main cause of reflection crack is the coupling effect of temperature and load.

Reflection cracks are mainly transverse cracks, and their spacing depends on factors such as climatic and hydrological conditions, overlay thickness, and crack resistance of surface materials. When the temperature difference between day and night is large, the thickness of the surface layer is thin, and the crack resistance of the surface layer material is poor, and the spacing generated by the reflection crack is small; otherwise, it is large.

3. Influencing Factors of Structure and Material Design of Stress Absorbing Layer

3.1. Functional Characteristics of Stress Absorption Layers. According to the antireflection crack mechanism of the stress absorption layer, it must have the following functional characteristics [20–23]:

TABLE 1: Influence of driving load on road surface.

Load distance from crack position	The relative displacement of both sides the crack	The stress affected by the surface layer
Approach to	Larger	High shear stress
Top surface	No or less	Bending tensile stress
Bear off	Larger	High shear stress
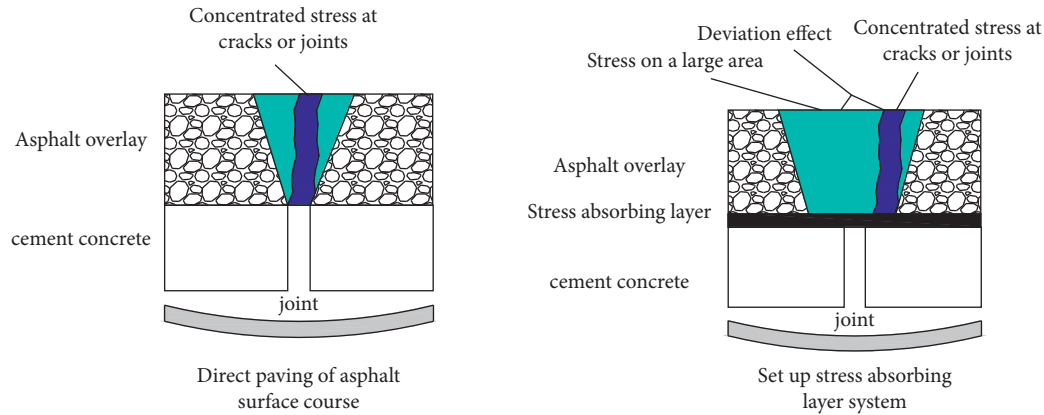
FIGURE 1: Principle diagram of antireflection crack of stress absorption layer.

High elasticity: the greater the recoverable elastic deformation of the structural layer, the better the performance of relieving load stress, which is conducive to reducing the vertical deformation of the overlay and improving the fatigue resistance of the surface layer.

Strong flexibility: the low temperature flexibility of stress absorption layer can alleviate temperature stress. When the temperature stress is generated on the old road surface, the stress absorbing layer with high flexibility will produce large plastic deformation, so as to weaken the additional stress.

Water loss resistance: stress absorbing layer should have the ability to resist water damage. The stress absorbing layer forms asphalt film on the asphalt pavement, which can prevent the filtration of rainwater; that is, it has good waterproof performance, cuts off the penetration of surface water into the old road surface, ensures the stability of the original road base, and prolongs the service life of the road surface.

Interlayer bonding: the stress absorbing layer should have high viscosity, which can bond each structural layer well and provide transition and connection for the structural layers of two different materials. Good bonding performance can not only dissipate and alleviate the stress concentration caused by cracks, but also improve the overall strength and stability of the structure.

3.2. Principle of Preventing Reflection Crack by Stress Absorption Layer. The stress absorption layer is a functional layer with good fatigue resistance and low modulus added between the old pavement and the asphalt concrete surface layer. It can delay the extension of the road surface reflection crack, focus on the stress diffusion, reduce the peak stress, and slow speed of crack propagation and the deviation from the position of the cracks on the surface at the grass-roots level [23], as shown in Figure 1.

4. Influence of Modulus and Thickness of Stress Absorbing Layer on Pavement Stress

In this paper, the stress of pavement structure layer will be simulated by the three-dimensional finite element method, and the influence of the thickness and modulus of stress absorption layer on asphalt surface layer will be studied [24–30]. A reasonable range of modulus and thickness of stress absorption layer is proposed to weaken the stress to the greatest extent, so as to prevent and reduce the generation of reflection cracks.

4.1. Model Building. Taking the asphalt overlay of old cement concrete pavement as an example, the three-dimensional model of asphalt pavement structure of stress absorption layer of cement concrete pavement with the stress absorption layer is established by using the ABUQUS finite element program, as shown in Figures 2 and 3. The influence of the change of modulus and thickness of stress absorbing layer on the stress distribution and change of asphalt pavement structure layer is analyzed [30].

The size of cement concrete pavement board is $5.0 \, m \times 4.5 \, m \times 0.24 \, m$, and the expanded foundation size is $16.01 \, m \times 15.5 \, m \times 9 \, m$. The three-dimensional structure of the stress absorbing layer of the asphalt pavement structure layer is shown in Figure 2. X is the driving direction, Y is the cross section direction of the road, Z is the depth direction of the road, and Figure 3 is the meshing of the finite element calculation of the model.

4.2. Influence of Modulus on Road Surface. Standard single axle and double wheel axle loads are used to calculate the load. According to the research, when the load acts on one side of the original crack, the damage to the overlay is the
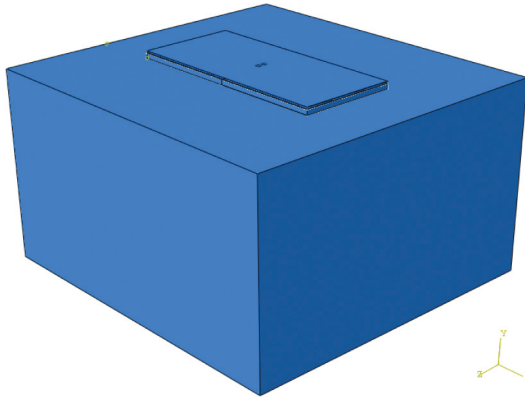
FIGURE 2: 3D model of asphalt pavement structure layer.

FIGURE 4: Calculation diagram of seam of overlay.
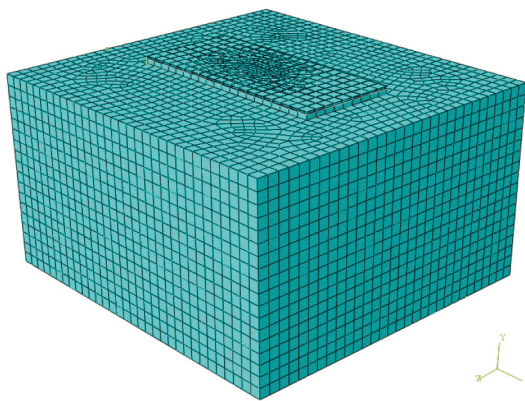
FIGURE 3: Grid division of asphalt pavement structure layer.
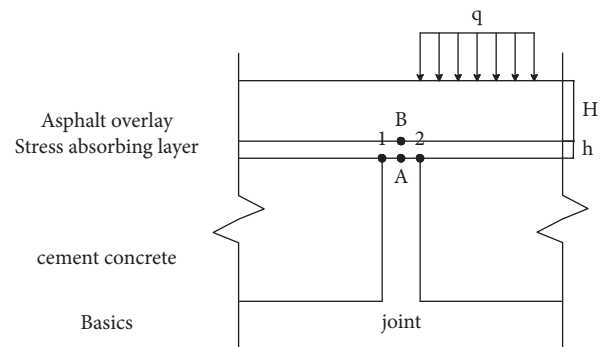
FIGURE 5: Calculation diagram of joint of stress absorption layer.

greatest. Therefore, partial load is selected as the load position for the calculation in this paper [30]. Figures 4 and 5 show the position of partial loads applied on the overlay road surface and the overlay road surface with stress absorbing layer.

In this paper, the modulus of asphalt concrete surface layer is 1200 MPa, and the thickness is 10 cm. The modulus range of stress absorption layer is 200 MPa~1200 MPa, and the thickness range is 1 cm~3 cm. The calculation parameters of pavement structure layer are shown in Table 2.

In order to analyze the influence of the modulus of the stress absorbing layer on the overlay pavement, finite element numerical analysis method is used to calculate the stress on the top and bottom of the overlay layer and the bottom of the stress absorbing layer with different modulus of stress absorbing layer. The relationships between the tensile stress σ_X, first principal stress σ_1, equivalent stress σ_{Mises}, maximum shear stress τ_{Max} and the modulus of stress absorption layer are shown in Figures 6–8.

As can be seen from Figure 6, the values of tensile stress σ_X, first principal stress σ_1, equivalent stress σ_{Mises}, and maximum shear stress τ_{Max} decrease with the increase of the modulus of the stress absorption layer, but they are not obvious. It can be concluded that the change of the modulus of the stress absorption layer has little effect on the stress of the top surface of the overlay layer.

As can be seen from Figure 7, the stress at the bottom of the overlay layer is greatly affected by the modulus of the stress absorbing layer. With the increase of the modulus of the overlay layer, the values of tensile stress σ_X, first principal stress $\sigma1$, equivalent stress σ_{Mises}, and maximum shear stress τ_{Max} increase. When the modulus increases from 200 MPa to 600 MPa, the increasing trend is very fast. From 600 MPa to 1200 MPa, the growth trend slows down.

As can be seen from Figure 8, the modulus of the stress absorbing layer has an important effect on the stress at the bottom. With the increase of the modulus, the bottom tensile stress σ_X, the first principal stress σ_1, the equivalent stress σ_{Mises} and the maximum shear stress τ_{Max} also increase. Therefore, it is necessary to set up a low modulus stress absorption layer to benefit the overlay layer and its own structural layer.

Therefore, in order to determine the reasonable modulus range of the stress absorbing layer, the relationships between the tensile stress σ_X, the first principal stress σ_1, the equivalent stress σ_{Mises}, the maximum shear stress τ_{Max} and the vertical shear stress τ_{XZ} and the pavement depth are calculated by finite element numerical values, as shown in Figures 9–12.

It can be seen from Figures 9–12 that the maximum shear stress τ_{Max}, tensile stress σ_X, first principal stress $\sigma1$ and equivalent stress σ_{Mises} decrease gradually with the increase of the depth of road surface.

Figure 11 shows that the vertical shear stress τ_{XZ} decreases obviously with the increase of the modulus of stress absorbing layer when the layer depth is less than 6 cm. At the depth of 6 cm, the modulus of the stress-absorbing layer is 200 MPa, and τ_{XZ} is −0.019 MPa, while at 1200 MPa τ_{XZ} is

TABLE 2: Calculation parameters of asphalt pavement structure layer.

The structure layer	The thickness of the (cm)	Modulus of elasticity E (MPa)	Poisson's ratio
Asphalt overlay	10	1200	0.25
Stress absorbing layer	1~3	200~1200	0.30
Old cement concrete pavement layer	24	30000	0.15
The foundation		100	0.35
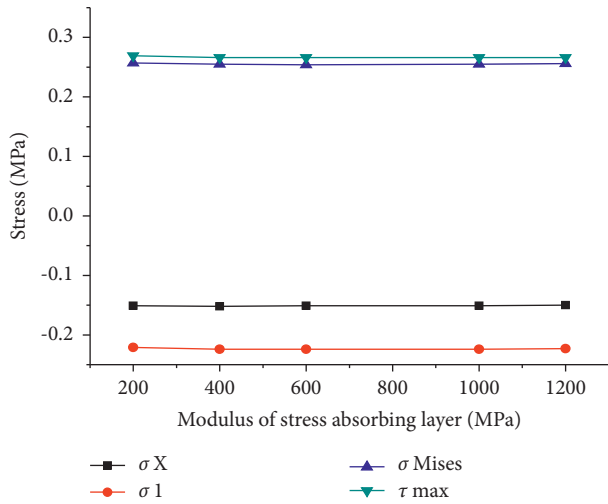
FIGURE 6: The stress on the top of the overlay varies with the modulus of the stress absorbing layer.
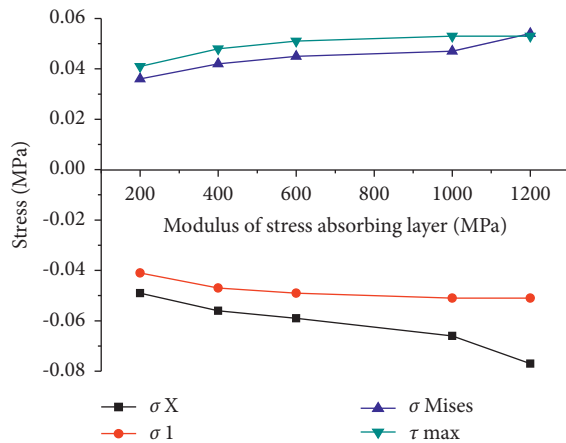
FIGURE 7: The stress at the bottom of the overlay varies with the modulus of the stress absorbing layer.

FIGURE 8: The bottom stress of stress absorbing layer varies with the modulus of stress absorbing layer.
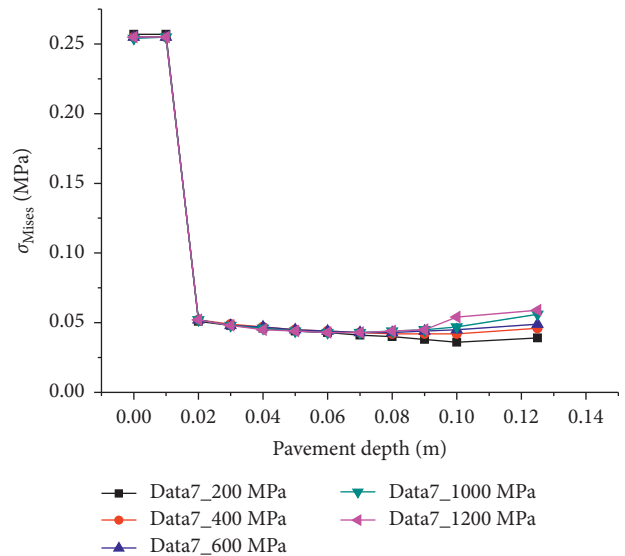
FIGURE 9: The equivalent stress σ_{Mises} is distributed along the road depth.

−0.018 MPa, and the stress decreased by about 4.9%. Figures 10–13 also have the same rule. When the depth of the overlay is less than 2 cm, the tensile stress decreases gradually with the increase of the modulus. When the depth of overlay is less than 4 cm, the maximum shear stress decreases with the increase of modulus. Therefore, the modulus of the stress absorbing layer should not be too low.

It can be seen from Figures 9–13 that when the pavement depth is greater than 6 cm, all stresses should decrease with the decrease of modulus, which is more prominent in Figures 10 and 11. Therefore, the stress absorbing layer with low modulus is reasonable.

In conclusion, when the modulus of stress absorption layer is between 400 MPa and 600 MPa, it can play an important role in dissipating stress and can also have flexibility. The overall strength of pavement structure will not be reduced because the modulus is too low.

4.3. Analysis of the Influence of Stress Absorbing Layer Thickness on Overlay Layer. The thickness of the stress absorbing layer is 0 cm, 1 cm, 1.5 cm, 2.5 cm, and 3 cm (where the thickness is 0, meaning that no stress absorbing
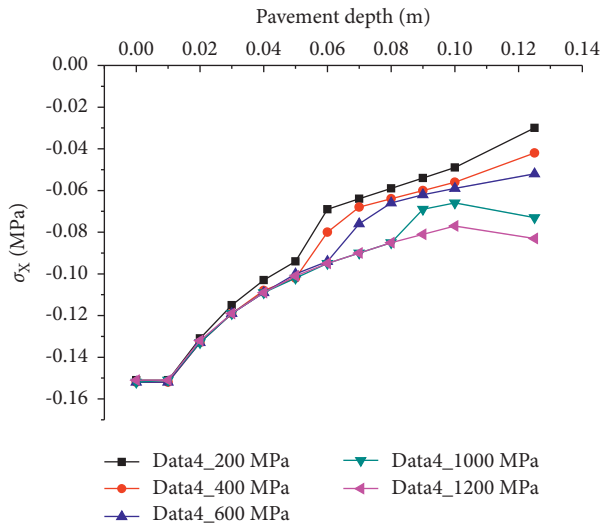
Figure 10: The tensile stress, σ_X, is distributed along the pavement depth.
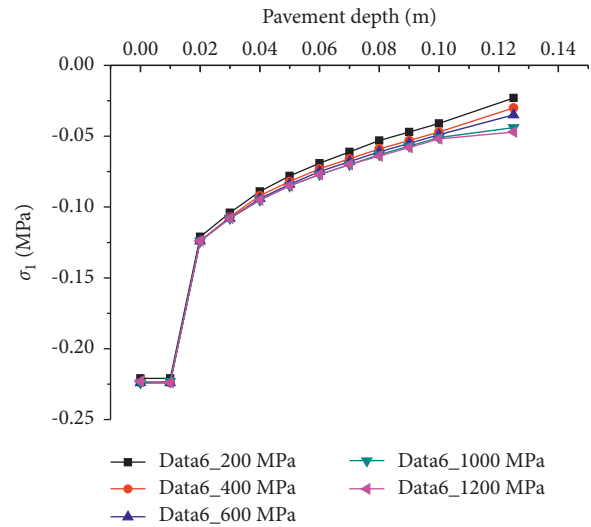
Figure 12: The first principal stress $\sigma 1$ is distributed along the depth of the road surface.
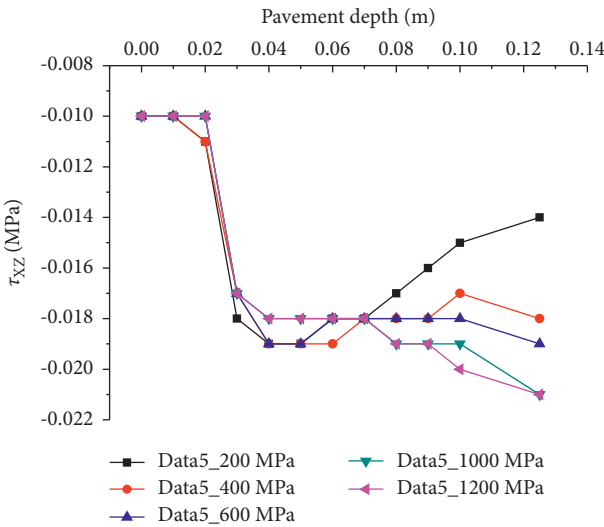
Figure 11: Vertical shear stress τ_{XZ} is distributed along the pavement depth.
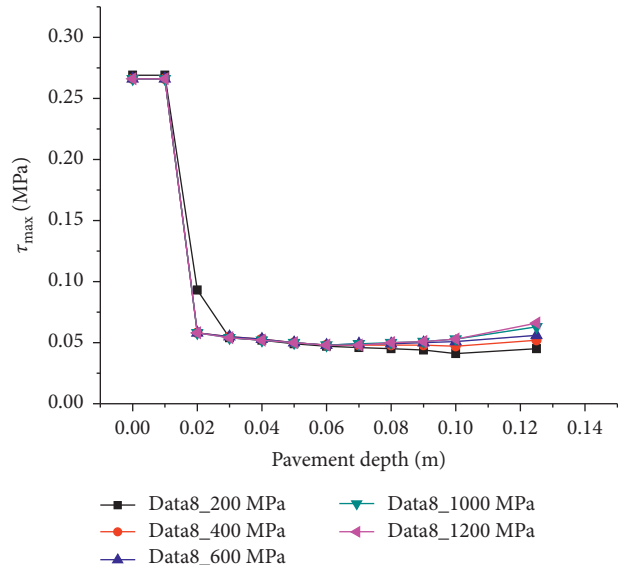
Figure 13: Max shear stress $\tau_{\max}$ is distributed along the depth of the road surface.

layer is added). According to the finite element calculation results, the relationships between the tensile stress σ_X, first principal stress $\sigma 1$, equivalent stress σ Mises and maximum shear stress τ_{Max} at the bottom of the stress absorbing layer with the thickness of the stress absorbing layer are plotted, as shown in Figures 14 and 15.

Figures 14 and 15 show that when the modulus is 400 MPa and 600 MPa, the tensile stress σ_X, the first principal stress σ_1, the equivalent stress σ_{Mises} and the maximum shear stress τ_{Max} decrease with the increase of the thickness of the stress absorbing layer, indicating that the thickness of the stress absorbing layer has little influence on the change of the stress on the top of the layer.

It can be seen from Figures 16 and 17 that the changes of 400 MPa and 600 MPa are similar. The tensile stress σ_X, first principal stress σ_1, equivalent stress σ_{Mises} and maximum

shear stress τ_{Max} decrease with the increase of stress absorption layer thickness. From the unpaved stress absorbing layer to the overlaying stress absorbing layer with the thickness of 1 cm, the stress value is greatly reduced, indicating that the effect of the applied stress absorbing layer is remarkable. When the thickness of the stress absorbing layer increases from 1.0 cm to 2.5 cm, the stress on the bottom surface of the overlay continues to decrease, and the trend of stress reduction is weaker than that of 0-1 cm. When the thickness changes from 2.5 cm to 3 cm, the trend of stress reduction is weaker than that of 1–2.5 cm.

As can be seen in Figures 18 and 19, when the thickness of the stress absorbing layer increases from 1.0 cm to 2.5 cm, the tensile stress σ_X, the first principal stress σ_1, the equivalent stress σ_{Mises} and the maximum shear stress τ_{Max}
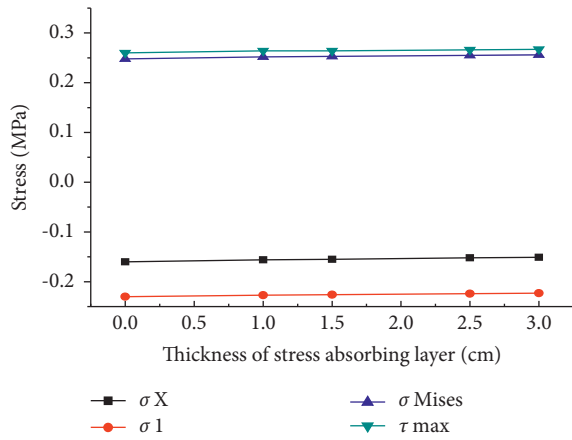
FIGURE 14: Add the top surface stress of the layup layer varies with thickness (the modulus of the stress absorbing layer is 400 MPa).

FIGURE 15: Plus the top surface stress of the layup changes with thickness (the modulus of the stress absorbing layer is 600 MPa).

FIGURE 16: The stress on the bottom surface of the plus layer varies with thickness (the modulus of the stress absorbing layer is 400 MPa).
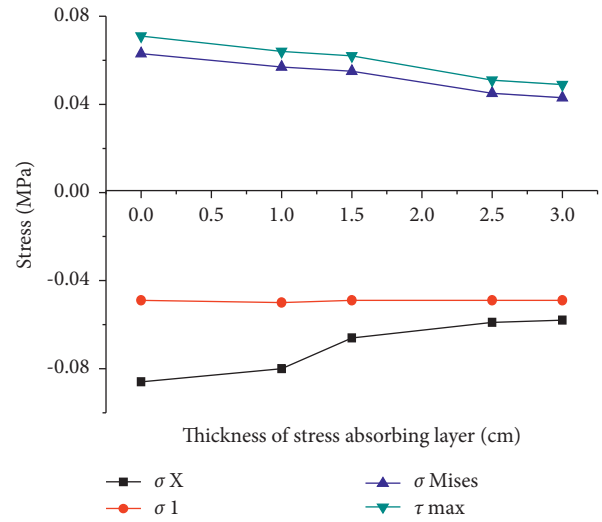
FIGURE 17: Stress at the bottom surface of the stress absorption layer varies with thickness (the modulus of the stress absorbing layer is 600 MPa).
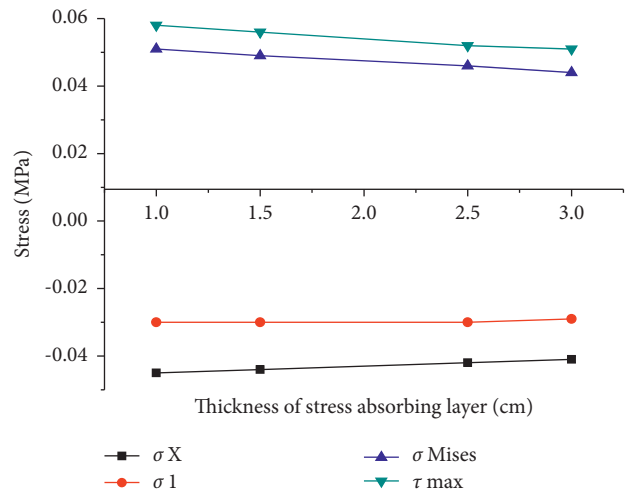
FIGURE 18: Stress at the bottom of the stress absorption layer varies with thickness (the modulus of the stress absorbing layer is 400 MPa).
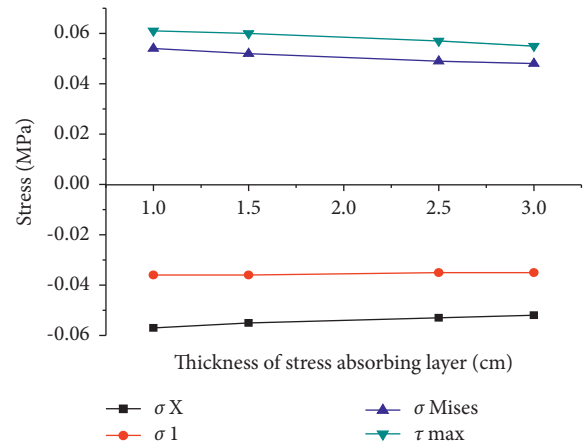
FIGURE 19: Stress at the bottom surface of the stress absorption layer varies with thickness (the modulus of the stress absorbing layer is 600 MPa).

Table 3: Correlation between the void fraction and seepage coefficient.

	Void fraction V_v (%)	The coefficient of water seepage ml/min	Water seepage of specimen (−Don't pour through; +Pouring through)	Regression relation	Correlation coefficient between the void fraction and seepage coefficient
Stress absorbing layer	1.5	0	−		
	2.0	0	−	$y = 3.5714x − 6.0714$	$R^2 = 0.8929$
	3.0	6	−		
AC-13	4.5	0	−		
	5.6	21	−		
	6.7	84	+	$y = 83.504x − 426.47$	$R^2 = 0.9518$
	8.4	263	+		
	10	445	+		
AC-16	3.7	26	−		
	4.5	32	−		
	5.6	41	−	$y = 5.9536x^2 − 53.065x + 146.22$	$R^2 = 0.996$
	6.3	44	+		
	9.6	186	+		
SMA-16	3.5	9	−		
	4.7	46	−		
	7.2	134	+	$y = 1.1249e^{0.6879x}$	$R^2 = 0.9606$
	8.4	273	+		
	9.3	782	+		
AC-20	3.2	0	−		
	3.6	8	−		
	4.9	12	−	$y = 33.446x^2 − 269.69x + 523.51$	$R^2 = 0.9907$
	5.7	43			
	7.8	411	+		

decrease significantly. When the thickness changes from 2.5 cm to 3 cm, the stress value of the stress absorbing layer tends to decrease.

In conclusion, the increase of the thickness of the stress absorbing layer has a significant impact on stress reduction, and the effect is the most obvious when the thickness changes from 1.0 cm to 2.5 cm. When the thickness changes from 2.5 cm to 3 cm, the stress reduction effect decreases. The greater thickness of the stress absorption layer will cause the vertical deformation of the pavement structure and reduce the overall strength of the pavement. Therefore, it is suggested that the thickness of the stress absorption layer should be 1 cm~2.5 cm.

4.4. Voidage of Mixture in Stress Absorbing Layer. According to the function requirement of the stress absorbing layer to prevent water damage, a reasonable index is raised on the mixture voidage of the stress absorbing layer [31]. When the old road surface adds the asphalt surface, the infiltration of moisture will lead to loose and peeling mixture particles. When water enters the pavement structure, the mechanical strength of pavement structure will be reduced. The water damage of asphalt surface is related to the voidage of mixture. The larger voidage of mixture compaction will lead to the damage of asphalt surface. In a certain range of voidage, the influence of voidage change on antiwater damage performance is not obvious. Therefore, this paper selects four kinds of different grades and then uses the water seepage meter to test the water seepage situation under different void rates in indoor according to the requirements

of highway asphalt pavement construction technical specifications, as shown in Table 3.

The test result shows that the water permeability coefficient of asphalt mixture with different grades is different under the same void ratio. When the void ratio is greater than a certain quantitative value, the water permeability coefficient will increase sharply, and there is a good correlation between the water permeability coefficient and the void ratio. It is generally considered that when the water seepage coefficient exceeds 400 mL/min, it is not acceptable. At this time, the asphalt pavement will produce serious water seepage and increase the generation of water damage. However, the water seepage coefficient of stress absorption layer asphalt mixture is less than 10 mL/min, which is far less than the requirement of 200 mL/min in the specification.

It can be inferred that the stress absorbing layer has a good waterproof and pervasive function compared with asphalt mixture from Table 3. The stress absorbing layer prevents the rain from the surface layer from the old concrete plate to the original base, avoids the base to produce new water damage, and ensures the stability of the base. So, according to the impermeability test of stress absorbing layer, it is feasible to design the void ratio of the stress absorption layer mixture between 1.0% and 2.5%.

5. Add Numerical Simulation of Stress Absorbing Layer

In this paper, the modulus is set as 600 MPa, and the stress changes on the top and bottom of the stress absorbing layer

TABLE 4: Calculation results of stress absorption layer of 2.5 cm thickness and unpaved asphalt pavement structure.

Stress absorbing layer thickness	Stress position	σ_X	σ_1	σ_{Mises}	τ_{max}
2.5 cm	Asphalt layer top surface	−0.152	−0.225	0.255	0.267
	The bottom surface of the asphalt layer	−0.058	−0.047	0.046	0.052
0 cm (no paving)	Asphalt layer top surface	−0.161	−0.232	0.248	0.2620
	The bottom surface of the asphalt layer	−0.085	−0.0479	0.065	0.070

of asphalt surface with a thickness of 2.5 cm and the stress absorbing layer of asphalt surface without the stress absorbing layer are calculated. The calculation results are shown in Table 4.

It can be seen from Table 4 that the addition of 2.5 cm stress absorbing layer has little effect on the stress on the top of asphalt layer, which is basically consistent with the previous analysis. When the stress absorbing layer of the asphalt layer is not laid, the tensile stress σ_X, the equivalent effect force σ_{Mises}, and the maximum shear stress τ_{max} values are −0.085, 0.065, and 0.070, respectively. After laying 2.5 cm stress absorption layer, the values become −0.058, 0.046, and 0.052, which are 31.7%, 29.2%, and 25.7% lower than the original values, respectively. The stress reduction effect is obvious, which can prevent or reduce reflection cracks.

6. Conclusion

In summary, the mechanism of the generation and development of reflection cracks is studied, the functional characteristics of stress absorption layer are analyzed, and the principle of antireflection crack is clarified. Besides, the influence of modulus and thickness of stress absorption layer on pavement is studied. The detailed description and explanation of the effect of stress absorption layer on preventing reflection crack have been obtained by numerical simulation. The key findings of the current work are listed as follows:

(1) Through the research on the formation principle of reflective cracks, it can be seen that the main purpose of the stress absorption layer is to add a thin asphalt concrete layer with good fatigue resistance and low modulus between the old pavement and the asphalt pavement, so as to delay the expansion of reflective cracks on the pavement.

(2) According to the antireflection crack mechanism of the stress absorbing layer, it is proposed that the stress absorbing layer must have the functional requirements of high elasticity, low temperature flexibility, water damage resistance, and interlayer bonding.

(3) The effect of thickness and modulus of stress absorbing layer on the stress of surfacing layer is analyzed by finite element method. It is suggested that the modulus of the stress absorbing layer should be 400 MPa~600 MPa, and the thickness should be 1 cm~2.5 cm.

(4) The stress reduction effect of the stress absorbing layer is simulated. The overlay thickness is 2.5 cm,

the modulus is 600 MPa, and the tensile stress σ_X, equivalent stress σ_{Mises} and maximum shear stress τ_{Max} decreased by 31.7%, 29.2%, and 25.7%, respectively. The stress reduction effect is obvious. It can prevent or reduce reflection cracks.

(5) According to the indoor impermeability test of stress absorption layer, it is proposed that the design void ratio of stress absorption layer mixture is between 1.0% and 2.5%.

Data Availability

The data used to support the findings of this study are included within the article.

Conflicts of Interest

The authors declare that they have no conflicts of interest.

References

[1] M. A. Caltabiano and J. M. Brunton, "Refletion craeking in asphalt overlays," *Proceedings of AAPT*, vol. 60, pp. 310–331, 1991.

[2] Ishai, "ExPerimental and analytical model for the role of reinforced asphalt membranes in retardation of refleeting cracking," *Proceedings of AAPT*, vol. 62, pp. 130–149, 1993.

[3] H. S. Chang, *Predietion of Thermal Reflection Cracking in West Texas*, Texas Transprotation Institute, Research Report, Bryan, TX, USA, 1976.

[4] M. Aston, "Model for thermally induced reflection cracking of portland cement concrete Pavement with reiforced asphalt conerete overiay transportation Research record," in *Proceedings of the Road Safty on Five Continers Conferences*, pp. 83–93, TX, USA, October 1987.

[5] J. Zheng and H. Guan, "Finite element analysis of thermo-viscoelasticity of thermosized reflective cracks," *China Journal of Highway and Transport*, vol. 3, pp. 1–5, 2001.

[6] J. Wang and X. Zhu, "Stress intensity factor of crack-containing highway structure under dynamic load," *Chinese Journal of Vibration Engineering*, vol. 16, no. 1, pp. 114–118, 2003.

[7] F. Zhou, *Measures to Prevent Reflection Cracks and Their Analysis*, Doctoral Thesis of Tongji University, Shanghai, China, 1998.

[8] Y. Sun and Y. Zhao, "Viscoelastic damage analysis of asphalt pavement with reflection cracks," *Journal of Shenyang Institute of Architecture and Engineering (Natural Science Edition)*, vol. 18, no. 2, pp. 97–100, 2002.

[9] Q. Gu and L. Peiyi, "Study on the mechanism of reflection crack of asphalt overlay on old rigid pavement," *Journal of China Highway*, vol. 9, no. 2, pp. 11–18, 1995.

[10] F. Zhang, "Application of glass fiber grille in pavement engineering," *Journal of Shandong Institute of Building Materials*, 1998.

[11] X. Wang, J. An, and Z. Wang, "Application and design of geosynthetics in asphalt pavement," *Geotechnical Mechanics*, vol. 25, no. 7, pp. 1093–1098, 2004.

[12] Y. Huang, Z. Guo, and P. Huang, "Fatigue performance of fabric reinforced asphalt concrete," *Highway Traffic Science and Technology*, vol. 16, no. 4, pp. 8–11, 1999.

[13] W. Liao, *Study on Structure and Material of Asphalt Overlay on Old Cement concrete Pavement Based on Stress Absorption Layer*, Doctoral Thesis of Wuhan University of Technology, Wuhan, China, 2007.

[14] R. S. Yijiang, "APPlication of cracking and seating and use of fibers to control reflective cracking," *Transportation Research Reeord*, vol. 1388, pp. 150–159, 1993.

[15] M. R. Thompson, "Breaking cracking and seating conerete pavements," *National Cooperative Highway Research Program*, vol. l44, 1989.

[16] L. Wang and D. Liu, "Comparative analysis of asphalt macadam and graded macadam transition layer in preventing reflection cracks in semi-rigid base," *Northeast Highway*, vol. 32, pp. 10–122, 2002.

[17] B. Yang, "Study on asphalt overlay structure of old cement concrete pavement," Doctoral Thesis of Chang'an University, Xi'an, China, 2005.

[18] A. A. A. Molenaar, J. C. P. Heerbens, and J. H. M. Verhoeven, "Effects of stress absorbing membrane interlayes," *Proceedings of AAPT*, vol. 55, pp. 206–219, 1986.

[19] X. Zhang, G. Zou, and Z. He, "Study on evaluation method of anti-reflection crack ability of asphalt mixture," *Journal of South China University of Technology*, vol. 29, no. 7, pp. 88–91, 2001.

[20] G. Zou, X. Zhang, and S. Wang, "Study on evaluation of reflection crack resistance of asphalt mixture by impact toughness," *Highways*, vol. 10, pp. 119–122, 2004.

[21] G. Ye, "Test method for prevention of reflection cracks in asphalt pavement," *Central-South Highway Project*, vol. July 12, pp. 28–34, 1997.

[22] J. Lian, *Study on Stress Absorption Layer of Cement Concrete Pavement*, Master's degree thesis, Chang'an University, Xi'an, China, 2009.

[23] J. Zhang, T. Yu, and Y. Wanglin, "Reflection crack propagation analysis and crack prevention measures of asphalt overlay," *Chongqing Architecture, Construction and Technology*, vol. 11, pp. 53-54, 2006.

[24] Z. Li, S. Chen, and C. Yi, "Numerical simulation of determining the thickness of Sampave stress absorbing layer," *Science of Hebei University of technology*, vol. 4, pp. 82–85, 2008.

[25] B. Yang, W. Liao, S. Chen, and B. Wang, "Numerical simulation analysis of stress absorption layer to alleviate the stress concentration of asphalt concrete overlay," *Highway*, vol. 11, pp. 106–109, 2007.

[26] Q. Yang and J. Ning, "Sha qinglin early damage and countermeasures of expressway asphalt pavement," *Journal of Changsha University of Technology (Natural Science Edition)*, vol. 3, no. 3, pp. 1–6, 2006.

[27] W. Liao, S. Chen, and J. Liu, "Experimental study on pavement performance of asphalt mixture with stress absorption layer," *Highway Transportation Technology*, vol. 3, pp. 11–16, 2009.

[28] Y. Ming and P. Kui, "Mechanism and prevention measures of reflection cracks in asphalt concrete overlay," *Highway Transportation Technology*, vol. 5, pp. 41–44, 2012.

[29] X. Huijie, "Prevention and treatment of reflection cracks in asphalt concrete overlay of cement concrete pavement," *Highway*, vol. 8, pp. 36–38, 2009.

[30] Z. Hao, J. Liu, and J. Chang, "Study on the effect of HDPE stress absorbing layer in preventing reflective cracks," *Lecture Notes in Civil Engineering*, vol. 1, pp. 331–341, 2020.

[31] J. Han, D. Liu, Y. Guan et al., "Study on shear behavior and damage constitutive model of tendon-grout interface," *Construction and Building Materials*, vol. 320, Article ID 126223, 2022.

Hindawi

Research Article

Analysis of the Bearing Capacity of a Steel Structural Member after Reinforcement

Chen Chen,[1] Yake Tang,[1] Liang Zhang,[1] Kai Niu,[1] Xiangrui Meng,[2] Meng Yang,[2] and Juncai Liu [2]

[1]*State Grid Henan Economic Research Institute, Zhengzhou, 450052, China*
[2]*School of Civil Engineering, Shandong University, Jinan 250061, China*

Correspondence should be addressed to Juncai Liu; liujuncaiw@163.com

To improve the bearing capacity of existing angle steel structures, a new and cost-effective reinforcement method for increasing the load-bearing capacity is proposed. This method uses steel pipes as auxiliary materials and clamps the reinforced angle steel and the auxiliary materials through fixtures to ensure that they are deformed together. The influence of the fixture spacing, the size of the reinforced angle steel member, the slenderness ratio of the members, the size of the auxiliary steel pipe, and other parameters on the reinforcement effect is studied. The results show that the smaller the fixture spacing is, the more obvious the improvement of the bearing capacity is, and the reasonable fixture spacing is related to the angle steel leg width. The larger the slenderness ratio of the member is, the more obvious the reinforcement effect of the scheme is. The steel pipe size has a significant impact on the reinforcement effect of the scheme.

1. Introduction

Due to the large slenderness ratio and special section form, hot-rolled steel members of steel structures have serious tension and compression asymmetry. When these members are subjected to bending moments and pressures, instability and damage often occur, and the material strength cannot be fully utilized. The failure of angle steel structure is mostly extreme point instability failure. When the weak members of a steel structure are unstable, the bearing capacity decreases rapidly, causing a chain reaction in local areas, which leads to the overall collapse of the structure. In recent years, with the continuous increase in load, the bearing performance of some steel structures cannot meet the existing design requirements [1, 2].

At present, scholars worldwide have studied reinforcement schemes for steel structures with different types and service states. The reinforcement of angle steel structures can be divided into two categories: adding transverse support members and strengthening the restraint on the buckling behavior of weak members [3, 4]. The overall bearing capacity of a steel structure can be effectively improved by adding

transverse support [5, 6]. Albermani et al. [7] added transverse supports to the weak parts of a transmission tower to improve the bearing capacity of the tower. By carrying out experiments, Albermani et al. [7] studied the influence of parameters such as different forms of transverse supports and locations of transverse supports on the bearing capacity of the steel structure. Yang et al. [8] established a numerical model for a steel structure and studied the effect of transverse partitioning on the wind resistance calculation of the tower. This researcher concluded that a reasonable setting of the transverse partition can prevent the premature appearance of local formation and reduce the internal force of the main material. However, the calculation scheme of the bearing capacity is not clear after adding transverse support, and the additional support needs to be effectively connected to the original structure through special design, so there are difficulties in design and construction. Strengthening the restraint on the buckling behavior can reinforce weak members, and this kind of reinforcement has various forms, and reasonable reinforcement forms can be selected according to different types of transmission towers and design requirements[9, 10]. Scholars worldwide have carried out a series of studies on the

buckling behavior of restrained angle steel. Adding auxiliary materials is an economical and effective way to provide restraint to angle steel. Mills et al. [11] used the form of parallel auxiliary materials to constrain the buckling behavior of angle steel. Lu and coworkers[12] reinforced the original angle steel by drilling holes in the main material and connecting plates to connect auxiliary materials. These investigators carried out substructure tests to study the influence of bolt cross connectors on the bearing performance of transmission towers. Welding and bolted connections are common connections between auxiliary materials and angle steel. The welding residual stress and bolted connection can damage the original angle steel [13–16]. A kind of strengthening scheme, which is convenient for construction and has little influence on the original structure, is to connect auxiliary material to the original angle steel effectively through a fixture [17, 18].

Commonly used auxiliary materials include angle steel, steel plates, channel steel, and other open section steel members with poor buckling capacity. Fixtures with complex forms have reduced practicability and reinforcement convenience. In this paper, a new scheme for improving the bearing capacity of angle steel is proposed, which uses a steel pipe as an auxiliary material to reinforce the original angle steel. The bearing capacity of the steel pipe is much higher than that of the steel member with the same specification because of its symmetrical cross section and isotropic mechanical properties. The use of fixtures to connect auxiliary materials and angle steel reduces the secondary damage to angle steel components.

2. Model Establishment

2.1. Finite Element Modeling. In the new antibuckling capacity improvement scheme, a steel pipe is adopted as an auxiliary material; this pipe is fixed to the inner side of the angle steel by using fixtures and bolts, as shown in Figure 1. By tightening the bolts, a pretightening force is applied to the steel tube and the angle steel to strengthen the cooperative work between them.

The finite element model of the component was established in ABAQUS to study the buckling shape and bearing capacity of the component before and after reinforcement. The component is modeled by a solid element, which is divided into 8-node hexahedral solid elements (C3D8R). Figure 2 is a schematic diagram of mesh division. The mesh size is determined according to the force complexity of different components. Bolts, fixtures, and angle steel parts with complex forces are divided into small meshes, and the mesh size is controlled at 1/500 of the maximum length of the parts. The steel pipe mesh size is controlled at 1/100 of the maximum length of the part. The end plate mesh size is controlled at 1/10 of the maximum length of the part. Both ends of the angle steel are fixed to the end plate, and both ends of the steel pipe are 250 mm away from the end plate. To ensure that the axial displacement is applied to the members, one end of the member is completely fixed, and only the axial displacement is released at the other end.
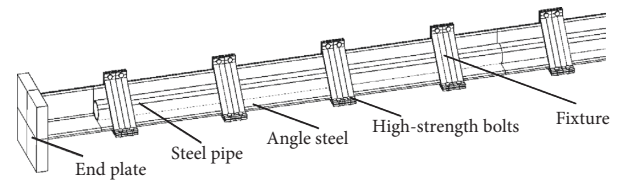
Figure 1: Component model.
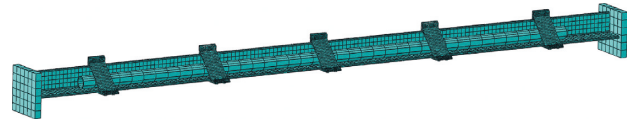
Figure 2: Finite element model.

The angle steel component, steel pipe, and fixture use Q355 steel. Steel is assumed to be an ideal elastic-plastic material. It is assumed that the material is completely elastic before the yield point and completely plastic after the yield point. The constitutive model of the material is shown in Figure 3. The stress-strain curve can be approximately replaced by a double straight line model. The fixture is connected with grade 8.8 M12 bolts. Since the pretightening force of the bolt is the first analysis step that propagates throughout the loading process, it can be imposed to the cross section of the bolt by means of "bolt load" option in ABAQUS. Three analysis steps are defined in the process of pretightening force analysis. At first step, a small pretightening force is applied in order to make convergence easier. In the second step, a large pretightening force is applied. In the third and subsequent steps, the fix at current length method is selected to maintain the adjustment of the pretightening force.

2.2. Component Selection. To study the influence of different parameters on the reinforcement effect of angle steel, numerical models of various components were established, and parametric research of a new reinforcement scheme was carried out. Specifications of various components are shown in Table 1. A total of 27 components were selected for parameter analysis.

Fixtures and bolts need to be strong enough to ensure that their failure occurs after the bar buckles and produces a large deformation. The thickness of the steel plate used in the fixture is uniformly determined to be 6.0 mm, and the width of the fixture is uniformly 80.0 mm. The section size of the fixture varies proportionally with the size change in the angle steel. Figure 4 is a schematic diagram of fixture installation. In component number such as L100×10G57SR75-1150, L100×10 represents limb width of angle steel which is 100 mm, limb thickness is 10 mm, G57 represents the steel pipe diameter which is 57 mm, SR75 represents angle steel member slenderness ratio which is 75, and −1150 represents fixture spacing which is 1150 mm.
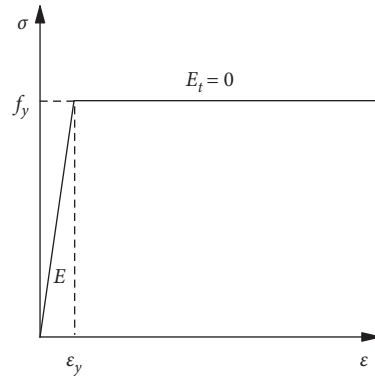
FIGURE 3: Bilinear constitutive model of steel.

TABLE 1: Component specification sheet.

Member number	Section size of angle steel (mm)		Section size of steel tube (mm)		Slenderness ratio of angle steel	Length of angle steel (mm)	Fixture spacing (mm)	The ratio of the fixture spacing to angle steel limb width
	Limb width (l)	Limb thickness (h)	Outer diameter (D)	Wall thickness (t)				
L63 × 5G0SR75-0	63	5	—	—	75	1875	—	—
L100 × 10G0SR75-0	100	10	—	—	75	3000	—	—
L140 × 14G0SR75-0	140	14	—	—	75	4125	—	—
L63 × 5G34SR75-587	63	5	34	2.0	75	1875	587	9.32
L63 × 5G34SR75-392	63	5	34	2.0	75	1875	392	6.22
L63 × 5G34SR75-295	63	5	34	2.0	75	1875	295	4.68
L63 × 5G34SR75-235	63	5	34	2.0	75	1875	235	3.73
L100 × 10G57SR75-1150	100	10	57	4.0	75	3000	1150	11.5
L100 × 10G57SR75-765	100	10	57	4.0	75	3000	765	7.65
L100 × 10G57SR75-575	100	10	57	4.0	75	3000	575	5.75
L100 × 10G57SR75-460	100	10	57	4.0	75	3000	460	4.60
L100 × 10G57SR75-385	100	10	57	4.0	75	3000	385	3.85
L100 × 10G57SR75-325	100	10	57	4.0	75	3000	325	3.25
L140 × 14G76SR75-1712	140	14	76	5.5	75	4125	1712	12.23
L140 × 14G76SR75-1142	140	14	76	5.5	75	4125	1142	8.16
L140 × 14G76SR75-855	140	14	76	5.5	75	4125	855	6.11
L140 × 14G76SR75-685	140	14	76	5.5	75	4125	685	4.89
L140 × 14G76SR75-570	140	14	76	5.5	75	4125	570	4.07
L140 × 14G76SR75-490	140	14	76	5.5	75	4125	490	3.50
L100 × 10G57SR55-575	100	10	57	4.0	55	2180	575	5.75
L100 × 10G57SR95-575	100	10	57	4.0	95	3700	575	5.75
L100 × 10G57SR115-575	100	10	57	4.0	115	4500	575	5.75
L100 × 10G40SR75-575	100	10	40	2.5	75	3000	575	5.75

Table 1: Continued.

| Member number | Section size of angle steel (mm) | | Section size of steel tube (mm) | | Slenderness ratio of angle steel | Length of angle steel (mm) | Fixture spacing (mm) | The ratio of the fixture spacing to angle steel limb width |
	Limb width (l)	Limb thickness (h)	Outer diameter (D)	Wall thickness (t)				
L100 × 10G45SR75-575	100	10	45	2.5	75	3000	575	5.75
L100 × 10G50SR75-575	100	10	50	3.0	75	3000	575	5.75
L100 × 10G63.5SR75-575	100	10	63.5	4.0	75	3000	575	5.75
L100 × 10G70SR75-575	100	10	70	5.0	75	3000	575	5.75
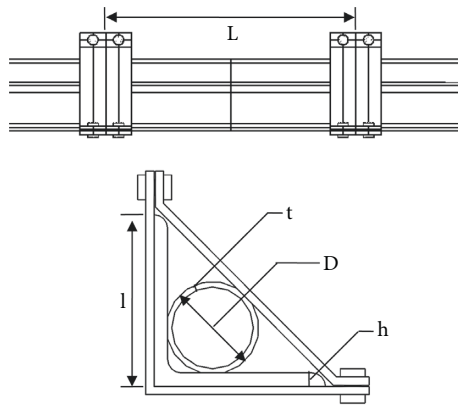
Figure 4: Fixture installation diagram.

3. Parameter Analysis of the New Reinforcement Scheme

The effect of a new reinforcement scheme on the bearing capacity of an angle steel member is complicated, as it is influenced by the fixture spacing, component slenderness ratio, size of the steel pipe and the angle steel component, fixture width, and bolt arrangement on the fixture. In this paper, four parameters, including the fixture spacing, size of the angle steel member, slenderness ratio, and size of the steel pipe, were selected for analysis, and the influence rule of parameter change on the bearing performance of the original angle steel member was studied. The improvement rate of the bearing capacity after reinforcement is defined as α.

$$\alpha = \frac{c_1 - c_2}{c_2} \times 100\%, \tag{1}$$

where α is the improvement rate of the bearing capacity after reinforcement, c_1 is the bearing capacity of the component after reinforcement, and c_2 is the bearing capacity of the original angle steel.

3.1. Fixture Spacing. In this paper, angle steel components of L63 × 5 mm, L100 × 10 mm, and L140 × 14 mm were selected to study the influence of the fixture spacing. The angle steel component, steel pipe, and other hot-rolled steel members

have a definite specification. To ensure a single variable, the relative size of the steel pipe and angle steel limb was fixed in the same range. The outside diameter of the steel pipe is 50–60% of the width of the angle steel limb, the wall thickness of the steel pipe is 35%–40% of the wall thickness of the angle steel limb, and the cross-sectional area of the steel pipe is 25%–35% of the angle steel member. The component specifications are shown in Table 1.

When the section size of the angle steel reinforcement is L63 × 5 mm, as shown in Figure 5, the bearing capacity of the component increases with decreasing fixture spacing. The maximum bearing capacity is exhibited on the L63 × 5G34SR75-235 member with the smallest fixture spacing, and the maximum bearing capacity is 85.4% of the tensile yield capacity of the member. The bearing capacity of reinforced components is negatively correlated with fixture spacing. When the fixture spacing is 587 mm and 392 mm, the bearing capacity of the member is increased by 7.8% and 14.8%, respectively. Compared with the angle steel member, the bearing capacity is not significantly improved. When the fixture spacing is 295 mm and 235 mm, the lifting rate of the bearing capacity is 37.7% and 41.3%, respectively. When the fixture spacing is less than 295 mm, with decreasing fixture spacing, the bearing capacity of the component does not improve significantly, indicating that there is a reasonable range of fixture spacing. When the fixture spacing is less than a reasonable range, the bearing capacity cannot be improved
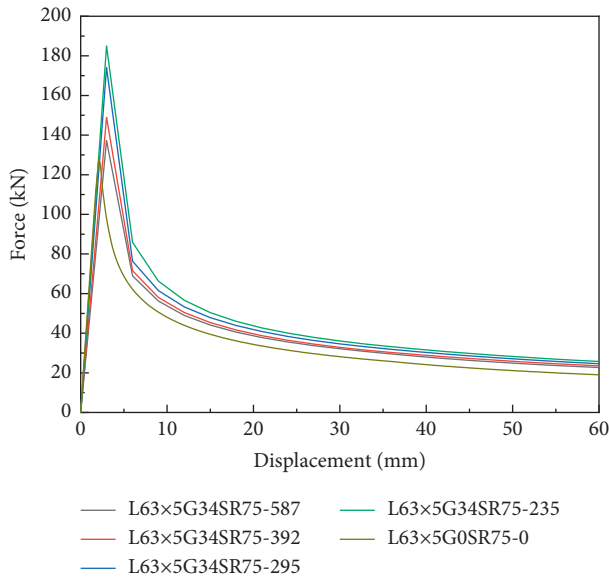
Figure 5: Force-displacement curve (L63 × 5 mm).

effectively. When the fixture spacing is greater than a reasonable range, the bearing capacity of the component does not improve significantly.

The buckling morphology of each component before and after reinforcement is shown in Figure 6. Initial defects should be given for the buckling analysis of angle steel components. The initial defect is uniformly set to 1‰ of the length of the angle steel. When applying initial defects, the component is regarded as a whole, and initial defects are applied to the steel pipe and angle steel. In this paper, the first-order buckling mode of the member is taken as the application form of the initial defect, and the first-order buckling mode of the member is determined by the nonlinear buckling analysis of the member. The coordinates of each element of the member in the first-order buckling mode are multiplied by the corresponding scale factor and then introduced into the static analysis. When the original angle steel member buckles, the stress concentration is obvious in the middle and both ends of the component, as shown in Figure 6 for member L63 × 5G0SR75-0. Large displacement and deformation occur in the middle part. Members L63 × 5G34SR75-587, L63 × 5G34SR75-392, and L63 × 5G34SR75-295 are similar to the original angle steel component in terms of their flexural morphology, with large deformation in the middle. The buckling shape of member L63 × 5G34SR75-235 is slightly different, and the buckling point of the member is moved up, but all the members suffer from overall buckling instability.

The original angle steel member is reinforced with a new reinforcement scheme, and the buckling bearing capacity of the original angle steel can be effectively improved by reasonably setting the fixture spacing. The buckling characteristic of the member, that is, the overall buckling instability, exhibits no obvious change. After reinforcement, the ductility of the angle steel member demonstrates no obvious improvement.

Figure 7 shows the force-displacement curves of the L100 × 10 mm angle steel before and after reinforcement. After reinforcement, the buckling bearing capacity of L100 × 10G57SR75-765, L100 × 10G57SR75-575, L100 × 10G 57SR75-460, L100 × 10G57SR75-385, and L100 × 10G57SR 75-325 increases significantly, and the lifting rate A exceeds 50.0%. When the distance between the fixtures is more than 765 mm, the increase in the buckling capacity of the components is small.

After reinforcement, the ductility of the member is significantly improved. After the bearing capacity of the member reaches the maximum value, with a continuous increase in the end displacement, the bearing capacity of the member decreases gradually. The members L100 × 10G57SR75-460, L100 × 10G57SR75-385, and L100 × 10G57SR75-325 exhibit the best ductility performance.

Figure 8 shows the buckling shape of each member. The members L100 × 10G0SR75-0 and L100 × 10G57SR75-1150 showed overall buckling. When the bearing capacity exceeds the buckling bearing capacity and then decreases rapidly, the ductility of the member with overall buckling is poor. L100 × 10G57SR75-575 first suffered from local buckling, and with a continuous increase in the displacement, the deformation of the middle part of the member increases, showing the overall buckling shape. When the member begins to buckle locally, its bearing capacity reaches the maximum value at the same time, the local buckling characteristic becomes increasingly obvious with an increase in the end displacement, and the bearing capacity of the member decreases slowly. When the end displacement continues to increase, the overall buckling of the member occurs, and the bearing capacity decreases rapidly. Component L100 × 10G57SR75-385 exhibits local buckling, and there is clear local deformation of the angle steel between the two fixtures near the end. After local buckling, the bearing capacity shows no obvious drop. With the increasing end displacement, the component shows good ductility.

With the reduction in the fixture spacing, the new reinforcement scheme has a more obvious effect on the bearing capacity of the angle steel member, the ductility of the components is significantly improved, and the bearing performance is improved. When the distance between the fixtures is less than 575 mm, the bearing capacity and ductility of the components are both improved. When the distance between the fixtures is greater than 575 mm, the ductility characteristics of the components are not obvious, and the effect of improving the bearing capacity is limited.

When the section size of the angle steel member increases to L140 × 14 mm, the bearing capacity of the components increases significantly with decreasing fixture spacing. When the fixture spacing is less than 855 mm, the buckling capacity of the components does not change significantly with decreasing fixture spacing. Therefore, when the fixture spacing is less than 855 mm, the influence of fixture spacing on the bearing capacity of the reinforced components is weakened.

The ductility of the component is improved after reinforcement. As shown in Figure 9, the members show a certain ductility after buckling. As shown in Figure 10, the
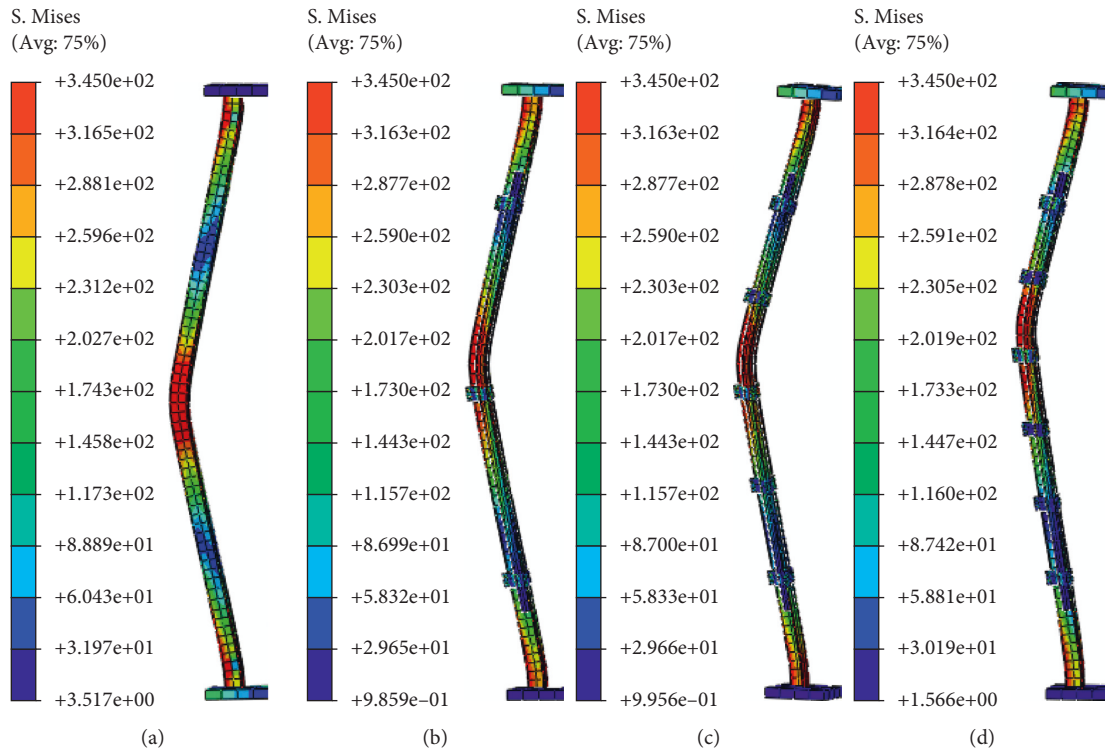
Figure 6: Member buckling shape (L63 × 5 mm). (a) L63 × 5G0SR75-0. (b) L63 × 5G34SR75-587. (c) L63 × 5G34SR75-295. (d) L63 × 5G34SR75-235.
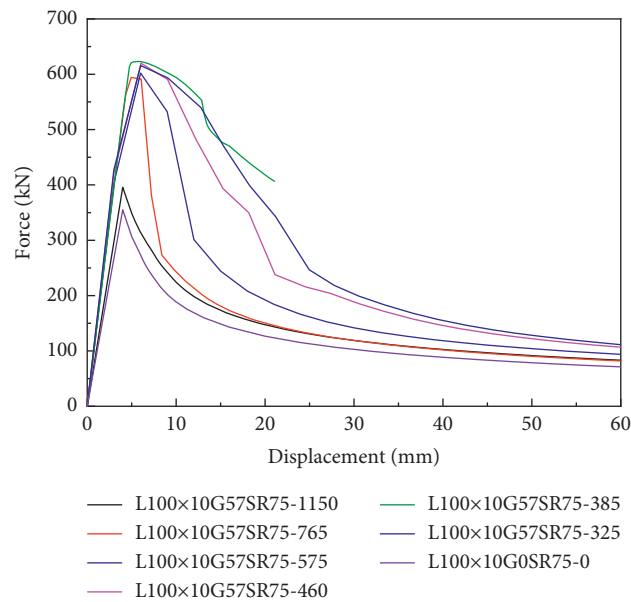
Figure 7: Force-displacement curve (L100 × 10 mm).

buckling characteristics of the members before and after reinforcement are referred to as global buckling. In member L140 × 14G0SR75-0, by increasing end displacement, the central deformation gradually increases, and, finally, overall buckling behavior occurs. With the increase in the end displacement of components L140 × 14G76SR75-1712, L140 × 14G76SR75-855, and L140 × 14G76SR75-570, the stress

concentration and slight local deformation first appeared at the connection between the angle steel and the end plate. As the displacement of the end plate continues to increase, the middle part of the member is deformed, but the deformation speed is significantly lower than that of the original angle steel member. After reinforcement, the member shows certain ductility characteristics. The angle steel member
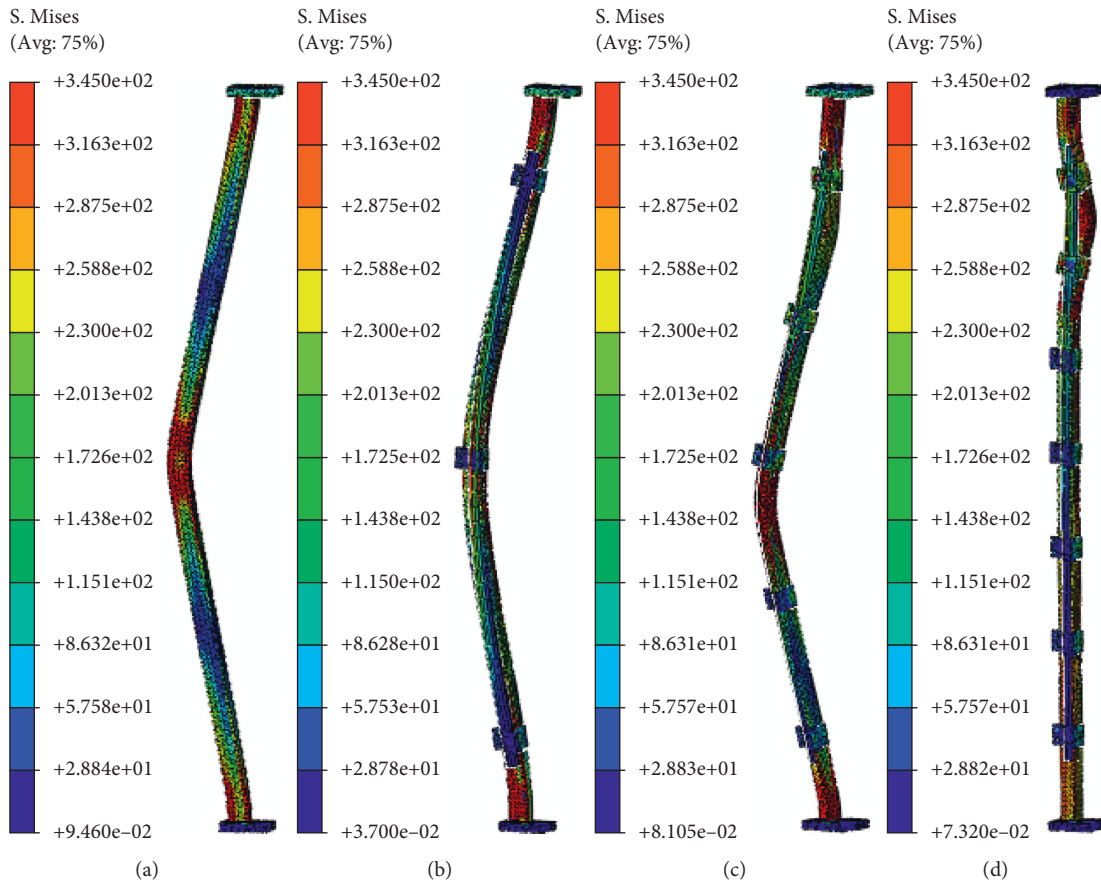
FIGURE 8: Member buckling shape (L100 × 10 mm). (a) L100 × 10G0SR75-0. (b) L100 × 10G57SR75-1150. (c) L100 × 10G57SR75-575. (d) L100 × 10G57SR75-385.
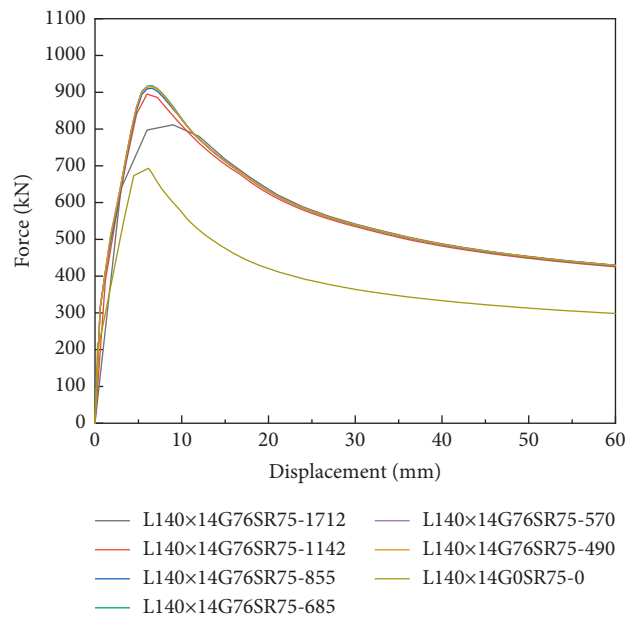
FIGURE 9: Force-displacement curve (L140 × 14 mm).
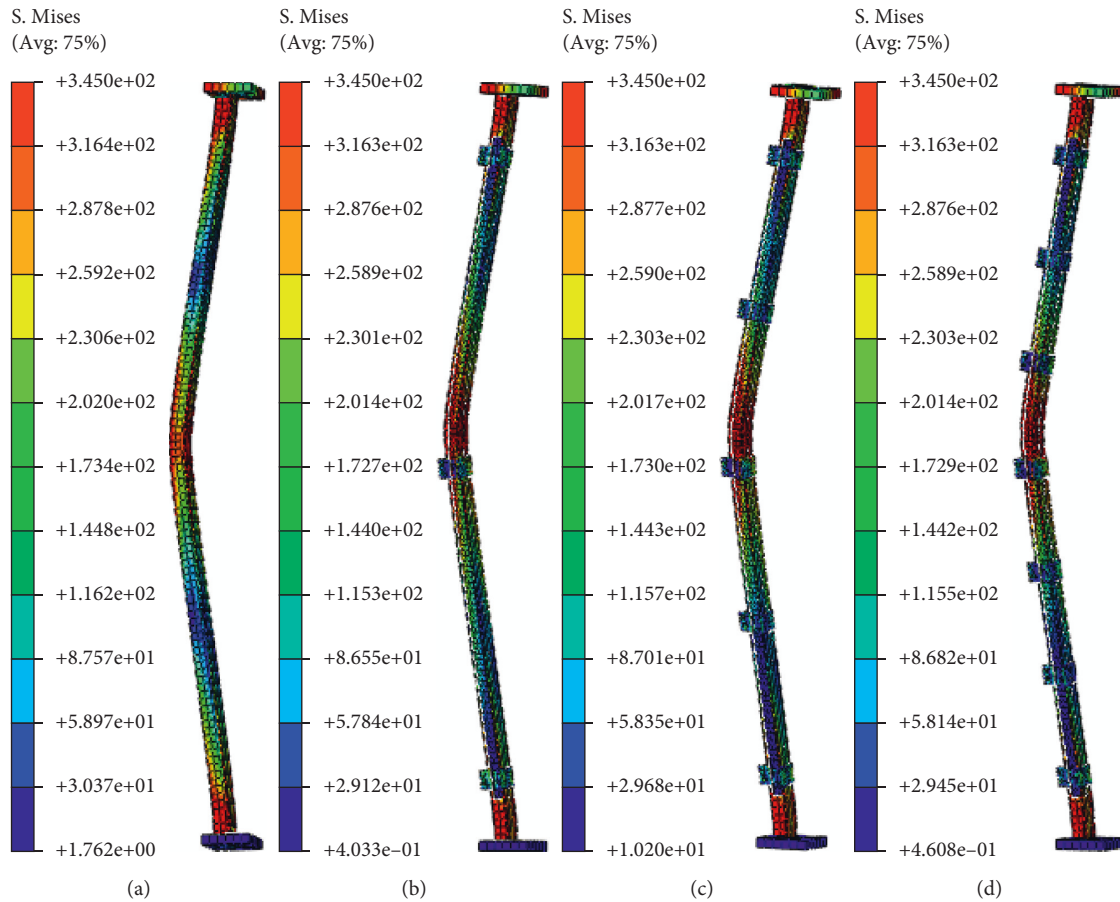
Figure 10: Member buckling shapes (L140 × 14 mm). (a) L140 × 14G0SR75-0. (b) L140 × 14G76SR75-1712. (c) L140 × 14G76SR75-855. (d) L140 × 14G76SR75-570.

L140 × 14G0SR75-0 has no steel pipe to constrain its overall buckling behavior; so the member cannot develop local buckling deformation. It shows obvious buckling characteristics and has poor ductility.

The improvement effect of the bearing capacity of the new reinforcement scheme is greatly affected by the distance between the fixtures; the smaller the distance between the fixtures is, the more obvious the effect of reinforcement. When the effect of reinforcement is considered, the smaller the fixture spacing is, the better the bearing capacity and ductility of the reinforced components can meet engineering requirements. Considering the economics of reinforcement and the convenience of construction, the larger the distance between the fixtures is, the lower the construction cost is, and the better the convenience of use is. Therefore, it is necessary to find a balance between the effect of reinforcement and economy.

The cross section of the angle steel member is L63 × 5 mm, and when the distance between the fixtures is less than 295 mm, the bearing capacity of the components cannot be effectively improved as the distance is further reduced. At this time, the ratio of the distance between the fixtures and the width of the angle steel legs is 4.68. In this paper, it is believed that when the angle steel member with a cross section of L63 × 5 mm is reinforced, the fixture spacing can be taken as 4.68 times the width of the angle steel leg to obtain good reinforcement and economy effects. The cross section of the angle steel is L100 × 10 mm. When the distance between the fixtures is less than 575 mm, the effect of increasing the bearing capacity is no longer obvious. When the distance between the fixtures is greater than 575 mm, the ductility of the reinforced member is not significantly improved. Considering bearing performance after reinforcement and the economy of reinforcement, it is considered reasonable to select the fixture spacing as 5.75 times the width of the angle steel legs. When the cross section of the angle steel is L140 × 14 mm, the distance between the fixtures is 6.11 times the width of the angle steel leg, which can meet the requirements of bearing capacity improvement and economy.

Based on the above analysis, a reasonable fixture spacing of an angle steel member with different specifications is different, and it has a proportional relationship with the leg width of the reinforced angle steel. Through the simulation of three different specifications of angle steel, the results indicate that when using this new reinforcement scheme to reinforce the transmission tower angle steel, the distance between the fixtures should not be greater than 5.00 times the width of the reinforced angle steel leg.

3.2. Influence of the Angle Steel Section Size. The new reinforcement scheme demonstrates a certain difference in the effect of reinforcement of different specifications of angle steel. Table 2 shows the improvement level of the bearing capacity of different specifications of angle steel. The slenderness ratio of the reinforced angle steel remains unchanged, the relative size of the steel pipe and the angle steel is maintained in the same range, and the maximum bearing capacity of the reinforced angle steel is taken. Comparing the improvement rate of the bearing capacity of different specifications of angle steel, the minimum value of the improvement rate of bearing capacity is 32.2%. It can be considered that this reinforcement scheme has a significant reinforcement effect on the angle steel member with a section size from L63 × 5 mm to L140 × 14 mm. There is a large fluctuation in the bearing capacity increase rate of angle steel of different specifications. It is believed that the reinforcement scheme is affected by the size effect to a certain extent. When the size of the reinforced angle steel is too small or too large, it will have a certain impact on the reinforcement effect, but the ideal reinforcement effect can still be achieved by rationally setting the distance between the fixtures. It can be considered that this reinforcement scheme has a good reinforcement effect on angle steel with different cross-sectional sizes and has strong versatility.

As shown in Figure 11, the larger the distance between the fixtures, the greater the load on the fixtures, the greater the stress on the fixtures, and the more obvious the strain. When the angle steel is subjected to pressure and overall buckling occurs, the fixture will tightly connect the steel pipe and the angle steel to realize the effect of constraining the buckling of the angle steel with the flexural bearing capacity of the steel pipe. The fixtures need to bear the force of the steel pipe and the angle steel at the same time. Therefore, to ensure the common deformation of the steel pipe and the angle steel, damage to the fixture needs to occur after damage to the angle steel or the steel pipe. In the parameter study of this paper, the thickness of the steel plate of the fixture is 6 mm. Neither the fixture nor the bolt is damaged before the large buckling deformation of the component occurs.

3.3. Slenderness Ratio of Angle Steel. Angle steel members have different slenderness ratios. To explore the influence of different slenderness ratios on the reinforcement effect of the new reinforcement scheme, four kinds of angle steel members with different slenderness ratios were selected for reinforcement. The section size of the strengthened angle steel is L100 × 10 mm, and the fixture distance is 575 mm. A steel pipe with an external diameter $D = 57$ mm and a wall thickness $t = 4$ mm is selected.

As shown in Figure 12, with an increase in the slenderness ratio of the angle steel members, the buckling bearing capacity of the original member decreases gradually. The buckling capacity of angle steel reinforced by the new reinforcement scheme is clearly improved, and the improvement rate of bearing capacity α is different under different slenderness ratios. The bearing capacity of strengthened members is different. By increasing slenderness ratio, the bearing capacity of the strengthened members also shows a descending trend, but the increase rate of the bearing capacity of the angle steel after reinforcement increases, indicating that the larger the slenderness ratio is, the more obvious the reinforcement effect of the new reinforcement scheme is, and the higher the bearing capacity improvement rate is.

This reinforcement scheme has a good reinforcement effect on angle steel members with slenderness ratios from 55 to 115. The greater the slenderness ratio is, the more obvious the reinforcement effect is.

The buckling modes of components with different slenderness ratios are different. When the slenderness ratio of the angle steel is small, the component first deforms locally near the end and continues to increase with the displacement of the end, and the component begins to demonstrate an overall buckling shape, as shown in Figure 13 for components L100 × 10G57SR55-575 and L100 × 10G57SR75-575. When the slenderness ratio of angle steel increases, there is no obvious local buckling phenomenon. With the increasing end displacement, the component presents overall buckling failure.

In summary, the slenderness ratio of components has a great influence on the reinforcement effect. The larger the slenderness ratio is, the higher the improvement rate of the bearing capacity of the new reinforcement scheme is, and the minimum value of the improvement rate of the bearing capacity is 25.4%. The new reinforcement scheme has a good effect on all kinds of slenderness ratio components.

3.4. Effect of Different Specifications of Steel Pipe on Reinforcement. When steel pipes with different cross-sectional sizes are used to reinforce a specific angle steel component, a steel pipe with a small cross-sectional size ensures that the reinforcement scheme has good economy and low reinforcement costs. The relative size of the steel pipe and the reinforced angle steel member will also affect the reinforcement effect.

The reinforced angle steel section is selected as L100 × 10 mm, the slenderness ratio of the angle steel is 75, and the fixture distance is determined to be 575 mm. Six kinds of steel pipes were selected for this research, and the component numbers are L100 × 10G40SR75-575, L100 × 10G45SR75-575, L100 × 10G50SR75-575, L100 × 10G57SR75-575, L100 × 10G 63.5SR75-575, and L100 × 10G70SR75-575.

As shown in Figure 14, compared with the original component, the bearing capacity of the component after reinforcement shows different degrees of improvement. The external diameter D of the steel pipe section used in component L100 × 10G40SR75-575 is 40 mm, and the wall thickness $t = 2.5$ mm. Compared with the original angle steel member, the buckling bearing capacity increased by 25.1%. The ratio of the external diameter of the steel pipe to the width of the reinforced angle steel is 0.4, the ratio of the wall thickness of the steel pipe to the thickness of the angle steel component is 0.25, and the cross-sectional area of the steel

TABLE 2: Bearing capacity comparison table.

Angle steel type	Bearing capacity before reinforcement (kN)	Bearing capacity after reinforcement (kN)	Increase amplitude (kN)	Increase rate α (%)
L63 × 5 mm	127.51	185.33	57.82	45.3
L100 × 10 mm	354.96	619.90	264.94	74.6
L140 × 14 mm	693.75	917.26	223.51	32.2

(a)

(b)

(c)

(d)

(e)

(f)
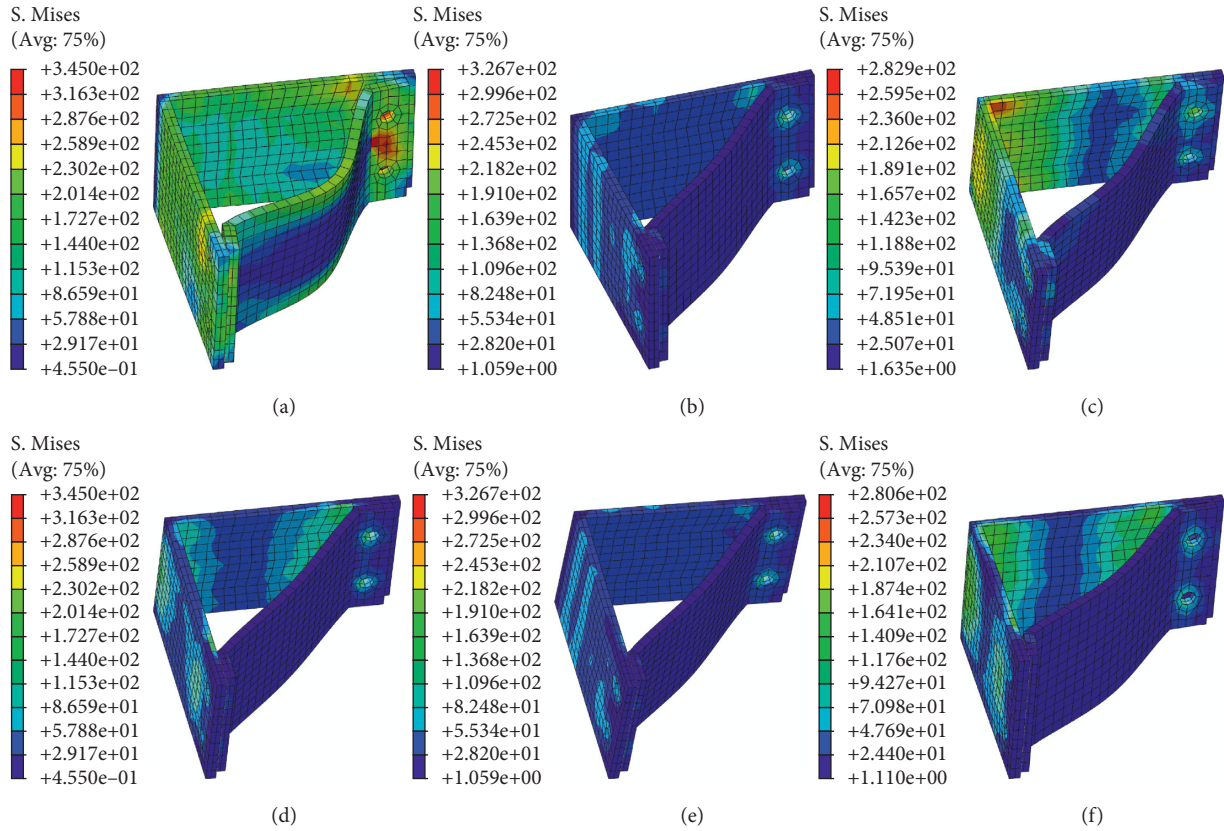
FIGURE 11: Fixture stress contours. (a) L100 × 10G57SR75-1150 end fixture. (b) L100 × 10G57SR75-575 end fixture. (c) L100 × 10G57SR75-385 end fixture. (e) L100 × 10G57SR75-575 middle fixture. (f) L100 × 10G57SR75-385 middle fixture.
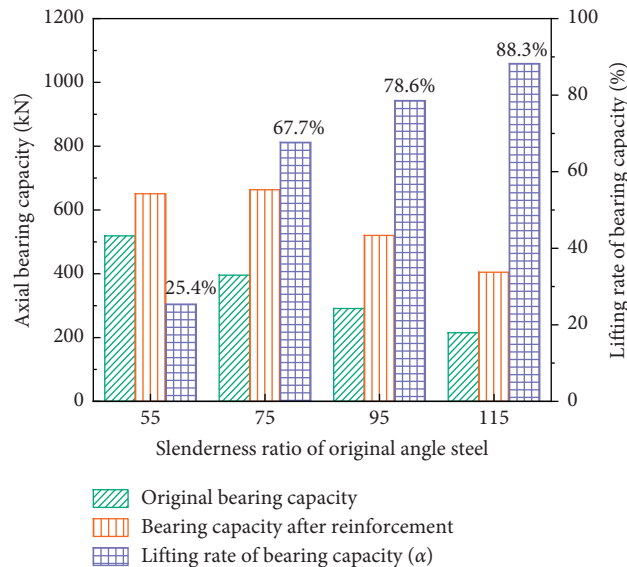
FIGURE 12: Effect of improving the bearing capacity with different slenderness ratios.
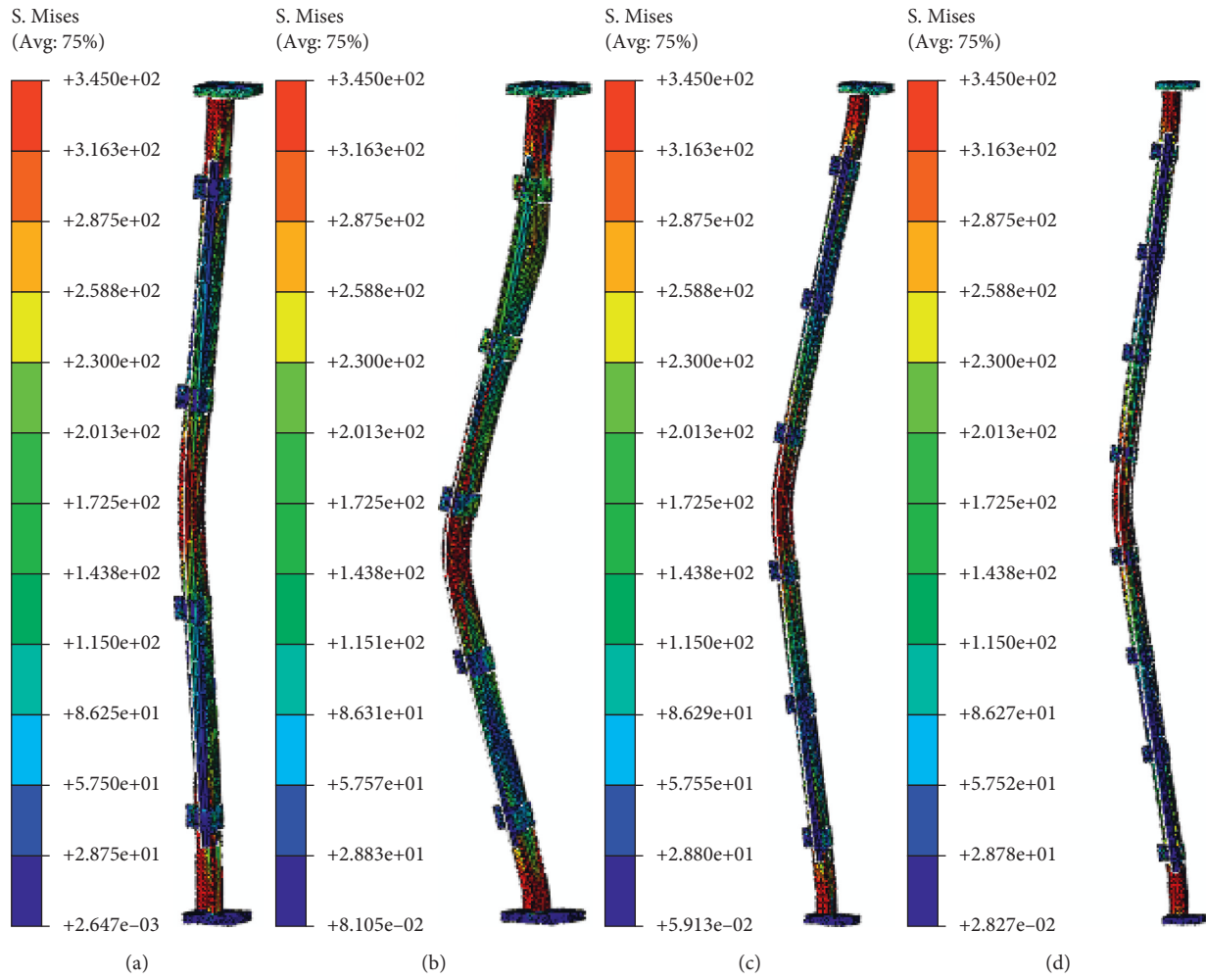
FIGURE 13: Buckling patterns of the members with different slenderness ratios. (a) L100×10G57SR55-575. (b) L100×10G57SR75-575. (c) L100×10G57SR95-575. (d) L100×10G57SR115-575.
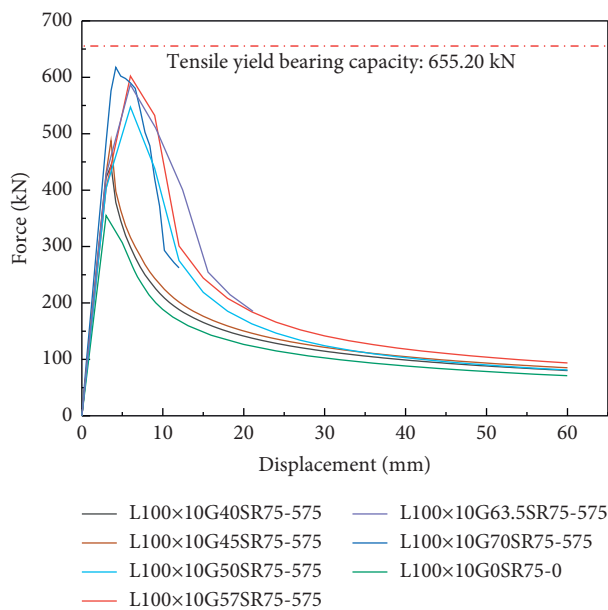
FIGURE 14: Effect of the different specifications of steel pipes on the reinforcement.

pipe is 15.3% of the cross-sectional area of the angle steel member. The steel pipe utilization rate is defined as β.

$$\beta = \frac{\alpha \cdot a_2}{a_1}, \tag{2}$$

where β is the steel pipe utilization rate, α is the angle steel bearing capacity improvement rate, a_1 is the ratio of the steel pipe section area, and a_2 is the angle steel sectional area.

The utilization ratio of steel pipe β is the relative relationship between the lifting ratio of angle steel bearing capacity α and the ratio of steel pipe to the angle steel area. The larger the angle steel bearing capacity increase rate α is, the better the reinforcement effect is. The cross-sectional area ratio of the steel pipe to angle steel reflects the economy of the new reinforcement scheme. The smaller the area ratio is, the lower the reinforcement cost is. The bearing capacity improvement level and reinforcement cost of angle steel are opposite to each other. When other conditions are the same, the larger the bearing capacity improvement rate α is, the larger the cross-sectional area of the steel pipe is needed, and the higher the reinforcement cost is. The smaller the ratio of the cross-sectional area of the steel pipe to the angle steel is, the lower the reinforcement cost is, but the increase rate of the bearing capacity decreases. The utilization ratio of steel pipe β reflects the relationship between the bearing capacity improvement and the reinforcement economy. When the slope of the curve is greater than 0, the growth rate of the bearing capacity improvement rate is greater than the growth rate of the ratio of the section area of the steel tube to the angle steel. Additionally, the larger the slope is, the more obvious the effect of increasing the section area of the steel pipe on the bearing capacity of the angle steel is. When the slope of the curve is less than 0, the increase in the bearing capacity lags behind the growth rate of the ratio of the cross-sectional area of the steel pipe and the angle steel. The smaller slope indicates that increasing the section of the steel pipe has less influence on the bearing capacity of the members.

When selecting steel pipes for reinforcement, it is necessary to make full use of the rising section of the steel pipe utilization curve to avoid excessive reinforcement costs caused by excessive falling sections. As shown in Figure 15, in this study, it is considered that the ratio of the sectional area of the steel pipe and the angle steel corresponding to the top of the rising section is reasonable. The optional section specifications of the steel pipe and angle steel are fixed. Therefore, considering the practical application of engineering, a reasonable ratio range of the cross-sectional area of the steel pipe and angle steel member should be given. The maximum value of steel pipe utilization rate β is 2.35, and the minimum value is 1.39. When steel pipe utilization rate β is greater than 2.0, it can be considered that the steel pipe utilization rate is at a high level. When the steel pipe utilization rate β is greater than 2.0, the corresponding interval of the ratio of the cross-sectional area of the steel pipe to the angle steel component is 17–34%. It can be considered that the reasonable interval of the ratio of the cross-sectional area of the steel pipe to the angle steel is 17–34%. When the

increase in the steel pipe utilization rate is fully utilized, the optimal interval of the ratio of the steel pipe to the angle steel component is 23–34%. This optimal interval not only ensures a high utilization rate of the steel pipe, but also makes the bearing capacity improvement rate as high as possible. When the original angle steel member with a cross-sectional size of L100 × 10 mm is reinforced, the ratio of the cross-sectional area of the selected steel pipe to the cross-sectional area of the angle steel component is within the range of 23–34%, which can guarantee the reinforcement effect and the economy of the reinforcement scheme.

As shown in Figure 16, when the section size of the steel pipe is $D = 70$ mm and the wall thickness is $t = 5.0$ mm, local buckling occurs. When the section size of the steel pipe is $D = 57$ mm and the wall thickness is $t = 4.0$ mm, local buckling occurs slightly in the early stage, and an obvious global buckling characteristic occurs by increasing end displacement. When the section size of the steel pipe is $D = 50$ mm and the wall thickness is $t = 3.0$ mm, the component presents overall buckling characteristics. When the section size of the steel pipe is $D = 40$ mm and the wall thickness is $t = 2.5$ mm, the component also presents overall buckling characteristics. The bending capacity of the steel pipe determines the buckling capacity and buckling form of the angle steel component. When the flexural rigidity of steel pipes with high section sizes is larger, the lateral constraint provided to the original angle steel component is stronger. At this time, the force of the angle steel member on the steel pipe cannot make the steel pipe bend as a whole, and the buckling capacity of the angle steel member is improved. The simulation results show that the larger the size of the steel pipe is, the better the ductility of the angle steel member during buckling is, but the improvement of this ductility is limited. As shown in Figure 14, the force-displacement curves of members L100 × 10G57SR75-575, L100 × 10G63.5SR75-575, and L100 × 10G70SR75-575 decrease slowly with the increasing end displacement after the buckling load reaches a peak. The ductility of the original angle steel member and the member strengthened with a 40 mm external diameter of steel pipe and $t = 2.5$ mm wall thickness is poor. The bearing capacity of the member decreases rapidly with increasing end position after the buckling point. When the steel pipe size increases to an external diameter of $D = 57$ mm and a wall thickness of $t = 4.0$ mm, the ductility of the component is significantly improved. With the increase in the steel pipe size, the ductility of component L100 × 10G70SR75-575 shows no significant improvement compared with that of component L100 × 10G57SR75-575. This indicates that when the steel pipe size increases to a certain value, the improvement in the ductility of the component by continuously increasing the section size of the steel pipe gradually decreases.

Combined with Figure 16, it can be found that the postbuckling ductility is related to the buckling characteristics. The overall buckling deformation of the member is restrained at the initial buckling stage, and local deformation occurs, which can effectively improve the ductility of the member at the initial buckling stage.
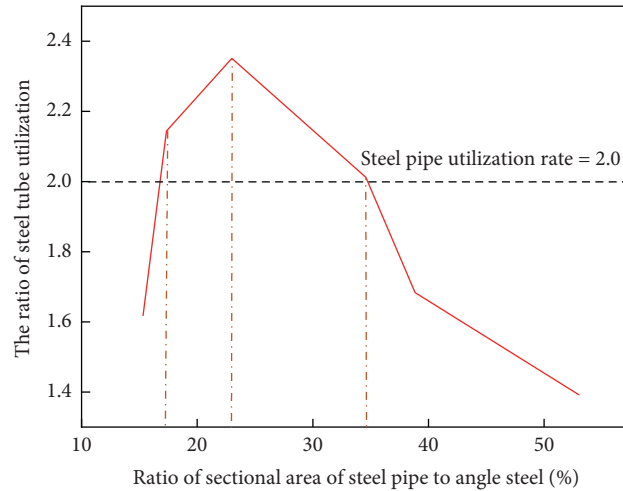
FIGURE 15: Utilization ratio curve of the steel pipe.
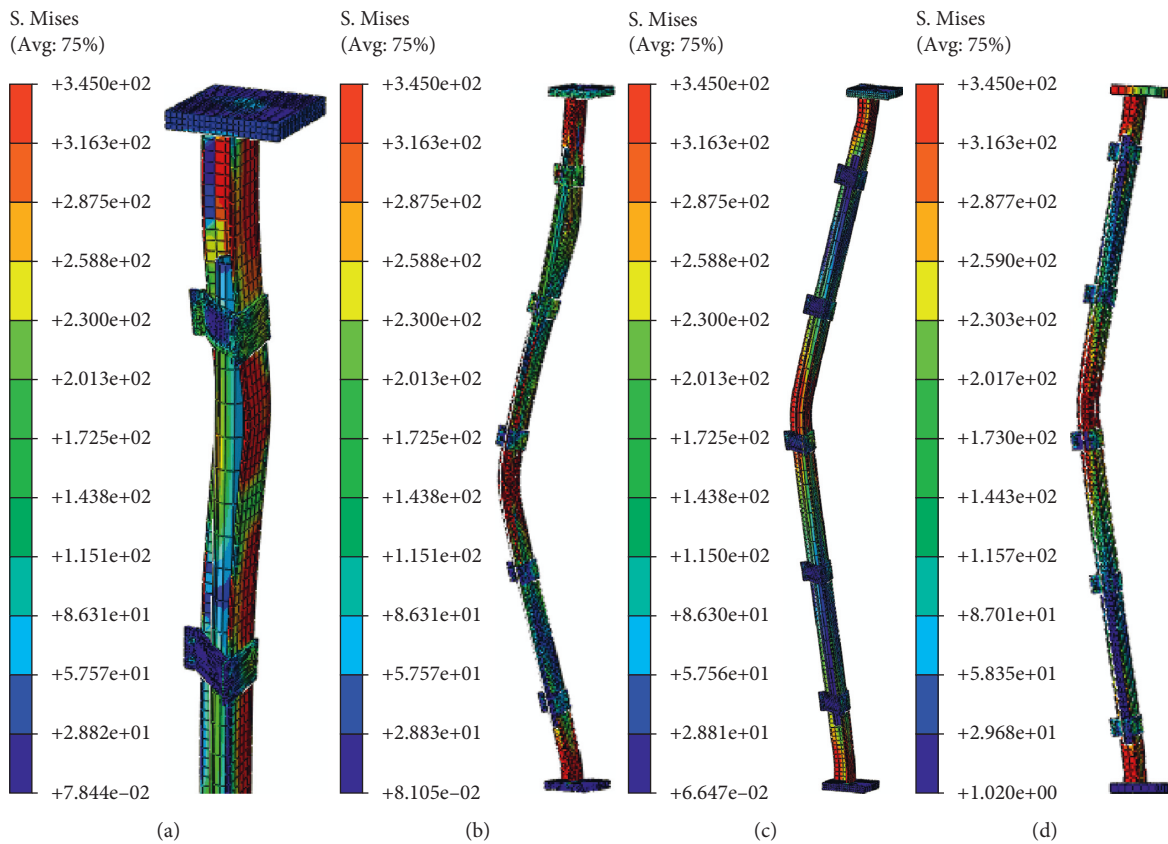
FIGURE 16: Buckling patterns of different steel pipe members. (a) L100×10G70SR75-575. (b) L100×10G57SR75-575. (c) L100×10G50SR75-575. (d) L100×10G40SR75-575.

Through the analysis of various components, considering the reinforcement effect and cost of the new reinforcement scheme, it is considered that it is reasonable to select the cross-sectional area of the steel pipe as 23–34% of the cross-sectional area of the angle steel member. At this time, the reinforcement cost is low, the reinforcement effect is remarkable, and the component shows good ductility when damaged.

4. Conclusions

In this paper, a new buckling bearing capacity enhancement scheme is proposed. The steel pipe is used as the auxiliary material, and the steel pipe is connected with the angle steel member through the clamp, so as to avoid the adverse effect of the bolt connection and welding on the bearing capacity of the original angle steel. The effects of fixture spacing, angle

steel size, member slenderness ratio, and steel pipe speci-fication on the reinforcement effect were studied through numerical analysis. The following conclusions are drawn.

(1) The reinforcement effect is highly correlated with the fixture distance. The smaller the fixture distance is, the greater the improvement rate of the bearing capacity of the component is. and there is a rea-sonable range of fixture spacing.

(2) There is a correlation between the reasonable dis-tance and the width of the reinforced angle steel limb. When the ratio of the fixture distance to the width of the reinforced angle steel limb is less than 5, it is considered that the reinforcement scheme has a good bearing capacity improvement effect, and the bearing capacity improvement rate is greater than 50%.

(3) The slenderness ratio of angle steel affects the re-inforcement effect of the new bearing capacity im-provement scheme. The larger the slenderness ratio of angle steel is, the larger the bearing capacity improvement rate is, and the more obvious the bearing capacity improvement effect is.

(4) Different steel pipe specifications affect the rein-forcement effect of the new scheme. Considering the effect of reinforcement and the economy, it is considered reasonable that the sectional area of the circular steel pipe is 23–34% of the angle steel.

Data Availability

The data used to support the findings of this study are available from the corresponding author upon request.

Conflicts of Interest

The authors declare that they have no conflicts of interest.

Acknowledgments

References

[1] C. Lu, X. Ma, and J. E. Mills, "Modeling of retrofitted steel transmission towers," *Journal of Constructional Steel Research*, vol. 112, pp. 138–154, 2015.

[2] K. M. Alsilevanai and M. Özakça, "Comparison of various bracing system for self-supporting steel lattice structure towers," *American Journal of Civil Engineering*, vol. 5, no. 2, pp. 60–68, 2017.

[3] F. Albermani, S. Kitipornchai, and R. W. K. Chan, "Failure analysis of transmission towers," *Engineering Failure Analysis*, vol. 16, no. 6, pp. 1922–1928, 2009.

[4] N. Hoveidae and B. Rafezy, "Overall buckling behavior of all-steel buckling restrained braces," *Journal of Constructional Steel Research*, vol. 79, pp. 151–158, 2012.

[5] Y. Zhuge, J. E. Mills, and X. Ma, "Modelling of steel lattice tower angle legs reinforced for increased load capacity," *Engineering Structures*, vol. 43, pp. 160–168, 2012.

[6] Q. Xie and L. Sun, "Failure mechanism and retrofitting strategy of transmission tower structures under ice load," *Journal of Constructional Steel Research*, vol. 74, pp. 26–36, 2012.

[7] F. Albermani, M. Mahendran, and S. Kitipornchai, "Upgrading of transmission towers using a diaphragm bracing system," *Engineering Structures*, vol. 26, no. 6, pp. 735–744, 2004.

[8] W. Yang, X. Li, and Y. Yang, "Analysis of weak parts of narrow transmission towers and the reinforcement measure," in *Proceedings of the 2015 Sixth International Conference on Intelligent Systems Design and Engineering Applications (ISDEA)*, pp. 143–146, IEEE, Guiyang, China, August 2015.

[9] Q. Xie and L. Sun, "Experimental study on the mechanical behavior and failure mechanism of a latticed steel trans-mission tower," *Journal of Structural Engineering*, vol. 139, no. 6, pp. 1009–1018, 2013.

[10] P. Feng, S. Bekey, Y.-H. Zhang, L.-P. Ye, and Y. Bai, "Ex-perimental study on buckling resistance technique of steel members strengthened using FRP," *International Journal of Structural Stability and Dynamics*, vol. 12, no. 01, pp. 153–178, 2012.

[11] J. E. Mills, X. Ma, and Y. Zhuge, "Experimental study on multi-panel retrofitted steel transmission towers," *Journal of Constructional Steel Research*, vol. 78, pp. 58–67, 2012.

[12] C. Lu, X. Ma, and J. E. Mills, "Cyclic performance of bolted cruciform and splice connectors in retrofitted transmission tower legs," *Thin-Walled Structures*, vol. 122, pp. 264–285, 2018.

[13] C. Lu, X. Ma, and J. E. Mills, "The structural effect of bolted splices on retrofitted transmission tower angle members," *Journal of Constructional Steel Research*, vol. 95, pp. 263–278, 2014.

[14] E. Baran, T. Akis, G. Sen, and A. Draisawi, "Experimental and numerical analysis of a bolted connection in steel transmis-sion towers," *Journal of Constructional Steel Research*, vol. 121, pp. 253–260, 2016.

[15] Y. Yao, W. Ling Xu, and Z. You Jia, "Stability and rein-forcement analysis of weathering steel high voltage trans-mission tower," *IOP Conference Series: Materials Science and Engineering*, vol. 637, no. 1, Article ID 012009, 2019.

[16] H. C. Yıldırım, H. Remes, and A. Nussbaumer, "Fatigue properties of as-welded and post-weld-treated high-strength steel joints: the influence of constant and variable amplitude loads," *International Journal of Fatigue*, vol. 138, Article ID 105687, 2020.

[17] H. Komatsu, K. Ishii, and A. Fukushima, "Experimental study on buckling strength of angle steel compression members with built-up bracing," *Kou kouzourombunshuu*, vol. 16, no. 62, pp. 62_27–62_34, 2009.

[18] J. Denton, D. Windsor, and J. Mills, "Effectiveness of load sharing connections for the reinforcement of steel lattice tower leg members," in *Proceedings of the Australian Struc-tural Engineering Conference*, p. 1054, Australia, 2005.

Research Article

Study on Progressive Failure of Hard Rock Tunnel After Excavation Under High Stress

Daning Zhong [iD],[1] Jianlin Chen,[1] Hui Zhou [iD],[2] Xiangrong Chen,[1] and Yali Jiang[1]

[1]*PowerChina Huadong Engineering Corporation, Hangzhou 310014, China*
[2]*State Key Laboratory of Geomechanics and Geotechnical Engineering, Institute of Rock and Soil Mechanics,*
 Chinese Academy of Sciences, Wuhan 430071, China

Correspondence should be addressed to Daning Zhong; zhong_dn@hdec.com

The analysis and simulation of brittle failure of hard rock tunnels under high stress is essential for understanding and mastering the brittle failure characteristics of rock masses and for analyzing and regulating the stability of surrounding rocks in underground projects. The rupture and deformation of hard brittle basalt in the dam site area is one of the key problems faced by Baihetan Hydropower Station. In the paper, the spalling characteristics of the surrounding rock on the right bank of the exploratory tunnel are summarized. CDEM (continuum-based discrete element method) is used to carry out the numerical simulation and the fracture energy model considering cohesive force weakening and friction angle strengthening is adopted. The indoor test simulations are conducted first to verify the effectiveness of the model. Then the simulation of the right bank exploratory tunnel is conducted to study the brittle failure of the surrounding rock. The results are compared with the field exposure, and the stress and displacement of characteristic points of the surrounding rock are analyzed. The numerical results are in good agreement with the damage situation in the field and reflect the brittle failure characteristics of basalt under high-stress conditions, which helps to reasonably grasp the damage situation of the surrounding rock and take corresponding support measures, and also proves the superiority of CDEM method in solving hard rock fracture, providing a technical reference for similar hard rock brittle failure problems in engineering.

1. Introduction

Under high-stress conditions, the excavation of hard rock tunnels will cause rapid adjustment of secondary stress field of the surrounding rock, which may lead to damage destabilization phenomena such as local spalling, collapse, or even rock burst of surrounding rock, seriously threatening the project progress and personnel safety [1–3]. Only by fully understanding the damage mode of surrounding rock under different conditions and accurately grasping its damage mechanism, can corresponding control measures be formulated to ensure engineering safety. Therefore, it is necessary to gain better insight into the failure characteristics and mechanisms of hard rock tunnels [4, 5].

In recent years, many scholars have performed uniaxial compression [6], biaxial compression [7], and true-triaxial unloading tests [8, 9] on rock or rocklike specimens to simulate the spalling failure of the tunnel, but these studies focused on the material failure and did not consider the effects of the tunnel space structure. To analyze the influence of tunnel space structure on hard rock fracture, some scholars have employed rock specimens with a central hole to simulate the failure behavior of tunnels at a laboratory scale and focused on the crack propagation around the holes [10–12].

Because of the difficulties in reproducing the failure characteristics during laboratory tests and the rapid development of computational capacity, numerical methods have been increasingly used to simulate the failure characteristics of hard rock tunnels. The most representative work is the research related to the damage of the Canadian underground test tunnel. Martin firstly studied the cohesion loss and stress path effect of hard rock rupture in 1997 [13], based on which Hajiabdolmajid et al. [14, 15] proposed the CWFS (cohesion

weakening and friction strengthening) model, Diederichs et al. [16, 17] proposed DISL (damage initiation and spalling limit) model to reproduce the formation of V-shaped damage zone. With reference to the CWFS model, Jiang et al. [18] proposed the hard rock intrinsic model, considering the effect of surrounding rock deterioration. All of the above are developed in the context of continuous media. However, because the displacement of adjacent interfaces must be coordinated in FEM, it is challenging to reach convergence in simulations. Some scholars adopted discrete-based methods such as PFC2D [19], DEM [20, 21], and DDA [22] to study related fracture issues in hard rock. However, the entire failure process from continuum to discontinuum in these studies was not captured. So, the combined finite discrete element method has been gradually confirmed and adopted by scholars to solve related problems [23–26]. For example, Zhong et al. [23] and Vazaios et al. [24] adopted the finite discrete element method to reproduce the V-shaped failure of the URL test tunnel.

Baihetan hydropower station in China is the largest power station under construction, and the underground powerhouse area is a high ground stress area with four types of basalt erupted at the dam site with internal crypto microfracture developed and elastic-brittle damage characteristics, determining that Baihetan is facing the critical rupture deformation problem of hard, brittle surrounding rocks [27]. Based on this, many scholars have carried out indoor uniaxial and triaxial tests to study the basic mechanical characteristics of basalt [28, 29]. Besides, during the excavation of the powerhouse, many typical hard rock damage phenomena such as spalling, rupture, and spray layer cracking have occurred [30, 31]. So, it is necessary to study the fracture deformation of hard, brittle basalt surrounding rocks.

In order to deeply study the brittle failure characteristics of basalt under high stress, several exploratory tunnels were arranged on each side of the left and right banks of the dam site area. In this paper, we first introduce the exploratory tunnel arrangement and the damage of the surrounding rock in exploratory tunnels. Then select the brittle intrinsic model and use CDEM [32] to compare indoor tests and numerical simulations for model validation. Lastly, simulate the exploratory tunnel excavation, analyze the brittle failure process of the surrounding rock, compare it with the field exposure, and analyze the stress and displacement of the surrounding rock in order to better recognize the brittle failure characteristics of basalt under high-stress conditions, and at the same time provide a reference for similar damage cases encountered in engineering.

2. Overview of Baihetan Underground Exploration Tunnels

2.1. Background of the Project. Baihetan Hydropower Station is one of the four-step power stations in the lower reaches of the Jinsha River, which will become the second-largest giant hydropower station after the Three Gorges after completion. In order to analyze the distribution of ground stress on the left and right banks, several exploratory tunnels are laid on

each bank, and their location distribution is shown in Figure 1. The right bank tunnels consist of PD62 and its branch tunnels, which are mainly divided into four different orientations on the plane, among which PD62-2 is axially N80°E, orthogonal to the axis of the main tunnel, while PD62-4 and PD62-3 are axially N10°W, in line with the direction of the main tunnel. The left bank tunnels consist of PD61 and its branch tunnels; the orientations are not discussed here.

2.2. Spalling Characteristics of the Right Bank Exploration Tunnel. This paper takes the exploratory tunnels on the right bank as a research object. A detailed investigation of the spalling characteristics, including spatial distribution and intensity level, of the five exploratory tunnels, has been obtained, as shown in Figure 2.

The spalling is the direct manifestation of hard, brittle basalt under the action of large initial in-situ stress. The overall spalling on the right bank shows two basic patterns as follows:

(1) The relationship between the spalling intensity of the exploration tunnel is

$$PD62 - 2 \approx PD62 > PD62 - 1 > PD62 - 3 \approx PD62 - 4. \tag{1}$$

(2) The spalling in PD62-2 is located in the top arch of the exploratory tunnel, while the spalling in the rest of the exploratory tunnels is generally inclined to the side arch on the upstream side of the river valley, as shown in Figure 3. The maximum spalling depth in PD62-2, PD62, PD62-1, and PD62-4 is 0.7 m, 0.7 m, 0.5 m, and 0.7 m, respectively. Regarding damage morphology, the spalling in both PD62-2 and PD62 shows typical V-shaped features, with the tip of the V shape extruding a distinct rupture shape and a large rupture depth. The spalling in PD62-1 also shows a typical V shape in general, but the tip morphology is poorer and slightly flatter compared to PD62-2 and PD62. Influenced by the gently inclined structural surface, the spalling of PD62-4 is significantly different from the other three tunnels. Although the most intense spalling part in PD62-4 also has a greater rupture depth, the morphology is much more soothing than the above tunnels. So the deeper spalling in PD62-4 can be considered as a special case, and will not be considered in the paper.

3. Mechanical Model of Basalt and Model Validation

3.1. Mechanical Model. The strain-softening model is commonly used to represent the postpeak weakening characteristics of rock mass in conventional continuum analysis. The strain-softening model assumes that the cohesion and frictional strength of the rock mass constitute its peak strength before plastic deformation occurs, and then both start to lose simultaneously and gradually decrease with
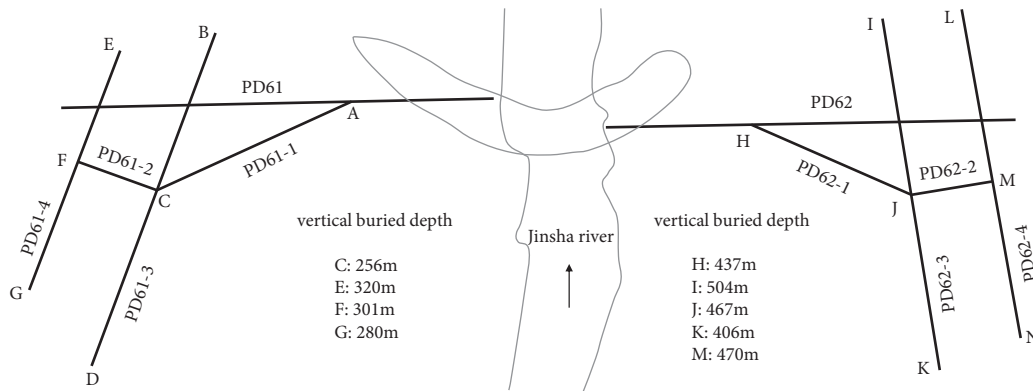
FIGURE 1: Distribution of exploration tunnels on the left and right bank.
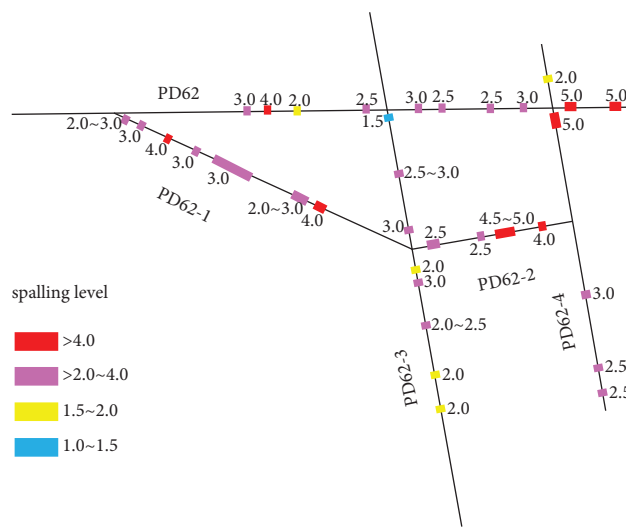
FIGURE 2: Spalling features of the tunnels on the right bank.
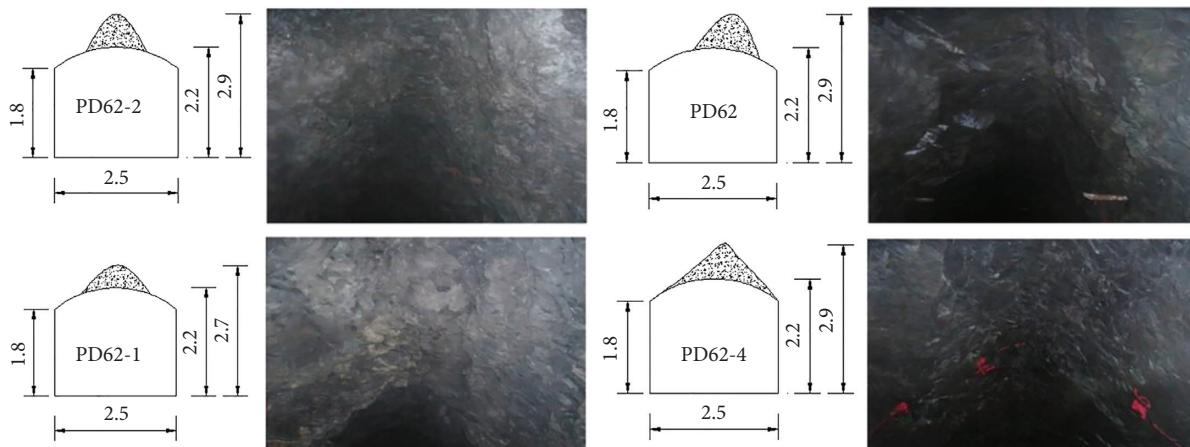
FIGURE 3: Spalling features of tunnels on the right bank.

increasing strain. However, Martin [13] found in their study of the URL test tunnel that only the cohesive force comes into play at the initial moment and gradually decreases with the development of damage, while the frictional strength comes into play and gradually increases with the development of damage, i.e., the CWFS model. Hajiabdolmajid et al. [14, 15] reproduced the V-shaped damage of the URL test tunnel based on CWFS, verifying the accuracy and feasibility of CWFS in simulating the deformation damage of the granite in the URL tunnel.

After summarizing the results of cyclic loading and unloading tests of amygdaloidal basalt, Chang [28] obtained the evolution of cohesion and internal friction angle with internal variables by fitting plastic internal variables based on the M-C yield criterion. The fitting results confirm that basalt also has similar properties to CWFS. This property must be considered in the calculation to describe the brittle damage behavior of basalt.

In CDEM, the intrinsic model is implemented in the following way: the finite element part uses a linear elastic model, and the elastic intrinsic incremental relations are

$$\Delta\sigma_{ij} = \left(K - \frac{2}{3}G\right)\Delta\theta\delta_{ij} + 2G\Delta\varepsilon_{ij}. \tag{2}$$

$\Delta\sigma_{ij}$, $\Delta\varepsilon_{ij}$ refer to the average stress increment and average strain increment. $\Delta\theta$ is the volumetric strain increment. K and G are the bulk modulus and shear modulus of the material, respectively.

The fracture energy model is used for the discrete element part, which is essentially the maximum tensile stress model, and the M-C model, considering the linear softening effect of strength and the strengthening effect of friction angle. Firstly, the normal and tangential contact forces at the next time step on the interface are calculated using the incremental method as follows:

$$\begin{cases} F_n(t_1) = F_n(t_0) - K_n \times \Delta d_n, \\ F_s(t_1) = F_s(t_0) - K_s \times \Delta d_s. \end{cases} \tag{3}$$

F_n, F_s are the normal and tangential force; K_n, K_s are the normal stiffness and tangential stiffness, which are obtained by inheriting from the element stiffness. Δd_n, Δd_s are the relative displacement increments in normal and tangential directions. Subsequently, equation (4) is used for the determination of tensile damage and the correction of normal contact force and tensile strength.

$$\begin{cases} \text{if} - F_n(t_1) \geq \sigma_t(t_0)A, \\ \\ F_n(t_1) = -\sigma_t(t_0)A, \quad \sigma_t(t_1) = -\frac{\sigma_0^2}{2G_t}d_n + \sigma_0. \end{cases} \tag{4}$$

σ_0, $\sigma_t(t_0)$, and $\sigma_t(t_1)$ are the tensile strength of the interface at the initial time, this time, and the next time, respectively; d_n is the normal relative displacement on the interface at this time; G_t is the tensile fracture energy; and A is the area of the interface.

Equation (5) is used for the determination of shear damage and the correction of tangential contact force and cohesive force and internal friction angle.

$$\begin{cases} \text{if } F_s(t_1) \geq F_n(t_1)\tan\varphi + c(t_0)A, \\ \\ F_s(t_1) = F_n(t_1)\tan\varphi + c(t_0)A, \\ \\ c(t_1) = -\frac{c_0^2}{2G_s}d_s + c_0, \\ \\ \varphi(t_1) = n\varphi_0 \,(n \geq 1). \end{cases} \tag{5}$$

c_0, $c(t_0)$, and $c(t_1)$ are the cohesion of the interface at the initial time, this time, and the next time, respectively; d_s is the tangential relative displacement on the interface at this time and G_t is the shear fracture energy. φ_0 is the internal friction angle on the interface at the initial moment; n is the multiplication of the increase of internal friction angle, the value of which depends on the specific analysis.

3.2. Model Validation. In order to verify whether the above model can reflect the characteristics of the mechanical behavior of basalt under different confining pressures, the triaxial test curves of basalt with confining pressures of 0, 10, 30, and 70 MPa are compared with the numerical simulation curves, as shown in Figure 4. Among them, when the confining pressure is between 0 MPa and 10 MPa, the compaction section of the test curve is significant. Regardless of this compression deformation, the numerical simulation is compared with indoor test results, as shown on the right side of Figures 4(a) and 4(b). It can be seen from Figure 5 that numerical simulation curves of the fracture energy model can match well with test curves, indicating that the model can better reflect the brittle fall process of basalt under different confining pressures.

4. Numerical Simulation of Exploration Tunnel

4.1. Geometric Model. In discontinuous analysis, the good or bad calculation results are closely related to the element size. Referring to the numerical simulation of the URL test tunnel in Canada by Vazaios [24], the grid is divided as shown in Figure 5.

According to the actual excavated dimensions of the exploration tunnel, the simulated sidewall height of the exploration tunnel is 1.8 m, the top height is 2.2 m, and the bottom side width is 2.5 m. The size of the whole model section is 40 m × 40 m. Area 1 is the cave-shaped part to be excavated off, and its grid size transitions from 0.2 m to 0.03 m. Area 2 is a square area adjacent to the cavity, where the cracks appear first during excavation, with a section of 10 m × 10 m, and a small enough grid size of 0.03 m to accurately capture the crack expansion. The section of area 3 is 20 m × 20 m, with the grid size from 0.03 m to 1.5 m; area 4 is 40 m × 40 m, with the grid size from 1.5 m to 2.5 m. The total number of elements is 299662.

4.2. Geostress and Boundary Conditions. Taking PD62-2 exploratory tunnel as the simulation object, the geostress direction is approximated as follows [33]: the maximum principal stress orientation is in the N-S direction, the dip angle is nearly horizontal, and the size is 26 MPa; the middle principal stress is nearly horizontal, and the size is 18 MPa; the minimum principal stress is vertical, and the size is 10 MPa.

The boundary conditions adopted in the calculation are: a normal displacement constraint is applied at the bottom, a surface force of 26 MPa is applied at the left and right sides, and a surface force of 10 MPa is applied at the top.
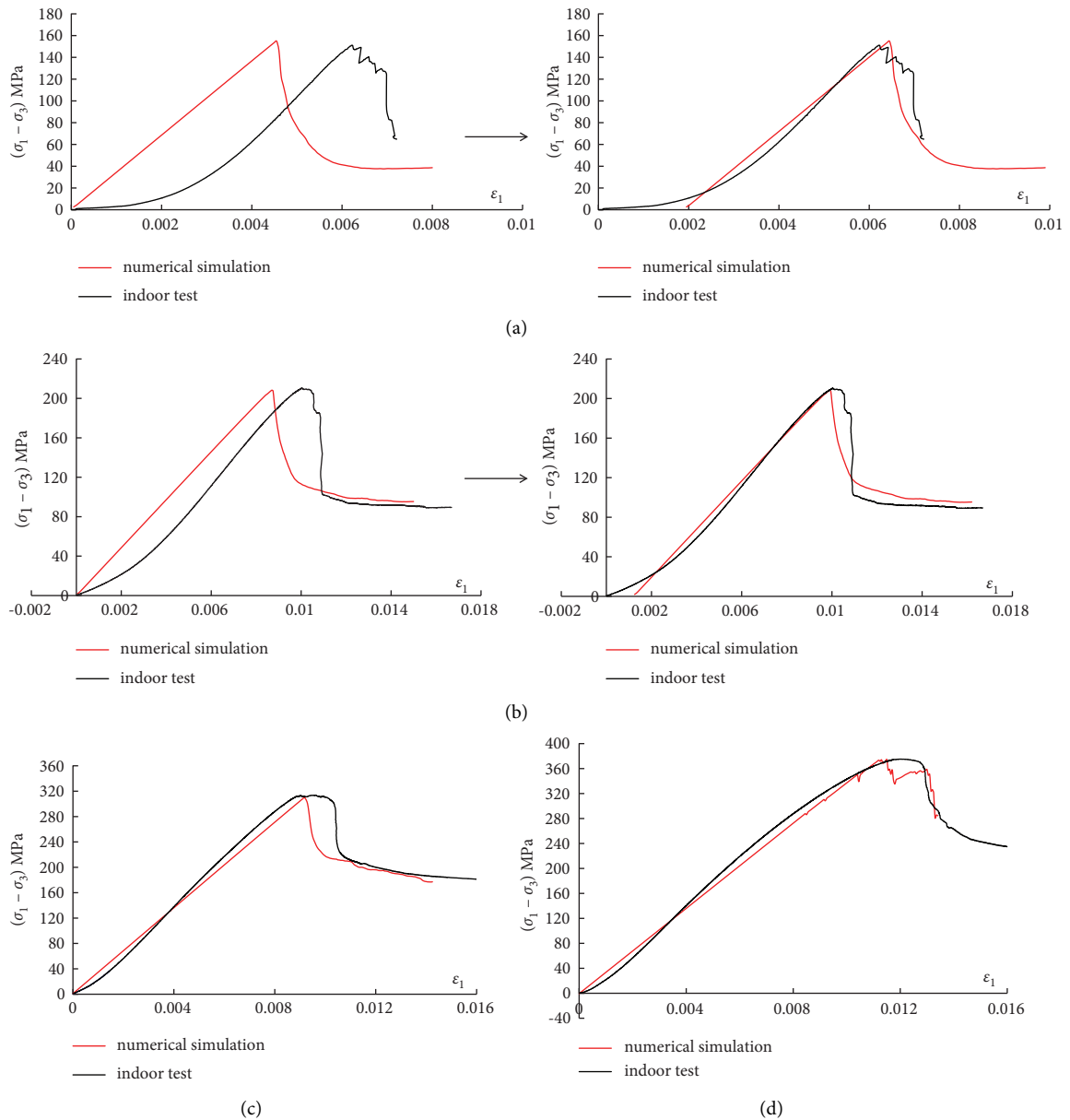
FIGURE 4: Contrast between numerical simulation and rock experiments under different confining stresses: (a) confining stress 0 MPa, (b) confining stress 10 MPa, (c) confining stress 30 MPa, and (d) confining stress 70 MPa.

4.3. Calculation Steps and Mechanical Parameters. Before the start of excavation calculation, the initial stress field of the model needs to be obtained first. The whole calculation process lasts for 800000 steps. Then the excavation of the exploratory tunnel is carried out. In order to eliminate the 3D effects caused by the actual excavation and to ensure the accuracy of the 2D calculation results, Vlachopoulos and Diederichs [34] proposed four methods to achieve the approximation of the 2D simulation to the 3D excavation. Curran et al. [35] introduced the face replacement method in detail.

In this paper, the face replacement method will also be used to approximate the 3D excavation effect. In brief, it is to continuously weaken the deformation modulus of the element in area 1, and after each modulus replacement, 5000

steps are calculated to reach a temporary equilibrium, and so on for five times. Eventually, the elements inside the exploratory tunnel are excavated one at a time, and then 10,000 steps are calculated to observe the fracture evolution of the surrounding rocks.

After several trial calculations for parameter adjustment, the final mechanical parameters used in the numerical simulation are shown in Table 1. The deformation modulus replacement is shown in Table 2.

5. Results Analysis

5.1. Fracture Evolution of Surrounding Rock. Figure 6 shows the evolution process of internal cracks in PD62-2, obtained by numerical simulation. The initial time step of formal
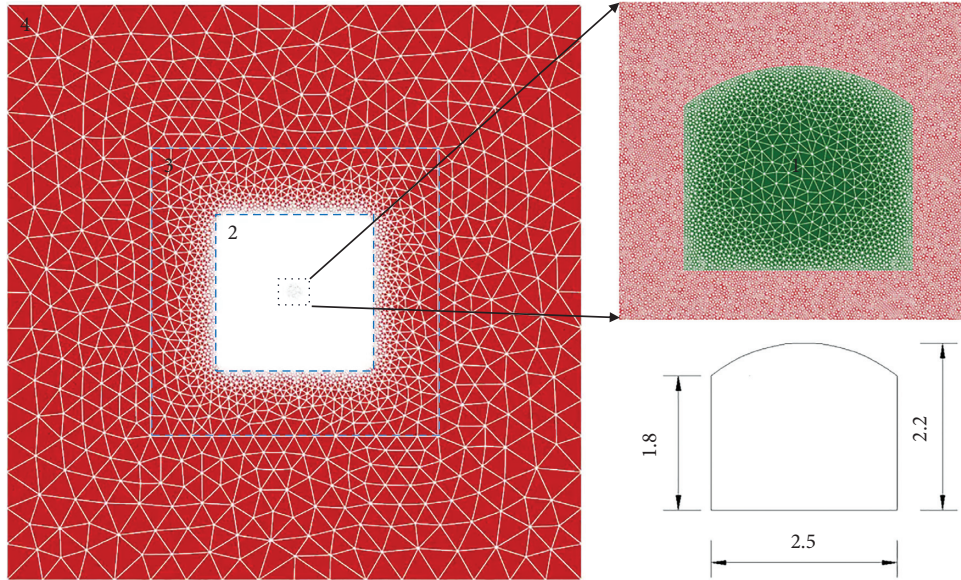
FIGURE 5: Model of numerical simulation.

TABLE 1: Microparameters for simulation.

Parameters	Values
Density ρ/kg/m^3	2800
Initial deformation modulus E/GPa	10
Poisson's ratio ν	0.25
Cohesion c/MPa	25
Tensile strength of intact rock σ_{ti}/MPa	8
Internal friction angle at initial time φ°	5
Multiplication of the increase of internal friction angle n	10
Dilatancy angle ψ°	10
Tensile fracture energy/Pa.m	50
Shear fracture energy/Pa.m	500

TABLE 2: Deformation modulus used in different stages.

The stages of simulated excavation	1	2	3	4	5
Elastic modulus/GPa	5	3	1	0.5	0.1

excavation is 825100, and the results are output every 1000 steps, for a total of 10 times.

As can be seen from the figure, the cracks first appeared at the bottom corners of the left and right sidewalls. Then, with the expansion of cracks at the bottom, small cracks began to appear at the top of the exploratory tunnel. With the advancement of the calculation step, cracks at the bottom and the top arch gradually expanded and connected. When calculating 10000 steps, that is, the total number of calculation steps is 835100, the crack propagation of the bottom and top arch basically reaches a stable state. At this time, the top arch forms a much more significant V-shaped failure, and the rock mass is broken and spalled. The cracks on both sides of the bottom also gather and connect to the middle depth, forming the shape of V-shaped cracks, but the rock mass is significantly less broken than the top arch.

During the calculation, the damage of the one-dimensional spring, i.e., contact element, is monitored. Three variables are statistically output, as shown in Figure 7. Among them, the total damage of spring is the proportion of elements that have been damaged. The total rupture of a spring is the proportion of elements that have not only been damaged but also have had their cohesion and tensile strength reduced to zero. The current damage of spring is the proportion of elements that are now in a damaged state. It can be seen from the figure that after the tunnel starts excavation, all three curves increase continuously with the advance of calculation steps. Before the 831500 calculation steps, the failure speed of the spring was faster; after that, the failure speed of the spring gradually decreased, and finally showed a convergence trend. Among them, the current damage ratio of the spring almost stops increasing, which has good correspondence with Figure 7.

5.2. Comparison between Simulated and Observed Fracture.

We compare the failure of the exploratory tunnel finally obtained by numerical calculation with the field observation, as shown in Figure 8. As for the top arch, the numerical results are in good agreement with the field observations. The maximum depth of crack extension is about 0.7 m, and the failure depth of the top of PD62-2 is also about 0.7 m. The crack range of the crown arch calculated by numerical calculation is slightly larger than the field observation results, but under the combined action of surrounding rock stress and self-weight stress, the surrounding rock spalling and falling are concentrated in the core area of the crown arch, which is consistent with the field observation. In the numerical calculation, the bottom plate of the exploration tunnel also forms a penetrating crack, and the final shape is roughly V-shaped. This is because the stress boundary conditions applied in this paper are generally symmetrical, so the calculated failure area is also generally symmetrical. However, unlike the top arch, the bottom plate does not form a significant crushing failure.
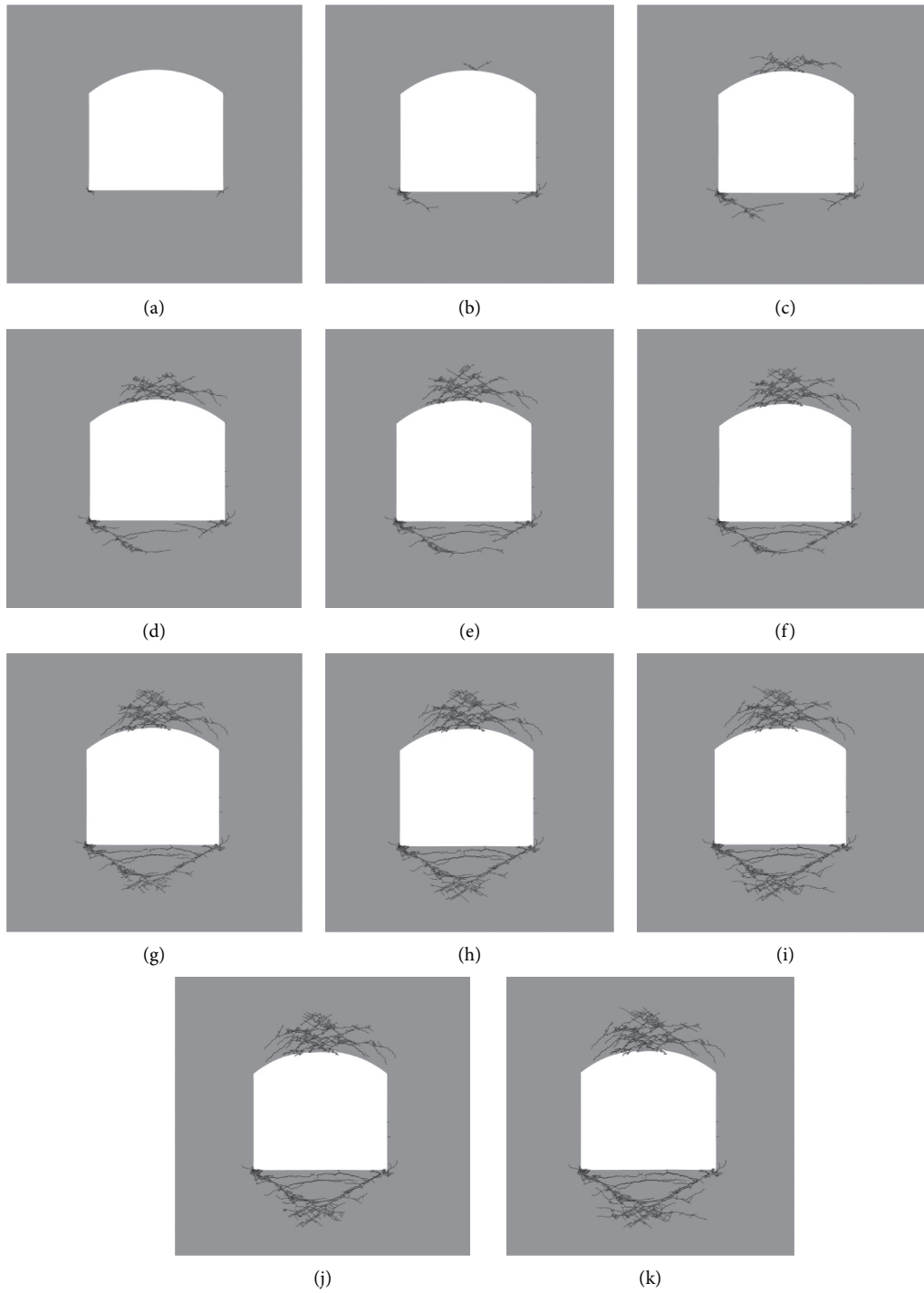
Figure 6: The evolution of cracks in PD62-2: (a) 825100, (b) 826100, (c) 827100, (d) 828100, (e) 829100, (f) 830100, (g) 831100, (h) 832100, (i) 833100, (j) 834100, and (k) 835100.

In general, the numerical results can better reflect the spalling failure of the surrounding rock, and the calculation results are reliable.

5.3. Stress Analysis of Surrounding Rock. In order to further analyze the calculated damage to the top arch and bottom floor of the surrounding rock, 6 measurement points were taken at different depths of the top arch and bottom floor, respectively. Among them, the distance from the top arch 1#~6# to the tunnel top is 0 m, 0.3 m, 0.4 m, 0.5 m, 0.7 m, and 1 m, respectively; the distance from the bottom floor 1#~6# to the tunnel bottom is 0 m, 0.5 m, 0.6 m, 0.9 m, 1.0 m, and 1.1 m, respectively. The evolution curves of the minimum principal stress of each measurement point at the top and bottom of the tunnel with the calculation step after tunnel
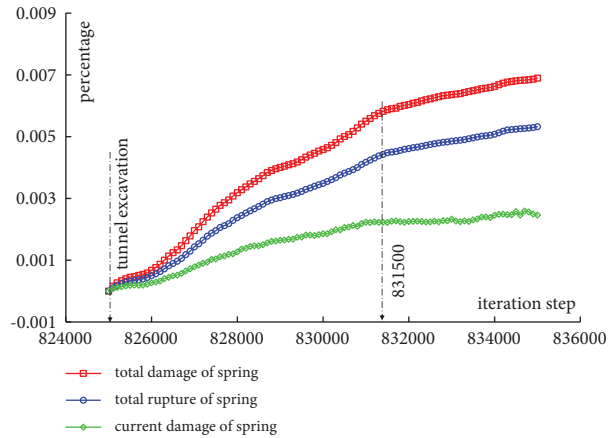
FIGURE 7: The statistics of spring rupture.
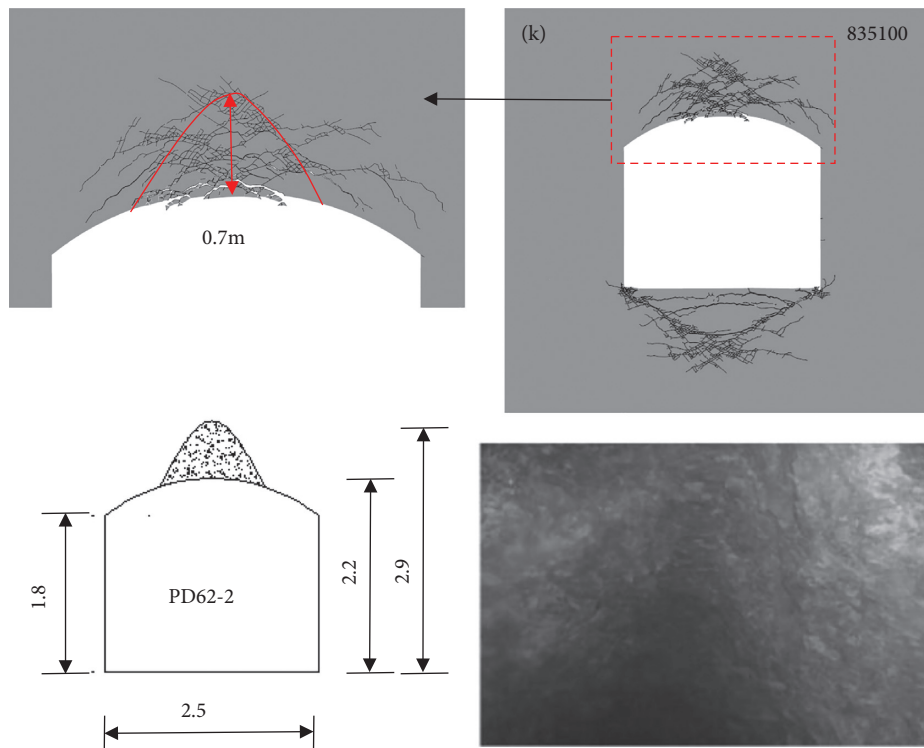
FIGURE 8: Comparisons of calculated results and field phenomena of spalling failure in PD62-2.

excavation are counted. The analysis results are shown in Figure 9.

Firstly, for the top arch, the trend of the minimum principal stress at measurement points 1#~5# is to increase gradually with the excavation, and then to decrease at a certain point, and the deeper the measurement point is buried, the less significant the drop. At measurement point 6#, the minimum principal stress no longer has a drop process, but always grows slowly with the iteration step. The crack expansion pattern at the moment of stress drop from 1# to 5# measurement points is plotted on the top of the curve, and it can be seen from the figure that the moment when the stress starts to drop is the moment when the crack starts to expand at that location, and the position of each measurement point

in the figure coincides with the crack boundary. We take the 1# measurement point as an example, which is a point close to the tunnel top. When the tunnel is first excavated, the minimum principal stress at this point gradually increases. It can be seen from Figure 6 that there is no crack at the top of the tunnel at the initial time, and the stress is accumulating. When the calculation reaches 826400 steps, the minimum principal stress begins to fall rapidly, and cracks are produced here due to the rapid release of energy. The cracks continue to expand and connect in the subsequent process, and the minimum principal stress has been at a low level and no longer rises. 2#~5# measurement points can be analyzed similarly. Finally, when the calculation stops at 835100 steps, that is, the crack is in a stable state, the minimum principal
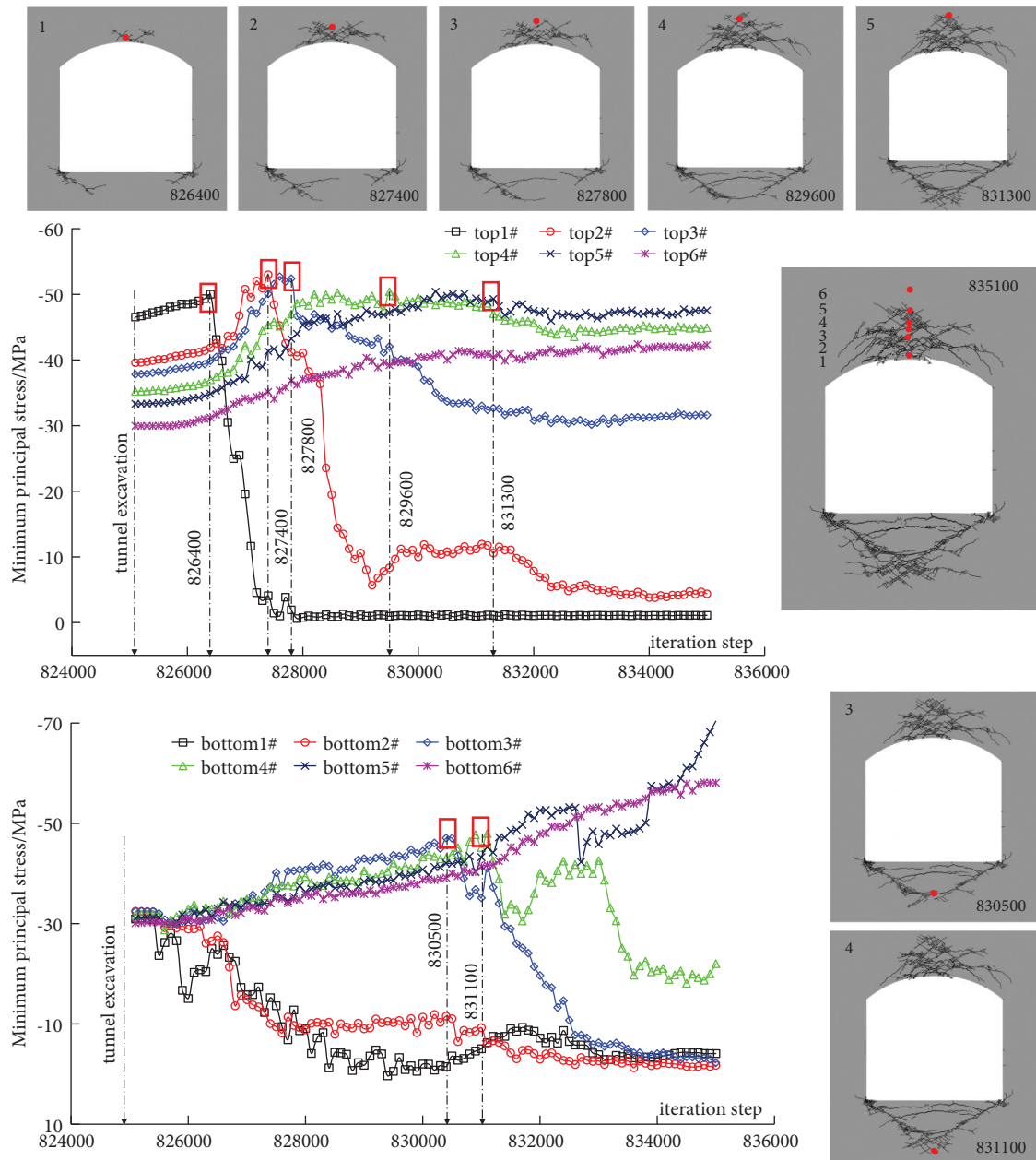
FIGURE 9: The principal stress curve at characteristic points of the surrounding rock mass.

stress at each measurement point also reaches a stable state, and the crack extends to the vicinity of measurement point 5#, the buried depth of this point is about 0.7 m, which is consistent with the measured failure depth, further verifying the accuracy of the calculation.

The minimum principal stress of each measurement points on the bottom floor can be roughly divided into three cases: (1) the principal stress of measurement points 1# and 2# always decreases slowly; (2) the principal stress of measurement points 3# and 4# increases first and then decreases; and (3) the principal stress of measurement points 5# and 6# always increases slowly. Among them, due to the unloading effect of tunnel excavation, cracks start to appear at the bottom of the tunnel at the beginning, and initially penetrate at 829100 steps, forming a V-shaped failure. 1# and

2# measurement points are located on the inner side of the V-shaped failure, so the principal stress decreases continuously with the unloading. While 3# and 4# measurement points are located on the outer side of the V-shaped failure, the crack gradually expands deeper as the iteration proceeds until 830500 and 831100 steps, when 3# and 4# measurement points begin to show stress drop one after another. Since the maximum depth of crack propagation is near measurement point 4#, no cracks are generated at measurement points 5# and 6#, and their principal stresses keep growing slowly.

5.4. Deformation Analysis of Surrounding Rock. Similar to the stress analysis of surrounding rock, 6 measurement points are taken at different depths of the tunnel top and
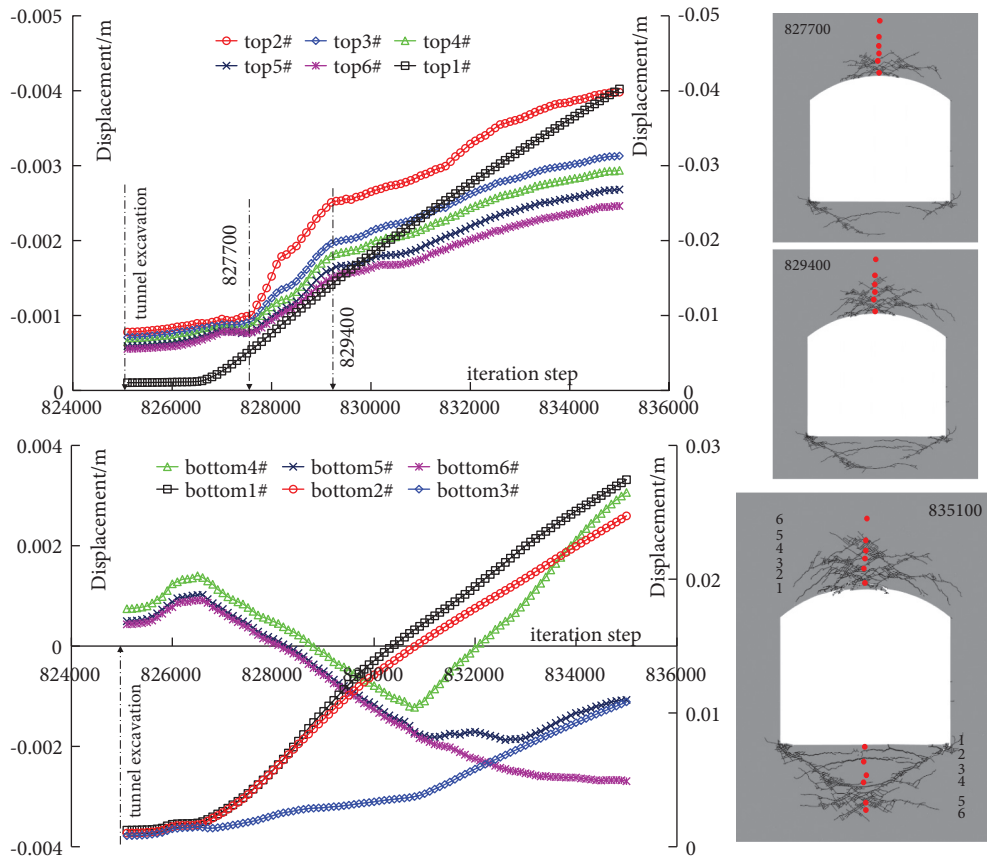
FIGURE 10: The displacement curve at characteristic points of the surrounding rock mass.

bottom to analyze the surrounding rock deformation. Among them, the distribution of measurement points from 1# to 6# in the top arch is the same as that in the stress analysis, and the distance of each point from 1#~6# in the tunnel bottom is 0 m, 0.2 m, 0.4 m, 0.5 m, 0.8 m, and 0.9 m, respectively. The evolution curves of the vertical displacement of each measurement point at the top and bottom of the tunnel with the calculation step after tunnel excavation are counted. The analysis results are shown in Figure 10.

Firstly, for the top arch, the vertical displacement of measurement points 1#~6# shows an increasing trend in general, indicating that with the continuous sprouting, expansion, and connection of cracks, the surrounding rock is continuously spalling downward, resulting in the increasing vertical displacement. Among them, the vertical displacement of measurement point 1# is one order of magnitude higher than that of other measurement points, because the point is close to the free face of the tunnel top, and the point is most vulnerable to the unloading effect. The vertical displacement of measurement points 2#~5# begins to increase rapidly at 827700 calculation steps, and the growth rate begins to slow down at 829400 calculation steps. It can be seen from Figure 6 that the interval between 827700 and 829400 steps is the stage of rapid crack propagation at the tunnel top. After 829400 steps, the V-shaped failure of the crack has been formed, the crack propagation speed gradually slows down, and the growth trend of vertical

displacement is basically consistent with the propagation trend of the crack.

Similar to the minimum principal stress distribution law of the bottom floor, the vertical displacement of each measurement point of the bottom floor can be roughly divided into three cases: (1) the vertical displacement of measurement points 1#, 2#, and 3# always increases slowly; (2) the vertical displacement of measurement points 4# and 5# decreases first and then increases; and (3) the vertical displacement of measurement point 6# always decreases slowly. Among them, 1#, 2#, and 3# measurement points are in the inner side of the V-shaped failure of the bottom floor. With the tunnel excavation and unloading, the bottom floor crack penetration causes the bottom floor to bulge upward. Therefore, the vertical displacement of these three measurement points is increasing in the upward direction. Moreover, the displacement growth rate of 1# and 2# is larger than that of 3#, which conforms to the law that the closer to the free surface, the larger the displacement is. 4# and 5# measurement points are located in the area covered by the continuous expansion of subsequent cracks. When there is no crack, the overall displacement direction is downward under the action of self-weight stress. After the crack is generated, the displacement direction changes to upward and keeps growing. The 6# measurement point is located at the crack boundary during stable propagation, and its vertical displacement is less affected by crack propagation, and the displacement direction is always downward.

In general, the trend of stress and deformation at characteristic points of surrounding rock can better reflect crack propagation, which proves that the calculation results are reliable.

5.5. Essence of the Spalling. According to the stress and deformation analysis, the essence of spalling can be obtained. The underground tunnel produces stress unloading during excavation. Before the tunnel excavation, the rock mass only bears the action of the initial stress and is in a stable state of three-dimensional compression. After the excavation, the rock mass around the tunnel is unloaded, all the in-situ stress around the tunnel is released, and the rock mass is in a two-dimensional or one-dimensional stress state. The original equilibrium state of the surrounding rock stress field is broken, and the original approximately uniform initial stress field becomes an obvious uneven stress field. Stress concentration occurs in some surrounding rock areas, and the stress concentration areas continue to migrate to the interior of the surrounding rock, resulting in a certain high-stress area in the interior of the surrounding rock. When the adjusted stress state reaches the limit state of rock mass, the rock mass is damaged, and cracks begin to form in the surrounding rock of the tunnel boundary with the highest stress concentration and expand with the increase in pressure. It can be seen that the stress mutation caused by tunnel excavation and unloading, and local high stress, are the main causes of surrounding rock damage.

At the same time, the progressive failure of the surrounding rock is also reflected by the simulation of the roof spalling process. Firstly, the stress of the surrounding rock begins to adjust after the excavation of the exploratory tunnel, and the tangential stress of the top arch keeps increasing while the vertical stress keeps decreasing, resulting in circumferential splitting cracks in the hard, brittle basalt of the top arch. Furthermore, the deterioration of the stress condition of the top arch and the further deterioration of the surrounding rock make the splitting cracks propagate to the depths and the oblique intersecting shear cracks appear. Finally, the further propagation of shear cracks provides boundary conditions for the falling of flake rocks, resulting in the spalling of surrounding rock.

6. Conclusions

As the largest hydropower station under construction, the failure simulation of the hard, brittle surrounding rock in Baihetan underground exploration tunnel is of great significance to reveal the brittle failure characteristics of basalt. In this paper, the brittle constitutive model of basalt is studied in depth. The finite discrete element method CDEM is used to simulate the brittle failure of the surrounding rock, analyze the stress and displacement of the characteristic points, and compare them with the in-situ observed failure so as to test the rationality of the in-situ stress, constitutive model, and mechanical parameters. The main conclusions are as follows:

(1) The finite discrete element method (CDEM) is used to simulate the indoor uniaxial and triaxial tests. The fracture energy constitutive model considering cohesion weakening and friction angle strengthening can better simulate the brittle failure behavior of basalt under different confining pressures.

(2) In the numerical simulation of the exploratory tunnel, the maximum depth of crack propagation in the top arch of PD62-2 is about 0.7 m, which is consistent with the depth of surrounding rock spalling observed in the field. The stress and displacement of surrounding rock characteristic points further verify the accuracy of the calculation, which strongly illustrates the reasonableness and practicability of the constitutive model and mechanical parameters adopted in this paper.

(3) Using CDEM, the brittle failure mechanism of hard surrounding rock under high stress can be obtained, which intuitively presents the evolution process of progressive failure of surrounding rock and provides scientific and technical support for the design and construction of tunnels.

Due to the problem of computational efficiency, numerical simulation is limited to two-dimensional calculations, which needs to be improved in the future.

Data Availability

The data used to support the findings of this study are available from the corresponding author upon request.

Conflicts of Interest

The authors declare that there are no conflicts of interest regarding the publication of this paper.

Acknowledgments

References

[1] X.-T. Feng, H. Xu, S.-L. Qiu et al., "In situ observation of rock spalling in the deep tunnels of the China Jinping underground laboratory (2400 m Depth)," *Rock Mechanics and Rock Engineering*, vol. 51, no. 4, pp. 1193–1213, 2018.

[2] F. Gong, Y. Luo, X. Li, X. Si, and M. Tao, "Experimental simulation investigation on rockburst induced by spalling failure in deep circular tunnels," *Tunnelling and Underground Space Technology*, vol. 81, pp. 413–427, 2018.

[3] Y. Luo, F. Gong, D. Liu, S. Wang, and X. Si, "Experimental simulation analysis of the process and failure characteristics of spalling in D-shaped tunnels under true-triaxial loading conditions," *Tunnelling and Underground Space Technology*, vol. 90, pp. 42–61, 2019.

[4] M. N. Abdul, Z. E. Muhammad, R. Hafeezur, and Y. Handyu, "Geological and geomechanical heterogeneity in deep hydropower tunnels: a rock burst failure case study," *Tunnelling*

and Underground Space Technology, vol. 84, pp. 507–521, 2019.

[5] K. Efstratios, H. John, H. Jim, and T. Pascal, "Discrete element modelling of the bucking phenomenon in deep hard rock mines," *International Journal of Rock Mechanics and Mining Sciences*, vol. 80, pp. 346–356, 2015.

[6] L. Jacobsson, K. Appelquist, and J. E. Lindkvist, "Spalling experiments on large hard rock specimens," *Rock Mechanics and Rock Engineering*, vol. 48, no. 4, pp. 1485–1503, 2015.

[7] N. Cho, C. D. Martin, D. C. Sego, and J. Jeon, "Dilation and spalling in axially compressed beams subjected to bending," *Rock Mechanics and Rock Engineering*, vol. 43, no. 2, pp. 123–133, 2010.

[8] X. G. Zhao, J. Wang, M. Cai et al., "Influence of unloading rate on the strainburst characteristics of Beishan granite under true-triaxial unloading conditions," *Rock Mechanics and Rock Engineering*, vol. 47, no. 2, pp. 467–483, 2014.

[9] K. Du, M. Tao, X. Li, and J. Zhou, "Experimental study of slabbing and rockburst induced by true-triaxial unloading and local dynamic disturbance," *Rock Mechanics and Rock Engineering*, vol. 49, no. 9, pp. 3437–3453, 2016.

[10] B. J. Carter, E. Z. Lajtai, and Y. Yuan, "Tensile fracture from circular cavities loaded in compression," *International Journal of Fracture*, vol. 57, no. 3, pp. 221–236, 1992.

[11] R. Wong, P. Lin, and C. A. Tang, "Experimental and numerical study on splitting failure of brittle solids containing single pore under uniaxial compression," *Mechanics of Materials*, vol. 38, no. 1, pp. 142–159, 2006.

[12] X. Liu, S. Yang, Y. Huang, and Cheng, "Experimental study on the strength and fracture mechanism of sandstone containing elliptical holes and fissures under uniaxial compression," *Engineering Fracture Mechanics*, vol. 205, pp. 205–217, 2019.

[13] C. D. Martin, "Seventeenth Canadian geotechnical colloquium: the effect of cohesion loss and stress path on brittle rock strength," *Canadian Geotechnical Journal*, vol. 34, no. 5, pp. 698–725, 1997.

[14] V. Hajiabdolmajid, P. K. Kaiser, and C. D. Martin, "Modelling brittle failure of rock," *International Journal of Rock Mechanics and Mining Sciences*, vol. 39, no. 6, pp. 731–741, 2002.

[15] V. Hajiabdolmajid, P. Kaiser, and C. D. Martin, "Mobilised strength components in brittle failure of rock," *Géotechnique*, vol. 53, no. 3, pp. 327–336, 2003.

[16] M. S. Diederichs, P. K. Kaiser, and E. Eberhardt, "Damage initiation and propagation in hard rock during tunnelling and the influence of near-face stress rotation," *International Journal of Rock Mechanics and Mining Sciences*, vol. 41, no. 5, pp. 785–812, 2004.

[17] M. S. Diederichs, "The 2003 Canadian Geotechnical Colloquium: mechanistic interpretation and practical application of damage and spalling prediction criteria for deep tunnelling," *Canadian Geotechnical Journal*, vol. 44, no. 9, pp. 1082–1116, 2007.

[18] Q. Jiang, X. Feng, T. Xiang, and G. Su, "Rockburst characteristics and numerical simulation based on a new energy index: a case study of a tunnel at 2,500 m depth," *Bulletin of Engineering Geology and the Environment*, vol. 69, no. 3, pp. 381–388, 2010.

[19] X. Li, W. Cao, Z. Zhou, and Y. Zou, "Influence of stress path on excavation unloading response," *Tunnelling and Underground Space Technology*, vol. 42, pp. 237–246, 2014.

[20] K. Duan, Y. Ji, W. Wu, and C. Y. Kwok, "Unloading-induced failure of brittle rock and implications for excavation-induced strain burst," *Tunnelling and Underground Space Technology*, vol. 84, pp. 495–506, 2019.

[21] L. Hu, G. Su, X. Liang, Y. Li, and L. Yan, "A distinct element based two-stage-structural model for investigation of the development process and failure mechanism of strainburst," *Computers and Geotechnics*, vol. 118, no. C, Article ID 103333, 2020.

[22] G. Q. Chen, M. C. He, and F. S. Fan, "Rock burst analysis using DDA numerical simulation," *International Journal of Geomechanics*, vol. 18, no. 3, pp. 1–12, 2018.

[23] D. N. Zhong, J. L. Chen, H. Zhou et al., "Techniques for progressive failure simulation of hard brittle surrounding rockmass: taking the URL test tunnel as an example," *Advances in Civil Engineering*, vol. 2021, Article ID 8449905, 12 pages, 2021.

[24] I. Vazaios, N. Vlachopoulos, and M. S. Diederichs, "Assessing fracturing mechanisms and evolution of excavation damaged zone of tunnels in interlocked rock masses at high stresses using a finite-discrete element approach," *Journal of Rock Mechanics and Geotechnical Engineering*, vol. 11, no. 4, pp. 701–722, 2019.

[25] P. Hamdi, D. Stead, D. Elmo, and J. Töyrä, "Use of an integrated finite/discrete element method-discrete fracture network approach to characterize surface subsidence associated with sub-level caving," *International Journal of Rock Mechanics and Mining Sciences*, vol. 103, pp. 55–67, 2018.

[26] L. F. Trivino and B. Mohanty, "Assessment of crack initiation and propagation in rock from explosion-induced stress waves and gas expansion by cross-hole seismometry and FEM-DEM method," *International Journal of Rock Mechanics and Mining Sciences*, vol. 77, pp. 287–299, 2015.

[27] C. Q. Zhang, Z. J. Liu, C. S. Zhang, H. Zhou, Y. Gao, and J. Hou, "Experimental study on rupture evolution and failure characteristics of aphanitic basalt," *Rock and Soil Mechanics*, vol. 40, no. 7, pp. 1–11, 2019, in Chinese.

[28] Z. R. Chang, "Study on Mechanical Characteristics and Evolution of Mechanical Parameters of Hard and Brittle basalt," Master thesis, Shenyang University of Technology, Shenyang, China, 2019.

[29] C. S. Zhang, Y. S. Zhu, W. J. Chu, and N. Liu, "Mechanical behaviors of basalt at Baihetan hydropower station and simulation with Hoek-Brown constitutive model," *Chinese Journal of Rock Mechanics and Engineering*, vol. 38, no. 10, pp. 1964–1978, 2019, in Chinese.

[30] Y. S. Zhu, H. C. Zhu, A. C. Shi, and G. T. Meng, "Complicated block stability analysis of Baihetan hydropower station based on distinct element method," *Chinese Journal of Rock Mechanics and Engineering*, vol. 30, no. 10, pp. 2068–2075, 2011, in Chinese.

[31] G. T. Meng, Y. L. Fan, Y. L. Jiang, W. He, Y. B. Pan, and Y. Li, "Key rock mechanical problems and measures for huge caverns of Baihetan hydropower plant," *Chinese Journal of Rock Mechanics and Engineering*, vol. 35, no. 12, pp. 2549–2560, 2016, in Chinese.

[32] S. H. Li, J. G. Wang, B. S. Liu, and D. P. Dong, "Analysis of critical excavation depth for a jointed rock slope using a face-to-face discrete element method," *Rock Mechanics and Rock Engineering*, vol. 40, no. 4, pp. 331–348, 2007.

[33] Q. Jiang, X. T. Feng, D. P. Xu, Y. Zhao, Y. L. Jiang, and K. Huang, "Evaluation method of general geostress based on spalling features of wall rock," *Rock and Soil Mechanics*, vol. 32, no. 5, pp. 1452–1459, 2011, in Chinese.

[34] N. Vlachopoulos and M. S. Diederichs, "Appropriate uses and practical limitations of 2D numerical analysis of tunnels and

tunnel support response," *Geotechnical & Geological Engineering*, vol. 32, no. 2, pp. 469–488, 2014.

[35] J. H. Curran, R. E. Hammah, and T. E. Yacoub, "A two-dimensional approach for designing tunnel support in weak rock," in *Proceedings of the 56th Canadian Geotechnology Conference*, Winnipeg, Canada, September 2003.

Research Article

Study on Settlement Influence of Newly Excavated Tunnel Undercrossing Large Diameter Pipeline

Qian Xu [ID],[1] **Wenchao Zhang** [ID],[1,2] **Cheng Chen** [ID],[2] **Jun Lu** [ID],[1] **and Peng Tang** [ID][3]

[1]*School of Civil Engineering, NANTONG VOCATIONAL UNIVERSITY, Nantong, Jiangsu 226007, China*
[2]*School of Rail Transportation, Soochow University, Suzhou, Jiangsu 215000, China*
[3]*Nanjing Construction Engineering Group Co., Ltd, Nanjing, Jiangsu 211100, China*

Correspondence should be addressed to Cheng Chen; 3542368460@qq.com

With the rapid development of tunnel construction, there will be an increasing number of engineering cases about undercrossing existing pipelines. During the undercrossing process, the settlement control of existing pipelines is relatively strict. If the construction is not handled properly, the existing pipelines will cause a larger settlement, which will affect their normal use. This paper takes an existing pipeline project in Nanjing as the research object and uses numerical simulation to explore the influence of different excavation sequences and grouting reinforcement scopes on the existing pipelines above the newly built tunnels when using shallow tunnel excavation. The results show that the sections are constructed first on both sides of the construction, and the middle section is constructed subsequently, which not only increases the excavation speed but also the pipeline deformation is smaller, especially in controlling the differential settlement on both sides of the pipeline. By studying the relationship between the grouting reinforcement range and the vertical distance from the newly built tunnel to the existing pipeline, it is found that the soil engineering effect within 0.3 d above the arch line is more reasonable, and the feasibility of the proposed scheme is verified through actual monitoring data. This research can provide a reference for similar projects in the future.

1. Introduction

With the rapid development of underground engineering construction in China, underground pipelines will inevitably be encountered during the construction process [1, 2]. In the early stages of construction, pipelines usually migrate to other places, but the migration of pipelines will cause disturbance to the existing stratum. At the same time, it will cause uneven stress and strain redistribution of the pipeline, which is very detrimental to the pipeline and the construction project [3]. Therefore, it is important to choose reasonable construction methods and reinforcement measures to ensure the safety of the project and pipeline engineering crossing municipal pipelines.

Many scholars have studied the deformation of pipelines caused by tunnel underpasses. The main methods include analytical [4–15], numerical simulation [16–20], and model tests [21–28]. Zhang et al. [10] analyzed the influence of tunnel excavation in different soil layers on existing pipelines based on continuum elasticity theory using mathematical Hankel transformation and a transfer matrix and compared the results with published centrifuge model test results to verify the accuracy of the parameter values and the validity of the method. Based on the Winkel foundation model, Lin et al. [14] improved the relevant parameters to study the deformation of adjacent existing connecting pipelines caused by the soil deformation caused by tunnel excavation, and compared the calculation results with continuous pipeline deformation, field measured data, and centrifugal test data. The parameters of the pipeline joints, pipeline stiffness, and relative location of the pipe tunnels are analyzed. Lin et al. [15] deduced the existing pipeline deformation and internal force caused by tunnel underpass construction based on the Euler–Bernoulli beam theory and the Pastmank foundation model, mainly considering the gap between the pipe and soil and the pipe-tunnel clamp caused

by the volume loss during the tunnel excavation process. Based on the angle factor, an analytical solution for the pipeline and the overlying ground was established, and the accuracy of the analytical solution was verified by on-site measured data and model test results. Luo et al. [20] used ABAQUS software to simulate the pipeline stress and deformation of a polyethylene pipeline under the condition of surface subsidence and considered that the polyethylene pipeline and the subsidence section are perpendicular to each other. Xu et al. [21] conducted a finite element parameter study on the mechanical behavior of the existing pipeline caused by the excavation of the nearby deep foundation pit, considering the influence of factors such as the relative position of the excavation and the pipeline, the diameter of the tunnel, the size of the excavation, and the tunnel protection measures on the tunnel. Vorster et al. [22] used the centrifuge model test to analyze the surface displacement, vertical displacement of the pipeline, pipeline bending moment, and surrounding soil strain caused by tunnel excavation under different stratum loss rate conditions and compared the results of the centrifugal model test with theoretical solutions. Marshall et al. [23] studied the effect of tunnel excavation in sandy soil layers for pipes with different stiffness characteristics through centrifugal model tests and analyzed the soil strain and pipe bending characteristics. Saiyar et al. [25] used a centrifuge model to study the effect of the formation of normal faults on node pipelines. The results showed that when the soil plastic shear strain area caused by the formation of a normal fault passes through the pipeline node and is located between the two nodes, the maximum turning angle of the pipeline node caused by the former is larger than that of the latter. Ng et al. [26] studied the influence of tunnel construction on existing tunnels through centrifuge model tests. The results showed that with the increase in the soil loss rate, the tunnel settlement deformation and bending moment gradually increased. Ma et al. [28] used a centrifuge model to study the influence of double-track tunnel excavation on the upper pipeline under different excavation sequences and layouts.

In summary, the current research on pipeline deformation caused by tunnel undercrossing is abundant, but there are many new conditions encountered in actual engineering, and the research can be further improved. For example, previous studies mainly focused on the influence of single-line or double-line tunnels on pipelines, and there are few studies on the impact of the excavation methods of the three-line tunnel on the pipeline. Second, there is less research about the deformation of the large-diameter pipelines caused by tunnel construction. Different construction schemes can make different influences on the pipeline, which also increases the risk of pipeline damage. Therefore, this paper introduced the project background in section 1, then studied the influence of different excavation schemes and advanced deep-hole grouting prereinforcement schemes on pipeline deformation in section 2 and section 3, the optimal construction schemes were proposed and verified by monitoring data in section 4. The conclusions were obtained in this paper can provide some references for similar projects in the future.

2. Background

The total construction length of the project is 2700 m, and the underground excavation tunnel, which is 500 m in length, is underneath the operating pipeline. The diameter of the pipeline is 2400 mm, and the vertical distance from the pipeline to the underground excavation section is 5 m. The diameter of the tunnel is 6 m, and the width is 5 m. The underground excavation and the overall project location map are shown in Figure 1 and Figure 2.

According to the geological survey report, the strata of the underground excavation section are mainly ④ sandy silt, ⑤ clay, and ⑥ silty clay. During the construction process, it is easy to collapse and experience local instability of the initial supporting structure. The parameters of the strata are shown in Table 1.

3. Optimization Analysis of the Tunnel Construction Scheme

The tunnel excavation method has a greater impact on the deformation of the underground pipeline, especially because there are three tunnels in this project, which has a large section, so the selection of the excavation method is particularly important. Combining the actual situation of the project, the stability of the large-diameter pipeline, which is crossed beneath by the multihole shallow buried tunnel, is calculated and analyzed by the MIDAS GTS finite element software to obtain the influence of the tunnel construction scheme on the pipeline deformation. The three tunnel construction plans are shown in Table 2.

Taking into account the influence of the model boundary conditions on the calculation results, the dimensions are 500 m in the x-direction, 400 m in the y-direction, and 30 m in the z-direction. The stratum, tunnel, pipeline, and grouting reinforcement are modeled by solid elements, the tunnel support is simulated by shell elements, the soil layer is modeled by Mohr–Coulomb, the tunnel structure is modeled by elastomer, and the boundary of the top surface of the model is set as a free boundary. Fixed constraints are set on the surrounding boundary and the bottom boundary. The formation parameters are shown in Table 1, the pipeline parameters are shown in Table 3, and the overall model diagram is shown in Figure 3. The different excavation steps are shown in Figure 4.

Scheme one: the order of construction is from left to right, namely, construct section A first, then construct section B, and finally construct section C.

The displacement cloud of the pipeline displacement in the first scheme is shown in Figure 5. Figure 5 shows that the maximum settlement of the pipeline is approximately 45.5 mm, and the differential settlement at both ends of the pipeline is approximately 11 mm. This is mainly due to unloading after the tunnel excavation, which causes the redistribution of stress and causes a certain amount of settlement in the upper strata and thus leads to the deformation of the pipeline, but because of the different excavation sequence, both ends of the pipeline will have differential settlement.
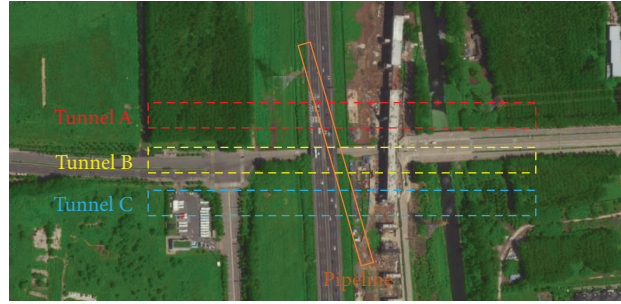
Figure 1: Floor plan between underground excavation and pipeline.
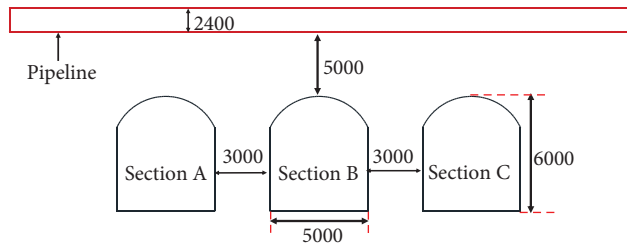
Figure 2: Sectional drawing of underground excavation (units: mm).

Table 1: Soil parameters.

Soil types	Depth (m)	γ (kN/m3)	c (MPa)	φ (°)	ν	E (MPa)
① Miscellaneous Fill	1.78	16.3	10.1	8	0.35	5.3
②Silty clay	2.55	19.2	31.2	26	0.3	6.2
③Clay	2.32	20.7	46	16	0.31	21
④Sandy silt	2.31	22.1	9.2	19	0.28	16
⑤Clay	2.61	48	47.2	16	0.31	21
⑥Silty clay	12.35	20.5	33.1	24	0.3	6.2

Table 2: Construction methods.

Constructions schemes	Sequence of construction
1	A section ⟶B section ⟶C section
2	B section ⟶A and C sections
3	A and C sections ⟶B section

Table 3: Parameters of the pipeline.

Structure name	Diameter (mm)	γ (kN/m3)	E (GPa)	v
Pipeline	2200	25	30	0.2

The displacement cloud of the pipeline displacement in the second scheme is shown in Figure 6. It can be seen from the displacement cloud diagram that the maximum deformation of the pipeline is approximately 36.6 mm, and the differential settlement at both ends of the pipeline is approximately 13 mm. Compared with the previous excavation sequence, the maximum deformation of the pipeline has been reduced by 8.9 mm, but the differential settlement at both ends of the pipeline has increased by 2 mm.
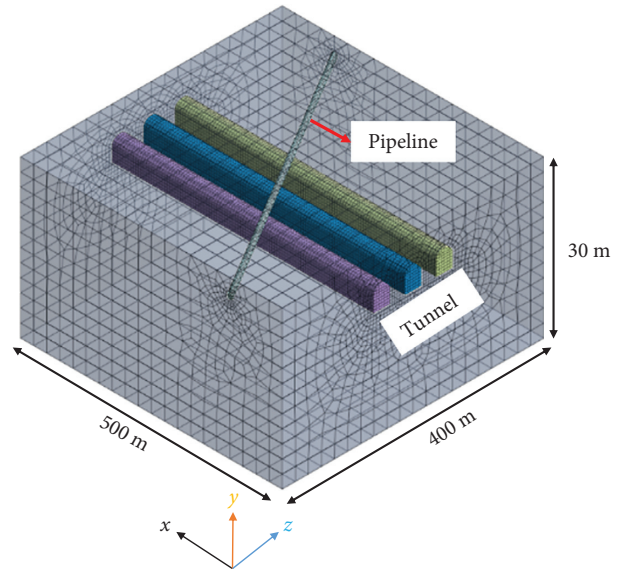
Figure 3: 3D model diagram.

The displacement cloud of the pipeline displacement in the third scheme is shown in Figure 7. The maximum deformation of the pipeline is approximately 35.5 mm, and the

(a)

(b)

(c)
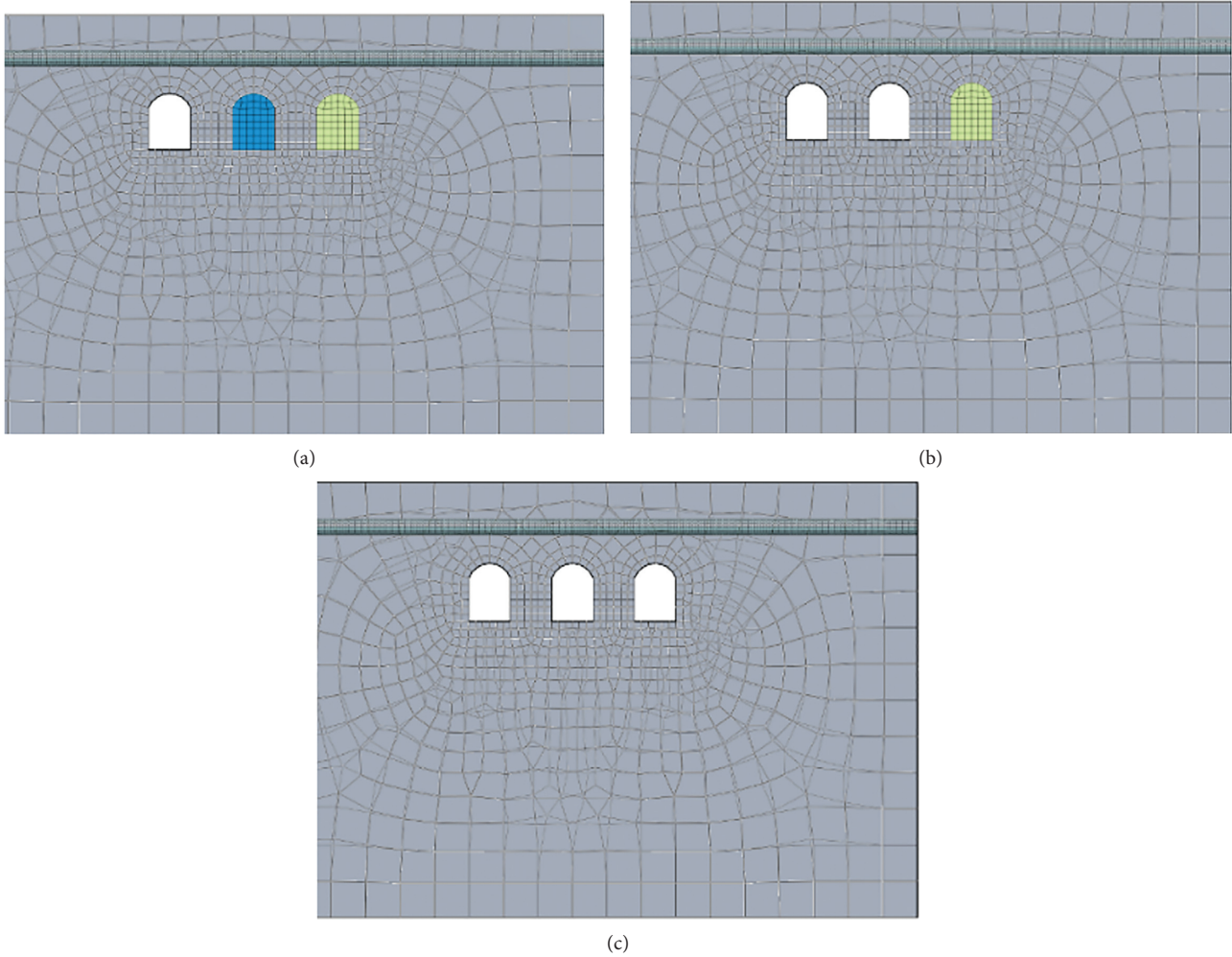
FIGURE 4: Excavation steps: (a) step 1: excavate section A, (b) step 2:excavate section B, and (c) step 3: excavate section C.
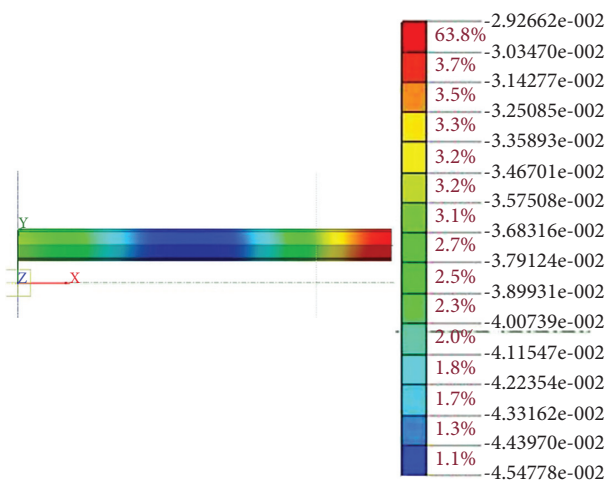
FIGURE 5: Pipeline deformation cloud map.
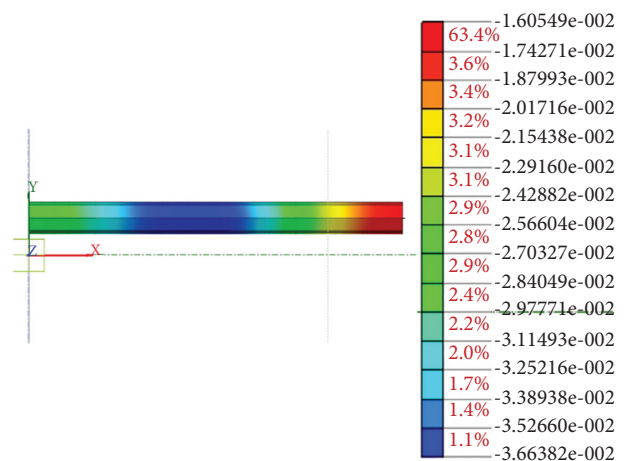
FIGURE 6: Pipeline deformation cloud map.

differential settlement at both ends of the pipeline is approximately 10 mm. Compared with the above two excavation sequences, it can be found that the pipeline deformation caused by the current excavation sequence is

moderate. At the same time, the differential settlement value at both ends of the pipeline is the smallest, indicating that the pipeline itself suffers the least disturbance.
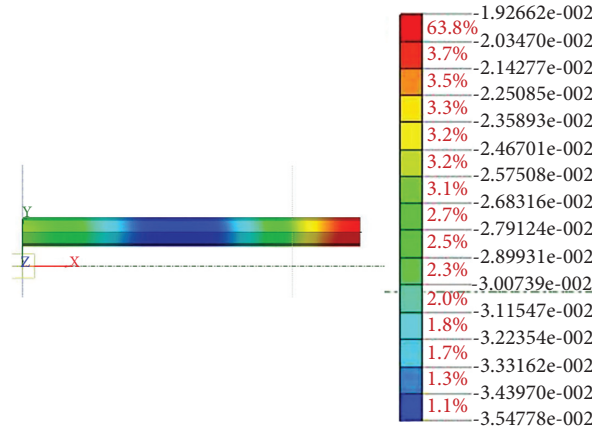
FIGURE 7: Pipeline deformation cloud map.

TABLE 4: Comparison of simulation results of construction schemes.

Construction scheme	Maximum settlement of pipeline (mm)	Differential settlement on both sides of pipeline (mm)	Construction period
1	45.5	11	Longer
2	36.6	13	Moderate
3	35.5	10	Moderate

Scheme comparisons are shown in Table 4. Table 4 shows that the pipeline settlement caused by the first scheme is the largest, and the second scheme is the smallest. However, the settlement difference of the pipeline in the second and third schemes is only 1.1 mm, the differential settlement at both ends of the pipeline caused by the second scheme is the largest, and the construction period is also considered. After comprehensive consideration, the third scheme was selected as the construction sequence for this project.

4. Research on the Prereinforcement Scheme of Advanced Deep-Hole Grouting under Shallow Excavation

On the basis of the second section, the third scheme was selected and combined with the requirements of this project, and the range of deep-hole grouting was simulated. The soil parameters after grouting are listed in Table 5. In addition, find a construction plan that can not only meet the construction requirements but also reduce the project cost, which can further guide the construction.

The first scheme: the soil is reinforced within 0.1 d (0.5 m) above the arching line, and the reinforced section is shown in Figure 8.

The displacement cloud of the pipeline displacement in the first scheme is shown in Figure 9. The maximum settlement of the pipeline is approximately 35.3 mm, and the differential settlement at both ends of the pipeline is approximately 13 mm. Compared with Figure 7, the maximum settlement values of the pipeline are similar, it shows that the first reinforcement scheme is not effective in controlling settlement.

TABLE 5: Parameters of the soil after grouting.

γ (kN/m3)	c (kPa)	φ (°)	E (MPa)	N
2100	40	35	80	0.3

The second scheme: the soil is reinforced within 0.3 d (1.5 m) above the arch line, and the reinforced section is shown in Figure 10.

The displacement cloud of the pipeline displacement in the second scheme is shown in Figure 11. The maximum settlement of the pipeline is approximately 29.7 mm, and the differential settlement at both ends of the pipeline is approximately 6 mm. Compared with Figure 9, the settlement value of the pipeline in the first reinforcement scheme is smaller than that in the second reinforcement scheme, indicating that increasing the grouting range can effectively control the pipeline settlement.

The third scheme: the soil is reinforced within 0.5 d (2.5 m) above the arch line, and the reinforced section is shown in Figure 12.

The displacement cloud of the pipeline displacement in the third scheme is shown in Figure 13. The maximum settlement of the pipeline is approximately 28.5 mm, and the differential settlement at both ends of the pipeline is approximately 4 mm. Compared with Figure 11, the settlement value of the pipeline in the third reinforcement scheme is smaller than that in the second reinforcement scheme, but the difference in value is only 1.2 mm, indicating that the third grouting reinforcement scheme can further control the settlement of the pipeline. However, the effect of controlling the pipeline settlement is not obvious.
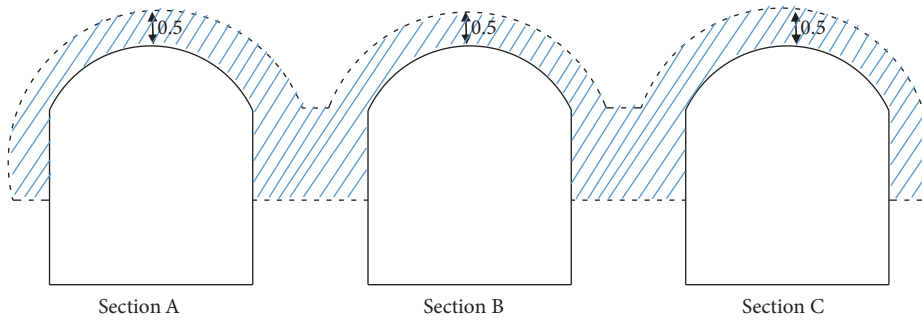
FIGURE 8: Reinforced section view.
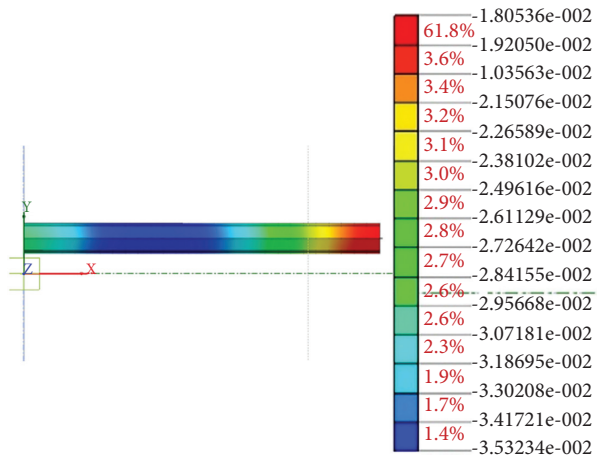
FIGURE 9: Pipeline deformation cloud map.
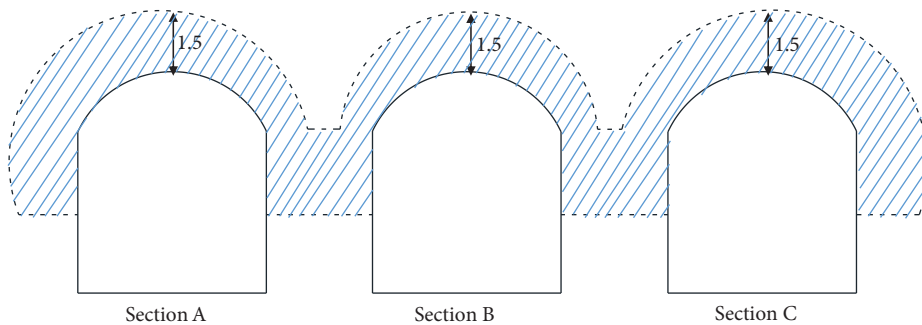
FIGURE 10: Reinforced section view.

The calculation results of the model are shown in Table 6. Table 6 shows that the pipeline deformation in Scheme 1 is the largest, with a value of 35.3 mm, which is close to the allowable specification value (35 mm). Therefore, the solution does not meet the requirements; although the maximum pipeline deformation in scheme 3 is the smallest, the difference between the pipeline and scheme 2 is only 1 mm, and considering the difficulty of construction and the cost of the project, scheme 2 is more cost-effective, so scheme 2 is selected as the final project construction plan.

5. Actual Monitoring Data Analysis

According to the above analysis, in the actual project, deep-hole grouting reinforcement is carried out on both sides of the tunnel, the reinforcement range is 1.5 m above the arch line, and then underground excavation is carried out. The above construction steps are carried out alternately. Until the tunnel is completed, the middle tunnel is finally excavated. The construction process is the same as that on both sides.
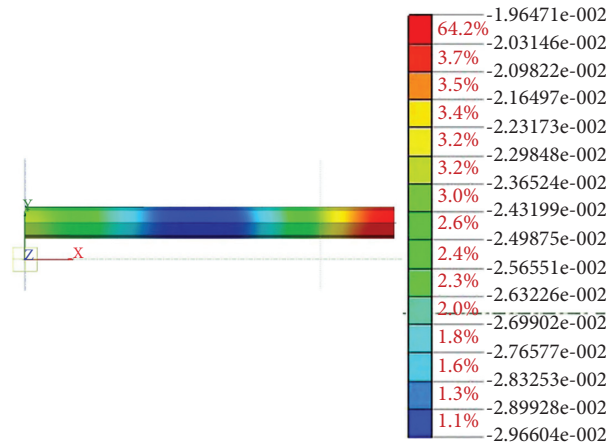
Figure 11: Pipeline deformation cloud map.

Section A   Section B   Section C
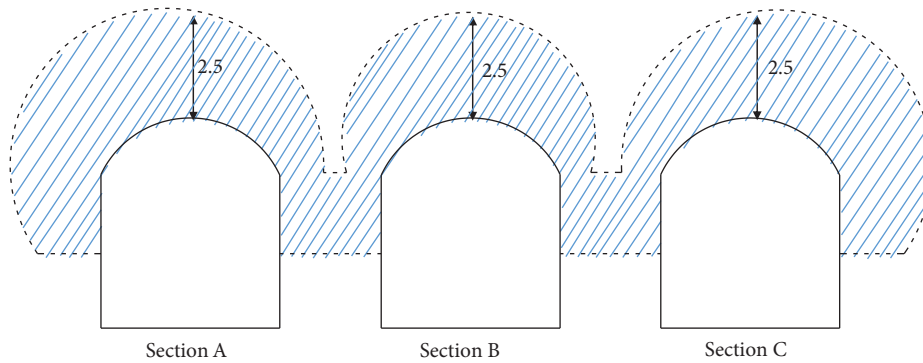
Figure 12: Reinforced section view.
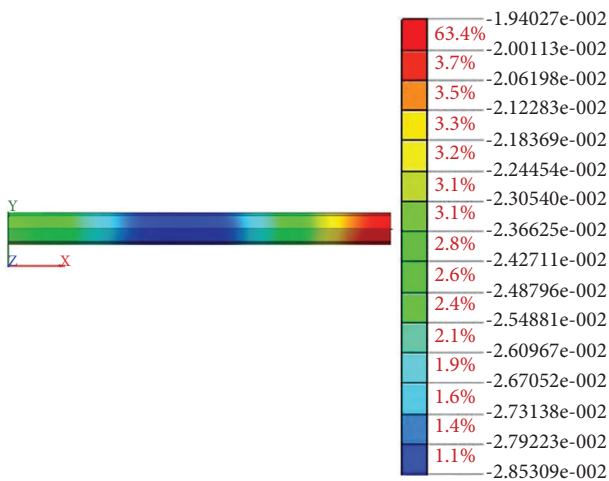
Figure 13: Pipeline deformation cloud map.

There are three rows of monitoring points, which are used to monitor surface subsidence and tunnel vault subsidence, arranged in the direction of the centerline of the digging section. A total of 48, such as point A1', are directly above point A1. There are nine pipeline settlement monitoring points, which are distributed along the pipeline

through boreholes. The layout of the measuring points is shown in Figure 14.

5.1. Pipeline Settlement. Figure 15 shows that the settlement value of monitoring point J5 is the largest because it is affected by the superposition of three tunnel excavations. The final settlement value is approximately 23 mm, which is smaller than the result of the numerical simulation (29.6 mm). The main reason may be that there are various uncertain factors during the actual construction. For example, there will be certain errors in the quality of the slurry and the scope of grouting that will cause a difference between the monitoring value and the simulated value of the pipeline, but the settlement meets the requirements of the construction regulations (35 mm).

5.2. Tunnel Vault Subsidence. Figure 16 shows that the settlement value of the tunnel vault along the direction of undercutting gradually decreases. The maximum settlement values of the three tunnels are 21.6 mm (A1), 26.1 mm (B1), and 21.2 mm (C1), and the settlement value at point B1 is the largest because the settlement at this point is affected by the excavation of the three tunnels, which coincides with the settlement law of the pipeline.

TABLE 6: Comparison of simulation results of construction schemes.

Grouting schemes	Reinforcement range (m)	Maximum settlement of pipeline (mm)
1	0.5	35.3
2	1.5	29.6
3	2.5	28.5
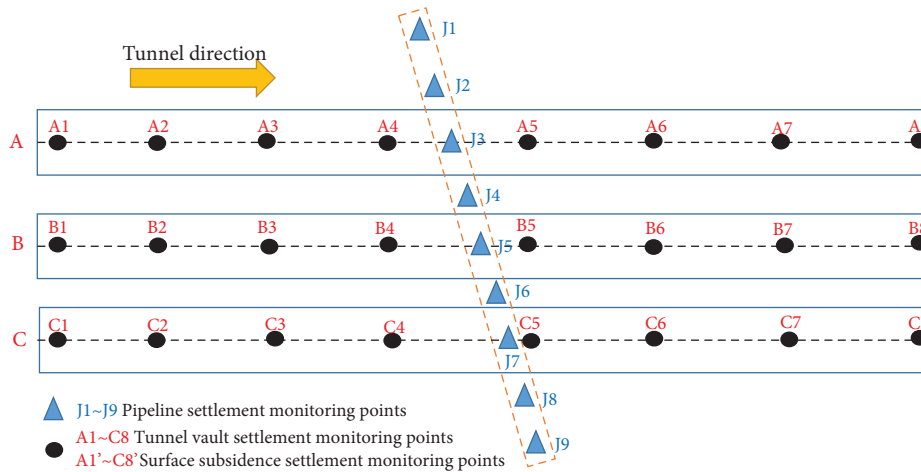
FIGURE 14: Monitoring point layout plan.
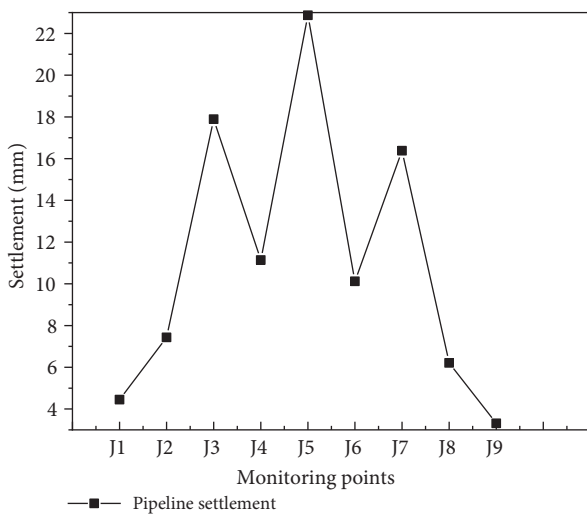
FIGURE 15: Pipeline settlement curve.
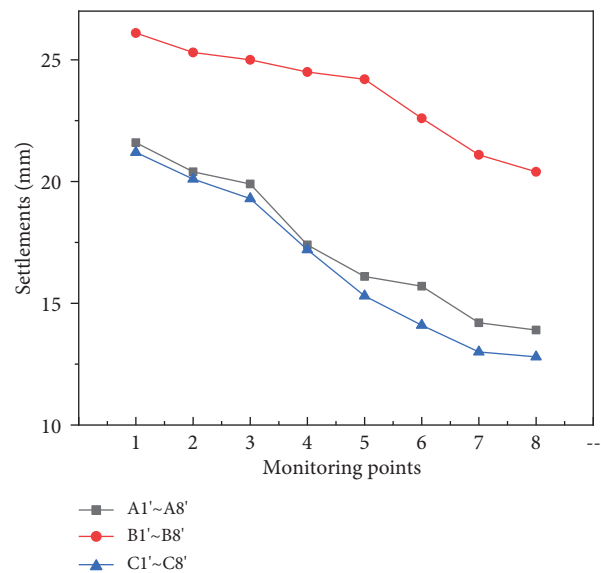
FIGURE 16: Tunnel vault settlement curve.

5.3. Surface Subsidence.

Figure 17 shows that the settlement value of the ground surface gradually decreases along the direction of the undercut. The maximum settlement value of the ground surface above the three tunnels is 13.2 (A1'), 14.1 (B1'), and 12.9 (C1'), and the settlement value of point B1' is the largest because the settlement of this point is affected by the excavation of the three tunnels, which is consistent with the settlement law of the pipeline and the tunnel vault. At the same time, due to the self-stabilizing ability of the soil, the surface settlement value at the same vertical position is smaller than that of the tunnel vault. Monitoring points C7' and C8' did not collect relevant data due to the failure of the monitoring equipment.
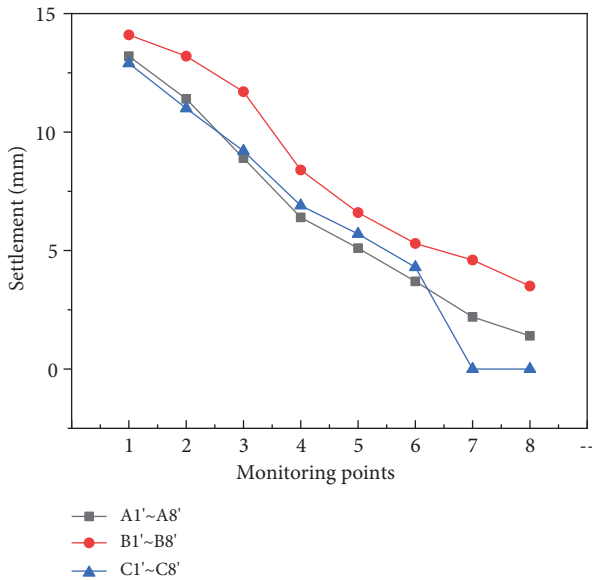
FIGURE 17: Surface settlement curve.

6. Conclusions

(1) According to the numerical simulation results, it can be found that different tunnel excavation sequences will cause the deformation of the pipeline in the upper soil, but the magnitude of the deformation is different. The excavation method, which constructs the tunnels on both sides at the same time and then constructs the middle tunnel, not only increases the excavation speed but also controls the pipeline deformation better than the other two schemes, especially in terms of differential settlement on both sides of the pipeline.

(2) By studying the relationship between the grouting reinforcement range and the vertical distance between the new tunnel and the existing pipeline, it is found that when the deep-hole grouting range is approximately 0.1d above the arch line, the pipeline deformation during tunnel excavation is large. When the reinforcement range is 0.5 d, the pipeline deformation is minimal, but the difference between scheme 2 and scheme 3 is small, and many other factors need to be considered, such as project cost and actual construction difficulty; thus, it is more reasonable to choose a reinforcement range of 0.3 d in scheme 2.

(3) The actual monitoring data show that the cumulative settlement value of the ground surface and pipeline gradually increases, and the final settlement values are 14.1 mm and 23 mm, respectively, which are less than the 30 mm and 35 mm required in the specification, indicating that the excavation plan and grouting method proposed in this paper are feasible, which can provide references for similar projects in the future.

References

[1] X. J. Zhang, "Research on the influence of shallow - buried excavation tunnel passing through existing pipelines in muddy soil," *Journal of Railway Engineering Society*, vol. 37, no. 7, pp. 77–83, 2020.

[2] Y. K. Sun, W. Y. Wu, and T. Q. Zhang, "Analysis on the pipeline settlement in soft ground induced by shield tunneling across buried pipeline," *China Railway Science*, vol. 30, no. 1, pp. 80–85, 2009.

[3] S. J. Wang, "Influence of tunneling construction on buried pipelines paralleled with running tunnel," *China Civil Engineering Journal*, vol. 47, no. S2, pp. 334–338, 2014.

[4] R. J. Mair, K. Soga, and A. Klar, "Soil-pipe interaction due to tunnelling: comparison between Winkler and elastic continuum solutions," *Géotechnique*, vol. 55, no. 6, pp. 461–466, 2005.

[5] A. Klar, A. M. Marshall, K. Soga, and R. J. Mair, "Tunneling effects on jointed pipelines," *Canadian Geotechnical Journal*, vol. 45, no. 1, pp. 131–139, 2008.

[6] F. Wang, H. Huang, Z. Yin, and Q. Huang, "Probabilistic characteristics analysis for the time-dependent deformation of clay soils due to spatial variability," *European Journal of Environmental and Civil Engineering*, pp. 1–19, 2021.

[7] J. Han, D. Liu, Y. Guan et al., "Study on shear behavior and damage constitutive model of tendon-grout interface," *Construction and Building Materials*, vol. 320, Article ID 126223, 2022.

[8] A. Klar and A. M. Marshall, "Shell versus beam representation of pipes in the evaluation of tunneling effects on pipelines," *Tunnelling and Underground Space Technology*, vol. 23, no. 4, pp. 431–437, 2008.

[9] A. M. Marshall and A. Klar, "Linear elastic tunnel pipeline interaction: the existence and consequence of volume loss equality," *Géotechnique*, vol. 65, no. 9, pp. 788–792, 2015.

[10] C. Zhang, J. Yu, and M. Huang, "Effects of tunnelling on existing pipelines in layered soils," *Computers and Geotechnics*, vol. 43, pp. 12–25, 2012.

[11] Z. Zhang, M. Zhang, and Q. Zhao, "A simplified analysis for deformation behavior of buried pipelines considering disturbance effects of underground excavation in soft clays," *Arabian Journal of Geosciences*, vol. 8, no. 10, pp. 7771–7785, 2015.

[12] J. Yu, C. Zhang, and M. Huang, "Soil-pipe interaction due to tunnelling: assessment of Winkler modulus for underground

pipelines," *Computers and Geotechnics*, vol. 50, no. 5, pp. 17–28, 2013.

[13] M. Huang, X. Zhou, J. Yu, C. F. Leung, and J. Q. W. Tan, "Estimating the effects of tunnelling on existing jointed pipelines based on Winkler model," *Tunnelling and Underground Space Technology*, vol. 86, no. 4, pp. 89–99, 2019.

[14] X. T. Lin, R. P. Chen, and H. N. Wu, "Three-dimensional stress-transfer mechanism and soil arching evolution induced by shield tunneling in sandy ground," *Tunnelling and Underground Space Technology*, vol. 93, Article ID 103104, 2019.

[15] C. G. Lin, M. S. Huang, F. Nadim, and Z. Liu, "Tunnelling-induced response of buried pipelines and their effects on ground settlements," *Tunnelling and Underground Space Technology*, vol. 96, no. 2, Article ID 103193, 2020.

[16] A. Klar, T. E. Vorster, K. Soga, and R. J. Mair, "Elastoplastic solution for soil-pipe-tunnel interaction," *Journal of Geotechnical and Geoenvironmental Engineering*, vol. 133, no. 7, pp. 782–792, 2007.

[17] Y. Wang, J. Shi, and C. W. W. Ng, "Numerical modeling of tunneling effect on buried pipelines," *Canadian Geotechnical Journal*, vol. 48, no. 7, pp. 1125–1137, 2011.

[18] W. C. Zhang, N. Wu, P. Jia, X. Zhou, H. Li, and G. Wang, "Study the mechanical performance of excavation under asymmetrical pressure and reinforcement measures," *Arabian Journal of Geosciences*, vol. 14, no. 18, 2021.

[19] J. Shi, Y. Wang, and C. W. W. Ng, "Buried pipeline responses to ground displacements induced by adjacent static pipe bursting," *Canadian Geotechnical Journal*, vol. 50, no. 5, pp. 481–492, 2013.

[20] X. Luo, S. Lu, J. Shi, X. Li, and J. Zheng, "Numerical simulation of strength failure of buried polyethylene pipe under foundation settlement," *Engineering Failure Analysis*, vol. 48, pp. 144–152, 2015.

[21] X. Xu, H. F. Schweiger, and H. Huang, "Influence of deep excavations on nearby existing tunnels," *International Journal of Geomechanics*, vol. 13, no. 2, pp. 170–180, 2013.

[22] T. E. Vorster, A. Klar, K. Soga, and R. J. Mair, "Estimating the effects of tunneling on existing pipelines," *Journal of Geotechnical and Geoenvironmental Engineering*, vol. 131, no. 11, pp. 1399–1410, 2005.

[23] A. M. Marshall, A. Klar, and R. J. Mair, "Tunneling beneath buried pipes: view of soil strain and its effect on pipeline behavior," *Journal of Geotechnical and Geoenvironmental Engineering*, vol. 136, no. 12, pp. 1664–1672, 2010.

[24] J. W. Shi, Y. Wang, and C. W. W. Ng, "Three-Dimensional centrifuge modeling of ground and pipeline response to tunnel excavation," *Journal of Geotechnical and Geoenvironmental Engineering*, vol. 142, no. 11, Article ID 04016054, 2012.

[25] M. Saiyar, I. D. Moore, and W. A. Take, "Kinematics of jointed pipes and design estimates of joint rotation under differential ground movements," *Canadian Geotechnical Journal*, vol. 52, no. 11, pp. 1714–1724, 2015.

[26] C. W. W. Ng, T. Boonyarak, and D. Mašín, "Three-dimensional centrifuge and numerical modeling of the interaction between perpendicularly crossing tunnels," *Canadian Geotechnical Journal*, vol. 50, no. 9, pp. 935–946, 2013.

[27] C. W. W. Ng, T. Boonyarak, and D. Masin, "Effects of pillar depth and shielding on the interaction of croosing multi-tunnels," *Journal of Geotechnical and Geoenvironmental Engineering*, vol. 141, no. 6, Article ID 04015021, 2015.

[28] S. Ma, Y. Shao, Y. Liu, J. Jiang, and X. Fan, "Responses of pipeline to side-by-side twin tunnelling at different depths: 3D centrifuge tests and numerical modelling," *Tunnelling and Underground Space Technology*, vol. 66, no. 6, pp. 157–173, 2017.

Research Article

A Nonlinear Prediction Model of Antislide Pile Top Displacement Based on MIC-SVR for Jurassic Landslides

Zhiping Huang,[1] **Manman Dong** ⓘ**,**[2] **Xi Du,**[3] **and Yongping Guan**[4]

[1]*School of Civil Engineering & Architecture, Jishou University, Jishou, Hunan, China*
[2]*Department of Engineering Management, Changshu Institute of Technology, Changshu, China*
[3]*School of Environment and Architecture, University of Shanghai for Science and Technology, Shanghai, China*
[4]*Taizhou Transportation Investment Group, Taizhou, China*

Correspondence should be addressed to Manman Dong; manmandong@cslg.edu.cn

Academic Editor: Qian Chen

In this study, a nonlinear prediction model of antislide pile top displacement is proposed. Based on the quantitative analysis of the rock mass structure characteristics of the soft and hard interbedded sliding bed in the Jurassic strata, the post-thrust force and geometric characteristics of the top of antislide pile displacement, and bending moment, the main controlling factors affecting the displacement of the top of antislide pile were determined by maximal information coefficient (MIC). Through orthogonal experiment design and 3DEC numerical experiment, a database of main controlling factors (sliding bedrock inclination, thrust size, embedded depth, and pile section size) of pile top displacement was established and a nonlinear prediction model of the displacement of the top of antislide pile based on the main controlling factors was proposed. Finally, two engineering examples were used to validate the performance of this model, with the comparisons of four prediction methods (SVR, MIC-SVR, LSTM, and ELMAN). The results show that the MIC-SVR model has a practical reference value for the prediction of the displacement of the top of an antislide pile in the Jurassic landslide in the Three Gorges Reservoir Area.

1. Introduction

Landslides widely occur in the Three Gorges Reservoir Region in China [1–4]. Antislide piles balance the thrust of the upper sliding body on the sliding surface through the embedded force and passive resistance of the embedded section to stabilize the ground and are widely used to improve the stability of slopes and prevent their excessive movements [3, 5, 6].

In the analysis of antislide piles, the laminated rock structure is usually modeled as an equivalent homogeneous or horizontally stratified body. Martin and Chen [7] examined the effects of spatial variations in soil displacement on the response of piles and pile groups caused by lateral soil movements using a numerical modeling method. Conte et al. [8] conducted a study on the response of reinforced concrete piles under horizontal loading in multilayered soils

composed of silty sand and sandy silt. Klar et al. [9] layered the antislide pile and the rock and soil around the pile and then used the numerical results of each layer to study the three-dimensional interaction characteristics between the pile and the foundation rock and soil. Lei et al. [10] studied the response of laterally loaded piles in multilayered elastic soils using a separation-based continuum model. Mylonakis et al. [11] proposed a method for calculating the internal force of a single pile or group of piles in multilayer soil based on the generalized Winkler foundation model. Salgado et al. [12] proposed a semianalytical method for the analysis of pile groups embedded in multilayered elastic soils. Dong et al. [13] studied the mechanical characteristics of stabilizing piles embedded in layered bedrock through numerical tests and model tests. Fattah [14–17] estimated the bearing capacity of open-ended model piles in different conditions, and the end bearing, vertical, and horizontal displacement of

the pile group model were investigated in dry soil under horizontal excitation.

The Three Gorges Reservoir Area is a high incidence area of landslide geological disaster in China, strata of all ages are developed, among which Jurassic strata are the most widely distributed, the number of landslides developed in this stratum accounts for about 67% of the total number of landslides in the whole reservoir area, and the volume accounts for 65% [18]. In the Jurassic strata of the Three Gorges Reservoir Area, there are a large number of sandstone and mudstone interlayers in the rock structure, which is different from the homogeneous rock structure, and shear stress concentration often occurs under the action of gravity, leading to the overall destruction of the weak layer to produce landslides, which needs urgent treatment [13]. The FLAC3D numerical method is used to analyze the influence of the slope angle, thickness similarity ratio, and layer thickness ratio of the sliding bedrock layer on the force and deformation characteristics of the antislide pile [19]. The K method is used to horizontally divide the rock mass foundation coefficient of the sliding bed into n layers, and the displacement of the top of the antislide pile is calculated [20]. The mechanical characteristics of antisliding piles considering the integrated foundation coefficient of sliding beds on composite inclined rock masses are studied.

At present, there are relatively few considerations about the structural surface development of the rock mass in the embedded section. The influence of the structural characteristics of the sliding bedrock mass and the geometric parameters of the antisliding pile should be further studied. Therefore, the influence of the mechanical characteristics of the rock mass and the geometric parameter characteristics of the antislide piles on the internal force and deformation of the antislide piles are analyzed, which has important theoretical significance for the design of antislide piles for Jurassic landslides.

The pile top displacement of antislide piles is an important indicator for monitoring the effect of antislide piles. At present, the displacement of the pile top used for antislide piles is mainly calculated by the combination of theoretical calculations, model tests, and numerical tests, and few machine learning methods are used to study the top displacement of antislide piles. With the development of computer applications, big data mining and machine learning methods have been widely used in geotechnical engineering, especially in landslide displacement prediction. Therefore, it is necessary to develop antislide pile top displacement predictions based on machine learning.

In summary, based on the quantitative analysis of the rock mass structure characteristics of the soft and hard interbedded sliding bed in the Jurassic strata, the post-thrust force and geometric characteristics of the top of antislide pile displacement, and bending moment, the main controlling factors affecting the displacement of the top of antislide pile were determined by maximal information coefficient (MIC).

Through orthogonal experimental design and 3DEC numerical experiments, a database of the main controlling factors (sliding bedrock inclination, thrust size, embedded depth, and pile section size) of pile top displacement was established, and a nonlinear prediction model of the displacement of the top of an antislide pile based on the main controlling factors was proposed.

2. Methodology

2.1. Maximal Information Coefficient. The maximal information coefficient (MIC) is a distinct correlation statistic, and MIC measures the association relationship of both linear and nonlinear relationships between input and output variables [21]. The MIC is an excellent data correlation calculation method that has higher accuracy than mutual information (MI).

MIC is aimed at the relationship between two variables that are discretized in a two-dimensional space. The current two-dimensional space is divided into a certain number of intervals in the x and y directions, the scatter points falling in each grid are checked, and the problem of joint probability in mutual information is solved. The calculation formula of MIC is as follows:

$$
\begin{aligned}
\text{mic}(x; y) &= \max_{a*b<B} \frac{I(x; y)}{\log_2 \min(a, b)}, \\
\text{MIC}[x; y] &= \max_{|X||Y|<B} \frac{I(x; y)}{\log_2(\min(|X|, |Y|))}.
\end{aligned}
\tag{1}
$$

In the formula, a and b are the number of divided grids in the x and y directions, which are essentially grid distributions, and B is a variable. Generally, the size of B is approximately 0.6 of the amount of data.

2.2. Support-Vector Regression. Support-vector regression (SVR) is a nonlinear regression prediction model based on the principle of structural risk minimization, which works by finding the best regression hyperplane in the high-dimensional feature space. The most widely used model is the ε-SVR model based on the insensitive loss function ε, which is determined by the hyperplane [22].

To establish the nonlinear relationship between the displacement of the pile top and the main control factor determined by the MIC, the training samples are mapped into the high-dimensional feature space through a nonlinear mapping function φ, and then, the correlation between the displacement of the pile top and the main control factor is fitted by the regression estimation function $f(x)$ in the high-dimensional feature space, where f(x) is the following:

$$
f(x) = W^T \varphi(x) + b,
\tag{2}
$$

where W^T is the independent variable function coefficient, $\varphi(x)$ is the nonlinear mapping function, and b is the offset.

The ε-insensitive loss function is used to transform the estimated function into a function minimization problem [23].

$$\text{minimize } \frac{1}{2}\mathbf{w}^T\mathbf{w} + C\sum_{i=1}^{i=l}(\xi_i + \xi_i^*),$$

$$\text{subjected to }\begin{cases} \left(\mathbf{w}^T\varphi(\mathbf{F}_i) + b\right) - JRC_i \leq \varepsilon + \xi_i \\ JRC_i - \left(\mathbf{w}^T\varphi(\mathbf{F}_i) + b\right) \leq \varepsilon + \xi_i^* . \\ \xi_i, \xi_i^* \geq 0, i = 1, \ldots, l. \end{cases} \quad (3)$$

In the formula, C is the penalty parameter, which represents the degree of punishment for samples that exceed the error.

Using Lagrangian and optimal conditions, the following dual problem can be obtained [23]:

$$\text{minimize } \frac{1}{2}(\boldsymbol{\alpha} - \boldsymbol{\alpha}^*)^T\mathbf{Q}(\boldsymbol{\alpha} - \boldsymbol{\alpha}^*) + \varepsilon\sum_{i=1}^{i=l}(\alpha_i + \alpha_i^*) + \sum_{i=1}^{i=l}JRC_i(\alpha_i - \alpha_i^*)$$

$$\text{subjected to }\begin{cases} e^T(\boldsymbol{\alpha} - \boldsymbol{\alpha}^*) = 0 \\ 0 \leq \alpha_i, \alpha_i^* \leq C, i = 1, \ldots, l, \end{cases} \quad (4)$$

among $\begin{aligned} Q_{ij} &= K(\mathbf{F}_i, \mathbf{F}_j) \\ K(\mathbf{F}_i, \mathbf{F}_j) &= \phi(\mathbf{F}_i)^T\phi(\mathbf{F}_j) \end{aligned}$ where α_i and α_i^* are Lagrangian multipliers; $\mathbf{e} = 1, \ldots, 1^T$ is the unit vector; $\mathbf{Q}$ is a $l \times l$ positive semidefinite matrix; and $K(\mathbf{F}_i, \mathbf{F}_j)$ is the kernel function that transfers the operations in the high-dimensional feature space to the low-dimensional input space through the kernel technique [23]. It should be noted that the commonly used kernel functions include the radial basis function (RBF), sigmoid function, linear function, and polynomial function. The RBF kernel function, which is the most extensive and can effectively deal with nonlinear problems, is used in this study. The model solution of the dual form is as follows [24]:

$$f(\mathbf{F}) = \sum_{i=1}^{i=l}(-\alpha_i + \alpha_i^*)K(\mathbf{F}_i, \mathbf{F}) + b,$$

$$K(\mathbf{F}_i, \mathbf{F}_j) = e^{-g\|F_i - F_j\|^2}, \quad (5)$$

where g is the width parameter of the RBF kernel function, which controls the complexity of the SVR solution. The insensitive loss parameter ε, the penalty parameter C, and the RBF kernel function parameter g will greatly affect the generalization ability and prediction accuracy of the SVR model; therefore, the three parameters need to be uniformly optimized.

2.3. Predictive Model Building Steps.
Sample databases and actual engineering examples are used as training samples and test samples, respectively. LIBSVM is used to train the model, and the grid search method with a concise algorithm and easy implementation is adopted to optimize the parameter combination (g, ε, and C). The solution obtained by the grid search is the optimal solution in the grid delineation,

and the training error caused by random sampling is eliminated through cross validation. Then, the stable and reliable prediction model is obtained.

The main control factor in the training sample is used as the input variable, and the corresponding antislide pile top displacement is used as the target output variable. The support-vector regression model is trained based on the optimal parameter combination obtained by grid search and cross test. By calling the libsvmtrain function of LIBSVM, the support vector x_i, the support-vector coefficient $(-\alpha + \alpha*)$, and the deviation constant D can be obtained, and then, the pile top displacement prediction equation based on the support-vector regression can be obtained. The obtained pile top displacement prediction equation can be used to predict the pile top displacement of antislide piles (see Figure 1).

3. Main Factors of the Top Displacement of the Antislide Pile

3.1. Discrete Element Modeling.
To study the influence of each parameter on the deformation of the top of the antisliding pile, a 3DEC discrete element model was established, as shown in Figure 2. The dimensions of the sliding bed are $33\,\text{m} \times 21\,\text{m} \times 30\,\text{m}$. The relevant mechanical parameters are shown in Table 1. To highlight the regularity of the influence of the structural characteristics of the sliding bedrock on the deformation of the pile tops, the following improvements were made to the model. (1) In the model, only the embedded section of the antisliding pile is considered, and the effect of the sliding body on the antislip pile is simplified to a horizontal rectangular uniform load. (2) Due to the small scope of the model and the fact that the antisliding piles are placed in the sliding section where the sliding surface is gently sloping, the sliding surface of the model is assumed to be horizontal. (3) Given that the row monopile can be
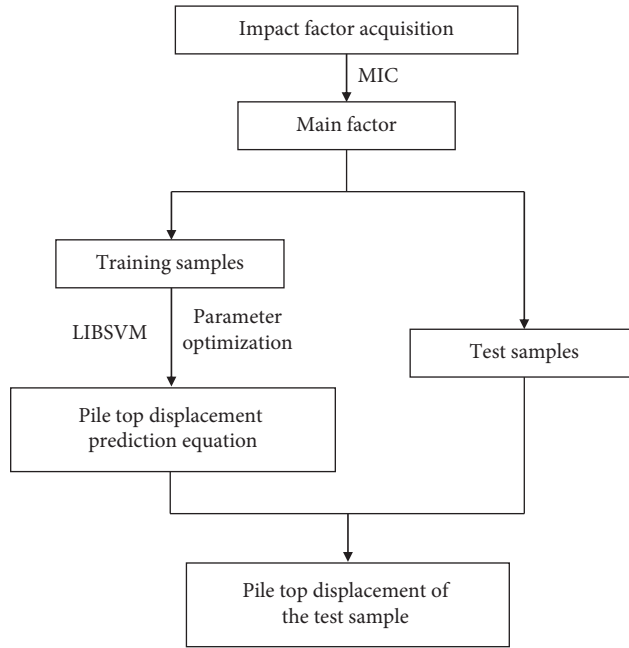
Figure 1: Prediction process of pile top displacement based on MIC-SVR.
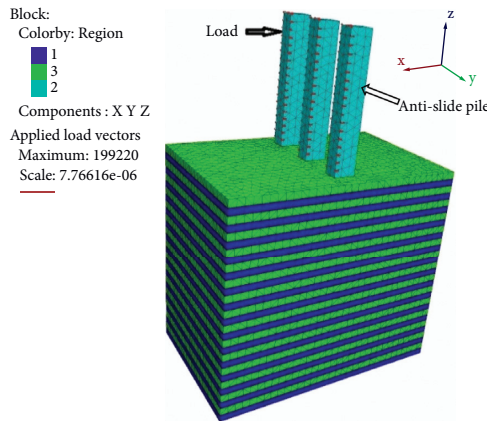
Figure 2: Numerical model.

Table 1: The mechanical parameter of rock.

Category	Bulk modulus (Pa)	Shear modulus (Pa)	Normal stiffness (kPa)	Tangential stiffness (kPa)	Unit weight (kN/m^3)	Cohesion (Pa)	Internal friction angle (°)
Soft rock	1.67×10^9	0.56×10^9	—	—	24.3	2.9×10^5	20
Hard rock	10×10^9	10.9×10^9	—	—	26.5	6.6×10^6	48
Rock layer	—	—	1×10^8	1×10^7	—	0.2×10^6	26
Antislide pile	12×10^9	30×10^9	—	—	30	—	—
Pile rock contact surface	—	—	1.2×10^9	0.1×10^9	—	0.4×10^6	33.8

reduced to a plane strain problem, a total of three antisliding piles are considered, and the intermediate pile is the subject of study [25]. The model is divided before calculation, and the size of mech is 1 m.

Solid element is used to simulate rock, and antislide piles were simulated using solid. The perfect elastic-plastic model (cons = 2) was used for the rock, and the elastic model was adopted to define the behavior of the antislide piles. The

Coulomb sliding failure principal model (jcons = 1) was used for the rock strata. For construction method of the antislide piles, location of the antislide piles is first excavated in the landslide using "tunnel" code, and subsequently, contact surface is used to simulating the interaction of solid element between rock and the antislide piles. Boundary conditions are as follows: normal displacement constraints are applied to the front and rear of the sliding bed, fixed constraints are applied to the bottom boundary, and a horizontal uniform load q in the $-x$ direction is applied to the loaded section of the antisliding pile.

3.2. Influence of Critical Parameters on the Horizontal Displacement of the Antislip Pile

3.2.1. Structural Characteristics of the Soft and Hard Interbedded Layers of Bedrock. To study the influence of the structural characteristics of the soft and hard interbedded layers of bedrock on the displacement of the antisliding pile, the inclination, layer thickness ratio, and single group thickness are selected as the influencing factors for analysis in this study. In the model established in this section, the antisliding pile section size is $2\,m \times 3\,m$, the pile length is $30\,m$, the embedded section is $12\,m$, and the horizontal load q is $290\,kPa$.

(1) Inclination of Soft and Hard Interbedded Layers of Bedrock. Since some scholars have pointed out that the influence of the inclination of the counter-inclined rock formation on the antisliding pile is small [19], only the influence of the inclination of the positive-inclined rock formation on the antisliding pile is studied here. The range of rock inclination is 0°~40°, and five parameters are designed as follows: 0°, 10°, 20°, 30°, and 40°. A layer thickness ratio of 1 : 1 (hard rock thickness over soft rock thickness) was used in the model for both hard and soft rocks.

The effect of different inclinations on the displacement of antisliding piles is shown in Figure 3. As seen from the figure, the displacement of antisliding piles corresponding to different inclinations basically show a similar trend with the depth of embedment, while the horizontal displacement of the piles increases with increasing distance from the bottom of the piles and reaches the maximum displacement at the top of the piles. When the inclination angle increases from 0° to 20°, the change in inclination angle has basically no effect on the pile top displacement. When the inclination angle increases from 20° to 40°, the pile top displacement more significantly increases. Compared to an inclination of 0°, the pile top displacement increases by 6.0% and 12.1% for inclination angles of 30° and 40°, respectively, as shown in Figure 4.

(2) Layer Thickness Ratio of Soft and Hard Interbedded Layers of Bedrock. To study the effect of different layer thickness ratios of soft and hard rock on the pile displacement of antisliding piles and considering that the sliding bed of Jurassic stratigraphic landslide in the Three
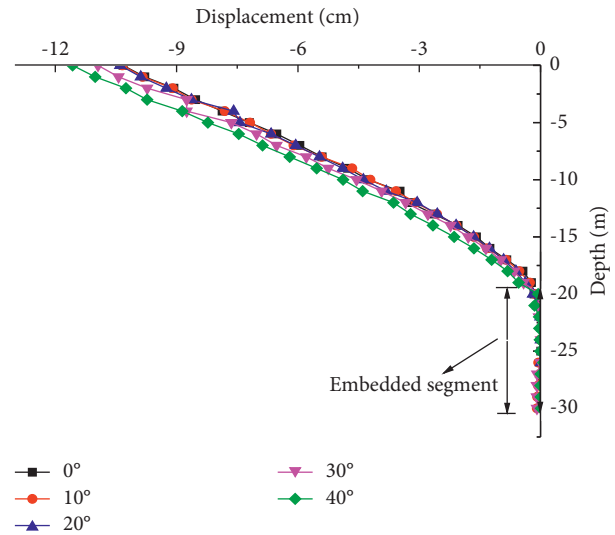
FIGURE 3: The influence of inclination on the displacement of antislide pile.
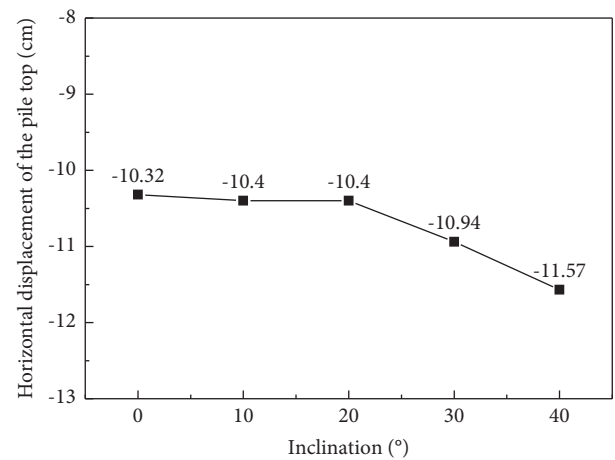
FIGURE 4: Relationship between the inclination and displacement of the antislide pile.

Gorges Reservoir Area is mostly soft and hard interlayer or there are soft and weak interlayers, five groups of layer thickness ratios of soft and hard rock are designed in this paper, namely, 1 : 9, 1 : 7, 1 : 5, 1 : 3, and 1 : 1. The inclination of the soft and hard rock used in the model is 0°, and the thickness of the single group is $2\,m$.

The effect of different soft and hard rock layer thickness ratios on the displacement of the antisliding pile is shown in Figure 5. As seen from figure, the displacement of the antisliding pile with different rock layer thickness ratios shows a similar trend with the burial depth. In contrast, the horizontal displacement of the pile increases with the distance from the bottom of the pile and reaches the maximum displacement at the top of the pile. With the increase in the layer thickness ratio, the horizontal displacement of the top of the pile shows an increasing linear trend, and the growth is within 3% (see
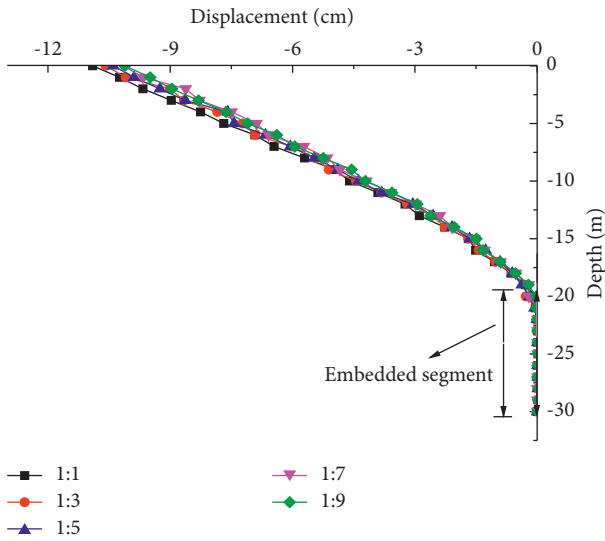
FIGURE 5: The influence of the layer thickness ratio on the displacement of the antislide pile.
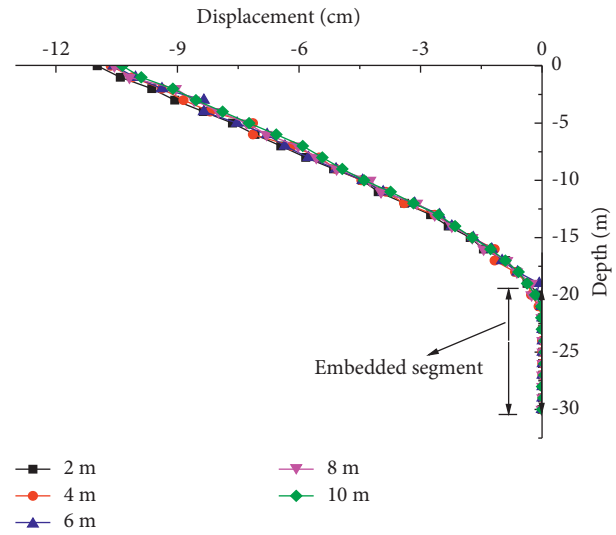
FIGURE 7: The influence of the single group thickness of rock on the displacement of the antislide pile.
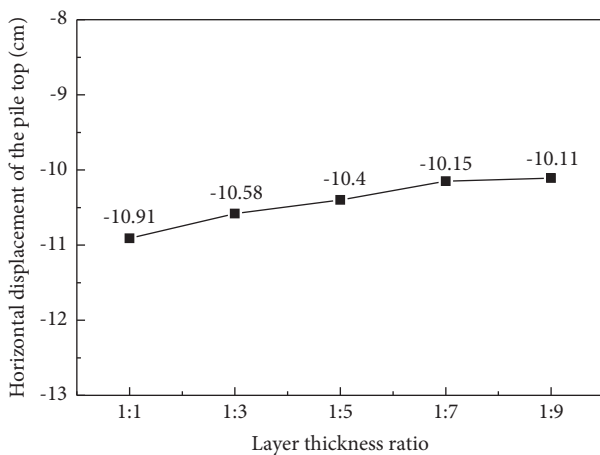
FIGURE 6: Relationship between the layer thickness ratio and displacement of the antislide pile.

Figure 6). This indicates that the influence of the rock layer thickness ratio on the horizontal displacement of the pile top of the antisliding pile is relatively small.

(3) Thickness of a Single Group of Soft and Hard Interbedded Layers of Bedrock. To study the effect of the single group thickness of soft and hard interlayer rock formations on the displacement of antisliding piles, five groups of soft and hard rock layer thickness ratios are designed in this study, namely, 2 m, 4 m, 6m, 8 m, and10 m. The inclination of soft and hard rock used in the model is 0°, and the layer thickness ratio is 1 : 1.

The effect of the thickness of the single group of different rock layers on the displacement of the antisliding pile is shown in Figure 7. As seen from the figure, the displacement of the antisliding pile corresponding to the thickness of a single group of different rock layers shows a similar trend with the depth of burial, with the

displacement of the top of the antisliding pile being the largest, and the displacement of the pile gradually decreases downward along the top of the pile, tending to zero when it reaches the bottom. When the thickness of the single group of rock layers increases from 2 m to 4 m, the maximum increase in the horizontal displacement of the pile top is approximately 3%, and the rest of the increase in the horizontal displacement of the pile top with the increase in the thickness of the single group is minimal (see Figure 8). This shows that the thickness of a single group of rock layers has a negligible effect on the horizontal displacement of the top of the antisliding pile.

3.2.2. Postpile Thrust of the Antisliding Pile. To study the influence of the postpile thrust on the displacement of the antisliding pile, the influence of the sliding body on the pile is transformed into the magnitude of the postpile thrust to be considered. This study establishes the numerical calculation model of the embedded solid section of an antisliding pile under different thrust conditions, and the postpile thrusts are 1000 kN/m, 1250 kN/m, 1500 kN/m, 1750 kN/m, and 2,000 kN/m. The other parameters in the model are kept consistent in Section 3.2.1.

The effect of different postpile thrusts on the displacement of the antisliding pile is shown in Figure 9. As seen from the figure, the displacement of the antisliding pile corresponding to different postpile thrusts basically shows a similar trend with burial depth, with the displacement of the top of the antisliding pile being the largest, and the displacement of the pile gradually decreases downward along the top of the pile, tending to zero when it reaches the bottom of the pile. The horizontal displacement of the top of the pile shows a gradual increase with the increase in the postpile thrust, when the thrust is between 1250 kN/m and 1750 kN/m, and the horizontal displacement of the top of the pile shows a uniform increase in approximately 20%. When the thrust force is greater than 1750 kN/m, the rate of growth
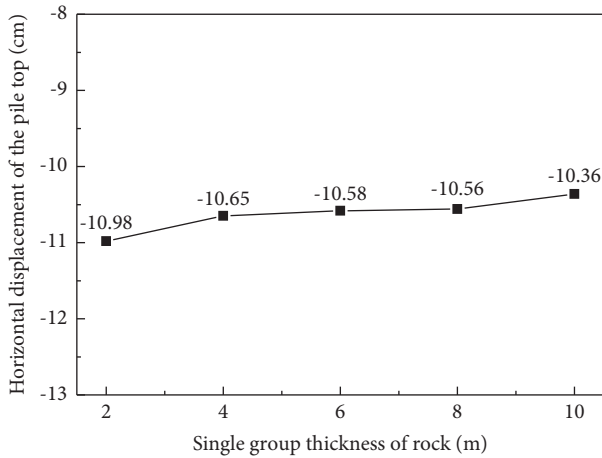
Figure 8: Relationship between the single group thickness of rock and displacement of the antislide pile.
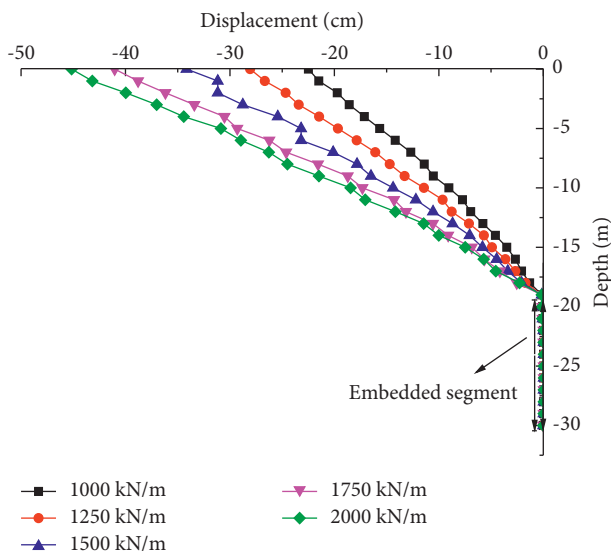
Figure 9: The influence of postpile thrust on the displacement of the antislide pile.
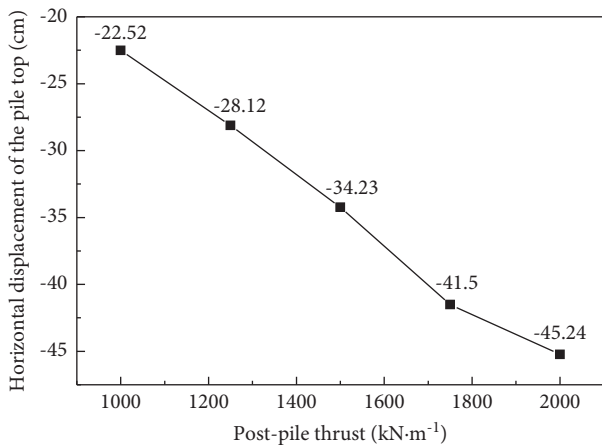
Figure 10: Relationship between postpile thrust and displacement of the antislide pile.

of the horizontal displacement at the top of the pile appears to start slowing down (see Figure 10). This indicates that the magnitude of the postpile thrust has a significant effect on the horizontal displacement of the pile top of the antisliding pile.

3.2.3. Characteristics of the Geometric Parameters of the Antisliding Piles. To study the influence of geometric parameters on the displacement of antisliding piles, the embedded depth and section size are selected as parameters for analysis in this study. In the model established in this section, the inclination of the soft and hard rock used is 0°, the layer thickness ratio is 1:1, the thickness of a single group of soft and hard rock layers is 2, and the horizontal load q is 290 kPa.

(1) Depth of Embedded Antisliding Piles. To study the effect of different embedment depths on the displacement of antisliding piles, five sets of embedment depth models are designed in this study, namely, 7 m, 9 m, 11 m, 13 m, and 15 m. The antisliding pile section size is 2 m × 3 m, and the pile length is 30 m.

The effect of different embedment depths on the displacement of antisliding piles is shown in Figure 11. The displacement of antisliding piles corresponding to different embedment depths shows a similar trend with the depth of embedment, with the displacement of the top of the antisliding pile being the largest and the displacement of the pile gradually decreasing downward along the top of the pile and tending to zero when it reaches the bottom of the pile. As shown in Figure 12, when the embedded depth of the antisliding pile increases from 7 m to 9 m, the displacement of the top of the antisliding pile significantly decreases. When the embedded depth of the antisliding pile is greater than 9 m, the change in the displacement of the top of the pile is minimal. Therefore, when designing antisliding piles, it is important to consider not only the stability of the project but also the financial requirements to find a reasonable embedment depth to give sufficient stability to the landslide.

(2) Section Size of the Antisliding Pile. To study the effect of different section sizes on the displacement of antisliding piles, five sets of section sizes were designed in this study, namely, 2 m × 3 m, 2.5 m × 3 m, 2.5 m × 3.5 m, 3 m × 3.5 m, and 3 m × 4 m. In addition, the embedded depth of antisliding piles was 12 m, and the pile length was 30 m.

The effect of different section sizes on the displacement of antisliding piles is shown in Figure 13. As seen from the figure, the displacement of antisliding piles corresponding to different section sizes shows a similar trend with the burial depth, with the displacement of the top of the antisliding pile being the largest, and the displacement of the pile gradually decreasing downward along the top of the pile, tending to zero when it reaches the bottom of the pile. As shown in Figure 14, for section sizes of 2 m × 3 m, 2.5 m × 3 m, 2.5 m × 3.5 m, and 3 m × 3.5 m, changing the antisliding pile section width results in an extremely small trend of change in the displacement of the pile body, while a substantial
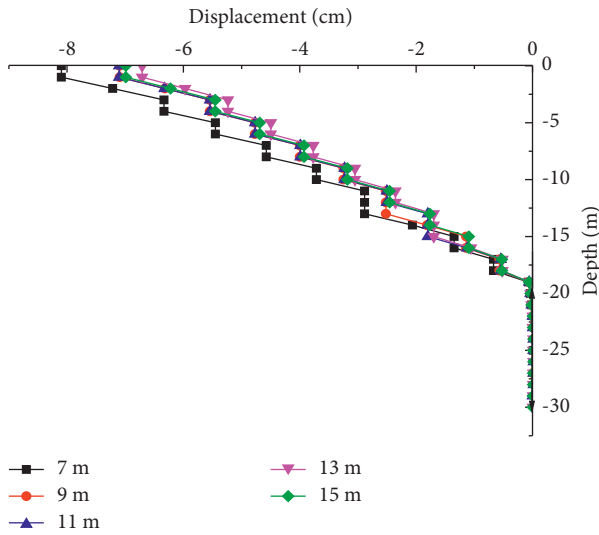
FIGURE 11: The influence of embedded depth on the displacement of antislide pile.
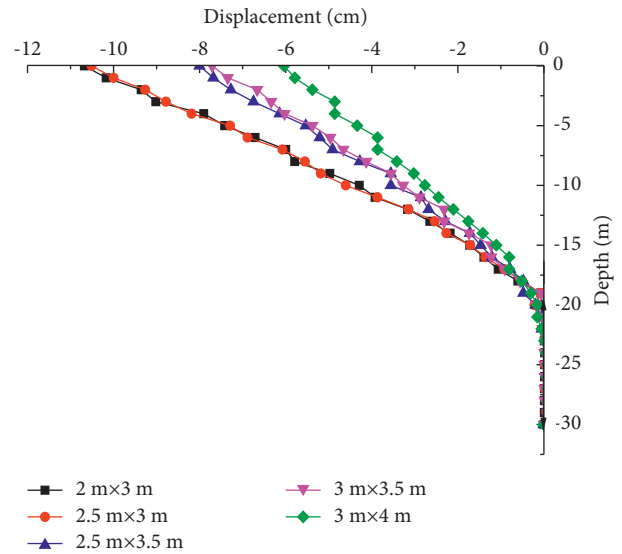
FIGURE 13: The influence of section size on the displacement of antislide pile.
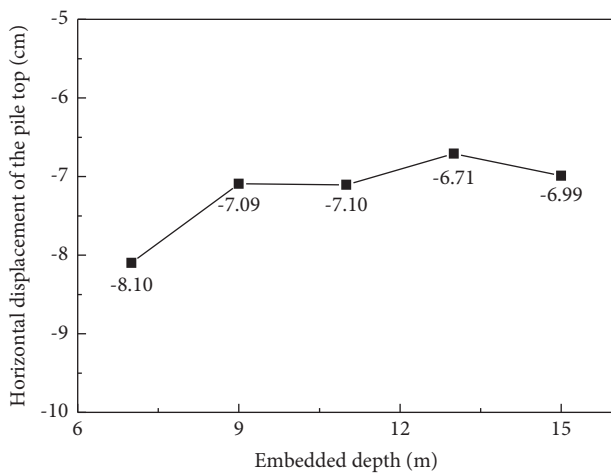
FIGURE 12: Relationship between embedded depth and displacement of antislide pile.
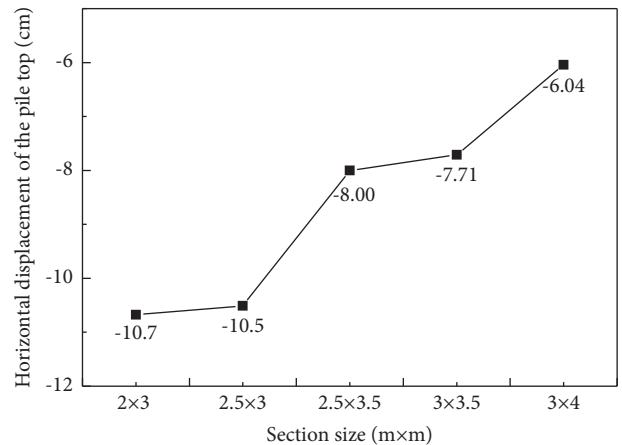
FIGURE 14: Relationship between section size and displacement of antislide pile.

reduction in the displacement of the top of the antisliding pile occurs when the pile section size is changed from 2.5 m × 3 m to 2.5 m × 3.5 m. The above study results show that the effect of the section length of the antislip pile is greater than the effect of the section width.

3.3. Orthogonal Experimental Design.
Orthogonal experimental design is a method to scientifically arrange and analyze multifactor tests using orthogonal tables [26]. With the advantages of ease of use, short cycle time, and good results, orthogonal designs have been widely used in geohazard research [27, 28].

Combined with the results of the above parametric analysis, this test determined six factors: layer thickness ratio of soft and hard rock, the thickness of a single group, the inclination of the slide bed rock, thrust magnitude, embedded depth and pile section size as independent variables, and displacement of the

top of the antisliding pile as dependent variables, and carried out a six-factor, five-level orthogonal design, with the factor level table shown in Table 2.

MATLAB software was used to generate orthogonal tables [29] containing a total of 120 sets of tests, and the pile top displacements were calculated using the discrete element numerical simulation software 3DEC. The physical and mechanical parameters and boundary conditions of the model are the same as those of the numerical tests in the previous section. The data from the 120 orthogonal design test results can be considered a sample database regarding the displacements between the pile tops of the soft and hard rock masses of the considered sliding strata and its six independent variables.

3.4. Determination of the Main Control Factor for the Top Displacement of the Antisliding Pile.
The MIC values were calculated for the dependent variable (the top displacement of the antisliding pile) and the six influencing factors (rock dip, layer

TABLE 2: Factor level.

Level	Tested level					
	Inclination (°)	Layer thickness ratio	Single group thickness (m)	Thrust (kN/m)	Embedded depth (m)	Section size (m)
1	0	1 : 1	2	1000	7	2 × 3
2	10	1 : 3	4	1250	9	2.5 × 3
3	20	1 : 5	6	1500	11	2.5 × 3.5
4	30	1 : 7	8	1750	13	3 × 3.5
5	40	1 : 9	10	2000	15	3 × 4

thickness ratio, single group thickness, thrust magnitude, embedment depth, and antisliding pile size), and for the six independent variable influencing factors in relation to each other. The results of the calculations are shown in the table below (see Table 3).

From the MIC values between the antisliding pile top displacement and the six influencing factors, it can be seen that the influences of the antislip pile top displacement are in descending order: postpile thrust > embedded depth > pile section size > rock inclination > single group thickness > layer thickness ratio. The most significant influence on the pile top displacement is the magnitude of the postpile thrust, with the MIC value of the pile top displacement reaching 0.725. Within the sliding bedrock structure feature group, the most influential pile top displacement is the inclination of the soft and hard interbedded rock layers in the sliding bed, suggesting that the inclination of the soft and hard interbedded layers of bedrock contains more information about the variation in pile top displacement. In the group of geometric characteristics of antisliding piles, both the embedded depth and cross-sectional dimensions significantly affect the displacement of the top of the pile, with the MIC values of 0.629 and 0.598, respectively. Therefore, in the case of soft and hard interbedded rock in the sliding bed, the postpile thrust magnitude, pile section size, embedment depth, and rock inclination can be used as the dominant combination of factors to control when predicting the displacement of the top of the antisliding pile.

4. Pile Top Displacement Prediction Model Based on MIC-SVR

4.1. Model Constitution. In this section, four factors, namely, the inclination angle, thrust, embedment depth, and pile cross-sectional size of the soft and hard interlayer of the sliding bed, were used as independent variables, and the displacement of the top of the antisliding pile was used as the dependent variable. A total of 71 sets of experiments were designed on this basis. The discrete element numerical simulation method (3DEC) was used to simulate each set of tests, with the same physical and mechanical parameters and boundary conditions of the model as the numerical tests in the previous chapter. The 71 datasets can be considered as a sample database on the relationship between the pile top displacements and the independent variables considering the soft and hard interbedded layers of bedrock, as shown in Table 4.

4.2. Pile Top Displacement Prediction Model Based on MIC-SVR. Using 71 sets of data as the training database, with the four principal control factors as input variables and their

corresponding antisliding pile top displacements as output variables, the optimal combination of parameters $\varepsilon = 0.001$, $C = 0.8745$, and $g = 8.3913$ for the support vector regression was obtained based on grid search and cross validation. Based on the optimal combination of parameters, the optimal SVR model for the prediction of the displacement of the top of the antisliding pile can be obtained. The comparison results between the predicted values of the displacement of the top of the antisliding pile and the numerical test results are shown in Figure 15. The comparison shows that the maximum error between the predicted pile top displacement and the numerical test results is 0.008 m, and most of the errors are small and basically negligible. Therefore, the SVR model obtained through training can well reflect the nonlinear relationship between the antisliding pile top displacement values and the selected primary control factors. The support vector x_i, the support-vector coefficients ($-\alpha, +\alpha *$), and the deviation constant D can be obtained by calling the libsvmtrain function of LIBSVM [30], and 71 support vectors and support-vector coefficients are generated. The value of the deviation constant D is -0.0901. According to equation (6), the prediction equation for pile top displacement based on support-vector regression is obtained as follows:

$$y = \sum_{i=1}^{i=71} \left(-\alpha + \alpha_i^* \right) e^{-8.3913\|x_i - x\|} - 0.0901. \tag{6}$$

Figure 15 shows a comparison between the predicted and numerical test values of pile top displacement for 71 sets of antisliding piles, with a coefficient of determination R^2 of approximately 96.88% for both sets of data. The results indicate that the accuracy of the established support-vector regression equation is high and is applicable to the prediction of pile top displacement for subsequent examples.

5. Practical Example Validation and Comparative Analysis

5.1. Practical Example Validation. Both the Majiagou No. 1 Landslide and Zhangfeimiao Landslide are located in the Jurassic strata of the Three Gorges Reservoir Area [13, 31], and both landslides use antisliding piles as the support measure. The main control factors and the measured displacement data at the top of the antisliding piles are shown in Table 5.

Equation (6) was used to predict the top displacement of the antislip piles for both landslides. By substituting the inclination, postpile thrust, embedment depth, and pile

Table 3: MIC values between the pile top displacement of the antislide pile and influencing factors.

MIC value	Inclination	Layer thickness ratio	Single group thickness	Postpile thrust	Embedded depth	Section size	Displacement
Inclination	1	0.006	0.006	0.006	0.006	0.003	0.565
Layer thickness ratio	0.006	1	0.012	0.004	0.005	0.001	0.315
Single group thickness	0.006	0.012	1	0.002	0.002	0.002	0.327
Postpile thrust	0.006	0.004	0.002	1	0.005	0.001	0.757
Embedded depth	0.006	0.005	0.002	0.005	1	0.002	0.629
Section size	0.003	0.001	0.002	0.001	0.002	1	0.598
Displacement	0.565	0.315	0.327	0.757	0.629	0.598	1

Table 4: Sample database.

Specimen	Inclination (°)	Postpile thrust (kN/m)	Embedded depth (m)	Section size (m)	Displacement (m)
1	10	1500	15	3×3.5	0.124
2	0	1250	11	2.5×3.5	0.092
3	20	1250	15	2×3	0.126
4	10	1250	13	2×3	0.124
5	0	1500	7	2.5×3	0.149
6	0	1500	9	3×3.5	0.126
7	0	1000	13	2.5×3.5	0.077
8	10	1750	7	2×3	0.205
9	20	1000	15	2×3	0.110
10	10	1750	15	3×3.5	0.154
11	40	1500	11	2.5×3	0.240
12	0	1000	9	2.5×3.5	0.081
13	30	1500	9	2.5×3	0.155
14	0	1750	9	3×4	0.107
15	10	1250	9	2.5×3	0.141
16	10	1750	11	2.5×3.5	0.140
17	30	1250	11	2×3	0.212
18	0	2000	11	3×3.5	0.168
19	0	1000	7	2×3	0.112
20	20	1500	11	2.5×3.5	0.168
21	20	1250	7	3×4	0.118
22	20	1250	7	3×3.5	0.130
23	10	2000	7	2.5×3.5	0.225
24	10	1000	7	2.5×3	0.119
25	20	2000	13	2.5×3	0.228
26	30	1750	11	2.5×3	0.223
27	30	1250	13	2.5×3.5	0.110
28	40	1750	13	2×3	0.309
29	40	1250	9	2.5×3.5	0.255
30	20	1000	9	2.5×3	0.100
31	10	1000	9	3×3.5	0.090
32	10	2000	7	2.5×3.5	0.225
33	0	2000	11	3×3.5	0.157
34	0	1250	13	2.5×3	0.116
35	30	2000	9	2×3	0.230
36	10	1500	9	3×4	0.108
37	10	1750	11	3×3.5	0.151
38	40	1000	7	3×3.5	0.162
39	30	1750	13	3×3.5	0.314
40	10	1000	13	2.5×3.5	0.083
41	20	2000	13	2.5×3	0.203
42	20	1750	9	2.5×3.5	0.180
43	20	1500	7	3×3.5	0.163
44	10	1500	13	3×4	0.100
45	40	1750	9	2×3	0.250
46	0	1250	15	2.5×3	0.117

Table 4: Continued.

Specimen	Inclination (°)	Postpile thrust (kN/m)	Embedded depth (m)	Section size (m)	Displacement (m)
47	30	1000	11	3×4	0.098
48	40	1000	11	3×3.5	0.103
49	20	1500	9	3×3.5	0.156
50	0	1500	11	2×3	0.134
51	0	1250	13	3×3.5	0.096
52	20	1750	13	2.5×3.5	0.147
53	30	1000	15	2.5×3.5	0.086
54	0	1750	7	3×4	0.128
55	40	1250	7	2.5×3.5	0.201
56	20	1250	11	3×4	0.123
57	30	2000	9	2×3	0.233
58	0	1500	13	2×3	0.143
59	0	1750	15	2.5×3	0.171
60	20	1750	7	2.5×3	0.204
61	30	1500	15	2.5×3.5	0.140
62	20	1000	13	3×3.5	0.085
63	20	1000	9	2×3	0.108
64	10	1000	11	2.5×3	0.100
65	30	1000	11	2.5×3	0.113
66	10	1250	11	2×3	0.125
67	30	1250	9	3×3.5	0.140
68	30	1000	13	3×4	0.070
69	20	1750	11	2×3	0.182
70	0	1750	9	2.5×3.5	0.141
71	10	1500	13	2×3	0.162
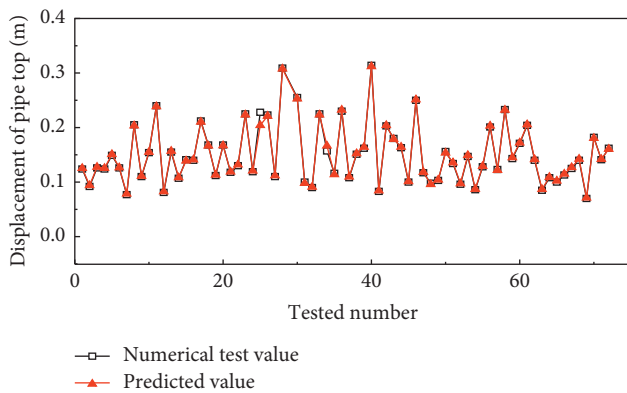
Figure 15: Comparison of the numerical test value and the predicted value.

section size into equation (6) for both landslides, the antisliding pile top displacement y can be calculated to be 0.1447 m and 0.092 m, respectively. The predicted pile top displacement of the Majiagou No. 1 Landslide is approximately 3.5% smaller than the actual value, and the antislip pile top displacement of the Zhangfeimiao Landslide is approximately 8% smaller than the actual value, which indicates that the prediction equation of pile top displacement proposed in this study has good accuracy.

5.2. Comparative Analysis of Predictive Models. To further validate the feasibility of the MIC-SVR prediction model proposed in this study, the prediction results of the Elman neural network, support-vector regression (SVR), and long

short-term memory neural network (LSTM) were simultaneously selected in this section for comparison and analysis with the actual values of the two landslides, as shown in Figure 16.

As seen from Figure 16, for the Majiagou No. 1 Landslide, the predictions of the SVR, LSTM, ELMAN, and MIC-SVR models proposed in this study are 14.53 cm, 10.2 cm, 9.3 cm, and 14.47 cm, respectively, and compared to the measured value (15.0 cm), all predictions are small, decreasing by approximately 3.2%, 32%, 38%, and 3.5%. For the Zhangfeimiao Landslide, the predictions of the SVR, LSTM, ELMAN, and MIC-SVR models proposed in this study are 9.3 cm, 7.1 cm, 5.1 cm, and 9.2 cm, respectively, all of which are still smaller than the measured value (10.0 cm), with reductions of approximately 7%, 29%, 49%, and 8%, respectively. For the Zhangfeimiao Landslide, the predictions of the SVR, LSTM, ELMAN, and MIC-SVR models proposed in this study are 9.3 cm, 7.1 cm, 5.1 cm, and 9.2 cm, respectively, all of which are still smaller than the measured value (10.0 cm), with reductions of approximately 7%, 29%, 49%, and 8%, respectively. Combining the comparative prediction results of the two landslides, the SVR model and the MIC-SVR model proposed in this study have higher prediction accuracy, and the results are better than those of the other two prediction models. However, compared with the SVR model, the prediction model proposed in this study, which uses MIC-based screening out the main control factors and circumvents the factors with less influence, not only has a greater advantage in the prediction of pile top displacement of antisliding piles but also reduces the calculation samples and greatly improves the working efficiency. Therefore, the MIC-SVR prediction model proposed

TABLE 5: The main control factors and the measured value of the antislide pile.

Landslide name	Inclination (°)	Postpile thrust (kN/m)	Embedded depth (m)	Section size (m)	Displacement (m)
Majiagou No. 1	28°	1062.66	8	2 ∗ 3	0.15
Zhangfeimiao	5°	1200	11	2.75 × 3.5	0.10
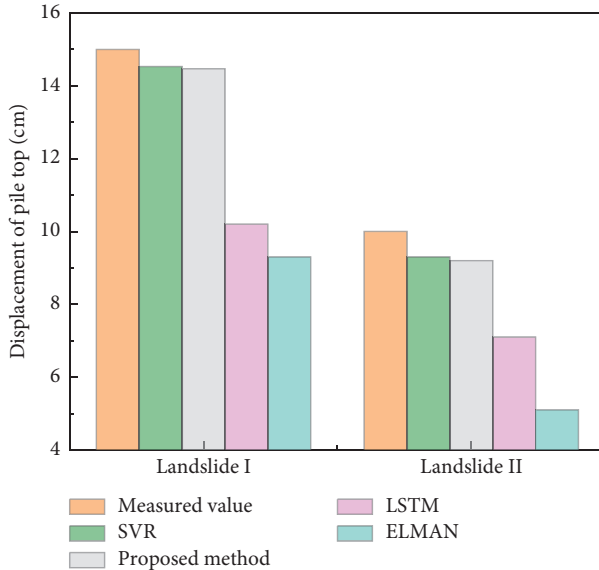
FIGURE 16: Comparison between the measured value and the predicted value of different methods.

in this study is feasible in practical engineering applications and can better reflect the corresponding relationship between the main influencing factors of the antisliding pile deformation and top displacement of the antisliding pile.

6. Conclusions

(1) The largest influence on the pile top displacement is the magnitude of the postpile thrust, which has an MIC value of 0.725. The most significant influence on the pile top displacement is the inclination of the soft and hard interlayer in the sliding bedrock structure characteristic group. The embedded depth and pile section size of the antisliding pile in the geometry characteristics group greatly influence the pile top displacement, with MIC values of 0.629 and 0.598, respectively. In the case of soft and hard interbedded rock, the postpile thrust, pile section size, embedment depth, and rock inclination are the main control factors in predicting the pile top displacement of the antisliding pile.

(2) A database of pile top displacement concerning the main control factors (sliding bedrock inclination, postpile thrust, embedded depth, and pile section size) was established, and the optimal combination of parameters for SVR was obtained based on grid search and cross validation. On this basis, a nonlinear prediction model of pile top displacement based on the main control factors was developed. The prediction model proposed in this study (MIC-SVR)

was compared with SVR, LSTM, and ELMAN by combining practical examples of the Majiagou No. 1 Landslide and Zhangfeimiao Landslide. The prediction model proposed in this study avoids the factors with small influence, reduces the calculation sample, and improves the working efficiency.

Data Availability

The data used to support the findings of this study are included in the article.

Conflicts of Interest

The authors declare that there are no conflicts of interest.

Acknowledgments

References

[1] J. Ma, Y. Wang, X. Niu, S. Jiang, and Z. Liu, "A comparative study of mutual information-based input variable selection strategies for the displacement prediction of seepage-driven landslides using optimized support vector regression," *Stochastic Environmental Research and Risk Assessment*, 2022.

[2] H. H. Zhu, B. Shi, J. F. Yan, J. Zhang, C. C. Zhang, and B. J. Wang, "Fiber Bragg grating-based performance monitoring of a slope model subjected to seepage," *Smart Materials and Structures*, vol. 23, no. 9, pp. 1–12, 2014.

[3] J. Han, D. Liu, Y. Guan et al., "Study on shear behavior and damage constitutive model of tendon-grout interface," *Construction and Building Materials*, vol. 320, Article ID 126223, 2022.

[4] Y. K. Wang, H. M. Tang, J. S. Huang, T. Wen, J. W. Ma, and J. R. Zhang, "A comparative study of different machine learning methods for reservoir landslide displacement prediction," *Engineering Geology*, vol. 298, Article ID 106544, 2022.

[5] L. L. Chen, W. G. Zhang, Y. Zheng, D. M. Gu, and L. Wang, "Stability analysis and design charts for over-dip rock slope against Bi-planar sliding," *Engineering Geology*, vol. 275, Article ID 105732, 2020.

[6] J. W. Ma, X. X. Niu, H. M. Tang, Y. K. Wang, T. Wen, and J. R. Zhang, "Displacement prediction of a complex landslide in the Three Gorges Reservoir Area (China) using a hybrid computational intelligence approach," *Complexity*, vol. 2020, Article ID 2624547, 15 pages, 2020.

[7] G. R. Martin and C. Y. Chen, "Response of piles due to lateral slope movement," *Computers & Structures*, vol. 83, no. 8–9, pp. 588–598, 2005.

[8] E. Conte, A. Troncone, and M. Vena, "Nonlinear three-dimensional analysis of reinforced concrete piles subjected to horizontal loading," *Computers and Geotechnics*, vol. 49, pp. 123–133, 2013.

[9] A. Klar and S. Frydman, "Three-dimensional analysis of lateral pile response using two-dimensional explicit numerical scheme," *Journal of Geotechnical and Geoenvironmental Engineering*, vol. 128, no. 9, pp. 775–784, 2002.

[10] G. Lei, H. Tang, and W. Wu, "A pile-soil separation concerned model for laterally loaded piles in layered soils," *Recent Advances in Modeling Landslides and Debris Flows*, Springer Series in Geomechanics and Geoengineering, Germany, pp. 211–228, 2015.

[11] G. Mylonakis and G. Gazetas, "Settlement and additional internal forces of grouped piles in layered soil," *Géotechnique*, vol. 48, no. 1, pp. 55–72, 1998.

[12] R. Salgado, F. S. Tehrani, and M. Prezzi, "Analysis of laterally loaded pile groups in multilayered elastic soil," *Computers and Geotechnics*, vol. 62, pp. 136–153, 2014.

[13] M. Dong, L. Wang, B. Shahbodagh, X. Du, S. Deng, and Z. Sun, "Effect of the soft and hard interbedded layers of bedrock on the mechanical characteristics of stabilizing piles," *Applied Sciences*, vol. 10, no. 14, p. 4760, 2020.

[14] M. Y. Fattah, H. H. Karim, and M. K. M. Al-Recaby, "Investigation of the end bearing load in pile group model in dry soil under horizontal excitation," *Acta Geotechnica Slovenica*, vol. 18, no. 1, pp. 79–106, 2021.

[15] M. Y. Fattah, H. H. Karim, and M. K. M. Al-Recaby, "Vertical and horizontal displacement of model piles in dry soil with horizontal excitation," *Proceedings of the Institution of Civil Engineers-Structures and Buildings*, vol. 174, no. 4, pp. 239–258, 2021.

[16] M. Y. Fattah, W. H. S. Al-Soudani, and M. Omar, "Estimation of bearing capacity of open-ended model piles in sand," *Arabian Journal of Geosciences*, vol. 9, no. 3, pp. 1–14, 2016.

[17] M. Y. Fattah and W. H. S. Al-Soudani, "Bearing capacity of open-ended pipe piles with restricted soil plug," *Ships and Offshore Structures*, vol. 11, no. 5, pp. 501–516, 2016.

[18] X. X. Liu, Y. Y. Xia, X. S. Zhang, and R. Q. Guo, "Effects of drawdown of reservoir water level on landslide stability," *Chinese Journal of Rock Mechanics and Engineering*, vol. 24, no. 8, p. 6, 2005.

[19] R. Yong, *Interaction between Thrust Load Caused Landslideand Antislide Pile in Jurassic Strata in Three Gorges Reservoir Region*, China University of Geosciences, Wuhan, China, 2014.

[20] H. Z. Zhan, L. Q. Wang, C. S. Wang, and N. Zhang, "Study of mechanical characters of anti-sliding piles considering differentfoundation coefficients of sliding bed [J]," *Rock and Soil Mechanics*, vol. 35, no. S2, pp. 250–256, 2014.

[21] D. N. Reshef, Y. A. Reshef, H. K. Finucane et al., "Detecting novel associations in large data sets," *Science*, vol. 334, no. 6062, pp. 1518–1524, 2011.

[22] P. Samui, "Slope stability analysis: a support vector machine approach," *Environmental Geology*, vol. 56, no. 2, pp. 255–267, 2008.

[23] A. J. Smola and B. Schölkopf, "A tutorial on support vector regression," *Statistics and Computing*, vol. 14, no. 3, pp. 199–222, 2004.

[24] C. S. Wang, *Quatitative Evaluation Methods for Roughness and Peak Shear Strength of Rock Joints*, China University of Geosciences, Wuhan, China, 2019.

[25] The Second Survey and Design Institute of the Ministry of Railways, *Anti-slide Pile Design and Calculation*, China Railway Press, Beijing, China, 1983.

[26] Y. Y. Li, *Experimental Design and Data Processing (Version 2) (M)*, Chemical Industry Press, Beijing, China, 2013.

[27] H. H. Yao, A. X. Wu, Y. M. Wang, and H. C. Xia, "Stability analysis of stope retention pillars in broken rock conditions," *Journal of University of Science and Technology Beijing*, vol. 33, no. 4, p. 400, 2011.

[28] X. Y. Fan, S. J. Tian, and X. D. Duan, "Study of topography factors influence on motion parameters for seismic slope-toe landslides," *ChineseJournalofRockMechanicsandEngineering*, vol. 33, no. s2, p. 4056, 2014.

[29] S. Q. Pang and S. S. Lu, "Construction method of orthogonal table and MATLAB realization," *China Health Statistics*, vol. 34, no. 2, pp. 364–367, 2017.

[30] Z. H. Sun, L. Q. Wang, J. Q. Zhou, and C. Wang, "A new method for determining the hydraulic aperture of rough rock fractures using the support vector regression," *Engineering Geology*, vol. 271, Article ID 105618, 2020.

[31] J. Liu, "Response characteristics of landslide treatment project to reservoir water level change-an example the Zhangfeimiao landslide in the Three Gorges reservoir area," *Yangtze River*, vol. 51, no. 1, pp. 129–135, 2020.

Research Article

Nonlinear Seismic Response Based on Different Site Types: Soft Soil and Rock Strata

Meng Xiao [ID],[1,2] **Jie Cui** [ID],[1,2] **Ya-dong Li** [ID],[1,2] **and Van-Quang Nguyen** [ID][3]

[1]*School of Civil Engineering, Guangzhou University, Guangzhou 510006, China*
[2]*Guangdong Provincial Engineering and Technology Research Center of Geo-Structure Safety and Protection, Guangzhou 510006, China*
[3]*Department of Civil Engineering, Vinh University, 182 Le Duan Street, Vinh city, Vietnam*

Correspondence should be addressed to Ya-dong Li; liyadong@gzhu.edu.cn

Site condition is an important part of urban underground space development and construction. The seismic fortification of the site plays an important role in the safety of the whole project. To study the seismic dynamic response of the site under different geological conditions, seismic waves of different intensities (Chichi wave and Kobe wave) were input to a rock site with good geological conditions and a soft soil site, respectively. In this paper, the dynamic responses of these two types of free sites were calculated and analyzed using DEEPSOIL numerical simulation software. The dynamic responses of different types of sites under strong shock and persistent earthquakes are discussed under the equivalent linear and nonlinear conditions, and the related dynamic parameters are studied. The results show that the equivalent linear method is more effective than the nonlinear method, especially in the calculation of the strong nonlinear soft soil response induced by strong earthquakes. The amplification effect is more obvious in rock layer sites under strong earthquakes, and the "weakening" effect of soft soil sites is more obvious. Arias's strength values show that both types of sites are safe under the incident of the two waves, but soft soil sites have better seismic performance. The results calculated by the equivalent linear method are larger and more unsafe; in particular, in the case of a strong earthquake with a stronger nonlinear Kobe wave, the results are more inaccurate. The purpose of this study is to provide a reference for seismic design and reinforcement measures of underground engineering.

1. Introduction

Site seismic response analysis is an important part of site seismic safety evaluation. It is of great reference value to the design of seismic-sensitive dynamic parameters of sites and structures, which will affect the subsequent design and construction of underground space and structure. In recent years, the macroscopic seismic damage data and the observation records of strong earthquakes have proved that the site conditions not only have an important influence on the peak acceleration and spectral shape of ground motion but also have a very close relationship with the seismic response and earthquake damage mechanism of different types of engineering structures. Some scholars have studied the seismic response of soft soil sites. Huang et al. [1] adopted

the one-dimensional equivalent linearized frequency domain analysis method to study the seismic response of the site in the deep soft soil overburden area of Shanghai and established a dynamic analysis model. Taking El Centro seismic wave as an example, the acceleration response and spectral characteristics of the seismic response of the soil in the Shanghai area are analyzed. The results show that the surface peak ground acceleration (PGA) of the soft soil site has amplification characteristics when the seismic category is 7°; that is, the site peak ground acceleration (PGA) is equal to 0.1 g. The spectral composition of surface acceleration has the characteristics of low-frequency amplification and high-frequency filtering. The preeminent period of the response spectrum of ground motion acceleration also tends to move towards the long period direction. Huang et al. (2000)

conducted an experimental study on the site seismic response of soft soil sites with soft interlayers in Hong Kong. Through analysis, they found that the weak interlayer magnified the long period of response spectrum and reduced the dynamic intensity of the earthquake. In addition, they also proposed a normalized design response spectrum for such sites. Cao et al. [2] constructed a seismic response analysis model for various soil layers based on soft soil sites in the Jianghuai region of China. They analyzed the effects of the buried depth and thickness of the soft layer on the peak surface acceleration of soft soil under three kinds of strong earthquake conditions. The results show that the peak surface acceleration and the amplification coefficient of the soil layer decrease with the increase of the buried depth and thickness of the soft layer. When the buried depth and thickness of the soft interlayer exceed a certain value, the site begins to have a shock absorption effect. The deeper the buried depth and thickness of the soft layer are, the higher the ground vibration intensity is, and the more obvious the shock absorption effect is. Ma et al. [3] conducted a series of large-scale drainage dynamic triaxial tests to study the dynamic characteristics of saturated sand and gravel soil in Nanning and established a model which can accurately predict the dynamic deformation characteristics of saturated round gravel.

Numerical analysis and model test methods are often used to analyze site seismic response. One-dimensional site response methods are commonly used nonlinear methods and equivalent linear methods. The equivalent linear method approximates the nonlinear problem and is not as accurate as the nonlinear method in calculating the seismic induced site dynamic response. DEEPSOIL (Hashash et al. [4]) is one-dimensional site seismic response analysis software that allows linear, equivalent linear, and time-domain nonlinear analyses of the site and considers the effects of pore water pressure. From the engineering practical point of view, DEEPSOIL numerical software provides the best time-domain nonlinear elastoplastic calculation. Sun et al. [5] proposed the method of global equivalent shear strain and compiled the calculation program of seismic response of soil layer based on equivalent linearization, which can be used to simulate the amplification of strongly nonlinear site earthquakes under strong earthquakes. Wang et al. compared and verified the computational results of weakly coupled nonlinear site response simulated by Abaqus and one-dimensional liquefaction site seismic response calculated by DEEPSOIL v6.0, and obtained more accurate propagation characteristics of high-frequency seismic waves and filtering effect of liquefaction site. Zhang et al. [6] established a soft soil site model with DEEPSOIL software and analyzed the seismic response of a typical III type soft soil site (according to Chinese industry standards). They studied the sensitivity of fitting parameters and the effects of equivalent linear method and time-domain nonlinear method on response spectrum of peak acceleration and surface acceleration and pointed out the shortcomings of equivalent linear method in analyzing the seismic response of soft soil sites. Gao et al. [7] used the FLUSH finite element analysis program to calculate the surface acceleration peak

value and acceleration response spectrum under three different input waves and different replacement rates in the two-dimensional reinforced composite foundation site. Based on some site conditions in the loess area, Liao et al. [8] obtained the dynamic parameters of soil: dynamic shear modulus G and equivalent viscous damping ratio D, through dynamic triaxial tests. A heterogeneous soil layer model considering the wave velocity and the depth of weak interlayer was established. El Centro wave was input to the bottom of bedrock for experimental simulation. The results show that the soft interlayer in the loess stratum will reduce the maximum acceleration of seismic response and the ground acceleration. Ou et al. studied the dynamic response of concrete dam of large mud dump reservoir induced by artificial synthetic seismic waves and simulated it with viscoelastic artificial boundary.

The study of urban underground space often involves the interaction and response of soil and structure, mainly considering the dynamic response of structures (Ma et al. [9], Chen et al. [10], Han et al. [11], Wang et al. [12]). However, the nonlinear problem of the site under earthquake and the amplification effect of the site are also very important. In this paper, the seismic dynamic response of the actual engineering sites was analyzed on the basis of the theory of seismic engineering, combined with the geological exploration data in the two actual engineering sites. In order to study the seismic dynamic response of the site under different geological conditions, seismic waves of different intensities (Chichi wave and Kobe wave) were input to a rock site with good geological conditions in Nanning City, Guangxi Province, China, and a soft soil site with bad geological conditions in the coastal area of Guangdong Province, China. Moreover, the effects of different types of earthquakes and site geological conditions on the dynamic parameters of site seismic response were discussed using the DEEPSOIL v7.0 numerical simulation software, and the site safety and amplification effects were also analyzed.

2. Engineering Projects

Baoneng City Square Project of Nanning Wuxiang New Area is located in Yongning District, Nanning City. The site belongs to the denuded hilly remnant geomorphic unit. The site is near Yongjiang River. No surface water is found on the site. The groundwater is mainly upper stagnant water, and the surface roughness is of class B (according to Chinese industry standards). Field earthquake basic intensity is 7°, and seismic fortification intensity is 7°. The soil of the building site is classified as II (according to Chinese industry standards). The basic seismic acceleration of the design is 0.10 g. The surface bearing capacity is high, and the upper stagnant water mainly occurs in the plain fill, red clay, and gravel. The stable water level depth is 0.50 m–20.40 m, and the stable water level elevation is 74.16 m–105.79 m. The main replenish source is surface water, which is greatly affected by the season. The bedrock fissure water mainly occurs in strongly weathered argillaceous siltstone, strongly weathered calcareous siltstone, strongly weathered siliceous rock, and moderately weathered calcareous siltstone (the

local limestone sections are manifested as karst cave fissure water). During the survey, the stable water level elevation is 65.27 m–98.98 m, and the water quantity is relatively stable. The equivalent shear wave velocity of the overlying soil of the site is 170.00–200.00 m/s. Through sorting out the geological prospecting data of Baoneng City Square in Wuxiang New District of Nanning and the headquarter base of Nanning Qianhai Life Insurance, unified stratigraphic parameters are selected for calculation after statistical analysis. The soil parameters are shown in Table 1, and the parameters in this table will be used to represent the specific geological types in part areas of Nanning in the subsequent seismic dynamic response analysis.

The soft soil site is based on a geological survey report of the data of 384 boreholes drilled in an engineering site in the coastal soft soil area of Guangzhou. Most of the strata in the coastal areas of Guangzhou are mainly composed of silt, with a thickness of about 10–30 m. According to the geological origin, the site strata are successively divided into quaternary system (Q^{ml}), grain filling soil <1-3>, marine and continental strata (Q^{mc}), silt layer <2-1>, diluvial layer ($Q^{al + pl}$), fine sand layer <3-1>, medium sand layer <3-2>, eluvial soil (Q^{el}), and hard plastic sandy clay layer <4-1>; the bedrock is mainly Yanshanian granite (γ), strongly weathered layer <5>, moderately weathered layer <6>, and slightly weathered layer <7>. The physical and mechanical parameters of soil in each layer are shown in Table 1. Soil parameters of soft soil base are shown in Table 2.

3. Calculation Model and Analysis Method

3.1. Theory and Model.
The MRDF pressure-dependent hyperbolic model [13], a non-Masing model inherent in DEEPSOIL software, was used to describe the hysteretic behavior of media loading and unloading. By introducing the reduction factor, the modulus reduction curve and damping curve can be fitted simultaneously. The damping performance is improved as follows:

$$\xi_{\text{MasingHysteretic}} = F(\gamma_{\text{Max}}) * \xi_{\text{Masing}}, \tag{1}$$

where $F(\gamma_m)$ is the reduction factor calculated by the function of γ_m, γ_m is the maximum shear strain experienced by the soil at any given moment, and ξ_{Masing} is the hysteretic damping calculated by Masing rule based on the modulus reduction curve.

In this calculation, we adopted the MRDF-Darendeli model, which was proposed by Darendeli in 2001 and improved the reduction coefficient on the basis of the MRDF pressure-dependent hyperbolic model. This formula is a modified hyperbolic model based on experience, which is used to predict the nonlinear dynamic response of different types of soil. The developed model is implemented as a simplification factor in the following form:

$$F(\gamma_m) = P_1 \left(\frac{G(\gamma_m)}{G_0} \right)^{P2}, \tag{2}$$

where γ_m is the maximum shear strain experienced at any given time; $G(\gamma_m)$ is the shear modulus at γ_m; and P_1, P_2, and P_3 are the fitting parameters. By setting $P_1 = 1$ and $P_2 = 0$, the reduction factor is equal to 1 (regardless of the value of P_3), and the model is reduced to the extended Masing criteria.

Figure 1 shows the models established under two different geological conditions. Model 1 is the model under geological conditions in Nanning area, and model 2 is the model under soft soil conditions. The profile of model 1 has a total depth of 115 m, a natural frequency of 0.9646 (Hz), and a natural period of 1.037 seconds. Model 2 has a total depth of 62 m, a natural frequency of 0.8071 (Hz), and a natural period of 1.239 seconds. It can be seen that model 1 is dominated by relatively hard rock strata, while model 2 has poor geological conditions and is dominated by silt.

3.2. Input Parameters.
Figures 2 and 3 show acceleration time history curves of two different types of input seismic waves. The peak acceleration of the first type of seismic wave is no more than 0.2 g, while the peak acceleration of the second type of seismic wave is no more than 0.8 g. The first type of seismic wave lasts longer than the second, which can be described as a short, strong earthquake.

Figures 4 and 5 show variation of peak spectral acceleration with the period (response spectrum) and the relationship between Fourier amplitude and frequency (Fourier amplitude spectrum) after input of different seismic waves, respectively. It can be seen that the peak spectral acceleration of Kobe input seismic wave exceeds 2.5 g at low period and that of Chichi input seismic wave is about 0.5 g. As shown in Figure 5, the Fourier amplitude of the two seismic waves is very large at low frequencies, and the maximum value of Kobe input wave is 0.6 g-s, which is twice that of Chichi's input wave 0.3 g-s.

Figure 6 shows Fourier amplitudes and 5% damped spectral acceleration of the two input seismic waves. It shows that the amplitude of the two kinds of seismic waves is higher at low frequency and low periods. The 5% damping spectrum acceleration amplitude of the Kobe input wave is more than 2.5 g, and that of the Chichi input wave is about 0.5 g.

4. Numerical Analysis

The simplification of some parameters is involved in time-history analysis and spectrum analysis, and the meaning of parameter representation is explained as follows: peak spectrum acceleration (PSA); peak spectrum acceleration (PSV); peak ground acceleration (PGA); equivalent linear (EL).

Arias intensity I_a is a quantity proposed by the American scientist Arias to calculate the total intensity of ground motion using strong earthquake records. It is an important dynamic parameter that can be used to judge the degree of the earthquake disaster. It describes the overall energy released by the observed field point vibration, that is, vibration amplitude, frequency, and other information. Compared with other ground motion parameters, it can reflect the whole situation of the vibration more comprehensively. Wang et al. [14] studied the dynamic influencing factors of a landslide triggered by the Wenchuan earthquake and

TABLE 1: Soil parameters of a project in Nanning area.

Order	Name	H (m)	f_{ak} (kPa)	ρ (g/cm^3)	Vs (m/s)
1-3	Plain fill	5	\	1.80	130
2-1	Hard plastic red clay	15	200	1.90	320
2-2	Plastic red clay	4	160	1.82	200
2-3	Gravel	2	300	2.21	600
3-1	Broken limestone	6	700	2.12	550
4-2	Highly weathered argillaceous siltstone	13	450	1.95	520
4-3	Strongly weathered calcareous siltstone	11	600	1.96	530
4-4	Highly weathered siliceous rock	20	420	1.98	580
5-1	Limestone	12	5000	2.23	610
5-2	Moderately weathered calcareous siltstone	6	2600	2.45	620
5-3	Breccia	21	1200	2.50	700

TABLE 2: Soil parameters of soft soil base.

Order	Name	H (m)	f_{ak}/f_a (kPa)	ρ (g/cm^3)	Vs (m/s)
1-1	Plain fill	1	\	1.8	130
2-1	Silt	25	40	1.62	110
3-1	Fine silt	3	100	1.80	230
3-2	Medium-coarse sand	3	180	1.90	300
4-1	Hard plastic sandy clay	2	250	1.93	550
5	Intensely weathered granite	2	500	2.10	520
6	Moderately weathered granite	6	2500 ~ 3000	2.40	550
7	Breezy granite	20	8000 ~ 10000	2.50	600

discussed the influence relationship between the Arias intensity parameters and the degree of the earthquake disaster. In that paper, the severity of landslides is differentiated by Arias intensity I_a. Taking the unidirectional Arias intensity $I_a = 2$ m/s as the boundary, I_a values in the two horizontal directions of the key disaster area and the sub-key disaster area are all greater than 2 m/s, while those in the general area and other areas are almost less than 2 m/s. When the sum of the two horizontal energy releases is taken as the criterion, $I_a = 4$ m/s can be taken as the criterion. Dong et al. [15] discussed the simulation accuracy of seismic liquefaction of sandy soil foundation, by carrying out shaking table test and using OpenSees software for numerical simulation, and verified the accuracy of Arias strength in the horizontal direction as anti-liquefaction strength. However, Arias intensity is closely related to the seismic records in the specific region, and the amplitude of Arias intensity may vary significantly in different areas of the same disaster zone due to the influence of earthquake source, propagation path, and local site conditions. Therefore, the seismic damage level of specific sites still needs to be analyzed by combining Arias strength with other site dynamic parameters and relevant data.

4.1. Output Time-History Analysis.
According to Figure 7, the value of acceleration calculated by the equivalent linear method is larger than that calculated by the nonlinear method. In the nonlinear calculation results, the amplitude of acceleration of the two types of seismic waves is similar, and the acceleration duration of the output of the Chichi wave is longer. By comparing the output PGA value in Figure 7 with the acceleration input in Figures 2 and 3, it can

be seen that the acceleration peak value in Figure 7 is greater than those in Figures 2 and 3, in both model 1 and model 2 when input in both Kobe wave and Chichi wave. The actual output values are amplified, indicating that the sites have a magnifying effect. In model 1, the acceleration amplitude of Kobe's output wave is obviously much smaller than that of the input wave, while the peak values of Chichi's input wave and output wave are similar. Model 2 weakens both the Chichi wave and the Kobe wave. However, the weakening of the Kobe wave is more serious. Therefore, affected by the site conditions, seismic waves will be magnified and reduced to varying degrees. The site amplification effect of model 1 rock site is more obvious than that of model 2 soft soil site. The results of the equivalent linear calculation of site acceleration are too large. The results of nonlinear calculation considering the nonlinear behavior of soil materials are more accurate, especially in the dynamic response analysis of soft soil and clay sites. The equivalent linear method is more inaccurate in calculating the result of soft field than that of sites in good soil conditions.

4.2. Acceleration Spectrum Analysis.
Figure 8 shows the surface response spectra of model 1 and model 2, respectively. As can be seen, when the equivalent linear calculation is adopted, the output results of the Kobe seismic wave differ greatly, and the results are not accurate. The two different sites reduced the Kobe wave more than the Chichi wave. In model 2, due to the damping effect of the soil, the soft soil site has a more obvious weakening effect on the peak spectral acceleration, especially for the sudden strong earthquake like the Kobe wave. Because the intensity of the Kobe wave is larger than that of the Chichi wave, the nonlinear
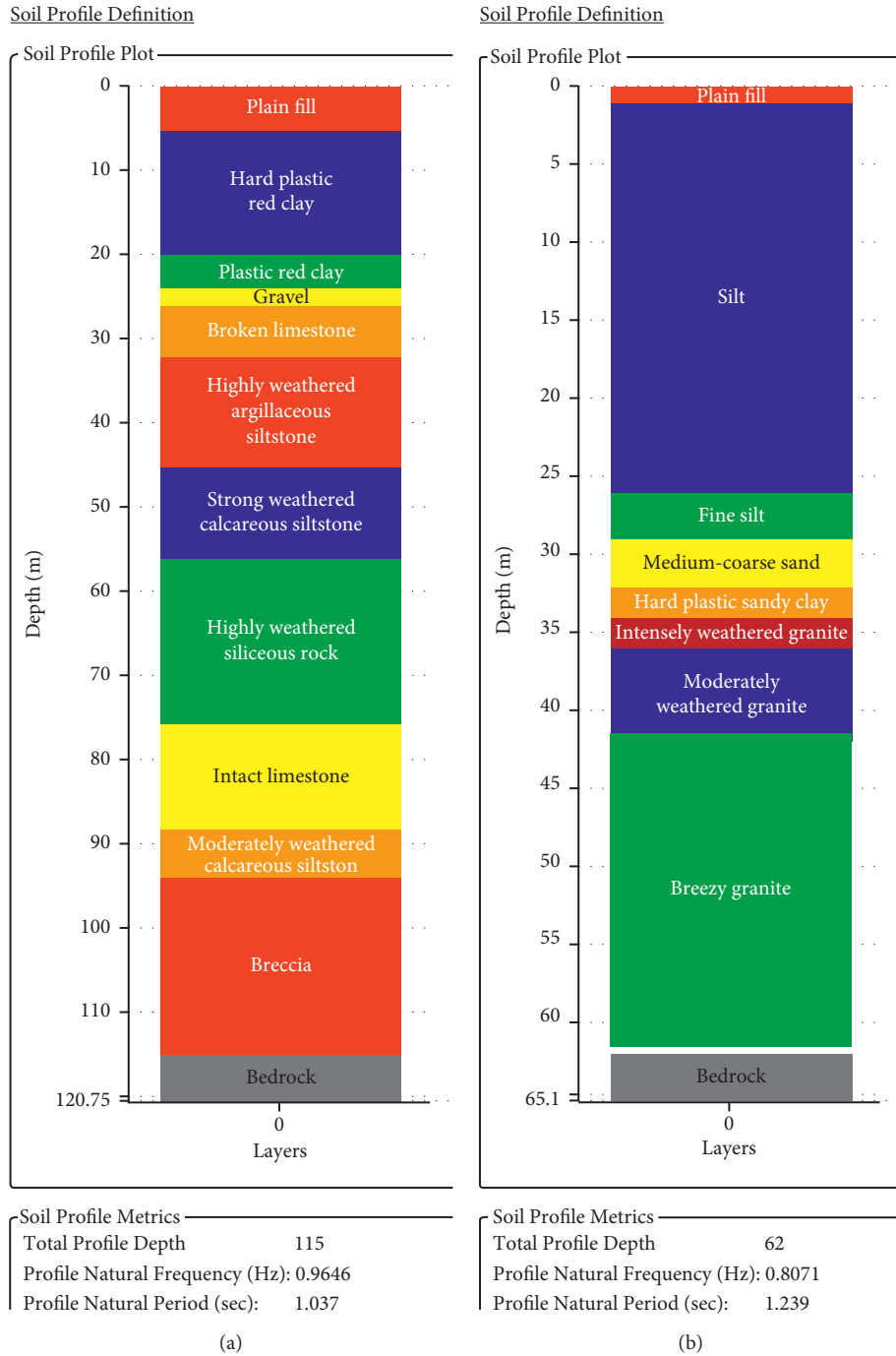
Figure 1: Establishment of the model: (a) model 1 and (b) model 2.

characteristic is stronger. Therefore, the error in performing equivalent linear calculations is larger. Furthermore, this error is amplified in the rock strata with larger elastic modulus and better soil conditions. In model 2, the calculation error of the soft soil layer is very large, partly because of its stronger nonlinearity. In addition, the amplification effect of the site is also reflected in Figure 8. The PSA values in Figure 8 are all larger than the acceleration values of Chichi and Kobe wave input in Figures 2 and 3. The peak acceleration at the surface is magnified by the site more obviously.

4.3. Time-History Response to Arias Strength. Figure 9 shows the variation of Arias intensity with time when the seismic waves recorded by Chichi and Kobe were input. The results show that the damage degree caused by different types of seismic wave input is also very different in various types of sites. The results of the equivalent linear calculation are different from those of nonlinear calculation. There is a great difference between the equivalent linear and nonlinear calculations when using the Kobe seismic wave. The calculation result of the linear equivalent of the two seismic waves is generally larger than that of the nonlinear one.
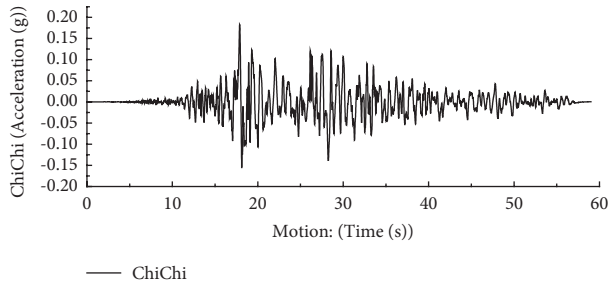
FIGURE 2: Acceleration time history of Chichi motion.
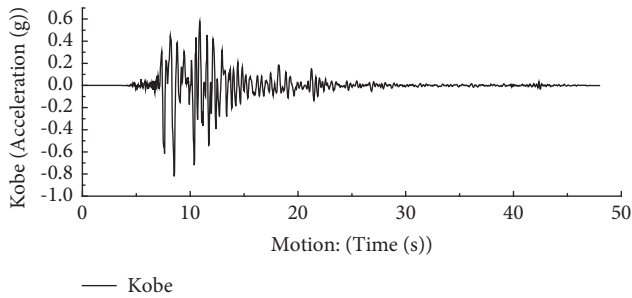
FIGURE 3: Acceleration time history of Kobe motion.
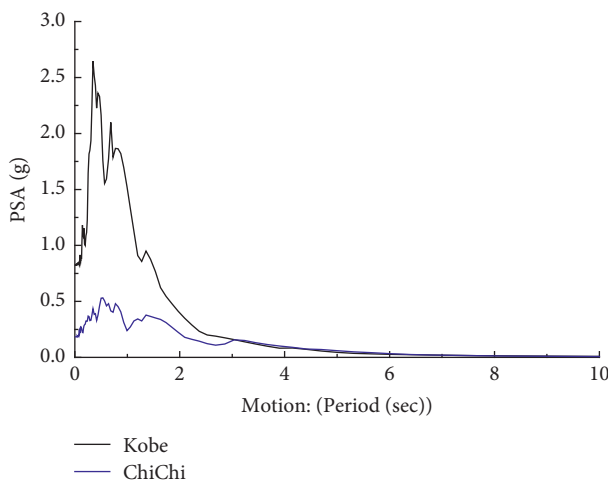
FIGURE 4: Response spectra of input motions.

FIGURE 5: Fourier amplitude spectrum of input motions.
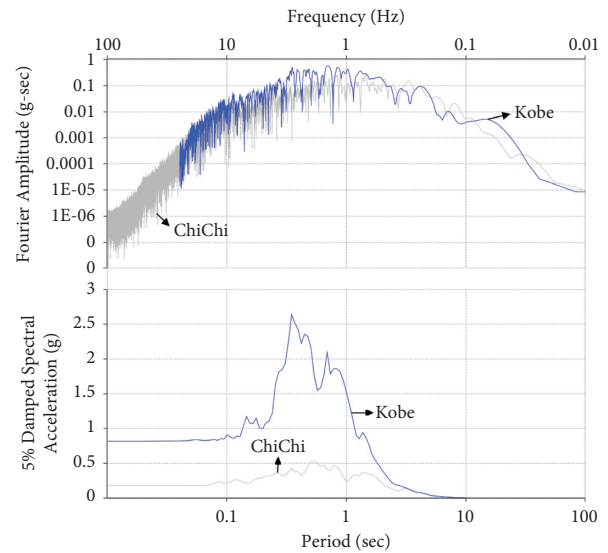
FIGURE 6: Fourier amplitudes and 5% damped spectral acceleration of two input seismic waves.

Except for the Chichi seismic wave input in model 1, the calculation results of the equivalent linearity are close to the results of the nonlinear Arias intensity. For strong earthquakes, the calculation accuracy of the equivalent linear method is low. For soft soil, the nonlinear nature of the soil itself is strong, and the error of the equivalent linear method is also large. Considering that the seismic wave and the soil are nonlinear, the results obtained by the nonlinear method are more reliable.

From the perspective of Arias strength value, the soft soil site can significantly reduce the sudden strong earthquakes. In contrast, persistent low-intensity earthquakes can dramatically reduce site safety. The intensity of Arias did not exceed 2 m/s after the input of two different types of earthquakes at the two sites; both sites are safe. In model 1,

when Chichi wave is incident, Arias intensity results calculated by equivalent linearity and nonlinearity are very close. This is because the nonlinearity of the rock site is weak and the nonlinearity of the seismic wave is weaker than that of the Kobe wave. In Model 2, Arias's strength exceeds 2 m/s when Kobe wave is input into soft soil site for equivalent linear calculation, which deviates greatly from other calculation results. At this time, the Kobe wave belongs to a strong earthquake and has strong nonlinear characteristics. In addition, with the strong nonlinearity of the soft soil layer, the result of the equivalent linear calculation is more inaccurate. For strong earthquakes, the calculation accuracy of the equivalent linear method is low. For soft soil, the nonlinear property of soil is strong, and the calculation error of the equivalent linear method is too large. Because both seismic waves and soil are nonlinear, the results calculated by the nonlinear method are more reliable.
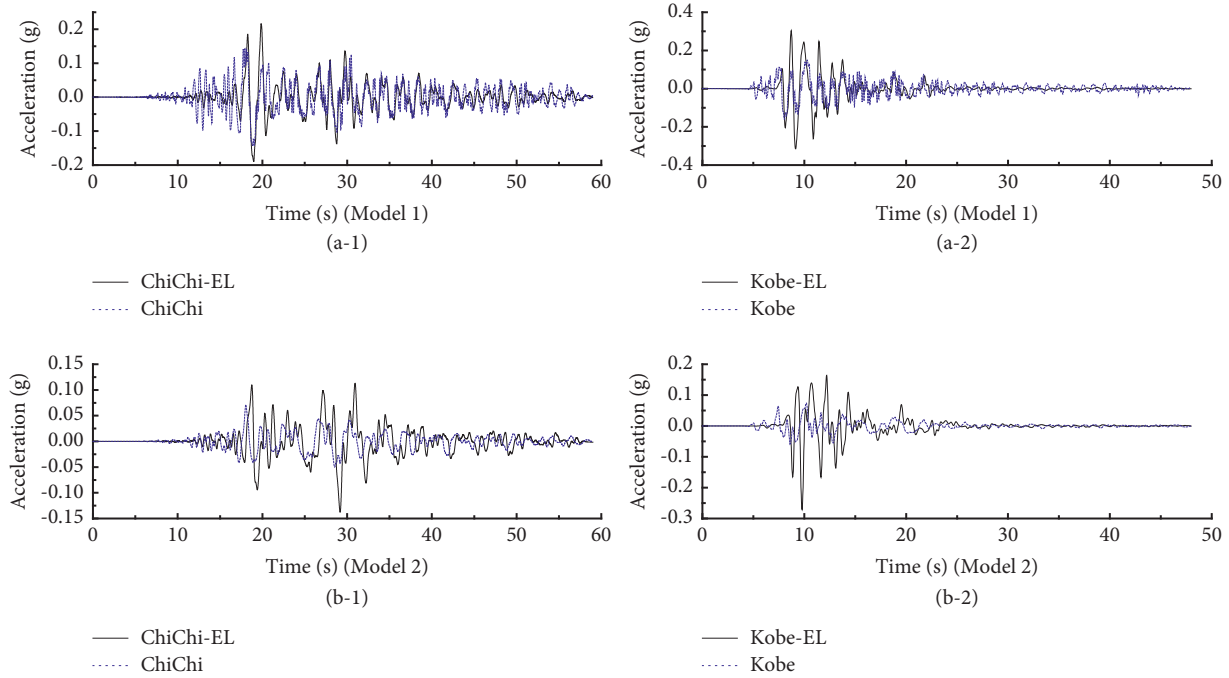
Figure 7: Surface time-domain acceleration response of (a) model 1 and (b) model 2.
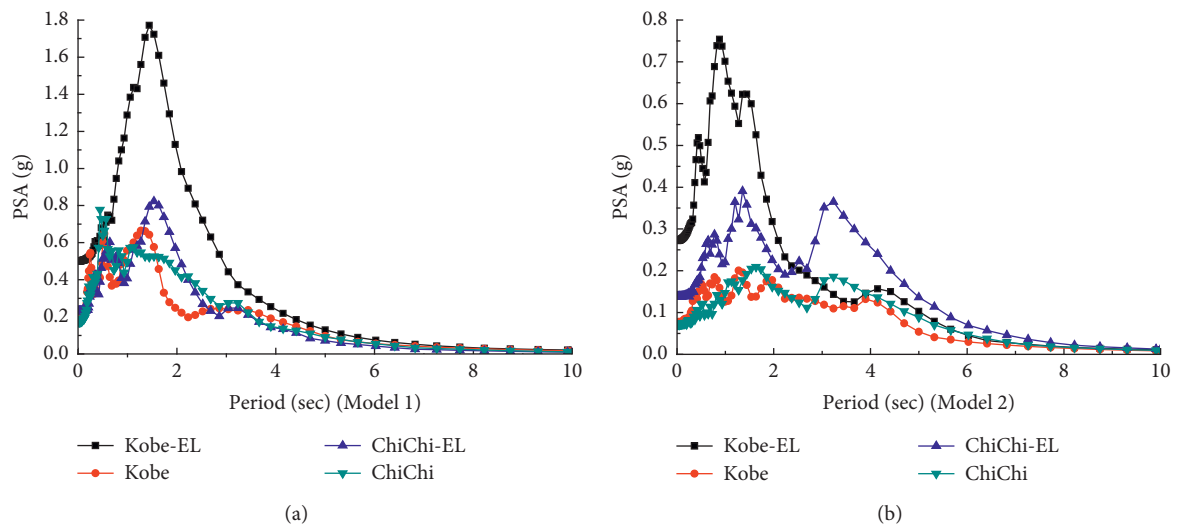
Figure 8: Surface response spectra of (a) model 1 and (b) model 2.

4.4. Analysis of Dynamic Parameters of Soil Profiles. The sections of two numerical simulation models with different geological conditions are analyzed. The variation of the maximum displacement, the maximum ground peak acceleration, and the ratio of maximum shear stress to vertical effective stress with soil depth were studied, and the calculated results are drawn in Figures 10–12.

Figure 11 shows the variation of the maximum displacement of soil layer with depth in model 1 and model 2. Model 1 shows that different kinds of seismic waves have different influences on the deep soil, and the effect of the

input Kobe seismic wave on the deep soil layer is greater than that of the Chichi wave. However, in model 2, where the soil layers are soft, the Kobe input wave has no special influence on the deep soil layer.

Figure 10 shows the variation of the maximum acceleration of soil layers with depth in model 1 and model 2. It shows that the stiff soil layer has a more obvious dynamic response to the Kobe input wave, and the ground peak acceleration is larger, while the soft soil layer is less sensitive to strong earthquakes. In the deep stiff stratum, the peak acceleration decreases with the increase of depth. In model 2,

(a)

(b)
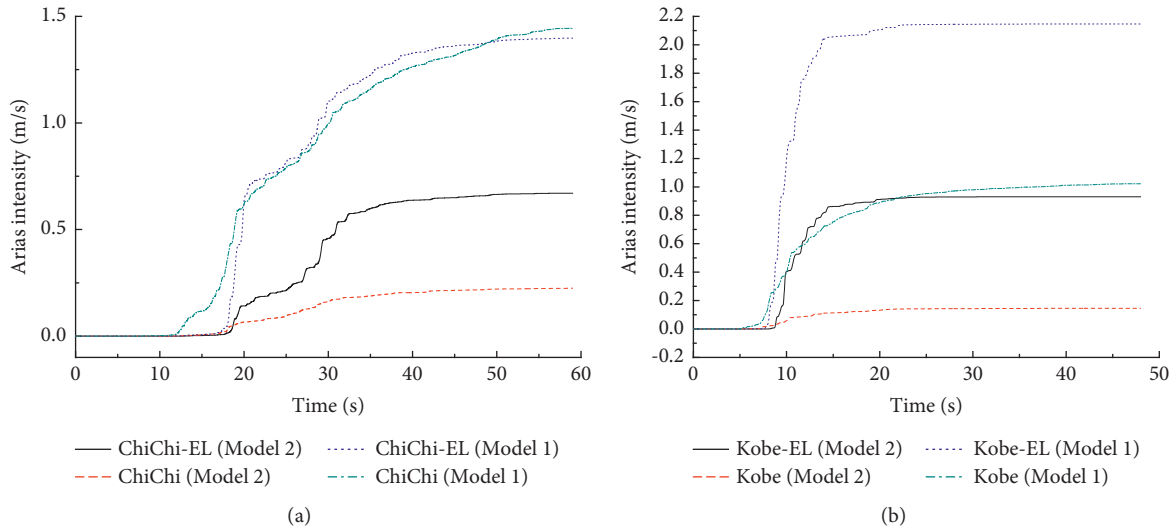
Figure 9: Time-domain response of Arias strength: (a) Chichi and (b) Kobe.

(a)

(b)
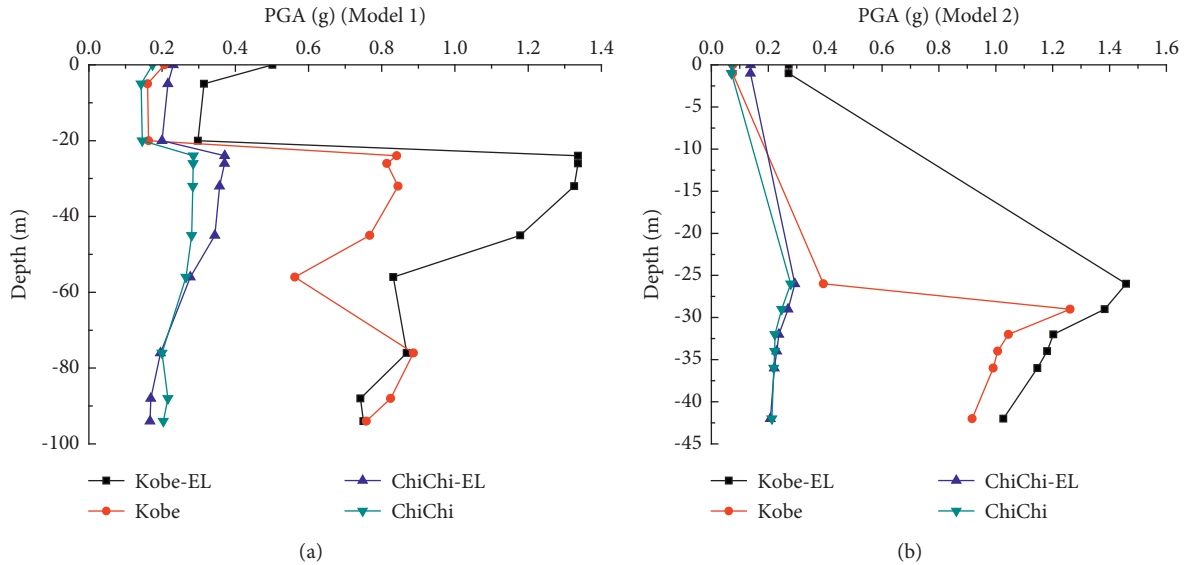
Figure 10: Maximum acceleration of soil in model 1 and model 2.

(a)

(b)
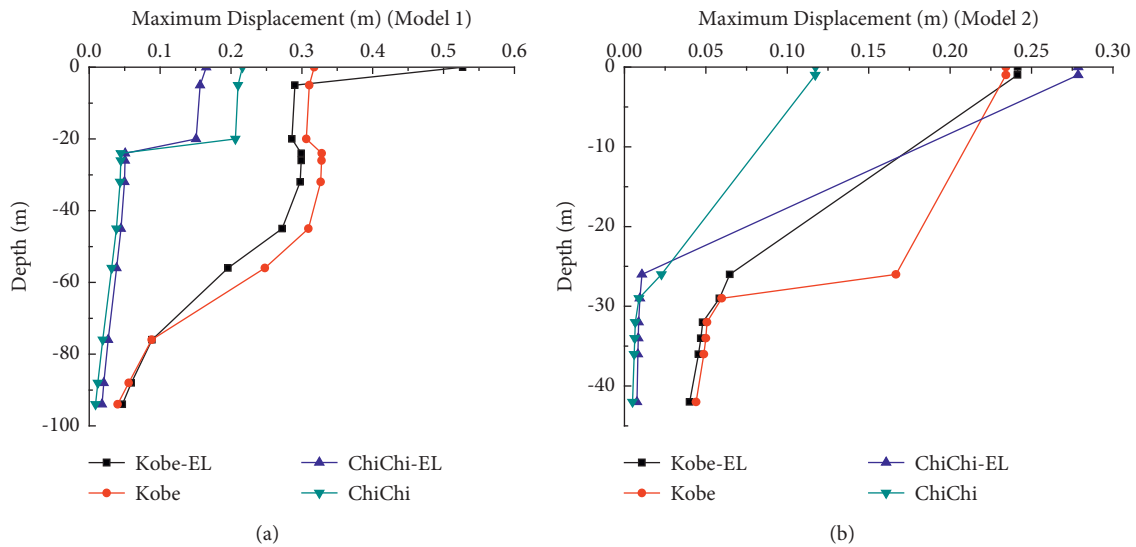
Figure 11: The maximum displacement of soil in (a) model 1 and (b) model 2.
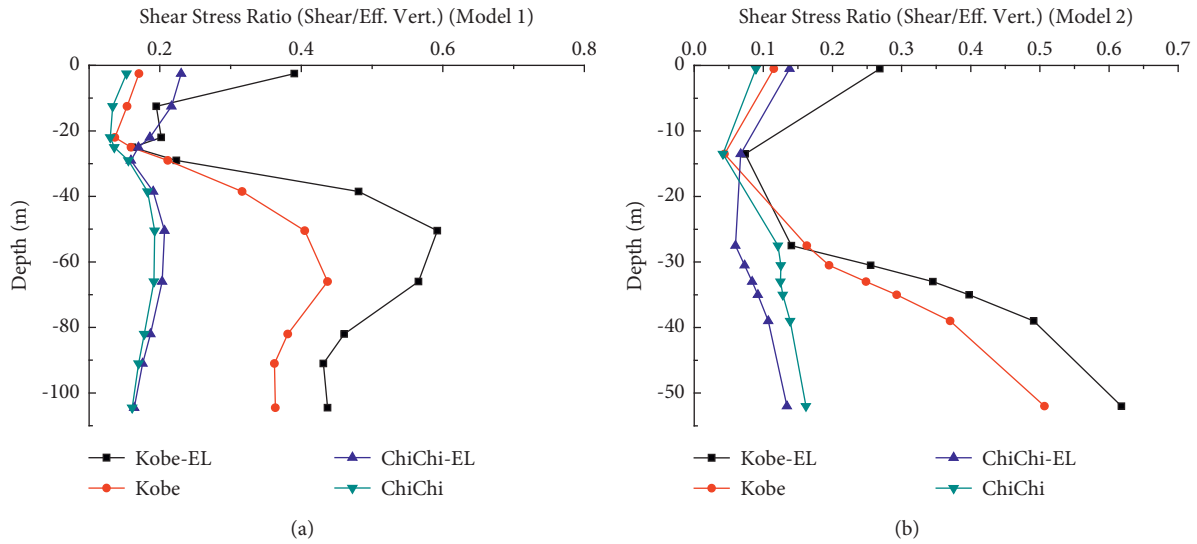
Figure 12: The ratio of maximum shear stress to vertical effective stress varies with depth in model 1 and model 2.

when two different seismic waves are input, the peak acceleration in the overlying soft soil layer increases with the depth, since the greater the vertical stress the soil is subjected to, the deeper the soil layer is. The vertical stress compacts and consolidates the weak soil layer, so the acceleration increases accordingly.

Figure 12 shows the variation of the ratio of maximum shear stress to vertical effective stress with soil depth under different site conditions. It can be seen from the figure that the ratio of the maximum shear stress to the vertical effective stress in model 1 is greater than that in model 2. Because the upper soil layer of model 2 is the silt layer, the soil damping is relatively large, and it is not sensitive to earthquake response. In model 2, the ratio of shear stress to vertical effective stress in the upper part of the soil layer is small, while the ratio of maximum shear stress to vertical effective stress in the bottom sandy bedrock layer is large, and it increases with the increase of depth. As the soil layer deepens, the degree of consolidation of soil deepens. Meanwhile, due to the constitutive characteristics of deep soil, the stress in the soil gradually increases with depth. As a result, the ratio of maximum shear stress to vertical effective stress turns with greater depth.

5. Conclusions

This paper studies the seismic response of different types of sites, aiming to provide the basis and data reference for the seismic fortification design of sites. The research results of this paper are summarized as follows:

(1) The soil itself is a nonlinear medium, so the nonlinear calculation method is more accurate than the equivalent linear calculation, especially for soft soil sites with more obvious nonlinear properties. In addition, seismic waves are not harmonics, and the nonlinear nature of seismic waves is simplified using the equivalent linear method, which leads to

generally larger calculation results. Therefore, it is better to adopt the nonlinear method in the seismic dynamic calculation.

(2) The Kobe wave is stronger than the Chichi wave, but the main peak duration is shorter than the Chichi wave. Due to the large damping of soft soil, the weakening effect of soft soil is very obvious for sudden strong earthquakes, but for the continuous low-intensity earthquake, the acceleration response of soft soil will be greater. Harder soil and rock help the spread of earthquakes and therefore have greater acceleration. In addition, they are more sensitive to strong earthquakes, and the site amplification effect of earthquakes is more obvious.

(3) Acceleration, surface spectral acceleration, Arias strength, maximum acceleration of each layer of soil, and the ratio of maximum shear stress to vertical effective stress with depth are calculated using Kobe wave and Chichi wave; the equivalent linear calculation results are always larger than the nonlinear calculation results. However, the equivalent nonlinear calculation result of soil displacement with depth is not the maximum. The influence of Kobe wave on soil displacement is greater, and the influence on deep soil is also greater. In soft soil field with Kobe wave incident, the result of the equivalent linear calculation is more inaccurate because both seismic wave and field are highly nonlinear. However, the results of the equivalent linear calculation are close to those of nonlinear calculation in the rock field with Chichi wave incidence.

(4) From the perspective of Arias strength value, especially the soft soil site, sudden strong earthquakes are more obviously weakened by the site. Therefore, soft soil sites are safer than rock sites during strong earthquakes. However, the continuous low intensity earthquake will make the soft soil site safety factor

sharply decreased. The surface displacement caused by the earthquake is large, and the influence decreases with depth, which is related to the property of the soil layer and the vertical stress of soil increasing with depth. The deep soil in the rock layer is more significantly affected by a sudden strong earthquake [16–18].

Data Availability

Some or all data, models, or codes generated or used during the study are available from the corresponding author upon request.

Conflicts of Interest

The authors declare that they have no conflicts of interest.

Acknowledgments

References

[1] Y. Huang, Y. E. Wei-min, Y. Q. Tang, and T. L. Chen, "Characteristic analysis for seismic ground response of soft soils in Shanghai," *Chinese Journal of Underground Space and Engineering*, vol. 1, no. 5, pp. 773–778, 2005, (in China).

[2] J. F. Cao, Y. L. Tong, L. I. Guang et al., "Effect of soft soil layer on ground motion peak," *Journal of Seismological Research*, vol. 36, no. 2, pp. 192–197, 2013, (in China).

[3] S. Ma, Z. Duan, Y. Liu, B. Wang, and Y. Shao, "Large triaxial test study on dynamic characteristics of round gravel," *Arabian Journal of Geosciences*, vol. 13, p. 816, 2020.

[4] Y. M. A. Hashash, M. I. Musgrove, J. A. Harmon et al., *DEEPSOIL 7.0, User Manual*, Board of Trustees of University of Illinois at Urbana-Champaign, Urbana, Kolkata, 2020.

[5] R. Sun and X. M. Yuan, "Holistic equivalent linearization approach for seismic response analysis of soil layers," *Chinese Journal of Geotechnical Engineering*, vol. 43, no. 4, pp. 603–612, 2021, (in China).

[6] H. Zhang, Z. Wang, Z. Ze-hui, and H. B. You, "The study of seismic response in soft soil site based on DEEPSOIL," *Technology for Earthquake Disaster Prevention*, vol. 10, no. 2, pp. 291–304, 2015, (in China).

[7] Y. P. Gao, L. I. Kai-jing, and J. Dai, "Effects of Composite Foundation on Site Seismic Response," *Rock and Soil Mechanics*, no. z1, Academia Sinica, (in China), pp. 211–214, 2009, (in China).

[8] H. J. Liao and B. H. Zhu, "Selsmic response analysis of the ground surface in loess site," *J. Xi'an Inst. of Metall. & Cons. Eng*, vol. 23, no. 3, pp. 331–338, 1991, (in China).

[9] S. Ma, Y. Shao, and Y. Liu, "Responses of pipeline to side-by-side twin tunnelling at different depths: 3D centrifuge tests and numerical modelling," *Tunnelling and Underground Space Technology*, vol. 66, pp. 157–173, 2017.

[10] Y. Chen, Z. Wen, P. Jia, J. Han, and Y. Guan, "Dynamic behavior of an embedded foundation under horizontal vibration in a poroelastic half-space," *Applied Sciences*, vol. 9, no. 4, p. 740, 2019.

[11] J. Han, D. Liu, Y. Guan et al., "Study on shear behavior and damage constitutive model of tendon-grout interface," *Construction and Building Materials*, vol. 320, Article ID 126223, 2022.

[12] X. Wang, Y. Wu, J. Cui, C. Q. Zhu, and X. Z. Wang, "Shape characteristics of coral sand from South China Sea," *Journal of Marine Science and Engineering*, vol. 8, no. 10, p. 803, 2020.

[13] C. Phillips and Y. Hashash, "Damping formulation for nonlinear 1D site response analyses," *Soil Dynamics and Earthquake Engineering*, vol. 29, pp. 1143–1158, 2009.

[14] X. Y. Wang, N. I. E. Gao-zhong, and L. Zhang, "Study on the relationship between triggered slippage and ARIAS intensities in wenchuan earthquake," *Journal of Basic Science and Engineering*, vol. 18, no. 4, pp. 645–656, 2010, (in China).

[15] R. Dong, J. Li-ping, Z. D. Shan, L. Zhang, and T. J. Liu, "Seismic liquefaction characteristics of saturated sand with a low permeable covering layer," *China Earthquake Engineering Journal*, vol. 42, no. 4, pp. 955–988, 2020, (in China).

[16] O. U. Xiao-duo, P. E Yuan-shen, and Z. H Yi-he, C. H. Jin and Y. A Yu-lu, Analysis of dynamic calculation model and seismic response of concrete dam of large bauxite tailings reservoir," *Journal of Basic Science and Engineering*, vol. 30, no. 1, pp. 76–88, 2019, (in China).

[17] Y. L. Wong, X. Guo, Y. F. Yuan, and K. T. Chau, "Influence of soft sandwich layer on seismic response in Hong Kong," *Journal of Natural Disasters*, vol. 9, no. 1, pp. 109–116, 2000, in China.

[18] W Yan-zhen, Z Ding-feng, C Guo-xing, and K. Liang, "A new nonlinear effective stress method for one-dimensional seismic site response analysis and its validation," *Chinese Journal of Geotechnical Engineering*, vol. 43, no. 3, pp. 502–510, 2021, (in China).

Research Article

Study on the Mechanism and Effect of a Partition Wall Controlling Foundation Pit Deformation in the Soft-Soil Area

Chunlei Feng [ID],[1] Dingli Zhang,[2] Hualao Wang,[1] and Xuan Zhang[1]

[1]*Bridge and Tunnel Research Center, Research Institute of Highway, Ministry of Transport, Beijing 100088, China*
[2]*Key Laboratory for Urban Underground Engineering of Ministry of Education, Beijing Jiaotong University, Beijing 100044, China*

Correspondence should be addressed to Chunlei Feng; fclbjtu@163.com

Based on the soft-soil layer and several practical subway stations projects, the effect of partition wall main parameters on internal force and the deformation of retaining structure was thoroughly investigated via numerical simulation and orthogonal experiment. Results show that the influence of distance between partition wall and retaining structure, L, on controlling the internal forces of the retaining structure and maximum ground settlement, is more obvious; the maximum settlement can be reduced by more than 60%. Moreover, the influence of partition wall depth under the ground, H, within a certain range can substantially reduce the maximum lateral palisade structure; the lateral displacement can be reduced by about 50%; however, within the scope of the economic, the stiffness of the partition wall, E, with impact on retaining structure internal force and deformation is relatively weak. Finally, the applicability of the research results is verified.

1. Introduction

The deformation control measures of foundation pit engineering can be divided into three categories [1]: ensuring the stability of the foundation pit itself during the construction process, improving the ability of the surrounding environment to resist deformation, and cutting off or reducing the influence of soil deformation on the surrounding environment through the partition method. In a soft-soil area, a partition wall in the form of cast-in-place pile, mixing pile, and so on has been used in many projects as the main measure to control the influence of foundation pit deformation on the surrounding.

At the moment, studies on the engineering application of partition walls in the domestic and overseas are primarily focused on two aspects: (1) the pilot-isolation pile-wall system used to control the impact of tunnel excavation on the surrounding environment is studied, and the key influencing factors [2] and theoretical model [3] of the system are summarized by combining analytical solutions and numerical simulation methods. (2) pile-wall partition

wall (hereinafter referred to as partition wall) is used to control the influence of foundation pit or tunnel excavation on adjacent buildings (structures). The most commonly used methods are numerical simulation [4–10] and orthogonal test [11], or partition wall design parameters are discussed using the evaluation index of partition wall control effect [12, 13]. Moreover, the majority of existing studies concentrate on the qualitative analysis of the impact of changing the main design parameters of partition walls on the deformation control effect of surrounding buildings (structures). The favorable change range and reasons of each parameter on the control effect cannot be accurately determined. Hence, the partition wall still needs to rely on engineering experience for design and construction. Furthermore, the research background is primarily for a specific project, and the research conclusion's general applicability is limited. As a result, the mechanism of partition wall control over foundation pit deformation needs to be investigated further.

In this study, based on the foundation pit engineering of the Tianjin Metro Line 5 and Line 6 in China, and based on

the analysis of the measured displacement data of the retaining structure and surface settlement and existing literature [14] on the study of the deformation law of foundation pit excavation of metro station in this soft-soiled area, the finite element analysis and orthogonal test combining the small strain characteristics of soil are used. The calculation theory of "similar structure" double-row piles is used to establish a quantitative relationship between the partition wall design parameters and deformation control effect. Finally, the prediction theory of the foundation pit deformation by Kung et al., based on the reliability method, is used to validate its mechanism of action, thereby making control measures more reasonable and effective.

2. Applicable Conditions and Mechanism of the Partition Wall: A Brief

For a building with high-protection grade in the adjacent foundation pit, the distance between the foundation pit retaining structure and the protected object should be more than 1.2 ~ 1.5 times the excavation depth of the foundation pit. If the minimum safe distance cannot be met and the stiffness of the envelope is already high, the tracking compensation method, foundation underpinning method, and partition method [15] are commonly used as protection measures. The tracking compensation method is one of them. It belongs to the "dynamic deformation control" category, and its main principle is to timely supplement ground loss through grouting during the foundation pit construction process to ensure that the construction technology and grouting time grasp requirements are high. The main principle of the foundation underpinning method is to improve the bearing capacity of the foundation by strengthening the soil beneath the foundation of the building before excavation to control the settlement of the building. However, this method causes significant soil disturbance, and improper operation will aggravate the uneven settlement of the building.

As shown in Figure 1, the partition wall is usually placed between surrounding buildings (structures) and the foundation pit as the primary control measure to cut off the propagation path of foundation pit deformation. The range of plane setting is generally at least equal to the range of buildings requiring settlement control, and the range of vertical setting must generally pass through the possible slip surface. It primarily constructs palisade structures and excavates lateral Earth pressure and friction resistance caused by differential settlement. To some extent, it can share the Earth pressure on retaining structures and limit the deformation of development restrictions, while also improving the ability of shear slip surface and reducing the foundation settlement caused by building precipitation and the effect of content. In comparison to the previous two control measures, the construction speed is fast and the operation is simple.

3. Project Background

3.1. Project Summary.
The Tianjin Metro Line 5 starts from Shuangjie, Beichen District, in the north and ends at Liyuantou, Xiqing District, in the south. The total length of

$45°-(\varphi/2)$

Partition wall   Retaining structure
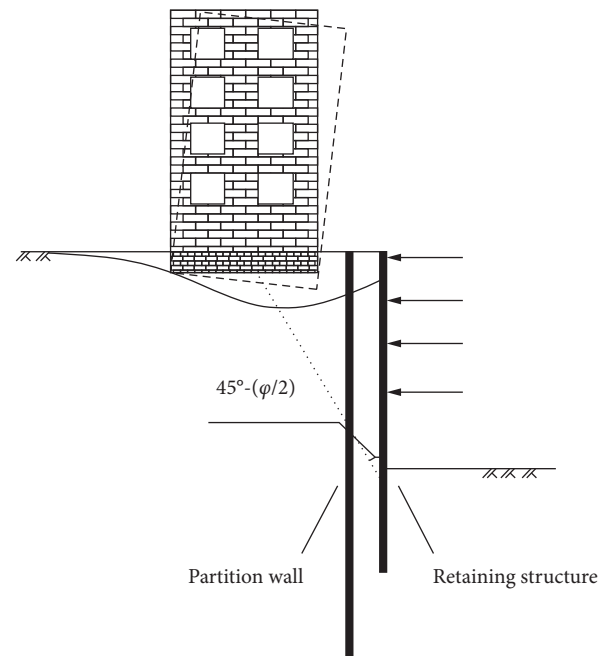
FIGURE 1: Schematic for the layout of the partition wall.

the line is 34.8 km, including a 33 km underground line and a 1.8 km ground line and transition section. Line 6 starts from Dabizhuang in the north and ends at Meilin Road in the south. The total length of the line is 41.6 km, including the 39.8 km underground line, 0.8 km ground line and transition section, and 1.0 km elevated line. The two lines run through the East, West, North, and South of Tianjin, covering a wide area, and the regional stratum represents the characteristics of the typical soft-soil layer in Tianjin.

3.2. Metro Station Foundation Pit Standardization.
In this study, a total of 20 excavation pits of the Tianjin Metro station, which are combined forms of inner support and ground wall, are collected with an open-cut method of Line 5 and Line 6. Summarizing and analyzing the basic parameters, physical and mechanical parameters of stratum, excavation process, and excavation depth of each layer of the 20 foundation pits, we standardized the subway foundation pits in this area. The statistical results are shown in Tables 1 and 2.

Based on the above statistical results and related design schemes, the main parameters of the standardized model are obtained, as shown in Table 3. The average value of each index in Table 1 is used to calculate the basic parameters of the foundation pit and underground continuous wall. In this study, the internal support uses the layout form with the highest proportion, which is one concrete support and three steel supports, and the specifications are based on the weak comprehensive stiffness.

3.3. The Rationality Verification of the Standardized Model.
In this study, for finite element analysis, the HSS (rolling soil model with small strain stiffness) constitutive model [16, 17]

TABLE 1: The basic statistics of the excavation with an open cut.

Serial number	Station	Excavation length L (m)	Excavation width B (m)	Excavation depth He (m)	Depth of retaining structure into soil H (m)	The wall thickness t (m)
1	Dan Bei road station	199.9	19.5	16.2	33	0.8
2	Vocational college station	241.6	20.5	16.4	29	0.8
3	The Huaihe river road station	205.4	20.7	16.8	34.4	0.8
4	Chishing road station	203.8	20.7	16.9	34.7	0.8
5	Siyuan road station	191.08	20.7	17.0	31.9	0.8
6	JianChang way station	294.2	20.7	16.7	34	0.8
7	Yueyahe road station	183.8	20.7	16.7	41.5	0.8
8	LingBin road station	153.6	37.6	16.9	31.1	0.8
9	Nanhezhuang station	202.4	20.7	15.4	32.5	0.8
10	Dabizhuang station	205.5	20.7	16.8	32	0.8
11	Admiralty street station	499.9	20.7	16.6	34.1	0.8
12	Xuzhuangzi station	228.5	20.7	16.5	32	0.8
13	Affiliated middle school station	307.6	29.6	16.8	30.5	0.8
14	North of bamboo station	167	23.1	24.0	42	1
15	Yibin road station	207	20.7	15.9	31.6	0.8
16	Anshan west road station	223.3	22.7	16.8	29.0	0.8
17	Day tow station	284.3	20.7	16.6	31.5	0.8
18	First central hospital station	180.6	40.6	16.8	29.6	0.8
19	Yukon beam way station	235	20.7	16.9	30.5	0.8
20	Cultural centre station	168	25.05	24.5	52.6	1

TABLE 2: Main excavated conditions of the foundation pit.

Working condition	The construction content	Excavation depth
I	Initial geostress	—
II	Construction of retaining structure and partition wall	—
III	1 m excavation, set up the first concrete support	1 m
IV	The first layer of soil excavation, set up a second steel support	4 m
V	The second layer of soil excavation, set up a third steel support	4 m
VI	The third layer of soil excavation, set up the fourth steel support	4 m
VII	The fourth layer of soil excavation, excavation to the end	4 m

TABLE 3: Main parameters of the normalized model.

Basic dimension of foundation pit	Excavation length, L/m	229.12	
	Excavation width, B/m	23.35	
	Excavation depth, H_e/m	17.34	
Partition wall	Wall thickness, t/m	0.8	
	Subsurface depth, H/m	33.86	
	Stiffness, E/Mpa	3.15×10^4	
Inner support	Support types	One concrete support	Three steel supports
	Support materials	C30	Q235
	Section size/mm	800×800	$\Phi 609 \times 16$
	Horizontal spacing	3	6

was used to take 1/2 of the central axis of the above-standard foundation pit long side. To ensure the accuracy of the finite element analysis results, the calculation results were compared to relevant statistics in [13]. Physical and mechanical parameters of site soil layer are shown in Table 4, where γ is the weight of the soil, c' is the effective cohesion of

TABLE 4: Physicomechanical parameters of the soils in the site.

Strata	Soil thickness (m)	γ (kN/m³)	c' (kPa)	φ' (°)	$E_{s0.1\sim0.2}$ (MPa)	E_{50}^{ref} (MPa)	$E_{\text{oed}}^{\text{ref}}$ (MPa)	E_{ur}^{ref} (MPa)	G_0^{ref} (MPa)	$\gamma_{0.7}$ (10⁻³)	K (m/d)
Artificial fill layer	3.6	18.5	12.4	16.1	4.38	4.38	4.38	26.28	70.96	0.1	0.02
Silty clay	2.5	19.6	14	22.5	6.03	6.21	6.02	30.04	60.27	0.1	0.02
Silty clay	1.9	19.2	16	28.6	6.32	6.17	6.34	31.54	63.65	0.1	0.2
Silt	1.5	19.5	7.2	32.5	8.12	8.34	8.05	40.05	80.75	0.1	0.2
Silty clay	4.6	19.2	12.6	19.6	6.02	6.34	6.07	30.09	60.86	0.1	0.2
Silty clay	2.9	19.8	21.65	31.95	6.34	7.12	6.35	31.58	63.33	0.1	0.02
Silt	5	20.3	7.5	39.1	54.31	62.11	54.04	162.11	270.21	0.1	3
Silty clay	1.8	20.1	7.8	27.2	21.94	23.88	21.97	109.52	219.01	0.1	0.02
Silt	7.2	20.1	6.5	38.5	54.02	51.54	54.03	162.22	270.65	0.1	3
Silty clay	8.4	20.5	15.3	25.8	20.75	24.71	20.77	111.51	207.05	0.1	0.02

the soil, φ' is the effective internal friction angle of the soil, $E_{S,1\sim2}$ is the compression modulus of the soil, E_{50}^{ref} is the secant stiffness in standard drained triaxial test, $E_{\text{oed}}^{\text{ref}}$ is the tangent stiffness for primary oedometer loading, E_{ur}^{ref} is the unloading/reloading stiffness at engineering stains, G_0 is reference shear modulus at very small strains, and $\gamma_{0.7}$ is the shear strain at which $G_s = 0.722G_0$. Figure 2 and Table 5 show the specific calculation and comparison results, which agree with the measured values. As a result, further research can be conducted on this basis.

According to the measured and calculated results, the ground surface settlement mode after foundation pit excavation in Tianjin metro station is consistent with the settlement mode corrected by Ou et al. [18], as shown in Figure 3. The relative distance between the maximum settlement point and the retaining structure is one-third the main influence range, where d is the horizontal distance between any settlement point on the surface and the retaining structure in the same plane and PIZ is the main area affected by surface settlement.

4. Analysis of the Influence of Partition Wall Design Parameters on Deformation Control

4.1. A Brief Introduction of the Orthogonal Finite Element Test. As illustrated in Figure 4, partition walls are constructed using the abovementioned standardized model, and an orthogonal test is performed to evaluate the impact of design parameters. Because the majority of the partition walls in existing practical projects are in the form of a continuous pile arrangement, this paper simplifies the partition wall composed of piles into the form of a continuous wall by reducing the size and stiffness; i.e., plate element is used for simulation.

First, the orthogonal test determined three primary partition wall design parameters: the horizontal distance between the partition wall and the same side retaining structure, the stiffness parameter, and the depth below ground. Second, during the orthogonal test, the partition wall was set within the range of settlement increase area (i.e., the horizontal distance between the maximum surface settlement point and the retaining structure) to observe the effect of the partition wall on the maximum surface

settlement and the internal force of the retaining structure at the same time, as shown in Figure 5.

To establish the connection between partition wall design parameters and retaining structure, this study will use the ratio form of analysis parameters for testing, as shown in Table 6, where L_0, E_0, and H_0 are the horizontal distances between the maximum surface settlement and the same side retaining structure, the stiffness parameters of the retaining structure, and the depth of the soil, respectively. There are three factors involved in the test, each with four levels. Under the condition that the number of tests is minimized, it is appropriate to use Table $L_{16}(4^5)$ to arrange the test plan with a total of 16 tests. Each test plan and calculation result are shown in Table 7, among which the test results are the deformation of the foundation pit after the last step of excavation.

4.2. Comprehensive Analysis of Test Results. The test results show that the three factors have varying degrees of influence on the deformation control of the foundation pit (Table 8, Figure 6). Among them, L/L_0 has the most obvious influence on the partition wall, retaining structure and surface settlement, and is used as the main factor to study the mechanism of partition wall deformation control in this study. H/H_0 mainly affects the maximum lateral movement of the retaining structure. However, the change of E/E_0 has a relatively weak influence on foundation pit deformation. After comprehensive consideration, the rigidity of the partition wall was set as a medium in the follow-up study, i.e., $E/E_0 = 0.4$.

Based on the influence of the above factors on deformation control, this study obtained the influence law of L/L_0 and H/H_0 by increasing the value density of each factor and further analyzed the control mechanism of the partition wall on this basis.

5. Mechanism Analysis of Partition Wall Design Parameters on Deformation Control

5.1. The Influence of L/L_0 on Surface Subsidence δv. The influence of L/L_0 on surface settlement is mainly reflected in two aspects. The first is the change of settlement groove form. When $L/L_0 \leq 0.6$, the settlement form is a traditional groove
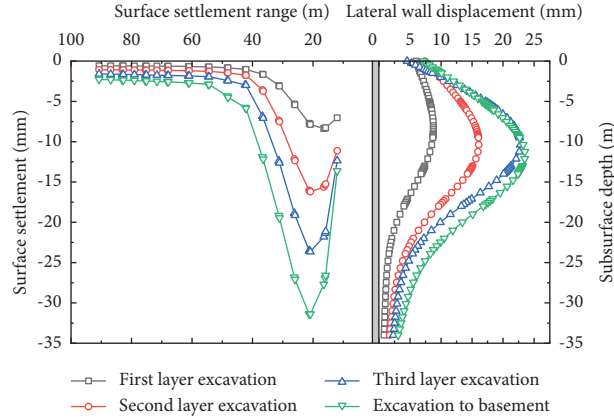
FIGURE 2: Surface settlement and lateral wall displacement of each excavated condition of the subway station foundation pit.

TABLE 5: Deformation comparison between analytical and measured values.

Working condition	Maximum surface settlement		Maximum lateral displacement of the retaining structure	
	Measured mean value	Calculated value	Measured mean value	Calculated value
First layer excavation and layer internal support	12.77	11.06	7.77	8.77
Second layer excavation and layer internal support	18.38	17.20	15.35	16.08
Third layer excavation and layer internal support	22.71	23.65	20.41	22.80
Excavation to basement	26.66	31.01	20.34	23.51

shape, and the soil settlement between the partition wall and enclosure structure is very small (Figure 7(a)). When $L/L_0 > 0.6$, the partition wall divides the form of the settlement trough into double grooves, resulting in two troughs (there are two troughs for "maximum surface settlement" in the test results in Table 7: No. 4, 8, 12, and 16), and the maximum settlement is located between the retaining structure and the partition wall, as shown in Figure 7(b).

The second is the influence on the maximum surface settlement δ_{vm}. When $L/L_0 \leq 0.6$, δ_{vm} is controlled within the range of $7 \sim 11$ mm. Compared with the other side without a partition wall, the surface settlement decreases by >60% and the control effect is obvious. When $L/L_0 > 0.6$, the value of δ_{vm}, which is outside the partition wall, changes in the range of 5 mm~7 mm, with little difference from that when $L/L_0 \leq 0.6$, while the value of δ_{vm} between the partition wall and the retaining structure changes in the range of 15~25 mm.

Simultaneously, when compared to the other two test results, the maximum value of internal force and lateral displacement of the retaining structure also appears at an inflection point near $L/L_0 = 0.6$, and the maximum value of internal force and lateral displacement presents an upward trend. Resultantly, when $L/L_0 > 0.6$, the ability of the partition wall to control deformation gradually weakens as L/L_0 increases.

For this phenomenon, from a mechanical point of view, when $L/L_0 < 0.6$, the partition wall is located in $d/\text{PIZ} < 0.2$, within the scope of the partition wall, and the retaining structure to provide the friction resistance of f is larger than the soil subsidence that occurs between the two because of the gravity on the walls of f' negative skin friction resistance, as shown in Figure 8. When $L/L_0 = 0.6$ ($d/\text{PIZ} > 0.2$), f is the largest, i.e., $f_{max} = f'$. When $L/L_0 > 0.6$, the dead

weight of soil and f' between the two walls gradually increase. Moreover, while $f < f'$, the partition wall's control effect on the deformation is relatively weakened.

$$\frac{L}{L_0} \begin{cases} \leq 0.6, & \dfrac{d}{\text{PIZ}} \leq 0.2, \quad f \geq f', \\[2ex] > 0.6, & \dfrac{d}{\text{PIZ}} > 0.2, \quad f < f'. \end{cases} \tag{1}$$

5.2. Influence of L/L_0 on Maximum Internal Force MD of Retaining Structure.

Due to the influence trend of L/L_0 on the change of maximum internal force of partition wall and retaining structure, this study introduces the calculation theory of Earth pressure distribution model of the "similar structure" double-row pile (Figure 9(a)) and analyzes the mechanism of L/L_0's influence on control effect from the mechanical perspective. Based on the theory, the ratio of active Earth pressure between the partition wall and retaining structure is calculated in the range of L/L_0, which is beneficial to control the deformation.

$$\Delta_P = \frac{p_{aG}}{p_{aD}}, \tag{2}$$

where p_{aG} and p_{aD} are the active Earth pressure acting on partition wall and retaining structure, respectively.

As illustrated in Figure 9(b), it is assumed that there is active Earth pressure σ_a acting on both the partition wall and retaining structure per unit length. Ignoring the interaction between the soil and structure, the soil between the two walls
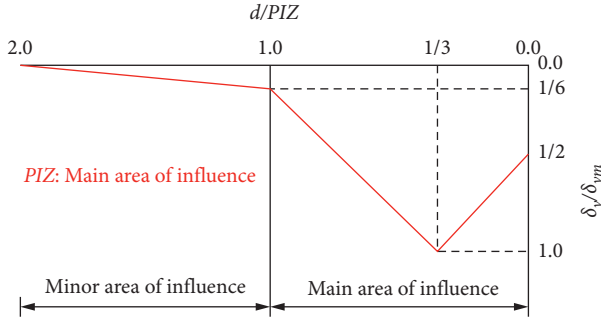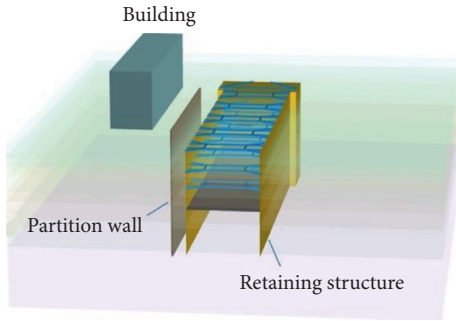
FIGURE 3: Surface settlement model.

FIGURE 4: Schematic of the normalized model excavation.

will produce equal Earth pressure $\Delta\sigma_a$ on the front and rear walls, resulting in equal stress on both.

$$p_{aG} = \sigma_a - \Delta\sigma_a, \tag{3}$$

$$p_{a\,D} = \sigma_a + \Delta\sigma_a. \tag{4}$$

Assuming that the ratio of $\Delta\sigma_a$ to σ_a is the same at different depths,

$$\Delta\sigma_a = \alpha\sigma_a, \tag{5}$$

where α is the Earth pressure distribution coefficient, which can be obtained by substituting it into (3) and (4) as follows:

$$\begin{aligned} p_{aG} &= (1 - \alpha)\sigma_a, \\ p_{a\,D} &= (1 + \alpha)\sigma_a. \end{aligned} \tag{6}$$

Accordingly, (2) can be expressed as

$$\begin{aligned} \Delta_P &= \frac{p_{aG}}{p_{a\,D}} \\ &= \frac{1 - \alpha}{1 + \alpha}. \end{aligned} \tag{7}$$

The Earth pressure distribution coefficient is calculated by dividing the weight of the sliding soil by the proportion of sliding between the partition wall and the retaining structure, i.e.,

$$\alpha = \frac{2L}{L_0'} - \left(\frac{L}{L'}\right)^2, \tag{8}$$

where $L_0' = H_e \tan(45° - \varphi/2)$ is the horizontal distance between the intersection of the active slip surface and the pit surface and the retaining structure. After substituting (8) into (7), the following is obtained:

$$\Delta_P = \frac{\left((L/L_0') - 1\right)^2}{2 - \left((L/L_0') - 1\right)^2}. \tag{9}$$

Since the traditional calculation method L_0' is determined according to the Rankine Earth pressure theory, and the existence of the retaining structure in practice will affect the distribution of the slip surface in the ideal state, the method of improving the starting position of the slip surface in [19] is used to determine the calculation of L_0'.

We assume that the vertical distance between the improved sliding crack surface A and the excavation surface of the foundation pit is t (Figure 10). In other words, at point A, the active Earth pressure is equal to the passive Earth pressure.

$$\sigma_{Aa} = \sigma_{Ap}, \tag{10}$$

i.e.,

$$k_a \gamma (H + t) = k_p \gamma t + 2c\sqrt{k_p}, \tag{11}$$

where γ is the weight of soil, c is the cohesion of soil, H is the excavation depth of foundation pit, and k_a and k_p are the active and passive Earth pressure coefficients of soil, respectively. Accordingly,

$$t = \frac{k_a \gamma H - 2c\sqrt{k_p}}{(k_p - k_a)\gamma}. \tag{12}$$

According to the above improvements, the standardized model parameters are used for trial calculation. Accordingly,

$$L_0' = (H_e + t)\tan\left(45° - \frac{\varphi}{2}\right) = 10.2m, \tag{13}$$

where φ takes the mean value $\overline{\varphi}'$ of the effective internal friction angle of silty clay typically distributed in the soft-soil area, and the horizontal distance L_0 between L_0' and maximum surface settlement and retaining structure is the same. Therefore, L_0 replaces L_0' in the following.

To compare the relationship between Δ_P and the internal force distribution between the partition wall and retaining structure, the internal force distribution ratio of the two is defined as

$$\Delta_M = \frac{M_G}{M_D}, \tag{14}$$

where M_G and M_D are the maximum bending moments of the partition wall and retaining structure, respectively, which are calculated using the finite element method. Simultaneously, the orthogonal test L/L_0 values were substituted in (9) for calculation. To make the investigation and establishment of the relationship between Δ_P and Δ_M, this study uses semilogarithmic coordinates to fit
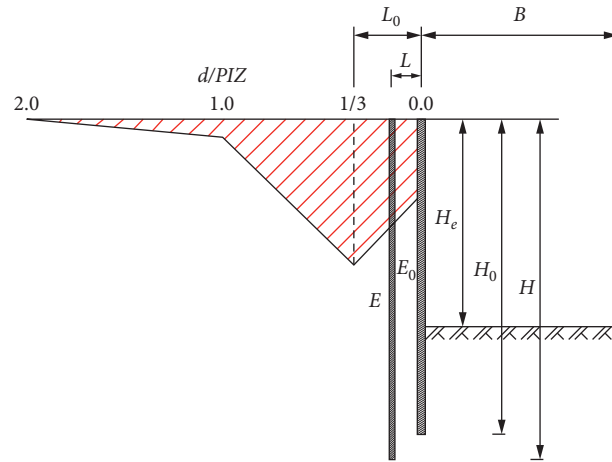
FIGURE 5: Schematic of the relationship between partition wall and foundation pit.

TABLE 6: Main factors and levels of the orthogonal test.

Factors		Test conditions			
		Condition 1	Condition 2	Condition 3	Condition 4
A	L/L_0	0.2	0.4	0.6	0.8
B	E/E_0	0.2	0.4	0.6	0.8
C	H/H_0	1	1.2	1.4	1.6

TABLE 7: Orthogonal test table.

Test number	L/L_0	E/E_0	H/H_0	Partition wall		Retaining structure		The Earth's surface
				Maximum bending moment (kN·m)	Maximum lateral (mm)	Maximum bending moment (10^3kN·m)	Maximum lateral (mm)	The largest settlement (mm)
1	0.2	0.2	1.6	260.12	14.31	1.21	12.82	9.91
2	0.4	0.2	1	219.43	15.71	1.21	15.71	12.15
3	0.6	0.2	1.4	141	10.61	1.23	12.78	7.74
4	0.8	0.2	1.2	83.26	8.3	1.34	14.38	15.59 (6.28)
5	0.2	0.4	1.4	423.5	13.53	1.15	12.46	9.62
6	0.4	0.4	1.2	335.15	12.94	1.14	12.69	9.78
7	0.6	0.4	1.6	215.67	9.64	1.22	12.28	6.94
8	0.8	0.4	1	133.05	8.69	1.34	14.98	16.34 (6.83)
9	0.2	0.6	1	563.08	16.18	1.12	15.3	12.75
10	0.4	0.6	1.6	424.08	11.26	1.11	11.35	8.25
11	0.6	0.6	1.2	279.01	10.19	1.21	12.86	7.74
12	0.8	0.6	1.4	157.4	7.39	1.34	13.93	15.3 (5.47)
13	0.2	0.8	1.2	655.39	13.15	1.06	12.52	9.81
14	0.4	0.8	1.4	499.5	11.12	1.09	11.39	8.29
15	0.6	0.8	1	333.2	10.9	1.20	13.53	8.61
16	0.8	0.8	1.6	181.34	6.99	1.34	13.74	15.18 (5.07)

TABLE 8: Average of the different levels for each factor.

| Level	Partition wall						Retaining structure						The Earth's surface		
	Maximum bending moment (kN·m)			Maximum lateral (mm)			Maximum bending moment (kN·m)			Maximum lateral (mm)			The largest settlement (mm)		
	$\overline{A}$	$\overline{B}$	$\overline{C}$	$\overline{A}$	$\overline{B}$	$\overline{C}$	$\overline{A}$	$\overline{B}$	$\overline{C}$	$\overline{A}$	$\overline{B}$	$\overline{C}$	$\overline{A}$	$\overline{B}$	$\overline{C}$
1	475.5	175.9	312.2	14.3	12.2	12.9	1140	1250	1220	13.3	13.9	14.9	10.5	9.0	10.1
2	369.5	276.8	338.2	13.0	11.2	11.2	1140	1210	1190	12.8	13.1	13.1	9.6	8.3	8.4
3	242.2	355.9	305.4	10.3	11.3	10.7	1220	1200	1200	12.9	13.3	12.6	7.8	8.6	7.8
4	138.8	417.4	270.3	7.8	10.5	10.6	1340	1170	1220	14.3	12.8	12.6	5.9	7.9	7.5
R	336.8	241.4	67.9	6.5	1.9	2.3	200	80	30	1.5	1.1	2.3	4.6	1.1	2.6
Factor to sort	1	2	3	1	3	2	1	2	3	2	3	1	1	3	2
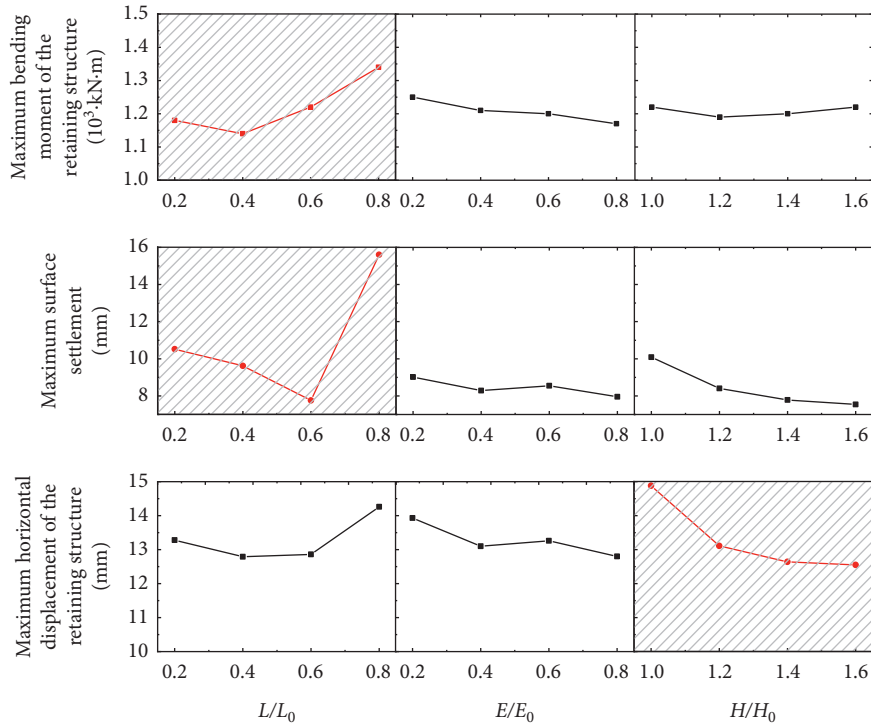
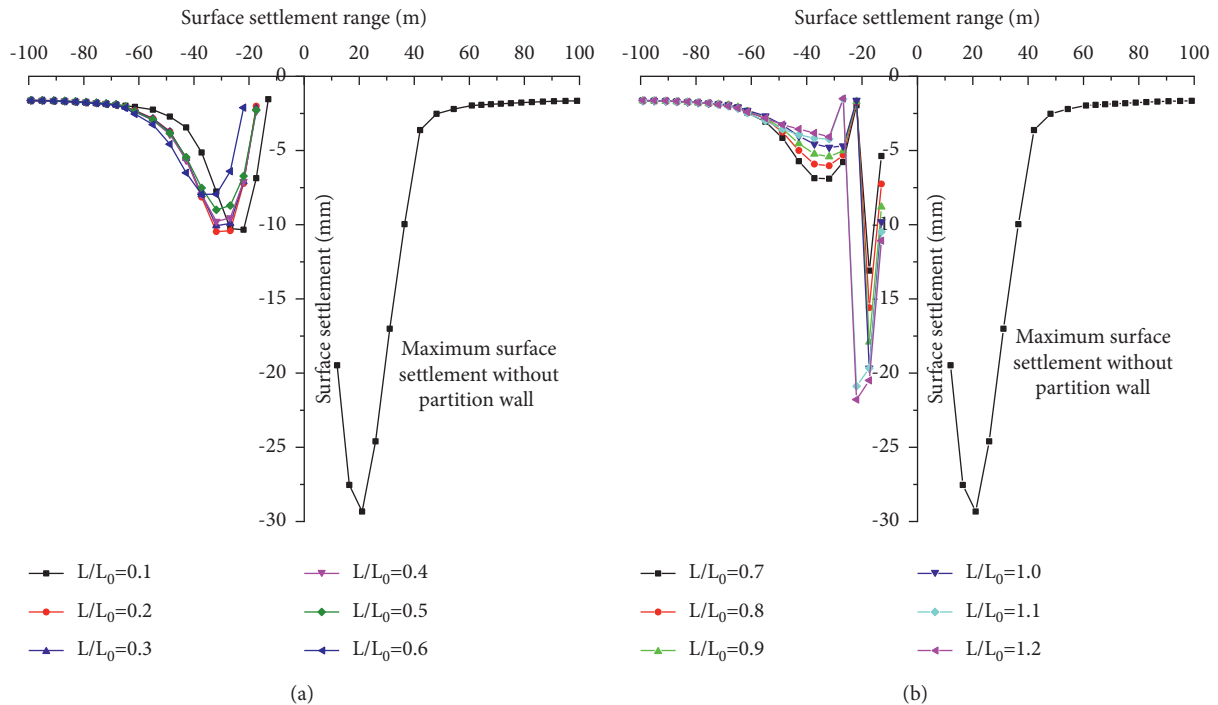FIGURE 6: Trends of the affection at different levels.

(a)

(b)

FIGURE 7: Affection of L/L_0 on the maximum ground settlement and the settlement form. (a) $L/L_0 \leq 0.6$. (b) $L/L_0 > 0.6$.

$\Delta_M - \ln(L/L_0)$ curve and $\Delta_P - \ln(L/L_0)$ curve, respectively (Figure 11).

By comparing the relationship between Δ_P and L/L_0 and between Δ_M and L/L_0, it is observed that the changing trend of the two curves is the same, i.e., the partition wall's Earth pressure gradually decreases with the increase of L/L_0, which

is consistent with the orthogonal test analysis result. Consequently, the Earth pressure distribution theory of double-row piles can also be used to determine the internal force distribution between the partition wall and the retaining structure, and the relationship between the two can be expressed as
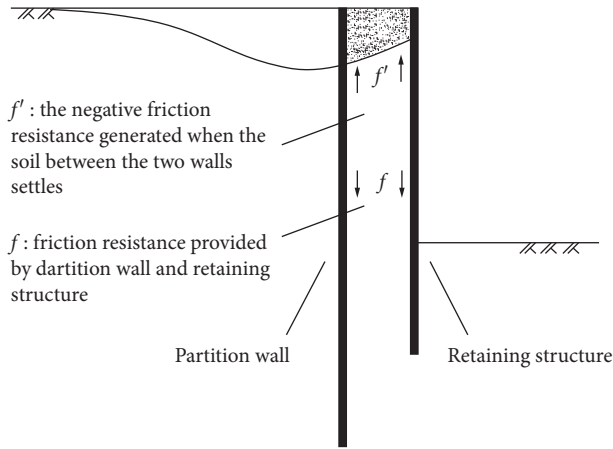
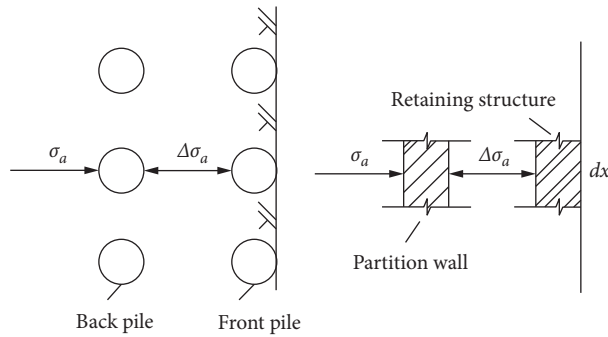FIGURE 8: Schematic of the force diagram for ground settlement.

f': the negative friction resistance generated when the soil between the two walls settles

f: friction resistance provided by dartition wall and retaining structure

Partition wall   Retaining structure

FIGURE 9: Schematic of the soil-stress comparison.
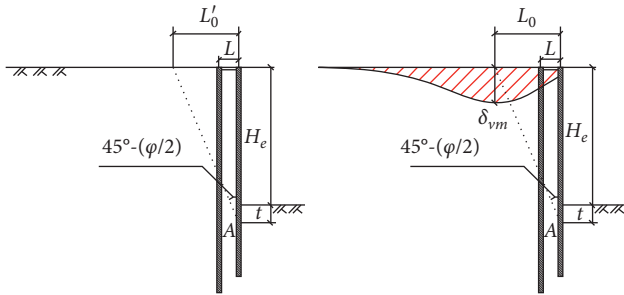
Back pile   Front pile

FIGURE 10: Schematic of the modified slip surface.

$$\Delta_M = \Delta_P + 0.05. \qquad (15)$$

Therefore, according to the actual engineering situation, the partition wall is set within the range conducive to the control of the retaining structure's internal force. Following the determination of the maximum internal force of the retaining structure during the design stage, (15) can be used to quantitatively analyze the influence of L/L_0 on the partition wall to share the retaining structure internal force, internal force control, and retaining structure deformation.

5.3. The Influence of H/H_0 on the Maximum Lateral Movement δhm of the Retaining Structure.
In addition to the partition wall's position ratio L/L_0, the ratio of the depth below the

$$\Delta_M = -0.2\ln(L/L_0) + 0.04$$

$$\Delta_P = -0.2\ln(L/L_0) - 0.01$$

$\ln(L/L_0)$

■ Ratio of earth pressure distribution
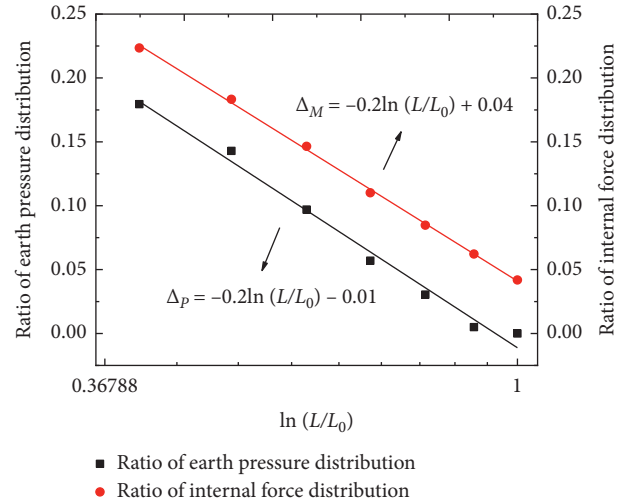● Ratio of internal force distribution

FIGURE 11: Relation curve of $\Delta_M - \ln(L/L_0)$ and $\Delta_P - \ln(L/L_0)$.

ground H/H_0 also has an obvious effect on controlling the retaining structure's maximum lateral movement. Based on the study of L/L_0, to analyze the specific influence of H/H_0 to δ_{hm}, we set $L/L_0 = 0.6$ (which is the optimal position), the H/H_0 value 0.5 ~ 2.0 for finite element analysis, normalizing the analysis results of δ_{hm}, and exponential function is used to describe the relationship between maximum lateral movement control and H/H_0, as shown in Figure 12.

When δ_{hm}^{con} is the lateral movement of the retaining structure when H/H_0 changes in the range of 0.5 ~ 2.0, and δ_{hm} is the maximum lateral movement of the retaining structure when no partition wall is set ($H = 0$),

$$\delta_{hm}^{con} = \delta_{hm}\left(3e^{-\left(3.6H/H_0\right)} + 0.5\right). \qquad (16)$$

It can be seen from the relationship curve between δ_{hm}^{con} and H/H_0 that, with the increase of partition wall penetration depth, the maximum lateral movement of the retaining structure can be reduced to ~50% of that without a partition wall. When $H/H_0 \leq 1.2$, the larger the value of H is, the more obvious the control effect on the maximum lateral movement of the retaining structure is. However, when $H/H_0 > 1.2$, the maximum lateral shift almost does not continue to decrease.

In summary, before constructing a partition wall, the maximum lateral displacement of the retaining structure should be predicted using hydrogeological conditions of the actual engineering, the type of foundation pit, and the overall stiffness of the supporting structure. Secondly, in the risk assessment stage of engineering, according to the requirements of the foundation pit itself and the surrounding environment, the control target of the retaining structure deformation is set. Finally, based on the determining L/L_0, the penetration depth of the partition wall is calculated according to (16).

5.4. Applicability Verification of Action Mechanism.
Based on the applicability of the constitutive model used in the finite element analysis, this study uses the prediction method of
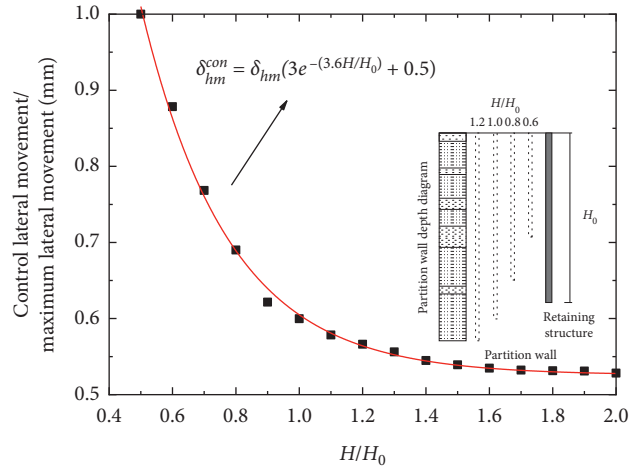
FIGURE 12: Relation curve between δ_{hm}^{con} and H/H0.

- The measured mean value in Tianjin area
- This paper standardizes the calculated values of the model
- Results of orthogonal test No. 11
- Predicted values of Kung et al. before controlling deformation
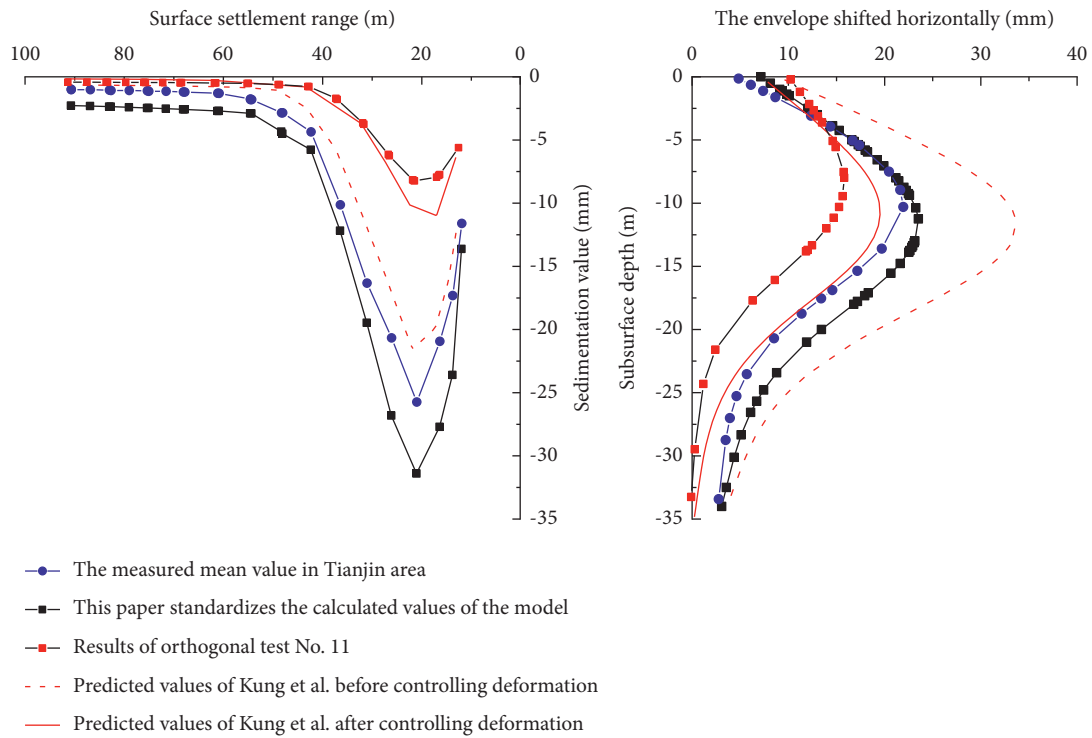- Predicted values of Kung et al. after controlling deformation

FIGURE 13: Result comparison among Kung et al.'s estimated and measured values and finite element calculation.

surface settlement outside the pit proposed by Kung et al. [20] using the reliability theory for soft soil and medium-hardness clay to verify the applicability of the partition wall controlling foundation pit deformation mentioned above in soft soil. The main steps for this are as follows.

Firstly, according to the main parameters of the standardized model of foundation pit in this paper, $\delta_{hm} = 34.74655$ mm, $R = 0.66557$, and $\delta_{vm} = 23.12637$ mm were calculated using the prediction method of Kung et al. before the control deformation. The predicted results were then compared to the average and maximum values of the

measured surface settlement and lateral displacement of the retaining structure in the Tianjin foundation pit, as well as the calculated value of the finite element in this paper, and Figure 13 depicts the outcome of this comparison. Kung et al. calculated Tianjin's soft-soil area. The predicted value δ_{hm} is larger and δ_{vm} is lower than the measured average value. However, both are within the variation range of the measured value statistics [14] in this area (20 mm $\leq \delta_{hm} \leq 40$ mm, 10 mm $\leq \delta_{vm} \leq 30$ mm).

Second, setting $L/L_0 = 0.6$ and $H/H_0 = 1.2$, we successively obtained the results determined by Kung et al. after

setting the partition wall. The predicted values of the method were $\delta_{hm}^{con} = 12.86$ mm and $\delta_{vm}^{con} = 7.74$ mm, and the predicted results were in good agreement with the calculated results of the No. 11 orthogonal test with the same parameter setting, as shown in Figure 13.

According to the results of the above analysis, the deformation prediction method proposed by Kung et al. can accurately predict the foundation pit deformation in Tianjin's soft-soil area. At the same time, the results of the analysis validate the study on the mechanism of the partition wall in soft-soil areas.

6. Conclusion

(1) The horizontal distance L between the partition wall and enclosure structure mainly affects the internal force of enclosure structure and surface settlement outside pit. When $L/L_0 < 0.6$, i.e., the partition wall is within the range of $d/PIZ < 0.2$, the frictional resistance f provided by the partition wall and the retaining structure is greater than the negative frictional resistance f' caused by the dead weight on the wall when the soil between the two is settled, and f is the maximum when $L/L_0 = 0.6$ ($d/PIZ > 0.2$), i.e., $f_{max} = f'$. At this point, the maximum surface settlement is inversely correlated with L/L_0. When $L/L_0 > 0.6$, the dead weight of soil between the two walls increases gradually with f'; i.e., f is less than f', and the maximum surface settlement is positively correlated with L/L_0. In this case, the control effect of the partition wall on deformation is relatively weakened.

(2) The Earth pressure distribution theory of "similar structure" double-row pile is introduced to analyze its action mechanism, and the distribution relationship of Earth pressure and internal force between the partition wall and retaining structure is obtained, so that its influence can be quantified based on the influence trend of L/L_0 on the maximum internal force of partition wall and retaining structure.

(3) In addition to the partition wall position ratio L/L_0, the ratio of the depth below the ground surface H/H_0 also has an obvious effect on controlling the maximum lateral movement of the retaining structure δ_{hm}. With the increase of partition wall penetration depth, the maximum lateral movement of the retaining structure can be reduced by ~50% of that without a partition wall. When $H/H_0 \leq 1.2$, the maximum lateral movement of the retaining structure can be controlled more clearly by increasing H. However, when $H/H_0 > 1.2$, the maximum lateral shift almost does not continue to decrease.

(4) Based on the abovementioned findings, the applicability of the partition wall mechanism controlling foundation pit deformation in soft soil was confirmed by implementing the prediction method of foundation pit deformation proposed by Kung et al.

Abbreviation

L: Length of the foundation pit's retaining structure
B: Width of the foundation pit's retaining structure
H_e: Excavation depth of the foundation pit's retaining structure
H: Depth of the foundation pit's retaining structure
t: Partition wall thickness
E: Stiffness of the partition wall
L_0: Horizontal distances between the maximum surface settlement and the same side retaining structure
E_0: Stiffness parameters of the retaining structure
H_0: Depth of the soil
p_{aG}: Active Earth pressure acting on partition wall
p_{aD}: Active Earth pressure acting on retaining structure
L_0': Horizontal distance between the intersection of the active slip surface and the pit surface and the retaining structure
M_G: Maximum bending moments of the partition wall
M_D: Maximum bending moments of the retaining structure
δ_{hm}: Horizontal displacement of the containment structure
δ_{vm}: Surface subsidence
δ_{hm}^{con}: Lateral movement of the retaining structure
γ: Weight of the soil
c': Effective cohesion of the soil
φ': Effective internal friction angle of the soil
$E_{S,1\sim2}$: Compression modulus of the soil
E_{50}^{ref}: Secant stiffness in standard drained triaxial test
$E_{oe\_d}^{ref}$: Tangent stiffness for primary oedometer loading
E_{ur}^{ref}: Unloading/reloading stiffness at engineering stains
G_0: Reference shear modulus at very small strains
$\gamma_{0.7}$: Shear strain at which $G_s = 0.722G_0$.

Data Availability

The measured data used to support the findings of this study are included within the article.

Conflicts of Interest

The authors declare that they have no conflicts of interest.

Acknowledgments

References

[1] G. Liu and W. Wang, *Handbook for Foundation Pit Engineering*, China Architecture And Building Press, Beijing, China, 2009.

[2] Y. Xiang, S. He, M. Zhang, Z. Cui, and S. Ma, "Constraint effect of pilot-drift and separation-pile structure on ground movements induced by shallow tunneling," *Chinese Journal of Rock Mechanics and Engineering*, vol. 23, no. 19, pp. 3317–3323, 2004.

[3] H. Yao, M. Wang, D. Zhang, and C. Hao, "Mechanism of a drift-pile system and analysis of its horizontal displacement," *China Civil Engineering Journal*, vol. 39, no. 4, pp. 105–109, 2006.

[4] W. Fei, "Application of isolation piles to deformation control of deep foundation pits close to buildings with shallow foundation," *Chinese Journal of Geotechnical Engineering*, vol. 32, no. S1, pp. 265–270, 2010.

[5] J. Zhai, J. Jia, and X. Xie, "Practice of partition wall in the building protection projects near deep excavation," *Chinese Journal of Underground Space and Engineering*, vol. 6, no. 1, pp. 162–166, 2010.

[6] H. Ying, T. Li, Y. Yang, and X. Xie, "Effect and application of partition walls in protecting adjacent buildings from deep foundation pits," *Chinese Journal of Geotechnical Engineering*, vol. 33, no. 7, pp. 1123–1129, 2011.

[7] H. Ying, T. Li, and W. Wang, "Optimization design of partition wall in deep excavations based on 3-D numerical simulation," *Rock and Soil Mechanics*, vol. 33, no. 1, pp. 220–226, 2012.

[8] E. Bilotta and G. Russo, "Use of a line of piles to prevent damages induced by tunnel excavation," *Journal of Geotechnical and Geoenvironmental Engineering*, vol. 137, no. 3, pp. 254–262, 2011.

[9] A. D. Mariano, J. M. Gesto, A. Gens, and H. Schwarz, "Ground deformation and mitigating measures associated with the excavation of a new metro line," *Geotechnical Engineering in Urban Environments*, pp. 1901–1906, Millpress Science, Rotterdam, Netherlands, 2007.

[10] J. Han, D. Liu, Y. Guan et al., "Study on shear behavior and damage constitutive model of tendon-grout interface," *Construction and Building Materials*, vol. 320, Article ID 126223, 2022.

[11] X. Ji, W. Zhao, S. Li, and Z. Zhou, "Application of isolation piles on metro tunnel for side-crossing the buildings with shallow foundation," *Journal of Northeastern University*, vol. 34, no. 1, pp. 135–139, 2013.

[12] J. Yan, *The influence of pile foundation in life-cycle on adjacent existing tunnel*, Ph.D Thesis, Shanghai Tong-ji University, Shanghai, China, 2007.

[13] G. Zheng, Y. Du, and Y. Diao, "Optimization analysis of efficiency of isolation piles in controlling the deformation of existing tunnels adjacent to deep excavation," *Chinese Journal of Rock Mechanics and Engineering*, vol. 34, no. S1, pp. 3499–3509, 2015.

[14] M. Ge, *Study on Deformation Law and Influencing Factors of Foundation Fit Excavation in Soft Soil Area of Tianjin*, Beijing Jiaotong University, Beijing, China, 2016.

[15] G. Zheng and Y. Jiao, *Deep Foundation Pit Engineering Design Theory and Engineering Application*, China Architecture and Building Press, Beijing, China, 2010.

[16] J. B. Burland, ""Small is beautiful"-the stiffness of soils at small strains," *Ninth Laurits Bjerrum Memorial Lecture, Canadian Geotechnical Journal*, vol. 26, no. 4, 1989.

[17] T. Benz, *Small strain stiffness of soils and its numerical consequences*, Institute of Geotechnical Engineering, University of Stuttgart, Stuttgart, Germany, [Ph.D], 2007.

[18] Z. Ou, *Analysis and Design Theory and Practice of Deep Excavation Engineering*, Science and technology books co. LTD, Taipei, Taiwan, 2002.

[19] G. T. Kung, C. H. Juang, E. C. Hsiao, and Y. M. Hashash, "Simplified model for wall deflection and ground-surface settlement caused by braced excavation in clays," *Journal of Geotechnical and Geoenvironmental Engineering*, vol. 133, no. 6, pp. 731–747, 2007.

[20] Kunming University of Science and Technology, *Theoretical Analysis and Numericial Calculation of Retaining Structure with Double-Row Piles*, Kunming University of Science and Technology, Kunming, China, 2013.